AN EXPERIMENTAL CHARACTERIZATION OF 3-D TRANSITIONAL SHOCK WAVE BOUNDARY LAYER INTERACTIONS AT MACH 6

A Dissertation

by

ANDREW NORBERT LEIDY

Submitted to the Office of Graduate and Professional Studies of
Texas A&M University
in partial fulfillment of the requirements for the degree of

DOCTOR OF PHILOSOPHY

Chair of Committee,	Rodney D.W. Bowersox
Committee Members,	Diego A. Donzis
	Simon W. North
	Edward B. White
Head of Department,	Rodney D.W. Bowersox

May 2019

Major Subject: Aerospace Engineering

ABSTRACT

Hypersonics is of current national interest, but improved understanding of fundamental flow physics is required for safe and efficient vehicle design. The objective of the present study was to expand the knowledgebase of shock wave boundary layer interaction flows during transition at a high Mach number since these interactions are likely to occur on hypersonic aircraft. The approach was to experimentally determine how the dynamics of the shock structure, the fluctuations within it, and the resulting thermal and acoustic loads, change as the flow evolves through its transitional regime. Tests were conducted on a canonical cylinder-induced 3-D shock wave boundary layer interaction geometry at Mach 5.8 in the Actively Controlled Expansion hypersonic wind tunnel. The model was tested in different configurations to isolate the effects of the boundary layer trips and the shock generator. The interaction excited a 40 kHz (possibly second mode) instability, causing transition just downstream of the separation shock. A transitional boundary layer was only achieved on the baseline model with trips at Re=7M/m, which demonstrated that a transitional incoming boundary layer is not required to produce a transition interaction. Time-resolved schlieren imaging revealed disturbances emerging from the supersonic jet and ascending the cylinder with a characteristic frequency near 20 kHz. The separation shock motion frequency was O(*1 kHz*) and was fed by disturbances originating near the base of the cylinder. The film coefficient was found to be the heat transfer parameter of interest since it scaled roughly linearly with Reynolds number. It revealed fundamental differences in heating at the reattachment arc for configurations with and without trips and indicated higher heating in that region for a laminar SBLI. Cylinder sweep had an impact on fluctuation levels and thermal loads. Sweeping the cylinder back 15

degrees significantly reduced the extent of the interaction and dropped the RMS pressure fluctuations and heating loads at the base of the cylinder by roughly 50%. Alternatively, sweeping the cylinder forward 15 degrees led to fluctuations on the order of the freestream static pressure and the highest heating levels observed for this campaign.

DEDICATION

For my friends and family who supported me throughout this long campaign

ACKNOWLEDGMENTS

There are many people to thank for the completion of this work. Thank you to my advisor, Dr. Rodney D.W. Bowersox, for taking me on as an undergraduate and sticking with me throughout my studies. Thank you for providing me the opportunity to take on two exciting and relevant projects, and for building such an eclectic lab, which has given me exposure to multiple disciplines relevant to wind tunnel testing and hypersonics. The time spent working in your lab has provided me confidence toward my future endeavors.

Thank you to my committee members, Drs. Diego A. Donzis, Simon W. North, and Edward B. White. Thank you for your suggestions and encouragement. I am proud to have you all on my committee because you are not only great researchers, but outstanding teachers as well.

Thank you to all of the members of the NAL, past and present. Seeing the work, brilliance, and accomplishments of Michael Semper, Chi Mai, Jerrod Hofferth, Alex Craig, and Nicole Sharp, set the bar high. Thank you to Ian Neel, with whom I worked closely throughout our time as graduate students. Thank you for your help over and over again, your friendship, and working so hard to make this lab a better place. Thank you to Ian, Heather Kostak, and Farhan Siddiqui for helping me complete an ambitious run matrix, running the tunnel at all hours, day and night. Thank you to Nathan Tichenor, Cecil Rhodes, Evan Marcotte, Chris Russo, Brianne McManamen, Rodrigo Sanchez-Gonzalez, Nick Gawloski, Shanae Smith, Silverio Canchola, Casey Broslawski. I have great memories of working with you all. Thank you to Rebecca Marianno and Colleen Leatherman for all of your efforts outside of the lab to keep it running smoothly.

Thank you to William Seward and Zahir Udovicic for machining my models and many other parts for me and other students at the lab. We appreciate the effort and extra hours you both

put in to get our campaigns started on time. Thank you to the students and staff at the Oran W. Nicks Low Speed Wind Tunnel for your help through the years and for keeping us in the loop about tours and the arrival of cool airplanes.

Thank you to Helen Reed and members of the Computational Stability and Transition Laboratory, especially Travis Kocian, Alex Moyes, and Daniel Mullen. Our group meetings provided me much insight to the work of computationalists and the information experimentalists should provide them.

Thank you to Catherine McGinley and Luther Jenkins for choosing me to be a part of the Flow Physics and Control Branch at LaRC. Thank you to Amanda Chou and Rudy King for mentoring me during my two stints as an intern with the branch. I am thankful for how much you taught me in only a few months.

Thank you to those who helped form my character. Having a supportive family has been tremendous. Thank you to my dad, Joe, who taught me that the easiest way is seldom the best way. Thank you to my mom, Sandra, who taught me to always expect the best out of myself. Thank you to Robert, my younger brother, for showing me what it's like to start a career and not letting me forget that he's made it.

Thank you to my Hopewell middle school coaches, especially Karl Murphy, who taught me how to train and the importance of consistency and developing good habits. Your tough practices helped me power through some late nights.

Thank you to my Round Rock high school math and science teachers, Robert Cole, Bradford Freeman, and Joan Gambrell. Thank you for preparing me so well for college. Freshman year was a breeze.

Thank you to the top of the AERO class of ‘12, especially Sai Patel, Ben Wilcox, Travis Kocian, and Robert Long. You all pushed me to do my best, helped me through homework assignments (notably AERO structures), and prepared with me for exams. It was great working with you all.

Thank you to now Bishop David Konderla and Fr. Brian McMaster for the culture you fostered at St. Mary’s. Thank you for supporting programs like Aggie Awakening and The Rock. Thank you to Jonathan Hollkamp, Kristin O’Brien, Katelin (Diguette) Jara, Huy Phan, Marcin Jurek, Daniel Steck, and Anne Voltin, for your friendship and encouraging words when I needed them the most. Thank you to Helen (Bain) Farrar. Without you I would have never pursued a Ph.D.

Above all, I offer this work up to my Lord and Savior Jesus Christ, who gives me confidence that everything will work out.

CONTRIBUTORS AND FUNDING SOURCES

Contributors

This work was supervised by a dissertation committee consisting of Professor R.D.W. Bowersox (advisor) and Professors D.A. Donzis and E.B. White of the Department of Aerospace Engineering and Professor S.W. North of the Department of Chemistry.

Funding Sources

Graduate study was supported by a graduate research assistantship from Texas A&M University. This work was funded by the U.S. Office of Naval Research and OUSD(R&E)/Basic Research Office under award numbers N00014-15-1-2269 and N00014-18-1-3020, respectively. The views and conclusions contained herein are those of the author and should not be interpreted as necessarily representing the official policies or endorsements, either expressed or implied, of the ONR or the United States government.

NOMENCLATURE

Letters

A	Area, Hot-wire Calibration Constant
B	Hot-wire Calibration Constant
D	Dimensional
E	Uncertainty
H	Cylinder Height
IR	Infrared
L	Length
M	Mach Number
M/m	Million per Meter
O( )	Order
Re	Reynolds Number
S	Separation Length
Sr	Strouhal Number
St	Stanton Number
T	Temperature
U, u	Relevant Velocity Component or Velocity Magnitude
V	Voltage
X	Streamwise Coordinate
Y	Tunnel-based Vertical Coordinate
c_p	Specific Heat

d	Cylinder Diameter
f	Frequency
h	Height of Trips or Film Coefficient
k	Thermal Conductivity
n	Number of Shock Crossings or Hot-wire Calibration Constant
p	Pressure
q	Heat Flux
t	Time
w	Spacing of the Trips
x	Streamwise Coordinate from Leading Edge
x’	Streamwise Coordinate from Front of Cylinder
y	Distance Above Model
z	Spanwise Coordinate from Model Centerspan
α	Thermal Diffusivity
β	Local Shock Angle
γ	Intermittency or Specific Heat Ratio
δ	Boundary Layer Thickness
ε	Emissivity Coefficient
ζ	Distance into Model
θ	Cylinder Angular Coordinate
μ	Dynamic Viscosity
ρ	Density

Subscripts

B	Bridge
c	Crossing
e	Boundary Layer Edge
i	Intermittent
n	Normal to Surface
sep	Separation
t	Total or Throat
trip	Relating to the Trips
w	Wall
x	Related to the Coordinate x
0	Total
1	Upstream of the Shock
2	Downstream of the Shock
∞	Freestream

Acronyms and Abbreviations

AC	Alternating Current
ACE	Actively Controlled Expansion
AEDC	Arnold Engineering Development Complex
AFOSR	Air Force Office of Scientific Research
AHW	Army Advanced Hypersonic Weapon
ALTP	Atomic Layer Thermopile

BAM6QT	Boeing/AFOSR Mach 6 Quiet Tunnel
BL	Boundary Layer
CEV	Crew Exploration Vehicle
CFD	Computational Fluid Dynamics
CTA	Constant Temperature Anemometry
DAQ	Data Acquisition
DARPA	Defense Advanced Research Projects Agency
DC	Direct Current
DNS	Direct Numerical Simulation
fps	Frames-per-second
FSO	Full Scale Output
HEG	High Enthalpy Shock Tunnel Göttingen
HIFiRE	Hypersonic International Flight Research Experimentation Program
LabVIEW	Laboratory Virtual Instrument Engineering Workbench
LaRC	NASA Langley Research Center
LE	Leading Edge
LED	Light-emitting Diode
LES	Large Eddy Simulation
M6QT	NASA Langley Mach 6 Quiet Tunnel
MATLAB	Matrix Laboratory
NACA	National Advisory Committee for Aeronautics
NAL	National Aerothermochemistry and Hypersonics Laboratory

NASA	National Aeronautics and Space Administration
NI	National Instruments
NO	Nitric Oxide
ONR	U.S. Office of Naval Research
PDF	Probability Density Function
PEEK	Polyether Ether Ketone
PIV	Particle Image Velocimetry
PLIF	Planar Laser Induced Fluorescence
PLS	Planar Laser Scattering
PSD	Power Spectral Density
PSP	Pressure Sensitive Paint
RANS	Reynolds-Averaged Navier-Stokes
RMS < >	Root Mean Square
SBLI(s)	Shock Wave / Boundary Layer Interaction(s)
SRA	Strong Reynolds Analogy
TSP	Temperature Sensitive Paint
UI	Upstream Influence
XSBLI(s)	Transitional Shock Wave / Boundary Layer Interaction(s)

TABLE OF CONTENTS

Page

LIST OF FIGURES

Page

LIST OF TABLES

Page

1. INTRODUCTION

1.1 Motivation

1.1.1 The Nature of Hypersonic Flight

Hypersonics is characterized by several distinct features that separate it from other flow regimes. Hypersonic flow over a body results in thin shock layers, thick entropy layers, viscous interactions between shock waves and boundary layers, low density effects, and high temperature effects where real gas calculations, nonequilibrium ramifications, and chemical reactions become important [1]. The physical manifestation of these phenomena on a vehicle is shown in Figure 1.

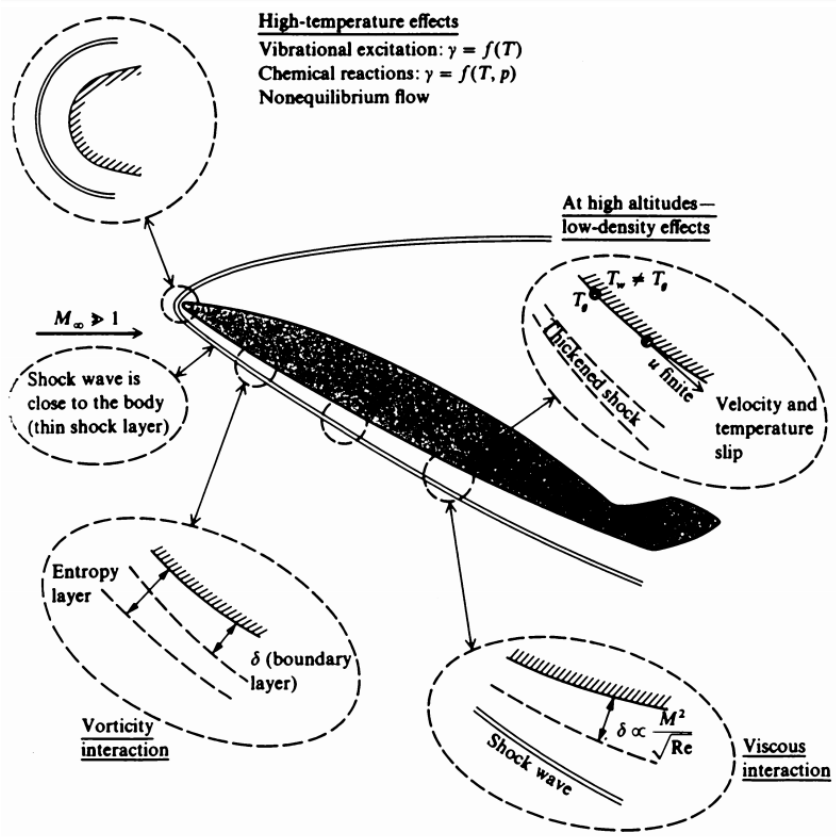

Figure 1. A hypersonic vehicle and its associated flowfield (reprinted from [1])

Sometimes, hypersonics can allow for simplifications [1]. The Mach number independence principle asserts that certain aerodynamic quantities such as pressure coefficients, lift, wave-drag, and flowfield structures – like shock wave shapes and Mach wave patterns – become independent of Mach number. The shock relations can reach a hypersonic limit, and Newtonian impact theory can predict the pressure distribution on a surface based solely on incident flow angle. While these simplifications make the calculations much easier, the cost is accuracy. Some of the greatest challenges holding back progress in the development of hypersonic flight vehicles fall within uncertainties in the fundamental aerodynamics.

An order-one issue in hypersonics is kinetic thermal loading. Its importance cannot be overstated as it dictates the configuration design of most hypersonic vehicles. Overprediction of the heat flux will lead to an unnecessarily bulky and inefficient design which will add cost to the mission. Underprediction in any region on a vehicle could have catastrophic consequences [2]. The regions of highest heat transfer occur at or near areas of the body where the flow stagnates. Where stagnation occurs, the kinetic energy from the flow is converted into heat, some of which is convectively transferred into the body.

There are a few regions on a vehicle where the flow will stagnate. Most apparent are the upstream surfaces that see the flow first, like the nose or leading edges of wings or fins. Significant steps or cavities, which may be present due to fabrication tolerances or sensor installations, can lead to recirculating, stagnating flow [3]. A third and perhaps less intuitive region of separated and stagnated flow can be caused by shock wave boundary layer interactions (SBLIs). While the sites of stagnation point heating on upstream surfaces are obvious, the exact location, spatial extent, and magnitude of heat transfer – which can be several times higher than upstream stagnation heat transfer rates – for an SBLI are not always well known [4].

1.1.2 The Prevalence of Viscous Interactions

Interactions between a shock wave and a viscous boundary layer represent complex flow phenomena that are associated with a wide range of features, including transonic airfoils, high-speed inlets and control surfaces, wing-fuselage junctions, missile base flows, reaction control jets, and over-expanded nozzles [5]. Some of these flows and interactions are diagrammed in Figure 2. Essentially, an SBLI will occur wherever the vehicle shape deviates from a simple, smooth surface.

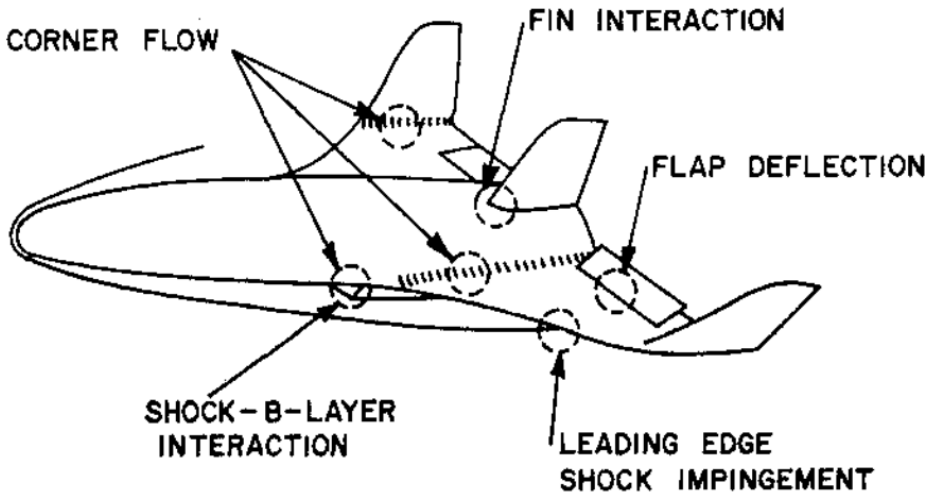

Figure 2. Regions of strong viscous interaction on a high Mach number vehicle (reprinted from [4])

Aside from the extreme thermal loads found at flow reattachment, unsteady pressure waves can also precipitate deleterious effects, including aircraft buffeting, inlet instability, and aerostructure fatigue when the low-frequency, high-amplitude (up to 185 dB or more) pressure oscillations couple to panel resonant frequencies [6]. For example, the associated wall pressure fluctuations have significant energy content between 10 and 1000 Hz [5], the range of typical resonant frequencies of flat panels on high Mach number aircraft [7]. Pozefsky et al. indicate that such loading

for a generic air-breathing trans-atmospheric vehicle, combined with high heating, poses a severe threat to local structural integrity [8]. Accurate predictions of fluctuating loads are vital to structural and materials engineers who must account for these phenomena in designing aerospace structures with adequate fatigue life, particularly for high Mach number vehicles.

The topic of SBLIs has been studied extensively in the time since the first manned supersonic flight. One of the earliest reviews by Green identified four important areas where SBLIs will occur: transonic airfoils, high-speed inlets, nozzles at off-design conditions, and near control flaps [9]. Many other reviews on SBLIs exist. In the decades that followed, there were several that provided chronological snapshots of the state-of-the art at the time with extended discussions of the physics as well as experimental and numerical techniques [10-16]. Dolling [6] and Smits and Dussauge [14] reviewed work in supersonic SBLIs through the early to mid-1990s, including discussions of the unsteady flowfields and some early thoughts on driving mechanisms. In 2001, Dolling reviewed the topic, and presented the experimental and computational capabilities after 50 years of research as well as areas that should be of focus moving forward [17]. Points of emphasis included the need for more closely tied experimental and computational campaigns and the need for experimental work on interactions involving transitional boundary layers to potentially shed light on how the transitional boundary layer state affects the interaction properties. He also anticipated further study could provide insight into the peak heating and unsteady characteristics of turbulent flows. Clemens and Narayanaswamy [5] recently reviewed the topic with a focus on the origin of the low-frequency unsteadiness within the interaction. Knight reviewed experimental and computational efforts for interactions involving hypersonic transitional boundary layers dating back to the 1990s [18].

As previously alluded, SBLIs can arise from a number of geometric configurations. One example flow structure is a shock wave cast off by an upstream object impinging on an established boundary layer. The structure is described by Green [9] and diagrammed as Figure 3.

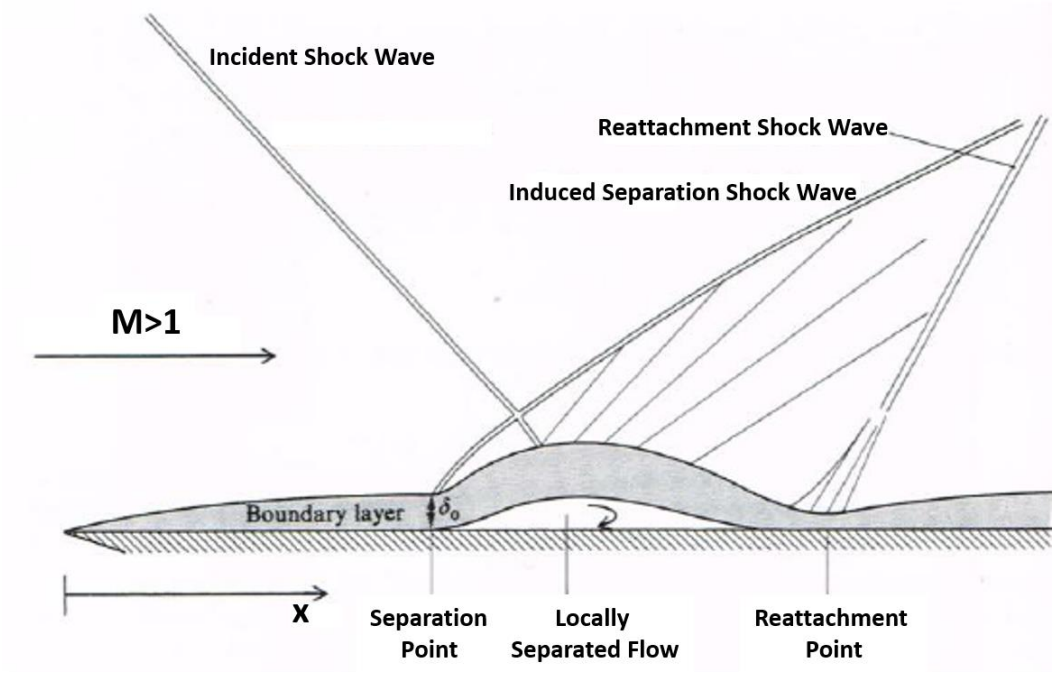

Figure 3. Schematic of an impinging shock wave / boundary layer interaction (modified from [1])

The incoming shock causes an adverse pressure gradient which may or may not be strong enough to separate the flow. If flow separation occurs, there will be a circulation bubble, and the surface may be subjected to temperatures on the order of the total conditions. Heat transfer will be even more extreme at reattachment. This is the type of interaction that infamously occurred on an X-15 test flight in 1968 when a shock cast from the dummy ramjet met and burned through the pylon that was securing it to the fuselage. The aftermath is given by Neumann [19] in Figure 4. The black bars (across the bottom of the pylon and on the left side of its root) indicate the burned interaction regions.

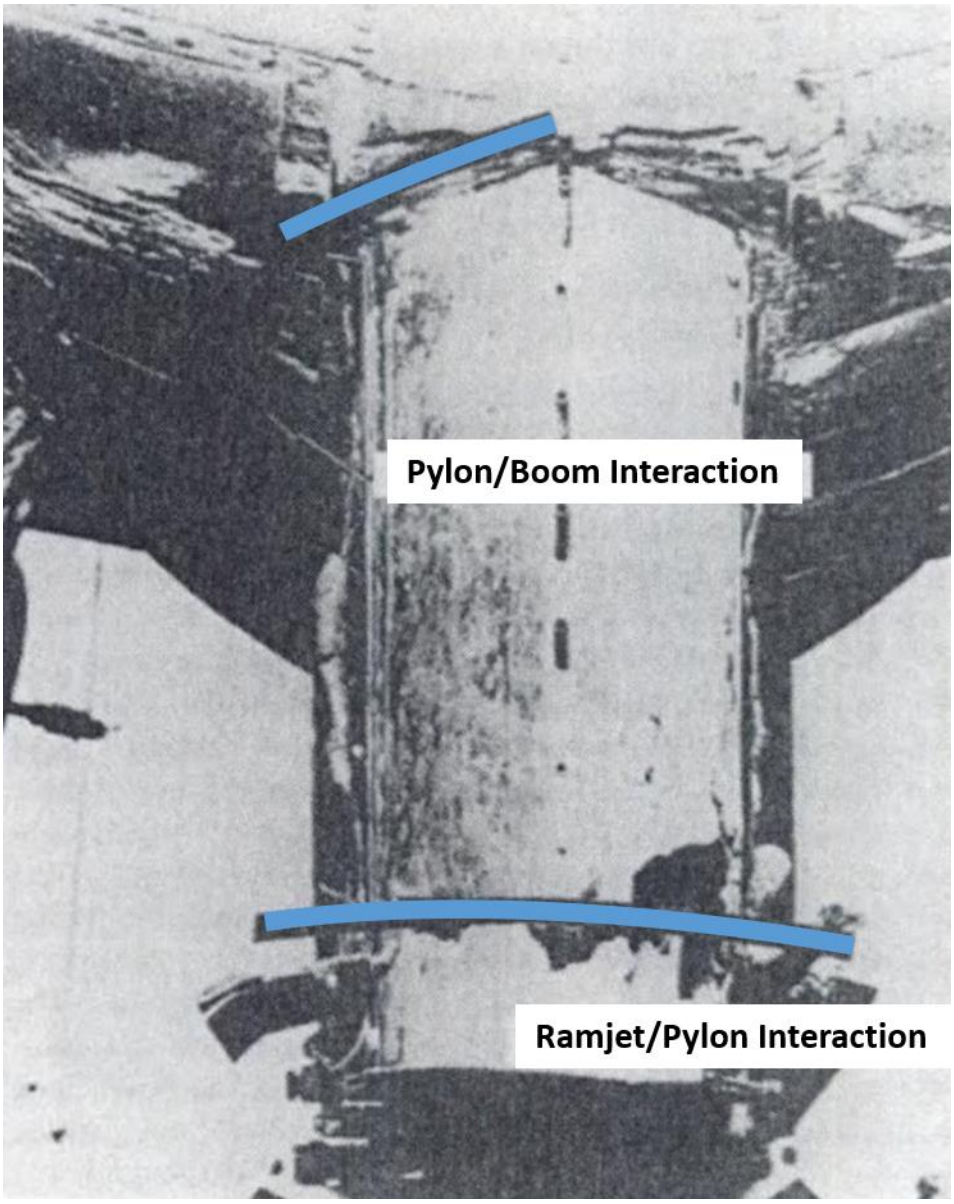

Figure 4. Damage to the X-15 from shock wave impingement (modified from [19])

A second SBLI configuration is geometry-based and manifests as a shock offset from some downstream feature interacting with the boundary layer. Control surfaces, fins, corners, and junctions can all trigger this type of interaction. In this case, the region of flow separation is upstream

of the body that triggers the shock. The 2-D version of this interaction caused by a compression ramp is sketched in Figure 5. Note that the adverse pressure gradient from the corner is strong enough to cause the flow to separate. The compression waves at the separation point coalesce into a separation shock wave. Another shock reattaches the flow downstream of the corner. The research presented in this dissertation will focus on a 3-D version of this geometry-based interaction.

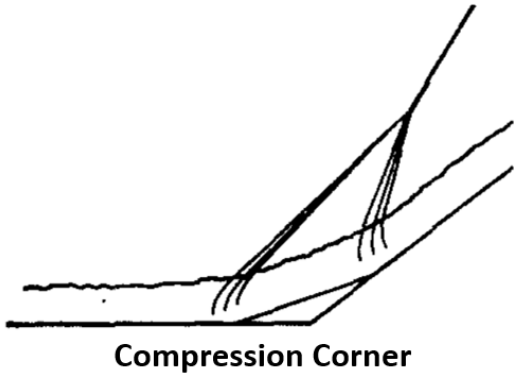

Figure 5. A two-dimensional separated SBLI structure (modified from [9])

The spatial extent and the dynamics within the separated region depend on the state of the incoming boundary layer, and being able to predict the state of the boundary layer on a hypersonic vehicle is a significant aerodynamic challenge in its own right [20]. The region of separated flow will be largest for an incoming laminar boundary layer. As a boundary layer transitions, streamwise momentum is drawn closer to the wall and works to resist flow separation. Therefore, the region of separation will be at a minimum for a fully turbulent boundary layer, and the spatial extent of a transitional SBLI will fall somewhere in between.

This experimental effort is part of a recent push to better understand SBLIs that occur in instances where the incoming boundary layer is transitioning from laminar to turbulent flow. Until

recently, very few studies have been conducted on such interactions, with the bulk of the experimental effort going into understanding the fundamental behavior of interactions within a fully developed turbulent boundary layer [21]. This has been argued to be the most probable type of interaction to occur on actual aerospace vehicles [4]. Conversely, computational resources have been diverted into the study of laminar SBLIs since they are fully resolvable, aside from cases with considerable flow nonequilibrium [22]. Unfortunately, laminar SBLIs rarely occur on actual vehicles, so our understanding of them means little in practice.

Much less research has been conducted on transitional SBLIs. Currently it is not possible to fully resolve a transitional or turbulent SBLI using a direct numerical simulation (DNS) due to the complexity of the interaction and the large range of scales. In fact, most hypersonic simulations are done using either a RANS or LES approach. Unfortunately, turbulence models are lacking for both of these methods. A cause for concern is that the transition location often must be specified, which is undesirable as the transition location must either be determined empirically or tuned in order to give the best results on a case by case basis [23]. Transition also cannot evolve naturally using these models.

Even more motivating into the study of transitional SBLIs is the recent emphasis on the development of unpowered boost-glide systems such as the DARPA/AF Falcon HTV-2 and the Army Advanced Hypersonic Weapon (AHW) [24], which have led to the significant interest in the design of vehicles with substantial runs of laminar flow for aerodynamic efficiency. On these vehicles, boundary layer transition will occur farther aft where SBLIs are more prevalent. In addition, a recent campaign in the Purdue Boeing/AFOSR Mach 6 Quiet Flow Ludwieg Tube examined the effectiveness of boundary layer trips on the initial compression surface of a representative X-51

forebody using temperature sensitive paint to characterize the increase in surface heating that results from the onset of turbulent flow [25]. The tunnel was run under noisy (nozzle bleed slots closed) and quiet (bleed slots open) conditions. Under noisy conditions, conditions in which the freestream disturbance levels are similar to those in a conventional wind tunnel, the inlet trips were seen to be effective in transitioning the flow almost immediately. In contrast, when the tunnel was run in quiet mode, where the freestream disturbance levels are similar to flight-like conditions, the trips were shown to be less effective and transition was delayed. This study shows that many hypersonic inlets are potentially closer to the margin between transitional and turbulent flow than previously thought.

1.2 Research Objectives, Approach, and Contributions

1.2.1 Research Objective and Approach

The overarching research objective of the present study is to expand the basic understanding of shock wave boundary layer interaction flows during transition at a high Mach number.

The approach to accomplish the research objective was to experimentally document the flow structure in a canonical shock wave boundary layer interaction flow as the interaction state was varied from fully laminar to fully turbulent. The primary test configuration is shown in Figure 6, where the shock generator is a cylinder normal to a flat surface. A parametric study on cylinder sweep angle was also performed as part of the study. With high levels of computuational uncertainty for key quantites in transitional SBLIs, including separation distance and thermal and pressure loads, there is a need for high-quality, archival data for validating computational efforts and for future comparisons with DNS simulations. The Actively Controlled Expansion hypersonic

wind tunnel, housed within the Texas A&M University National Aerothermochemistry and Hypersonics Laboratory, was employed for this measurement campaign. This facility is well suited for this problem due to the available broad Mach (5- 8) and Reynolds number (Re/m ~ $2x10^5$ – $1x10^7$) ranges, and a freestream environment that has received considerable characterization [26,27]. A combination of boundary layer tripping and Reynolds number regulation allowed for the interaction to be swept from fully laminar through transition to fully turbulent [28].

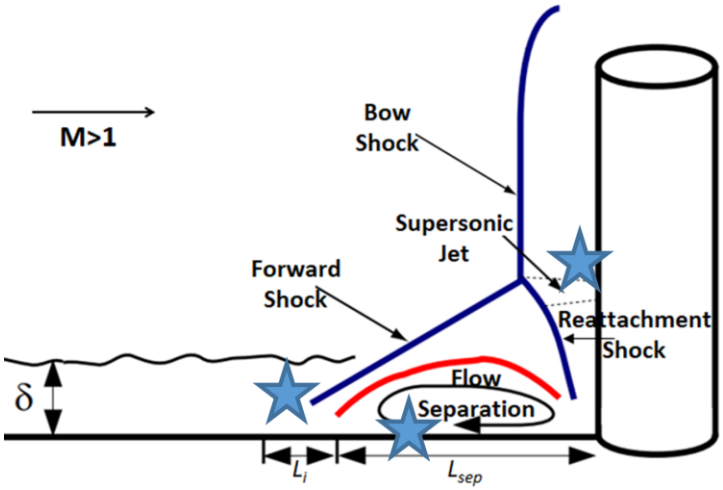

Figure 6. Unsteady features amenable to dynamical study

The principal question addressed in this study was: How do the dynamics of shock structure, especially the motion of the separation shock foot, triple point, shock-induced supersonic jet, and fluctuations within the separated region, change as the interaction evolves through transition?

A multitude of analyses methods were employed. First, high-speed schlieren flow visualization was used to monitor the motion of the shock structure. Second, high-frequency response pressure transducers were used to monitor the surface pressure spectral response within the interaction as the interaction is swept from fully laminar through transition to fully turbulent. Third,

infrared thermography provided the surface temperature of the model and the shock generator for all flow conditions. Fourth, to enhance the usefulness of the study for simulation and model assessment, the freestream was characterized using a high-frequency response pitot (Kulite) and a hot-wire probe. Fifth, the model geometry and roughness were documented using laser profilometry. With these instruments, profile and surface data were acquired at different streamwise and spanwise positions to characterize the state of the tripped boundary layer.

1.2.2 Expected Contributions and Impact

The primary contributions to the field from this study are the database and the subsequent analyses that extend the current state of knowledge on transitional SBLIs. The impact has the potential to be substantial as the data fill a clear void in the knowledgebase, where these measurements on a comparable geometry for any interaction state at a freestream above Mach 5 are unavailable. Additional scientific contributions include the first use of focused schlieren to examine specific planes within a 3-D SBLI, and the use of a swept cylinder to provide insight directly translatable to the advantages of geometric sweep on hypersonic vehicles.

2. LITERATURE REVIEW

This chapter first describes the SBLI being investigated – the flow structure resulting from the interaction of a right-cylinder mounted upright on a flat plate. This simplified geometry is analogous to a blunted fin on a vehicle body or a wing-fuselage junction and allows for effective study of the structure of a 3-D SBLI. It is important to note that the upstream features and scaling of the interactions between a cylinder or a hemicylindrically-blunted fin and the flat plate on which it is affixed are nearly identical [29]. Results from both configurations will be referenced from the literature. The similarity of the SBLI for these configurations is consistent with the free interaction hypothesis [30]. That is, a boundary layer undergoes separation in a manner that is independent of the original cause. Since the separation commences well upstream of the disturbance, the flow near the separation point is unaffected by the geometric detail of the protuberance.

After discussion of the structure, diagnostic techniques used to study the structure of this SBLI in past experiments are described. From there, a historical background is provided for this experimental configuration chronicling the evolution of supersonic cylinder-mounted flat plate experiments in step with the sophistication of wind tunnel diagnostics. A comprehensive table showing all supersonic experiments involving a cylinder or a blunted fin mounted on a plate is given as Appendix A. Following that section is a short review of the recent hypersonic experimental campaigns that have set out to study XSBLIs. The table for those experiments is given as Appendix B. The next section describes the two other XSBLI campaigns involving similar geometries: that by Murphree et al. at the University of Texas at Austin Mach 5 wind tunnel and the concurrent campaign by Lash et al. at the University of Tennessee Space Institute (UTSI) Mach 2

wind tunnel. The final section of this chapter details the flat plate boundary layer transition campaign by Semper and Bowersox, which set the stage for the experiments presented herein.

2.1 General Structure

To visualize the 3-D SBLI that results from a cylinder mounted on a flat plate in a supersonic freestream, it is instructive to first look at the features on the plane of symmetry – at the plate centerspan. A schematic of a turbulent SBLI is given as Figure 7. The prominent flow feature is the lambda shock structure, which can be broken into three regions: the central region, the free end, and the root [31]. The central region, which is characterized by the inviscid bow shock generated by the cylinder, only exists if the cylinder is tall enough relative to its diameter. Once the cylinder reaches an asymptotic height, increasing the height further only works to extend the central region. Dolling and Bogdonoff suggested as a general rule that *H/d* should be larger than 2.4 to achieve the asymptotic result [32]. At the free end, the shock curves over the top of the cylinder and continues to propagate downstream, eventually relaxing to the Mach angle.

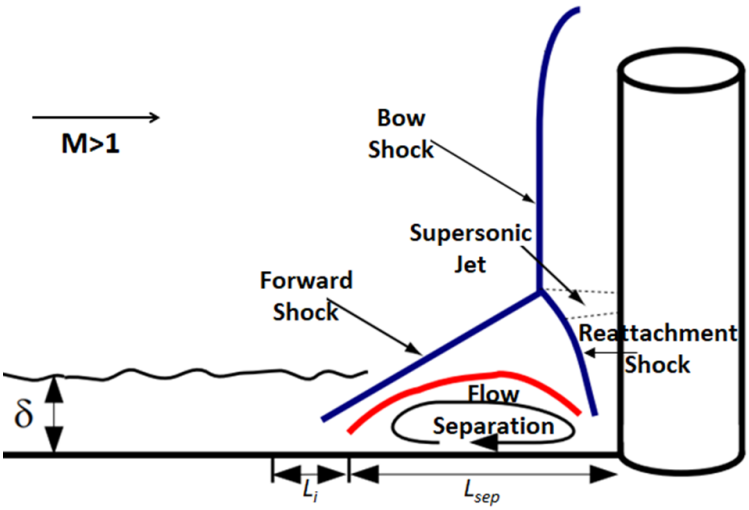

Figure 7. Centerspan cylinder-induced SBLI structure

The root region contains the features of interest for this study. The presence of the cylinder facilitates an adverse pressure gradient upstream of it, which is strong enough to separate the flow. As a result of the separation, the incoming flow is deflected, and a separation shock forms. This shock is the upstream leg of the lambda shock and intersects the bow shock at the triple point. The downstream leg of the lambda is the weaker flow reattachment shock, which causes high heating rates near the base of the cylinder. An important feature that leads to heat transfer rates and total pressures above the stagnation values on a small portion of the cylinder is the supersonic jet, which is the result of a Type IV Edney interaction [33]. The flow that passes just below the triple point encounters two oblique shock waves (the separation and reattachment shocks) and remains supersonic closer to the protuberance. The Edney interaction is given in Figure 8, where incoming supersonic freestream flow is from the right. This jet impingement even leads to higher heating rates than would an incident shock wave [34].

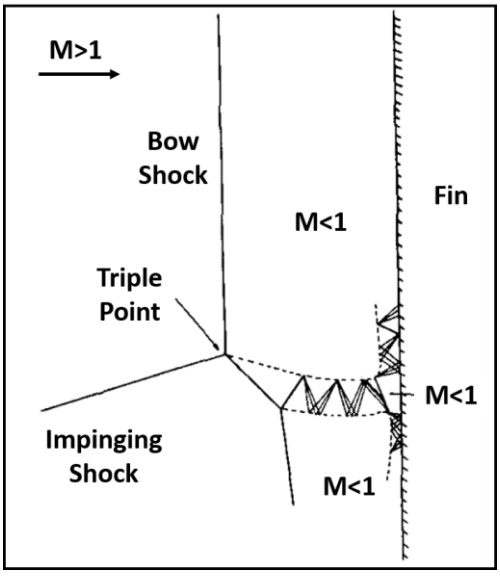

Figure 8. Type IV Edney interaction flow features (modified from [33])

The structure for a cylinder-induced transitional SBLI has an additional feature. An upstream influence shock is positioned upstream of the forward shock. The upstream influence shock is weaker as it has a smaller shock angle but still separates the boundary layer. Its intersection with the bow shock may be at or above the triple point depending on the stage of transition. The upstream reach of the upstream influence shock also varies with the state of the interaction. As the interaction tends toward turbulent, the upstream influence shock will collapse and may be indistinguishable from the forward shock. An annotated schlieren image displaying a cylinder-induced transition SBLI from the present campaign is pictured in Figure 9.

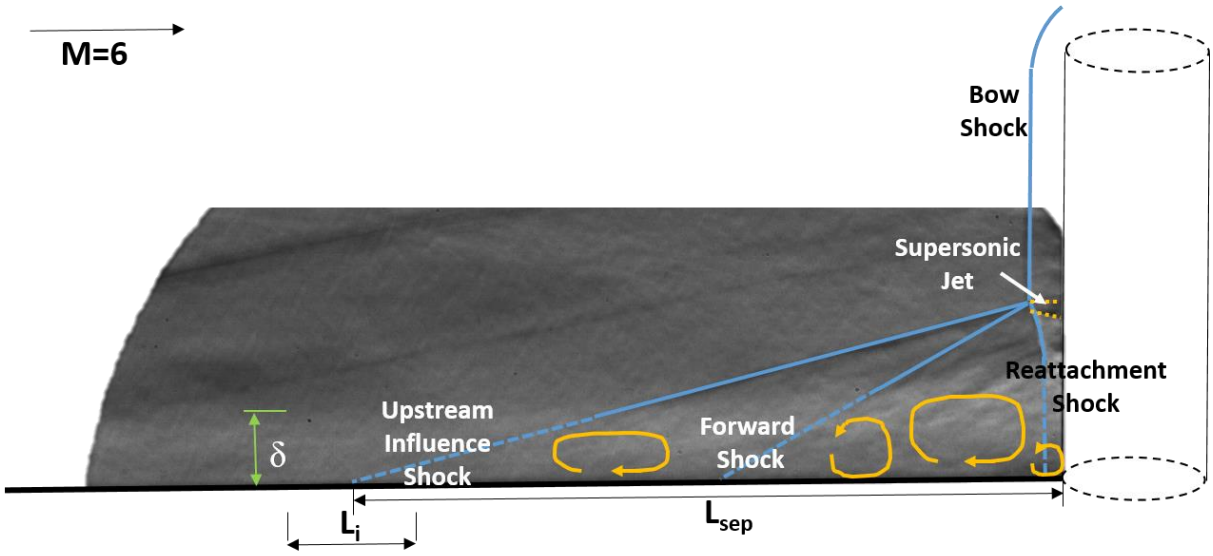

Figure 9. Shock structure for a cylinder-induced XSBLI in a Mach 6 freestream

Just downstream of the separation shock, the separated boundary layer rolls up to form a system of vortices within the lambda shock structure. The primary vortex, located at the separation line, induces a system of counter-rotating vortices within the separated region. This vortex system is swept around the base of the cylinder and each vortex assumes the characteristic shape which led to its name - the horseshoe vortex. The number and spread of these vortices are determined by

the state of the boundary layer and the Reynolds number [35]. A diagram showing the centerspan structure and the horseshoe vortices along the span is given as Figure 10.

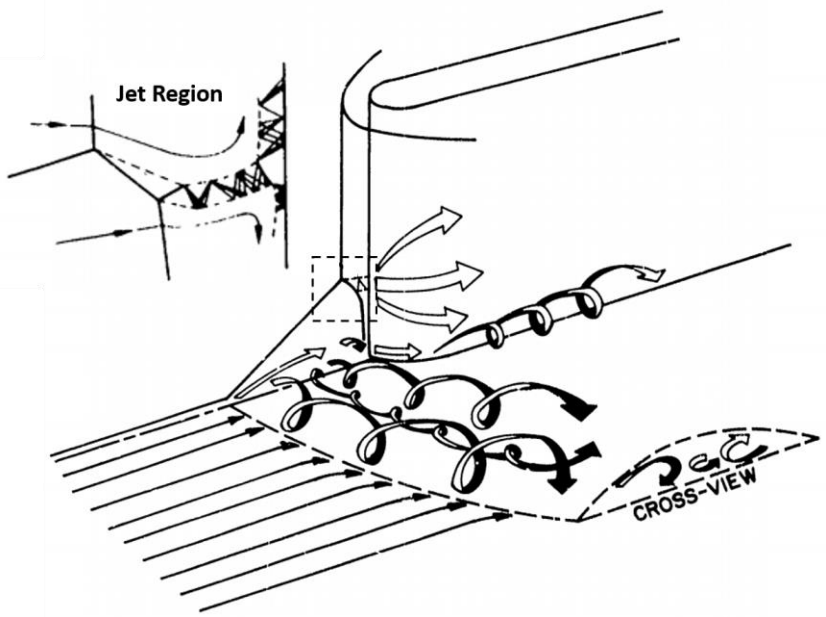

Figure 10. Centerspan and vortical structure within a blunt fin-induced SBLI (modified from [34])

Since the SBLI is unsteady, due to the intrinsic oscillatory behavior and pulsating, scavenging action of the horseshoe vortices, the spatial influence of the interaction changes with time [36]. The movement of the separation point about its mean position, and the fluctuating pressures ahead of the fin, are an order of magnitude larger than for comparable two-dimensional flows [37]. The vortices comprising the separated flow bring high-energy flow into close proximity with the surface, resulting in extremely high pressures and heating rates on the surface in the immediate vicinity of the fin leading edge. In this small region, surface pressures approaching the pitot pressure of the freestream flow, and heating rates exceeding 10 times the undisturbed surface values, have been measured [36].

Focusing back to the plane of symmetry, the separation distance, L_{sep}, is the minimum distance from the front of the cylinder to the separation line. The intermittent length, L_i, is the difference in the maximum and minimum separation distances. The upstream influence (UI) location, which is characterized by an initial rise in temperature or pressure from the undisturbed values, is just upstream of the flow separation.

For a cylinder that meets the asymptotic result, at a given boundary layer state, the most significant flow separation scaling parameter is the cylinder diameter (d). As mentioned in the introduction, the amount of separation largely depends on the state of the boundary layer. For a laminar interaction, the separation distance ranges from 6-9 cylinder diameters [34], with maximum UI distances measured between 9d and 12d [38]. Separation distances measured from oil flow are typically 10-20% less than UI distances estimated from the initial pressure rise [39]. For turbulent interactions, the separated region collapses significantly. Westkamper used oil-flow visualization data from his own experiments and results from others to conclude that the separation distance is 2.65d for a Mach numbers 2 to 21 and a wide range of Reynolds numbers [40].

The wake of the cylinder has its own distinct flow regions. Couch produced a sketch (Figure 11) of surface streaklines, based on oil flow visualization, on the plate in the vicinity of the cylinder [41]. The flow regions were divided as (1) the reversed-flow region upstream of the cylinder, (2) the flow impingement or vortex region downstream of Region 1, and (3) the wake core. The flow features that comprise Region 1 have already been discussed. Region 2 is characterized by a “herringbone” flow pattern [42], which is indicative of flow impingement on the plate surface. The flow passing over the reversed flow in Region 1, continues around the cylinder and is the source of the impingement downstream of it. The horseshoe vortices that constitute the separation

produce wakes and unsteadiness far downstream of the cylinder. It is hypothesized that unsteadiness in Region 2 is caused by a jet of high-momentum fluid that originates at the shock system in front of the cylinder [43,44]. Region 3 is located within the wake-core neck compression shock and consists of streamlines that are directed away from the plane of symmetry toward the bounding shock. At downstream distances greater than 5*d*, the flow on each side of the boundary is aligned and the wake boundary is indistinct.

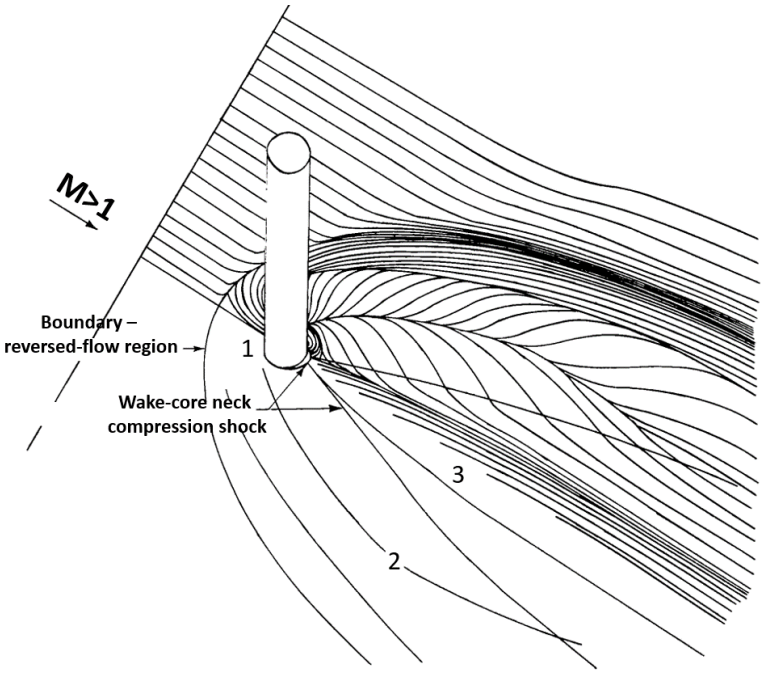

Figure 11. Cylinder wake surface streaklines (modified from [41])

2.2 Diagnostic Techniques for Studying SBLIs

Quite a few diagnostics have been used for studying SBLIs of this configuration. Several of these techniques have been available since the 1950s for the first cylinder-induced SBLI wind

tunnel tests and have evolved to become what they are today, while other nascent diagnostics have arisen from the development of technology.

2.2.1 Oil Flow Visualization

Surface oil flow has been used since the beginning to characterize the flow pattern at the surface of the plate. The oil can take different forms. Commonly used is silicone oil mixed with some sort of a pigment such as fluorescent powder. Kerosene-based mixtures have also been used. Methods for oil application have varied, but generally the oil is applied uniformly or in some pattern prior to a run.

Oil flow visualization allows the experimentalist to determine the average location of certain flow features like separation because the oil will collect at these locations. The oil tends to follow streamlines near the surface as it spreads, so tracking its motion can be useful. This technique does have its drawbacks. Often, the oil patterns are difficult to interpret. It is important to document the initial application as it may have an effect on the resultant pattern. The oil must be the correct consistency. If the viscosity is too low, the oil could blow away, and if it is too high it won't move quickly enough. There have been experiments where the oil is injected from inside the model to the surface during a run. While this insures oil will remain for longer runs, the injection of mass changes the flowfield. Tunnel unstart and subsequent depressurization of the supply line may drastically change the oil pattern. It is best to film the spread of the oil throughout the run to ensure that the end pattern is representative of the flow condition. The oil composition can also help to combat unstart effects as the kerosene-based mixtures dry in large gradient regions during the run.

For this SBLI configuration, the oil allows the experimentalist to see the separation distance, L_{sep}. That is, the oil tends to collect at the most downstream position of separation for this unsteady interaction [45]. Vortices within the separation and the form of the wake are also evident from the oil pattern. Streaklines on the cylinder itself can also be identified.

2.2.2 Surface Pressure Measurements

SBLIs are often studied by measuring the pressure on the model surface. These measurements are made by machining a hole into the model and either filling that port with a pressure transducer or a segment of tubing that runs to a pressure measurement device. The transducer or tubing should be sealed and flush with the model surface to minimize disturbances to the flowfield and fluctuation measurement inaccuracies [46].

Assuming the pressure transducer or measurement device is well calibrated and suited for the range of study, fairly accurate measurements can be made for the duration of a run. Some drawbacks are that these are "point" measurements and the model must be machined for sensor insertion. Larger transducers will add some uncertainty as to where the measurement is actually being made. To map out the entire surface with sufficient resolution would require many transducers, which will add to the cost of the campaign. Potting the transducers into the model can be difficult, and it is impossible to get most transducers flush with a curved surface. While tubing allows for the transducer or measurement device to be away from the model, it reduces the frequency response and adds the possibility of leaks.

A less intrusive diagnostic for obtaining the surface pressure field is pressure sensitive paint. Generally, the paint is sprayed on the model surface. Once in the tunnel, an ultraviolet light source causes the paint to fluoresce. The intensity of the fluorescent light is quenched by oxygen

molecules and therefore depends on the pressure of the flow. Pressure sensitive paint gives the pressure field for the entire surface, and the resolution is only limited by that of the camera taking the images of the light intensity. However, these measurements are less accurate than those of pressure transducers. Painting in even coats can be difficult, and any imperfections will show up in the final pressure mapping. The coating may alter the wall surface roughness or geometry, changing the flowfield. The pressure range is generally fairly large, so sensitivity may be a problem. Also, the paint photo-degrades relatively quickly, so a campaign may require multiple calibrations of the same sample or reapplications. The highest frequency response is order 10 kHz, compared to O(*100 kHz*) for a Kulite pressure transducer and O(*1 MHz*) for a PCB pressure transducer.

Mean pressure measurements at different streamwise positions upstream of the cylinder allow the experimentalist to determine where the flow begins to separate and the pressure profile in the separated region. Measurements on the cylinder itself indicate a pressure rise from the supersonic jet as well as the profile and point of circumferential separation on the cylinder. Transducers with high-frequency response can resolve the pressure fluctuations at the separation shock and the high-frequency content within the interaction.

2.2.3 Surface Heat Flux Measurements

The main quantity of interest for early SBLI studies was heat flux. Heat flux can be determined from several different devices. Most commonly, heat flux is derived from surface temperature measurements by way of a heat conduction model. Thermocouples can be mounted at the surface in the same manner as pressure transducers in Section 2.2.2. Infrared (IR) cameras are non-

intrusive and give surface temperature maps by measuring the irradiance of light within a wavelength band that can be converted to temperature through a calibration. Thin film gauges can be applied to the model surface and will output heat flux based on the temperature of each side of the film and a 1-D conduction model.

Thermocouples are cheap and accurate but again only produce point measurements. Care must be taken at the junction as the output will be the mean temperature of the junction. IR cameras produce full surface temperature maps but are expensive, require a special tunnel window, and necessitate the model be made of (or coated with) a material with high emissivity and low thermal conductivity. Thin film sensors can output heat flux directly but, again, are point measurements and generally suffer from poor frequency response like most thermocouples and IR cameras. More recently developed heat flux probes with much higher frequency response, including Schmidt-Boelter gauges and Atomic Layer Thermopiles (ALTPs), have not been used yet in these studies.

Heat flux measurements allow the experimentalist to determine the locations of highest heating and to quantify the heat flux of the jet on the cylinder. Measurements on the plate indicate the horseshoe heating bands of the vortices in the separated region and the highest heat transfer at the reattachment shock just upstream of the cylinder.

2.2.4 Pitot Pressure

Pitot measurements have been made on this interaction in an effort to map out the flowfield above the surface of the plate [47]. These measurements are generally made with tubing facing the flow, either with a small pressure transducer embedded or with the tubing leading to a transducer. Generally, the tubing is attached to a traverse which allows for taking measurements of a segment of the flow during a run.

Traversing a pitot probe allows for the quick acquisition of spatially precise measurements, especially if there are several probes in the flow forming a rake. The spatial resolution can be as precise as the smallest tubing. Again, with tubing leading to a transducer, there is a possibility for leaks and the frequency response will be lessened. Pitot measurements are highly intrusive and will change the flowfield.

Pitot measurements do not give good results in the separated region and any measurements upstream of the cylinder interfere with interaction.

2.2.5 Hot-wire/Hot-film Anemometry

Hot-wires have not been used to study this interaction, but thin platinum hot-films have been used to measure surface fluctuations [45]. Hot-wire or hot-film anemometers serve as one element in the Wheatstone bridge. The sensor is connected to a unit, which balances the bridge and contains a feedback loop to maintain the wire at a set resistance defined by a temperature for a constant temperature anemometer (CTA). The voltage across the bridge is the output and is a function of total temperature and mass flux.

Hot-wires provide a means for obtaining precise, high-resolution, high-frequency response (usually greater than 100 kHz) flowfield measurements. They are commonly used for boundary layer surveys or measurements across shock waves. Hot-films provide the same information either in the flow or on the surface, but generally have a lower frequency response. Unfortunately, hot-wires are extremely fragile and difficult to manufacture and repair.

Hot-wires are not a viable option for characterizing this interaction due to their intrusive and fragile nature. Optimally placed surface hot-films allow the experimentalist to study the motion and intermittency of the separation shock wave and potential disturbances within the separated region.

2.2.6 Schlieren Imaging

Schlieren imaging is ubiquitous in high-speed wind tunnel testing. A standard z-type schlieren setup, given by Settles [48], is shown in Figure 12. The light going through the test section is collimated and any density gradients cause the light to refract. The knife edge on the imaging side cuts half of the light, which causes flow features that have density gradients – notably shock waves – to appear light or dark compared to the remaining image.

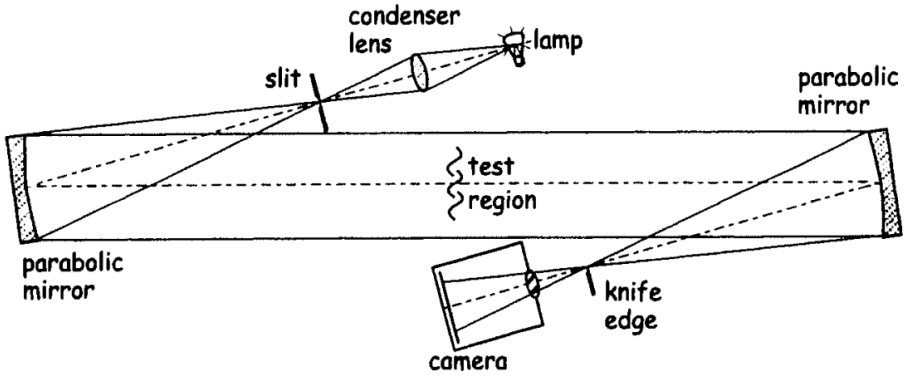

Figure 12. Standard Z-type schlieren configuration (reprinted from [48])

Schlieren is great for imaging shock waves and determining boundary layer thickness and flow separation. Today, high-speed cameras allow for time-resolved images. In standard form, schlieren is a path integrated technique, so it may be unclear which plane is contributing the flow

features in the image. Shutter speed is an important parameter. Features are only sharp for short integration times, but reducing the exposure reduces the light in the image.

Schlieren in the streamwise-wall normal plane allows the experimentalist to visualize the lambda flow structure and the incoming boundary layer. Streamwise-spanwise schlieren conducted in concert with oil flow provide an image containing the inviscid bow shock as well as the surface streaklines [49].

2.2.7 Flow Tracer Methods

Flow tracer methods have only been used in recent campaigns to characterize this cylinder-induced SBLI. These are optical techniques that use seeded particles or molecules to map flow properties. In particle image velocimetry (PIV), particles are seeded into the tunnel supply and a laser beam is conformed into a sheet directed into the flow to illuminate a plane. The particles within that plane scatter the light and the points of scattered light are traced with time. Back-to-back images are processed to give the "instantaneous" velocity on that plane. Averaging velocity fields from many image pairs gives the mean velocity.

Another flow tracer method is planar laser scattering (PLS). This method takes advantage of tracer state properties to indicate temperature characteristics within a plane. For example, finely atomized ethanol may be seeded into the settling chamber of a supersonic tunnel, where it evaporates and mixes with the air supply. As it expands through the nozzle, it becomes a fog. Similar to PIV particles, the fog scatters the light from a laser sheet which is projected into the area of interest. In regions of higher heating – like the separated region for this interaction – the ethanol evaporates and there is little scattering.

Flow tracers can elucidate many types of flow features. PIV provides instantaneous and average velocity fields. From there, flow separation and vorticity can be identified. PLS provides information on the flow temperature and density. A decrease in scatter could indicate separated flow, a turbulent boundary layer, or the presence of a strong shock. Scatter increases across a "weak-enough" shock since the particle density increases while the temperature doesn't increase enough to keep it in a fog state. As such, PLS results are sometimes difficult to interpret. They also provide very little quantitative data. Both of these methods require particles small enough to faithfully trace the flow. Samimy and Lele recommend a Stokes number of <0.5 for PIV [50]. Flow densities and seed densities must be high enough for adequate imaging.

These techniques provide the experimentalist with much information otherwise lacking regarding the structure of the separated region. PIV on a plane just above the surface provides a velocity map, clearly showing the extent of flow separation. PLS indicates incoming boundary layer states, the separation shock, and the separated region upstream of the cylinder.

2.3 Cylinder-Induced SBLI Historical Background

This section discusses the majority of all cylinder, or blunt fin, induced SBLI experiments that have ever been performed. The subsections categorize the experiments by objective, which generally aligns with chronology. The table given in Appendix A may be a helpful reference when reading this section.

2.3.1 Early Years (1952-1968)

The experimental configuration consisting of a cylinder mounted on a flat plate has been tested in supersonic wind tunnels for a long time. The first study was conducted by Gowen and

Perkins at NACA Ames in 1952 [49]. That study worked to characterize the pressure distribution on cylinders at low supersonic Mach numbers (1.49, 1.98, and 2.9) with turbulent plate incoming boundary layers. Although it mainly focused on the measurements away from the plate, and the pressure measurement spatial resolution was sparse, Figure 13 taken from their research memorandum clearly shows a local rise in the cylinder drag coefficient that can be attributed to increased leading edge pressure from the SBLI.

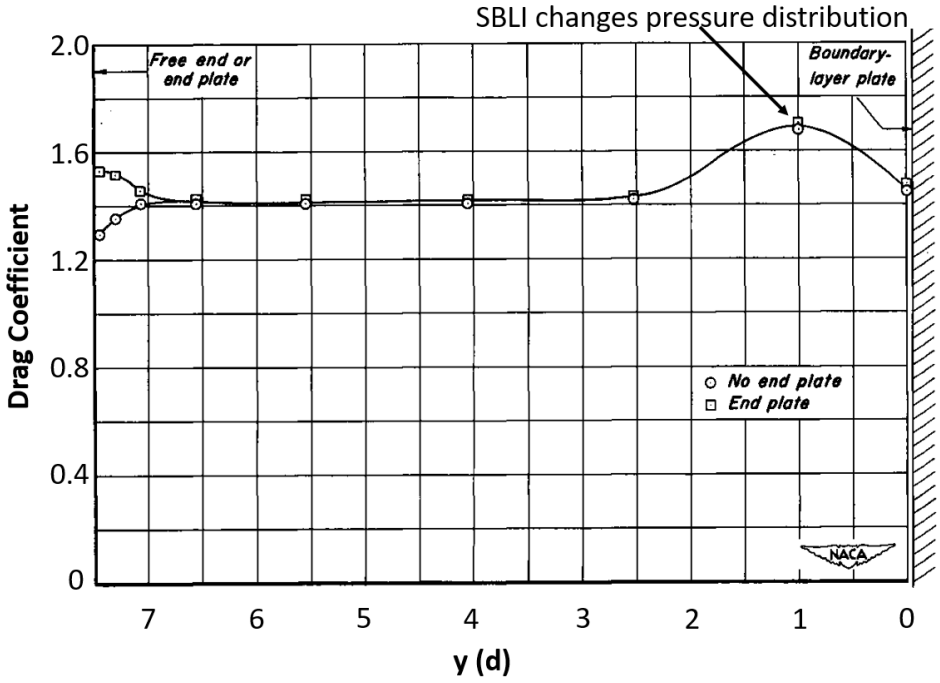

Figure 13. Longitudinal drag coefficient distribution on a circular cylinder with and without an end plate for *Re*=7.4E5 and Mach 1.98 (modified from [49])

In 1957, at Wright Patterson Air Force Base, Bloom and Pallone measured elevated heat flux levels on a thermocouple instrumented plate upstream of various-sized cylinder protuberances with Mach 6 incoming flow [51]. The cylinders, perpendicularly mounted to the plate, generated heating levels of 2-4 times the undisturbed value on the plate surface located upstream of the cylinder. Plates with cylinders swept 45 degrees forward or back showed slightly higher or lower

values, respectively. In 1958, Burbank and Strass ran a campaign in the then NACA Langley Unitary Tunnel to map out the heat flux on the plate, which had a turbulent incoming boundary layer, and on the cylinder for Mach 2.65 and Mach 3.51 freestream flows [52]. In addition to plate heat flux contour maps, the heat flux profile on the leading edge of the Mach 3.51 cylinder demonstrated elevated heating near the area of the expected supersonic jet. Additional results from the campaign were published in Burbank et al. [42]. The heat flux was measured on the plate at different boundary layer heights, which were achieved by either positioning the plate flush with the tunnel wall or moving it into the freestream. Results showed that the heat transfer was locally higher for the thinner boundary layer case, suggesting that a thicker boundary layer provides a damping effect. Surber [53] used these data to create a model for calculating the heat transfer in the vicinity of protuberances, while Truitt [54] created boundary layer growth angle, skin friction, and pressure rise models.

In 1962, Sykes produced the most complete study on cylinder-induced SBLIs up until that point [31]. His tests at Mach 1.96 gave the first schlieren images to clearly show the separation shock structure and higher resolution surface pressure contour maps. He also determined that the root shock structure, which he noted as the lambda-shock, and the triple point location do not change shape once the cylinder reaches a certain length relative to its diameter. Figure 14 gives a sketch of the centerspan shock structure upstream of the cylinder and the pressure coefficient on the front of the cylinder as a function of the cylinder height.

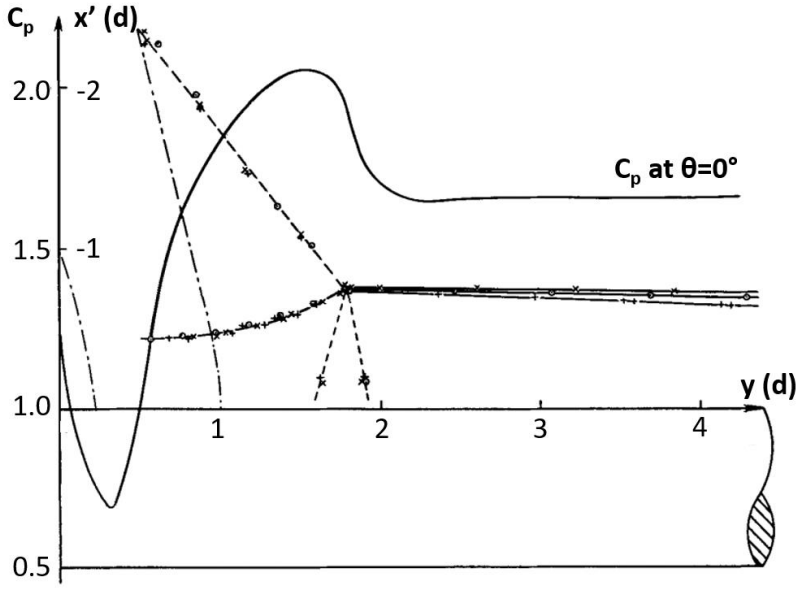

Figure 14. Shock shape and stagnation pressure distribution at root (modified from [31])

Experiments were conducted on a hemicylindrically-blunted fin configuration in 1963 by Kaufman and Meckler [55]. Testing was done at Wright Patterson to map out pressure and heat flux for Mach 5 and 8 freestream flow. Ray and Palko studied the effect of sweeping a blunt fin on an inclined plate [56]. These experiments were conducted at the Arnold Engineering Development Complex (AEDC) with Mach numbers of 6, 8, and 10, and with laminar incoming boundary layers. Their configuration produced two separate SBLIs, one caused by the impingement of the plate leading-edge shock on the cylinder and one caused by the bow shock and the plate boundary layer. However, when the cylinder was swept back such that the angle between the plate and cylinder was larger than 120 degrees, the separation of the plate boundary layer was no longer observed. Beckwith made a similar finding with a cylinder at LaRC at Mach 4.15 [57]. The 20-degree swept cylinder showed boundary layer separation in the schlieren image, but it was not observed when the cylinder was swept back 60 degrees. Bushnell used this lack of separation to effectively

isolate the effect of the leading-edge shock impingement on the cylinder for highly swept cylinders [58].

Price and Stallings conducted a more systematic study on swept fins for sweep angles ranging from 0 to 75 degrees with Mach 2.3 to 4.44 freestream [59]. Pressure measurements were made on the plane of symmetry to map out separation. Increasing the leading-edge sweep from 0 to 30 degrees sharply decreased both the extent of the upstream disturbed flow (the separation area) and the root pressure level. At a sweep angle of 75 degrees, the effect of the protuberance was barely perceptible. Despite the impact of the sweep, this study concluded that a given sweep angle produces a separation distance that still varies linearly with diameter. The peak pressure ratios within the interaction increased with freestream Mach number.

Several Soviet studies were performed near the end of this era using all of the diagnostic tools mentioned previously [60-63]. Voitenko et al. investigated the form of the separation line, the pressure distribution, and the flow direction on the surface near cylinders of different diameter and height for a Mach 2.5 freestream with a turbulent flat plate boundary layer [60]. They noted that for cylinders of "infinite effective height," the separation distance varies linearly with the cylinder diameter. They also offered a streamline model, which demonstrates the lambda shock, flow reversal, and centerspan and horseshoe vortices of the SBLI based on their surface oil flow and schlieren. The same group completed a subsequent study with better spatial resolution on the pressure measurements at Mach 3.11 [61]. Avduevskii and Medvedev ran a similar campaign for swept cylinders with both laminar and turbulent boundary layers for freestream Mach 2 to 6 [63]. They focused mainly on the effect of increasing the cylinder sweep angle on the separation distance.

Other experiments were run at different Mach numbers and/or with slightly different configurations (cylinders or fins, upright or swept, yaw [64]). All of these experiments focused on some combination of heat flux, surface pressure, schlieren/shadowgraph, and surface oil flow separation measurements [65-78].

During these early years of supersonic testing, there were several experiments with similar configurations tested at NASA Langley. These included flow over a plate with a ramp mounted upstream of a cylinder [79], plates with multiple cylinders to demonstrate the interaction between them [42,52,80], and flow over a pitched plate with the cylinder offset from the plate. Using this last configuration, Bushnell aimed to study the SBLI from the plate leading-edge shock impinging on the cylinder without the influence of the SBLI being investigated in this work [81]!

2.3.2 Separation Scaling and Flow Structure (1968-1984)

In 1968, Edney provided a physical explanation for the large increase in the local heat-transfer rate near the impingement point of a shock on a blunt body [33]. He took schlieren images along with pressure and temperature measurements on a glass hemisphere at Mach 4.6. A plate was mounted below the hemisphere at different angles of attack to generate impinging shocks at different locations on the hemisphere model. These different impingement locations led to different shock formations. When impingement occurred within the subsonic portion of the bow shock layer – as will always be the case on the front part of a cylinder – Edney noted a triple-shock interference pattern that leads to the formation of an embedded supersonic jet. High peak heating rates and total pressures above the stagnation pressure result in this region. Edney demonstrated that the total pressure could be estimated by preforming the first few oblique shock computations.

The structure and flow properties of the shock formation upstream of glass hemisphere is given in Figure 15.

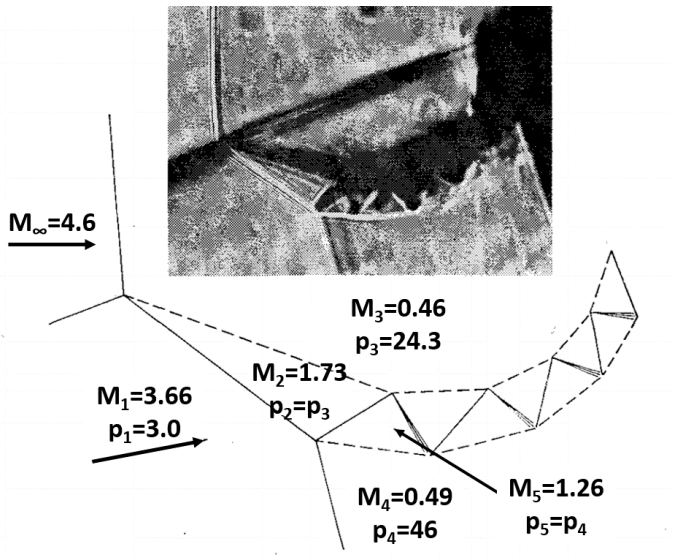

Figure 15. Supersonic embedded jet upstream of blunt object (modified from [33])

The supersonic jet is a hallmark feature of the cylinder-induced SBLI, and the shock formation now bears his namesake as the Type IV Edney interaction.

Westkaemper ushered in this era by introducing a separation distance correlation for cylinder-induced SBLIs involving incoming turbulent boundary layers [40]. Westkaemper used separation data from nine experimental campaigns, including his own, which were conducted at different Mach numbers, with different boundary layer thicknesses, and with cylinders of different height and diameter. The separation distance was defined based on the experimental diagnostic as either the outer edge of separated oil or the first rise in temperature or pressure when compared to the same plate without a cylinder. Like Sykes, Westkaemper implied that there is an asymptotic height for a given cylinder – an *H/d* for which the separation region will not change. For cylinders

of H/d > 1.13, he concluded that S/d=2.65. For shorter cylinders, the correlation is given by Eq. (2.1), below.

$$\frac{S}{d} = 2.42\left(\frac{H}{d}\right)^{0.7} \tag{2.1}$$

Figure 16 shows data from Westkaemper, and the sourced data, along with the correlation.

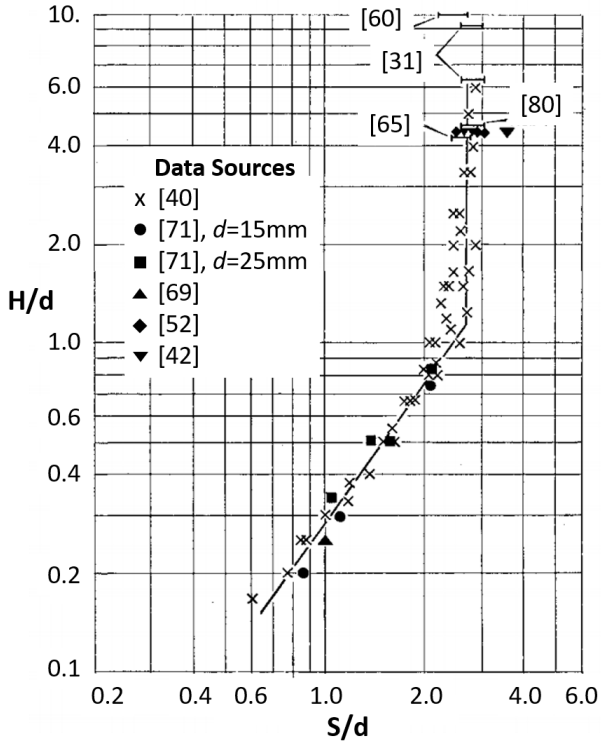

Figure 16. Separation distance based on cylinder length and diameter (modified from [40])

In 1969, Mashburn followed up Westkaemper with many more experiments in the same tunnel [82]. He characterized separation by the initial rise in pressure rather than the farthest point influenced in the oil flow. The cylinders ranged from 4.8 to 38.1 mm in diameter (3/16 to 1.5 in.) and 1.6 to 38.1 mm in height (1/16 – 1.5 in.). In general, the separation distance data showed strong

agreement with Westkaemper. The main discrepancy was at the asymptotic solution, where Mashburn saw S/d=3 or 3.25 from the pressure transducers, while Westkaemper saw very near 2.65 for every case from the oil. Another interesting note is that Mashburn never observed separation from his transducer data with the 4.8 mm diameter cylinder, even at 38.1 mm height. He suggested that enough flow was able to escape around the protuberance so that the resulting adverse pressure gradient was not strong enough to initiate separation.

Also, in 1969, Couch was the first to comprehensively measure the wake of the cylinder using a rake for total pressure and temperature measurements as well as surface mounted pressure transducers [37]. Her measurements at LaRC included copious boundary layer profiles at several streamwise locations and were used to map out the mean wake flow. Since then, data characterizing the wake of a mounted cylinder have been sparse. Recent studies by Danehy et al. [83] and Bathel et al. [84] have used advanced optical techniques to measure the velocity and temperature downstream of cylindrical roughness elements. Based on positioning suggestions from Danehy, Wheaton and Schneider measured the shedding frequency behind such an element using a pitot probe and a hot-wire [85].

In 1971, Lucas attempted to measure the pitot pressure in the separated region for Mach 2.99 in a tunnel at AEDC [47]. However, he found that the probe, which was traversed in the streamwise direction by extension from the front of the fin, interfered with the flowfield based on the data from the sensor and the high-speed, 1 microsecond exposure, schlieren images.

In 1972, Kaufman et al. conducted the first study aimed at looking at separation distances based on the known incoming boundary layer states [34]. A fin was placed at different streamwise positions on the plate and the separation distance was determined from high-speed schlieren images. The resulting plot for Mach 2.5, 3, and 4 transitional and turbulent boundary layers is given

as Figure 17. Here, *S/d* is plotted as a function of cylinder position on the plate, where a position value of unity corresponds to the first point of fully turbulent flow. They noted a large variation in separation distance for given points within the transitional boundary layer. Although their Reynolds and Mach number ranges were limited, Kaufman et al. noted separation distance appeared independent of both parameters. The group added to the campaign the following year by showing the variation in separation distance and surface pressure for a Mach 3 turbulent incoming boundary layer on a fin [36].

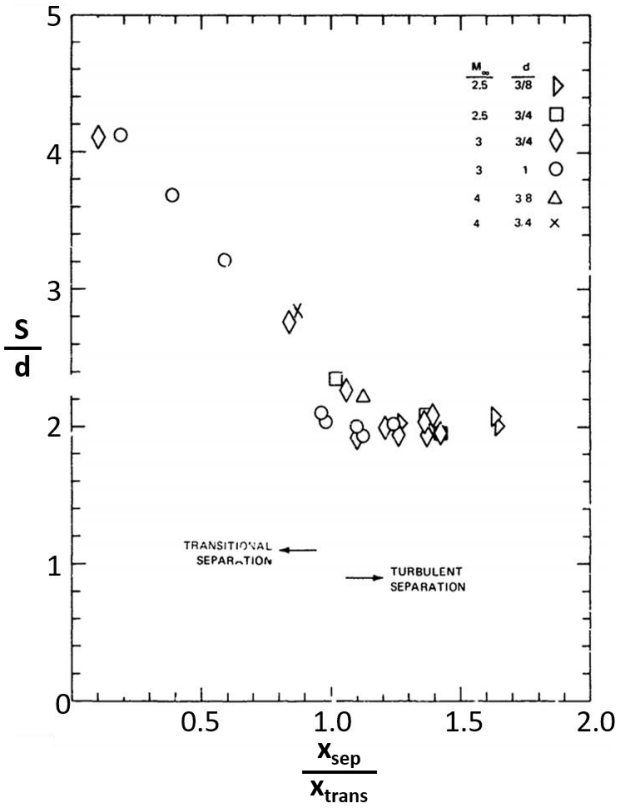

Figure 17. Separation distance for transitional and turbulent incoming boundary layers (modified from [34])

From experiments by Young et al. [86], Korkegi described the effects of a transitional boundary layer on the separation line shape [87]. As the fin bow shock location moves outboard

and downstream, it crosses the location for undisturbed boundary layer transition on the plate surface. At this point, there is an inflection in the separation line shape, as shown in Figure 18. Downstream of this location, the transitional separation line approaches the turbulent separation line shape.

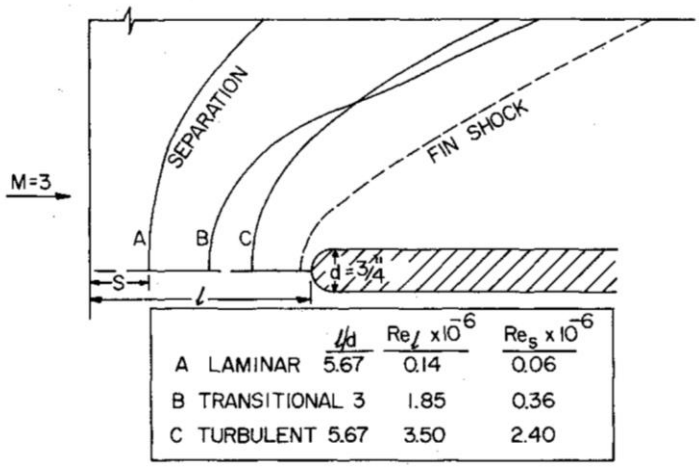

	l/d	$Re_l \times 10^{-6}$	$Re_s \times 10^{-6}$
A LAMINAR	5.67	0.14	0.06
B TRANSITIONAL	3	1.85	0.36
C TURBULENT	5.67	3.50	2.40

Figure 18. SBLI oil flow separation for different incoming boundary layer states (reprinted from [87])

Sedney commenced his experiments on this SBLI configuration in 1966 at the Ballistic Research Laboratories, Aberdeen Proving Ground, in Maryland. His simultaneous oil flow and shadowgraph imaging to map the structure of a Mach 2 turbulent interaction was not published until 1972 [88], but it gave similar conclusions regarding the presence of vortices within the separation region as tests conducted with pressure transducers [60]. Building on that study, Sedney and Kitchens conducted tests from Mach 1.5-4.5 on turbulent incoming boundary layers [35]. They used mostly "small" obstacles, which were defined as cylinder height less than boundary layer height. From this study they concluded that the separation distance does not scale with diameter for small protuberances and that the Westkaemper correlation often predicts a larger separation than was observed. Their data show that the separation distance increases with Mach number, but

since boundary layer thickness also grows with Mach number, it is unclear from the study which parameter has more influence on the separation. Surface flow patterns on cylinders of different aspect ratios are given in Figure 19. Note that boundary layer thickness is used as the normalizing parameter. Side view sketches of the separated region (like that in Figure 20a) were generated based on the number of separation and attachment points observed in the oil (Figure 20b) and the jet-maze model of Norman [89].

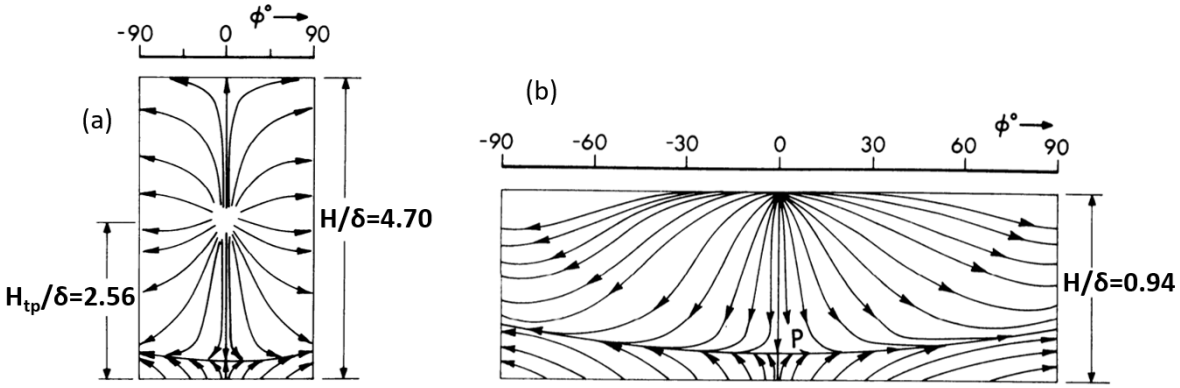

Figure 19. Sketches of surface flow patterns on (a) large and (b) small protuberances (modified from [35])

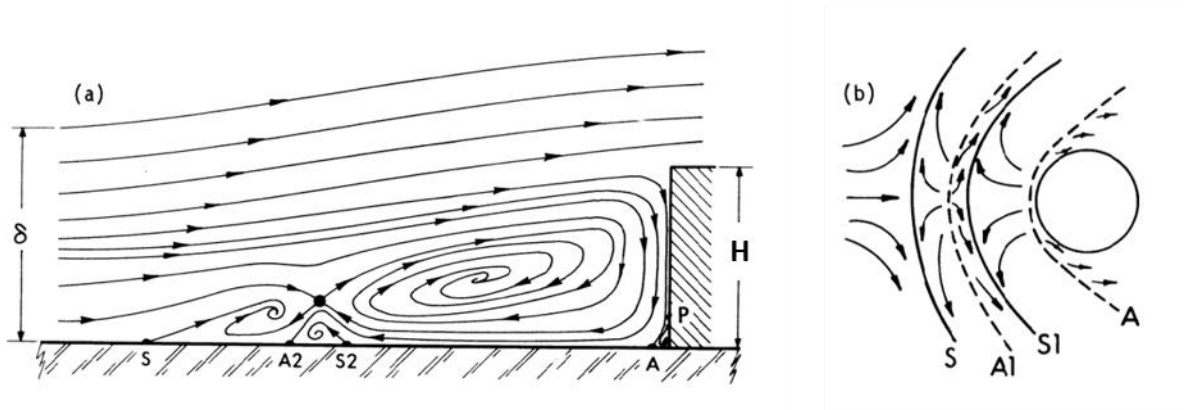

Figure 20. Four vortex system (a) side view on plane of symmetry configuration and (b) plan-view sketch of separation and reattachment (modified from [35])

Sedney and Kitchens [90] also created a separation distance model in the same vein as Westkaemper for each Mach 2.5 and Mach 3.5 datasets, suggesting the dependence of separation distance on Mach number.

In 1979 [91] and 1980 [92], Baker gave further insight into the structure of the separation vortices for laminar and turbulent incoming boundary layers, respectively. Baker conducted his experiments in a subsonic smoke tunnel, which allowed for velocimetry measurements of the vortex system, through frame-by-frame analysis of images collected at 64 Hz. He also took hot-wire and surface pressure measurements. The hot-wire measurements suggested that increasing the Reynolds number for a laminar incoming boundary layer causes the separated region to first increase from 2 to 4 to 6 vortices, then exhibit a regular oscillatory motion, and finally an irregular unsteady behavior. A diagram of a 4-vortex system is given as Figure 21. This system looks nearly identical to the one sketched by Sedney and Kitchens [35].

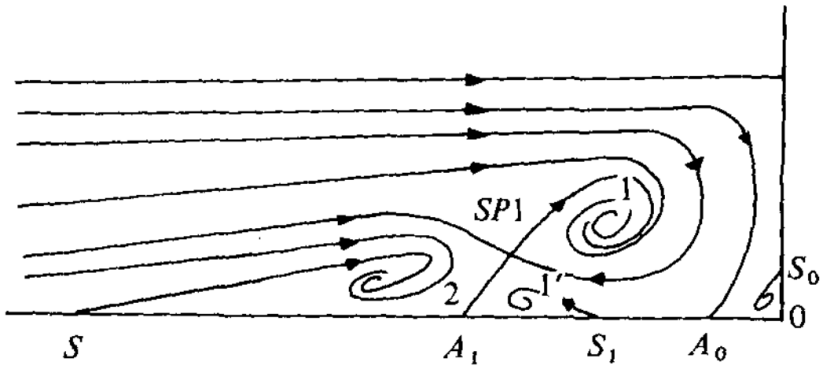

Figure 21. Sketch of subsonic 4-vortex system side view on plane of symmetry (reprinted from [91])

Hung and Clauss conducted an extensive study at NASA Ames using Mach 5.3 flow with cylinders of different heights and diameters at varying Reynolds numbers to produce incoming laminar and turbulent boundary layers [38]. Their primary goal was to improve the database and

generate correlations relating separation distance for short cylinders. From surface heat flux measurements, they found that every cylindrical protuberance eventually triggered boundary layer transition on an otherwise laminar plate. Within the separation region, they noted reattachment points from the horseshoe vortices, with the number determined from Winkelman's postulation that heating peaks correspond to reattachment points [93]. Hung and Patel generated heat flux contour maps for both plate and cylinder surfaces [94]. In addition, they tested with block protuberances and showed that the equivalent width block produces heating of greater magnitude and extent than its cylindrical counterpart.

Beginning in the late 1970s, Dolling et al. published several papers that involved measuring the separation distance ahead of a blunt fin with oil flow, pressure transducers, and copper slug calorimeters [32,39,95-101]. They also took pressure measurements on the fin leading edge. These Princeton campaigns were conducted in a Mach 3 freestream with turbulent incoming boundary layers. The first major conclusion the group made was that the separation scales with the diameter of the fin, and therefore, caution should be taken in making comparisons with a 2-D step as that scaling parameter is the incoming boundary layer thickness [97]. Schlieren photos of their interaction showed differences in the flow features in that some had a distinct separation shock, while others showed several fainter waves. Dolling and Bogdonoff then clarified what should be considered a "large" protuberance [99]. Sedney previously described small protuberances as $h<\delta$ and stated "the asymptotic result is obtained rather quickly for $h<\delta$" [35]. Dolling and Bogdonoff asserted that this is not necessarily true since the asymptotic result depends on the location of the triple point, which is highly dependent on the cylinder diameter. They suggested it is misleading to consider the protuberance as tall if it does not have an asymptotic result. Dolling and Bogdonoff

further stated that the cylinder should have an H/d >=2.4 to be considered semi-infinite for the asymptotic result [32].

Dolling et al. continued testing at Princeton with fins of different diameter, plate or tunnel floor mounted, for different d/δ ratios [100]. They observed that thicker boundary layers relative to the diameter worked to damp the interaction, pushing separation farther upstream but reducing the peak pressure. They also mapped out the surface pressure along the span to provide surface pressure contour maps. One of these is given as Figure 22.

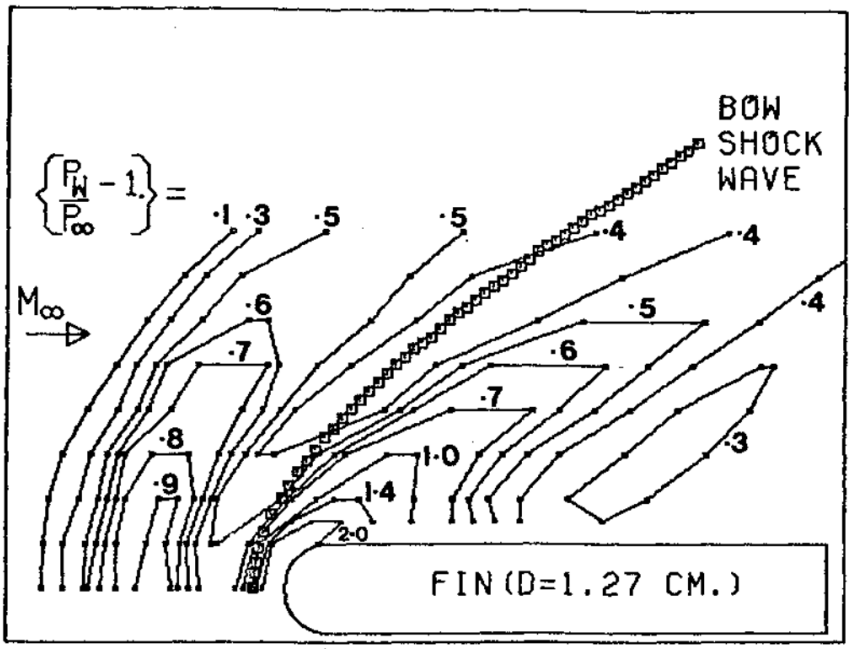

Figure 22. SBLI surface pressure contour map (reprinted from [100])

In 1984, Ozcan and Holt wrapped up the era by conducting tests with a laminar incoming boundary layer at Mach 2.36 freestream [102]. Their oil flow showed surface horseshoes consistent with the vortex configuration in Figure 8, but laser velocimetry could not confirm the flow structure and instead indicated that the flow within the region is unsteady. Ozcan and Yuceil later

mapped out the static pressure for a turbulent incoming boundary layer with different cylinder aspect ratios in the transonic tunnel at the Istanbul Technical University [103].

2.3.3 Quantifying Unsteady Effects (1969-1971; 1980-present)

In 1969, Robertson started a campaign to characterize frequencies within the separated flow region [37,104]. His tests were conducted at transonic speeds from Mach 0.6 to 1.6 and were the first to quantify the unsteady fluctuations. His surface-mounted microphone pressure transducers provided a linear response to 20 kHz. Robertson concluded from his oil flow visualization that there should be two vortices opposing the flow. He observed the highest fluctuation levels between these two vortices and at the inner region, just upstream of the cylinder base.

More than a decade later, Dolling and Bogdonoff were next to make pressure fluctuation measurements upstream of the cylinder [100]. They used Kulite pressure transducers in their turbulent Mach 3 interaction studies. These Kulites have a resonance peak above 100 kHz, but protective screens limit the maximum linear response to around 50 kHz. From their measurements, Dolling and Bogdonoff could not definitively say the proposed vortical structures were correct, but they did map out the flow region in terms of static pressure and RMS fluctuation levels and relate it to what they observed from kerosene lampblack surface flow visualization. On the centerspan, starting outside of the interaction and moving toward the fin: they first observed a peak in the static pressure fluctuations, followed by the primary separation line from oil flow visualization, then a peak in static pressure, a peak in fluctuations, the inviscid bow shock, and finally a peak in both pressure and fluctuations just ahead of cylinder. This sequence is summarized in Figure 23. Dolling and Bogdonoff also observed that the intensity of the fluctuations increases with increasing d/δ. Fomison and Stollery [105] later showed that the pressure fluctuation levels ahead of a

sharp fin are an order of magnitude less than those measured by Dolling and Bogdonoff on their hemicylindrically-blunted fins.

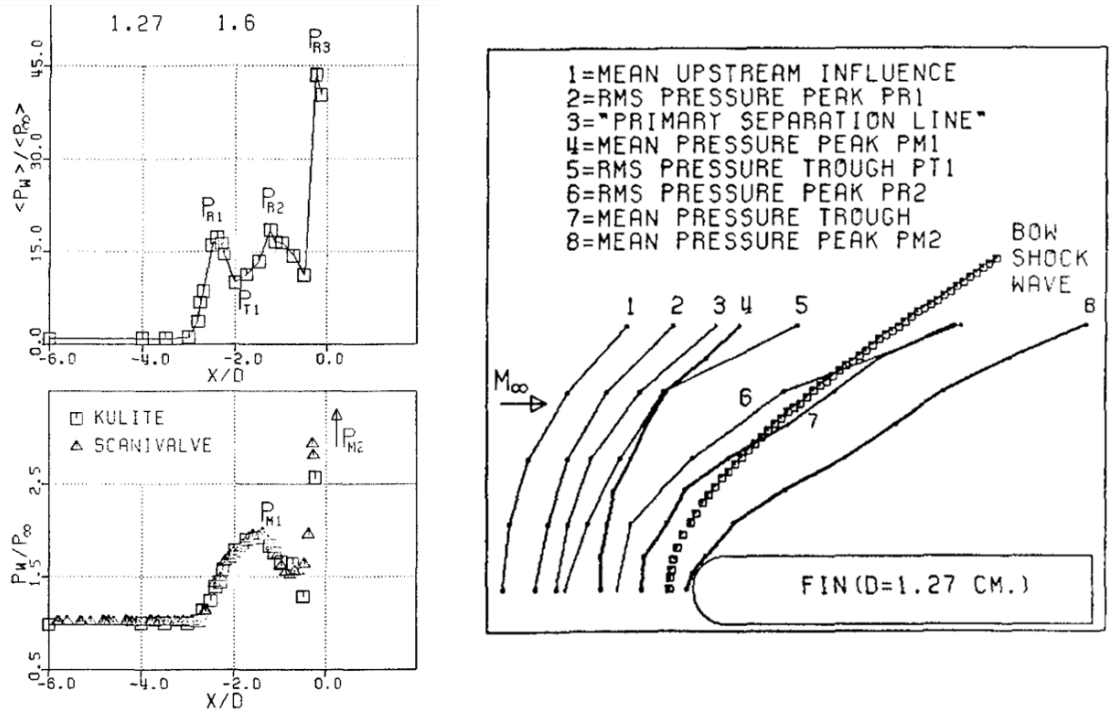

Figure 23. RMS surface pressure fluctuations (top left), surface pressure (bottom left), and sequence of surface diagnostic features (right) (reprinted from [100])

In 1986, at the University of Texas Mach 5 tunnel, Gramman and Dolling investigated how the location of the oil flow separation line – which has a frequency response of near zero and intuitively represents a mean location for separation – compares to the separation location determined from thin hot-film sensors [45]. The sensors had a frequency response of 10 kHz and were positioned on the plate surface at the location of oil flow separation arc initially and then progressively moved upstream. The intermittency of the signal was calculated at each sensor position. For this study, intermittency was determined using a conditional sampling method, where fluctuation levels above a certain threshold indicated that the sensor was within the interaction. An intermittency of one corresponds to a sensor always being within the interaction. Gramman and Dolling

found an intermittency value near unity at the oil separation line, meaning the separation shock is generally located upstream of the oil-indicated separation line. They also provided a flowfield model explaining how mean shear stress at the wall can be in the downstream direction even when the flow is separated for a major fraction of the time. They asserted that the instantaneous separation point is at the extension of the separation shock foot to the surface of the plate.

Dolling and his group continued characterizing separation shock-induced surface pressure unsteadiness using Kulite pressure transducers on this turbulent SBLI configuration for the next decade. Dolling and Brusniak developed a conditional sampling algorithm capable of discriminating between shock-induced pressure fluctuations and those generated by the turbulence in the boundary layers upstream and downstream of the shock [106]. This method used a two-threshold approach that converted the raw pressure signal into a box-car plot, showing when the separation shock was upstream or downstream of the transducer. This conversion is shown in Figure 24.

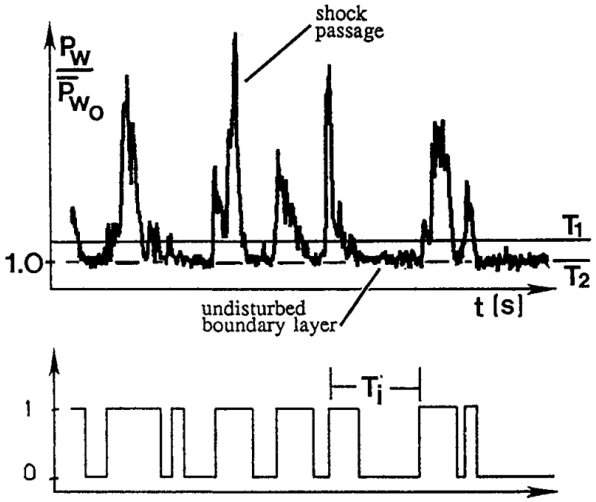

Figure 24. Conversion of pressure signal into a "boxcar" using a two threshold approach (reprinted from [106])

They added "zero-crossing frequency" to the analysis in 1989, which is the number of times the shock crosses the transducer in a second [106]. This is given as Eq. (2.2).

$$f_C = \left[\frac{1}{n}\sum_{i=1}^{n} t_r^{i+1} - t_r^i\right]^{-1} \tag{2.2}$$

where *n* is the number of shock crossings.

Figure 25 shows the zero-crossing frequency as a function of the intermittency (where the sensor is located relative to the separation shock) for cylinders of different diameters. The figure indicates that f_c is higher for the smaller diameter cylinder. Dolling and Brusniak suggest this is because the separation shock travels less distance with a smaller cylinder, while the speed in either direction remains roughly the same.

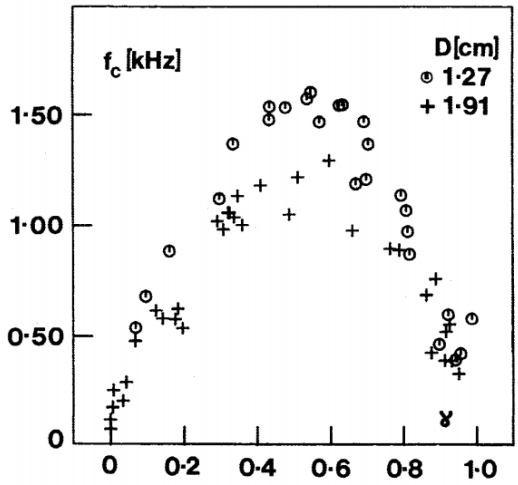

Figure 25. Zero-crossing frequency plot for different cylinders (reprinted from [106])

In the same tunnel, Baade used cross-correlations and other more direct statistical methods to determine the shock speeds in the upstream and downstream directions and the effects of cylinder diameter and boundary layer thickness on those speeds [107]. He showed that the maximum shock speed was around 15% of the freestream velocity and that the maximum speed does not

depend on the location of the separation shock or the size of the cylinder. From that campaign and previous experiments, the group concluded that the shock motion is not closely linked to the structure of the incoming boundary layer, but rather the downstream separated flow. This similar conclusion was postulated by Thomas [108].

Dolling and Smith showed the effect of separation shock intermittency on power spectral density (PSD) plots [109]. To generate Figure 26, five Kulite transducers were mounted at different locations relative to the interaction. Low-frequency content is dominant in the intermittent region, while the content is broadband and at higher frequencies in the separated region. Dolling and Smith also noted that a smaller incoming boundary layer increases the frequency corresponding to the peak signal in the PSD.

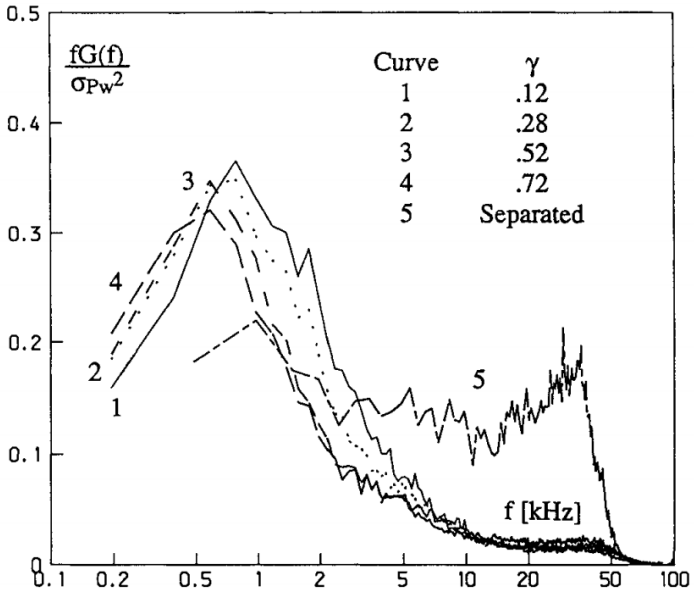

Figure 26. Evolution of the power spectrum through the intermittent region (reprinted from [109])

From previous work Dolling and Brusniak asserted that the shock motion is low-frequency O(*1 kHz*) and separation distance fluctuates O(*d*) from the location of the oil separation line to the

UI line [110]. They also postulated that the separation bubble expands and contracts randomly like a balloon. The pulsating nature of the separation was reemphasized by Dolling [6]. In that study, surface mounted Kulites were lined up on the centerspan from the intermittent region to the separated region. Cross correlations between the signals show large negative maxima that increase in time with increased distance between transducers into the separation, suggesting that pressure disturbances propagate upstream. Ensemble-averaged pressure histories indicate upstream propagation of large pressure pulses prior to changes in direction of the shock. Brusniak and Dolling concluded that the high-frequency boundary layer fluctuations continue into the separated region, and pulses within this region trigger the motion of the separation shock [29], which differs from the prior belief that the separated flow is solely responsible for the shock motion [107]. Brusniak and Dolling also suggested that mean wall pressure distributions can be used to predict unsteady aspects of the separated flowfield. Ünalmis and Dolling followed up on sourcing the unsteadiness by relating upstream pitot measurements to surface pressure measurements outside and within the interaction [111].

Gonsalez and Dolling studied the unsteadiness of interactions caused by blunt fins, sharp fins, and compression ramps at different angles of yaw [112]. They calculated effective Strouhal numbers based on the frequency corresponding to the peak observed in the PSDs for different sized cylinders. The effective Strouhal number was calculated using Eq. (2.3).

$$Sr = \frac{L_i f_c}{U_e} \tag{2.3}$$

where L_i is the length of the intermittent region defined as the distance from γ=0.05 to γ=0.95, f_c is the maximum zero-crossing frequency, and U_e is the streamwise component of the velocity at the undisturbed boundary layer edge. A value near 0.022 was found for multiple cylinder diameters as

well as for the other shock generator geometries tested. An inverse relationship between intermittent length and zero-crossing frequency works to keep the Strouhal number constant and is shown in Figure 27. Gonzales and Dolling also took measurements off-centerspan and stated that the mean shock speed, in both the upstream and downstream directions, is around 3% of the magnitude of the freestream.

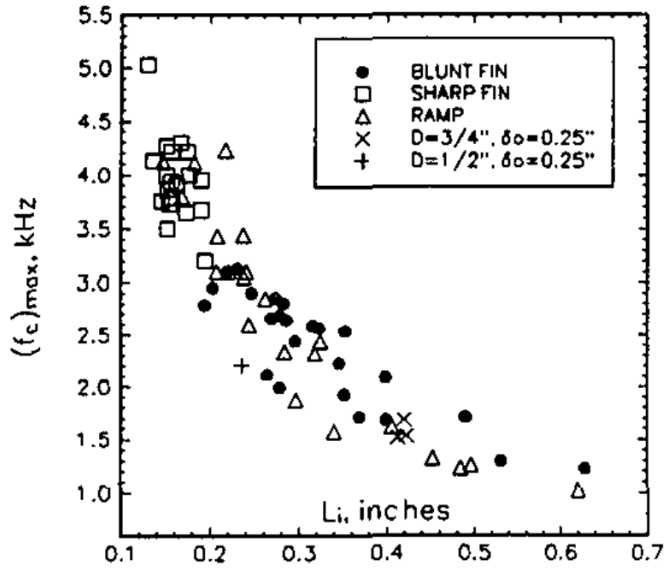

Figure 27. Maximum zero-crossing frequency as a function of intermittent length (reprinted from [112])

Dolling and Rodi experimented with protuberances of disparate leading edges including hemicylindrical, flat, wedge-shaped, and elliptical [113]. They found that the leading-edge drag coefficients correlated well with the separation distance. Hence, a fin with a hemicylindrical leading edge and one with a 53-degree wedge leading edge have the same drag coefficient and create the same upstream flow separation distance. Kleifges and Dolling built on the extensive mean surface pressure swept protuberance data of Price and Stallings [59] and Hussain [114]. Both of those studies noted the interaction scale decreases dramatically as a blunt fin is swept back from 0

to 30 degrees. Hussain concluded from surface oil flow visualization that the same structure of counterrotating horseshoe vortices is present but becomes more compressed with the sweep.

Kleifges and Dolling added pressure fluctuation data for swept blunt fins as well as sharp and flat-faced fins [115]. They used five different angles of sweep on the blunt fins from 0 to 45 degrees. Kleifges and Dolling noted a decrease in the magnitude of pressure fluctuations as well as the same decrease in interaction size that was previously observed. The centerspan wall pressure as a function of upstream distance for the five sweepback angles is plotted in Figure 28. The intermittent length also decreased but to a proportionally lesser extent than the separation length. The shock frequency was shown to increase, which is consistent with the postulation of a same shock speed over a smaller intermittent distance. Cross-correlations gave evidence of upstream turbulent boundary layer disturbances influencing shock movement. Increasing the bluntness (flattening the leading edge) created larger separation but a smaller intermittent distance for the same separation distance [116].

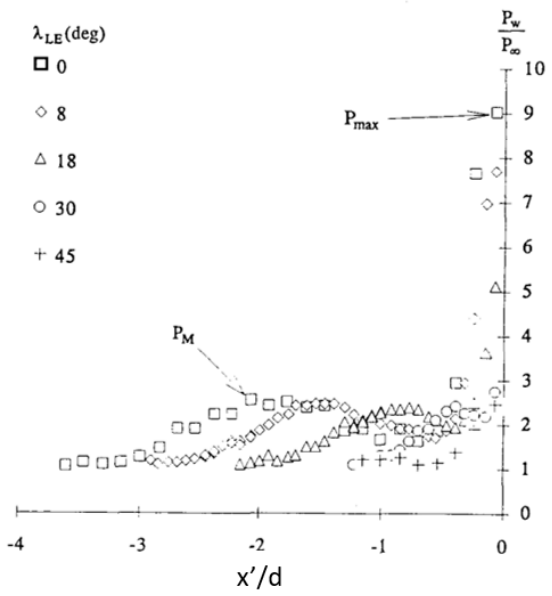

Figure 28. Effect of sweep on mean centerspan wall pressure (modified from [115])

There were contributions from other research groups as well during this time. Work continued in the high Reynolds number tunnel at Princeton, where a Mach 3 blunt fin-induced interaction was imaged using Rayleigh scattering [117]. Surface pressure measurements were also taken within the interaction [118], and the continuous wavelet transform was later performed on these data to provide insight regarding the motion of the separation shock and incoming turbulent boundary layer pressure fluctuations [119]. Poggie et al. later suggested that the Plotkin model provides justification for the conversion of broadband turbulent boundary layer disturbances to low-frequency shock motion [120] using datasets from [29,112,118].

Several campaigns commenced abroad near the turn of the millennium. In Japan, Aso et al. generated fast response heat flux measurements using thin film gauges and fluctuating pressure measurements with Kulites on a Mach 4 turbulent interaction [121,122,123]. From these measurements they computed standard deviations and higher moments of the pressure fluctuations as a function of position and concluded that sophisticated turbulent modeling would be necessary to resolve the interaction. More recently, Itoh and Mizoguchi used high-speed schlieren and surface mounted Kulites in a Mach 10 gun tunnel to examine the unsteadiness for a laminar cylinder-induced SBLI [124]. They observed the same low-frequency separation shock movements and attributed the source as the pulsating vortex system within the separation, which is fed by the high-speed freestream. Ozawa and Laurence used ultra-fast-response temperature sensitive paint and high-speed schlieren imaging for large and small cylindrical protuberances in Mach 1.2 flow [125].

In China, Shifen and Qingquan utilized fast response heat flux and surface pressure measurements at Mach 7.8 and 5 to show that both quantities are intermittent, and the frequency of the separation shock motion is less than 2.5 kHz [126]. In South Korea, Yu et al. performed oil flow

visualization and IR thermography to measure the heat transfer to the model surface for cases of different cylinder sweep [127].

At the University of Southampton, liquid crystal thermography was the primary method for estimating heat flux for laminar [128,129] and turbulent [130] interactions in Mach 6.7 freestream. Raju et al. at the National Aerospace Laboratories in Bangalore, India, used pressure sensitive paint for investigating turbulent interactions [131]. Houwing et al. [132] and Fox et al. [133] at the Australian National University used NO PLIF to visualize the shock structure and flow features for laminar and transitional boundary layers, respectively.

2.4 Recent Hypersonic Transitional SBLI Campaigns

The previous section asserts a great many laminar and turbulent SBLI studies of similar geometry. However, experimental campaigns employing any geometry to study hypersonic transitional SBLIs are scarce. There were some early studies [134-136] that noted three major effects of a transitional interaction compared to a laminar interaction. These include a reduced upstream influence, a larger pressure gradient at reattachment, and a higher surface pressure spike within the separation. Correlations were also generated to predict the peak heat transfer [137,138].

More recently, complementary experimental and computational efforts were made comparing static pressure and heat transfer on a hollow cylinder flare [139-141]. Close agreement between computations and experiments were observed on the cylinder upstream of the interaction; however, the peak computed heat transfer and pressure are substantially below the experimental peak values [140]. The experimentally measured peak heat transfer rate for a naturally occurring transitional SBLI was 3.4 times that of a fully turbulent SBLI [142], a result consistent with Longo [143]. Bur and Chanetz measured heat transfer rates 4-5 times lower for a tripped transitional

boundary layer than a naturally occurring one [141]. Benay et al. suggest that the higher heating may be due to the presence of observed Görtler vortices [140].

There have been several campaigns within the past decade that have put more emphasis into the interaction dynamics. The following subsections will examine the accomplishments of those experiments.

2.4.1 Impinging Shock

2.4.1.1 Willems et al. (2013, 2015)

The setup for this Mach 6 campaign consisted of a flat plate testbed with a shock-generating wedge positioned above it. The wedge was mounted at a 4-degree deflection and could be traversed to impart the shock at different streamwise positions on the plate. The tunnel Reynolds number was also varied to influence the state of the incoming boundary layer. A schlieren image depicting the configuration is given as Figure 29. The plate had removable inserts for different diagnostics. A PEEK insert allowed for IR thermography. A second insert was instrumented with Kulites to look at low-frequency shock motion, and another insert was instrumented with PCBs and an ALTP to measure the second mode instability.

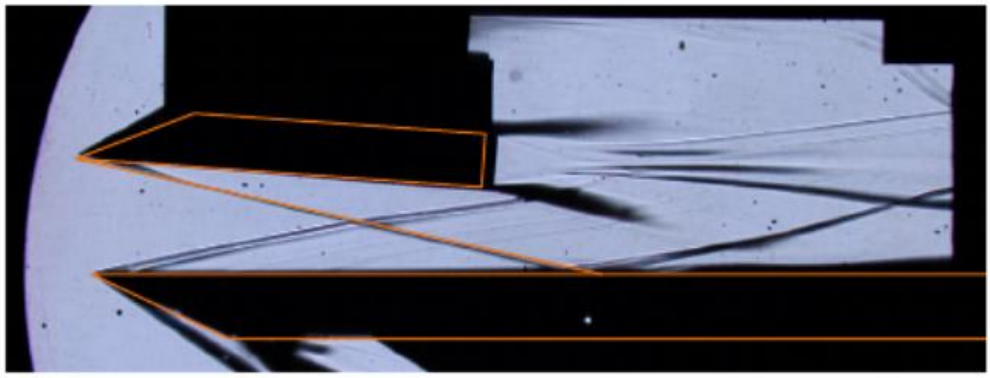

Figure 29. Impinging shock generated by wedge above model (reprinted from [145])

The study concluded that the impact of the impinging shock on the downstream boundary layer depends on the "free transition" location – where the boundary layer would transition without the influence of the shock [144]. If impingement is close to this location, a turbulent boundary layer will result. If the incoming boundary layer is laminar and far from transitional, it will relaminarize after the interaction. This study also showed that higher heat transfer rates occur for an incoming transitional boundary layer a turbulent one.

Willems et al. provided further insight to the same experimental dataset and concluded that the shock motion from the Kulites was near or below 1 kHz. A wavelet analysis of the PCB and ALTP signals showed that these modes were similar to naturally occurring second modes but at much lower frequencies [145]. The analysis also allowed for visualizing the breakup of the wavelet packages into turbulent structures.

2.4.1.2 Schülein (2014), Sandham et al. (2014)

Schülein conducted Mach 6 experiments using the same geometry as Willems and varied the incoming boundary layer state through freestream Reynolds number regulation. Schülein used high-speed shadowgraphy and introduced a transition intermittency factor (γ) based on the surface heat flux distribution to describe the state of the boundary layer. He found that a shock impinging on a BL with γ=0.05 (nearly laminar) produced the highest heat-flux intensification levels, and suggested this to be a consequence of the shock being the shortest way from a thin laminar boundary layer to a fully turbulent state [146].

Sandham et al. compared the data from Willems and Schülein with DNS computations and with high enthalpy data from HEG. The cross-validation between the experiments and DNS was considered a success, adding confidence that DNS will be able to provide data not accessible to

experiments [147]. Complementary DNS could not be provided for the experiments in HEG due to the low cold wall viscosity values. The experimental setup was similar in HEG, except the model had a slightly rounded leading edge of radius 0.16 mm to achieve a transitional incoming boundary layer. Thermocouples were used to obtain heat flux distributions and thin film gauges provided high-frequency data to extract the intermittency.

2.4.1.3 Erdem et al. (2013)

The testbed for this Mach 5 campaign was a hollow cylinder PEEK model. It was surrounded by a cowl, which deflected the flow 7 degrees and generated an impinging shock around the model circumference. Figure 30 depicts the configuration. The cowl was positioned at different streamwise stations to impart a shock on different model boundary layer states (1 laminar state and 4 transitional from IR thermography). A number of diagnostics were used in this extensive campaign including schlieren imaging, IR thermography, shear sensitive liquid crystals, PSP, PIV, and surface mounted Kulite transducers.

The IR thermography showed that the impingement on "laminar" point caused the largest heat flux values. Since the free transition location was determined from IR, it is possible that the boundary layer at the "laminar" location was unstable or in the early stages of transition. The liquid crystals revealed high levels of wall shear inside the separated region, downstream of the impinging shock position. PIV indicated high levels of turbulence above the separated region, signifying shock-triggered transition behavior [148].

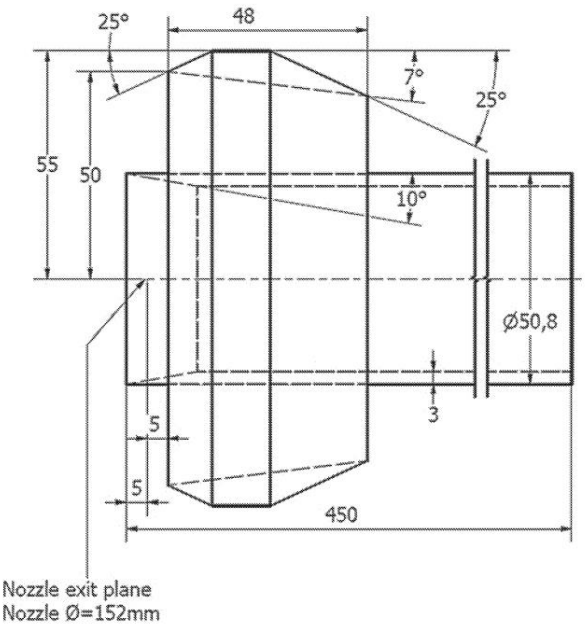

Figure 30. Impinging shock generated by a cowl surrounding a hollow cylinder (reprinted from [148])

2.4.2 Geometry-based Shock

2.4.2.1 Estruch-Samper et al. (2012, 2013) and Vanstone et al. (2013)

This set of Mach 8.9 experiments was performed on a blunted cylinder with downstream flare in the Imperial College gun tunnel. The model was designed with a large nose radius for a laminar boundary layer at the interaction, and trips were added to study transitional and turbulent cases. A sketch of the model and flow features is given in Figure 31. Estuch-Samper et al. used thin film gauges and high-speed schlieren imaging to track turbulent spots and to visualize the influence of the boundary layer state on separation at the 8-degree flare [149].

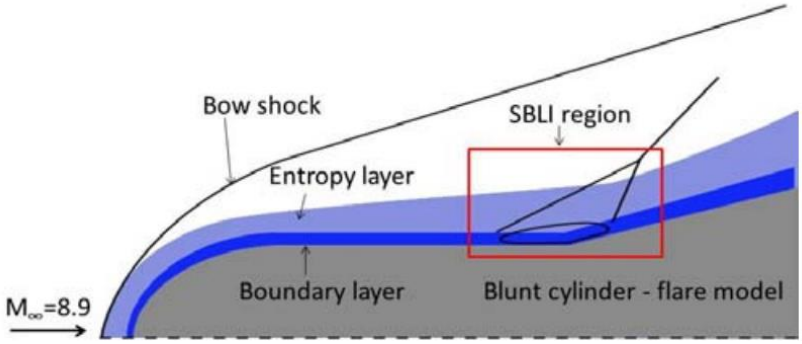

Figure 31. Blunted cylinder with downstream flare (reprinted from [149])

The following year, the group performed a systematic trip study in which diamond and square shaped trips of different heights were placed at one of two streamwise locations on the model. Additional thin film gauges and Kulite pressure transducers were added for heat transfer and static pressure comparisons with computations. Heat transfer rates within the transitional and turbulent interactions were measured as an order of magnitude higher than those for the laminar cases [150].

Vanstone et al. used a trip configuration that brought a high intermittency of turbulent spots into the SBLI. Based on Kulite pressure measurements at different axial locations, the group concluded that the length of the separation bubble and the time taken for a turbulent spot to convect past a given point are important length and time scales, respectively [151].

Vanstone further analyzed these experiments and examined a reduced turbulent spot intermittency case where the spot spacing was large enough to consider the collapse and reestablishment pairs to be independent. He concluded that the separation bubble collapse time was short compared to turbulent spot passage and was also short in relation to the adjustment of the surrounding flow. Surface pressure measurements within this transitional SBLI were higher than

those for the laminar fully separated and the turbulent collapsed cases. Vanstone made some preliminary measurements using toluene PLIF, and compared his results to CFD simulations that used an in-house operator split Godunov solver with a Baldwin-Lomax turbulence model [23].

2.4.2.2 McKiernan et al. (2016, 2017)

Edelman et al. introduced a finite span compression corner model and provided preliminary TSP and PCB measurements. The model was tested under quiet and noisy conditions in the BAM6QT to highlight the effect of freestream disturbances on the interaction for a given Reynolds number. Drawings of the model are given as Figure 32. This study presented results for a ramp angle of 30 degrees. Heat transfer maps suggest that transition occurs upstream of the slice under noisy flow, and the PCB spectra corroborate this since there is no indication of flow separation. The spectra for quiet flow suggest that the boundary layer transitions just prior to reattachment [152]. The resulting reattachment gives heat transfer rates around 2.5 times those with noisy flow. In Gray et al., oil flow visualization was added as a diagnostic for 10, 20, and 30 -degree ramps [153].

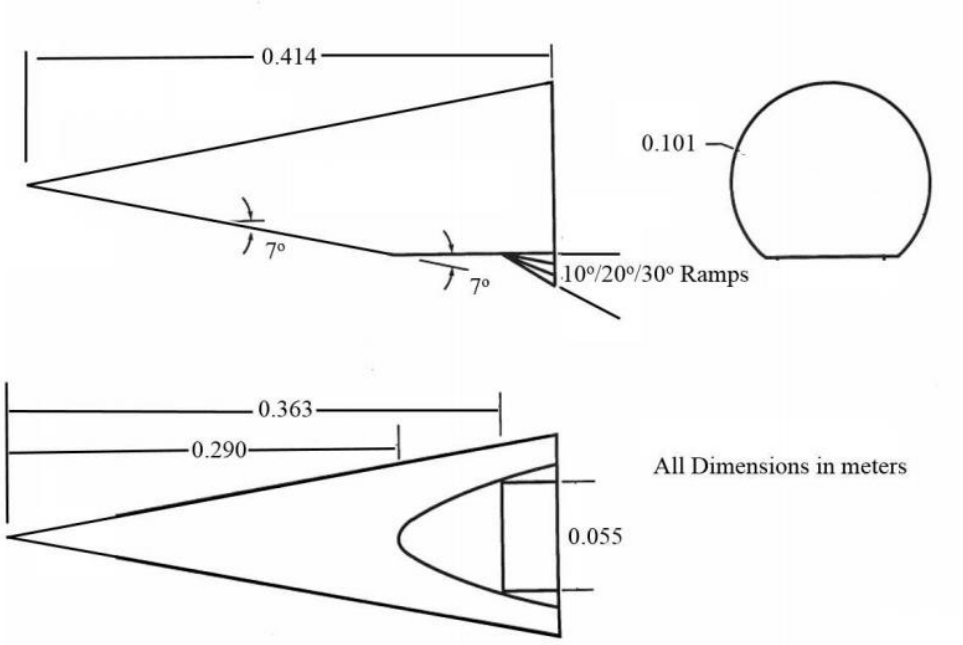

Figure 32. Conic model with downstream ramp (reprinted from [152])

In Chynoweth et al., the flow reattachment ramps were extended in order to determine the effect of the free shear layer on transition. This also meant the start of the ramp was moved 4 cm upstream. Only a 20-degree ramp was used for these TSP and PCB experiments. By varying the Reynolds number, they were able to achieve laminar, transitional, and fully turbulent boundary layers at reattachment for noisy flow and laminar and transitional (or at least broadband unstable) for quiet flow. The heat transfer mapping was noted as different for quiet flow as hot streaks extended along the edges of the ramp, and a region of heating was present about 1 cm off the centerspan [154].

2.4.2.3 Wagner et al. (2017)

Wagner et al. tested a flat plate / compression corner configuration in the high enthalpy HEG at Mach 7.4. The model wall temperature was varied from T_w/T_0 of 0.1 to 0.3. A sharp leading

edge and a heated wall proved to be destabilizing and resulted in an incoming transitional boundary layer of high intermittency [155]. The blunted leading edge resulted in a transitional boundary layer of low intermittency, which produced higher heat flux values and pressure spikes consistent with the results of Sandham et al. [147]. Complementary 2-D RANS-based simulations were also performed. The effect of the leading edge on the state of the boundary layer and separation within the SBLI is depicted in the schlieren images below (Figure 33).

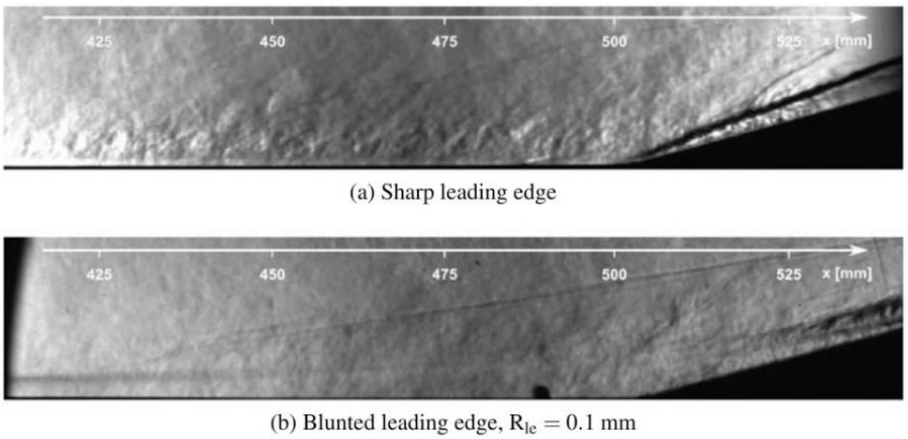

Figure 33. Transitional interactions at a compression corner for (a) high intermittency and (b) low intermittency (reprinted from [155])

2.5 Other Cylinder-Induced Transitional SBLI Campaigns

This section will summarize the findings of two experimental campaigns – a Mach 5 campaign by Murphree et al., which was completed in 2009, and a Mach 2 campaign by Lash et al., which is current.

2.5.1 Murphree et al. – Mach 5

The experiments by Murphree et al. followed a long line of cylinder-induced turbulent SBLI studies in the University of Texas Mach 5 tunnel. Prior to their campaign, Hood showed that transitional SBLI tests were possible in the tunnel by running at a lower total pressure and by positioning the shock-generator more upstream on the plate [156]. In Murphree et al., the group used PLS to image the spanwise-streamwise plane just above the surface of the plate [157]. They were able to distinguish different boundary layer states with this technique based on the identification of turbulent spots as dark patches. PLS was also used to identify the separation shock and flow separation for different incoming boundary layer states. Spark schlieren photography and surface visualization were also conducted. In Murphree et al., they showed that PLS and PIV give the same qualitative flow separation fields ahead of the cylinder [158]. They also concluded that transitional interactions resulting from an untripped boundary layer exhibit similar flow separation as those generated by tripping.

For his dissertation work, Murphree ran at a freestream unit Reynolds number of 50 million per meter (M/m), compared to 65M/m for the turbulent studies, and with the 9.53 mm (0.375 in.) diameter cylinder positioned between 96.8 and 125 mm (3.8-4.9 in.) downstream of the leading edge [159]. He used surface visualization, planar laser scattering, schlieren photography, and surface pressure measurements to provide a new description for both the mean interaction flowfield and its unsteadiness. From the schlieren, Murphree saw multiple separation shocks. The most upstream shock was termed the “upstream influence shock,” and was a relatively weak shock since its inclination angle was just slightly above the Mach angle. Closer to the cylinder, Murphree observed several more separation shocks had a larger inclination angles up to the triple point. He suggested the region upstream of the cylinder was comprised of two separated regions. The order

of diagnostic features from upstream to downstream within the first separated region is: an initial rise in pressure, the upstream influence shock, a plateau in the pressure, dry kerosene solution, and the development of fingerlike structures in the PLS, which is indicative of reattachment. Closer to the cylinder, the separated region extends farther from the wall, leading to steeper shock waves at the separation and higher surface pressures within it. A proposed model accounting for these observed features is presented as Figure 34.

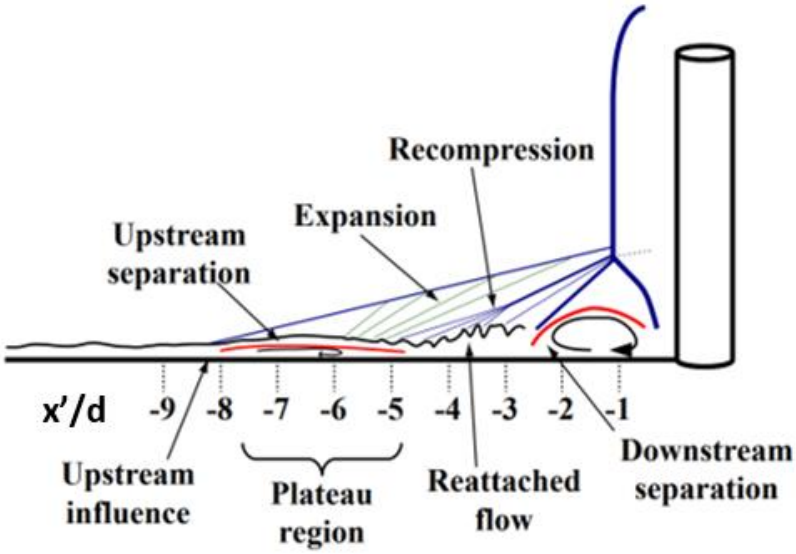

Figure 34. Conceptual model of the centerspan flowfield (modified from [159])

In terms of surface pressure fluctuation levels, the Kulite transducers showed low-frequency content consistent with interaction motion previously documented by the group. Within the reattached region, the fluctuations turned more broadband. Similarly, near the turbulent separation shock, the low-frequency disturbances were more prevalent but became broadband close to the cylinder face. A map showing the frequency distribution of the pressure fluctuations on the centerspan corresponding to scaling from the sketch is given as Figure 35.

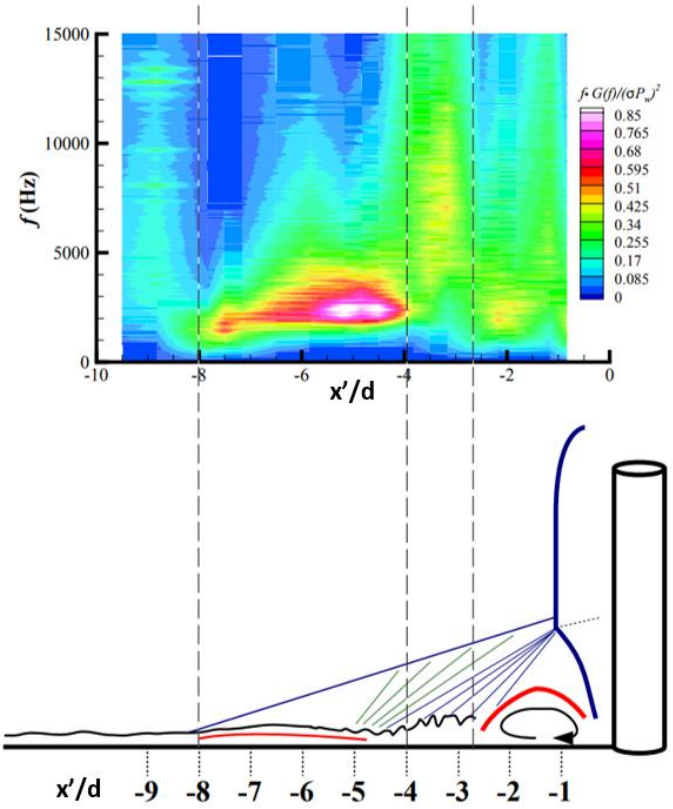

Figure 35. Pressure fluctuation frequency content on the plane of symmetry (modified from [159])

2.5.2 Lash et al. – Mach 2

The experiments by Lash et al. take place in the UTSI Mach 2 tunnel, run at a unit Reynolds number near 30M/m. Oil flow visualization was first conducted to determine the streamwise positioning of the 3.18 mm (0.125 in) diameter cylinder for transitional flow [160]. When positioning the cylinder closer to the leading edge, the oil showed separation was nonuniform, and there was evidence of unsteadiness in the separation distance – both indications of transitional incoming flow. With the cylinder positioned farther downstream, the separation front was pushed back into a symmetric arc about the centerspan – indicative of turbulent incoming flow. A comparison of

the oil flow with the cylinder positioned 8 and 25 diameters downstream of the leading edge is given as Figure 36(a) and Figure 36(b), respectively.

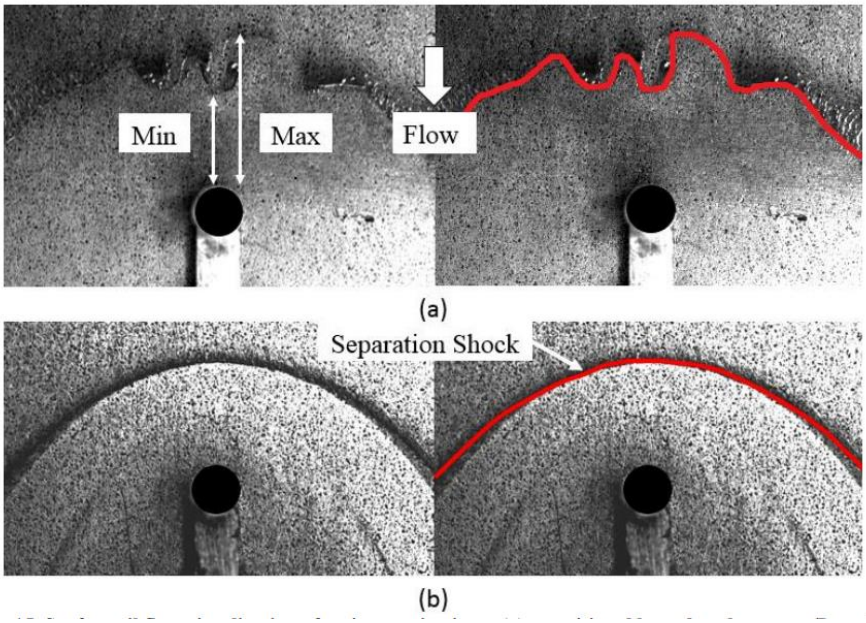

Figure 36. Oil flow visualization of the interaction in a (a) transitional boundary layer and (b) fully turbulent boundary layer (reprinted from [160])

Lash et al. also used high-speed schlieren and a MATLAB script to track the shock structure, in particular the motion of what are termed the upstream influence shock, the forward shock foot, and the trailing shock foot. These are indicated by the green, red, and blue lines, respectively, of the SBLI below in Figure 37. Some specifics regarding the shock tracking code are presented in Combs et al. [161].

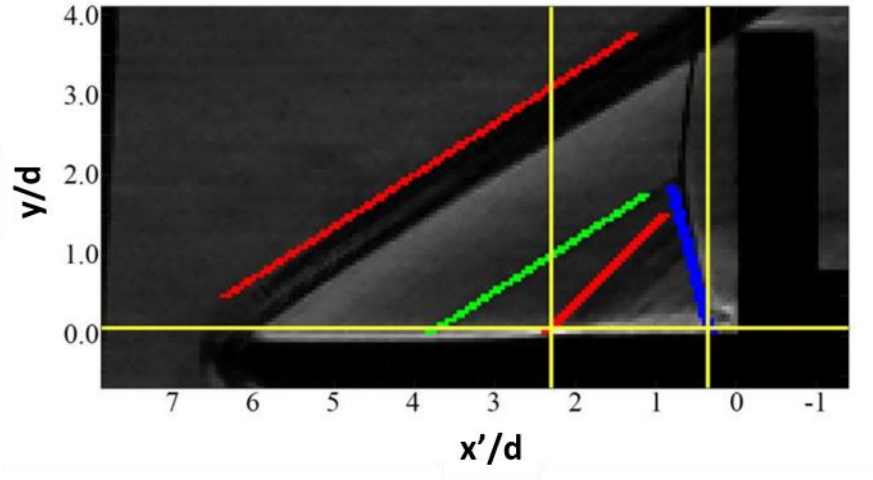

Figure 37. Shock waves identified by MATLAB code (modified from [160])

Lash et al. noted that the maximum unsteadiness in shock position occurred when the cylinder was positioned in the same location on the plate as what was concluded a transitional boundary layer from the incoming oil flow. Probability density functions of forward shock positions indicate both transitional and turbulent incoming boundary layers follow roughly Gaussian distributions with the mean turbulent position slightly closer to the cylinder (2.15*d* vs 2.4*d*), much more variance in the transitional position, and slightly more skew upstream for the transition forward shock position. The mean upstream influence shock, which was not present in all images, averaged a distance of 4*d* with some instances between 5*d* and 6*d*.

Further high-speed schlieren analysis was done in Lash et al. [162]. In this paper they concluded that sampling at 100 kHz provides time-resolved shock motion, that the upstream influence shock appears to be emanating from the forward shock, and that the upstream influence shock intermittency decreases as the cylinder is moved farther back on the plate. They also looked at representative frequencies defined by the shock crossing a set position, both from the schlieren

and from a Kulite pressure transducer positioned near the mean forward shock position. Combs et al. compared the scaling found from the schlieren to PIV and PLS results [163]. Although that data contained more noise, the same trends were shown in terms of UI and forward shock positions. Figure 38 shows the qualitative diagnostic comparison, with positions of the upstream influence shock, forward shock foot, inviscid bow shock, delineated by (a), (b), and (c) respectively.

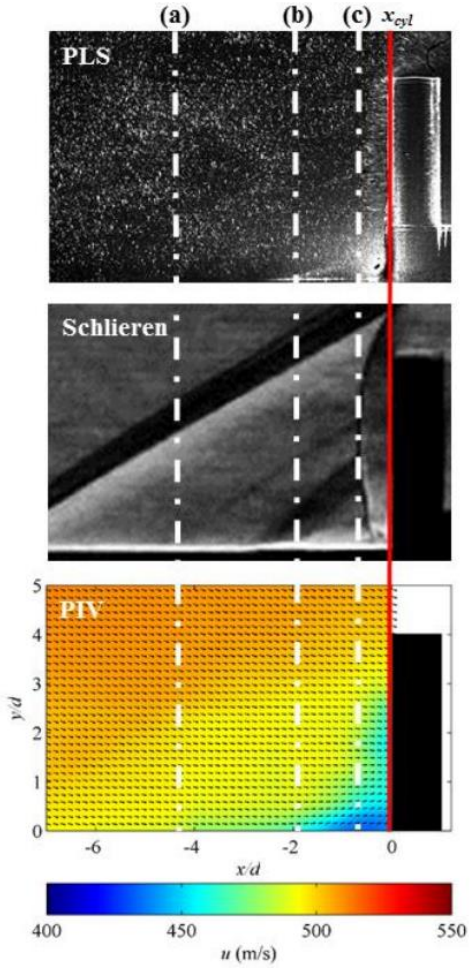

Figure 38. Plane of symmetry comparison between PLS, schlieren, and PIV (reprinted from [163])

Lash et al. continued the campaign by introducing fast-response pressure sensitive paint to map the plate surface pressure [164]. They used the combined diagnostics of PSP with schlieren and oil flow with schlieren to determine if the surface methods had an influence on the shock structure, observed from the schlieren. A streamwise aligned comparison of the independent diagnostic results is given in Figure 39. The PSP surface mapping and the high-speed schlieren probability density function (PDF) indicate a larger influence from the cylinder than does the separation indicated by the oil, consistent with the findings of Gramann and Dolling [45].

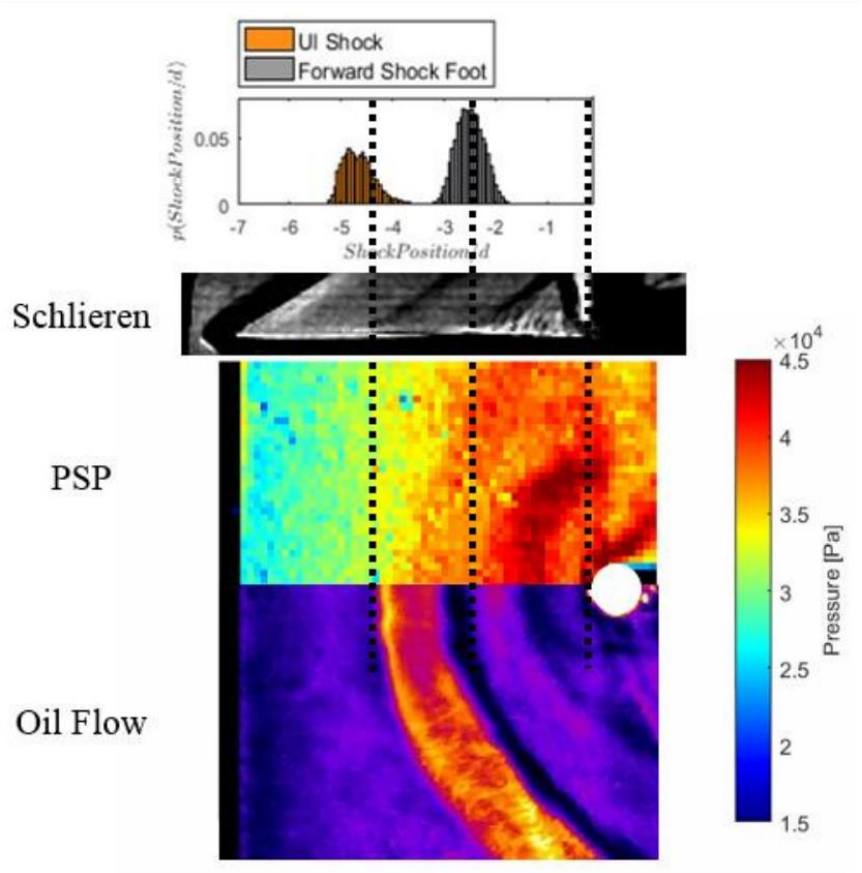

Figure 39. Scaling comparison between schlieren, PSP, and oil flow (reprinted from [164])

The PSP provided dynamic pressure data within the interaction. Every pixel in the Figure 40(a) map indicates the maximum frequency observed in its corresponding power spectral density plot. Similar to Figure 35 from Murphree, the low frequencies dominated in bands near the separation region. Likewise, the turbulent interaction, given in Figure 40(b) had higher frequency content separating bands of low-frequency dominance. Based on their position, Lash et al. attributed the low-frequency bands to the motion of the forward and trailing shock feet.

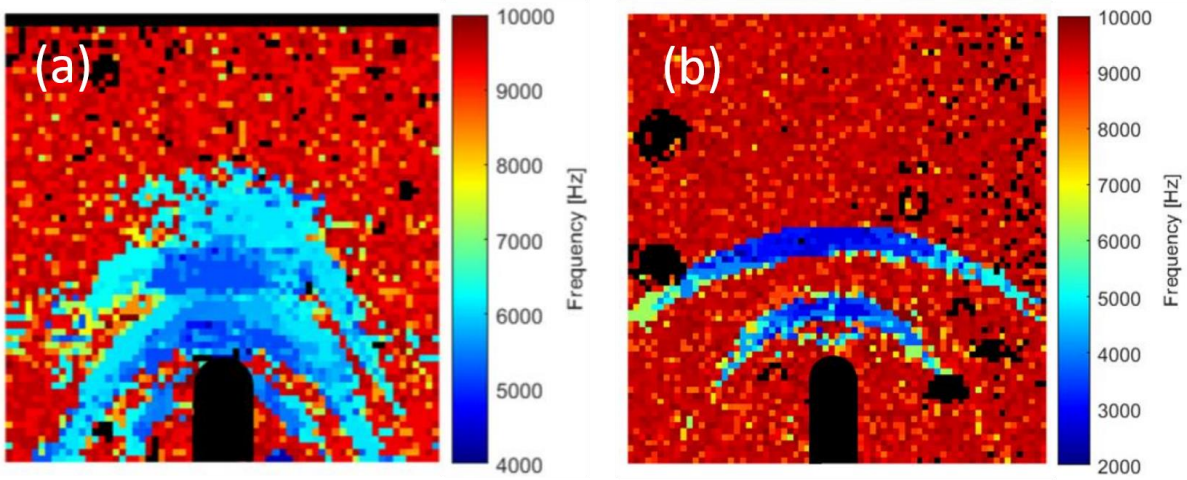

Figure 40. Dominant pressure fluctuation frequency maps for (a) transitional and (b) turbulent interactions (reprinted from [164])

Following that effort, Combs et al. [165] and Lindörfer et al. [166] conducted a joint experimental / computational effort to determine the impact of incoming turbulent boundary layer thickness on the separation distance. Combs et al. tested with cylinder diameters ranging from 1.6 mm to 19 mm and the cylinders were mounted on the tunnel wall and the flat plate. These test conditions resulted in a total range of δ/d values spanning 0.13-1.20. Lindörfer et al. used steady-state RANS simulations to determine the separation distance, defined as the first point of flow

reversal. The main conclusion from this joint effort was that the simulation overpredicted the extent of separation by up to a cylinder diameter in some cases. This combined effort also confirmed that the separation distance does indeed depend on the boundary layer thickness. Thicker boundary layers, for a given cylinder diameter, result in greater separation but lower peak pressures. Figure 41 shows the schlieren separation experimental data from this campaign (given by circles), along with the simulated conditions (triangles) and oil flow separation data from the literature (black squares).

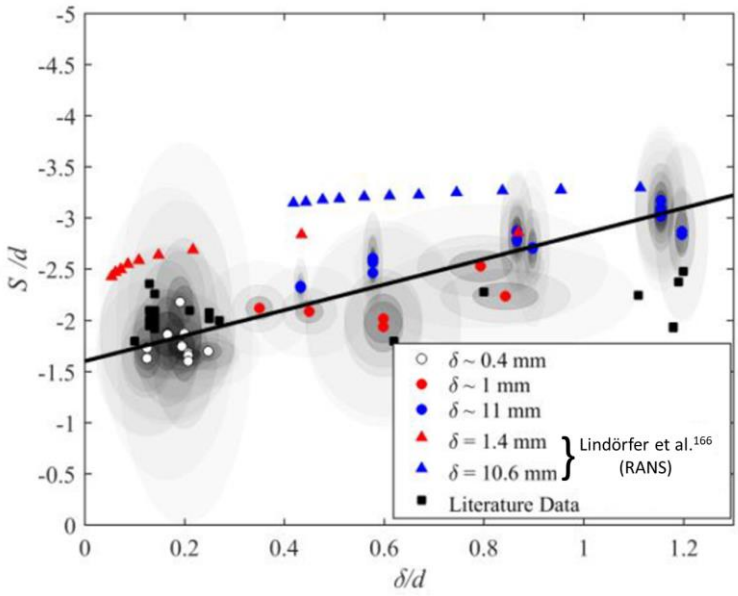

Figure 41. Separation distance dependence on boundary layer thickness (modified from [165])

2.6 Previous Boundary Layer Transition Experiments in ACE

The Actively Controlled Expansion (ACE) wind tunnel is the sister tunnel to the NASA Langley Mach 6 Quiet tunnel (M6QT) at the National Aerothermochemistry and Hypersonics Laboratory (NAL). ACE was designed to have similar mass flow to the M6QT so that both tunnels

could share the same infrastructure. ACE is a conventional wind tunnel with an adjustable nozzle throat which allows for Mach 5-8 flow. Section 3.1 discusses the tunnel in greater depth. The throat height is often set to its Mach 6 configuration which provides the NAL the ability to conduct sensitive boundary layer transition experiments by running the same models in both the M6QT (low "flight-like" pressure fluctuation levels) and ACE (conventional tunnel pressure fluctuation levels).

Tripping a hypersonic boundary layer is difficult, particularly at the low Reynolds numbers in the ACE wind tunnel. Semper and Bowersox conducted experiments in ACE to examine a turbulent boundary layer at low Reynolds numbers [167]. The test model was a flat plate with a spanwise array of NASA diamond-shaped "pizza box" boundary layer trips positioned near the leading edge. Hot-wire anemometry was used to characterize the boundary layer at four streamwise positions and different stations along the span at the most downstream location – where turbulent flow was established.

Semper produced a contour map from pitot surveys at the most downstream location which showed little influence of the trips on the boundary layer uniformity [28]. His hot-wire measurements were transformed using Van Driest methods to match the laminar sublayer and log layer regions of the law of the wall. However, derived velocity fluctuations – based on Morkovin scaling – from the hot-wire measurements fell an order of magnitude short of what was expected from the literature. This could be due to the Strong Reynolds Analogy (SRA) assumptions in the conversion of fluctuation types or the strong variation in density across the boundary layer.

This experiment provided several lessons for the current campaign. Most importantly, it not only showed that boundary layer transition on a plate could be attained in ACE, but that the transitional region could take up an extensive portion of the plate. The model design for this current

campaign was based off his recommendation that the model should not span the tunnel due to sidewall effects which turn streamlines inward as flow progresses over the plate. The trips chosen for this study are similar to the trips used by Semper and his recommendation of performing spanwise surveys to reveal information about the periodicity of the trip wakes will be followed.

Other boundary layer transition experiments conducted in ACE include the Orion CEV transient growth campaign [168] and the current 2:1 elliptic cone HIFiRE-5 crossflow campaign [169]. The roughness-induced transient growth campaign was the first to heavily employ IR thermography in the ACE wind tunnel, which has now become routine for transition experiments at the NAL. The HIFiRE-5 crossflow instability campaign uses many of the same diagnostics as the current study to show the evolution of the instability to fully turbulent flow.

3. TECHNICAL APPROACH

To fulfill the research objectives and answer the questions presented in Section 1.2, a campaign was conducted in a hypersonic wind tunnel on a canonical geometry with diagnostics capable of characterizing the high-frequency dynamics of the interaction.

3.1 The ACE Wind Tunnel

The Actively Controlled Expansion wind tunnel was a continuous open-circuit hypersonic blowdown-vacuum tunnel housed at the NAL. The nozzle contour was designed using a combination of method of characteristics (custom program written by R.D.W. Bowersox) with viscous corrections, and full three-dimensional computational fluid dynamics (CFD). The tunnel could achieve Mach 5-7+ [26]. The Mach number was changed by inserting or removing shims between the frame and the planar contours, and the necessary throat height for a desired Mach number could be approximated by the inviscid area-Mach number relation, Eq. (3.1).

$$(\frac{A}{A_t})^2 = \frac{1}{M^2} * [\frac{2}{\gamma+1} * \left(1 + \frac{\gamma-1}{2}M^2\right)]^{\frac{(\gamma+1)}{(\gamma-1)}} \tag{3.1}$$

where M is the downstream Mach number, A is the downstream cross-sectional area, A_t is the cross-sectional area of the throat, and γ is the specific heat ratio (1.4 for air in this case). ACE had a maximum run time of 40 seconds, and the wait time between runs was approximately 3 hours. The unit Reynolds number range was 0.3-10M/m, which was directly tied to the regulated settling chamber pressure. A SolidWorks drawing of ACE is shown in Figure 42.

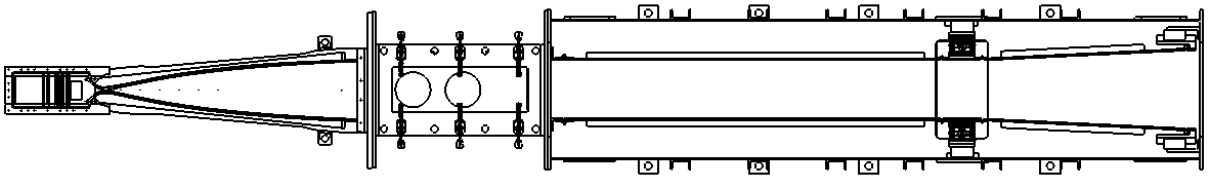

Figure 42. ACE wind tunnel schematic

3.1.1 Supporting Infrastructure

The compressed air supplying the tunnel was stored at a maximum pressure of 17.3 MPa (2500 psi) in an A.D. Smith 23.2 m^3 (820 $ft.^3$) cylindrical storage tank. The air supply was generated by two CompAir Reavell 5442 compressors, each with a pumping capacity of 3.7 standard cubic meters per minute (130 standard cubic feet per minute) [27]. Particulates, oil, and water, were removed from the air before it enters the tank from the compressors. Air from the tank traveled through a stainless steel 50.8 mm (2 in.) diameter pipeline until reached the "heater room," where it was regulated (Stra-Val) to a maximum pressure of 5.17 MPa (750 psi) and entered a Chromalox 535 kW circulation heater model GCHI-108-535P-E4. The primary reason for heating the air was to prevent liquefaction of the oxygen molecules as the air expanded through the nozzle.

From the "heater room", the air entered the laboratory through fiberglass insulated lines and passed through a second Stra-Val regulator, which was the primary control of the tunnel supply pressure. The air then passed through a 1-micron filter into the settling chamber of ACE. Electronic rope heaters were wrapped around the incoming pipes and filter. Electronic heating elements were fastened on the settling chamber. A tunnel run was not conducted until the settling chamber was elevated to the total temperature of the next anticipated run. To facilitate that, a tunnel preheating

that typically lasted between 5 and 10 minutes preceded a run to heat the components and promote thermal uniformity.

A run was generally initiated by pulling down a vacuum on the downstream end of the tunnel through a two-stage Venturi ejector. Air supplying the ejector traveled from the same compressed air storage tank through a carbon steel 0.102 m (4 in.) diameter pipeline. The air supply was regulated twice on the ejector at both stages using similar Stra-Val regulators. These regulators were heated during the winter to keep them functioning since the tolerances were tight. The Stage 2 regulators have historically proven to be the most sensitive and require annual servicing. The ejector typically established a back pressure of less than 1300 Pa (10 torr). Supporting infrastructure elements are displayed in Figure 43-46.

Figure 43. CompAir Reavell 5442 compressors

Figure 44. Air storage tank

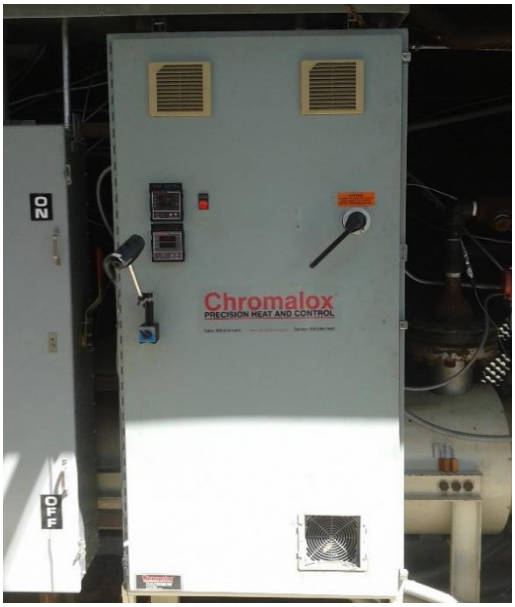

Figure 45. Chromalox heater

Figure 46. Two-stage ejector

3.1.2 Tunnel Design

Air entered the settling chamber of ACE through four 38.1 mm (1.5 in.) diameter braided steel hoses. Within the settling chamber, the air was conditioned as it passed through two "aerogrids" and three wire cloth mesh screens. The "aerogrids" were designed to promote flow uniformity, and the screens broke up large-scale turbulent structures into smaller, more easily dissipated, turbulent structures. Figure 47 shows a drawing of the settling chamber. Heat loss was minimized by virtue of three heating elements mounted to the sides and top of the settling chamber.

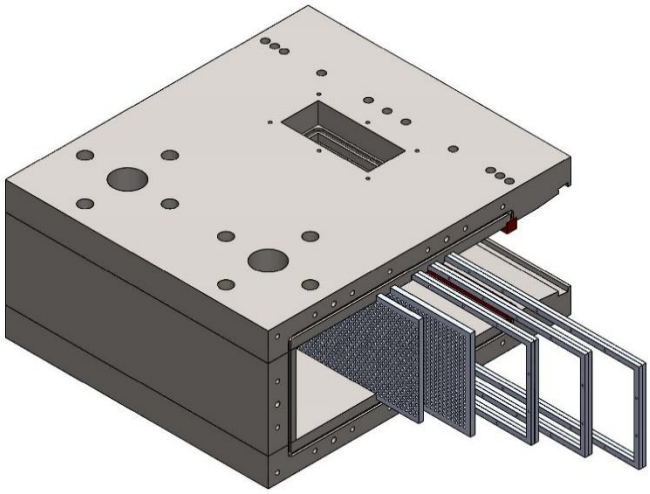

Figure 47. ACE settling chamber schematic

From the settling chamber, the air entered the nozzle and passed through the throat; the throat height was adjusted by changing the thickness of shims placed between the nozzle contour support brackets and the supporting frame. The shim locations are marked in Figure 48. As mentioned above, modifying the throat height alone controlled the Mach number since the downstream opening of the nozzle had a fixed height.

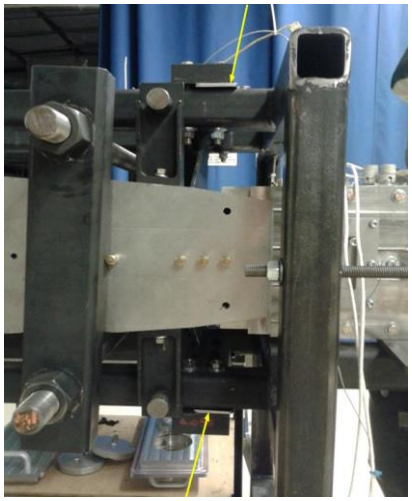

Figure 48. Adjustment shims at nozzle / settling chamber interface

Beyond the nozzle throat, the air expanded, reached condition, and entered the test section. The test section had constant cross-sectional dimensions of 0.232 m x 0.359 m (9.13 in. x 14.13 in.) and was 0.686 m (27.0 in.) long. It had three 0.127 m diameter (5 in.) access ports on the roof and floor that allowed for 0.152 m (6 in.) windows or plugs. The sidewalls on ACE were removable, so custom doors for mounting and optical access could be fabricated for a given experimental campaign.

After the air passed through the test section, it entered the diffuser where it once again became subsonic before exiting the laboratory through the ejector. The diffuser throat height should be adjusted in order to achieve the maximum efficiency and, correspondingly, a maximum Reynolds number range for a given testing configuration. More information on the diffuser can be found in Appendix C.

3.1.3 Instrumentation

The settling chamber pressure and temperature and the nozzle exit static pressure were the baseline flow measurements taken for every run in ACE. A pitot probe was welded to the top access port of the settling chamber and was connected to an Endevco 8540-200 (0–1.38 MPa full scale) piezoresistive pressure transducer to give the total pressure. An Omega exposed end type K thermocouple measured the temperature. Figure 49 shows the placement of these two measurement devices. An MKS Baratron 631C-10 capacitance manometer (0–1.33 kPa range) that was internally heated to 473 K, with no appreciable drift in zero or linearity at high temperatures, gave the static pressure reading. It was mounted on the nozzle sidewall, downstream of the last characteristic. The Baratron is shown in Figure 50. From this measurement and the total pressure, the Mach number of the freestream flow could be calculated using the isentropic flow relation, Eq. (3.2).

$$\frac{p_t}{p} = (1 + \frac{\gamma - 1}{2} M^2)^{\frac{\gamma}{\gamma - 1}} \tag{3.2}$$

or directly, Eq. (3.3)

$$M = \sqrt{\frac{2}{\gamma - 1} * [\left(\frac{p_t}{p}\right)^{\frac{\gamma - 1}{\gamma}} - 1]} \tag{3.3}$$

where M is the Mach number of the freestream flow, p_t is the total pressure as measured in the settling chamber, p is the static pressure as measured at the end of the nozzle contour, and γ is the specific heat ratio (1.4 for air).

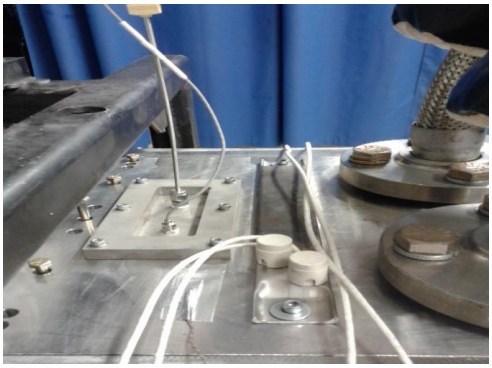

Figure 49. Settling chamber instrumentation

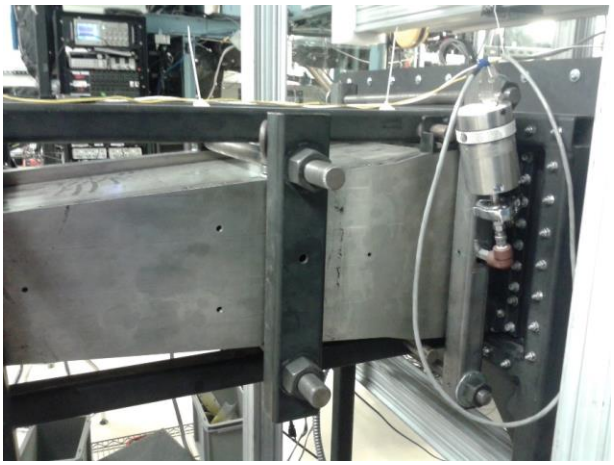

Figure 50. Static pressure measurement

More information about the design, installation, and preliminary calibration of the Actively Controlled Expansion tunnel can be found in Semper et al., Tichenor et al., and Tichenor [170,171,172]. More information about the infrastructure and instrumentation can be found in Mai [27]. Appendix D provides the ACE standard operating procedures.

3.1.4 Testing Conditions

The testing conditions for this campaign are summarized in Table 1. Note that the Mach number varies with freestream Reynolds number since increasing the Reynolds number leads to earlier transition on the nozzle walls and thicker boundary layers at the exit. This reduces the effective area ratio, which decreases the Mach number.

Table 1. Tunnel Conditions

Mach	Reynolds number	Total Temperature
5.75-5.9	0.5-8.5 M/m	430 K

3.2 Model Design and Evolution

3.2.1 Flat Surface

As mentioned in Section 2.6, the initial model design was based off the recommendations of Semper [28]. That is, to avoid tunnel sidewall effects the model should not span the entire test section and should have its sides tapered back at the Mach angle. The plate was machined of polyether ether ketone (PEEK) due to its high deflection temperature, high emissivity, and low thermal conductivity. These properties are especially beneficial for IR thermography since the material prevents surface reflections and mitigates lateral conduction that would smear the surface heating patterns from the flow features. The leading edge of the plate was blunted to a 1.6 mm (1/16 in.) radius and spanned 0.279 m (11 in.). The plate was swept back at the Mach 6 Mach angle of 9.6

degrees. The plate was mounted in the tunnel, centered spanwise, at a 2-degree downward angle-of-attack to promote stagnation on the top surface, which discouraged instabilities and flow separation on the leading edge.

Oil flow visualization was the first test conducted on this model. The oil was applied in streamwise segments across the span, as shown in Figure 52. This test made it clear that there was an influence near the lateral edges of the plate – not from the tunnel sidewalls, but from a difference in pressure on the upper and lower surfaces. The pressure gradient was caused by the top of plate having a higher pressure due to less of an entropy change from a smaller shock angle at the leading edge.

Building on this knowledge, a second PEEK model was designed, this time as a wedge. The model was a 1.3-degree half-angle wedge with a width of 0.279 m (11 in.), later trimmed to 0.248 m (9.75 in.). The leading edge was designed with a polynomial fit to match slope and curvature of the downstream wedge profile. Curvature mismatch can produce a pressure spike and receptivity source [173]. The polynomial and the natural incline of the wedge allowed for the leading edge to have a relatively small bluntness that should prevent flow separation [174]. The upper curve was defined by Eq. (3.4).

$$X = 373555Y^6 - 354050Y^5 + 49669.4Y^4 \tag{3.4}$$

where Y is the tunnel-based vertical coordinate, and X is the streamwise coordinate, and X=0 is the leading edge. Both variables have units of inches and $0<X<1.8$ and $0<Y<0.1$. The lower curve is symmetric about the X-axis.

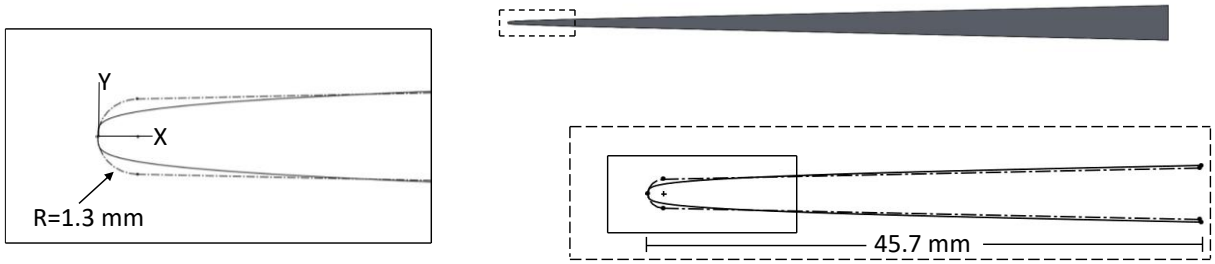

Figure 51. Side view of wedge model and leading edge

Figure 51 shows a side view of the 1.3-degree half-angle wedge as well as a close-up comparison with a 1.3 mm radius rounded leading edge of the same wedge angle (dashed profile on zoomed images). Note that the polynomial fit matches the slope and curvature at the interface with the wedge angle, which should improve the flow quality over the model.

Figure 52 gives a geometric comparison of the solid PEEK model designs as well as the preliminary oil flow for the front half of each model. Flow is from left to right in the figure. Oil at the surface is extremely sensitive to pressure effects due to low momentum near the wall. From the oil flow it is evident that the pressure gradient between the upper and lower surfaces no longer dominated the flowfield on the wedge. The wedge model provided for streamlines that were directed relatively straight downstream over much of its span, whereas the tapered plate gave fewer streamlines of that character near the leading edge, and the span of streamlines continued to shrink downstream because of the edge effects and the taper.

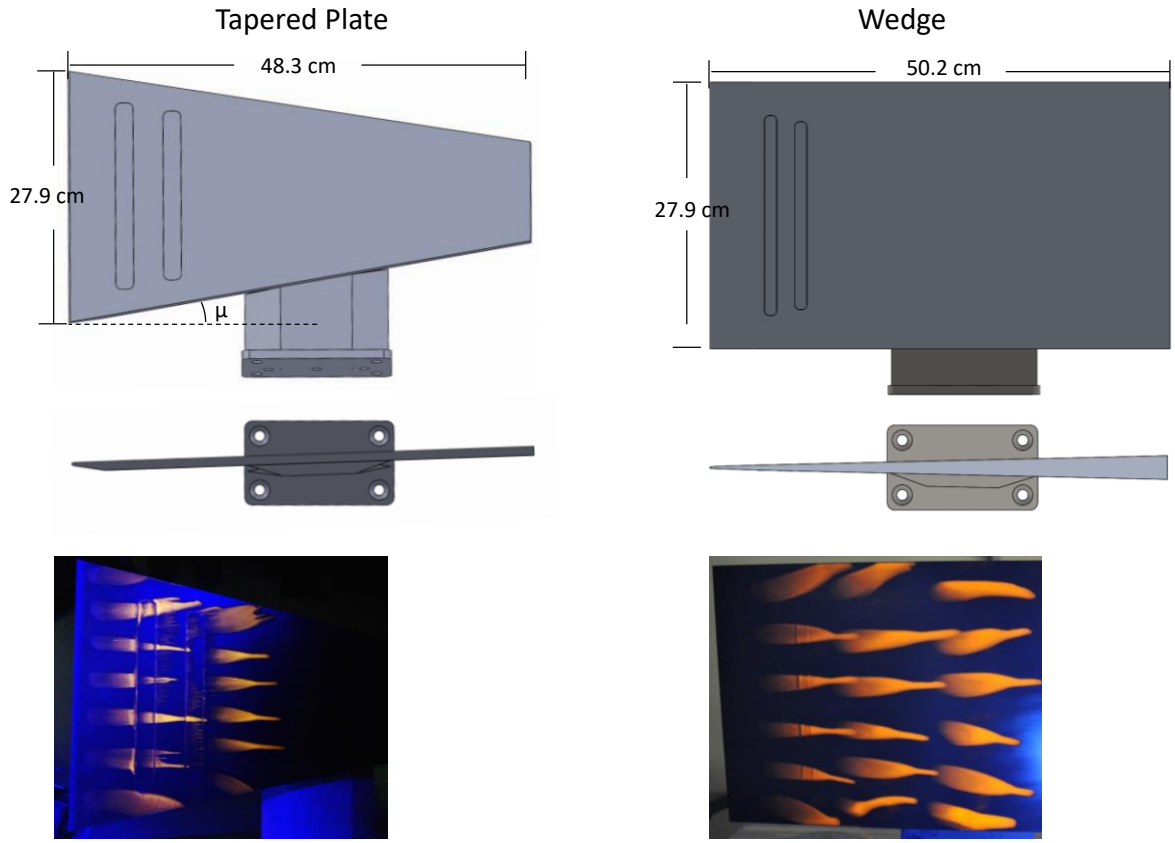

Figure 52. View of plate (left) and wedge (right) and preliminary oil flow (bottom)

Oil flow was also conducted on the wedge to observe the effect of span reduction on the extent of downstream streaklines. The original 0.279 m (11 in.) wedge was reduced by machining 15.9 mm (5/8 in.) off each side for a resulting span of 0.248 m. These results are presented in Figure 53.

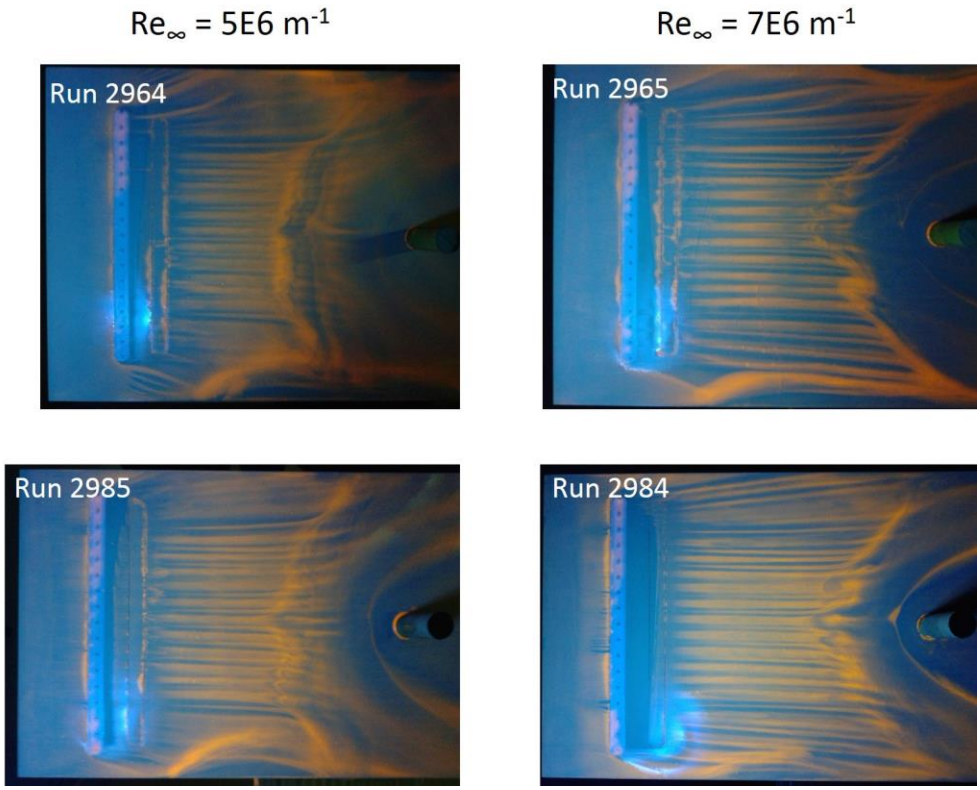

Figure 53. Edge effects before (top) and after (bottom) trimming the span of the wedge

The model was mounted from its left (picture bottom) on a strut which was attached to the door on the left side. While the edge effects may have been reduced by trimming the wedge for the right wall, the interaction with the strut remained the same for the reduced span, which resulted in an effective decrease in testing area.

The wedge PEEK model was used for tests reported in Leidy et al. [175]. While the model provided an excellent testbed for honing diagnostic techniques and collecting preliminary data on the SBLI, the leading edge was machined with some spanwise curvature, which can be observed in the profilometer scans in Appendix E. This prompted the development of another wedge model.

A new composite model was created for increased durability. The model frame was stainless steel, which worked to prevent warping of the leading edge during the machining process. The

cylinder was fastened to a PEEK insert, which allowed for IR thermography of the flow separation ahead of the cylinder. The boundary layer trips were the same height, spacing, and streamwise positioning as those used for past experiments. The insert directly downstream of the trips allowed for design flexibility in using this wedge for other experiments. These front two inserts were both secured from the back of the wedge so that the interfaces between the frame and the inserts had minimal steps. The inserts were taped on the back to prevent suction or blowing effects.

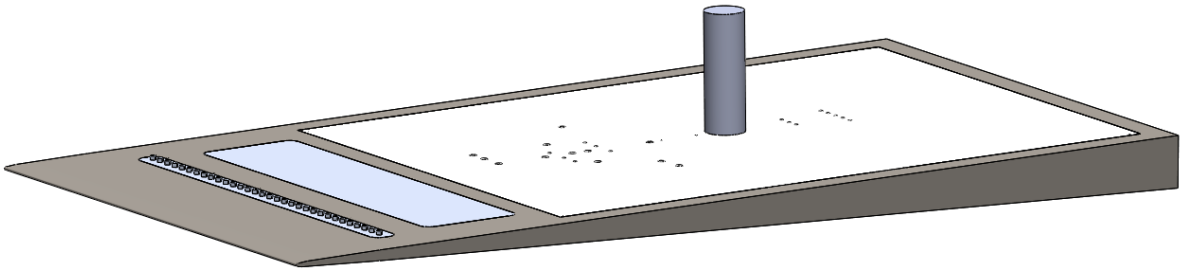

Figure 54. Test model: stainless shell and PEEK insert

Some key dimensions are given in Figure 55. The wedge was approximately 0.482 m (19 in.) long and 0.254 m (10 in.) wide, which left a 5.1 cm (2 in.) gap between the wedge and the sidewall on both sides. The 6.35 mm (0.25 in.) PEEK insert began 0.152 m (6 in. or 8*d*) upstream of the cylinder, which allowed for visualizing the full interaction with IR thermography. The most upstream part of the mounting strut was 15.9 mm (5/8 in.) upstream of the cylinder, compared to 114 mm (4.5 in.) previously, which mitigated the influence of the strut on the interaction being studied.

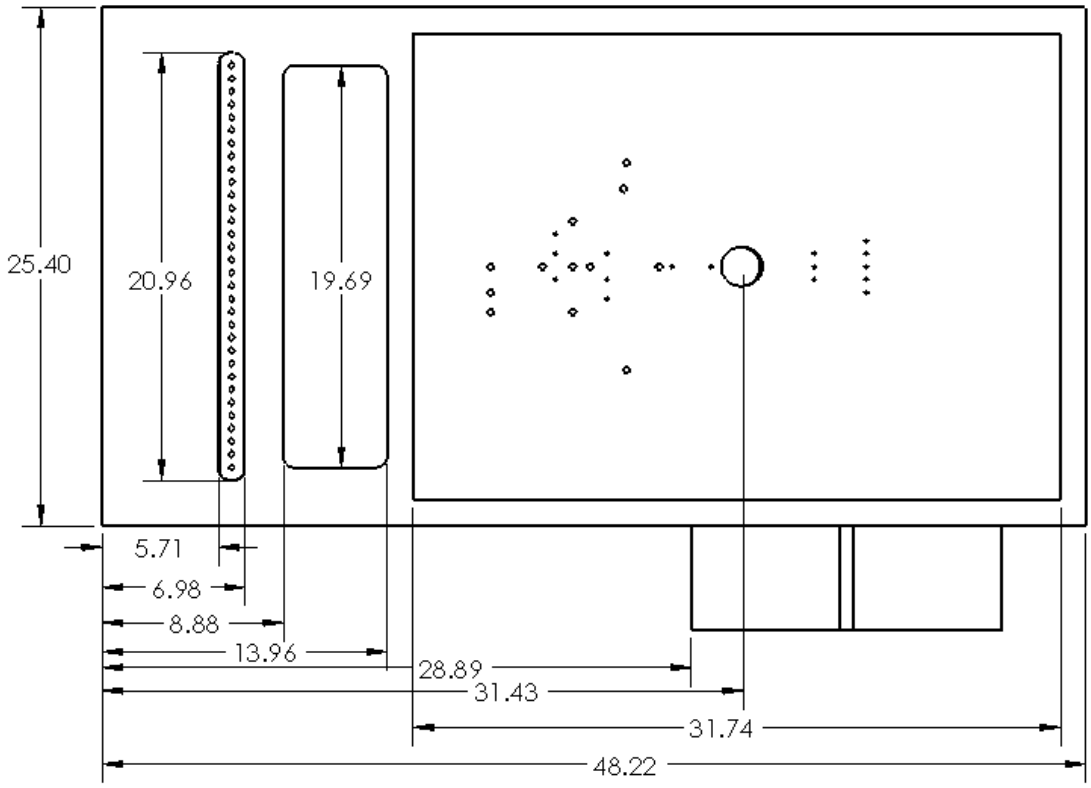

Figure 55. Top view of wedge with dimensions in centimeters

Figure 56 is a diagram of the wedge from the bottom view. The diagram indicates the bolt types and locations. The back of the PEEK insert had tapped holes for 6-32 bolts. During assembly, it was important to apply pressure to the PEEK surface, so the bolts would not strip the threads. The diagram does not include the 1.6 mm (1/16 in.) thick steel cover plate in order to allow for the viewing of the pressure ports on the underside of the PEEK. The positioning of these holes will be discussed further in Section 4.2

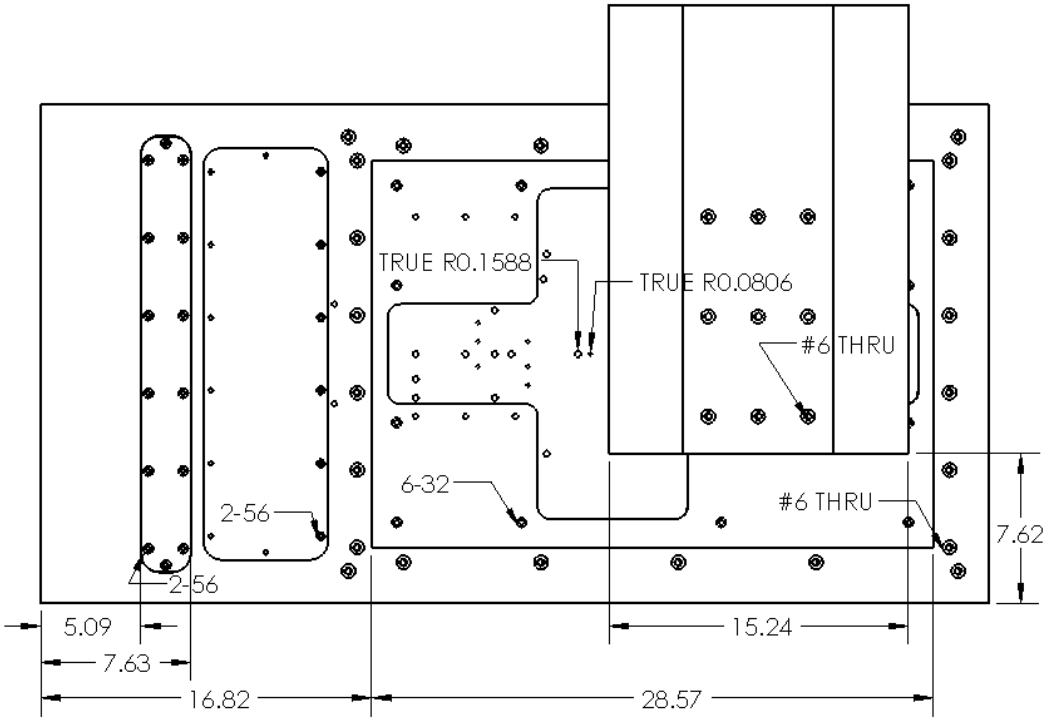

Figure 56. Bottom view of wedge with dimensions in centimeters

3.2.2 Boundary Layer Trips

A study aimed at characterizing the efficacy of arrays of diamond-shaped, "NASA pizza-box," trips was carried out on the solid PEEK wedge model in the preliminary studies of Leidy et al. [175]. Semper used the same trip shape at a spacing $w_{trip}=2\delta$ and height $h_{trip}=1.33\delta$, where δ was defined as the point at which the total enthalpy recovers to 99.5% of the freestream value [28]. Knowing that transition could be initiated by relatively close and tall trips, the purpose of the trip study was to determine if other configurations could trip the flow more effectively with less of a lasting effect to the mean flow.

Reshotko and Tumin suggested that the spanwise disturbance wavelength should be 3 to 3.5 times the boundary layer thickness for optimal disturbance growth [176]. Therefore, trips were

made with w_{trip} ranging from 2-5δ, where δ is approximately 3.2 mm (0.125 in.) as estimated from schlieren imaging and analytically from [177] for a freestream Reynolds number of 3M/m. Figure 57 shows a top view of the solid PEEK wedge with the geometry defined and the parameters that were adjusted in preliminary testing denoted in red. The corner-to-corner trip span was set to the boundary layer thickness. Trip heights of h_{trip}=0.3δ, h_{trip}=0.6δ, and h_{trip}=δ were tested.

The trips inserts were printed of polycarbonate in layers 0.18 mm (7 µin.) thick. They were fastened to the back of the wedge with #2-56 screws that could be adjusted to make the insert-wedge interface flush on the testing surface. The inserts were taped over on the back of the model to prevent jets or suction to the upper surface. Preliminary tests showed the front row of trips to be most effective, so the rear row was fitted with a blank insert for the data presented here.

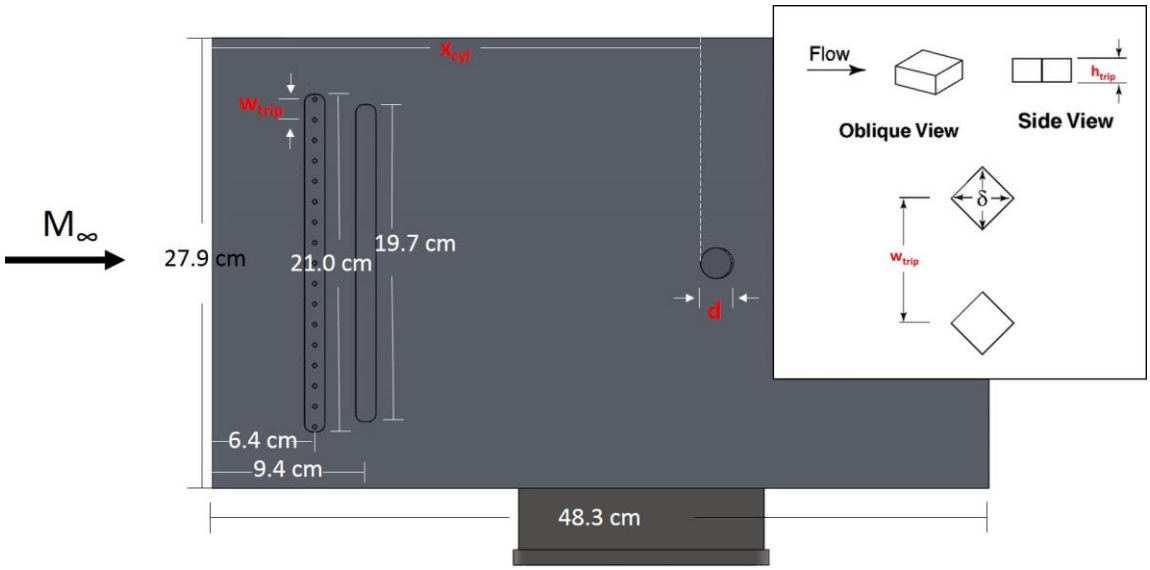

Figure 57. Top view of wedge and trip row details with adjustable parameters in red

Separation distances observed in oil flow visualization (L_{sep}) were used for these preliminary experiments to characterize the state of the SBLI based on the dependence of separation on

boundary layer state reported in literature. Tests were conducted at two Reynolds numbers (5M/m and 7M/m) for the spanwise trip arrays described above. A summary is given in Table 2.

Table 2. PEEK model oil flow visualization summary

Run Number	Cylinder x-loc (cm)	Re (M/m)	w_{trip} (δ)	h_{trip} (δ)	L_{sep} (d)
2957	38.1	5.1	2	0.6	3.5-4.0
2958	38.1	4.9	3	0.6	5.5-6.0
2959	30.5	5.0	3	0.6	6.0-6.5
2963	30.5	7.0	2	0.6	2.7
2964	30.5	5.2	4	0.6	5.5-6.0
2965	30.5	7.1	4	0.6	3.5-4.5
2966	30.5	7.1	5	0.6	3.5-4.0
2967	30.5	4.8	5	0.6	6.0-6.5
2969	30.5	4.9	5	0.3	6.0-6.5
2971	30.5	7.0	5	0.3	6.0-7.0
2972	30.5	5.0	4	0.3	6.5-7.0
2973	30.5	7.0	4	0.3	6.0-6.5
2984	30.5	7.1	4	0.6	3.5-4.5
2985	30.5	5.0	4	0.6	5.5-6.0

These tests showed separation scaling consistent with laminar, transitional, and turbulent, boundary layer states. Figure 58 gives a representative run for each state.

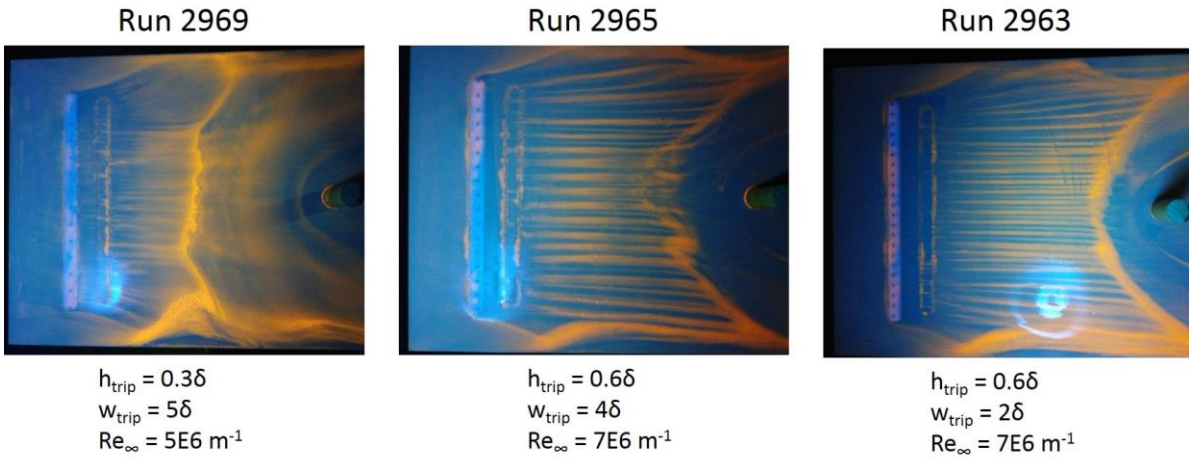

Figure 58. Oil flow showing the effect of different trips on the interaction state. The interaction is laminar (left), transitional (center), and turbulent (right)

Table 2 suggests that the farther spaced trips were less effective in triggering transition based on larger oil flow separation distances (L_{sep}) when compared $w_{trip}=2\delta$ for the same Reynolds number. The L_{sep} value of 2.7d from ACE Run 2963 is consistent with the data presented by Westkaemper for a turbulent incoming boundary layer [40]. This trip configuration was the only to produce a pattern consistent with a turbulent interaction at Re=7M/m. Since all three interaction states could be achieved by varying the Reynolds number, the $h_{trip}=0.6\delta$, $w_{trip}=2\delta$ array (32 total elements on the composite wedge) was used for all subsequent testing.

3.2.3 Cylinder Characteristics and Placement

Preliminary IR thermography runs were conducted with either a 19.1 mm (0.75 in) or 31.8 mm (1.25 in.) diameter cylinder positioned 26.7 cm (10.5 in.) downstream from the leading edge. The cylinder height was only 31.8 mm (1.25 in.) for both diameters tested, so it did not meet the minimum H/d=2.4 criteria set forth by Dolling and Bogdonoff [32]. From these tests, it was evident

that the 31.8 mm diameter cylinder that met the asymptotic height criterion would cause too much blockage and the interaction region was quite large, so it could be influenced by edge effects on the wedge. Under the same train of thought, more recent oil flow and schlieren runs were conducted using a 12.7 mm (0.5 in.) diameter cylinder. Diameter reduction to this extent did not prove to be helpful as the separation line still extended to the span, a smaller cylinder would reduce the resolution of measurements when scaled to the cylinder diameter, and, most importantly, using the 12.7 mm diameter cylinder significantly reduced the interaction disturbances, which lessened the quality of the schlieren. Therefore, a cylinder 19.1 mm (0.75 in.) in diameter and 57.2 mm (2.25 in.) in height was used for all composite model testing. The cylinder was made of black PEEK, allowing for IR thermography on its surface.

The placement of the cylinder was optimized based on the ability to generate three interaction states and minimize other factors that could influence the SBLI. From the oil flow runs in [175], it was clear laminar, transitional, and turbulent interactions could be established, given our tunnel unit Reynolds number range, with the cylinder positioned 0.305 m (12 in.) downstream of the leading edge. This position was not optimal for the schlieren as the interaction could not be observed given the existing doors. Therefore, tests were conducted with the cylinder positioned 0.406 m (16 in.) downstream of the leading edge, which still allowed for the boundary layer states. However, other flow features came into view at that position. A shock originating from the nozzle / test section interface met the cylinder just above the supersonic jet. Also, the strut would have more of an influence of the left side of the wedge with the cylinder that far downstream. Therefore, the cylinder was placed 0.305 m downstream and new doors were fabricated to facilitate schlieren imaging of the separated region.

Following tests with a right cylinder perpendicularly mounted to the wedge, various (15-degree forward, 15-degree back, and 30-degree back) swept 19.1 mm diameter cylinders were tested at the same streamwise mounting location to determine the effect of sweep angle on the separation region extent and dynamics for different SBLI states. A sketch depicting the cylinder configurations relative to the wedge is given as Figure 59.

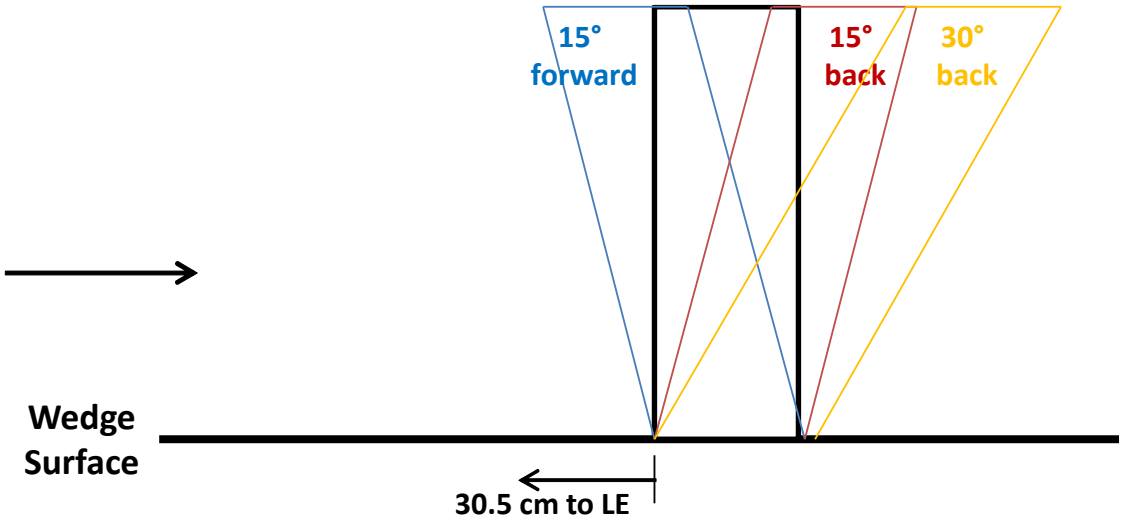

Figure 59. Side view showing swept cylinder positioning

3.2.4 Model Mounting

The model was bolted to a strut which was fastened on a removable door. A triple-jointed monitor display frame connected the door to the external extruded aluminum frame that surrounded the tunnel and allowed for the door to easily move into and out of position. A cut-away schematic showing this configuration as well as the position of the IR camera for most of the early

runs (up to ACE 3010) is given in Figure 60. For the composite model runs, the camera utilized a 50-mm lens and was positioned farther from the model (Figure 69).

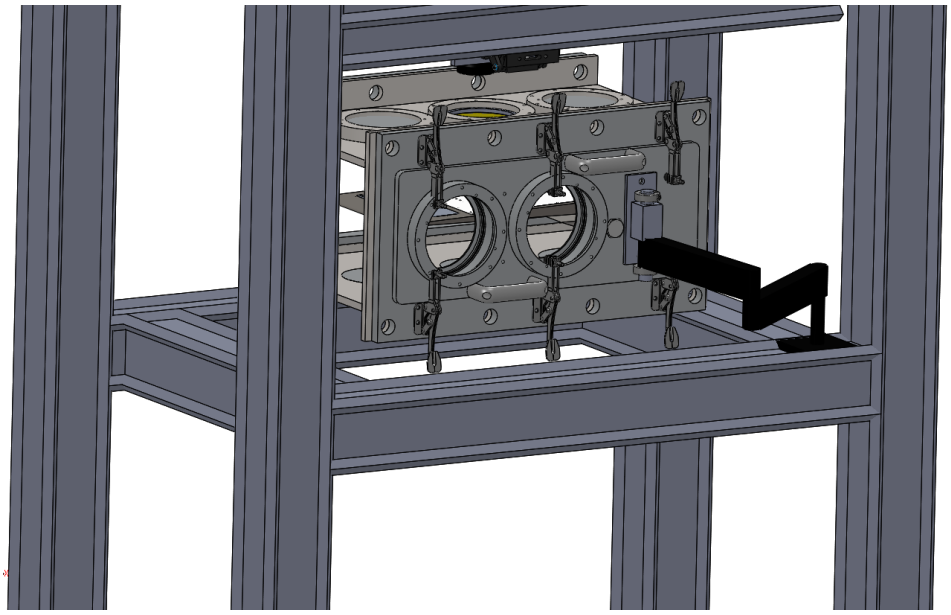

Figure 60. Cutaway image showing removable door

Tunnel preheating was executed with a blank door in place. When preheating was completed, the blank was removed and the model rotated into position. Positioning the model outside of the flow during the tunnel preheating allowed for the initial model temperature to be consistent between runs. It also allowed for larger changes in temperature to occur, which works to reduce the uncertainty in the calculated heat flux. Another benefit to this setup was that oil could be applied more easily outside of the tunnel for surface visualization runs.

3.3 Experimental Characterization

Surface laser profilometer scans from the leading edge to behind the trips of both wedge models were made to provide, with more precision than the design drawings, the exact geometry tested. These scans also provide information regarding surface roughness height and periodicity. Scans from the fully PEEK model and the composite model are given in Appendix E.

The freestream conditions were characterized at the location of the model leading edge using a hot-wire anemometer and a Kulite pressure probe. The data collection techniques were similar to those reported in Sections 3.4.1 and 3.4.3, respectively. These results are presented in Section 4.3.

3.4 Diagnostics

Section 2.2 reviews the techniques used in past experimental campaigns to characterize cylinder-induced SBLIs. This section will describe the facility-specific methods for the techniques related to this campaign.

3.4.1 Hot-wire Anemometry

In addition to characterizing the freestream environment, a hot-wire anemometer was used to evaluate the incoming boundary layer at various streamwise and spanwise positions, measure the jump across the leading-edge shock at three streamwise stations, and assess content in the wake of the cylinder. Hot-wires are sensitive to both total temperature and mass flux. The wire temperature loading factor was set to τ=0.8 (T_w=774K), which was intended to effectively isolate the mass flux sensitivity. Mass flux measurements were made using a 6.3 micrometer (0.25 µin.) diameter

TSI hot-wire and manually-adjusted A.A. Lab Systems AN-1003 constant temperature anemometer (CTA), set in its 1:1 symmetric bridge mode and shown in Figure 61.

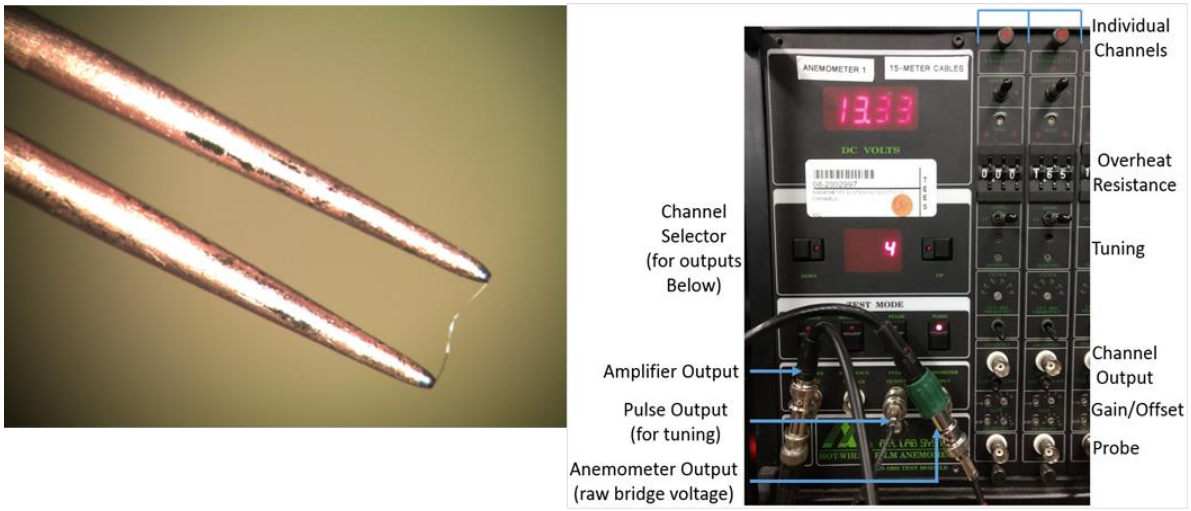

Figure 61. TSI hot-wire probe (left) and A.A. Lab Systems user interface (right)

The wire was tuned in the flow by adjusting the damping and ferric screws on the interface to maximize the flat-response frequency range. The wire responses to pulses before, during, and after the tuning run are shown in Figure 62. These plots were monitored in real-time using a National Instruments PC1-5122 digitizer/oscilloscope card and an NI SignalExpress Project. The 3-dB roll-off, as indicated by the horizontal dashes in Figure 62 (right) did not occur until above 180 kHz at the tuning Reynolds number of 5M/m. In general, the tuning tends to improve slightly with increased Reynolds number until a point where the wire becomes unstable. No effort was made to adjust for the reduced response from 10-180 kHz relative to the response below 10 kHz.

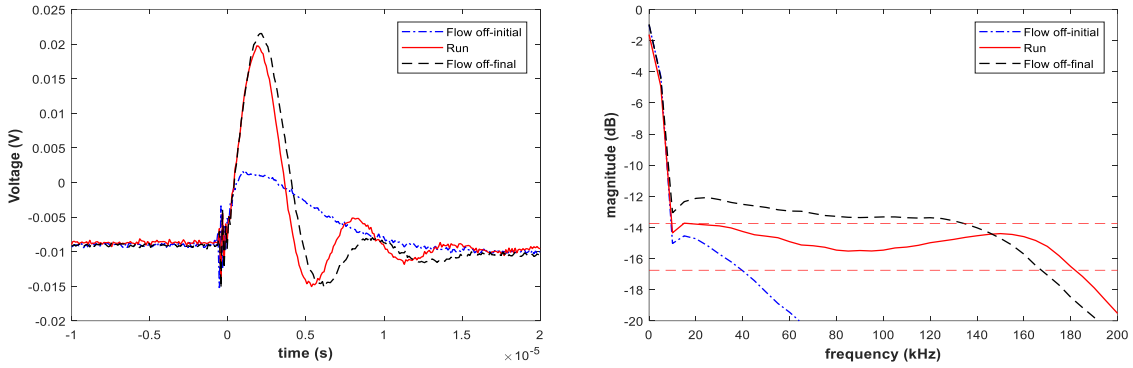

Figure 62. Hot-wire tuning pulse test: temporal (left) and frequency response (right)

The tunnel was started at a low Reynolds number for each run to maximize the chance for wire survival. With the flow established, the anemometer was switched to "operate", and the tunnel pressure was quickly ramped above the testing condition, held for a few seconds, and then brought to condition. This procedure was done to minimize the variation in total temperature during the run. Following data collection, the Reynolds number was intentionally reduced prior to unstart to help preserve the wire.

Calibration Run 3346 shown in Figure 63 underscores the effect of total temperature on the output voltage for a given mass flux. The total temperature was continually increasing with Reynolds number on the ramp up. At the peak mass flux, the tunnel was near its nominal 430 K and held that condition for the duration of the ramp down. The curve representing the ramp up portrays a lower mass flux than that on the ramp down due to the total temperature difference. The power law fit constants (general form of Kings Law [178] – Eq. (3.5)) for the two calibration up and down ramps are presented in Table 3.

$$V_B^2 = A + B(\rho u)^n \tag{3.5}$$

where V_B^2 is the bridge voltage, ρu is the mass flux and A, B, and n are calibration constants.

Table 3. Hot-wire calibration constants for King's Law

Wire S/N	Run number	Re_∞ range (M/m)	A	n	B
71331007	3346	1.7→5.9	0.881	0.694	1.997
71331007	3346	5.9→0.55	0.499	0.859	2.456
71331006	3481	2.6→5.7	1.345	0.569	0.793
71331006	3481	5.7→0.72	0.495	0.824	2.333

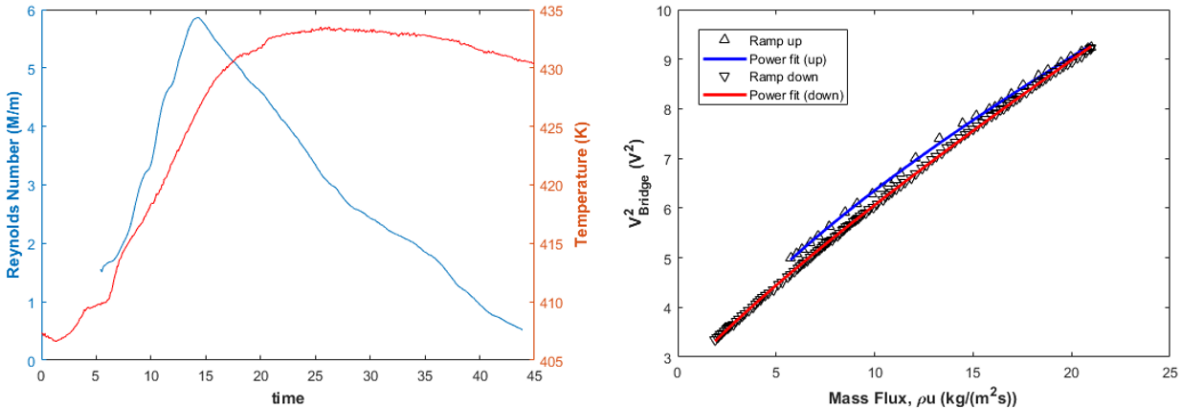

Figure 63. Temperature effect on hot-wire calibration curve

The power law fit can be modified to account for the variation in total temperature by adding a normalization factor [179]. The total temperature normalized equation is given as Eq. (3.6), and these curve-fit constants are in Table 4. Figure 64 shows data from the same Run 3346 and the corresponding fit. The data from the Reynolds number ramp up and down show significantly better agreement. Temperature normalized calibrations were used to calculate mass flux for the hot-wire surveys presented in Section 5.1.

$$\frac{T_t}{430K}V_B^2 = A + B(\rho u)^n \tag{3.6}$$

where T_t is the tunnel total temperature in K.

Table 4. Temperature normalized hot-wire calibration constants

Wire S/N	Run number	Re_∞ range (M/m)	A	n	B
71331007	3346	0.55-5.9	0.599	0.804	2.298
71331006	3481	0.72-5.7	0.586	0.776	2.168

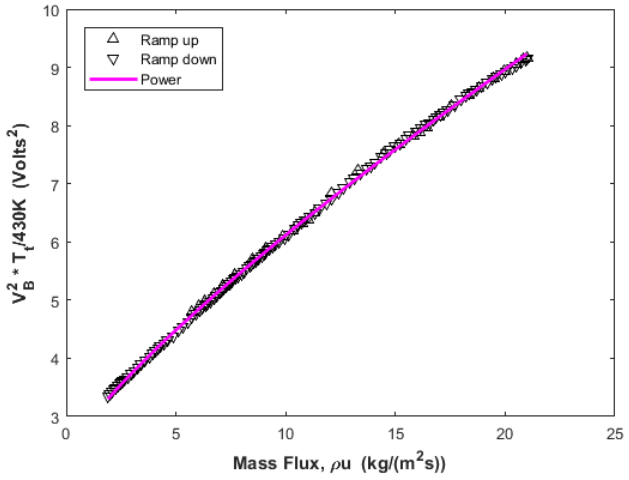

Figure 64. Total temperature normalized hot-wire calibration curve

The motion of hot-wire was coupled to a two-axis traversing system consisting of two Aerotech PRO165 linear stages with stated 6-micron resolution in both directions (vertical and spanwise relative to the model). Due to tunnel vibration and potential misalignment of the traverse structure relative to the tunnel, the estimated uncertainty in the distance above the model and the spanwise coordinate was estimated as 0.1 mm based on schlieren and infrared imaging, respectively. Figure 65 depicts the experimental setup and the positioning of the diagnostics. Figure 66 provides a closer look at the sliding seal that enables transverse motion of the probe (left), along with the hot-wire anemometer positioned in the tunnel (right).

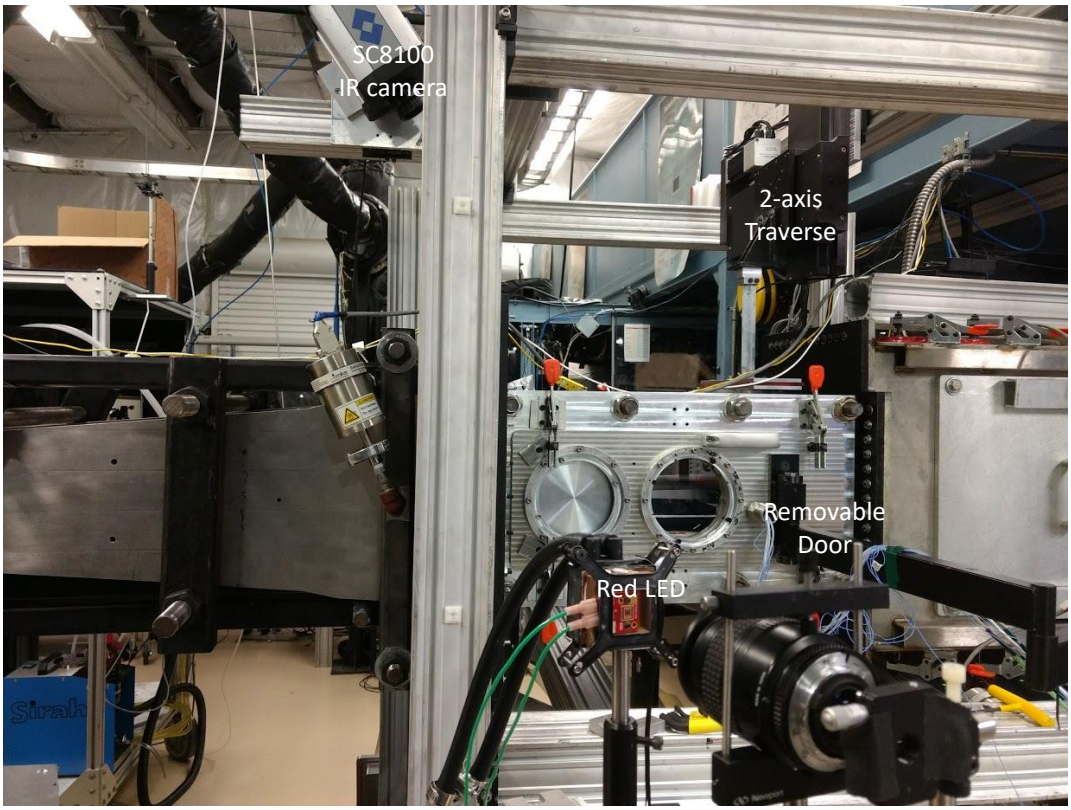

Figure 65. Photograph of hot-wire setup

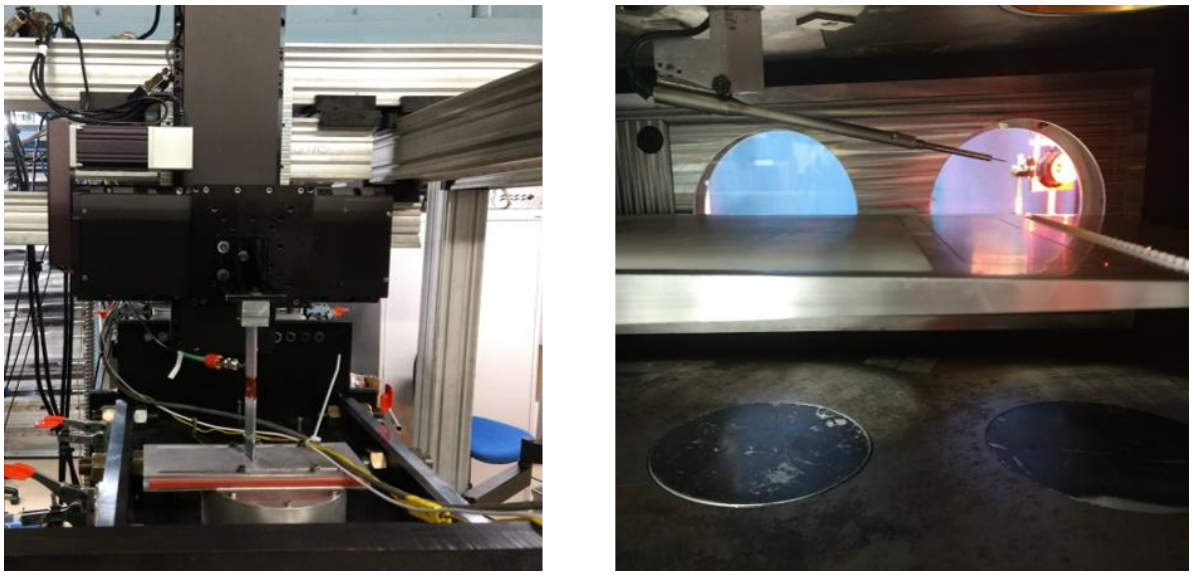

Figure 66. Hot-wire traverse sliding seal (left) and probe in tunnel (right)

From the anemometer interface, the "anemometer output" signal is the raw bridge voltage, and the "amplifier output" signal is the bridge voltage with an applied gain and offset from within the anemometer. Four different signals were sampled at 500 kHz for each run. These signals included **(1)** the amplified output (*x1.5* gain), **(2)** the amplified low-pass output – filtered at 200 kHz using an 8-pole Bessel filter element in a Krohn-Hite chassis, **(3)** the amplified low-pass filtered output – split from (2), and then – AC coupled (1 kHz) and gained (*x2*) by a Stanford Research Systems SR560 low-noise preamplifier and filter, and **(4)** the raw bridge voltage output directly from the anemometer. All of these signals were evaluated against each other for consistency in terms of output voltage magnitude and fluctuation levels. Similarly, AC- and DC- coupled signals were sampled for the freestream pressure measurements. Sampling time for each point was generally 100 ms.

Data were acquired by a linking of two NI USB-6366 X-Series DAQ systems, each of which had 8 channels and a maximum sampling rate of 2 MS/s per channel (the FastDAQ). Three channels were used to obtain tunnel conditions (total temperature, total pressure, and static pressure), leaving up to 13 fast-channels to sample the hot-wire anemometer, pressure transducers, or a camera trigger. A LabVIEW code, written in-house and modified by this author, controlled the traverse and was generally configured to sample only the number of channels required for a given test in order to minimize each file size. The front panels of this and other virtual instruments (VIs) utilized during the campaign are presented and explained in Appendix I. The motion of the Aerotech PRO165 linear stages could also be controlled using Ensemble Motion Composer software.

3.4.1.1 Boundary Layer Surveys

Accurate measurements of the inflow conditions are critical to the evaluation of the behavior of the SBLI. Hot-wires were chosen for the boundary layer profiles because they enable higher frequency measurements at finer spatial resolution than pitot probes. The purpose of these measurements was to characterize the boundary layer entering the interaction region, so the cylinder was removed from the wedge for these experiments. It should be noted that these are not true boundary layer profiles as the traverse moves vertically within the tunnel and the surface of the wedge is 1.3 degrees relative to horizontal; however, the difference is streamwise position that this creates is negligible for the analysis conducted herein. Boundary layer surveys were executed with (Runs 3357-73; 3378-90) and without (Runs 3471-75) the trip array. The positions for survey points were determined prior to each run and were saved as a .csv file that was read into the LabVIEW VI.

The initial probe position was generally outside of the boundary layer. The probe was typically stepped down to the wall in 6 relatively large steps. It was then raised in millimeter or submillimeter increments. The purpose of this strategy was to provide a coarse survey of the entire boundary layer in case the tunnel unstarted or the wire broke during the upward traverse. The upward moving survey was typically given more clout due to its finer resolution and less variation in the tunnel conditions. However, the mass flux and fluctuation profiles rarely had much discrepancy for repeated points on the upward and downward surveys. After each traversing step, the probe would settle and was sampled at 500 kHz for 100 ms. Several samples were taken at each position for initial surveys. The data (mass flux, mass flux fluctuations, and spectra) were similar for each sample at a given location, providing confidence that the probe was properly settled for

each measurement after movement. Figure 67 depicts the location of the surveys relative to the surface of the model. A summary of hot-wire surveys is provided in Table 5.

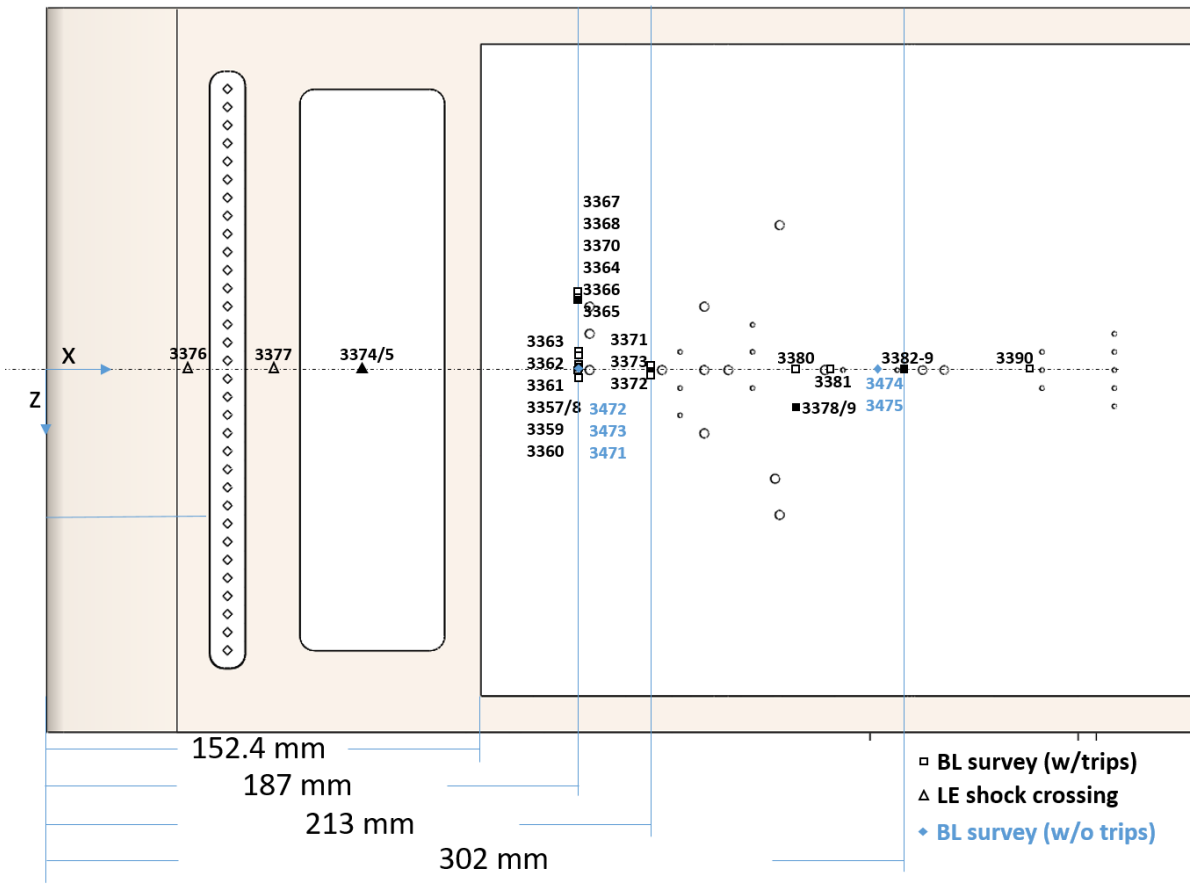

Figure 67. Hot-wire measurement locations

Table 5. Placement of hot-wire surveys

Run Number	Streamwise coordinate, x (mm)	Spanwise coordinate, z (mm)	Normal distance range, y (mm)	Re_x
3357	187	-0.7	1.5-10.9	9.2E5
3358	187	-0.7	2.9-21.9	9.1E5
3359	187	0.9	2.5-19.0	9.4E5
3360	187	3.4	3.2-21.7	9.2E5
3361	187	-2.5	3.4-21.4	9.0E5
3362	187	-4.1	2.8-18.8	9.0E5
3363	187	-6.1	3.0-17.5	9.1E5
3364	187	-24.6	2.4-16.4	9.5E5
3365	187	-24.0	2.2-20.7	9.3E5
3366	187	-24.2	3.1-19.1	9.1E5
3367	187	-29.0	2.7-20.2	9.4E5
3368	187	-27.2	2.7-22.2	9.5E5
3370	187	-24.8	3.2-21.7	9.1E5
3371	213	-1.6	2.7-19.7	1.06E6
3372	213	2.0	2.8-21.3	1.06E6
3373	213	-1.0	3.2-15.6	1.09E6
3374	106	≈0	16.4-46.4	5.2E5
3375	106	≈0	16.1-42.1	5.3E5
3376	58	≈0	16.9-36.9	2.9E5
3377	82	≈0	5.8-38.8	4.2E5
3378	264	9.9	5.6-29.6	1.31E6
3379	264	9.9	5.4-29.4	1.29E6
3380	264	0.0	3.8-28.8	1.32E6
3381	276	0.6	4.3-32.3	1.35E6
3382	302	0.6	3.2-28.1	1.48E6
3384	302	0.5	3.5-28.5	2.26E6
3385	302	0.8	3.4-28.4	2.25E6
3387	302	1.0	2.3-27.2	2.08E6
3388	302	0.8	15.0	11-22E5
3389	302	0.8	15.0	2-15E5
3390	346	0.8	3.0-20.0	2.57E6
3471	187	0.4	1.6-21.6	9.0E5
3472	187	-1.6	0.8-20.8	8.9E5
3473	187	0.0	1.5-21.5	8.9E5
3474	293	-1.2	2.9-22.9	1.36E6
3475	293	0.7	3.3-23.3	1.42E6

3.4.1.2 Leading-Edge Shock Traverses

Hot-wire measurements were made across the leading-edge shock, near the center span, at different streamwise locations to quantify the effects of the shock on freestream disturbances (Runs 3374-3377). The process for taking these data was essentially the same as for the boundary layer surveys without emphasis on getting close to the wall. Line sketches of the approximate vertical extent of the scans are overlaid on a schlieren image in Figure 68. Note that the schlieren setup was not aligned perfectly with the model. This manifests in some distortion in the image, most notably on the trip array and shocks, which appear thicker than they were in reality.

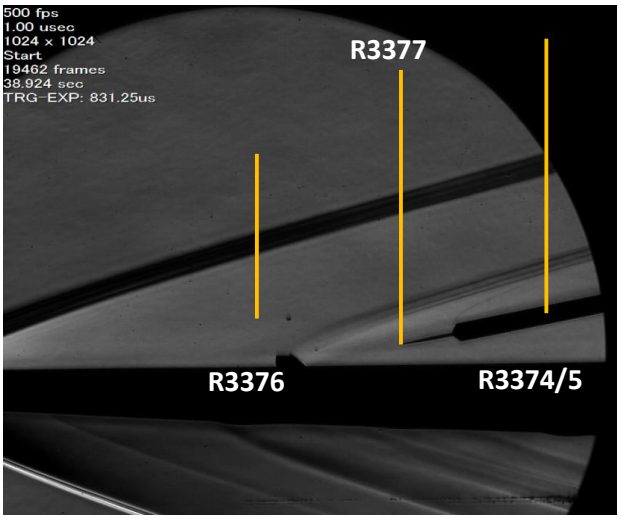

Figure 68. Approximate hot-wire probe paths (vertical yellow lines) for characterization of the leading-edge shock, overlaid on a schlieren image.

3.4.1.3 Cylinder Wake

The cylinder was added to the wedge testbed for these hot-wire runs in an effort to measure dominant shedding frequencies within the wake. Surveys were taken at two stations. The first was above a surface mounted Kulite sensor and the second was 1.7*d* downstream of the cylinder center

and 2.0*d* off centerspan, the position recommended by Danehy and measured by Wheaton behind a cylindrical roughness element [85]. The sampling time was extended for these wake surveys from 100 ms to 400 ms at each point. This reduced the uncertainty due to random errors and was made possible because fewer sampling points were required since the spatial resolution for these measurements was not as critical as for boundary layer surveys.

3.4.2 Oil Flow Visualization

The fluorescent oil was a well-mixed solution of Blaze Orange pigment sample from Day-Glo Color Corp. and 100 cSt (10^{-4} m^2s^{-1}) Esco silicon fluid in a volumetric ratio of 1/4 teaspoon to 1 fluid ounce (1:24). Preliminary oil flow tests were conducted on each model to test for flow directionality and uniformity over the model surface. The oil was distributed as roughly 13 mm (0.5 in.) diameter dots spaced approximately 38 mm (1.5 in.) apart along the span at different streamwise stations. Tests to observe the surface streaklines within and around the SBLI involved painting a thin coat of oil across the span from roughly 152 mm (6 in.) upstream of the cylinder to the back of the wedge. This essentially meant painting the entire PEEK insert on the composite model.

Prior to every run, the model surface was wiped with an acetone-covered cloth to remove any residual dust or oil from prior tests. The elimination of oil from previous tests was especially important as its signature would be seen in subsequent testing. New oil was applied to the model after the tunnel preheating, immediately prior to its insertion for testing. A Nikon D5000 camera was mounted above the test section center window port to track the oil flow during the preliminary model runs and the initial interaction runs. Blacklights were directed through the same window to illuminate the fluorescent oil.

The oil flow visualization test runs required a modification to the ACE standard operating procedure. After running the tunnel for 15 seconds (the surface streakline pattern was well-established by this time), the tunnel supply ball valve located just upstream of the settling chamber was closed prior to the normal shutdown sequence. Therefore, only a small amount of air passed over the model following the tunnel unstart. The Nikon footage indicated there was never an appreciable shift in the oil pattern due to the unstart, or ensuing air passage, when following this procedure. The model was then removed from the tunnel, and a door-blank was secured in its place. The blacklights were quickly positioned above the model. Pictures were taken using a 16-megapixel Motorola Moto G4 Plus phone camera of the final oil configuration. These were taken within 5 minutes of model removal since, after that time, the oil and pigment showed signs of separation and spread, creating unnecessary additional uncertainty in the measurement. The image capturing process was generally performed in concert with the tunnel operator draining the supply line.

3.4.3 High-Frequency Surface Pressure Measurements

PCB and Kulite fast-response pressure transducers provided dynamic surface pressure measurements on the solid PEEK and composite wedge models. The PCB and Kulite specifications are listed in Tables 6 and 7, respectively. The PEEK model utilized two PCB model 132A31 sensors, each of which had split black and red leads connected back to the sensor. The composite model used as many as six of the newer model 132B38 sensors for a given run. The 132B38 sensors have a coaxial cable attachment, a round (as opposed to square) sensing element, and better placement of the sensing element in the center of the sensor face. Both PCB models were powered by an in-line signal conditioner from the manufacturer. The conditioner provided a constant 4 mA

excitation current to the built-in amplifier. The PCB output is high-pass filtered by built-in electronics and has a stated 3-dB cutoff at 11 kHz. The stated resonant frequency for both models is above 1 MHz, and the response is reported to be flat to approximately 300 kHz [180]. Attempts to calibrate the sensors in a shock tube are ongoing at Purdue University [153].

Table 6. PCB 132B38 transducer specifications

Property	Value	
Measurement Range	345 kPa	50 psia
Full-Scale Output	7V (nom.)	
Resolution	7 Pa	0.001 psi
Temperature Range	248 to 352 K	-13 to 175 °F
Diameter	3.18 mm	0.125 in.
Resonant Frequency	>1MHz	

The Kulite pressure transducers used in this campaign were model XCE-062-15A. These sensors are described by the manufacturer as "high temperature and ultraminiature," but they also share the same sensitivity specifications as the XCS-062-15A sensors used by Murphree [159]. The sensors used in this campaign were A-screen, meaning the sensing element for each transducer is recessed in a cavity. While the diaphragm resonant frequency is around 200 kHz, the screen limits the flat response to roughly 80 kHz [181].

The Kulite transducers were connected to a custom-built power supply and conditioning box built by J.W. Hofferth. The circuit design was modified from one developed by the S.P. Schneider research group at Purdue University. The box provided a DC and AC signal output for each sensor. The original signal was gained by 100 and low-pass filtered with a first-order RC circuit at 482.5 kHz to generate the DC output. This signal was further refined by high-pass filtering at 842 Hz and gaining by 28.9 to produce the AC output.

Table 7. Kulite XCE-062-15A transducer specifications

Property	Value	
Measurement Range	0-103 kPa	0-15 psia
Full-Scale Output	100 mV (nom.)	
Diameter	1.7 mm	0.066 in.
Resonant Frequency	200 kHz	
Combined Error (non-linearity, hysteresis, and repeatability)	0.1% FSO BFSL (typ.)	
Compensated Temperature Range	298 to 508 K	80 to 450 °F
Temperature Sensitivity Shift	± 1.8%/100 K	± 1%/100 °F
Temperature Zero Shift	± 1.8%/100 K	± 1%/100 °F

The AC-coupled PCB and Kulite signals were generally low-pass filtered at 1 MHz and 200 kHz, respectively, using 8-pole Bessel filters of unity gain for anti-aliasing. The filtering units were housed within 2-channel Krohn-Hite FMB3002 chassis. Occasionally, a PCB was instead low-pass filtered at 1 MHz and unity gain through a Stanford Research Systems SR560 low-noise preamplifier and filter.

The oil flow visualization results aided in determining the location of the pressure ports on both models. Justification for the positioning of each port on the composite model is provided in Section 4.2.

Many pressure sensor configurations were tested on the composite model, but no more than 5 PCBs and 4 Kulites were ever run at a time. These sensors were rotated to take measurements at all port locations. The configurations for all runs are defined in the Pressure Transducer Configuration Table (Appendix G). Unused ports were plugged using either steel or Teflon rod stock. Effort was made to mount both the sensors and plugs flush with the surface, and both plugs and sensors were sealed from the back of the PEEK insert with fingernail polish. Testing different

sensors at the same port for similar flow conditions was important to verify repeatability. It also helped to indicate whether features within the spectra were sensor specific.

Spectra (PSDs) from these measurements were generated using Welch's method. In general, a Hamming window was used of size 1024 (2^{10}) with 50% overlap, which led to a frequency resolution of roughly 2 kHz.

3.4.4 Infrared Thermography

The FLIR SC8100 was used to measure the surface temperature of the model. The indium antimonide detector is sensitive to mid-wavelength infrared radiation within the range of 3-5 micrometers. The camera can sample at 132 frames-per-second (fps) at a resolution of 1024 x 1024 pixels and is capable of detecting temperature differences as small as 25 mK [182]. Tests conducted on the fully PEEK model utilized a 17-mm lens, with the detector positioned approximately 0.18 m (7.0 in.) above the wedge surface. Tests performed on the composite model utilized a 50-mm lens, with the detector located 0.61 m (24 in.) from the surface. The later configuration proved to introduce less barrel lens distortion.

The camera was generally positioned above the wedge and directed vertically down to visualize the interaction heating on the model surface. However, there were some runs where the heating on the cylinder was of interest, so the camera was moved upstream and directed back at 34 degrees with respect to vertical for those runs. Figure 69 presents a diagram of both configurations.

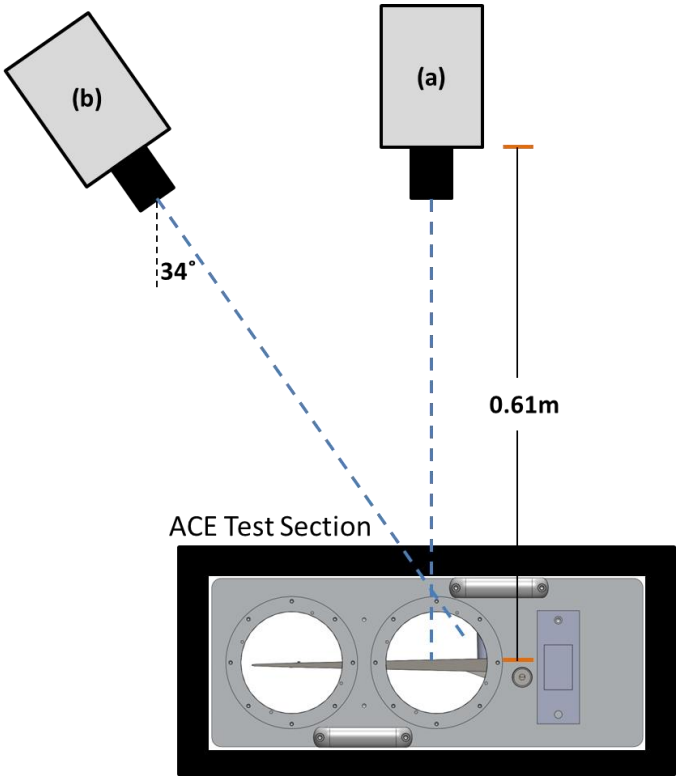

Figure 69. IR camera configuration for measurements on (a) wedge surface and (b) cylinder face

The camera was calibrated using an anodized aluminum calibration plate for 4 different integration times (1 ms, 2 ms, 4 ms, 8 ms), known as "presets" in the FLIR ResearchIR software, which was configured to collect the data. More details about the calibration are reported in Appendix F. Most of the test runs in this campaign used the 1 ms and 8 ms exposure presets, with each sampled at 15 Hz. The 1 ms exposure allowed for measurements up to 415 K, which was higher than the temperature seen at any location within the interaction region at any time during the run. The 8 ms exposure allowed for more precise temperature measurements below 325 K, which proved helpful for characterizing the flow upstream of the SBLI.

Data collection was manually triggered at the opening on the 4 in. air-line supplying the ejector. From there, 1024 x 1024 resolution data were sampled at 15 Hz for the duration of the run

and tunnel unstart. The unstart of the tunnel caused a sudden frame-to-frame jump in surrounding temperature that was used to link the IR dataset to the tunnel conditions for each run.

In order to achieve a better understanding of the heating distribution on the front of the cylinder, a first-order coordinate transformation was applied to produce maps in the local spanwise-normal (z-y) coordinate system, followed by some interpolation to get the cylinder co-ordinates theta-wedge normal (theta-y). The coordinate transformations for a sample temperature map are shown in Figure 70.

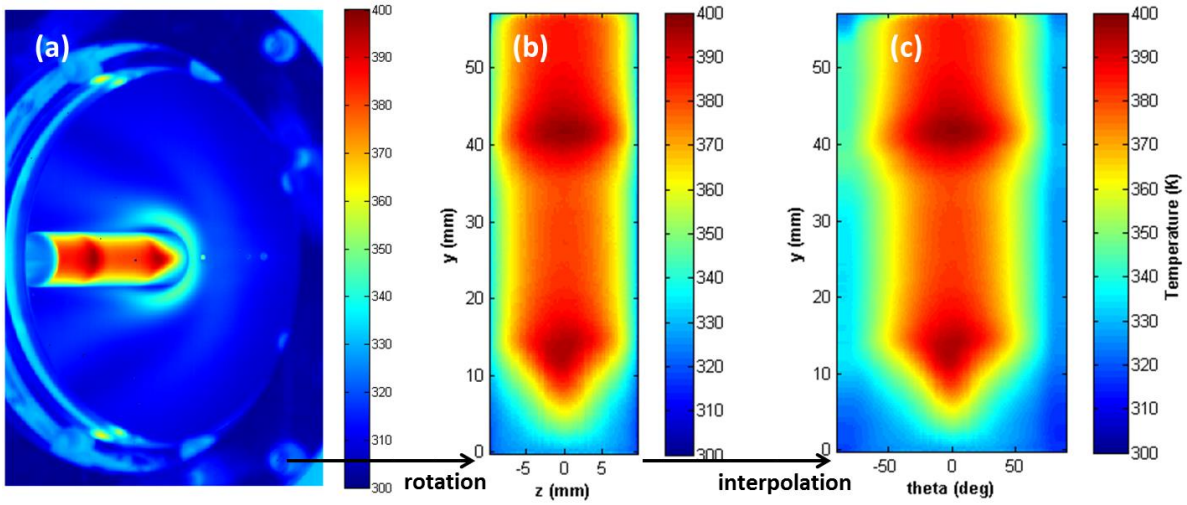

Figure 70. Temperature map coordinate transformation from (a) raw field-of-view to (b) front of cylinder to (c) around front of cylinder, for a sample frame within Run 3484

There are, however, some cautions when interpreting these temperature values. For example, the coordinate transformation is first-order, so no correction has been made for distance from the lens; it is purely a rotational transformation. As a consequence, there is minor distortion in the transformed images that manifests in contraction at the base of the cylinder and stretching near the

top. Another caution is the effect of directional emissivity. The emissivity coefficient (ε) of the surface depends on the angle (θ) between the direction normal to the emitting surface and the direction of the emitted radiation (the viewing angle). This relationship is described by Eq. (3.7).

$$\varepsilon(\theta) = \varepsilon_n \cos(\theta)^{\frac{a}{b\cos(\theta)}} \tag{3.7}$$

where ε_n is the emissivity value when viewed normal to the surface, and a and b are fitted constants. Cerasuolo [183] studied the directional emissivity of PEEK and found ε_n=0.91, a=0.030, and b=1.35. The camera signal is a function of the emissivity, and its effect can be propagated through the non-linear relationship to temperature. Running [184] suggested viewing angles greater than 60 degrees reduce the emissivity enough to lead to significant uncertainties in heat flux. For this experimental setup, the viewing angle θ is computed using Eq. (3.8).

$$\theta = \arccos(\cos(\theta_1) * \cos(\theta_2)) \tag{3.8}$$

where θ_1 is the angle formed by the camera orientation and the front normal of the cylinder, and θ_2 represents the circumferential position on the cylinder with respect to its front. For a perpendicular cylinder, $\theta_1 \cong 55$, θ_2 values above 30 degrees will map heat flux values considerably lower than reality.

IR data from the full run were exported into MATLAB to perform calculations to convert surface temperatures to heat flux values using an in-house code, written by I.T. Neel [185], similar to that of Juliano et al. [186] and Borg et al. [187]. The heat flux map at each sampled frame was approximated from the base equation for one-dimensional conductive heat transfer, given below as Eq. (3.9).

$$q = -k \frac{\partial T}{\partial \zeta} \tag{3.9}$$

where T is the temperature and ζ is the distance into the wedge, directed opposite the wall-normal. This process followed approximating the temperature distribution within the wedge from the general equation, Eq. (3.10).

$$\frac{\partial T}{\partial t} = \alpha \frac{\partial^2 T}{\partial \zeta^2} \tag{3.10}$$

where t is time and α is the thermal diffusivity, defined as Eq. (3.11).

$$\alpha = \frac{k}{\rho c_p} \tag{3.11}$$

where k and ρ are the thermal conductivity and the density, respectively, as provided by the distributor of the PEEK (Professional Plastics), and c_p is the estimated specific heat capacity based on specifications from other distributors. These thermal properties as well as code parameters for the heat flux calculation are presented below in Table 8.

The derivatives in Eq. (3.10) were approximated using a forward-time, central-space (FTCS) scheme. This finite difference scheme is presented as Eq. (3.12).

$$\frac{T_{i+1,j} - T_{i,j}}{\Delta t} = \frac{\alpha(T_{i,j-1} - 2T_{i,j} + T_{i,j+1})}{(\Delta \zeta)^2} + \mathcal{O}(\Delta \zeta^2) \tag{3.12}$$

where the first temperature index is temporal and the second is spatial, Δt is the temporal step size given by the camera sampling frequeny of 15 Hz, and $\Delta \zeta$ is the spatial step size, which was set just above $\sqrt{2\alpha \Delta t}$ to maximize the nodes while still maintaining scheme stability. The initial temperature distribution within the wedge was set to the initial wall temperature. The time dependent surface temperature provided by the IR thermography was used as the surface boundary condition. The back-boundary condition for the solid PEEK model was isothermal (initial surface temperature) at a penetration depth of roughly half the model thickness. The PEEK insert for the composite model is backed by air, so the back-boundary condition was set to adiabatic at a depth of 6.35 mm.

For comparison, the code was also run with an isothermal boundary at the same depth, and the maximum difference in heat flux values was less than 0.1%. This is in agreement with the inability of the camera, with a <25mK sensitivity, to detect the steel frame beneath the edges of the PEEK plate during a run.

With the temperature distribution within the model approximated for the entire run, the temperature gradient at the surface was evaluated from the wall temperature and the two nodes below it. The heat flux approximation is given in Eq. (3.13).

$$q \approx \frac{-k(-\frac{3}{2}T_{n,0} + 2T_{n,1} - \frac{1}{2}T_{n,2})}{\Delta\zeta} \tag{3.13}$$

where i=n is a given time and j=0 is the surface.

Table 8. Heat flux calculation values

Thermal Properties			Code Parameters		
Thermal Conductivity	k	0.26 W m^{-1} K^{-1}	Time step	Δt	0.0667 s
Density	ρ	1310 kg m^{-3}	Node Step	$\Delta\zeta$	0.13 mm
Specific Heat	c_p	1500 J kg^{-1} K^{-1}	Material thickness		6.4 mm
Thermal Diffusivity	α	1.3E-7 m^2 s^{-1}			

An important consideration when interpreting heat flux results is that heat flux varies for a given Reynolds number because the surface temperature increases during the run. More heat is transferred to a colder wall. Therefore, a more appropriate parameter that should be independent of exposure is the convective heat transfer coefficient (film coefficient), defined by Eq. (3.14).

$$h = \frac{q}{T_0 - T_w} \tag{3.14}$$

where q is the local surface heat flux, T_0 is the tunnel total temperature (replacing the more conventionally used T_{aw}), and T_w is the local surface wall temperature. Independence from the

freestream conditions is achieved through further reduction to the Stanton number, which is a non-dimensional parameter that indicates the ratio of convective heat transfer to the thermal capacity of the fluid. In effect, it further normalizes the film coefficient by the freestream mass flux and specific heat of the air. Stanton number is defined by Eq. (3.15).

$$St = \frac{q}{\rho_\infty u_\infty c_p \left(T_0 - T_w\right)} \tag{3.15}$$

3.4.5 High-Speed Schlieren Imaging

High-speed schlieren images were captured using a Photron FASTCAM SA-Z CMOS camera, which has a maximum frame rate of 2.1 million fps at a reduced resolution. Multiple frame rates and resolutions were used throughout this campaign to visualize the extent and dynamics of the interaction region. The shutter time was generally set to 1/800k seconds (1.25 μs) to effectively freeze the flow structure within each frame, yielding clearer images of the SBLI. The setup was similar to the z-type configuration, diagrammed in Figure 12. The light source was a red-amber (616 nm) LED lighting module model PT-121-RAX-L15l-MPH. The LED was typically run continuously at 3.4 V and 21.5 A, which was the maximum output of the adjustable power supply (Extech 382275). The light was oriented through a Nikon camera lens, which was used as a condenser to focus it onto a cut-off slit. The lens and slit were positioned such that the light was concentrated but would also fully and uniformly illuminate the parabolic mirror (Edmund Optics). After reflection off the other parabolic mirror on the imaging side of the tunnel, the light was focused onto a black razor blade, which served as the knife edge and was positioned to reduce the light intensity by a factor of approximately two. Following the cutoff, it was focused using one of

two plano-convex lenses, depending on the desired field-of-view, onto the camera detector. A photo of the high-speed schlieren imaging system is shown in Figure 71.

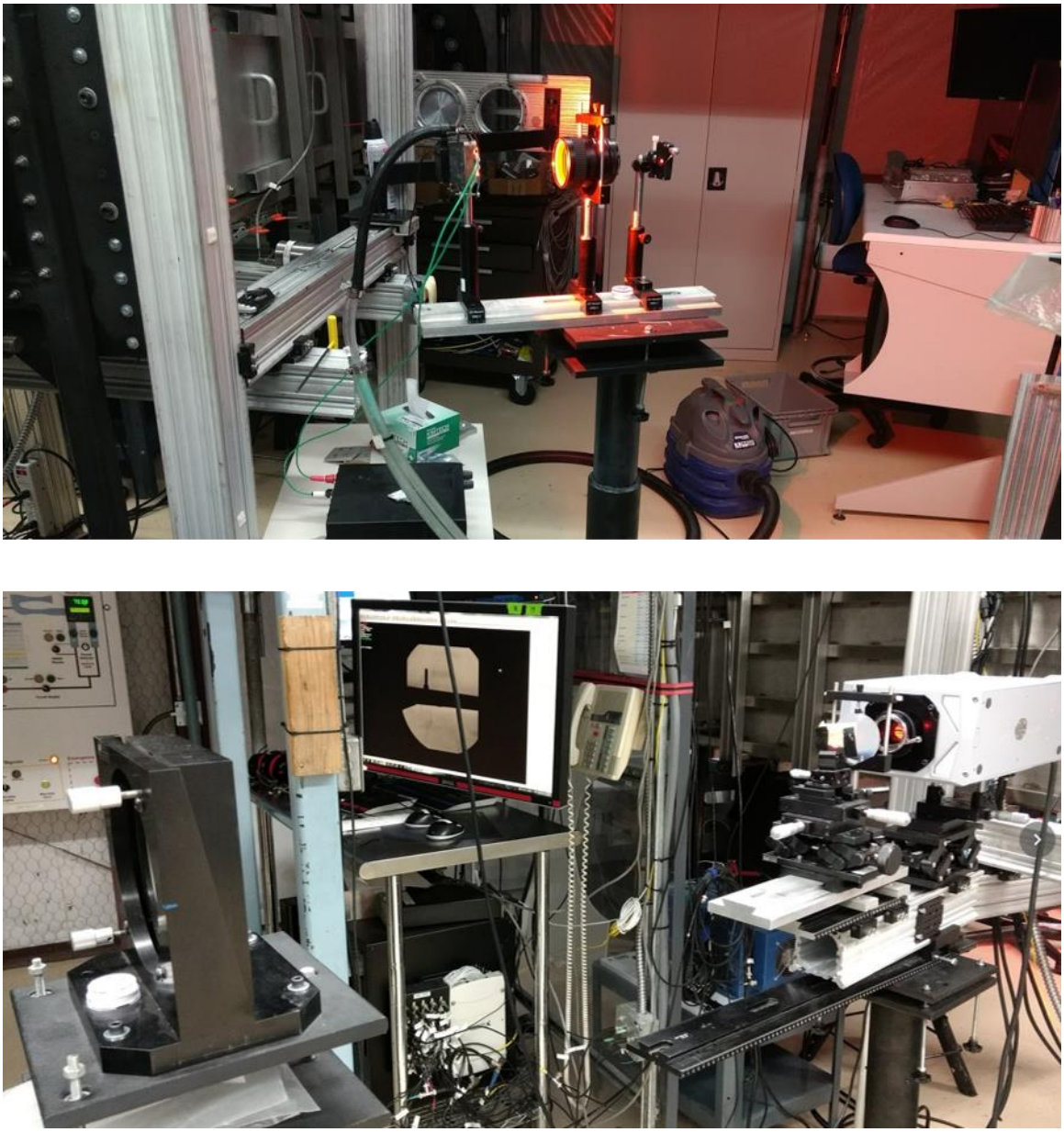

Figure 71. Schlieren setup around ACE: source side (top) and collection side (bottom)

The camera interfaced with the M6QT-DAQ PC via Ethernet cable and was controlled using the Photron FASTCAM Viewer (PFV) software package. Screenshots from the software and the settings are provided and explained in Appendix I.

Each tunnel run had a specific schlieren imaging objective. For example, some tunnel runs were Reynolds number sweeps, for which the schlieren images were acquired at 500 fps, to study the impact of the changing state of the boundary layer on the interaction region. This frame rate allowed the entire run to be captured at full 1024 x 1024 resolution. For other runs, schlieren images were sampled at much higher rates. A second group of runs were conducted to track the motion of the upstream influence separation shock. The frame rate was set to 150k fps and the resolution was 456 x 128 for the perpendicularly mounted cylinder configuration. Sampled continuously, the camera would only be able to sample for 2.616 seconds using these settings. Therefore, the camera was triggered to acquire 50k frames every six seconds. During the run, the tunnel Reynolds number was stepped rather than swept. Conditions were held constant during the data acquisition period (1/3 second every 6 seconds). A third group of runs was directed on the triple point and area directly upstream of the cylinder. The sampling rate was 240k fps and the resolution was 120 x 256. A similar stepped Reynolds number procedure followed. A diagram showing the positions of the boxes of reduced resolution relative to the model and flow structure is given as Figure 72. The resolutions and sampling rates varied slightly for the swept cylinder runs. These quantities are outlined in the Campaign Run Log and the High-speed Schlieren Table (Appendix G).

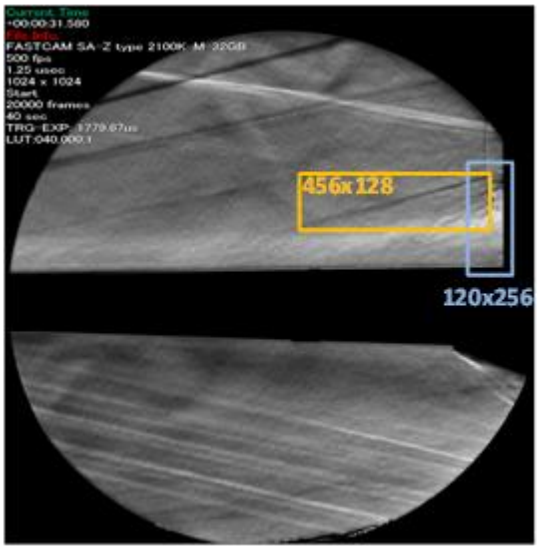

Figure 72. High-speed schlieren resolution placement

An unfortunate feature of the FASTCAM SA-Z is the inability to choose the position of reduced resolution on the sensor – it is set to the center of the detector. Therefore, the camera was traversed up/down and right/left to position it properly for each run.

The time-resolved schlieren images were reduced through spectral analysis and shock tracking. Spectral analysis utilized Welch's method to determine the PSD for each pixel in the schlieren images. 256 points comprised each periodogram. The frequency resolution was 586 Hz and 938 Hz, for 150 kHz and 240 kHz sampling, respectively. By generating a power spectrum at each pixel, maps indicating locations of dominant frequencies could be assembled.

The shock and disturbance waves for each frame were detected using the following line-detecting algorithm.

(1) Subtract the mean of the 50k frame batch from every frame.

(2) Set each pixel value to 1 or 0 based on its intensity relative to pixels above and below it. Shocks and disturbances of interest are dark, so if the intensity of the pixel is less than the

[mean(pixels 2:7)-threshold] above and below the given pixel, that pixel is assigned a value of 1. (using pixels offset 2 through 7 proved to give narrow, well-defined lines)

(3) Reduce noise by setting each pixel value to 0 if all of its surrounding pixels are 0.

(4) Conduct a Hough transform [188] on each frame to detect lines present in the frame. Threshold values will need to be set depending on the desired features for detection.

(5) Eliminate lines outside of the anticipated slope range.

(6) Convert from the polar Hough coordinates back to Cartesian coordinates and relate these to the field-of-view positions given in Appendix G.

This procedure is illustrated in the figures below and allows for viewing the progression of shock and disturbance waves with time. Figure 73 shows the isolation of lines. Figure 74 demonstrates the application of the Hough transform. Figure 75 presents the geometry in terms of the model-based coordinate system. The detected lines were placed in model-based coordinates by relating points on the lines to the coordinates of the vertices of the field-of-view box. Shock-tracking results were converted into the model-based coordinate system for propagation of the shocks to the surface, which allowed for estimation of movement distance along the surface and comparison with findings of the surface-based diagnostics.

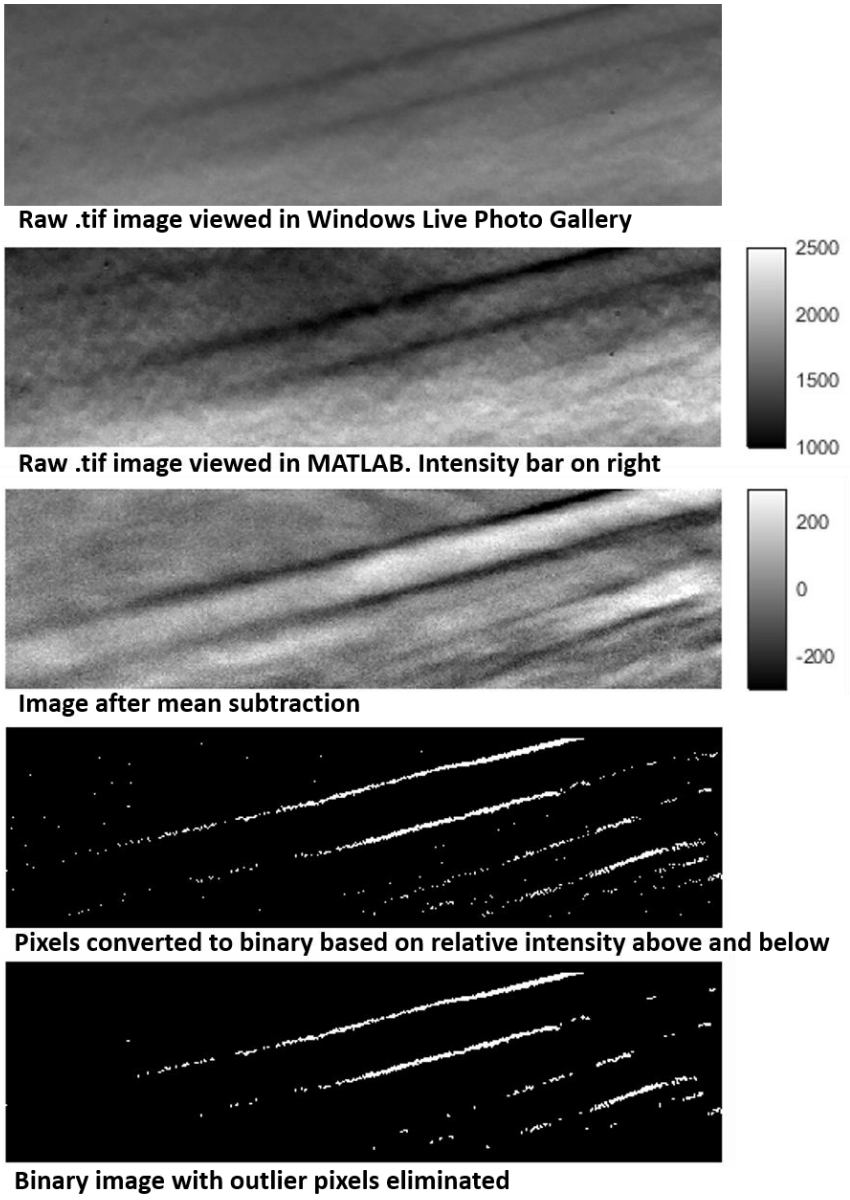

Figure 73. Line isolation procedure demonstated for Frame 24, Run 3443, *Re*=3.7M/m

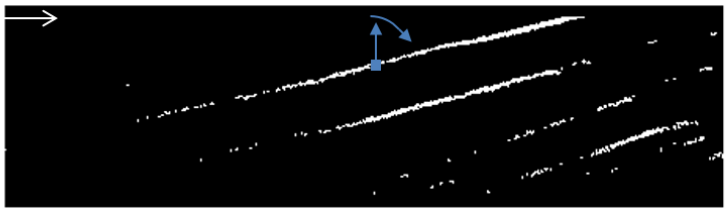

Directional scans occur for each pixel of value 1. The "hits" are tallied in terms of distance(ρ) and angle (θ) from the reference pixel

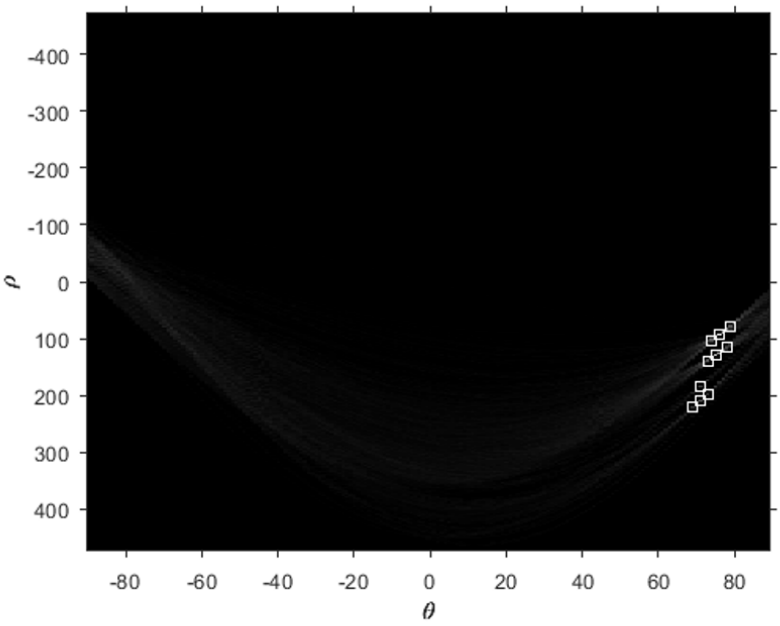

Results in Hough space of "voting" from the above image. The squares denote the most common (θ,ρ) overlap and represent lines in image space

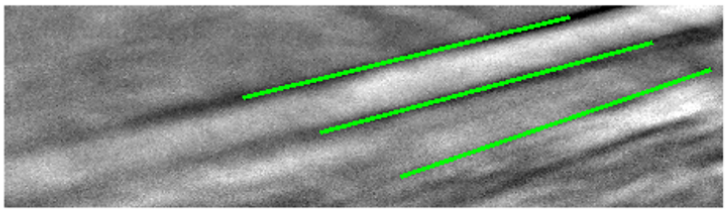

Lines that meet the length threshold and correct angle range are plotted on top of the mean-subtracted image

Figure 74. Hough transform demonstration and resulting fit lines

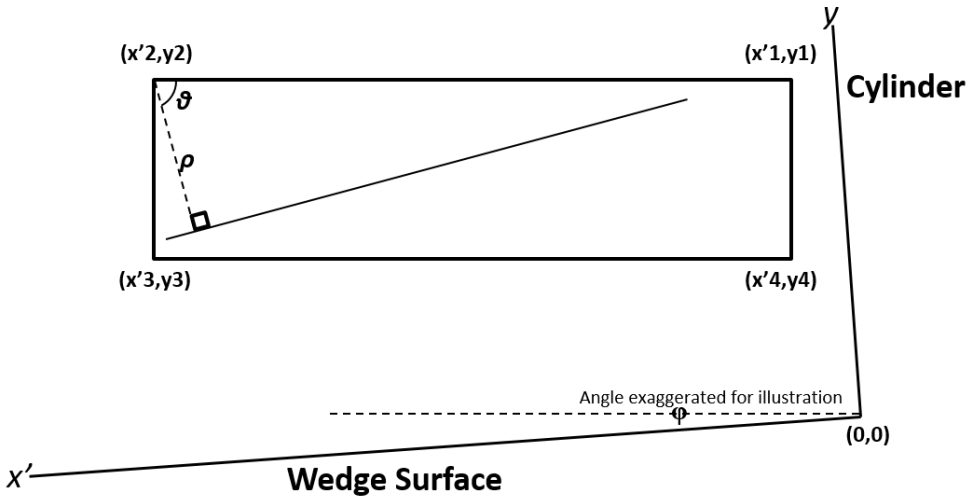

Figure 75. Transformation to model-based coordinates

3.4.6 Focused Schlieren Deflectometry

A focused schlieren imaging setup built by J.W. Hofferth [189] based on the lens-and-grid configuration detailed by Weinstein [190] was utilized to view the shock structure in different planes of this 3-D SBLI. The focused schlieren technique is essentially the culmination of multiple conventional schlieren systems, with multiple sourcing lines and cut-off lines, imaged together through one lens. The advantage of this configuration is it allows for the visualization of density gradients in a single spanwise-normal plane, whereas conventional schlieren integrates across the span. With a conventional schlieren system, flow features outside the region of interest, or even outside of the tunnel (air currents in the room), are visible in the final image. A schematic of the layout is given as Figure 76. The components for this campaign remained unchanged from those used by Hofferth [189], with the exception of the source and cut-off grids and the detector. F. Siddiqui commissioned the printing (FineLine Imaging) of higher quality grids that had sharper

lines separating regions of increased opacity from regions of increased transparency, which improved the quality of the image. The FASTCAM SA-Z was set in place of the avalanche photodetector since visualizing a portion of the interaction was desired over measuring frequency content at a specific point. Photographs of the setup are given in Figure 77.

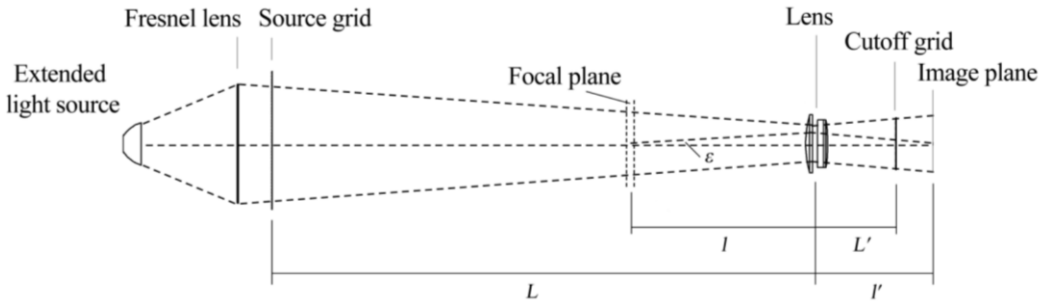

Figure 76. Lens-grid type focused schlieren schematic using nomenclature from Weinstein [190]

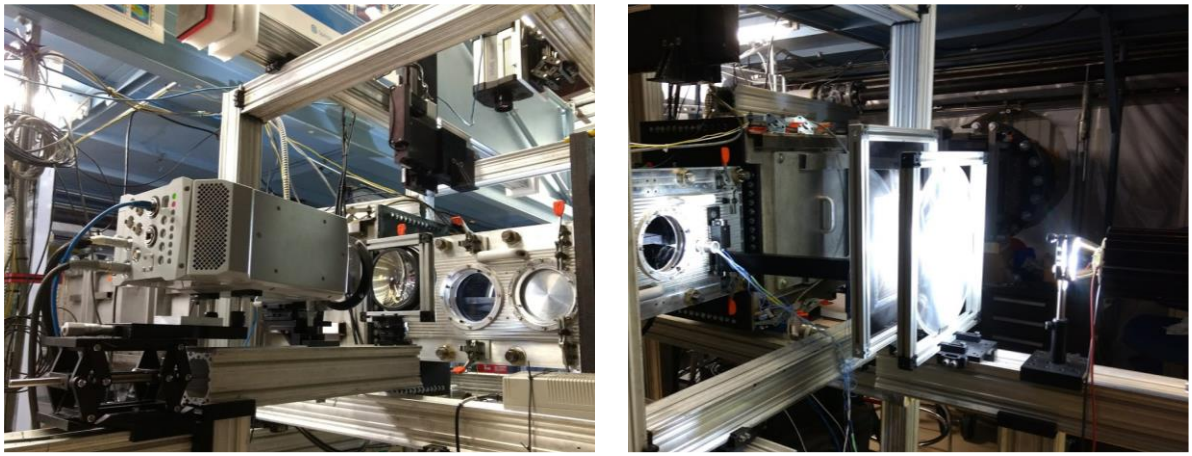

Figure 77. Focused schlieren setup: camera side (left) and source side (right)

Due to space limitations, with only 0.66 m (26 in.) separating the tunnel side wall from the source grid, the model was fixed in the tunnel. Therefore, the wall temperature was elevated for

these runs, with the initial temperature averaging around 360 K on the PEEK insert. Focused schlieren imaging was the only diagnostic technique for which the model was not removed while preheating. The technique was utilized for two SBLI configurations: (1) cylinder swept 15 degrees forward on model and (2) cylinder mounted perpendicularly on wedge. The trip array was in position for both configurations and the tunnel conditions were held constant at *Re*=5M/m.

A feature of the focused schlieren technique is that the focal plane is directly tied to the image plane. Therefore, traversing the camera in the direction of the optics shifts the spanwise-normal plane of focus in the same tunnel spanwise direction. For Run 3490, the camera was traversed at a velocity of 250 µm/s (moving the plane of focus 640 µm/s), and the entire run was captured at 500 fps. Subsequent runs (Run 3492 and 3494) were conducted by stepping the position of the camera in small increments toward the center plane, and acquiring at reduced resolutions (232 x 384 and 184 x 512, respectively) at a frame rate of 150k fps, in order to track the flow features for a given plane in a time-resolved fashion.

3.5 Uncertainty Analysis

3.5.1 Tunnel Conditions

Uncertainty values for the Endevco 8540-200 (settling chamber pressure) and the MKS Baratron 631C-10 (static pressure) are provided by the manufacturer. The combined uncertainty of the Endevco, due to temperature dependence, non-linearity, non-repeatability, and pressure hysteresis, is 2.4% full scale output (FSO) assuming 430 K testing conditions. The Baratron is much more accurate, with an uncertainty of 0.5% of its reading. However, measuring static pressure through a port in the tunnel wall adds a fair bit of uncertainty. The uncertainty in the static pressure was assumed to be 5%. The total temperature was measured using an Omega type K thermocouple

(with a standard uncertainty of 2.2 K) in the settling chamber. By definition, isentropic expansion assumes the total temperature remains the same. Some heat is lost to the nozzle, so the total temperature is estimated to be within 1% of the value reported. The Mach and Reynolds number are derived values based on the measured quantities. From Clark [191] the relative uncertainty in Mach number as a function of the relative total and static pressure uncertainties is given by Eq. (3.16).

$$\frac{E_{M_\infty}}{M_\infty} = (\theta'_{M_\infty})^{-1} * \left[\left(\frac{E_{p_\infty}}{p_\infty}\right)^2 + \left(\frac{E_{p_t}}{p_t}\right)^2\right]^{0.5} \tag{3.16}$$

where θ'_{M_∞} is the relative sensitivity coefficient, defined by Eq. (3.17).

$$\theta'_{M_\infty} = -\frac{\gamma M_\infty^2}{1 + \frac{\gamma - 1}{2} M_\infty^2} \tag{3.17}$$

The uncertainty in Mach number depends on the flow conditions since the uncertainty in the total pressure is a fraction of the FSO of the transducer, rather than the value it measures. For *Re*=5M/m, the uncertainty in the Mach number is 1.5%. The value increases with decreasing Reynolds number.

The uncertainty in the freestream Reynolds number is given by Eq. (3.18).

$$\frac{E_{Re}}{Re} = \left[\left(\frac{E_{\rho_\infty}}{\rho_\infty}\right)^2 + \left(\frac{E_{u_\infty}}{u_\infty}\right)^2 + \left(\frac{E_{\mu_\infty}}{\mu_\infty}\right)^2\right]^{0.5} \tag{3.18}$$

where the 3 uncertainty values are a direct or indirect function of the instrumentation uncertainty ($\rho_\infty = f(p_t, T_t)$, $u = f(M, T_t)$, and $\mu_\infty = f(T_t)$) and are calculated in a similar manner. The resulting uncertainty in Reynolds number is 7% for *Re*=5M/m. Relative uncertainty increases with decreasing Reynolds number.

3.5.2 Diagnostic Specific

3.5.2.1 Hot-wire Anemometry

Improvements were made on the analysis of the hot-wire data from [193], which cited the calibration as a significant source of error, since the total temperature for a given run is not exactly the same as that during the calibration. Temperature normalization, as detailed in Section 3.4.1, makes the tunnel total temperature dependence negligible. The analysis does not take into consideration the total temperature variation throughout the boundary layer. Deviation from the expected values is observed near the surface, where heat from the wire is lost through radiation to the wall. The resulting heat flux values at positions within ~3 mm of the surface are higher than reality. The uncertainty in hot-wire position, above the wall and spanwise, is 0.1 mm. The uncertainty in streamwise position is 1 mm.

Random errors are a major contributor to the spectral and RMS uncertainties. The PSD plots were generated from 97 averages, which corresponds to an uncertainty of 10.2% at a given PSD value. The RMS fluctuations were calculated by using the trapezoid rule approximation of the PSD integration, which added a maximum uncertainty of 14%. The uncertainty from the integral approximation constitutes an overestimation since the data are skewed toward higher frequencies, and much content is held in the first few points.

3.5.2.2 Surface Pressure Measurements

The contributors to uncertainty in the Kulite output are combined error (non-linearity, hysteresis, and repeatability), temperature effects on sensitivity and zero shift, and calibration. The uncertainty for most Kulite transducers is low since the majority of the model does not heat up significantly during the run. Upstream Kulites (T5-T7; T12-T14) have a maximum uncertainty of

0.8%. The downstream Kulites heat up a bit more, particularly T20. The uncertainty for a sensor at that port is 3.1%. PCBs were created as time of arrival sensors, so precise specifications are not reported. They are calibrated dynamically by the manufacturer using a single 50 psia test point. The sensitivity values are generally close (within a few percent) to the stated calibration but can also be very far off. This author knows of an instance when a group of sensors was sent back to the manufacturer for different connectors and ended up coming back with very different calibrations!

The uncertainty in the position of the transducers on the composite model relative to the leading edge is 0.5 mm and relative to other transducers and the base of the cylinder is 0.1 mm. Uncertainty in the relative positioning of the transducers to the cylinder on the PEEK model is higher since that model had no alignment holes for positioning the cylinder.

There are a few contributing sources to the spectral and RMS uncertainties. Many of the spectra for the baseline cases hit the noise floor at frequencies within the presented domains or even within the RMS integration bounds. Therefore, the spectra portray overestimations of the actual energy content at frequencies where the content is below the noise floor. The RMS values are impacted by overestimation as well, but the contribution of the noise floor to the RMS is generally negligible. The PSD plots were generated from 390 averages, which corresponds to an uncertainty of 5.1% at a given PSD value due to random error. As with the mass flux fluctuations, the RMS pressure fluctuations were calculated by using the trapezoid rule approximation of the PSD integration. The uncertainty from the integral approximation tended to overestimate the values but to a lesser extent than for the hot-wire anemometer since the spectra were not as far skewed.

3.5.2.3 Infrared Thermography

The calibration curves for eight trials presented in Appendix F demonstrate less than 2 K variability between all curves over the entire temperature range (290-415 K). These calibrations were done using a similar configuration to the experiments, with the exception of quiescent air, which is expected to have a negligible impact. There may also be a slight difference in the emissivity of the PEEK model (or insert) compared to the black camera calibration plate. Uncertainties in these values propagate directly to uncertainties of the model surface temperature. For the present study, the emissivity values were assumed to be equal, except for at extreme viewing angles.

The heat transfer parameter values have uncertainties originating from the material properties, data processing, and initial condition assumptions. The PEEK thermal specifications (Table 8) are from the distributor, but it is unclear what methods were used to measure these values and the dependence on temperature. The heat conduction equation provides some relief in that uncertainties in the material properties only tend toward a square-root effect on the heat flux. For example, a thermal diffusivity that is 10% too high will only increase the heat flux by around 5%. The 1-D heat conduction processing code introduces some uncertainty in the estimation of heat flux by way of temperature gradient at the surface, which has some convergence time and is influenced by changing freestream conditions. The model typically sat in the tunnel for 1-2 minutes before a run, which caused the surface temperature to increase.

The assumption that the temperature on the model surface and throughout the material was the same at the start of the run is a major contributor of uncertainty to the heat flux and derived parameters. Figure 78 (right) demonstrates the effect of changing the initial internal material temperature on the heat flux. Run 3428 considers the average heat flux in the reattachment arc region, and Run 3398 considers an upstream region (Regions 1 and 3, respectively, from Section 6.3.1).

Heat flux values were computed using different initial temperature distributions for both runs. The first distribution, "Tsurf," is explained above and was used for the analysis in the current campaign. This temperature was 309.6 K for Run 3428 and 308.1 K for Run 3398. A second initial temperature distribution assumed that all nodes below the surface were equal to room temperature (293 K). The figure indicates a significant difference in heat flux that is slow to converge. The heat flux within the reattachment arc is much higher in magnitude; however, the difference in heat flux is not proportionally greater than the upstream heating. Rather, the offsets, which are severe initially and vary from 0.8-2.0 kW/m^2 for t>8 s, show good agreement for a given time across the duration of both runs.

The example above demonstrates some initial condition uncertainty bounds. The two runs chosen had high initial temperatures relative to the majority of IR runs (most had initial temperatures between 299 K and 303 K). The true heat flux for the given regions falls between the profiles and is likely much closer to the result obtain from the surface temperature internal distribution. However, without a better model for the initial internal temperature distribution, its contribution to the uncertainty will be high.

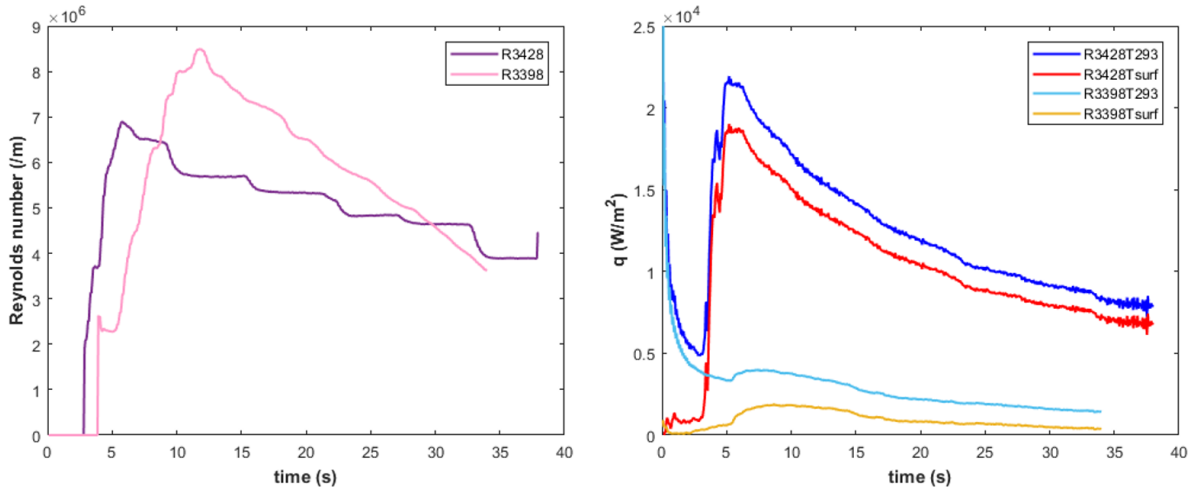

Figure 78. Heat conduction code sensitivity to initial conditions

Neglecting lateral conduction gives a slight underestimation of heat transfer in areas of highest temperature. Normalization of heat flux introduces further uncertainty from the total temperature measurement (Section 3.5.1). Uncertainties in film coefficient and Stanton number are affected by uncertainties in total temperature, particularly in regions where the difference between total temperature and model wall temperature are the lowest.

3.5.2.4 High-speed Schlieren Imaging

Several factors contribute to the estimate in the uncertainty of the shock position. Many of the time-resolved schlieren runs did not have reference geometry (surface or cylinder) in the field-of-view. Therefore, snapshots were taken after each of those runs using a 50.8 mm square (2”x2”) glass line grid target. The lines on the target were spaced every millimeter. The position of the reduced resolution field-of-view was related back to the full frame through the target. This method contributes to an uncertainty of 0.2 mm in the relative positioning of the field-of-view vertices.

However, there is also uncertainty due to slight movement in the model upon tunnel startup. The combined field-of-view position uncertainty, for the values listed in Appendix G, is 0.5 mm.

Many of the shocks are not well-defined and do not form straight lines in the schlieren images, which leads to uncertainties in shock tracking. Extrapolating lines of uncertain slope to the surface further contributes to an uncertainty of 2 mm for the location of shock intersection with the wedge. As with the other diagnostics, the PSD analysis is subject to random errors. The data generally provide 390 periodogram averages, which results in an uncertainty of 5.1%.

3.6 Proposed Run Schedule

This section presents objective questions along with preliminary answers based on capability expectations of the diagnostics. The proposed run matrix (Table 9) was designed to answer the following questions.

1. **How do the dynamics of shock structure, especially the motion of the separation shock foot, triple point, shock-induced supersonic jet, and fluctuations within the separated region, change as the interaction evolves through transition?**

   High-speed schlieren will be used to monitor the motion of the shock structure. High-frequency response pressure transducers will monitor the surface pressure within the interaction. Reynolds number sweeps will be conducted by increasing the total pressure within a run to vary the interaction state from laminar, through transition, to turbulent.

2. **What effect do the trips have on the downstream boundary layer profiles at different streamwise and spanwise positions?**

Pitot and/or hot-wire boundary layer profiles will be generated at different streamwise positions. For a given streamwise position, profiles will be generated at different spanwise positions to determine the influence of the trip wakes on the evolving boundary layer.

3. **How does the spanwise positioning behind the trips affect the surface pressure dynamics with and without a shock generator?**

   The positioning of the high-frequency pressure transducers is such that some will be roughly centered behind a trip and underneath its wake and some are behind a gap and out of the wake. Monitoring adjacent transducers will indicate the positional effect.

4. **How does the protuberance sweep angle affect the separation scaling and dynamics for a transitional SBLI?**

   High-speed schlieren, high-frequency pressure transducers, and IR thermography will be used to monitor the interaction with cylinders of different sweep angles.

The following run matrix was generated following the oil flow visualization experiments and the machining of the pressure ports in the composite model. It represents what was believed to be the minimum required to answer the objective questions.

Table 9. Proposed run matrix

Run	Question addressed	Description	Re
1	characterization	Freestream hot-wire at wedge LE location (no model)	Sweep
2*	characterization	Hot-wire traverse across leading-edge shock: upstream of trips	High
3*	characterization	Hot-wire traverse across leading-edge shock: downstream of trips	High
4*	3	Pressure sensor config 1, IR on wedge: trip wake heating, Full run schlieren on LE and trips	Sweep
5*	3	Pressure sensor config 2, IR on wedge: trip wake heating, HS schlieren on LE and trips	Stepped
6*	3	Pressure sensor config 3, IR on wedge: trip wake heating, Full run schlieren downstream	Sweep
7*	3	Pressure sensor config 4, IR on wedge: trip wake heating, HS schlieren downstream	Stepped
8*	2	HW (Kulite) traverse BL survey: directly upstream of a most upstream PCB	High
9*	2	HW (Kulite) traverse BL survey: directly upstream of an adjacent most upstream PCB	High
10*	2	HW (Kulite) traverse BL survey: directly upstream of a transitional interaction located PCB	High
11*	2	HW (Kulite) traverse BL survey: directly upstream of an adjacent transitional interaction located PCB	High
12*	2	HW (Kulite) traverse BL survey: at cylinder face location	High
13*	2	HW (Kulite) traverse BL survey: adjacent to cylinder face location	High
14	3	Pressure sensor config 1, Full run schlieren, IR on wedge	Sweep
15	3	Pressure sensor config 2, Full run schlieren, IR on wedge	Sweep
16	3	Pressure sensor config 3, Full run schlieren, IR on wedge	Sweep
17	3	Pressure sensor config 4, Full run schlieren, IR on wedge	Sweep
18	1,3	Pressure sensor config 1, HS schlieren on separation shock, IR on wedge	Stepped
19	1,3	Pressure sensor config 2, HS schlieren on separation shock, IR on wedge	Stepped
20	1,3	Pressure sensor config 3, HS schlieren on separation shock, IR on wedge	Stepped
21	1,3	Pressure sensor config 4, HS schlieren on separation shock, IR on wedge	Stepped
22	1,3	Pressure sensor config 1, HS schlieren on supersonic jet, IR on cylinder	Stepped
23	1,3	Pressure sensor config 2, HS schlieren on supersonic jet, IR on cylinder	Stepped

Table 9 Continued

Run	Question addressed	Description	Re
24	1,3	Pressure sensor config 3, HS schlieren on supersonic jet, IR on cylinder	Stepped
25	1,3	Pressure sensor config 4, HS schlieren on supersonic jet, IR-cylinder	Stepped
26	additional contribution	Focused Schlieren – HS on separation shock, adjusting spanwise plane of focus	Constant
27	4	15 deg swept cylinder, IR – camera angled to see cylinder and wedge, Full run schlieren	Sweep
28	4	30 deg swept cylinder, IR – camera angled to see cylinder and wedge, Full run schlieren	Sweep
29	4	30 deg swept cylinder, IR – camera angled to see cylinder and wedge, HS schlieren on separation shock	Stepped
30	4	15 deg swept cylinder, IR – camera angled to see cylinder and wedge, HS schlieren on separation shock	Stepped

* No cylinder mounted

It may be instructive to repeat BL surveys at a given location for a couple additional, lower Reynolds numbers. More angles of sweep could be tested.

4. PRELIMINARY RESULTS

This chapter presents IR thermography, surface pressure measurements, and high-speed schlieren imaging on the solid PEEK wedge model as well as oil flow measurements on the composite wedge model. The oil flow visualization directly influenced the placement of high-frequency surface pressure transducers on the composite model. Tunnel freestream measurements are presented in Section 4.3. A complete run log outlining the testing conditions and diagnostic techniques for all models used in this campaign is given in Appendix G.

4.1 Solid PEEK Wedge Model

With flow uniformity and directionality requirements met, preliminary experiments were conducted using the solid PEEK model as the testbed. Oil flow visualization was primarily used to identify the efficacy of the different trip arrays. As such, the interaction separation distances are noted in Section 3.2.2.

Simultaneous IR thermography and surface pressure measurements were carried out on this model for three Reynolds number sweep runs: (Run 3007) model with no trips and no cylinder, (Run 3008) model with trips and no cylinder, and (Run 3010) model with trips and cylinder. Heat flux maps for these three configurations at four Reynolds numbers were obtained through the calculations outlined in Section 3.4.4 and are given in Figure 79. A comparison of the first two rows in Figure 14 (Run 3007 and Run 3008) shows the effect of the trips on the heat transfer rate. At low Reynolds numbers, like Re=3.0M/m and Re=3.5M/m, the maps look much the same between the two runs, but as the Reynolds number increases, the heat transfer rate elevates to much higher

levels with the trips. The effect of the trips on the heat transfer is substantial. The lower heat transfer rates seen for Run 3007, at all Reynolds numbers, are consistent with those of a laminar boundary layer. The much sharper increase in heat transfer rate with Reynolds number over the course of Run 3008 is indicative of the changing state of the boundary layer.

The final two rows give the effect of adding a shock generator to a flowfield where the state of the boundary layer is governed by the Reynolds number. Upstream of the separated region, the surface heat transfer for Runs 3008 and 3010 look virtually identical, indicating an upstream bound for the interaction. The vortices within the separated region pull the high energy mean flow closer to the wall, elevating the surface heat transfer. The highest heating is where the flow reattaches at the base of the cylinder. At the low Reynolds numbers, L_{sep} is measured between 5.5d and 6.0d depending on the position along the span. This value agrees with the measured separation shock offset distance from the oil flow.

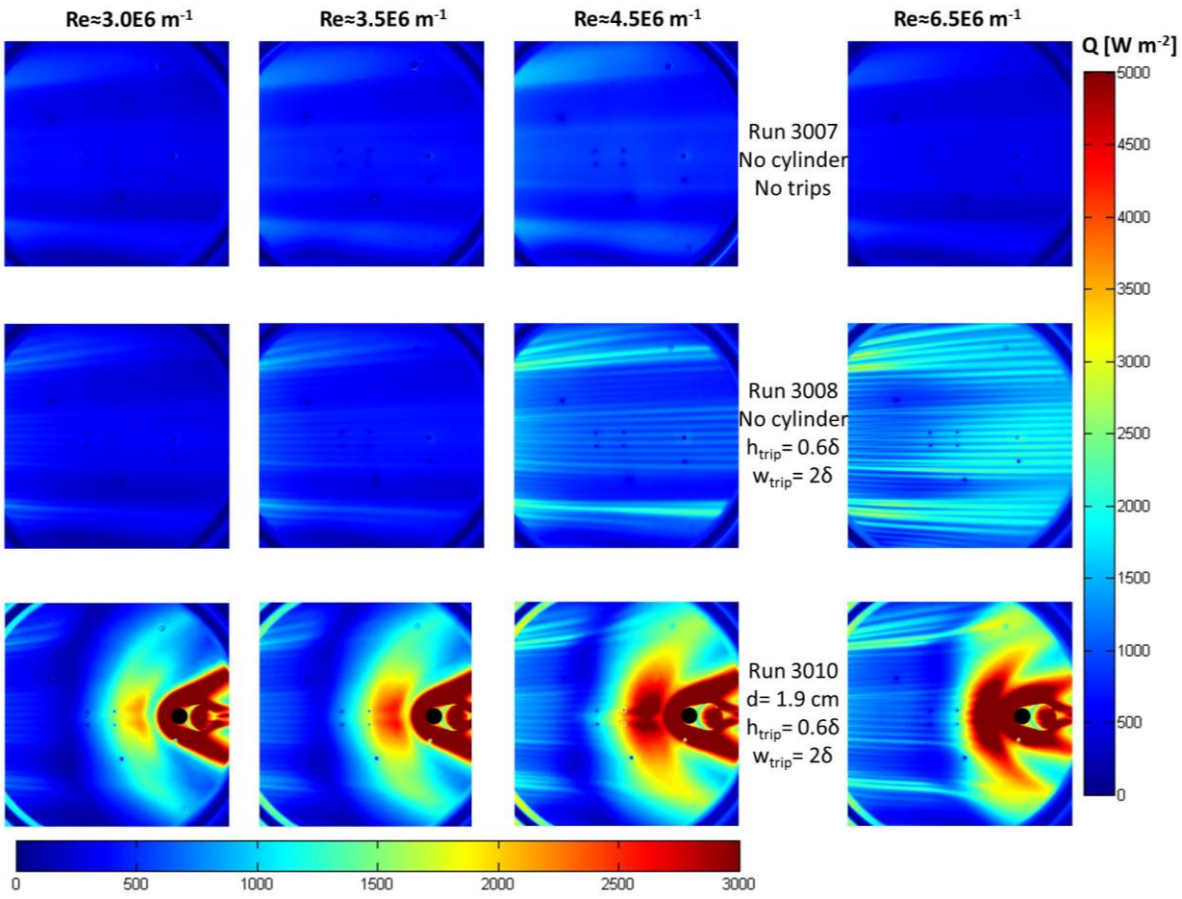

Figure 79. IR thermography derived heat flux maps

The locations for the two Kulite and two PCB pressure transducers, relative to the heat flux map at *Re*=3.5M/m are provided in Figure 80. The dimensioned positions relative to the cylinder are given in Leidy et al. [175].

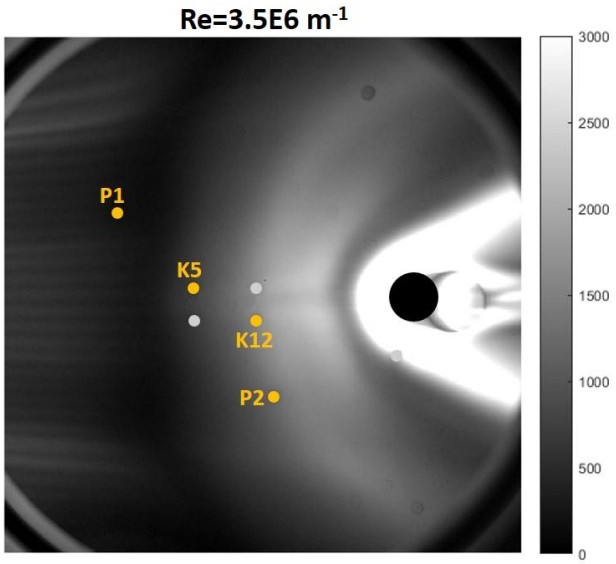

Figure 80. Pressure transducer locations

The power spectral density plots for Run 3007 (no trips, no cylinder) for each of the four pressure transducers are in Figure 81. The legend gives the freestream Reynolds number in millions. The Kulite sensors are plotted over a frequency scale of 0-100 kHz, while the PCB transducers are on a scale of 0-500 kHz. The Kulites and PCBs indicate that signal increases with Reynolds number across the entire frequency range, although the signal is near the noise floor for much of the range. The spectra do not appear to change shape across the frequency range with increasing Reynolds number for any sensor, and, therefore, there is no indication of a change from a laminar boundary layer.

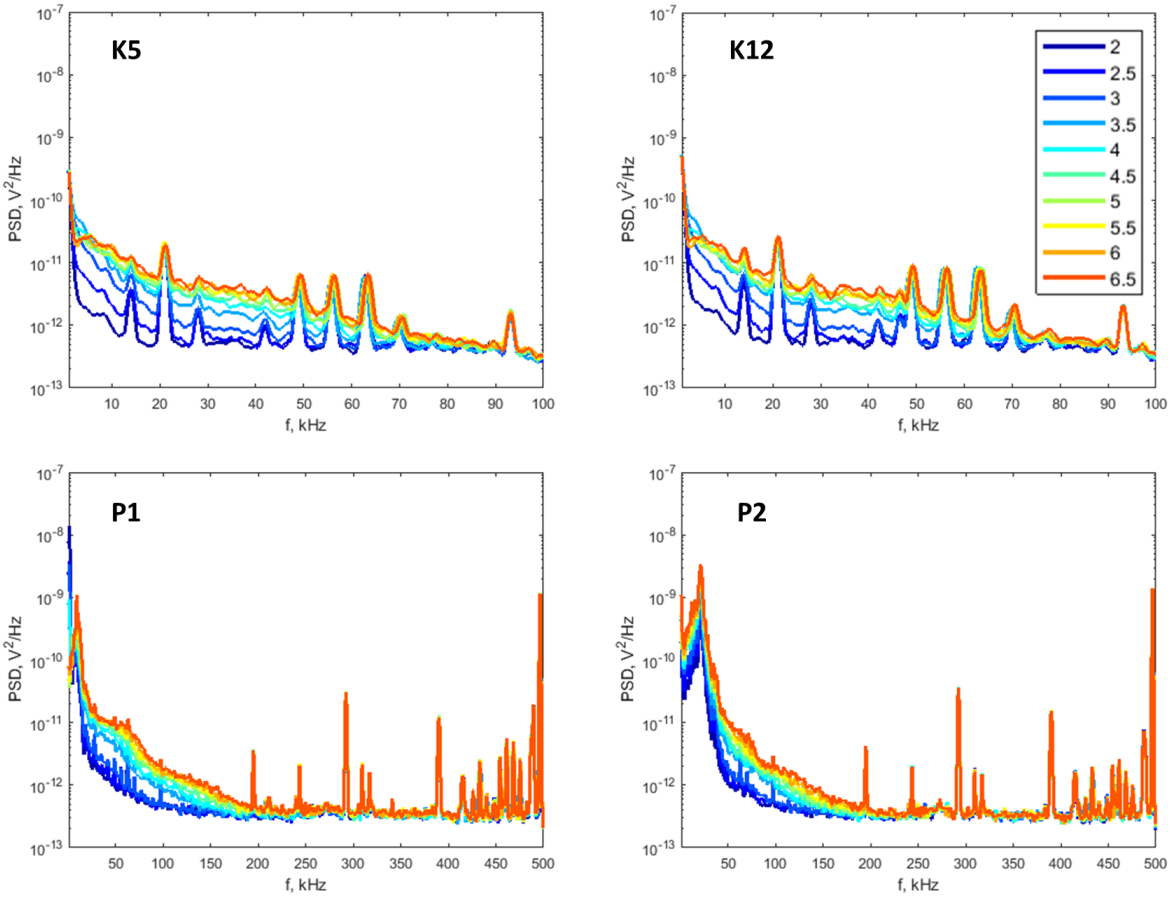

Figure 81. Run 3007 PSDs: no trips, no cylinder

The trips were in place for Run 3008, and the PSD plots for each sensor are shown below as Figure 82.

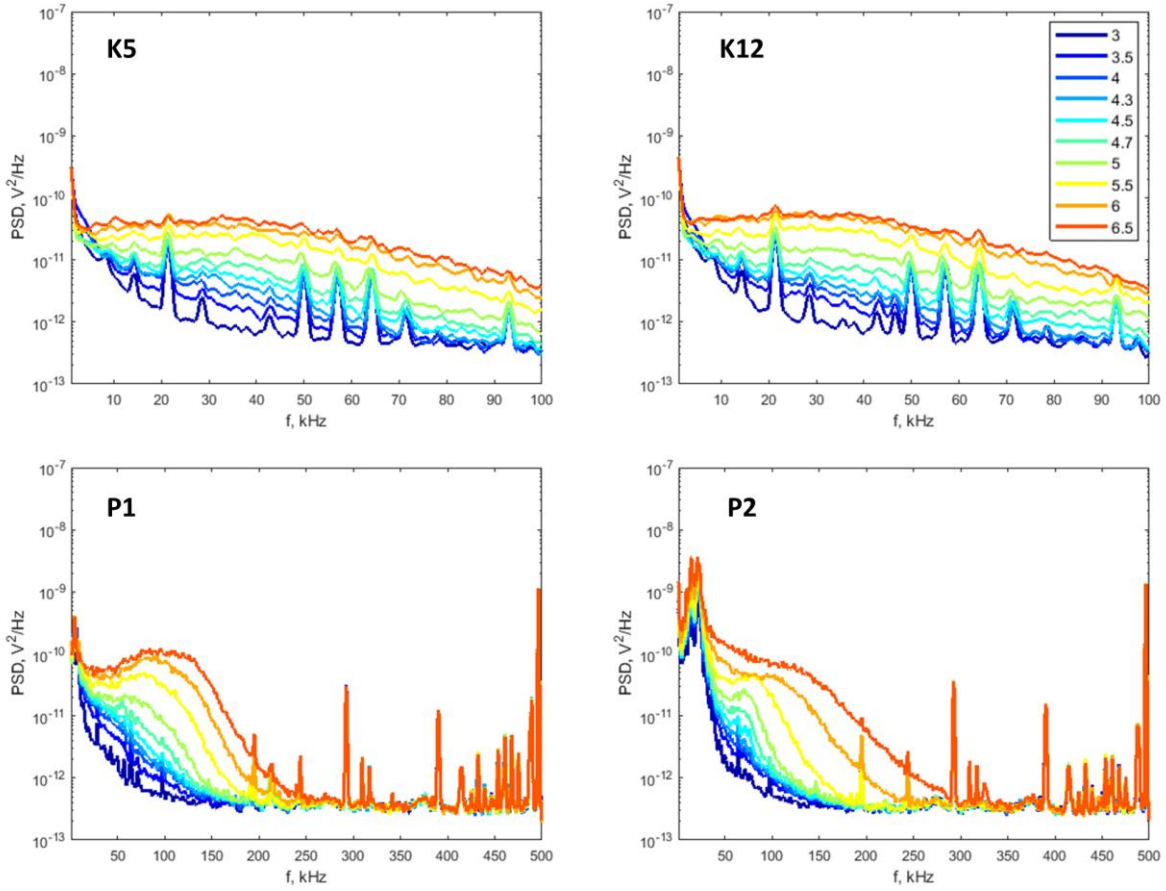

Figure 82. Run 3008 PSDs: trips, no cylinder

All of the transducers indicate a change in PSD form with increasing Reynolds number. The Kulite and PCB sensors give nearly identical spectral content over the lowest two freestream Reynolds numbers (3.0M/m and 3.5M/m) as compared with Run 3007. The spectra at *Re*=4.5M/m break form from the previous run and also portray broadening of shape. There is much more broadening of the spectra over the frequency range at the highest two Reynolds numbers (6.0M/m and 6.5M/m). For the Kulite transducers, the signal at these Reynolds numbers is nearly entirely independent of the noise floor. Although the Kulites show the stronger signal at these Reynolds numbers for the frequency range up to 100 kHz, the PCBs give the true extent of the broadening on the

frequency range. The upstream PCB shows elevated signal at *Re*=6.5M/m up to 250 kHz, while the downstream PCB demonstrates continued broadening and elevated signal up to 300 kHz. Sensor P1 indicates a local signal peak just below a frequency of 100 kHz from *Re*=5.5M/m to *Re*=6.5M/m. Downstream, at P2, the peak is near this frequency for *Re*=5.0M/m to *Re*=5.5M/m, while a spectral shift blankets this peak into higher frequencies at higher Reynolds numbers, characteristic of the transitioning boundary layer. Therefore, the frequency just below 100 kHz may be representative of an instability caused by the trips.

The 1.9 cm diameter cylinder was added to the previous configuration for Run 3010, and the PSD plots are shown below as Figure 83.

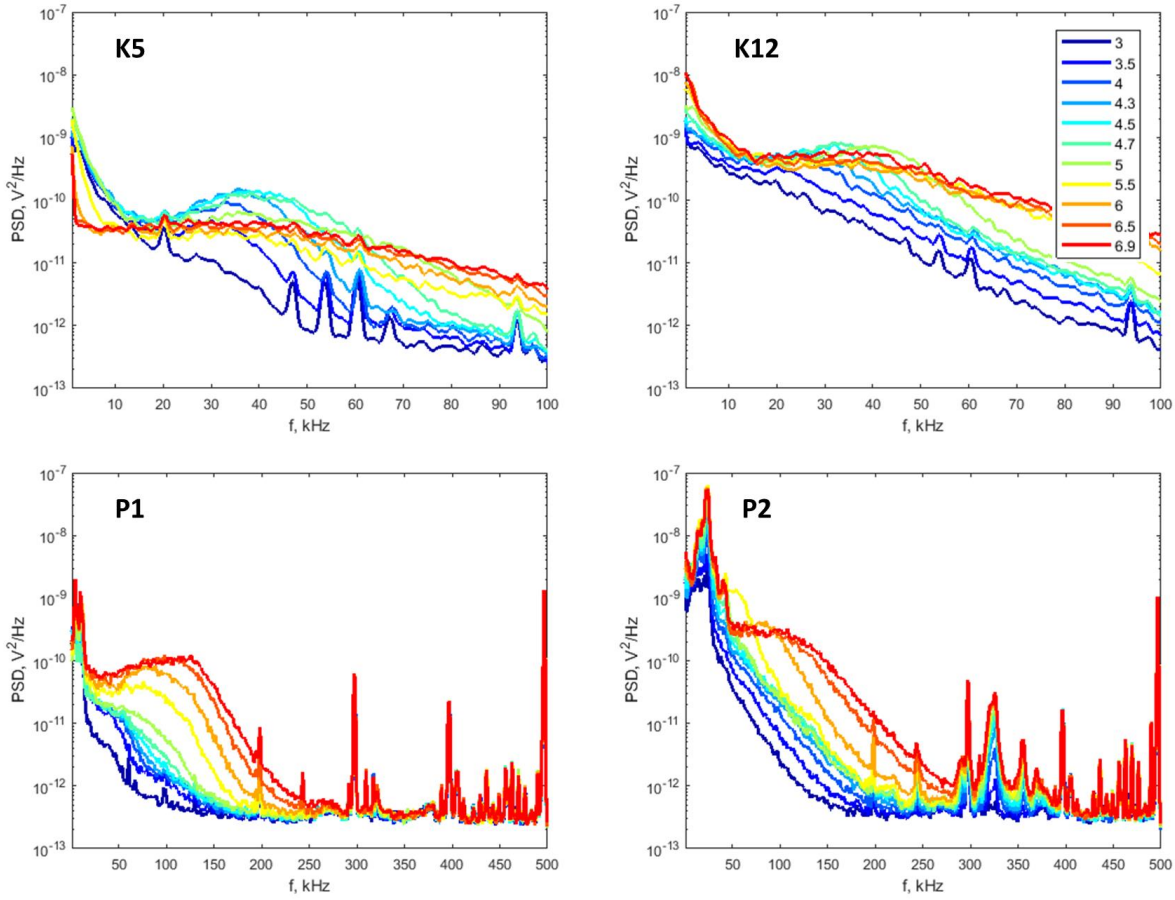

Figure 83. Run 3010 PSDs: trips and cylinder

The positioning of the transducer with respect to the cylinder clearly affects the spectral content. For example, PCB transducer P1 is measured 5.8 cylinder diameters upstream of the front of the cylinder and is offset 5.1*d* from the centerspan. The oil flow and IR show this sensor to be near the separated region at low Reynolds numbers. While the signal is slightly strengthened at low frequencies and low Reynolds numbers when compared to Run 3008, it changes little at the higher Reynolds numbers. This is consistent with the reduction of L_{sep} as the interaction transitions. P2 is measured only 2.5*d* upstream of the cylinder and is also offset 2*d*. The oil flow and IR show it to be located just outside of the separation shock for a turbulent interaction. The PSD values for

frequencies less than 70 kHz jump by more than an order of magnitude across the Reynolds number range when compared to Run 3008. However, the highest Reynolds number case produces a similar signal between frequencies of 150-300 kHz. This may be because the sensor is located upstream of the separation at *Re*=6.5M/m.

The Kulite transducers tell a similar story. K5 is measured 4.1*d* upstream of the cylinder and only 0.3*d* off the centerspan. The oil flow and IR indicate this sensor to be in the separated region at low Reynolds numbers. The lowest Reynolds numbers have PSD values that are over an order of magnitude higher for frequencies less than 40 kHz. The highest two Reynolds numbers show nearly the same spectral content as for Run 3008, meaning the separated region does not reach far enough upstream to impact the measured signal. The local PSD signal maximum for *Re*=4.0M/m to *Re*=4.7M/m at frequency just under 40 kHz is interesting in that the separation shock is expected just upstream of the sensor for these conditions. This dominant frequency may be related to the transient nature of the shock or the separation vortex. K12 is measured 2.8*d* upstream of the cylinder and 0.3*d* off the centerspan. The oil flow and IR show this sensor just outside of the separation shock for a turbulent interaction. The PSD plots for all Reynolds numbers across the entire frequency range are elevated from the previous run. This result makes sense because the total pressure, and therefore, the magnitude of the fluctuations should be highest in the recirculation region near the cylinder. There is another frequency peak for *Re*=4.5M/m to *Re*=5.0M/m at a frequency near 40 kHz. This peak is not as distinct and occurs at a slightly higher Reynolds number, meaning the separation shock is farther downstream and closer to this sensor. Again, the 40 kHz frequency is believed to be characteristic of the separated region within this transitional shock/boundary layer interaction.

Following these tests, the cylinder was removed and positioned 0.406 m (16 in.) downstream of the leading edge, so the interaction region could be imaged with schlieren. Schlieren videos were taken of a full Reynolds number sweep run (at 500 fps) run at low exposure times (about 1.25 μs). Although these images are not time-resolved, they provide insight into the structure and further corroborate the separation scaling from the oil flow. Since the cylinder is positioned farther downstream, the freestream Reynolds number is less for transitional and turbulent interactions.

Sample schlieren images for (a) laminar, (b) transitional, and (c) turbulent interactions are shown in Figure 84. Flow is from left to right. The shock wave coming into the interaction from the middle left is from the nozzle / test section interface and is a contributing reason for positioning the cylinder farther upstream in subsequent testing. The viewing diameter of the window is 0.127 m (5 in.).

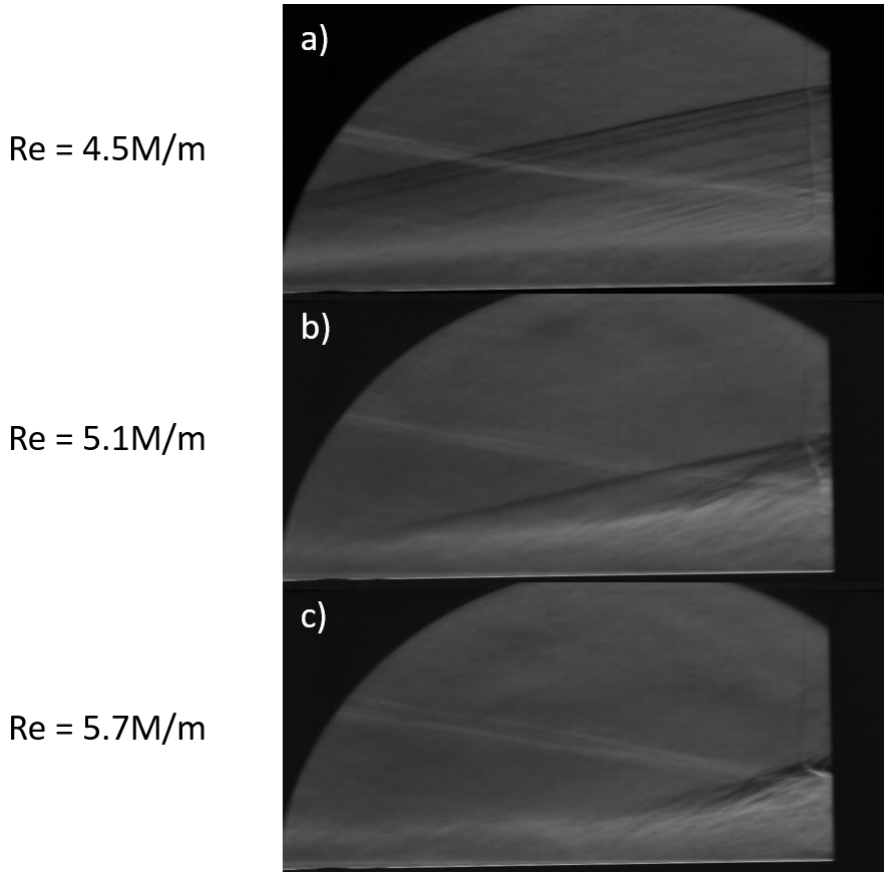

Figure 84. Schlieren images showing different interaction states

4.2 Composite Wedge Model

The diffuser height was optimized for maximum Reynolds number and oil flow visualization was conducted on the composite model to verify similar flow patterns regarding the trips and edge effects as the solid PEEK model (Runs 3203-14). A series of oil flow runs were conducted at different Reynolds numbers to determine separation distances across the transitional boundary layer range (Runs 3269-77). These results are given as Figure 85.

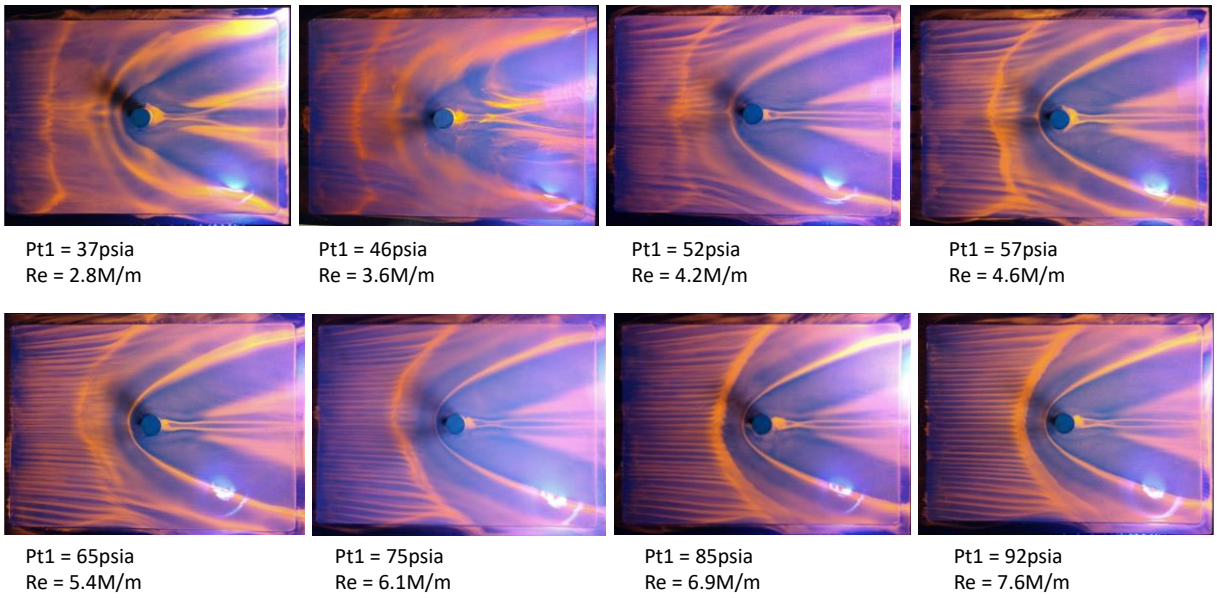

Figure 85. Oil flow maps for a series of Reynolds numbers

The positioning of the oil flow separation line resulting from the upstream influence shock follows the expected trend with increasing Reynolds number. For a freestream Reynolds number of 2.8M/m, the separation distance is between 5.2*d* and 5.5*d* upstream of the cylinder. At 4.6M/m, there is more variation across the span and the distance is between 3.3*d* and 3.9*d*. By *Re*=7.6M/m, the separation and flow features are consistent with those of a turbulent SBLI. The interaction appears symmetric across the span and there is little variation in the separation distance (2.5-2.7*d*). The measured separation values for all runs are given in Table 10.

Table 10. Composite model oil flow separation summary

Run Number	Re_∞ (10^6 m^{-1})	L_{sep} (d)
3270	2.8	5.2-5.5
3271	3.6	5.0-5.2
3277	4.2	3.8-4.5
3269	4.6	3.3-3.9
3272	5.4	3.2-3.8
3273	6.1	2.8-3.4
3274	6.9	2.5-2.7
3276	7.6	2.5-2.7

Another interesting feature is the evidence of separation and reattachment in the form of additional horseshoe vortices downstream of the primary vortex. For instance, three additional horseshoes are clearly defined at *Re*=2.8M/m. The most downstream of these three is near the base of the cylinder and signifies flow reattachment. At 4.2M/m, two full-bands downstream of the primary vortex are observed. By 4.6M/m, the band directly downstream the primary band begins to merge with the primary band out near the center of the span but is still distinct outboard. The merging progresses as the Reynolds number increases and the interaction region shrinks; however, there is still outboard evidence of this secondary band at 7.6M/m.

The oil flow separation lines were traced and overlaid. The resulting map was used to systematically distribute surface pressure ports. Two Kulite ports and a PCB port from the solid PEEK model were placed in the same location on the composite model for comparison.

A composite map featuring the separation lines at each Reynolds number (Figure 86) was generated to provide insight as far as the positioning of the sensors upstream and within the SBLI. Ahead of the oil separation line, three PCB ports were inserted to measure pressure fluctuations in the incoming boundary layer for all test runs. The spanwise spacing was such that two sensors were positioned directly downstream of trips, while the third was directly downstream of the center

of a gap. This was to characterize the spanwise influence of the trips. Another row of three PCBs and two rows of three Kulites were positioned farther downstream to quantify the influence of the trip wakes both within and outside of the SBLI. Several more PCB and Kulite transducer ports were added to the centerspan to achieve more measurements for comparison with Murphree [159]. PCBs were positioned outboard from the centerspan to determine that spatial effect on high-frequency fluctuations. Kulites were positioned in the wake of the cylinder to measure if similarities in the frequency content exist in the upstream separation and the wake.

These justifications are consistent with the general priorities of characterizing the spectral content (1) along the centerspan (2) at several ports for a given streamwise location (influence of the trips), (3) far off-centerspan within the interaction, and (4) in the wake. Figure 86 also indicates the position of the transducers on the previous model, labeled in red as P1 (now T3), P2, K5 (T7), and K12 (T12). A dimensioned diagram demarcating the position of each transducer port (T1-T28) is given as Figure 87. The dimensions are in terms of cylinder diameter (19.1 mm), which is the first-order scaling parameter for the interaction. Table 11 summarizes the sensor positions. Coordinates are referenced to the front and center of the cylinder. The distribution of these pressure ports should provide insight to measurement goals listed above.

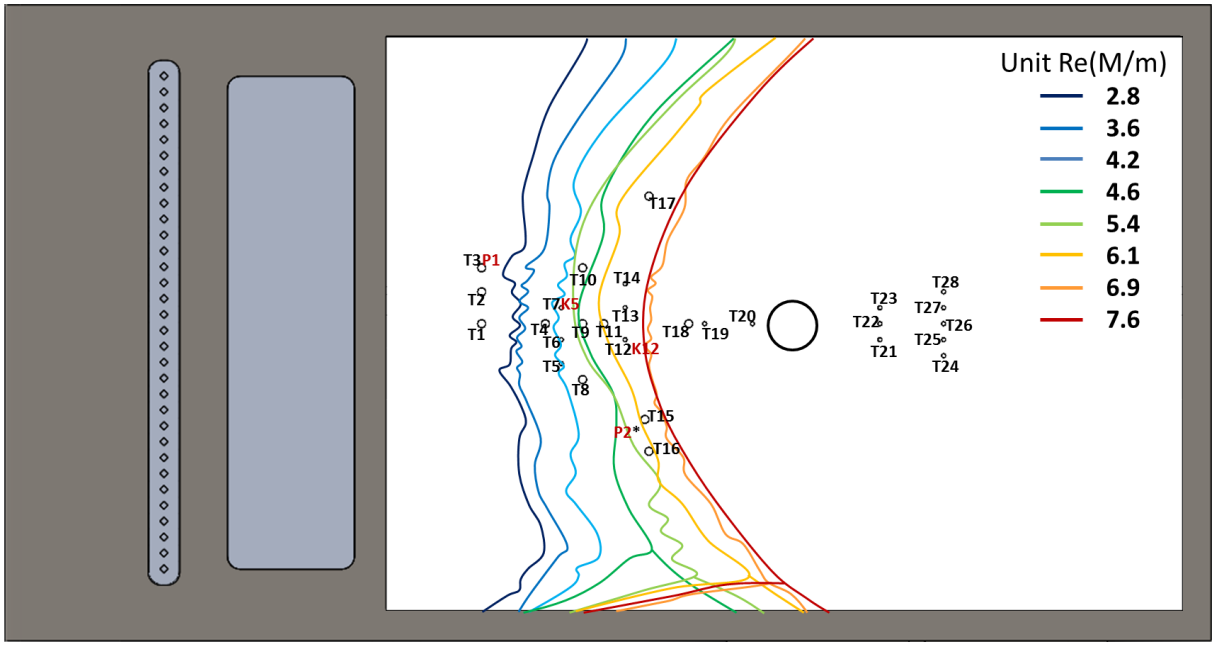

Figure 86. Separation lines from oil flow visualization and pressure port locations

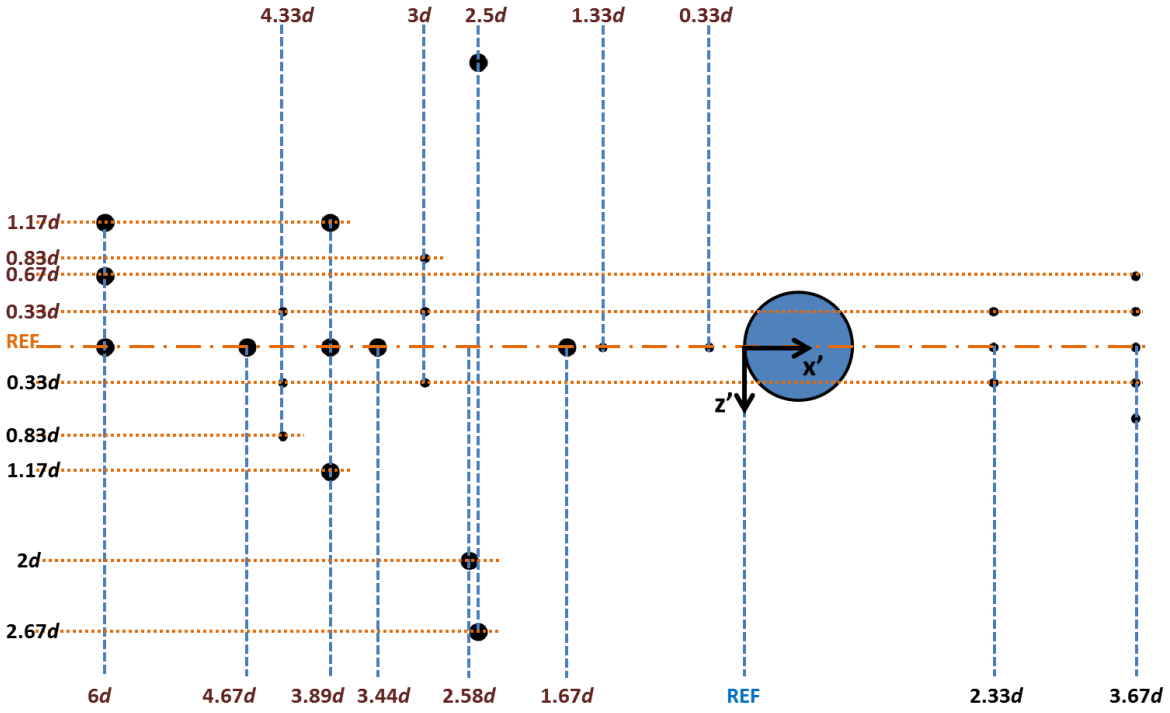

Figure 87. Transducer port locations relative to the front of the cylinder

Table 11. Transducer port locations

Sensor	Type	*x'* (mm/in./*d*)	*z'* (mm/in./*d*)
T1	PCB	(-) 114 / 4.5" / 6*d*	0
T2	PCB	(-) 114 / 4.5" / 6*d*	(-) 12.7 / 0.5" / 0.67*d*
T3	PCB	(-) 114 / 4.5" / 6*d*	(-) 22.2 / 0.88" / 1.17*d*
T4	PCB	(-) 88.9 / 3.5" / 4.67*d*	0
T5	Kulite	(-) 82.6 / 3.25" / 4.33*d*	15.9 / 0.63" / 0.83*d*
T6	Kulite	(-) 82.6 / 3.25" / 4.33*d*	6.4 / 0.25" / 0.33*d*
T7	Kulite	(-) 82.6 / 3.25" / 4.33*d*	(-) 6.4 / 0.25" / 0.33*d*
T8	PCB	(-) 74.1 / 2.92" / 3.89*d*	22.2 / 0.88" / 1.17*d*
T9	PCB	(-) 74.1 / 2.92" / 3.89*d*	0
T10	PCB	(-) 74.1 / 2.92" / 3.89*d*	(-) 22.2 / 0.88" / 1.17*d*
T11	PCB	(-) 65.6 / 2.58" / 3.44*d*	0
T12	Kulite	(-) 57.2 / 2.25" / 3*d*	6.4 / 0.25" / 0.33*d*
T13	Kulite	(-) 57.2 / 2.25" / 3*d*	(-) 6.4 / 0.25" / 0.33*d*
T14	Kulite	(-) 57.2 / 2.25" / 3*d*	(-) 15.9 / 0.63" / 0.83*d*
T15	PCB	(-) 49.2 / 1.94" / 2.58*d*	38.1 / 1.5" / 2*d*
T16	PCB	(-) 47.6 / 1.88" / 2.5*d*	50.8 / 2" / 2.67*d*
T17	PCB	(-) 47.6 / 1.88" / 2.5*d*	(-) 50.8 / 2" / 2.67*d*
T18	PCB	(-) 31.8 / 1.25" / 1.67*d*	0
T19	Kulite	(-) 25.4 / 1" / 1.33*d*	0
T20	Kulite	(-) 6.4 / 0.25" / 0.33*d*	0
T21	Kulite	44.5 / 1.75" / 2.33*d*	6.4 / 0.25" / 0.33*d*
T22	Kulite	44.5 / 1.75" / 2.33*d*	0
T23	Kulite	44.5 / 1.75" / 2.33*d*	(-) 6.4 / 0.25" / 0.33*d*
T24	Kulite	69.9 / 2.75" / 3.67*d*	12.7 / 0.5" / 0.67*d*
T25	Kulite	69.9 / 2.75" / 3.67*d*	6.4 / 0.25" / 0.33*d*
T26	Kulite	69.9 / 2.75" / 3.67*d*	0
T27	Kulite	69.9 / 2.75" / 3.67*d*	(-) 6.4 / 0.25" / 0.33*d*
T28	Kulite	69.9 / 2.75" / 3.67*d*	(-) 12.7 / 0.5" / 0.67*d*

4.3 Tunnel Freestream Measurements

Tunnel freestream measurements were made using a pitot probe and hot-wire anemometer positioned at the same streamwise location as the model leading edge [193]. The primary purpose

for the measurements was to provide accurate inflow conditions necessary for computational simulations.

4.3.1 Pressure Fluctuations

Total pressure measurements were acquired using a pitot probe, instrumented with a high-frequency Kulite pressure transducer (XCEL-100-5A). These were made at the tunnel center span, 106 mm (4.18 in.) downstream of the nozzle-test section interface. Four signals were sampled at 400 kHz using a NI USB-6366 X-Series DAQ system. The signals included DC coupled (gain x100) and low-pass filtered at 100 kHz using a 8-pole Bessel filter in a Krohn-Hite chassis, AC (842 Hz) coupled (gain x2890) with the same 100 kHz low-pass filter, as well as the raw DC and AC coupled signals without the 100 kHz anti-aliasing filter. PSD plots were formed from the AC filtered signal using Welch's method. 2048 points comprised each periodogram, which utilized a Hamming window. The frequency resolution was 195 Hz. ACE run 3290 and 3291 were both conducted by sweeping through Reynolds numbers anticipated for testing on the model. The fluctuation levels presented from these runs were generated by integrating the PSDs using the trapezoid rule over the range of approximately 1 kHz to 100 kHz. PSD plots for Run 3291 are given in Figure 88 (left), and the fluctuation levels for both freestream pitot runs are plotted in Figure 88 (right).

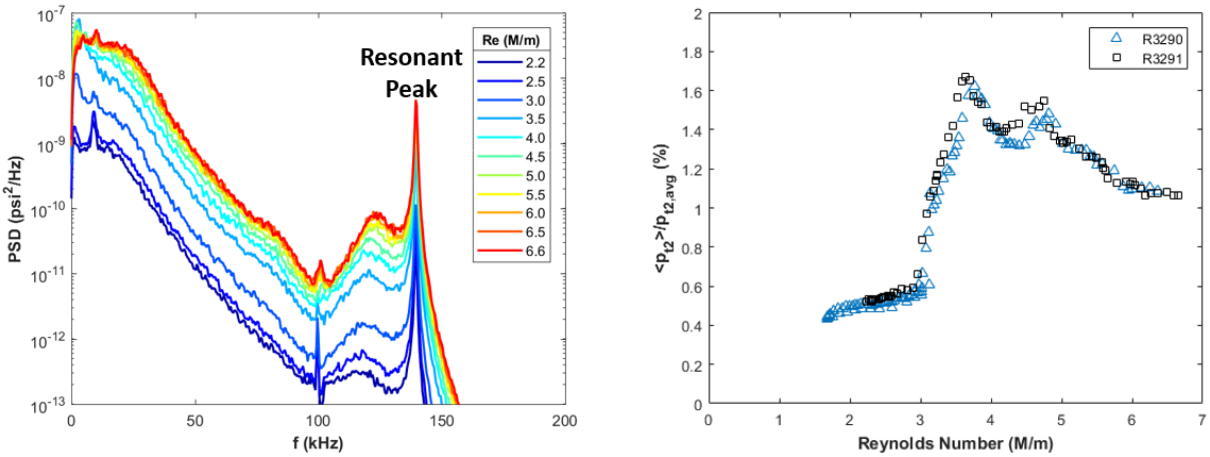

Figure 88. Freestream pitot PSD plots (left) and normalized RMS pressure fluctuations (right)

The pressure fluctuation levels are similar for both runs and consistent with those reported by Mai and Bowersox [192] and Semper et al. [26]. The most notable feature in the fluctuation profile is the jump from roughly 0.6% to 1.7% near a Reynolds number of 3M/m, which is due to the transitioning of the nozzle sidewalls. This is an important characteristic of the ACE tunnel because it allows for investigation into the effects of freestream noise on the transition process. This same jump is observed in the spectra, where the greatest energy gap is between 3.0 and 3.5 M/m. The energy rise across the frequency domain is nearly uniform with increasing Reynolds number. The shape of the spectra and the slope from 25 to 100 kHz are similar for all conditions. Most of the energy is held in the lower frequencies (<25 kHz), and no dominant frequency manifests at any Reynolds number.

4.3.2 Mass Flux Fluctuations

Mass flux measurements were made using a hot-wire anemometer set to a high overheat. The specifications, signals acquired, and data processing are all outlined in Section 3.4.1. Measurements from Runs 3340 and 3341 were taken at the same position as the pitot measurements. PSD plots for Run 3340 are given in Figure 89 (left), and the mass flux fluctuation levels for both freestream hot-wire runs are plotted in Figure 89 (right). The plot indicates the points on the Reynolds number ramp up and ramp down for each run. The fluctuation levels appear to be path independent.

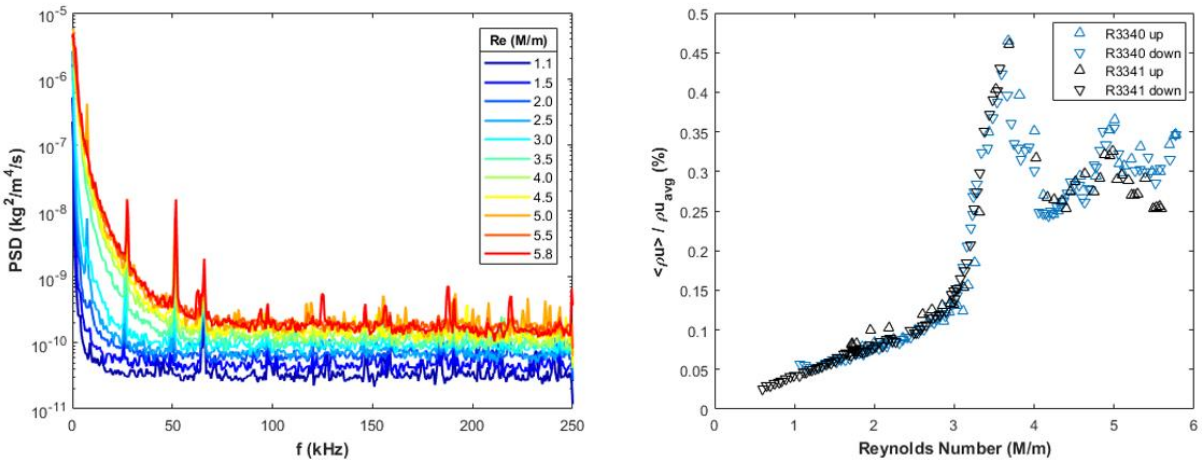

Figure 89. Freestream hot-wire PSD plots (left) and normalized RMS mass flux fluctuations (right)

The mass flux fluctuation and pressure fluctuation trends are similar in that the spectra show energy concentrated in the lower frequencies, and the disturbance levels roughly triple near *Re*=3M/m. The mass flux fluctuations represent a smaller fraction of the total in comparison to the pressure fluctuations and taper off more quickly as the Reynolds number is reduced below 3M/m.

5. INCOMING BOUNDARY LAYER CHARACTERIZATION

This chapter presents data from hot-wire boundary layer surveys, infrared thermography, and surface mounted Kulite and PCB fast-response pressure transducers, taken with and without the array of boundary layer trips. These measurements were made without the shock generating cylinder in an effort to characterize the inflow.

5.1 Hot-wire Anemometry

Hot-wire boundary layer surveys were taken at different stations to achieve the following goals: (1) quantify dominant frequencies to classify instabilities, (2) determine the effect of spanwise position behind the trips on the boundary layer profile and fluctuation levels, and (3) establish the inflow conditions required for transitional and turbulent SBLIs [193]. The surveys were generally conducted at *Re*=5M/m since that flow condition was shown to produce a transitional SBLI. Several surveys with trips were made at *Re*=7M/m for comparison.

5.1.1 No Trips

Boundary layer profiles were generated at two axial locations (x=187mm and x=293mm) without the trip array to characterize the baseline laminar boundary layer. Boundary layer profiles from Run 3473 (x=187mm) and Run 3475 (x=293mm) are given in Figure 90 (left). The profiles indicate that the boundary layer height is roughly 11 mm at x=187mm. The fluctuation profiles for all runs are also plotted below (Figure 90, right). The fluctuations are very low throughout the boundary layer (~0.2%), which suggests the anticipated laminar flow. The spectra from Run 3473 are plotted in Figure 91. Note that they are similar in shape (nearly all energy concentrated <25

kHz) and even lower in magnitude (static vs. pitot) than the freestream measurements shown in Figure 89.

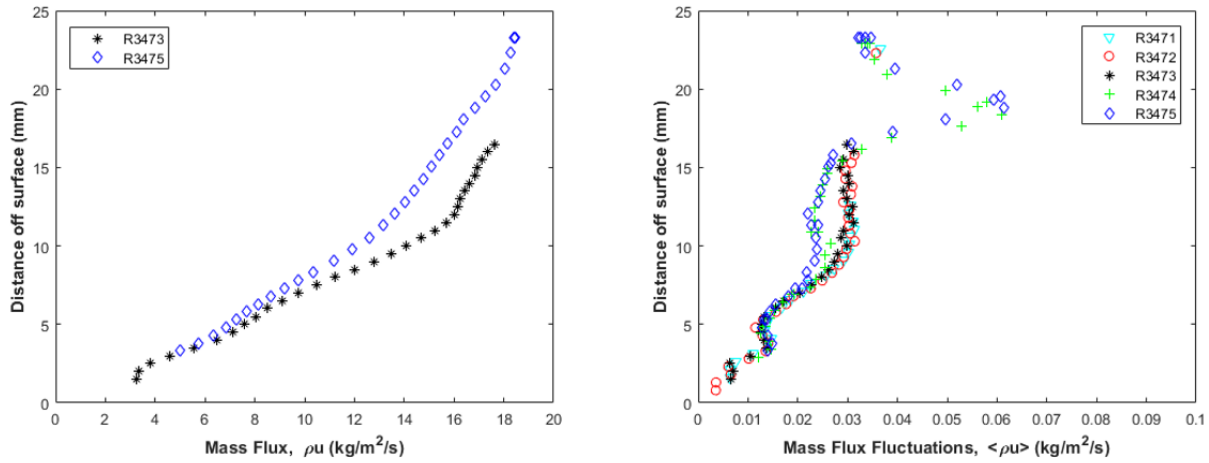

Figure 90. Untripped boundary layer profiles (left) and fluctuations (right)

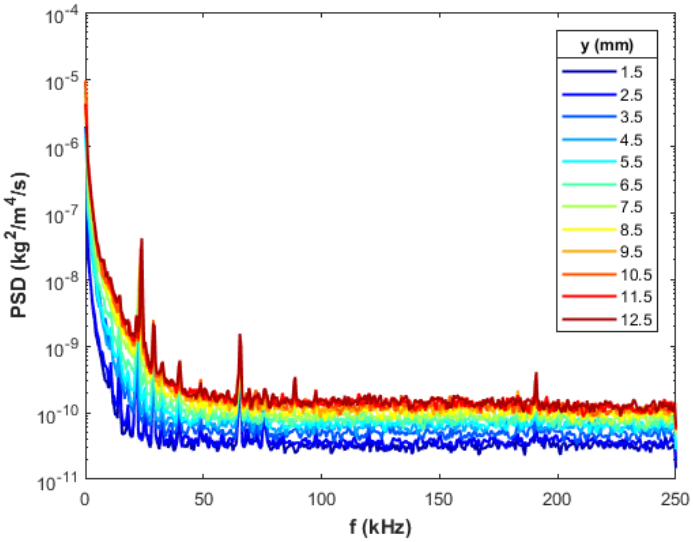

Figure 91. Untripped boundary layer spectra (Run 3473)

5.1.2 With Trips

5.1.2.1 Axial Measurements

Profile data were acquired at several axial locations near the centerspan of the model. The untripped (Runs 3471-3473) and tripped (Runs 3357-3363) surveys at x=187mm are compared in Figure 92. The mass flux (top) and fluctuation (bottom) profiles are provided in absolute (left) and normalized (right) units.

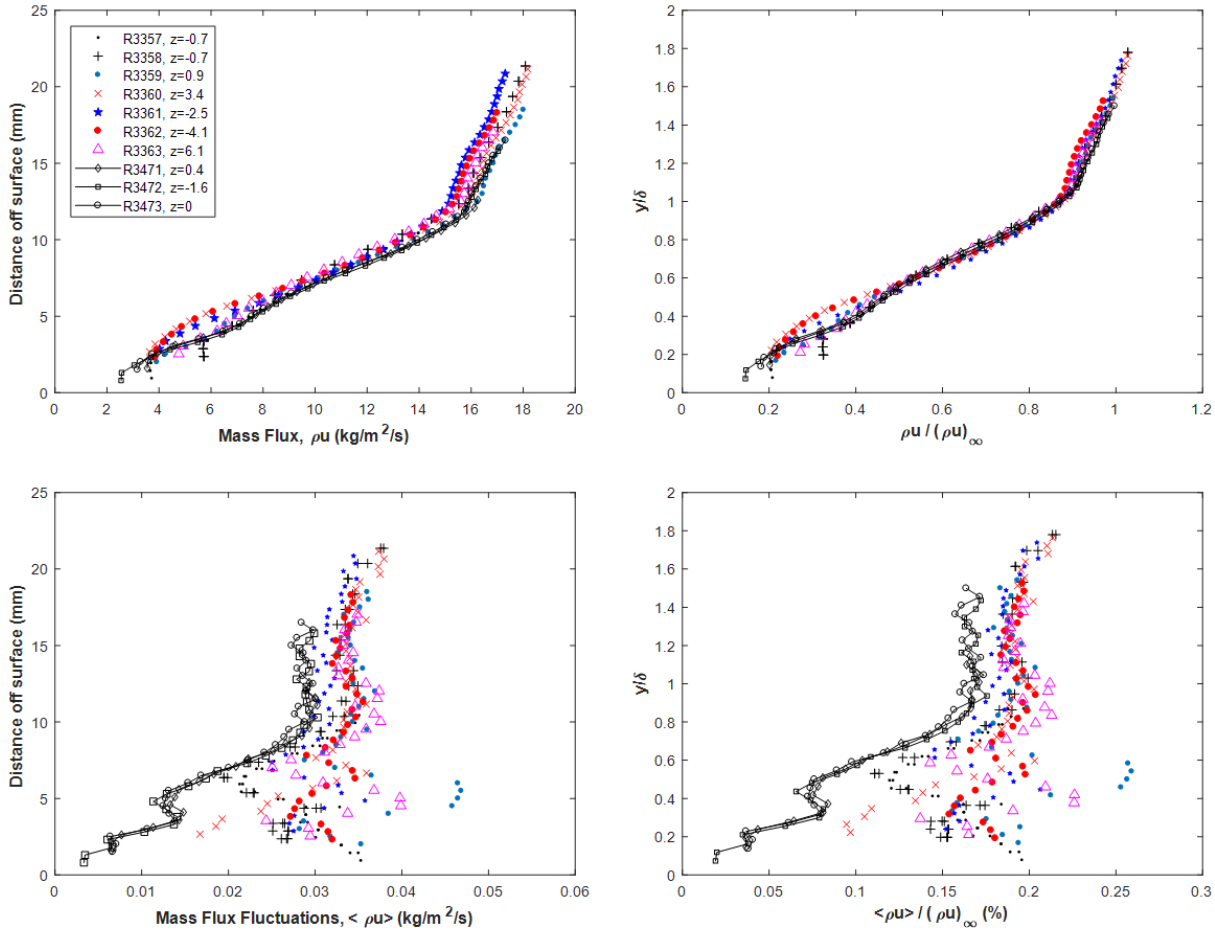

Figure 92. Mass flux (top) and fluctuation (bottom) profiles at x=187mm

In general, the tripped and untripped boundary layers produced similar mean mass flux boundary layer profiles. There is more variation near the wall for the tripped runs, and the boundary layer appears to be roughly 1.0 to 1.5 mm (~10%) thicker. When normalized by the boundary layer thickness and the freestream mass flux, the curves collapse further, particularly for y/δ >0.5. This suggests that the tripped boundary layer was laminar at x=187mm for a freestream Reynolds number of 5M/m. However, the fluctuation profiles show a significant difference between the untripped and tripped cases. First, the RMS fluctuation magnitudes outside the boundary layer are nominally 15% higher for the tripped cases. This is not surprising given that the trips produced waves and shear layers, which could yield additional fluctuations. For the untripped cases, the fluctuation amplitudes lessen near the wall, and the profiles possess a local minimum at y/δ=0.5, an inflection near y/δ=0.4, and a local maximum at y/δ=0.3. For the tripped cases, there appear to be a slight systematic peak near y/δ=1, which is consistent with Semper and Bowersox [167]. The z=-2.5mm profile is the exception. Moreover, the shapes of the profiles generally follow those for the untripped cases, including the minimum, inflection, and maximum. However, the amplitudes and locations of the extrema are dependent on spanwise position. This is not too surprising given that the trips are expected to generate a complex system of shear layers and secondary flows. Additional inspection is required to discern systematic dependency on z for the tripped cases with respect to the streak locations. This is discussed in Section 5.1.2.2.

Three boundary layer profiles were acquired 213 mm downstream of the leading edge at different spanwise locations as listed in Table 5 (Runs 3371, 3372, and 3373). All three showed higher fluctuation levels within the boundary layer compared to x= 187, 264, 276, and 302 mm, at the same flow condition (Re=5M/m). The x=213mm profiles are plotted in Figure 93. The fluctuation levels are highest near the wall (around 2 percent of the local mass flux). Spectra from Runs

3371 and 3372 (Figure 94) demonstrate instability growth between 40 and 80 kHz when compared to the "no trips, no cylinder" spectra in Figure 91. The spectra are broadest at a height of roughly 6-7 mm above the model, which is above the position of maximum fluctuations and just more than half-way to the boundary layer edge. The sharp spectral peaks are attributed to either strain gauging or prong vibrations.

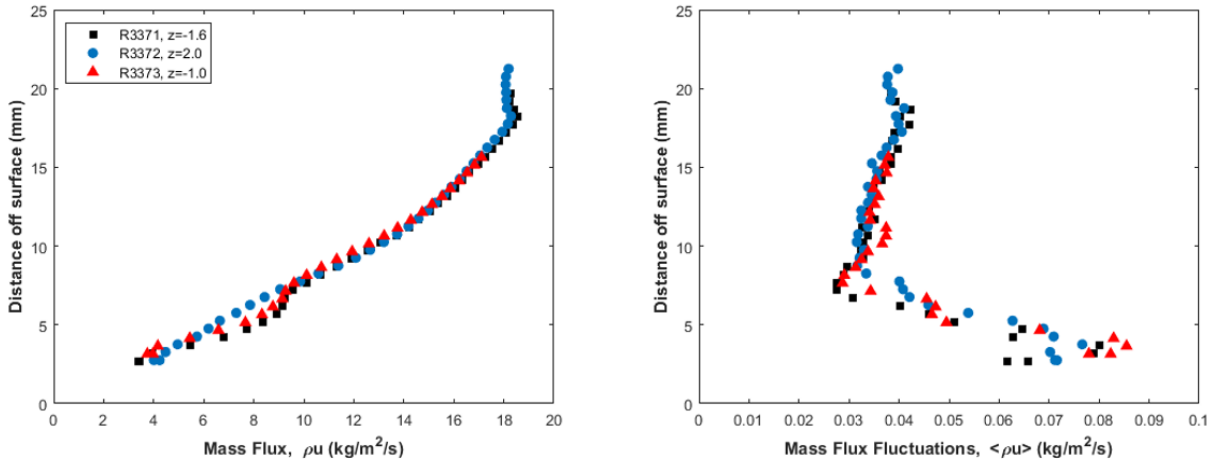

Figure 93. Mass flux (left) and fluctuation (right) profiles at *x*=213mm

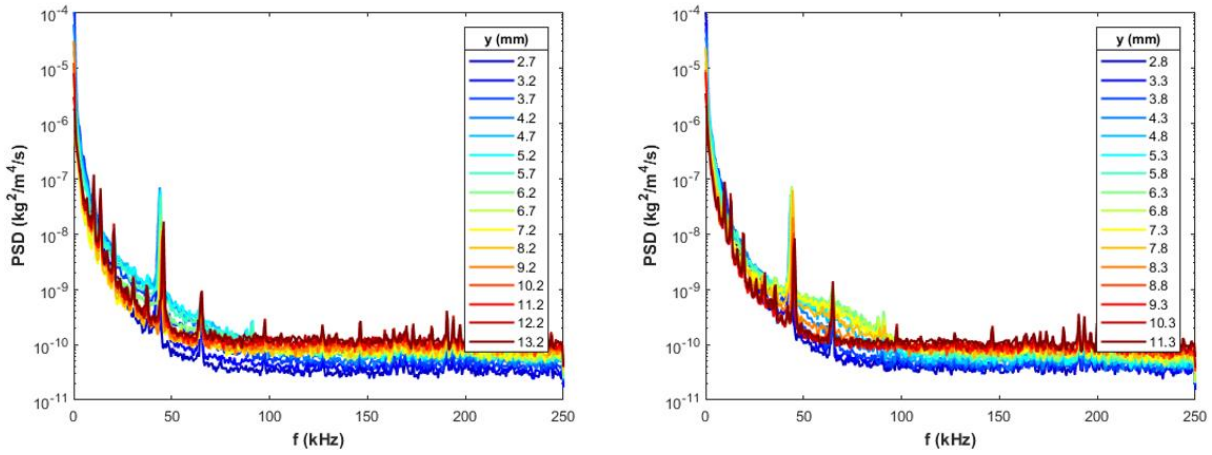

Figure 94. Hot-wire spectra for Run 3371 (left) and Run 3372 (right)

Farther downstream, fluctuation levels remain comparatively low to the experiments performed by Semper and Bowersox at a similar Reynolds number [167]. That study indicates late transitional or turbulent boundary layers at the same positions. Earlier transition is not surprising for that study since taller trips that extended past the boundary layer edge were utilized. The lower fluctuation levels in this study suggest that the boundary layer is still laminar. However, the fluctuation profile shapes at x = 264, 276, and 302 mm are qualitatively similar to Semper and Bowersox. Specifically, the peak in the fluctuations near y=7mm (roughly 60% of the boundary layer height) agrees with the far downstream observations in Ref. [167]. Boundary layer and fluctuation profiles for the five axial locations are given in Figure 95.

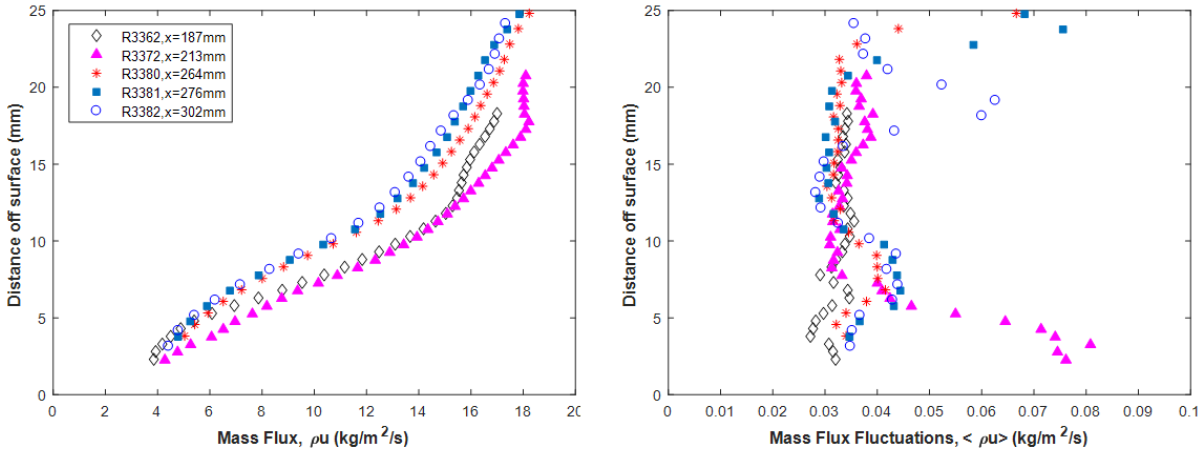

Figure 95. Mass flux (left) and fluctuation (right) profiles at different axial locations

Higher Reynolds number tests, near Re=7M/m, were also performed at x = 302 and 346 mm. Boundary layer and fluctuation profiles from those runs are plotted in Figure 96, and spectra from Run 3387 (x=302mm, Re=6.9M/m) and Run 3390 (x=346 mm, Re=7.5M/m) are plotted in Figure 97. The wire was not calibrated above 22 kg/m^2/s, so points near the boundary layer edge extend beyond the calibration.

Spectral deviations from the laminar signature for both runs are most pronounced between 10 and 12 mm above the wall, which is also near the boundary layer edge. The broadening of the spectra for Run 3387 appear to be characteristic of the beginning stages of transition, where energy from the instability peak begins to cascade down to higher frequencies. The survey for Run 3390 was conducted at a higher model Reynolds number, and the spectra for this run appear to be further down the transition process, with higher energies across the frequency domain. The boundary layers do not appear to be fully turbulent for either of these surveys; the fluctuation levels are too low.

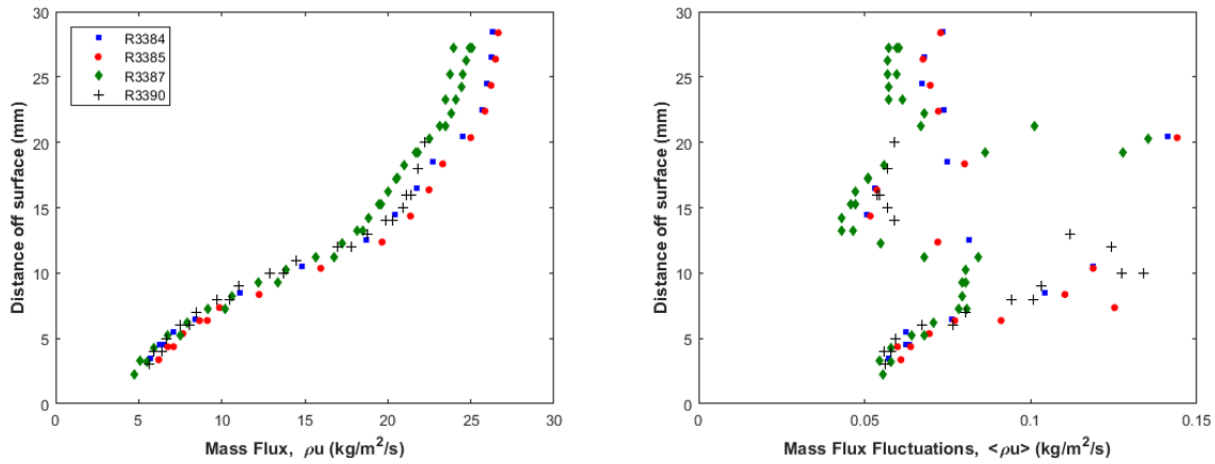

Figure 96. Mass flux (left) and fluctuation (right) profiles for *Re*=7M/m

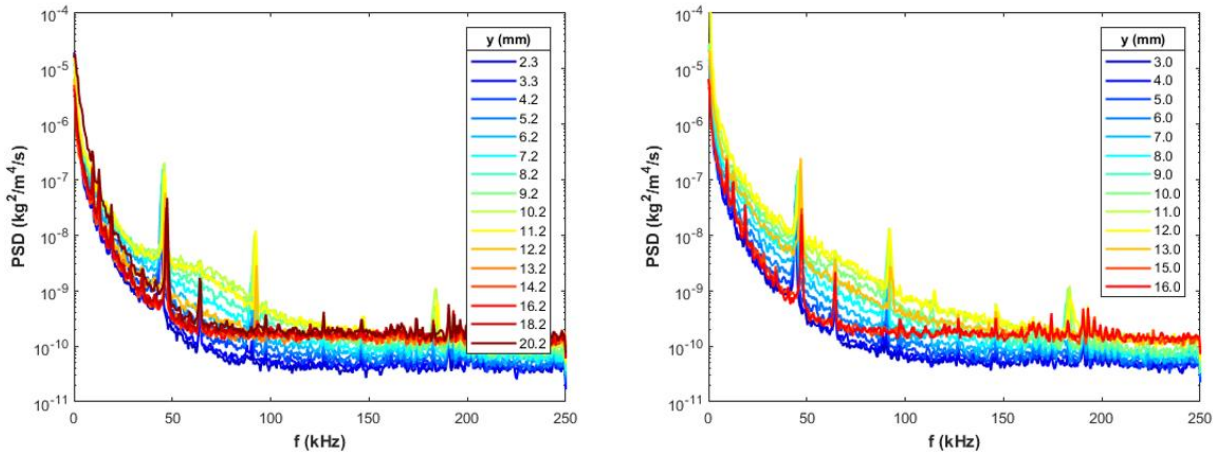

Figure 97. Hot-wire spectra for Run 3387 (left) and Run 3390 (right)

5.1.2.2 Streak Effects

One of the goals of this study was to determine the effect of the trip wakes on the boundary layer profiles and fluctuation levels by acquiring data at different spanwise stations. Figure 92 displays evidence of this dependency. Hence, a systematic inspection was performed during Runs 3364-3370 at x=187mm, which is near the outside PCB (z between -29 mm and -24 mm) where the trip wakes are well-defined. Infrared imaging was used to visualize the hot-wire position relative to surface heating streaks and the PCB pressure sensor ports. The infrared images of the wire at the closest point to the model are given in Figure 98. The bright streaks are areas of higher surface heating where the high energy flow from the freestream penetrates closer to the model. The probe was positioned above a hot-streak in slightly different spanwise positions for Runs 3364-3366, 3370. It was above a cold streak for Runs 3367 and 3368. The boundary layer profile and fluctuation levels are plotted in Figure 99. The probe position is summarized in the left figure legend. In the outer 50% of the boundary, the mean flow profiles overlapped (left plot in Figure 99). Runs 3364 and 3370 showed similar profiles, as expected since they were essentially at the

same location directly over a hot streak. The profiles for Runs 3365 and 3366 were also similar as both were shifted by 0.5 mm, but still over a streak. Runs 3367 and 3368 were on opposite sides of the same cooler region between streaks, and Run 3368 showed the largest difference in the inner half of the boundary layer. This was likely the result of the secondary flow created by the trips.

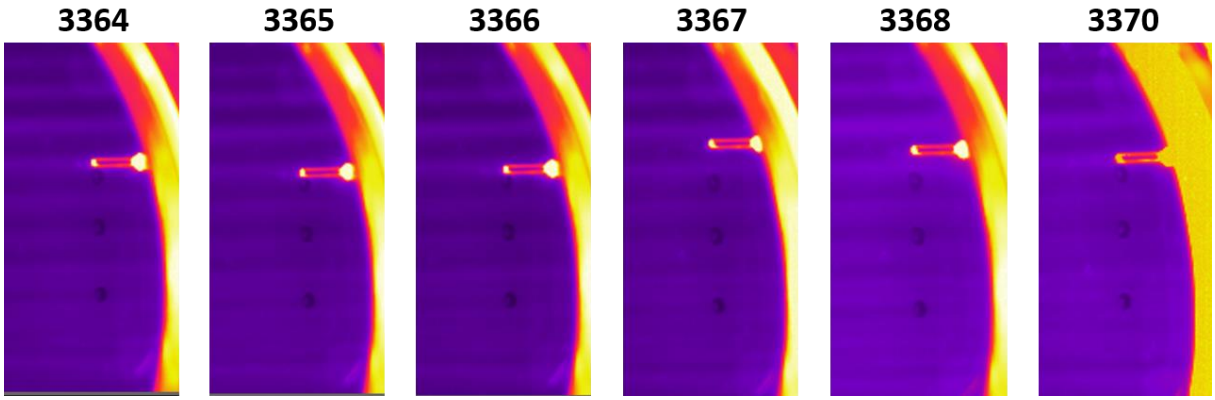

Figure 98. Hot-wire position relative to surface streaks and PCB ports

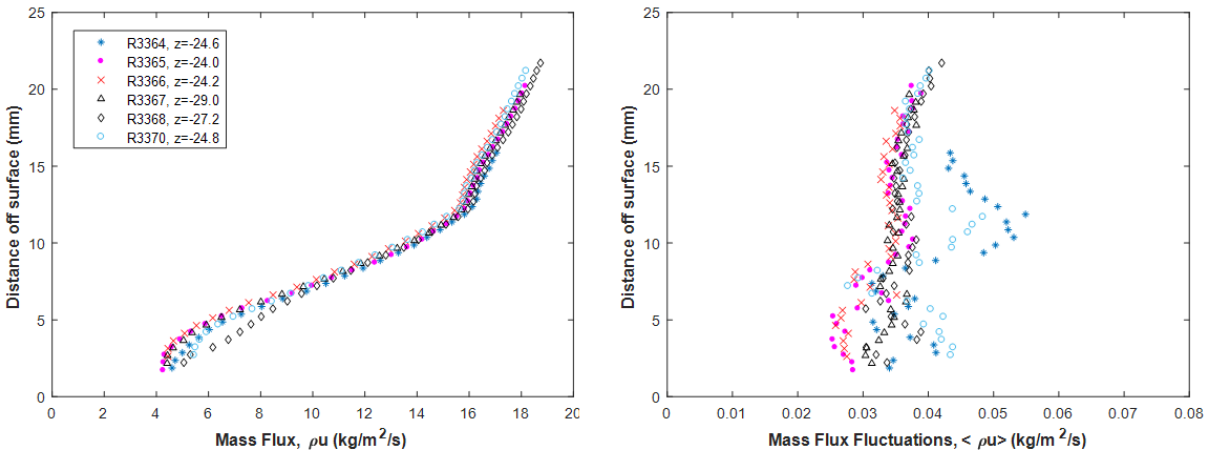

Figure 99. Spanwise variation in mass flux (left) and fluctuations (right) behind trips

The fluctuation profiles appear repeatable and show systematic dependence on location with respect to location of the hot streak. First, the profiles directly over the hot streak (Runs 3364 and 3370) have a peak near the outer edge of the boundary layer (y≈12 mm), which is similar to the instability growth seen in Semper and Bowersox [167]. Moving closer to the wall, two extrema, similar to those in Figure 92, are observed. The two off-center runs (3365 and 3366) do not show the peak in the outer layer, but do show the extrema near the wall, but with a minimum near y=4mm. Trends for the profiles over the cold streaks (Runs 3367 and 3368) are difficult to discern. None of these runs reached fluctuation levels, at any point, as high as those seen ~4 mm above the wall at x=217mm.

5.1.2.3 Leading-Edge Shock Surveys

Since the leading edge is blunted according to the polynomial in Section 3.2.1, the resulting model shock has curvature. The measured shock angle with respect to the freestream is noted in Table 12 for each of Runs 3374-77. Although these shock angles do not seem much larger than the Mach angle or oblique shock angle (9.9 and 10.7 degrees, respectively) for the Mach 5.82 freestream, they work to significantly increase the density and hence mass flux across the shock (see CFD solution – Appendix J). Table 12 provides the theoretical jump in mass flux across the shock, which can be calculated using a reduction of the Rankine-Hugoniot oblique shock jump relations, Eq. (5.1).

$$\frac{\rho_2 V_2}{\rho_1 u_1} = \sqrt{sin^2\beta + \left(\frac{\rho_2}{\rho_1}\right)^2 cos^2\beta} \tag{5.1}$$

where β is the local shock angle measured from the schlieren (see Figure 68).

Table 12. Leading-edge shock traverses

Run Number	Streamwise Position, x (mm)	Measured Shock Angle (deg)	Freestream Mass Flux ($kg/m^2/s$)	Mass Flux Across Shock ($kg/m^2/s$)
3374 (3375)	106	14.6	17.7 (17.9)	30.4 (30.7)
3376	58	16.3	17.8	35.3
3377	82	15.3	18.2	33.2

The mass flux and fluctuation levels are provided in Figure 100. It is important to note that the wire was not calibrated above 22 $kg/m^2/s$. The higher mass flux values plotted are curve-fit estimates and are intended to show the sharp jump in mass flux across the shock and the relaxation as the wire approaches the wedge. Although the agreement with the theoretical mass flux values directly across the shock is very good, there is significant experimental uncertainty regarding these points. The effect of the shock angle on the response complicates the interpretation of the data in Figure 100. These data show that, while moving toward the wedge from the freestream, the fluctuations appear to "relax" to values below those observed in the freestream above the upper shock jump. This trend is readily seen in the fluctuation profile at x=82mm (Run 3377). In the freestream (y=35mm), the fluctuation level is ~0.055 $kg/m^2/s$. The shock is located near y=30mm, and below that, the root-mean-square of the fluctuations appears to steadily drop to ~0.045 $kg/m^2/s$ at y=17mm. The jump at y=12mm is the result of trip generated shocks that are portrayed in Figure 68. The Run 3375 spectra (Figure 101) do not indicate appreciable differences within any of the regions but show broadband elevated content at shock crossings (leading edge at y=39.1mm and trips at 22.1 mm). As the fluctuation levels "relax" after both shock crossings, the spectra maintain form but slowly reduce in magnitude.

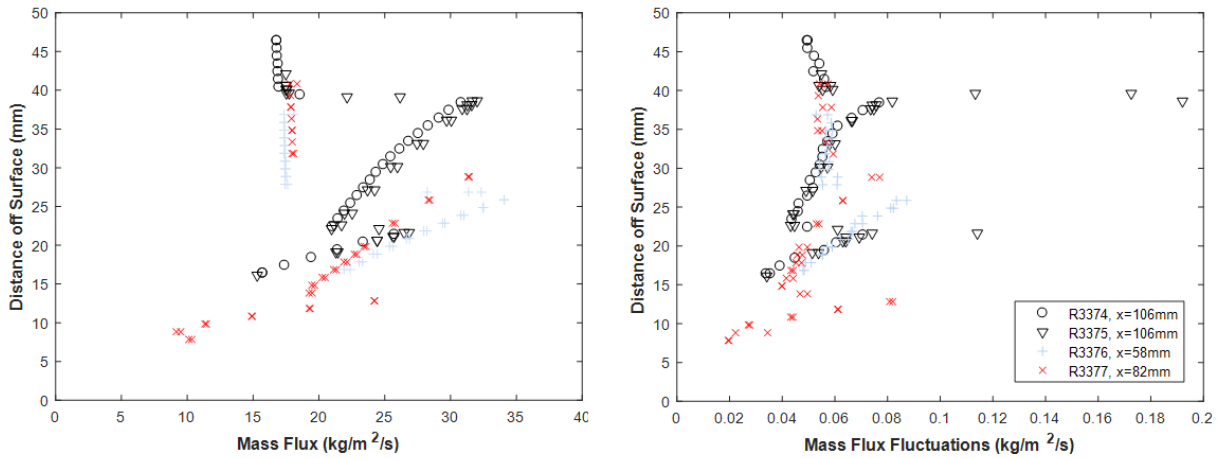

Figure 100. Leading-edge shock mass flux (left) and fluctuation (right) profiles

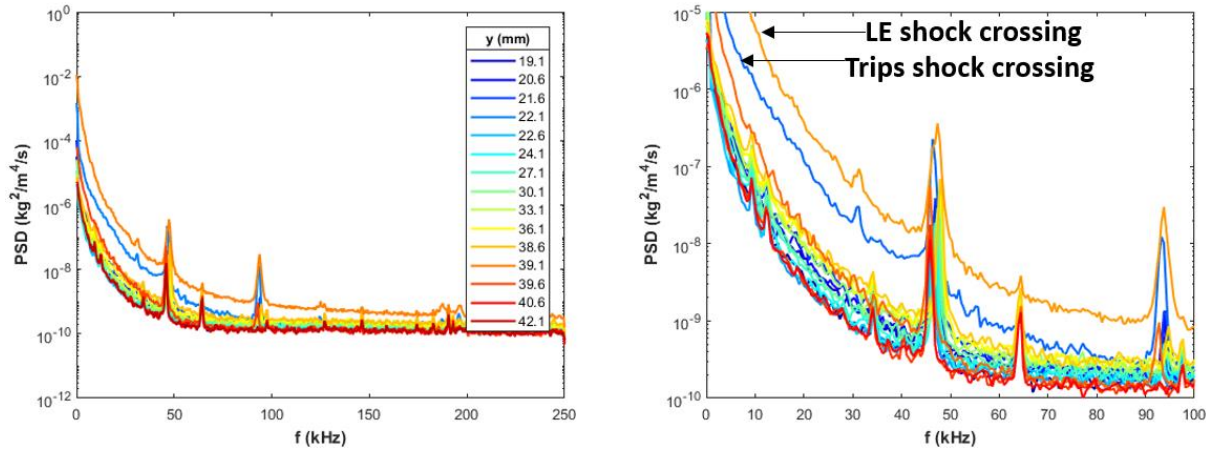

Figure 101. Hot-wire spectra from shock crossing (Run 3375)

5.2 High-frequency Surface Pressure Measurements

5.2.1 No Trips

Run 3469 served as the baseline configuration in that neither the cylinder nor the trips were present. Sample PCB (T1) and Kulite (T14) spectra, plotted to 500 kHz and 200 kHz, respectively, are given in Figure 102. Perhaps the most notable feature when comparing these plots is the ele-

vated signal in the PCB from 0-50 kHz, roughly two orders of magnitude higher than the corresponding Kulite signal. This elevated low-frequency content is not believed to be physical and will receive further consideration later in Section 6.2.1. Both sets of spectra show little content overall but indicate some growth with Reynolds number. The Kulite spectra suggest that most of the energy is contained within the low frequencies (<20 kHz) but give some indication of instability growth by the hump near 40 kHz. This frequency is in excellent agreement with the expected second mode instability frequency based on boundary layer scaling, Eq. (5.2).

$$f \cong \frac{U_e}{2\delta} \tag{5.2}$$

where U_e is the boundary layer edge velocity and δ is the boundary layer thickness. The model boundary layer edge velocity about 860 m/s and the boundary layer thickness was measured near 11 mm (Section 5.1). Spectra for all Reynolds numbers merge with the noise floor by 100 kHz. The background noise in the PCBs is too high to observe the instability growth at 40 kHz, and there is no signal change across the Reynolds number range above 200 kHz. RMS surface pressure fluctuations from all sensors in terms of Reynolds number are plotted in Figure 103. These levels were calculated by integrating the PSDs over a frequency range using Eq. (5.3).

$$g_{RMS} = \sqrt{\int_{f_1}^{f_2} PSD(f)df} \tag{5.3}$$

The Kulites were integrated from 0-100 kHz and the PCBs from 50-300 kHz. The Kulite fluctuations show some influence from the freestream as there is a peak just above *Re*=3M/m. The RMS values for both transducer sets are artificially high due to the signal proximity to the noise floor. Still, the lack of spectral content and the fluctuation levels suggests that the incoming flow is laminar.

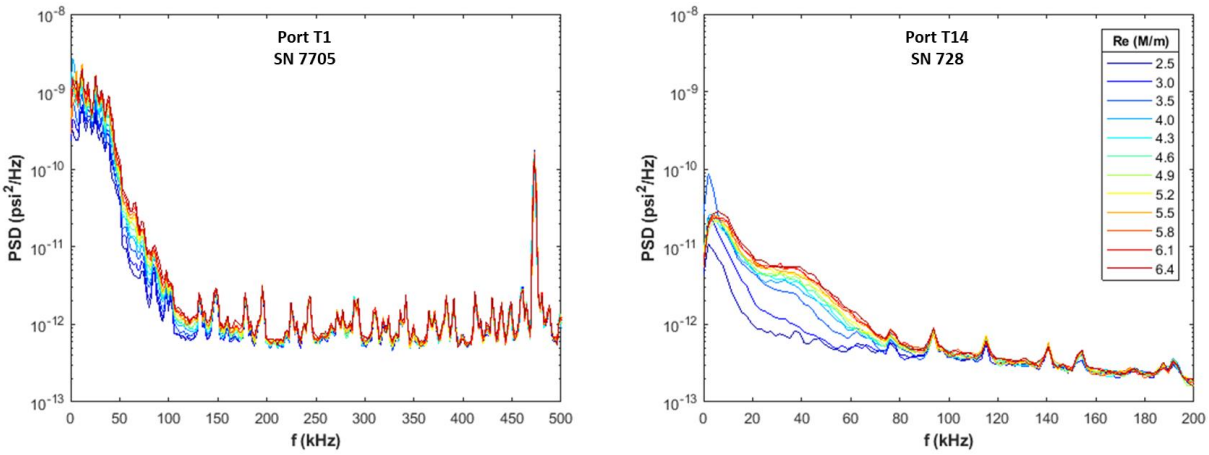

Figure 102. PCB (left) and Kulite (right) spectra for "no trips, no cylinder"

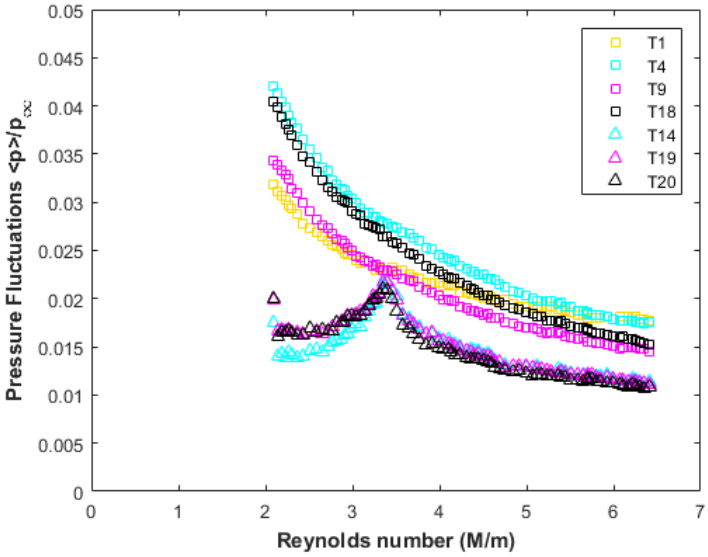

Figure 103. RMS fluctuations from all transducers for "no trips, no cylinder"

5.2.2 With Trips

The addition of trips prompted change in the frequencies of energy concentration. Spectra from the Kulite transducers at an upstream (x=222mm) and a downstream (x=298mm) location are

given in Figure 104. There are signs of growth near 40 kHz, but the peak is far from distinct, and the frequency response of the sensor is such that the signal is naturally expected to roll off near 80 kHz. A change in slope in the *Re*=6M/m spectra is observed near 120 kHz. The Kulites display signal growth with increasing Reynolds number and a broadband jump in signal near 7M/m.

While no discernable features are observed in the baseline PCB spectra (Run 3469, Figure 102), the addition of trips prompts growth of an instability near 115 kHz. This feature starts to take shape around a Reynolds number of 5M/m and becomes the dominant feature at 6M/m. A sudden elevation in and broadening of the spectra past 300 kHz is observed when the Reynolds number exceeds 7M/m. The spectra suggest there is no dependence on spanwise position. For a given streamwise station, the signal is roughly the same for a sensor located directly downstream of a trip as for a sensor downstream of a gap. The influence of streamwise position is depicted in Figure 105, where Port T1 (left) is located roughly 83 mm upstream of T18 (right). The instability peak becomes less distinct farther downstream, and that energy appears to redistribute to higher frequencies. A 115 kHz frequency corresponds to a Strouhal number of 0.43 based on the trip width and edge velocity.

The redundancy of testing different sensors in the same port allowed for spectral comparisons. This was especially important for the PCB sensors, which have been known for erroneous factory calibrations. PCB sensors 7705, 7629, and 7707 were all tested in T1, and Kulite sensors 728 and 726 were tested in port T6 for the same "trips, no cylinder" model configuration. The spectra at several commonly tested Reynolds numbers are plotted below in Figure 106. While there is some variability in the signal levels across the frequency domain, the spectra follow the same trends and are at the same levels for a given Reynolds number. This suggests that the manufacturer supplied PCB calibrations are accurate and corroborates the static in situ Kulite calibrations. PCB

content for frequencies 0-50 kHz is discussed in Section 6.2.1. Comparisons using other runs and involving all other sensors were made, and the variation in the data is similar [194].

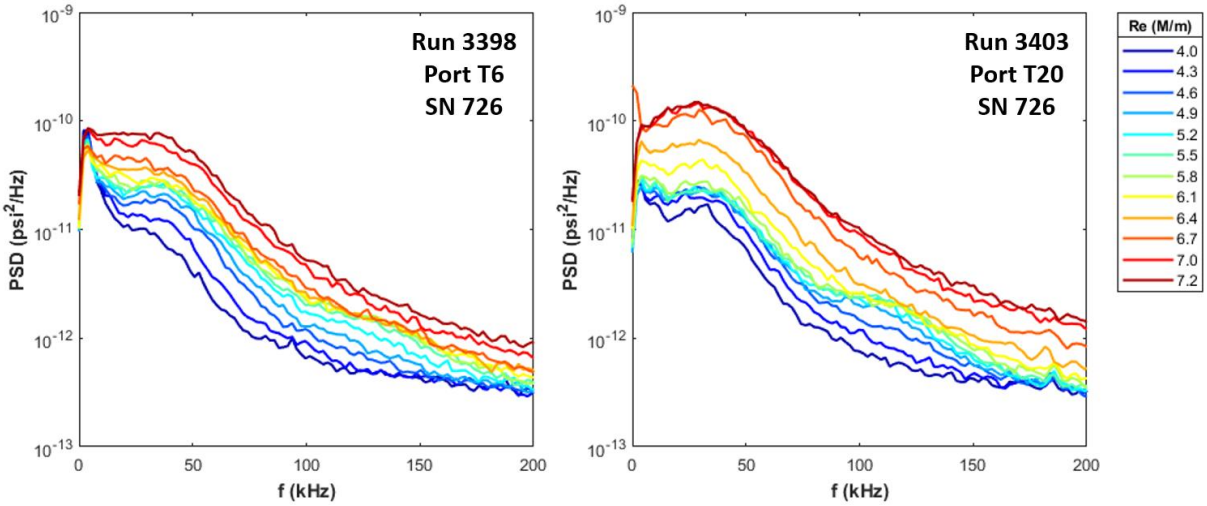

Figure 104. Kulite spectra at *x*=222mm (left) and *x*=298mm (right) for "trips, no cylinder"

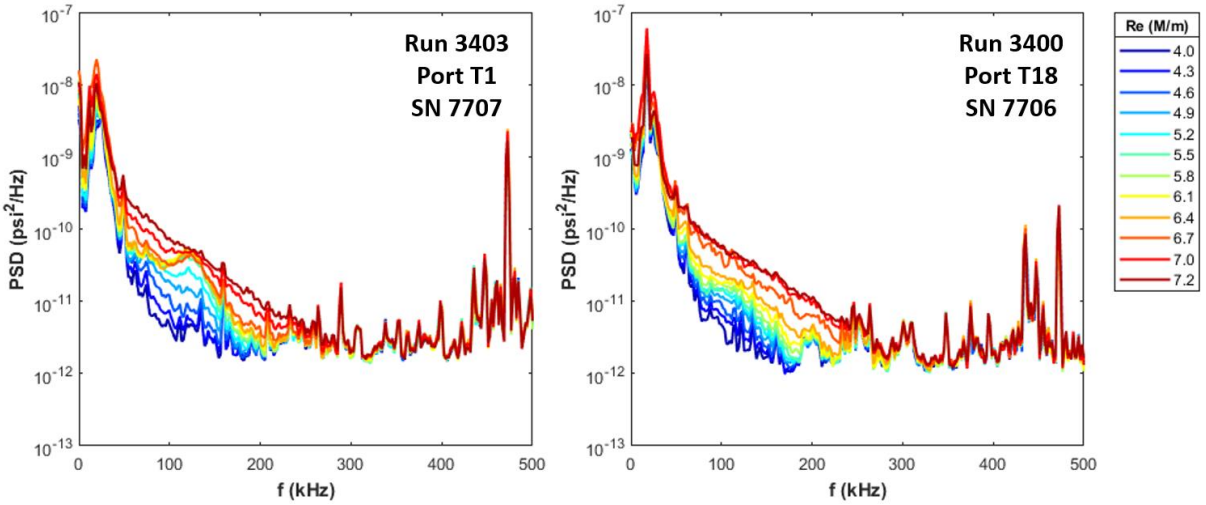

Figure 105. PCB spectra at *x*=191mm (left) and *x*=273mm (right) for "trips, no cylinder"

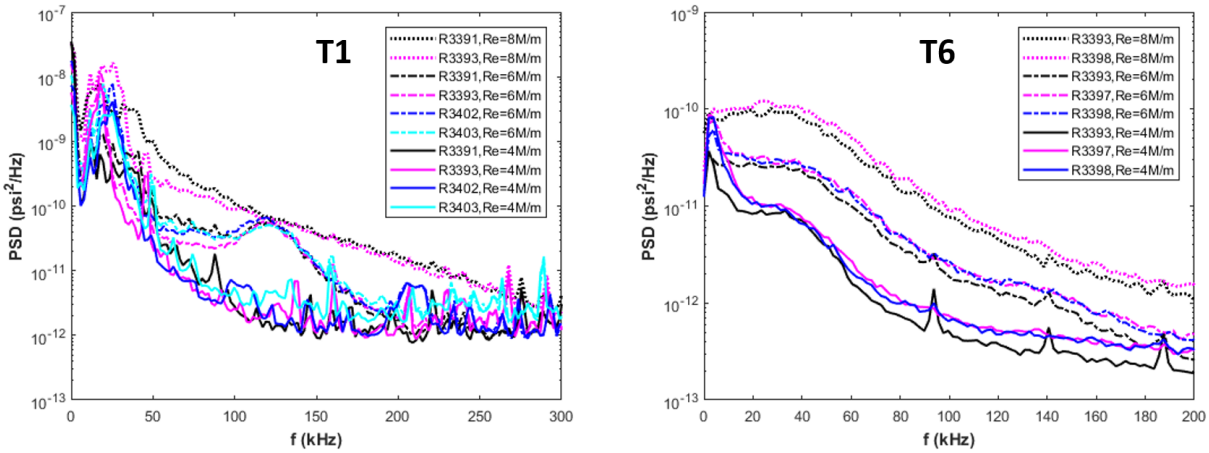

Figure 106. Spectral comparison between different PCB (left) and Kulite (right) transducers located at the same port

5.3 IR Thermography

5.3.1 No Trips

Run 3469 served as the focus for "no trips, no cylinder" surface measurement characterization. The IR camera was directed at the wedge surface and temperature maps were acquired throughout the run. Surface temperature was converted to heat flux, film coefficient, and Stanton number following the process described in Section 3.4.4. Maps of these three parameters at different Reynolds numbers are presented in Figure 107. It is easier to determine boundary layer transition from heat flux than surface temperature; however, both of these parameters are influenced by the temperature of the flow relative to the model surface. Temperature normalization is achieved through the film coefficient, and the Stanton number further promotes facility independence through mass flux normalization. Further analysis of these parameters is presented in Section 6.3.1.

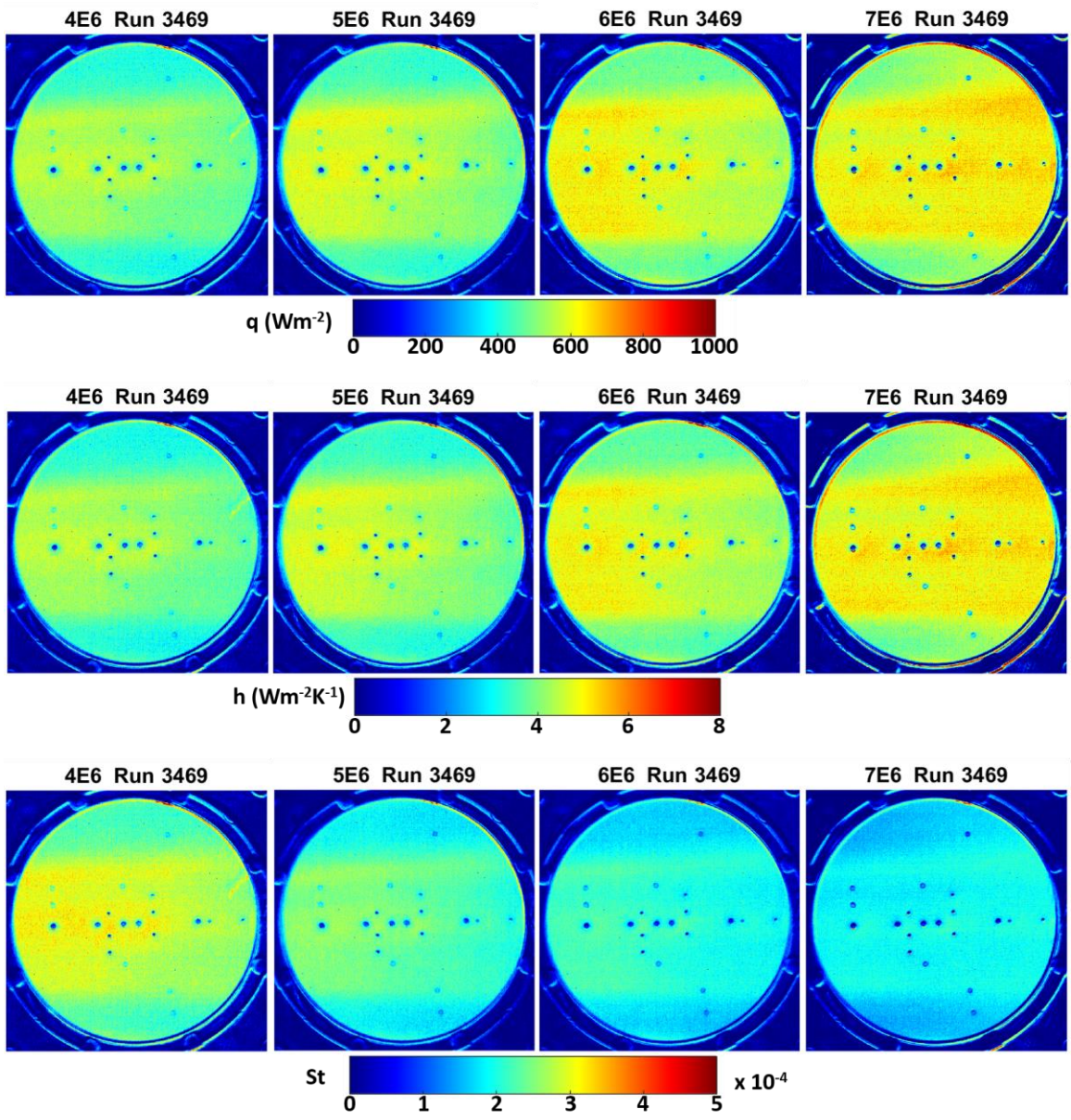

Figure 107. Surface heating parameter maps for base model at different Reynolds numbers

The maps in Figure 107 indicate that the convective heat transfer to the model wall is minimal. Heat flux values range from roughly 400-800 Wm^{-2}, film coefficient from 3-6 $Wm^{-2}K^{-1}$, and Stanton numbers from 0.0001-0.0004, over the Reynolds number range of 4.0-7.0 M/m. These

baseline values are provided for comparison with the other configurations. A notable feature from these plots is that both the heat flux and the film coefficient distributions increase with Reynolds number, but the Stanton number decreases, meaning that the mass flux normalization outpaces the heat transferred into the model.

5.3.2 With Trips

The addition of trips adds defining features to the heating maps. The wakes, which trail downstream behind the center of all trips, induce elevated heat transfer to the surface. Evidence of the wakes is observed in the maps of all heat transfer parameters (q, h, St) for Run 3421 plotted in Figure 108. The cooler streaks still demonstrate heating levels above those of the reference non-tripped configuration. For Reynolds numbers between 4.0 and 6.0 M/m, the Stanton number for a given segment of the map is roughly twice the unperturbed configuration. The ratio jumps further near *Re*=7M/m, where the heat flux suddenly ascends and Stanton number values are 3-4 times the nontripped values. Figure 109 provides a finer look at the sudden rise in Stanton number by plotting maps for Reynolds number between 6.5 and 7.4 M/m with a resolution of 0.1M/m. It is clear from Figure 108 that the Stanton number does not rise much between *Re*=4.0M/m and *Re*=6.0M/m, but there is a significant difference between maps on different rows in a given column (0.5M/m difference) of Figure 109. These maps do not present a well-defined transition front; however, the sudden jump in Stanton number supports the idea that the boundary layer is becoming transitional near *Re*=7M/m.

Figure 110 provides profile plots at two different streamwise locations (*x*=187mm and *x*=292mm) for several different Reynolds numbers during the same upsweep of Run 3421. These profiles provide insight to the magnitude of the heating oscillations caused by the trip wakes. The

amplitudes are higher at the x=187mm location, with peak-to-valley Stanton number values of roughly 0.0002, which is around twice the mean value at x=292mm. The trip insert is positioned at x=64mm, so this result indicates that the influence of the trips on the mean flow weakens farther downstream. The profile plots also clearly represent the difference in Stanton number across the span between Re=6.5M/m and Re=7.0 M/m. In fact, for z-values of -40 to 20 mm, there is not much difference in the Stanton number profiles from 3.0-6.5 M/m. Between z of 20 to 40 mm, the Re=6.5M/m curve is elevated a bit from the lower Reynolds number curves, possibly suggesting earlier transition on that portion of the model. The profiles at both streamwise stations are all much higher for Re=7.0M/m to Re=8.0M/m.

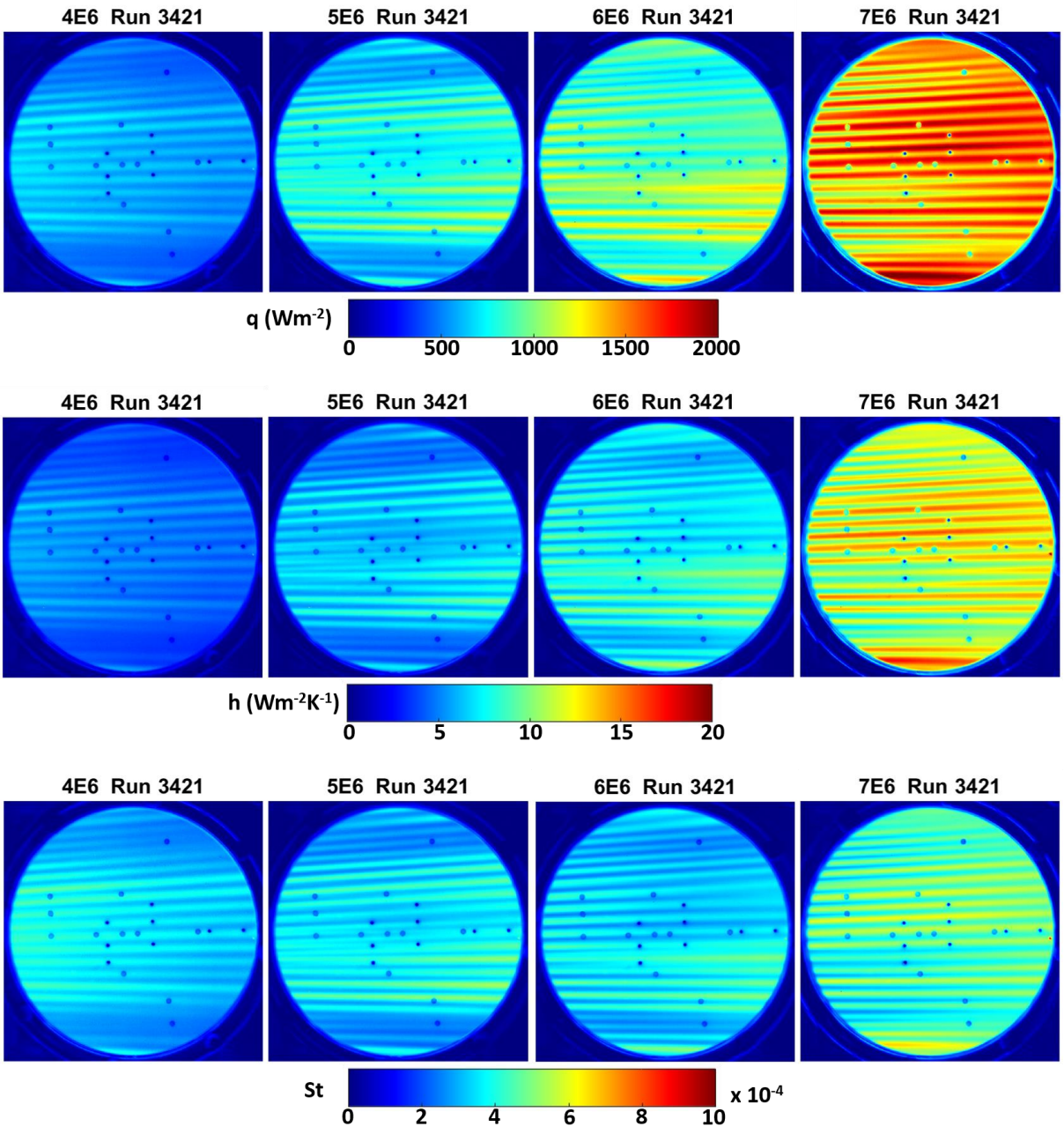

Figure 108. Surface heating parameter maps for model with trips at different Reynolds numbers

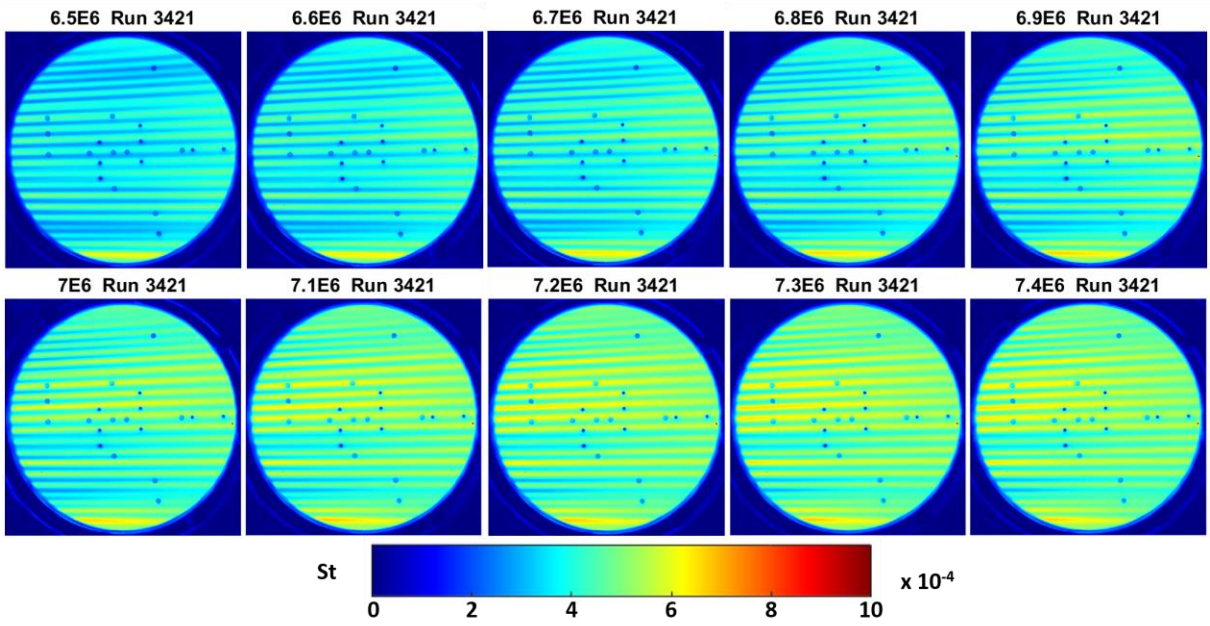

Figure 109. Stanton number maps showing jump in heating near *Re*=7M/m

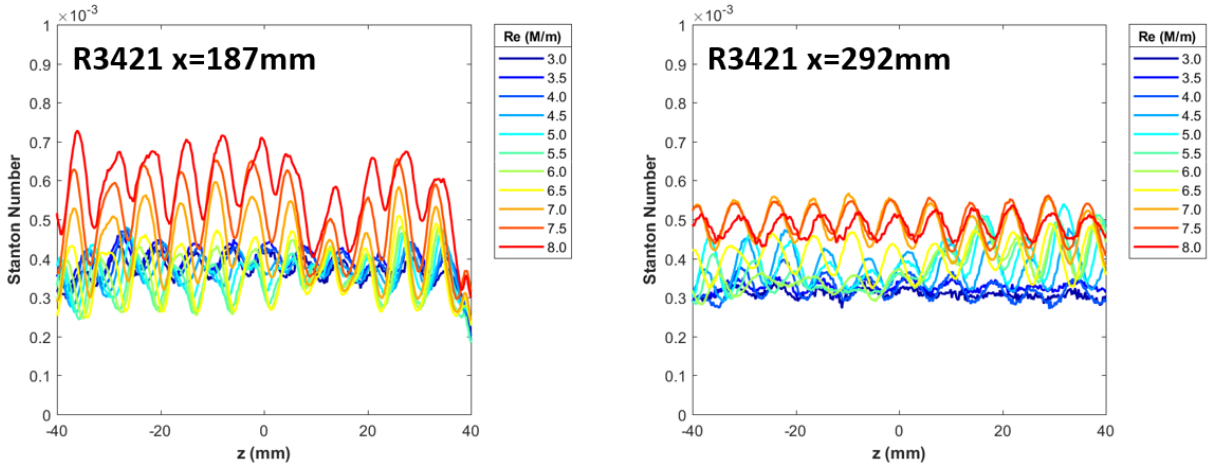

Figure 110. Stanton number spanwise profiles in the upstream (left) and downstream (right) portions of view

5.4 Summary

The diagnostics suggest that the incoming boundary layer on the model without trips is laminar. The hotwire surveys and PCBs indicate low fluctuation levels that grow across the frequency domain with increasing Reynolds number. The Kulites portray the development of an instability near 40 kHz, which is the expected frequency for second mode. IR thermography shows that heat transfer to the model is minimal for all conditions.

The addition of trips promotes spectral growth at higher Reynolds numbers for the hotwires and pressure transducers. Some hot-wire traces indicate instability growth between 40 and 80 kHz at *Re*=5M/m. The spectra broaden and appear transitional, albeit at the beginning stages, at *Re*=7M/m. The Kulite spectra maintain evidence of the 40 kHz instability across the Reynolds number range but show traces of another instability near 115 kHz. They also indicate a sudden broadband rise in content around a Reynolds number of 7M/m. The PCB spectra more prominently display the 115 kHz trip-induced instability since a PCB responds better to those higher frequencies than does a Kulite. The instability peak is generally more pronounced in the upstream PCB spectra, which suggests that the wakes weaken as they progress downstream. PCBs also show a broadband spectral jump around *Re*=7M/m, and content is observed out to 300 kHz.

While the surface mounted pressure transducers indicate no spanwise variation in spectra due to positioning behind the trips, the hot-wire anemometer portrays some variation – most notably in the mass flux fluctuation levels. The trip wakes in the IR thermography are significantly more conspicuous. Hot streaks trail each element and continue downstream over the length of the model. This leads to a spanwise profile of heating peaks and valleys. The Stanton number profiles show that the amplitude of the oscillations decreases farther downstream, which is expected since there should be less distortion to the mean flow as the distance increases and the wakes lose energy.

As with the pressure spectra, there is a jump in Stanton number near 7M/m, indicative of a transitioning boundary layer.

6. SBLI RESULTS

This chapter summarizes the testing configurations and offers the results obtained from the surface mounted pressure transducers, IR thermography, and high-speed schlieren imaging. Hot-wire measurements from the wake of the cylinder and focused schlieren images and spectral maps are also presented Finally, the influence of freestream noise on the state of the interaction is considered.

6.1 Campaign Structure

Several stages of measurements were made on the composite model in an effort to independently investigate the variables influencing the SBLI. The model configurations and diagnostics are summarized in Table 13, and show some semblance to the proposed runs in Section 3.6. The complete run log is in Appendix G. Following the hot-wire characterization tests reported in Section 5.1, surface pressure and heat flux measurements were made for “trips, no cylinder” configuration (Sections 5.2 & 5.3). The next wave of tests more prominently featured the high-speed schlieren in addition to the surface diagnostics on the “trips, cylinder” configuration. These diagnostics were all performed simultaneously for the remainder of the campaign. The transitional SBLI was achieved for this set of runs. The fourth major wave of tests removed the trips, but kept the cylinder. Following those experiments, a single baseline run was performed on a no trips, no cylinder configuration. The final group of tests included the trips and focused on the effect of cylinder sweep. A sketch showing side-views of the swept cylinder mounting is given in Figure 59. The front and center of the base was in the same position for all sweep angles, and the cylinder height was constant. Centerspan measurements were the focus for the swept cylinder runs.

Table 13. Testing configurations and diagnostics

Run Numbers	Configuration	Diagnostics
3357-3390	Trips, no cylinder	Hot-wire, IR, HS schlieren (full run)
3391-3403, 3421	Trips, no cylinder	PCBs & Kulites, IR, HS schlieren (full run)
3422-3444	Trips, cylinder	PCBs & Kulites, IR (wedge and cylinder), HS schlieren (full run and time-resolved)
3458-3468	No trips, cylinder	PCBs & Kulites, IR (wedge and cylinder), HS schlieren (full run and time-resolved)
3469	No trips, no cylinder	PCBs & Kulites (single arrangement), IR (wedge), HS schlieren (full run)
3471-3475	No trips, no cylinder	Hot-wire, PCBs & Kulites (single arrangement), IR (wedge), HS schlieren (full run)
3476-3480	Cylinder wake	Hot-wire, PCBs & Kulites (single arrangement), IR (wedge), HS schlieren (full run)
3482-3489	Trips, angled cylinder	PCBs & Kulites (single arrangement), IR (wedge and cylinder), HS schlieren (full run and time-resolved)
3482-3484	15 deg back	
3485-3486	30 deg back	
3487-3489	15 deg forward	
3490-3494	Trips, cylinder	PCBs & Kulites (single arrangement), IR (wedge), focused schlieren (full run and time-resolved)
3490-3492	15 deg back	
3494	perpendicular	

The surface pressure and temperature measurements were taken simultaneously with the high-speed schlieren imaging. The goals of the schlieren dictated the acquisition of the pressure measurements [194]. For example, schlieren images were taken at 500 fps for an entire Reynolds number sweeping run to track the evolution of the shock structure. With constantly changing freestream conditions, many small duration high-frequency pressure measurements were made with sampling times of 100 ms. The resulting spectra from those measurements have higher uncertainty due to the changing conditions and random errors but allow for tracking progression of energy in the frequency domain with Reynolds number. The Reynolds number stepped runs, which were held at condition for the time-resolved schlieren imaging, also allowed for longer pressure samples. The transducers were sampled for 1.5 seconds at each condition during those runs. A comparison in tunnel conditions for a swept and a stepped run is shown below in Figure 111. IR

measurements were sampled at 15 Hz for two different integration times for all test runs. The IR camera defaulted to position A (directed straight down on the wedge) but was generally in position B (directed at the cylinder face) when the impinging jet predominated the high-speed schlieren field-of-view.

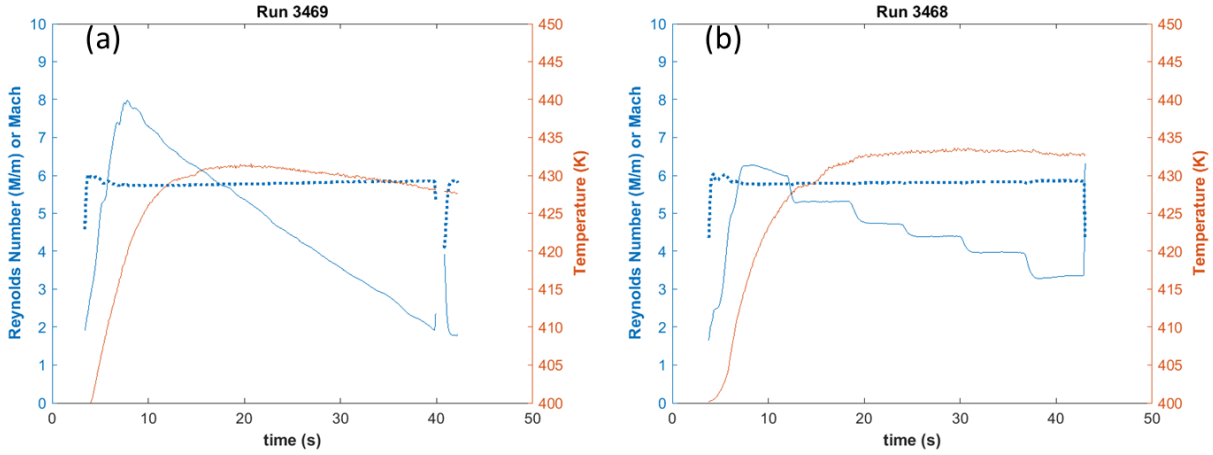

Figure 111. Representative tunnel conditions for (a) swept *Re* run and (b) stepped *Re* run. Mach number is denoted by the blue dotted line

6.2 High-frequency Surface Pressure Measurements

6.2.1 General

Many surface pressure transducer configurations were utilized during this campaign to verify repeatability and to determine if features within the spectra were sensor specific. The "no trips, no cylinder" PCB spectral data in Section 5.2.1 indicated the signal between 0-50 kHz as nearly two orders of magnitude higher than the corresponding Kulite signal. Elevated PCB signal was a common theme for all runs and for all PCB sensors. Reviewing the data from every sensor and for all runs provided some answers regarding the inconsistencies in the spectra [194].

For example, in the “trips, no cylinder” configuration, sensors S/N 7705 and 7707 were positioned in port T1 for Runs 3391-2 and 3402-3, respectively. A comparison of the spectra, plotted to 300 kHz, is given in Figure 112. From 0 to 50 kHz, the 7707 signal is peakier compared to the broader band, but lower amplitude, 7705 signal. However, the low-frequency behavior was not simply sensor dependent. Sensor 7705 was also run in T8, where it produced a sharp peak near 25 kHz. A comparison between the spectral content of sensor 7705 for ports T1 and T8 is given in Figure 113. Therefore, the observed elevated <50 kHz content is neither location dependent nor sensor dependent and cannot be physical since there is no evidence in the Kulite spectra. Additionally, this noise is not consistent for a given run or data collection channel.

PCB sensors have some sensitivity to acceleration, so it was believed that the signal could be due to some small-scale movement of the model. However, personal correspondence with M. Wason, who calibrates these transducers in the Purdue shock tunnel, gave indication that vibrations were not the cause since the spectra do not have the same signature (elevated broadband peaks at multiple frequency bands out to ~1 MHz). Whatever the cause, it is clear that content below 50 kHz from the PCB sensors cannot be trusted for this campaign. Therefore, PCB spectra are presented from 50-300 kHz in the following subsections.

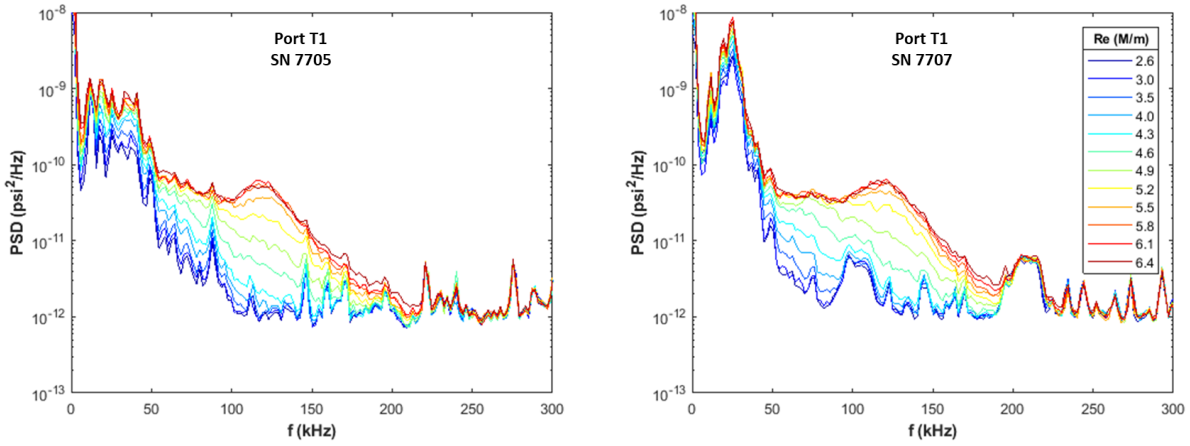

Figure 112. Different PCB sensors located at the same port (T1); Run 3391 (left) and Run 3402 (right)

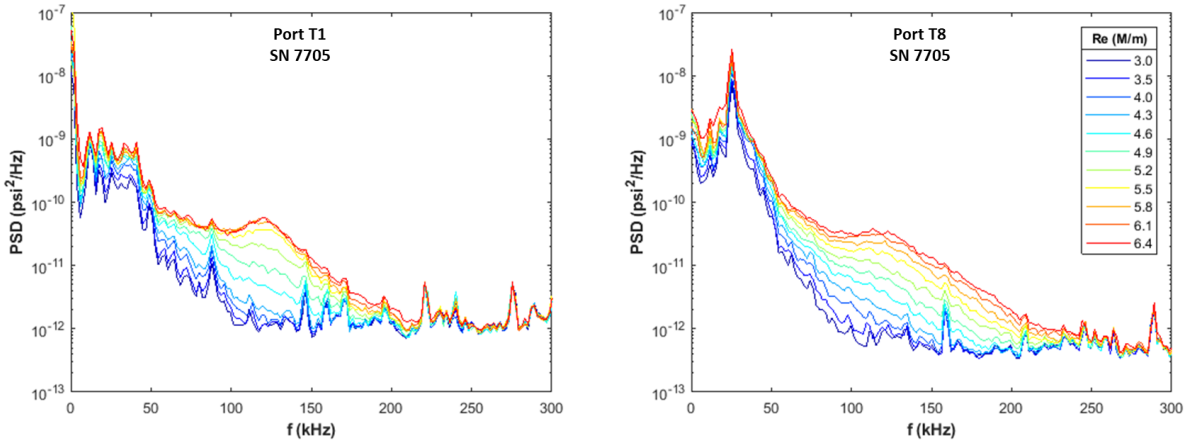

Figure 113. PCB 7705 spectra for Run 3391 (left) and Run 3403 (right)

6.2.2 Baseline "no trips, cylinder"

Evaluating the SBLI without trips provided for a low disturbance laminar incoming boundary layer for comparison. The PCB transducers (Figure 114, left) indicate minimal content above the baseline for Ports T1-T4 and T9. The spectra broadened at locations closer to the cylinder

(Figure 114, right), but the RMS fluctuations are still only one-half to two-thirds of the corresponding signal with trips at the measured positions.

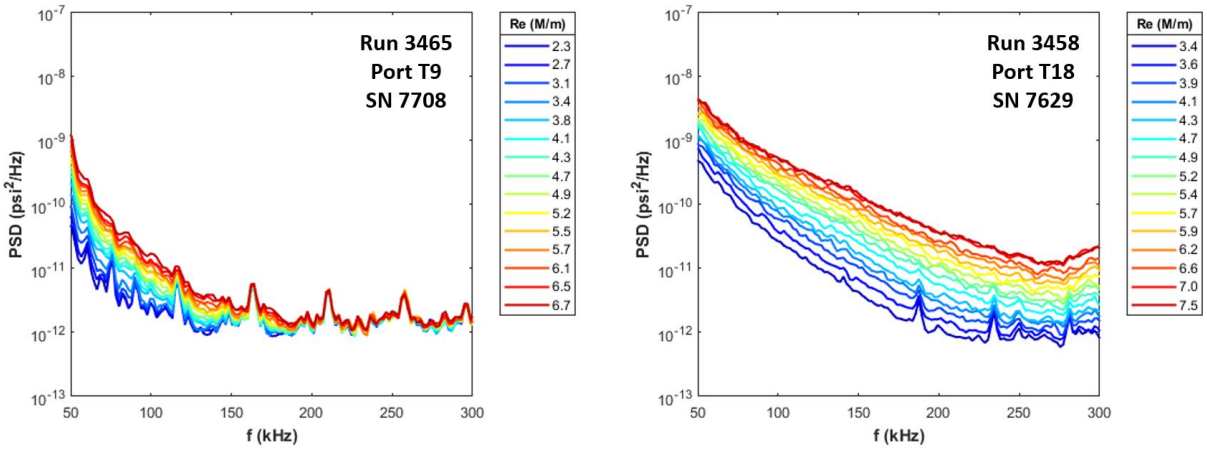

Figure 114. PCB spectra for the "no trips, cylinder" configuration. T9 (left) spectra have minimal content, while T18 (right) spectra are elevated and broad

The Kulites demonstrate noteworthy cylinder-induced instability growth. The presence of the cylinder appears to excite the existing 40 kHz potentially second mode instability, elevating the magnitude of the energy peak. The most upstream Kulites, located 4.33*d* upstream of the cylinder, and represented by Port T5 in Figure 115 (left), clearly show the growth of the instability with Reynolds number; however, higher frequency spectral content is minimal as the cylinder alone is not enough to transition the boundary layer at this position. Things appear to change farther downstream. Figure 115 (right) give the spectra at the next downstream Kulite station (x'=-3d). The signal at T12 is higher for all Reynolds numbers, and the instability peak near 40 kHz is less distinct. The spectra are also broader, suggesting the boundary layer may be more transitional in nature.

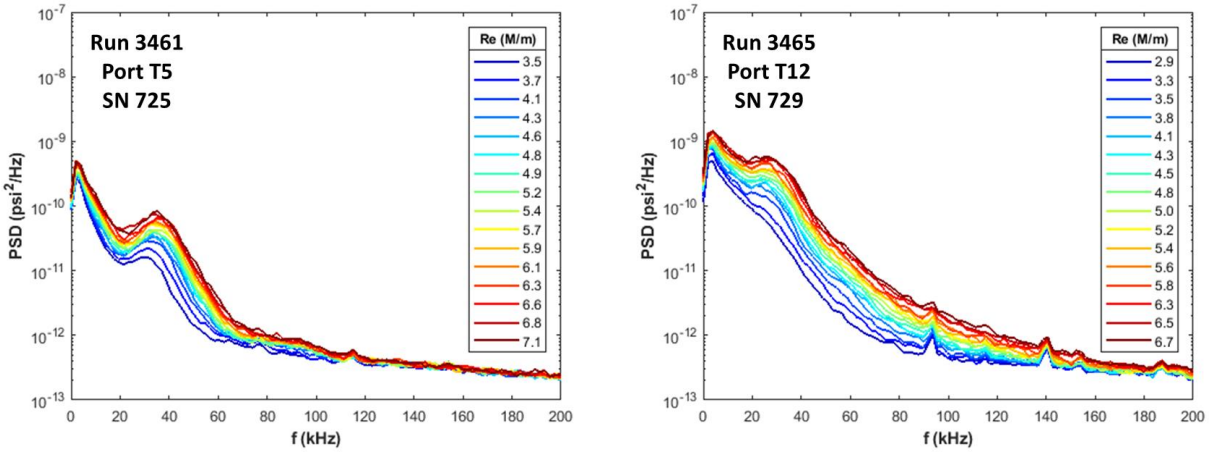

Figure 115. Kulite spectra for the "no trips, cylinder" configuration. T5 (left) shows instability growth, and T12 (right) depicts growth and broadening of the spectra

6.2.3 Transitional "trips, cylinder"

The spectra appear very much the same as the "trips, no cylinder" configuration in the most upstream PCBs (T1-T3), given in Figure 116 (left). Spectra from *Re*=4-5M/m begin to show some nonuniform marginal growth in T4, located 4.67*d* upstream of the cylinder, but the 115 kHz instability remains a prominent feature in the T4 spectra (Figure 116, right).

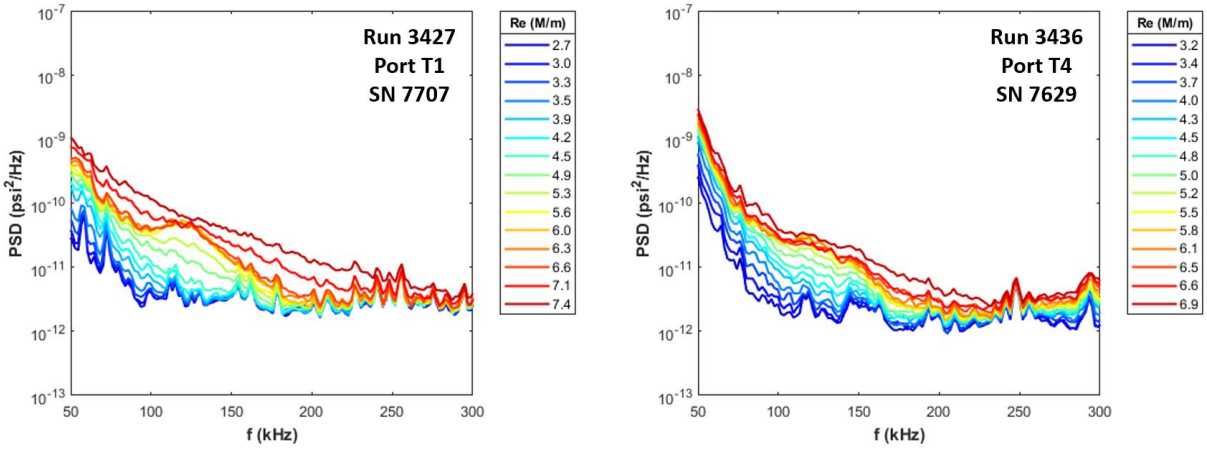

Figure 116. Upstream PCB spectra for "trips, cylinder" at T1 (left) and T4 (right)

More significant changes are observed at the x'=-4.33d Kulite transducer ports. The spectra for Port T5 are presented in Figure 117 (right). Like T4, there is some growth at the Reynolds numbers near 4M/m when compared to the previous model configuration. More significantly, there are low-frequency peaks near the same Reynolds numbers. These peaks represent the motion of the separation shock. The maximum amplitude occurs at Re=4.2M/m, and these lower frequencies will be examined more closely later in this subsection.

More substantial differences are also witnessed in the T9 (x'=-3.89d) spectra (Figure 117, left). The signal is slightly elevated for all Reynolds numbers, which effectively washes out the 115 kHz instability peak. The highest Reynolds number spectra are least affected since the surface influence of the interaction generally does not reach this far upstream.

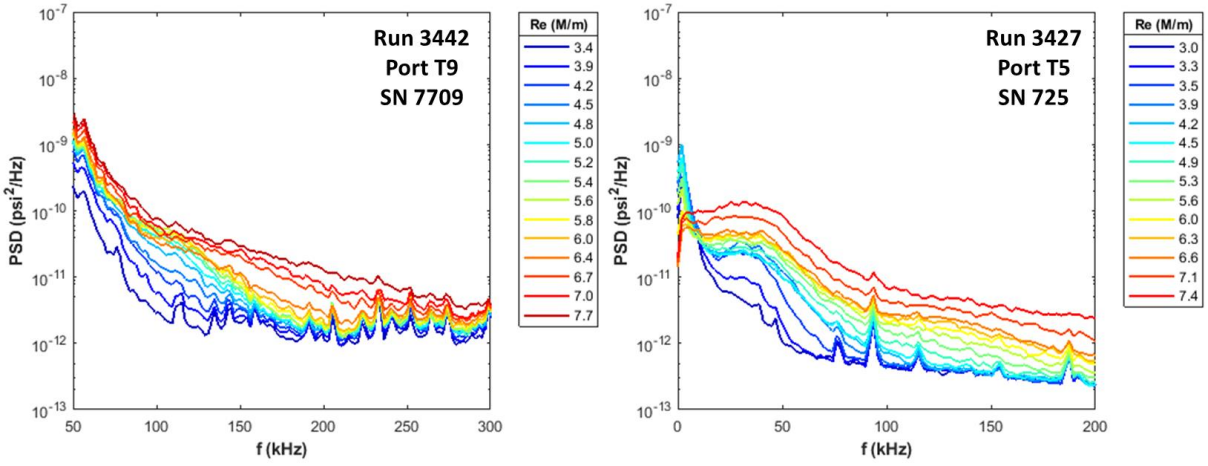

Figure 117. PCB (left) and Kulite (right) spectra indicating the first significant deviations from the baseline "trips, no cylinder" spectra

Continuing downstream, PCB Port T11 is located 3.44d upstream of the cylinder, and its spectra are given in Figure 118 (left). The elevation in content from the previous port is quite apparent. For example, the T9 spectrum for Re=5.6M/m reaches the noise floor around 200 kHz.

The T11 spectra are above the 300 kHz noise floor for Reynolds number at or above 3.4M/m. The RMS fluctuations see the most significant rise for Reynolds numbers between 4 and 6 M/m. This makes sense since the flow is separated above both ports below 4M/m, and the schlieren only indicates high fluctuation levels at the base of the cylinder for low Reynolds numbers [193]. There is not much of an RMS increase above 6M/m since the bulk of the interaction is downstream of both ports at that Reynolds number.

The next streamwise station (x'=-3d) features three Kulites, which provide particularly interesting results. Spectra from T14 are shown in Figure 118 (right), and a closer look is provided in Figure 119 (right). These spectra show evidence of modal growth. For this set of spectra, an instability peak becomes evident at *Re*=3.4M/m. It grows and shifts right until it reaches its highest amplitude at *Re*=4.9M/m at a frequency just above 40 kHz. As the Reynolds number continues to increase, the magnitude of the instability peak decreases, but the spectra broaden, leading to an increase in RMS fluctuations. This same behavior was observed near the same frequencies in the transducers K5 and K12 on the solid PEEK model [175].

Another feature of the T14 spectra is the elevated low-frequency content, which reaches a maximum for *Re*=6.4M/m. This indicates that the separation shock at 4.9M/m is located upstream of T14 and suggests that the modal instability growth occurs just downstream of the separation shock. The low-frequency peaks from T5 and T14 were better resolved using the stepped Reynolds number Runs 3439 and 3428, in which each Reynolds number was held constant while sampling for 1.5 seconds. The window size was changed from 1024 (2^{10}) to 4096 (2^{12}) and 16384 (2^{14}) to plot these spectra, for frequency resolutions of 488 Hz and 128 Hz, respectively. Spectra for T5 are plotted in Figure 119 (left), with the bold lines representing the spectra from the 2^{14} window. For T5, the highest peak is for *Re*=3.9M/m at a frequency of 1.22 kHz. For T14 (Figure 119,

center), this occurs for *Re*=6.9M/m at a frequency of 1.47 kHz. These values are consistent with frequencies previously observed for separation shock motion at Mach 5 [159]. The position of the sensors is also in agreement with the position of the separation shock for the Reynolds numbers represented based on the schlieren imaging (Section 6.4).

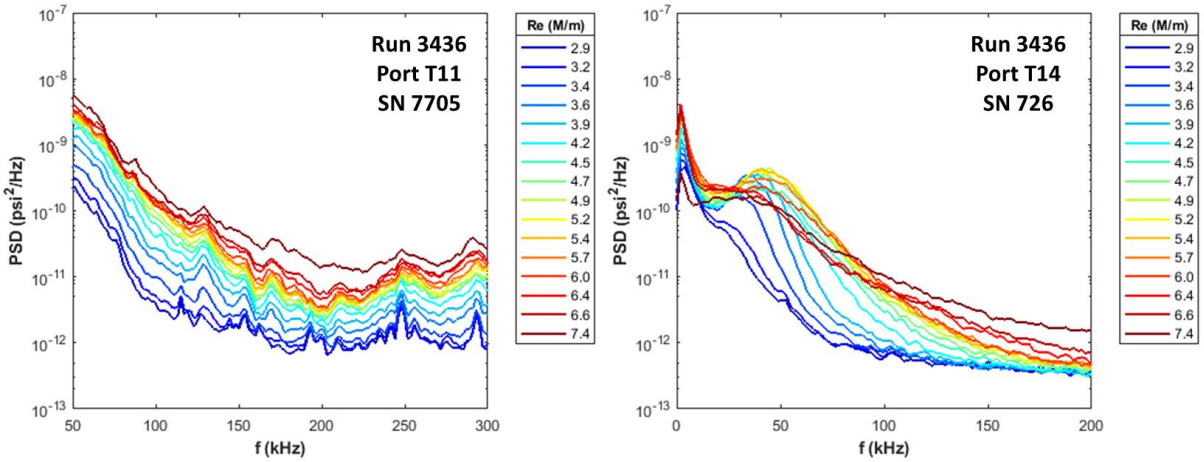

Figure 118. PCB (left) and Kulite (right) spectra for transducers placed near separation for transitional SBLIs

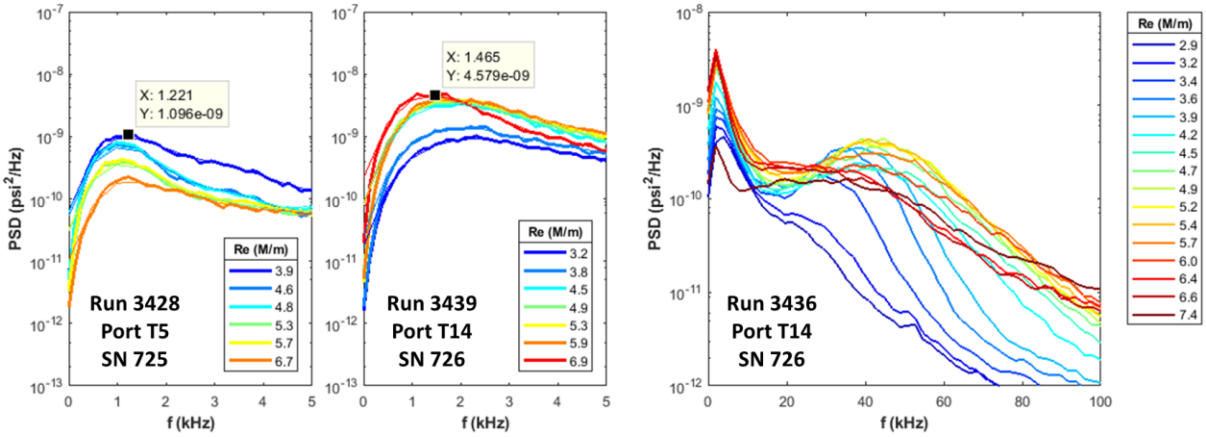

Figure 119. A closer look at the low-frequency Kulite peak due to separation shock motion (left and center) and modal instability growth (right)

The most downstream centerspan PCB sensor is Port 18, located 1.67*d* upstream of the cylinder. This sensor is positioned within the interaction for all Reynolds numbers, and the spectra reflect it (Figure 120, left). The signal is at least an order of magnitude higher across the frequency domain for *Re*>6.5M/m when compared to the baseline "trips, no cylinder" spectra. Content is even observed for *Re*=2.9M/m beyond 150 kHz. The Kulite transducer in Port 19 (*x'*=-1.33*d*) measured a signal two orders of magnitude above the baseline value for all Reynolds numbers in frequencies of 0-50 kHz. Its spectra are in Figure 120 (right).

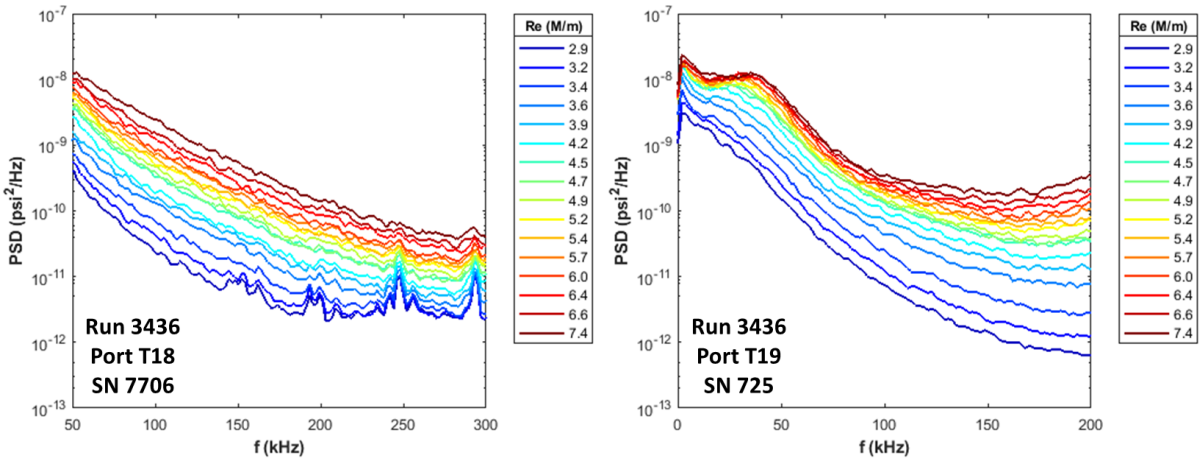

Figure 120. PCB (left) and Kulite (right) spectra for transducers positioned within the SBLI at all Reynolds numbers

Several PCB transducers were placed well off the centerspan in order to characterize the effect on the spectra. T16 and T17 are symmetrically located 2.67*d* off the centerspan and 2.5*d* upstream of the cylinder. T15 is located 2*d* off-centerspan and 2.58*d* upstream (near P2 on the solid PEEK model). The spectra from transducers at Ports 15-17 are compared to the spectra from a transducer at T11 in Figure 121. The composite oil flow separation map (Figure 86) indicates that separation occurs for all four of these ports near *Re*=6M/m. The spectra all look similar to

each other. The outboard sensors do not seem to present any more or less high-frequency content than what is observed on the centerspan.

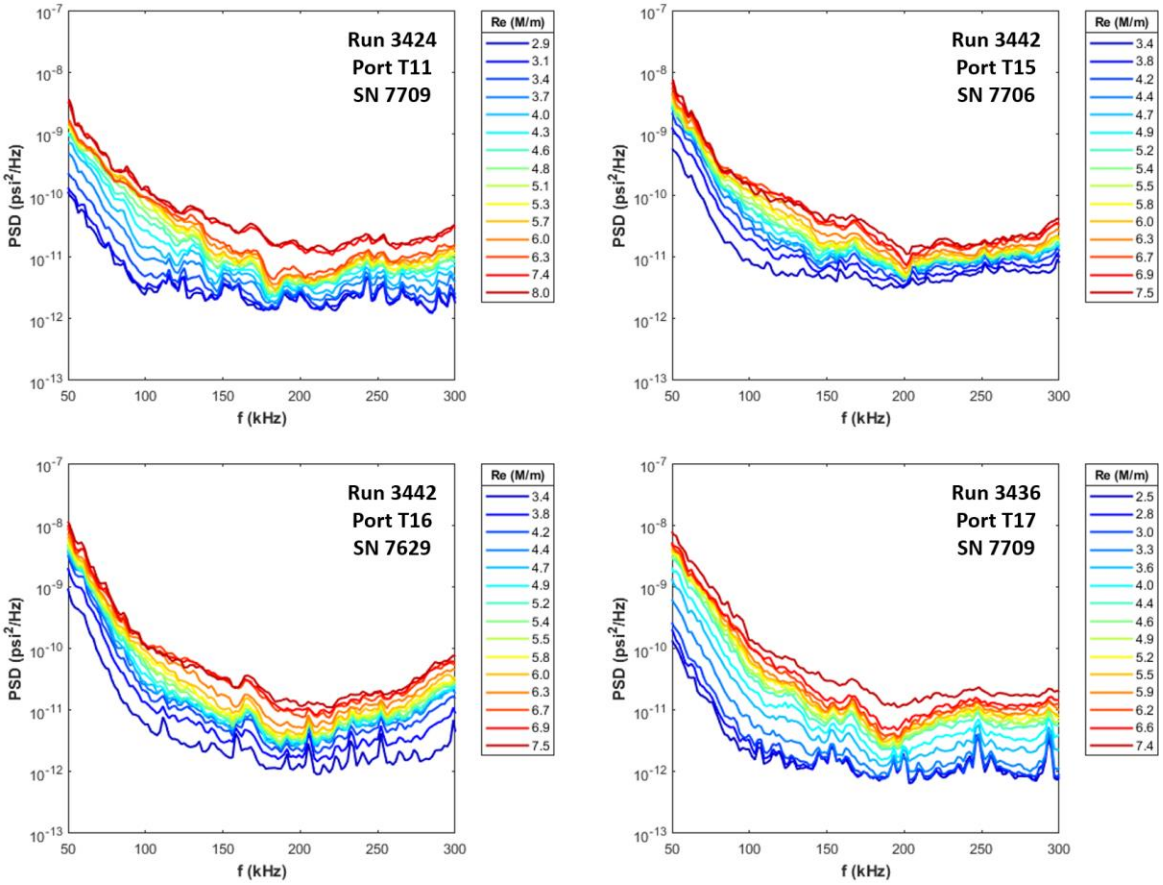

Figure 121. Spectral comparison of outboard PCBs to a PCB at centerspan port T11

Spectra from Kulites positioned in the wake were also considered. Figure 122 presents these at ports T21 (first row behind cylinder, outboard), T22 (first row, centered), T24 (second row behind cylinder, outboard), and T25 (second row). The spectra are broadband, similar to those of T19 (Figure 120, right), but do not show any signs of the 40 kHz instability. All wake spectra indicate broad low-frequency peaks, with local maxima near 20 kHz. The RMS pressure fluctuations measured with all four transducers in the wake are roughly 50% of those measured at T19.

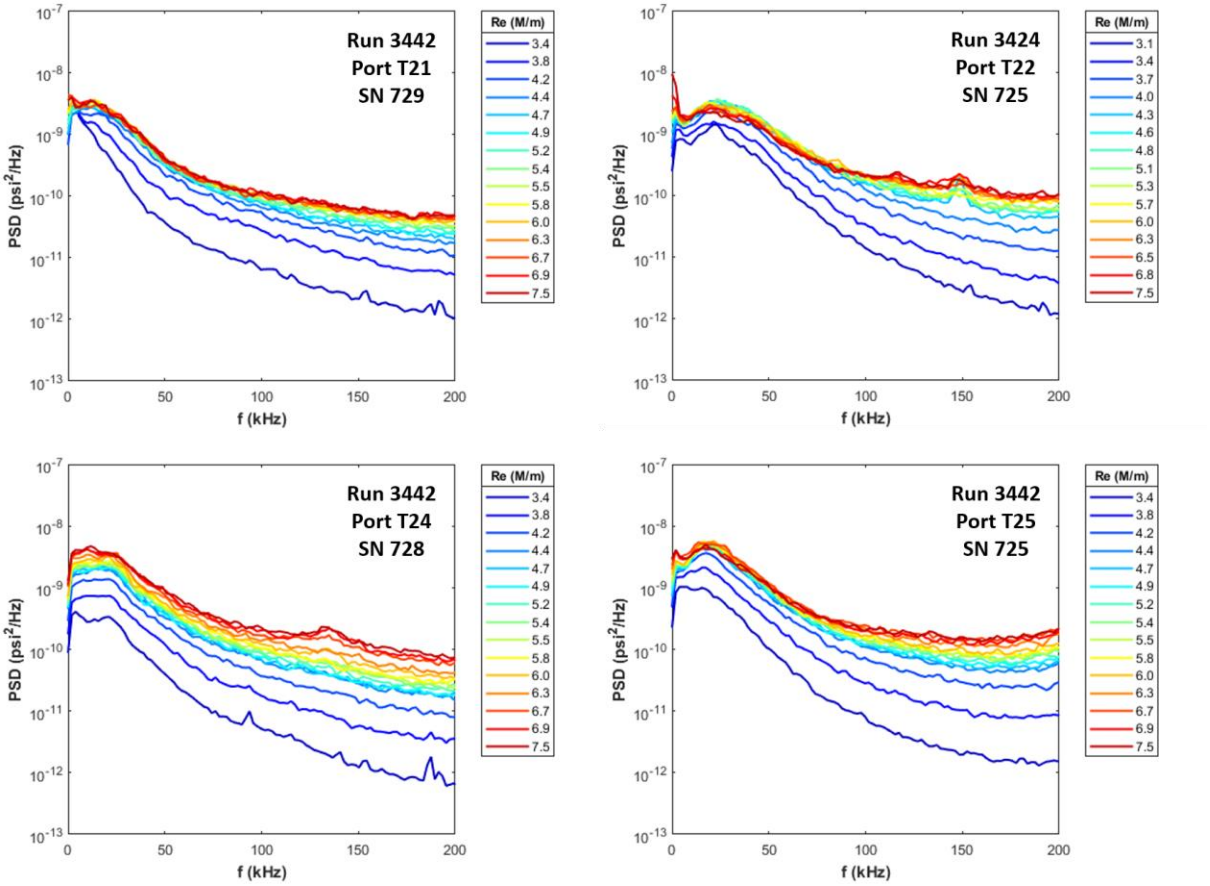

Figure 122. Spectral comparison of Kulites in the wake

6.2.4 Effect of Cylinder Sweep

The shock generator sweep angle has a significant impact on the extent of the interaction as well as the amplitude of the pressure fluctuations within the interaction. Run 3485 was conducted with a 30-degree swept cylinder and instrumentation in place along the model centerspan. Although the RMS values are higher than the baseline "trips, no cylinder" configuration for all ports, the spectra appear much the same in form (Figure 123, left) as the baseline through Port T11. At that port, the RMS value of the 30-degree swept cylinder configuration is roughly 25% higher across the full Reynolds number range than the baseline value. Significant differences from

the baseline do not become apparent until Port T18 (x'=-1.67d), spectra pictured in Figure 123 (right), and even then the magnitudes of the fluctuations are only at the same levels as for T9 (x'=-3.89d) in the conventional perpendicular cylinder case.

Higher levels are observed for the 15-degree swept cylinder configuration. The RMS fluctuation levels for this setup are marginally higher than for the 30-degree setup for the four most upstream centerspan PCB ports (T1, T4, T9, T11). The only perceptible difference in the T11 spectra for the 15-degree swept configuration (Figure 124, left) and those for the 30-degree swept setup is a slight increase in content for Reynolds numbers near 6M/m. By Port T18, the differences are more apparent as the spectra (Figure 124, right) are broader and higher in magnitude. The RMS levels are just above those from T11 (x'=-3.44d) for the perpendicular configuration and are nearly identical to the levels, at the same T18 port, for the "no trips, cylinder" configuration.

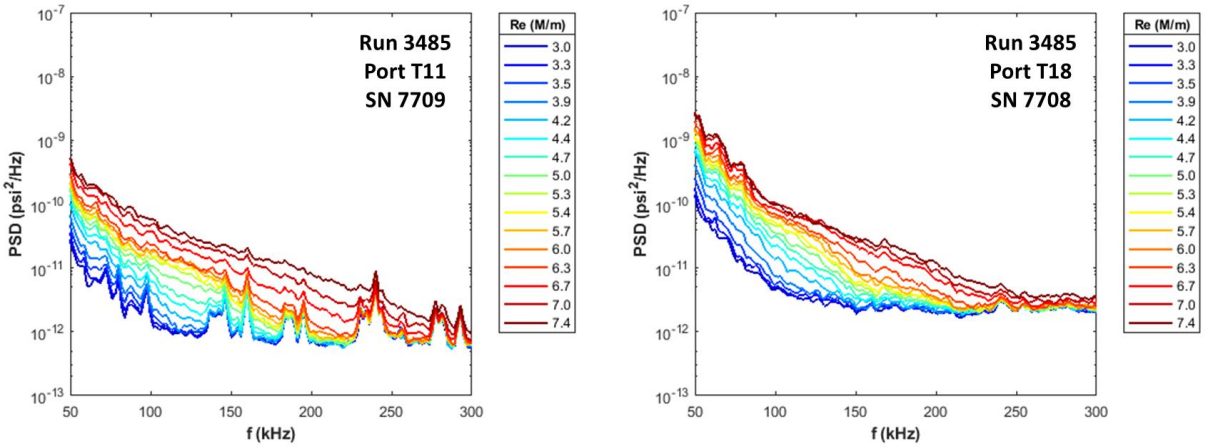

Figure 123. PCB spectra for the 30-degree swept back cylinder

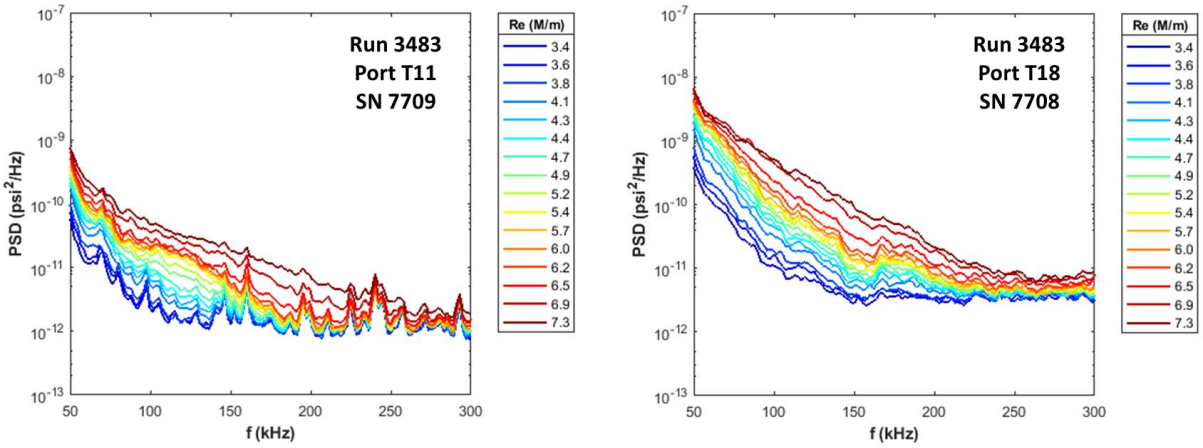

Figure 124. PCB spectra for the 15-degree swept back cylinder

Sweeping the cylinder forward significantly increases fluctuation levels across the board and greatly extends the upstream influence. A 15-degree forward sweep produced spectra at Port T1 (Figure 125, left), which is 6*d* upstream of the cylinder base, similar to those at T11 for the perpendicular configuration. Closer to the cylinder, at T18, the spectra (Figure 125, right) are at substantially higher levels at all frequencies for all Reynolds numbers than for any other configuration. The RMS pressure fluctuations, integrated from 50-300 kHz, hover around 50% of the freestream static pressure for *Re*=4.0-7.5M/m.

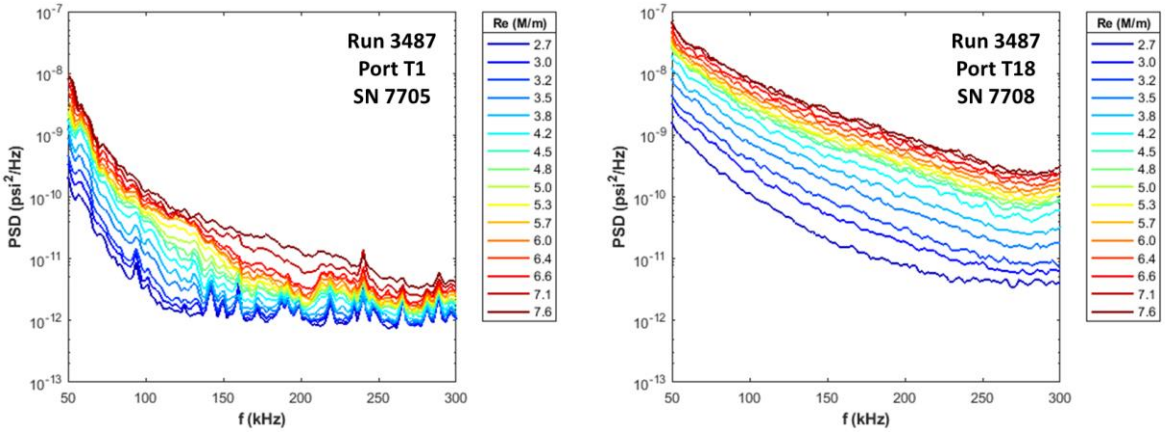

Figure 125. PCB spectra for the 15-degree swept forward cylinder

A look at the spectra from centerspan Kulite T19 (x'=-1.33d) is provided in Figure 126. The frequency range has been plotted to 100 kHz in this figure. The low-frequency peaks in the 30-degree swept cylinder spectra suggests that the separation shock periodically passes over this transducer at the highest freestream Reynolds number conditions, comparable to what is seen in the spectra for the perpendicular cylinder at x'=-3d. From there, the spectra increase in magnitude across the frequency domain as the cylinder sweep angle trends forward. The spectra are roughly two orders of magnitude higher for the 15-degree forward swept cylinder configuration as compared to the 30-degree swept back setup.

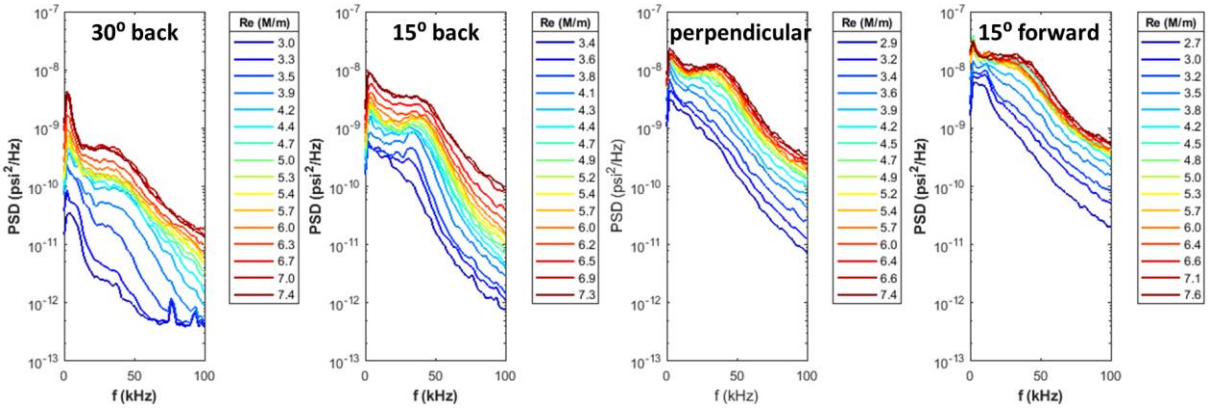

Figure 126. Spectral comparison for a Kulite at T19 for different cylinder sweep angles

6.2.5 Summary and Trends

RMS fluctuation profiles were generated for each port along the centerspan for the different testing configurations. The first five plots in Figure 127 give these fluctuation levels for PCB sensors at Ports T1, T4, T9, T11, and T18. These RMS values were computed by taking the square root of the integrated spectra from 50-300 kHz. The Kulite RMS values in the final plot are for T19 and involved spectral integration from 0-100 kHz.

A great deal can be gathered from this figure. First it should be noted that the baseline values from the "no trips, no cylinder" and the "trips, no cylinder" configurations are higher than reality and are largely set by the noise floor. That is a reason why the normalized RMS values are not plotted below *Re*=3M/m. It is interesting that the measured fluctuation levels with a shock generator are always higher than the baseline, even for cases where the interaction appears to be confined to a region downstream of the transducer location. For example, T1 and T4 should be well upstream of an interaction caused by a 30-degree swept back cylinder or even a perpendicular

cylinder with a high freestream Reynolds number; however, the observed higher fluctuation levels suggest that the cylinder has some far-reaching influence through the boundary layer.

Another significant point is the effect of cylinder sweep on fluctuations. While sweeping the cylinder forward 15 degrees produces fluctuations on the order of the freestream static pressure, sweeping it back 15 degrees greatly reduces the extent of the interaction and reduces the RMS fluctuations near the shock generator (T18 and T19) by roughly 50 percent when compared to the perpendicular cylinder case.

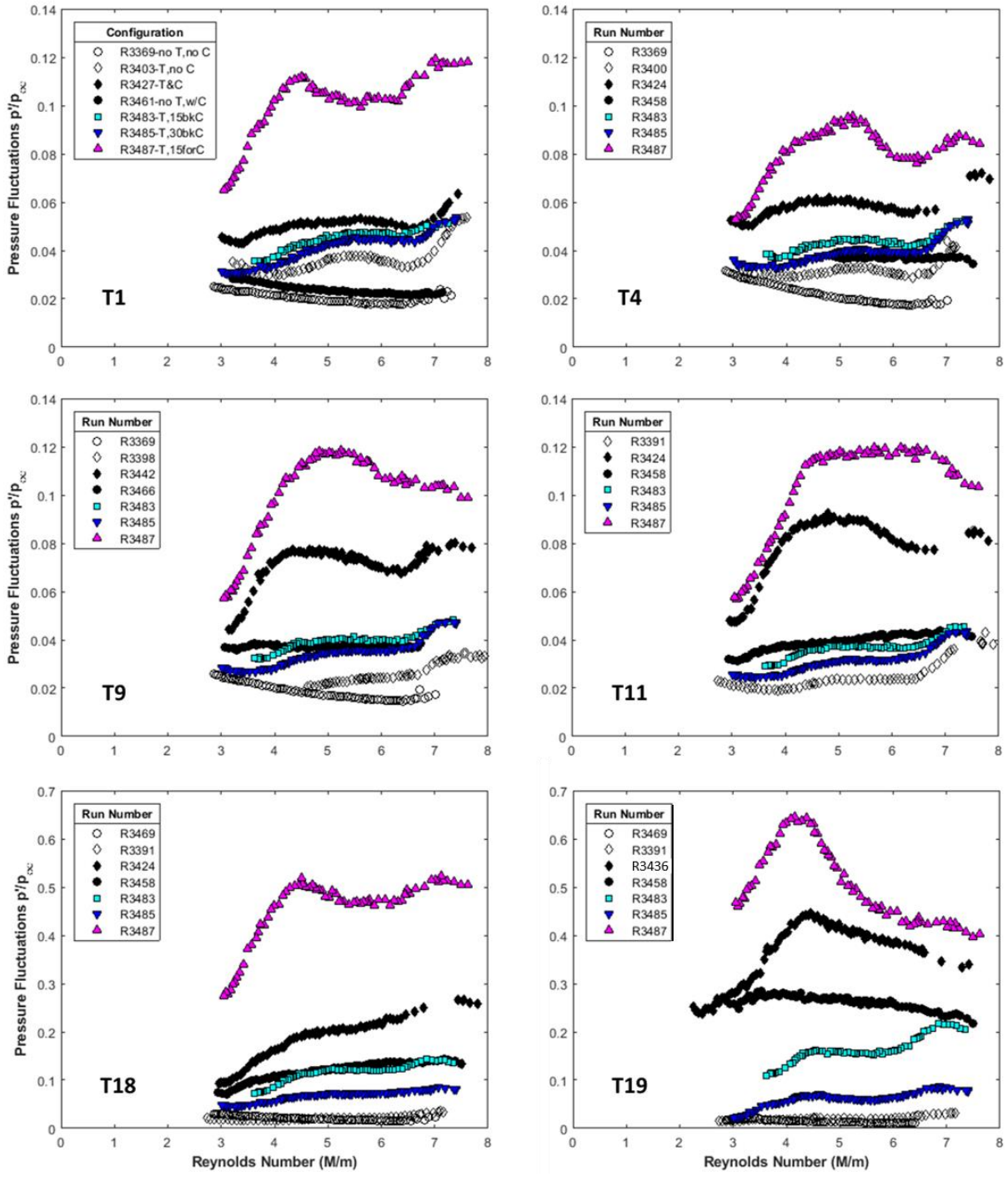

Figure 127. RMS fluctuations of pressure transducers positioned at different ports

6.3 IR Thermography

6.3.1 General

While a goal for this campaign is to provide precise measurements for a CFD validation, it is also important to report data in terms of normalized quantities that experimentalists at other facilities can use for comparison. As mentioned in Section 5.3.1, and further demonstrated in this section, heat flux values vary dramatically in the regions of highest heating over the course of a run in the same freestream. The film coefficient and Stanton number are normalized parameters that should provide more consistent results [194].

To illustrate why heat flux is not the primary heat transfer parameter reported in this paper, heat flux maps on the cylinder face from the same run at times *t1* and *t2* are shown in Figure 128 and are labeled as *Q(t1)* and *Q(t2)*. These maps are wildly different, and the washed-out map at *t2* is not indicative of the nature of heat transfer at that Reynolds number. The character of this run is shown in the upper left plot of the figure. The conditions considered are roughly the same Reynolds number, but are taken more than 20 seconds apart. This time difference leads to a nearly uniform increase of 50K on the cylinder face. The temperature and heat transfer parameter profiles are given in the bottom plot of Figure 128. The squares denote parameters at *t1*, and the triangles are for *t2*.

The profile plots demonstrate that the heat flux parameters *Q*, *h*, and *St* follow the same trends at *t1*, but only *h* and *St* show any semblance of these trends at *t2*. Again, the heat flux plot is washed-out because less heat is transferred to regions that are already at higher temperatures. While the film coefficient and Stanton number trends are consistent for a given Reynolds number, the magnitudes show some variation. There are several potential reasons for this as reported in

Section 3.5.2.3, but the variation in the data was minimized for the reported results by only considering points on the downward Reynolds number ramps or steps. More time at a set condition and less dramatic changes in condition allow the heat flux code to generate a more representative material internal temperature distribution that is important for accurate heat flux estimation at the surface.

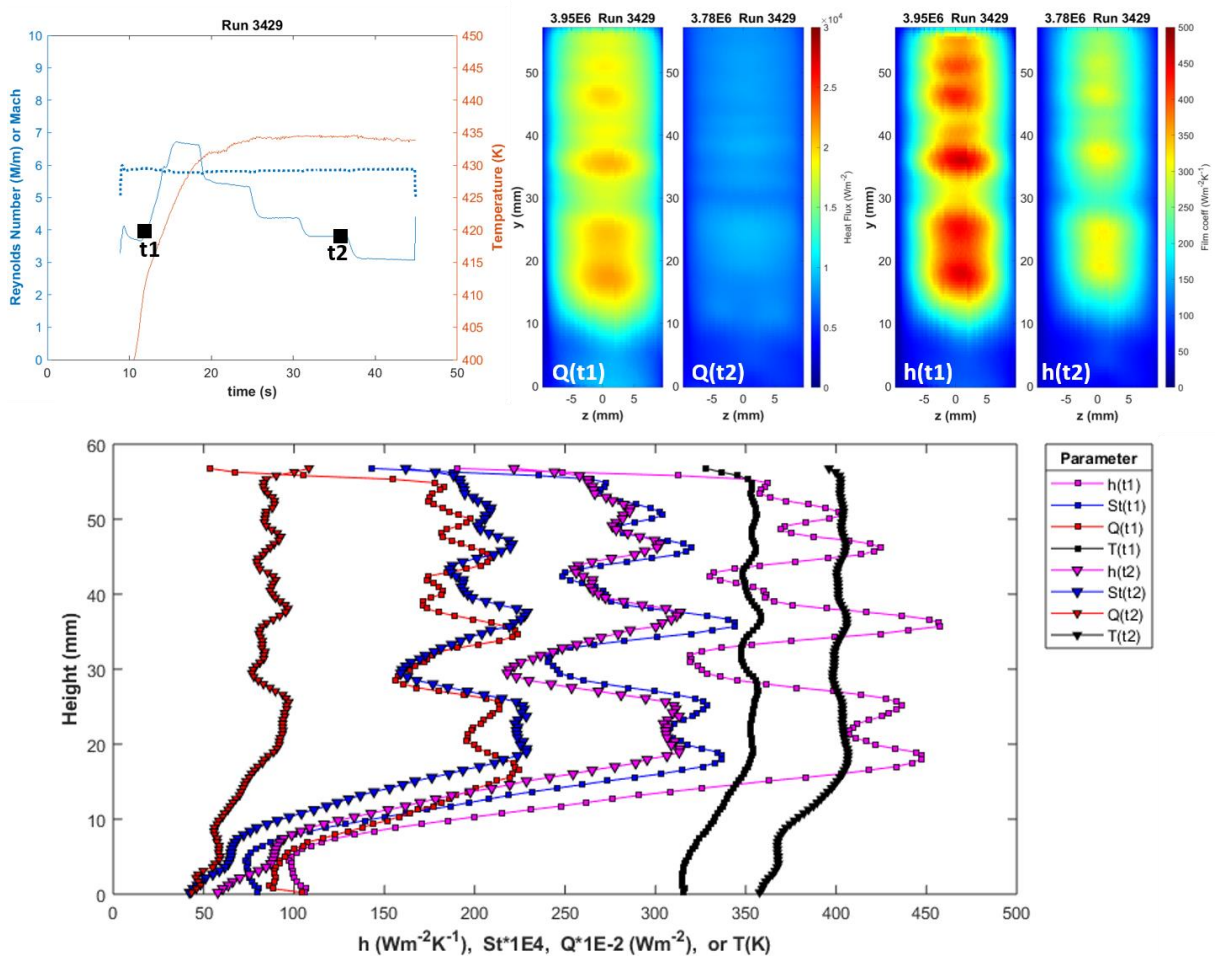

Figure 128. Surface temperature influence on heat transfer parameters

In addition to the full field-of-view and cylinder surface maps, this section will consider heating parameters in the regions illustrated in Figure 129. Region 1 is a 12.7 x 3.2 mm box that is located at the reattachment arc where the highest heating occurs. It is centered spanwise and is positioned between the upstream face of the cylinder and the trailing edge of K20. Region 2 represents the centerspan of the model. The region is a 19.1 x 134 mm box with its downstream edge centered on and tangent to the front of the cylinder. Region 3 (20.9 x 20.9 mm) is an outboard region used to contrast the high-heating region of the reattachment arc. The center of Region 3 is located 80 mm upstream of the cylinder and 32 mm off the centerspan.

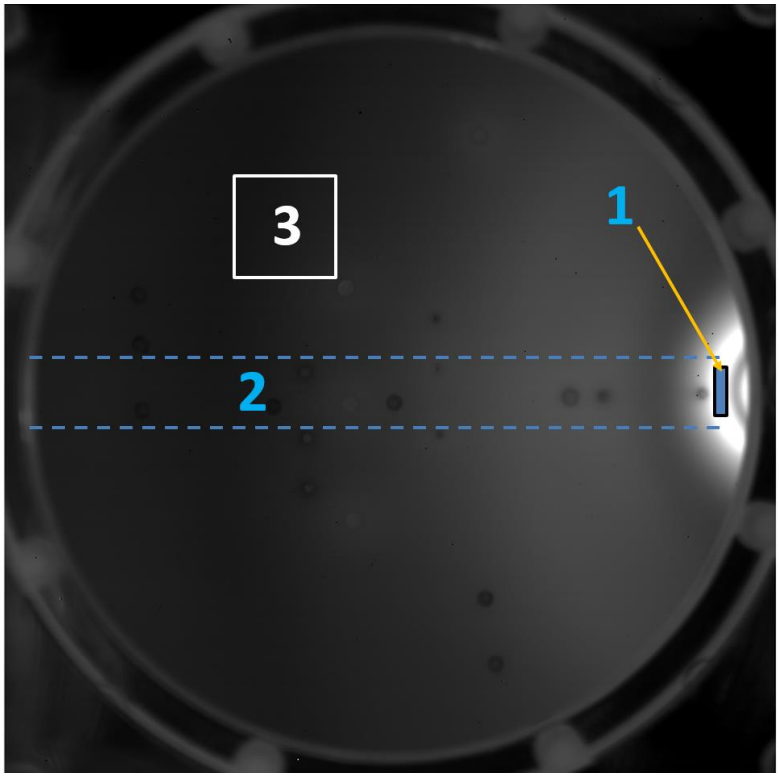

Figure 129. Regions for consideration on heating parameter maps

Figure 130 presents tunnel conditions and surface heating parameters over the course of a Reynolds number stepped run for Regions 1 and 3. The Reynolds number for Run 3467 was initially brought to just above 8M/m. This ramp quickly brought the tunnel total temperature to condition. On the surface, the reattachment arc average temperature rose over 70K in 5 seconds, while the average temperature in the outboard region only increased a couple degrees in that same time span. The tunnel unstarted on the first step down. The unstart resulted in a sudden decrease in surface temperature at the reattachment arc and an increase everywhere else. The impact of the unstart is apparent in all of the heating parameter plots. After hypersonic flow was reestablished, all of the heating parameters resumed trends observed prior to the unstart. The temperature at reattachment continued to increase throughout the run which worked to reduce the convective heat flux into that region. The temperature increase in the outboard region was much more gradual, so the heat flux was more reflective of the changing run conditions. By normalizing the heat flux by the difference in total and wall temperature, the film coefficient represents the stepped nature of the Reynolds number in both regions. The relationship between *h* and *Re* appears to be nearly linear, which is why the film coefficient was chosen as the primary heat transfer parameter of interest in the following sections. Mass flux normalization essentially leads to a constant value of Stanton number on the back half of the run which makes sense given the relationship between *h* and *Re*.

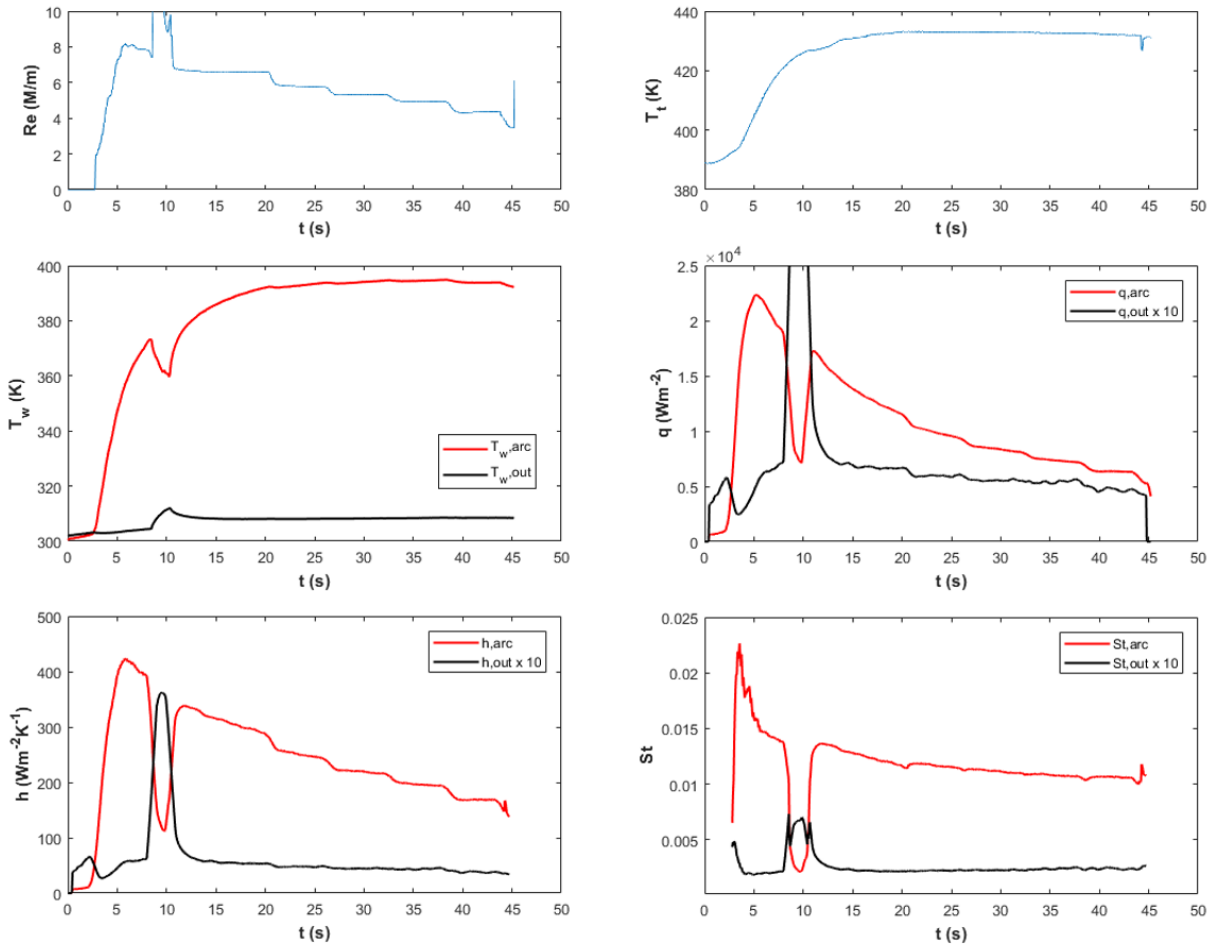

Figure 130. Testing conditions and heating parameters for Run 3467 (typical stepped run with an unstart)

For comparison, the outboard Region 3 of Run 3490 was evaluated. The wall temperature was elevated for this run because the focused schlieren setup necessitated that the model remain in the tunnel for its preheating. The Reynolds number was held near a constant 5M/m. As a result, the wall temperature rise was less and the heating parameters reflected it with lower magnitudes. Despite the near constant freestream conditions, all of the heating parameters demonstrate a gradual slope down with time, which essentially demonstrates that the normalizations are not perfect.

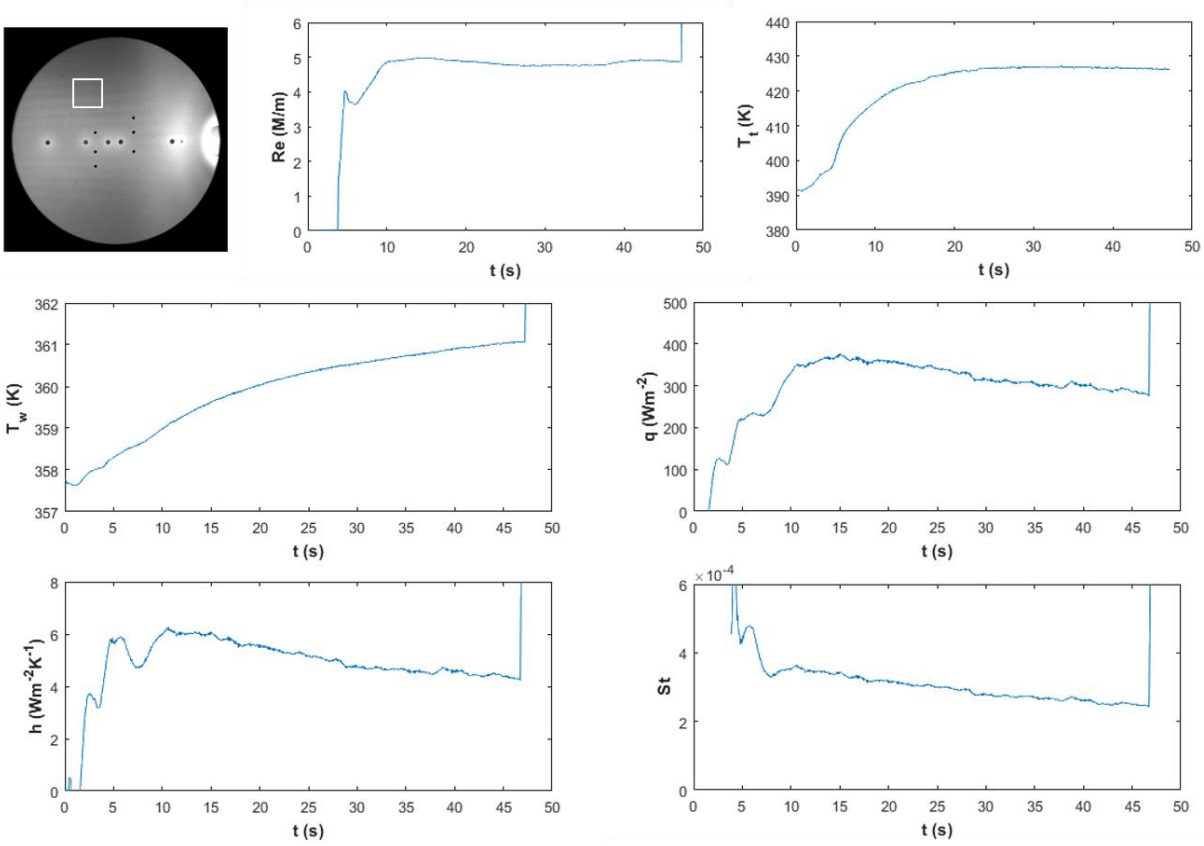

Figure 131. Testing conditions and heating parameters for Run 3490 (elevated model wall temperature)

6.3.2 Baseline "no trips, cylinder"

Adding the shock generator caused the heat transfer to increase by one or two orders of magnitude in some locations above "no trips, no cylinder". Figure 132 shows film coefficient maps at roughly the same Reynolds numbers as in Figure 107 for comparison. The top row of Figure 132 plots *h* from 0-50 $Wm^{-2}K^{-1}$ scale for an appreciation of the heating extent of the SBLI. The bottom row plots h on a 0-400 $Wm^{-2}K^{-1}$ scale to demonstrate the magnitude of maximal heating and its proximity to the base of the cylinder. The cylinder is drawn in as a circle on the right side of all of these maps for clarity.

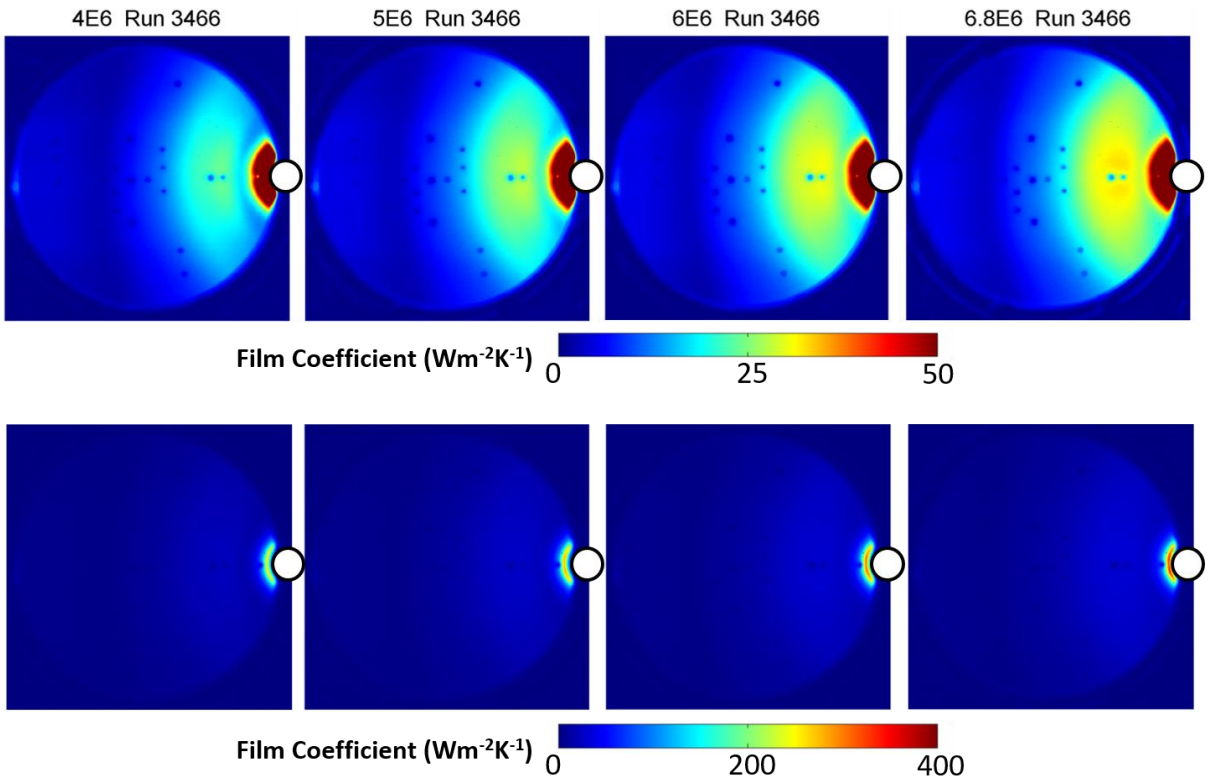

Figure 132. Film coefficient maps for "no trips, cylinder" at different Reynolds numbers (columns) on different scales (rows)

Central region (Region 2 on Figure 129) film coefficient profiles were extracted from Run 3458 at different Reynolds numbers over the sweep. The profiles (Figure 133, left) show the same trends as the maps in Figure 132, but make for easier film coefficient magnitude comparison for many Reynolds numbers. The maps indicate an initial rise (dark blue to medium blue) at x'/d=-4.0 for Re=4M/m and x'/d=-4.7 for Re=6.8M/m. The profiles show shallow ramps up at the same offset distances. This trend agrees with the observations of [91] that the interaction size increases with Reynolds number for a laminar SBLI. A second rise in heat transfer occurs between x'/d=-3.1 and -2.5 for Re = 7.0 and 4.0 M/m, respectively. This rise continues for all Reynolds numbers until a local maximum is reached around x'/d=-1.5. The heat transfer then decreases and reaches a

local minimum near x'/d=-0.8 (now slightly farther away for lower *Re* and slightly closer for higher *Re*). From there it rises precipitously, reaching a peak value near x'/d=-0.1. This represents the location of the reattachment shock, which is most easily estimated from the zoomed plot in Figure 133 (right).

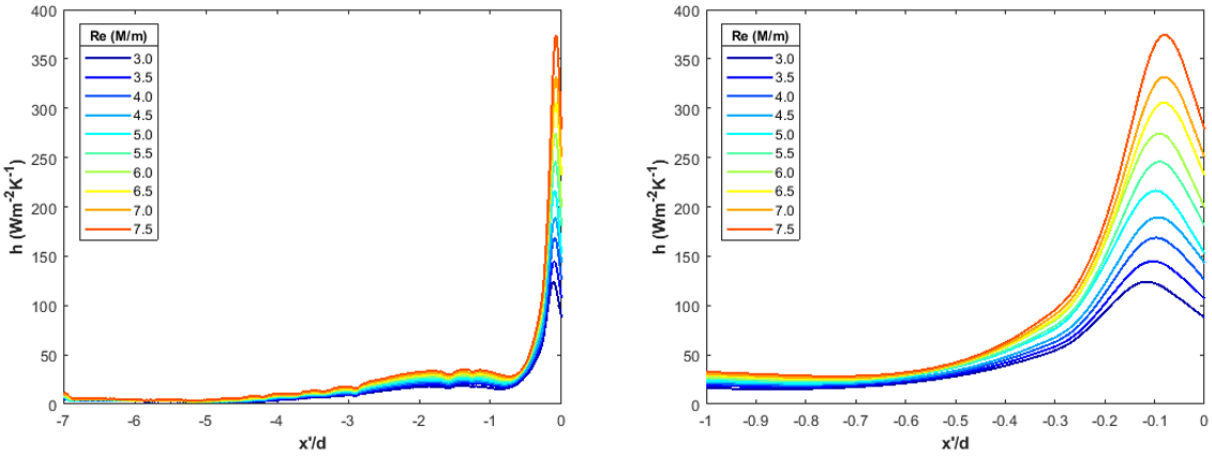

Figure 133. Film coefficient profiles along the model centerspan (Region 2) for Run 3458 from x'/d=[-7,0] (left) and x'/d=[-1,0] (right)

A closer look at the arc heating (Region 1) for multiple runs is presented in Figure 134. The lines represent swept Reynolds number runs, while the symbols are for stepped Reynolds number runs. Runs 3458 and 3461 were both quick ramps up and slow ramps down, and the lines plotted are from the ramps down. Run 3466 was a slow ramp up. The stepped runs involved quick ramps up and decreasing Reynolds number at each step. Data points on the stepped runs were taken roughly 1 second before the end of the step to allow the internal material temperature time to respond to the new condition.

The data agree nicely. With the exception of Run 3466, all of the tests show a near linear fit between *h* and *Re*, with similar slope and offset. Run 3466 was conducted differently and shows

a more gradual slope; still, there is less than 50 $Wm^{-2}K^{-1}$ deviation from all the runs over the Reynolds number range.

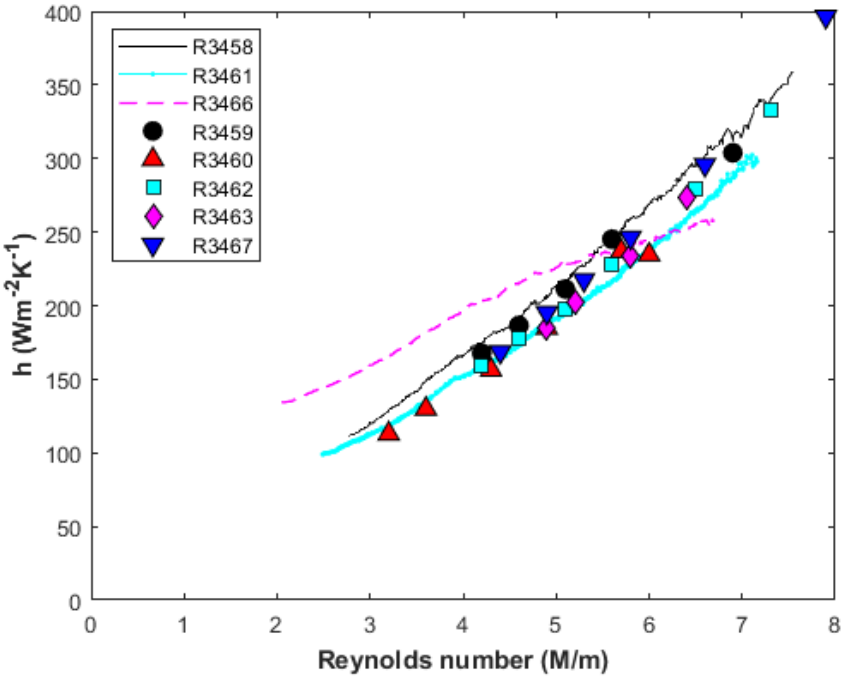

Figure 134. Reattachment arc (Region 1) heating as a function of Reynolds number without trips

6.3.3 Transitional "trips, cylinder"

The addition of trips changes the form of the interaction heating. Figure 135 illustrates the influence of the trips and the heating characteristics of a transitional SBLI. The rows in the figures put the plots on different scales, and a circle is drawn in each plot to represent the cylinder. The heating for the "no trips, cylinder" laminar SBLI configuration is roughly uniform in extent and seems to scale with Reynolds number. The areas of highest heating are closely confined to within 0.5*d* of the base of the cylinder. Conversely, the extent and magnitudes of heating for the "trips,

cylinder" setup changes with Reynolds number as the boundary layer transitions. The interaction collapses to the base of the cylinder, while the separation distance extends only slightly for the laminar SBLI. As the interaction collapses, the region of elevated heating becomes more expansive.

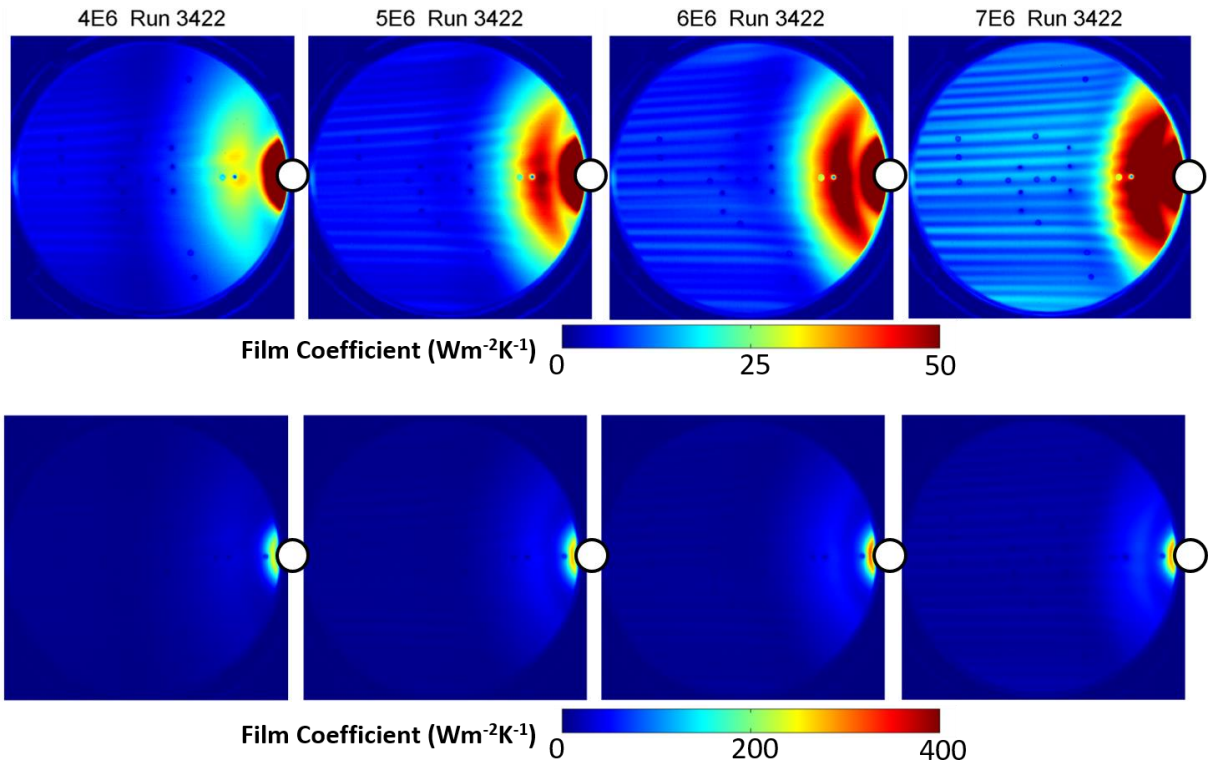

Figure 135. Film coefficient maps for "trips, cylinder" at different Reynolds numbers (columns) on different scales (rows)

Center region (Region 2 on Figure 129) film coefficient profiles were extracted from Run 3442 at different Reynolds numbers over the sweep. Both the maps and the profiles demonstrate the spatial collapse in initial temperature rise with increasing Reynolds number. The profiles show essentially the same values of h at x'/d=-2.2 for all Reynolds numbers. This distance represents the initial rise in heating for Re=7.5M/m. Re=3.0M/m reaches a local maximum near x'/d=-1.5,

which is the same distance as that for all Reynolds numbers for "no trips, cylinder". The higher Reynolds numbers achieve progressively higher local maxima at positions that are increasingly close to the cylinder. The *Re*=7.5M/m reaches its local maximum at *x'/d*=-0.9. The value of 76.1 $Wm^{-2}K^{-1}$ is considerably higher than the corresponding "no trips, cylinder" value of 34.9 $Wm^{-2}K^{-1}$. The ensuing local minima also show significant offset distance variation with Reynolds number, ranging from *x'/d*=-0.8 to -0.5 for *Re*=3.0 and 7.5 M/m, respectively. The heating peak is located closer to the cylinder than for "no trips, cylinder"; however, the value of 320 $Wm^{-2}K^{-1}$ for "trips, cylinder" is lower than the 374 $Wm^{-2}K^{-1}$ for the no trips run.

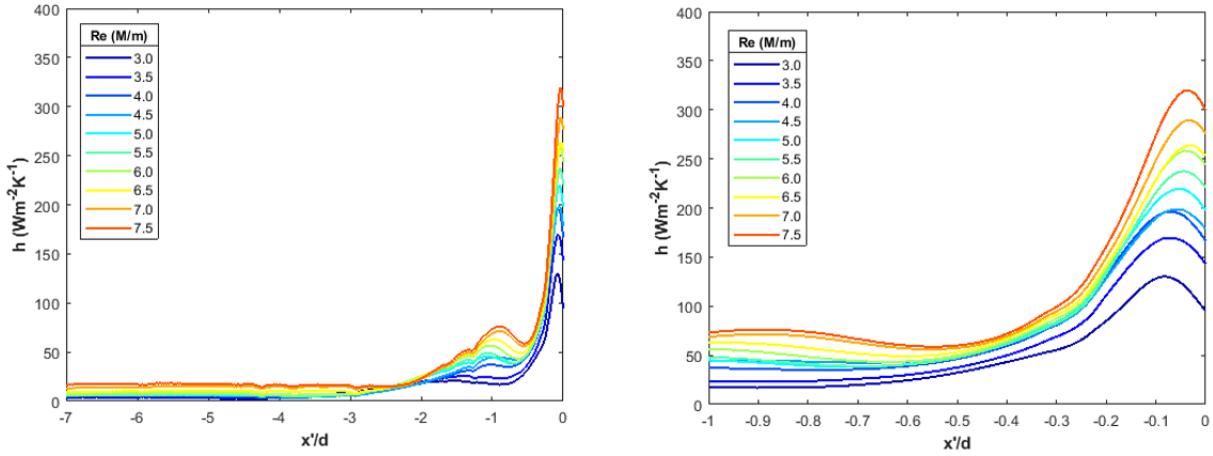

Figure 136. Film coefficient profiles along the model centerspan (Region 2) for Run 3442 from *x'/d*=[-7,0] (left) and *x'/d*=[-1,0] (right)

Figure 137 presents a closer look at the arc heating for a number of runs. Again, the swept Reynolds number runs are lines, and the stepped runs are symbols. Runs 3422 and 3427 are downward swept runs. The reattachment arc heating does not follow the same linear form with Reynolds number as for the "no trips, cylinder" configuration. There appears to be a linear region between *Re*= 3.5 to 6.5 M/m for most runs; however, the heating slope tends to tail off above that Reynolds

number range. This contributes to film coefficient values that are lower than corresponding values for “no trips, cylinder”, which is a surprising result since “no trips, cylinder” produces a laminar SBLI, while “trips, cylinder” produces a near turbulent SBLI above *Re*=6.5M/m. Another feature from Figure 137 is the sudden rise in film coefficient at a Reynolds number of just over 3M/m. This rise corresponds almost perfectly with the increase in freestream disturbances, which suggests that there is some coupling between the freestream disturbances, the 40 kHz (potentially second mode) instability, and the instability from the trips, to produce this effect.

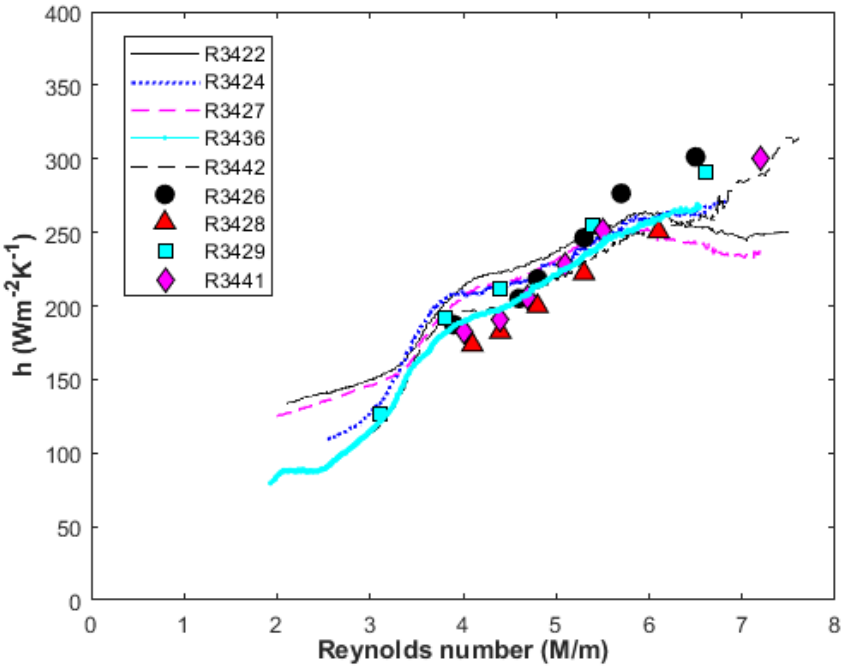

Figure 137. Reattachment arc (Region 1) heating as a function of Reynolds number with trips

6.3.4 Effect of Cylinder Sweep

Film coefficient maps of the region upstream of the cylinder were created (Figure 138) to evaluate the effect of sweep angle on heating distribution. The top row of maps is for the configuration with a cylinder swept back 30 degrees. The center row is for a cylinder swept back 15 degrees, the bottom row gives maps for a cylinder swept forward 15 degrees. As expected, the interaction involving the cylinder swept back 30 degrees features minimal heating, particularly at the low Reynolds numbers. The film coefficients within the interaction at 4M/m are not much higher than those produced by the trips alone. The heating footprint is also comparatively small. Heating from the 15-degree swept back configuration is higher but still significantly reduced from that produced by the perpendicular cylinder. The film coefficients produced by the 15-degree forward case are substantially higher, and the elevated heating arc extends roughly a cylinder diameter farther upstream than that from the perpendicular cylinder.

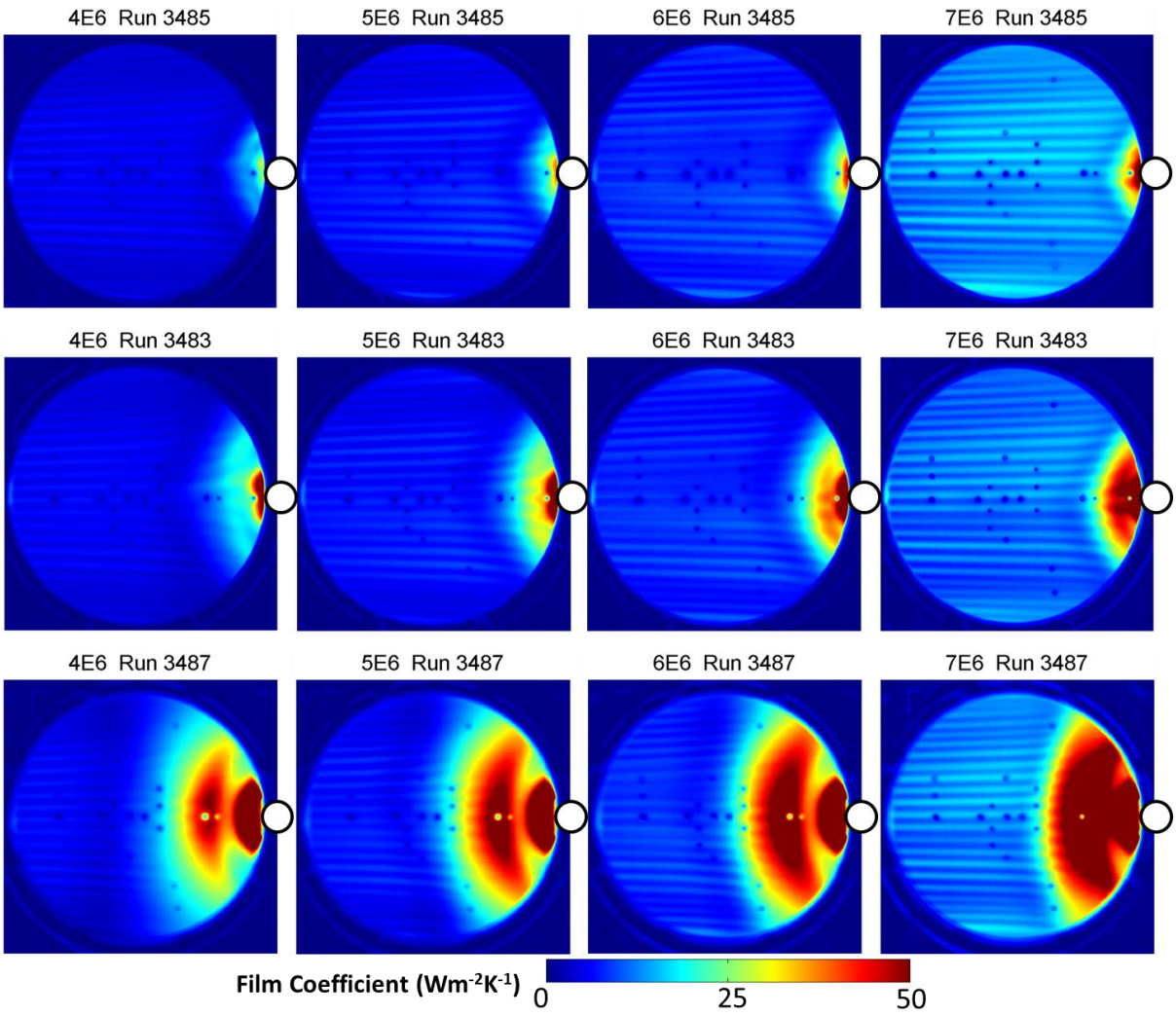

Figure 138. Film coefficient maps with trips and swept cylinders at different Reynolds numbers (columns). The cylinder is swept 30 degrees back in the top row, 15 degrees back in the center row, and 15 degrees forward in the bottom row

The position of the camera for the maps in Figure 138 makes it impossible to measure the peak heating caused by the reattachment shock for the 15-degree swept forward case since the cylinder is blocking the view. Therefore, the angled camera images were used to evaluate this feature. Figure 139 provides film coefficient maps for three different Reynolds numbers at each cylinder sweep angle. The colorbar is scaled to highlight the salient features for each configuration.

These maps indicate that the heat transfer to the model is highly dependent on the sweep angle. Heating at the reattachment arc is significantly lower when the cylinder is swept and is much lower than what is seen on the cylinder itself. However, the heat transfer at reattachment for the 15-degree swept forward case is higher (>800 $Wm^{-2}K^{-1}$) than was observed at any location for any other run during this campaign.

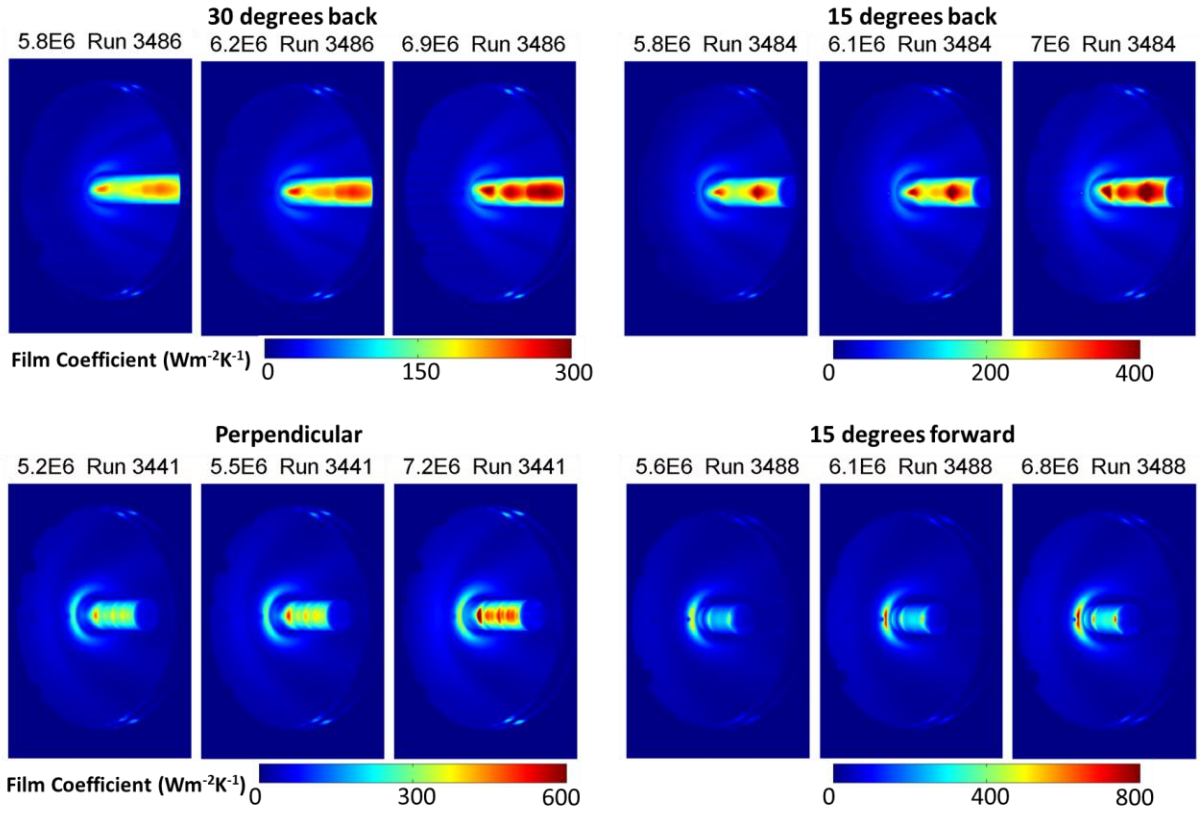

Figure 139. Film coefficient maps (tilted camera) for different cylinder sweep angles at different Reynolds numbers

The film coefficient maps shown in Figure 139 were transformed to view the heating on the cylinder and are given for the 30 degrees back, 15 degrees back, and 15 degrees forward configurations as Figures 140-142. The cylinder heating maps are on the same 0-500 $Wm^{-2}K^{-1}$ scale

as those reported in the previous subsection. The maps for the 30-degree swept cylinder appear a bit different since the top part of the cylinder is blocked from view by the tunnel. As a result, the height is reduced and curvature appears at the top of the maps from the coordinate transformation. Heating at any Reynolds number for this case is comparatively low. As expected, the 15 degrees swept back case produces heating levels between 30 degrees and perpendicular. The 15-degree swept forward configuration maps are in Figure 142. It should be noted that the minimum camera viewing angle for these measurements is 70 degrees, which not only leads to increased perspective image distortion but also directional emissivity concerns. The surface heating values depicted in this figure are lower than in reality and should only be considered qualitatively. It is, however, noteworthy that this configuration seems to be the only one with elevated heating near the cylinder base.

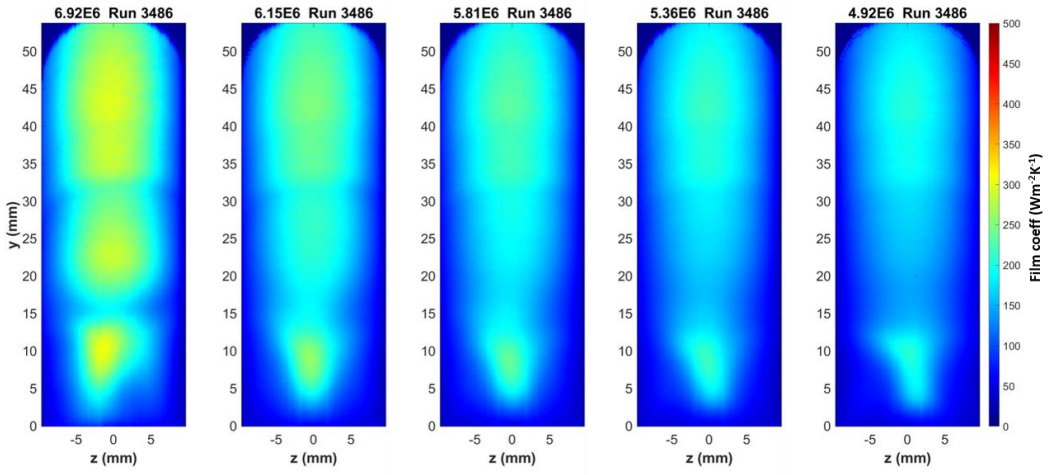

Figure 140. Film coefficient maps of the cylinder: 30 degrees swept back (with trips)

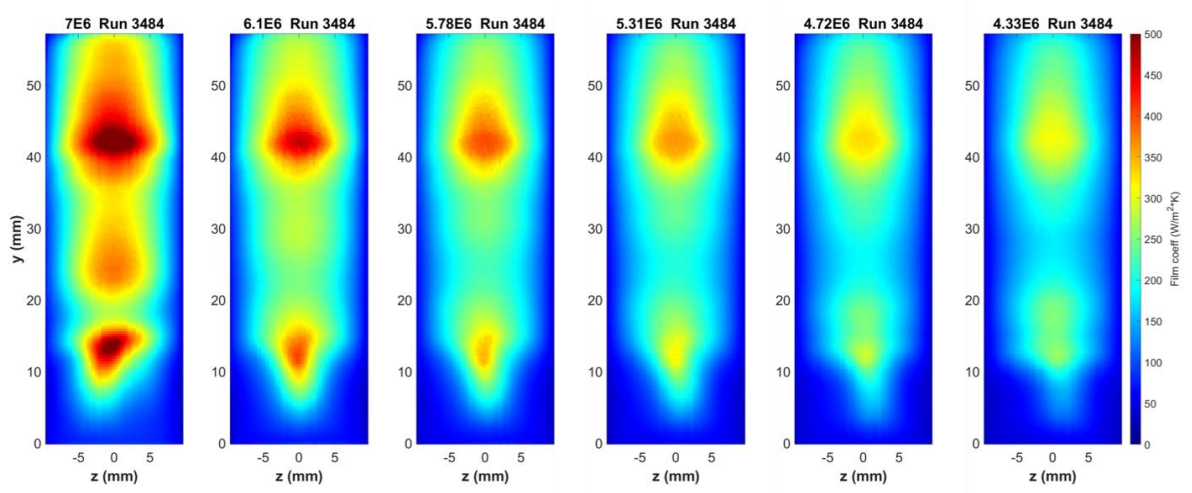

Figure 141. Film coefficient maps of the cylinder: 15 degrees swept back (with trips)

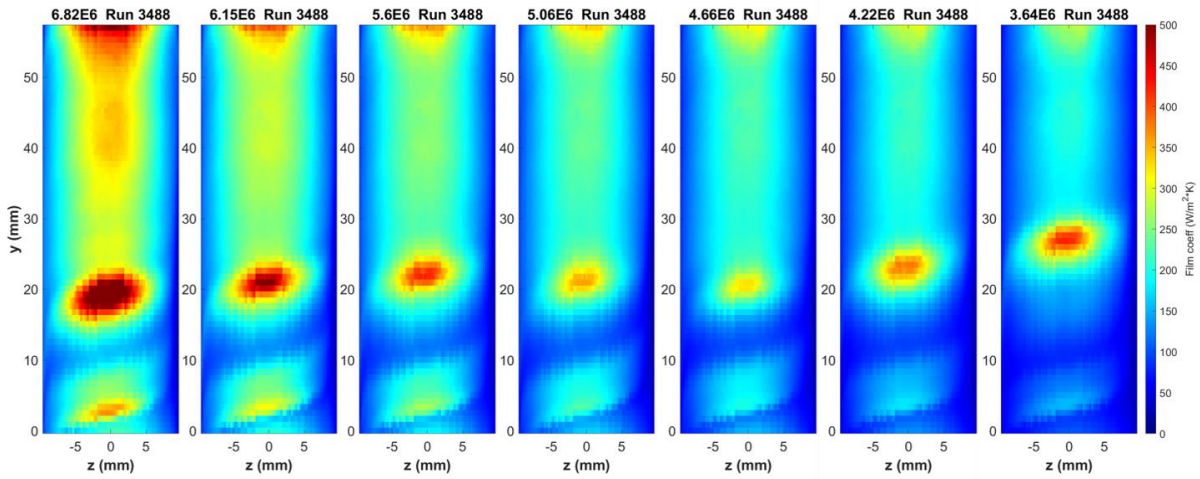

Figure 142. Film coefficient maps of the cylinder: 15 degrees swept forward (with trips)

6.3.5 Summary and Trends

The highest Reynolds number film coefficient maps for each configuration were converted to profile plots for easier comparison (Figure 143). The highest heating regions occurred for Runs 3429 and 3441, which were both of the "trips, cylinder" configuration. Film coefficients in excess of 700 $Wm^{-2}K^{-1}$ resulted from supersonic jet impingement and were concentrated roughly 17 mm above the base of the cylinder. Sweeping the cylinder back lowered both the magnitude of heat transfer and the position of the jet. Film coefficients on the cylinder with trips were higher than those without trips across the profile.

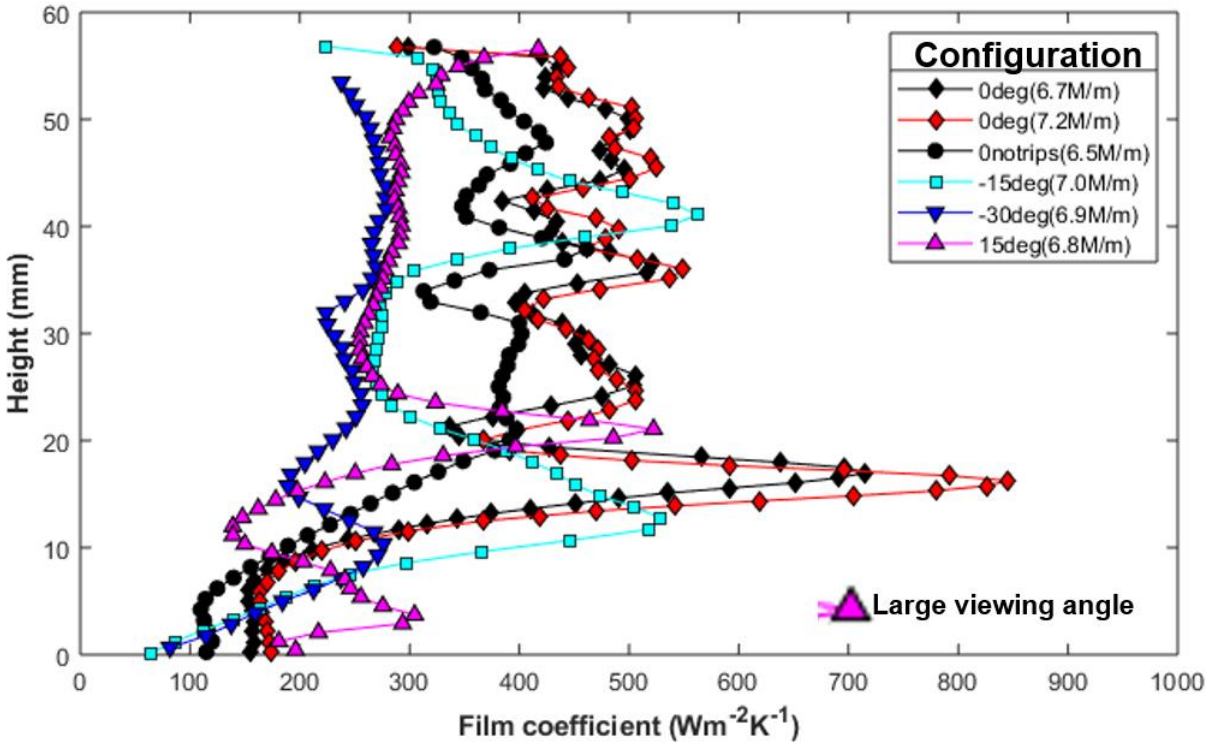

Figure 143. Film coefficient profiles up the center face of cylinder at Reynolds numbers near 7M/m

6.4 High-speed Schlieren Imaging

6.4.1 Shock Structure

The Reynolds number swept runs with full resolution 1024 x 1024 schlieren images allowed for tracking the evolution of the shock structure as the interaction was swept through transition. The SBLI interaction extent and positioning of the relevant flow features is highly dependent on the interaction state, which was dictated by the freestream Reynolds number and the configuration. Schlieren images demonstrating the effect of sweeping through transition on the shock structure for "trips, cylinder" (Run 3424) are shown in Figure 144. Flow is from left to right in these images and the cylinder is the vertical right boundary. The upstream distance from the base of the cylinder, normalized by the cylinder diameter is sketched below the images. It should be emphasized that the features at all of the Reynolds numbers tested are unsteady. The wave motion is time-resolved when sampling at 150k and 240k fps. Spatially, the interaction region contracts as it transitions from laminar to turbulent flow. Increasing momentum closer to the wall forces the shock structure to collapse, and the extent of the interaction is at its minimum when the boundary layer is turbulent.

As first reported in Leidy et al. [193], the contraction of the interaction is not the only feature that can be observed in these images. The evolution of the incoming boundary layer is striking. At *Re*=3M/m, it is faint and blurred with no visible structure, characteristic of laminar flow in a low-density facility. At *Re*=5M/m, flow structure commences within the boundary layer, and by the maximum Reynolds number tested, 8M/m, the structures appear sharper and better defined. This is expected from a transitioning boundary layer. Also, at *Re*=3M/m, there is very little visible near the base of the cylinder. The upstream influence separation shock is clear, but the forward shock foot that precedes the chaotic separation at higher Reynolds number is not. By

Re=4M/m, more structure begins to form at the base of the cylinder and the position of the forward shock foot can be inferred. The intersection of the upstream influence shock and the bow shock is above the triple point. At 5M/m, the intersections of the upstream influence shock, the forward shock, the bow shock, and the reattachment shock are at roughly the same point. At 6M/m, the forward shock foot is well-defined. As the Reynolds number continues to increase, the triple point height is reduced. Its movement seems to cast off structures, which propagate up and down the cylinder. These disturbances are very distinct at *Re*=5M/m. The frequency content of these structures will be explored later in the section. Another feature evident from the schlieren is the propagation of disturbance waves from the separation at the base of the cylinder toward the upstream influence shock. The outward movement of the disturbance waves is most apparent at the lower Reynolds numbers since the waves travel a greater distance. Tracking of the separation shock and the disturbance waves is also reported later in this section.

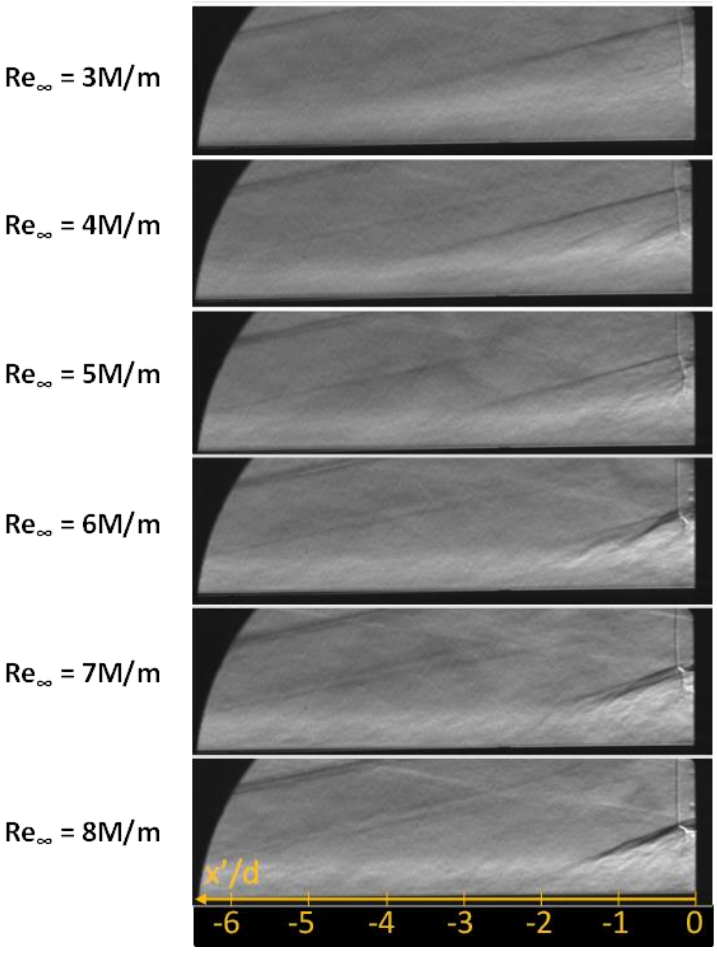

Figure 144. Schlieren images showing the evolution of the XSBLI with Reynolds number

Conversely, the interaction structure does not change nearly as much when no trips are present. The sequence of schlieren images for "no trips, cylinder" is presented in Figure 145. The images at *Re*=3M/m look nearly identical for both runs, with the separation shock extending far upstream and few disturbances within the interaction. The differences become increasingly apparent as the Reynolds number increases because the separation shock never collapses down for "no trips, cylinder"; in fact, the separation distance appears to slightly increase. To be sure, disturb-

ances do increase within the interaction with increasing Reynolds number. Several discrete disturbance waves appear by *Re*=5M/m, but the large region of chaotic features at the base of the cylinder, bounded by a distinct forward shock, never appears.

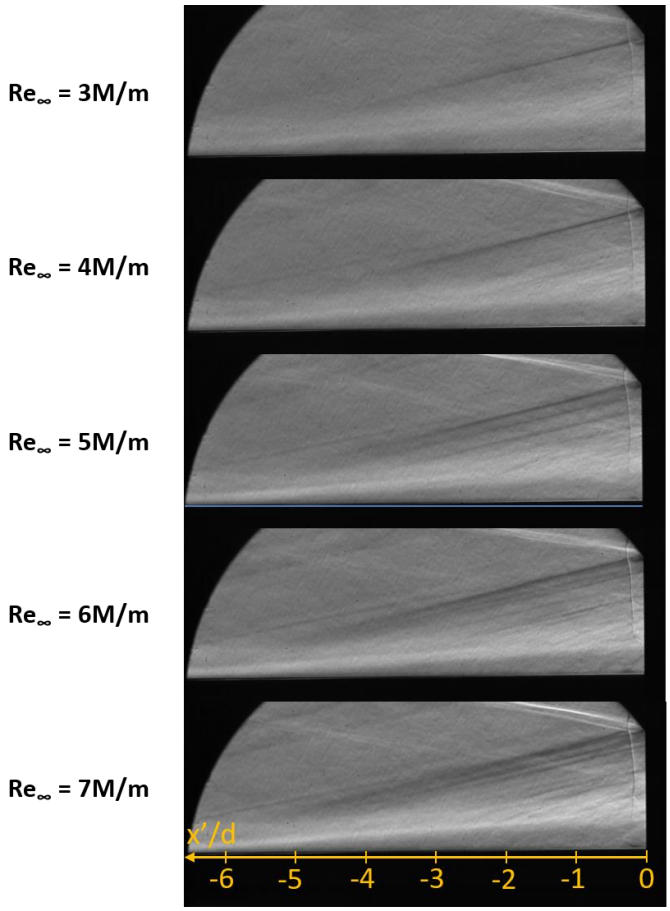

Figure 145. Schlieren images of the "no trips, cylinder" laminar SBLI

The effect of angling the cylinder back 15 degrees (Run 3483) is demonstrated in Figure 146. In comparison to "trips, cylinder" (Figure 144), the shocks and features are much fainter, which indicates lower disturbance levels. Sweeping the cylinder back reduces the streamwise extent of the interaction. The separation distance is closer to the cylinder at *Re*=3M/m, and continues

to be throughout the Reynolds number sweep. Although the disturbances are reduced, the swept cylinder, in conjunction with the trips, produces a transition SBLI at the higher Reynolds number, as indicated by the collapsing shock structure and the definitive presence of both an upstream influence shock and forward shock.

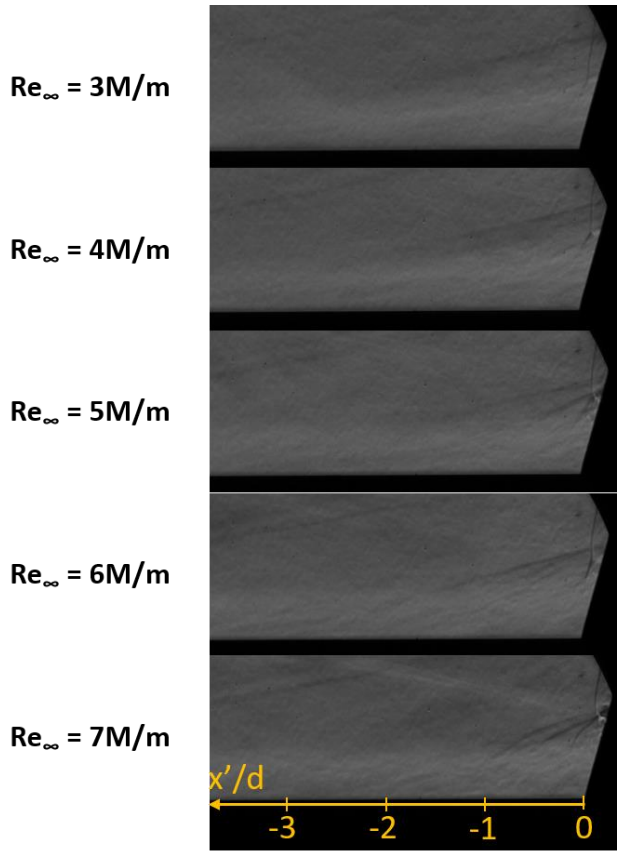

Figure 146. Schlieren images with the cylinder swept back 15 degrees

The reduced disturbance trend continued for Run 3485 where the cylinder was swept back 30 degrees (Figure 147). It is difficult to even identify a separation shock at the lower Reynolds numbers. The structure is evident at Re=6M/m, but the reach of the separation shock is significantly reduced as are the features at the base of the cylinder.

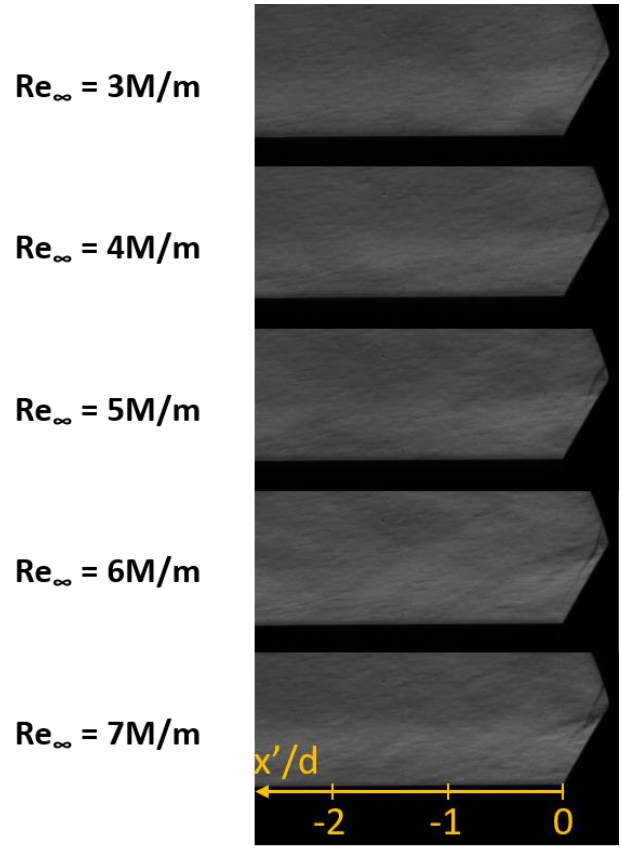

Figure 147. Schlieren images with the cylinder swept back 30 degrees

On the other hand, sweeping the cylinder forward increases the disturbances which works to enhance the contrast of the features. The cylinder was swept forward 15 degrees for Run 3487 (Figure 148). The structure already begins collapsing to the cylinder around *Re*=2M/m. An additional feature only observable in the forward swept configuration for all conditions is a small recirculation bubble at the base of the cylinder. At 3M/m, the intersections of the upstream influence shock and two weaker disturbance shocks with the bow shock appear to cause weak jets, similar in form to the supersonic jet on the perpendicular cylinder. At 4M/m, a forward shock foot emerges, establishes a triple point, and produces higher intensity jet impingement on the cylinder. As the Reynolds number increases, the upstream influence shock contracts to the forward shock

and the disturbances at the base of the cylinder show more structure and energy. The upstream influence shock merges with the forward shock at *Re*=7M/m. In addition to increasing the disturbance levels at every flow condition, the forward swept cylinder appears to accelerate the transitioning process in comparison to the perpendicular cylinder.

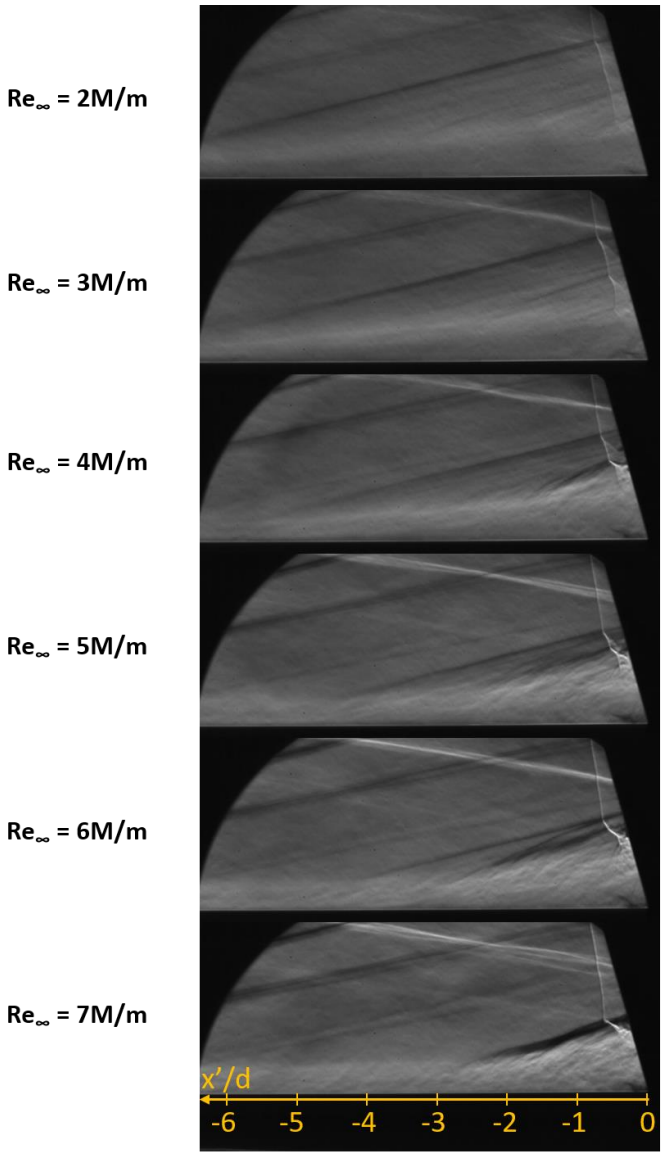

Figure 148. Schlieren images with the cylinder swept forward 15 degrees

6.4.2 Spectral Content

Dominant frequencies within the interaction were observed by taking PSDs of pixels for a set of the 50k images. As mentioned above, the disturbances that ascend the cylinder from the supersonic jet are an interesting flow feature, and their time-resolved motion could be tracked using the 120 x 256 pixel, 240k fps, viewing window. Images from high-speed videos (Run 3429) are presented in Figure 149 at the four Reynolds numbers surveyed for the analysis. Flow is again from left to right with the cylinder on the right and the base model below. The points sampled are indicated by crosshairs on the *Re*=6.6M/m image in Figure 149. The annotated points 1-3 are physically located 0.4 mm upstream of the cylinder and 27.4, 26.8, and 26.1 mm above the wedge surface, respectively. Point 4 is located upstream of the bow shock, 9.2 mm upstream of the cylinder and 24.9 mm above the wedge; it serves for comparison.

For each point, a PSD was generated using 50k consecutive images. The spectra are plotted in Figure 150, where the frequency resolution is 938 Hz. The PSD plots give results consistent with what is expected from the high-speed videos. At *Re*=6.6M/m, the disturbances are most distinct, and a broadband peak around 20 kHz appears clearly in the spectra. The magnitude of the Point 3 peak is the highest, which makes sense if the disturbances emanate from the triple point since Point 3 is the closest. It follows that the ascending disturbances lose an increasing amount of energy for Point 2 and Point 1. Point 4 gives no content of note, which is encouraging because no features are present at the higher Reynolds numbers. By *Re*=5.4M/m, Point 3 is no longer highest in magnitude. This is because the triple point rises with decreasing Reynolds number. The rising disturbances cannot ascend past the sampled point if the triple point is covering it. The triple point brings its own frequency content which explains the broadening of the spectrum. This trend con-

tinues at *Re*=4.4M/m. The overall energy is less which is expected because the jet-induced disturbances are blurred and no longer distinct. By *Re*=3.8M/m the broadband peak at 20 kHz is not observed, and there is additional low-frequency content. This is the result of the separation shock crossing over all four points sampled.

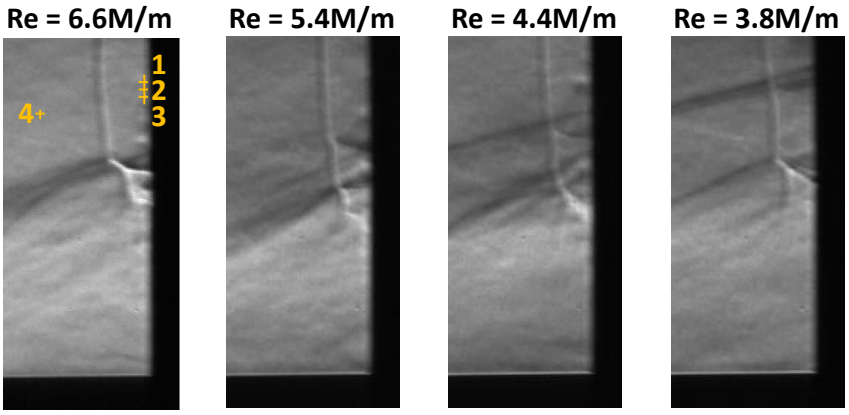

Figure 149. Sample images from disturbance ascension analysis

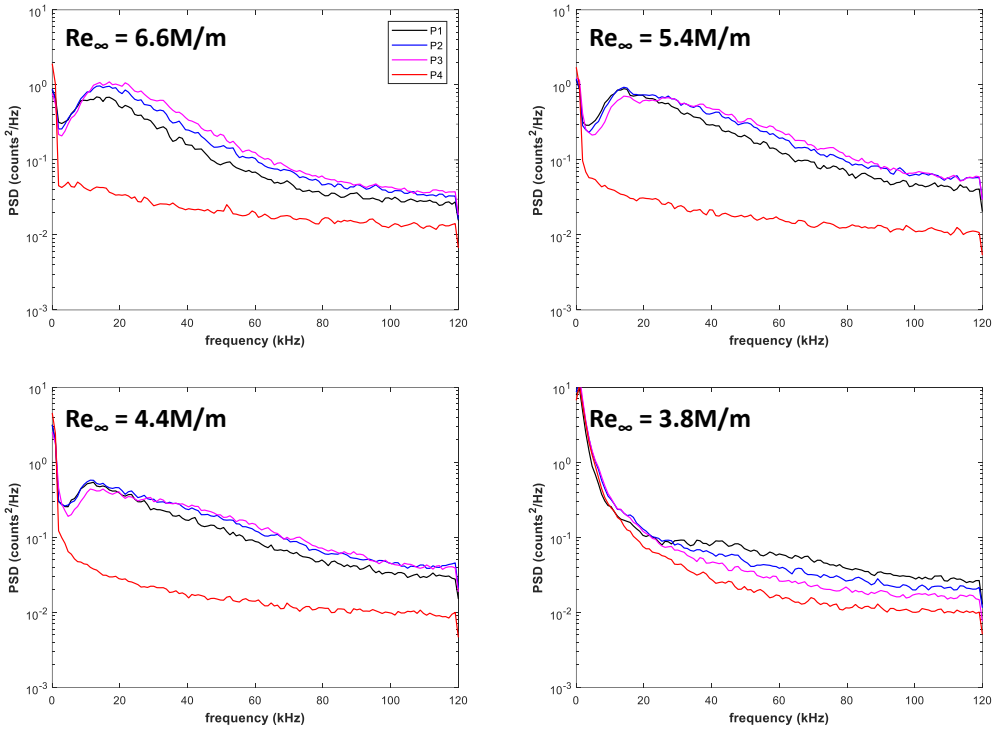

Figure 150. Disturbance ascension PSD plots for 4 locations at each Reynolds number

Following the above results, which were first reported in [193], PSDs were taken at every pixel for every condition to produce maps of dominant frequencies and maps of energy content. The dominant frequencies maps were generated by taking the frequency that corresponded to a peak in the PSD, for each pixel, and plotting that frequency value as a contour over the space. The energy content maps represent the PSD value for the frequency in the dominant frequency maps. In other words, this is the maximum PSD value for the spectrum at each pixel. The frequency resolution was enhanced to 500 Hz for these computations.

Figure 151 displays the maps described above (right) as well as a schlieren image showing points and lines probed for later consideration (far left) and an RMS counts fluctuations map (left center), which was produced by integrating the spectra from 0.5 to 120 kHz. The points were

chosen to be representative of the features in the interaction. Point 1 is outside of the interaction, Point 2 is across the bow shock, Point 3 is on the upstream influence shock, Point 4 is on the forward shock, Point 5 is on the supersonic jet, and Point 6 is within the separated region. The lines were chosen because they demonstrate significant variation in the spectra. L1 crosses through the triple point and passes through the disturbances that roll up from that point, L2 is just above the model wall, and L3 crosses the bow shock.

The RMS map provides insight to the distribution of energy. The incoming flow above the interaction has the lowest fluctuation levels; these increase across the bow shock. The highest fluctuation levels are on the cylinder side of the triple point, at the supersonic jet. High RMS levels continue, from the jet, up the cylinder and physically represent the disturbances described above. The upstream influence and forward shocks are positioned relatively close together for this flow condition, so they produce a large region of elevated fluctuations, and the shocks are not distinguishable from each other. The intensity within the separated region is higher than the freestream but lower than the shock structure. The fluctuation levels near the model wall increase in the region closest to the base of the cylinder.

The dominant frequencies map indicates that the majority of points in the interaction have peak PSD values at zero frequency, despite the mean values being subtracted before evaluation. Therefore, the non-zero frequency values truly represent foremost frequencies. The map indicates low frequencies (500 to 1500 Hz) are prevalent for both forward shocks (as expected), but also for the triple point and the entirety of the supersonic jet. The only region where high frequencies (17 to 27 kHz) are dominant is above the jet, near the face of the cylinder. This is the region in which cylinder ascending disturbances are at their highest intensity.

Comparisons can be made between the peak PSD value map and the RMS map to give clues regarding the spectra. For example, the upstream influence shock and the forward shock are distinct in the dominant frequency map, which indicates that the PSD value is a sharp peak. Likewise, the supersonic jet shows better definition. Conversely, there is little evidence for the disturbances rising from the jet, or any activity at the base of the cylinder, on the peak PSD value map. The RMS map shows these features because the peaks are broadband.

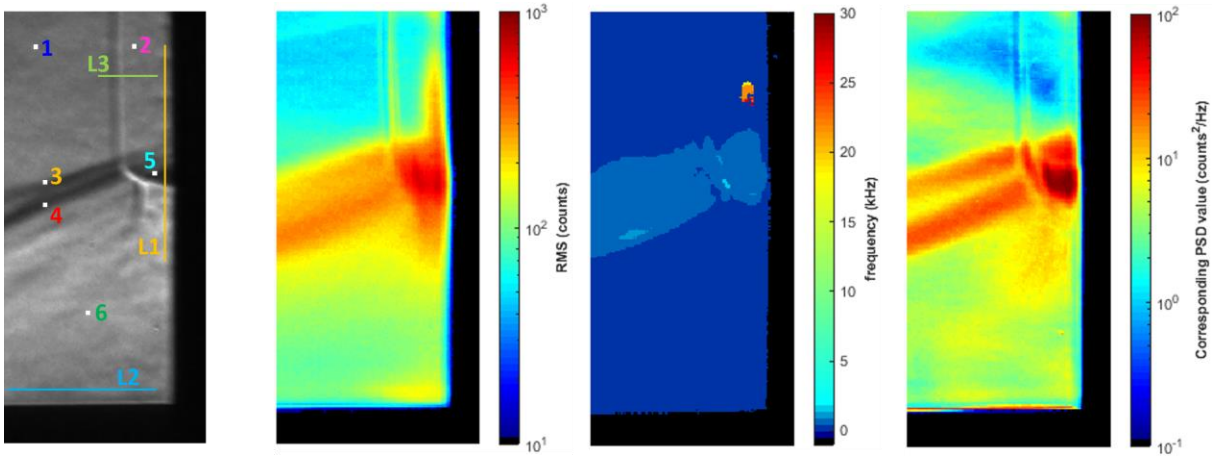

Figure 151. Schlieren-based maps for Run 3429, *Re*=6.6M/m. From left to right: raw high-speed schlieren image indicating positions for later PSD display, RMS fluctuations, dominant frequencies, and maximum PSD values

Analysis of the PSD plots in Figure 152 gives better clarity to the dynamics of the interaction. The upper left plot shows PSDs at the points depicted on the schlieren image in Figure 151. The spectrum for Point 1 indicates baseline fluctuation level outside of the interaction. The levels increase for Point 2 across the bow shock, as the content shifts up nearly uniformly for all frequencies. The spectrum at Point 6 (within the separated region) is similar in its broadband shape and still higher in energy than the spectra at the first two points. The spectra representing the upstream

influence shock (Point 3), forward shock (Point 4), and supersonic jet (Point 5) are all similar in shape with comparatively high fluctuation levels concentrated in the lower frequencies. The UI shock is less intense than the forward shock. The supersonic jet has PSD values roughly 3-5 times the shock values across the frequency domain.

Line L1 is positioned approximately 0.4 mm upstream of the cylinder. Spectra from 10 points on the line, at different heights above the model, are plotted in the upper right of Figure 152. The first two spectra are below the supersonic jet and show fairly broadband content that increases in intensity with proximity to the jet, where the highest levels are seen. The disturbances that travel up the cylinder take form above the supersonic jet. The broad spectral peak (15 to 30 kHz) from the disturbances is highest in magnitude and frequency close to the jet, and both decrease with increasing height above the surface.

Line L2 is located approximately 1.1 mm above the surface of the wedge. The spectra from x'<-7.7mm are essentially the same. Between 7.7 and 3.6 mm from the cylinder surface, the spectra increase across the frequency domain and again overlap for the final points that are displayed. The spectra near the base of the cylinder indicate a peak between 20 and 25 kHz. Line L3 is located around 26.2 mm above the model surface and crosses through the bow shock, which is located near x'=-4.2mm. The spectra from the points closest to the cylinder show effects from the disturbances that rise from the jet. Points near the shock indicate elevated low-frequency content up to 10 kHz, before a sharp drop-off.

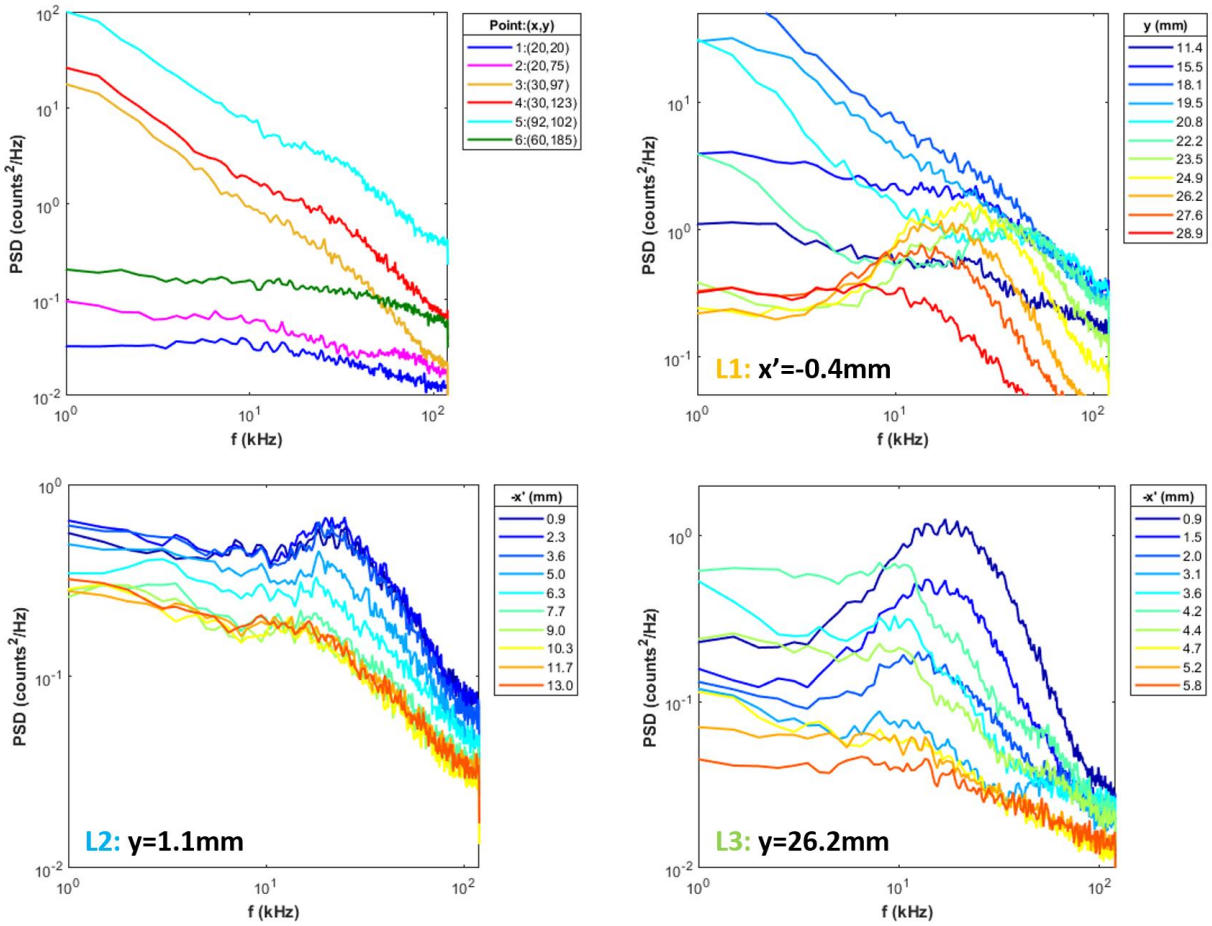

Figure 152. PSD plots for the points and lines indicated in Figure 151

The same maps displaying RMS fluctuations, dominant frequencies, and corresponding PSD values are given in Figure 153 for *Re*=5.4M/m and in Figure 154 for *Re*=4.4M/m. The color scale for all maps is the same as previous. The intensity in the main features (shocks and supersonic jet) decreases with Reynolds number. The dominant frequency maps show the low frequencies of the upstream influence shock and the jet but only partially define the forward shock. The high-frequency peaks related to the jet-induced disturbances exist but no longer rises to absolute maxima levels. The overwhelming presence of zero-frequency content washes out physical features in the maximum PSD values maps. The specific spectra that comprise the lower Reynolds number

maps are presented for the points (Figure 155) and for line L1 (Figure 156) as outlined in Figure 151. The points are not at the same pixel locations for each Reynolds number; rather, the points were chosen to be in the same position relative to the features (shocks).

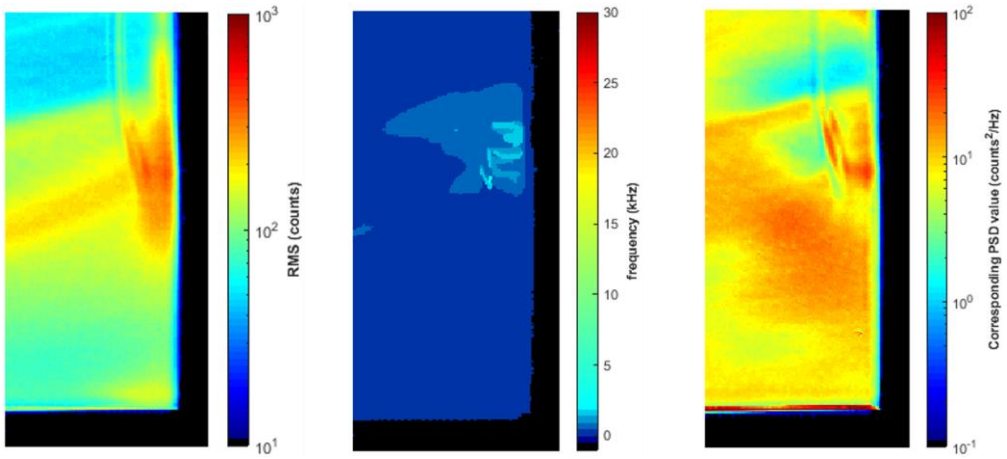

Figure 153. Schlieren-based maps for Run 3429, *Re*=5.4M/m. From left to right: RMS fluctuations, dominant frequencies, and maximum PSD values

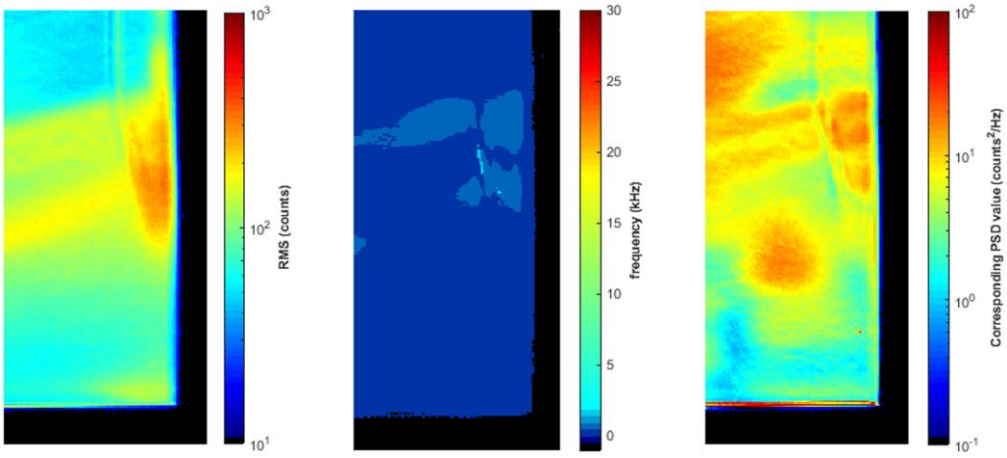

Figure 154. Schlieren-based maps for Run 3429, *Re*=4.4M/m. From left to right: RMS fluctuations, dominant frequencies, and maximum PSD values

The spectra for Points 1 and 2 (upstream and downstream of the bow shock) look similar through transition. Point 6, located within the separation, is fairly consistent as well but indicates some spectra broadening with increasing Reynolds number. The spectra for Point 3 (on the upstream influence shock) are generally lower in magnitude than those for Point 4 (on the forward shock). However, the low-frequency content, which is dominant for both separation shocks, is higher for the upstream influence shock at lower transitional Reynolds numbers. This follows since the upstream separation shock appears better defined at those conditions. The most precipitous rise in content throughout the transition process is observed at the supersonic jet. The spectra increase by nearly an order of magnitude throughout across the frequency domain as the interaction transitions through a Reynolds number range of 4.4 to 6.6 M/m. The spectra on L1 indicate that disturbances continue to rise up the cylinder throughout the transition process, and the characteristic frequency is near 20 kHz. However, the magnitudes of the disturbance peaks at Re=5.4M/m and Re=4.4M/m are not higher than the zero-frequency PSD value. That only occurs when the interaction state becomes more turbulent.

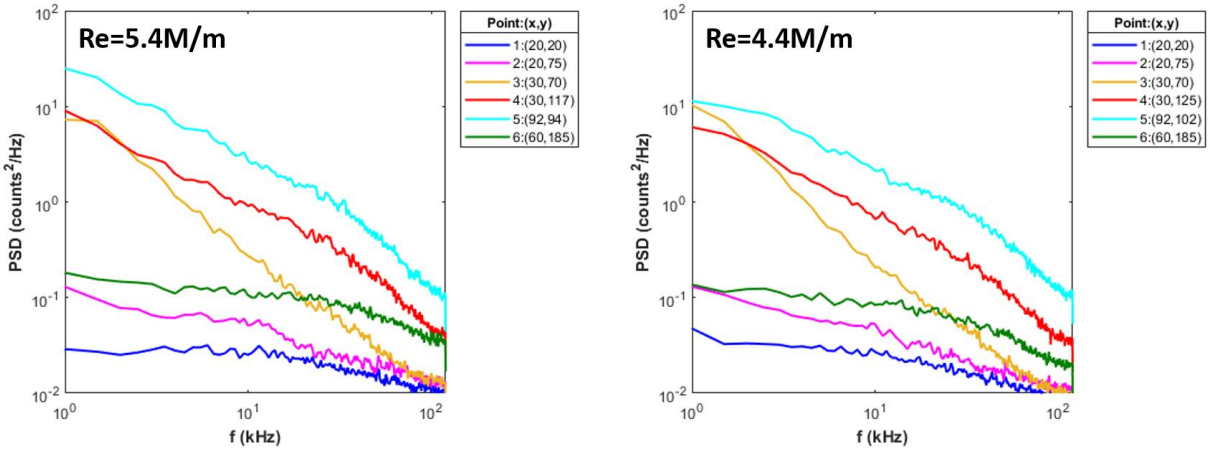

Figure 155. PSD plots for the points indicated in Figure 151 at *Re*=5.4M/m (left) and *Re*=4.4M/m (right)

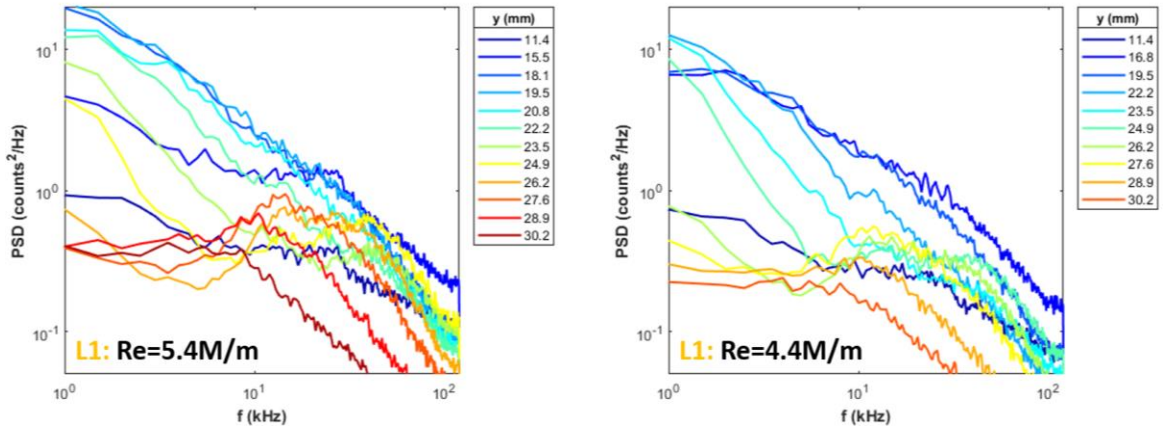

Figure 156. PSD plots for points on L1 at *Re*=5.4M/m (left) and *Re*=4.4M/m (right)

6.4.3 Shock Tracking

The shock tracking results provide significant insight to the disturbance wave and upstream influence separation shock motion. Both of these features are observed in the schlieren image of *Re*=4M/m in Figure 144 where the disturbance wave is between the forward shock foot and the upstream influence shock. That disturbance wave originated from the high-frequency, high-intensity, circulation at the base of the cylinder and progressed outward toward the separation shock. Shock tracking, even displayed in terms of the Hough coordinate, ρ, elucidates some important trends. Figure 157 portrays such results for the first 1000 frames of Run 3443 at 3.7M/m. The distance, ρ, is the magnitude of the distance from the upper left corner of the field-of-view. A larger ρ value means that the shock or disturbance wave is closer to the wedge surface. The primary wave is the farthest shock away from the wedge for a given frame and represents the position of the upstream influence shock. Secondary and tertiary waves are additional disturbance waves that are within the same frame.

Inspection of Figure 157 provides insight to the character of the motion. The prevailing trend is that primary wave points originate at high ρ values and tend to lower ρ with increasing frame. Once at a ρ between 90 and 110, the slope of descent levels out and the ρ value is held more or less constant for several frames. Physically, this indicates that once the shock reaches a distant position, it stalls at that position rather than continuing farther upstream. After a period of time, the shock dies out, and another shock, positioned closer to the cylinder, becomes the new primary shock and repeats the trend. This "shock replacement" dynamic contrasts the literature, where the separation shock is reported to be oscillatory [5,29]. It is unclear if the motion observed in the schlieren imaging is representative of all SBLIs or is a function of the geometry for the present transitional interaction; however, it may be related to the "disappearing" of the upstream influence shock observed in [162]. The slope formed by the data points in the figure is related to the shock speed, and the offset between the lines of sloping points is related to the characteristic frequency of separation shock motion.

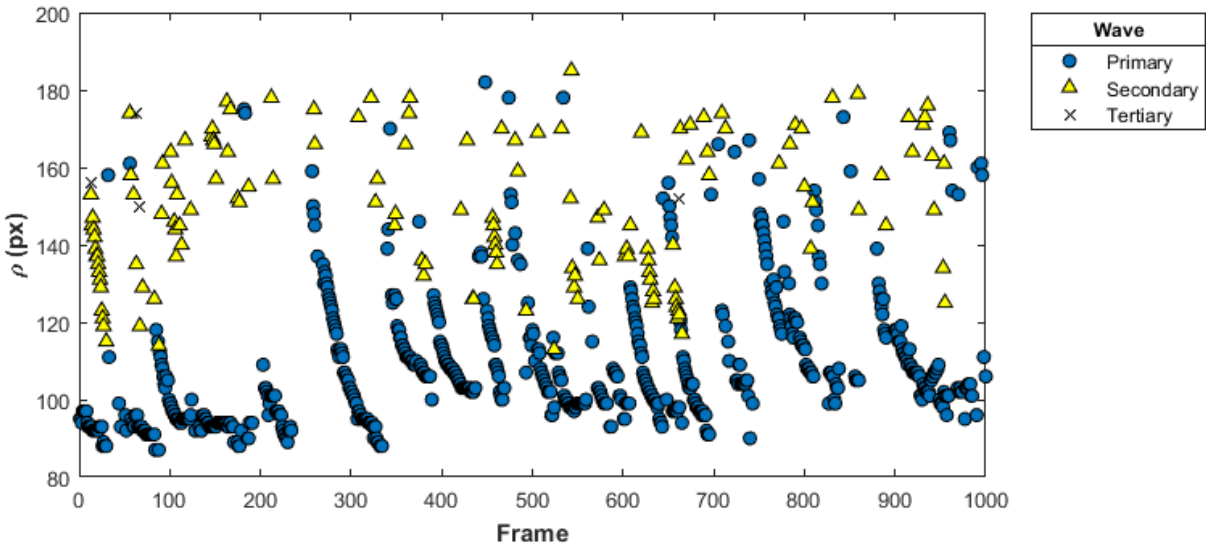

Figure 157. Shock tracking with Hough coordinate ρ (Run 3443, *Re*=3.7M/m)

The coordinates were transformed to model-based, and the lines representing shock and disturbance waves were extrapolated to the wedge surface to determine the streamwise intercept position relative to the base of the cylinder. The same data are plotted in Figure 158 in terms of wedge intercept position and time. At first glance, Figure 158 appears to be Figure 157 mirrored about the horizontal axis. While it is not a perfect mirror, the trend makes sense because the reference distance is from below, rather than above the wave. The data show that the greatest percentage of wedge intercept values are from *x'/d* = -7 to -5 for the 1000 frames presented at *Re*=3.7M/m.

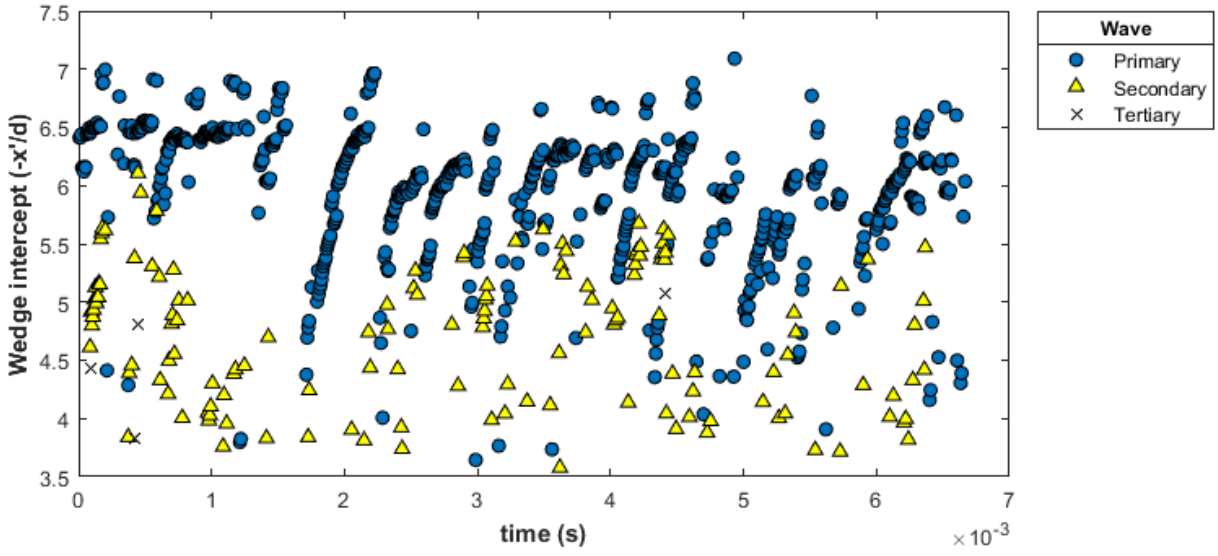

Figure 158. Upstream influence shock / wedge intercept from shock tracking (Run 3443, *Re*=3.7M/m)

The wedge intercept values for the primary waves are displayed in a histogram format in Figure 159. The left plot shows that nearly 40% of frames from the same 1000 frame dataset have intercept values between *x'/d* of -6.5 and -6.0. The data are skewed toward lesser separation, demonstrating the tendency of the upstream influence shock to pause near the end of its travel. The histogram built from the full set of frames at *Re*=3.7M/m indicates no significant changes to the

trend. The overall shape of the histogram is similar to that of the upstream influence probability density function presented by Lash et al. [162]. Both sets of data have similar variation about the mean separation and comparable skew.

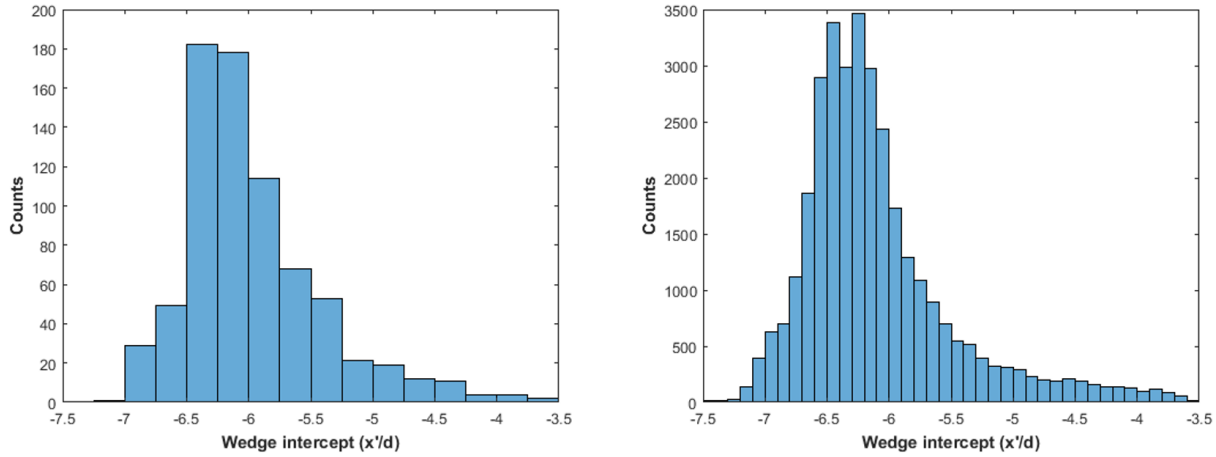

Figure 159. Shock / wedge intercept histogram for 1000 sample dataset (left) and for all samples of Run 3443, *Re*=3.7M/m (right)

The outward motion of the waves is more difficult to perceive visually at Reynolds numbers above 4M/m since the shock structure collapses and the disturbances travel a lesser distance. The shock tracking code still indicates that "shock replacement" motion applies at higher transitional Reynolds numbers as evidenced by Figure 160, which presents the motion for 1000 frames at *Re*=5.2M/m. Figure 161 gives the wedge intercept position for frames at *Re*=6.9M/m. The interaction is close to turbulent at that Reynolds number. The data do not show a distinct pattern, partly due to the shape of the shocks, which have reduced length and are often not linear. The motion may be oscillatory at this condition, but it is unclear visually or based on the intercept positions.

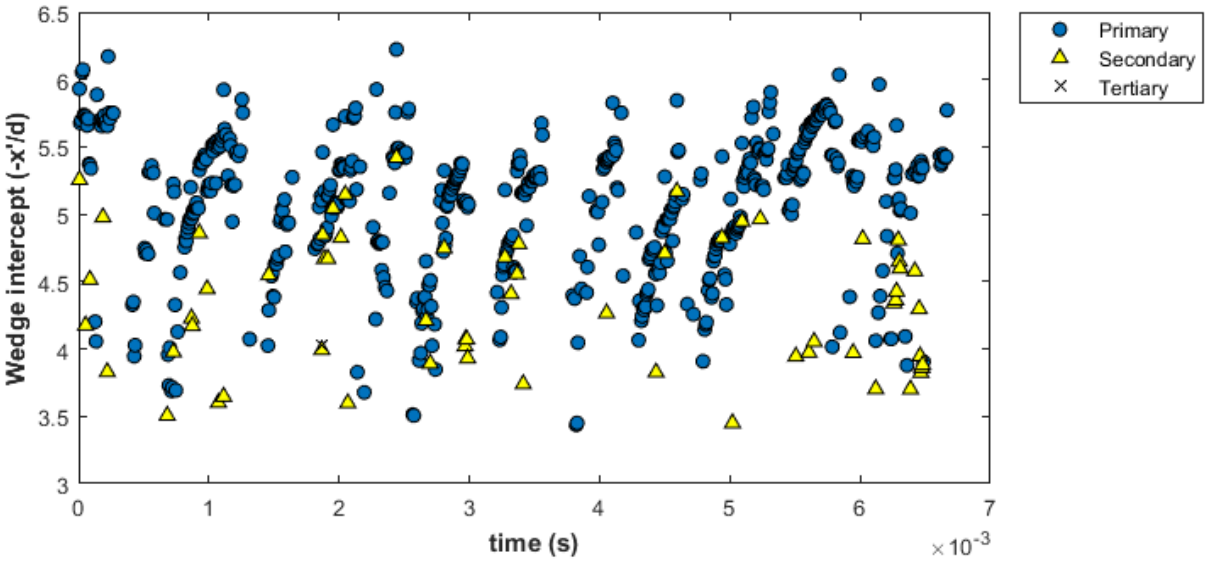

Figure 160. Upstream influence shock / wedge intercept from shock tracking (Run 3443, *Re*=5.2M/m)

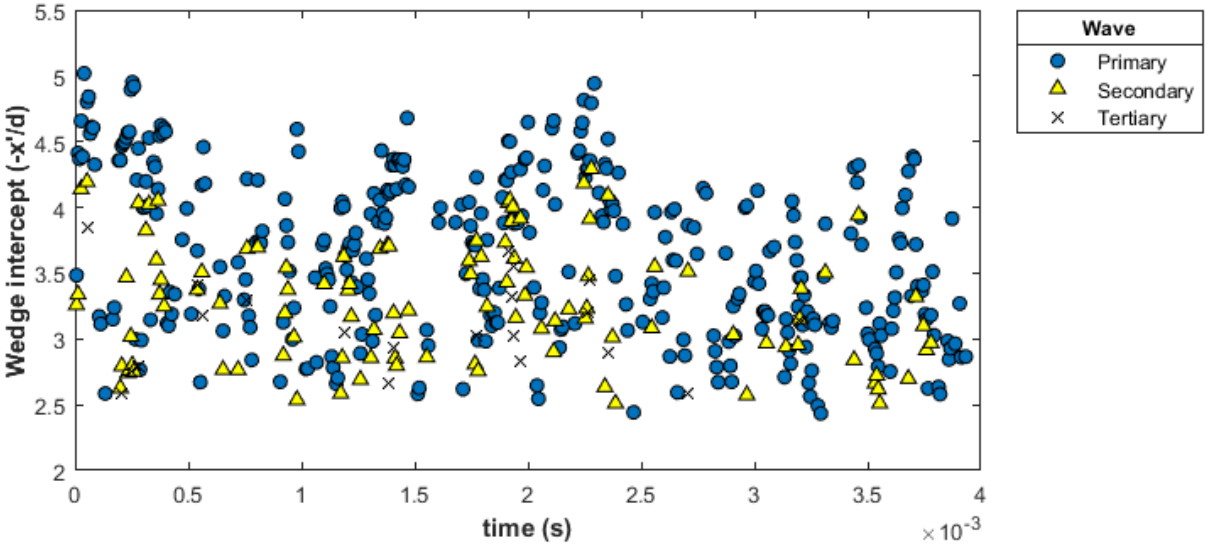

Figure 161. Separation shock / wedge intercept from shock tracking (Run 3443, *Re*=6.9M/m)

6.5 Other Measurements

6.5.1 Cylinder Wake

Hot-wire surveys were conducted in the wake of the cylinder in an effort to compare spectral content with that observed upstream of the shock generator. The first survey (Run 3476) was made without the trip array in place above K3 in port T24. The following run (Run 3477) surveyed the location studied by Wheaton [43], and Run 3479 consisted of identical measurements on the model with trips. The probe was held in a fixed position for Run 3480, and the Reynolds number was swept in an effort to identify a dominant frequency.

Mass flux and fluctuation profiles (Figure 162) indicate that the surveys with and without trips were conducted in the wake. Both the mass flux and fluctuations are elevated significantly above what was observed in the upstream boundary layer. The trips configuration results in far greater fluctuations in the wake, particularly away from the wall. However, the spectra from both of these runs, as well as the other two runs, indicate no notable frequency peaks (Figure 163).

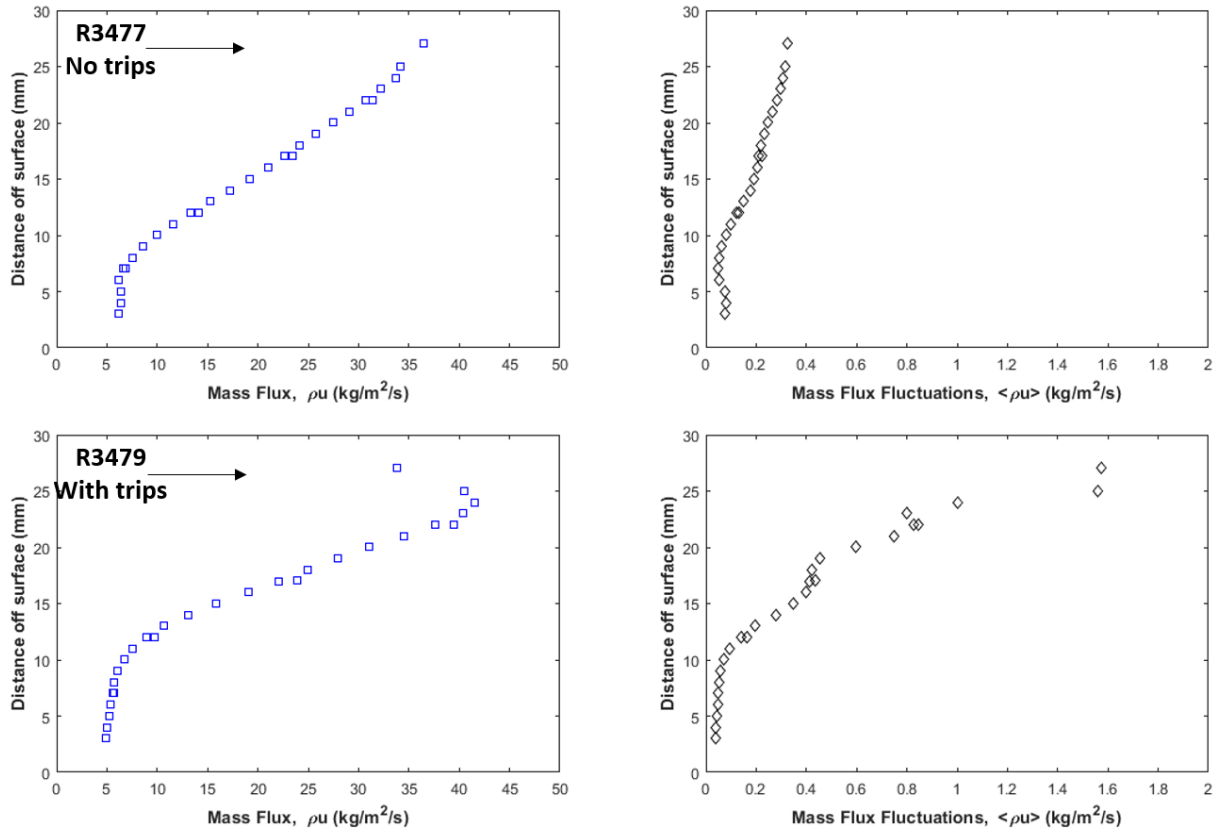

Figure 162. Mass flux (left) and fluctuation (right) profiles in cylinder wake without (top) and with (bottom) trips

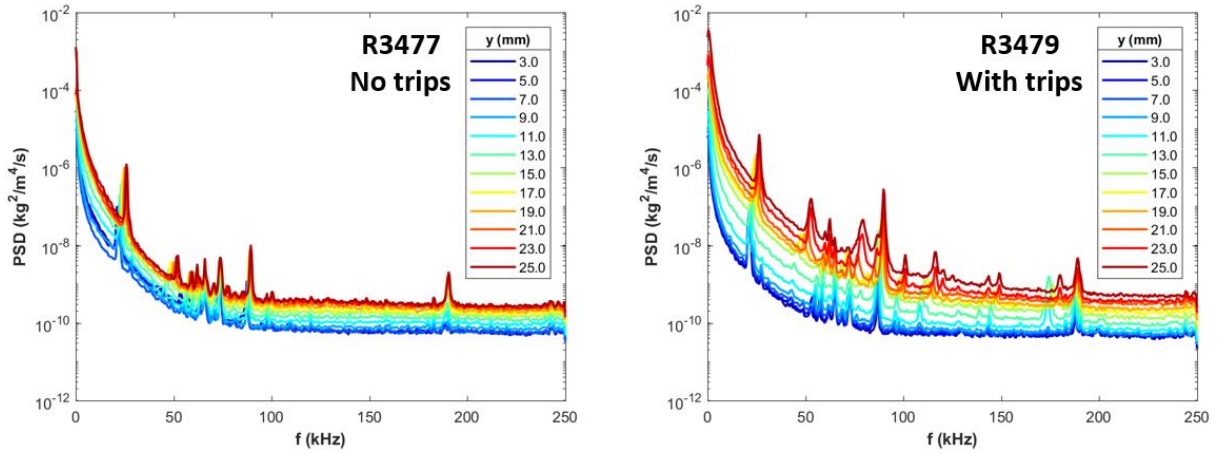

Figure 163. Hot-wire spectra in cylinder wake: Run 3477 (left) and Run 3479 (right)

6.5.2 Focused Schlieren

The first focused schlieren run, Run 3490, was sampled in full resolution as the imaging plane was swept into focus. The field-of-view was considerably smaller than that of the conventional schlieren; the full 1024 x 1024 resolution corresponded to only a 34 x 34 mm square for the focused schlieren. Nevertheless, it was able to capture the features near the triple point, including the supersonic jet, for the 15-degree swept forward cylinder. Figure 164 depicts the relative fields-of-view for 216 x 256 conventional schlieren (Run 3488, left) and 1024 x 1024 focused schlieren (Run 3490, right). The 232 x 384 reduced resolution used for time-resolved motion is inset on the full focused schlieren image.

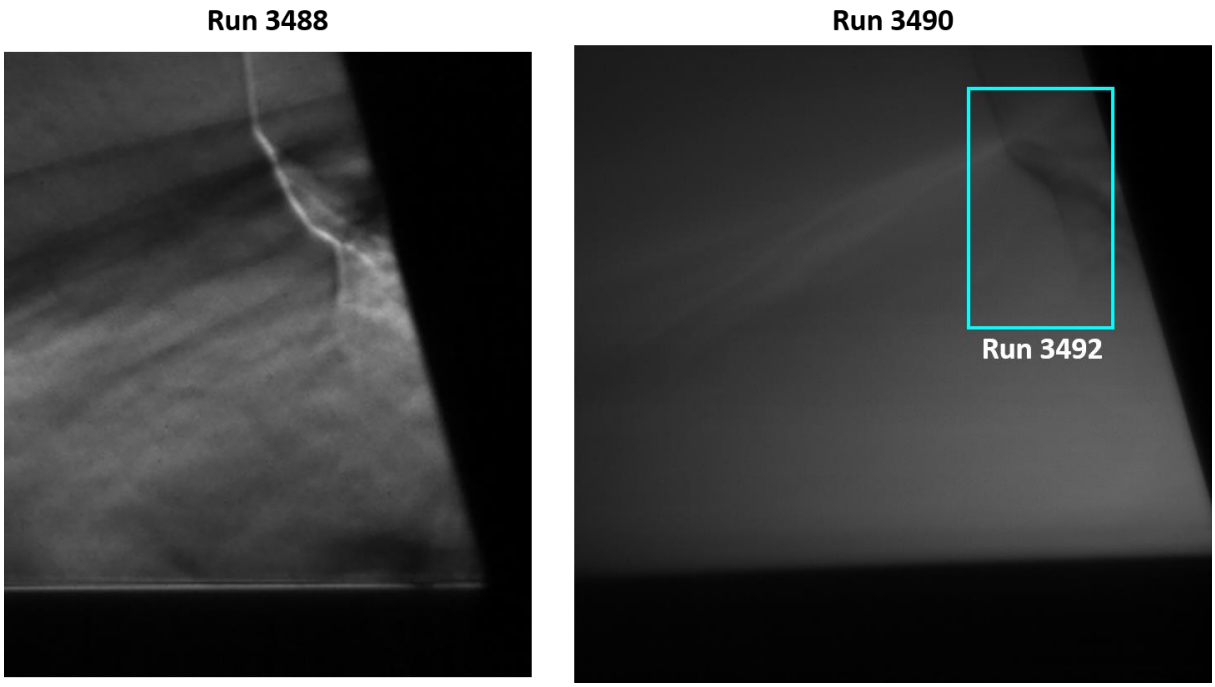

Figure 164. Field-of-view comparison of conventional (time-resolved) schlieren (left) and focused schlieren (right), with the time-resolved focused resolution inset

Time-resolved focused schlieren imaging was performed for the same model configuration in Run 3492. The resolution was reduced, so the field-of-view was only 7.7 x 12.8 mm, which was barely enough to capture the supersonic jet. Figure 165 displays a progression of image as the plane of focus was moved to the centerspan of the model (z=0).

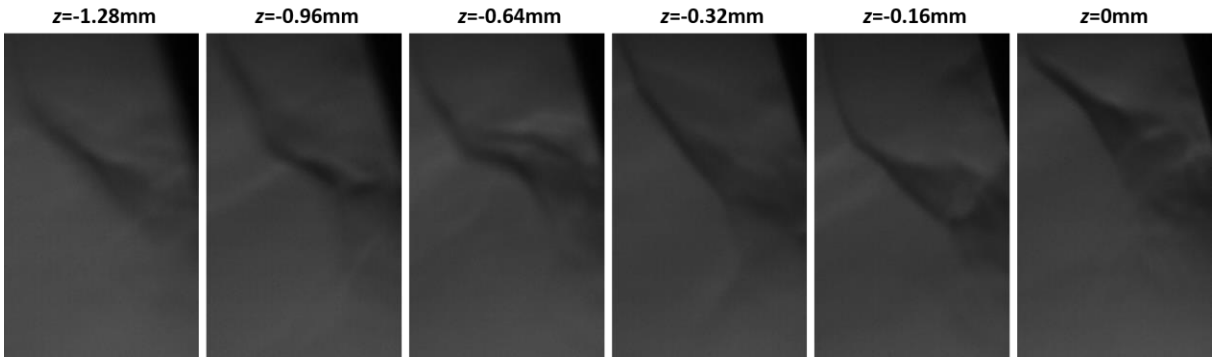

Figure 165. Focused schlieren images as the plane of focus was stepped in Run 3492, with focal plane z=0 on the right

Comparisons were made between the observed dynamics for conventional and focused schlieren. Maps of dominant frequency and maps of RMS normalized by the maximum RMS value are given in Figure 166 for conventional (top, Run 3488, *Re*=5.1M/m) and focused (bottom, Run 3492, *Re*=4.9M/m) schlieren at the z=0 plane of focus. It was necessary to normalize the fluctuations due to lower overall lighting for focused schlieren versus conventional. Although the focused schlieren only captures the supersonic jet and a small portion of the forward shock foot, the data between the two imaging techniques show excellent agreement over the region. The low-frequency nature of the supersonic jet and forward shock foot motion, and the intensity distribution, are captured well with focused schlieren. The consistency between these diagnostics inspires confidence that the interaction features observed in the conventional schlieren for this campaign were present at or near the plane of symmetry.

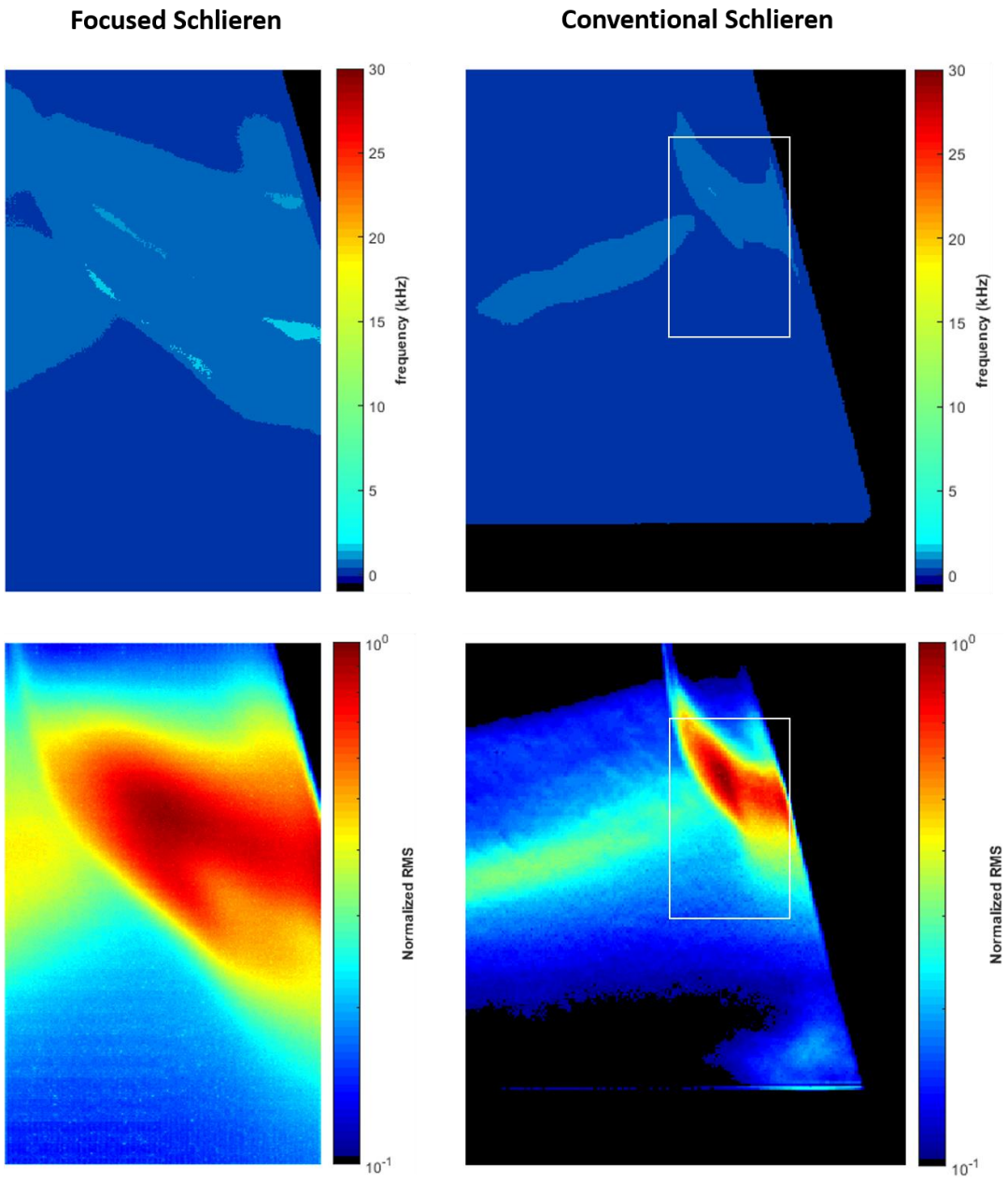

Figure 166. Comparison of dominant frequencies (top) and RMS fluctuations (bottom) between focused schlieren (left) and conventional schlieren (right)

The perpendicular cylinder was traded in for the swept cylinder for the Run 3494. Unfortunately, the image lighting was reduced for this run because much of the illumination was blocked by the tunnel wall due to the proximity of the window edge to the front edge of the cylinder. The

jet was positioned near the bottom of the field-of-view in an effort to visualize the ascending disturbances. The left image in Figure 167 gives the focused schlieren field-of-view relative to a full resolution, conventional schlieren image (Run 3427, *Re*=5.0M/m). The center image is a sample focused schlieren image at the model centerspan. The jet is visible toward the bottom of the image, but there is little contrast, particularly in the upper portion. PSDs (Figure 168) were taken at points on line L. The right image of Figure 167 is the map of dominant frequencies, which shows low-frequency content, ranging from 500 Hz to 2 kHz, in the region near the triple point. These frequencies are consistent with those observed with the conventional schlieren.

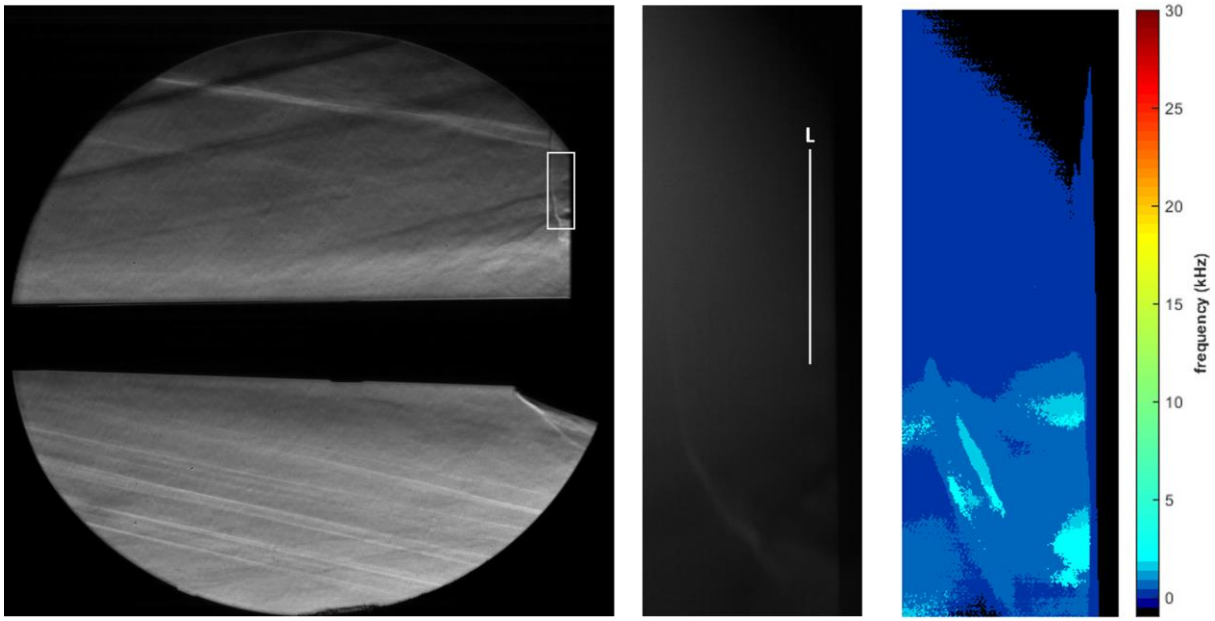

Figure 167. Conventional schlieren image with the focused schlieren resolution inset (left), sample focused schlieren image at *z*=0 (center), and dominant frequency map from all *z*=0 images (right)

The RMS fluctuations are given in Figure 168 (left). The highest content is observed near the triple point and the supersonic jet, as expected. The image also shows higher fluctuation levels near the cylinder, above the triple point. The elevated levels are due to the disturbances that ascend

the face of the cylinder. PSDs from points along the aforementioned line L are presented in Figure 168 (right). The spectra look similar to those presented in Figure 156, albeit noisier and at lower levels, caused by the poor lighting and lack of contrast in the group of focused schlieren images.

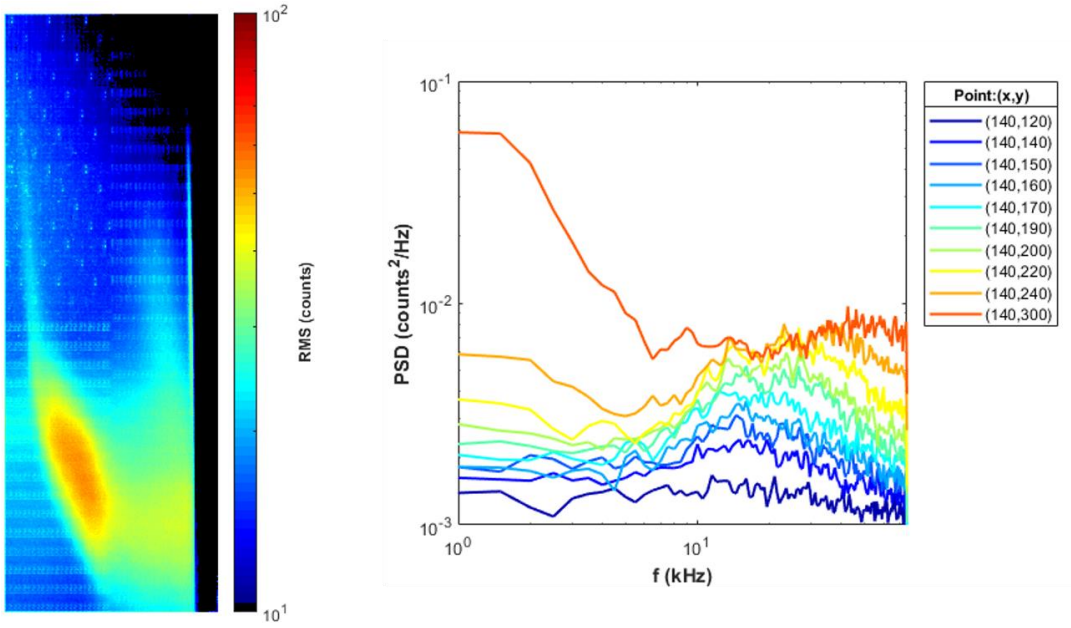

Figure 168. RMS fluctuation map (left) and PSDs from points along line L (right) from the focused schlieren images at *z*=0

6.6 Influence of Freestream Noise on Transition

Results from the present study suggest that freestream noise had a significant impact on the interaction transition process. Spectral plots in waterfall format are presented for Kulite sensors placed within the interaction in Figure 169. The upstream Kulites (x'=-4.33d) are depicted above the downstream Kulites (x'=-3d) in the figure. The spectra at the same streamwise locations look similar. This is expected since the total spanwise spacing between the three sensors is only 22.2

mm. It should be noted that ports T12 and T13 are directly behind T6 and T13, respectively. T5 and T14 are offset to the left and right, respectively, to measure the influence of spanwise position behind the trips. The effect of placement behind a trip or a gap appears negligible.

The spectra at all locations show a sudden rise in amplitude and broadening just below *Re*=3.5M/m, which is consistent with the rise in freestream noise (Figure 170, bottom). Both sets of spectra, upstream and downstream, indicate high amplitudes at low frequencies. These occur near *Re*=5M/m upstream and near *Re*=6M/m downstream, which are the expected conditions for separation shock motion. The upstream plots show instability growth near 40 kHz around 4M/m. They also indicate the transition of the incoming boundary layer around 7M/m since the interaction is downstream of the transducers at that Reynolds number. The downstream plots provide higher amplitudes of the 40 kHz instability at 4M/m and also show another peak near 5.5M/m. The spectra broaden considerably above that Reynolds number, indicative of the interaction transitioning.

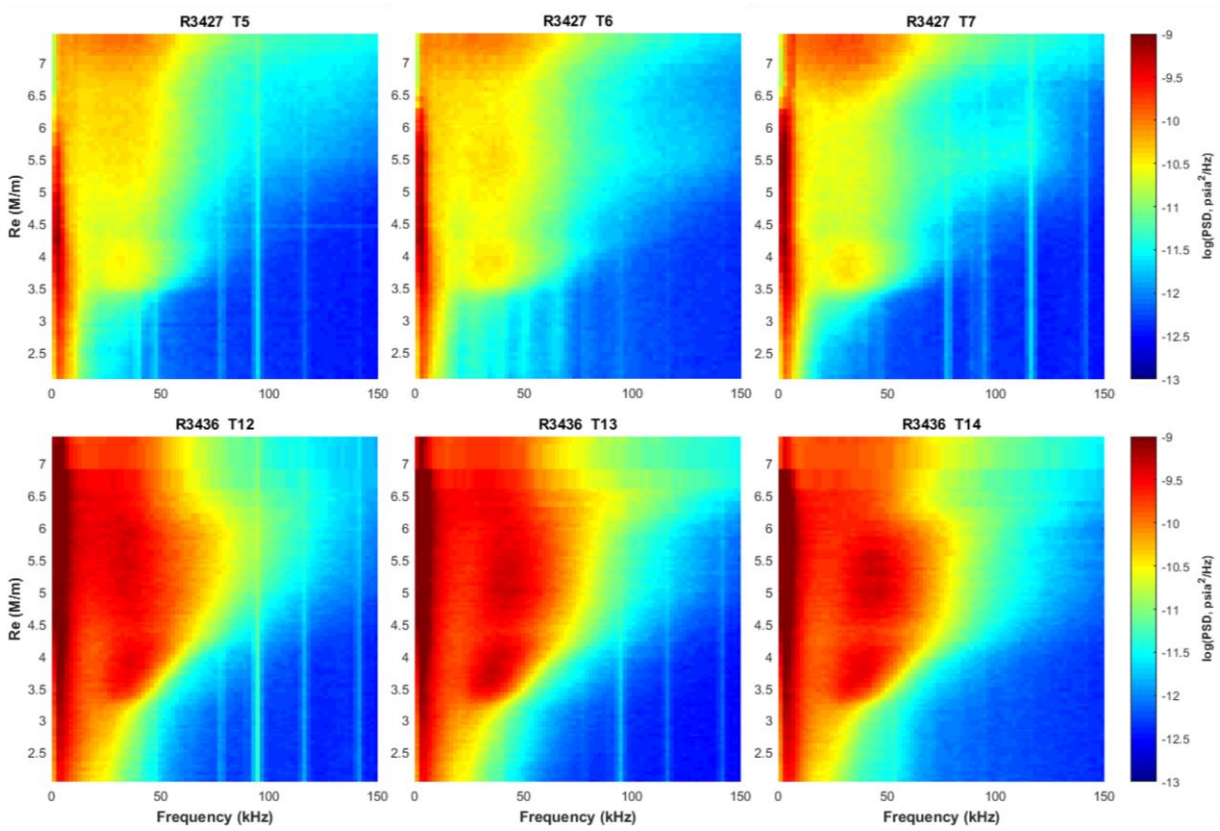

Figure 169. Spectral maps for Kulite transducers demonstrating transition in the "trips, cylinder" configuration. T12 is behind T6. T13 is behind T7

Figure 170 presents the average film coefficient within the reattachment arc as a function of Reynolds number for several runs, both with and without trips. This plot is a combination of Figure 134 and Figure 137. It allows for easier comparison between the two configurations and the freestream noise, which is plotted at the bottom of Figure 170. The heating comparison shows that both configurations have roughly the same heating at the reattachment arc at low Reynolds numbers. At around 3M/m, both the freestream noise and the heating for the configuration with trips increase substantially. The heating slope for the transitional SBLI is roughly constant between 3.5 and 6.0 M/m, but is lower than that for the laminar SBLI, which has a constant slope across

the entire Reynolds number range. The laminar SBLI heating overtakes that of the transitional / turbulent SBLI for Reynolds numbers above 6M/m.

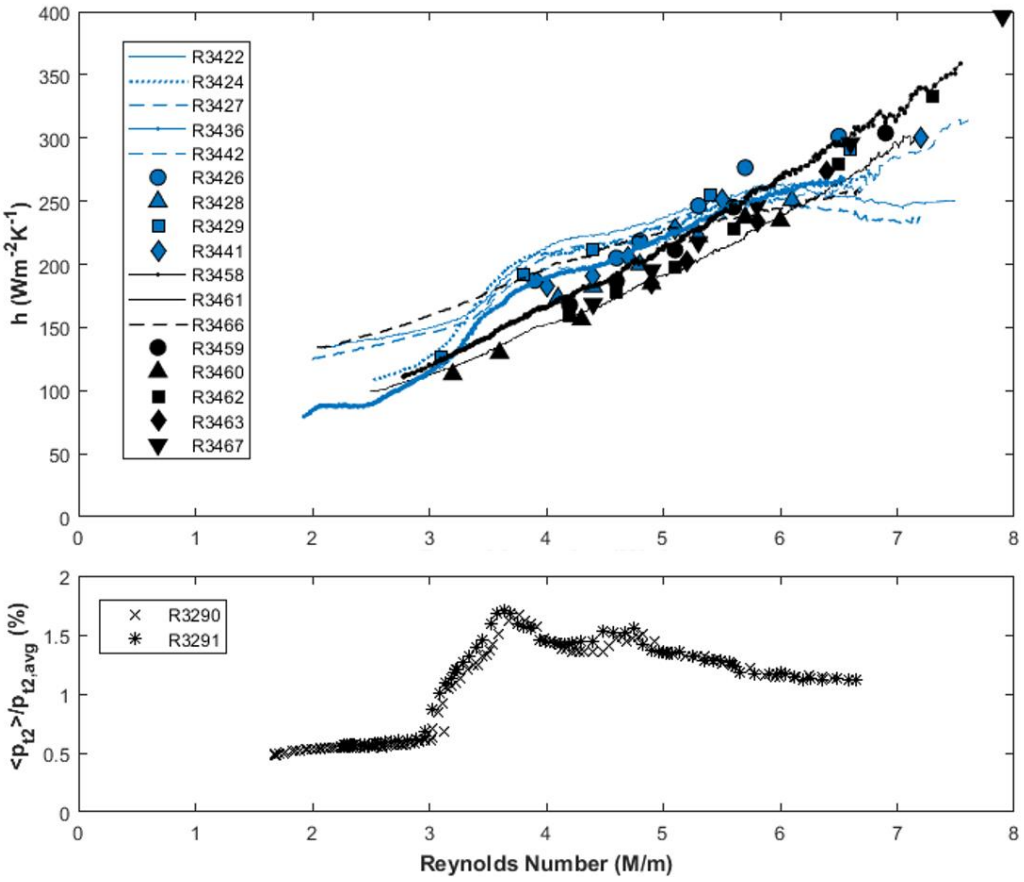

Figure 170. Reattachment arc heating (top) with trips (blue) and without trips (black) and freestream pressure fluctuations (bottom)

The extrapolation of the separation shock to the wedge is plotted as a function of Reynolds number for the "trips, cylinder" and "no trips, cylinder" configurations in Figure 171. The shock / wedge intercept was determined using the shock tracking code described in Section 3.4.5 and implemented in Section 6.4.3. The separation distance increases slightly with Reynolds number for "no trips, cylinder", as suggested by Figure 145. The shock intercept distance begins decreasing

just below *Re*=3.5M/m for the configuration with trips. Therefore, the shock structure begins to contract under conditions of elevated freestream noise. The interaction collapses most rapidly between 3.5 and 4.5 M/m and continues to reduce in extent until around *Re*=7M/m. The extrapolated intercept of the separation shock with the wedge is around 3*d* from the front of the cylinder at the highest Reynolds numbers tested, when the interaction is near its turbulent state.

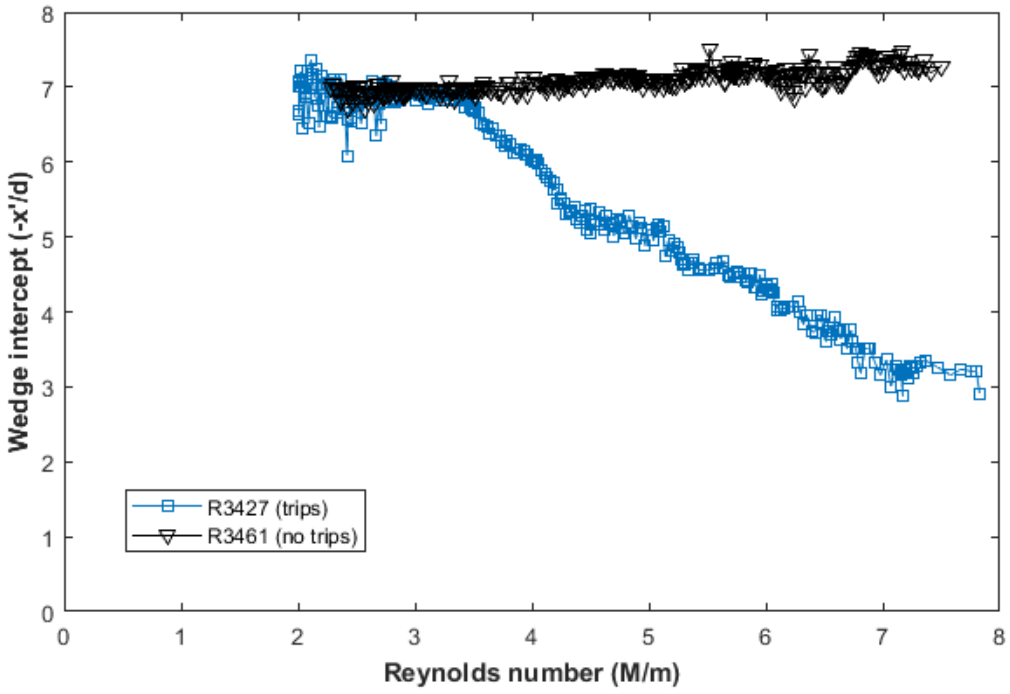

Figure 171. Separation shock / wedge intercept with Reynolds number from schlieren images

In summary, a jump in freestream noise is a feature in the ACE wind tunnel, characterized by RMS pressure fluctuations increasing by a factor of three near *Re*=3M/m. The freestream noise levels were not anticipated to be a catalyst for transition in the present campaign as it was believed that some combination of trip disturbances and cylinder-induced adverse pressure gradient would lead to transition at a suitably high Reynolds number. However, the surface pressure spectra within

the separated region of the interaction, the surface heating at the base of the cylinder, and the initiation of interaction contraction, all indicate that freestream noise played a role in the transition process in conjunction with the 40 kHz base model instability, the trips, and the cylinder.

7. CONCLUDING REMARKS AND RECOMMENDATIONS

This chapter reviews the impact of the study in terms of the available literature, addresses the research objective questions with results obtained from the experiments, and provides recommendations for follow-up tests that would offer further insight into 3-D transitional shock wave boundary layer interactions.

7.1 Impact of Study

The primary contributions to the field from this study are the database and the subsequent analyses that aim to extend the current state of knowledge on transitional SBLIs. The long-term impact has the potential to be substantial as the data fill a clear void in the knowledgebase. Prior to this campaign, high-frequency surface pressure measurements, time-resolved high-speed schlieren images, and heat transfer maps on comparable geometries for any incoming boundary layer state at a freestream above Mach 5 were unavailable.

SBLIs of similar configuration to the present experiment have been studied extensively. The present study provides a comprehensive list that puts this work in context with the literature and provides future researchers a starting point for a literature review. Early cylinder-induced SBLI experiments focused on measuring thermal and pressure loads, in particular magnitudes and locations of maxima. Oil flow visualization and schlieren imaging then became important tools to map out the interaction structure. Also, during that time, the effects of cylinder height and incoming boundary layer thickness were evaluated. Following those studies, the dynamics for turbulent interactions took the forefront. Dolling and Bogdonoff [32,39,100] began using surface mounted Kulite pressure transducers at Princeton University. Dolling continued work studying the motion

of the separation shock with his group at the University of Texas. Most recently, advanced laser diagnostics have been used to measure more specific features within the interaction and in the protuberance wake. In total, over 100 campaigns have been conducted on similar geometries but few of the studies have been devoted to transitional SBLIs.

The present campaign was carefully conducted with future CFD validation efforts in mind. The geometry and surface roughness were measured across the model. Freestream pressure and mass flux fluctuations were quantified at the same streamwise position as the model leading edge. The model was designed to minimize the pressure gradient between the upper and lower surfaces. It was mounted 50.8 mm away from each sidewall to minimize that influence. The strut was positioned on the downstream portion of the model to minimize impact on flow upstream of the cylinder. Oil flow visualization indicated these strategies to be successful as streamlines were directed straight back for the majority of the span. The model was set outside of the tunnel during the preheating and inserted just before the run, which led to consistent surface temperatures. Hot-wire surveys were taken at different streamwise and spanwise positions within the boundary layer and across the leading-edge shock. Every effort was made to mount the transducers and plugs flush with the model surface. The IR camera was calibrated prior to the campaign using the same tunnel setup, with the exception of quiescent air. The pressure transducer data, high-speed schlieren, and IR thermography were all synchronized to the tunnel operating conditions.

For transitional interactions, Murphree [159] raised the question if the incoming boundary layer were transitional or if transition were caused by the protuberance. This campaign showed that the presence of the cylinder excited the 40 kHz (potentially second mode) instability and led to boundary layer transition just downstream of the separation shock. The interaction state proved to be ahead of the incoming boundary layer state in the transitioning process. Hot-wire boundary

layer surveys indicated instability growth for *Re*=5M/m, while oil flow visualization and schlieren imaging showed a transitional SBLI under the same conditions. Stanton number maps and surface pressure transducer spectra suggested incoming boundary layer transition near *Re*=7M/m. At that Reynolds number, the interaction was near turbulent based on the observed separation distances from the oil flow and schlieren.

A particularly important feature of the present campaign was the goal to isolate key variables through configuration modifications. Pressure fluctuations and thermal loads were quantified for all configurations, and fluctuations in the schlieren images were evaluated for interactions with and without boundary layer trips as well as at different sweep angles. This made it possible to explain many of the results. For instance, Kulite spectra revealed a 40 kHz peak on the base model. This peak grew with the protuberance in place, but the roll-over signature of instability-induced transition was not observed. The trip array without the protuberance prompted an additional instability peak near 115 kHz. With both the trips and cylinder in place, the 40 kHz instability was excited to the point of transitioning just downstream of the separation shock.

Many other discoveries were made during this campaign. An important, and unexpected result, was the film coefficient dependence on Reynolds number at the reattachment arc. The reattachment arc represents the region of highest heating on the wedge portion of the model. Heating was shown to be higher for a laminar SBLI (configuration without trips) than for transitional or turbulent SBLIs at the same freestream conditions. This finding may be related to those of Benay et al. [140] and Bur and Chanetz [141], who observed higher heat transfer for untripped interactions. The present study also suggested reattachment arc heating dependence on the freestream noise for the transitional SBLI.

Data from this campaign will be useful for contemporary studies. Cylinder-induced XSBLIs experiments using similar diagnostics are currently taking place in the Mach 2 blowdown tunnel at the University of Tennessee Space Institute. Comparisons will be made between the present campaign, the UTSI (Lash et al.) Mach 2 campaign, and the UT (Murphree et al.) Mach 5 campaign, to determine the role of Mach number on interaction dynamics and thermal loading. Clemens and Narayanaswamy [5] recently reviewed the cause for low-frequency separation shock oscillations. The present study observation of low-frequency waves which propagate outward from the chaotic recirculating flow at the base of the cylinder to the separation shock provides additional evidence for disturbance-fed separation shock motion.

This campaign clearly demonstrates separation shock motion that is not oscillatory, a discovery not mentioned in literature. The present study shows that the separation shock primarily moves away from the cylinder when the interaction is transitional. As the interaction becomes turbulent, the nature of the shock motion becomes less clear in the schlieren because less distance is traveled. The separation shock may oscillate for turbulent interactions, which would be consistent with what is reported in literature.

7.2 Objective Questions Revisited

The experiments conducted during the present campaign provided insight to the transition process, separation shock motion, and thermal and acoustic loading, that is potentially more significant than the answers to the original research questions. The original questions posed in Section 3.6 are answered below.

How do the dynamics of shock structure, especially the motion of the separation shock foot, triple point, shock-induced supersonic jet, and fluctuations within the separated region, change as the interaction evolves through transition?

The surface fluctuations were measured using PCB and Kulite pressure transducers, and the separation shock motion and fluctuations within the interaction were tracked using schlieren photography. The defining feature of the interaction as it was swept through transition was the modal growth of a 40 kHz instability that transitioned just downstream of the upstream influence separation shock. The representative low-frequency (1.0-1.5 kHz) of the shock was similar to reports from other studies; however, the character of its motion was not oscillatory. Rather, shock tracking of the time-resolved schlieren images showed the separation shock motion could be better described as "shock replacement". The forward shock and supersonic jet were likewise characterized by high-amplitude, low-frequency fluctuations, which significantly increased in intensity through transition. The fluctuations within the separation, between the legs of the lambda shock structure, were broadband throughout but were elevated in magnitude near the merger of the model and cylinder. A 20 to 25 kHz peak was observed just upstream of the cylinder base. Disturbances were cast up the shock generator from the triple point. They appeared vortical in nature and resulted in broadband spectral peaks near 20 kHz. The disturbances that rise up from the supersonic jet were present throughout the transition process but only became the dominant frequency of the region when the interaction became close to turbulent.

What effect do the trips have on the downstream boundary layer profiles at different streamwise and spanwise positions?

The influence of the trips was more prominently displayed by some diagnostics than others. The oil flow visualization and IR thermography demonstrated evidence of trip wakes back to the trailing edge of the model. The wakes caused streaks of higher temperature behind the center of every trip. The spanwise temperature variation caused by the wakes decreased distances farther from the trip array.

Hot-wire anemometry was used to characterize the boundary layer. At one streamwise station (x=187mm), the mean profile had the same shape at *Re*=5M/m, with and without trips, but the tripped boundary layer was about 10% thicker. The fluctuation levels were significantly higher (2-3x) with trips throughout the boundary layer. Fluctuation profiles showed more variation when the trip array was in place. Surveys were taken at different spanwise positions relative to wakes (observed using IR thermography). Surveys at similar positions produced similar fluctuation profiles. Fluctuation profiles and spectra from x=213mm demonstrated signs of instability growth at 5M/m with the trips. Spectra indicated the beginning stages of transition at stations farther downstream at *Re*=7M/m.

How does the spanwise positioning behind the trips affect the surface pressure dynamics with and without a shock generator?

Surface mounted PCB pressure transducers (and to a lesser extent, the Kulites) measured a 115 kHz trip-induced instability peak. The peak was not influenced by spanwise position; sensors located directly behind trips gave similar spectra to sensors located between the gaps. The instability peak became less pronounced farther downstream on the model. The addition of the cylinder increased the surface pressure levels tremendously within the interaction. However, no spanwise dependence was observed. The interaction trailed back as position deviated from the centerspan.

Comparing spectra from similar separation locations (as observed by the oil flow), revealed no additional features on the centerspan or outboard.

How does the protuberance sweep angle affect the separation scaling and dynamics for a transitional SBLI?

Sweeping the cylinder back contracted the shock structure, decreased the observable fluctuations within the separation, and reduced the surface RMS pressure fluctuations to near baseline levels in many of the upstream transducers. Closer to the base of the cylinder, the RMS fluctuations were reduced by roughly 50% when using a cylinder swept back 15 degrees compared to one mounted on the model perpendicularly. Conversely, sweeping the cylinder forward increased the extent and intensity of the interaction. As a result, pressure fluctuations rose across the board. RMS fluctuations at the base of the cylinder were measured to be on the order of the freestream static pressure. The highest heating levels detected during this campaign were at the reattachment arc for the forward swept cylinder.

The interaction dynamics were similar for comparable positions within each interaction. Deep within the separation, elevated levels of broadband surface pressure fluctuations were observed. High-frequency content was noted on the face of the cylinder. Low-frequency (~1 kHz) shock motion occurred for all configurations.

7.3 Recommendations for Future Work

The present experimental campaign provided a wealth of insight to 3-D transitional SBLIs. However, some of the data raise additional questions, and the following recommendations for future work are made.

From a model design perspective, the surface mounted transducers should be easier to access for configuration changes. Currently, to access the back cover on the underside of the model, the entire model must be removed from the strut on the removable door, and all of the cables must be disconnected and fed through a Conax fitting on the door. After resetting the transducers, the model must be remounted and the cables reconnected. The ability to swap the transducers in place would save time, as the current exchange took a minimum of six hours. Also, the trip array for the present campaign allowed for sweeping through transition, but future trip arrays should be machined for greater precision.

Additional effort should be made to find and eliminate the cause of the low-frequency noise in the PCBs. That noise was particularly unfortunate in this campaign as it obscured the primary feature in the spectra – the growth and evolution of the 40 kHz instability peak. The Kulites captured this peak well. For future campaigns, it would be helpful to have more Kulite transducers, placed both on the centerspan and outboard. The outboard PCBs did not indicate any differences in the spectra, but there could be some low-frequency discrepancies that would be better suited for the Kulites to detect.

Additional work should be undertaken in processing the IR thermography data. The heat flux is very sensitive to initial conditions, and the current practice of assigning the mean surface temperature as the initial temperature value to all nodes within the material is not accurate. Solutions for reduction of heat flux uncertainty include inserting the model into the tunnel immediately prior to the start of hypersonic flow to minimize the change in temperature on the surface, monitoring the temperature constantly from the moment the model is in the tunnel, using the high-speed data recorder to sample up to 132 Hz (while keeping the node spacing near the same value) to minimize the effect of the initial temperature values, and/or developing a better model for the

temperature distribution throughout the material with time (prior to the actual run) based on the temperature on the front and rear surfaces and the time in the tunnel.

Positioning the model lower in the test section may also be beneficial. Weak shocks from the nozzle / test section interface impinged on the interaction with the current setup. No impact from this impingement was observed in the schlieren, but clearance of these shocks above the cylinder would make for a better experiment.

Boundary layer surveys should be done using a pitot probe in addition to a hot-wire anemometer. Comparing spectra using different instrumentation allows for more confidence in differentiating between flow features or noise. Using a pulsed light source for the schlieren would allow for more light during the camera exposure, which would sharpen the contrast in the flow features. This could allow for a campaign involving cylinders of different diameters (including smaller) as smaller disturbances could be visualized. Examining the flow structure within the separation at different spanwise-normal planes is of interest. Testing this geometry in a high Mach number (thick boundary layers) facility that is more amenable to PIV (higher Reynolds numbers) would allow for better characterization of the separation.

The heating levels and pressure fluctuations within the interaction clearly indicate that the transition process was impacted by freestream noise in the present campaign. Repeating a similar study in a quiet facility would provide insight to the effect of freestream noise on transition for SBLIs.

REFERENCES

[1] J.D. Anderson, Jr. *Hypersonic and High Temperature Gas Dynamics*. AIAA, Reston, VA, 2000.

[2] M.S. Holden. A review of aerothermal problems associated with hypersonic flight. Reno, NV, 1986. AIAA Conference. AIAA Paper 86-0267). URL https://doi.org/10.2514/6.1986-267.

[3] W.L. Auxer, D.E. Nestler, and A.R. Saydah. Heat transfer to steps and cavities in hypersonic turbulent flow. *AIAA Journal*, 7(7):1368-1370, 1969.

[4] R.H. Korkegi. Survey of viscous interactions associated with high Mach number flight. *AIAA Journal*, 9(5):771-784, 1971. URL https://doi.org/10.2514/3.6275.

[5] N.T. Clemens and V. Narayanaswamy. Low-frequency unsteadinessof shock wave/turbulent boundary layer interactions. *Annual Review of Fluid Mechanics*, 46:469-492, 2014. URL https://doi.org/10.1146/annurev-fluid-010313-141346.

[6] D.S. Dolling. Fluctuating loads in shock wave/turbulent boundary layer interaction: tutorial and update. Reno, NV, 1993. AIAA Conference. AIAA Paper 93-0284. URL https://doi.org/10.2514/6.1993-284.

[7] J. Poggie, N.J. Bisek, R.L. Kimmel, and S.A. Stanfield. Spectral Characteristics of Separation Shock Unsteadiness. *AIAA Journal*, 53(1):200-214, 2015. URL https://doi.org/10.2514/1.J053029.

[8] P. Pozefsky, R.D. Blevins, and A.L. Laganelli. Thermo-Vibro Acoustic Loads and Fatigue of Hypersonic Flight Vehicle Structures. AFWAL-TR-89-3014, 1989.

[9] J.E. Green. Interactions between shock waves and turbulent boundary layers. *Progress in Aerospace Sciences*, 11:235-340, 1970. URL https://doi.org/10.1016/0376-0421(70)90018-7.

[10] W.L. Hankey and M.S. Holden. Two-Dimensional Shock-Wave Boundary Layer Interactions in High Speed Flows. AGARD-AG-203, 1975.

[11] J.M. Delery. Shock wave/turbulent boundary layer interaction and its control. Progress in Aerospace Sciences, 22:209-280, 1985. URL https://doi.org/10.1016/0376-0421(85)90001-6.

[12] G.S. Settles and D.S. Dolling. Swept Shock-Wave/Boundary Layer Interactions. In *Tactical Missile Aerodynamics: General Topics*. In *AIAA Progress in Astronautics and Aeronautics*, 141:505-574, 1992.

[13] A.G. Panaras. Review of the physics of swept-shock/boundary layer interactions. *Progress in Aerospace Sciences*, 31:173-244, 1995. URL https://doi.org/10.1016/0376-0421(95)00005-4.

[14] A.J. Smits and J. Dussauge. *Turbulent shear layers in supersonic flow*. AIP Press, New York, NY, 1996.

[15] G.S. Settles and D.S. Dolling. Tactical missile aerodynamics: general topics. In *AIAA Swept shock wave/boundary-layer interactions*, 1, 1997.

[16] D.D. Knight and G. Degrez. Shock wave boundary layer interactions in high Mach number flows – a critical survey of current numerical prediction capabilities. AGARD-TR-AR-319, Vol. 2, 1997.

[17] D.S. Dolling. Fifty years of shock wave/boundary layer interaction research: what next?, *AIAA Journal*, 39(8):1517-1531, 2001. URL https://doi.org/10.2514/2.1476.

[18] D.D. Knight and M. Mortazavi. Hypersonic shock wave transitional boundary layer interactions - a review. Denver, CO, 2017. AIAA Conference. AIAA Paper 2017-3124. URL https://doi.org/10.2514/6.2017-3124.

[19] R.D. Neumann. Special topics in hypersonic flow. Aerodynamic problems of hypersonic vehicles, AGARD Lecture Series 42(1), Van Karman Institute, Brussels, Belgium, 1972.

[20] S.P. Schneider. Summary of Hypersonic Boundary-Layer Transition Experiments on Blunt Bodies with Roughness. *Journal of Spacecraft and Rockets*, 45(6):1090-1105, 2008. URL https://doi.org/10.2514/1.37431.

[21] D.V. Gaitonde. Progress in shock wave/boundary layer interactions. *Progress in Aerospace Sciences*, 72:80-99, 2015. URL https://doi.org/10.1016/j.paerosci.2014.09.002.

[22] I. Nompelis, G.V. Candler, M.S. Holden, and T.P. Wadhams. Real gas effects on hypersonic shock wave laminar boundary layer interactions. Reno, NV, 2003. AIAA Conference. AIAA Paper 2003-443. URL https://doi.org/10.2514/6.2003-0443.

[23] Leon Vanstone. *Shock-Induced Separation of Transitional Hypersonic Boundary Layers*. PhD dissertation, Imperial College London, England, 2015.

[24] A.F. Woolf. Conventional prompt global strike and long-range ballistic missiles: background and issues. CRS Report 7-5700, 2017.

[25] M. P. Borg, S. P. Schneider, and T. J. Juliano. Effect of freestream noise on roughness-induced transition for the X-51A forebody. *Journal of Spacecraft and Rockets*, 45(6):1106-1116, 2008. URL https://doi.org/10.2514/1.38005.

[26] M.T. Semper, B.J. Pruski, and R.D.W. Bowersox. Freestream Turbulence Measurements in a Continuously Variable Hypersonic Wind Tunnel. Nashville, TN, 2012. AIAA Conference. AIAA Paper 2012-0732. URL https://doi.org/10.2514/6.2012-732.

[27] Chi Luong Nhat Mai. *Near-Region Modification of Total Pressure Fluctuations by a Normal Shock Wave in a Low-Density Hypersonic Wind Tunnel*. PhD dissertation, Texas A&M University, College Station, TX, 2014.

[28] Michael Thomas Semper. *Examining a Hypersonic Turbulent Boundary Layer at Low Reynolds Number*. PhD dissertation, Texas A&M University, College Station, TX, 2013.

[29] L. Brusniak and D.S. Dolling. Physics of unsteady blunt-fin-induced shock wave/turbulent boundary layer interactions. *Journal of Fluid Mechanics*, 273:375-409, 1994. URL https://doi.org/10.1017/S0022112094001989.

[30] D.R. Chapman, D.M. Kuehn, and H.K. Larson. Investigation of separated flows in supersonic and subsonic streams with emphasis on the effect of transition. NACA-TR-1356, 1958.

[31] D.M. Sykes. The supersonic and low-speed flows past circular cylinders of finite length supported at one end. *Journal of Fluid Mechanics*, 12(3):367-387, 1962. URL https://doi.org/10.1017/S0022112062000270.

[32] D. S. Dolling and S. M. Bogdonoff. Blunt fin-induced shock wave/turbulent boundary-layer interaction. *AIAA Journal*, 20(12):1674-1680, 1982. URL https://doi.org/10.2514/3.8003.

[33] B. E. Edney. Effects of shock impingement on the heat transfer around blunt bodies. *AIAA Journal*, 6(1):15-21, 1968. URL https://doi.org/10.2514/3.4435.

[34] L.G. Kaufman, R.H. Korkegi, and L.C. Morton. Shock impingement caused by boundary layer separation ahead of blunt fins. ARL-TR-72-0118, 1972.

[35] R. Sedney and C.W. Kitchens. The structure of three-dimensional separated flows in obstacle-boundary layer interaction. Brussels, Belgium: NATO. AGARD-CP-168, Paper No: 37, 1975.

[36] L.G. Kaufman, R.H. Korkegi, and L.C. Morton. Shock impingement caused by boundary-layer separation ahead of blunt fins. *AIAA Journal*, 11(10):1363-1364, 1973. URL https://doi.org/10.2514/3.50590.

[37] J.E. Robertson. Characteristics of the static and fluctuating pressure environments induced by three-dimensional protuberances at transonic Mach numbers. Wyle Lab. Res. Staff Rep. WR-69-3, 1969.

[38] F.T. Hung and J.M. Clauss. Three-dimensional protuberance interference heating in high speed flow. Pasadena, CA, 1980. AIAA Conference. AIAA Paper 80-0289. URL https://doi.org/10.2514/6.1980-289.

[39] D.S. Dolling and S.M. Bogdonoff. Experimental investigation of three-dimensional shock wave turbulent boundary layer interaction—an exploratory study of blunt fin induced flows," Princeton Univ. M.A.E. Rept. 1468, 1980.

[40] J.C. Westkaemper. Turbulent boundary-layer separation ahead of cylinders. *AIAA Journal*, 6(7):1352-1355, 1968. URL https://doi.org/10.2514/3.4747.

[41] L.M. Couch. Flow-field measurements downstream of two protuberances on a flat plate submerged in a turbulent boundary layer at Mach 2.49 and 4.44, NASA-TND-5297, 1969.

[42] P.B. Burbank, R.A. Newlander, and I.K. Collins. Heat transfer and pressure measurements on a flat-plate surface and heat-transfer measurements on attached protuberances in a supersonic turbulent boundary layer at Mach numbers of 2.65, 3.51, and 4.44. NASA-TN-D-1732, 1962.

[43] Bradley M. Wheaton. *Roughness-induced Instabilities in a Mach-6 Laminar Boundary Layer*. PhD dissertation, Purdue University, West Lafayette, IN, 2012.

[44] M.D. Bartkowicz, P.K. Subbareddy, and G.V. Candler. Numerical Simulations of Roughness Induced Instability in the Purdue Mach 6 Wind Tunnel. Chicago, IL, 2010. AIAA Conference. AIAA Paper 2010-4723. URL https://doi.org/10.2514/6.2010-4723.

[45] R.A. Gramann and D.S. Dolling. Unsteady separation in shock wave turbulent boundary layer interaction. Atlanta, GA, 1986. AIAA Conference. AIAA Paper 1986-1033. URL https://doi.org/10.2514/6.1986-1033.

[46] R.D. Hanly. Effects of Transducer Flushness on Fluctuating Surface Pressure Measurements. Hampton, VA, 1975. AIAA Conference. AIAA Paper 75-0534. URL https://doi.org/10.2514/6.1975-534.

[47] E.J. Lucas. Investigation of blunt fin-induced flow separation region on a flat plate at Mach numbers 2.5 to 4.0. AEDC-TR-70-265, 1971.

[48] G.S. Settles. *Schlieren and Shadowgraph Techniques: Visualizing Phenomena in Transparent Media*. Springer, New York, NY, 2001.

[49] F.E. Gowen and E.W. Perkins. Drag of circular cylinders for a wide range of Reynolds and Mach numbers. Nat. Adv. Committee Aero., NACA-RM-A52C20, 1952.

[50] M. Samimy and S.K. Lele. Motion of particles with inertia in a compressible free shear layer. *The Physics of Fluids*, 3(8):1915-1923, 1991. URL https://doi.org/10.1063/1.857921.

[51] M.H. Bloom and A. Pallone. Heat transfer to surfaces in the neighborhood of protuberances in hypersonic flow. WADC-TN-57-95, ASTIA-AD-118138, U.S. Air Force, 1957.

[52] P.B. Burbank and H.K. Strass. Heat transfer to surfaces and protuberances in a supersonic turbulent boundary layer. NACA-RM-L58E01a, 1958.

[53] T. E. Surber. Heat transfer in the vicinity of surface protuberances. *Journal of Spacecraft and Rockets*, 2(6):978-980, 1965. URL https://doi.org/10.2514/3.28330.

[54] R.W. Truitt. Hypersonic turbulent boundary layer interference heat transfer in vicinity of protuberances. *AIAA Journal*, 3(9):1754-1757, 1965. URL https://arc.aiaa.org/doi/10.2514/3.3241.

[55] L.G. Kaufman and L. Meckler. Pressure and heat transfer measurements at Mach 5 and 8 for a fin flat plate model. ASD-Tb-1 63-235, 1963.

[56] A.D. Ray and R.L. Palko. An investigation of the effects of shock impingement on a blunt leading edge. AEDC-TR-65-153, 1965.

[57] I.E. Beckwith. Experimental investigation of heat transfer and pressures on a swept cylinder in the vicinity of its intersection with a wedge and flat plate at Mach number 4.15 and high Reynolds numbers. NASA-TN-D-2020, 1964.

[58] D.M. Bushnell. Interference heating on a swept cylinder in the region of its intersection with a wedge at Mach number 8," NASA-TN-D-3094, 1965.

[59] E.A. Price and R.L. Stallings. Investigation of turbulent separated flows in the vicinity of fin-type protuberances at supersonic Mach numbers." NASA-TN-D-3804, 1967.

[60] D.M. Voitenko, A.I. Zubkov, and Y.A. Panov. Supersonic gas flow past a cylindrical obstacle on a plate. *Fluid Dynamics*, 1(1):84-88, 1966. URL https://doi.org/10.1007/BF01016276.

[61] D.M. Voitenko, A.I. Zubkov, and Y.A. Panov. Existence of supersonic zones in three-dimensional separation flows. *Fluid Dynamics*, 2(1):13-16, 1967. URL https://doi.org/10.1007/BF01024793.

[62] D.M. Voitenko, A.I. Zubkov, and Y.A. Panov. Supersonic gas flow past a cylindrical protuberance of a plate. JHU/APL Translation TG-230-T515, 1967.

[63] V.S. Avduevskii and K.I. Medvedev. Physical properties of the flow in the separation region for three-dimensional interaction of a boundary layer with a shock wave. *Fluid Dynamics*, 2(1):17-22, 1967. URL https://doi.org/10.1007/BF01024794.

[64] J.P. Thomas. Flow investigation about a fin plate model at a Mach number of 11.26. ARL-67-0188, 1967.

[65] P.S. Yip. Test report for phase 1 of the aerodynamic heating tests at the NACA Langley unitary plan wind tunnel. General Dynamics/Astronautics ZT-7-020-TN, 1958.

[66] R.A. Jones. Heat-transfer and pressure investigation of a fin-plate interference model at a Mach number of 6. NASA-TN D-2028, 1964.

[67] L. Siler and H. Deskins. Effect of shock impingement on the heat transfer and pressure distributions on a cylindrical leading edge model at Mach number 19. AEDC-TDR-64-228, 1964.

[68] E.A. Price, P.W. Howard, and R.L. Stallings. Heat-transfer measurements on a flat plate and attached fins at Mach numbers of 3.51 and 4.44. NASA-TN-D-2340, 1964.

[69] R.W. Halprin. Step induced boundary-layer separation phenomena. *AIAA Journal*, 3(2):357-359, 1965. URL https://doi.org/10.2514/3.2858.

[70] W. L. Francis. Experimental heat-transfer study of shock impingement on fins in hypersonic flow. *Journal of Spacecraft and Rockets*, 2(4):630-632, 1965. URL https://doi.org/10.2514/3.28253.

[71] E.F. Lucero. *Turbulent Boundary Layer Separation Induced by Three-Dimensional Protuberances on a Flat Plate*. M.S. thesis, University of Maryland, College Park, MD, 1966.

[72] W. Miller. Pressure distributions on single and tandem cylinders mounted on a flat plate in Mach number 5.0 flow. APL/JHU CR-25 (University of Texas DRL-538), 1966.

[73] R.S. Hiers and W.J. Loubsky. Effects of shock-wave impingement on the heat transfer on a cylindrical leading edge. NASA-TN-D-3859, 1967.

[74] J. Uselton. Fin shock/boundary-layer interaction tests on a flat plate with blunted fins at Minf = 3 and 5. AEDC-TR-67-113, 1967.

[75] D.G. Hall, J.A. Schetz, and P.J. Waltrup. Flowfield in the vicinity of cylindrical protuberances on a flat plate in supersonic flow. *Journal of Spacecraft and Rockets*, 5(1):127-128, 1968. URL https://doi.org/10.2514/3.29203.

[76] S. Dendrinos. Static and relative fluctuating pressure results of a wind tunnel investigation of subsonic and supersonic separated flow about cylindrical and Saturn V model protuberances. Wyle Laboratories WR-68-13, 1968.

[77] A.H. Whitehead. Flow field and drag characteristics of several boundary layer tripping elements in hypersonic flow. NASA-TN-D-5454, 1969.

[78] E.F. Lucero. Turbulent boundary layer separation induced by three dimensional protuberances. JHU/APL TG-1094, 1970.

[79] R.A. Newlander. Effect of shock impingement on the distribution of heat transfer coefficients on a right circular cylinder at Mach numbers of 2.65. 3.51, and 4.44. NASA-TN-D-642, 1961.

[80] T.E. Surber and R.B. Luning. Hypersonic heat flux and pressure measurements near a surface protuberance. North American Aviation NA-64-1194-1, 1965.

[81] D.M. Bushnell. Effects of shock impingement and other factors on leading-edge heat transfer. NASA-TN-D-4543, 1968.

[82] J.H. Mashburn. Turbulent boundary layer separation ahead of cylindrical protuberances in supersonic flow. ARL-TR-69-17, 1969.

[83] P.M. Danehy et al. High-speed PLIF imaging of hypersonic transition over discrete cylindrical roughness. Orlando, FL, 2010. AIAA Conference. AIAA Paper 2010-0703. URL https://doi.org/10.2514/6.2010-703.

[84] B.F. Bathel et al. Hypersonic laminar boundary layer velocimetry with discrete roughness on a flat plate. Chicago, IL, 2010. AIAA Conference. AIAA Paper 2010-4998. URL https://doi.org/10.2514/6.2010-4998.

[85] B.M. Wheaton and S.P. Schneider. Roughness-induced instability in a laminar boundary layer at Mach 6. Orlando, FL, 2010. AIAA Conference. AIAA Paper 2010-1574. URL https://doi.org/10.2514/6.2010-1574.

[86] F.L. Young, L.G. Kaufman, and R.H. Korkegi. Experimental investigation of interactions between blunt fin shock waves and adjacent boundary layers at Mach numbers 3 and 5. ARL-68-0214, 1968.

[87] R.H. Korkegi. Effect of transition on three-dimensional shock-wave/boundary-layer interaction. *AIAA Journal*, 10(3):361-363, 1972. URL https://doi.org/10.2514/3.50097.

[88] R. Sedney. Visualization of boundary layer flow patterns around protuberances using an optical-surf ace indicator technique. *The Physics of Fluids*, 15(12):2439-2441, 1972. URL https://doi.org/10.1063/1.1693890.

[89] R.S. Norman. *On Obstacle Generated Secondary Flows in Laminar Boundary Layers and Transition to Turbulence*. PhD dissertation, Illinois Institute of Technology, Chicago, IL, 1972.

[90] R. Sedney and C.W. Kitchens. Separation ahead of protuberances in supersonic turbulent boundary layers. *AIAA Journal*, 15(4):546-552, 1977. URL https://doi.org/10.2514/3.60658.

[91] C.J. Baker. The laminar horseshoe vortex. *Journal of Fluid Mechanics*. 95(2):347-367, 1979. URL https://doi.org/10.1017/S0022112079001506.

[92] C.J. Baker. The turbulent horseshoe vortex. *Journal of Wind Engineering and Industrial Aerodynamics*, 6(1-2):9-23, 1980. URL https://doi.org/10.1016/0167-6105(80)90018-5.

[93] A.E. Winkelmann. Flow visualization studies of a fin protuberance partially immersed in a turbulent boundary layer at Mach 5. NOL-TR-70-93, 1970.

[94] F.T. Hung and D.K. Patel. Protuberance interference heating in high-speed flow. Snowmass, CO, 1984. AIAA Conference. AIAA Paper 1984-1724. URL https://doi.org/10.2514/6.1984-1724.

[95] D.S. Dolling, C.D. Cosad, and S.M. Bogdonoff. Three-dimensional shock wave turbulent boundary layer interactions - a preliminary analysis of blunted fin-induced flows. Princeton University MAE Dept. Report 1354, 1977.

[96] D.S. Dolling, C.D. Cosad, and S.M. Bogdonoff. Three-dimensional shock wave turbulent boundary layer interactions - a parametric study of blunt fin-induced flows. Huntsville, AL, 1978. AIAA Conference. AIAA Paper 78-0159, 1978. URL https://doi.org/10.2514/6.1978-159.

[97] D.S. Dolling, C.D. Cosad, and S.M. Bogdonoff. An examination of blunt fin-induced shock wave turbulent boundary layer interactions. New Orleans, LA, 1979. AIAA Conference. AIAA Paper 79-0068, 1979. URL https://doi.org/10.2514/6.1979-68.

[98] D.S. Dolling and S.M. Bogdonoff. Experimental study of three-dimensional shock wave turbulent boundary layer interaction – scaling of sharp and blunt fin-induced flowfields. Princeton University MAE Dept. Report 1483, 1980.

[99] D.S. Dolling and S.M. Bogdonoff. Scaling of interactions of cylinders with supersonic turbulent boundary layers. *AIAA Journal*, 19(5):655-657, 1981. URL https://doi.org/10.2514/3.7805.

[100] D.S. Dolling and S.M. Bogdonoff. An experimental investigation of the unsteady behavior of blunt fin-induced shock wave turbulent boundary layer interactions. Palo Alto, CA, 1981. AIAA Conference. AIAA Paper 81-1287. URL https://doi.org/10.2514/6.1981-1287.

[101] D.S. Dolling. On upstream influence in shock wave turbulent boundary layer interaction. *The Aeronautical Journal*, 87(868):324-327, 1983. URL https://doi.org/10.1017/S0001924000051083.

[102] O. Ozcan and M. Holt. Supersonic separated flow past a cylindrical obstacle on a flat plate. *AIAA Journal*, 22(5):611-617, 1984. URL https://doi.org/10.2514/3.48492.

[103] O. Ozcan and B.K. Yuceil. Cylinder-induced shock-wave boundary-layer interaction. *AIAA Journal*, 30(4):1130-1132, 1992. URL https://doi.org/10.2514/3.11039.

[104] J.E. Robertson. Predictions of in-flight fluctuating pressure environments including protuberance induced flow. Wyle Laboratories WR-71-3, 1971.

[105] N.R. Fomison and J.L. Stollery. The effects of sweep and bluntness on glancing shock wave turbulent boundary layer interaction. AGARD Conference Proceedings, AGARD 428, Bristol, UK, 1987.

[106] D.S. Dolling and L. Brusniak. Separation shock motion in fin, cylinder, and compression ramp-induced turbulent interactions. *AIAA Journal*, 27(6):734-742, 1989. URL https://doi.org/10.2514/3.10173.

[107] H.A. Baade. Time series analysis of shock induced pressure fluctuations in supersonic interactive flow. Reno, NV, 1988. AIAA Conference. AIAA Paper 88-0176. URL https://doi.org/10.2514/6.1988-176.

[108] A.S.W. Thomas. The unsteady characteristics of laminar juncture flow. *The Physics of Fluids*, 30(2):283-285, 1987. URL https://doi.org/10.1063/1.866374.

[109] D.S. Dolling and D.R. Smith. Separation shock dynamics in Mach 5 turbulent interactions induced by cylinders. *AIAA Journal*, 27(12):1698-1706, 1989. URL https://doi.org/10.2514/3.10323.

[110] D.S. Dolling and L. Brusniak. Correlation of separation shock motion in a cylinder-induced, Mach 5, turbulent interaction with pressure fluctuations in the separated flow. Reno, NV, 1991. AIAA Conference. AIAA Paper 91-0650. URL https://doi.org/10.2514/6.1991-650.

[111] Ö.H. Ünalmis and D.S. Dolling. Experimental study of causes of unsteadiness of shock-induced turbulent separation. *AIAA Journal*, 36(3):371-378, 1998. URL https://doi.org/10.2514/2.373.

[112] J.C. Gonsalez and D.S. Dolling. Correlation of interaction sweepback effects on unsteady shock-induced turbulent separation. Reno, NV, 1993. AIAA Conference. AIAA Paper 93-0776. URL https://doi.org/10.2514/6.1993-776.

[113] D.S. Dolling and P.E. Rodi. Upstream influence and separation scales in fin-induced shock turbulent boundary layer interaction. *Journal of Spacecraft and Rockets*, 25(2):102-108, 1988. URL https://doi.org/10.2514/3.25957.

[114] S. Hussain. *A Study of the Interaction between a Glancing Shock Wave and a Turbulent Boundary Layer - The Effects of Leading Edge Bluntness and Sweep*. PhD dissertation, Cranfield Institute of Technology, England, 1985.

[115] K. Kleifges and D.S. Dolling. Control of unsteady shock-induced turbulent boundary layer separation upstream of blunt fins. Orlando, FL, 1993. AIAA Conference. AIAA Paper 93-3281. URL https://doi.org/10.2514/6.1993-3281.

[116] K. Kleifges and D.S. Dolling. Leading-edge sweepback and shape effects on fin-induced fluctuating pressures. *Journal of Spacecraft and Rockets*, 32(2):286-293, 1995. URL https://doi.org/10.2514/3.26608.

[117] D.R. Smith, J. Poggie, W. Konrad, and A.J. Smits. Visualization of the structure of shock wave turbulent boundary layer interactions using Rayleigh scattering. Reno, NV, 1991. AIAA Conference. AIAA Paper 91-0651. URL https://doi.org/10.2514/6.1991-651.

[118] T. Evans, K. Poddar, and A.J. Smits. Compilation of wall pressure data for a shock wave boundary layer interaction generated by a blunt fin. MAE Report 1908 T, Department of Mechanical and Aero-space Engineering, Princeton University, 1990.

[119] J. Poggie and A.J. Smits. Wavelet analysis of wall-pressure fluctuations in a supersonic blunt-fin flow. *AIAA Journal*, 35(10):1597-1603, 1997. URL https://doi.org/10.2514/2.18.

[120] J. Poggie and A.J. Smits. Experimental evidence for Plotkin model of shock unsteadiness in separated flow. Physics of Fluids, 17(1):018107, 2005. URL https://doi.org/10.1063/1.1833405.

[121] S. Aso, A. Tan, and M. Hayashi. The structure of aerodynamic heating in three-dimensional shock wave turbulent boundary layer interactions induced by sharp and blunt fins. Buffalo, NY, 1989. AIAA Conference. AIAA Paper 89-1854. URL https://doi.org/10.2514/6.1989-1854.

[122] S. Aso, S. Kuranaga and S. Nakao. Aerodynamic heating phenomena in three dimensional shock wave/turbulent boundary layer interactions induced by sweptback blunt fins. Reno, NV, 1990. AIAA Conference. AIAA Paper 90-0381. URL https://doi.org/10.2514/6.1990-381.

[123] S. Aso, S. Kuranaga, and M. Hayashi. Detailed measurements on unsteady properties in three-dimensional shock wave/turbulent boundary layer interaction induced by blunt fin at Mach number 4.

Honolulu, HI, 1991. AIAA Conference. AIAA Paper 91-1755. URL https://doi.org/10.2514/6.1991-1755.

[124] H. Itoh and M. Mizoguchi. Experiments on unsteadiness associated with cylinder-induced shock-laminar boundary layer interaction in hypersonic flow. Washington, DC, 2016. AIAA Conference. AIAA Paper 2016-3648. URL https://doi.org/10.2514/6.2016-3648.

[125] H. Ozawa and S.J. Laurence. Experimental investigation of the shock-induced flow over a wall-mounted cylinder. *Journal of Fluid Mechanics*, 849:1009-1042, 2018. URL https://doi.org/10.1017/jfm.2018.433.

[126] W. Shifen and L. Qingquan. Hypersonic turbulent separated flow past an unswept circular cylinder on a flat plate. *Acta Aerodynamica Sinica*, 10(1):38-44, 1992.

[127] M.S. Yu, J. Song, J.C. Bae, and H.H. Cho. Heat transfer by shock-wave/boundary layer interaction on a flat surface with a mounted cylinder. *International Journal of Heat and Mass Transfer*, 55(5-6):1764-1772, 2012. URL https://doi.org/10.1016/j.ijheatmasstransfer.2011.11.033.

[128] P.H. Schuricht and G.T. Roberts. Hypersonic interference heating induced by a blunt fin. Norfolk, VA, 1998. AIAA Conference. AIAA Paper 98-1579. URL https://doi.org/10.2514/6.1998-1579.

[129] O.R. Tutty, G.T. Roberts, and P.H. Schuricht. High-speed laminar flow past a fin–body junction. *Journal of Fluid Mechanics*, 737:19-55, 2013. URL https://doi.org/10.1017/jfm.2013.541.

[130] Z. Haq, G.T. Roberts, and R.A. East. Interference heating near fin/body junctions on hypersonic vehicles. Proceedings of the First European Symposium on Aerothermodynamics for Space Vehicles, European Space Agency SP-318, 1991, pp. 171-176.

[131] C. Raju and P.R. Viswanath. Application of PSP to the study of 3D shock-boundary layer interaction. Sendai, Japan, 2005. ICIASF 21st International Congress, 197-201. URL https://doi.org/10.1109/ICIASF.2005.1569923.

[132] A.F.P. Houwing, D.R. Smith, J.S. Fox, P.M. Danehy, and N.R. Mudford. Laminar boundary layer separation at a fin-body junction in a hypersonic flow. *Shock Waves*, 11(1):31-42, 2001. URL https://doi.org/10.1007/PL00004055.

[133] J.S. Fox, S. O'Byrne, A.F.P. Houwing, A. Papinniemi, P.M. Danehy, and N.R. Mudford. Fluorescence visualization of hypersonic flow establishment over a blunt fin. AIAA Journal, 39(7):1329-1337, 2001. URL https://doi.org/10.2514/2.1451.

[134] J.D. Gray. A correlation of axisymmetric laminar flow separation characteristics. Washington, DC, 1964. AIAA Conference. AIAA Paper 64-0475. URL https://doi.org/10.2514/6.1964-475.

[135] D.A. Needham and J.L. Stollery. Boundary layer separation in hypersonic flow. New York, NY, 1966. AIAA Conference. AIAA Paper 66-0455. URL https://doi.org/10.2514/6.1966-455.

[136] T. Kubota, L. Lees, and J. Lewis. Experimental investigation of supersonic laminar, two-dimensional boundary-layer separation in a compression corner with and without cooling. New York, NY, 1967. AIAA Conference. AIAA Paper 67-0191. URL https://doi.org/10.2514/6.1967-191.

[137] F.T. Hung and D.O. Barnett. Shockwave-boundary layer interference heating analysis. Washington, DC, 1973. AIAA Conference. AIAA Paper 73-0237. URL https://doi.org/10.2514/6.1973-237.

[138] K.S. Heffnert, A. Chpoun, and J.C. Lengrand. Experimental study of transitional axisymmetric shock-boundary layer interactions at Mach 5. Orlando, FL, 1993. AIAA Conference. AIAA Paper 93-3131. URL https://doi.org/10.2514/6.1993-3131.

[139] L. Vandomme, B. Chanetz, R. Benay, and J. Perraud. Transitional shock wave boundary layer interactions in hypersonic flow at Mach 5. Norfolk, VA, 2003. AIAA Conference. AIAA Paper 2003-6966. URL https://doi.org/10.2514/6.2003-6966.

[140] R. Benay, B.Chanetz, B. Mangin, L. Vandomme, and J. Perraud. Shock wave/transitional boundary-layer interactions in hypersonic flow. *AIAA Journal*, 44(6):1243-1254, 2006. URL https://doi.org/10.2514/1.10512.

[141] R. Bur and B. Chanetz. Experimental study on the PRE-X vehicle focusing on the transitional shock-wave/boundary-layer interactions. *Aerospace Science and Technology*, 13(7):393-401, 2009. URL https://doi.org/10.1016/j.ast.2009.09.002.

[142] D. Knight and M. Mortazavi. Hypersonic shock wave transitional boundary layer interactions - a review. *Acta Astronautica*. 151:296-317. URL https://doi.org/10.1016/j.actaastro.2018.06.019.

[143] J.M.A. Longo. Aerothermodynamics - a critical review at DLR. *Aerospace Science and Technology*, 7(6):429-438, 2003. URL https://doi.org/10.1016/S1270-9638(03)00036-1.

[144] S. Willems and A. Gülhan. Experiments on shock induced laminar-turbulent transition on a flat plate at Mach 6. EUCASS Conference, 2013.

[145] S. Willems, A. Gülhan, and J. Steelant. Experiments on the effect of laminar-turbulent transition on the SWBLI in H2K at Mach 6. *Experiments in Fluids*, 56:49, 2015. URL https://doi.org/10.1007/s00348-015-1904-z.

[146] E. Schülein. Effect of laminar-turbulent transition on the shock-wave/boundary-layer interaction. Atlanta, GA, 2014. AIAA Conference. AIAA-Paper 2014-3332. URL https://doi.org/10.2514/6.2014-3332.

[147] N.D. Sandham, E. Schülein, A. Wagner, S. Willems, and J. Steelant. Transitional shock-wave/boundary-layer interactions in hypersonic flow. *Journal of Fluid Mechanics*, 752:349-382, 2014. URL https://doi.org/10.1017/jfm.2014.333.

[148] E. Erdem, K. Kontis, E. Johnstone, N.P. Murray, and J. Steelant. Experiments on transitional shock wave – boundary layer interactions at Mach 5. *Experiments in Fluids*, 54:1598, 2013. URL https://doi.org/10.1007/s00348-013-1598-z.

[149] D. Estruch-Samper, B. Ganapathisubramani, L. Vanstone, and R. Hillier. Axisymmetric flare-induced separation of high-speed transitional boundary layers. Nashville, TN, 2012. AIAA Conference. AIAA-Paper 2012-0067. URL https://doi.org/10.2514/6.2012-67.

[150] D. Estruch-Samper, L. Vanstone, B. Ganapathisubramani, and R. Hillier. Effect of roughness-induced disturbances on an axisymmetric hypersonic laminar boundary layer. Grapevine, TX, 2013. AIAA Conference. AIAA Paper 2013-0083. URL https://doi.org/10.2514/6.2013-83.

[151] L. Vanstone, D. Estruch-Samper, R. Hillier, and B. Ganapathisubramani. Shock-induced separation of transitional hypersonic boundary layers. San Diego, CA, 2013. AIAA Conference. AIAA Paper 2013-2736. URL https://doi.org/10.2514/6.2013-2736.

[152] J.B. Edelman, B.C. Chynoweth, G.R. McKiernan, C.J. Sweeney, and S.P. Schneider. Instability measurements in the Boeing/AFOSR Mach-6 quiet tunnel. Washington, DC, 2016. AIAA Conference. AIAA Paper 2016-3343. URL https://doi.org/10.2514/6.2016-3343.

[153] K.A. Gray, B.C. Chynoweth, J.B. Edelman, G.R. McKiernan, M.P. Wason, and S.P. Schneider. Boundary-layer transition measurements in the Boeing/AFOSR Mach-6 quiet tunnel. Grapevine, TX, 2017. AIAA Conference. AIAA Paper 2017-0068. URL https://doi.org/10.2514/6.2017-0068.

[154] B.C. Chynoweth, J.B. Edelman, K.A. Gray, G.R. McKiernan, and S.P. Schneider. Measurements in the Boeing/AFOSR Mach-6 quiet tunnel on hypersonic boundary-layer transition. Denver, CO, 2017. AIAA Conference. AIAA Paper 2017-3632. URL https://doi.org/10.2514/6.2017-3632.

[155] A. Wagner, J.M. Schramm, K. Hannemann, R. Whitside, and J.P. Hickey. Hypersonic shock wave boundary layer interaction studies on a flat plate at elevated surface temperature. *Shock Wave Interactions*, 231-243. Springer, 2017.

[156] Egbert S. Hood. *Exploratory Experimental Study of Shock Wave/Transitional Boundary Layer Interactions*. Master's thesis, University of Texas at Austin, 2003.

[157] Z.R. Murphree, J. Jagodzinski, E.S. Hood, N.T. Clemens, and D.S. Dolling. Experimental studies of transitional boundary layer shock wave interactions. Reno, NV, 2006. AIAA Conference. AIAA Paper 2006-0326. URL https://doi.org/10.2514/6.2006-326.

[158] Z.R. Murphree, K.B. Yuceil, N.T. Clemens, and D.S. Dolling. Experimental studies of transitional boundary layer shock wave interactions. Reno, NV, 2007. AIAA Conference. AIAA Paper 2007-1139. URL https://doi.org/10.2514/6.2007-1139.

[159] Zachary Ryan Murphree. *Physics of Unsteady Cylinder-Induced Transitional Shock Wave Boundary Layer Interactions*. PhD dissertation, University of Texas at Austin, 2009.

[160] E.L. Lash, C.S. Combs, J.D. Schmisseur, P.A. Kreth, and E.A. Beckman. Developing an image-based analysis of the dynamics of transitional shock wave–boundary layer interactions. Washington, DC, 2016. AIAA Conference. AIAA Paper 2016-4320. URL https://doi.org/10.2514/6.2016-4320.

[161] C.S. Combs, P.A. Kreth, J.D. Schmisseur, and E.L. Lash. Image-based analysis of shock-wave/boundary-layer interaction unsteadiness. *AIAA Journal*, 56(3):1288-1293, 2018. URL https://doi.org/10.2514/1.J056390.

[162] E.L. Lash, C.S. Combs, P.A. Kreth, and J.D. Schmisseur. Experimental investigation of a cylinder-induced transitional shock wave–boundary layer interaction. Grapevine, TX, 2017. AIAA Conference. AIAA Paper 2017-0760. URL https://doi.org/10.2514/6.2017-0760.

[163] C.S. Combs, E.L. Lash, and J.D. Schmisseur. Investigation of a cylinder-induced transitional shock wave–boundary layer interaction using laser diagnostics. Washington, DC, 2016. AIAA Conference. AIAA Paper 2016-4321. URL https://doi.org/10.2514/6.2016-4321.

[164] E.L. Lash, C.S. Combs, P.A. Kreth, and J.D. Schmisseur. Study of the Dynamics of Transitional Shock Wave-Boundary Layer Interactions using Optical Diagnostics. Denver, CO, 2017. AIAA Conference. AIAA Paper 2017-3123. URL https://doi.org/10.2514/6.2017-3123.

[165] C.S. Combs, S.A. Lindörfer, P.A. Kreth, and J.D. Schmisseur. The role of boundary-layer thickness on cylinder-generated shock-wave/turbulent boundary-layer interactions, part II: experiments. Kissimmee, FL, 2018. AIAA Conference. AIAA Paper 2018-0824. URL https://doi.org/10.2514/6.2018-0824.

[166] S.A. Lindörfer, C.S. Combs, R.B. Bond, and J.D. Schmisseur. The tole of boundary-layer thickness on cylinder-generated shock-wave/turbulent boundary-layer interactions, part I: computations. Kissimmee, FL, 2018. AIAA Conference. AIAA Paper 2018-0380. URL https://doi.org/10.2514/6.2018-0380.

[167] M.T. Semper and R.D.W. Bowersox. Tripping of a hypersonic low-Reynolds-number boundary layer. *AIAA Journal*, 55(3):808-817, 2017. URL https://doi.org/10.2514/1.J055341.

[168] A.N. Leidy, E. Reshotko, F. Siddiqui, and R.D.W. Bowersox. Transition due to roughness on blunt capsule: comparison with transient growth correlation. *Journal of Spacecraft and Rockets*, 55(1):167-180, 2018. URL https://doi.org/10.2514/1.A33625.

[169] I.T. Neel, A.N. Leidy, N.R. Tichenor, and R.D. Bowersox. Influence of environmental disturbances on hypersonic crossflow instability on the HIFiRE-5 elliptic cone. Kissimmee, FL, 2018. AIAA Conference. AIAA Paper 2018-1821. URL https://doi.org/10.2514/6.2018-1821.

[170] M.T. Semper, N.R. Tichenor, R.D.W. Bowersox, R. Srinivasan, and S.W. North. On the design and calibration of an actively controlled expansion hypersonic wind tunnel. Orlando, FL, 2009. AIAA Conference. AIAA Paper 2009-0799. URL https://doi.org/10.2514/6.2009-799.

[171] N.R. Tichenor, M.T. Semper, R.D.W. Bowersox, R. Srinivasan, and S.W. North. Calibration of an actively controlled expansion hypersonic wind tunnel. Chicago, IL, 2010. AIAA Conference. AIAA Paper 2010-4793. URL https://doi.org/10.2514/6.2010-4793.

[172] Nathan Ryan Tichenor. *Characterization of the Influence of a Favorable Pressure Gradient on the Basic Structure of a Mach 5.0 High Reynolds Number Supersonic Turbulent Boundary Layer*. PhD dissertation, Texas A&M University, College Station, TX, 2010.

[173] R.E. Hanson, H.P. Buckley, and P. Lavoie. Aerodynamic optimization of the flat-plate leading edge for experimental studies of laminar and transitional boundary layers. *Experiments in Fluids*, 53(4):863-871, 2012. URL https://doi.org/10.1007/s00348-012-1324-2.

[174] W.S. Saric, H.L. Reed, and E.J. Kerschen. Boundary-layer receptivity to freestream disturbances. *Annual Review of Fluid Mechanics*, 34:291-319, 2002. URL https://doi.org/10.1146/annurev.fluid.34.082701.161921.

[175] A.N. Leidy, I.T. Neel, R.D.W. Bowersox, and J.D. Schmisseur. Influence of perturbations on 3-D hypersonic shock / laminar boundary interactions. Grapevine, TX, 2017. AIAA Conference. AIAA Paper 2017-1685. URL https://doi.org/10.2514/6.2017-1685.

[176] E. Reshotko and A. Tumin. Role of transient growth in roughness-induced transition. *AIAA Journal*, 42(4):766-770, 2004. URL https://doi.org/10.2514/1.9558.

[177] H. Schlichting. *Boundary-Layer Theory*. McGraw Hill, New York, NY, USA, 1979.

[178] L.V. King. On the convection of heat from small cylinders in a stream of fluid. *Philosophical Transactions of the Royal Society*, A 214:373, 1914.

[179] M.A. Kegerise, M. Sheplak, and E.F. Spina. Calibration of a constant-temperature hot-wire anemometer in a Mach 6 air flow. Technical Report MAME-95-402, Syracuse University Center for Hypersonics, Department of Mechanical and Aerospace Engineering, Syracuse University, Syracuse, New York, 1995.

[180] A. Chou, A.N. Leidy, R.A. King, B.F. Bathel, and G. Herring. Measurements of freestream fluctuations in the NASA Langley 20-inch Mach 6 tunnel. Atlanta, GA, 2018. AIAA Conference. AIAA Paper 2018-3073. URL https://doi.org/10.2514/6.2018-3073.

[181] S. Beresh, J. Henfling, R. Spillers, and B. Pruett. Fluctuating wall pressures measured beneath a supersonic turbulent boundary layer," Physics of Fluids, 23(7):075110, 2011. URL https://doi.org/10.1063/1.3609271.

[182] B.K. Crawford, G.T. Duncan, D.E. West, and W.S. Saric. Laminar-turbulent boundary layer transition imaging using IR thermography. *Optics and Photonics Journal*, 3(3):233-239, 2013. URL http://dx.doi.org/10.4236/opj.2013.33038.

[183] Salvatore Cerasuolo. *Heat Flux Measurements by Infrared Thermography in the Boeing/AFOSR Mach 6 Quiet Tunnel*. M.S. thesis, University of Naples Federico II, 2016.

[184] C. Running, M. Thompson, T. Juliano, and H. Sakaue. Boundary-layer separation detection for a cone at high angle of attack in Mach 4.5 flow with pressure-sensitive paint. Denver, CO, 2017. AIAA Conference. AIAA Paper 2017-3120. URL https://doi.org/10.2514/6.2017-3120.

[185] I.T. Neel, A.N. Leidy, and R.D.W. Bowersox. Preliminary study of the effect of environmental disturbances on hypersonic crossflow instability on the HIFiRE-5 elliptic cone. Grapevine, TX, 2017. AIAA Conference. AIAA Paper 2017-0767. URL https://doi.org/10.2514/6.2017-0767.

[186] T.J. Juliano, M.P. Borg, and S.P. Schneider. Quiet tunnel measurements of HIFiRE-5 boundary-layer transition. *AIAA Journal*, 53(4):832-846, 2015. URL https://doi.org/10.2514/1.J053189.

[187] M.P. Borg, R.L. Kimmel, and S. Stanfield. Traveling crossflow instability for the HIFiRE-5 elliptic cone. *Journal of Spacecraft and Rockets*, 52(3):664-673, 2015. URL https://doi.org/10.2514/1.A33145.

[188] R.O. Duda and P.E. Hart. Use of the Hough transformation to detect lines and curves in pictures. *Communications of the Association for Computing Machinery*, 15(1):11-15, 1972.

[189] Jerrod W. Hofferth. *Boundary-Layer Stability and Transition on a Flared Cone in a Mach 6 Quiet Wind Tunnel*. PhD dissertation, Texas A&M University, College Station, TX, 2013.

[190] L.M. Weinstein. Large-field high-brightness focusing schlieren system. *AIAA Journal*, 31(7):1250–1255, 1993. URL https://doi.org/10.2514/3.11760.

[191] E.L. Clark. Error Propagation equations for estimating the uncertainty in high-speed wind tunnel test results. SAND-93-0208C, 1993. URL https://www.osti.gov/servlets/purl/10162072.

[192] C.L.N Mai and R.D.W Bowersox. Effect of a normal shock wave on freestream total pressure fluctuations in a low-density Mach 6 flow. Atlanta, GA, 2014. AIAA Conference. AIAA Paper 2014-2641. URL https://doi.org/10.2514/6.2014-2641.

[193] A.N. Leidy, I.T. Neel, N.R. Tichenor, R.D.W. Bowersox, and J.D. Schmisseur. High-speed schlieren imaging and hot-wire characterization of cylinder-induced hypersonic shock boundary layer interactions. Atlanta, GA, 2018. AIAA Conference. AIAA Paper 2018-3703. URL https://doi.org/10.2514/6.2018-3703.

[194] A.N. Leidy, I.T. Neel, N.R. Tichenor, R.D.W. Bowersox, and J.D. Schmisseur. Cylinder-induced hypersonic transitional shock wave boundary layer interactions: pressure fluctuations and thermal loading. Orlando, FL, 2018. AIAA Conference. AIAA Paper AIAA 2018-5374. URL https://doi.org/10.2514/6.2018-5374.

[195] A.E. Winkelmann. Experimental investigations of a fin protuberance partially immersed in a turbulent boundary layer at Mach 5. NOLTR 72-33, 1972.

[196] J.W. Keyes and F.D. Hains. Analytical and experimental studies of shock interference heating in hypersonic flows. NASA TN D-7139, 1973.

[197] Oktay Özcan. An Experimental Investigation of Three Dimensional Boundary-Layer Separation in Supersonic Flow Past a Circular Cylinder on a Flat Plate. PhD. dissertation, University of California at Berkeley, 1982.

[198] N. Saida and H. Hattori. Shock wave-turbulent boundary layer interactions induced by a blunt fin. Transactions of the Japan Society for Aeronautical and Space Sciences, 27:67-77, 1984.

[199] N. Saida. Separation ahead of blunt fins in supersonic turbulent boundary layers. IUTAM Symposium, Palaiseau, France, 1985.

[200] D.S. Dolling and J.C. Narlo. Driving mechanisms of unsteady separation shock motion in hypersonic interaction flow. Proceedings of the Agard Conference on Aerodynamics of Hypersonic Lifting Vehicles, Agard 428, 1987.

[201] D.S. Dolling and D.R. Smith. Unsteady shock-induced turbulent separation in Mach 5 cylinder interactions. Reno, NV, 1988. AIAA Conference. AIAA Paper 88-0305. URL https://doi.org/10.2514/6.1988-305.

[202] S. Johnson and K. Murphy. Pressure-sensing performance of upright cylinders in a Mach 10 boundary-layer. NASA Technical Memorandum 4633, 1994.

[203] D. Barberis and P. Molton. Shock wave - turbulent boundary layer interaction in a three dimensional flow. Reno, NV, 1995. AIAA Conference. AIAA Paper 95-0227. URL https://doi.org/10.2514/6.1995-227.

[204] S.B. Verma and V. Gupta. Supersonic separation with obstructions. AIAA Journal, 34(4):849-851, 1995. URL https://doi.org/10.2514/3.13151.

[205] P.J. Barnhart and I. Greber. Experimental investigation of unsteady shock wave turbulent boundary layer interactions about a blunt fin. NASA Contractor Report 202334, 1997.

[206] D.S. Dolling, N.C. Clemens, and E.S. Hood. Exploratory experimental study of transitional shock wave boundary layer interactions. AFRL-SR-AR-TR-03-0046. Austin, TX, 2003.

[207] R. Mukund, P.R. Viswanath, A. Prabhu, and B. Vasudevan. Study of glancing and blunt fin shock-boundary layer interactions at low supersonic Mach numbers. Project document PD-EA-0316, National Aerospace Laboratories, Bangalore, India, 2003.

[208] Y.X. Hou, Ö.H. Ünalmis, P.C. Bueno, N.T. Clemens, and D.S. Dolling. Role of upstream boundary layer velocity fluctuations on unsteadiness of Mach 5 blunt-fin interactions. Technical Note submitted to AIAA Journal, May 10, 2004.

[209] P.C. Bueno, B. Ganapathisubramani, N.T. Clemens, and D.S. Dolling. Cinematographic planar imaging of a Mach 2 shock wave / turbulent boundary layer interaction. Reno, NV, 2005. AIAA Conference. AIAA Paper 2005-0441. URL https://doi.org/10.2514/6.2005-441.

[210] P.C. Bueno, J.L. Wagner, J.A. Searcy, B. Ganapathisubramani, N.T. Clemens, and D.S. Dolling. Experiments in unsteady forcing of Mach 2 shock wave/boundary layer interactions. Reno, NV, 2006. AIAA Conference. AIAA Paper 2006-0878. URL https://doi.org/10.2514/6.2006-878.

[211] K. Kontis, C. Lada, and H. Zare-Behtash. Effect of dimples on glancing shock wave turbulent boundary layer interactions. Shock Waves, 17(5):323-335, 2008. URL https://doi.org/10.1007/s00193-007-0114-x.

[212] D.P. Wang, Y.X. Zhao, Z.X. Xia, Q.H. Wang, and Z.B. Luo. Flow visualization of supersonic flow over a finite cylinder. Chinese Physics Letters, 29(8):084702-(1-4), 2012. URL https://doi.org/10.1088/0256-307X/29/8/084702.

[213] C.S. Kumar and K.P.J. Reddy. Hypersonic interference heating on flat plate with short three-dimensional protuberances. AIAA Journal, 52(4):747-756, 2014. URL https://doi.org/10.2514/1.J052658.

[214] E.J. Stephen, S.P. Morell, R. Decker, D.K. Hope, and T. McLaughlin. Flow interactions of small cylindrical protuberances and the supersonic turbulent boundary layer on a flat plate. National Harbor, Maryland, 2014. AIAA Conference. AIAA Paper 2014-0435. URL https://doi.org/10.2514/6.2014-0435.

[215] P.C. Quan, S.H. Yi, Y. Wu, Y.Z. Zhu, and L. He. Experimental investigation on the effects of swept angles on blunt fin-induced flow. AIAA Journal, 53(9):2805-2810, 2015. URL https://doi.org/10.2514/1.J053988.

[216] F. Avallone, D. Ragni, F.F.J. Schrijer, F. Scarano. G. Cardone. PIV-based study of a cylindrical roughness element in a hypersonic laminar boundary layer. Santa Barbara, California, 2015. In: 11th international symposium particle image velocimetry PIV.

[217] B.E. Rice, J.A. McKenzie, S.J. Peltier, C.S. Combs, C. Clifford, and B. Thurow. Comparison of 4-camera tomographic PIV and single-camera plenoptic PIV. Kissimmee, Florida, 2018. AIAA Conference. AIAA Paper 2018-2036. URL https://doi.org/10.2514/6.2018-2036.

[218] A. Pope and K.L. Goin. *High-Speed Wind Tunnel Testing*. Krieger Publishing, Malabar, FL., 1965.

[219] R. Sánchez-González, R. Srinivasan, R.D.W. Bowersox, and S.W. North. Simultaneous velocity and temperature measurements in gaseous flow fields using the VENOM technique. *Optics Letters*, 36(2):196-198, 2011. URL https://doi.org/10.1364/OL.36.000196.

[220] Ian T. Neel. *Influence of Environmental Disturbances on Hypersonic Crossflow Instability on the HIFiRE-5 Elliptic Cone*. PhD dissertation, Texas A&M University, College Station, TX, 2019.

APPENDIX A

CYLINDER (OR BLUNT FIN) -INDUCED SBLI EXPERIMENTS

Ref.	Authors	Year	Location (Affiliation)	Mach	Shock Gen.[1]	Reynolds (M/m)	BL state[2]	Diagnostics[3]
[49]	F.E. Gowen & E.W. Perkins	1952	NACA Ames	1.49, 1.98, 2.9	C	5.1 to 51.2	T	OF, P(cylinder), S(top down)
[51]	M.H. Bloom & A. Pallone	1957	Wright Patterson	6	C		T	TCs(model)
[65]	P.S. Yip	1958	NACA Langley	2.65,3.51	C		T	TCs(model)
[52]	P.B. Burbank & H.K. Strass	1958	NACA Langley	2.65,3.51	C	4.4 to 77	T	TCs(model&cylinder)
[31]	D.M. Sykes	1962	Univ. of Manchester	1.96	C	13.4	T	P(cylinder), S
[42]	P. B Burbank et al.	1962	NASA Langley	2.65,3.51,4.44	C	4.3 to 15.4	T	OF, P&TCs(model), Pitot(BL rake)
[55]	L.G. Kaufman & L. Meckler	1963	Wright Patterson (Grumman)	5,8	F			P&TCs(model)
[57]	I.E. Beckwith	1964	NASA Langley	4.15	C	56.7 to 142	T	P&TCs(model), S
[66]	R.A. Jones	1964	NASA Ames	6	C	2.36 to 28.7	L&T	TCs(model)
[67]	L. Siler & H. Deskins	1964	AEDC	19	C	0.94	L	P&TCs(cylinder)
[68]	E.A. Price et al.	1964	NASA Langley	3.51,4.44	F	8.2 to 13.8	T	TCs(model)
[80]	T.E. Surber & R.B. Luning	1965	North American Aviation, Inc.	12 to 21	C		L	P&TCs(model)
[58]	D.M. Bushnell	1965	NASA Langley	8	C	3.0-34	L&T	P&TCs(cylinder)
[56]	A.D. Ray & R.L. Palko	1965	AEDC	6,8,10	F	1.9-11.6	L	OF, P(Wiancko)&TCs(fin), Sh
[69]	R.W. Halprin	1965	UCLA (Douglas Aircraft Company, Inc.)	2.71	C		T	OF, P(model), S
[70]	W.L. Francis	1965	JPL (Ford)	9	F	0.59 to 3.7	L	P&TCs(fin)
[71]	E.F. Lucero	1966	APL (Johns Hopkins Univ.)	2.17	C		T	OF

[72]	W. Miller	1966	Univ. of Texas	4.88	C		T	P(cylinder), S
[60]	D.M. Voitenko et al.	1966	Moscow	2.5	C	132	T	OF, P(model&cylinder), S
[61]	D.M. Voitenko et al.	1967	Moscow	3.11	C	134	T	P(model&cylinder), Pitot(sep. region)
[63]	V.S. Avduevskii & K.I. Medvedev	1967	Moscow	2-6	C		L&T	OF, Pitot, S, Sh
[73]	R.S. Hiers & W.J. Loubsky	1967	NASA Ames	14	F	0.63	L	OF, TCs(fin), S
[59]	E.A. Price & R.L. Stallings	1967	NASA Langley	2.3-4.44	F	4.9-14.7	T	OF, P(model), Sh
[74]	J. Uselton	1967	AEDC	3,5	F			P(model)
[64]	J.P. Thomas	1967	Wright Patterson (Ohio St. Univ.)	11.26	F	2	L	P(model)
[75]	D.G. Hall et al.	1968	APL (Univ. of Maryland)	2.2	C	9.8	T	P(model), S
[86]	F.L. Young et al.	1968	Wright Patterson	3 and 5	F	1.77 to 4.65	**X**,T	OF, P(model), Pitot, Sh
[76]	S. Dendrinos	1968	NASA Marshall (Wyle Labs)	1.15,1.96	C	21, 24	T	OF, P(model), S
[40]	J.C. Westkaemper	1968	Univ. of Texas	4.9	C	37.8	T	OF, S
[82]	J.H. Mashburn	1969	Univ. of Texas	4.8	C	42.3	T	P(model)
[41]	L.M. Couch	1969	NASA Langley	2.49, 4.44	C	4.9,9.8	T	Wake: P(model), Pitot, total T
[77]	A.H. Whitehead	1969	NASA Langley	6.8	C	2 to 15	L	OF, P(cylinder)
[37]	J.E. Robertson	1969	AEDC (Wyle Labs)	0.6 to 1.6	C	4.9 to 14.8	T	OF, P(model), FP(to 20kHz), Pi-tot(BL)
[78]	E.F. Lucero	1970	APL (Johns Hopkins Univ.)	2.17	F	9.8	T	P(model)
[93]	A.E. Winkelmann	1970	Naval Ordinance Laboratory	5	F	9.2 and 24.3	T	OF, azobenzene sublimation, Pitot(BL) S, Sh
[47]	E.J. Lucas	1971	AEDC	2.5 to 4	F	18.8 to 31.6	T	OF, Pitot, S(1μs exp.)
[195]	A.E. Winkelmann	1972	Naval Ordinance Laboratory	5	F	9.2 and 24.3	T	OF, sublimation, P(model), RDF HF gauge, S
[34]	L.G. Kaufman et al.	1972	Wright Patterson	2.5, 3, 4	F	18.5, 31.5	**X**&T	OF, P(model&fin), Pitot(from fin), S(1μs exp.), Sh

[88]	R. Sedney	1972	Ballistic Research Laboratories, Aberdeen Proving Ground, Maryland (Martin Mari-etta Corp.)	2	C	13	T	OF, S(top down), Sh
[196]	J.W. Keyes & F.D. Hains	1973	NASA Langley (Bell Aerospace)	6	F	7.9, 25.6	T	P&TCs(fin), S
[36]	L.G. Kaufman et al.	1973	Wright Patterson	2.5, 3, 4	F	18.5, 31.5	**X**&T	OF, P(model), S(1μs exp.)
[35]	R. Sedney & C.W. Kitchens	1975	Ballistic Research Laboratories, Aberdeen Proving Ground, Maryland	1.5-4.5	C	2 to 25	T	OF, vapor screen, S, Sh(top down)
[90]	R. Sedney & C.W. Kitchens	1977	Ballistic Research Laboratories, Aberdeen Proving Ground, Maryland	1.5-4.5	C	2 to 25	T	OF, Sh(top down)
[95]	D.S. Dolling et al.	1977	Princeton Univ.	3	F	62	T	OF, P(model), HF(TCs&slug calorimeter)
[96]	D.S. Dolling et al.	1978	Princeton Univ.	3	F	62	T	OF, P(model), Sh
[97]	D.S. Dolling et al.	1979	Princeton Univ.	3	F	63	T	P(model&fin), S, Sh
[38]	F.T. Hung & J.M. Clauss	1980	NASA Ames	5.3	C	3.3, 16.4	L&T	TCs(model&cylinder)
[98]	D.S. Dolling & S.M. Bogdonoff	1980	Princeton Univ.	3	F	63	T	P(model&fin), S, Sh
[39]	D.S. Dolling & S.M. Bogdonoff	1980	Princeton Univ.	3	F	63	T	P(model-Kulites), S, Sh
[100]	D.S. Dolling & S.M. Bogdonoff	1981	Princeton Univ.	2.95	F	63	T	OF, P(model-Kulites&mean), S
[32]	D.S. Dolling & S.M. Bogdonoff	1982	Princeton Univ.	3	F	65	T	OF, P(model-contour&fin), S
[197]	O. Özcan	1982	Univ. of Cal.	2.36	C	2.5-16	L,**X**,T	OF, Laser vel., P(model), S
[101]	D.S. Dolling	1983	Princeton Univ.	3	F	65	T	P(model-Kulites)
[94]	F.T. Hung & D.K. Patel	1984	NASA Ames (Aerospace Corp. & Rockwell Intl. Corp.)	5.3	C	3.3,16.4	L&T	TCs(model&cylinder)
[102]	O. Özcan & M. Holt	1984	Univ. of Cal.	2.36	C	2.5-3.5	L	OF, Laser vel., P(model), S
[198]	N. Saida & H. Hattori	1984	Aoyama Gakuin Univ., Japan	1.98, 2.48	F	3.3, 16.4	L&T	P(model)

[199]	N. Saida	1985	Aoyama Gakuin Univ., Japan	2.48	F	40	T	OF, P(model), S
[114]	S. Hussain	1985	Cranfield Inst. of Tech., England	2.4	F	3	T	OF, T liquid crystals, P(model), S
[45]	R.A. Gramann & D.S. Dolling	1986	Univ. of Texas	4.96	C	55	T	OF, thin hot-films
[105]	N.R. Fomison & J.L. Stollery	1987	Cranfield Inst. of Tech., England	2.4	F	2.6	T	OF, P(model-Kulites&mean), vapor screen, S
[200]	D.S. Dolling & J.C. Narlo	1987	Univ. of Texas	5	C	55	T	FP(model-Kulites)
[113]	D.S. Dolling & P.E. Rodi	1988	Univ. of Texas	5	F	53	T	FP(model-Kulites)
[201]	D.S. Dolling & D.R. Smith	1988	Univ. of Texas	5	C	53	T	FP(model-Kulites)
[107]	H.A. Baade	1988	Univ. of Texas	5	C	55	T	FP(model-Kulites)
[121]	S. Aso et al.	1989	Kyushu Univ., Japan	3.95	F	61.5	T	HF(thin-film) and P(model-Kulites)
[109]	D.S. Dolling & D.R. Smith	1989	Univ. of Texas	5	C	53	T	FP(model-Kulites)
[122]	S. Aso et al.	1990	Kyushu Univ., Japan	4	F	12	T	OF, HF(thin-film), P(model-Kulites), S
[118]	T. Evans et al.	1990	Princeton Univ.	2.87	F	60	T	FP(model-Kulites)
[117]	D.R. Smith et al.	1991	Princeton Univ.	2.87	F	65	T	Rayleigh scattering
[110]	D.S. Dolling & L. Brusniak	1991	Univ. of Texas	5	C	53	T	OF, FP(model-Kulites)
[123]	S. Aso et al.	1991	Kyushu Univ., Japan	3.95	F	61.5	T	OF, FP(model-Kulites), S
[130]	Z. Haq et al.	1991	Univ. of Southampton, England	6.9	F		T	T sensitive liquid crystals
[126]	W. Shifen & L. Qingquan	1992	Academia Sinica, China	7.8, 5	C	35,47	T	HF(thin-film) and P(model-Kulites)
[103]	O. Özcan & B.K. Yuceil	1992	Istanbul Tech Univ., Turkey	1.7, 2.2	C	14.7, 12	T	OF, P(model-mean)
[112]	J.C. Gonsalez & D.S. Dolling	1993	Univ. of Texas	5	F	53	T	OF, FP(model-Kulites)

[115]	K. Kleifges & D.S. Dolling	1993	Univ. of Texas	4.95	F	49	T	FP(model-Kulites)
[29]	L. Brusniak & D.S. Dolling	1994	Univ. of Texas	4.95	F	53	T	OF, FP(model-Kulites)
[202]	S. Johnson & K. Murphy	1994	NASA Langley (Dryden & Langley)	10	C	1.6 to 6.6	T	P(cylinder-alt. for pitot rake)
[116]	K. Kleifges & D.S. Dolling	1995	Univ. of Texas	4.95	F	49	T	FP(model-Kulites)
[203]	D. Barberis & P. Molton	1995	Chatillon Cedex, France	1.97	F	9.27	T	OF, LDV, P(model), S
[204]	S.B. Verma & V. Gupta	1995	IIT Kanpur, India	1.6	C	36	T	OF
[205]	P.J. Barnhart & I. Greber	1997	Case Western Reserve Univ. (NASA Lewis)	2 to 5	F	10	T	OF, P(model-Kulites&mean), S
[111]	Ö.H. Ünalmis & D.S. Dolling	1998	Univ. of Texas	4.95	F	48	T	FP(model-Kulites) & Upstream Pi-tot
[128]	P.H. Schuricht & G.T. Roberts	1998	Univ. of Southampton, England	6.7	F	4.3	L	OF, T liquid crystals, S
[133]	J.S. Fox et al.	2001	Australian National Univ.	6.4	F	5.9	**X**	NO PLIF, TCs(model)
[132]	A.F.P. Houwing et al.	2001	Australian National Univ.	7.5	F	4.5	L	NO PLIF
[156]	E.S. Hood	2003	Univ. of Texas	5	C	50	**X**	OF
[206]	D.S. Dolling et al.	2003	Univ. of Texas	5	C	50	**X**	OF, S
[207]	R. Mukund et al.	2003	Nat. Aerospace Laboratories, India	1.8, 2.47	F		T	OF, P(model-mean)
[208]	Y.X. Hou et al.	2004	Univ. of Texas	5	F	50	T	FP(model-Kulites), PIV
[131]	C. Raju & P.R. Viswanath	2005	Nat. Aerospace Laboratories, India	1.8	F		T	PSP
[209]	P.C. Bueno et al.	2005	Univ. of Texas	2	C	33	T	Cinematographic PIV
[210]	P.C. Bueno et al.	2006	Univ. of Texas	2	C	33	T	PIV and PLS adding VGs to flow
[157]	Z.R. Murphree et al.	2006	Univ. of Texas	5	C	50	**X**	OF, PLS, S
[158]	Z.R. Murphree et al.	2007	Univ. of Texas	5	C	60	**X**	PIV, PLS

[211]	K. Kontis et al.	2008	Univ. of Manchester, England	0.8 and 1.4	F	18.4, 32.1	T	OF, P(model-mean), PSP, S
[159]	Z.R. Murphree	2009	Univ. of Texas	5	C	50	**X**	OF, PIV, PLS, FP(model-Kulites), S
[85]	B.M. Wheaton & S.P. Schneider	2010	Purdue Univ.	6	C	5.6 to 6.6	L	Wake: Pitot, hot-wire
[84]	B.F. Bathel et al.	2010	NASA Langley	10	C	1.7, 3.3	L	NO MTV
[83]	P.M. Danehy et al.	2010	NASA Langley	10	C	1.7, 3.3, 6.1	L	NO PLIF
[127]	M.S. Yu et al.	2012	Yonsei University, S. Korea	3	C	2.3	T	OF, IR
[212]	D.P. Wang et al.	2012	Nat. Univ. of Defense Tech., China	2.68	C		L	PLS
[129]	O.R. Tutty et al.	2013	Univ. of Southampton, England	6.7	F	5	L	OF, T liquid crystals, S
[213]	C.S. Kumar & K.P.J. Reddy	2014	Indian Inst. of Science	8	C	1	L	HF(thin-film)
[214]	E.J. Stephen et al.	2014	US Air Force Academy	3	C	3.5	T	OF, P(model-Kulites), S
[215]	P. Quan et al.	2015	Changsha Univ., China	3.4	F	39	T	NPLS, PIV
[216]	F. Avallone et al.	2015	Delft Univ. of Tech., Netherlands	7.5	C	14	L	PIV, IR
[124]	H. Itoh & M. Mizoguchi	2016	Nat. Defense Academy of Japan	10	C	2.9	L	P(model-Kulites), S(HS)
[163]	C.S. Combs et al.	2016	Univ. of Tennessee Space Inst.	2	C	30	**X**&T	PIV, PLS, S(HS)
[160]	E.L. Lash et al.	2016	Univ. of Tennessee Space Inst.	2	C	30	**X**&T	OF, S(HS)
[162]	E.L. Lash et al.	2017	Univ. of Tennessee Space Inst.	2	C	28	**X**&T	P(model-Kulites), S(HS)
[164]	E.L. Lash et al.	2017	Univ. of Tennessee Space Inst.	2	C	28	**X**&T	OF, PSP, S(HS)
[165]	C.S. Combs et al.	2018	Univ. of Tennessee Space Inst.	2	C	30	T	S(HS)
[217]	B.E. Rice et al.	2018	Univ. of Tennessee Space Inst. (AFRL, UTSI, & Auburn Univ.)	2	C	33	T	PIV
[125]	H. Ozawa & S.J. Laurence	2018	Tokyo Metropolitan Univ., Japan (TMU & Univ. of Maryland)	1.2	C	2.2 to 3.9	L	TSP&TCs(model), S(HS)

[1]The shock generator is either a cylinder (C) or a blunt fin (F)

[2]The boundary layer (BL) state is either laminar (L), transitional (**X**), or turbulent (T)

[3]The diagnostics are abbreviated as follows: OF=Oil Flow, P=Pressure(generally static), FP=Fluctuating Pressure, PSP=Pressure Sensitive Paint, T=Temperature, TCs=Thermocouples, HF=Heat Flux, IR=Infrared Thermography, LDV=Laser Doppler Velocimetry, MTV=Molecular Tagging Velocimetry, PIV=Particle Image Velocimetry, PLIF=Planar Laser Induced Fluorescence, PLS=Planar Laser Scattering, Sh=Shadowgraph, S=Schlieren, S(HS)=High-speed Schlieren(for time-resolved motion)

APPENDIX B

HYPERSONIC TRANSITIONAL SBLI EXPERIMENTS

Ref.	Authors	Year	Location	Mach	Reynolds (M/m)	Configuration	Diagnostics[4]
[144]	S. Willems & A. Gülhan	2013	DLR	6	3,6,12	Impinging shock caused by a wedge positioned above a sharp leading-edge flat plate model	FP(Kulites & PCBs), T(IR & coax TCs), HF(thin film & ALTP), S
[145]	S. Willems et al.	2015	DLR (German Aerospace Center)	6	3,6,12		
[146]	E. Schülein	2014	DLR (German Aerospace Center)	6	1.9 to 8.1	Impinging shock caused by a wedge positioned above a sharp leading-edge flat plate model	IR, Sh
[147]	N.D. Sandham et al.	2014	DLR & Univ. of South-ampton, England	6	14.2		TCs, HF(thin film)
[148]	E. Erdem et al.	2013	AeroPhysics Lab U of Glasgow	5	15.9	impinging shock caused by a cowl surrounding a hollow cylindrical model	FP(Kulites & PSP), IR, PIV, S
[149]	D. Estruch-Samper et al.	2012	Imperial College London	8.9	47.4	blunted cylinder with a downstream flare	HF(thin film), S(HS)
[150]	D. Estruch-Samper et al.	2013	Imperial College London	8.9	47.4		FP(Kulites), HF(thin film), toluene PLIF, S(HS)
[151]	L. Vanstone et al.	2013	Imperial College London	8.9	47		FP(Kulites), HF(thin film), S(HS)
[23]	L. Vanstone	2015	Imperial College London	8.9	47	blunted cylinder with a downstream flare and, separately, shock impingement from a cowl	FP(Kulites), HF(thin film), S(HS)
[152]	J.B. Edelman et al.	2016	Purdue	6	12.4	compression ramp on sharp cone subjected to quiet and noisy conditions	FP(PCBs), TSP, HF(Schmidt-Boelter)
[153]	K.A. Gray et al.	2017	Purdue	6	10.5-12.1		OF, FP(PCBs)
[154]	B.C. Chynoweth et al.	2017	Purdue	6	1.1-10.9		FP(PCBs), TSP, HF(Schmidt-Boelter)
[155]	A. Wagner et al.	2017	DLR	7.4	6.65	compression corner on flat plate with either a sharp or blunted leading edge	P, TCs, S(HS)

[4]The diagnostic abbreviations are the same as those listed in [3] at the end of Appendix A

APPENDIX C

NEW (STAINLESS) ACE DIFFUSER

Wind tunnel diffuser design is not an exact science. As [218] describes, "the tunnel designer must choose a configuration that he can reasonably expect to work on the basis of previous diffuser studies and hope it works well in his tunnel." An ideal diffuser would have a Mach number of 1 at the second minimum (resulting from upstream oblique shock reflections), and a normal shock downstream of this point to minimize entropy losses. For an empty test section, assuming perfectly uniform flow, and no viscous effects, the theoretical contour angle can be determined for a given second minimum streamwise position. However, getting a diffuser to perform at maximum efficiency in practice is difficult because the Mach number is variable, viscous effects are prominent, and the optimal second minimum area depends on test section blockage; it is model dependent. Therefore, the ability to adjust the diffuser throat height is paramount. With this in mind, the goals for the new diffuser were threefold.

Make adjustment of second minimum easier – as alluded above, there is an optimal diffuser throat height for each model. The throat height of the previous diffuser was modified by adjusting the position of nuts on a threaded rod both within and outside of the tunnel, seen in Figure C-172. The contours tended to be bound, so force was required to move the contour over any amount of distance. Accessing the rods was tedious as they had to be covered to prevent leaks. During adjustment, the contours appeared to bend rather than pivot. The new design keeps the throat height adjustment within the diffuser by fixing the contours to jacks which are secured to the floor and ceiling of the diffuser box. The jacks are accessed by opening a single door on the box, and bounding is eliminated through use of piano hinges and rails.

Extend the Reynolds number range of facility – the maximum freestream Reynolds number using the previous diffuser was about 7M/m. Tests are often done using the same model in both ACE and the M6QT, which is quiet to near 11M/m. Extending the Reynolds number range in ACE allows for a larger overlap in Reynolds number for comparison of freestream disturbance effects. The previous diffuser was bolted together and was sealed with O-rings that occasionally came out of position. Fixing the leaks by creating a diffuser that is welded together allows for a better vacuum and an increase in efficiency. The present diffuser is also longer, while keeping the second minimum in the same location relative to the test section. This reduces the angle between the contours downstream of the second minimum [218].

Use a material suitable for nitric oxide (and nitrogen dioxide) – NO is a common flow seed in our laboratory. It allows for simultaneous velocimetry and thermography [219], but is toxic and highly corrosive. The previous diffuser was comprised entirely of carbon steel, which readily oxidizes in the presence of NO and NO_2. The present diffuser is fully sealed and stainless.

Figure C-172. Contour of old diffuser: nuts on threaded rods for throat adjustment

The throat height for the present diffuser is adjusted by jacks located at the second minimum. These jacks are fastened to rails which allow for the streamwise kinematic motion due to changing contour angle with throat height; this prevents binding and bending of metal. A similar arrangement of rails is located at the downstream end of the diffuser. A model of the full contour is given in Figure C-173 and the rail assemblies are pictured in Figure C-174. The external box assembly is shown in Figure C-175 from both sides of the tunnel.

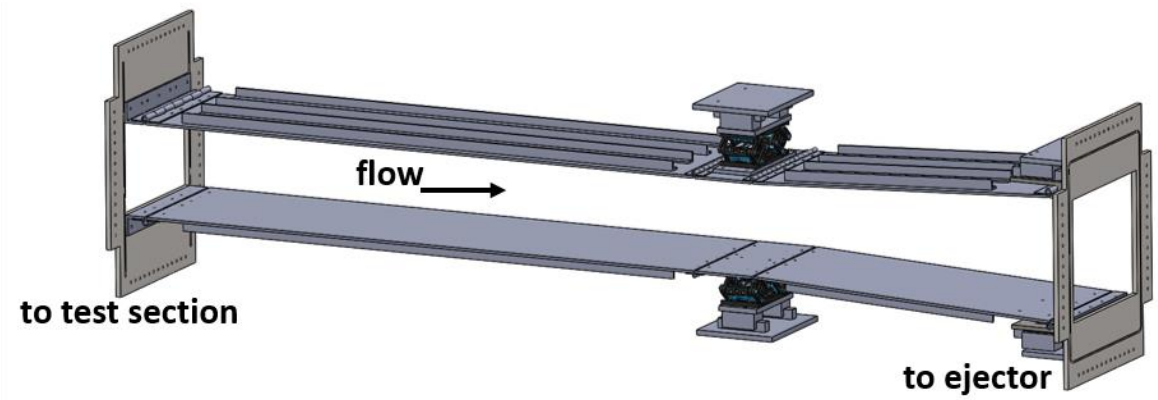

Figure C-173. Diffuser contour assembly

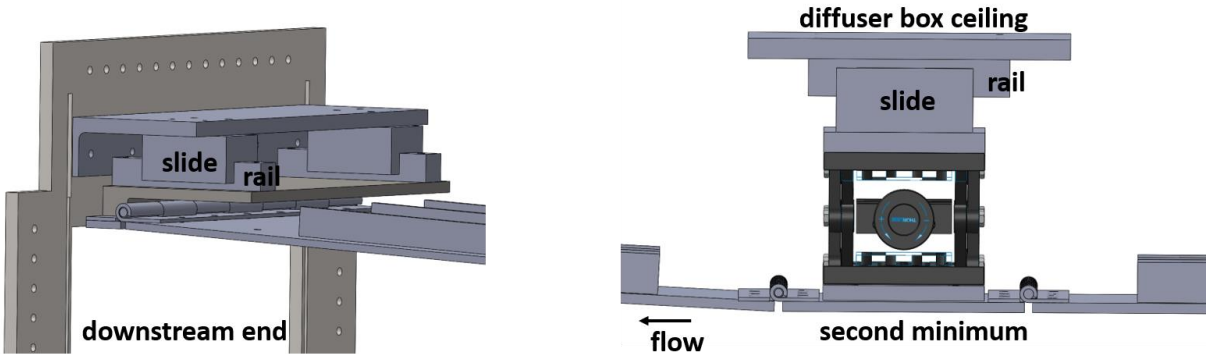

Figure C-174. Diffuser rail assemblies

Table C-14 gives the material list. Once the parts outlined in the table were machined, the interior was assembled. Parts were generally fastened with 1/4-20 thread-locking screws. The external box was built around the contour and was welded along all seams for an airtight assembly. Figure C-176 displays the diffuser during fabrication in the welding shop. Figure C-177 is a picture of the diffuser with the jack adjustment door removed.

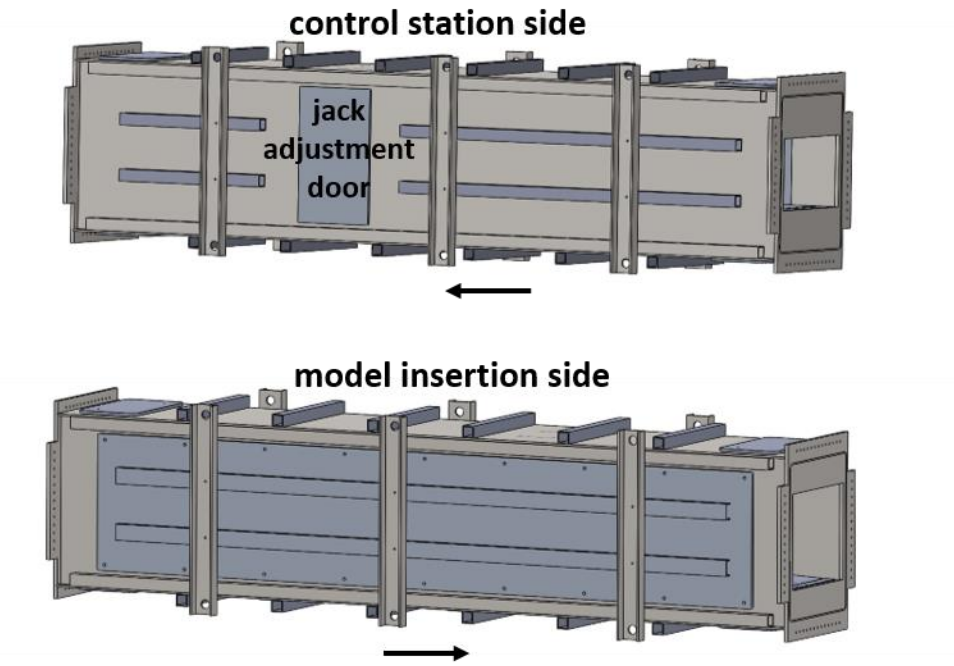

Figure C-175. Side views of external diffuser box

Figure C-176. Fabrication of stainless diffuser

Figure C-177. View inside diffuser from jack adjustment door

Table C-14. ACE diffuser material list

Outside			
SolidWorks Part Name	**Material**	**Size**	**Quantity**
left outside wall	stainless steel	100.5" x 21" x 0.25"	1
right outside wall	stainless steel	100.5" x 21" x 0.25"	1
wall mount	stainless steel	90" x 1" x 1/2"	2
outer top and bottom	stainless steel	100" x 17" x 0.25"	2
remove wall	aluminum	90" x 17" x 3/4"	1
square	stainless steel	96" x 1.5" x 0.12" thick	4
top and bottom square	stainless steel	17" x 1.5" x 0.12" thick	12
door	aluminum	17" x 10" x 5/8"	1
aluminum cbeam	aluminum	84" x 2" x 1" x 0.13" thick	2
upstream square	stainless steel	48" x 1.5" x 0.12" thick	2
downstream square	stainless steel	20" x 1.5" x 0.12" thick	2
cbeam holes	steel	26" x 3" x 1.5" x 0.25" thick	6
window	aluminum	14" x 8" x 5/8"	4
ACE diffuser - Test section end plate	stainless steel	24.5" x 20.5" x 0.50"	1
ACE ejector - Test section end plate	stainless steel	24.5" x 20.5" x 0.50"	1
Inside			
Note: all interior dimensions that are 14" cannot exceed 14" and must be cut if larger			
SolidWorks Part Name	**Material**	**Size**	**Quantity**
Contour			
upstream plate	stainless steel	58" x 14" x 0.25"	2
upstream hinge	stainless steel	14" x 3" x 0.12" thick	2
upstream angle	stainless steel	14" x 2" x 0.25" thick	2
mid hinge	stainless steel	14" x 2" x 0.090" thick	4
middle plate	stainless steel	14" x 6" x 0.25"	2
downstream plate	stainless steel	31.25" x 14" x 0.25"	2
hinge_back	stainless steel	14" x 3" x 0.12" thick	2
last plate	stainless steel	14" x 1.4" x 0.25"	2
upstream contour sup	stainless steel	52" x 1" x 1" x 0.1875" thick	8
downstream contour sup	stainless steel	22" x 1" x 1" x 0.1875" thick	8
Downstream slide assembly			
back angle	stainless steel	14" x 5" x 2"	2
cart	stainless steel		4

rail	stainless steel	6" long	4
cart plate	stainless steel	12" x 6 " x 1"	2
Central slide assembly			
mid base plate	stainless steel	10" x 8" x 0.5"	2
mid rail	stainless steel	5" long	4
cart	stainless steel		4
mid base jack plate	stainless steel	8" x 4" x 0.5"	2
L490 jack			2
mid contour jack plate	stainless steel	10" x 4" x 3/8"	2

APPENDIX D

ACE STANDARD OPERATING PROCEDURE

Starting a Work Day

-Turn on pipe, filter, and settling chamber heaters several hours before a run.
-Ensure compressors are set to "AUTO" and are without error.

Before a Hypersonic Run

Outside the lab:

-Open manual 2" ball valve.
-Switch on 2" and 4" actuators in compressor building.
-Open ejector covers and ball valves.
-Ensure ejector regulator heaters are on if air temperature is below 55°F.
-Turn on Chromalox supply heater.

Inside Lab:

-Supply 2.4 MPa (350 psi) to ejector regulators.
-Feed shop air to tunnel supply regulators.
-Ensure tunnel is secure.
-Find a second tunnel operator.
-Warn others in the lab that a run is about to happen.
-Open ACE knife gate valve.
-Open manual hypersonic tunnels ball valve.
-Verify SHR and M6QT valves are closed.
-Open manual ACE tunnel supply ball valve.
-Check cameras and set warning lights to yellow.

Preheating the Tunnel

-Open actuated 2" pipeline valve.
-Switch on Chromalox heating elements.
-Open actuated tunnel supply valve.
-Monitor the supply and heater element temperature closely.
-Preheat settling chamber to around 430 K for a Mach 6 run.
-Turn off tunnel supply and allow air to bleed through tunnel.

Immediately Prior to a Run

-Remove tunnel preheat door and rotate model into test section.
-Ensure data acquisition is ready.
-Check cameras, sound warning horn, and switch lights to red.

Hypersonic Test Run

-Open actuated 4” pipeline valve and switch on ejector regulators.
-Open tunnel supply when back pressure reaches 1300 Pa (10 torr).
-Conduct test. Tunnel can run for nearly 40 seconds.
-Shut down tunnel when done or when tank pressure drops below 1400 psi.
-Switch off ejector regulators, 4” pipeline valve, and 2” pipeline valve.
-Allow air to bleed through tunnel.
-Close actuated tunnel supply valve.
-Close manual ACE supply ball valve.
-Close ACE knife gate.

Shutting Down for the Day

-Close manual hypersonic ball valve.
-Close ejector regulator line at wall
-Depressurize shop airline.
-Close ejector valves and replace covers.
-Turn off Chromalox heater.
-Close manual 2” ball valve.
-Turn off actuators in compressor building.

APPENDIX E

MODEL PROFILOMETER SCANS

A series of laser profilometer scans were conducted on the composite and wedge models to characterize the geometry and surface roughness. The setup is pictured below in Figure E-178. The profilometer assembly was secured atop an optical table and the model was placed on a previous wedge model in order for the geometry of interest to be relatively flat compared to the traversing laser. This is important because the laser range must fall within a 6 mm bound, and the laser is most precise near the center of the range. The profilometer has the ability to traverse near 1 m in its *x*-direction and 80 mm in its *y*-direction.

Figure E-178. Setup of laser profilometer and model for leading-edge scans

A number of scans were done on both geometries and those comparing the upstream 75 mm of the composite and PEEK models are depicted in Figure E-179. These scans were performed starting at a front edge of the model, traversing across the span of the leading edge, stepping a Δy downstream, traversing back, and repeating downstream for the 75 mm distance. Δy was 0.5 mm for the PEEK model and 0.25 mm for the composite model. There were some small bands of readings that were clearly erroneous (NaN or extreme values) and these were smoothed with the remaining data. Data were not collected for the white square region in the PEEK wedge scan. The reason for this is not currently known. The contour maps in Figure E-179 were rotated be representative of the wedge models near zero AOA.

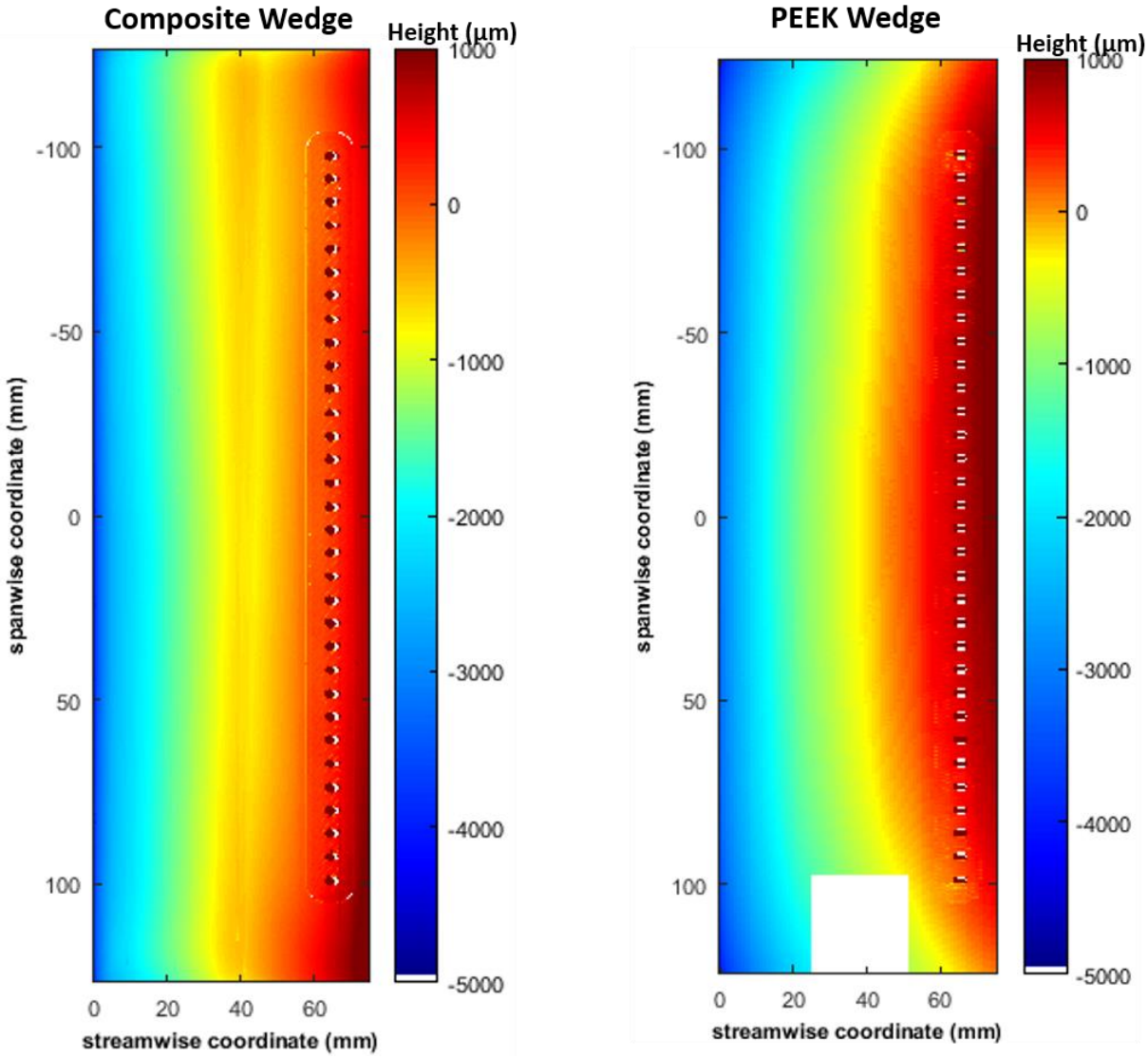

Figure E-179. Leading edge contour scan of composite model (left) and PEEK model (right)

Spanwise profiles from the above contour plots are presented in Figure E-180.

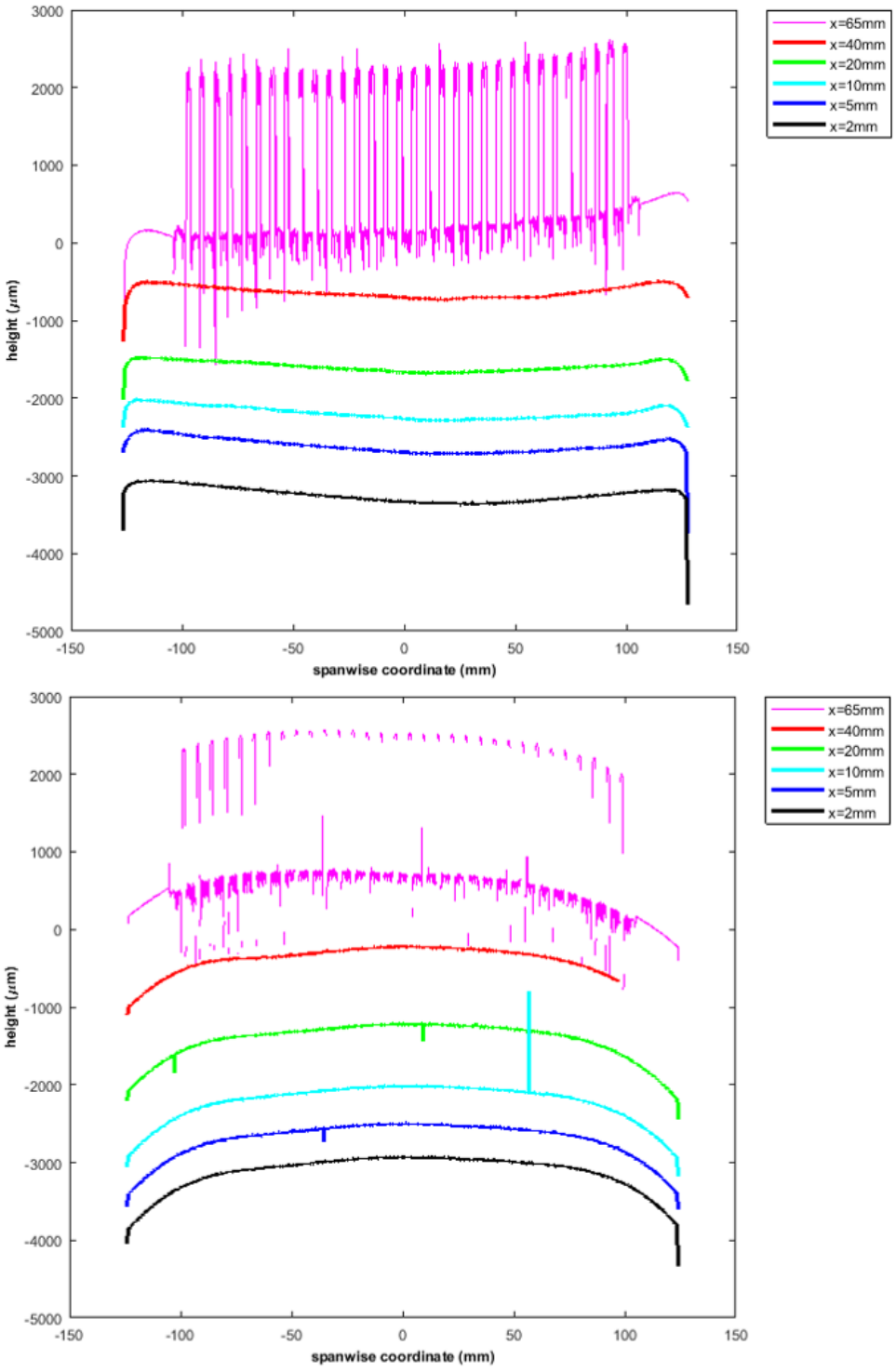

Figure E-180. Spanwise profiles of the composite model (top) and PEEK model (bottom)

The above figures quantitatively display the justification for a composite model. The leading edge is a significant improvement in uniformity, and the contours are directed across the span. The profile plots show that the measured trip height is roughly 1.8 mm, or 0.07 in. as defined.

Surface roughness profiles were also generated for each traverse across the span. A series of charts showing the process for obtaining a roughness profile for scan 20 of the composite model (5 mm downstream of the leading edge) is given in Figure E-181. This example only considers the central 10 cm of the span. The raw scan was first median filtered to account for the width of the laser beam. A best fit polynomial (here a quadratic) was then subtracted from the profile to leave only model waviness and roughness. From there, a length factor – lambda – was defined to separate these two components; each scan was broken into segments of lambda length (0.3 mm), and the roughness parameters are assessed for each segment. Peak-to-valley roughness height and RMS roughness as a function of streamwise position on the model are plotted in Figure E-182. The peak-to-valley values are roughly three times the RMS for all scans, as expected. The peak-to-valley roughness hovers near 4 microns for the composite model, which was lightly polished, compared to around double that for the machine finished PEEK. A more thorough description of this process and the roughness parameters is presented in [220].

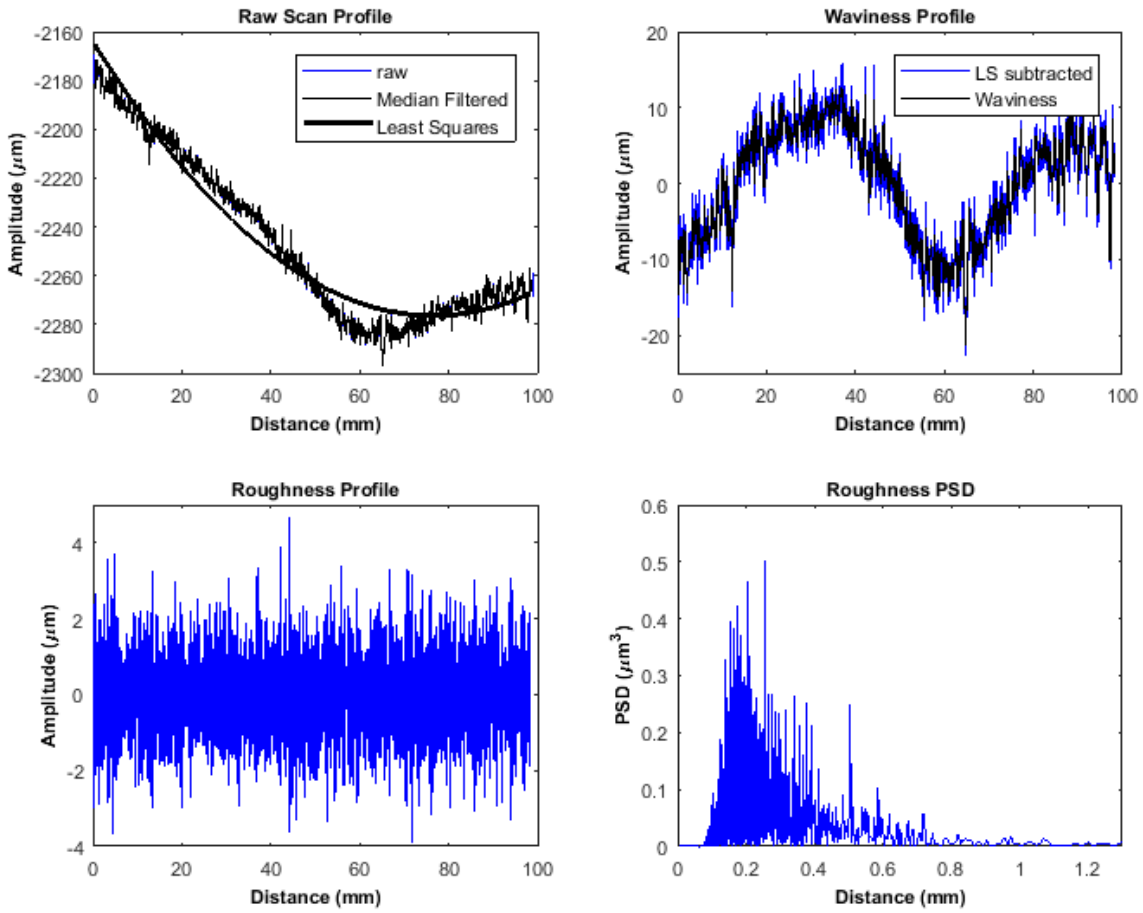

Figure E-181. Scan processing sequence to obtain surface roughness (composite model)

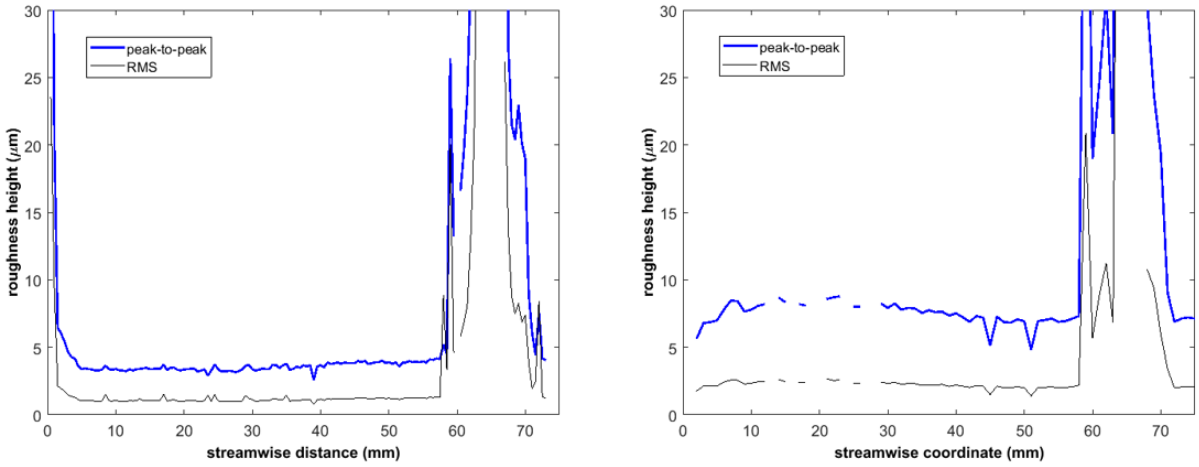

Figure E-182. Average roughness for composite model (left) and PEEK model (right)

APPENDIX F

FLIR SC8100 IR CAMERA CALIBRATION

Precise measurement of surface temperature was imperative for this campaign. The SC8100 has a factory calibration, but it gives no consideration for experimental setup, most notably, measuring irradiance through a 9.5 mm (3/8 in.) thick zinc selenide window. Therefore, an in situ calibration was performed on the IR camera.

The setup consisted of a high emissivity flat black aluminum calibration plate (from FLIR), resting on a hot plate and propped to the center of the test section. The camera was directed through the IR transmissive window from above the plate (Figure F-183) at different heights depending on which lens was used (plate was put into focus). The camera was wrapped in a cloth to minimize reflections from the room. A Type K thermocouple was mounted on the surface of the plate and connected to a DMM to read out the temperature. This readout was verified to be accurate by first measuring the temperatures of ice water and boiling water, which indicated 0.3° C and 100.0° C, respectively.

The calibration plate was slowly heated and points were only recorded when its temperature reached a steady value. A typical calibration from 20° C to 140° C took around 45 minutes to complete. The FLIR ResearchIR software was used for the calibration. The temperature readout from the DMM was input into the software at user-defined times. The measured temperatures were matched to camera counts (on a segment of the plate near the thermocouple) for 4 predefined integration times (1 ms, 2 ms, 4 ms, and 8 ms exposures). The radiance value is a value that is automatically generated by the software based on the input temperature and user-defined emissivity.

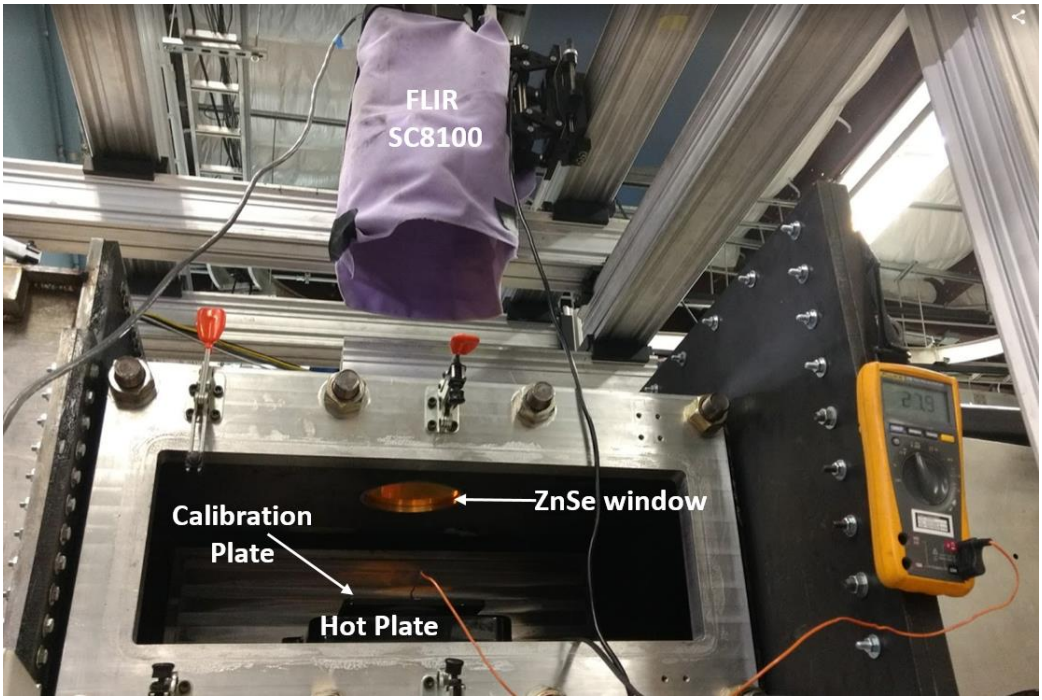

Figure F-183. IR camera calibration setup

Several methods for calibration were used prior to the final approach that was found to give consistent results. The first approach was to tape the thermocouple onto the plate using Kapton tape, which is rated to 260° C, well above what was needed for the calibration. A piece of silicone with adhesive backing was secured on top to reinforce the hold. At first glance, the calibration curves looked reasonable as there were no discontinuities in the temperature vs counts curve. However, after the calibration was finished, rearranging the thermocouple wire caused the reading to increase by roughly 5° C. That prompted the second approach which involved weighing down the junction onto the plate using the stainless cylinder on the right of Figure F-184. After that calibration, the cylinder was removed and the junction rotated, again causing a rise in the displayed temperature.

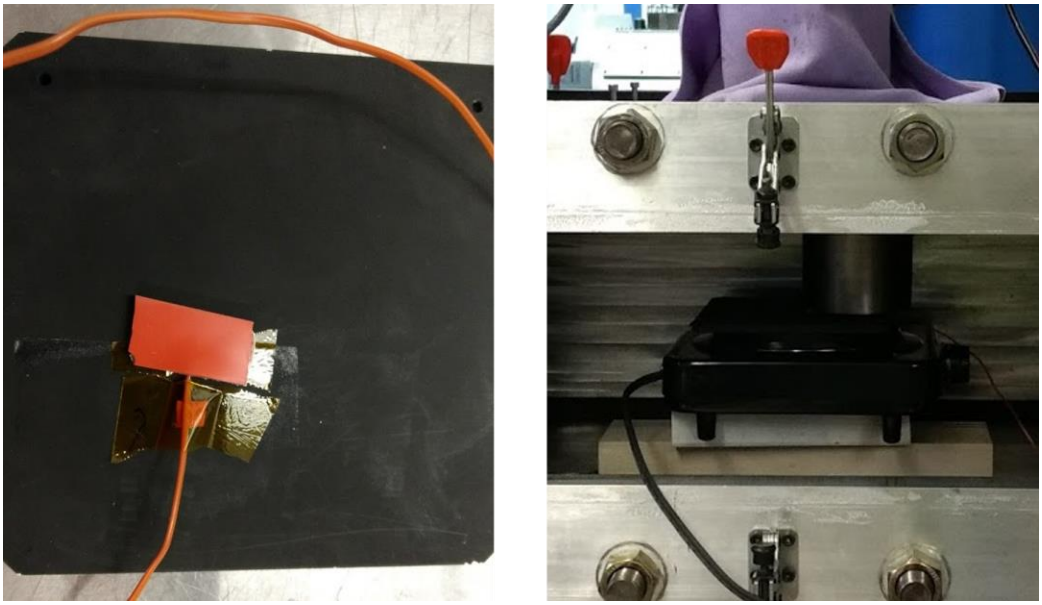

Figure F-184. Thermocouple taped to calibration plate (left) and held down by stainless cylinder (right)

The theory for this increase was that the temperature measured throughout the calibration was too low since only one side of the thermocouple junction was in contact with the plate and the other parts were either in contact with surrounding air or the tape, both of which were cooler than the surface of the plate. Therefore, rotating the junction on the hot surface after the calibration exposed the other sides of that bead to higher temperatures, which increased the displayed temperature.

The final mounting method involved drilling a hole into the plate, angled to the surface, as draw in Figure F-185. The thermocouple was then positioned in the hole and carefully backfilled with solder. Care was taken to not create a second junction. Slow, meticulous calibrations were even more critical (minimize temperature gradients through the calibration plate) for this configuration since the thermocouple was below the surface.

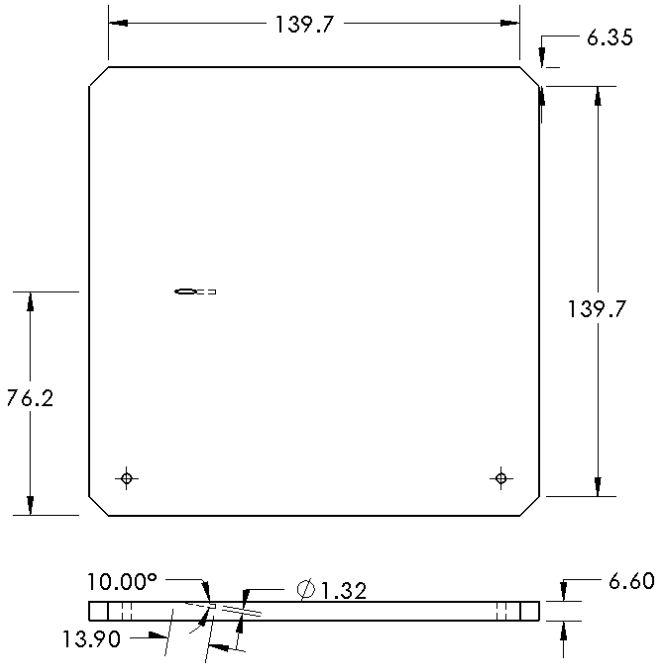

Figure F-185. Port for thermocouple in calibration plate. Dimensions are in mm

Calibrations were performed with the imbedded thermocouple using both the 17 mm and 50 mm lenses through two different (nominally identical) IR windows. Most calibrations were performed with the camera directed at the calibration plate surface but several were done at viewing angles of either 20 or 30 degrees. Figure F-186 plots all calibrations for the 1 ms exposure time. Note that the minimal variability in the data despite different windows and lenses.

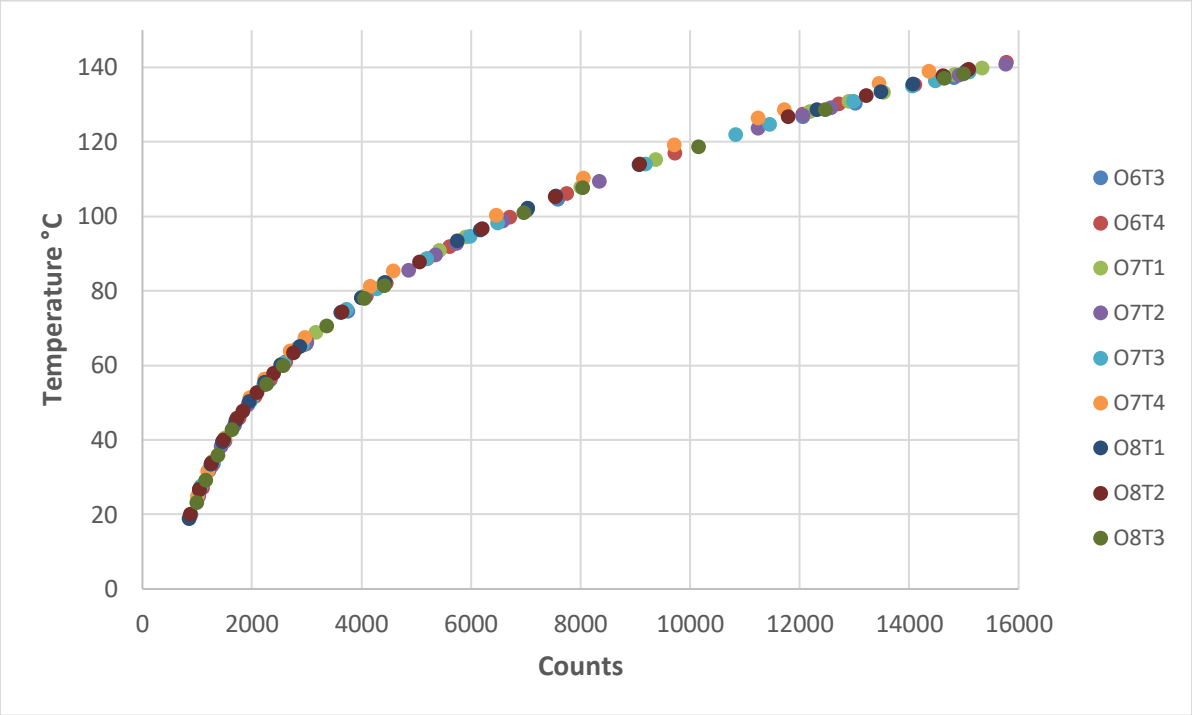

Figure F-186. Calibration points for all calibrations. Slight deviation only observed in O7T4, which was a 30° viewing angle

The tables give all of the calibrations for all of the exposure times tested.

06T3 - "New 3-O6". Unused window and 17mm lens.				
Temperature	**Counts**			
	8 ms	**4 ms**	**2 ms**	**1 ms**
33.7	8693.2	4478	2335.4	1303.1
56.2		8252.6	4244.6	2342
65.8		10603.2	5440.9	2993.9
74.7		13314.1	6830	3755
104.7			13780.5	7591.3
126.8				12067.2
130.5				13018.8
137.3				14816.9

06T4 - "Zoom 1-O6". Used window and 50mm lens.				
Temperature	**Counts**			
	8 ms	**4 ms**	**2 ms**	**1 ms**

27.2	7224.2	3739.4	1962.8	1100.2
33	8422.7	4346.1	2267.2	1265.4
39.8	10179.6	5233.8	2714.6	1508.8
45.9	12057.2	6179.7	3194	1769.6
51.8	14158.1	7257.8	3736.8	2063.3
56.4		8200.3	4220.4	2326.3
61		9274.8	4764.5	2622.2
65.7		10484.8	5380.6	2955.5
78.7		14523.2	7457.6	4095.4
82.1			8114.9	4455.3
88.7			9479.5	5205.1
91.9			10209.4	5608.8
99.8			12204.2	6706.1
106.3			14084.8	7754.2
117				9729.2
127.6				12066.5
130.2				12714.6
135.5				14105.2
138.9				15034.7
141.5				15785

07T1 - "Zoom 2". Used window and 50mm lens.				
Temperature	**Counts**			
	8 ms	**4 ms**	**2 ms**	**1 ms**
19.2	5476.3	2857.5	1520.6	858.4
27.5	7000.8	3622.8	1905.6	1067.3
34.2	8494.7	4375.9	2284.3	1272.8
40.6	10200.9	5244.6	2718.8	1508.6
51.2	13695.1	7012.2	3614.1	1995.1
55.9		7972.3	4102.8	2260.5
60.3		8972.2	4610.7	2536.3
64.6		10052.5	5156.5	2832.8
69		11281.7	5779.2	3172.8
78.5		14318	7343.9	4029.2
82.2			8033.5	4404.9
90.9			9897.3	5429.8
94.5			10764.5	5906.5
102.2			12816	7037.4
108			14539.3	8004.8
115.3				9373

128.2				12195.2
130.9				12906.2
133.4				13540.6
138.2				14837.2
139.9				15332.8

07T2 - "Zoom 3". Used window and 50mm lens.				
Temperature	**Counts**			
	8 ms	**4 ms**	**2 ms**	**1 ms**
25	6690.5	3464.1	1826.9	1025.1
31.8	8101.9	4178.6	2184.4	1220.1
38.3	9699.2	4992.3	2593.6	1442.8
44.1	11421.7	5862.6	3029.3	1679.5
49.5	13265.8	6791.7	3500	1936.4
54.8		7842.3	4033.7	2226.2
66.4		10655.2	5465.7	3006.5
85.7			8843	4860.5
89.8			9737.2	5353.7
92.8			10430.3	5735.7
98.8			11960.5	6581.9
101.7			12778.4	7030.5
109.5				8344.9
123.8				11248.2
127.2				12062
129.2				12575
138				14918.4
141				15764

07T3 - "Zoom-20deg". Used window and 50mm lens.				
Temperature	**Counts**			
	8 ms	**4 ms**	**2 ms**	**1 ms**
20	5680.8	2963.4	1573	886.7
27.7	7083.5	3664.9	1925.4	1079.9
33.9	8464.4	4362.9	2275.8	1271.6
40	10063.8	5175.3	2681.2	1493.1
45.7	11820.8	6056.7	3128.1	1737.3
50.6	13543.9	6938.1	3574.7	1980.9
55.1		7834.3	4021.6	2226.3
60.7		9102.9	4670.6	2580.5

65.6		10351.3	5302.2	2927.5
75.1		13200.9	6759.7	3730
80.6			7752.9	4277.4
88.7			9403.5	5191.4
94.7			10824.2	5981.7
98.3			11738.2	6489.1
114.1			14969.5	9191.4
122				10839.7
124.8				11458.3
131				12982.2
135.1				14058.9
136.5				14478.1
138.8				15098

07T4 - "Zoom-30deg". Used window and 50mm lens.				
Temperature	**Counts**			
	8 ms	**4 ms**	**2 ms**	**1 ms**
25	6620.2	3417	1810.8	1009.3
31.7	8011.8	4127.3	2163.8	1189
51.4	13945.8	7155.1	3682.9	1963.2
56.5		8233.6	4218.4	2235.8
63.9		10030.3	5131.3	2700.1
67.6		11060.1	5650.5	2965.5
81.4		15645.4	7976.9	4159.3
85.4			8808.5	4585.7
100.4			12448.9	6463.2
110.4			15484.1	8051.2
119.3				9717.1
126.5				11240.9
128.7				11719.5
135.7				13450.7
139.1				14367.3

08T1. Used window and 17mm lens.				
Temperature	**Counts**			
	8 ms	**4 ms**	**2 ms**	**1 ms**
18.9	5449	2846.1	1514.3	854.6
26.7	6837.2	3541	1863.3	1043.2
33.6	8353.6	4307.3	2249.2	1251.5

39.6	9913.6	5092	2644.5	1465.2
45.3	11655.2	5975.9	3087.3	1704.8
50.4	13437.2	6877.4	3544.6	1951.7
55.5		7915.3	4069.1	2234.9
60.2		8969.7	4613.2	2529.6
65.1		10217.9	5245	2871.6
74.2		12902.7	6622.7	3619.6
78.2		14211.4	7307.2	3993.8
82.4			8115.2	4432.8
93.5			10536	5757.4
96.5			11290	6171
102.3			12876.6	7041.8
105.5			13794.6	7553.6
114				9072.1
128.8				12321.8
133.5				13494.2
135.6				14071.8
137.6				14629.1
139.2				15058.7

08T2. Used window and 17mm lens.				
Temperature	**Counts**			
	8 ms	**4 ms**	**2 ms**	**1 ms**
20.1	5654.8	2948.9	1566.1	882.4
26.8	6863.9	3557.7	1869.9	1046.8
33.9	8447.3	4348	2270.9	1263.1
40.1	10076.8	5177.1	2684.8	1486.4
45.9	11905.4	6092.6	3151.4	1737.3
47.8	12600	6451.5	3332.6	1835.2
52.8	14431.7	7386.5	3807.1	2090.8
58		8498.4	4372.5	2395.7
63.5		9824	5050.2	2761.4
74.5		13038.5	6691	3651.1
87.9			9271.2	5057.6
96.8			11377.1	6208.3
105.4			13804.6	7540.6
114.1				9077.9
126.8				11799
132.5				13224.7
137.8				14617.7

139.5				15094.8

08T3 - "New 4-O8". Unused window and 17mm lens.				
Temperature	**Counts**			
	8 ms	**4 ms**	**2 ms**	**1 ms**
23.3	6490.8	3367.4	1775.8	997.4
29.3	7681.4	3961.1	2076.1	1159.4
36	9271.8	4761.5	2478.4	1377.6
42.8	11205.2	5740.4	2969.7	1643.1
55.1		8014.8	4125.4	2268.3
60.1		9151	4694	2576.1
70.6		12019.3	6157.9	3370.4
78		14447.9	7411.6	4054
81.5			8079.5	4419.8
101.1			12723.4	6964.1
107.7			14639.5	8037.6
118.8				10163.6
128.8				12475.9
137.1				14651.7
138.3				14994.4

Old calibration used for SciTech 2017				
Temperature	**Counts**			
	8 ms	**4 ms**	**2 ms**	**1 ms**
22.1	6089.3	3166.4	1815.9	1020
25	6754.9	3504.3	2004.7	1114.6
28	7132.9	3691.1	2105.1	1164.7
31	7970.7	4120	2344.4	1284.3
34	8469.8	4354.8	2470.7	1347.9
37	9373.8	4801.8	2719.2	1472.3
40	9929.6	5092.1	2874.8	1550.3
43	10993.9	5587.3	3162.7	1694.3
46	12132.4	6177.8	3483.2	1854.2
49	13115.1	6656.6	3754	1989.8
52	14068.4	7226.5	4061.4	2127.3
55	14901.9	7646.1	4286.9	2256.4
58		8209.1	4605.8	2415.9
61		8738	4888	2557
64		9485.4	5305.6	2766.1

67		10119.6	5661.9	2944.9
70		10297.7	5748.1	2988.4
73		11421.7	6397.7	3315.7
76		12530.3	7024.3	3630.1
79		13245.9	7429.7	3834.9
82		14348.7	8045.2	4145.4
85		14949	8439.2	4344.3
88			9117.1	4686.6
91			9555.8	4908.8
94			10539.5	5407.5
97			11160.5	5721.6
100			11937.2	6117.1
103			12700.2	6503.8
106			14613.1	7481.8
109			16050.2	8263.3
112				8784.6
115				9324.6
118				10041.6
121				10714.9
124				11424.9
127				12078.9
130				12925
133				13550.2
136				14484.8
139				15291.6
141				15799.7

APPENDIX G

CAMPAIGN RUN LOG

Run #	Date	Test Description/Notes	Diagnostics
First Model: Flat Plate at angle of attack. Span swept back at the Mach angle. Diffuser Height = 7.0" M=6.05@ Re =3.5M/m , M=5.89@ Re=7.8M/m			
2814	24/Nov/2015	Model mounted at -1.9° AOA. Reynolds number sweep 3.5-7.8M/m.	Schlieren (Nikon)
2815	24/Nov/2015	AOA of -1.9°. Re near 4.3M/m. First oil flow taken. Oil band applied parallel to leading edge.	Oil Flow Visualization
2816	25/Nov/2015	Similar to 2815. Re near 5.2M/m. Too much oil applied initially. Swirls are evident and streamlines are not straight back.	Oil Flow Visualization
2817	30/Nov/2015	Oil flow with rows of dots. Re held constant near 4.9M/m. Video taken.	Oil Flow Visualization
2818	1/Dec/2015	Repeated 2817. Re held near 4.8M/m. Streamlines on edges of plate are pulled over by the lower pressure of the bottom surface.	Oil Flow Visualization
2819	16/Dec/2015	Plate now shimmed to -1.1° AOA. Re held near 4.8M/m. Similar but less extreme curvature in oil pattern streamlines compared to 2814-2818.	Oil Flow Visualization
2820	20/Jan/2016	Shimmed to -1.1° AOA. Re near 4.5M/m. 3" Velcro trip centered on the span and near the leading edge. Heat streaks are evident downstream.	SC8100
2821	21/Jan/2016	Shimmed to -1.1° AOA. Re near 4.3M/m. Velcro trip spanning and near the leading edge. Streak pattern recorded.	SC8100
2822	21/Jan/2016	Shimmed to -1.1° AOA. Re near 4.3M/m. No Velcro. No discernable streak pattern in the IR.	SC8100
Second Model: 1.3-degree aluminum wedge model			
2834	16/Feb/2016	Aluminum 1.3-degree wedge. Re held near 3.4M/m. Oil streaks traveled downstream with little influence from model edge.	Oil Flow Visualization
Third Model: 1.3-degree PEEK wedge model. Diffuser Height = 7.0" M = 6.09@ Re=2.8M/m, M=5.94@ Re = 6.7M/m			
2847	20/Apr/2016	Wedge with 3-D printed polycarbonate trip insert in the back plug. Trip height = 0.17". 1 trip every 0.25" on span. Smooth insert in front trip port. Started tunnel at Re=3.5M/m, held, then swept up to 5.7M/m and held.	SC8100, Schlieren (Nikon)
2848	21/Apr/2016	Wedge with same trip insert in the front port. Smooth insert in downstream port. Started tunnel at Re=3.6M/m, held, then swept up to 5.8M/m and held.	SC8100, Schlieren (Nikon)
2849	21/Apr/2016	Wedge with RP poly trip insert in rear port. Smooth insert in front. Started tunnel at 3.5M/m, held, then swept up to 5.6M/m and held.	SC8100, Schlieren (Nikon)
2850	26/Apr/2016	Schlieren video of wedge with both sets of trips in place. Started at 3.6M/m, then driven up to 5.8M/m and held.	Schlieren (Nikon)

2851	26/Apr/2016	Oil flow of wedge with both sets of trips. Re sweep from 3.5 to 5.4 M/m.	Oil Flow Visualization
2855	29/Apr/2016	Wedge run with *new IR window*. Re held constant near 3.3M/m. Camera view through top middle window looking forward. Camera positioned near tunnel using 17-mm lens. Viewing area from first trip to 7.5" behind rear trip (which is also 7.5" measured up from the back edge). Both trips.	SC8100
2856	2/May/2016	Re held near 7.0M/m. Camera view through top middle window looking upstream. Both trips.	SC8100
2857	2/May/2016	Re held near 6.5M/m. Middle window looking downstream. Can see from 2.5" to 11" from the back edge. Both trips.	SC8100
2858	3/May/2016	Re held near 6.9M/m. Camera directed straight down the downstream window. Can see from back edge to 5.5" up from back. Turbulent front or some edge effect on downstream edge? Both trips.	SC8100
2859	5/May/2016	Re held near 6.5M/m. Rear window looking straight down. Can see from back edge to 5.5" up from back. New 0.07" height trips with same 0.25" spacing in both trip ports.	SC8100
2860	6/May/2016	Re held near 3.2M/m. Rear window looking straight down. Can see from back edge to 5.5" up from back. Same trips as 2859.	SC8100
2862	6/May/2016	Re held near 4.8M/m. Rear window looking straight down. Can see from back edge to 5.5" up from back. Same trips.	SC8100
2863	11/May/2016	Re held near 6.3M/m. Rear window looking straight down. Only front set of 0.07" height trips in place.	SC8100
2864	12/May/2016	Re held near 6.5M/m. Rear window looking straight down. Same trips.	SC8100
2865	12/May/2016	Re held near 6.5M/m. Middle window looking straight down. Same trips.	SC8100
2866	12/May/2016	Re held near 6.4M/m. Front window looking straight down. Same trips.	SC8100
2867	13/May/2016	Re near 6.7M/m. No trips. Camera straight through front window. Symmetric, hotter, streaks from leading edge still evident.	SC8100
2868	13/May/2016	Re near 6.6M/m. No trips. Camera straight through middle window. Streaks continue back.	SC8100
2869	17/May/2016	Re stepped and held at 3.3, 5.0, 6.4 M/m for ~8 sec at each. Camera focused on leading edge of wedge to see start of heat streaks. Streaks identified as potentially coming from machining lines on wedge 5.2" apart. Unclear why these cause such elevated heating over other machining lines.	SC8100
First Cylinder Runs			
2870	20/May/2016	Re stepped 3.4, 5.1, 6.3 M/m. A 0.75" diameter, 1.25" tall wooden dowel spray painted black was superglued to a position ~2.1" from the leading edge. It was positioned 0.5" toward the centerspan from one of the hot streaks. Camera was moved closer to tunnel for most zoomed look.	SC8100
2871	20/May/2016	Re stepped 3.4, 4.7, 6.6 M/m. Wedge model was shifted downstream in tunnel about an inch (door was rotated so windows would be at back of wedge).	SC8100
2877	31/May/2016	Re = 2.8, 3.4, 4.4, 6.7 M/m. 0.75" wooden dowel superglued 10.5" downstream from leading edge centered on span. No trips.	SC8100

2878	31/May/2016	Re = 2.8, 3.2, 4.3, 6.4 M/m. First set of short (0.07"), 0.25" spaced trips in front port.	SC8100
2879	1/Jun/2016	Re = 2.9, 3.3, 4.3, 6.7 M/m. Same trips, but with a 1.25" diameter, 1.25" tall wooden dowel.	SC8100
2880	1/Jun/2016	Re = 2.8, 3.3, 4.5, 6.5 M/m. Same 1.25" cylinder, but with no trips.	SC8100
Mach number change. Additional shims measure 0.084" M=7.58@ Re=2.4M/m, M=7.28@ Re=4.3M/m			
2881	2/Jun/2016	Same config as 2880. Attempted change to Mach 7. Felt leak on upper right side of settling chamber nozzle junction during preheat. Went through with run. Mach number closer to 7.5. Tunnel started near 3.8 M/m, then swept down to 2.4 and stepped to 3.4, and 4.3 M/m.	SC8100
Mach number change. Additional shims measure 0.094" M=7.06@ Re=3.2M/m, M=6.66@ Re=6.4M/m			
2884	6/Jun/2016	Redid run 2881 at new throat settings. Re = 3.2, 3.6, 5.0, 6.4 M/m.	SC8100
2885	7/Jun/2016	1.25" cylinder positioned 10.5" from leading edge. With same trip array. Re stepped 3.1, 3.5, 5.1, 6.3 M/m.	SC8100
2886	7/Jun/2016	Re = 2.9, 3.6, 4.9, 6.2 M/m. Configuration with trips and 0.75" diameter dowel.	SC8100
2887	7/Jun/2016	Re = 3.0, 3.6, 5.0, 6.5. Same 0.75" cylinder, but with no trips.	SC8100
2888	20/Jun/2016	Cylinder moved downstream on wedge to 16.5" from the LE, centered on span. No trips. Re = 3.3, 3.8, 5.1, 6.7 M/m.	SC8100
2889	20/Jun/2016	0.75" diameter cylinder with front set of short, closely spaced trips. Re = 3.1, 3.6, 5.2, 6.6 M/m.	SC8100
2890	21/Jun/2016	1.25" cylinder with front set of trips. Re = 3.1, 3.7, 5.2, 6.6 M/m.	SC8100
2891	21/Jun/2016	Same config as 2890. Re = 3.0, 3.7, 4.9, 6.6 M/m.	SC8100
2892	21/Jun/2016	1.25" cylinder with no trips. Re = 3.0, 3.5, 5.0, 6.6 M/m.	SC8100
2898	18/Jul/2016	Front row of trips and no cylinder. IR camera at rear window. Some streaks form at the end of run (higher Re) on left side in the line with a machine mark at front of wedge. Re = 3.0, 3.5, 4.9, 6.4 M/m.	SC8100
New Diffuser Installation. Diffuser Height = 7.0" M=7.00@ Re=3.2M/m			
2945	17/Oct/2016	Mach 7 Runs with 1.3° half angle wedge and cylinder shock generator. Runs were conducted at a settling chamber total pressure 60-65 psi (Re near 3.3M/m.) The temperature increased throughout each run. The front edge of the cylinder was 12" downstream of the leading edge with the front set of trips installed (0.07" tall, 0.25" spaced trips).	Oil Flow Visualization
2946	17/Oct/2016	Previous run repeated with less oil, and blacklights directed on upstream influence for better recording with Nikon. Re near 3.2M/m.	Oil Flow Visualization
2947	18/Oct/2016	Same cylinder position with no trips. Re near 3.3M/m.	Oil Flow Visualization
2948	18/Oct/2016	Front of cylinder 18" from leading edge with trips. Upstream influence not as defined as previous. Re near 3.2M/m.	Oil Flow Visualization
2949	19/Oct/2016	Front of cylinder 15" from the leading edge. Upstream influence returns. Re near 3.1M/m.	Oil Flow Visualization
Mach number change. Nozzle O-rings replaced. Additional shims measure 0.172" M=5.89@ Re=5.0M/m, M=5.82@ Re=7.0M/m			

2957	7/Nov/2016	Mach 6 Runs with 1.3° half angle wedge and 0.75" diameter, 2.25" tall cylinder shock generator. Cylinder positioned 15" from the leading edge. Re held constant at 5.1M/m. Front trips ~1 boundary layer thickness between each trip (spacing of 0.25") and ~60% BL height (0.07").	Oil Flow Visualization
2958	8/Nov/2016	Re held at 4.9M/m. Front trips ~2 boundary layer thicknesses between each trip (spacing of 3/8") and ~60% BL height (0.07").	Oil Flow Visualization
2959	11/Nov/2016	Front of cylinder shock generator move up to 12" from leading edge of wedge. Re = 5.0M/m. Front trips ~2 boundary layer thicknesses between each trip and ~60% BL height (0.07").	Oil Flow Visualization
2960	13/Nov/2016	Front trips ~1 boundary layer thickness between each trip and ~60% BL height (0.07"). Pressure ramp up until unstart at 8.3M/m.	Oil Flow Visualization
2961	13/Nov/2016	Front trips ~1 boundary layer thickness between each trip and ~60% BL height (0.07"). Ramp up to 7.6M/m and tried to hold condition. Only held for 2 seconds (maybe tape).	Oil Flow Visualization
2962	14/Nov/2016	Front trips ~1 boundary layer thickness between each trip and ~60% BL height (0.07"). Similar test but tunnel was not able to hold condition at Re = 7.8M/m.	Oil Flow Visualization
2963	14/Nov/2016	Front trips ~1 boundary layer thickness between each trip and ~60% BL height (0.07"). Held condition at 7.0M/m for 15 seconds until intentional unstart of the tunnel by closing supply ball valve.	Oil Flow Visualization
2964	17/Nov/2016	Re held at 5.3M/m. Front trips ~3 boundary layer thicknesses between each trip (0.5" spacing) and ~60% BL height (0.07").	Oil Flow Visualization
2965	17/Nov/2016	Re held at 7.1M/m. Front trips ~3 boundary layer thicknesses between each trip and ~60% BL height (0.07").	Oil Flow Visualization
2966	18/Nov/2016	Re held at 7.1M/m. Front trips ~4 boundary layer thicknesses between each trip (5/8" spacing) and ~60% BL height (0.07"). Ptot = 93psi.	Oil Flow Visualization
2967	18/Nov/2016	Re held at 4.8M/m. Front trips ~4 boundary layer thicknesses between each trip and ~60% BL height (0.07").	Oil Flow Visualization
2968	20/Nov/2016	Front trips ~4 boundary layer thicknesses between each trip and ~30% BL height (0.035"). Failed run - ejector regulator seemed stuck. Unscrewed both covers and regulator pistons/ packing nuts seemed fine. Determined it was just cold and raining - Heated bags of rice were added for future runs conducted when outside temperature was below 55^{o}F.	Oil Flow Visualization
2969	20/Nov/2016	Re held at 4.9M/m. Front trips ~4 boundary layer thicknesses between each trip and ~30% BL height (0.035").	Oil Flow Visualization
2970	20/Nov/2016	Re set to 7.3M/m. Front trips ~4 boundary layer thicknesses between each trip and ~30% BL height. Failed run - tunnel unstarted as tape came off bottom of wedge and off tunnel floor.	Oil Flow Visualization
2971	20/Nov/2016	Same as 2970 but worked. Re held at 7.0M/m.	Oil Flow Visualization
2972	21/Nov/2016	Re held at 4.9M/m. Front trips ~3 boundary layer thicknesses between each trip and ~30% BL height (0.035").	Oil Flow Visualization
2973	21/Nov/2016	Re set to 7.3M/m. Front trips ~3 boundary layer thicknesses between each trip and ~30% BL height (0.035"). Failed run (tape).	Oil Flow Visualization
2974	21/Nov/2016	Re set to 7.5M/m. Front trips ~3 boundary layer thicknesses between each trip and ~30% BL height. Failed run (unstarted - not sure why).	Oil Flow Visualization

2975	21/Nov/2016	Re held at 7.0M/m. Front trips ~3 boundary layer thicknesses between each trip and ~30% BL height.	Oil Flow Visualization
Diffuser height change - 8.0" now			
2984	23/Nov/2016	Re held at 7.1M/m. Wedge with 5/8" cut off each side (checking for sidewall and sting influence elimination) with front trips ~3 boundary layer thicknesses between each trip (0.5" spacing) and ~60% BL height (0.07"). Cylinder was placed 12" from the leading edge.	Oil Flow Visualization
2985	25/Nov/2016	Re held at 5.0M/m. Front trips ~3 boundary layer thicknesses between each trip and ~60% BL height (0.07"). Cylinder was placed 12" from the leading edge.	Oil Flow Visualization
2986	25/Nov/2016	Stepped Re = 3.3, 4.9, 7.0. Front trips ~3 boundary layer thicknesses between each trip and ~60% BL height (0.07"). Cylinder 12" from LE.	SC8100
2987	26/Nov/2016	Stepped Re = 3.5, 5.2, 7.3. Front trips ~3 boundary layer thicknesses between each trip and ~60% BL height (0.07"). Cylinder was removed.	SC8100
Diffuser height change - 7.125 now - SciTech 2017 runs M=6.02@ Re=3.0M/m, M=5.87@ Re=7.0M/m			
3007	17/Dec/2016	Instrumented wedge (2 PCB 132A31 sensors and 2 Kulite XCE-062-15A sensors). Sampled at 1MHz. PCBs filtered at 500kHz, Kulites at 100kHz. Model with no trips, no cylinder. Re sweep from 2.9 down to 1.9 up to 6.7 M/m.	SC8100, PCBs, Kulites
3008	17/Dec/2016	Instrumented Wedge, w=2*delta (1 delta btw each trip) h=0.6*delta trips, no cylinder. Re sweep from 2.7 to 2.0 to 6.7 M/m.	SC8100, PCBs, Kulites
3010	19/Dec/2016	Instrumented Wedge, trips and 0.75" diameter, 2.25" tall cylinder. Re sweep from 2.7 down to 2.0 up to 7.3 M/m.	SC8100, PCBs, Kulites
Mach number check M=5.91@ Re=3.0M/m, M=5.77@ Re=6.7M/m			
3046	16/May/2017	PEEK wedge. Closely spaced w=2*delta (1 delta btw each trip), h=0.6*delta pizza box trips in front wedge insert. Reynolds number sweep from 3.0 to 1.8 to 6.9 M/m. No leading-edge separation observed.	Schlieren (Nikon)
3047	16/May/2017	Re sweep from 3.0 up to 6.7 M/m. No signs of leading-edge separation.	Schlieren (Olympus)
3048	17/May/2017	Re sweep from 3.0 up to 6.7 M/m. Door was reversed and additional mounting holes were drilled in the bottom of the model to look at the cylinder/boundary layer interaction. Cylinder was 16" downstream of LE. Video captures later part of run with Re>=6M/m. Shock structure and separation scale look close to those for a turbulent SBLI.	Schlieren (Olympus)
3049	17/May/2017	Reynolds number sweep from 2.9 to 5.1 down to 1.8 M/m. Looking at SBLI. Cylinder is 15.5" downstream of LE. Video captures part of run with Re~=4M/m. Shock structure looks to be on laminar side of transitional - extends much farther upstream than Run 3048.	Schlieren (Olympus)
3050	18/May/2017	Reynolds number sweep from 3.3 to 6.8 M/m. Cylinder is 15.5" downstream of LE. Video captures part of run with Re>=6M/m. Shock structure looks close to turbulent.	Schlieren (Olympus)
3051	22/May/2017	Reynolds number sweep from 3.2 up to 7.1, down to 2.7 M/m. Cylinder is 15.5" downstream of LE. Video captures entire run at 500	Schlieren (Fastcam SA-Z)

		frames per second. Shutter speed is 1/800000 sec. Shock structure is directly influenced by the changing Re.	
3052	23/May/2017	Closely spaced trips removed and blank inserted. Re sweep from 3.2 to 7.0 to 1.7 M/m. Cylinder is 15.5" downstream of LE. Video captures entire run at 500 frames per second. Shutter speed is 1/800000 sec. Shock structure characteristic of laminar BL. Partial tunnel unstart in viewing area (did not reach static pressure tap) in the middle of run as pressure began ramping down.	SC8100, Schlieren (Fastcam SA-Z)
3053	23/May/2017	Blank still in both trip ports. Re held near 4M/m. Cylinder is 15.5" downstream of LE. Captured just over a second of runtime at 60k fps. Video shows 300 consecutive frames of that run spanning 5ms. Shutter speed is 1/800000 sec. Shock structure characteristic of laminar SBLI. Shocks/disturbance waves seem to propagate upward, away from the BL, until they meet the UI shock.	Schlieren (Fastcam SA-Z)
3054	23/May/2017	Closely spaced trips reinserted into upstream trip port. Reynolds number held near 4.5M/m. Cylinder is 15.5" downstream of LE. Captured just over a second of runtime at 60k fps. Video shows 300 consecutive frames of that run spanning 5ms. Shutter speed is 1/800000 sec. Shock structure still characteristic of laminar BL (maybe onset of transitional, but interaction region did not seem to change much).	Schlieren (Fastcam SA-Z)
3055	24/May/2017	Closely spaced trips. Reynolds number held near 5.7M/m. Cylinder is 15.5" downstream of LE. Captured just over a second of runtime at 60k fps. Video shows 300 consecutive frames of that run spanning 5ms. Shutter speed is 1/800000 sec. Shock structure transitional/turbulent.	Schlieren (Fastcam SA-Z)
3056	24/May/2017	Closely spaced trips. Reynolds number held near 5.1M/m. Cylinder is 15.5" downstream of LE. Captured just over a second of runtime at 60k fps. Video shows 300 consecutive frames of that run spanning 5ms. Shutter speed is 1/800000 sec. Shock structure transitional with a larger upstream influence than Run 3055.	Schlieren (Fastcam SA-Z)
3057	26/May/2017	No trips. Re held near 5.3M/m. Cylinder is 15.5" downstream of LE. Captured just over a second of runtime at 360k fps. Reduced resolution of 512 x 64. Shutter speed is 1/800000 sec. Laminar BL shock structure - rectangle focuses on region just below UI shock. Video shows 720 consecutive frames (2ms). Looking at upward movement of disturbance waves.	Schlieren (Fastcam SA-Z)
3058	28/May/2017	Closely spaced trips reinserted into upstream trip port. Used green LED as light source. Reynolds number held near 6.7M/m. Cylinder is 15.5" downstream of LE. Captured just over a second of runtime at 60k fps. Resolution of 896 x 368. Shutter speed of 1/4032000 sec. Near turbulent shock structure. First 300 frames saved at 10fps.	Schlieren (Fastcam SA-Z)
3059	28/May/2017	Closely spaced trips. Reynolds number held near 6.5M/m. Cylinder is 15.5" downstream of LE. Captured just over a second of runtime at 60k fps. Resolution of 896 x 368. Shutter speed of 1/6300000 sec. Near turbulent shock structure. First 300 frames saved at 10fps. More contrast in BL.	Schlieren (Fastcam SA-Z)
3060	28/May/2017	PEEK wedge. Closely spaced trips reinserted into upstream trip port. Used green LED as light source. Re held near 6.3M/m. Cylinder is 15.5" downstream of LE. Captured just over 2 seconds of runtime at 288k fps. Resolution of 256 x 128. Shutter speed of 1/6300000 sec. Near turbulent shock structure. First 300 frames saved at 10fps. More contrast in BL. Screw is 3/4" x 1/4"-20 SHCS.	Schlieren (Fastcam SA-Z)

Tunnel supply regulator serviced. Initial chatter but settled down by these runs Fourth Model: Composite Wedge Model on new removable door. Diffuser height = 7.9" Initial runs (3206-3248) with a 0.5" diameter, 2" tall Teflon cylinder Runs (3249-end) used the familiar 0.75" diameter, 2.25" tall cylinder M=5.88@ Re=3.5M/m, M=5.71@ Re=9.6M/m			
3203	9/Oct/2017	Oil flow on new composite wedge mounted on new door. No trips and an initial band of 50cs orange pigment oil painted right on leading edge. Re of 6.2M/m held for 3 seconds before unstart. Oil did not make it back past the second trip/plasma location. Need more bands/streaks of oil and longer run time.	Oil Flow Visualization
3204	10/Oct/2017	Reynolds number bounds test run. Tunnel stayed started to 118 psia (9.6M/m).	n/a
3205	10/Oct/2017	Held tunnel at 88 psi (Re=6.9M/m) for 12 seconds before manually close ACE supply ball valve to kill flow.	Oil Flow Visualization
3206	11/Oct/2017	Added 0.5" diameter, 2" tall cylinder and ran at 30 psia (Re = 2.4M/m). Held the condition for 20s.	Oil Flow Visualization
3207	11/Oct/2017	Tried to run the same config at Re=7.0M/m. Tunnel unstarted after 12s.	Oil Flow Visualization
Start of a series of diffuser height change runs to optimize for the cylinder configuration			
3208	12/Oct/2017	Diffuser height changed to 8.125". Ramped tunnel up to 7.4M/m. Tunnel unstarted after 2 seconds.	Oil Flow Visualization
3209	12/Oct/2017	Diffuser height changed to 7.75". Ramped tunnel up to 7.1M/m. Tunnel unstarted after 9 seconds.	Oil Flow Visualization
3210	12/Oct/2017	Diffuser height changed to 7.6". Ramped tunnel pressure up to 88 psia. It wandered on its own from 88 to 91 (6.9 to 7.2 M/m) and back again a few times. Brianne closed the manual ball valve at 1600 psia to unstart it. 20 second run.	Oil Flow Visualization
3211	12/Oct/2017	Tried to repeat the same test as 3210. Re held at 7.1M/m. Tunnel unstarted after 14s.	Oil Flow Visualization
3212	13/Oct/2017	Diffuser height changed to 7.5". Re of 7.2M/m held for 6s.	
Diffuser height set at 7 3/8" from here until end of campaign			
3213	13/Oct/2017	Re of 7.0M/m held for 13s. Still no trips.	Oil Flow Visualization
3214	13/Oct/2017	Re held near 5.0M/m for 23 seconds. Resulting oil pattern looks fairly clean.	Oil Flow Visualization
3218	19/Oct/2017	Schlieren using incandescent light source looking at the leading edge of the model. Sampled at 500 fps and 1/20k sec exposure. Re sweep from 3.1 to 1.1 up to 7.7 M/m.	Schlieren (Fastcam SA-Z)
3222	21/Oct/2017	Rigged up a voltage divider as the adjustable power supply got plasma-zapped at SHR. Sampled at 500 fps and 1/200k sec exposure. Re sweep from 3.2 to 1.2 to 7.4 M/m.	Schlieren (Fastcam SA-Z)
3223	21/Oct/2017	Same setup and same exposure but sampled at 140k fps to look at steadiness of flow passing over the leading edge. There appears to be no movement or indication of separation. Re held near 5.2M/m.	Schlieren (Fastcam SA-Z)
Start of schlieren struggles with 0.5" diameter cylinder			
3237	1/Nov/2017	Schlieren using incandescent light source looking at interaction region. Sampled at 500 fps and 1/20k sec exposure. Quality was poor with this long of an exposure. The separation was clearly present	Schlieren (Fastcam SA-Z)

		but flow features were not. Reynolds number sweep from 3.2 up to 7.7 M/m.	
3239	2/Nov/2017	Adjustable Extech 382275 30V, 20A power supply purchased. The red LED was used, set to the power supply maximum 3.4 V and 21.5 A. The frame rate was 500 fps and exposure of 1/4M sec. Re sweep from 3.2 to 8.2 M/m.	HS Schlieren, SC8100
3240	2/Nov/2017	Similar run as 3239, trying to adjust cutoff better during run. Re sweep from 3.2 to 6.7 M/m. The frame rate was 500 fps and exposure of 1/4M sec.	HS Schlieren, SC8100
3241	2/Nov/2017	Again, trying to adjust cutoff, but contrast does not seem to be improving. Re held at 2.4 for a while, then swept up to 4.3 M/m.	HS Schlieren, SC8100
3242	3/Nov/2017	Condenser lens and slit were positioned to put brightest portion (shape of LED) through the slit. The quality did not improve. Re sweep from 3.5 to 2.4 to 5.9 M/m.	HS Schlieren
3244	3/Nov/2017	For Runs 3237-42, optics were not all the same height. This was done to try to match the slope of the model in the tunnel relative to the lab floor and to eliminate glare off the model. Prior to 3244, the optics were made the same height again and the reflection was masked. However, the quality of the schlieren looked the same. Re sweep from 2.5 to 6.2 M/m.	HS Schlieren
3245	4/Nov/2017	Changed optic heights with Bowersox (effort to eliminate reflections off wedge surface). Same quality schlieren. Re swept from 3.0 to 5.3 M/m.	HS Schlieren
3246	6/Nov/2017	Optics changed back and wedge leveled in tunnel. No improvement to quality. Re sweep from 2.5 to 6.6 M/m.	HS Schlieren
3247	6/Nov/2017	Light slit on source side made smaller. This seemed to just make the entire image darker but did not improve the contrast. Re sweep from 2.5 to 6.5 M/m.	HS Schlieren
3248	8/Nov/2017	Substituted the red LED for the green LED which produces more lumens but the SA-Z is less sensitive to that band. The quality of the images was still poor. Re sweep from 2.5 to 6.5 M/m.	HS Schlieren
After this series of runs, it was concluded the optical setup was not the problem The 0.5" diameter cylinder did not produce the same levels of disturbances as the 0.75" diameter cylinder			
3249	8/Nov/2017	Returned to using a 0.75" diameter, 2.25" wooden dowel cylinder. The disturbances were much more distinct in the schlieren. Re sweep from 2.4 to 6.5 M/m.	HS Schlieren
3250	9/Nov/2017	The Re was stepped at 4.5, 5.0, 5.5, and 5.9 M/m (thought to be the transitional range). The rate was 500 fps, capturing the entire run. 1/4M sec shutter. The tunnel unstarted while holding the 5.9M/m condition for some reason.	HS Schlieren
3251	9/Nov/2017	High-speed sampling at 200k fps, reduced resolution, 1/6.3M sec shutter time. Re held near 2.8M/m.	HS Schlieren
3252	9/Nov/2017	Repeat of Run 3251, but more cutoff at light source trying to get more contrast in image. Re held near 2.8M/m. Disturbance waves may be more distinguishable. .tif files saved.	HS Schlieren
3253	9/Nov/2017	Similar fast sampling run at 200k fps. Re held constant around 3.5M/m.	HS Schlieren
3254	9/Nov/2017	Similar sampling. Re held near 4.3M/m.	HS Schlieren
3255	10/Nov/2017	Similar sampling. Re held near 6.4M/m. Vortices appear to roll up and down the cylinder above and below the triple point.	HS Schlieren

3257	12/Nov/2017	Higher frame rate: 480k fps. Shutter 1/6.3M sec. Schlieren resolution restricted to triple point and just above. 100k frames were sampled per trigger (every 3 seconds) with 13 triggers over the course of the run. Re stepped and not adjusted during each sampling. First 3 points before flow established. Images are good but dark. Re = 2.7,3.0,3.3,3.8,4.1,4.4,4.9,5.3,5.5,5.9 M/m.	HS Schlieren
3259	12/Nov/2017	Same style run as 3257 with less cut-off. Re = 2.6,2.8,2.9,3.1,3.3,3.6,4.0,4.2,4.5,4.9 M/m. Not sure if last point at 5.1M/m was captured.	HS Schlieren
3260	12/Nov/2017	Same style run. Wanted to get to higher Reynolds numbers. Re = 3.3,3.6,3.8,4.1,4.4,4.7,5.0,5.1,5.6,5.8 M/m.	HS Schlieren
3261	13/Nov/2017	Region of interest changed to separation shocks. Larger resolution, so frame rate reduced to 200k fps. 40k frames/interval, 14 intervals, 1/6.3M sec shutter. Re = 2.6,2.8,2.9,3.2,3.4,3.7,3.8,4.3,4.4,4.8 M/m	HS Schlieren
3265	21/Nov/2017	IR run looking straight down through the central top window port using the 50-mm IR lens. Re sweep from 2.8 to 7.5 M/m.	SC8100
3266	21/Nov/2017	IR run looking from upstream, with the camera rotated ~30° looking back at the wooden cylinder to see the heating pattern from the interaction and other tunnel features, like the trip shocks and interface shock. Re sweep from 2.6 to 7.5 M/m.	SC8100
Start of interaction oil flow campaign Thin coat of fluorescent oil mixture painted on entire PEEK insert just before model insertion Reynolds number set and held for ~15 seconds			
3267	22/Nov/2017	Re set at 3.0M/m. Oil looked smeared and messy. Repeated this condition in Run 3270.	Oil Flow Visualization
3268	22/Nov/2017	Re set at 3.7M/m. Oil looked smeared and messy. Repeated this condition in Run 3271.	Oil Flow Visualization
3269	22/Nov/2017	Cleaned wedge much more thoroughly with acetone before this run and all other oil flow runs. Re set at 4.6M/m. Measured separation distance between 3.3-3.9*d*.	Oil Flow Visualization
3270	22/Nov/2017	Re set at 2.8M/m. Measured separation distance between 5.2-5.5*d*.	Oil Flow Visualization
3271	22/Nov/2017	Re set at 3.6M/m. Measured separation distance between 5.0-5.2*d*.	Oil Flow Visualization
3272	27/Nov/2017	Re set at 5.4M/m. Measured separation distance between 3.2-3.8d.	Oil Flow Visualization
3273	27/Nov/2017	Re set at 6.1M/m. Measured separation distance between 2.8-3.4d.	Oil Flow Visualization
3274	27/Nov/2017	Re set at 6.9M/m. Measured separation distance between 2.5-2.7*d*.	Oil Flow Visualization
3276	28/Nov/2018	Re set at 7.6M/m. Measured separation distance between 2.5-2.7*d*.	Oil Flow Visualization
3277	28/Nov/2018	Re set at 4.2M/m. Measured separation distance between 3.8-4.5*d*.	Oil Flow Visualization
Tunnel freestream characterization at model LE streamwise location 4.18" DS of Nozzle-Test Section Interface			
3290	20/Jan/2018	Pitot probe mounted on sting through the top central window port. The tip of the probe was centered on the span and centered	Kulite XCEL-100-5A

		heightwise. The tunnel was started around 3.0M/m, ramped down to 1.8 and up to 6.5M/m. Points 24 to 129 apply. Data were sampled in 200ms increments at 200kHz. Low-pass filtered using Krohn-Hite 8-pole Bessel filter at 100kHz. Noticed a weird 60kHz peak, so decided to sample faster.	
3291	21/Jan/2018	Similar run as 3290 but sampled at 400kHz. Re sweep from 2.3 to 6.7 M/m. Points 21 to 98 apply.	Kulite XCEL-100-5A
3340	14/Mar/2018	Wire was positioned in same location as pitot probe. Sampled in 100ms increments at 500kHz and filtered at 200kHz. Re swept from 1.7 to 5.8, down to 1.1 M/m. Points [30:78,84:135,139:172] apply. There were two brief unstarts on the ramp down. The ramp down temperature was 433 +-3 K. Cal coeff (temp norm-see 3346) a=0.7694, n=0.7359, b=2.066.	AA Systems Hot-wire Anemometer
3341	15/Mar/2018	Repeatability run. Re sweep up from 1.7 to 5.5 M/m. Ramp down unstarted frequently at first but able to get to 0.5M/m.	Hot-wire
3346	20/Mar/2018	Hot-wire calibration run for 0.25 micro-inch (6.3 micro) TSI platinum iridium hot-wire, S/N 71331007. Positioned 2.5" downstream of nozzle/test section interface on center. Reynolds number sweep was from 1.7 up to 5.9, down to 0.55 M/m. Power law curve fit y=a*x^n+b established, where y=(Bridge Voltage)^2, x=rho*u, and a,b,c are constants. a=0.499, n=0.859, b=2.456 for points (118) starting at Re=5.52, ramp to max, and ramp down to 0.55 M/m. Up and down with temperature normalization (i.e. y=(Bridge Voltage)^2*T_t/430K) yields constants A=0.599, n=0.804, b=2.298. HW ovh set to 0.8.	Hot-wire
3349	27/Mar/2018	Calibration of the wire behind the leading-edge shock. Wire was positioned 2" downstream of the PEEK interface on the model and 9mm below the oblique shock. Later learned that every calibration will be different behind the shock depending on the location (shock curvature). Re sweep from 1.9 to 6.1 to 0.5 M/m.	Hot-wire
3350	30/Mar/2018	Prior to this run a thru hole was drilled in the rear corner of the model opposite the strut mount. A threaded rod allowed the model to be fixed to the tunnel to help consistently level the model within 0.1°. This run started at the location of 3349 and traversed up 25mm. Timing did not work for this run and needed to be repeated. Re held near 4.9M/m.	Hot-wire
3351	30/Mar/2018	Repeat of 3350. Moved 25mm in 0.5mm steps across the LE shock. Schlieren were taken at 500fps for the run, but the intersection of the LE shock and wire was already out of view. Fluctuation levels indicate the crossing of 3 features on this traverse. Re held near 4.8M/m.	Hot-wire and HS Schlieren
Start of Boundary layer survey campaign - With trips, no cylinder Hot-wire surveys sampled at 500kHz for 100ms at each point Schlieren (Fastcam SA-Z) was used to track the vertical distance of the wire off the wedge during the traverse The SC8100 indicated when the wire turned on and its spanwise location and relation to heat streaks The 50-mm IR lens was used, usually looking back at the probe at some angle			
3354	2/Apr/2018	Dummy probe positioned above front/center PCB located 1" DS of PEEK interface on model. IR camera angled to look back at probe through the top front window port. Schlieren through the downstream window. Wakes from trips do not look as uniform as remembered. Re held constant at 4.9M/m.	SC8100, HS Schlieren

3355	2/Apr/2018	Traverse was removed and IR camera was shifted to be above center window. This run showed that the streaks take distance to develop uniformity at Re near 5M/m.	SC8100
3356	2/Apr/2018	Dummy probe looking at movement during start/unstart and a traverse. There is a slight shift in either the model or traverse <1mm prompted by the start. Schlieren is necessary to estimate distance off model. Re held near 4.9M/m.	SC8100, HS Schlieren
3357	3/Apr/2018	Re held near 5.0M/m. x=187mm downstream of leading edge. z=-0.7mm off centerspan. The wire was traversed from 1.5 to 10.9 mm above the surface. Points were repeated during this survey to determine if the same signal was given after traverse motion. Points 9 to 47 are valid. This first group was taken near the most upstream SBLI influence location, near the centerspan - just upstream of the PCB port located there.	Hot-wire, SC8100, HS Schlieren
3358	3/Apr/2018	Re held near 4.9M/m. x=187mm downstream of leading edge. z=-0.7mm off centerspan. The wire was traversed from 2.9 to 21.9 mm above the surface. This survey was in the same position as Run 3357 and the resultant survey and fluctuation levels look similar. Points 7 to 54 are valid.	Hot-wire, SC8100, HS Schlieren
3359	3/Apr/2018	Re held near 5.0M/m. x=187mm downstream of leading edge. z=0.9mm off centerspan. The wire was traversed from 2.5 to 19.0 mm above the surface. Points 7 to 42 are valid.	Hot-wire, SC8100, HS Schlieren
3360	4/Apr/2018	Re held near 4.9M/m. x=187mm downstream of leading edge. z=3.4mm off centerspan. The wire was traversed from 3.2 to 21.7 mm above the surface. Points 7 to 45 are valid.	Hot-wire, SC8100, HS Schlieren
3361	4/Apr/2018	Re held near 4.8M/m. x=187mm downstream of leading edge. z=-2.5mm off centerspan. The wire was traversed from 3.4 to 21.4 mm above the surface. Points 7 to 44 are valid.	Hot-wire, SC8100, HS Schlieren
3362	4/Apr/2018	Re held near 4.8M/m. x=187mm downstream of leading edge. z=-4.1mm off centerspan. The wire was traversed from 2.8 to 18.8 mm above the surface. Points 7 to 40 are valid.	Hot-wire, SC8100, HS Schlieren
3363	4/Apr/2018	Re held near 4.9M/m. x=187mm downstream of leading edge. z=-6.1mm off centerspan. The wire was traversed from 3.0 to 17.5 mm above the surface. Points 7 to 37 are valid.	Hot-wire, SC8100, HS Schlieren
3364	5/Apr/2018	Re held near 5.1M/m. x=187mm downstream of leading edge. z=-24.6mm off centerspan. The wire was traversed from 2.4 to 16.4 mm above the surface. This group was taken near the most upstream SBLI influence location, off the centerspan where the trip wakes appeared more distinct. Points 7 to 36 are valid.	Hot-wire, SC8100, HS Schlieren
3365	5/Apr/2018	Re held near 5.0M/m. x=187mm downstream of leading edge. z=-24.0mm off centerspan. The wire was traversed from 2.2 to 20.7 mm above the surface. Points 7 to 45 are valid.	Hot-wire, SC8100, HS Schlieren
3366	5/Apr/2018	Re held near 4.9M/m. x=187mm downstream of leading edge. z=-24.2mm off centerspan. The wire was traversed from 3.1 to 19.1 mm above the surface. Points 7 to 40 are valid.	Hot-wire, SC8100, HS Schlieren
3367	5/Apr/2018	Re held near 5.0M/m. x=187mm downstream of leading edge. z=-29.0mm off centerspan. The wire was traversed from 2.7 to 20.2 mm above the surface. Points 7 to 43 are valid.	Hot-wire, SC8100, HS Schlieren
3368	5/Apr/2018	Re held near 5.1M/m. x=187mm downstream of leading edge. z=-27.2mm off centerspan. The wire was traversed from 2.7 to 22.2 mm above the surface. Points 7 to 47 are valid.	Hot-wire, SC8100, HS Schlieren

3369	6/Apr/2018	Failed run. Traverse jam	Hot-wire, SC8100, HS Schlieren
3370	6/Apr/2018	Re held near 4.8M/m. x=187mm downstream of leading edge. z=-24.8mm off centerspan. The wire was traversed from 3.2 to 21.7 mm above the surface. Points 7 to 45 are valid.	Hot-wire, SC8100, HS Schlieren
3371	6/Apr/2018	Re held near 5.0M/m. x=213mm downstream of leading edge. z=-1.6mm off centerspan. The wire was traversed from 2.7 to 19.7 mm above the surface. This group was taken near the centerspan about an inch downstream of the first group - near another PCB port. Points 7 to 42 are valid.	Hot-wire, SC8100, HS Schlieren
3372	6/Apr/2018	Re held near 5.0M/m. x=213mm downstream of leading edge. z=2.0mm off centerspan. The wire was traversed from 2.8 to 21.3 mm above the surface. Points 7 to 45 are valid.	Hot-wire, SC8100, HS Schlieren
3373	7/Apr/2018	Re held near 5.1M/m. x=213mm downstream of leading edge. z=-1.0mm off centerspan. The wire was traversed from 3.2 to 15.6 mm above the surface. Points 7 to 33 are valid.	Hot-wire, SC8100, HS Schlieren
3374	7/Apr/2018	Re held near 4.9M/m. Start of Leading-Edge Shock traversing runs. x=106mm downstream of LE at approximate centerspan. Traversed from 16.4 to 46.4 mm above surface. This location also crossed the trips shock. Points 1 to 33 are valid.	Hot-wire, SC8100, HS Schlieren
3375	7/Apr/2018	Re held near 5.0M/m. x=106mm downstream of LE at approximate centerspan. Same placement and goals as Run 3374, different traversing steps. Traversed from 16.1 to 42.1 mm above surface. Points 1 to 38 are valid.	Hot-wire, SC8100, HS Schlieren
3376	7/Apr/2018	Re held near 4.9M/m. x=58mm downstream of LE at approximate centerspan (located upstream of trips). Traversed from 16.9 to 36.9 mm above surface. Points 1 to 43 are valid.	Hot-wire, SC8100, HS Schlieren
3377	8/Apr/2018	Re held near 5.1M/m. x=82mm downstream of LE at approximate centerspan. Picks up trips shock and shear layer as well. Traversed from 5.8 to 38.8 mm above surface. Points 1 to 43 are valid.	Hot-wire, SC8100, HS Schlieren
3378	8/Apr/2018	Re held near 5.0M/m. x=264mm downstream of LE at z=9.9mm. Traversed from 5.6 to 29.6 mm above surface. Start of boundary layer surveys farther downstream. Points 13 to 35 are valid. (Probe wire grounded to tunnel for points 1 to 12).	Hot-wire, SC8100, HS Schlieren
3379	8/Apr/2018	Re held near 4.9M/m. x=264mm downstream of LE at z=9.9mm. Traversed from 5.4 to 29.4 mm above surface. Points 1 to 43 are valid.	Hot-wire, SC8100, HS Schlieren
3380	9/Apr/2018	Re held near 5.0M/m. x=264mm downstream of LE at z=0.0mm. Traversed from 3.8 to 28.8 mm above surface. Points 1 to 42 are valid.	Hot-wire, SC8100, HS Schlieren
3381	9/Apr/2018	Re held near 4.9M/m. x=276mm downstream of LE at z=0.6mm. Traversed from 4.3 to 32.3 mm above surface. Points 1 to 41 are valid.	Hot-wire, SC8100, HS Schlieren
3382	9/Apr/2018	Re held near 4.9M/m. x=302mm downstream of LE at z=0.6mm. Traversed from 3.2 to 28.1 mm above surface. Points 1 to 39 are valid.	Hot-wire, SC8100, HS Schlieren
3383	9/Apr/2018	Re held near 7.2M/m, but a short run to see if tunnel would stay started with dummy probe.	SC8100, HS Schlieren

3384	10/Apr/2018	Re held near 7.5M/m, but a short run. x=302mm downstream of LE at z=0.5mm. Traversed from 3.5 to 28.5 mm above surface. Points 1 to 16 are valid.	Hot-wire, SC8100, HS Schlieren
3385	10/Apr/2018	Re held near 7.5M/m, but a short run. x=302mm downstream of LE at z=0.8mm. Traversed from 3.4 to 28.4 mm above surface. Points 1 to 18 are valid.	Hot-wire, SC8100, HS Schlieren
3386	10/Apr/2018	Re held near 7.0M/m. Traverse jam.	Hot-wire, SC8100, HS Schlieren
3387	10/Apr/2018	Re held near 6.9M/m. x=302mm downstream of LE at z=1.0mm. Traversed from 2.3 to 27.2 mm above surface. Points 1 to 40 are valid.	Hot-wire, SC8100, HS Schlieren
3388	10/Apr/2018	Re sweep from 2.4, up to 7.4, and back down to 3.5M/m. Hot-wire probe was held in a fixed position where fluctuation levels seemed the highest in Run 3387. The position was x=302, y=10.0, z=0.8 mm. Points 2 to 86 are valid.	Hot-wire, SC8100, HS Schlieren
3389	11/Apr/2018	Re sweep from 1.8 to 5.0 to 0.6 M/m. Hot-wire probe was held in a fixed position where fluctuation levels seemed the highest in Run 3387. The position was x=302, y=10.0, z=0.8 mm. This run was done because Run 3388 did not go low enough and stopped right where the fluctuation levels increased due to the spike in F.S. noise near 3-3.5M/m. Points 2 to 117 are valid.	Hot-wire, SC8100, HS Schlieren
3390	11/Apr/2018	Re held near 7.5M/m, but run cut short by the tunnel unstarting and the wire breaking. x=346mm downstream of LE at z=0.8mm. Traversed from 3.0 to 20.0 mm above surface. Points 5 to 27 are valid.	Hot-wire, SC8100
Start of Surface Pressure (PCB and Kulite) Measurements Campaign Baseline Measurements: Trips and No Cylinder The SC8100 looked at heating and trip wakes in relation to the sensors			
3391	12/Apr/2018	Re sweep up from 2.7 to 8.3 M/m. Tunnel unstarted on way down at 7.7. Restarted from 7.3 down to 0.7 M/m. Points (52:59,74:150) apply. Sensor config included 5 PCBs and 3 Kulites, most sensors on centerspan. 100ms sample at 2MHz. PCBs filtered at 1MHz (K-H 8-pole Bessel for 4, SRS for 1). Kulites filtered at 200kHz (K-H 8-pole Bessel).	PCBs, Kulites, SC8100
3392	13/Apr/2018	Same configuration as Run 3391. Re stepped: 7.2, 6.0, 5.4, 4.9, 4.5, 4.0, 3.5, 3.1 M/m. 1.5s samples while holding condition. Points 4 to 11 apply.	PCBs, Kulites, SC8100
3393	14/Apr/2018	Re sweep up from 2.1 to 8.3 M/m. Tunnel unstarted on way down at 7.8. Restarted from 6.8 down to 0.8 M/m. Points (47:50,71:140) apply. Sensor config included 5 PCBs and 3 Kulites, looking at spanwise variation at same streamwise position (first PCB and Ku-lite rows). 100ms samples.	PCBs, Kulites, SC8100
3394	14/Apr/2018	Same configuration as Run 3393. Re stepped: 7.2, 5.5, 5.0, 4.5, 4.1, 3.6, 3.2, 2.7, 2.4 M/m. 1.5s samples while holding condition. Points 4 to 12 apply.	PCBs, Kulites, SC8100
3395	15/Apr/2018	Re sweep up from 2.4 to 8.4 M/m. Tunnel unstarted on way down at 8.3. Restarted then unstarted and restarted from 6.8 down to 2.2 M/m. Points (84:155) apply. Sensor config included 5 PCBs and 3 Kulites, looking at spanwise variation at same streamwise posi-tion (2nd PCB row, first Kulite row). 100ms samples.	PCBs, Kulites, SC8100
3396	15/Apr/2018	Non-run. Tunnel supply ball valve mishap.	PCBs, Kulites, SC8100

3397	15/Apr/2018	Re sweep up from 2.1 to 6.4 to 3.2 M/m. Points (21:53) ramp up; points (54:110) ramp down. Goal of a clean run without an unstart. Sensor config same as Run 3395. 100ms samples.	PCBs, Kulites, SC8100
3398	15/Apr/2018	Re sweep up from 2.3 to 8.5 to 3.0 M/m. Points (41:123) apply. Sensor config same as Run 3395. 100ms samples.	PCBs, Kulites, SC8100
3399	16/Apr/2018	Re sweep run that unstarted twice. Sampled for 1s by mistake. Will redo.	PCBs, Kulites, SC8100
3400	16/Apr/2018	Re sweep up from 2.2 to 8.4 M/m. Tunnel unstarted on way down at 8.0. Restarted from 7.1 down to 3.1 M/m. Points (60:118) apply. Sensor config included 5 PCBs and 4 Kulites, looking at outboard PCBs and 2nd row of Kulites. 100ms samples.	PCBs, Kulites, SC8100
3401	16/Apr/2018	Same configuration as Run 3400. Re stepped: 7.0, 5.6, 4.6, 4.0 M/m. 1.5s samples while holding condition. Points 4,7 to 9 apply.	PCBs, Kulites, SC8100
3402	17/Apr/2018	Re sweep up from 2.4 to 8.5 M/m. Restarted from 6.7 down to 2.5 M/m. Points (61:127) apply. Sensor config included 5 PCBs and 4 Kulites, looking at spanwise variation at same streamwise position (second PCB and Kulite rows). 100ms samples.	PCBs, Kulites, SC8100
3403	17/Apr/2018	Re sweep up from 2.5 to 7.6 M/m. Restarted from 7.3 down to 2.7 M/m. Points (53:110) apply. Same config as Run 3402. 100ms samples.	PCBs, Kulites, SC8100
IR Runs using similar Reynolds number sweep M=5.9@ Re=3.0M/m, M=5.77@ Re=7.0M/m			
3421	25/Apr/2018	Re sweep starting at 4.0, down to 2.0, back up to 8.0 M/m. Trip configuration with no cylinder. Schlieren looking at incoming boundary layer.	SC8100, HS Schlieren
3422	25/Apr/2018	Re sweep starting at 4.0, down to 2.1, back up to 7.6 M/m. Trip configuration with new cylinder (see below). Schlieren at 500 fps, 1.25 µs shutter.	SC8100, HS Schlieren
Surface Pressure (PCB and Kulite) Campaign Measurements: Trips and 0.75" diameter, 2.25" tall black PEEK cylinder			
3424	26/Apr/2018	Re sweep up from 1.8 to 8.0 M/m. Tunnel unstarted on way down at 7.5. Restarted from 6.8 down to 2.4 M/m. Points (65:137) apply. Sensor config included 5 PCBs and 3 Kulites, most sensors on centerspan. 100ms samples at 2MHz. PCBs filtered at 1MHz (K-H 8-pole Bessel for 4, SRS for 1). Kulites filtered at 200kHz (K-H 8-pole Bessel). IR down on wedge straight through top center window.	HS Schlieren, PCBs, Kulites, SC8100
3425	27/Apr/2018	Reynolds number stepped, Re = 6.6, 5.9, 5.6, 4.8 M/m (points 3 to 6). Same sensor config as 3424. Sampling for 1.5s. IR straight down on wedge. Schlieren resolution reduced (456 x 128) looking at separation shocks. 150k fps. Collected 50k frames (0.333s) every 6 seconds, corresponding to the stepped Re. Same 1.25 µs exposure.	HS Schlieren, PCBs, Kulites, SC8100
3426	27/Apr/2018	Reynolds number stepped, Re = 6.2, 5.3, 4.8, 4.4, 4.1 M/m (points 3 to 7). Same sensor config as 3424. Sampling for 1.5s. IR angled back to look at face of cylinder/near interaction of wedge. Schlieren resolution reduced (120 x 256) looking at the jet and cylinder base. 240k fps. Collected 50k frames (0.208s) every 6 seconds, corresponding to the stepped Re. Same 1.25 µs exposure.	HS Schlieren, PCBs, Kulites, SC8100
3427	27/Apr/2018	Re sweep down from 3.8 to 2.0 and up to 7.7 M/m. Clean run, tunnel stayed started. Points (45:124) apply. Sensor config included 5 PCBs and 4 Kulites, looking at spanwise variation at same streamwise position (first PCB and Kulite rows). 100ms samples. Schlieren	HS Schlieren, PCBs, Kulites, SC8100

		sampled at 500 fps. IR down on wedge straight through top center window.	
3428	27/Apr/2018	Reynolds number stepped, Re = 6.7, 5.7, 5.3, 4.8, 4.6, 3.9 (points 2 to 7). Same sensor config as 3427. Sampling for 1.5s. IR straight down on wedge. Schlieren resolution reduced (456 x 128) looking at separation shocks. 150k fps. Collected 50k frames (0.333s) every 6 seconds, corresponding to the stepped Re. Same 1.25 µs exposure.	HS Schlieren, PCBs, Kulites, SC8100
3429	27/Apr/2018	Reynolds number stepped, Re = 6.6, 5.4, 4.4, 3.8, 3.1 M/m (points 4 to 8). Same sensor config as 3427. Sampling for 1.5s. IR angled back to look at face of cylinder/near interaction of wedge. Schlieren resolution reduced (120 x 256) looking at the jet and cylinder base. 240k fps. Collected 50k frames (0.208s) every 6 seconds, corresponding to the stepped Re. Same 1.25 µs exposure.	HS Schlieren, PCBs, Kulites, SC8100
3436	28/Apr/2018	Re sweep up from 2.5 to 8.2 M/m. Tunnel unstarted on way down at 7.5. Restarted from 7.4(6.6?- steep sweep at beginning) down to 1.9 M/m. Points (56:150) apply. Sensor config included 5 PCBs and 4 Kulites, looking at spanwise variation at same streamwise position (second PCB and Kulite rows). 100ms samples. Schlieren sampled at 500 fps. IR down on wedge straight through top center window.	HS Schlieren, PCBs, Kulites, SC8100
3439	28/Apr/2018	Reynolds number stepped, Re = 6.9, 5.9, 5.3, 4.9, 4.5, 3.8, 3.2 (points 2 to 8). Same sensor config as 3436. Sampling for 1.5s. IR straight down on wedge. Schlieren resolution reduced (456 x 128) looking at separation shocks. 150k fps. Collected 50k frames (0.333s) every 6 seconds, corresponding to the stepped Re. Same 1.25 µs exposure.	HS Schlieren, PCBs, Kulites, SC8100
3441	28/Apr/2018	Reynolds number stepped, Re = 7.3, 5.6, 5.2, 4.7, 4.4, 4.1 M/m (points 3 to 8). Same sensor config as 3436. Sampling for 1.5s. IR angled back to look at face of cylinder/near interaction of wedge. Schlieren resolution reduced (120 x 256) looking at the jet and cylinder base. 240k fps. Collected 50k frames (0.208s) every 6 seconds, corresponding to the stepped Re. Same 1.25 µs exposure.	HS Schlieren, PCBs, Kulites, SC8100
3442	29/Apr/2018	Re sweep up from 2.1 to 8.4 M/m. Tunnel unstarted on way down at 8.2. Restarted from 7.7 down to 2.7 M/m. Points (45:139) apply. Sensor config included 5 PCBs and 3 Kulites, outboard PCBs, downstream Kulites. 100ms samples. Schlieren sampled at 500 fps. IR down on wedge straight through top center window.	HS Schlieren, PCBs, Kulites, SC8100
3443	29/Apr/2018	Reynolds number stepped, Re =6.9, 5.6, 5.2, 4.8, 4.3, 3.7 (points 3 to 8). Same sensor config as 3442. Sampling for 1.5s. IR straight down on wedge. Schlieren resolution reduced (456 x 128) looking at separation shocks. 150k fps. Collected 50k frames (0.333s) every 6 seconds, corresponding to the stepped Re. Same 1.25 µs exposure.	HS Schlieren, PCBs, Kulites, SC8100
3444	29/Apr/2018	Reynolds number stepped, Re = 6.8, 5.8, 5.3, 4.7, 4.0, 3.3 M/m (points 2 to 7). Same sensor config as 3442. Sampling for 1.5s. IR angled back to look at face of cylinder/near interaction of wedge. Schlieren resolution reduced (120 x 256) looking at the jet and cylinder base. 240k fps. Collected 50k frames (0.208s) every 6 seconds, corresponding to the stepped Re. Same 1.25 µs exposure.	HS Schlieren, PCBs, Kulites, SC8100
Surface Pressure (PCB and Kulite) Campaign Measurements: Without Trips and With 0.75" Diameter, 2.25" Tall black PEEK Cylinder			

3458	5/May/2018	Re sweep up from 2.7 to 8.8 M/m. Tunnel unstarted on way down at 8.4. Restarted from 7.5 down to 2.2 M/m. Points (48:140) apply. Sensor config included 5 PCBs and 3 Kulites, most sensors on centerspan. 100ms samples at 2MHz. PCBs filtered at 1MHz (K-H 8-pole Bessel for 4, SRS for 1). Kulites filtered at 200kHz (K-H 8-pole Bessel). Schlieren sampled at 30 fps. Exposure 1.25 µs. IR down on wedge straight through top center window.	HS Schlieren, PCBs, Kulites, SC8100
3459	5/May/2018	Reynolds number stepped, Re = 6.9, 5.5, 5.0, 4.6, 4.2 (points 3 to 6, 7?-psd higher at low f). Same sensor config as 3458. Sampling for 1.5s. IR straight down on wedge. Schlieren resolution reduced (456 x 128) looking at separation shocks. 150k fps. Collected 50k frames (0.333s) every 6 seconds, corresponding to the stepped Re. Same 1.25 µs exposure.	HS Schlieren, PCBs, Kulites, SC8100
3460	5/May/2018	Reynolds number stepped, Re = 6.1, 4.9, 4.3, 3.6, 3.2 M/m (points 3 to 7). Same sensor config as 3458. Sampling for 1.5s. IR angled back to look at face of cylinder/near interaction of wedge (not focused). Schlieren resolution reduced (120 x 256) looking at the jet and cylinder base. 240k fps. Collected 50k frames (0.208s) every 6 seconds, corresponding to the stepped Re. Same 1.25 µs exposure.	HS Schlieren, PCBs, Kulites, SC8100
3461	6/May/2018	Re sweep up from 2.7 to 8.7 M/m. Tunnel unstarted on way down almost immediately. Restarted from 7.3 to 2.3 M/m. Points (54:150) apply. Sensor config included 5 PCBs and 4 Kulites, looking at spanwise variation at same streamwise position (first PCB and Kulite rows). 100ms samples. Schlieren sampled at 500 fps. IR looking back on cylinder face.	HS Schlieren, PCBs, Kulites, SC8100
3462	6/May/2018	Reynolds number stepped, Re = 6.4, 5.6, 5.1, 4.6, 4.2 (points 4 to 8, HS schlieren for 4-7). Same sensor config as 3461. Sampling for 1.5s. IR straight down on wedge. Schlieren resolution reduced (456 x 128) looking at separation shocks. 150k fps. Collected 50k frames (0.333s) every 6 seconds, corresponding to the stepped Re. Same 1.25 µs exposure.	HS Schlieren, PCBs, Kulites, SC8100
3463	6/May/2018	Reynolds number stepped, Re = 6.4, 5.8, 5.2, 4.8 M/m (points 5 to 8). Same sensor config as 3461. Sampling for 1.5s. IR angled back to look at face of cylinder/near interaction of wedge (not focused). Schlieren resolution reduced (120 x 256) looking at the jet and cylinder base. 240k fps. Collected 50k frames (0.208s) every 6 seconds, corresponding to the stepped Re. Same 1.25 µs exposure.	HS Schlieren, PCBs, Kulites, SC8100
3464	7/May/2018	DAQ failed to record.	HS Schlieren, PCBs, Kulites, SC8100
3466	7/May/2018	Re sweep down from 3.8 to 2.0 and up to 7.7 M/m. Clean run, tunnel stayed started. Points (45:124) apply. Sensor config included 5 PCBs and 4 Kulites, looking at spanwise variation at same streamwise position (second PCB and Kulite rows). 100ms samples. Schlieren sampled at 500 fps. IR down on wedge straight through top center window (out of focus).	HS Schlieren, PCBs, Kulites, SC8100
3467	7/May/2018	Reynolds number stepped, Re = 8.0, 6.6, 5.8, 5.3, 4.9, 4.3 (points 2, 4-8). Same sensor config as 3465. Sampling for 1.5s. IR straight down on wedge. Schlieren resolution reduced (456 x 128) looking at separation shocks. 150k fps. Collected 50k frames (0.333s) every 6 seconds, corresponding to the stepped Re. Same 1.25 µs exposure.	HS Schlieren, PCBs, Kulites, SC8100
3468	8/May/2018	Reynolds number stepped, Re = 6.1, 5.3, 4.7, 4.4, 4.0, 3.3 M/m (points 3 to 8). Same sensor config as 3465. Sampling for 1.5s. IR	HS Schlieren, PCBs, Kulites, SC8100

		angled back to look at face of cylinder/near interaction of wedge. Schlieren failed due to optical blockage.	
Surface Pressure (PCB and Kulite) Campaign Measurements: Without Trips and Without Cylinder			
3469	8/May/2018	Quick Re ramp from 1.9 to 7.9 and slow ramp down to 2.0 M/m. Clean IR run without unstart. Schlieren looking at incoming BL. 100ms samples.	PCBs, Kulites, SC8100, HS Schlieren
Surface Pressure (PCB and Kulite) Campaign Measurements: Without Trips and Without Cylinder - Hot-wire Boundary Layer Surveys Hot-wire surveys sampled at 500kHz for 100ms at each point			
3470	8/May/2018	Re held near 4.8M/m. Traverse jam and DAQ error, no HW/sensor data.	Hot-wire, PCBs, Kulites, SC8100, HS Schlieren
3471	9/May/2018	Re held near 4.9M/m. x=187mm downstream of leading edge. z=0.4mm off centerspan. The wire was traversed from 1.6 to 21.6 mm above the surface. This group (3471-73) was taken at the same upstream location as Runs 3357-63 (those with trips). Points 1 to 35 are valid. 36 to 38 sweep down, but some higher signal in p-sensors. 30 ends traverse. 100ms samples.	Hot-wire, PCBs, Kulites, SC8100, HS Schlieren
3472	9/May/2018	Re held near 4.8M/m. x=187mm downstream of leading edge. z=-1.6mm off centerspan. The wire was traversed from 1.6 to 21.6 mm above the surface. Points 1 to 44 are valid. 45 to 48 sweep down. 38 ends traverse. 100ms samples.	Hot-wire, PCBs, Kulites, SC8100, HS Schlieren
3473	9/May/2018	Re held near 4.7M/m. x=187mm downstream of leading edge. z=0.0mm off centerspan. The wire was traversed from 1.6 to 21.6 mm above the surface. Points 1 to 38 are valid. 39 to 46 sweep down. 38 ends traverse. 100ms samples.	Hot-wire, PCBs, Kulites, SC8100, HS Schlieren
3474	10/May/2018	Re held near 4.7M/m. x=293mm downstream of leading edge. z=-1.2mm off centerspan. The wire was traversed from 1.6 to 21.6 mm above the surface. Points 1 to 42 are valid. 43 to 56 downsweep. 36 ends traverse. 100ms samples.	Hot-wire, PCBs, Kulites, SC8100, HS Schlieren
3475	10/May/2018	Re held near 4.9M/m. x=293mm downstream of leading edge. z=0.7mm off centerspan. The wire was traversed from 1.6 to 21.6 mm above the surface. Points 1 to 46 are valid. 47 to 57 downsweep. 36 ends traverse. 100ms samples.	Hot-wire, PCBs, Kulites, SC8100, HS Schlieren
Surface Pressure (PCB and Kulite) Campaign Measurements: Cylinder Wake Study - Hot-wire			
3476	11/May/2018	The hot-wire was positioned above K3(SN725) and traversed from 40 to 20 to 40 mm above surface (Points 1 to 21). Re held constant near 4.9M/m. 400ms samples. No trips.	Hot-wire, SC8100
3477	11/May/2018	The hot-wire was positioned at the coordinates suggested by Danehy and tested by Wheaton, HW at x''= 1.7*d* downstream of center, z' = 2.0*d* lateral of center. The wire was traversed from 3.0 to 25.0 (Points 6 to 28). Re held constant near 4.7M/m. 400ms samples. No trips.	Hot-wire, SC8100
3478	13/May/2018	The traverse jammed during this run. No data collected.	Hot-wire, SC8100
3479	13/May/2018	Same position and traverse as Run 3477. Trips were reinserted into the model. Re held constant near 4.9M/m. 400ms samples.	Hot-wire, SC8100
3480	14/May/2018	Hot-wire fixed in same position at a height of y= 5mm. Reynolds number was swept from 4.4 to 5.8 to 1.9 M/m. Points 6:118 apply. 100ms samples.	Hot-wire, SC8100

3481	14/May/2018	Hot-wire calibration run for same wire, S/N 71331006. Re sweep was from 2.6 up to 5.7, down to 0.72 M/m. Power law curve fit y=a*x^n+b established, where y=(Bridge Voltage)^2, x=rho*u, and a,b,c are constants. a=0.495, n=0.824, b=2.333 for points (153) starting at Re=5.69 ramped down to 0.72 M/m. Up and down with temperature normalization (i.e. y=(Bridge Voltage)^2*T_t/430K) yields constants A=0.586, n=0.776, b=2.168. HW ovh set to 0.8. 100ms samples.	Hot-wire
Surface Pressure (PCB and Kulite) Campaign Measurements: Swept Cylinder With Trips			
3482	17/May/2018	15° swept back cylinder. Tunnel unstarted several times. Last continuous segment provided some points. 100ms samples (pts 98-143).	HS Schlieren, PCBs, Kulites, SC8100
3483	17/May/2018	15° swept back cylinder. Repeat of Run 3482 trying to get those higher Re. 100ms samples (pts 36-147).	HS Schlieren, PCBs, Kulites, SC8100
3484	17/May/2018	15° swept back cylinder. The interaction is so small that only 1 fast schlieren run is needed. Re stepped (points 3-8): 7.0, 6.1, 5.7, 5.3, 4.7, 4.3. 208 x 256 resolution, 200k fps, 50k images, 1.25 µs. 1.5s samples.	HS Schlieren, PCBs, Kulites, SC8100
3485	17/May/2018	30° swept back cylinder. 100ms samples (pts 50-151).	HS Schlieren, PCBs, Kulites, SC8100
3486	18/May/2018	30° swept back cylinder. 1.5s samples looking at interaction. The interaction is so small that only 1 fast schlieren run is needed. Re stepped (points 4-8): 6.9, 6.1, 5.7, 5.3, 4.9. 208 x 256 resolution, 200k fps, 50k images, 1.25 µs.	HS Schlieren, PCBs, Kulites, SC8100
3487	18/May/2018	15° swept forward cylinder. 100ms samples (pts 33-127).	HS Schlieren, PCBs, Kulites, SC8100
3488	18/May/2018	15° swept forward cylinder. 1.5s samples looking at jet/base. Re stepped (points 3-9): 7.1, 6.1, 5.6, 5.1, 4.7, 4.2, 3.6. 216 x 256 resolution, 200k fps, 50k images, 1.25 µs.	HS Schlieren, PCBs, Kulites, SC8100
3489	18/May/2018	15° swept forward cylinder. 1.5s samples looking at separation shock. Re stepped (points 3-9): 7.4, ?, 5.3, 5.9, 4.5, 4.1, and 3.4 M/m. Point 4 is questionable but schlieren indicates tunnel was started. 256 x 256 resolution, 150k fps, 50k images, 1.25 µs.	HS Schlieren, PCBs, Kulites, SC8100
3490	19/May/2018	15° swept forward cylinder. Focused schlieren plane sweeping traverse. Re held near 4.9M/m. 100ms samples (pts 51-157).	Focused Schlieren, PCBs, Kulites, SC8100
3492	20/May/2018	15° swept forward cylinder. Focused schlieren plane stepped traverse. Re held near 4.9M/m. 1.5s samples (pts 3-8). 232 x 384 resolution, 150k fps, 30k images, 1/4.032M sec exp.	Focused Schlieren, PCBs, Kulites
3494	20/May/2018	Right cylinder. Focused schlieren plane stepped traverse. Re held near 4.9M/m. 1.5s samples (pts 3-8). 184 x 512 resolution, 150k fps, 30k images, 1/1.2444M sec exp.	Focused Schlieren, PCBs, Kulites

Pressure Transducer Configuration Table

This table indicates the distribution of surface mounted PCB and Kulite pressure transducers for each run. It gives the structure of the run, the Reynolds number range, and the points that were extracted to produce the PSDs given in Appendix H.

"Trips, no cylinder" - Sampled at 2MHz. Kulite LP=200kHz. PCB LP=1MHz. Swept Re sampled for 0.1s per point. Stepped for 1.5s per point.						
Configuration 1		Applicable Points				
Run	Re Style	Start1	End1	Start2	End2	Re (M/m)
3391	swept	52	59	74	150	8.2-7.5, 7.2-1.0
3392	stepped	4	11			7.2, 6.0, 5.4, 4.9, 4.5, 4.0, 3.5
Sensor Distribution						
Type	SN	Channel	Position			
PCB	7705	1	T1			
PCB	7707	2	T4			
PCB	7706	3	T9			
PCB	7709	4	T11			
PCB	7629	5	T18			
Kulite	726	1	T19			
Kulite	729	2	T20			
Kulite	728	3	T28			
Configuration 2		Applicable Points				
Run	Re Style	Start1	End1	Start2	End2	Re (M/m)
3393	swept	47	50	71	140	8.2-7.8, 6.8-1.6
3394	stepped	4	12			7.2, 5.5, 5.0, 4.5, 4.1, 3.6, 3.2, 2.7, 2.4
Sensor Distribution						
Type	SN	Channel	Position			
PCB	7705	1	T3			

PCB	7707	2	T2			
PCB	7629	3	T1			
PCB	7709	4	T15			
PCB	7706	5	T16			
Kulite	729	1	T7	power wire broke		
Kulite	728	2	T6			
Kulite	725	3	T5			
Kulite	726	4	T26			
Configuration 3		Applicable Points				
Run	Re Style	Start1	End1	Start2	End2	Re (M/m)
3395	swept	84	155			6.8-2.9
3397	swept	21	53	54	110	2.0-6.4, 6.4-3.3
3398	swept	41	123			8.4-3.1
Sensor Distribution						
Type	SN	Channel	Position			
PCB	7705	1	T10			
PCB	7709	2	T9			
PCB	7707	3	T8			
PCB	7706	4	T17			
PCB	7629	5	T16			
Kulite	728	1	T7			
Kulite	726	2	T6	did not respond for 3395		
Kulite	729	3	T5			
Kulite	725	4	T22			
Configuration 4		Applicable Points				
Run	Re Style	Start1	End1	Start2	End2	Re (M/m)
3399	swept	sampled for 1 sec				
3400	swept	60	118			7.2-3.1

3401	stepped	4	4	7	9	7.0, 5.6, 4.6, 4.0
Sensor Distribution						
Type	SN	Channel	Position			
PCB	7629	1	T4			
PCB	7705	2	T11			
PCB	7706	3	T18			
PCB	7709	4	T17			
PCB	7707	5	T15			
Kulite	726	1	T14			
Kulite	728	2	T13			
Kulite	729	3	T12			
Kulite	725	4	T19			
Configuration 5		Applicable Points				
Run	Re Style	Start1	End1	Start2	End2	Re (M/m)
3402	swept	61	127			6.7-2.5
3403	swept	35	40	53	110	7.6-2.8
Sensor Distribution						
Type	SN	Channel	Position			
PCB	7709	1	T3			
PCB	7706	2	T2			
PCB	7707	3	T1			
PCB	7629	4	T10			
PCB	7705	5	T8			
Kulite	728	1	T14			
Kulite	729	2	T13			
Kulite	725	3	T12			
Kulite	726	4	T20			
"Trips, cylinder" - Sampled at 2MHz. Kulite LP=200kHz. PCB LP=1MHz.						

Swept Re sampled for 0.1s per point. Stepped for 1.5s per point.						
Configuration 6		Applicable Points				
Run	Re Style	Start1	End1	Start2	End2	Re (M/m)
3424	swept	39	44	65	137	8.0-2.5
3425	stepped	3	6			6.6, 5.9, 5.6, 4.8
3426	stepped	3	7			6.2, 5.3, 4.8, 4.4, 4.1
Sensor Distribution						
Type	SN	Channel	Position			
PCB	7705	1	T1			
PCB	7707	2	T4			
PCB	7706	3	T9			
PCB	7709	4	T11			
PCB	7629	5	T18			
Kulite	728	1	T26	broken signal wire		
Kulite	729	2	T20			
Kulite	725	3	T22			
Kulite	726	4	T19			
Configuration 7		Applicable Points				
Run	Re Style	Start1	End1	Start2	End2	Re (M/m)
3427	swept	45	124			2.1-7.4
3428	stepped	2	7			6.7, 5.7, 5.3, 4.8, 4.6, 3.9
3429	stepped	4	8			6.6, 5.4, 4.4, 3.8, 3.1
Sensor Distribution						
Type	SN	Channel	Position			
PCB	7707	1	T1			
PCB	7706	2	T2			
PCB	7709	3	T3			
PCB	7705	4	T8			
PCB	7629	5	T10			

Kulite	729	1	T7			
Kulite	726	2	T6			
Kulite	725	3	T5			
Kulite	728	4	T28			
Configuration 8		Applicable Points				
Run	Re Style	Start1	End1	Start2	End2	Re (M/m)
3436	swept	56	150			7.4-2.0
3439	stepped	2	8			6.9, 5.9, 5.3, 4.9, 4.5, 3.8, 3.2
3441	stepped	3	8			7.3, 5.6, 5.2, 4.7, 4.4, 4.1
Sensor Distribution						
Type	SN	Channel	Position			
PCB	7629	1	T4			
PCB	7705	2	T11			
PCB	7706	3	T18			
PCB	7709	4	T17			
PCB	7707	5	T16			
Kulite	726	1	T14			
Kulite	728	2	T13			
Kulite	729	3	T12			
Kulite	725	4	T19			
Configuration 9		Applicable Points				
Run	Re Style	Start1	End1	Start2	End2	Re (M/m)
3442	swept	45	139			7.7-2.9
3443	stepped	3	8			6.9, 5.6, 5.2, 4.8, 4.3, 3.7
3444	stepped	2	7			6.8, 5.8, 5.3, 4.7, 4.0, 3.3
Sensor Distribution						
Type	SN	Channel	Position			
PCB	7707	1	T8			

PCB	7709	2	T9			
PCB	7705	3	T10			
PCB	7629	4	T16			
PCB	7706	5	T15			
Kulite	726	1	T20	shorted signal wire		
Kulite	729	2	T21			
Kulite	728	3	T24			
Kulite	725	4	T25			
"No trips, cylinder" - Sampled at 2MHz. Kulite LP=200kHz. PCB LP=1MHz. Swept Re sampled for 0.1s per point. Stepped for 1.5s per point.						
Configuration 10		Applicable Points				
Run	Re Style	Start1	End1	Start2	End2	Re (M/m)
3458	swept	48	140			7.5-2.9
3459	stepped	3	7			6.9, 5.5, 5.0, 4.6, 4.2
3460	stepped	3	7			6.1, 4.9, 4.3, 3.6, 3.2
Sensor Distribution						
Type	SN	Channel	Position			
PCB	7705	1	T1			
PCB	7707	2	T4			
PCB	7708	3	T17			
PCB	7709	4	T11			
PCB	7629	5	T18			
Kulite	725	1	T19			
Kulite	729	2	T20			
Kulite	728	3	T24			
Configuration 11		Applicable Points				
Run	Re Style	Start1	End1	Start2	End2	Re (M/m)
3461	swept	54	150			7.1-2.4

3462	stepped	4	8			6.4, 5.6, 5.1, 4.6, 4.2
3463	stepped	5	8			6.4, 5.8, 5.2, 4.8
Sensor Distribution						
Type	SN	Channel	Position			
PCB	7629	1	T1			
PCB	7707	2	T2			
PCB	7709	3	T3			
PCB	7705	4	T15			
PCB	7708	5	T16			
Kulite	725	1	T5			
Kulite	728	2	T6			
Kulite	729	3	T7			
Configuration 12		Applicable Points				
Run	Re Style	Start1	End1	Start2	End2	Re (M/m)
3466	swept	45	124			2.0-6.7
3467	stepped	2	2	4	8	8.0, 6.6, 5.8, 5.3, 4.9, 4.3
3468	stepped	3	8			6.1, 5.3, 4.7, 4.4, 4.0, 3.3
Sensor Distribution						
Type	SN	Channel	Position			
PCB	7707	1	T8			
PCB	7708	2	T9			
PCB	7705	3	T10			
PCB	7709	4	T17			
PCB	7629	5	T18			
Kulite	729	1	T12			
Kulite	728	2	T13			
Kulite	725	3	T14			
"No trips, no cylinder" - Sampled at 2MHz. Kulite LP=200kHz. PCB LP=1MHz.						

Swept Re sampled for 0.1s per point. Stepped for 1.5s per point.						
Configuration 13		Applicable Points				
Run	Re Style	Start1	End1	Start2	End2	Re (M/m)
3469	swept	35	128			7.6-2.1
*same transducer configuration kept through R3475						
Sensor Distribution						
Type	SN	Channel	Position			
PCB	7705	1	T1			
PCB	7707	2	T4			
PCB	7708	3	T9			
PCB	7709	4	T11			
PCB	7629	5	T18			
Kulite	728	1	T14			
Kulite	725	2	T19			
Kulite	729	3	T20			
Cylinder wake studies - Sampled at 500kHz for 400ms.						
Configuration 14		Applicable Points				
Run	Re Style	Start1	End1	Start2	End2	Re (M/m)
Configuration for R3476-R3480						
Sensor Distribution						
Type	SN	Channel	Position			
PCB	7707	1	T1			
PCB	7709	2	T4			
PCB	7629	3	T9			
PCB	7705	4	T11			
PCB	7708	5	T18			
Kulite	728	1	T19			
Kulite	729	2	T20	broke on install		
Kulite	725	3	T24			

"Trips, angled cylinder" - Sampled at 2MHz. Kulite LP=200kHz. PCB LP=1MHz. Swept Re sampled for 0.1s per point. Stepped for 1.5s per point.						
Configuration 15		Applicable Points				
Run	Re Style	Start1	End1	Start2	End2	Re (M/m)
3482	swept	98	143			6.8-3.0
3483	swept	36	147			7.3-1.0
3484	stepped	3	8			7.0, 6.1, 5.7, 5.3, 4.7, 4.3
3485	swept	50	151			7.4-1.6
3486	stepped	4	8			6.9, 6.1, 5.7, 5.3, 4.9
3487	swept	33	127			7.6-1.5
3488	stepped	3	9			7.1, 6.1, 5.6, 5.1, 4.7, 4.2, 3.6
3489	stepped	3	9			7.4, ?, 5.3, 5.9, 4.5, 4.1, 3.4
3490	5M/m	51	157			5
Sensor Distribution						
Type	SN	Channel	Position			
PCB	7705	1	T1			
PCB	7707	2	T4			
PCB	7629	3	T9			
PCB	7709	4	T11			
PCB	7708	5	T18			
Kulite	728	1	T19			
Kulite	725	2	T24			

IR Thermography Table

This table indicates the camera configuration, specifics for resolution reduction (x min, x max, y min, and y max are pixels on the full frame representing the bounds of the new resolution), frame syncing to the tunnel DAQ (tunnel end is DAQ unstart – condition every 1/10 sec, IR end is IR unstart – frame every 1/15 sec), and other notes for each run.

Trips, No cylinder - zoom lens using O7-T1 (2nd zoom calibration), IR maps reduced to 700x700 resolution. All processing from preset 0.									
Run	**Reynolds number style**	**tunnel end**	**IR end**	**x min**	**x max**	**y min**	**y max**	**Initial T (K)**	**Notes**
3391	QU, ramp D. 1 US	466	734	235	934	20	719	300.6	
3392	small file - computer error								
3393	QU, ramp D. 1 US	455	639	184	883	149	848	302.3	
3394	QU, step down	476	679	189	888	150	849	303.0	
3395	QU, ramp D. 2 US	482	704	190	889	147	846	301.6	
3396	Tunnel fail								
3397	QU, ramp D. short run	332	479	187	886	156	855	306.0	
3398	QU, ramp D	369	578	191	890	155	854	308.1	
3399	QU, ramp D. 2 US. short run	292	422	191	890	152	851	300.4	
3400	QU, ramp D. 1 US	353	515	192	891	158	857	303.3	
3401	QU, step down. 1 US	374	580	184	883	160	859	300.6	
3402	QU, ramp D. 1 US	381	556	182	881	156	855	301.3	
3403	QU, ramp D. 1 US	327	430	185	884	162	861	306.1	
3421	ramp D, ramp U	387	593	168	867	155	854	301.7	
Trips and Cylinder - zoom lens using O7-T1. Both wedge surface (700x700) and cylinder (600x400) reduced. "Default" preset=3. Also converted over P0.									
3422	ramp D, ramp U	359	552	167	866	150	849	300.1	
3424	QU, ramp D. 1 US	426	650	166	865	160	859	299.7	
3425	QU, step D	370	478	167	866	150	849	296.9	
3426	QU, step D	363	508	50	449	150	749	302.4	out of focus
3427	ramp D, ramp U	379	532	186	885	140	839	303.3	
3428	QU, step D	390	599	189	888	133	832	309.6	
3429	QU, step D	450	604	66	465	200	799	302.0	
3436	QU, ramp D. 2 US	473	723	196	895	126	825	299.2	out of focus
3439	QU, step D	477	636	190	889	130	829	301.1	out of focus
3441	QU, step D, 1 US	431	653	18	417	185	784	299.2	
3442	QU, ramp D. 1 US	439	614	173	872	139	838	298.9	

3443	QU, step D	447	658	179	878	144	843	300.9	starts skipping frames at 39.4sec
3444	QU, step D	428	511	50	449	150	749	302.7	starts skipping at 33.6sec
Cylinder, no trips - zoom lens using O7-T1. Both wedge surface (700x700) and cylinder (600x400) reduced. Preset=3.									
3458	QU, ramp D. 1 US	447	645	195	894	139	838	300.8	
3459	QU, step D. 1 US	409	589	200	899	138	837	305.8	
3460	QU, step D	412	584	85	484	180	779	305.5	out of focus
3461	QU, ramp D. 1 US	463	672	81	480	184	783	301.2	
3462	QU, step D. 1 US	451	653	168	867	142	841	306.4	
3463	Slow ramp U, step D	434	610	87	486	205	804	304.2	
3464	QU, ramp D. 1 US	409	573	87	486	200	799	300.6	
3466	ramp D, ramp U	404	616	162	861	96	795	304.6	out of focus
3467	QU, step D. 1 US	460	700	141	840	93	792	301.7	
3468	QU, step D	430	575	110	509	213	812	303.5	
No trips and no cylinder. Maps reduced to 700x700 resolution. Preset=0.									
3469	QU, ramp D	400	606	150	849	140	839	299.5	
Angled Cylinder. Both wedge surface (700x700) and cylinder (600x400) reduced. Preset=3.									
3482	QU, ramp D. 4 US	437	522	134	833	153	852	298.9	4 unstarts-lot of lost frames starting 33.3s
3483	QU, ramp D	449	692	131	830	156	855	301.4	
3484	QU, step D	473	721	76	475	154	753	304.1	
3485	QU, ramp D. 1 US	456	700	169	868	160	859	305.6	
3486	QU, step D	425	653	85	484	160	759	302.4	
3487	QU, ramp D	392	601	176	875	166	865	299.0	out of focus
3488	QU, step D	493	753	66	465	168	767	302.9	
3489	QU, step D. 1 US	480	730	139	838	164	863	304.0	
3490	Constant 5M/m	480	730	203	902	178	877	357.3	preheated model

Blue denotes the camera in position (b) – having view of cylinder, D=Down, QU=Quick Up, U=Up, US=Unstart

High-speed Schlieren Table

This table provides the conditions, resolution, sampling specifications, and position relative to the model for each high-speed schlieren run. The coordinates are for each vertex defining the location of the high-speed time-resolved schlieren box with respect to the front of the cylinder and the wedge surface. The cylinder base and a representative upstream point on the model surface (to find the angle of the model relative to the camera) are given in full resolution (FR – taken before the run to define the position) and reduced resolution (actually used for the run) coordinates.

"Trips, cylinder"		Resolution		model-based coordinates (mm)								cylinder base (px)		upstream (px)			
Run	Re (M/m)	Frame (x x y)	Spatial (px/cm)	-x'1	y1	-x'2	y2	-x'3	y3	-x'4	y4	x	y	x	y	samples per condition	rate (fps)
3422	2.1-7.6	1024 x 1024	74									948	474	53	484		500
3424	8.0-2.5	1024 x 1024	74									961	478	40	488		500
3425	6.6, 5.9, 5.6, 4.8	456 x 128	74.3	5.9	26.4	67.3	27.0	67.5	9.8	6.1	9.1	FR785	FR643	FR11	FR652	50k	150k
3426	6.2, 5.3, 4.8, 4.4, 4.1	120 x 256	74.3	-2.7	29.2	13.4	29.4	13.9	-5.0	-2.3	-5.2	93 FR545	220 FR604	0 FR245	221 FR607	50k	240k
3427	2.1-7.4	1024 x 1024	74									949	490	33	501		500
3428	6.7, 5.7, 5.3, 4.8, 4.6, 3.9	456 x 128	74.7	5.8	25.0	66.8	25.5	67.0	8.4	5.9	7.8	FR784	FR633	FR5	FR640	50k	150k
3429	6.6, 5.4, 4.4, 3.8, 3.1	120 x 256	74.4	-3.0	31.3	13.1	31.5	13.5	-2.9	-2.7	-3.1	93 FR545	233 FR617	0 FR282	234 FR620	50k	240k
3436	7.4-2.0	1024 x 1024	74									940	489	17	498		500
3439	6.9, 5.9, 5.3, 4.9, 4.5, 3.8, 3.2	456 x 128	73.7	5.8	26.1	67.7	26.6	67.8	9.2	6.0	8.7	FR782	FR640	FR27	FR646	50k	150k

3441	7.3, 5.6, 5.2, 4.7, 4.4, 4.1	120 x 256	73.7	-0.1	31.3	16.2	31.5	16.5	-3.2	0.2	-3.4	114 FR566	234 FR617	0 FR268	233 FR620	50k	240k
3442	7.7-2.9	1024 x 1024	74									954	501	28	512		500
3443	6.9, 5.6, 5.2, 4.8, 4.3, 3.7	456 x 128	74.3	5.3	25.6	66.7	26.3	66.9	9.1	5.5	8.3	FR780	FR637	FR12	FR647	50k	150k
3444	6.8, 5.8, 5.3, 4.7, 4.0, 3.3	120 x 256	74	-1.0	32.6	15.2	32.7	15.5	-1.9	-0.7	-2.0	111 FR562	241 FR625	0 FR282	242 FR627	50k	240k
"No trips, cylinder"				model-based coordinates (mm)								cylinder base (px)		upstream (px)			
Run	Re (M/m)	Frame (x x y)	Spatial (px/cm)	-x'1	y1	-x'2	y2	-x'3	y3	-x'4	y4	x	y	x	y	samples per condition	rate (fps)
3458	7.5-2.9	1024 x 1024	76									970	487	88	493		30
3459	6.9, 5.5, 5.0, 4.6, 4.2	456 x 128	76.3	0.2	32.4	60.0	32.8	60.1	16.1	0.3	15.6	FR742	FR688	FR15	FR693	50k	150k
3460	6.1, 4.9, 4.3, 3.6, 3.2	120 x 256	76.3	-3.0	35.6	12.7	35.7	13.0	2.2	-2.7	2.0	FR549	FR648	FR227	FR651	50k	240k
3461	7.1-2.4	1024 x 1024	76									987	481	69	490		500
3462	6.4, 5.6, 5.1, 4.6, 4.2	456 x 128	76	0.4	32.4	60.4	32.9	60.5	16.1	0.5	15.5	FR743	FR694	FR26	FR700	50k	150k
3463	6.4, 5.8, 5.2, 4.8	120 x 256	76.3	-2.6	37.7	13.1	37.9	13.4	4.3	-2.3	4.2	FR552	FR672	FR256	FR674	50k	240k
3466	2.0-6.7	1024 x 1024	76									962	470	68	481		500
3467	8.0, 6.6, 5.8, 5.3, 4.9, 4.3	456 x 128	75.3	4.3	28.5	64.8	29.0	65.0	12.0	4.4	11.5	FR772	FR662	FR3	FR668	50k	150k
"Trips, angled cylinder"				model-based coordinates (mm)								cylinder base (px)		upstream (px)			
Run	Re (M/m)	Frame (x x y)	Spatial (px/cm)	-x'1	y1	-x'2	y2	-x'3	y3	-x'4	y4	x	y	x	y	samples per condition	rate (fps)

3482	6.8-3.0	1024 x 1024	96									960	538	6	545		50
3483	7.3-1.0	1024 x 1024	96									951	533	32	538		50
3484	7.0, 6.1, 5.7, 5.3, 4.7, 4.3	208 x 256	96	-7.1	24.1	14.5	24.2	14.7	-2.5	-7.0	-2.6	141 FR548	234 FR619	0 FR145	232 FR621	50k	200k
3485	7.4-1.6	1024 x 1024	96									934	621	21	627		50
3486	6.9, 6.1, 5.7, 5.3, 4.9	208 x 256	95.7	-8.8	24.4	12.9	24.5	13.0	-2.2	-8.7	-2.3	124 FR531	233 FR618	0 FR129	234 FR620	50k	200k
3487	7.6-1.5	1024 x 1024	76.5									944	448	41	453		500
3488	7.1, 6.1, 5.6, 5.1, 4.7, 4.2, 3.6	216 x 256	76.4	-2.7	28.9	25.6	29.0	25.7	-4.6	-2.5	-4.7	194 FR598	221 FR605	0 FR194	221 FR606	50k	200k
3489	7.4, ?, 5.3, 5.9, 4.5, 4.1, 3.4	256 x 256	76.3	6.4	38.0	40.0	38.2	40.1	4.6	6.5	4.5	FR687	FR673	FR13	FR676	50k	150k
Focused schlieren				model-based coordinates (mm)								cylinder base (px)		upstream (px)			
Run	Re (M/m)	Frame (x x y)	Spatial (px/cm)	-x'1	y1	-x'2	y2	-x'3	y3	-x'4	y4	x	y	x	y	samples per condition	rate (fps)
3490	4.9	1024 x 1024	300														500
3492	4.9	232 x 384	300													30k	150k
3494	4.9	184 x 512	300													30k	150k

APPENDIX H

RUN CONDITIONS AND DATA

This appendix provides plots of the tunnel conditions as well as configurations and some relevant data. Tunnel unstart is indicated by a precipitous fall in Mach number or "jump" in Reynolds number on the condition plots.

Model 1: Flat plate at AOA

Run 2814

Model mounted at -1.9° AOA. Schlieren imaging of Re sweep (DSC_0446.avi).

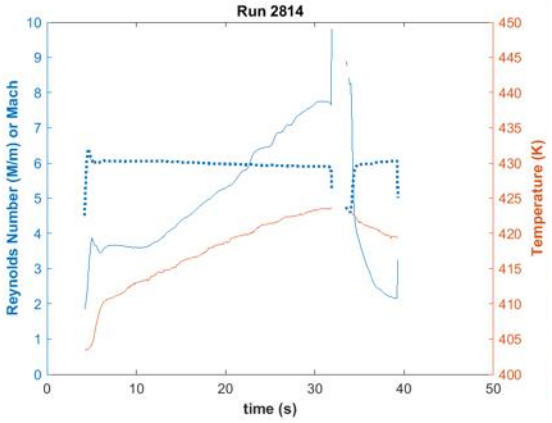

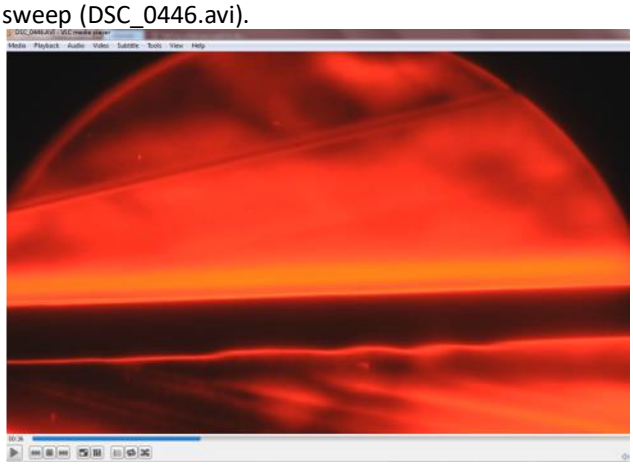

Run 2815

Model mounted at -1.9° AOA. Re near 4.3M/m. Oil flow visualization with initial band applied parallel to leading edge.

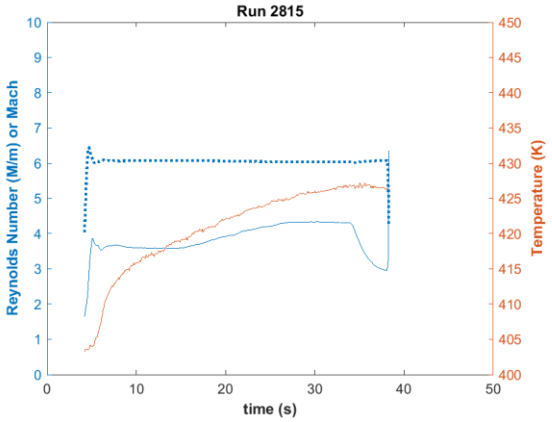

Run 2816

Model mounted at -1.9° AOA. Re near 5.2M/m. Oil flow visualization.

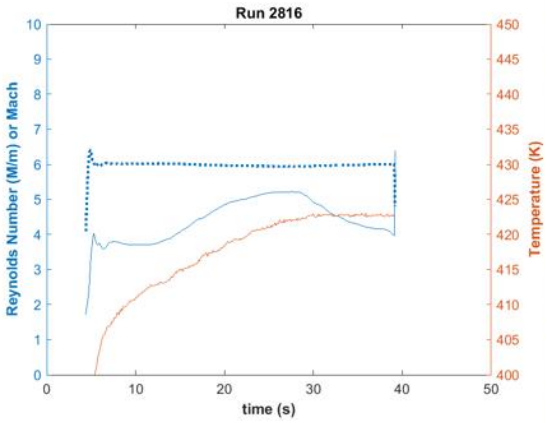

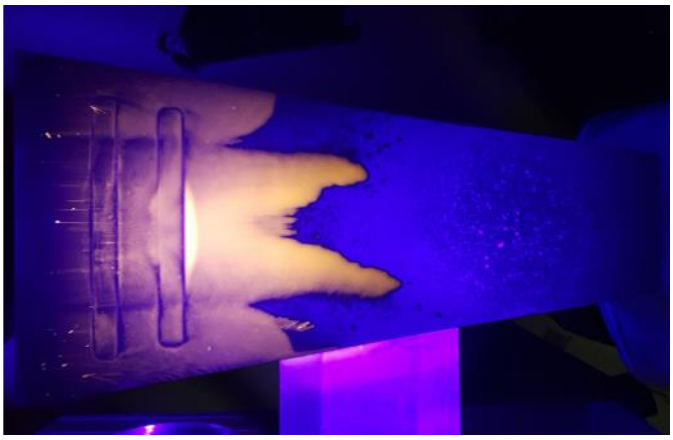

Run 2817

Model mounted at -1.9° AOA. Re near 4.9M/m. Oil flow visualization with row of dots.

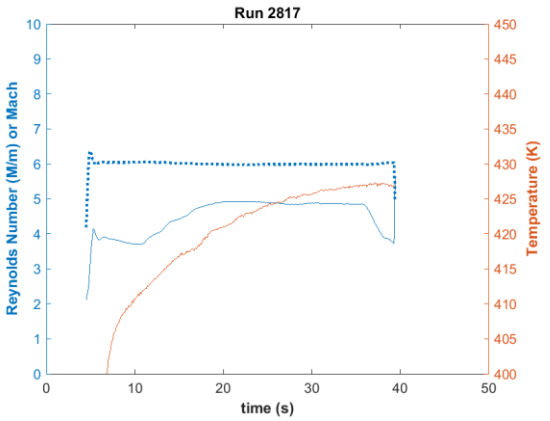

Run 2818

Repeat of previous run.

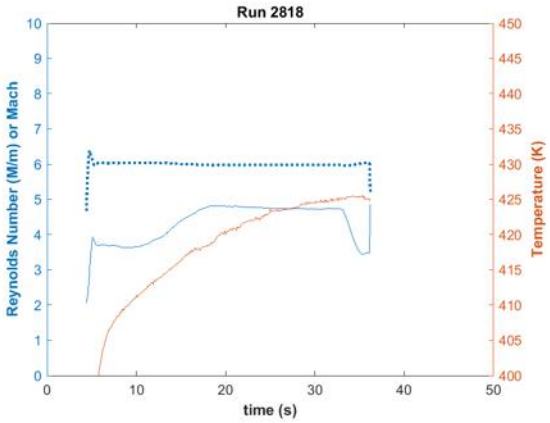

Run 2819

Model mounted at -1.1° AOA. Re near 4.8M/m.

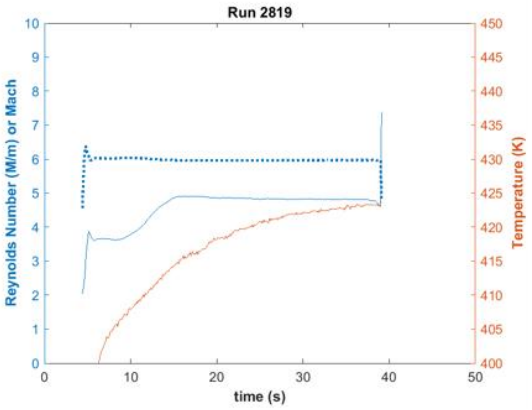

Run 2820

Model mounted at -1.1° AOA. Re near 4.5M/m. 3" Velcro trip centered on the span, near the leading edge. IR thermography.

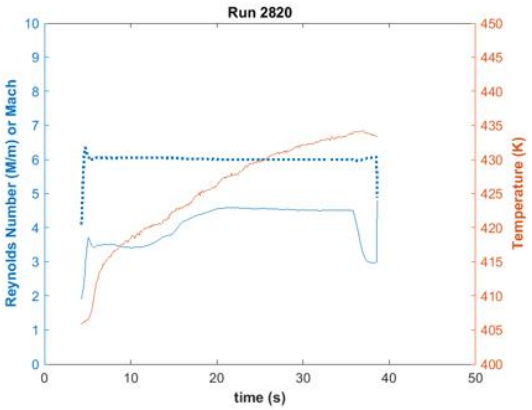

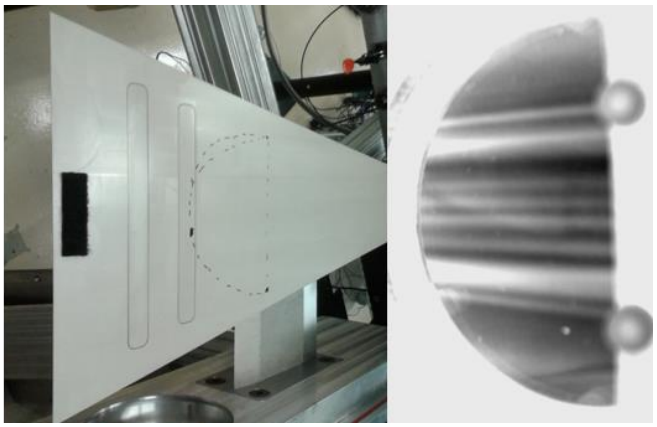

Run 2821

Similar run as previous. Re near 4.3M/m.

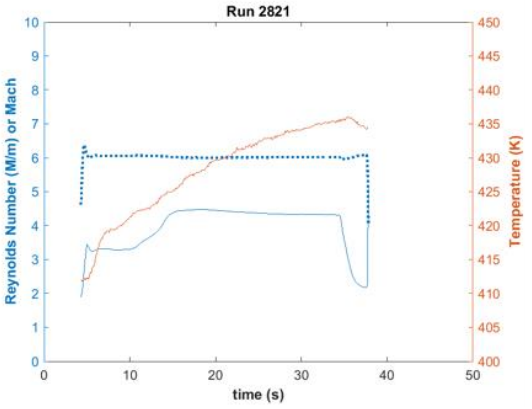

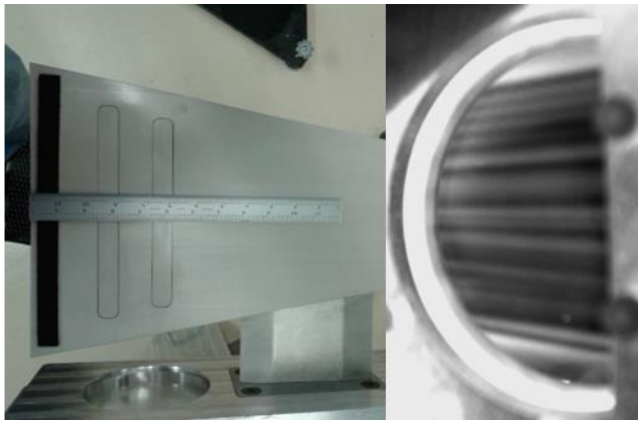

Run 2822

Model mounted at -1.1° AOA. Re near 4.3M/m. IR thermography with no Velcro.

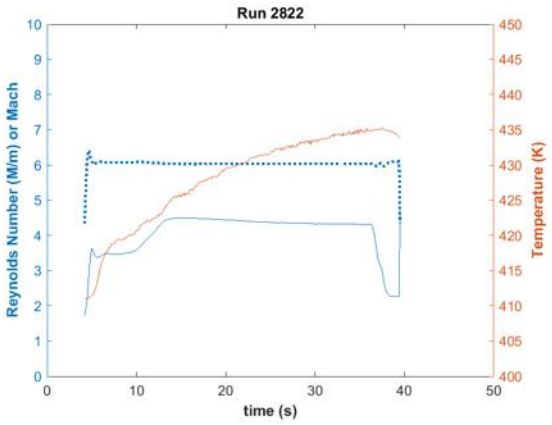

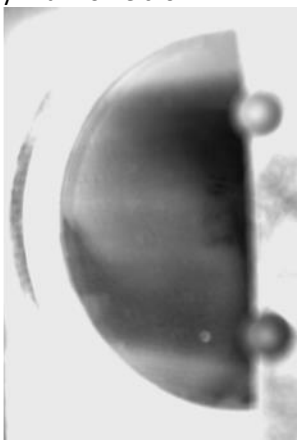

Model Positives:
-no influence from the tunnel sidewalls was observed
-IR thermography proved to be a success on the PEEK material

Model Drawbacks:
-a flat plate at negative AOA is necessary for leading edge flow attachment, but the pressure will always be higher on the upper surface of the model, which causes streamlines to curve over the edge
-sweeping the model at the Mach angle leads to a narrow span on downstream portion of model

Model 2: 1.3° aluminum wedge

Run 2834

Oil flow visualization with Re near 3.4M/m. Video is DSC_0523.avi.

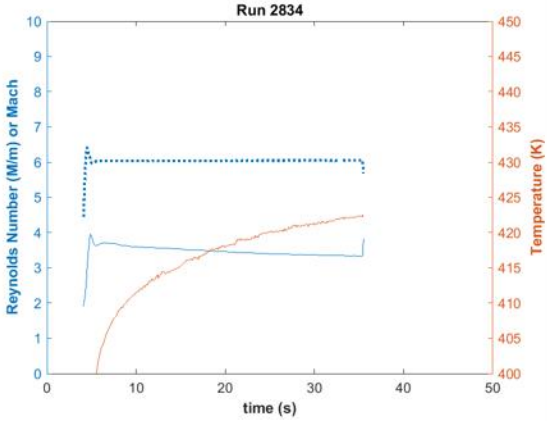

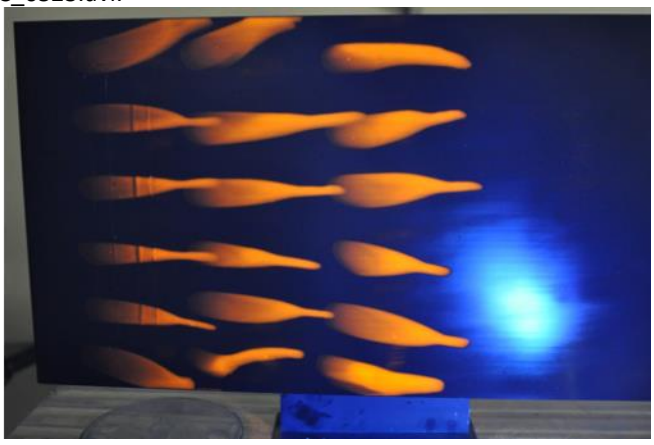

Model Positives:
-no influence from the tunnel sidewalls was observed
-streamlines trended straight back on model

Model Drawbacks:
-aluminum material is not suited for IR

Model 3: 1.3° PEEK wedge

Run 2847

IR thermography and schlieren on model with 0.17" diamond trip array in rear port. Re sweep.

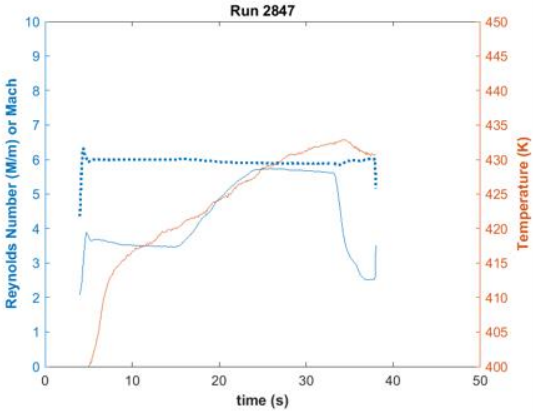

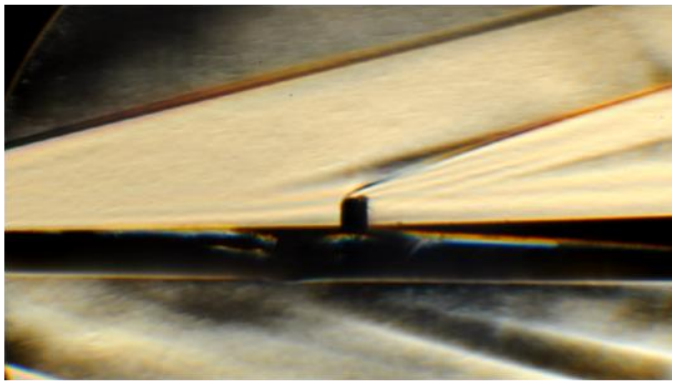

Run 2848

Trips moved to front port and Re sweep. Same diagnostics as previous.

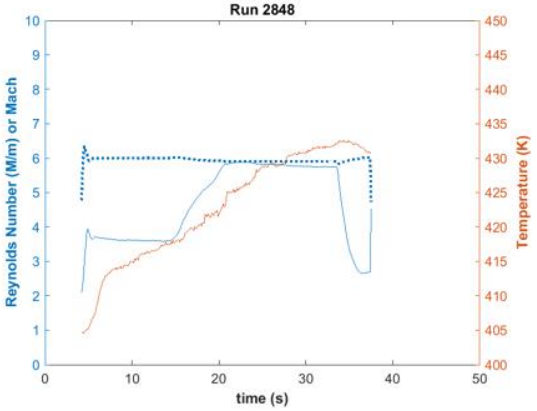

Run 2849

Trips again in rear port for Re sweep. Same diagnostics as previous.

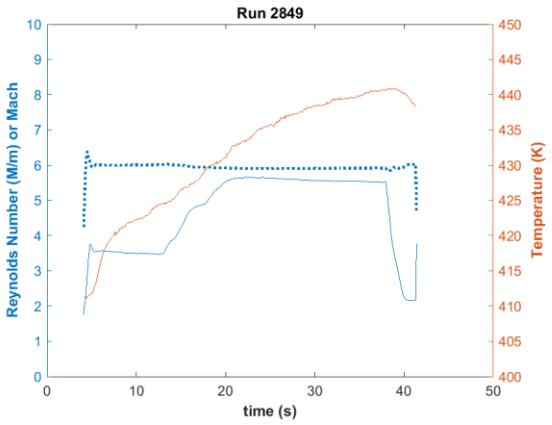

Run 2850

Schlieren with both sets of trips in place. Re sweep.

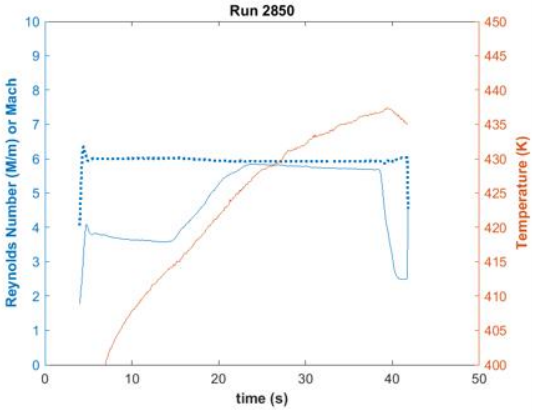

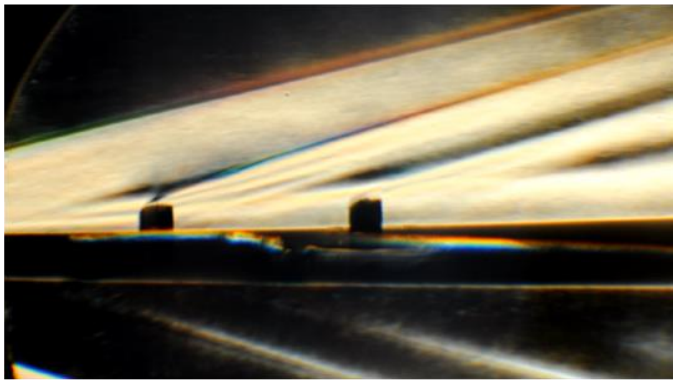

Run 2851

Oil flow with both sets of trips. Re sweep.

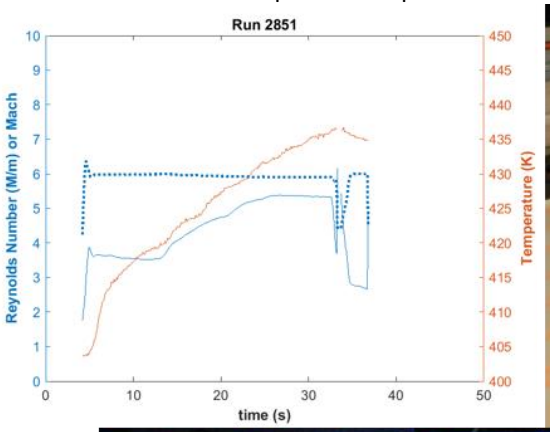

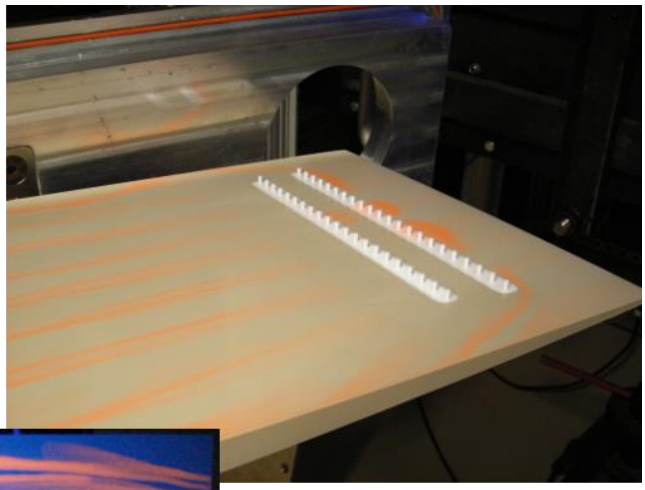

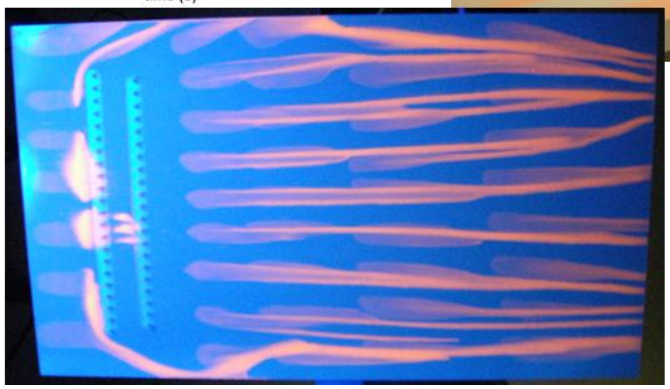

Run 2855

IR thermography through middle window port looking upstream. Both trips. Re held near 3.3M/m.

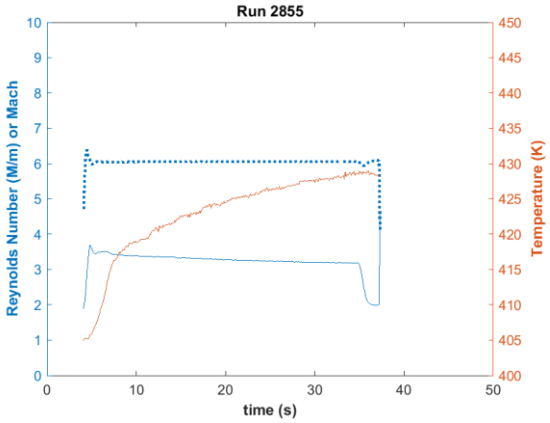

Run 2856

Same configuration and view as previous but Re held near 7M/m.

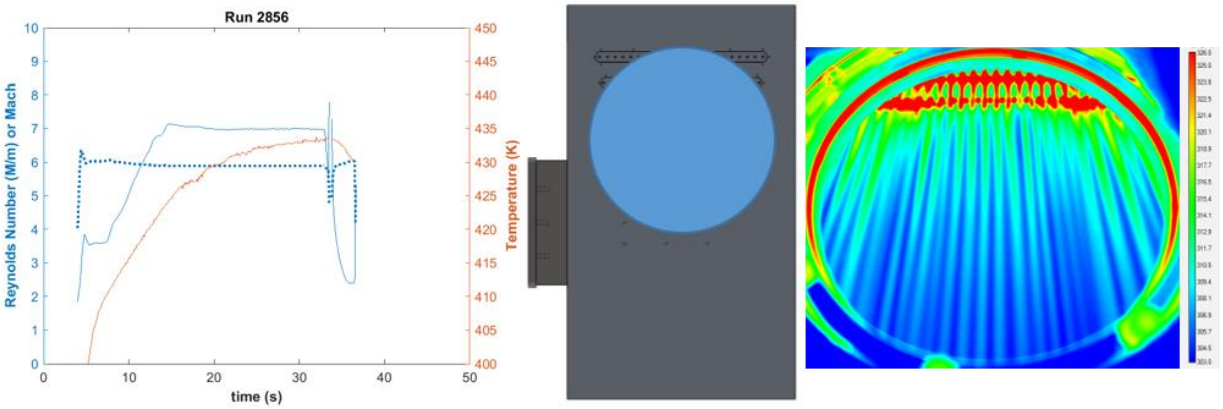

Run 2857

IR thermography through middle window looking downstream. Re held near 6.5M/m.

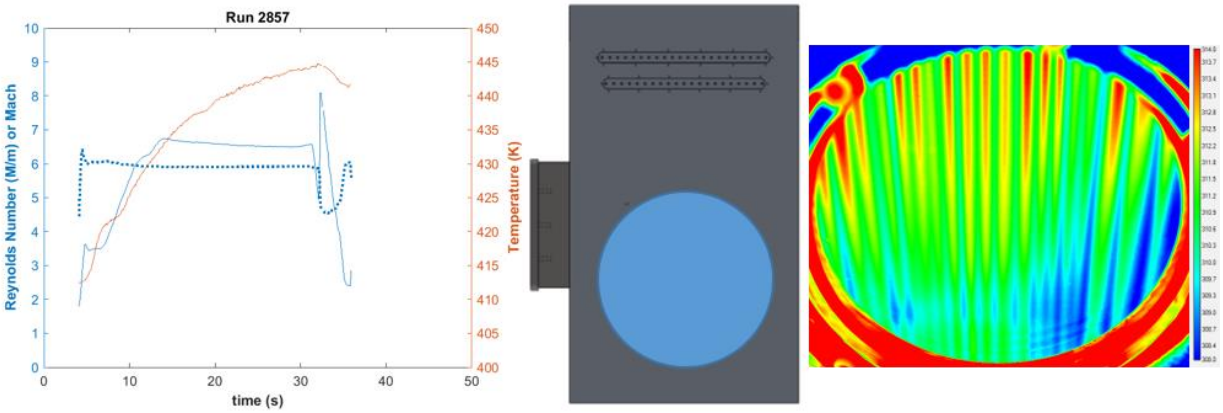

Run 2858

IR thermography directed straight down through downstream window. Re held near 6.9M/m.

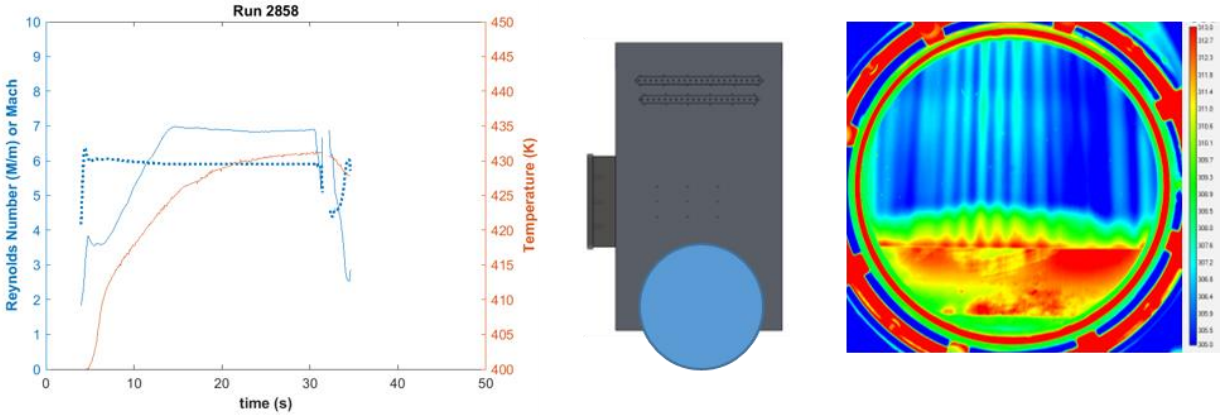

Run 2859

Same IR configuration as previous with new 0.07” trip heights. Re held near 6.5M/m.

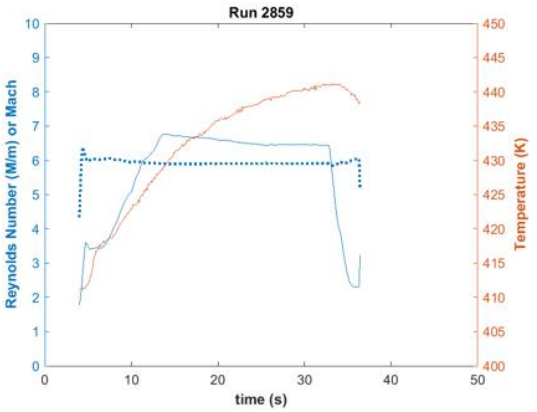

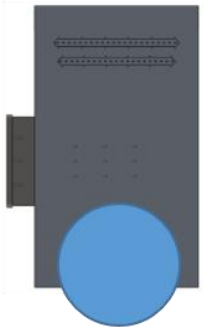

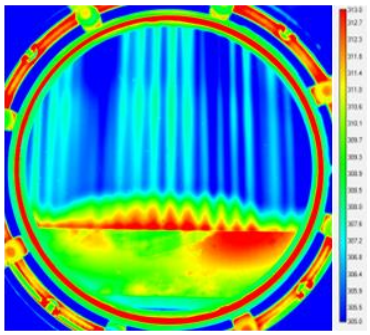

Run 2860

Same configuration as previous with Re held near 3.2M/m.

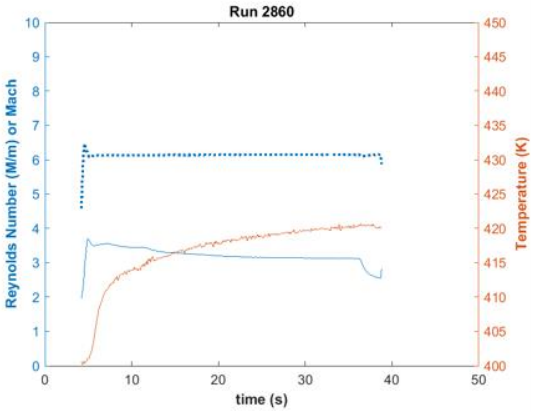

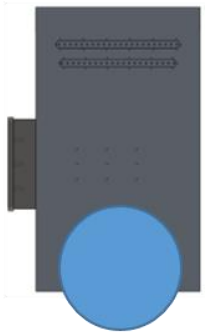

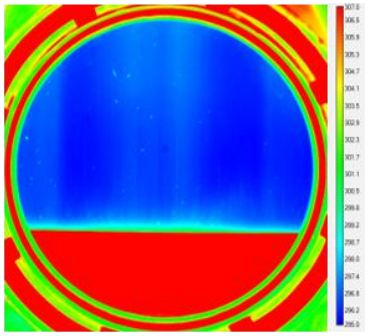

Run 2862

Same configuration as previous with Re held near 4.8M/m.

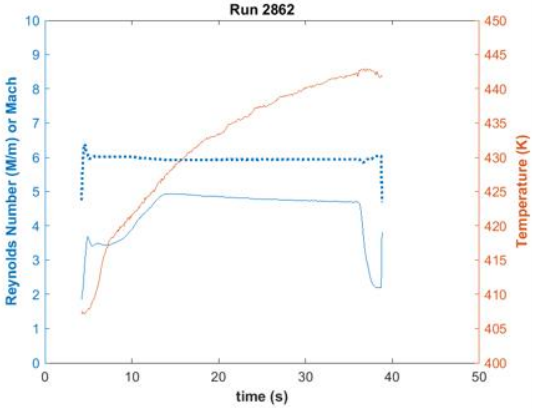

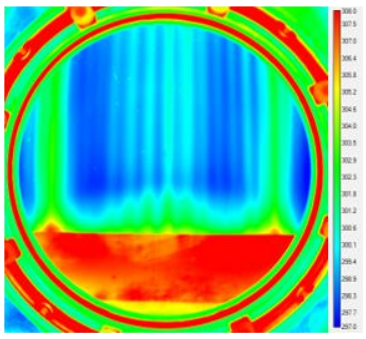

Run 2863

Only front set of 0.07” trips in place with IR straight down view through downstream window. Re held near 6.3M/m.

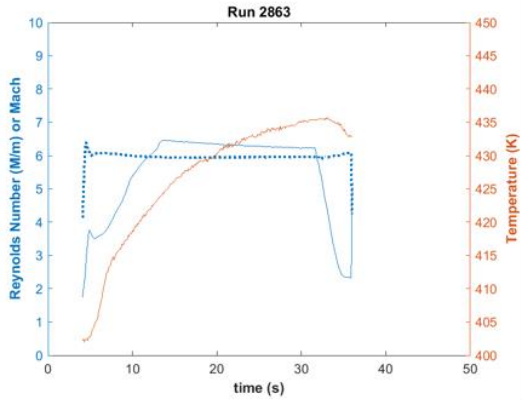

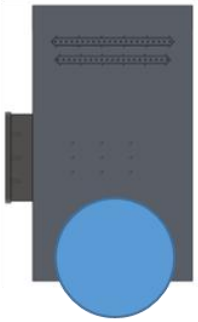

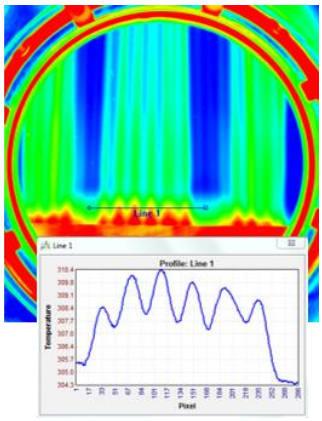

Run 2864

Same configuration and view as previous. Re held near 6.5M/m.

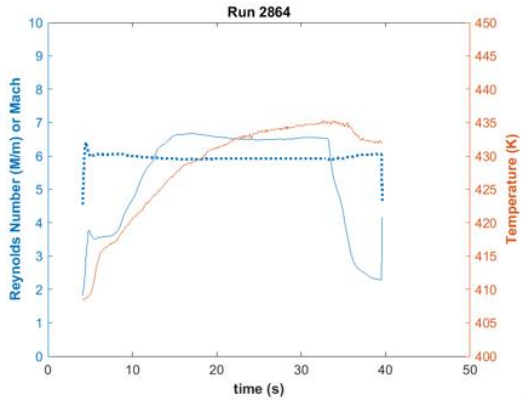

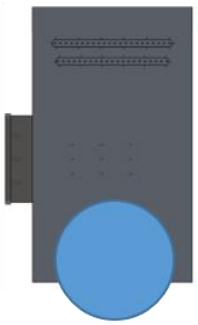

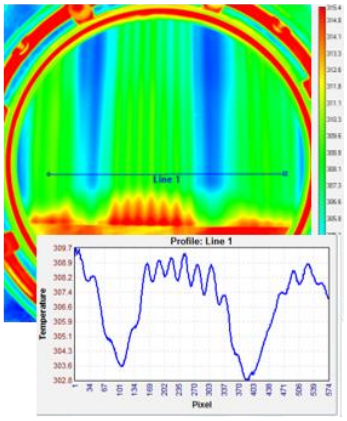

Run 2865

Same configuration but view straight through center window. Re held near 6.5M/m.

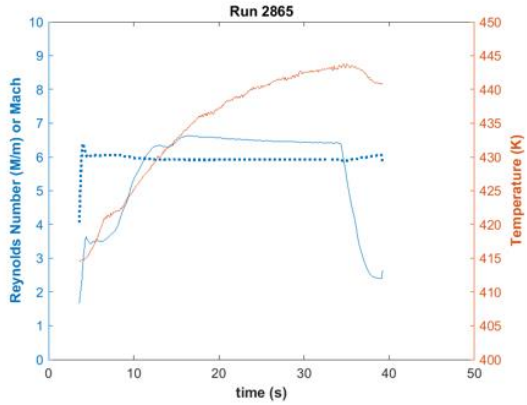

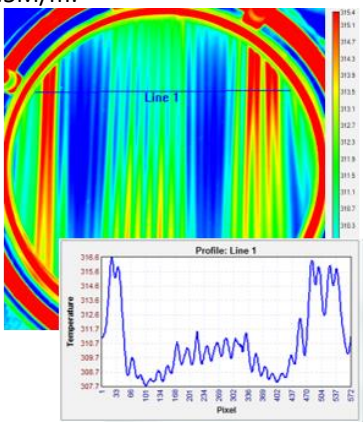

Run 2866

Same configuration but view straight through upstream window. Re held near 6.4M/m.

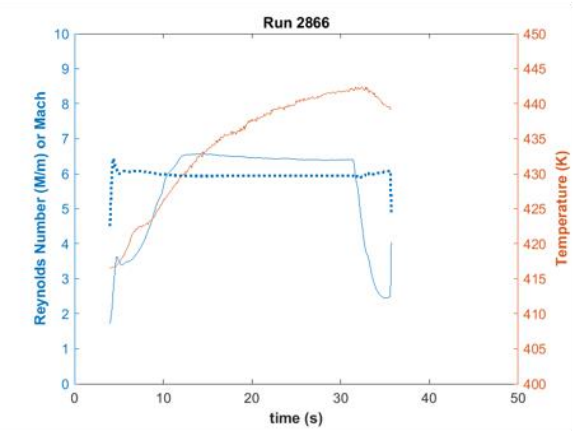

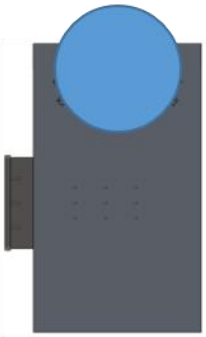

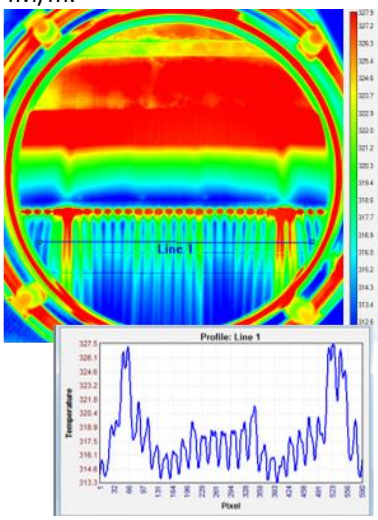

Run 2867

Same view but no trips. Re held near 6.7M/m.

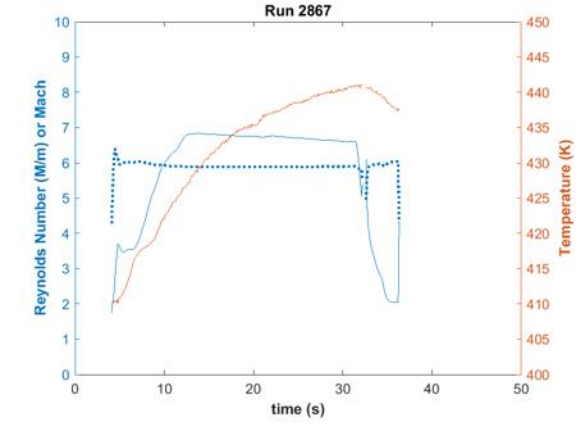

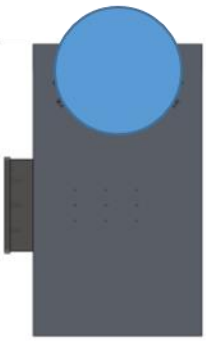

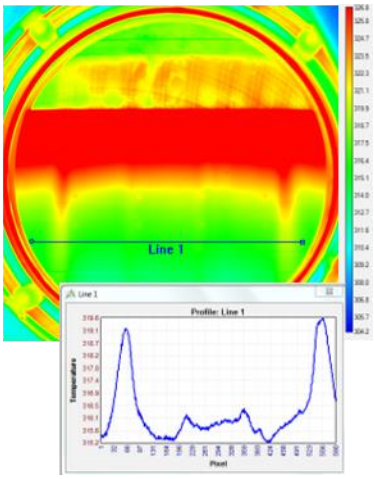

Run 2868

Same configuration as previous with camera directed through center window. Re near 6.6 M/m.

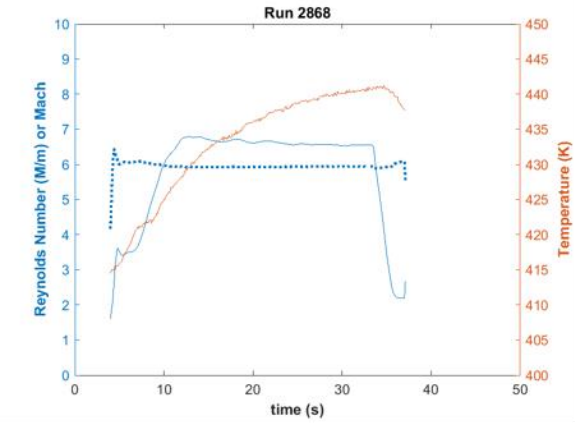

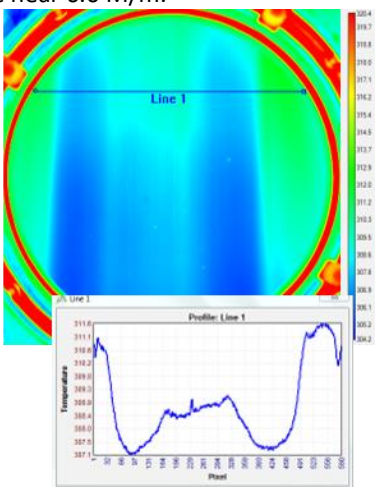

Run 2869

Camera again at upstream window looking at leading edge hot streaks and Re stepped.

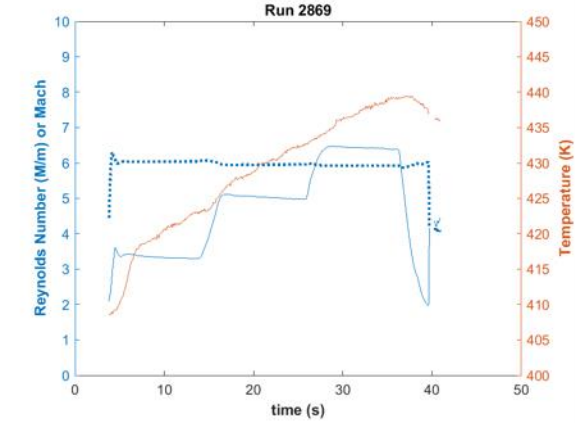

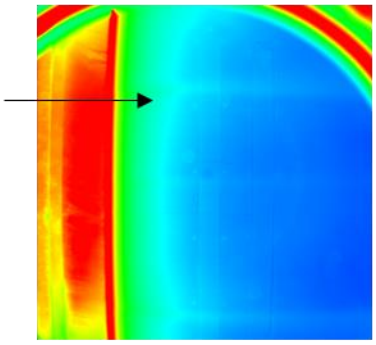

LE streaks are evident at all Re

First cylinder runs

Run 2870

A 0.75” diameter, 1.25” tall cylinder was placed 2.1” downstream of the leading edge near a hot streak. IR thermography was conducted at several Re. No trips.

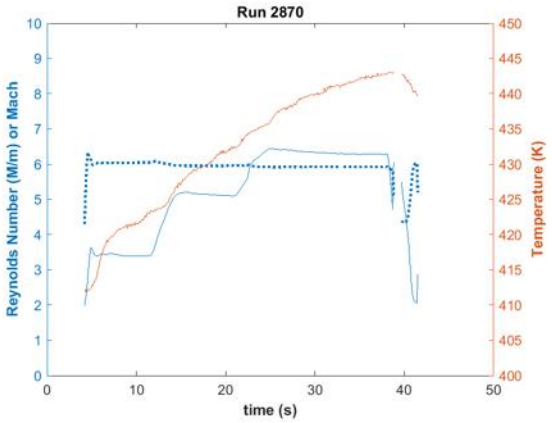

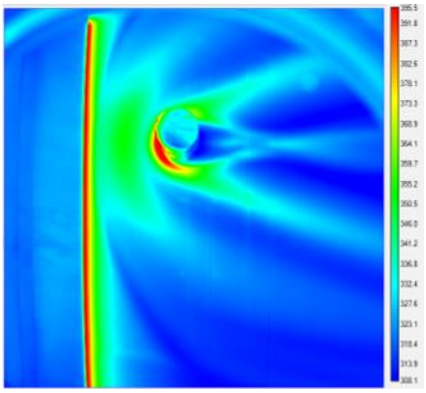

Run 2871

Same type of run with model positioned 1” farther downstream in tunnel.

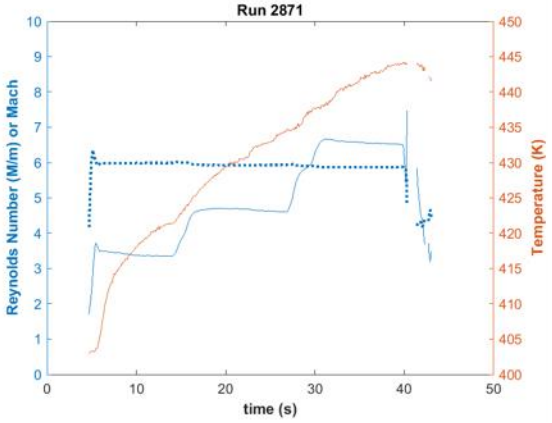

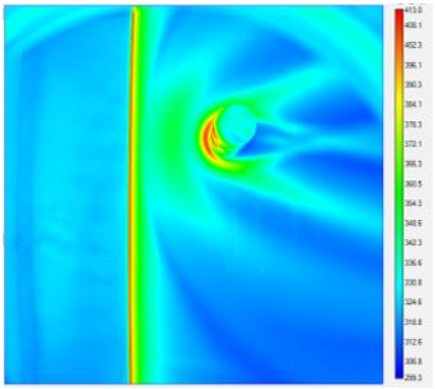

Run 2877

The same cylinder as previous was affixed 10.5” downstream of the leading edge. No trips. IR thermography.

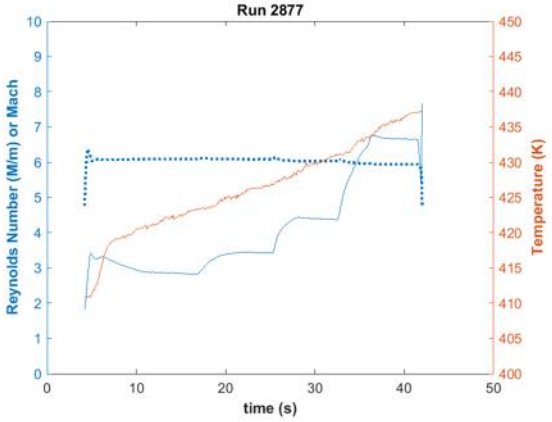

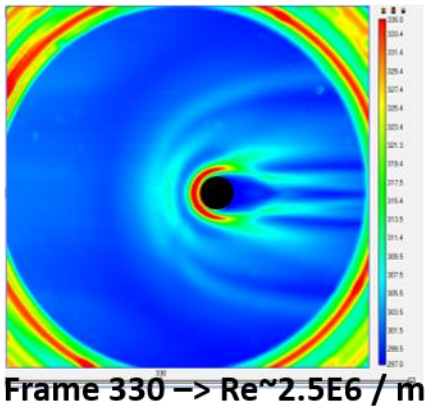
Frame 330 –> Re~2.5E6 / m

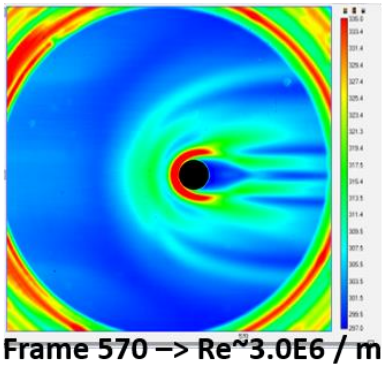
Frame 570 –> Re~3.0E6 / m

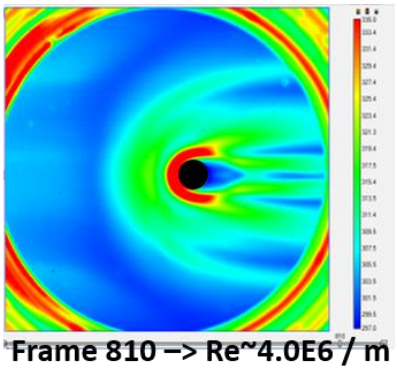
Frame 810 –> Re~4.0E6 / m

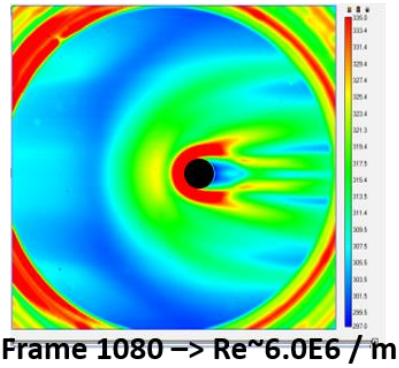
Frame 1080 –> Re~6.0E6 / m

Run 2878

Same configuration and run type with 0.07” trips in front port.

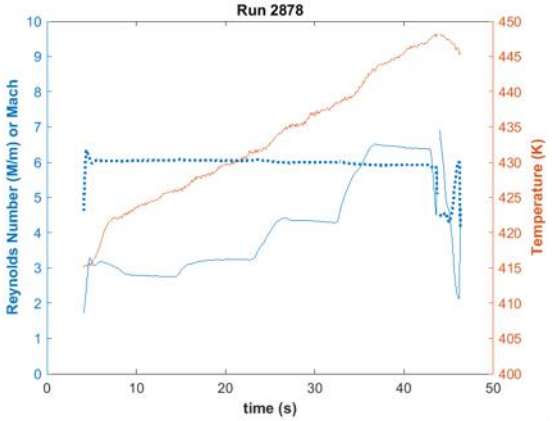

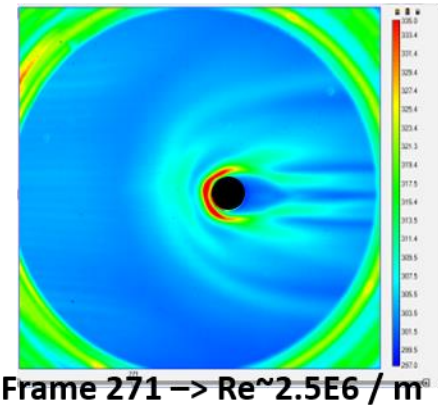
Frame 271 –> Re~2.5E6 / m

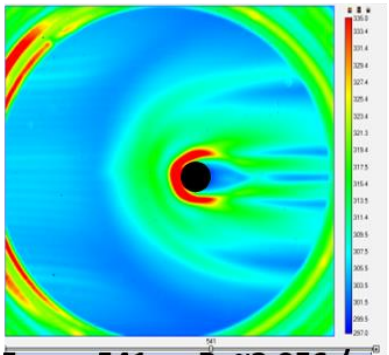

Frame 541 –> Re~3.0E6 / m

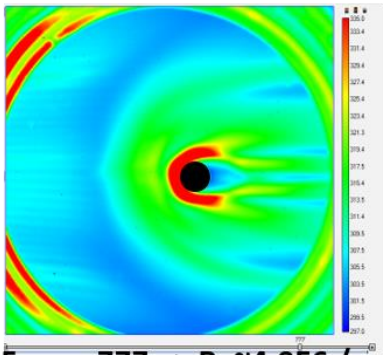

Frame 777 –> Re~4.0E6 / m

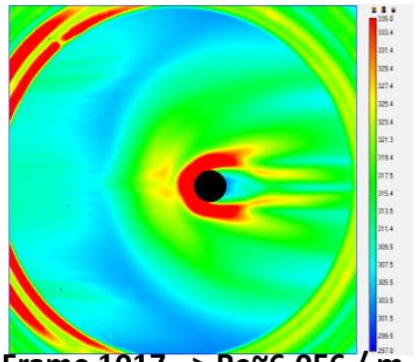

Frame 1017 –> Re~6.0E6 / m

Run 2879

IR thermography on same trips but now a 1.25” diameter, 1.25” tall cylinder located 10.5” downstream of LE.

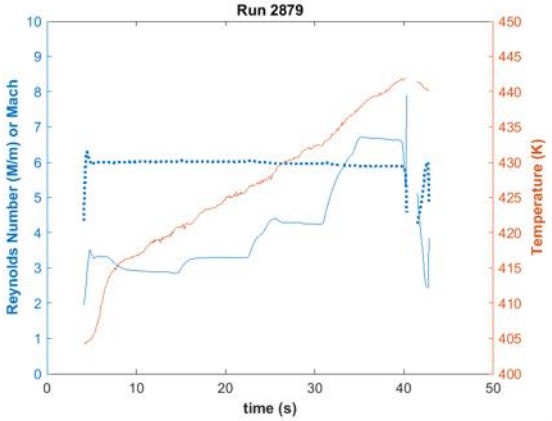

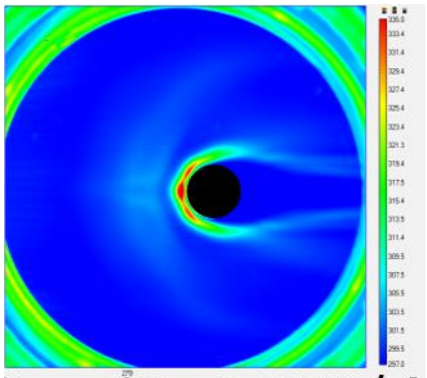

Frame 270 –> Re~2.5E6 / m

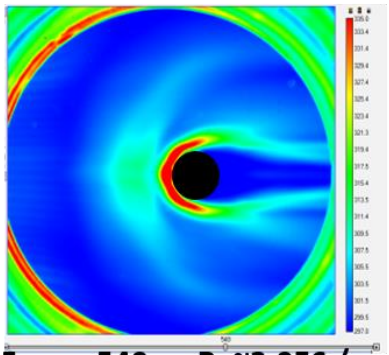

Frame 540 –> Re~3.0E6 / m

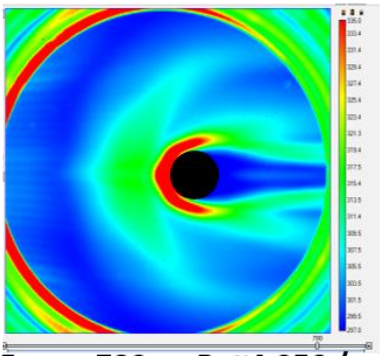

Frame 780 –> Re~4.0E6 / m

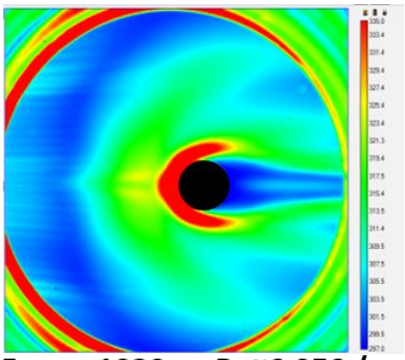

Frame 1020 –> Re~6.0E6 / m

Run 2880

IR thermography on same cylinder but no trips.

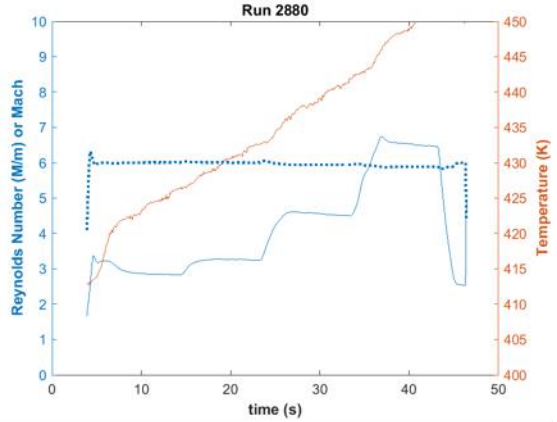

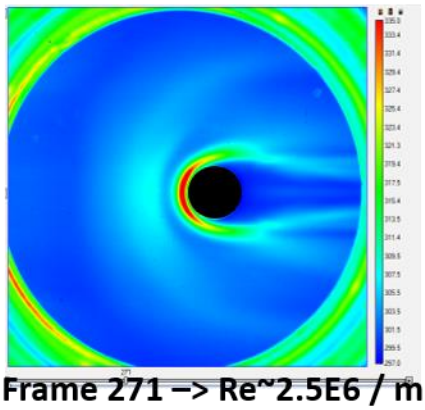
Frame 271 –> Re~2.5E6 / m

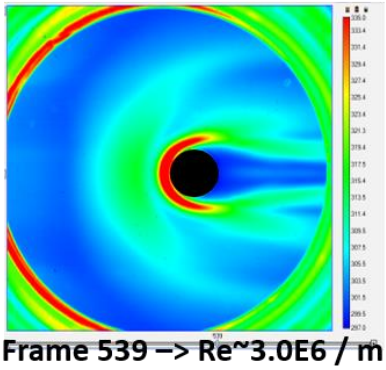
Frame 539 –> Re~3.0E6 / m

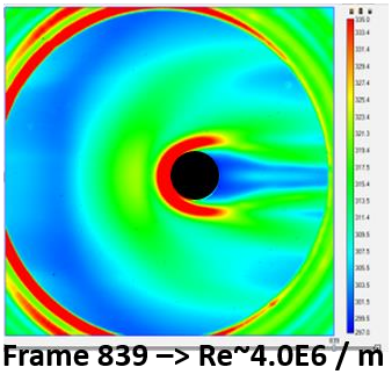
Frame 839 –> Re~4.0E6 / m

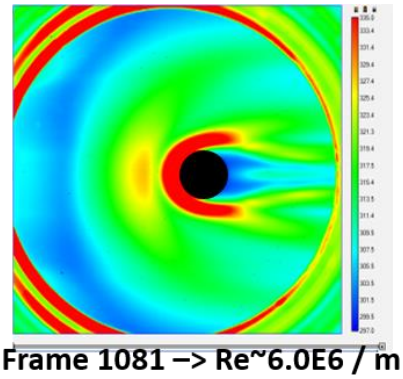
Frame 1081 –> Re~6.0E6 / m

Run 2881

IR thermography on same configuration as previous run but Mach number changed to near 7.5.

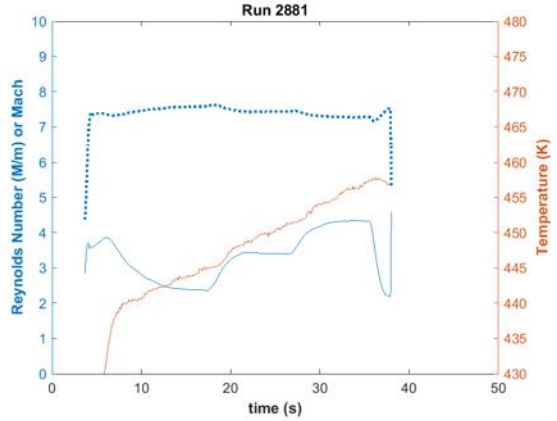

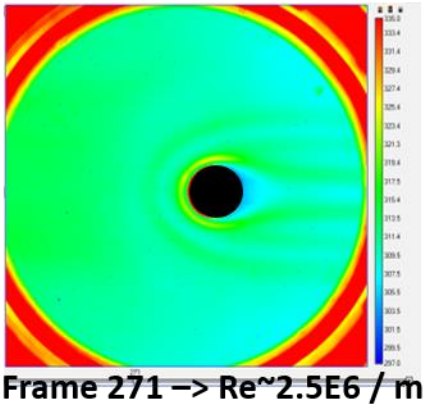
Frame 271 –> Re~2.5E6 / m

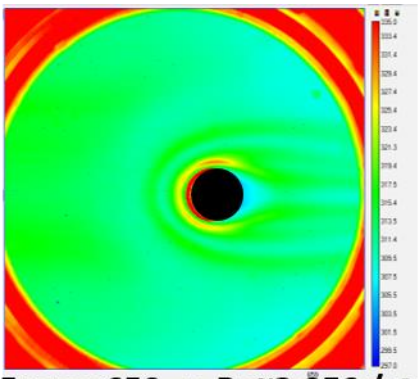

Frame 659 –> Re~3.0E6 / m

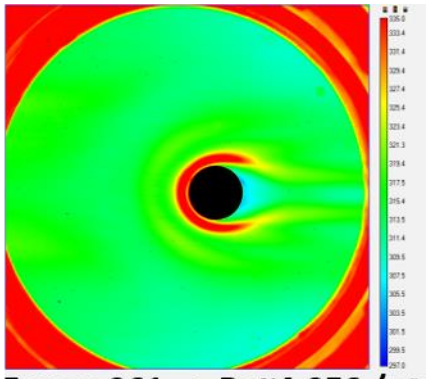

Frame 961 –> Re~4.0E6 / m

Mach 7 runs

Run 2884

IR thermography on same configuration as previous.

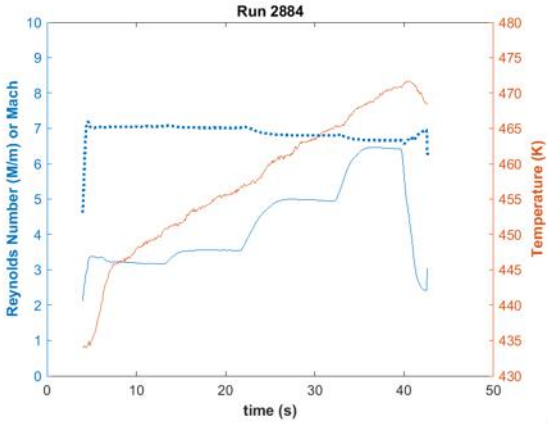

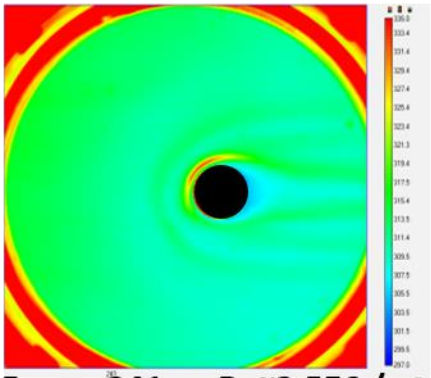

Frame 241 –> Re~2.5E6 / m

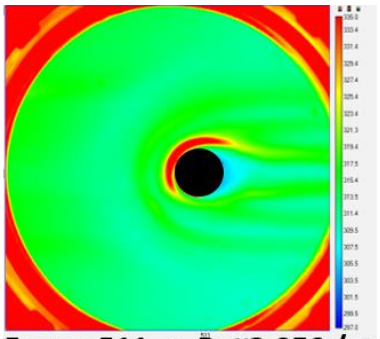

Frame 511 –> Re~3.0E6 / m

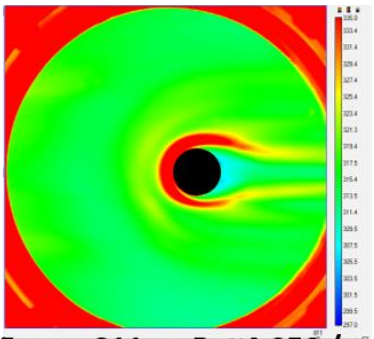

Frame 811 –> Re~4.0E6 / m

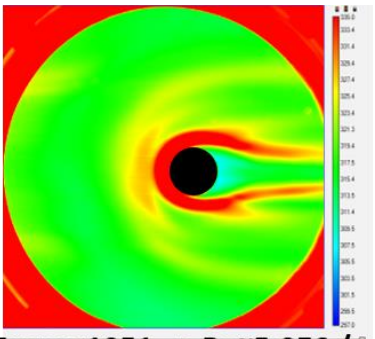

Frame 1051 –> Re~5.0E6 / m

Run 2885

IR thermography on same 1.25” diameter cylinder but now with trips.

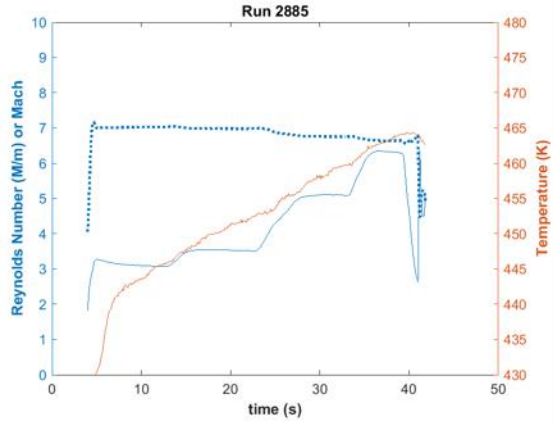

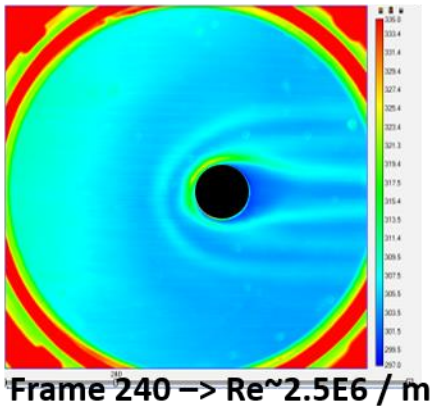

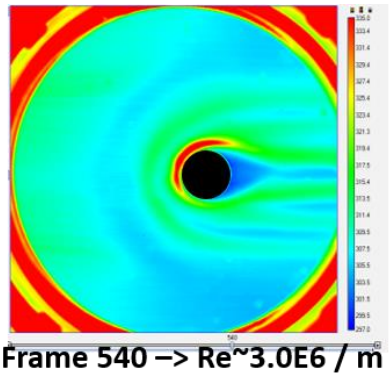

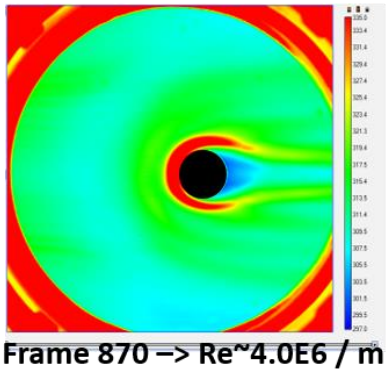

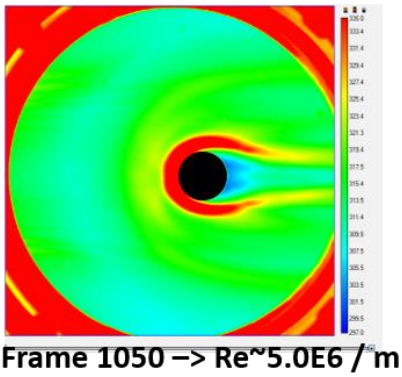

Run 2886

IR thermography on model with trips and 0.75” diameter cylinder.

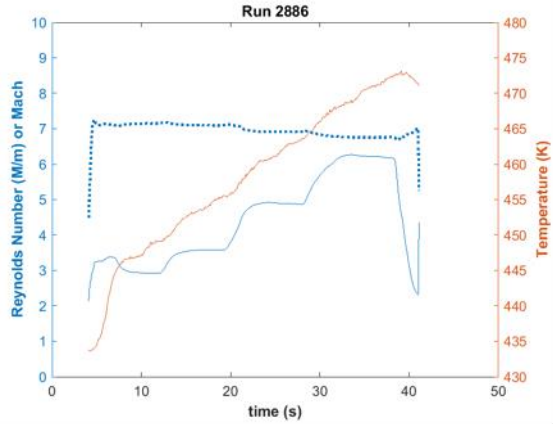

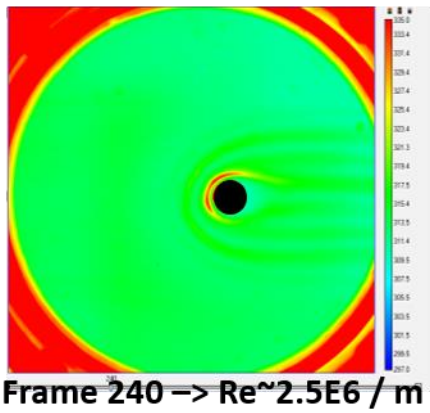

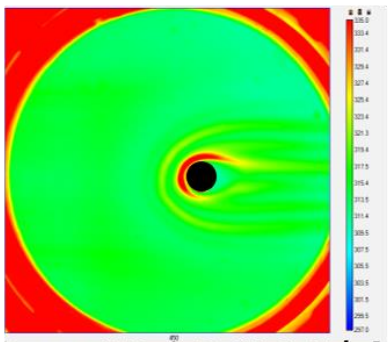

Frame 450 –> Re~3.0E6 / m

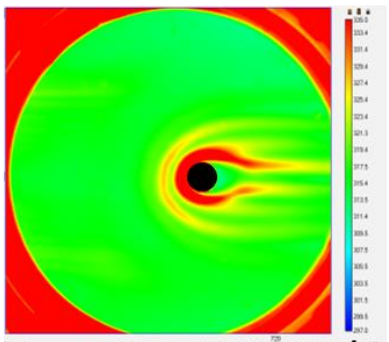

Frame 720 –> Re~4.0E6 / m

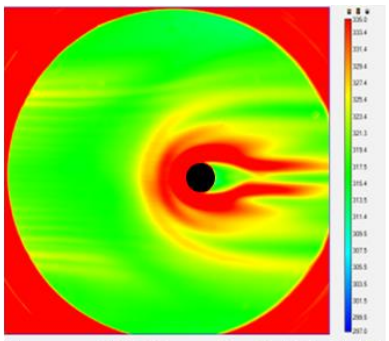

Frame 1020 –> Re~5.0E6 / m

Run 2887

IR thermography on model without trips and with a 0.75” diameter cylinder positioned 10.5” downstream of the leading edge.

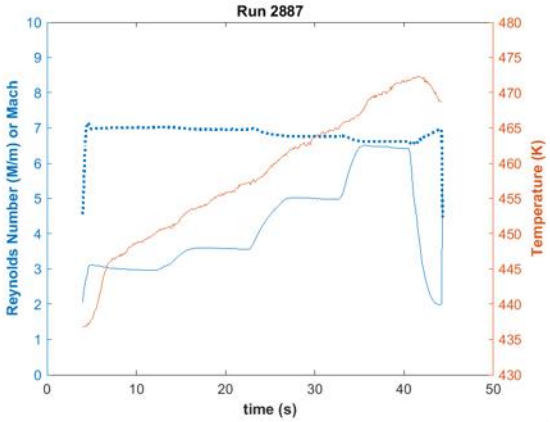

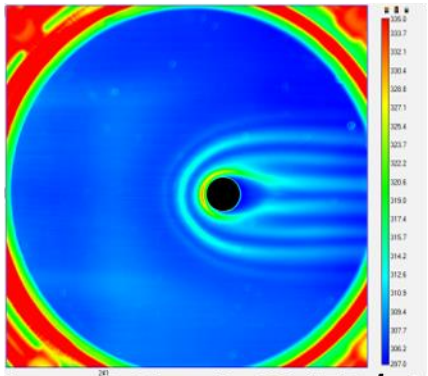

Frame 241 –> Re~2.5E6 / m

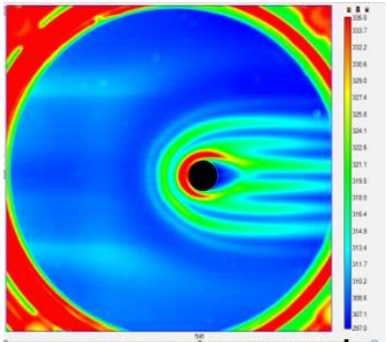

Frame 541 –> Re~3.0E6 / m

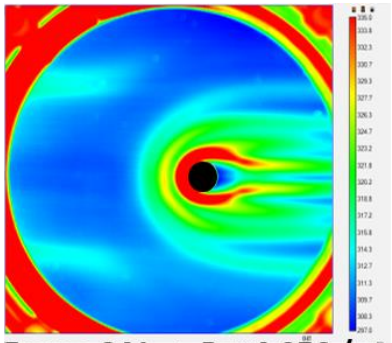

Frame 841 –> Re~4.0E6 / m

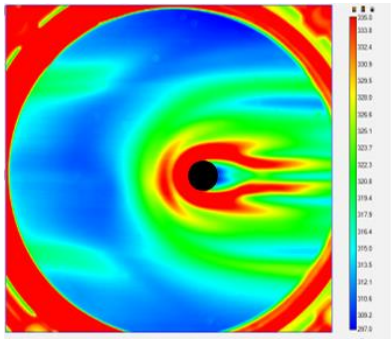

Frame 1081 –> Re~5.0E6 / m

Run 2888

IR thermography on model without trips and with a 0.75” diameter cylinder positioned 16.5” downstream of the leading edge.

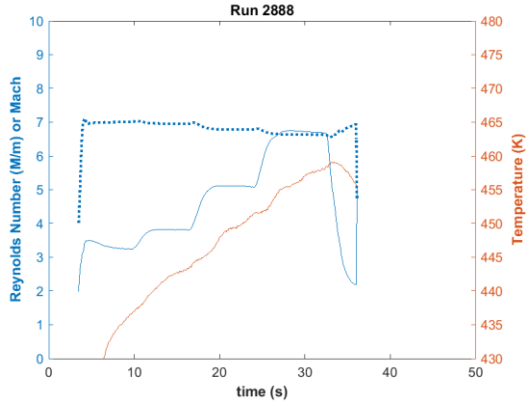

Run 2889

Same test as previous but with front set of 0.07” trips.

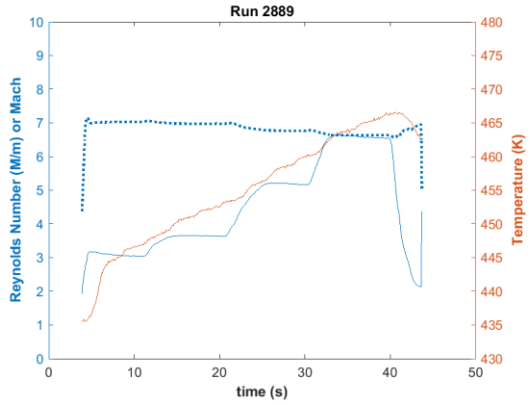

Run 2890

Same test as previous but with 1.25” diameter cylinder.

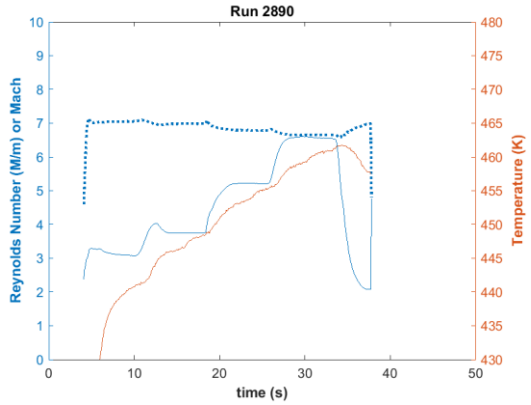

Run 2891

Repeat of previous run.

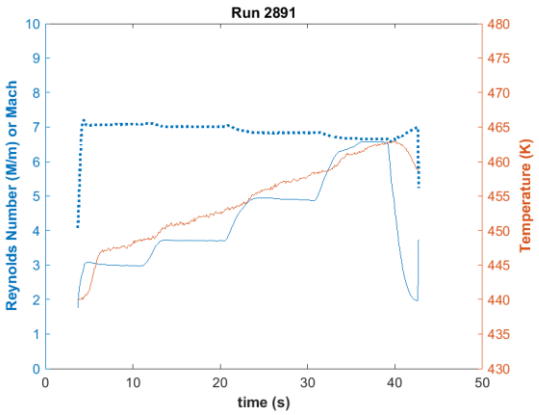

Run 2892

Same test as previous but with no trips.

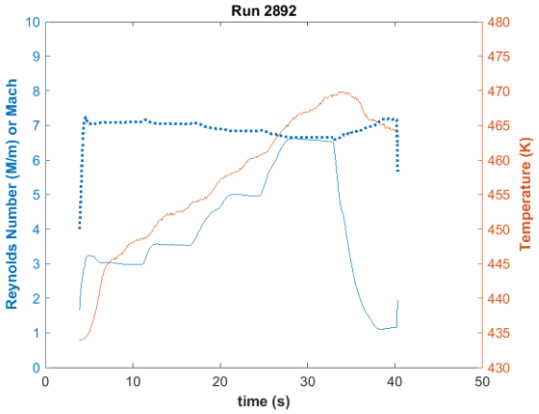

Run 2898

Front row of trips and no cylinder with IR camera directed through downstream window.

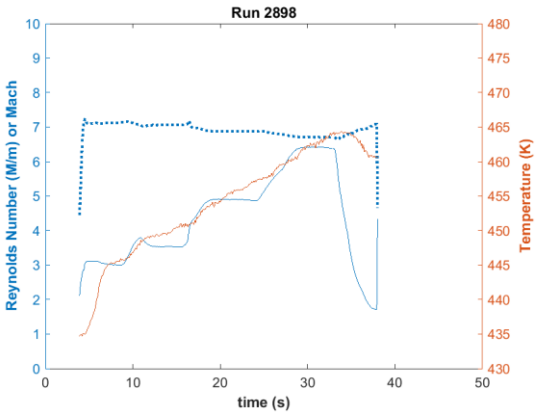

Run 2945

Oil flow visualization on the model with front set of trips and 0.75” diameter cylinder positioned 12” downstream. Re near 3.3M/m.

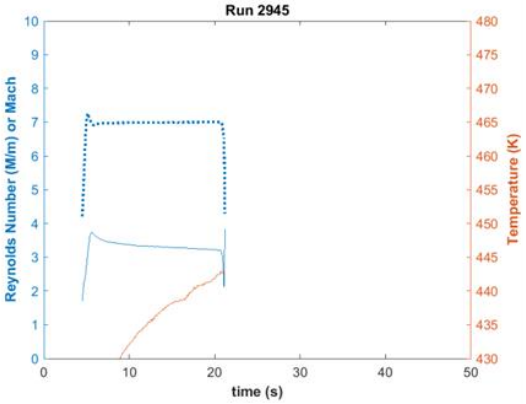

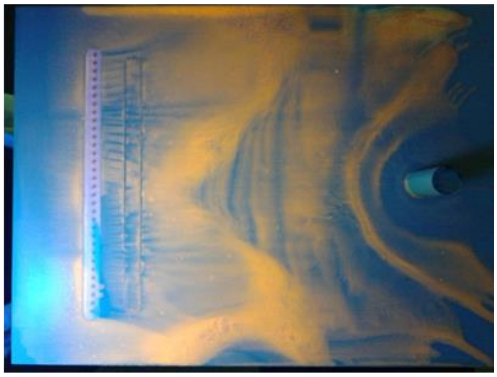

Run 2946

Repeat of previous run with less oil.

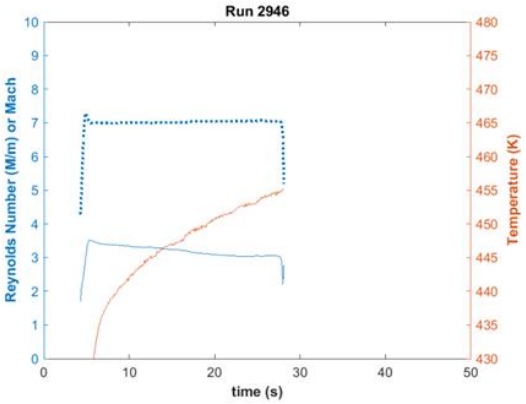

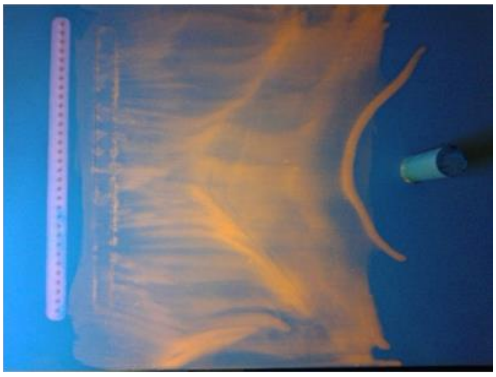

Run 2947

Same run as previous with no trips.

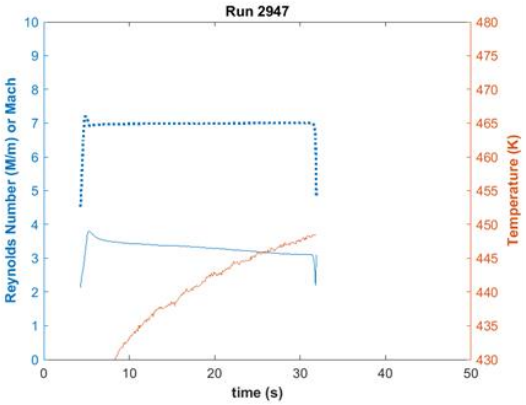

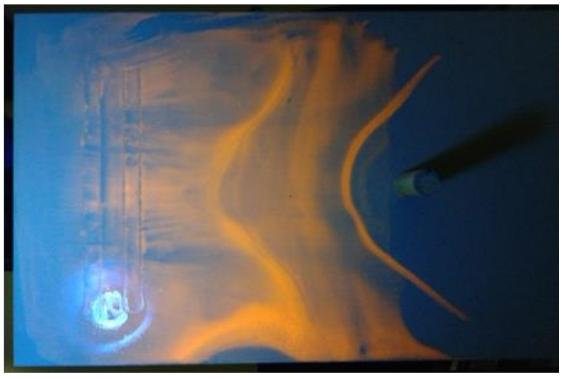

Run 2948

Oil flow on model with trips and with 0.75 diameter cylinder positioned 18” downstream. Re near 3.2 M/m.

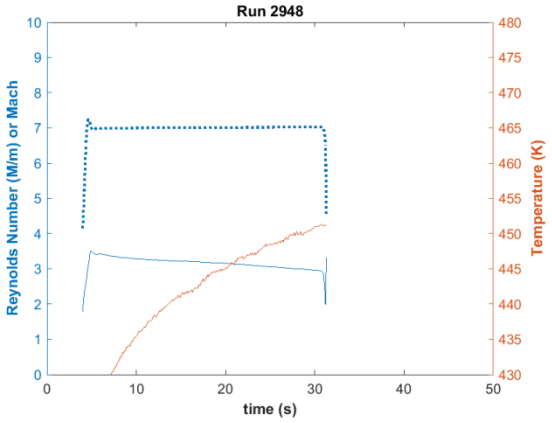

Run 2949

Oil flow on model with trips and with 0.75 diameter cylinder positioned 18” downstream. Re near 3.1 M/m.

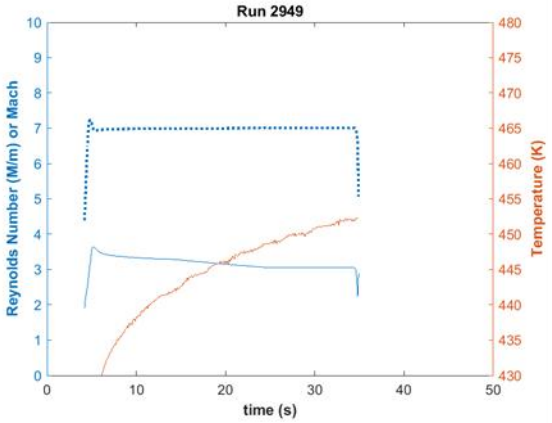

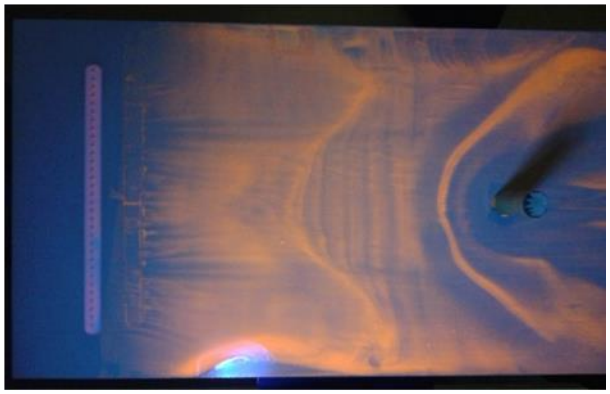

Return to Mach 6

Run 2957

Oil flow visualization on model with a 0.75” diameter, 2.25” tall cylinder placed 15” downstream from the leading edge. Re held near 5.1M/m. Front set of 0.07” trips with 2δ (0.25”) spacing.

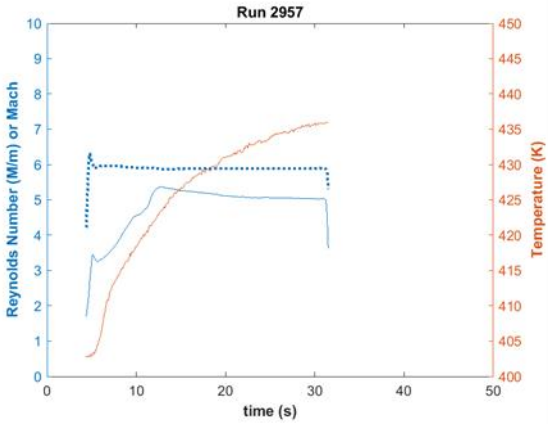

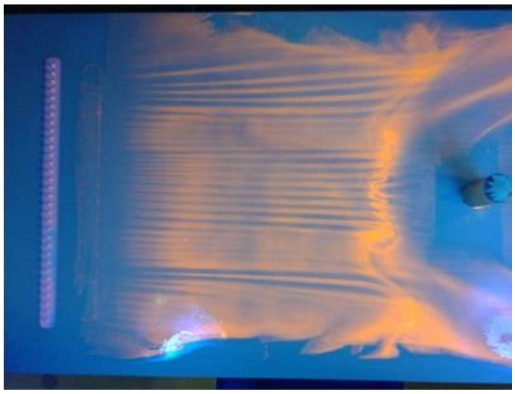

Run 2958

Oil flow visualization with 0.375” trip spacing. Re held near 4.9M/m.

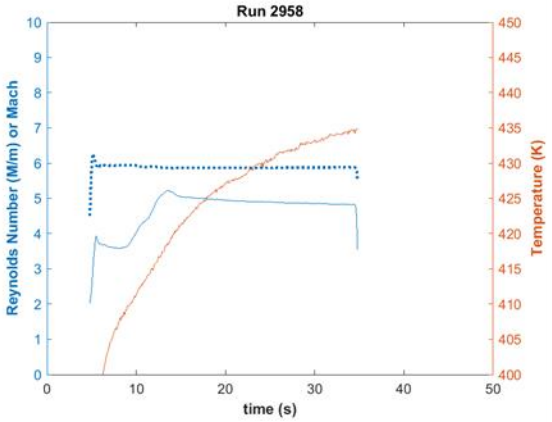

Run 2959

Oil flow on the same trips but cylinder moved upstream to 12” from leading edge. Re near 5.0M/m.

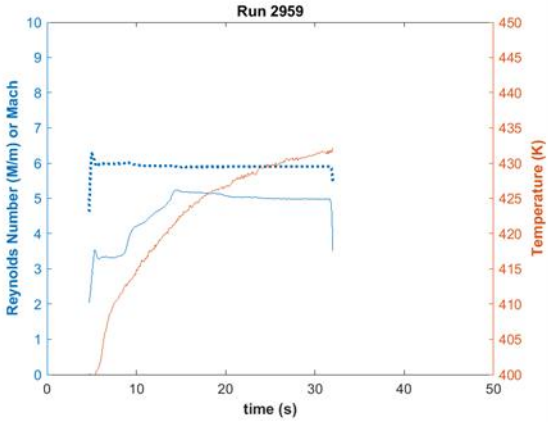

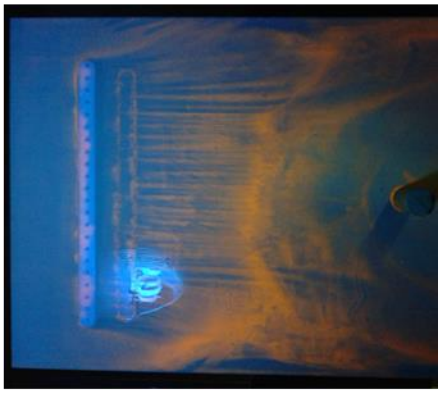

Run 2960

Oil flow with cylinder in same position but with 0.25” trip spacing. Re ramp until unstart at 8.3M/m.

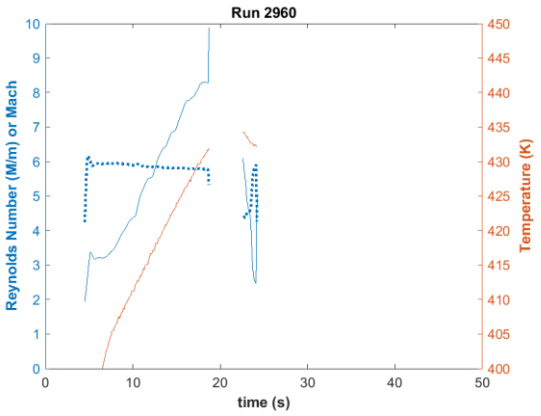

Run 2961

Oil flow with same configuration. Ramped up to Re of 7.6 M/m but tunnel unstarted after 2 seconds.

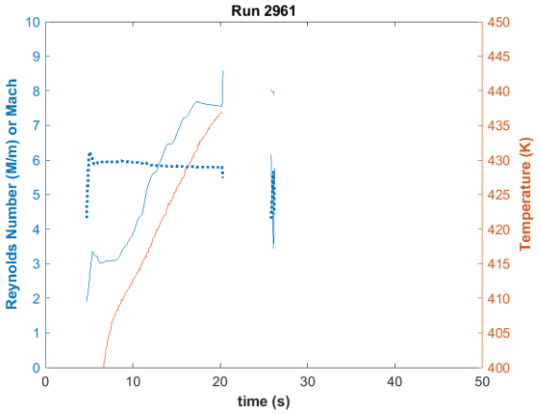

Run 2962

Oil flow with same configuration. Tunnel did not hold Re of 7.8M/m.

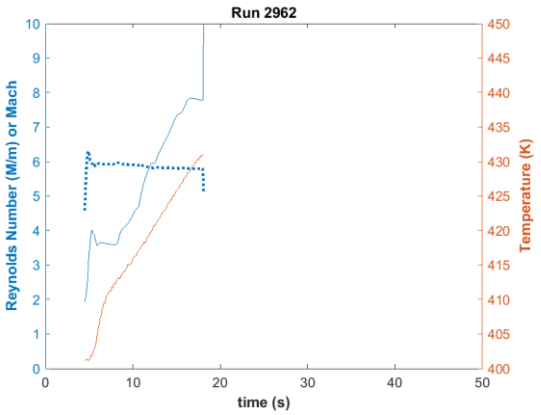

Run 2963

Oil flow with same configuration. 0.07” tall trips with 0.25” spacing and 0.75” diameter, 2.25” tall cylinder located 12” downstream of leading edge. Re held near 7.0M/m.

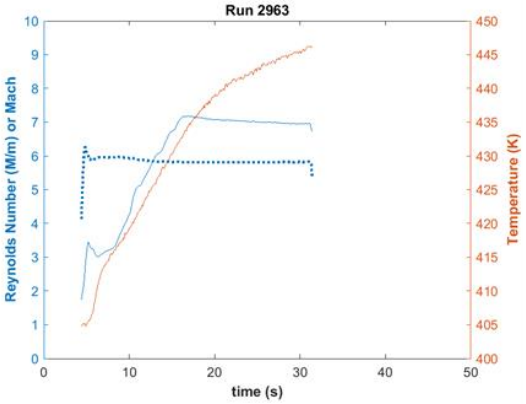

Run 2964

Oil flow with same configuration, except 0.5” spacing between trips. Re near 5.3M/m.

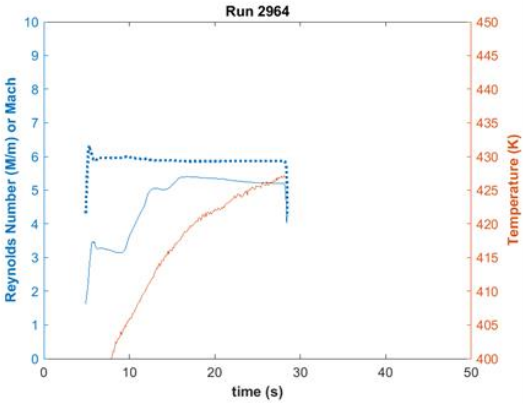

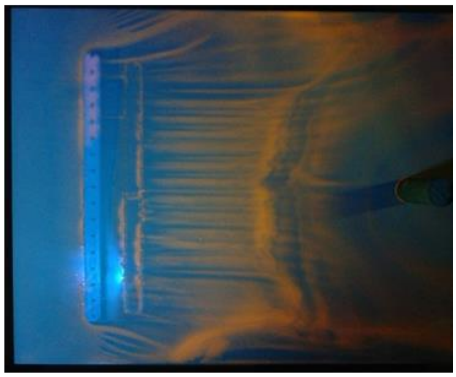

Run 2965

Oil flow on same configuration as previous with Re near 7.1M/m.

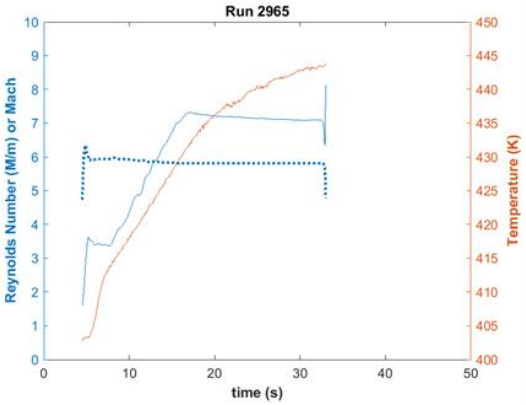

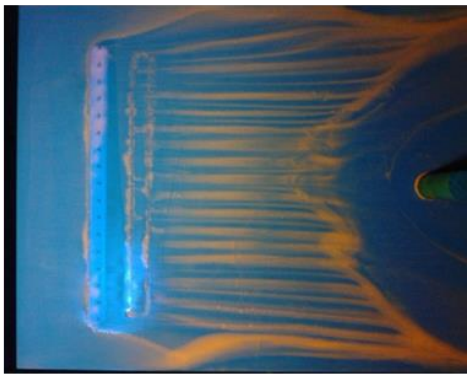

Run 2966

Oil flow on same configuration, except 0.625” spacing between trips. Re near 7.1 M/m.

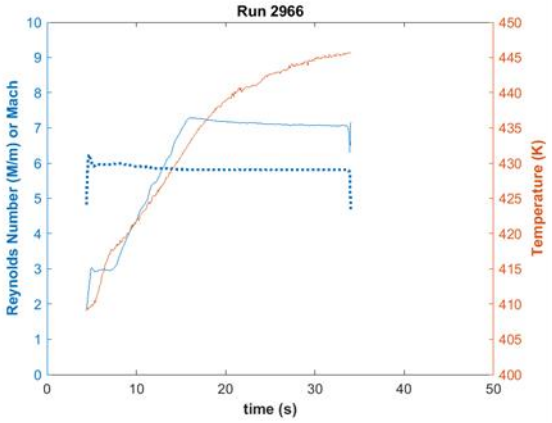

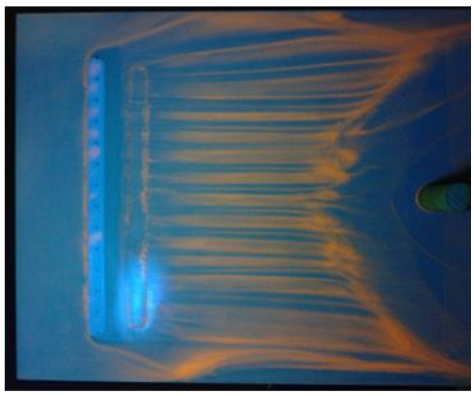

Run 2967

Oil flow on same configuration as previous but Re near 4.8M/m.

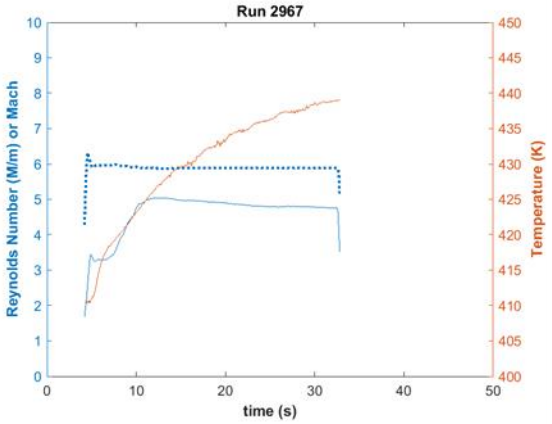

Run 2968. Same configuration as previous but shorter (0.035”) trips. Tunnel did not start as ejector regulators failed from cold temperatures.

Run 2969

Oil flow on configuration kept from 2968. Re held near 4.9M/m.

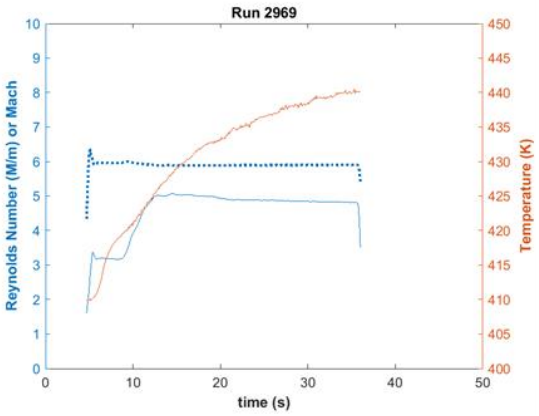

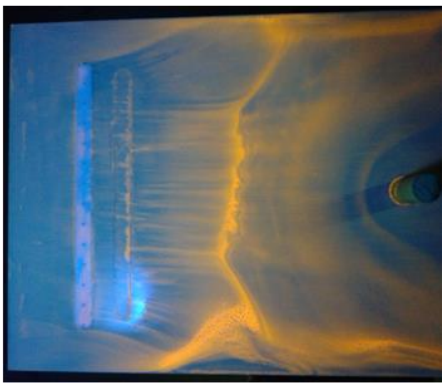

Run 2970

Oil flow on same configuration as previous run, but tunnel did not hold Re of 7.3M/m.

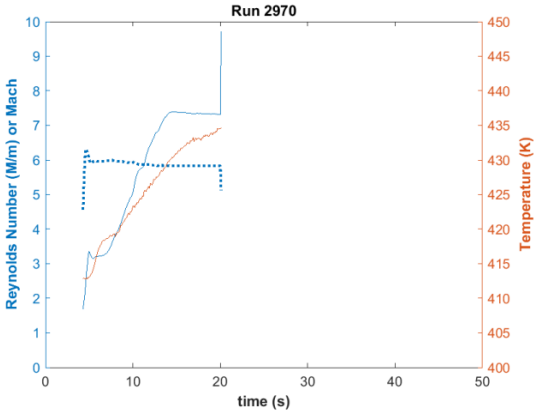

Run 2971

Repeat of 2970. Tunnel held Re of 7.0M/m.

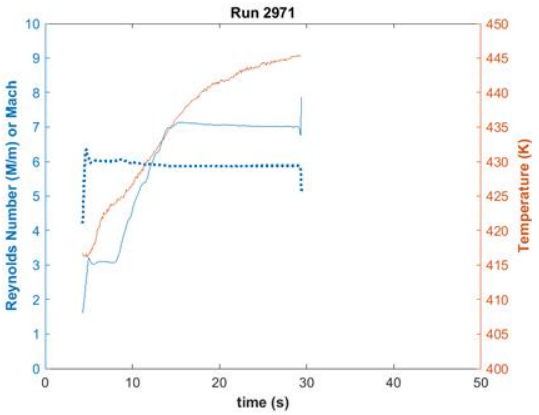

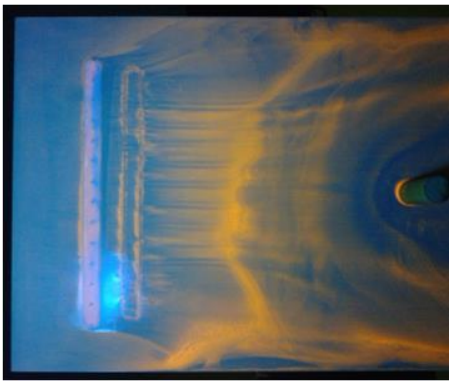

Run 2972

Oil flow on model with same cylinder and 0.035” tall trips and 0.5” spacing. Re held near 4.9M/m.

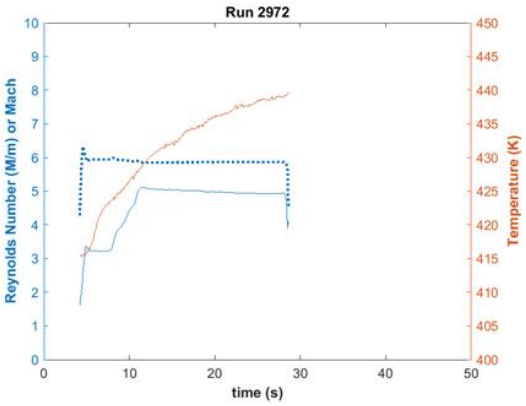

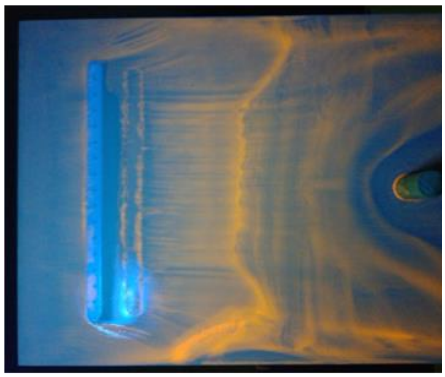

Run 2973

Oil flow on same configuration. Re of 7.3M/m failed.

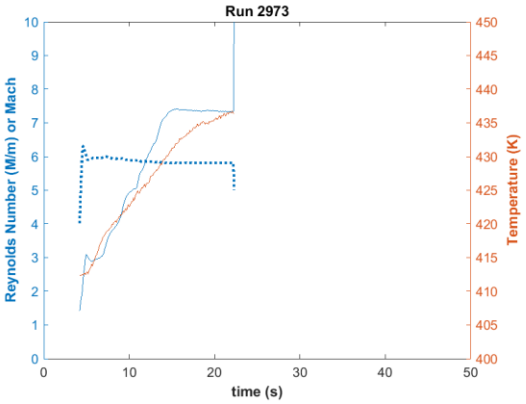

Run 2974

Repeat of previous again failed.

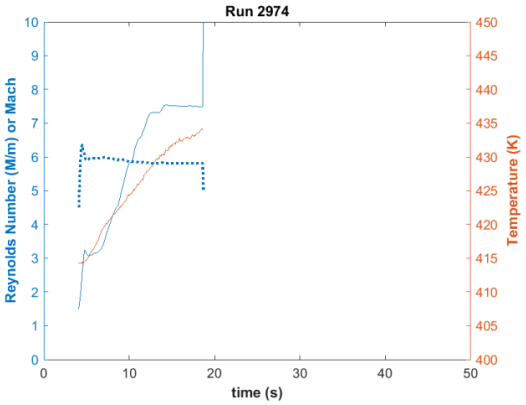

Run 2975

Repeat of previous held at Re of 7.0M/m.

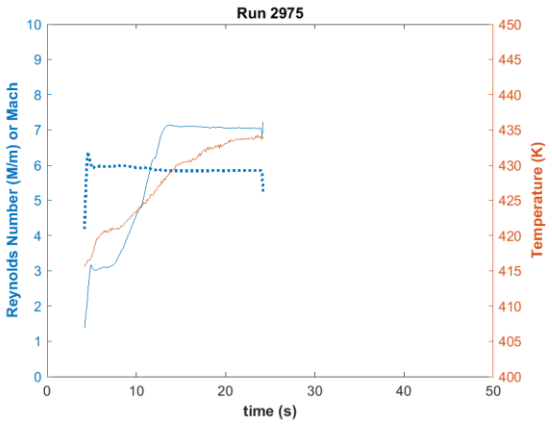

Model span reduced from 11" to 9.75"

Run 2984

Oil flow on model with 0.75" cylinder located 12" downstream of leading edge and front 0.07" tall, 0.5" spaced trips. Re held near 7.1M/m.

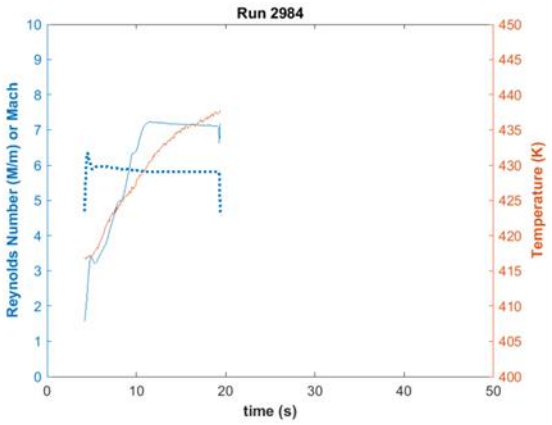

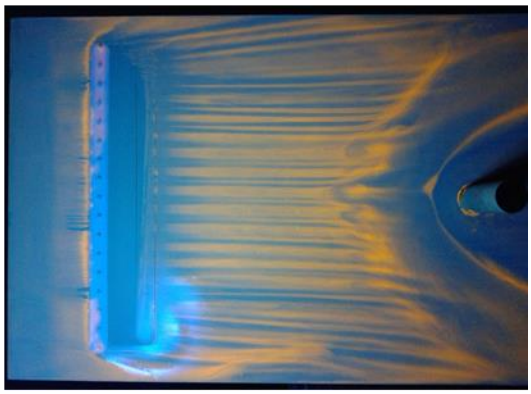

Run 2985

Oil flow on same configuration as previous, but Re held near 5.0M/m.

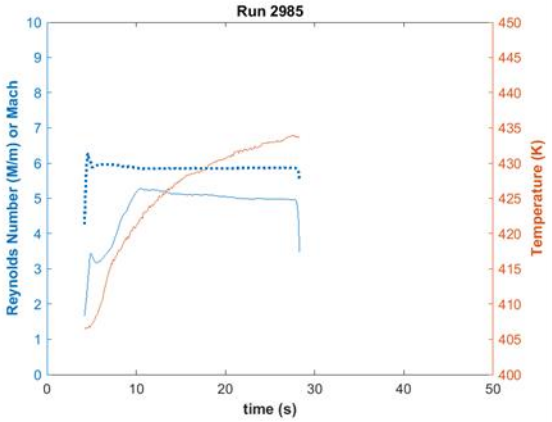

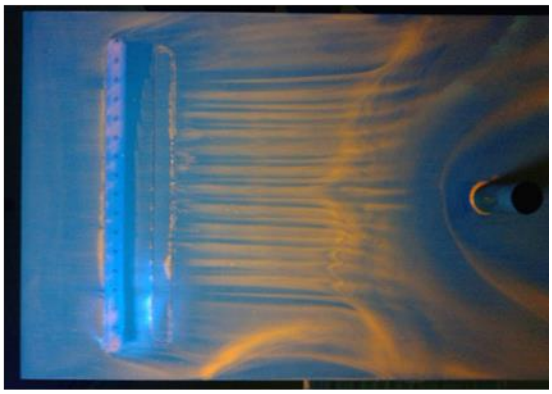

Run 2986

IR thermography on the same configuration at stepped Re.

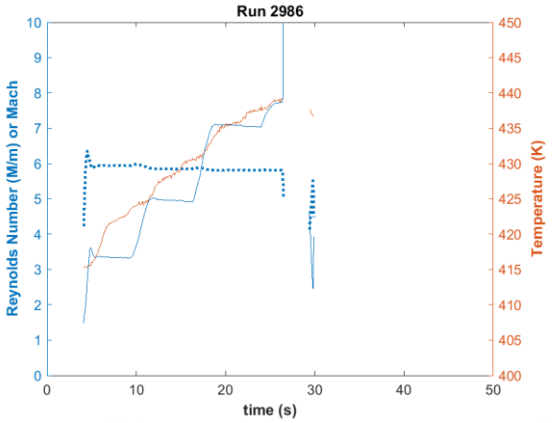

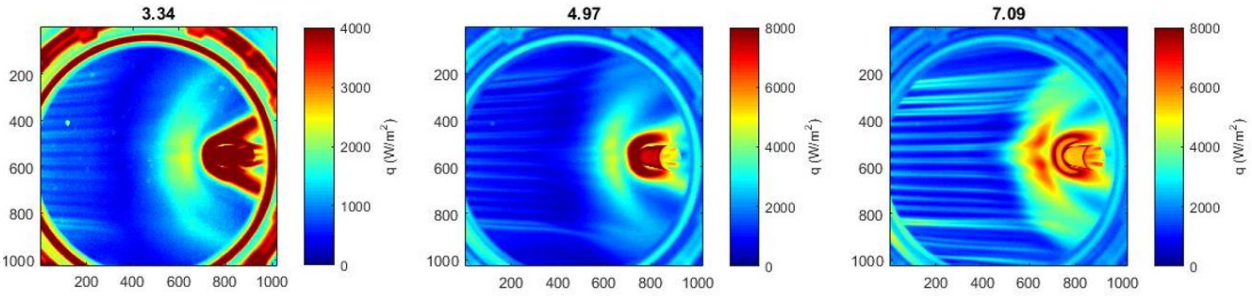

Run 2987

Same run as previous but without the cylinder.

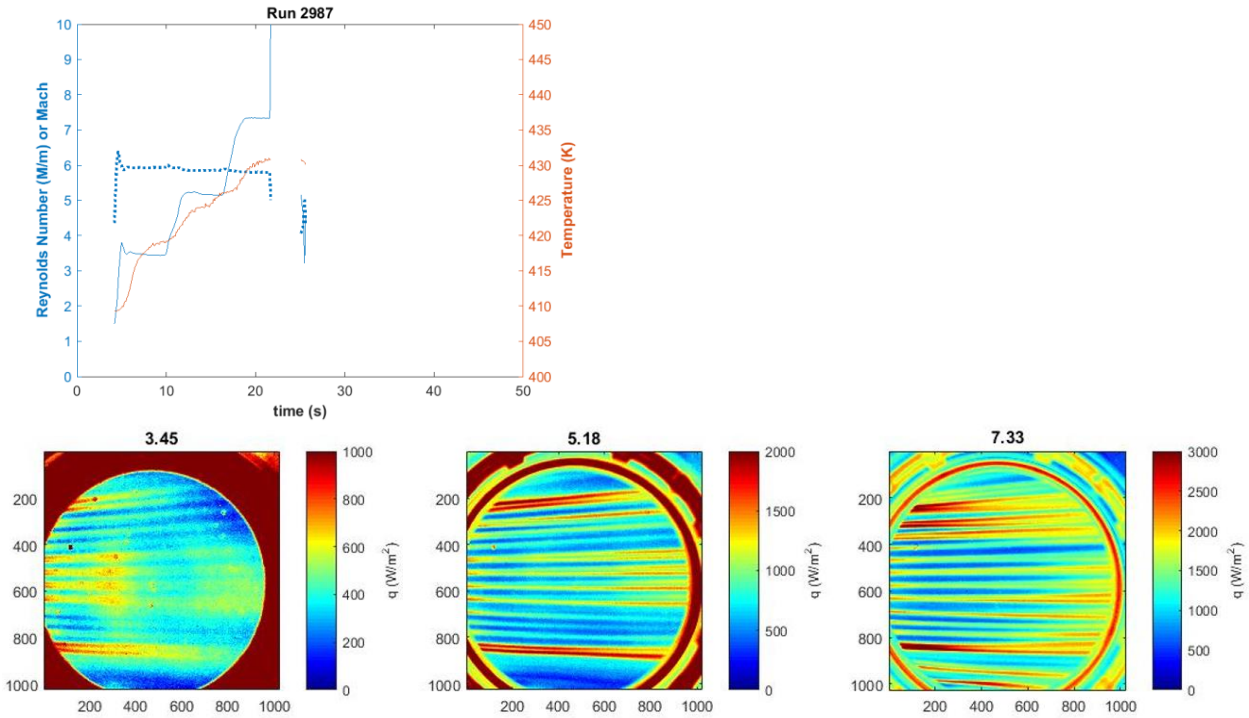

Run 3007

IR thermography and fast-response pressure measurements (2 Kulites, 2 PCBs) on the model with no trips and no cylinder.

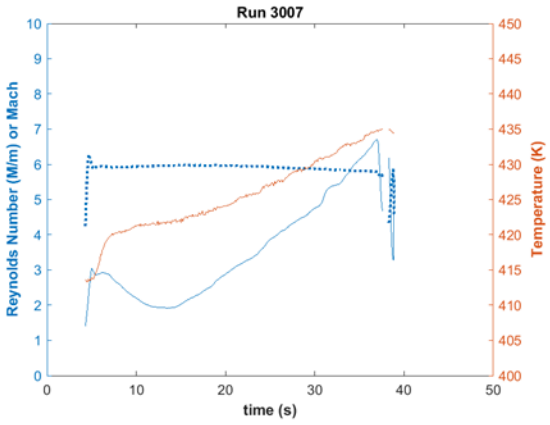

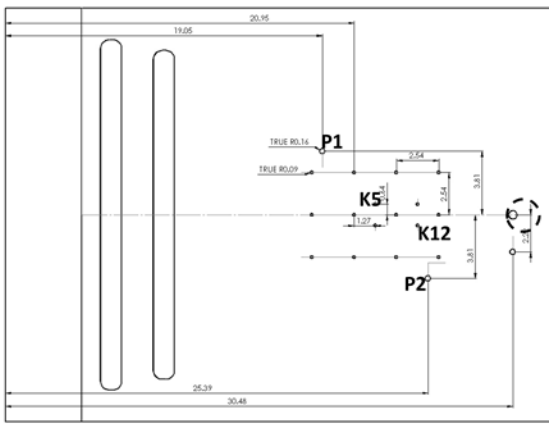

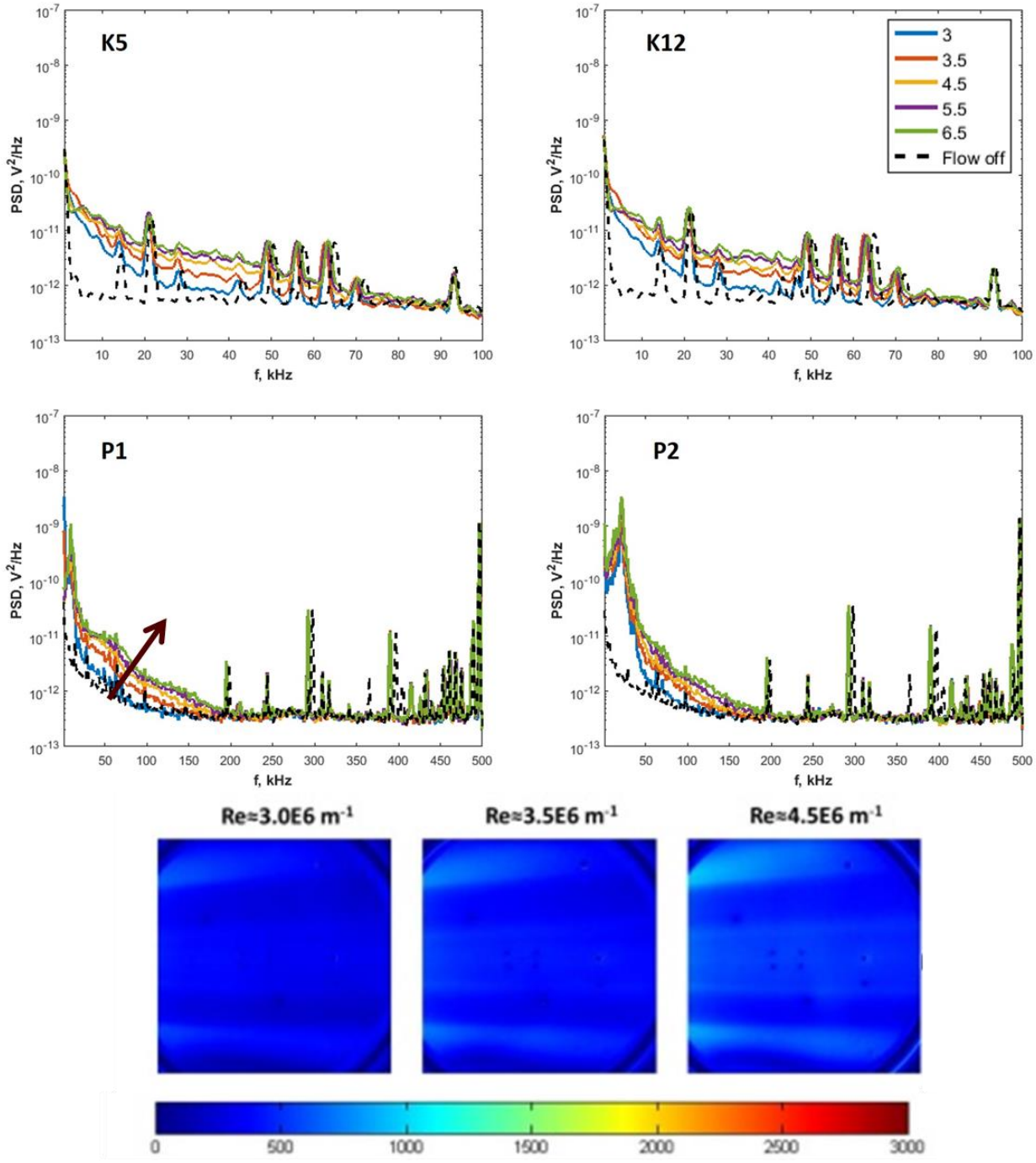
K5
K12
P1
P2
PSD, V²/Hz
f, kHz
3
3.5
4.5
5.5
6.5
Flow off
Re≈3.0E6 m⁻¹
Re≈3.5E6 m⁻¹
Re≈4.5E6 m⁻¹
0
500
1000
1500
2000
2500
3000

Run 3008

IR thermography and fast-response pressure measurements (2 Kulites, 2 PCBs) on the model with 0.07” tall, 0.25” spaced trips in front trip port and no cylinder.

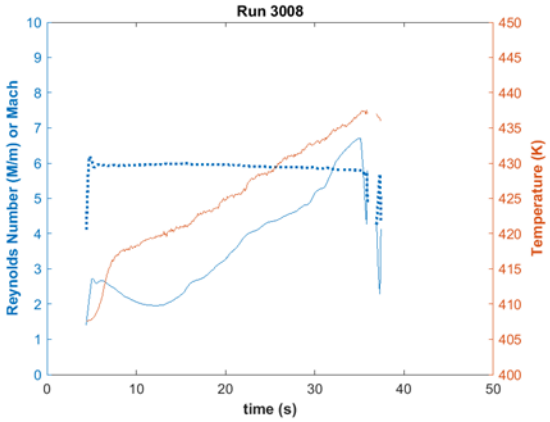

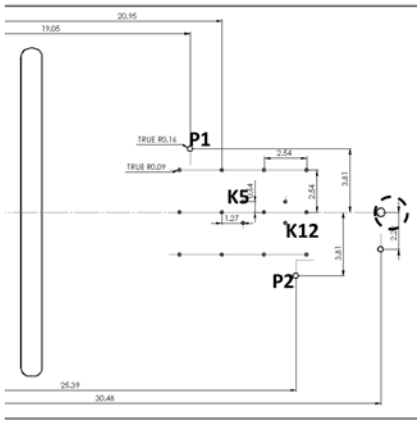

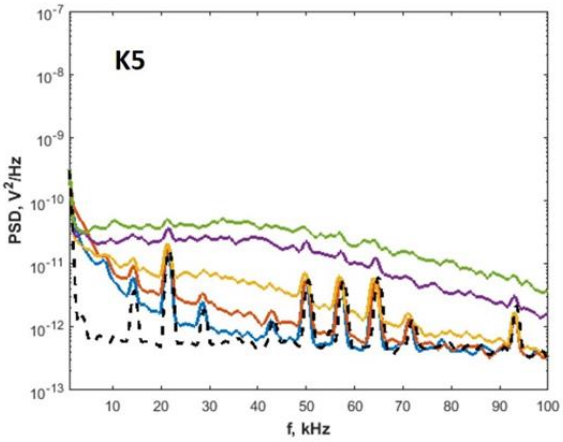

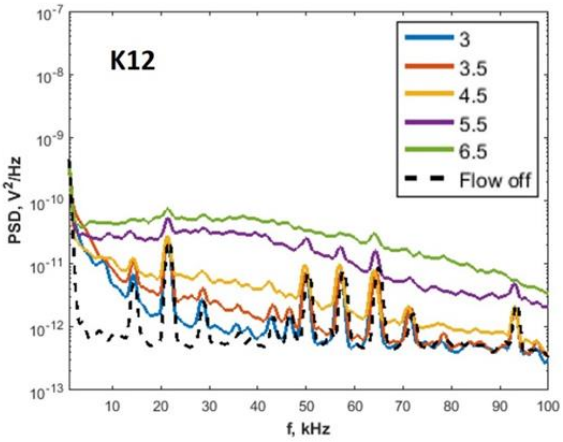

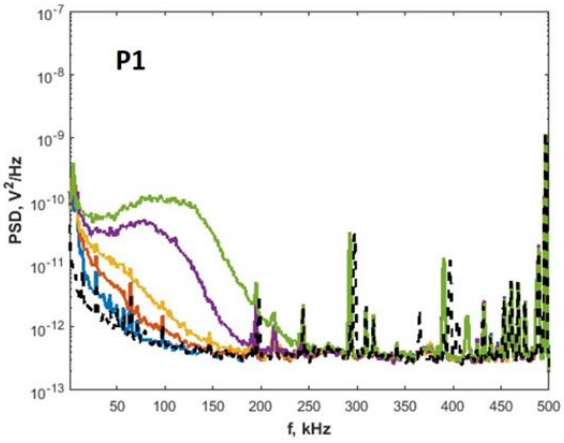

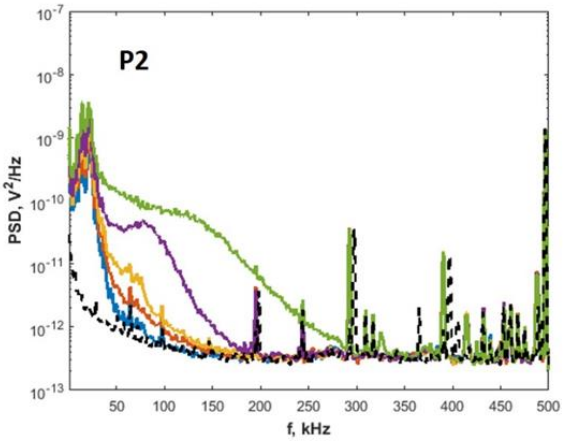

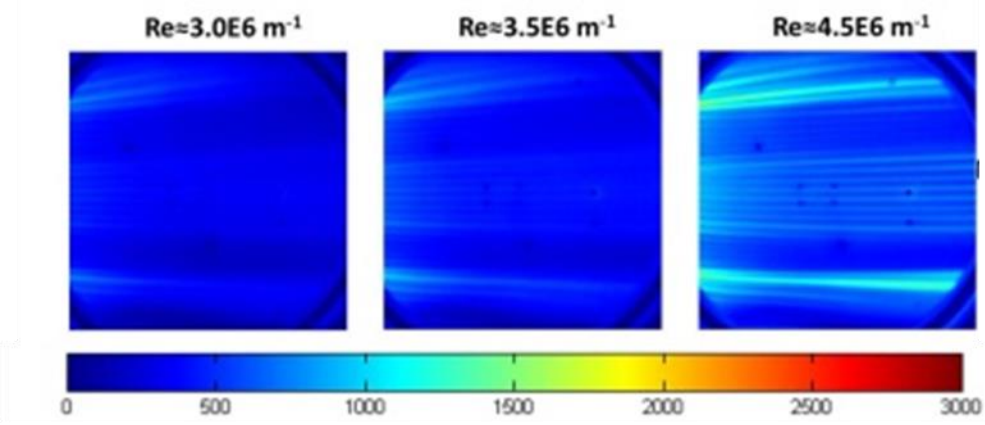

Run 3010

IR thermography and fast-response pressure measurements (2 Kulites, 2 PCBs) on the model with 0.07" tall, 0.25" spaced trips in front trip port and 0.75" diameter, 2.25" tall cylinder located 12" from leading edge.

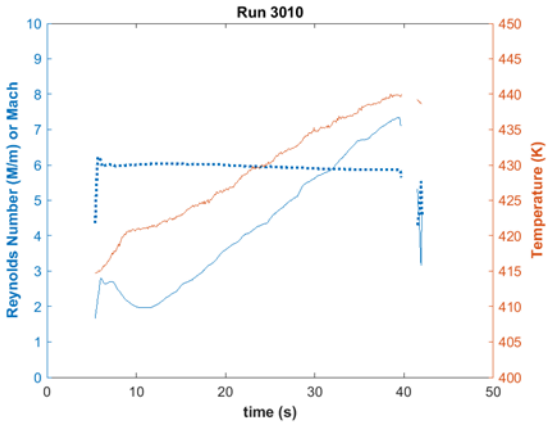

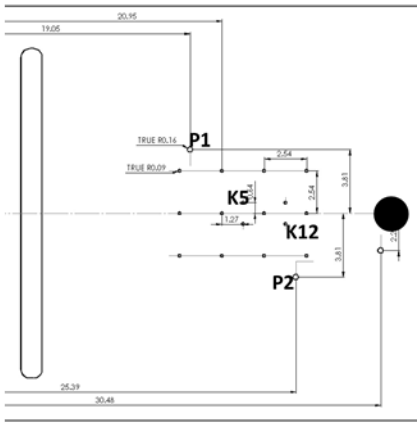

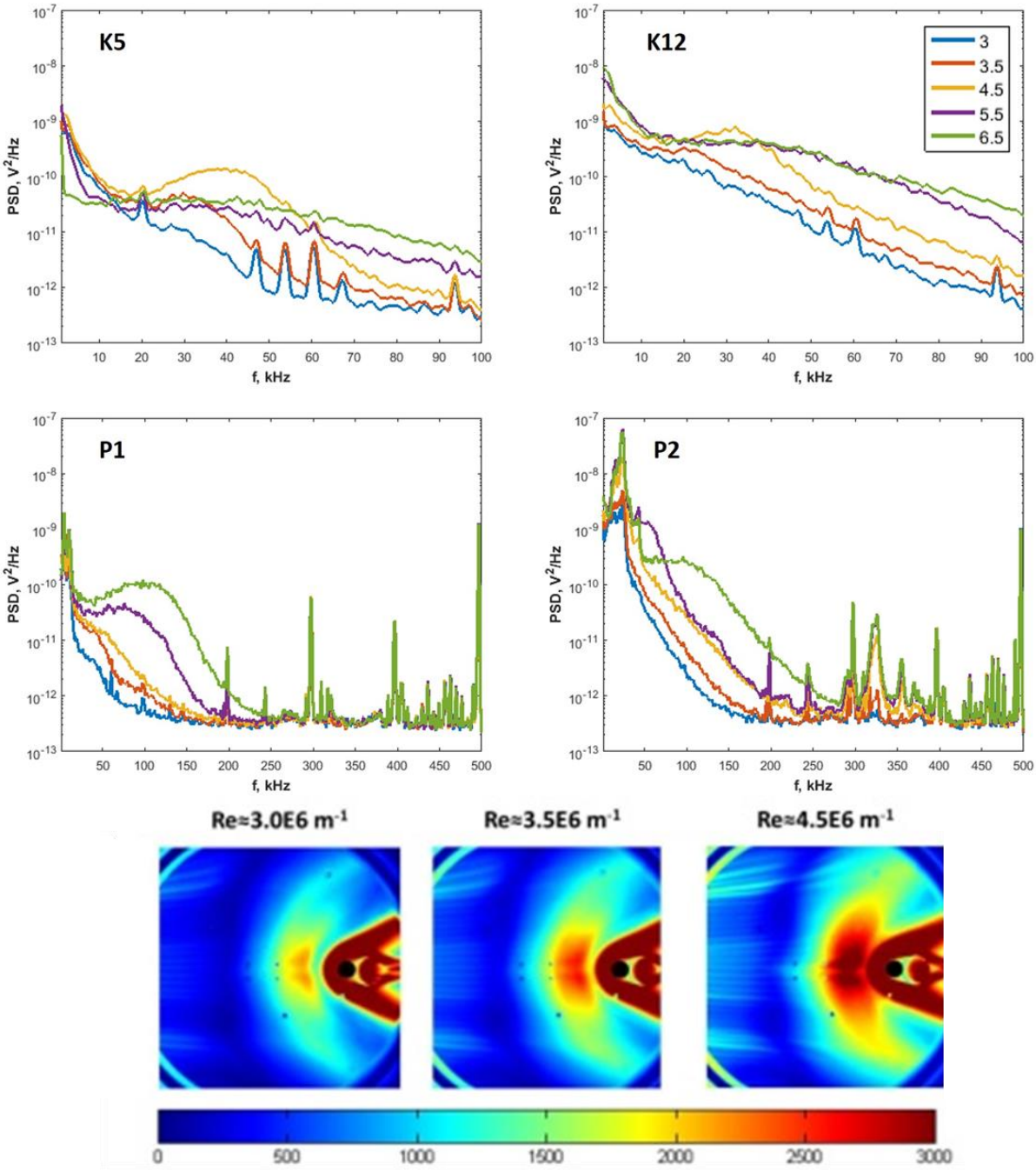
K5
K12
P1
P2
PSD, V²/Hz
f, kHz
3
3.5
4.5
5.5
6.5
Re≈3.0E6 m⁻¹
Re≈3.5E6 m⁻¹
Re≈4.5E6 m⁻¹
0
500
1000
1500
2000
2500
3000

Run 3046

Schlieren (Nikon) on model for a Re sweep. Not seeing leading edge separation.

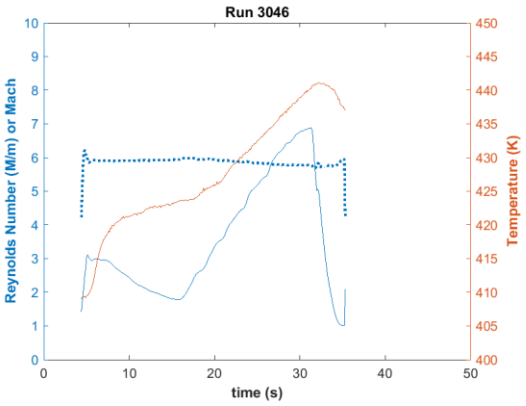

Run 3047

Schlieren (Olympus) on model for a Re sweep. Not seeing leading edge separation.

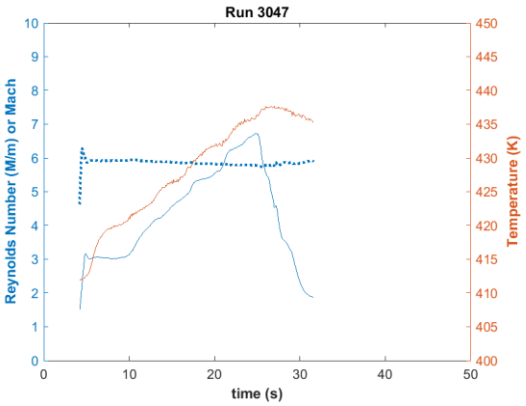

Run 3048

Door was reversed and mounting holes were drilled in model to allow for schlieren (Olympus) of interaction. Cylinder was positioned 16” downstream of leading edge. Video captures near Re of 6M/m.

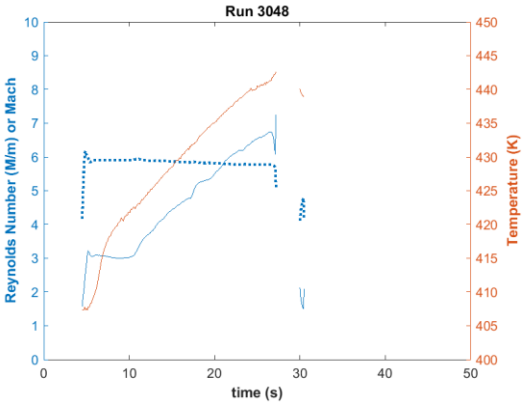

Run 3049

Cylinder repositioned to 15.5” downstream of leading edge. Re near 4M/m captured with schlieren video.

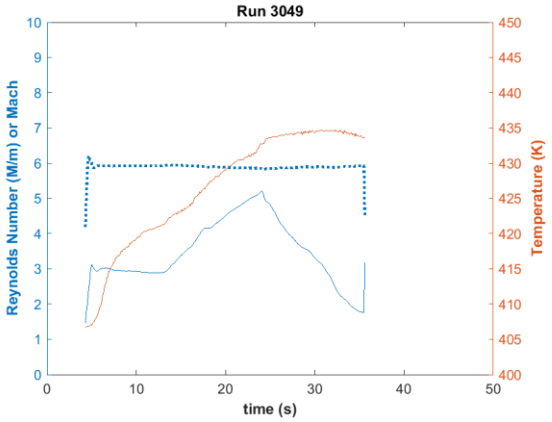

Run 3050

Same configuration as previous run with schlieren of interaction near Re of 6M/m.

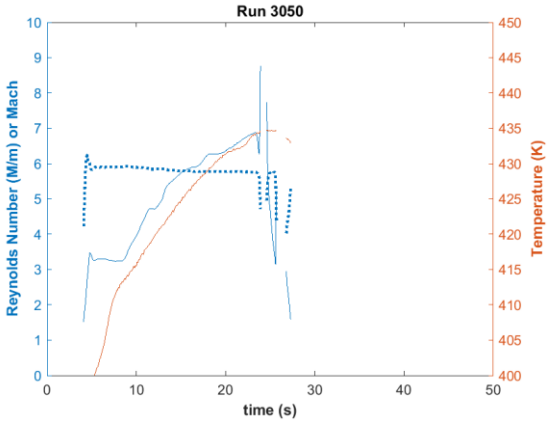

Run 3051

Schlieren for a Re sweep captured with the SA-Z at 500fps with an exposure of 1/800k seconds.

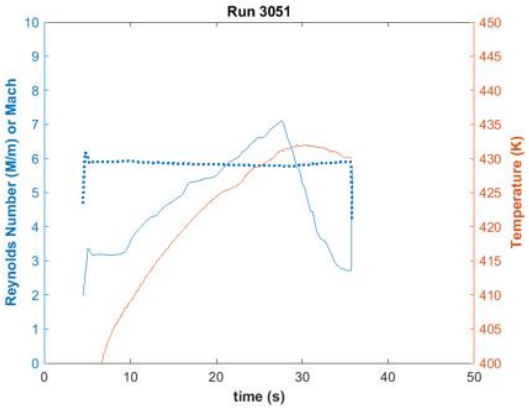

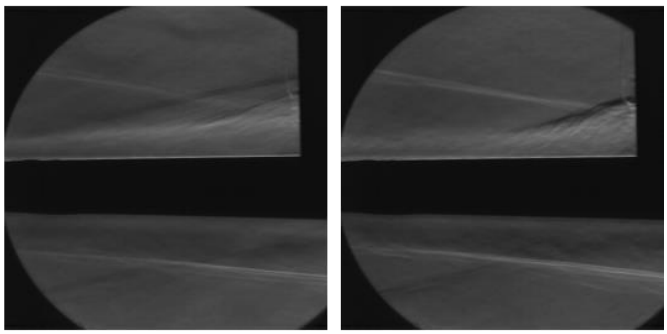

Run 3052

Same configuration as previous except trips were removed. Interaction was monitored using IR thermography and schlieren imaging with the same settings as the previous run.

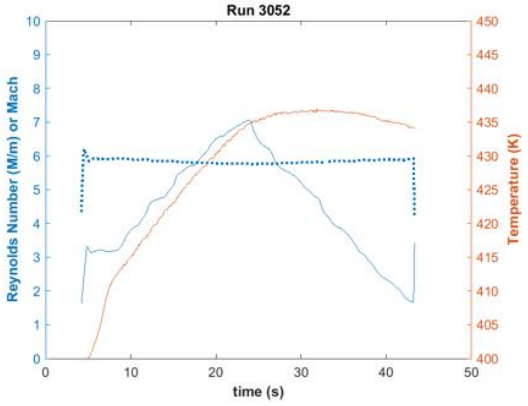

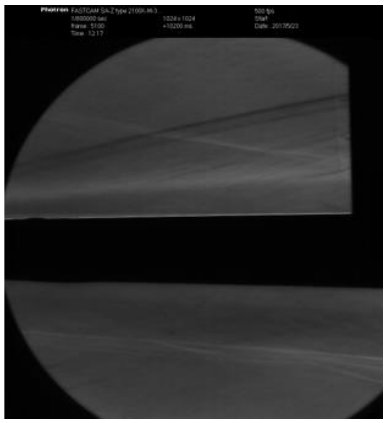

Run 3053

Schlieren imaging at 60k fps for the same configuration, holding a Re near 4M/m.

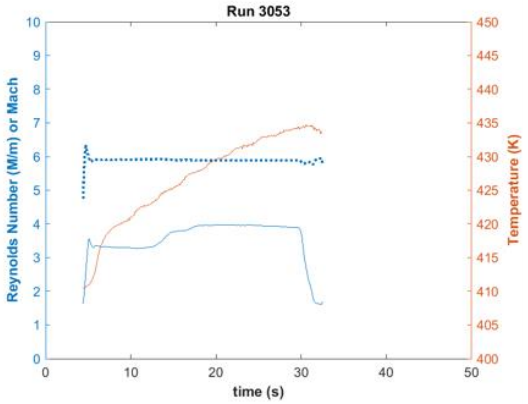

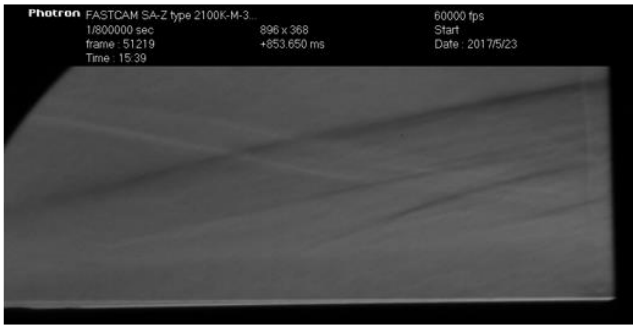

Run 3054

Trips reinserted and a similar schlieren run was conducted as the previous. Re near 4.5M/m.

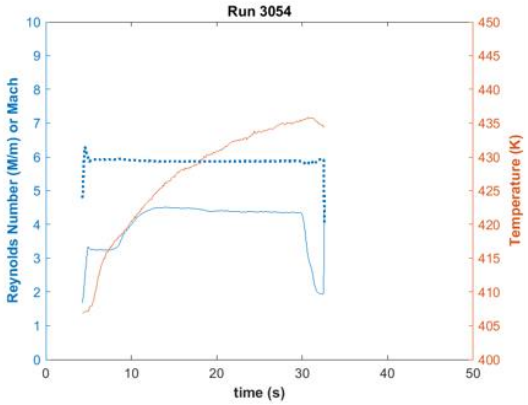

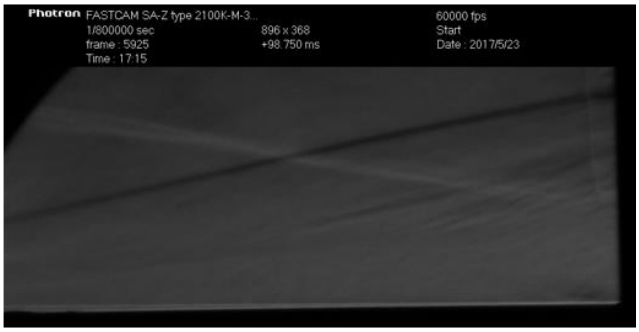

Run 3055

Same configuration and acquisition as above with Re near 5.7M/m.

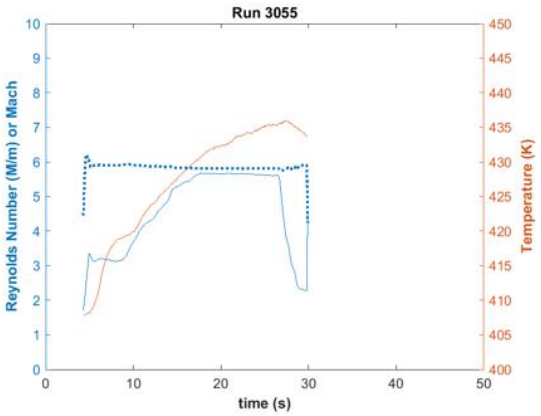

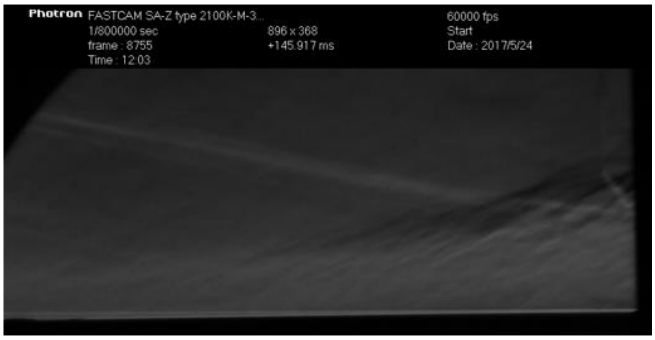

Run 3056

Same configuration and acquisition as above with Re near 5.1M/m.

Run 3057.

Schlieren imaging at 360k fps of region just below separation shock without the trips in place.

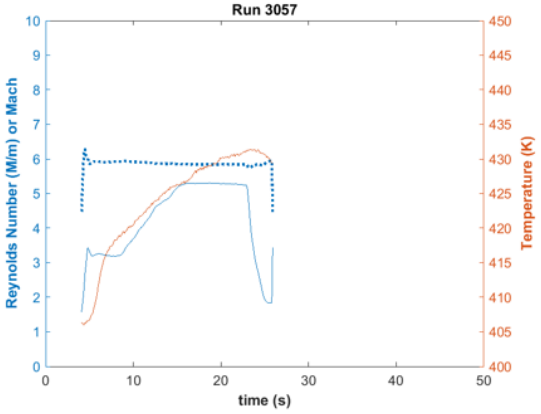

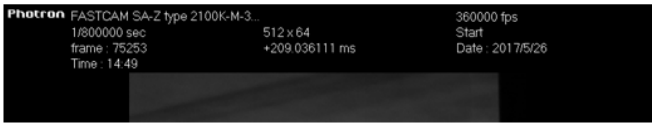

Run 3058.

Schlieren imaging at 60k fps of region near cylinder with trips reinserted. Re near 6.7M/m.

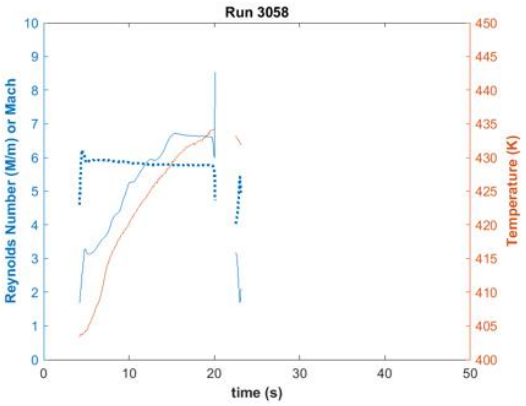

Run 3059.

Similar run as previous.

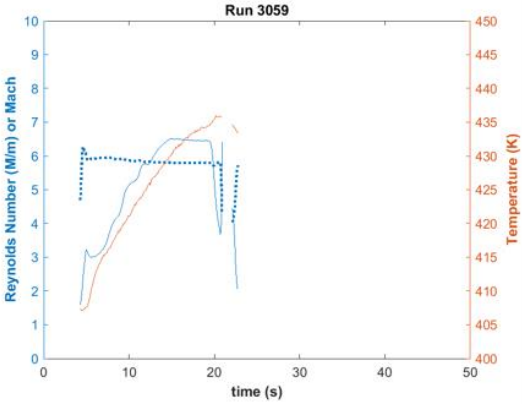

Run 3060.

Schlieren imaging at 288k of same configuration. Re near 6.3M/m.

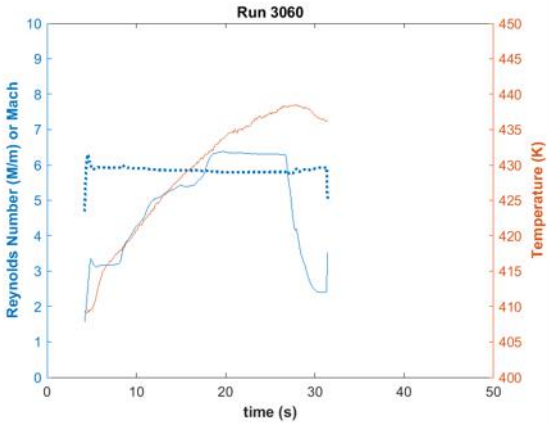

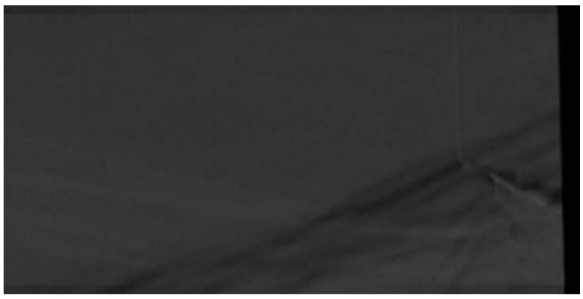

Model Positives:
-no influence from the tunnel sidewalls was observed
-streamlines trended straight back on model
-PEEK material allowed for IR thermography

Model Drawbacks:
-leading edge was machined with a spanwise bow
-mounting prevented high-speed schlieren of interaction

Model 4: 1.3° composite wedge

Preliminary Runs

Run 3203

Oil flow visualization on new model with a thin spanwise stripe painted on the leading edge.

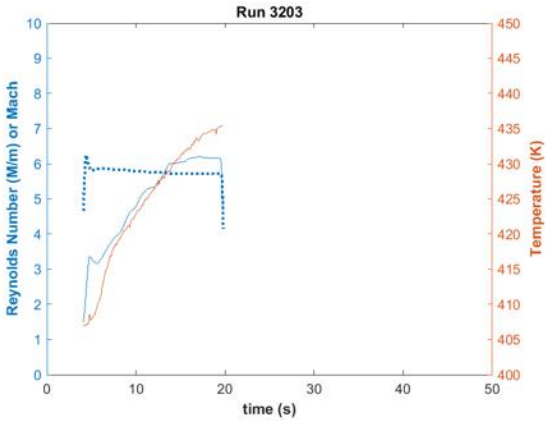

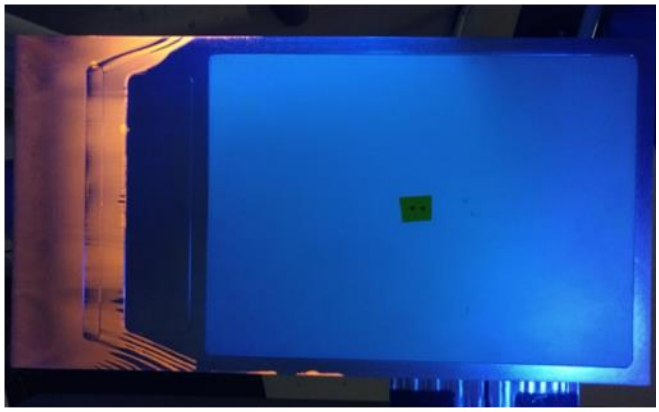

Run 3204

Reynolds number sweep up to find testing bounds.

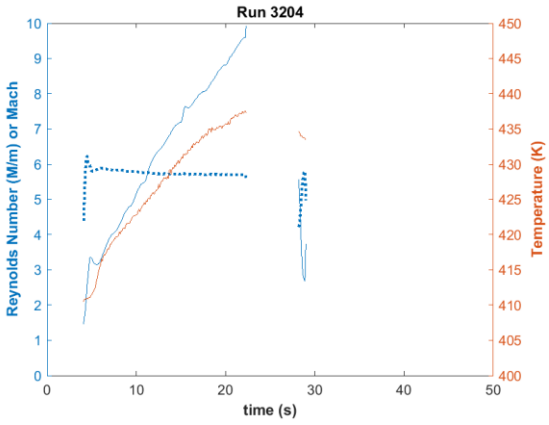

Run 3205

Oil flow visualization on model holding condition near 6.9M/m.

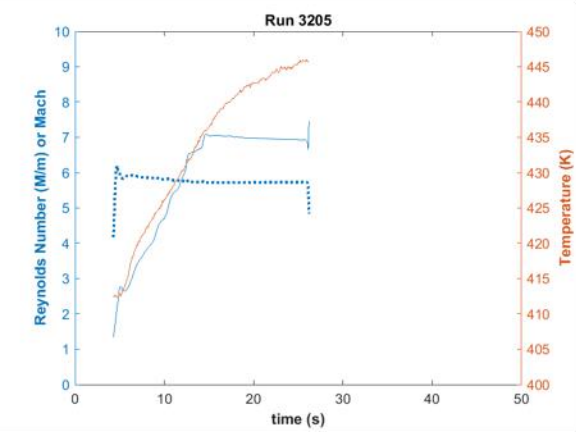

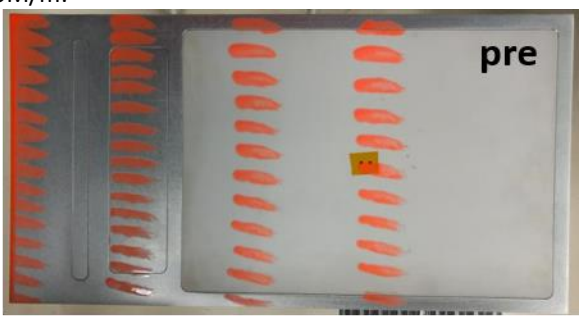

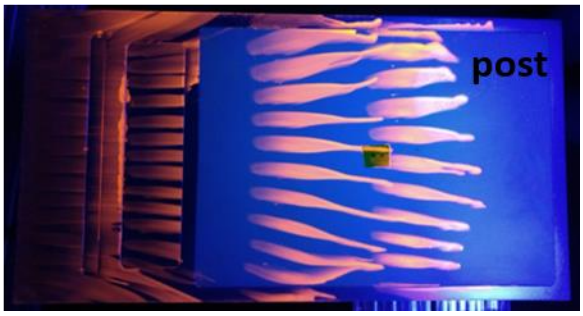

Run 3206

Oil flow visualization on model with a 0.5” diameter, 2” tall cylinder positioned 12” downstream of leading edge. Re held near 2.4M/m.

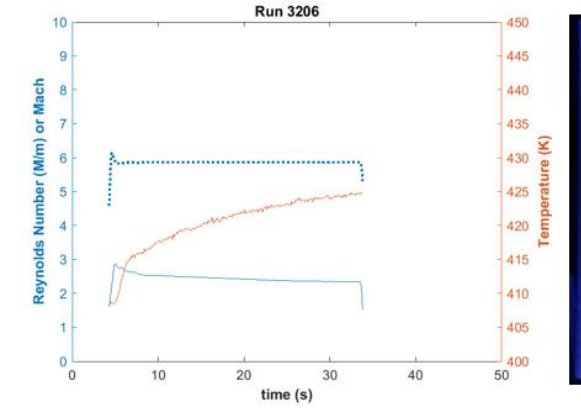

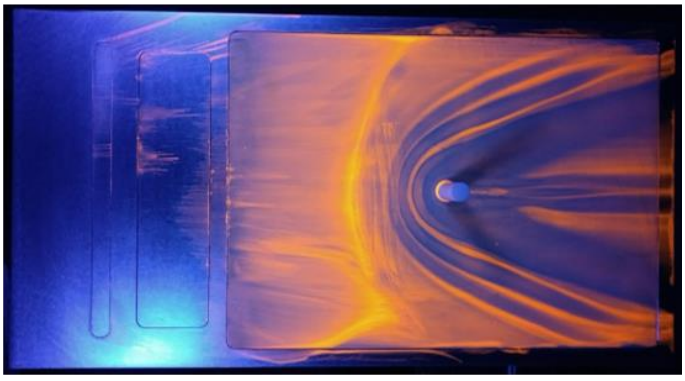

Run 3207

Same test as previous at Re of 7.0M/m.

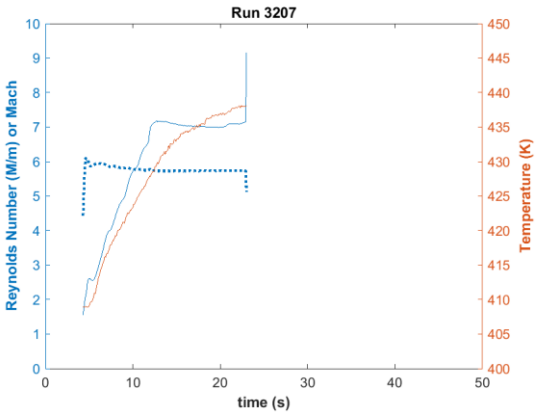

Run 3208

Repeat of previous test at a different diffuser setting.

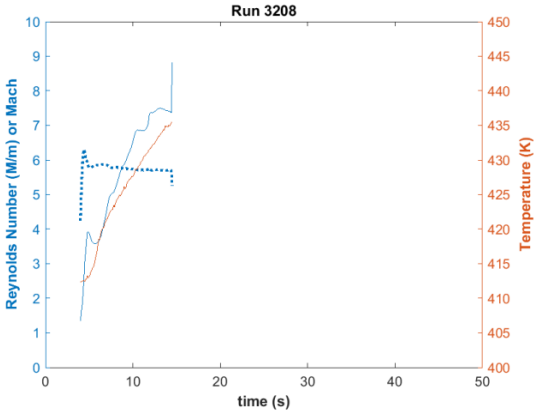

Run 3209

Repeat of previous test at a different diffuser setting.

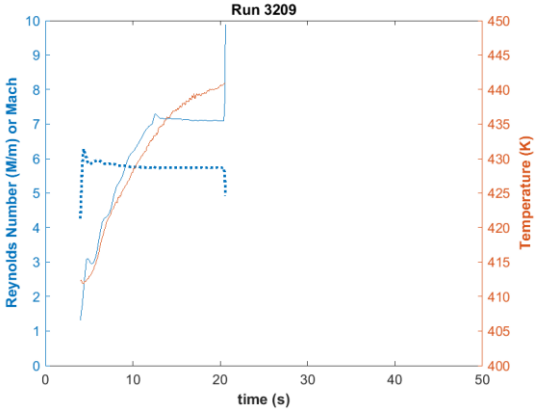

Run 3210

Repeat of previous test at a different diffuser setting.

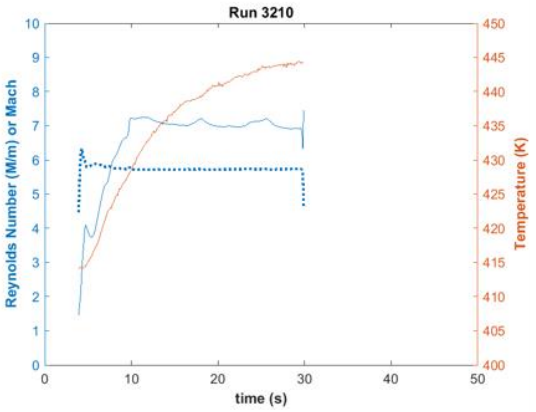

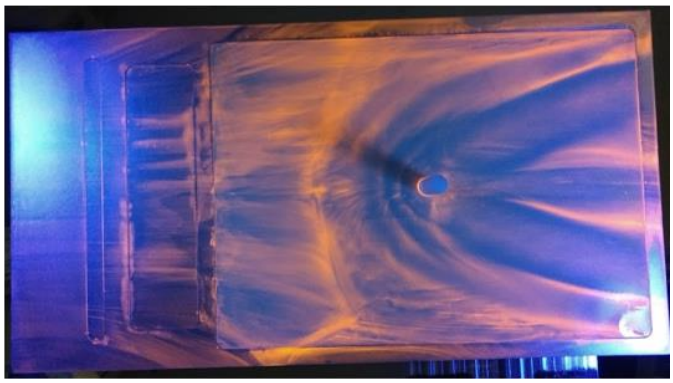

Run 3211

Repeat of previous test at a different diffuser setting.

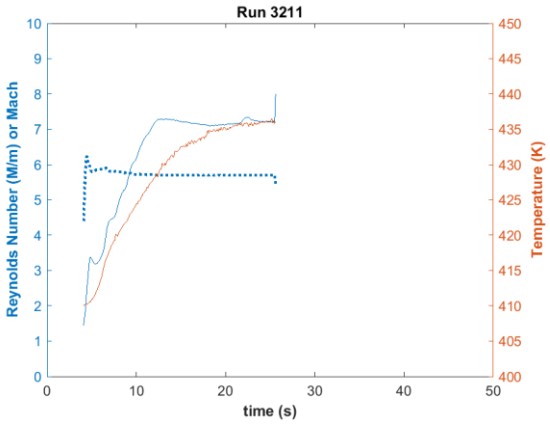

Run 3212

Repeat of previous test at a different diffuser setting.

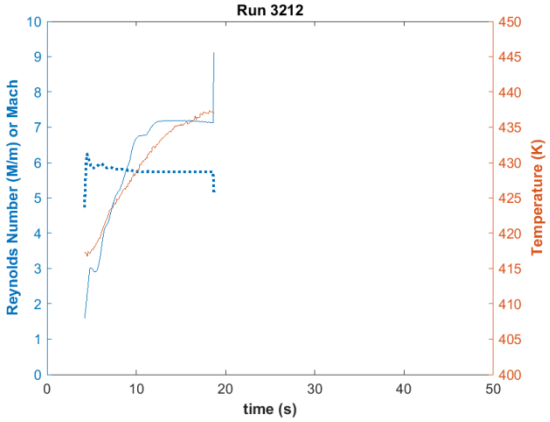

Run 3213

Repeat of previous test at a different diffuser setting. Oil flow visualization on model with a 0.5” diameter, 2” tall cylinder positioned 12” downstream of leading edge. Re held near 7.0M/m.

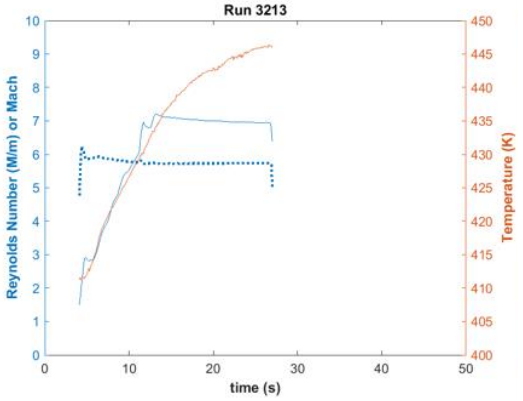

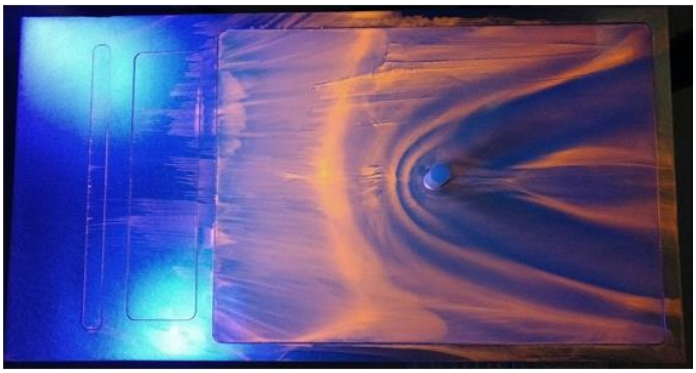

Run 3214

Repeat of previous test at a Re near 5.0M/m.

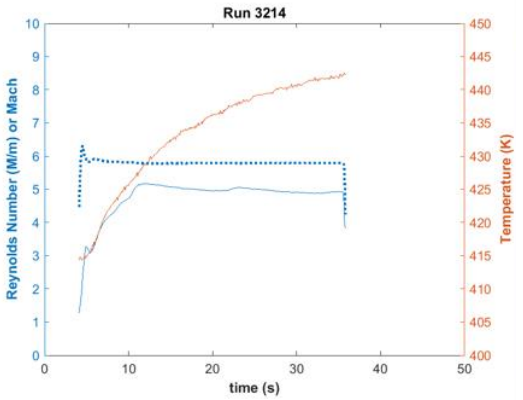

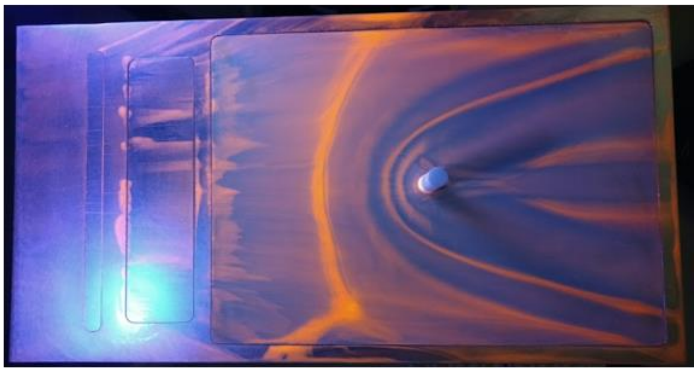

Run 3218

Schlieren using incandescent light source looking 500 fps at leading edge of model.

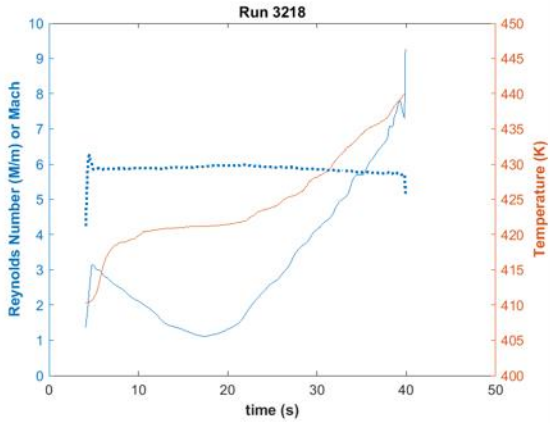

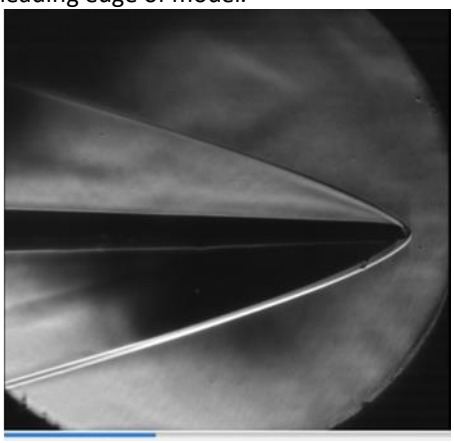

Run 3222

Schlieren using LED light source looking 500 fps at leading edge of model.

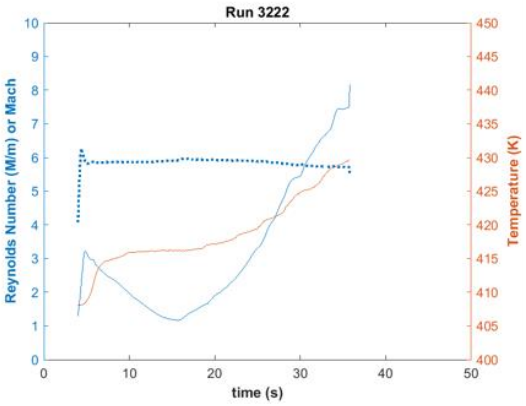

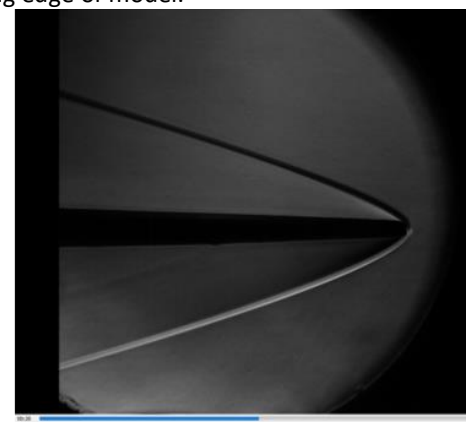

Run 3223

Schlieren looking 140k fps at leading edge of model.

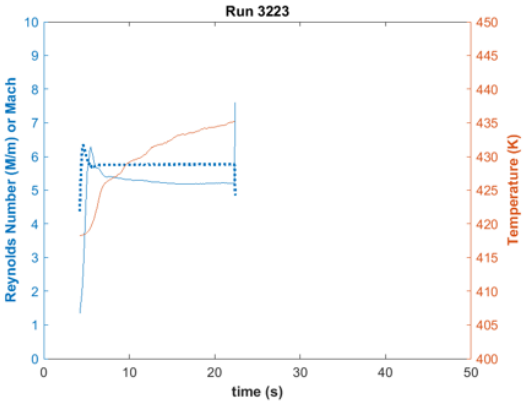

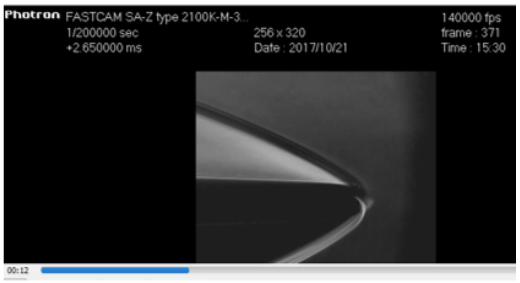

Run 3237

Schlieren at 500 fps using incandescent light source looking at interaction region from 0.5” diameter cylinder. Exposure time could only be reduced to 1/20k seconds and quality was poor.

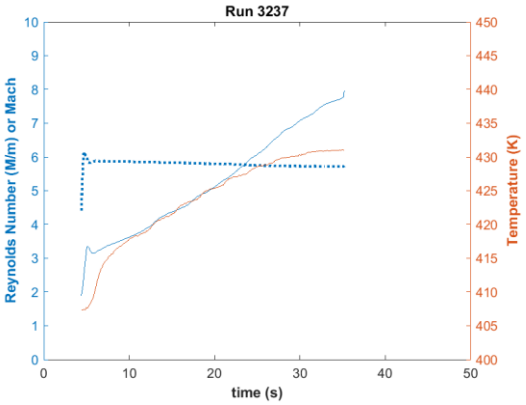

Run 3239

Schlieren of same interaction at 500 fps with LED for 1/4M exposure.

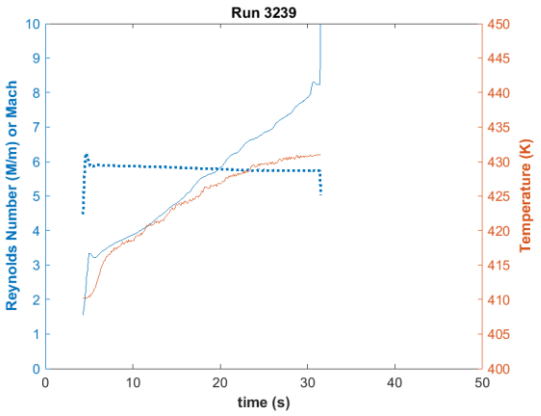

Run 3240

Repeat of previous run attempting to better adjust the cutoff.

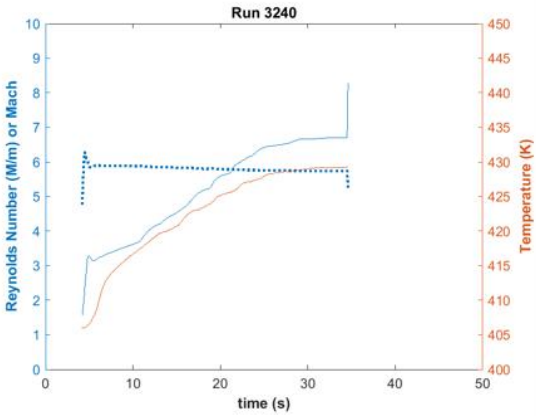

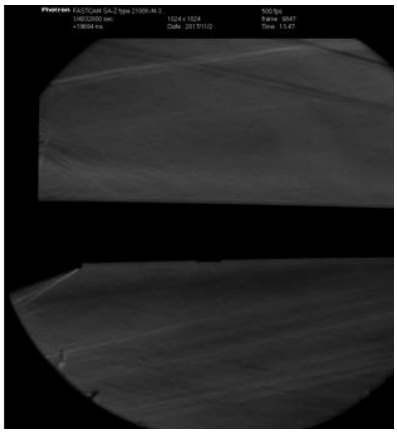

Run 3241

Repeat of previous run with still different cutoff and no improvement in contrast.

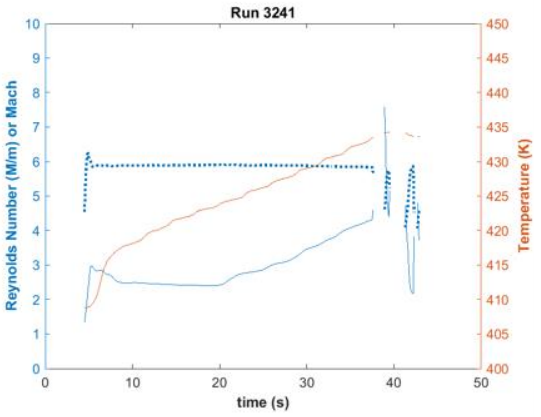

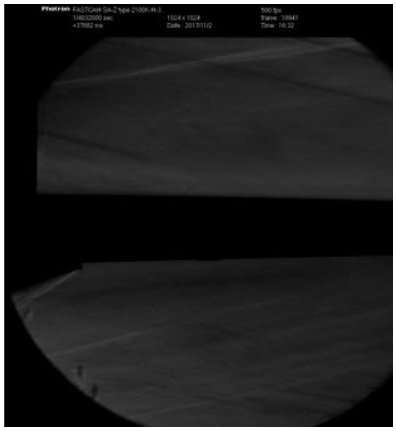

Run 3242

Repeat of previous run with slight adjustment of condenser lens and slit and no improvement.

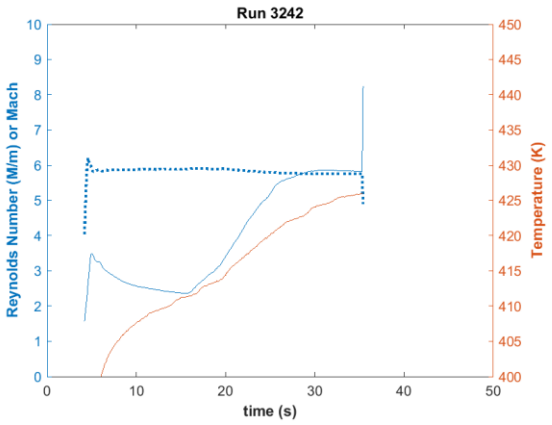

Run 3244

Repeat of previous adjusting optical heights. No improvement.

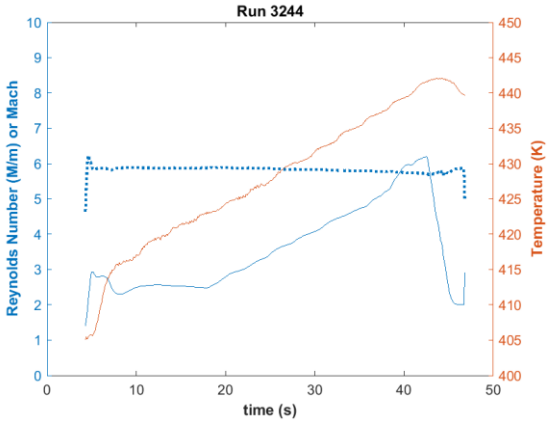

Run 3245

Repeat of previous adjusting optical heights. No improvement.

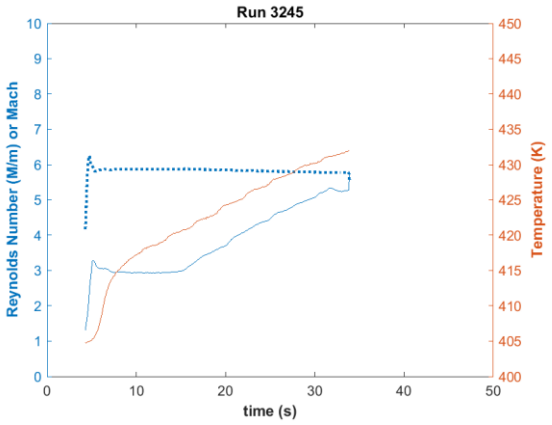

Run 3246

Repeat of previous adjusting optical heights. No improvement.

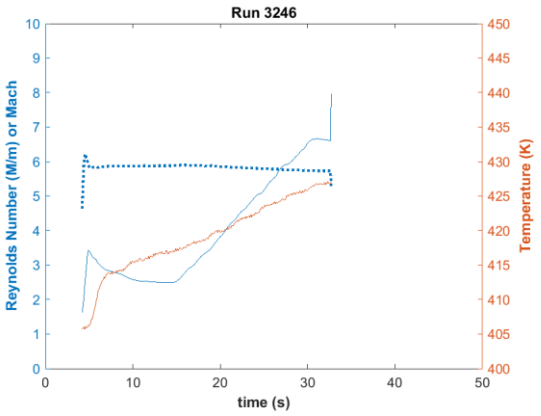

Run 3247

Repeat of previous with source slit made smaller. Darker, but no improvement in contrast.

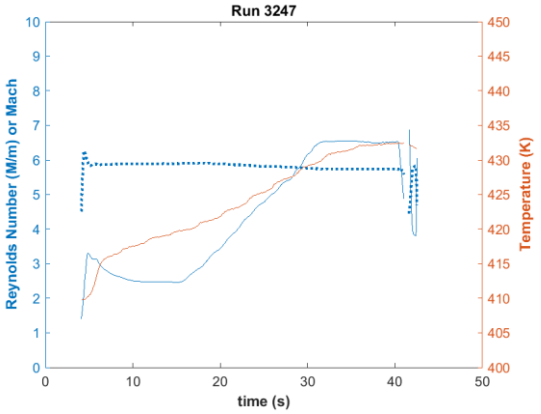

Run 3248

Repeat of previous substituting red LED for green LED. No improvement.

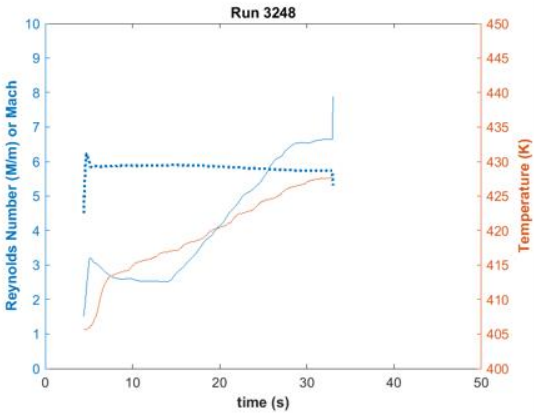

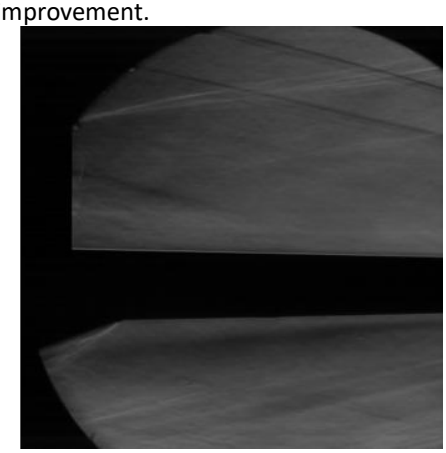

Run 3249

Returned to use of the 0.75” diameter, 2.25” tall cylinder, and schlieren quality improved.

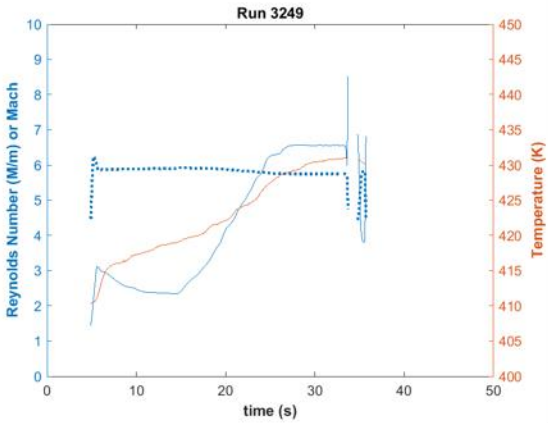

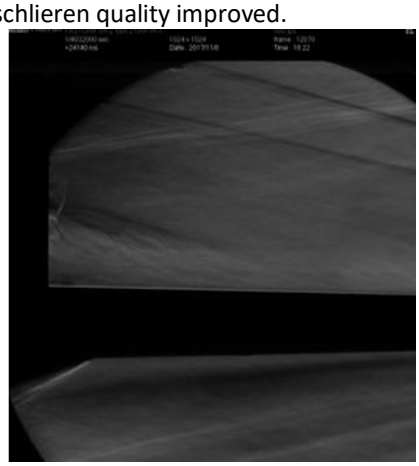

Run 3250

Schlieren at 500fps for a Re stepped run using an exposure of 1/4M seconds.

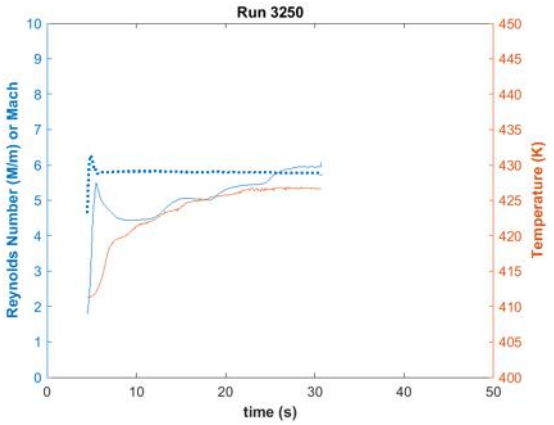

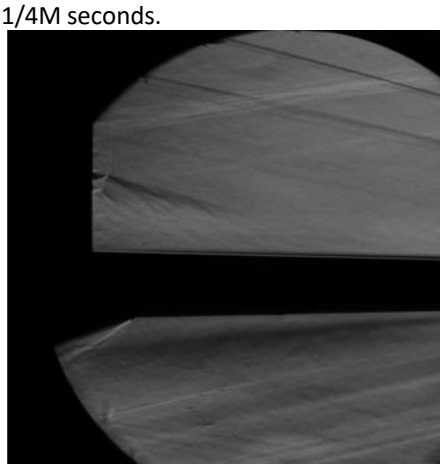

Run 3251

High-speed schlieren sampled at 200k fps. Re held near 2.8M/m.

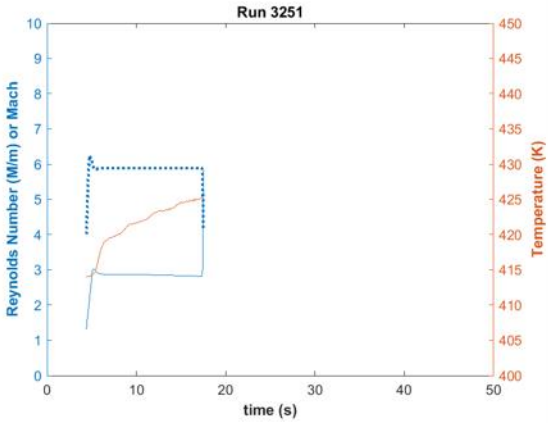

Run 3252

Repeat of previous run but with more cutoff.

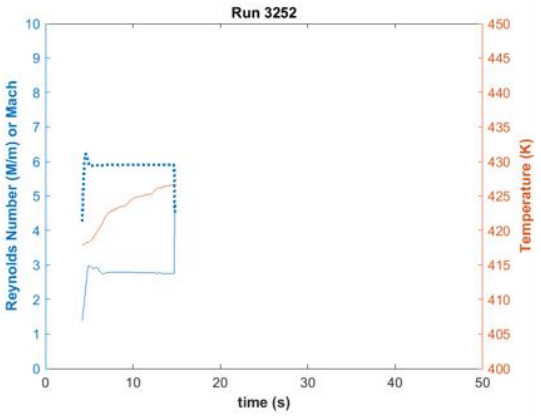

Run 3253

Same run configuration and sampling but at a Re of 3.5M/m.

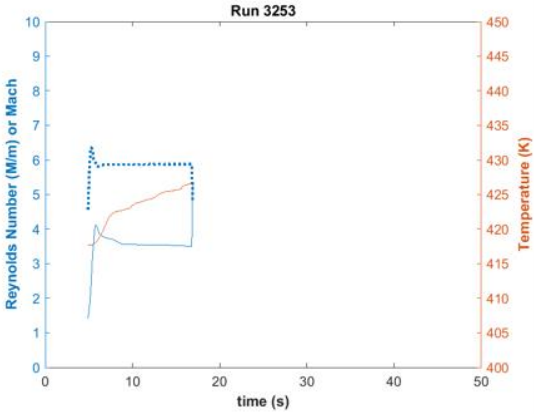

Run 3254

Same run configuration and sampling but at a Re of 4.3M/m.

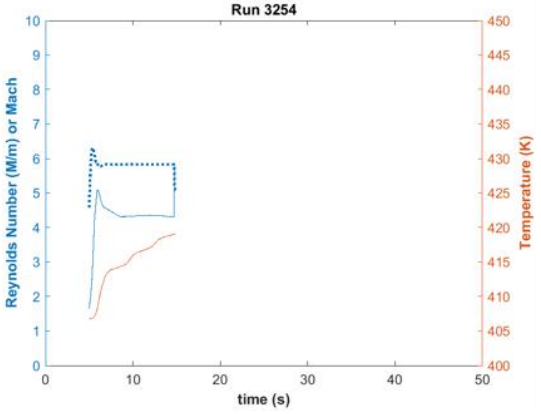

Run 3255

Same run configuration and sampling but at a Re of 6.4M/m.

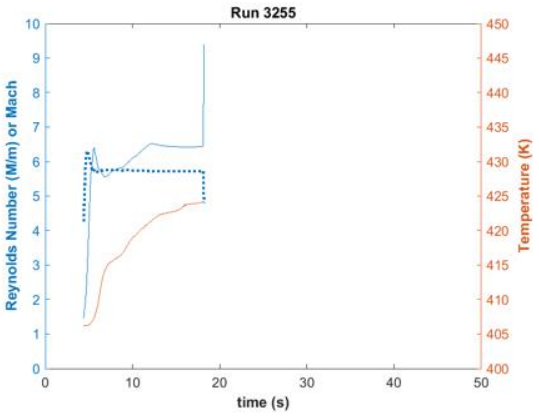

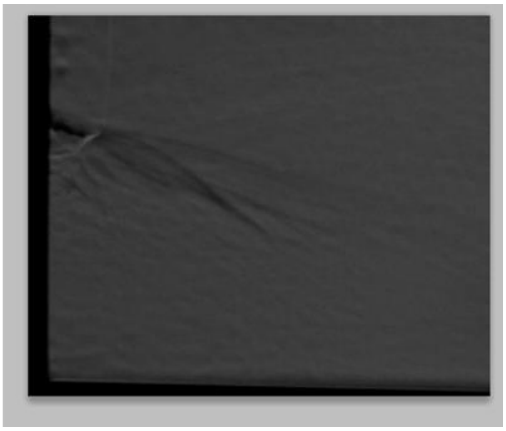

Run 3257

Schlieren run at 480k fps with 100k frames sampled every 3 seconds, allowing for Re steps.

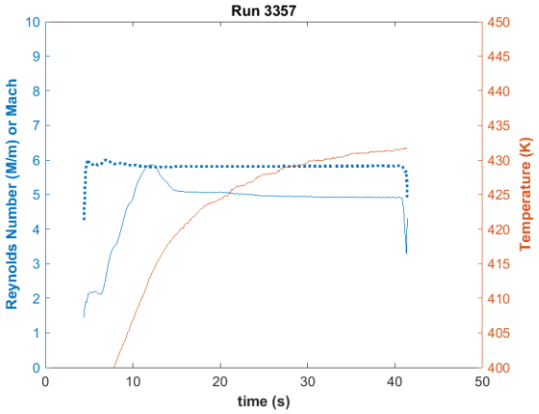

Run 3259

Similar run as previous with less cut-off.

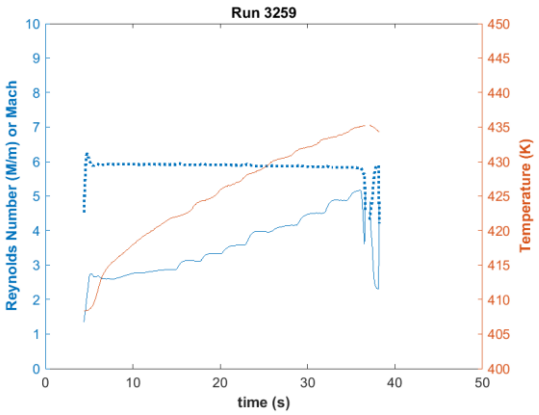

Run 3260

Similar run as previous but to a higher Re.

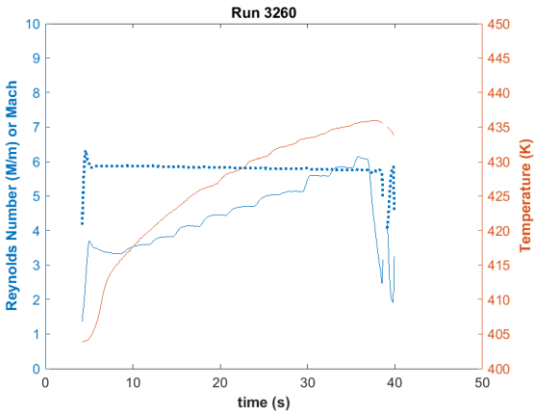

Run 3261

Region of interest shifted to separation shock and frame rate reduced to 200k. Similar stepped Re.

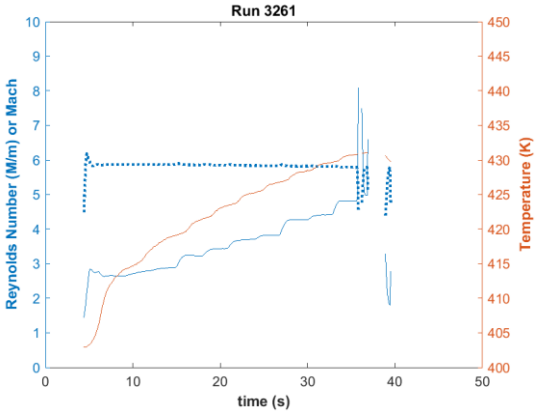

Run 3265

Infrared thermography looking straight down the central top window for a Re sweep.

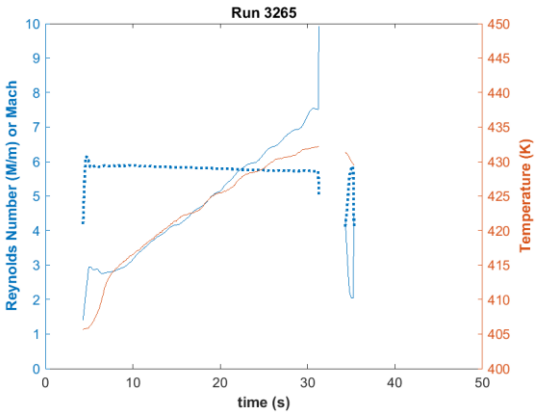

Run 3266

Infrared thermography angled back to measure temperature on the cylinder for a Re sweep.

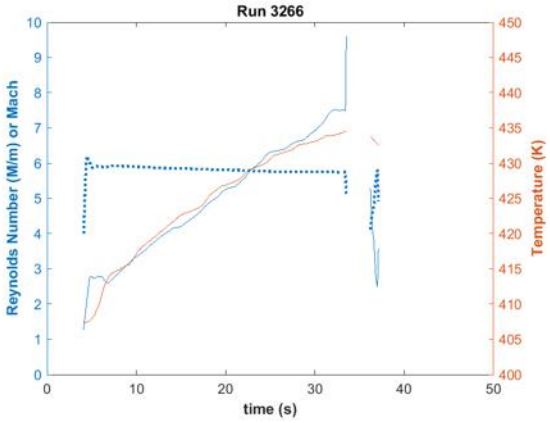

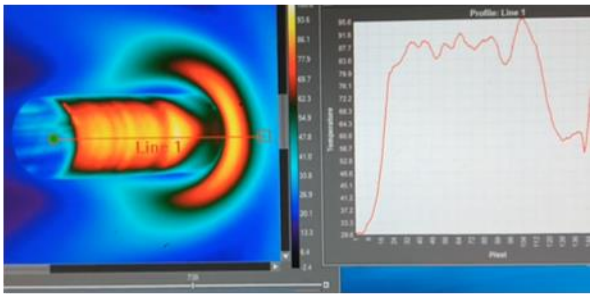

Oil flow mappings

Run 3267

Oil flow visualization at 3.0M/m.

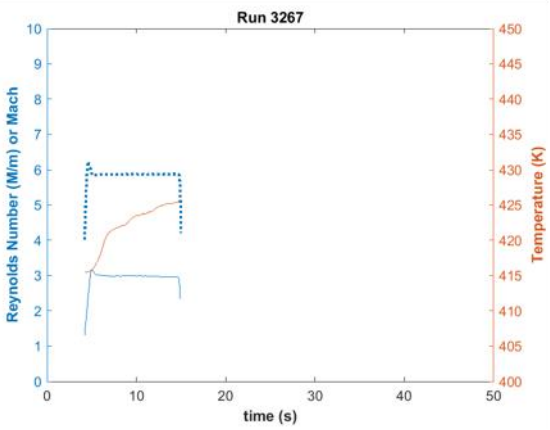

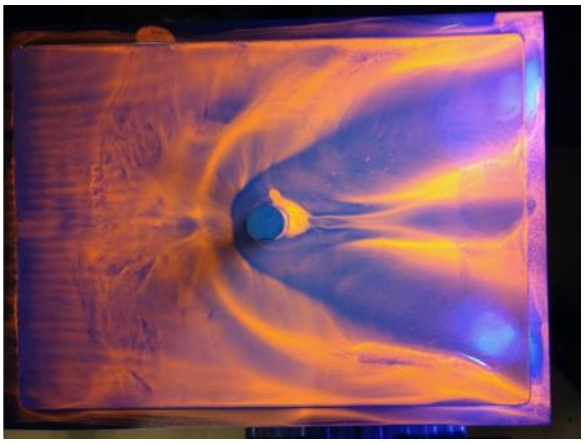

Run 3268

Oil flow visualization at 3.7M/m.

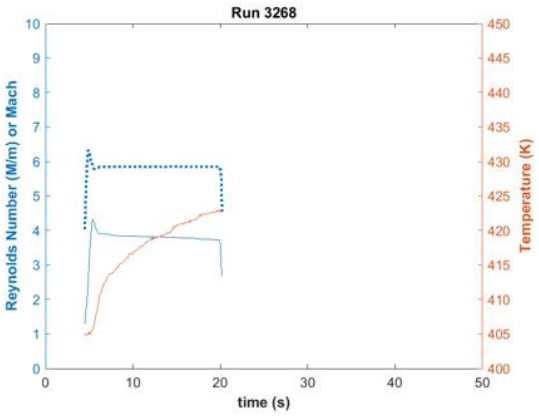

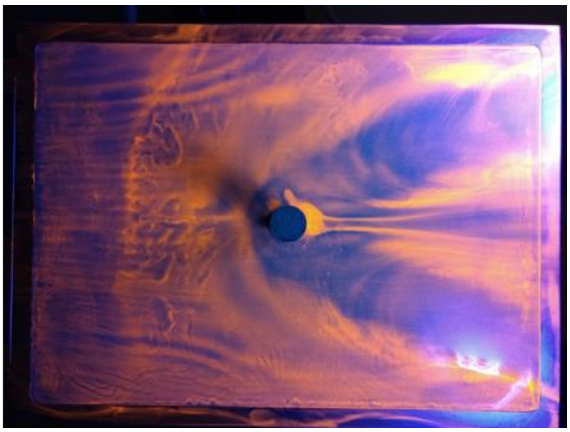

Run 3269

Oil flow visualization at 4.6M/m.

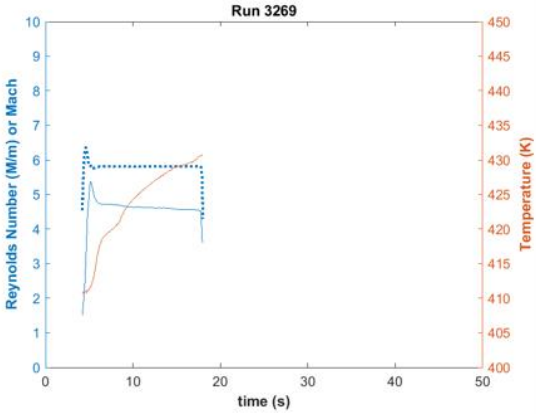

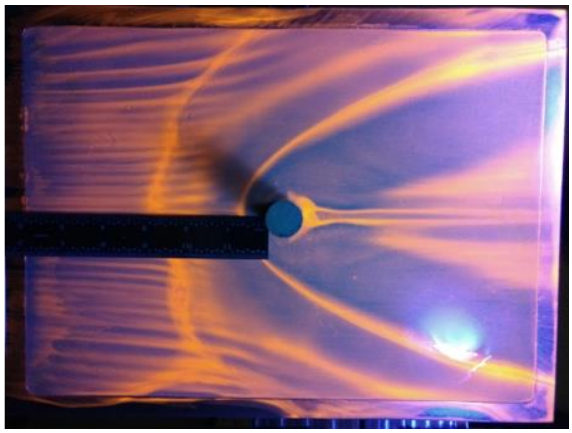

Run 3270

Oil flow visualization at 2.8M/m.

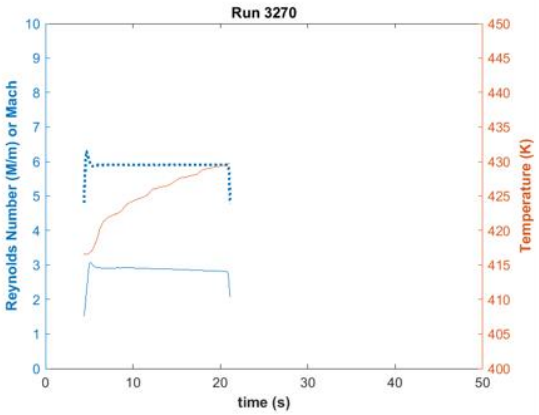

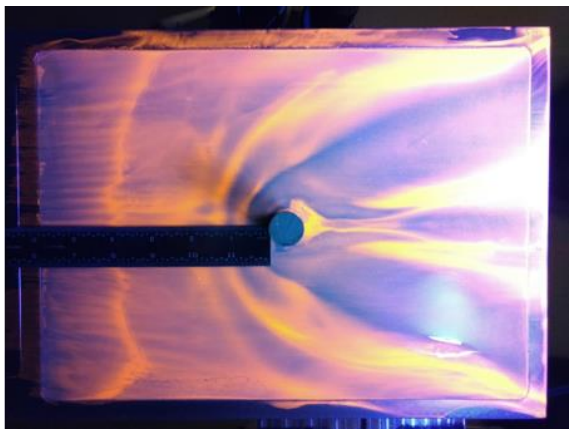

Run 3271

Oil flow visualization at 3.6M/m.

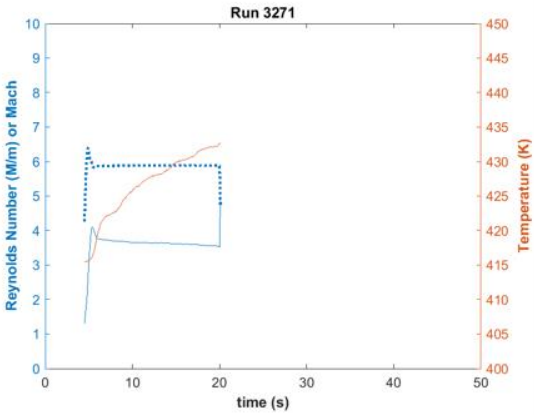

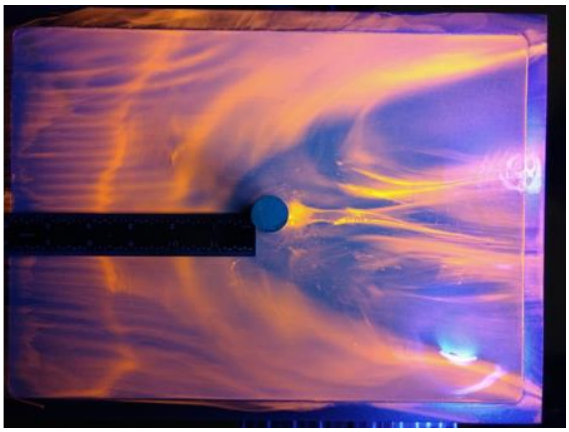

Run 3272

Oil flow visualization at 5.4M/m.

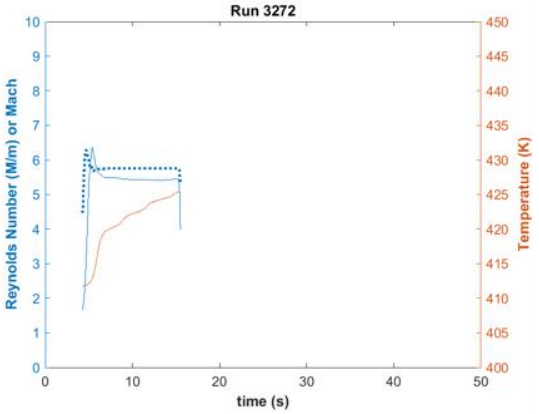

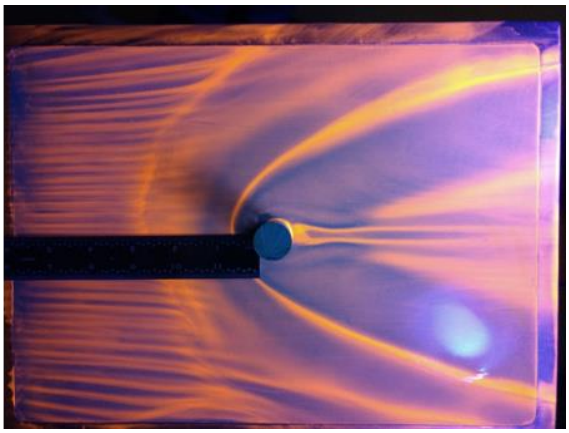

Run 3273

Oil flow visualization at 6.1M/m.

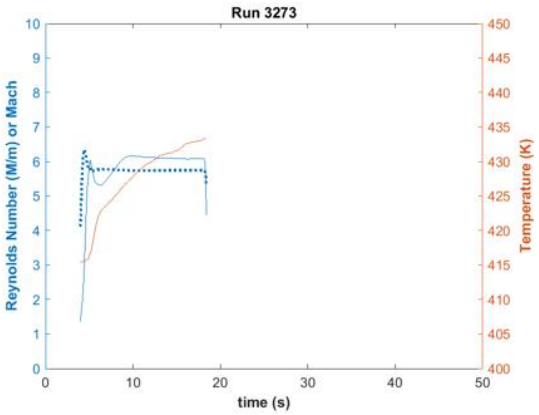

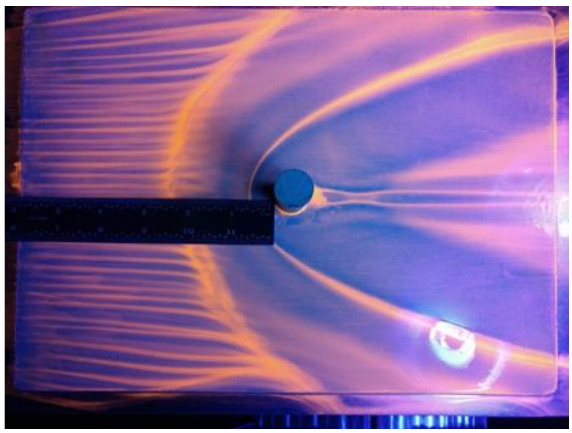

Run 3274

Oil flow visualization at 6.9M/m.

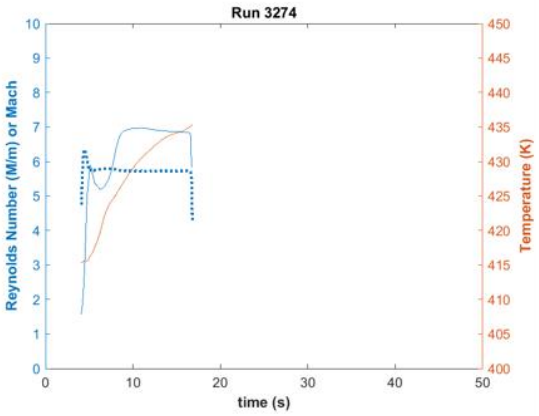

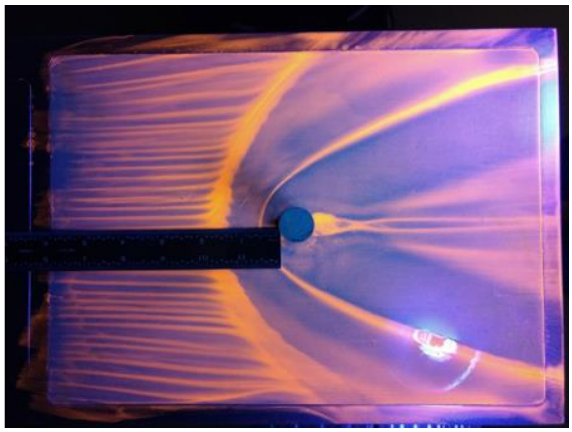

Run 3276

Oil flow visualization at 7.6M/m.

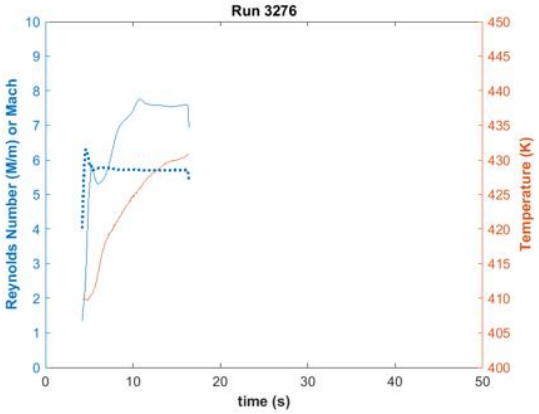

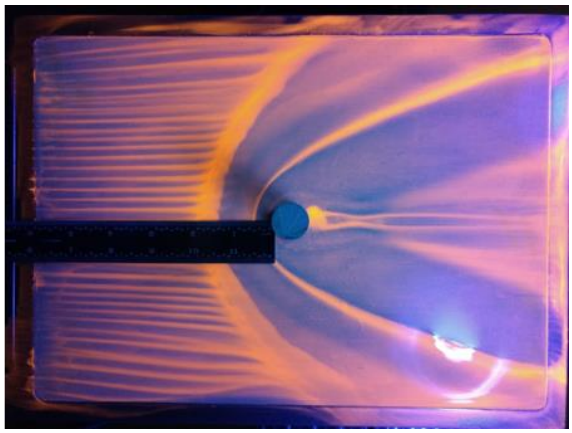

Run 3277

Oil flow visualization at 4.2M/m.

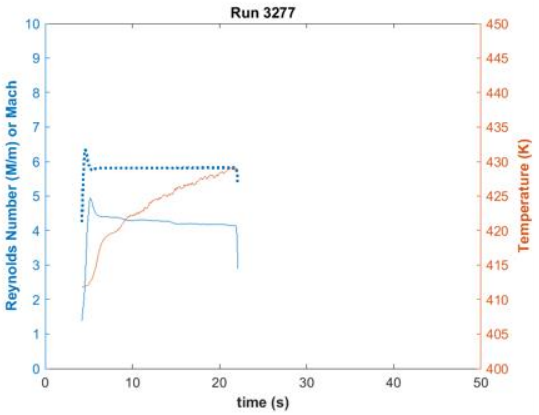

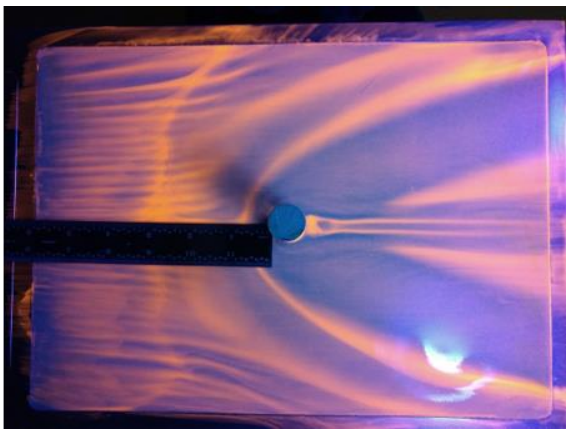

Tunnel freestream

Run 3290

Pitot measurement using a Kulite XCEL-100-5A at location in tunnel where model leading edge would be. Sampled at 200 kHz. Re sweep.

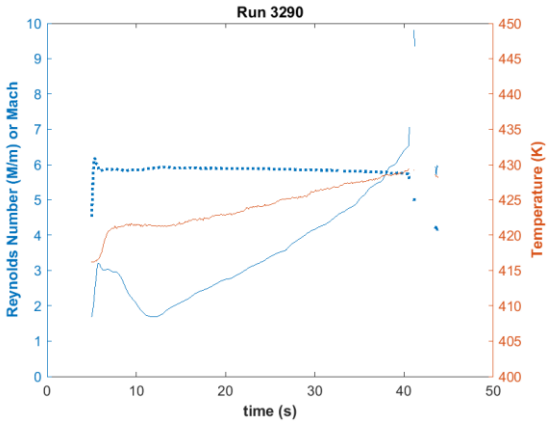

Run 3291

Repeat of previous run but sampled at 400 kHz.

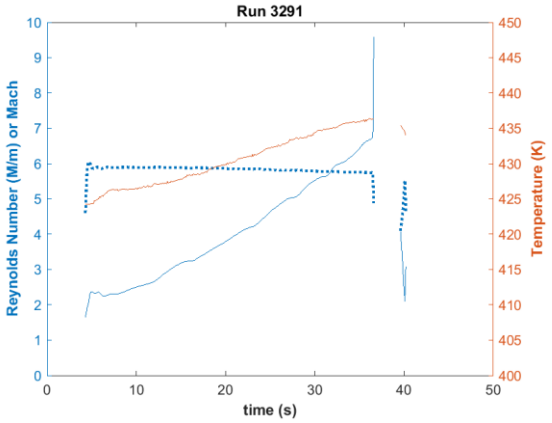

Run 3340

Hot-wire anemometry using AA Systems anemometer and TSI hot-wire. Wire was located at what would be the center of the model leading edge. Sampled at 500 kHz for a Re sweep. Ovh=0.8.

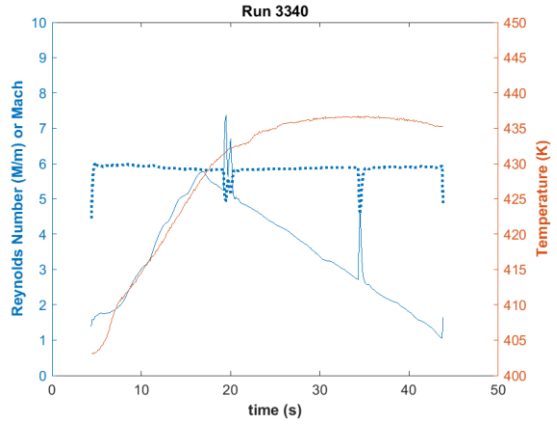

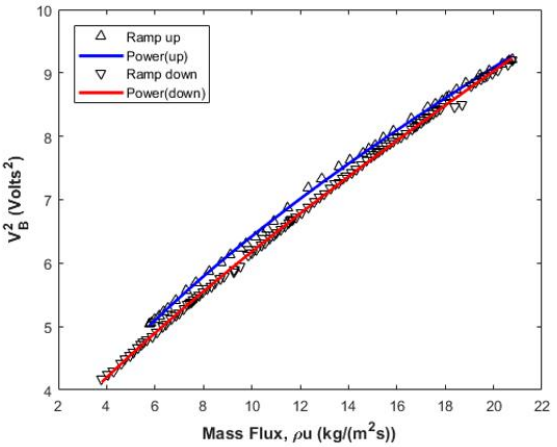

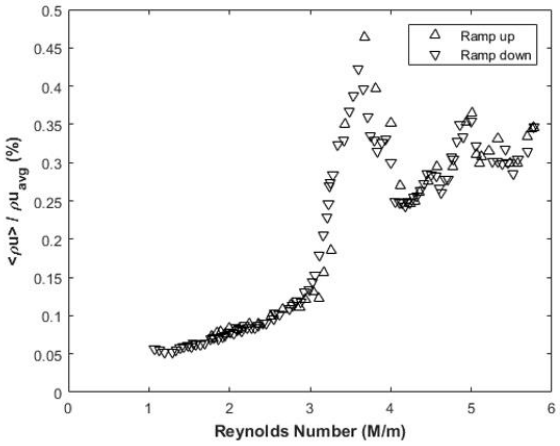

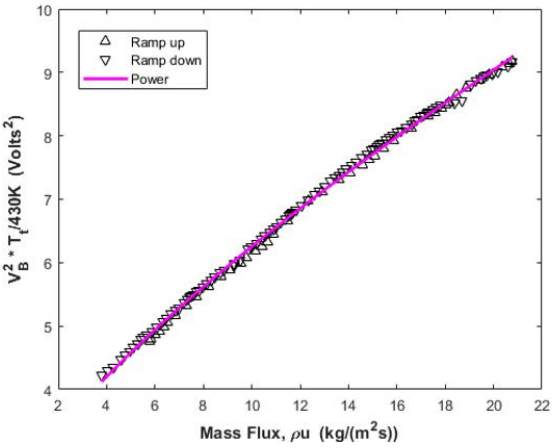

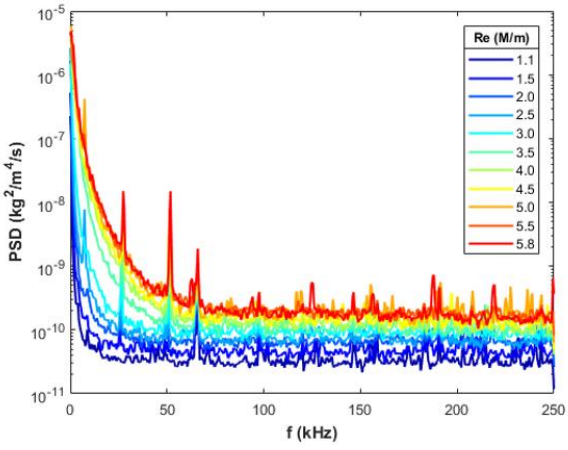

Run 3341

Repeat of previous run.

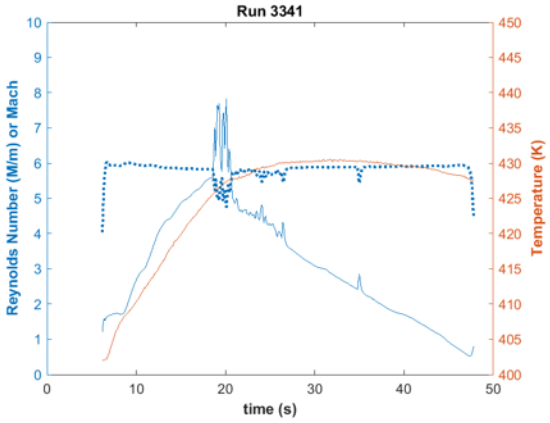

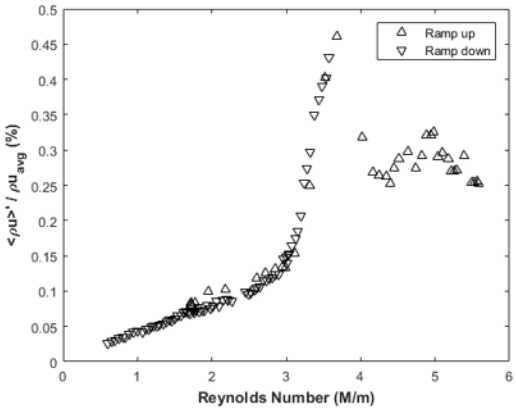

Run 3346

Hot-wire calibration run with wire positioned 1.7” upstream of what would be the model leading edge.

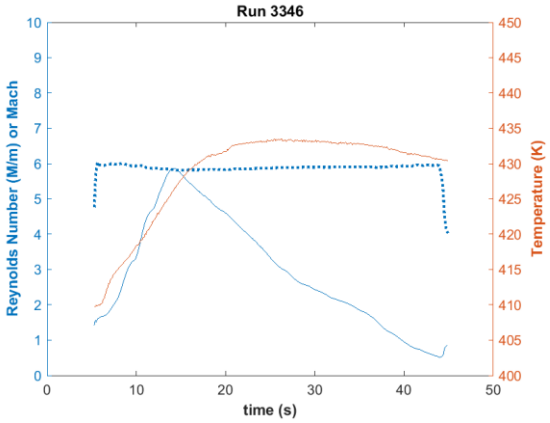

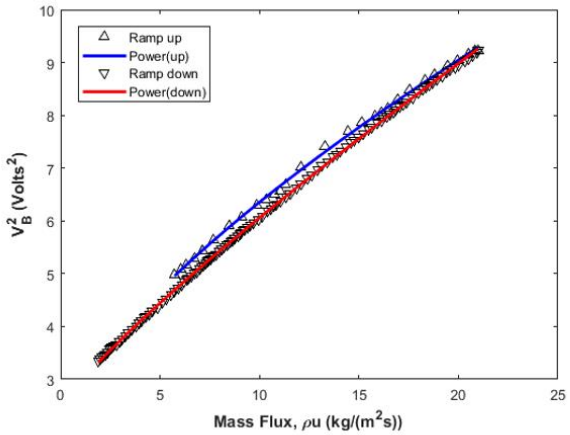

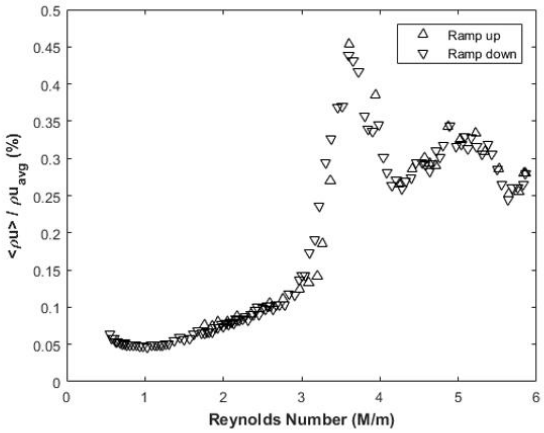

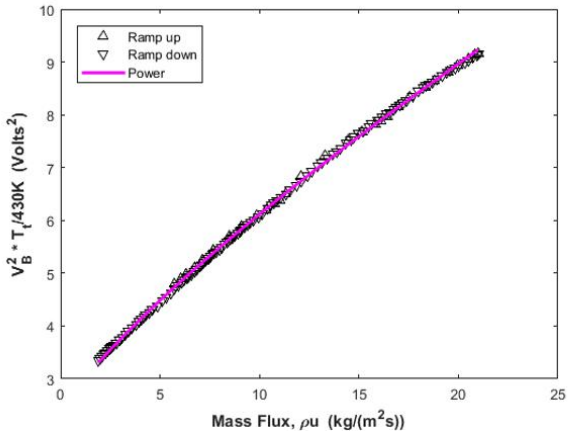

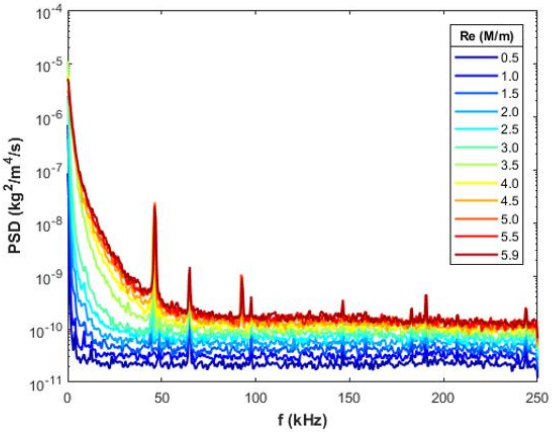

Run 3349

Hot-wire calibration behind the leading-edge shock.

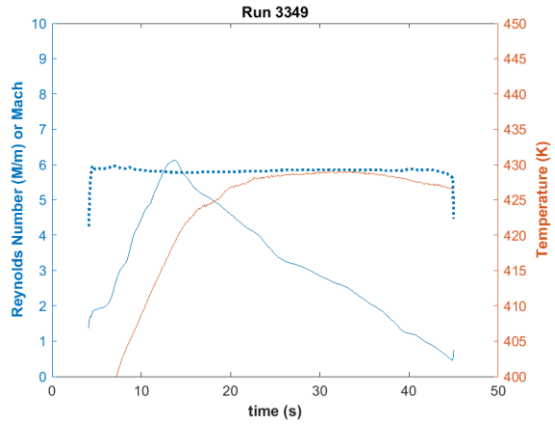

Run 3350

Hot-wire traverse behind the leading-edge shock. DAQ timing was off.

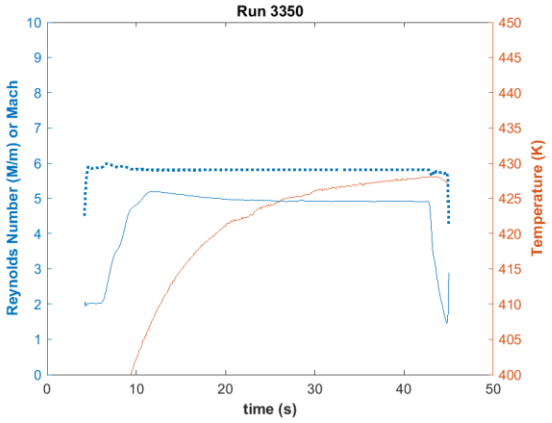

Run 3351

Repeat of previous run adding schlieren to track wire path.

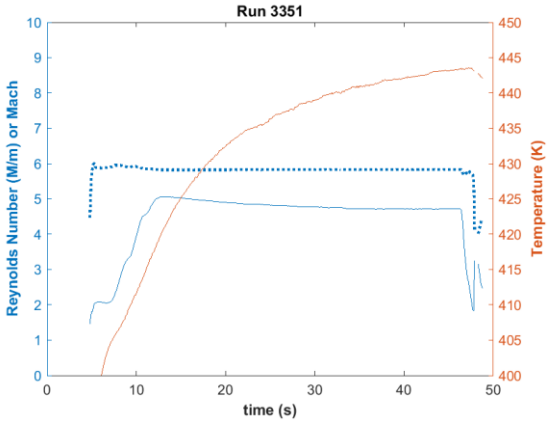

Hot-wire surveys

Run 3354

Dummy probe positioned above front/center PCB located 1" DS of PEEK interface on model. IR camera angled to look back at probe through the top front window port. Schlieren through the downstream window. Re held near 4.9M/m.

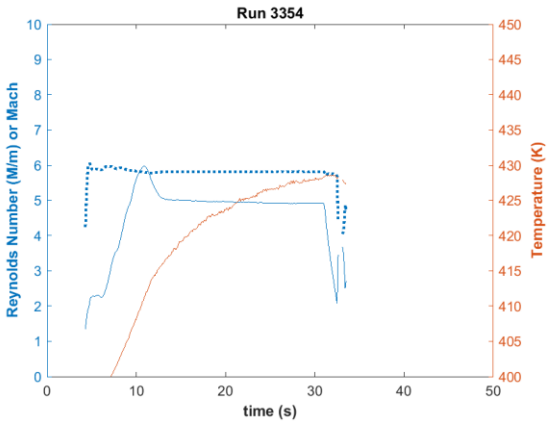

Run 3355

IR thermography was done through the central window to examine the heating streaks.

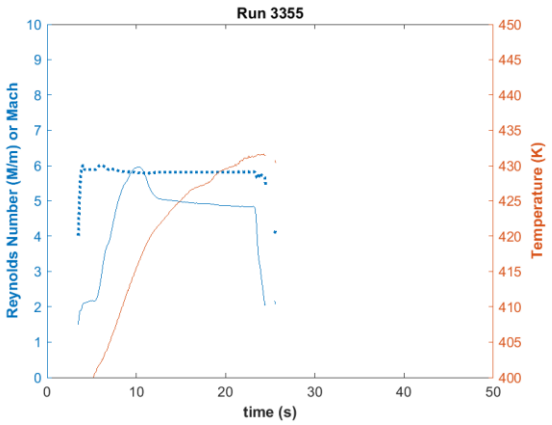

Run 3356

Dummy probe in same position as for 3354 to look at movement during start and unstart. Schlieren was used to estimate distance off model.

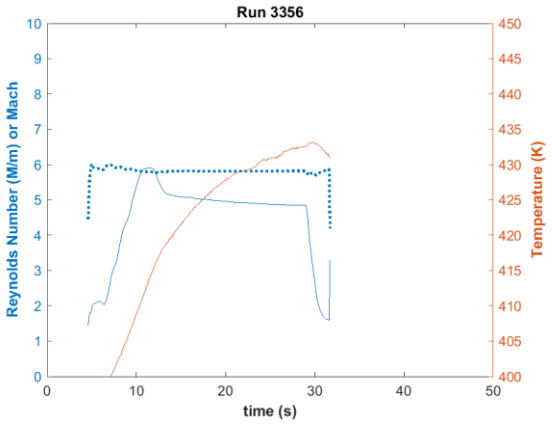

Run 3357

Hot-wire traverse at x=187mm, z=-0.7mm. Re near 5.0M/m.

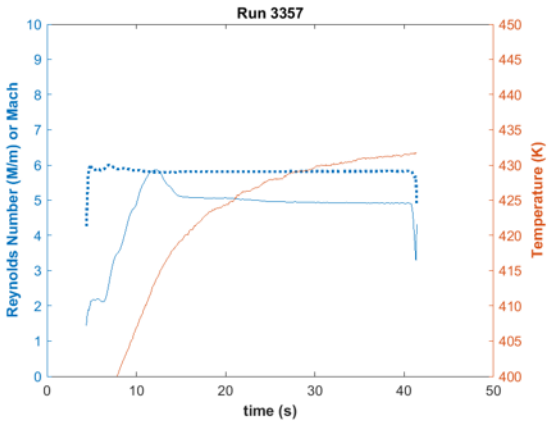

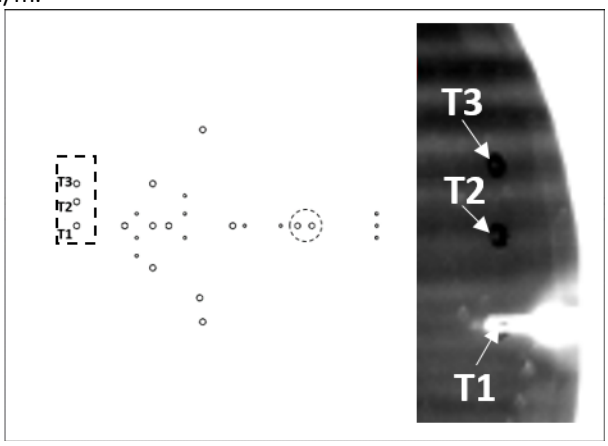

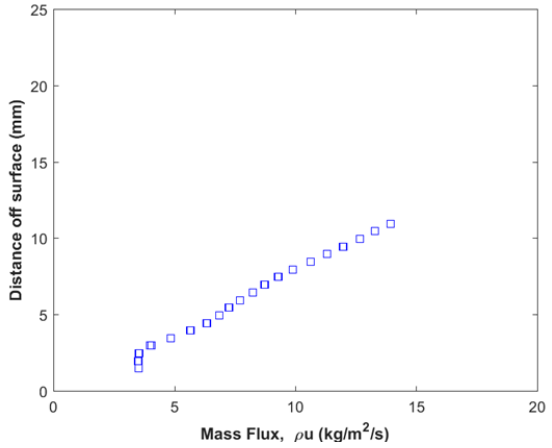

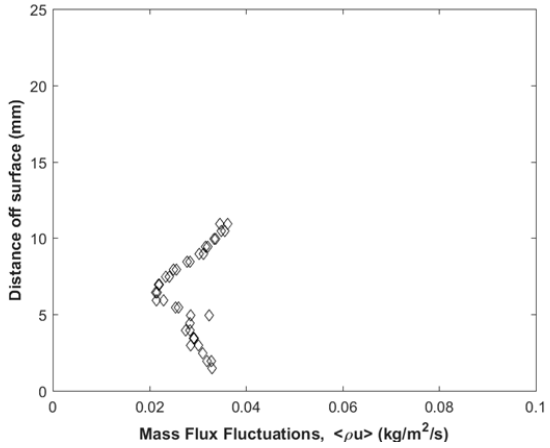

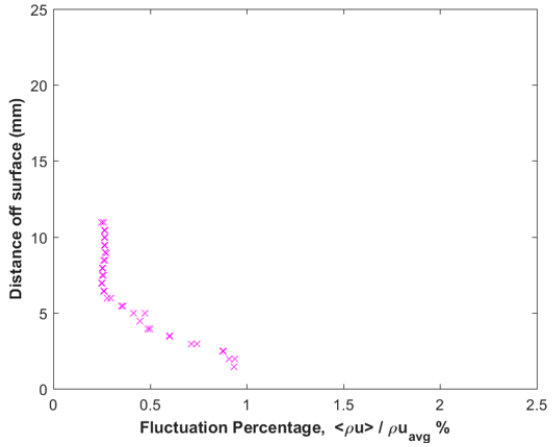

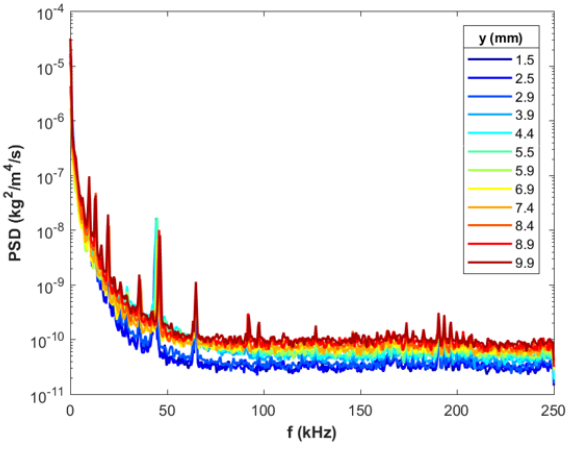

Run 3358

Repeat of previous run. Re near 4.9M/m.

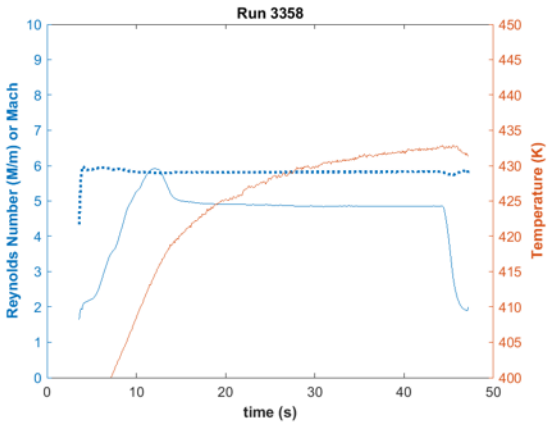

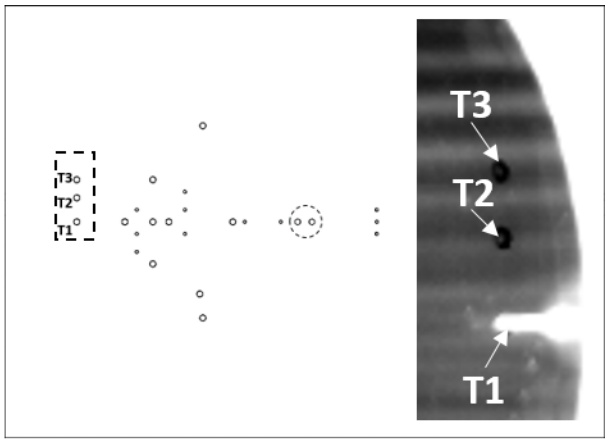

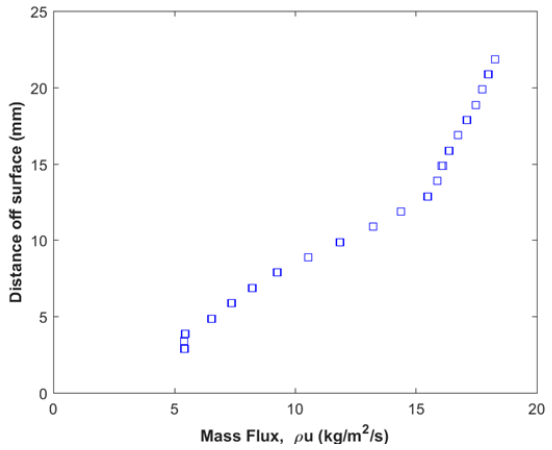

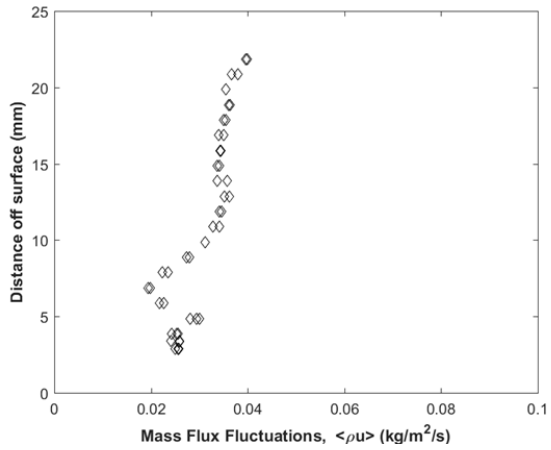

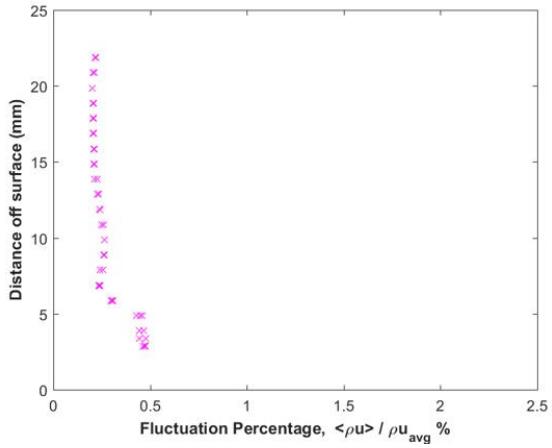

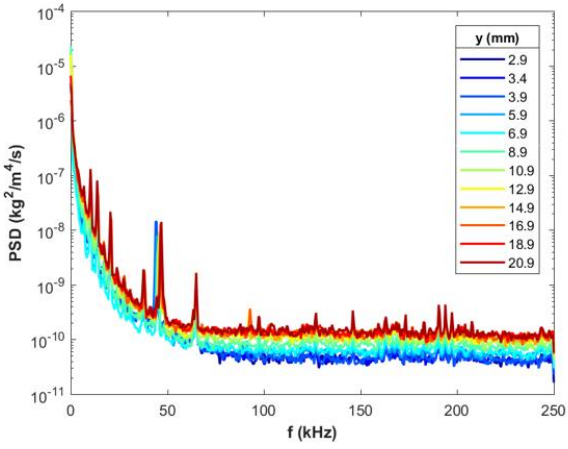

Run 3359

Hot-wire traverse at x=187mm, z=0.9mm. Re near 5.0M/m.

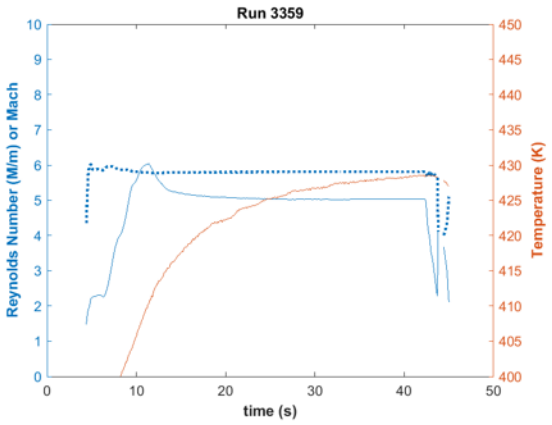

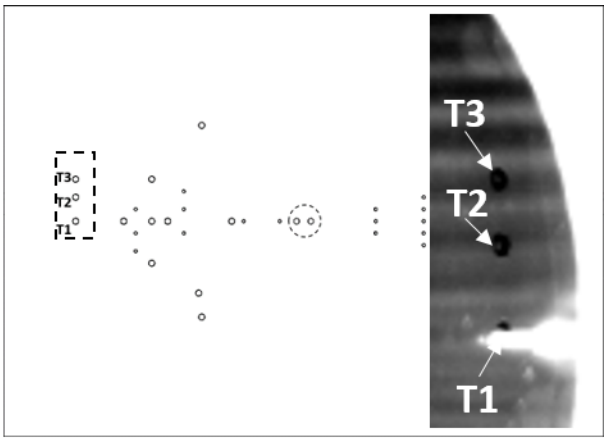

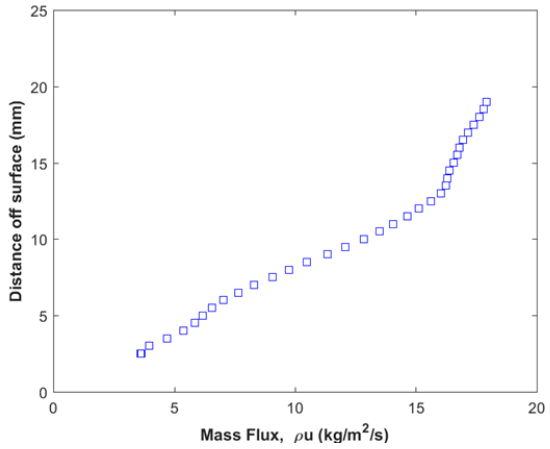

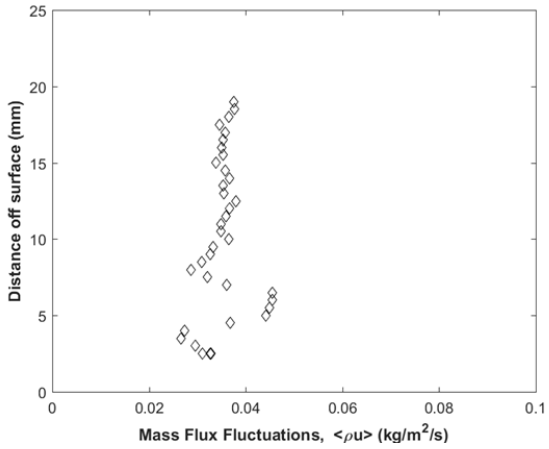

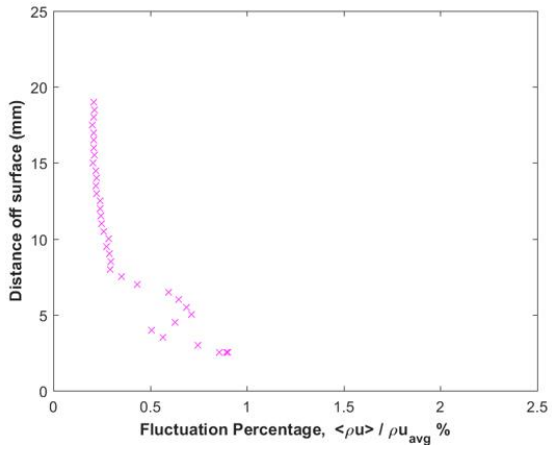

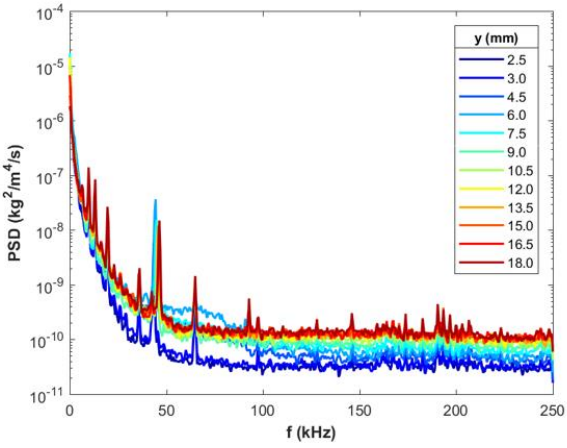

Run 3360

Hot-wire traverse at x=187mm, z=3.4mm. Re near 4.9M/m.

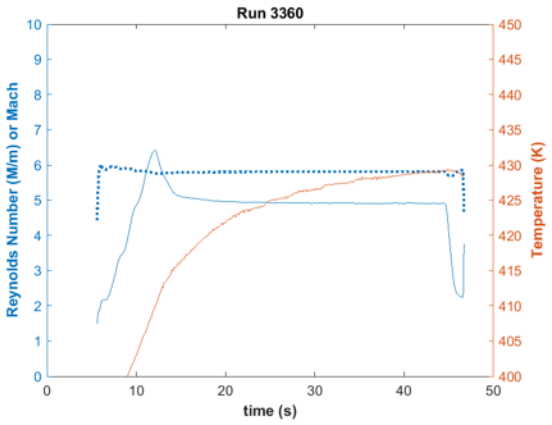

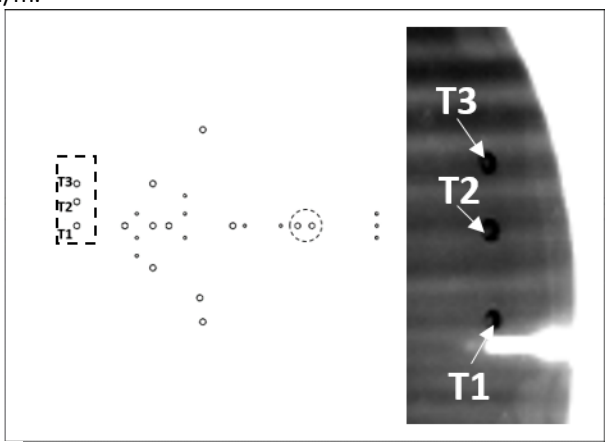

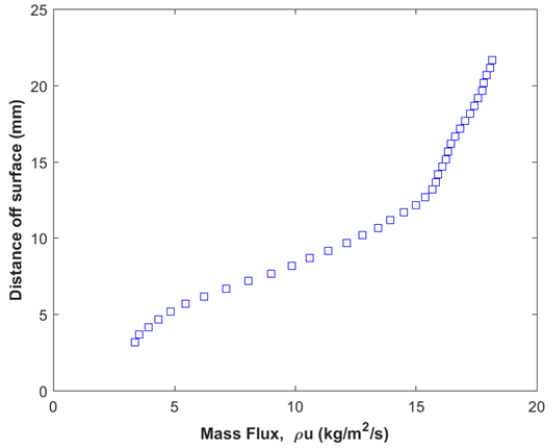

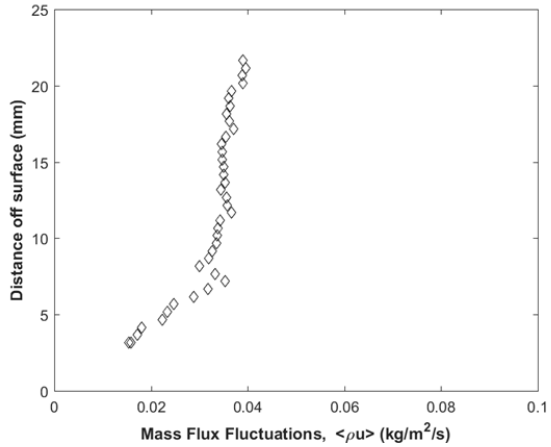

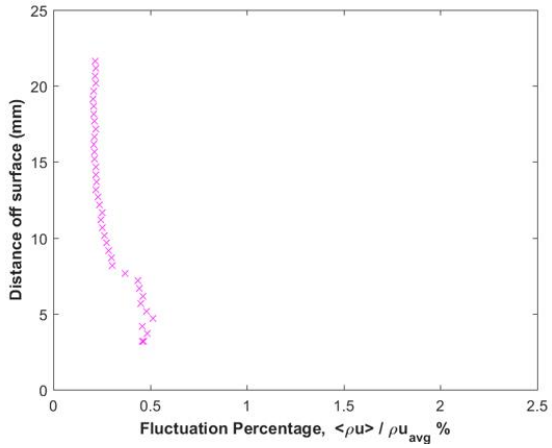

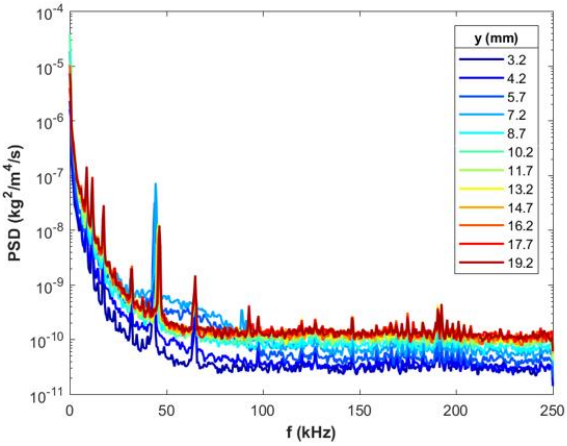

Run 3361

Hot-wire traverse at x=187mm, z=-2.5mm. Re near 4.8M/m.

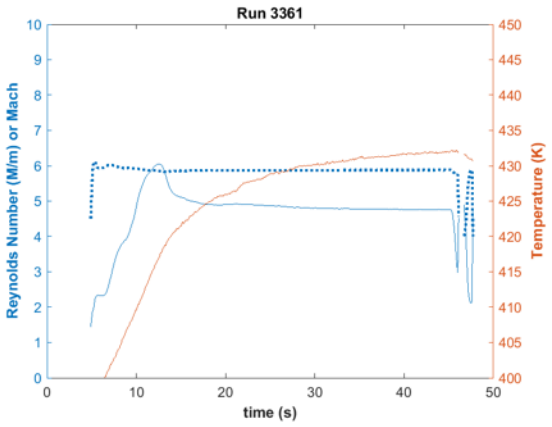

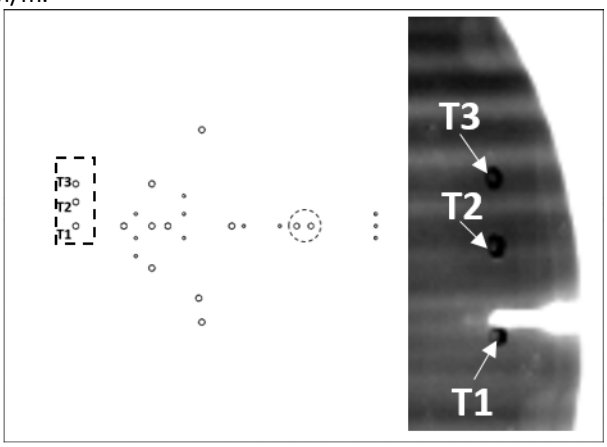

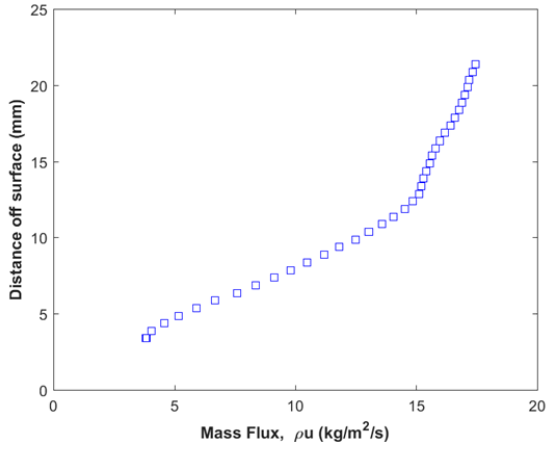

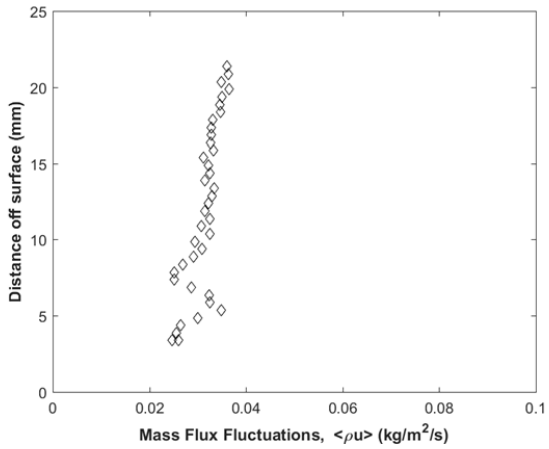

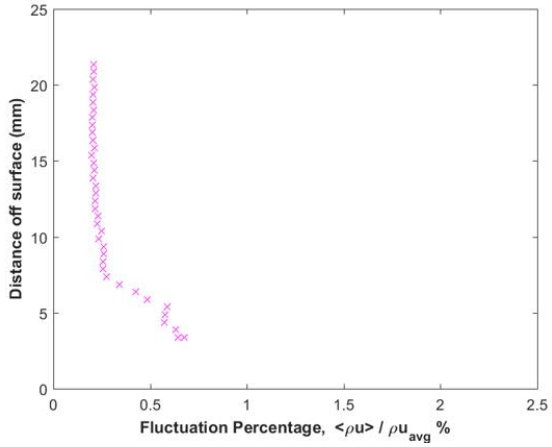

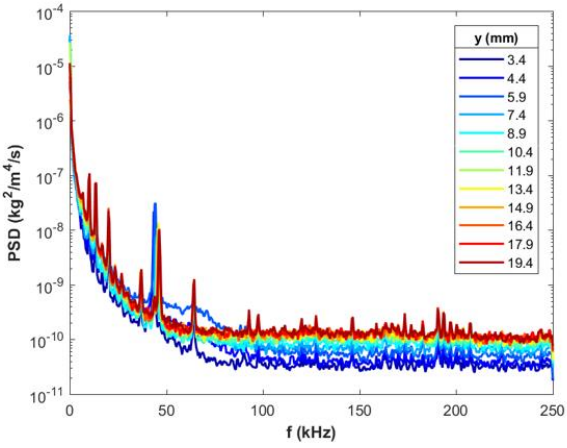

Run 3362

Hot-wire traverse at x=187mm, z=-4.1mm. Re near 4.8M/m.

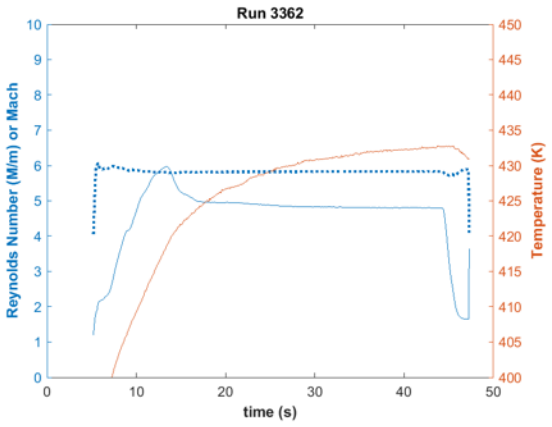

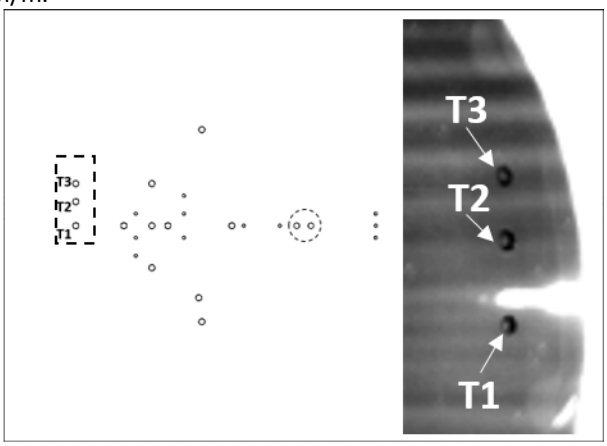

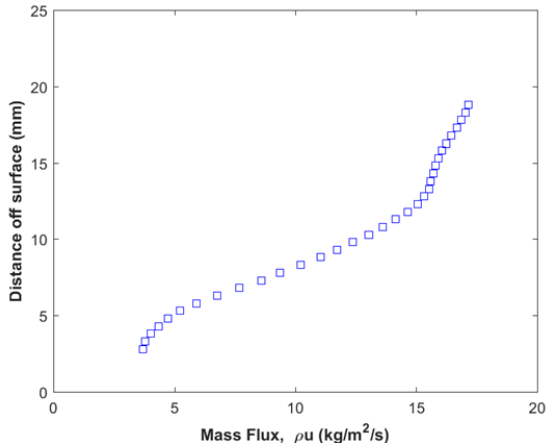

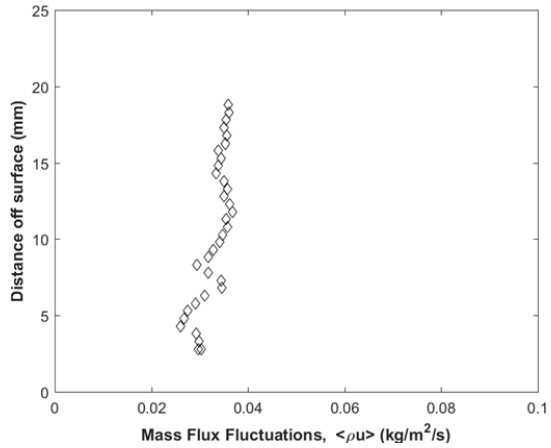

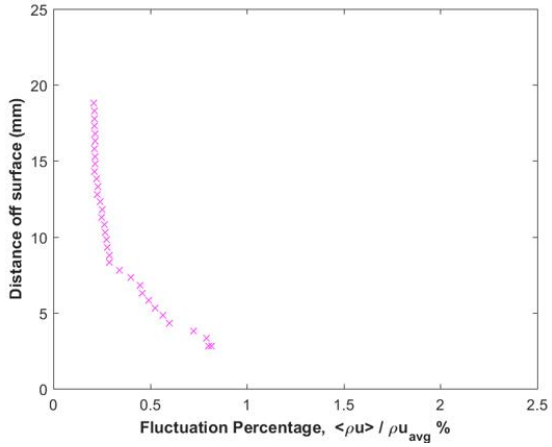

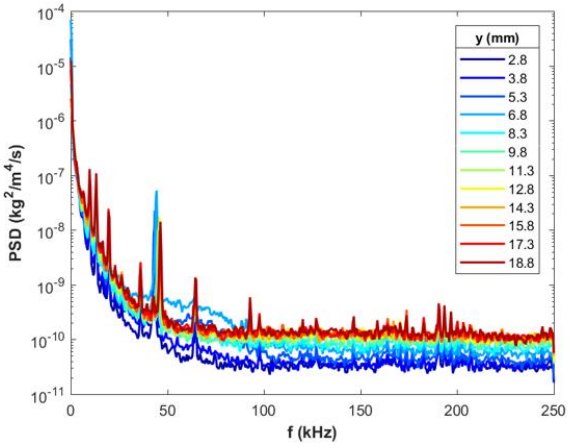

Run 3363

Hot-wire traverse at x=187mm, z=-6.1mm. Re near 4.9M/m.

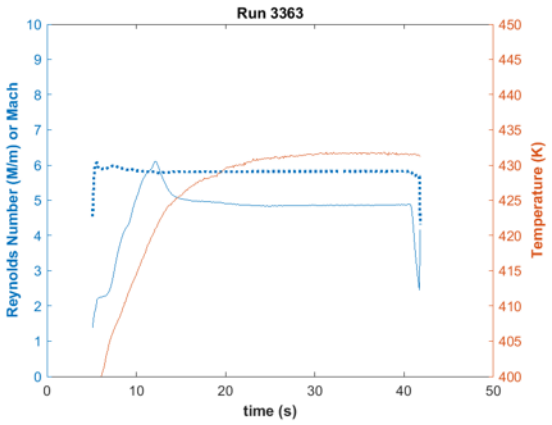

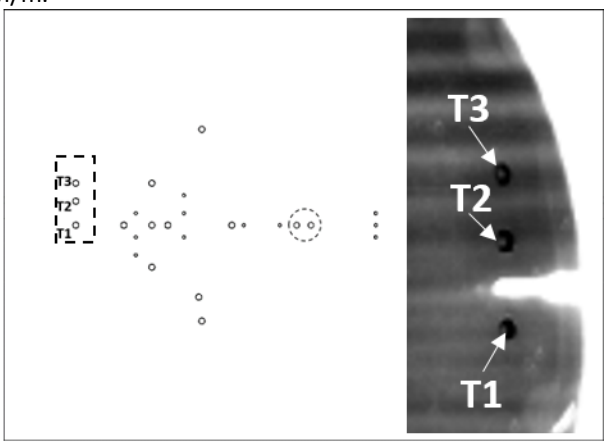

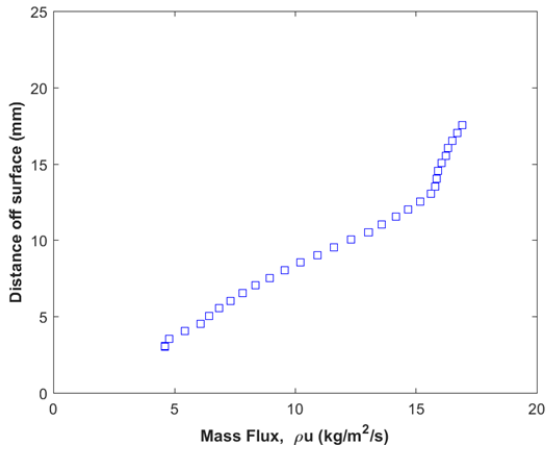

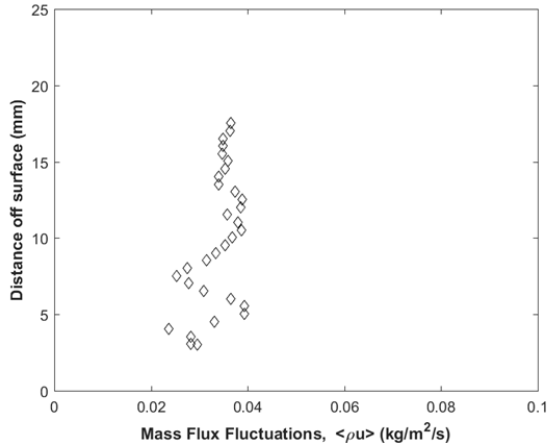

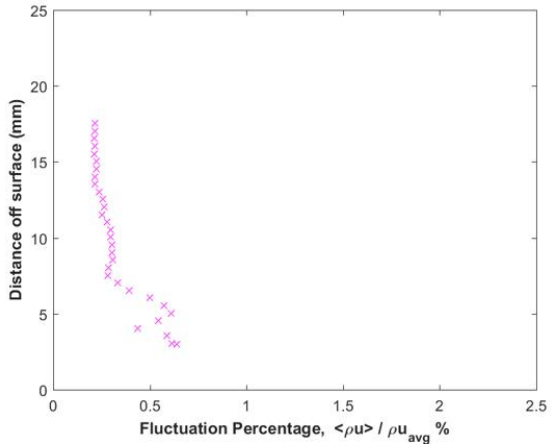

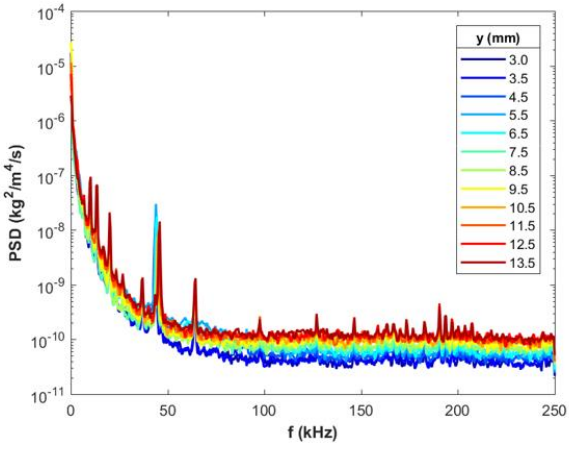

Run 3364

Hot-wire traverse at x=187mm, z=-24.6mm. Re near 5.1M/m.

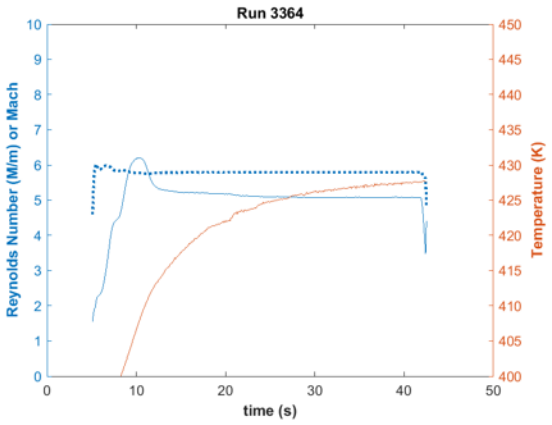

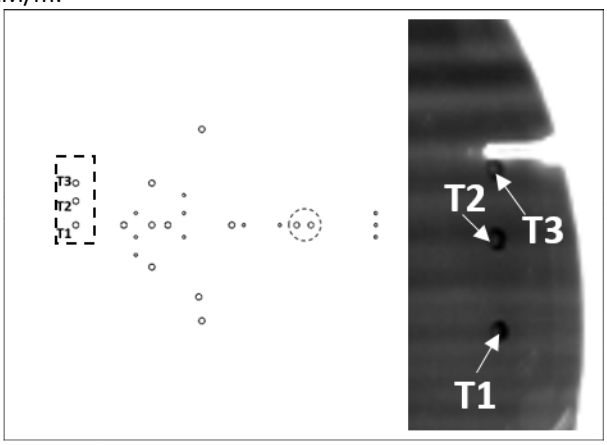

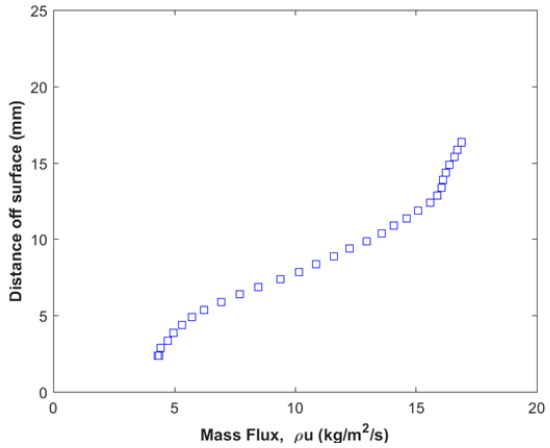

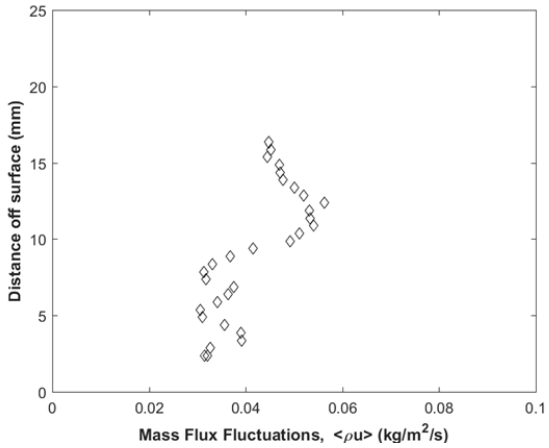

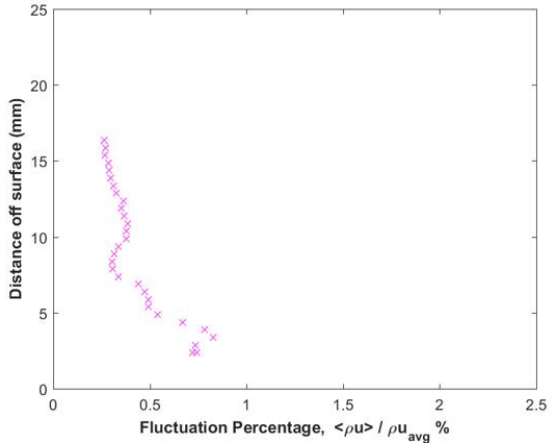

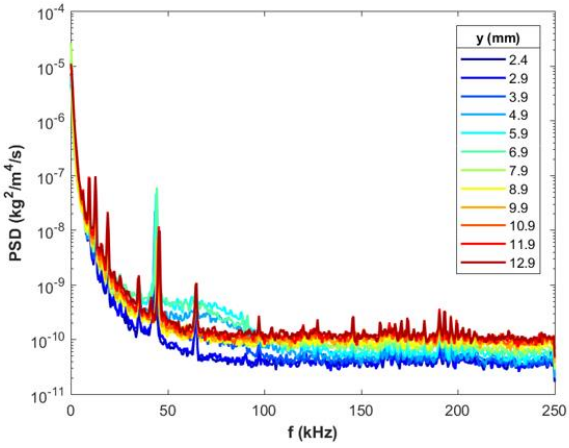

Run 3365

Hot-wire traverse at x=187mm, z=-24.0mm. Re near 5.0M/m.

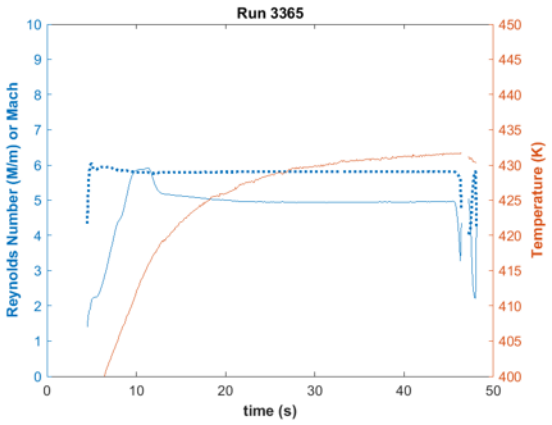

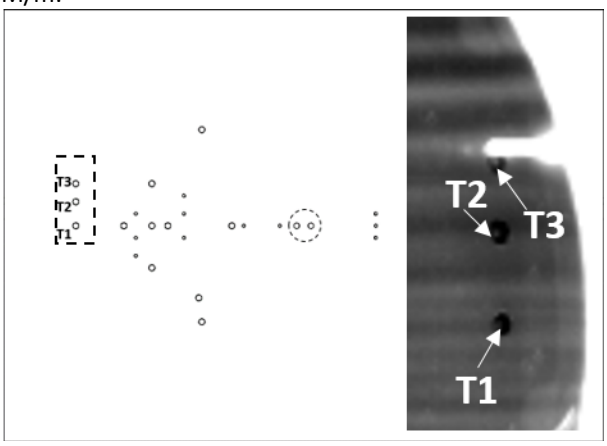

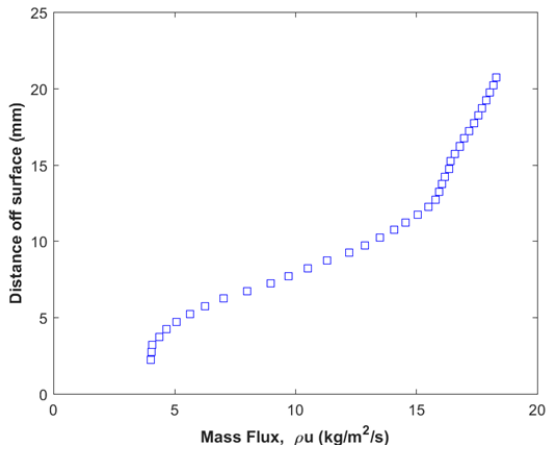

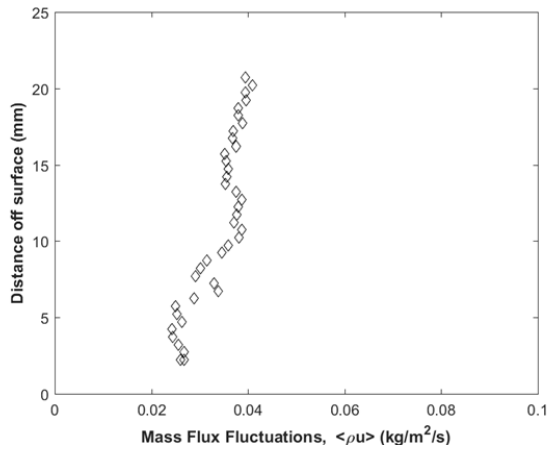

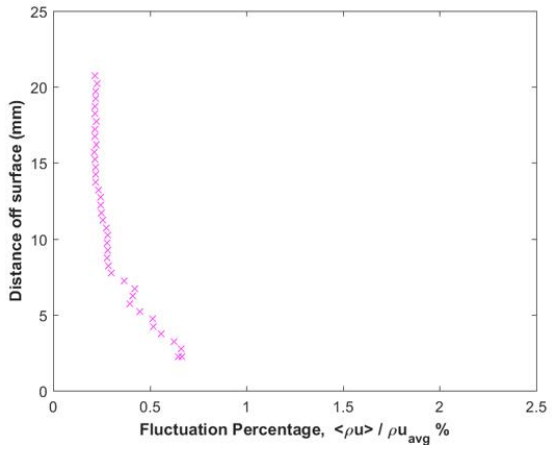

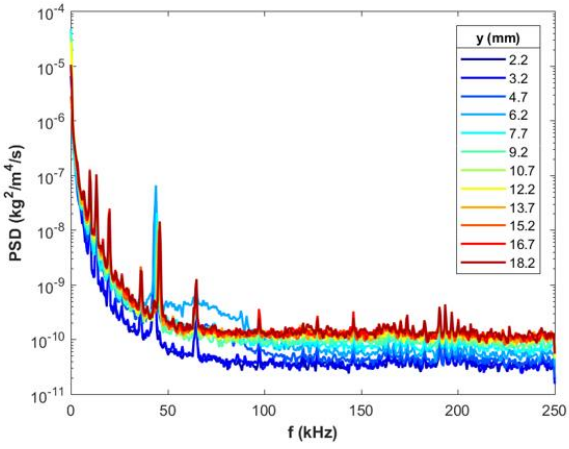

Run 3366

Hot-wire traverse at x=187mm, z=-24.2mm. Re near 4.9M/m.

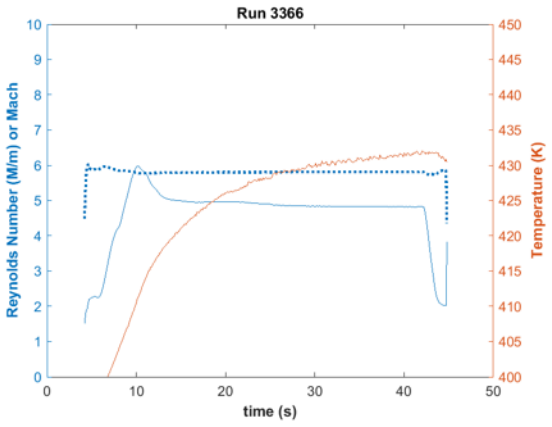

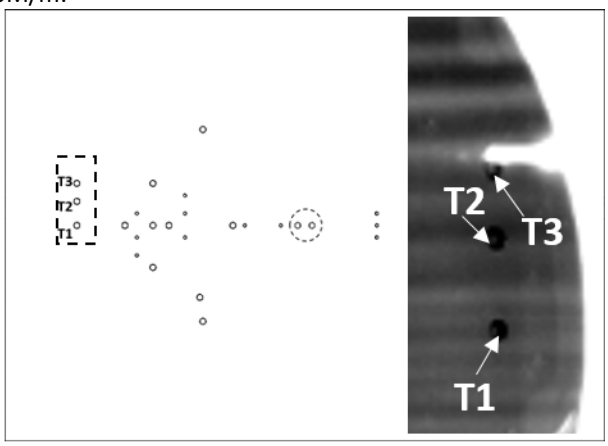

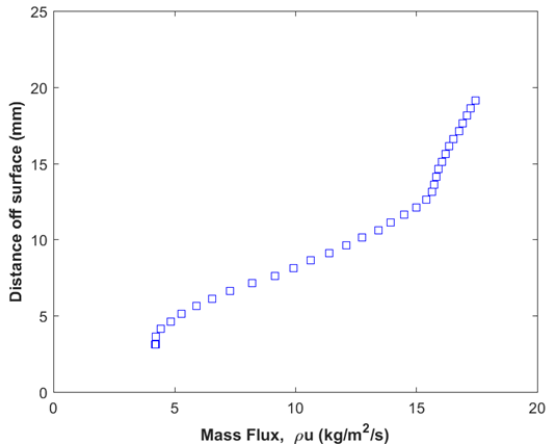

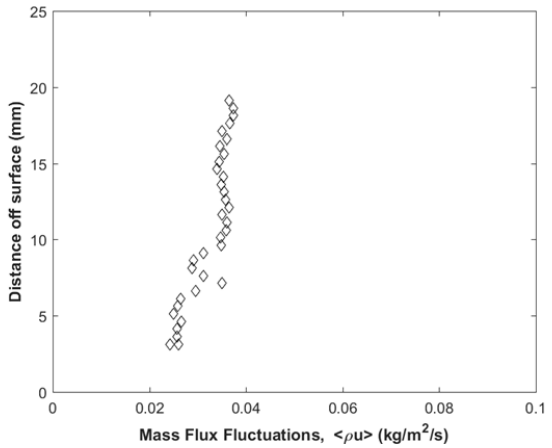

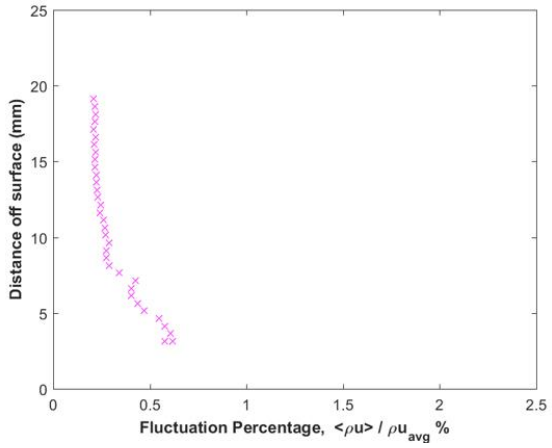

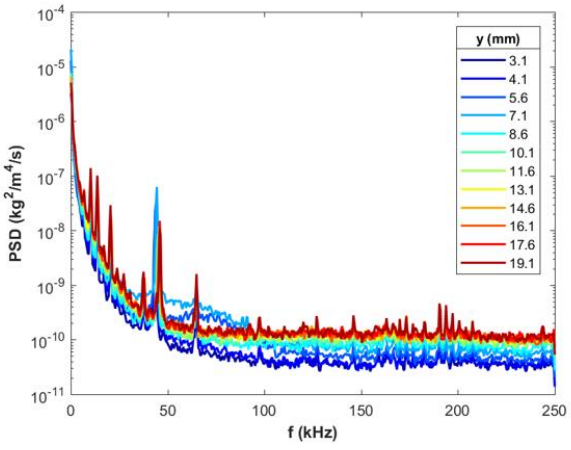

Run 3367

Hot-wire traverse at x=187mm, z=-29.0mm. Re near 5.0M/m.

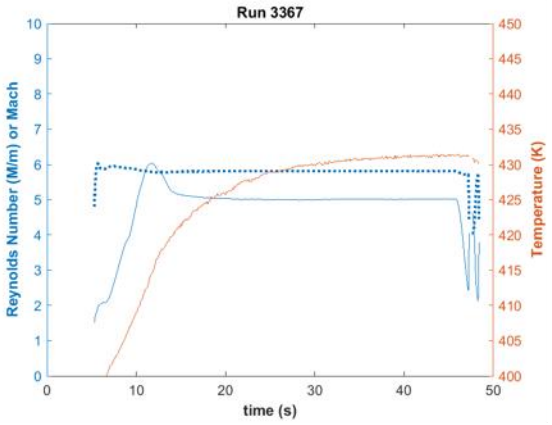

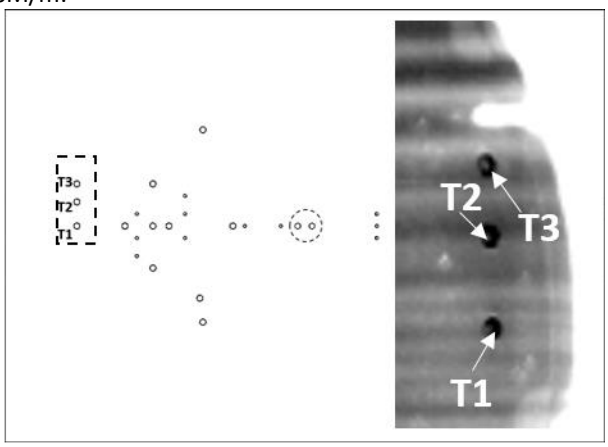

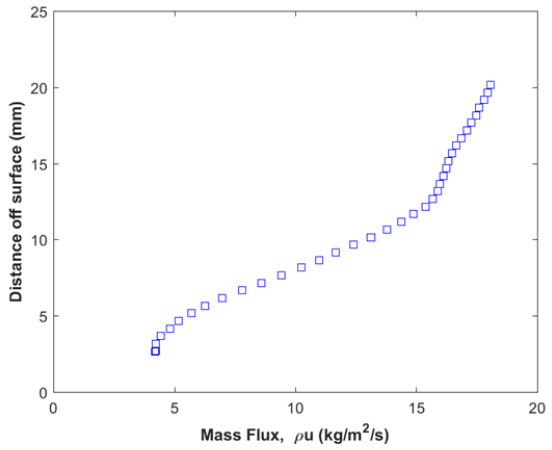

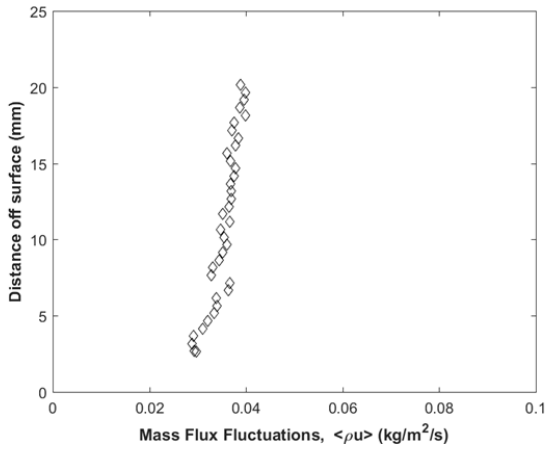

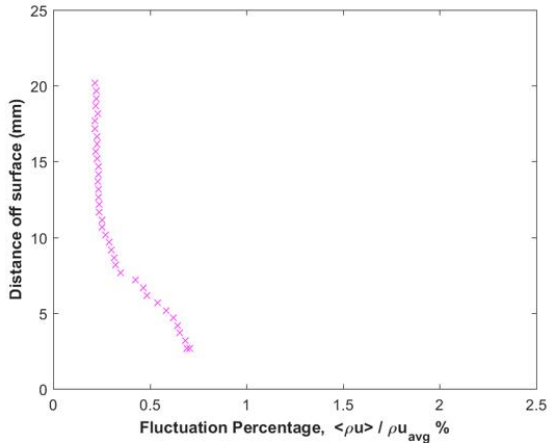

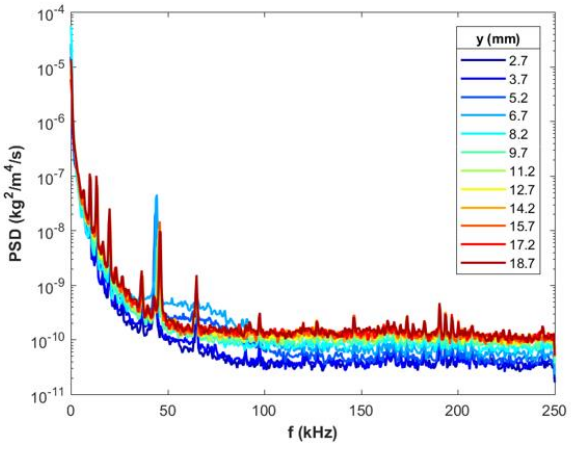

Run 3368

Hot-wire traverse at x=187mm, z=-27.2mm. Re near 5.1M/m.

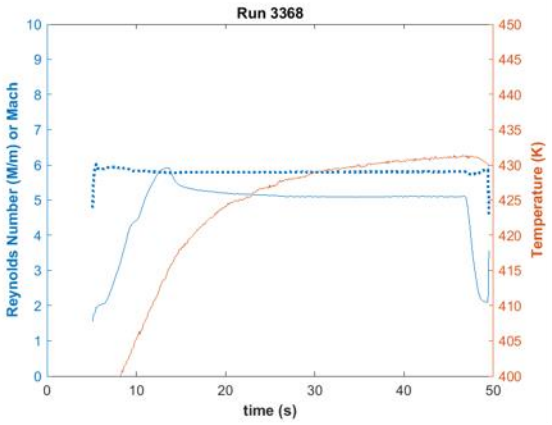

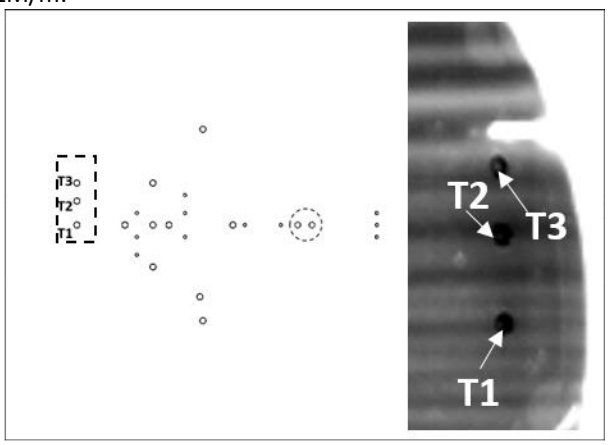

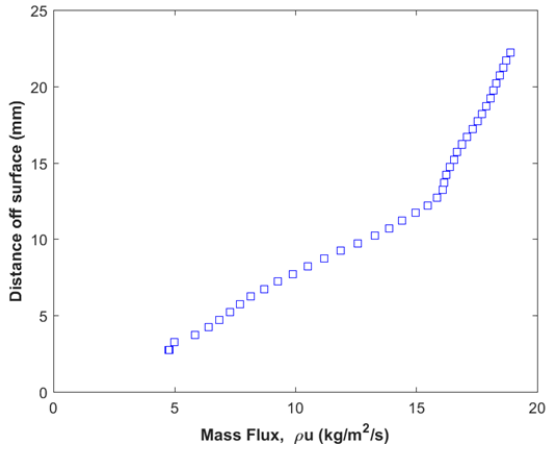

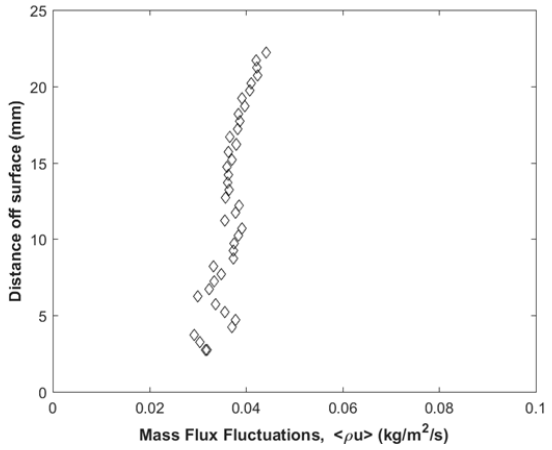

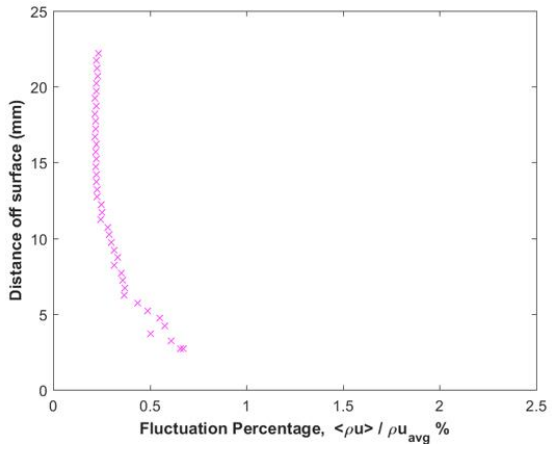

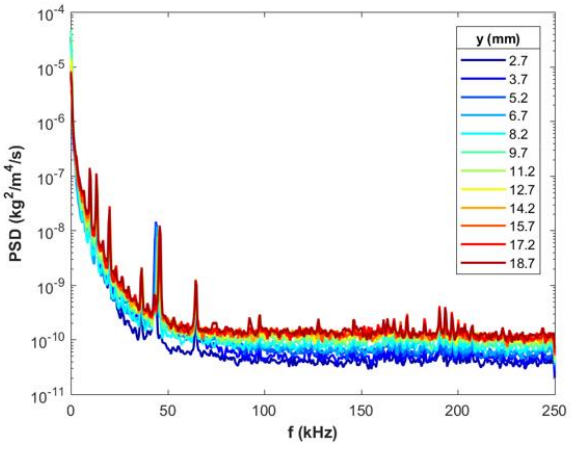

Run 3369. Failed run. Traverse jam.

Run 3370

Hot-wire traverse at x=187mm, z=-24.8mm. Re near 4.8M/m.

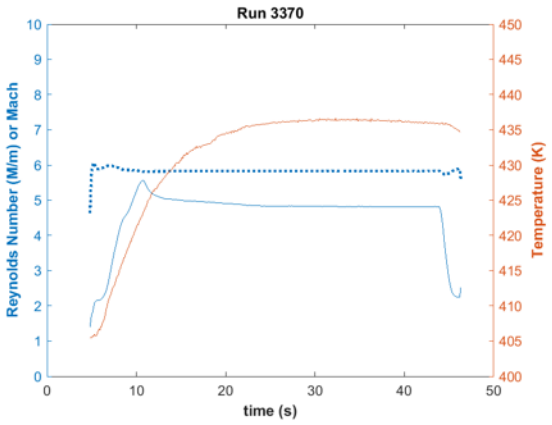

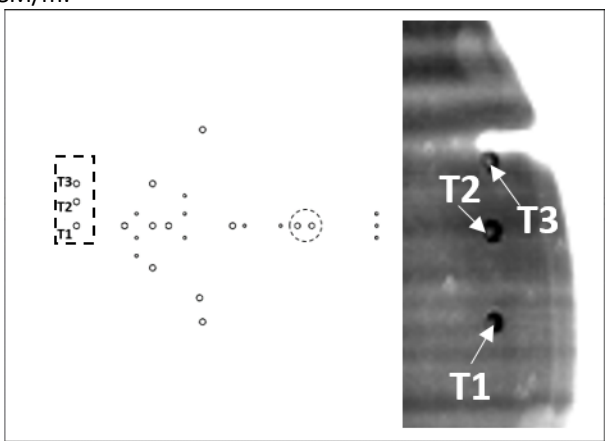

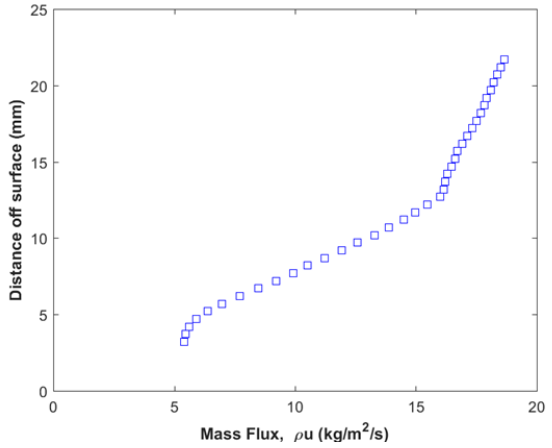

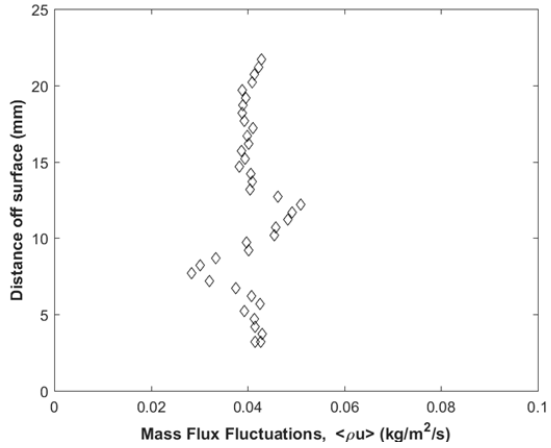

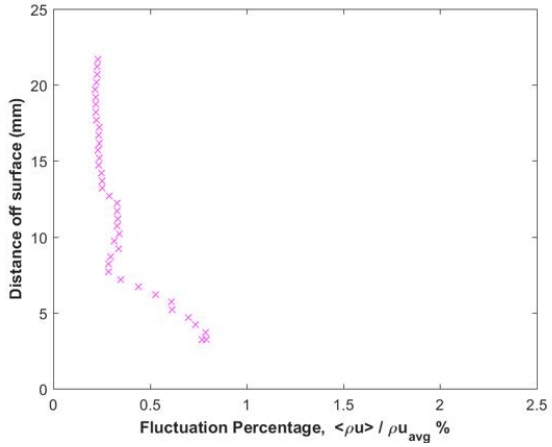

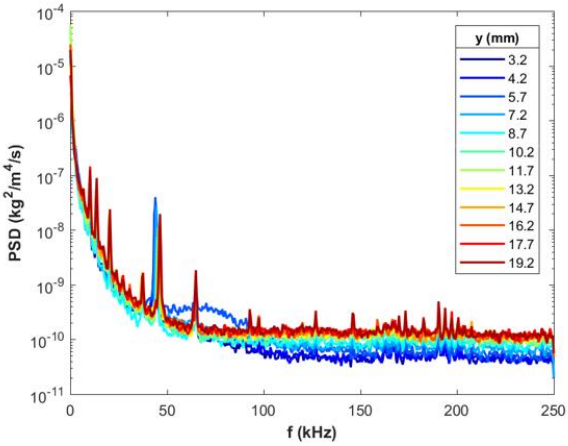

Run 3371

Hot-wire traverse at x=213mm, z=-1.6mm. Re near 5.0M/m.

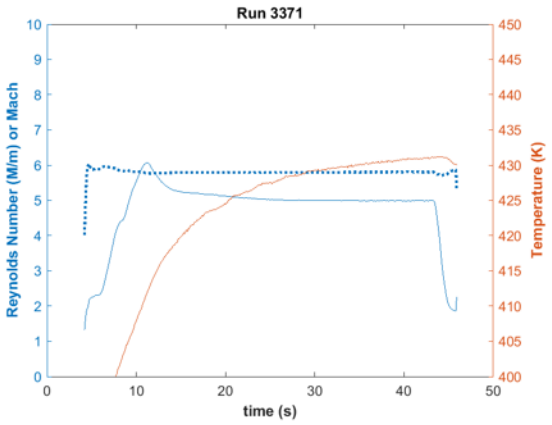

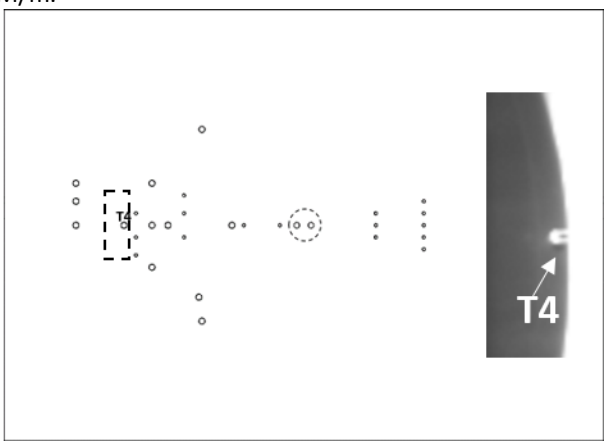

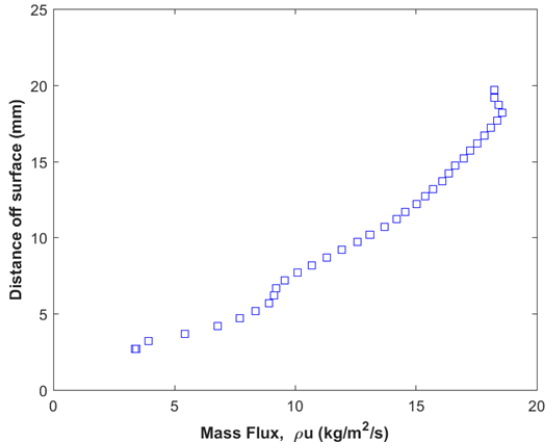

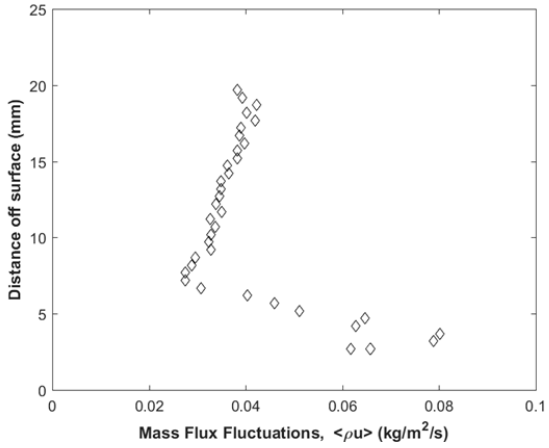

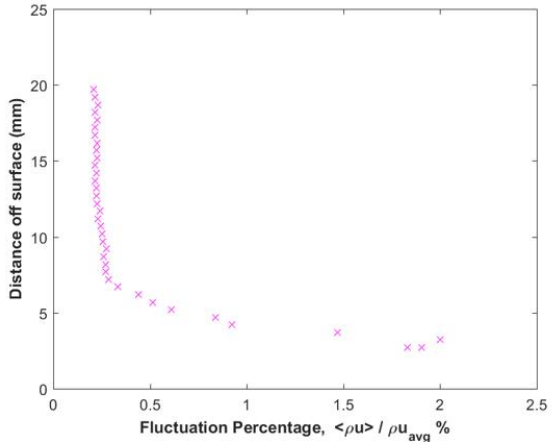

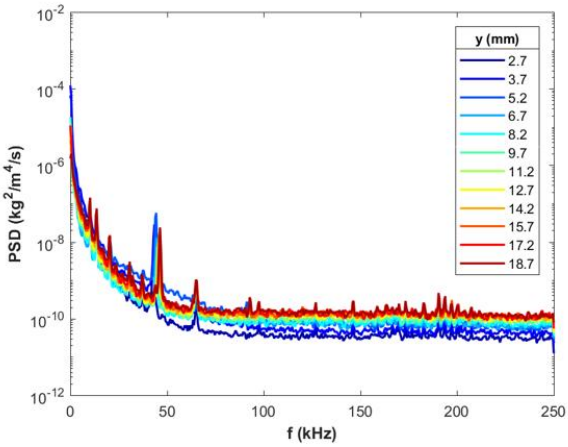

Run 3372

Hot-wire traverse at x=213mm, z=2.0mm. Re near 5.0M/m.

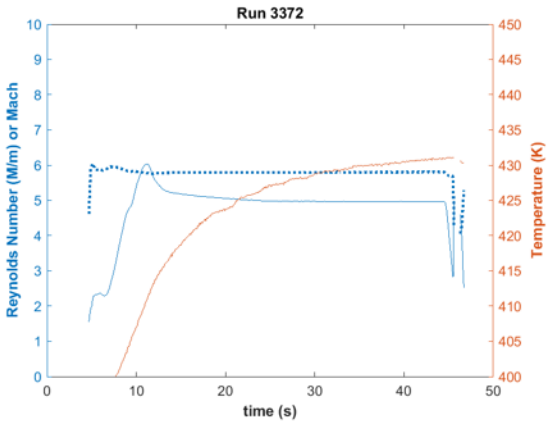

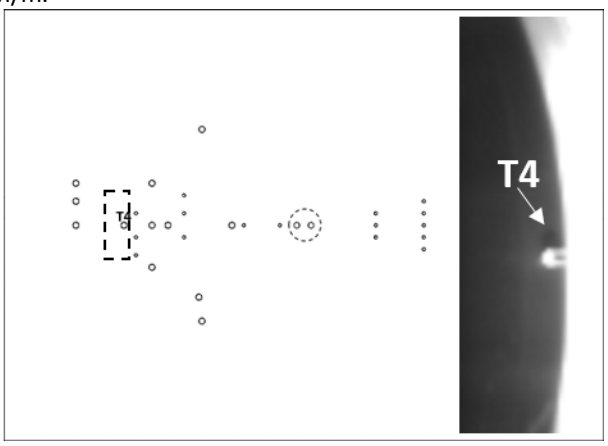

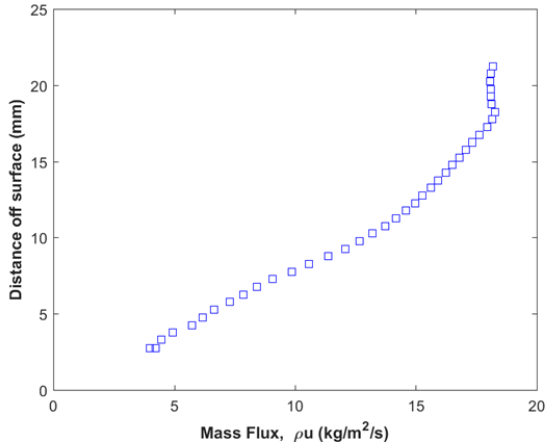

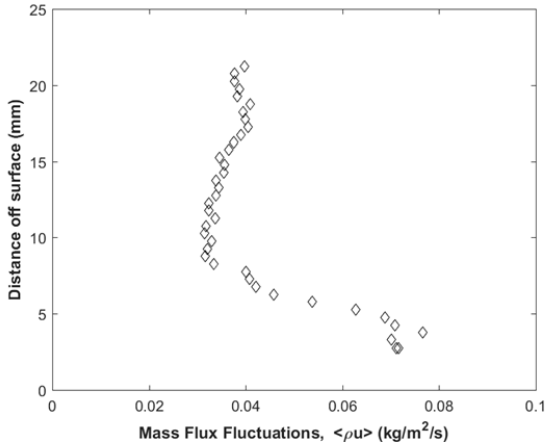

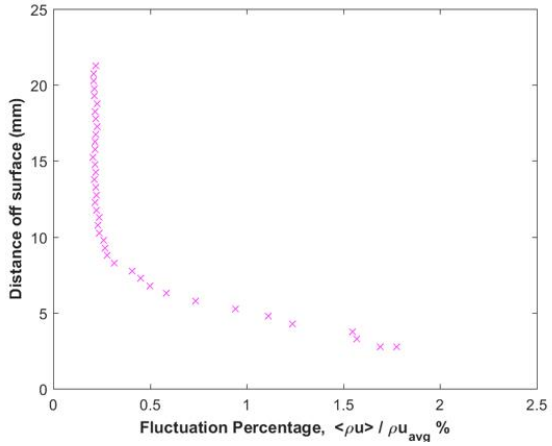

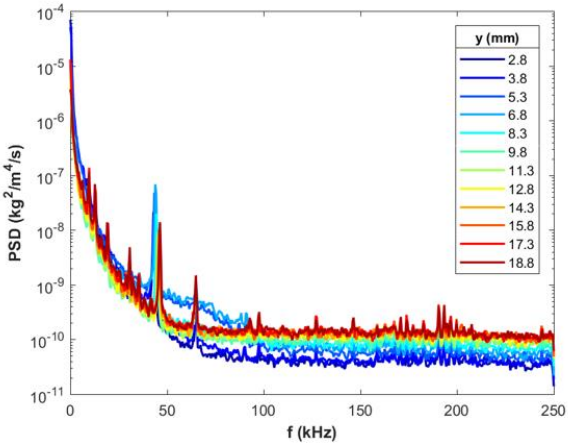

Run 3373

Hot-wire traverse at x=213mm, z=-1.0mm. Re near 5.1M/m.

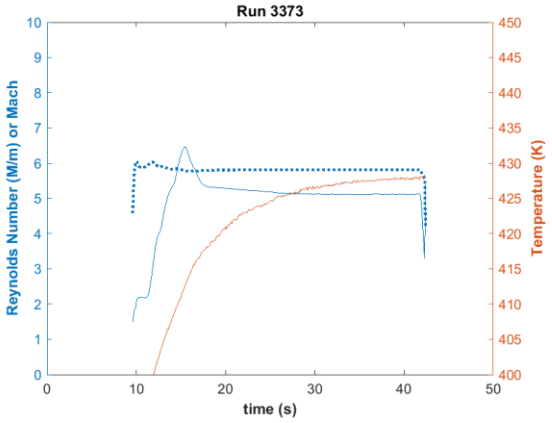

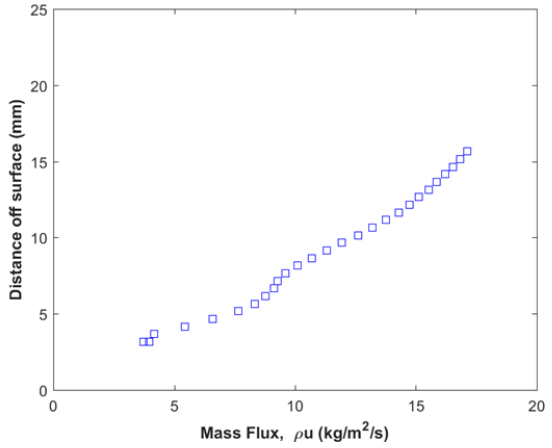

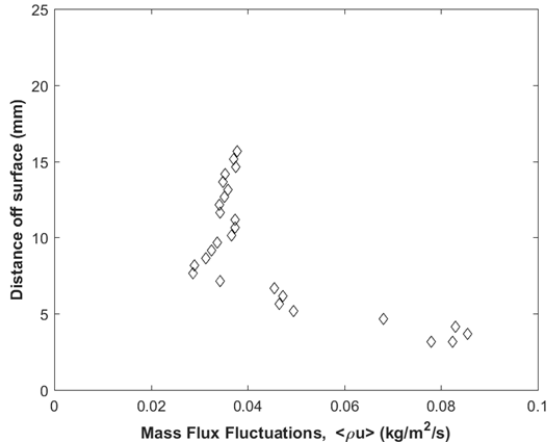

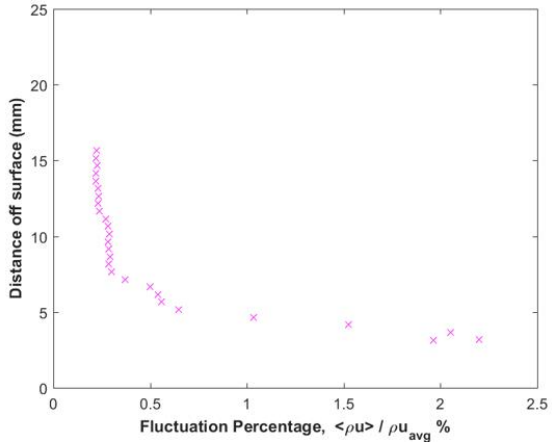

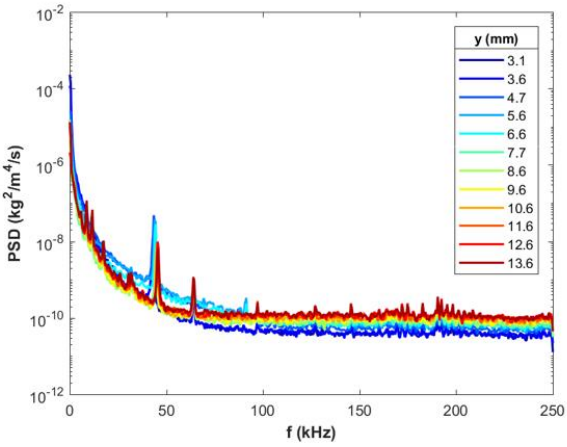

Run 3374

Hot-wire traverse across leading-edge shock at x=106mm, z=0mm. Re near 4.9M/m.

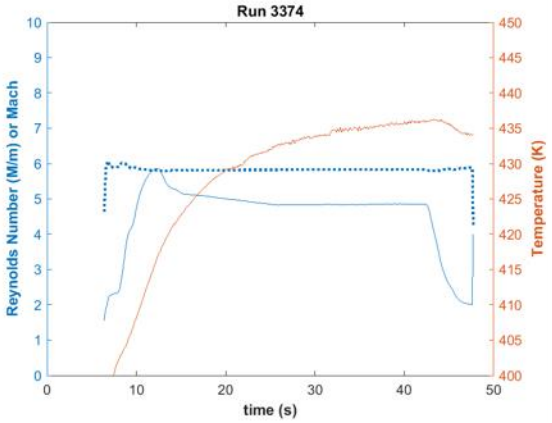

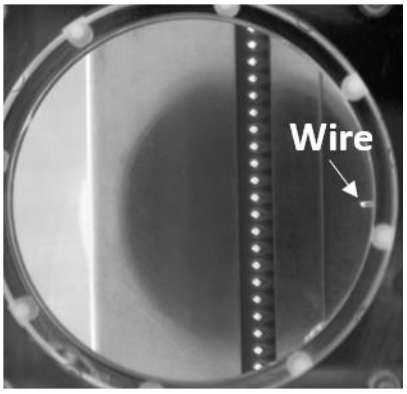

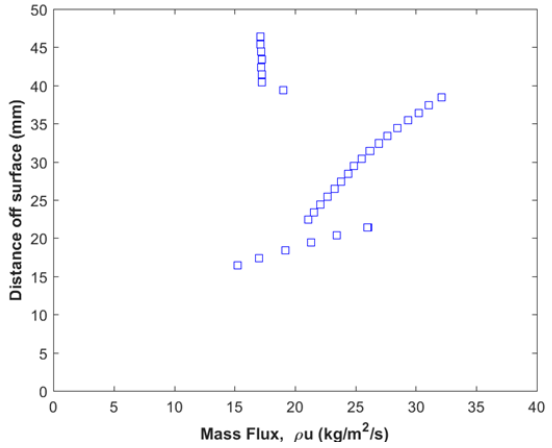

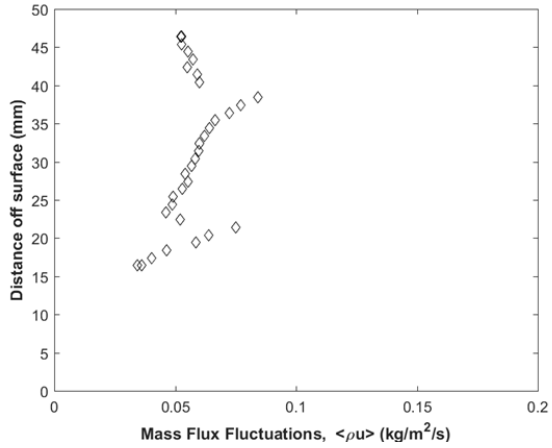

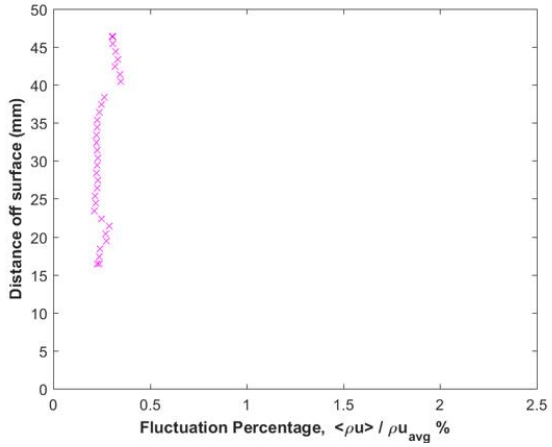

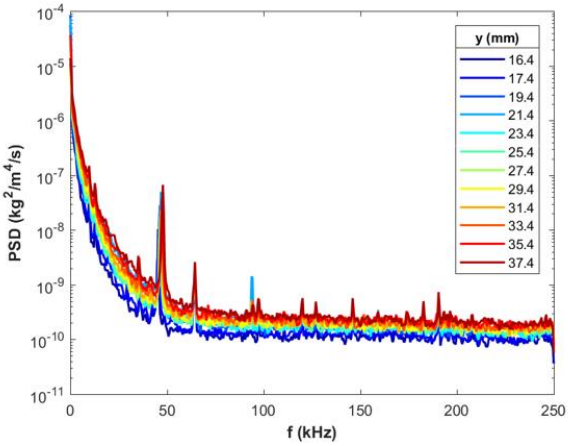

Run 3375

Repeat of same position as previous run, changing resolution. Re near 5.0M/m.

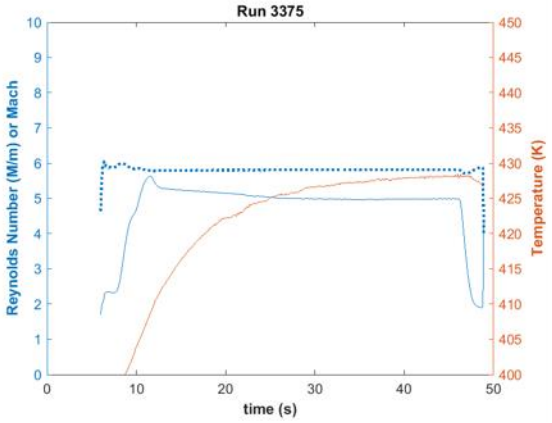

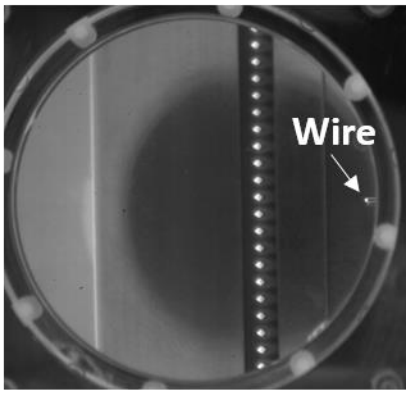

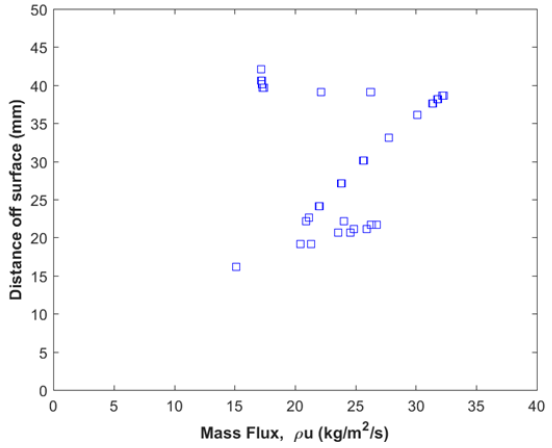

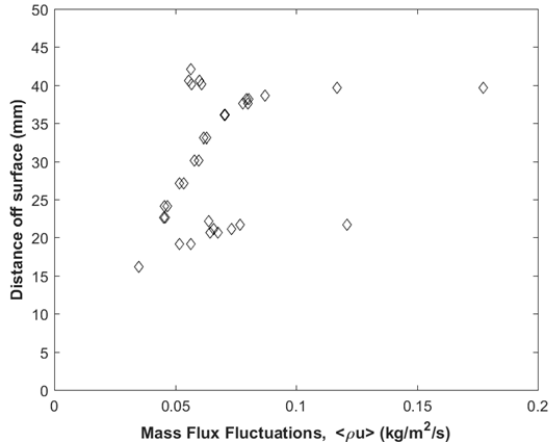

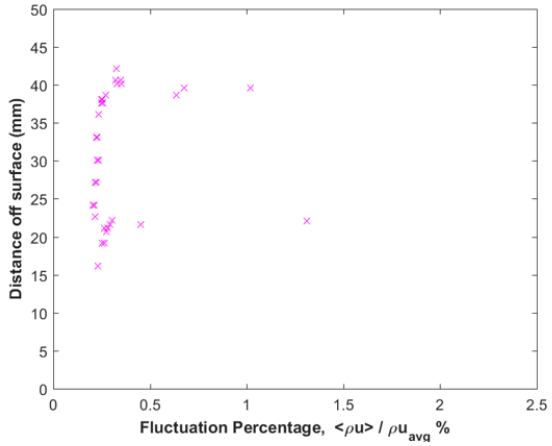

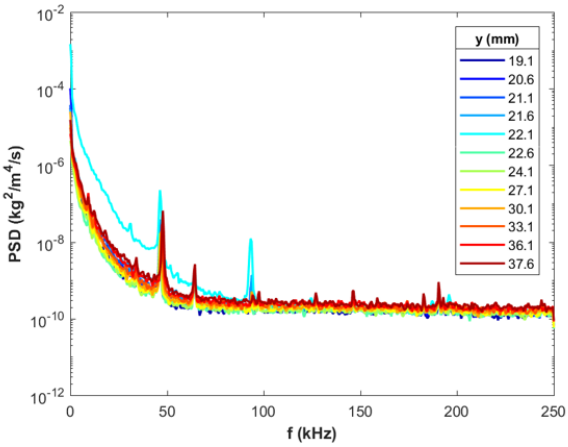

Run 3376

Hot-wire traverse across leading-edge shock at x=58mm, z=0mm. Re near 4.9M/m.

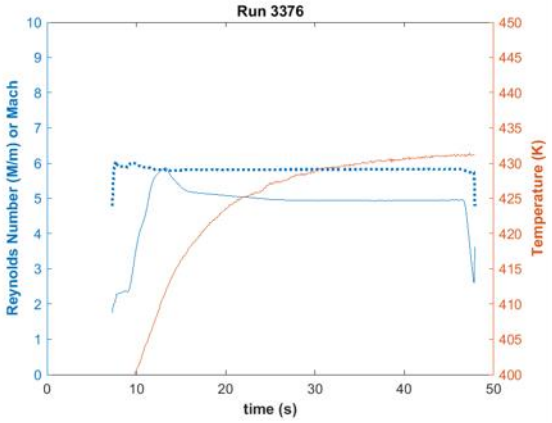

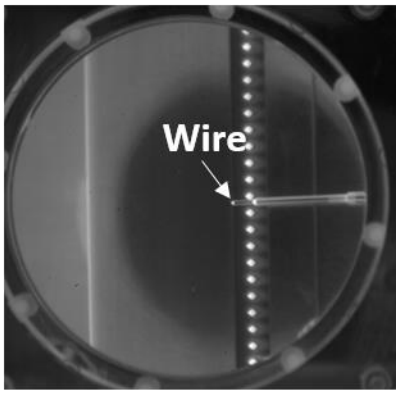

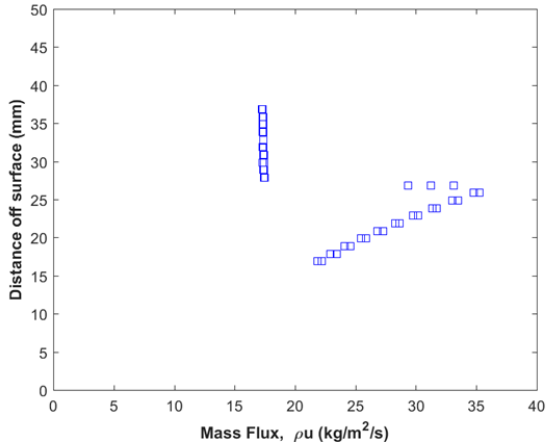

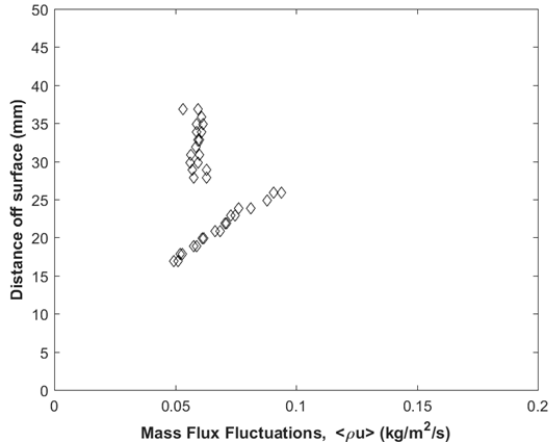

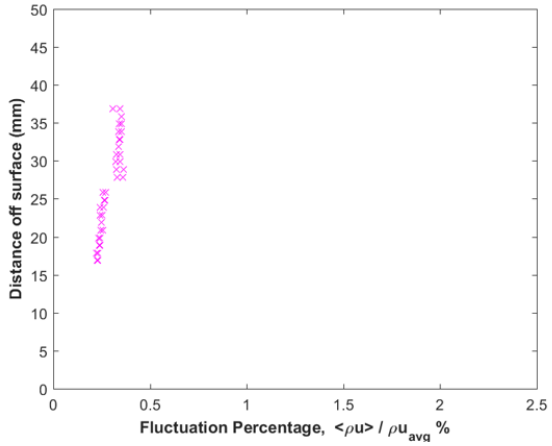

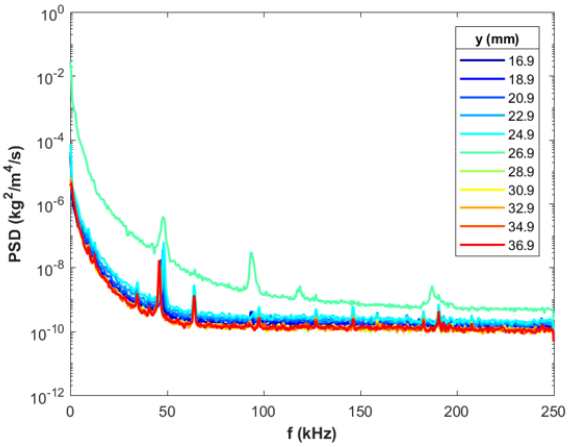

Run 3377

Hot-wire traverse across leading-edge shock at x=82mm, z=0mm. Re near 5.1M/m.

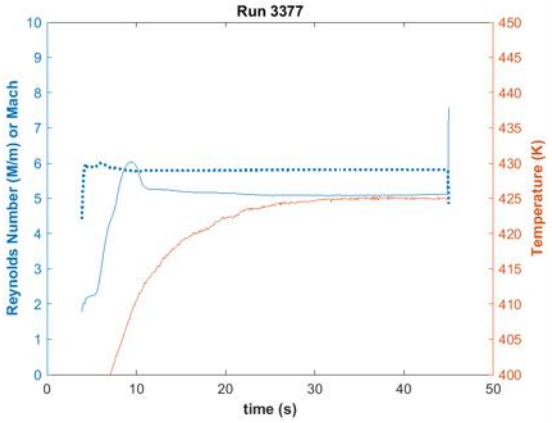

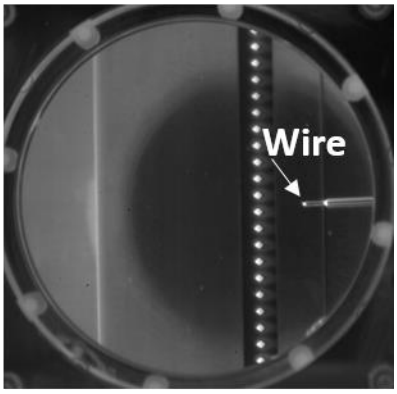

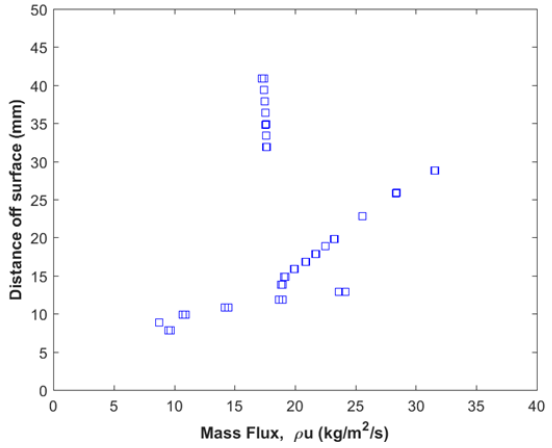

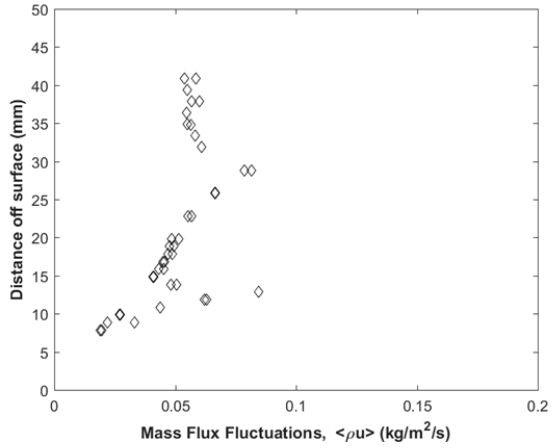

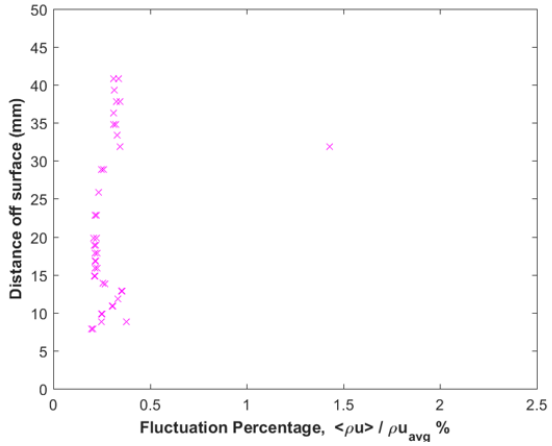

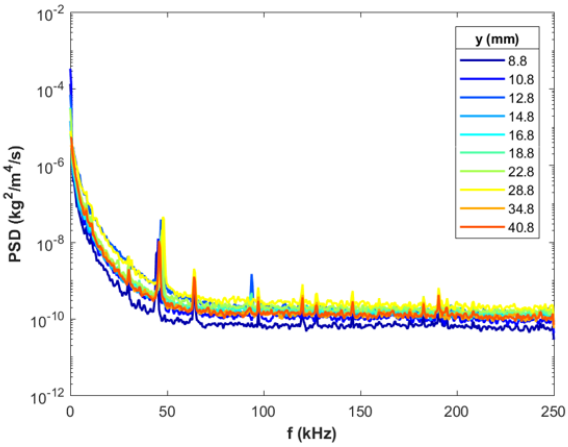

Run 3378

Hot-wire traverse at x=264mm, z=9.9mm. Re near 5.0M/m. Probe grounded to tunnel for points 1-12.

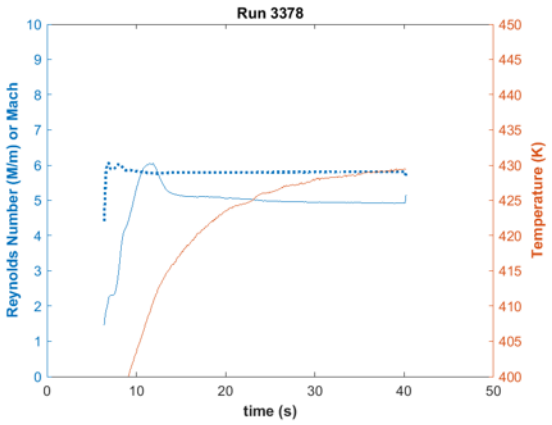

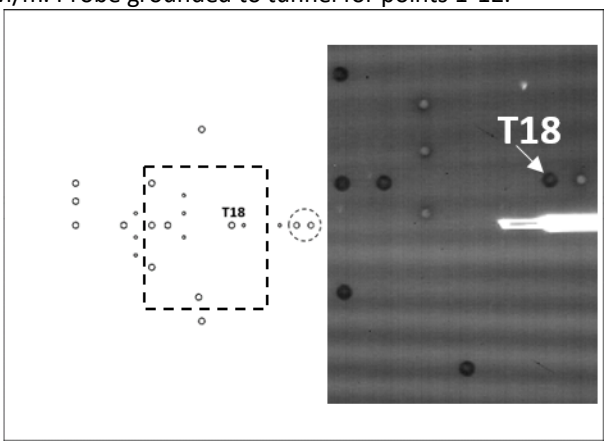

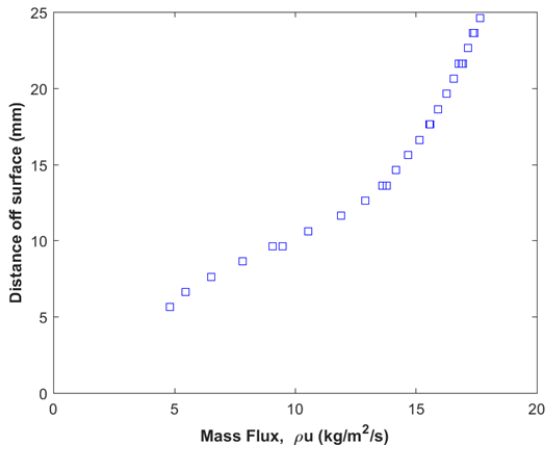

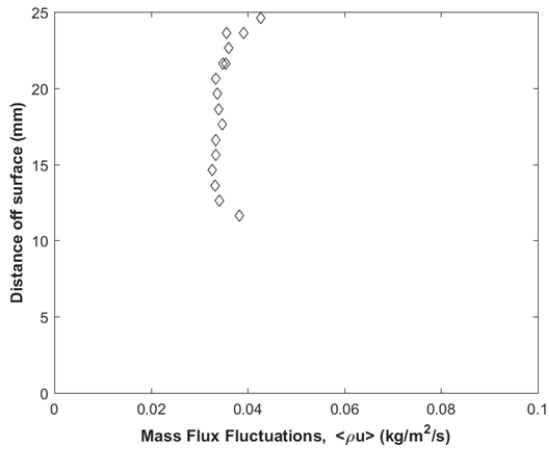

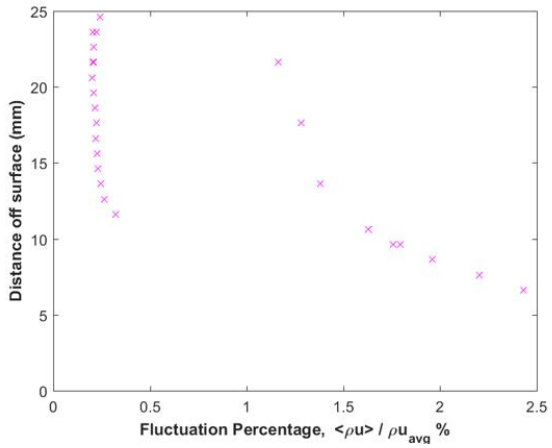

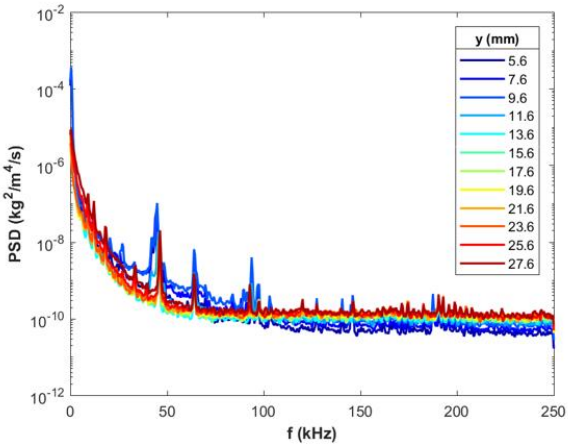

Run 3379

Repeat same traverse. Re near 4.9M/m.

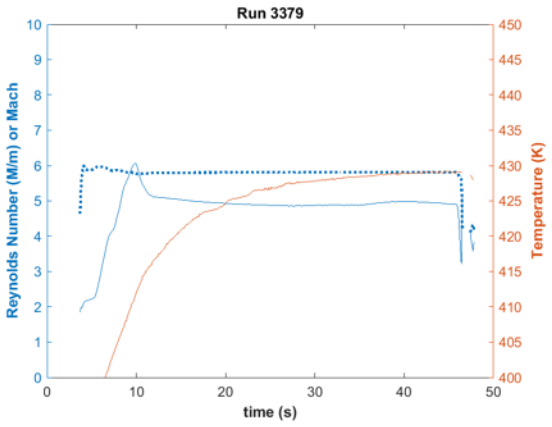

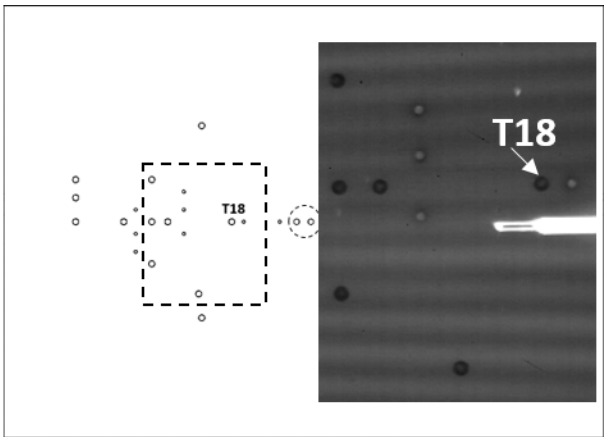

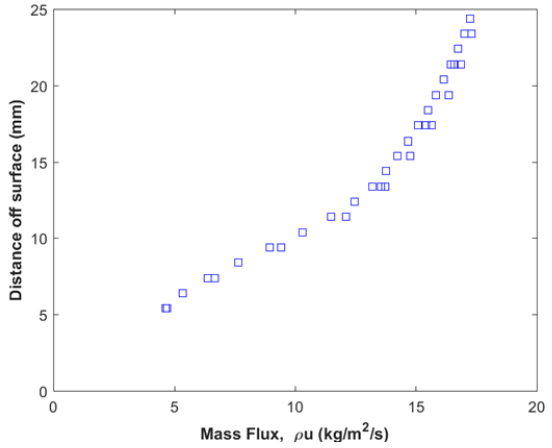

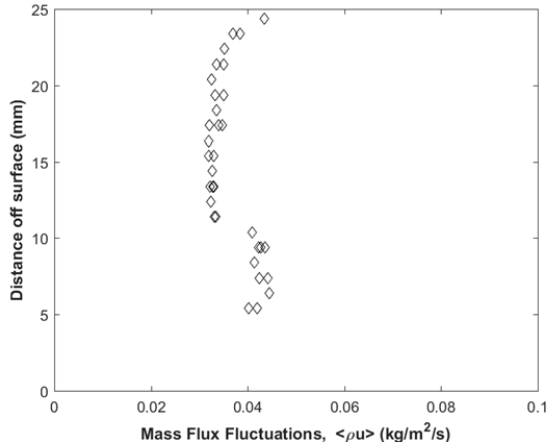

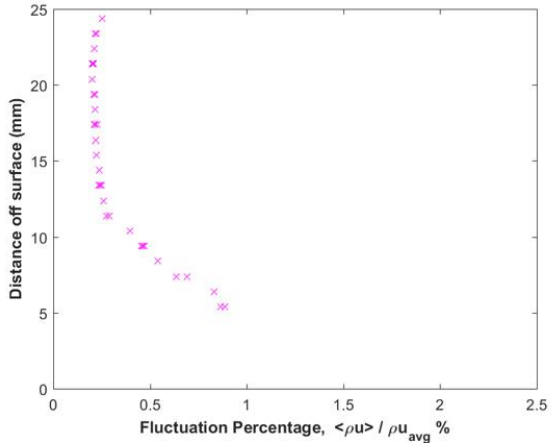

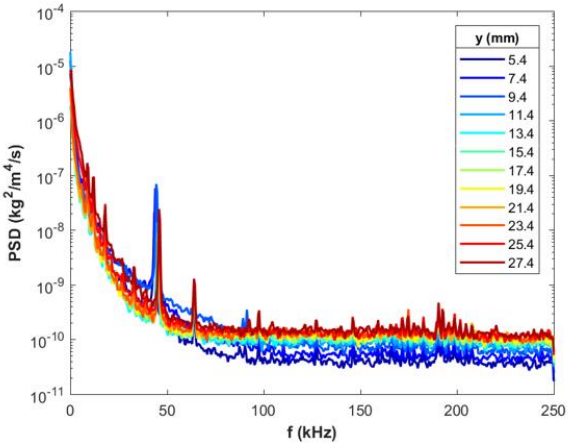

Run 3380

Hot-wire traverse at x=264mm, z=0.0mm. Re near 5.0M/m.

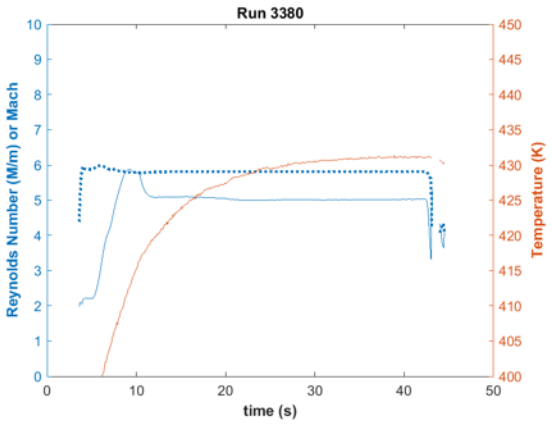

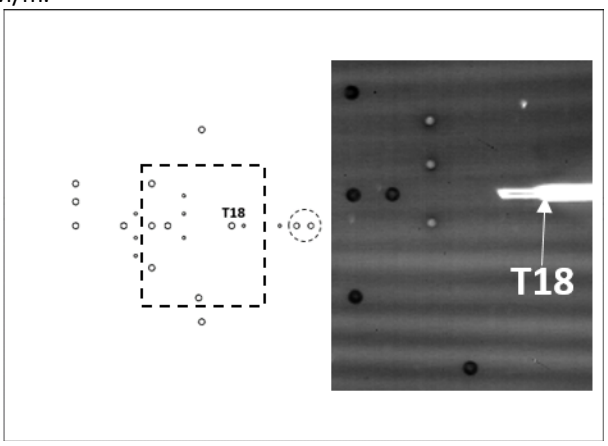

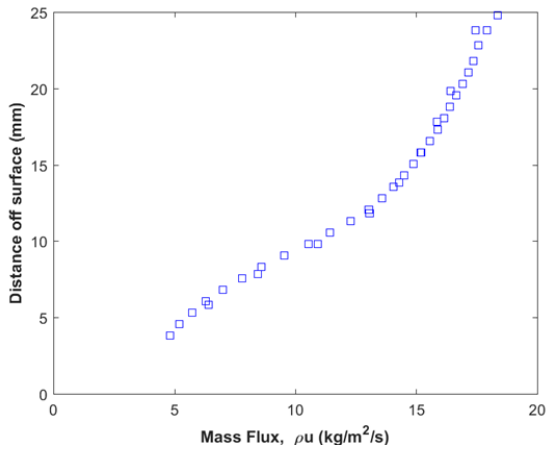

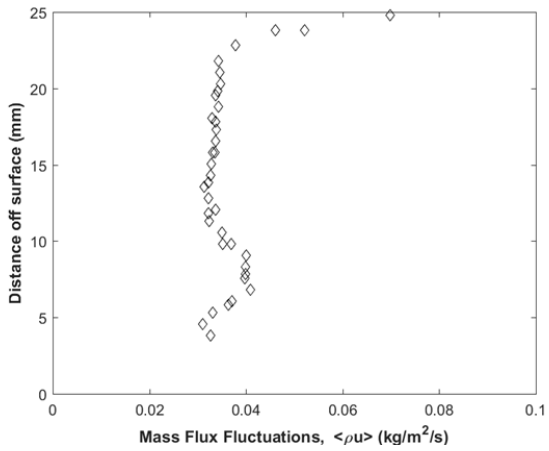

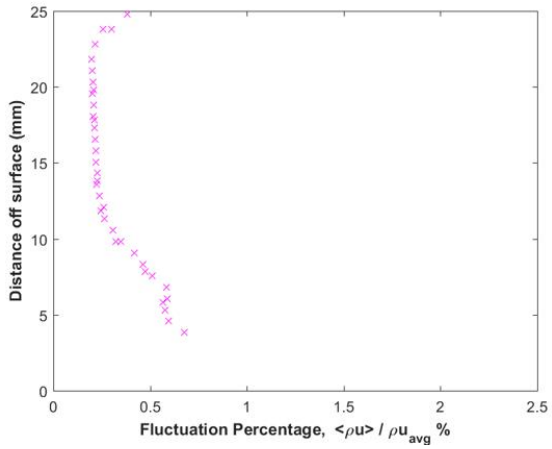

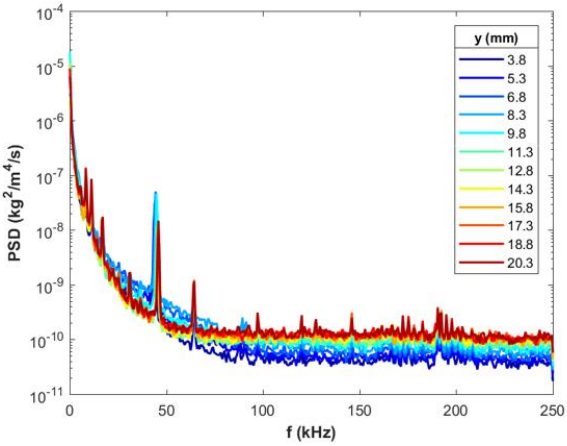

Run 3381

Hot-wire traverse at x=276mm, z=0.6mm. Re near 4.9M/m.

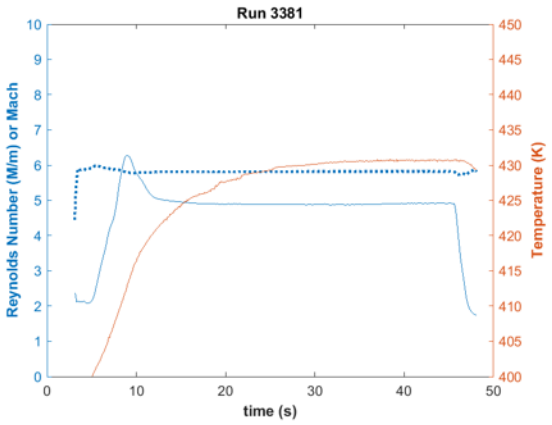

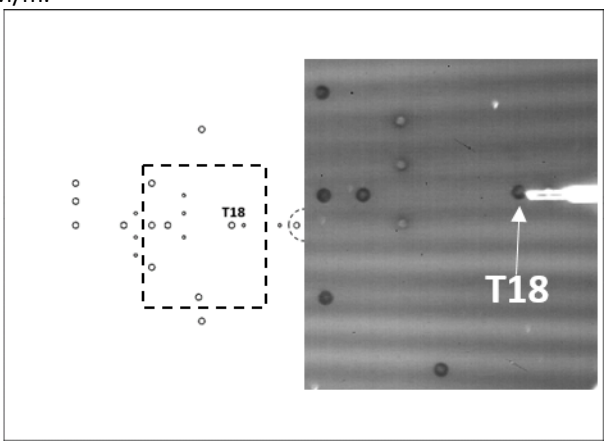

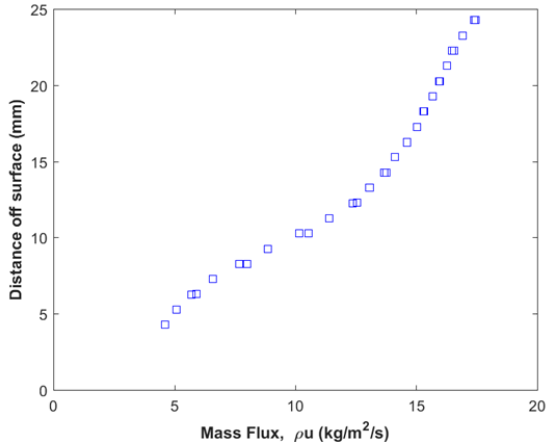

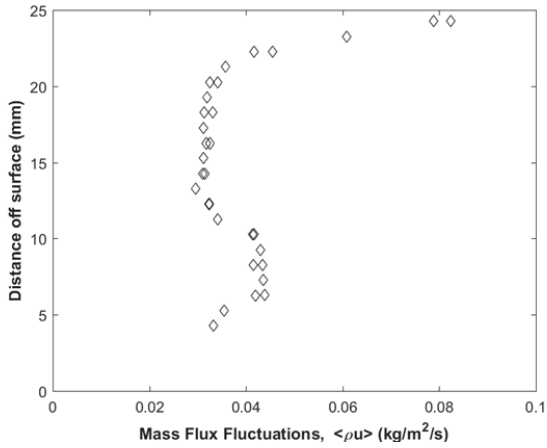

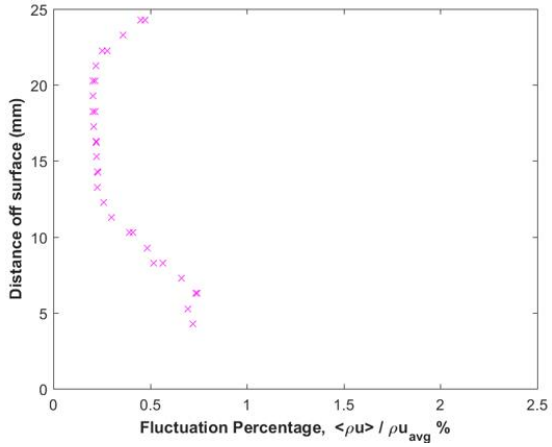

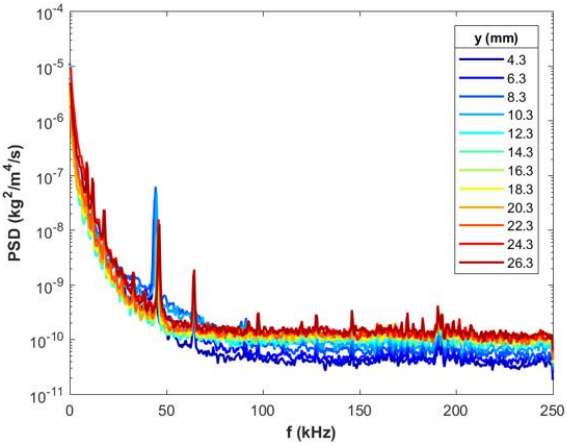

Run 3382

Hot-wire traverse at x=302mm, z=0.6mm. Re near 4.9M/m.

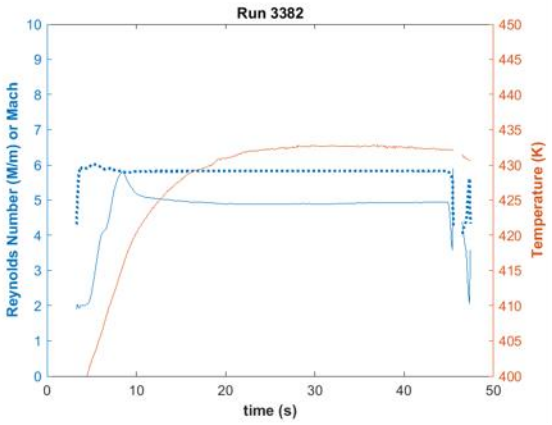

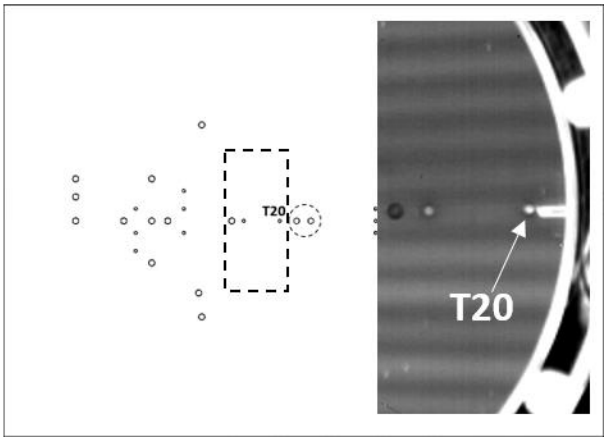

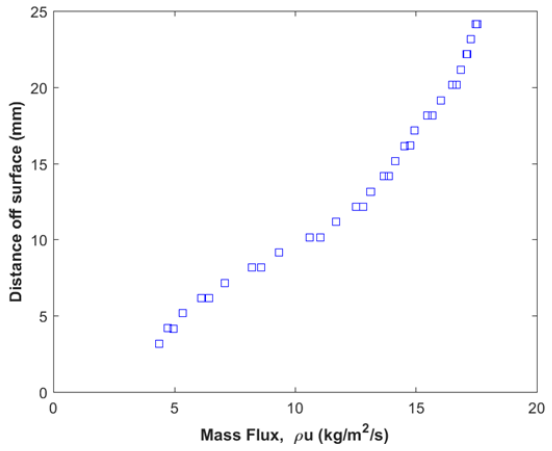

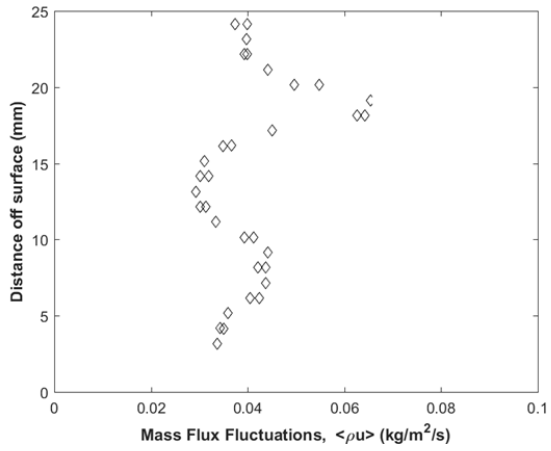

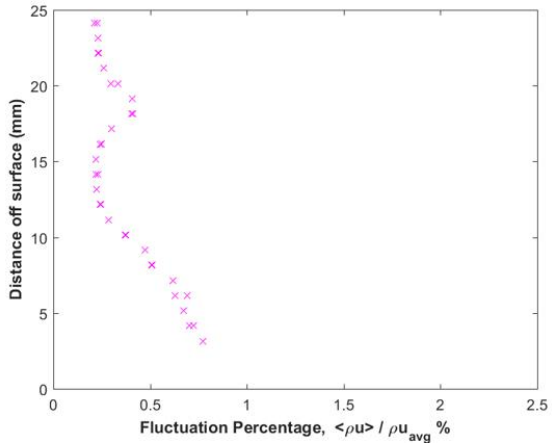

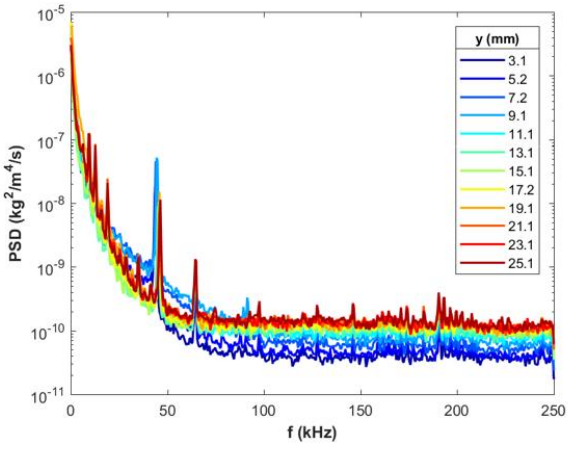

Run 3383

Same traverse with Re near 7.2M/m and dummy probe for higher Re.

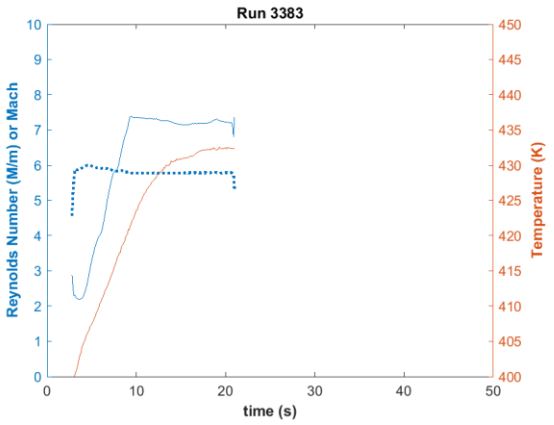

Run 3384

Repeat similar traverse with Re near 7.5M/m.

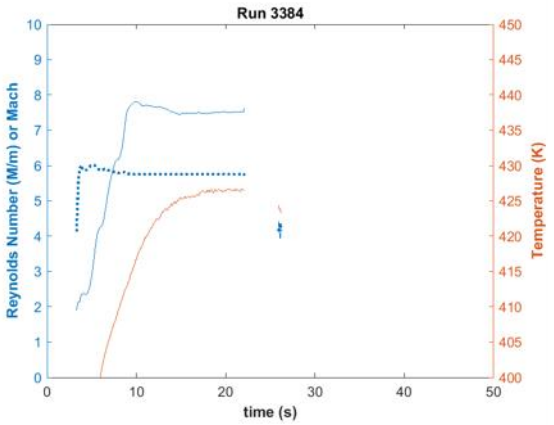

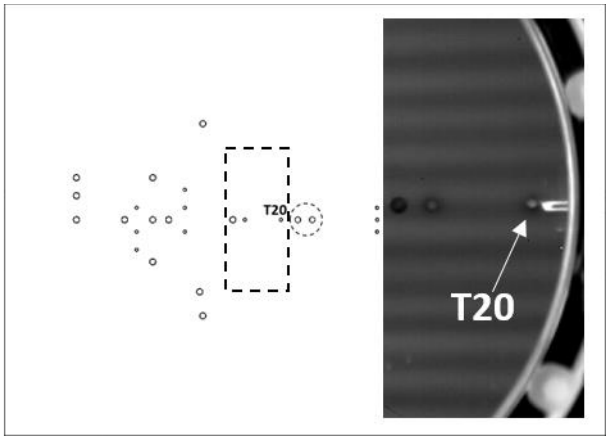

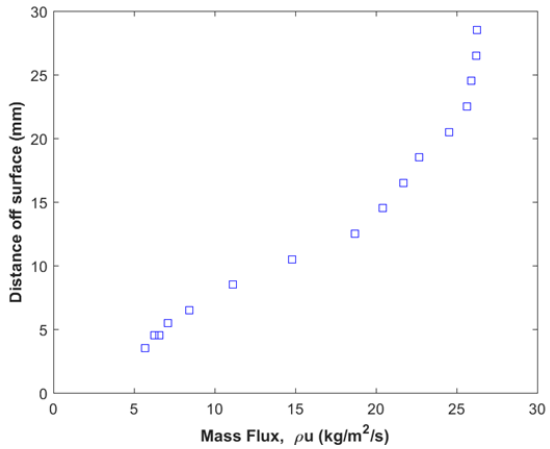

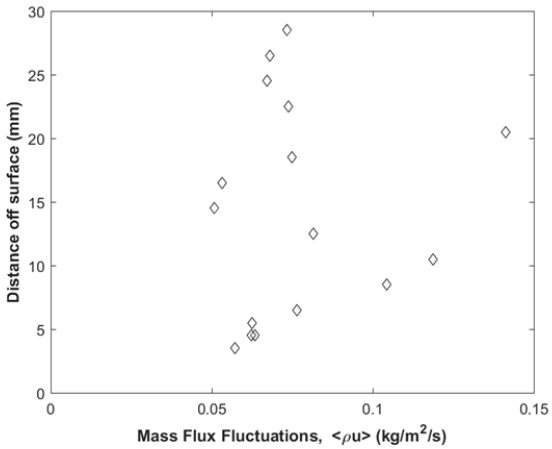

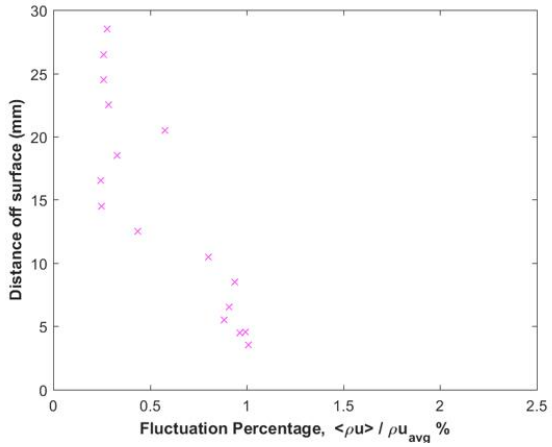

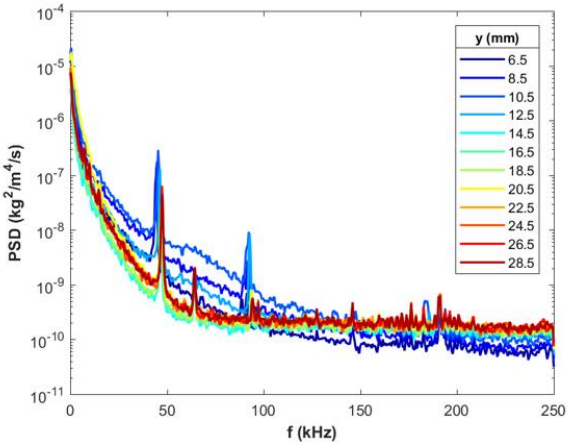

Run 3385

Repeat similar traverse with Re near 7.5M/m.

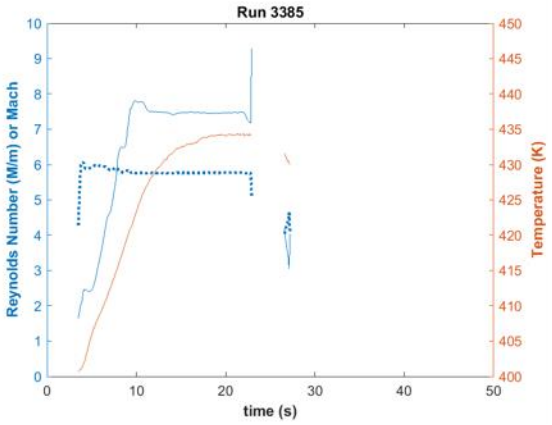

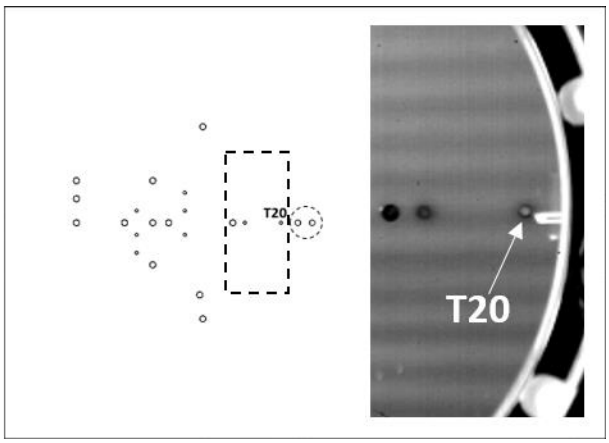

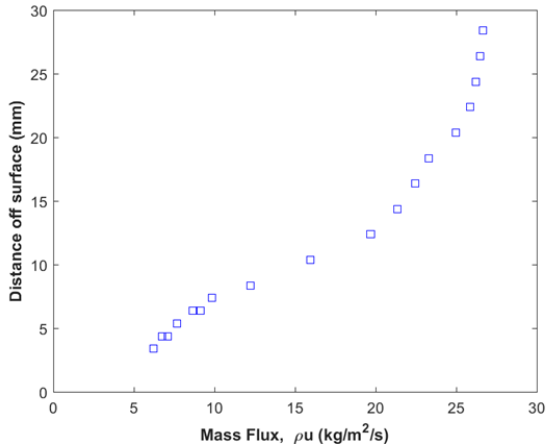

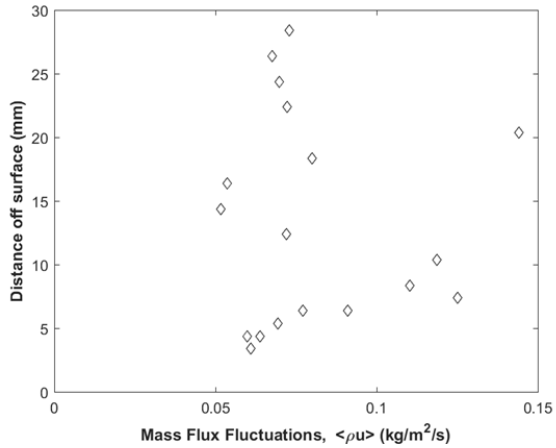

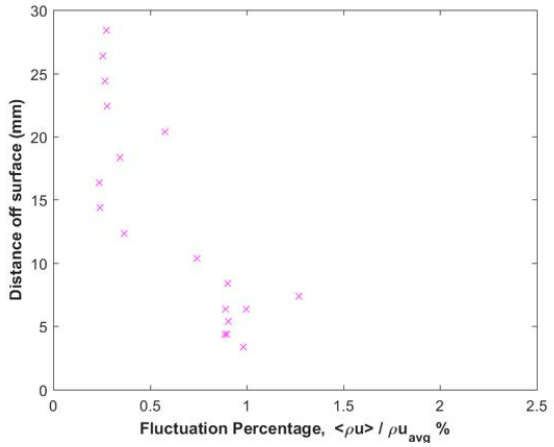

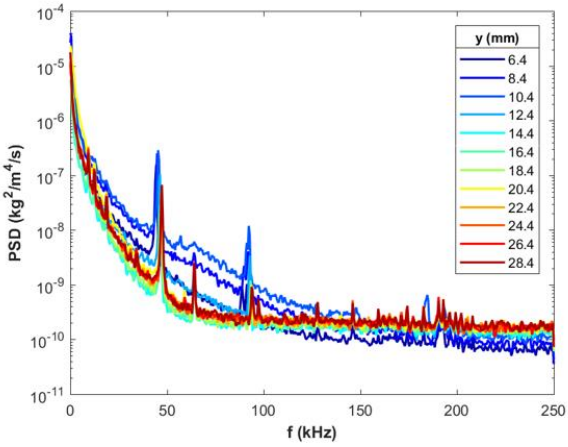

Run 3386

Repeat similar traverse with Re near 7.0M/m. Traverse jammed.

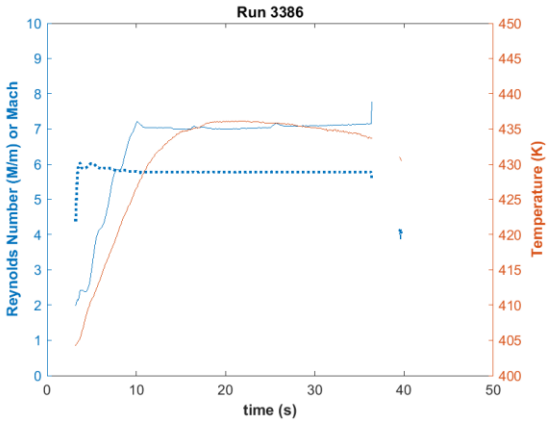

Run 3387

Repeat similar traverse with Re near 6.9M/m.

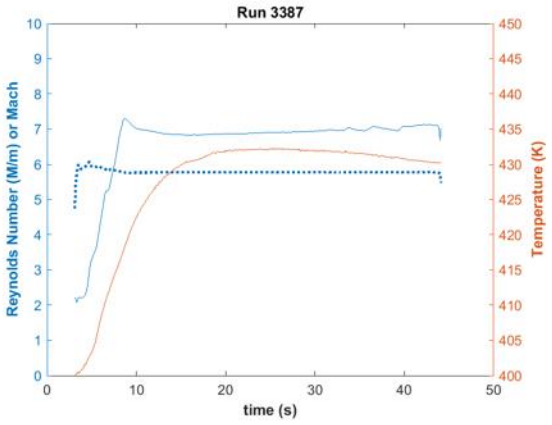

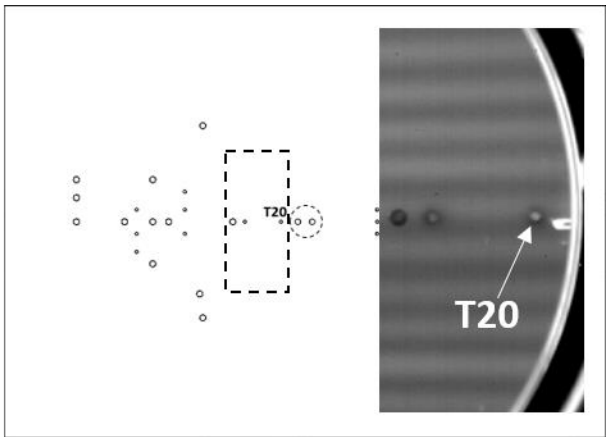

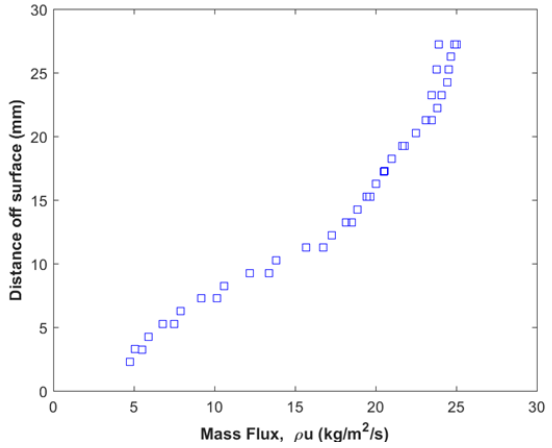

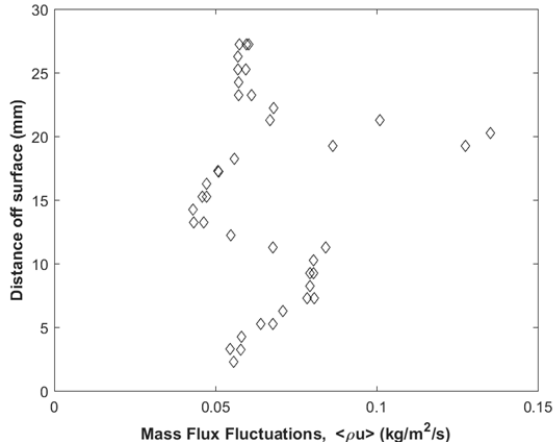

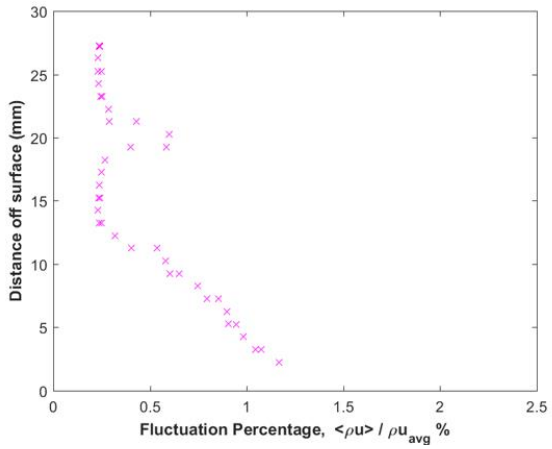

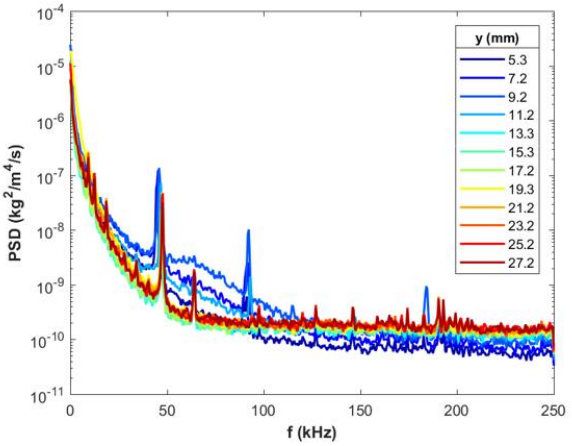

Run 3388

Hot-wire held in position at x=302mm, y=10.0mm, z=0.8mm. Re sweep.

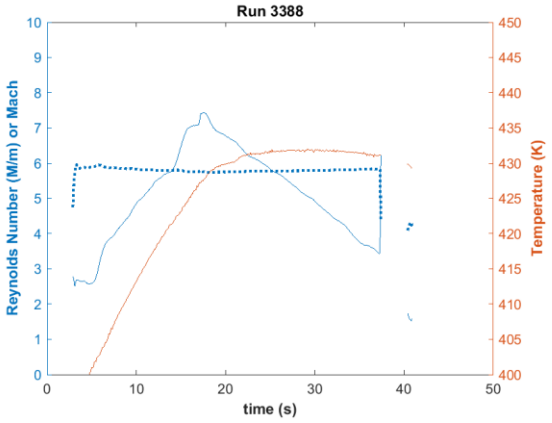

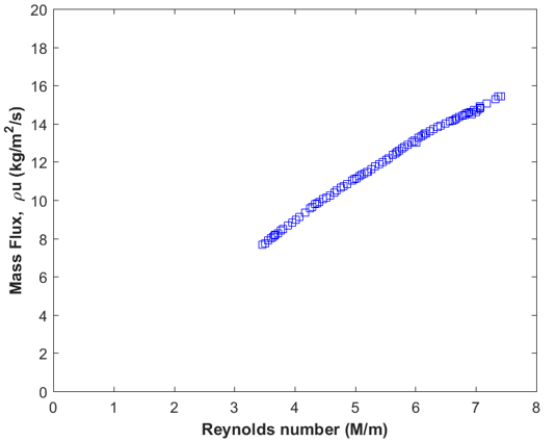

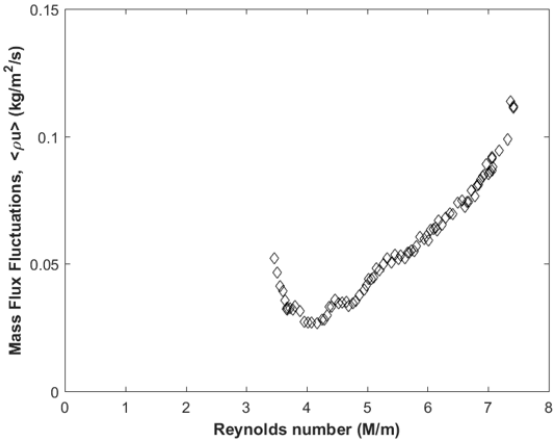

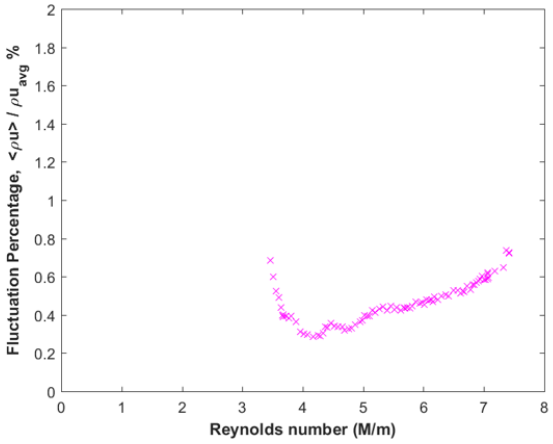

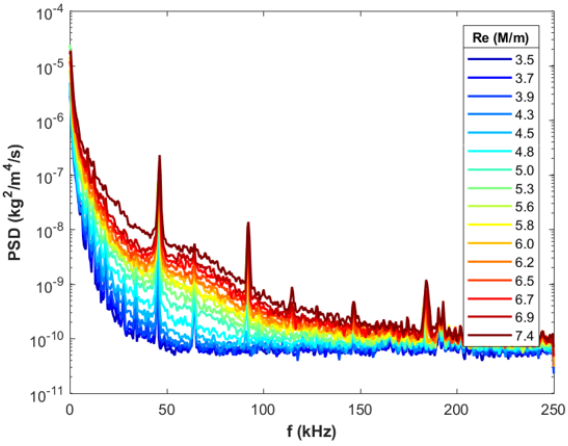

Run 3389

Repeat of previous going to lower Re.

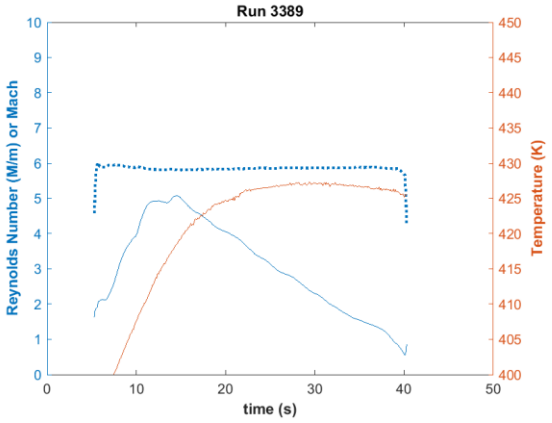

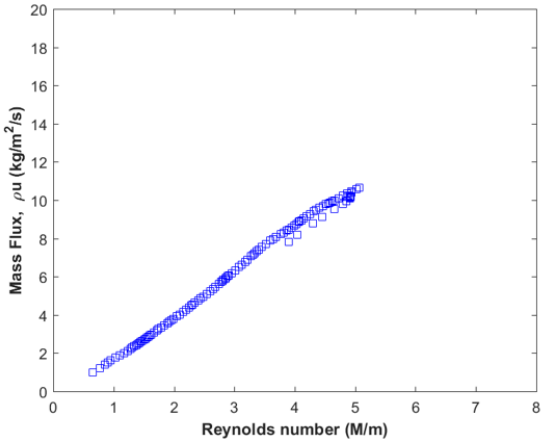

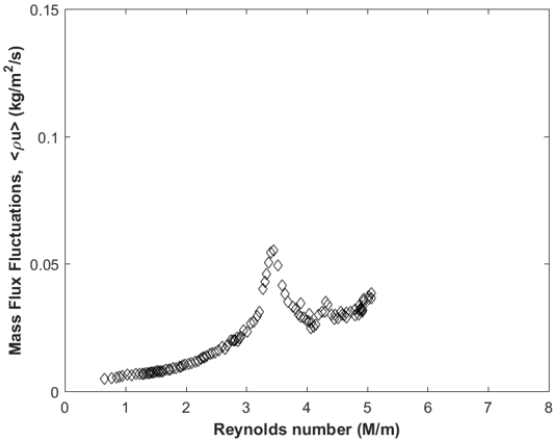

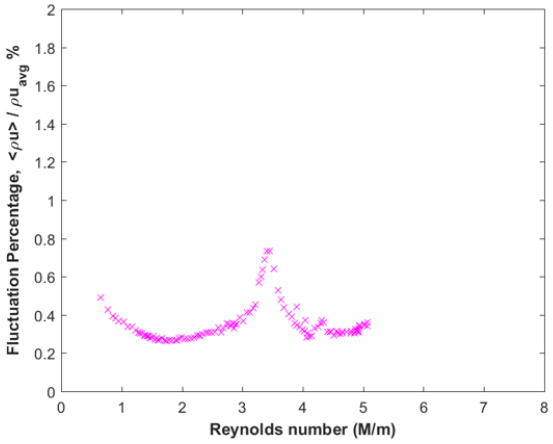

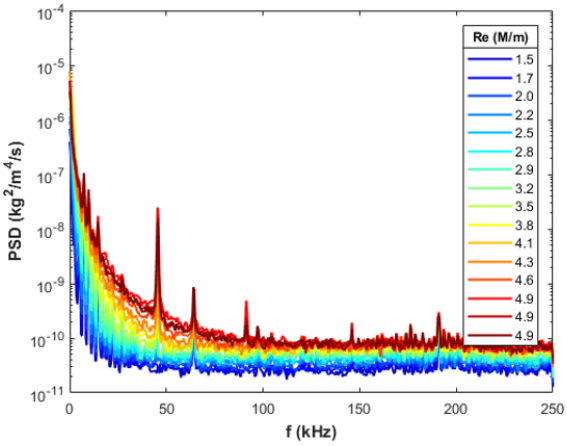

Run 3390

Hot-wire traverse at x=346mm, z=0.8mm. Re near 7.5M/m. Tunnel unstart broke wire.

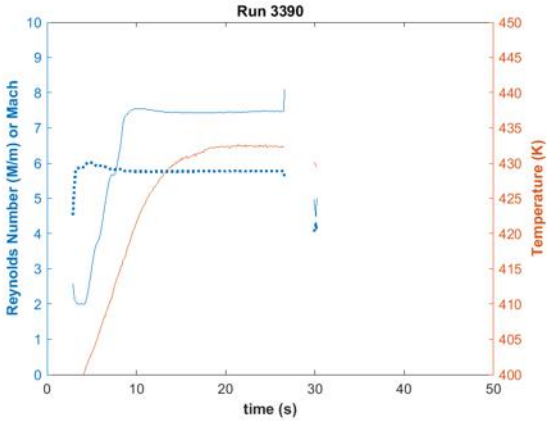

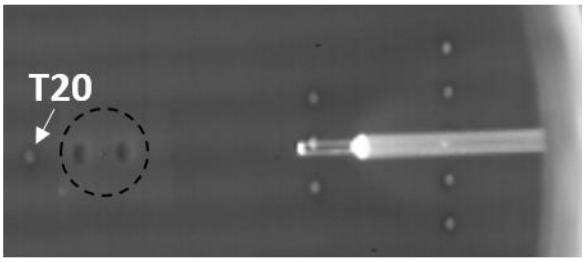

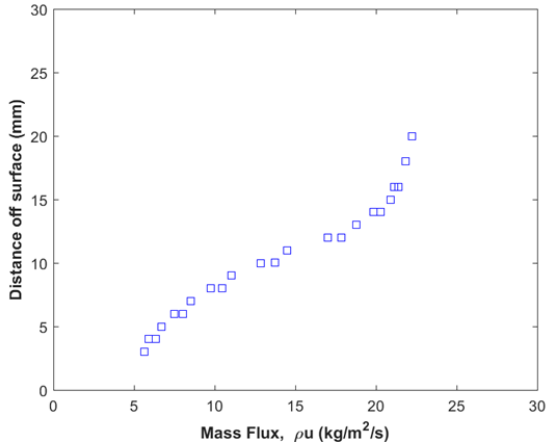

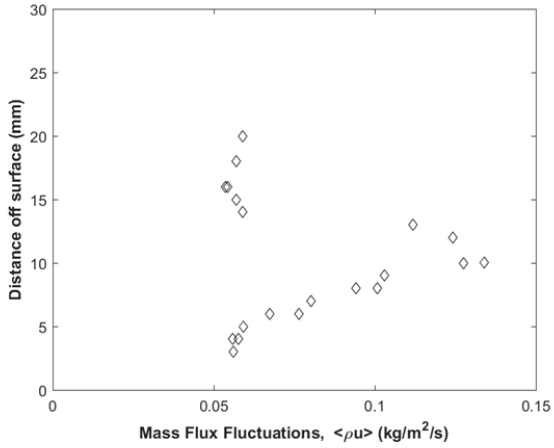

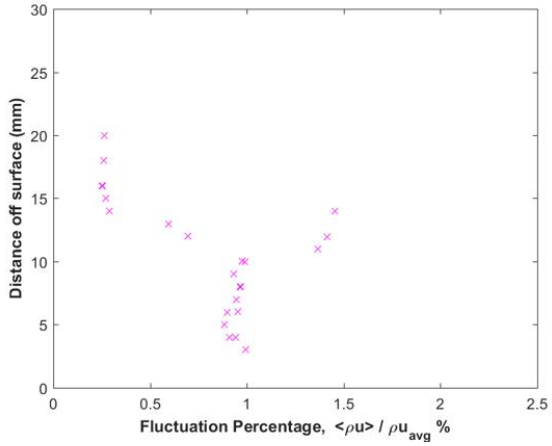

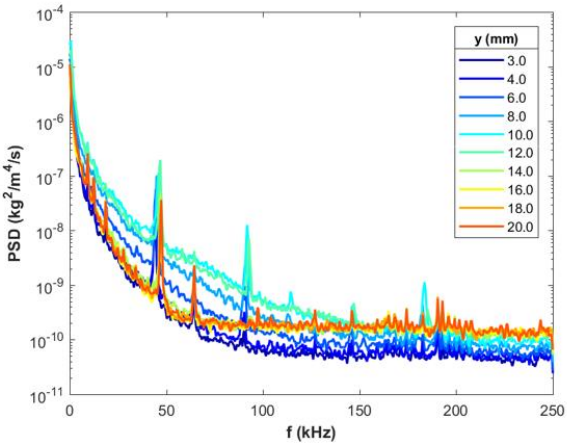

Trips, no cylinder

Run 3391

Surface pressure measurements and IR thermography made over a Re sweep.

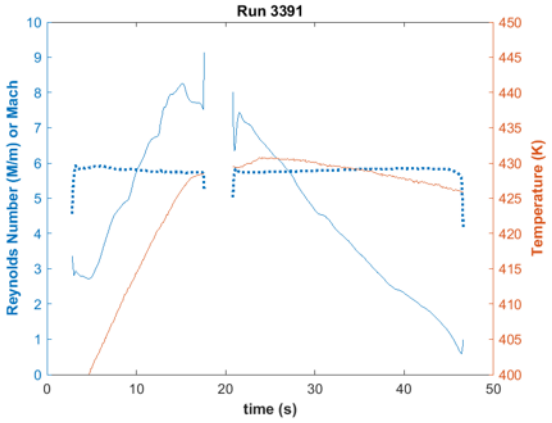

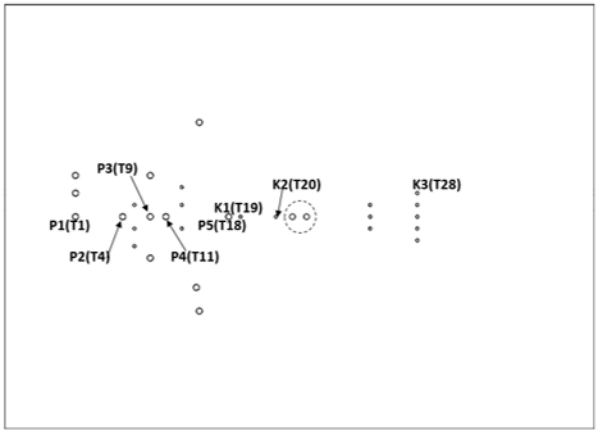

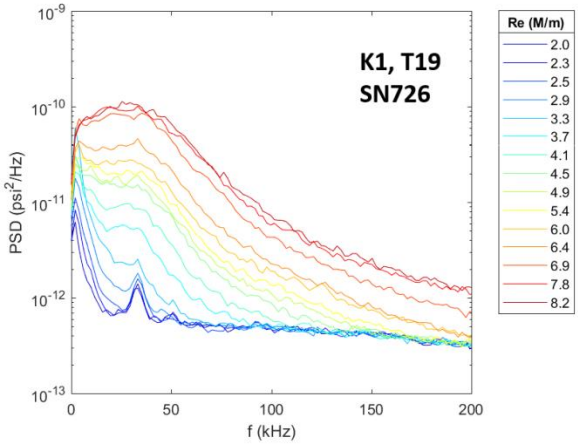

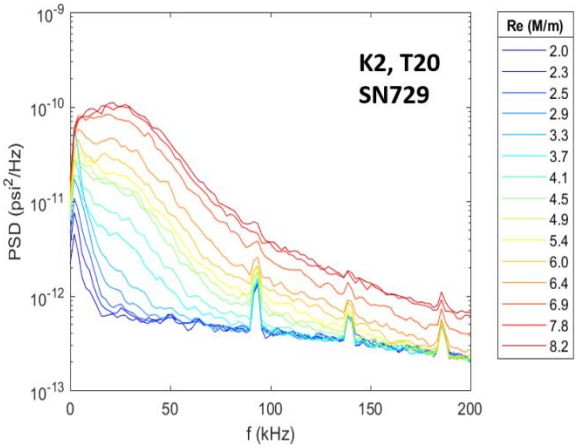

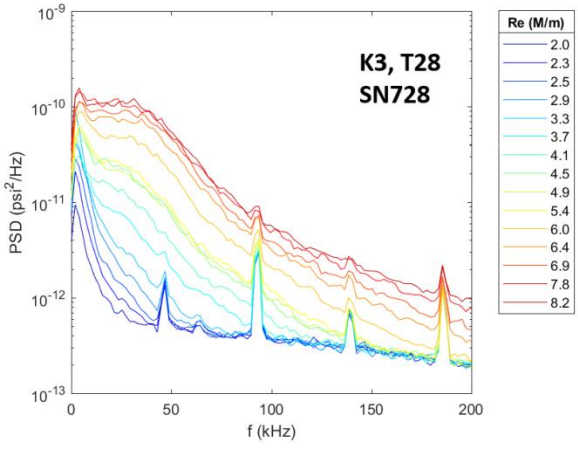

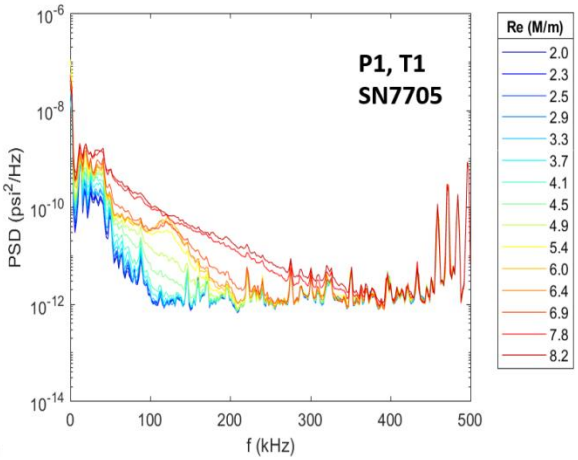

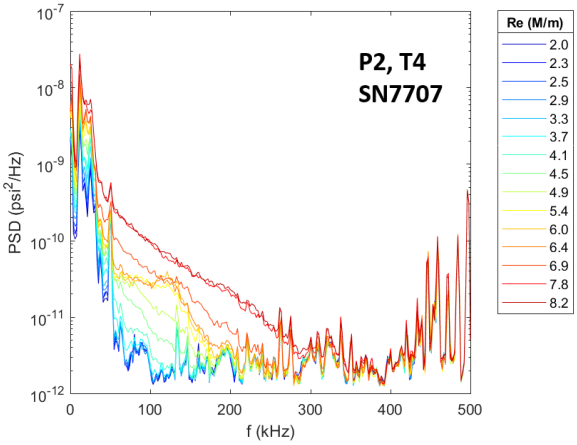
P2, T4
SN7707
PSD (psi²/Hz)
f (kHz)
Re (M/m)
2.0
2.3
2.5
2.9
3.3
3.7
4.1
4.5
4.9
5.4
6.0
6.4
6.9
7.8
8.2

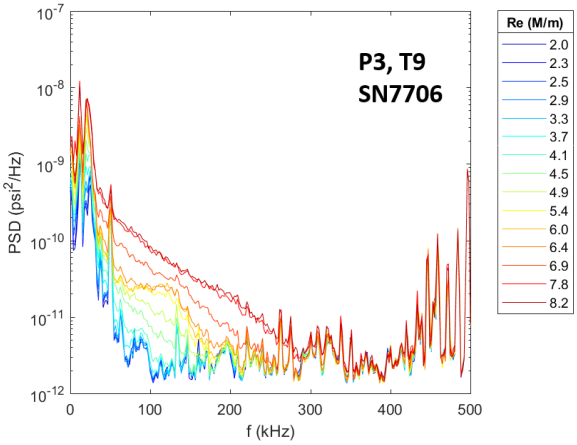
P3, T9
SN7706
PSD (psi²/Hz)
f (kHz)
Re (M/m)
2.0
2.3
2.5
2.9
3.3
3.7
4.1
4.5
4.9
5.4
6.0
6.4
6.9
7.8
8.2

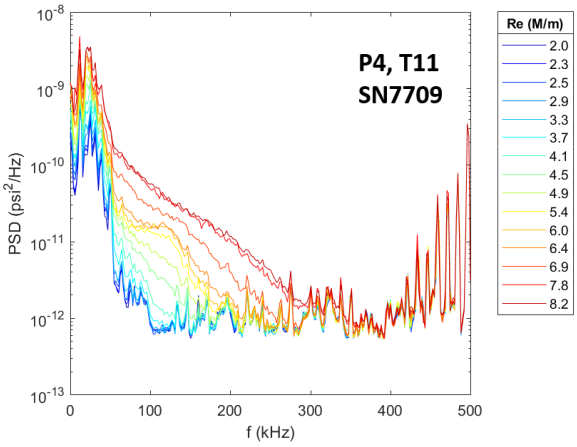
P4, T11
SN7709
PSD (psi²/Hz)
f (kHz)
Re (M/m)
2.0
2.3
2.5
2.9
3.3
3.7
4.1
4.5
4.9
5.4
6.0
6.4
6.9
7.8
8.2

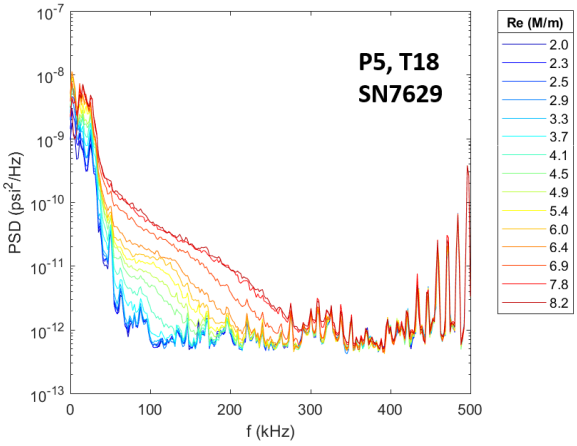
P5, T18
SN7629
PSD (psi²/Hz)
f (kHz)
Re (M/m)
2.0
2.3
2.5
2.9
3.3
3.7
4.1
4.5
4.9
5.4
6.0
6.4
6.9
7.8
8.2

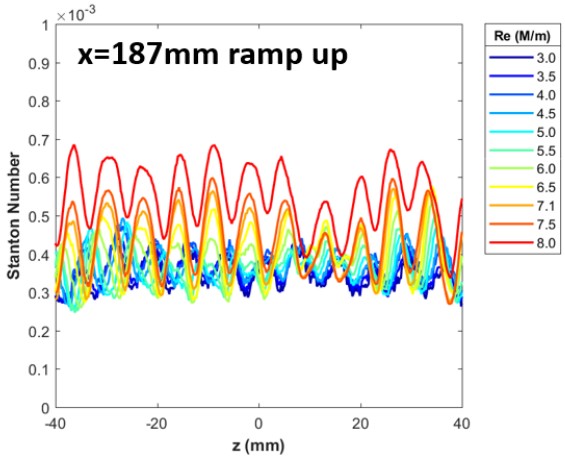
x=187mm ramp up
Stanton Number
z (mm)
Re (M/m)
3.0
3.5
4.0
4.5
5.0
5.5
6.0
6.5
7.1
7.5
8.0

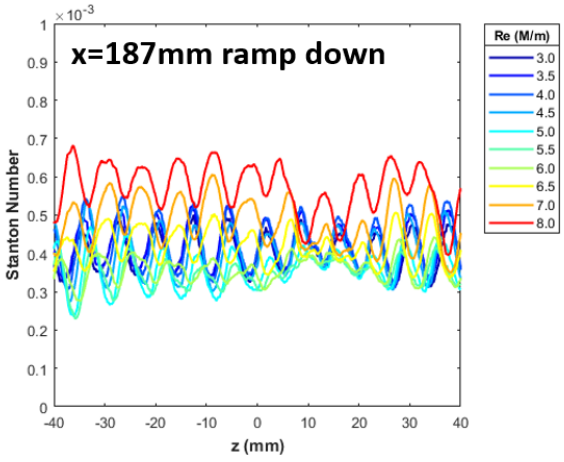
x=187mm ramp down
Stanton Number
z (mm)
Re (M/m)
3.0
3.5
4.0
4.5
5.0
5.5
6.0
6.5
7.0
8.0

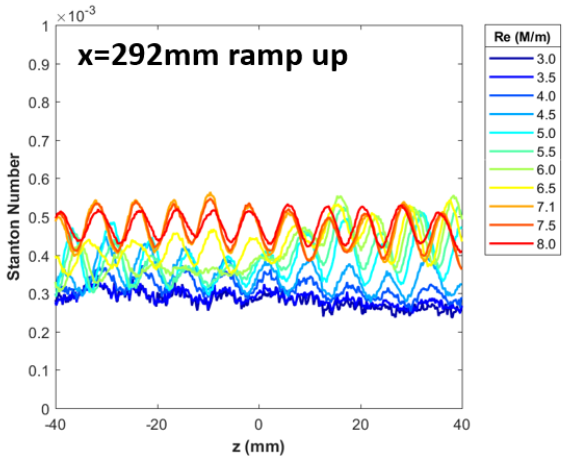

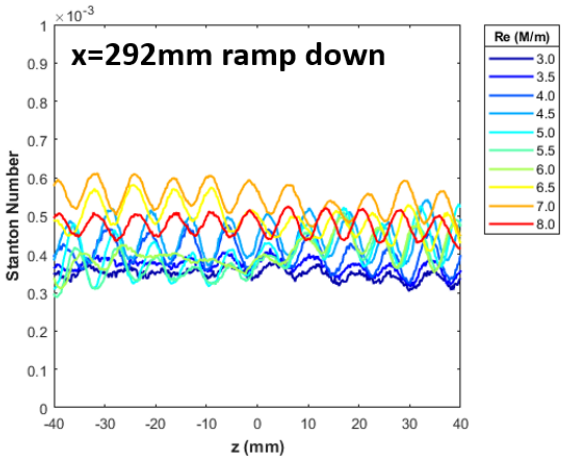

Run 3392

Surface pressure measurements and IR thermography made over Re steps.

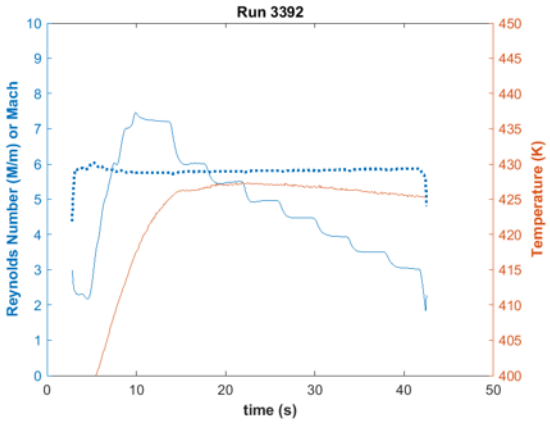

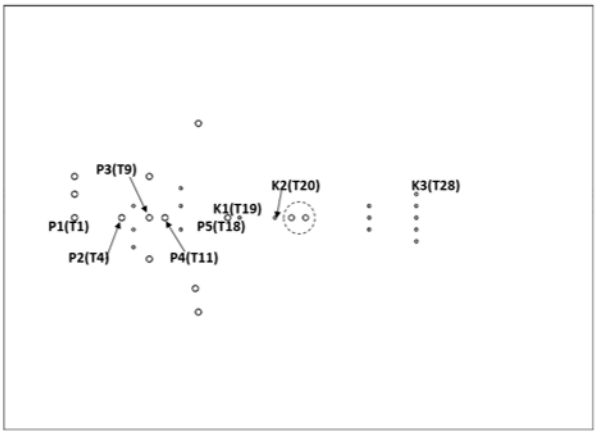

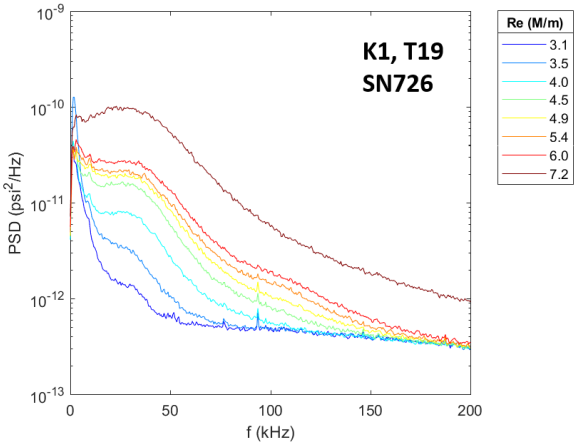

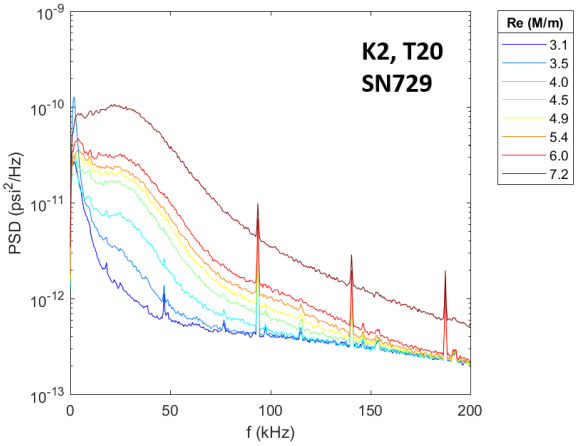

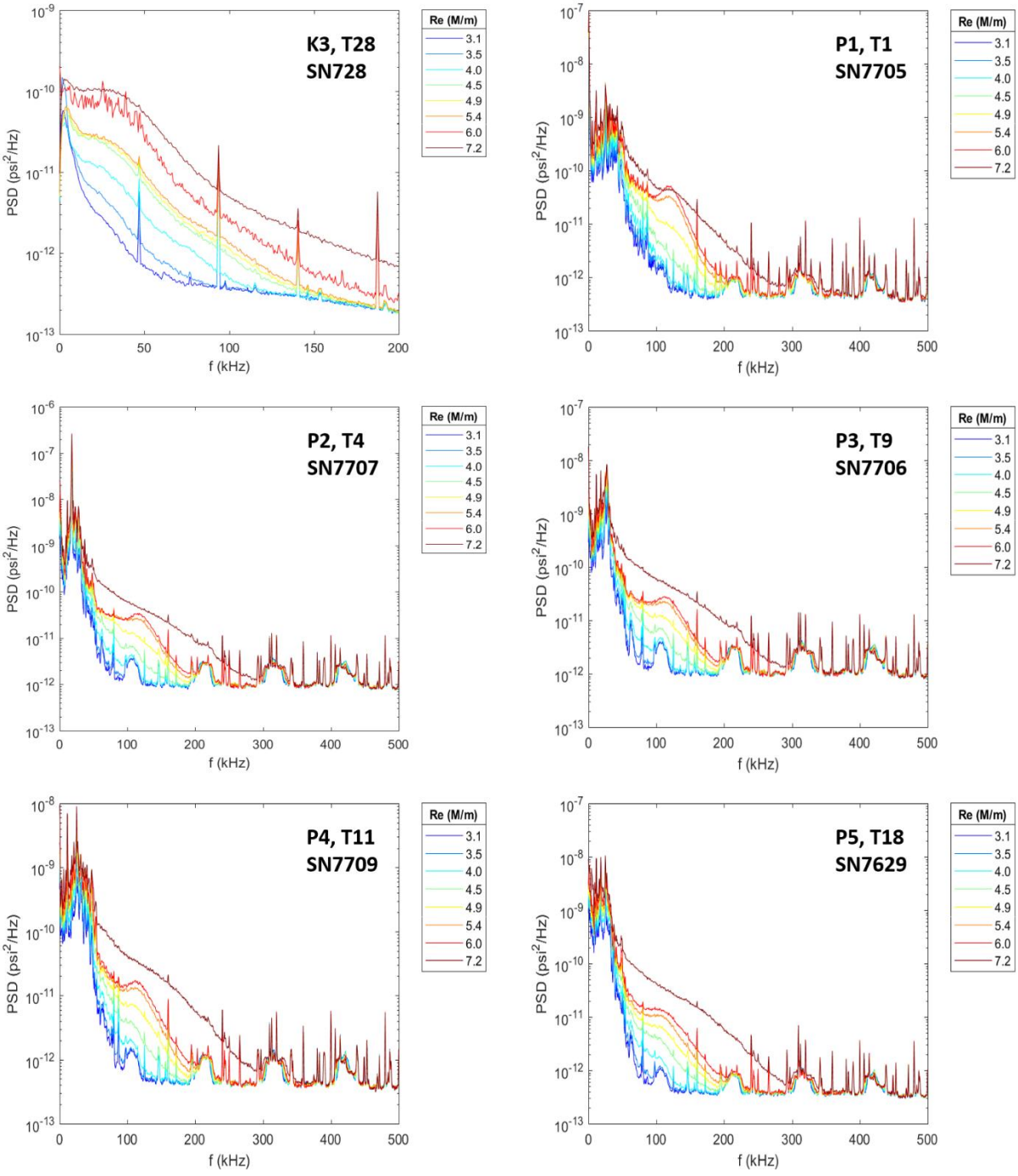
K3, T28
SN728
P1, T1
SN7705
P2, T4
SN7707
P3, T9
SN7706
P4, T11
SN7709
P5, T18
SN7629
PSD (psi²/Hz)
f (kHz)
Re (M/m)
3.1
3.5
4.0
4.5
4.9
5.4
6.0
7.2

Run 3393

Surface pressure measurements and IR thermography made over a Re sweep.

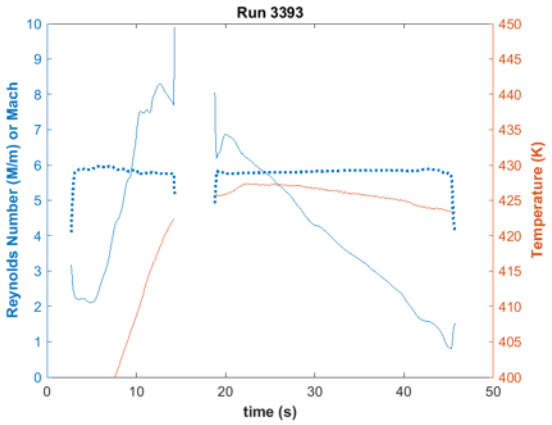

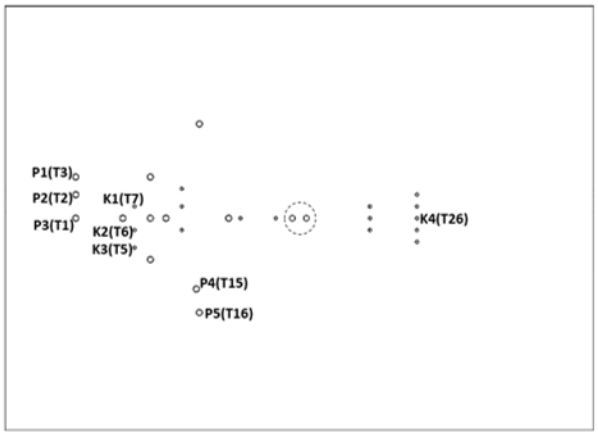

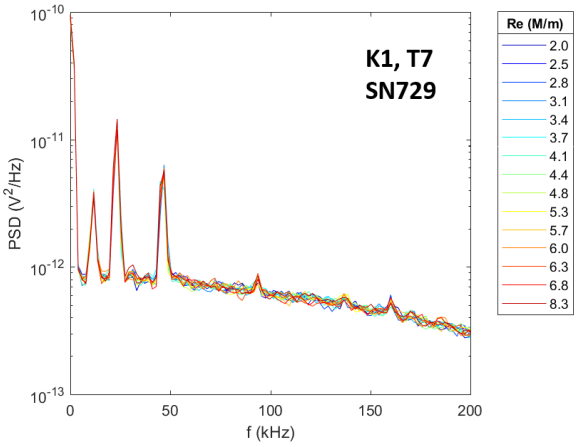

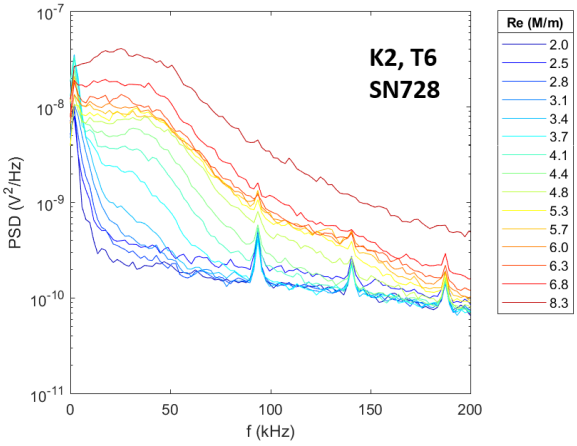

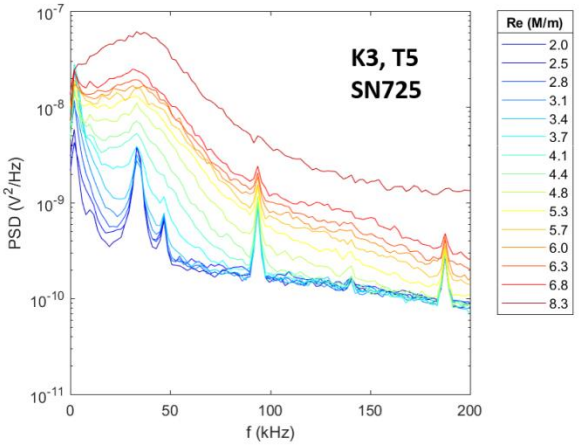

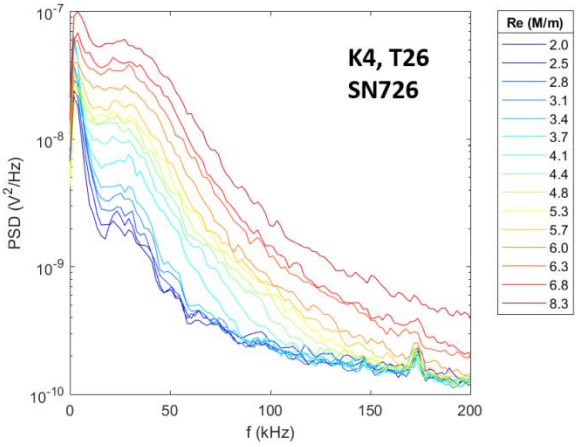

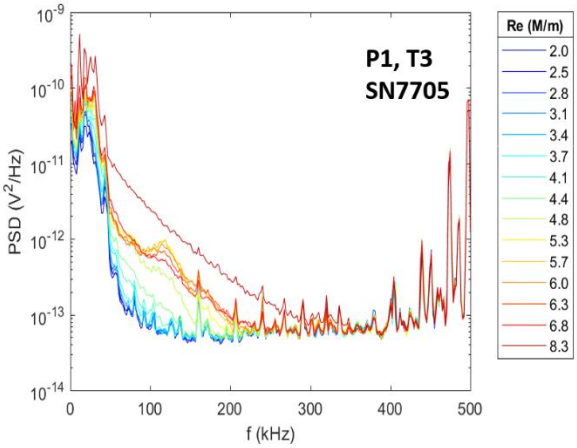
P1, T3
SN7705
PSD (V²/Hz)
f (kHz)
Re (M/m)
2.0
2.5
2.8
3.1
3.4
3.7
4.1
4.4
4.8
5.3
5.7
6.0
6.3
6.8
8.3

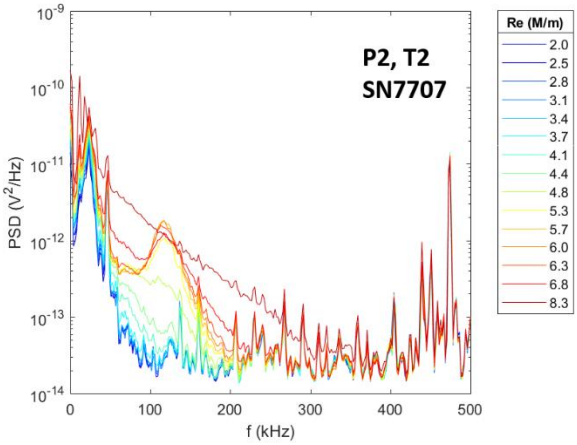
P2, T2
SN7707
PSD (V²/Hz)
f (kHz)
Re (M/m)
2.0
2.5
2.8
3.1
3.4
3.7
4.1
4.4
4.8
5.3
5.7
6.0
6.3
6.8
8.3

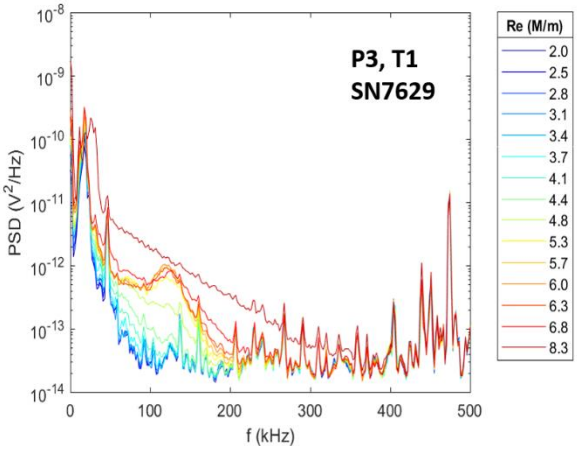
P3, T1
SN7629
PSD (V²/Hz)
f (kHz)
Re (M/m)
2.0
2.5
2.8
3.1
3.4
3.7
4.1
4.4
4.8
5.3
5.7
6.0
6.3
6.8
8.3

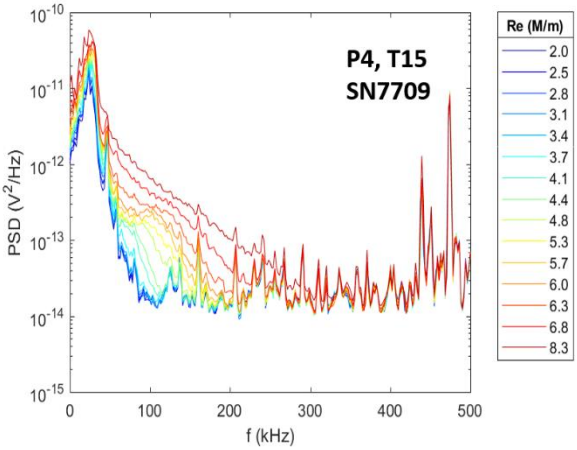
P4, T15
SN7709
PSD (V²/Hz)
f (kHz)
Re (M/m)
2.0
2.5
2.8
3.1
3.4
3.7
4.1
4.4
4.8
5.3
5.7
6.0
6.3
6.8
8.3

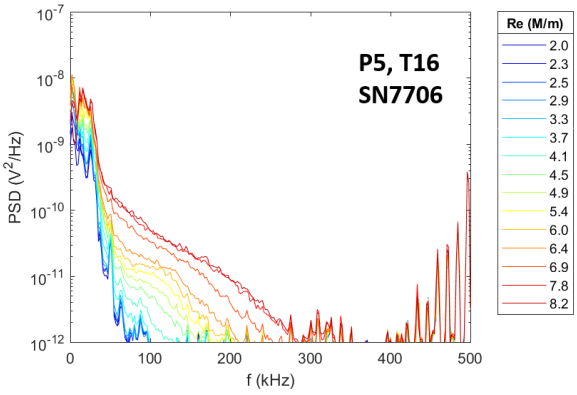
P5, T16
SN7706
PSD (V²/Hz)
f (kHz)
Re (M/m)
2.0
2.3
2.5
2.9
3.3
3.7
4.1
4.5
4.9
5.4
6.0
6.4
6.9
7.8
8.2

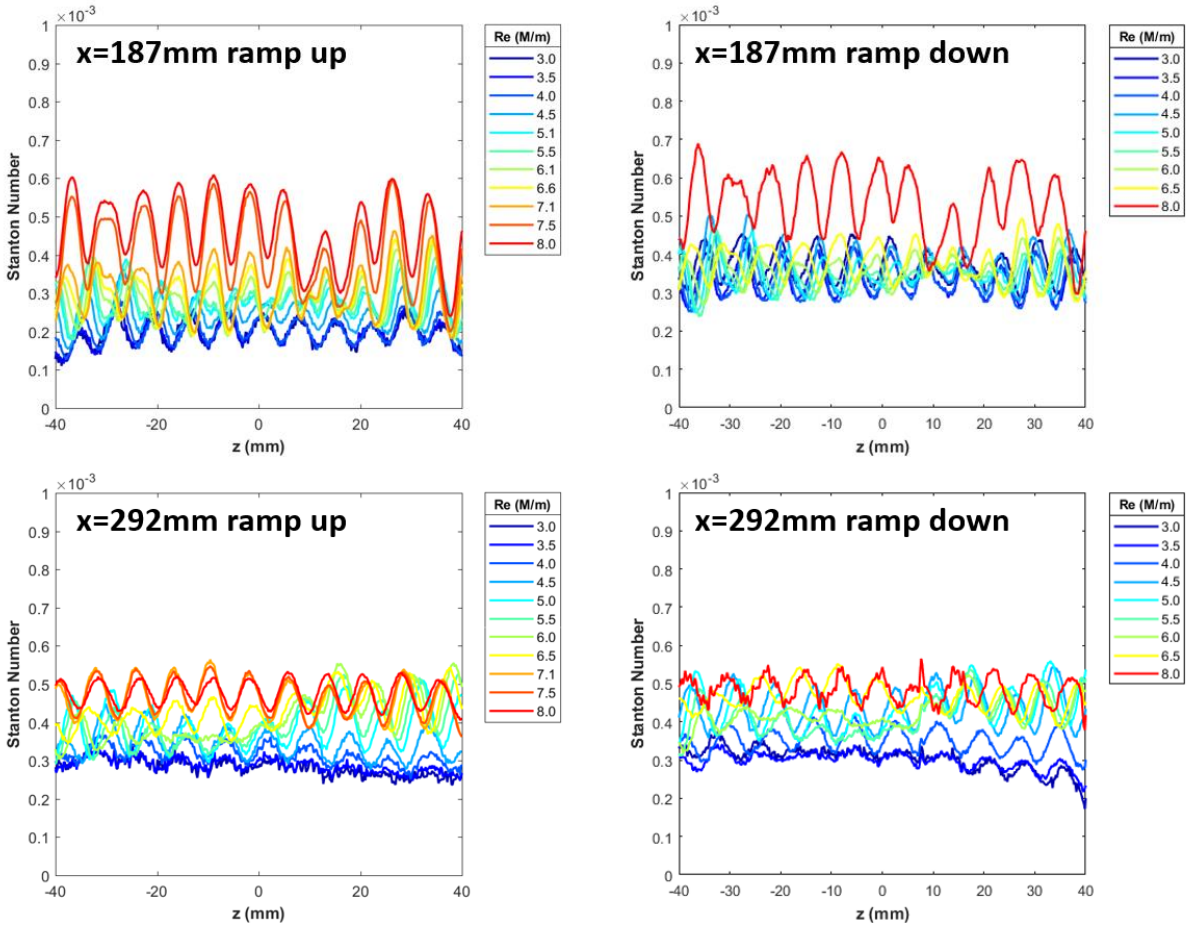

Run 3394

Surface pressure measurements and IR thermography made over Re steps.

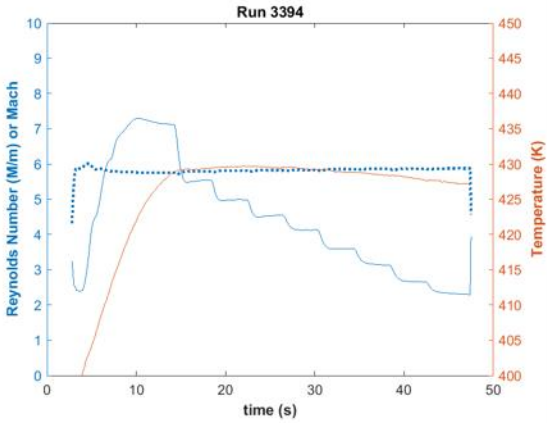

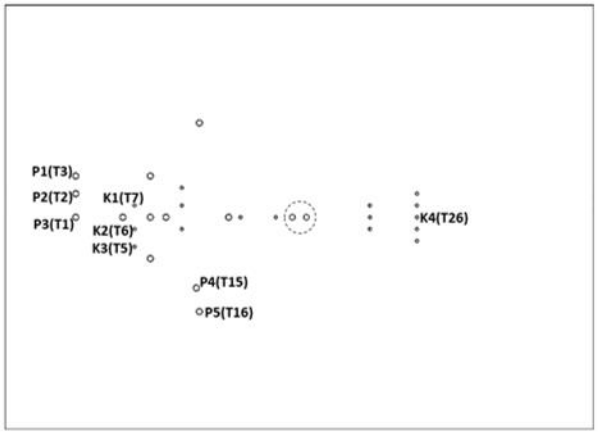

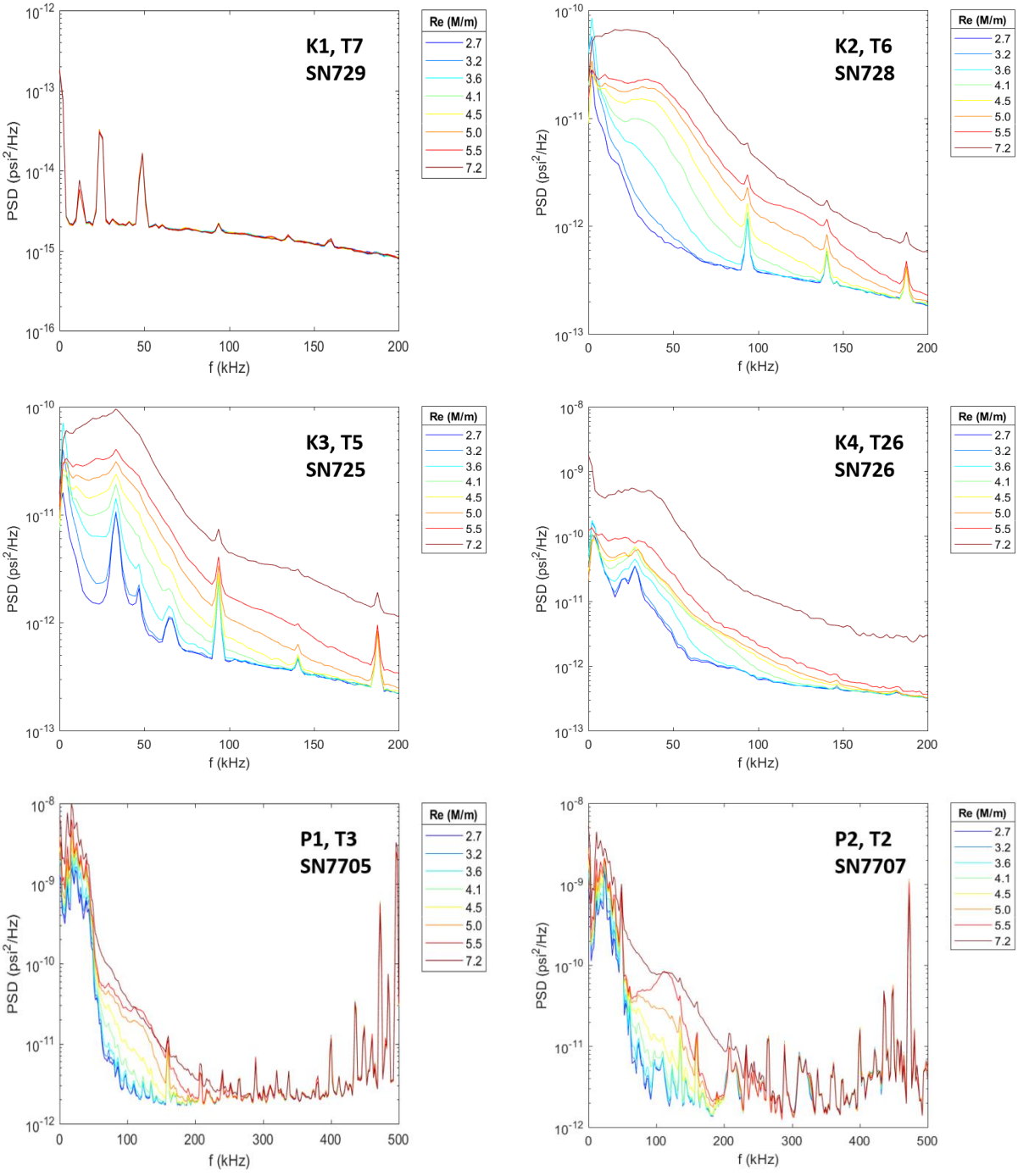
K1, T7
SN729
K2, T6
SN728
K3, T5
SN725
K4, T26
SN726
P1, T3
SN7705
P2, T2
SN7707
PSD (psi²/Hz)
f (kHz)
Re (M/m)
2.7
3.2
3.6
4.1
4.5
5.0
5.5
7.2

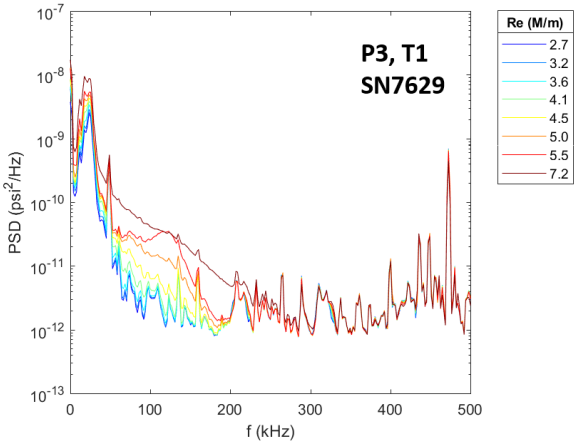
P3, T1
SN7629
PSD (psi²/Hz)
f (kHz)
Re (M/m)
2.7
3.2
3.6
4.1
4.5
5.0
5.5
7.2

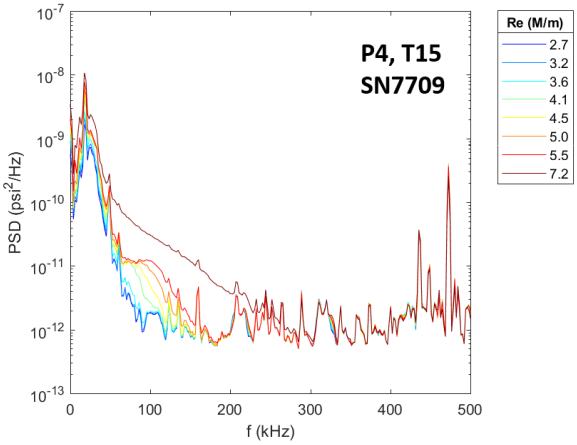
P4, T15
SN7709
PSD (psi²/Hz)
f (kHz)
Re (M/m)
2.7
3.2
3.6
4.1
4.5
5.0
5.5
7.2

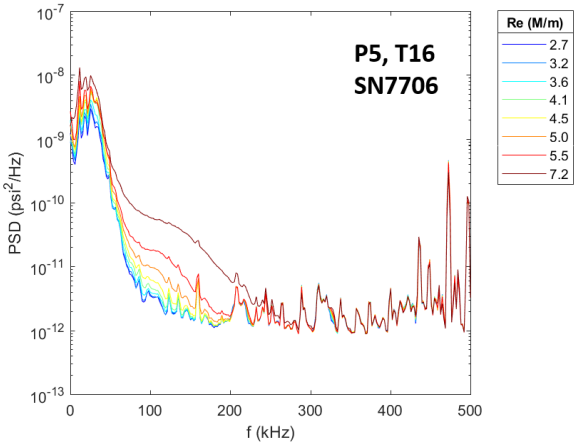
P5, T16
SN7706
PSD (psi²/Hz)
f (kHz)
Re (M/m)
2.7
3.2
3.6
4.1
4.5
5.0
5.5
7.2

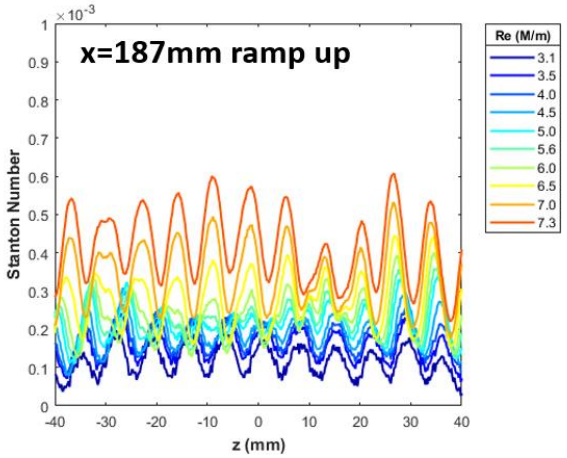
x=187mm ramp up
Stanton Number
z (mm)
Re (M/m)
3.1
3.5
4.0
4.5
5.0
5.6
6.0
6.5
7.0
7.3

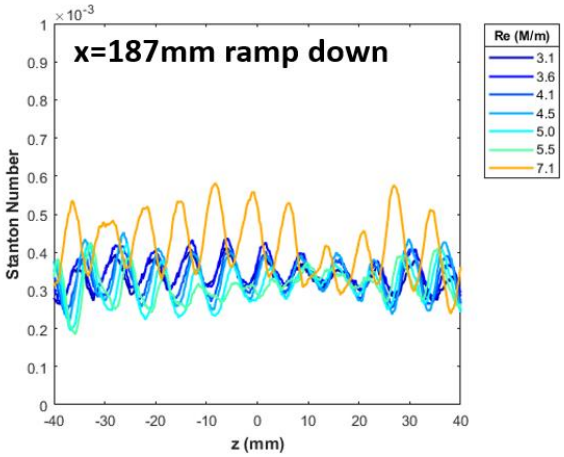
x=187mm ramp down
Stanton Number
z (mm)
Re (M/m)
3.1
3.6
4.1
4.5
5.0
5.5
7.1

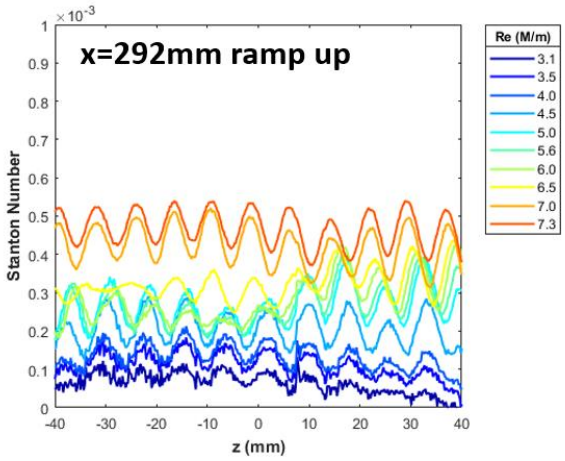

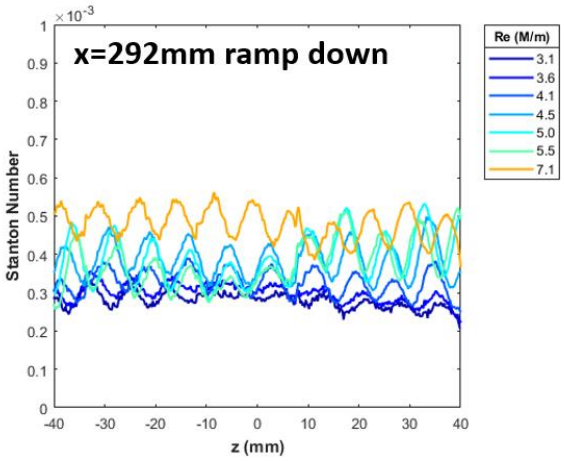

Run 3395

Surface pressure measurements and IR thermography made over a Re sweep.

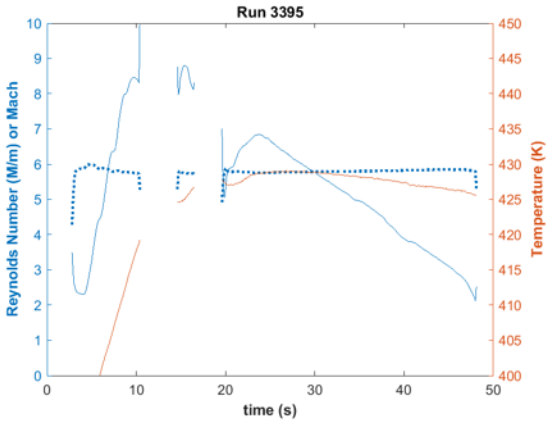

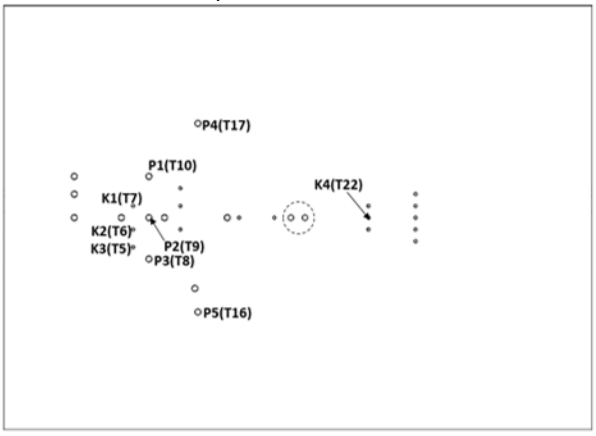

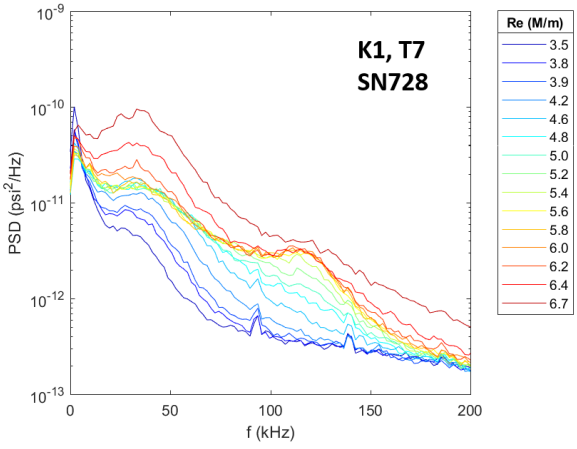

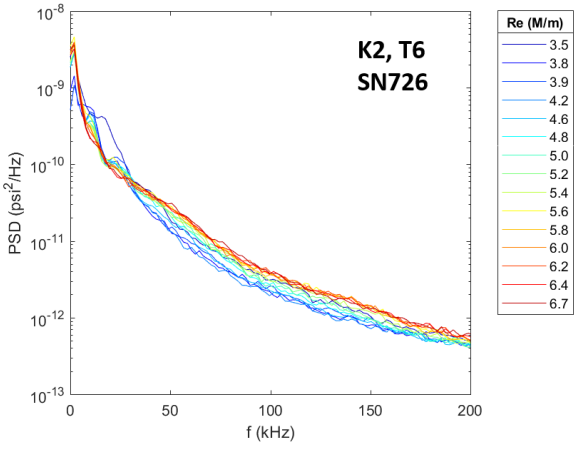

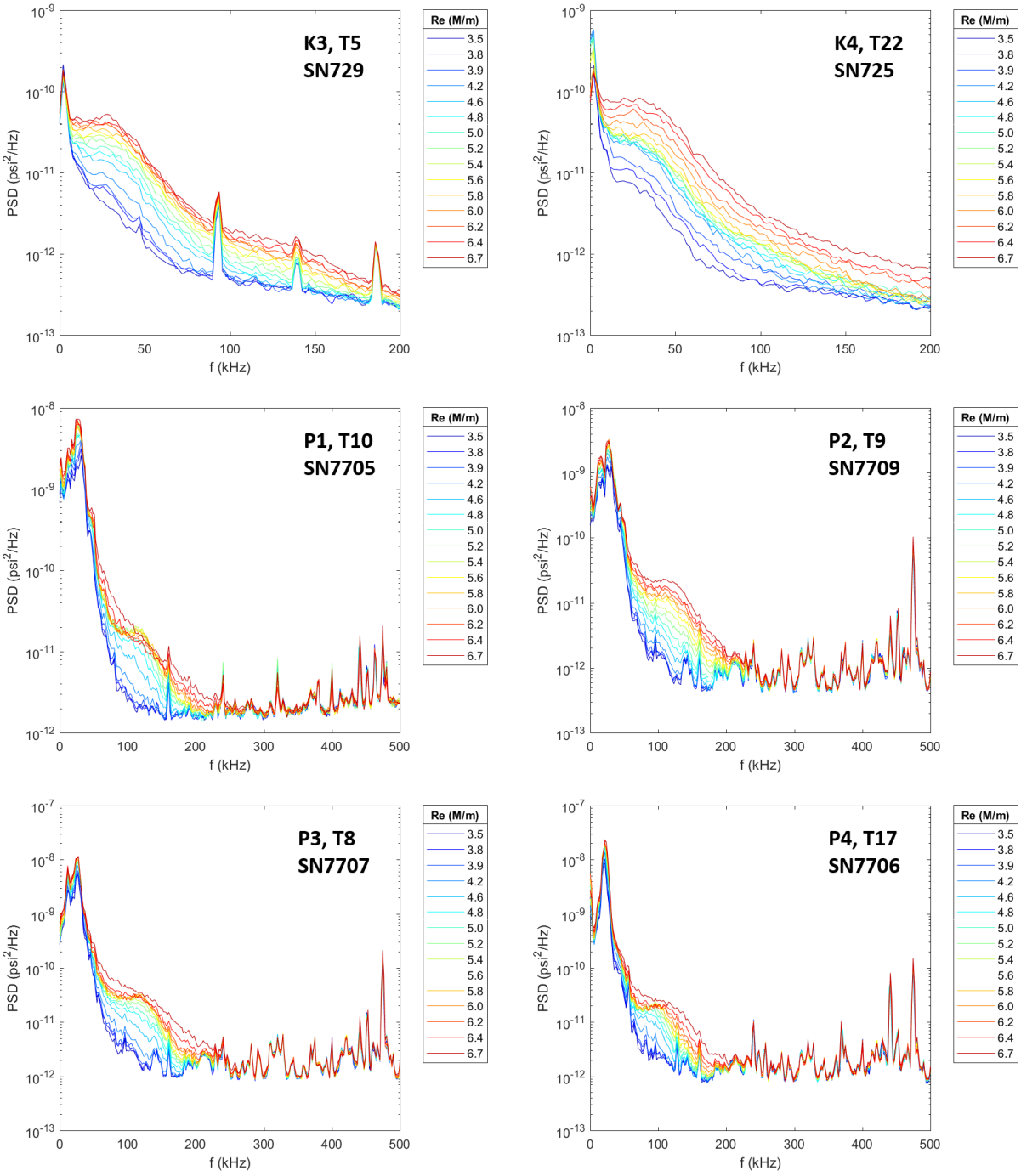
K3, T5
SN729
K4, T22
SN725
P1, T10
SN7705
P2, T9
SN7709
P3, T8
SN7707
P4, T17
SN7706
PSD (psi²/Hz)
f (kHz)
Re (M/m)
3.5
3.8
3.9
4.2
4.6
4.8
5.0
5.2
5.4
5.6
5.8
6.0
6.2
6.4
6.7

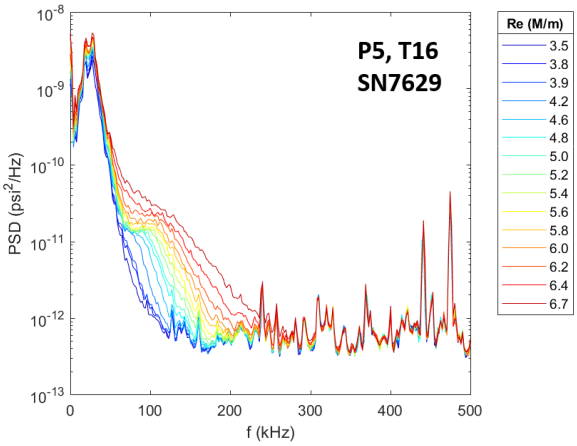

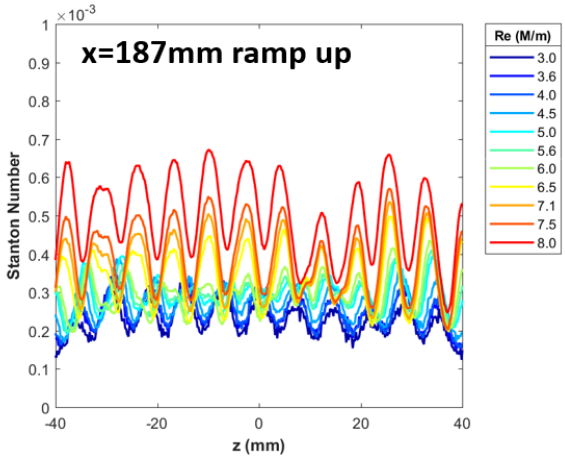

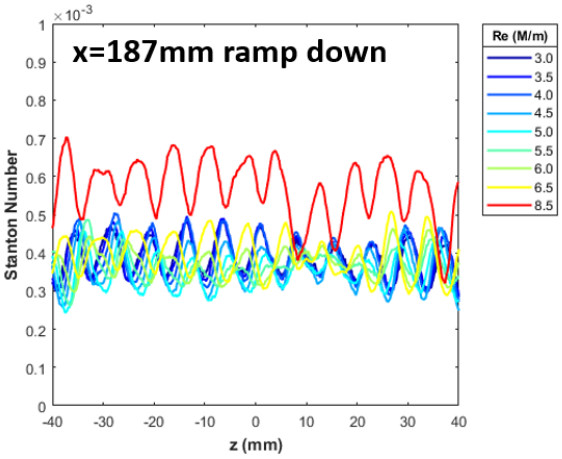

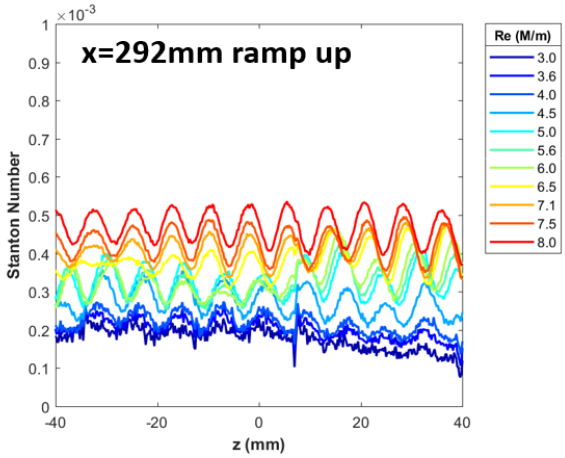

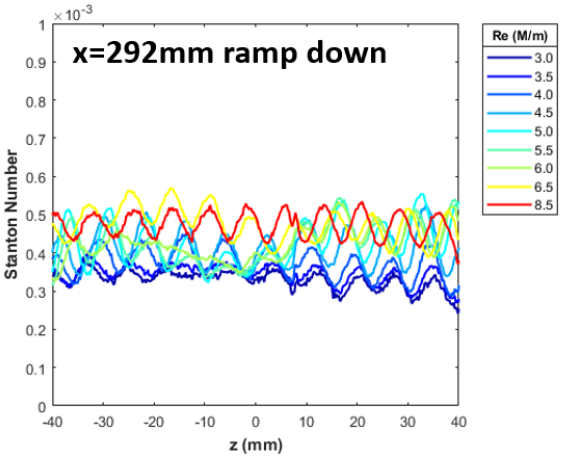

Run 3396. Not a run. Tunnel supply ball valve error.

Run 3397

Surface pressure measurements and IR thermography made over a Re sweep.

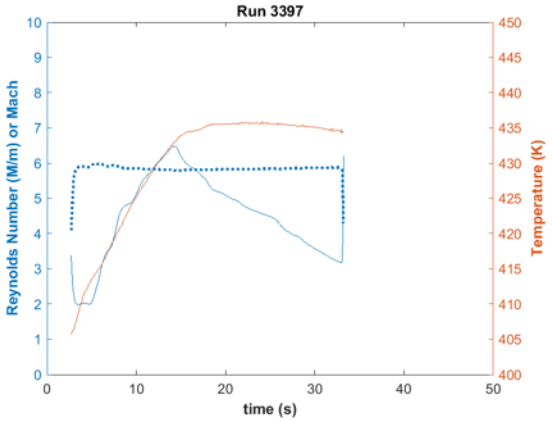

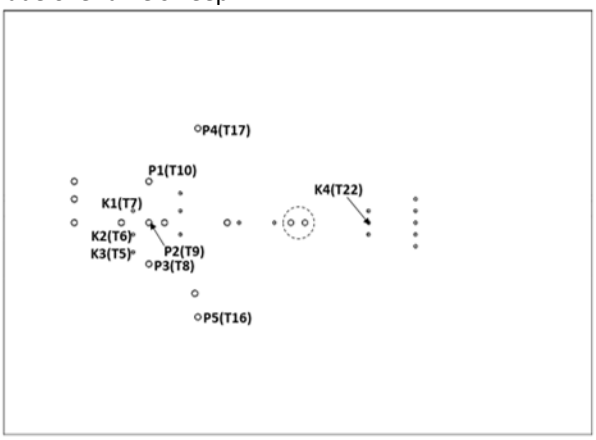

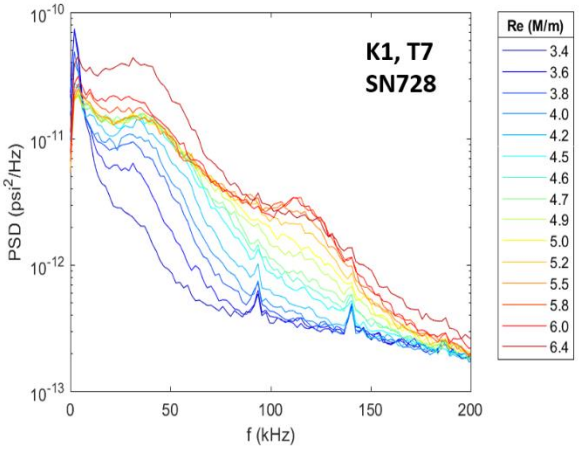

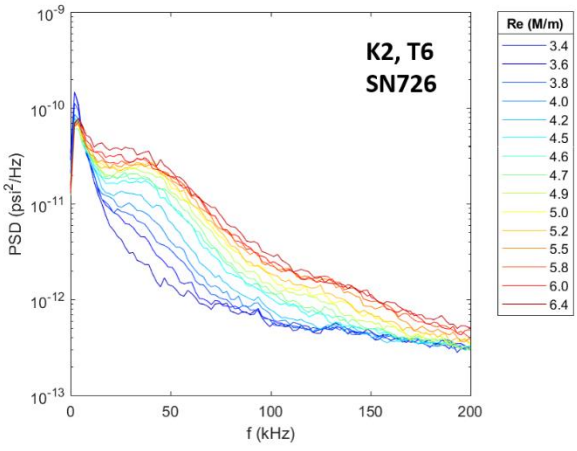

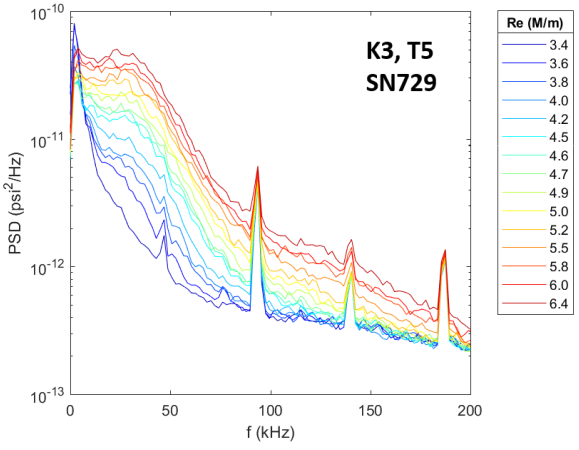

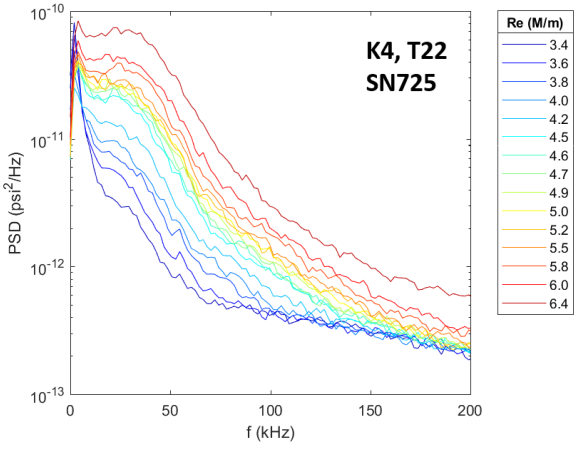

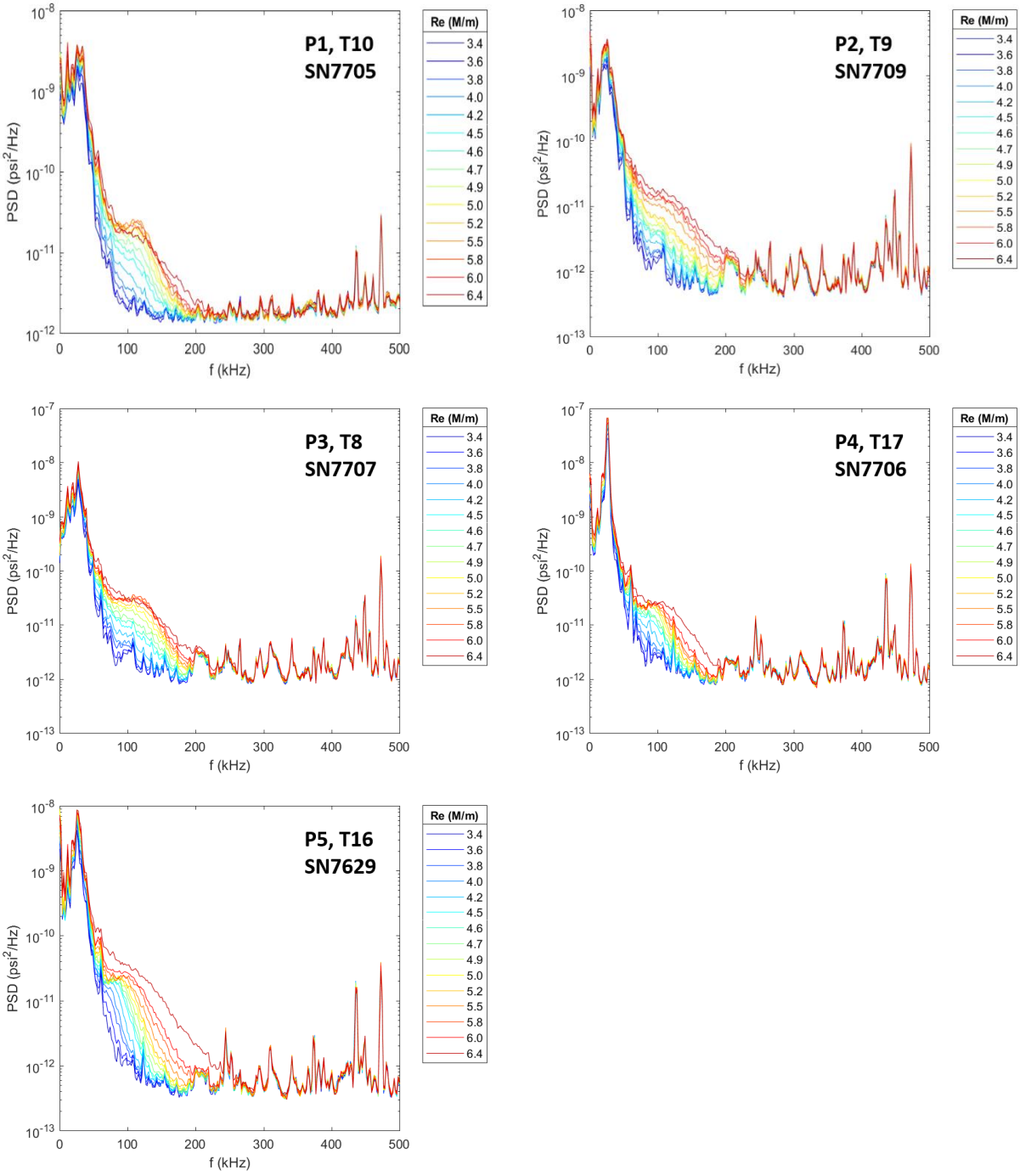
P1, T10
SN7705
P2, T9
SN7709
P3, T8
SN7707
P4, T17
SN7706
P5, T16
SN7629
PSD (psi²/Hz)
f (kHz)
Re (M/m)
3.4
3.6
3.8
4.0
4.2
4.5
4.6
4.7
4.9
5.0
5.2
5.5
5.8
6.0
6.4

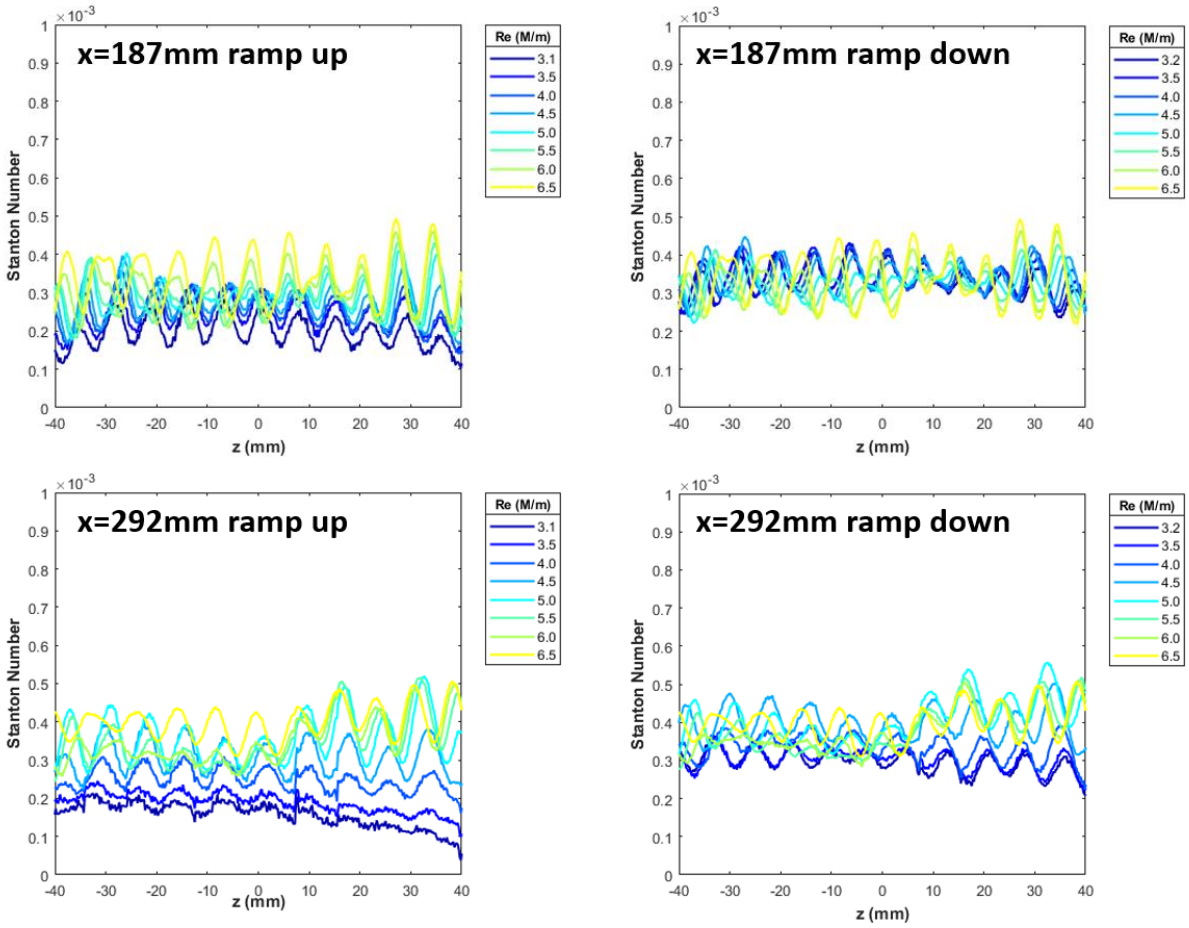

Run 3398

Surface pressure measurements and IR thermography made over a Re sweep.

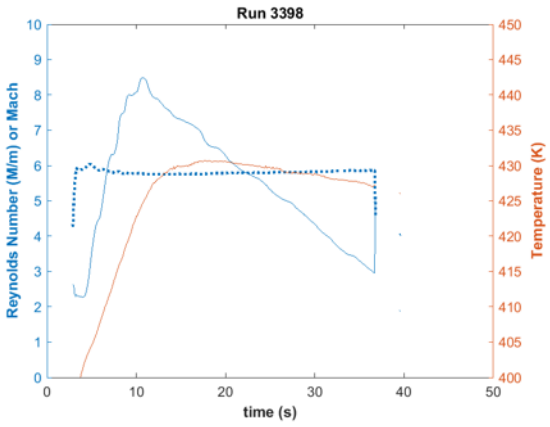

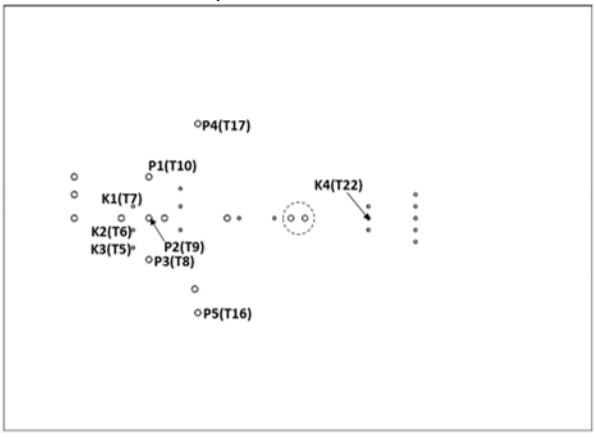

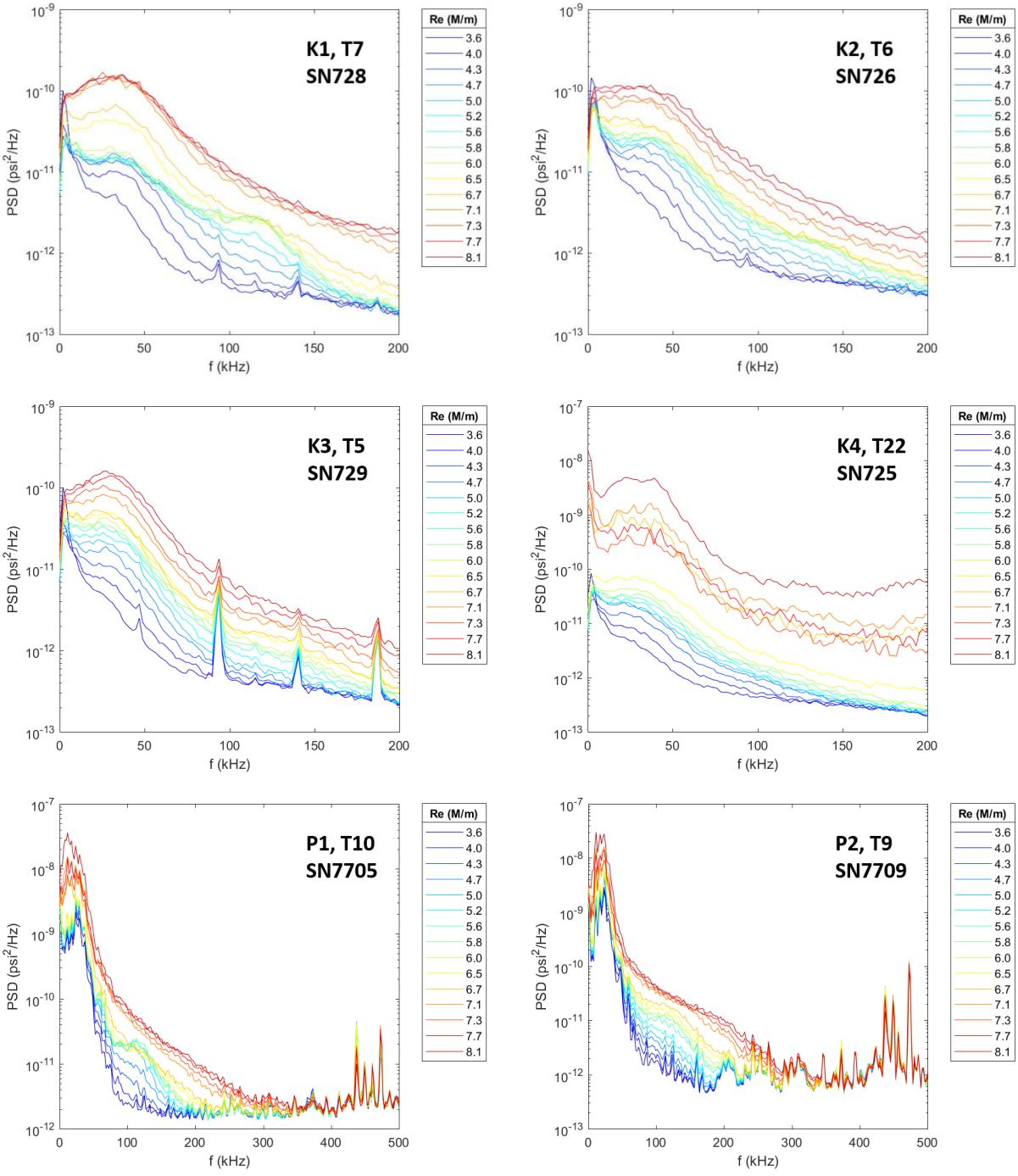
K1, T7
SN728
K2, T6
SN726
K3, T5
SN729
K4, T22
SN725
P1, T10
SN7705
P2, T9
SN7709
PSD (psi²/Hz)
f (kHz)
Re (M/m)
3.6
4.0
4.3
4.7
5.0
5.2
5.6
5.8
6.0
6.5
6.7
7.1
7.3
7.7
8.1

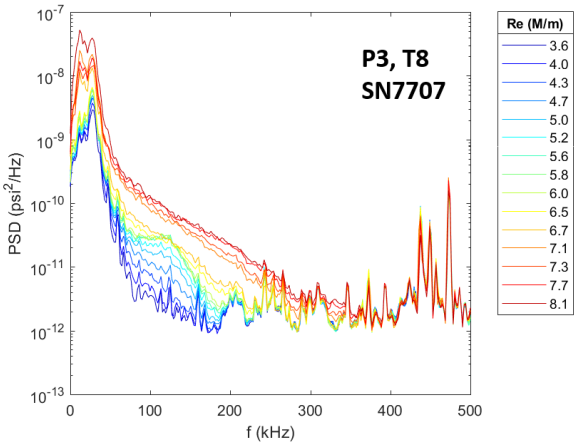
P3, T8
SN7707
PSD (psi²/Hz)
f (kHz)
Re (M/m)
3.6
4.0
4.3
4.7
5.0
5.2
5.6
5.8
6.0
6.5
6.7
7.1
7.3
7.7
8.1

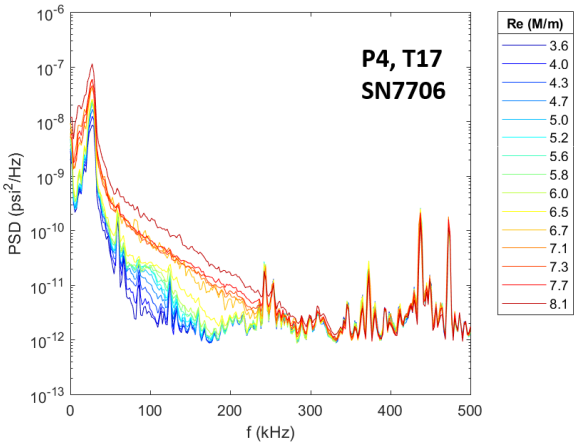
P4, T17
SN7706
PSD (psi²/Hz)
f (kHz)
Re (M/m)
3.6
4.0
4.3
4.7
5.0
5.2
5.6
5.8
6.0
6.5
6.7
7.1
7.3
7.7
8.1

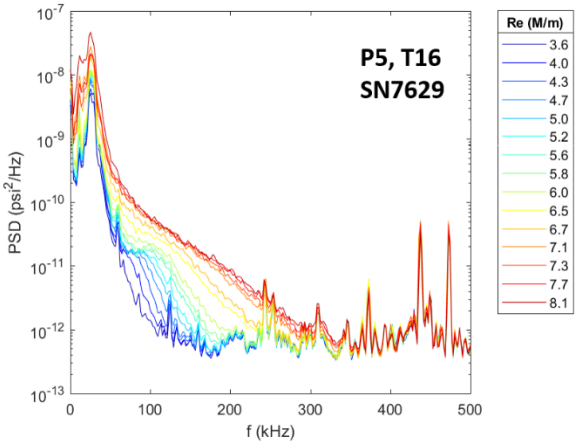
P5, T16
SN7629
PSD (psi²/Hz)
f (kHz)
Re (M/m)
3.6
4.0
4.3
4.7
5.0
5.2
5.6
5.8
6.0
6.5
6.7
7.1
7.3
7.7
8.1

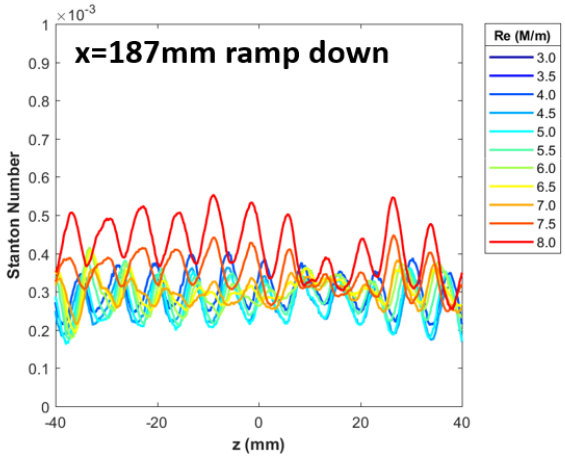
x=187mm ramp down
Stanton Number
z (mm)
Re (M/m)
3.0
3.5
4.0
4.5
5.0
5.5
6.0
6.5
7.0
7.5
8.0

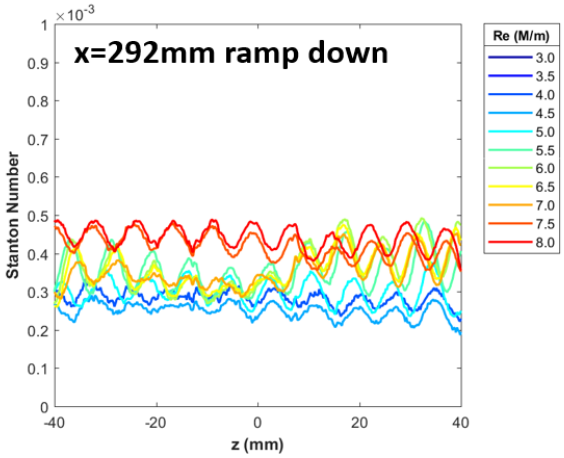
x=292mm ramp down
Stanton Number
z (mm)
Re (M/m)
3.0
3.5
4.0
4.5
5.0
5.5
6.0
6.5
7.0
7.5
8.0

Run 3399

Surface pressure measurements and IR thermography made over a Re sweep. Accidentally sampled transducers for 1s instead of 0.1s. Not a good looking run.

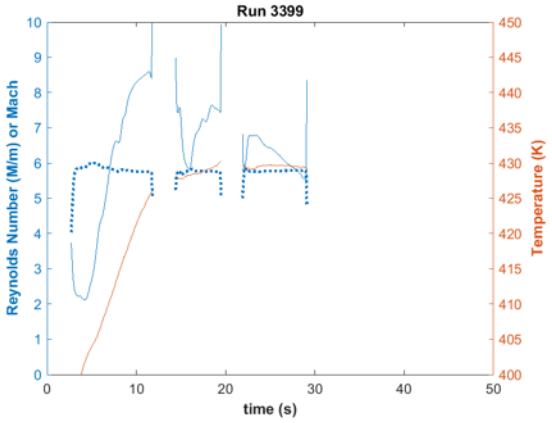

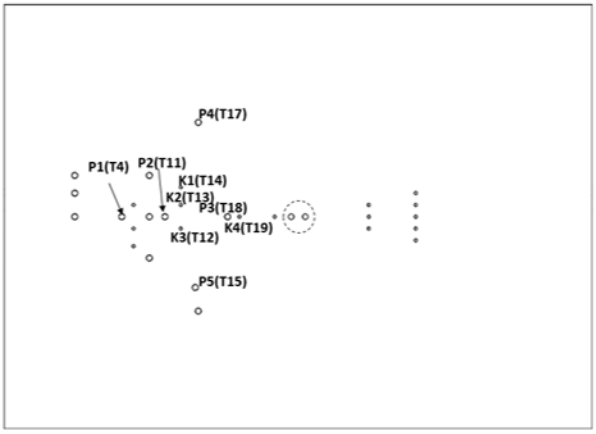

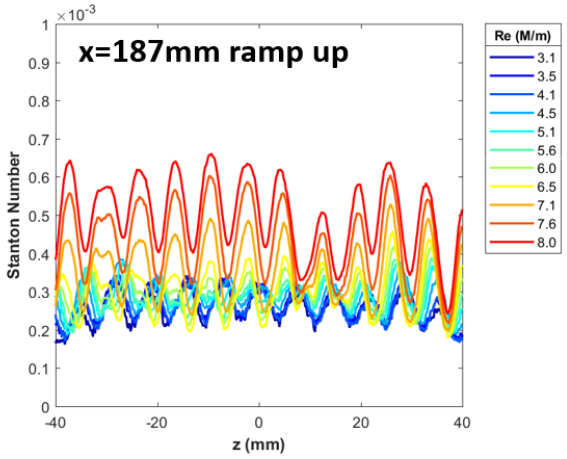

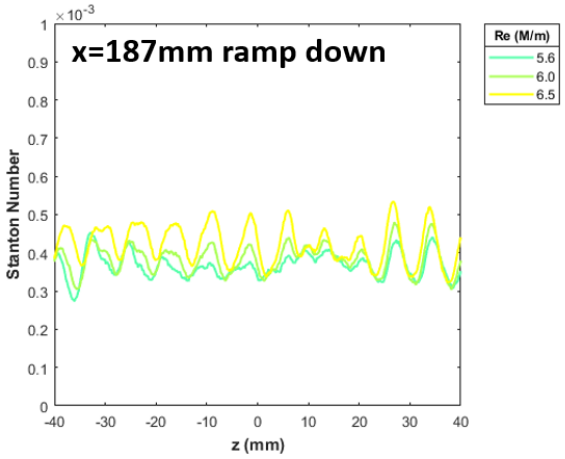

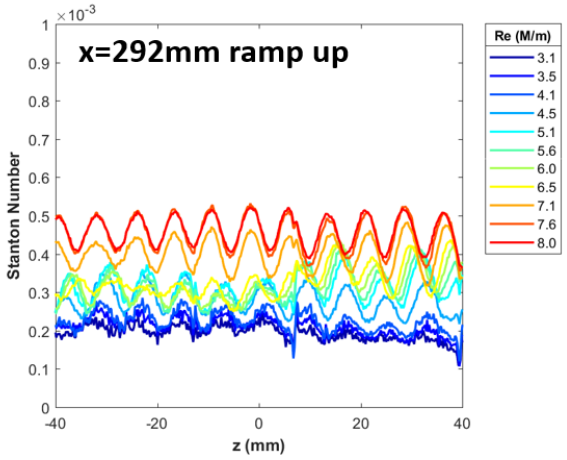

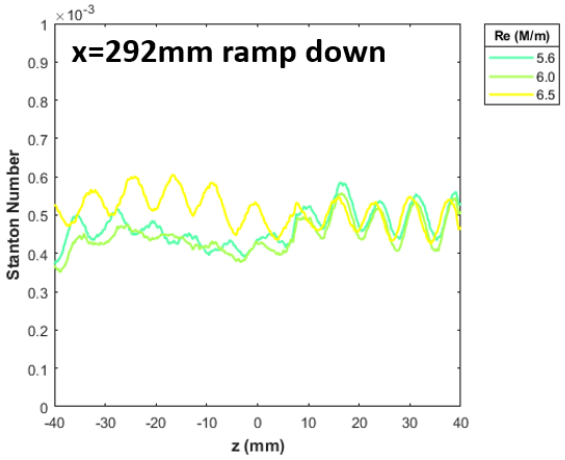

Run 3400

Surface pressure measurements and IR thermography made over a Re sweep.

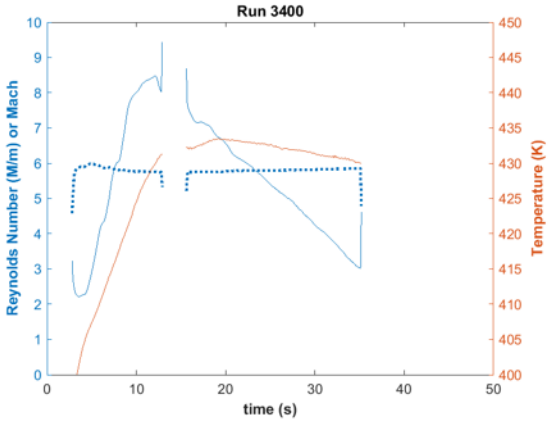

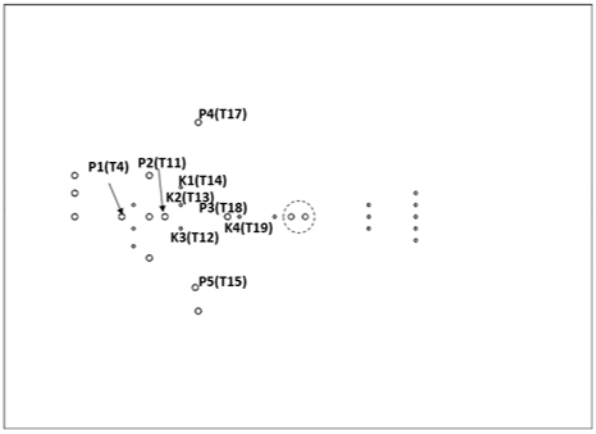

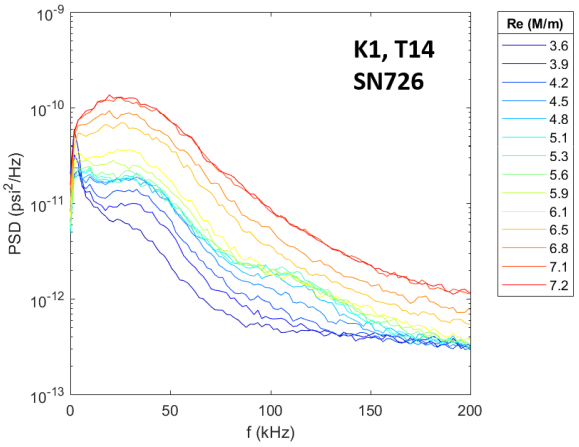

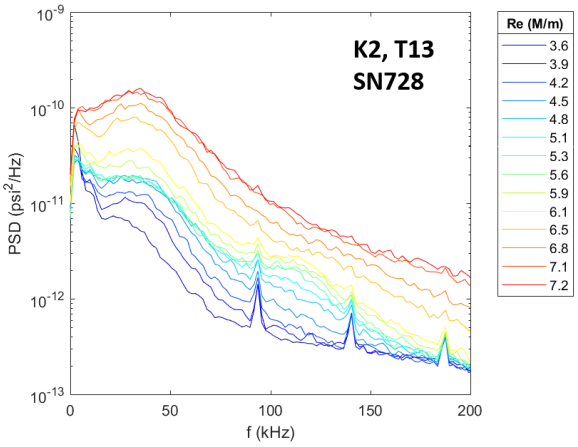

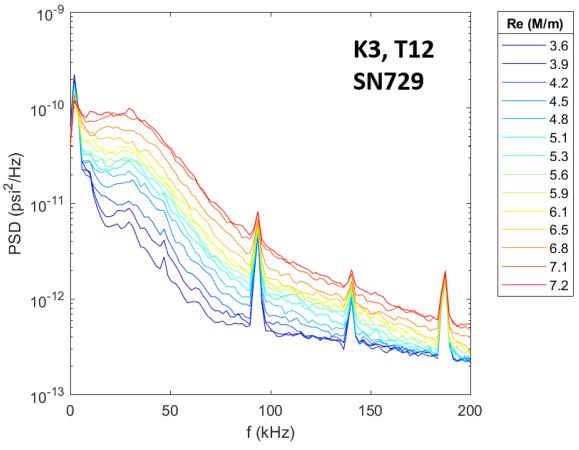

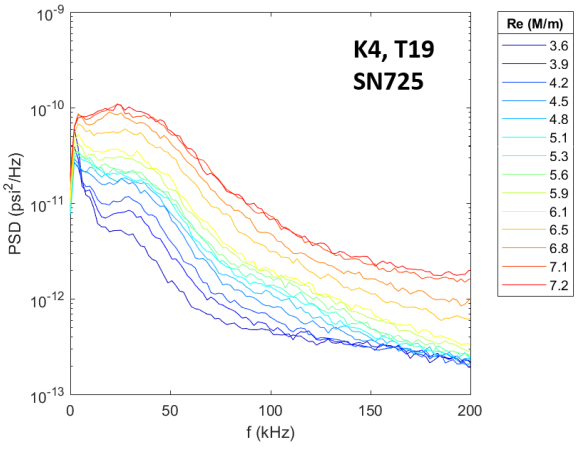

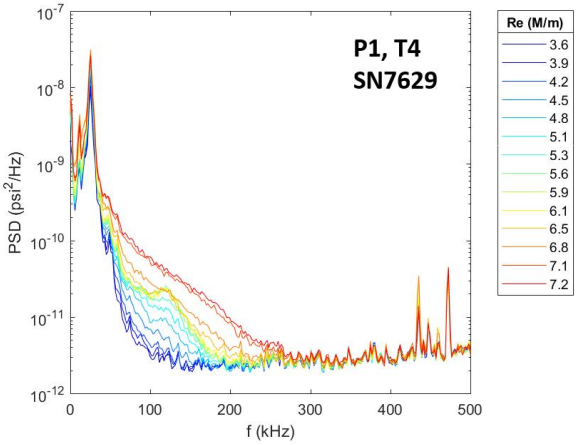
P1, T4
SN7629
PSD (psi²/Hz)
f (kHz)
Re (M/m)
3.6
3.9
4.2
4.5
4.8
5.1
5.3
5.6
5.9
6.1
6.5
6.8
7.1
7.2

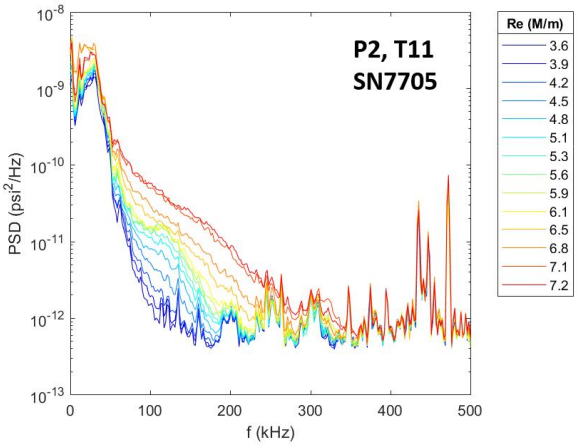
P2, T11
SN7705
PSD (psi²/Hz)
f (kHz)
Re (M/m)
3.6
3.9
4.2
4.5
4.8
5.1
5.3
5.6
5.9
6.1
6.5
6.8
7.1
7.2

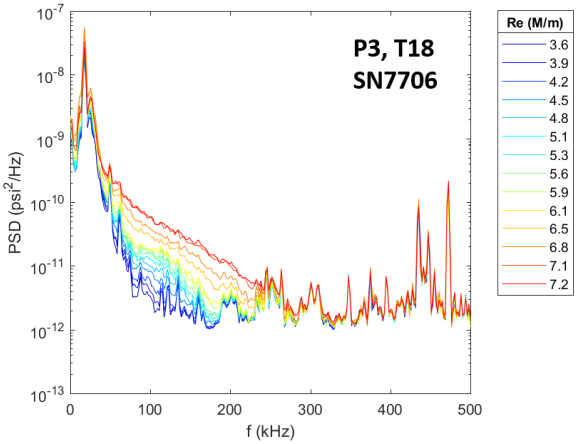
P3, T18
SN7706
PSD (psi²/Hz)
f (kHz)
Re (M/m)
3.6
3.9
4.2
4.5
4.8
5.1
5.3
5.6
5.9
6.1
6.5
6.8
7.1
7.2

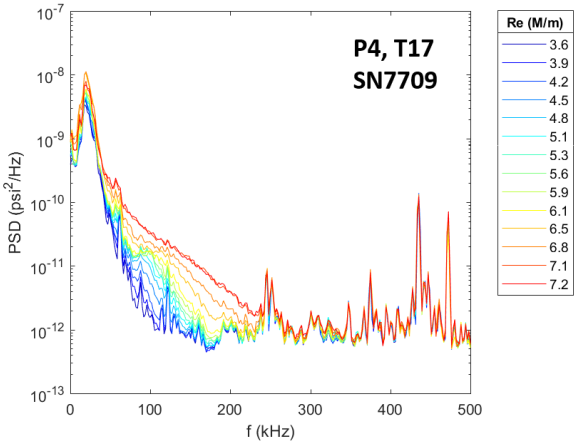
P4, T17
SN7709
PSD (psi²/Hz)
f (kHz)
Re (M/m)
3.6
3.9
4.2
4.5
4.8
5.1
5.3
5.6
5.9
6.1
6.5
6.8
7.1
7.2

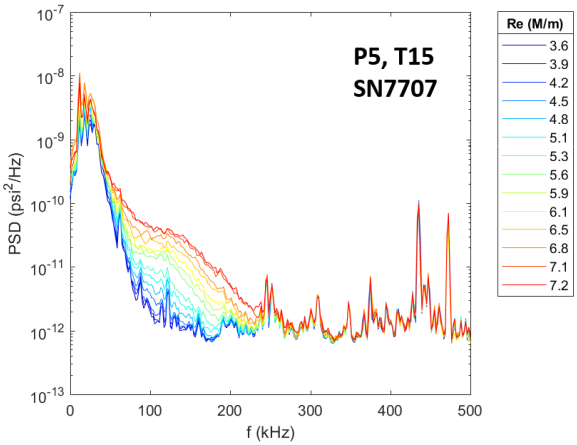
P5, T15
SN7707
PSD (psi²/Hz)
f (kHz)
Re (M/m)
3.6
3.9
4.2
4.5
4.8
5.1
5.3
5.6
5.9
6.1
6.5
6.8
7.1
7.2

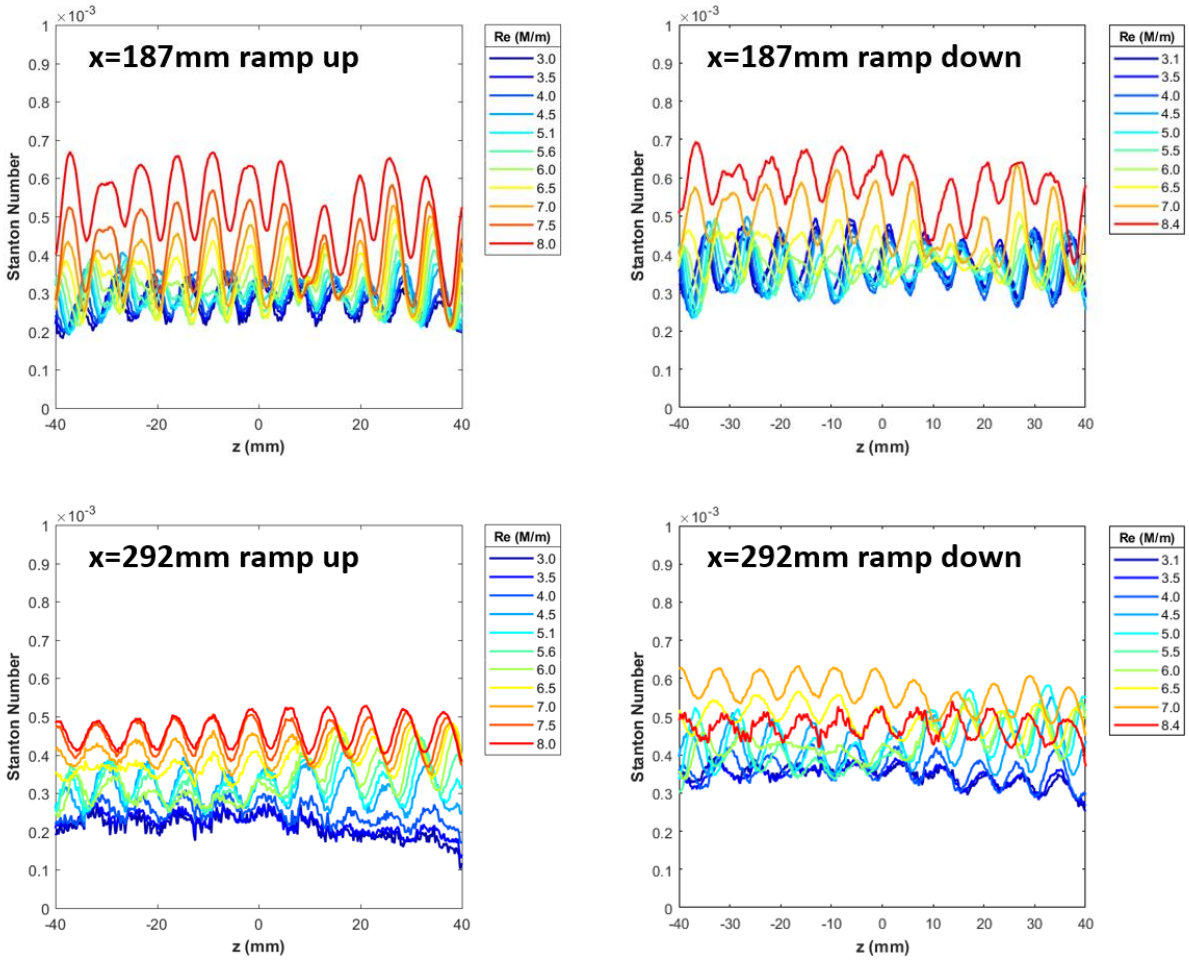

Run 3401

Surface pressure measurements and IR thermography made over Re steps.

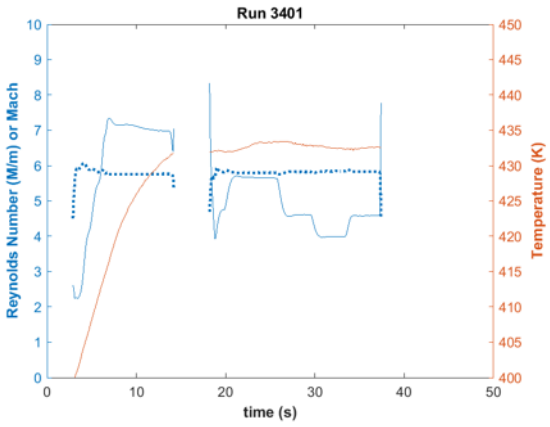

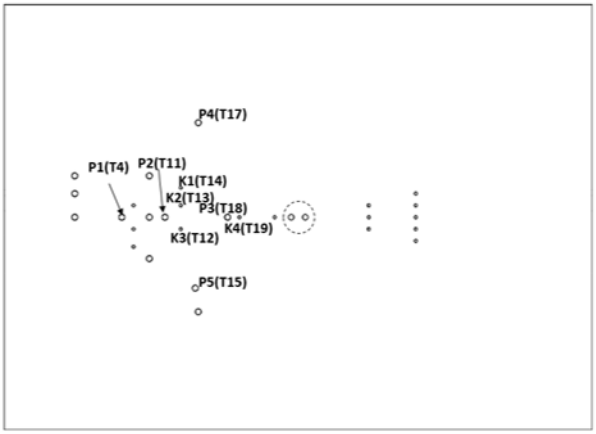

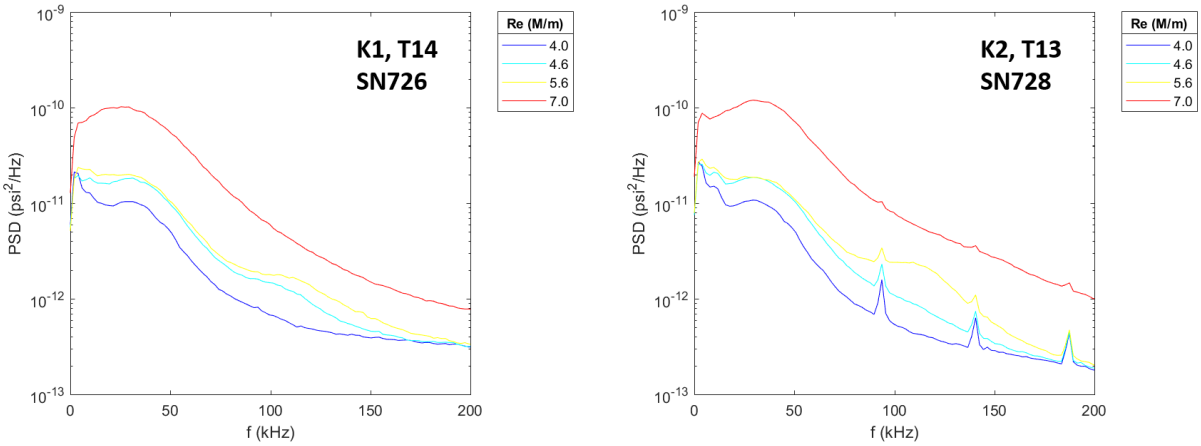
K1, T14
SN726
K2, T13
SN728
Re (M/m)
4.0
4.6
5.6
7.0
PSD (psi²/Hz)
f (kHz)

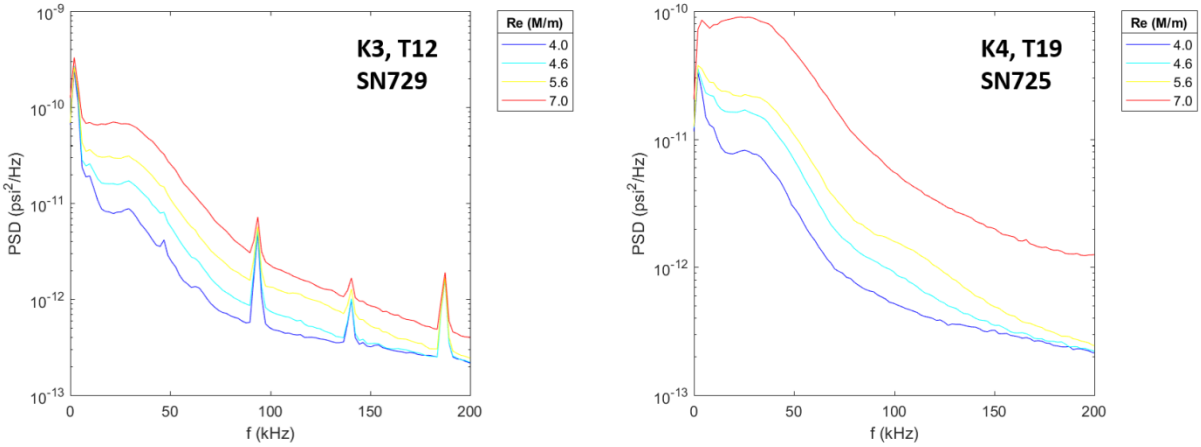
K3, T12
SN729
K4, T19
SN725
Re (M/m)
4.0
4.6
5.6
7.0
PSD (psi²/Hz)
f (kHz)

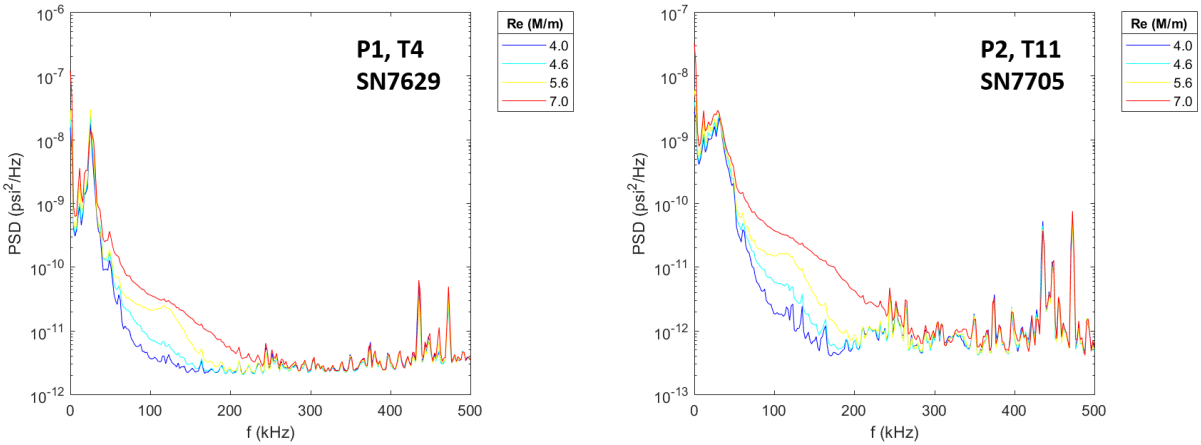
P1, T4
SN7629
P2, T11
SN7705
Re (M/m)
4.0
4.6
5.6
7.0
PSD (psi²/Hz)
f (kHz)

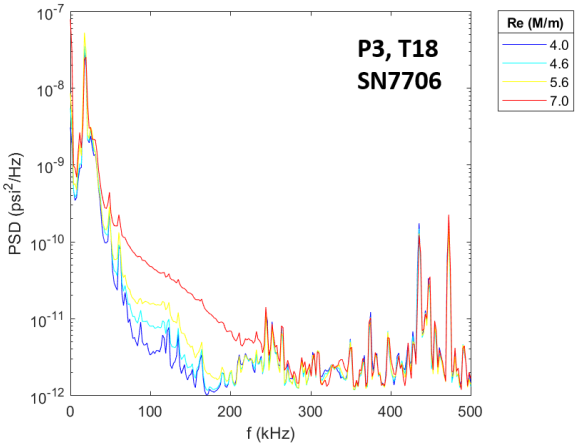
P3, T18
SN7706
Re (M/m)
4.0
4.6
5.6
7.0
PSD (psi²/Hz)
f (kHz)

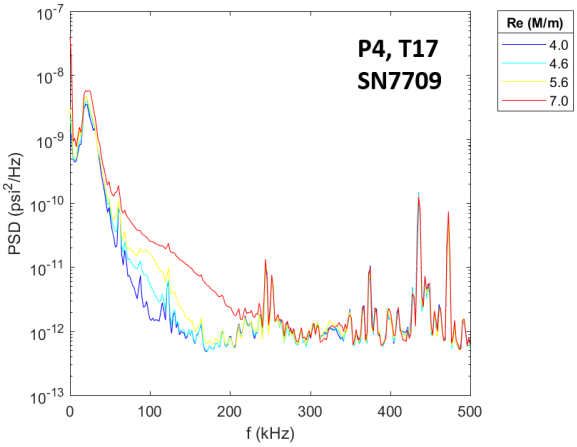
P4, T17
SN7709
Re (M/m)
4.0
4.6
5.6
7.0
PSD (psi²/Hz)
f (kHz)

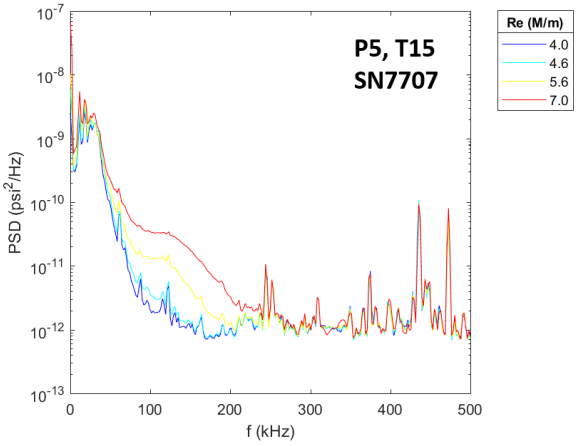
P5, T15
SN7707
Re (M/m)
4.0
4.6
5.6
7.0
PSD (psi²/Hz)
f (kHz)

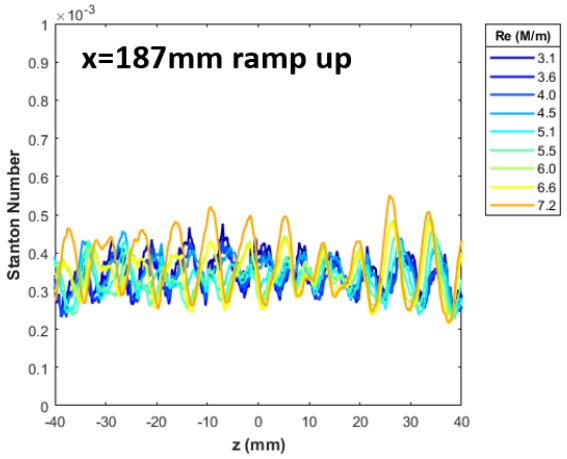
x=187mm ramp up
Re (M/m)
3.1
3.6
4.0
4.5
5.1
5.5
6.0
6.6
7.2
Stanton Number
z (mm)

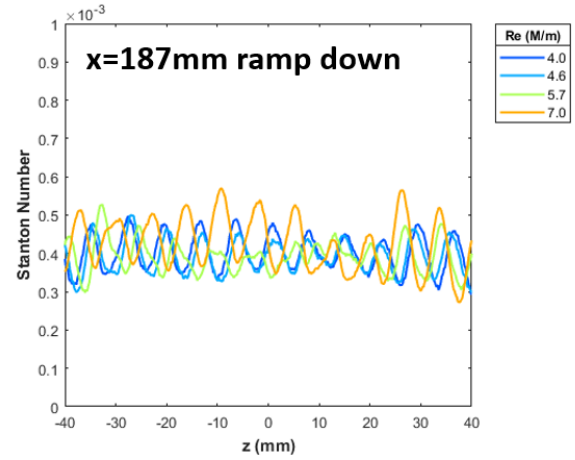
x=187mm ramp down
Re (M/m)
4.0
4.6
5.7
7.0
Stanton Number
z (mm)

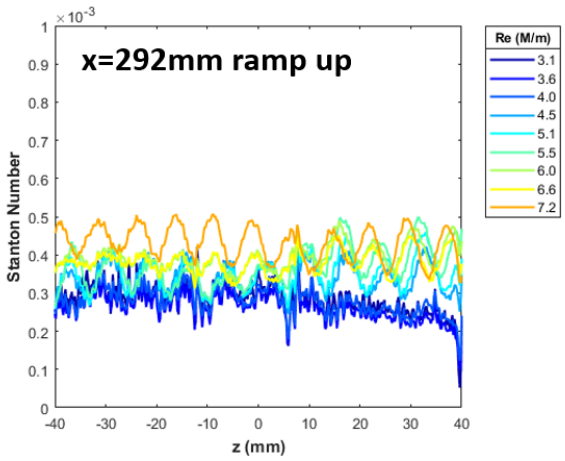

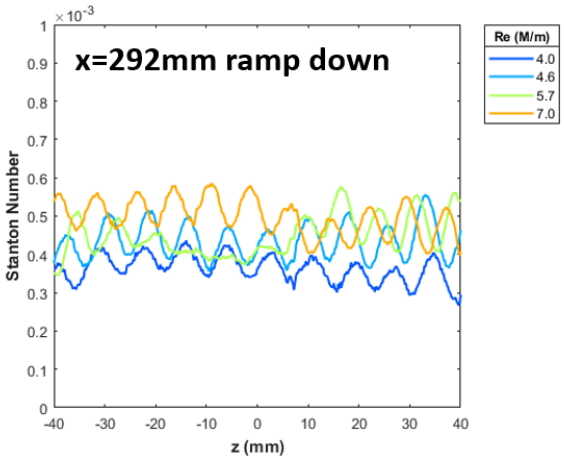

Run 3402

Surface pressure measurements and IR thermography made over a Re sweep.

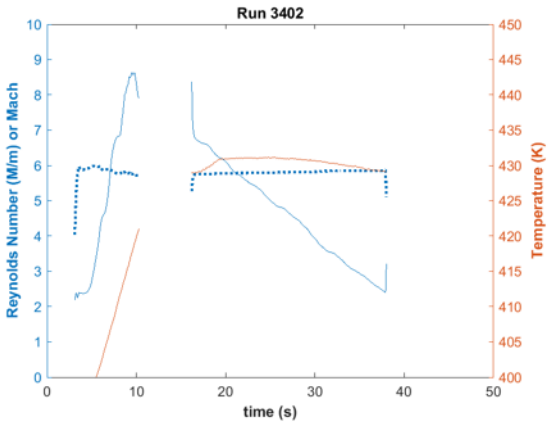

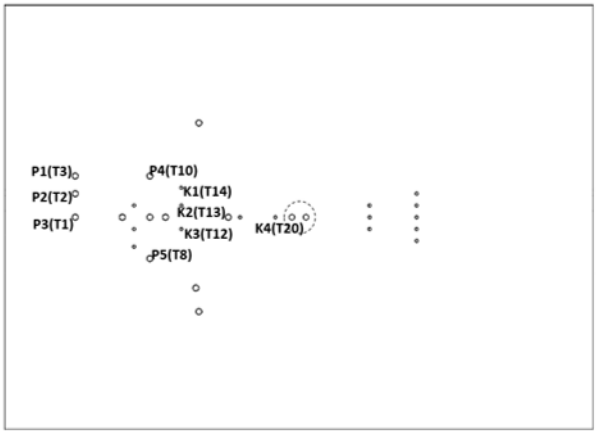

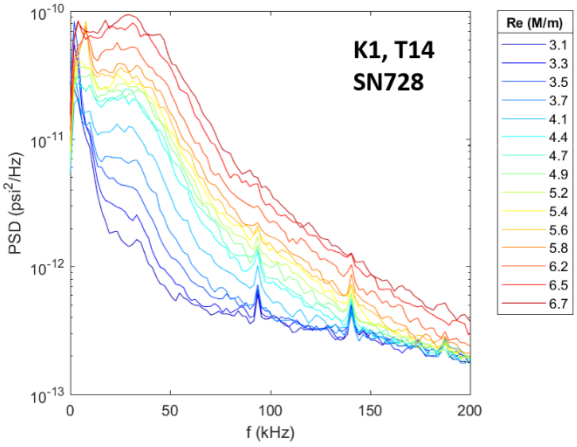

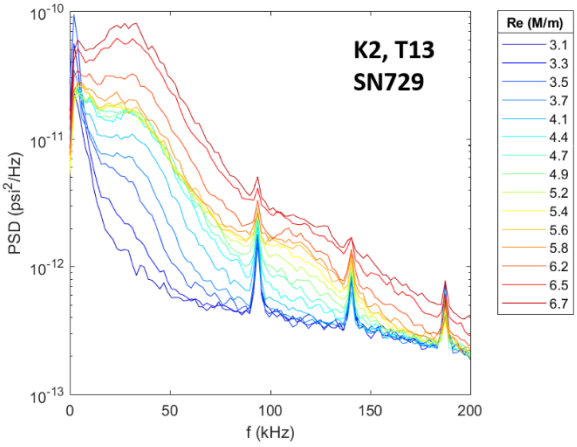

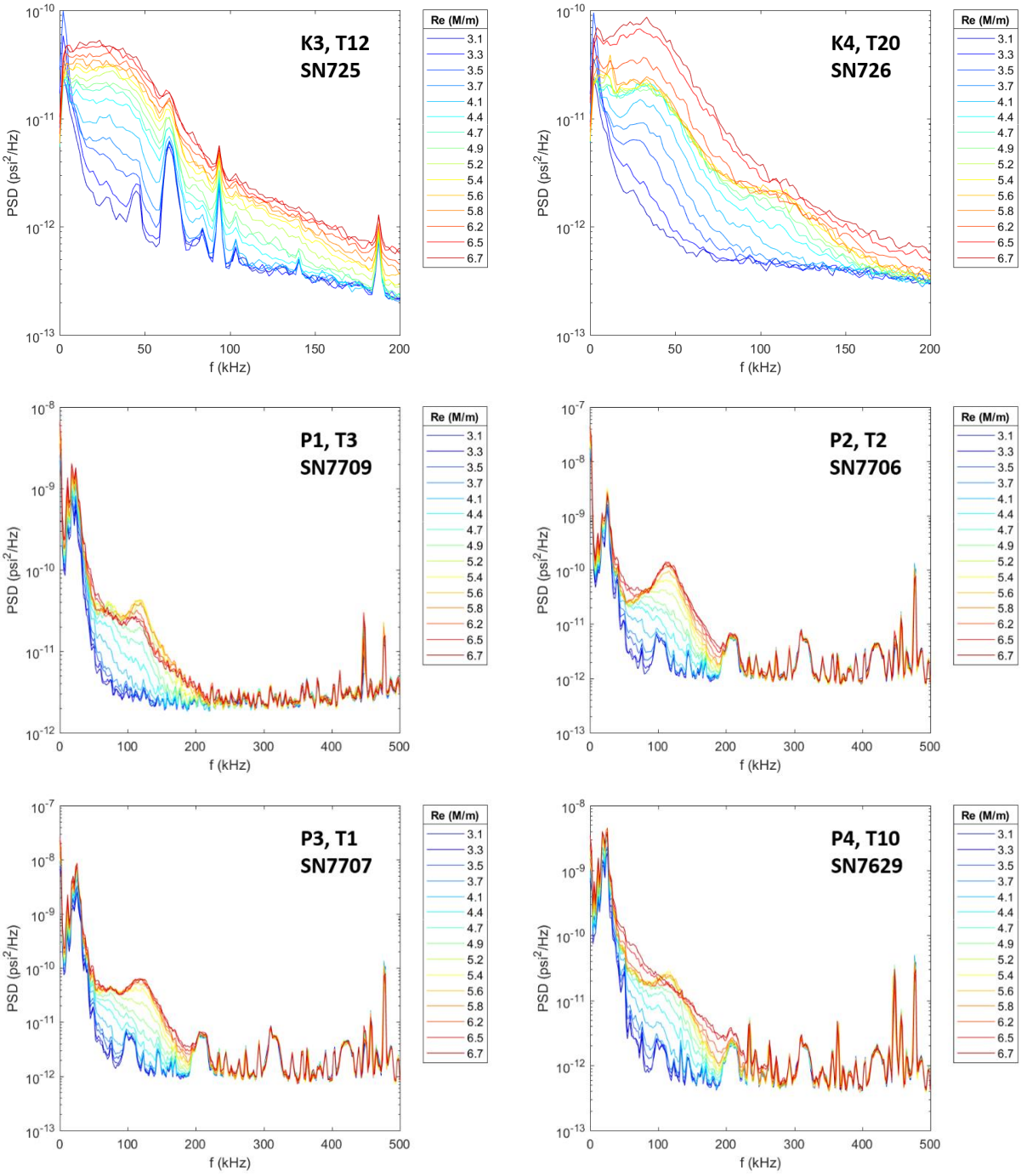
K3, T12
SN725
K4, T20
SN726
P1, T3
SN7709
P2, T2
SN7706
P3, T1
SN7707
P4, T10
SN7629
PSD (psi²/Hz)
f (kHz)
Re (M/m)
3.1
3.3
3.5
3.7
4.1
4.4
4.7
4.9
5.2
5.4
5.6
5.8
6.2
6.5
6.7

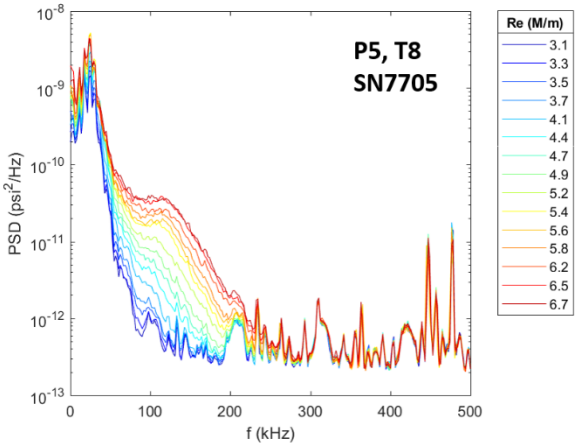
P5, T8
SN7705
PSD (psi²/Hz)
f (kHz)
Re (M/m)
3.1
3.3
3.5
3.7
4.1
4.4
4.7
4.9
5.2
5.4
5.6
5.8
6.2
6.5
6.7

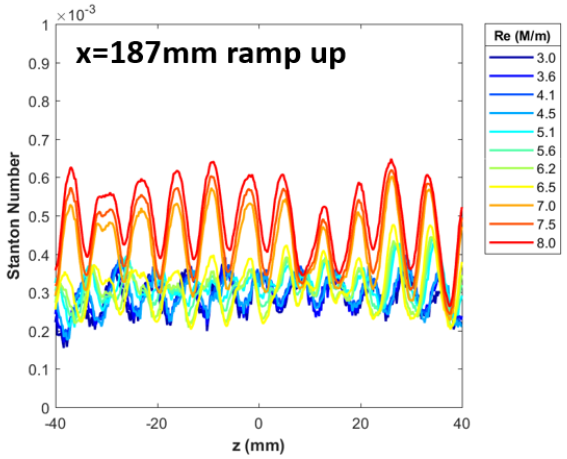
x=187mm ramp up
Stanton Number
z (mm)
Re (M/m)
3.0
3.6
4.1
4.5
5.1
5.6
6.2
6.5
7.0
7.5
8.0

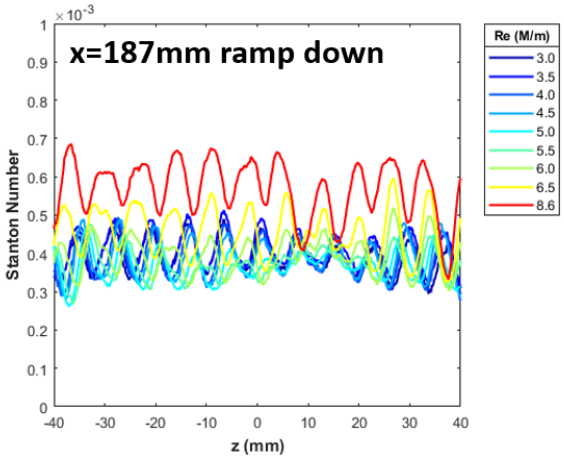
x=187mm ramp down
Stanton Number
z (mm)
Re (M/m)
3.0
3.5
4.0
4.5
5.0
5.5
6.0
6.5
8.6

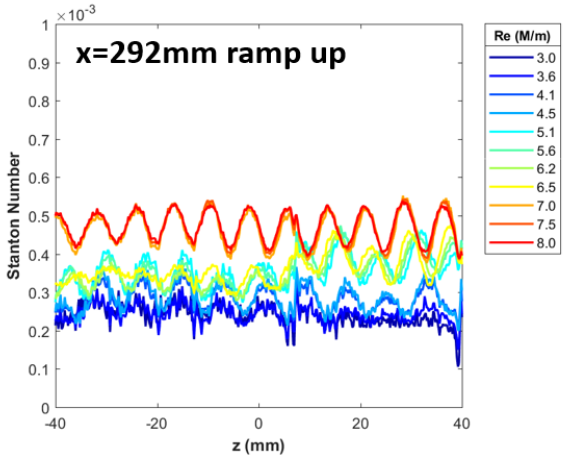
x=292mm ramp up
Stanton Number
z (mm)
Re (M/m)
3.0
3.6
4.1
4.5
5.1
5.6
6.2
6.5
7.0
7.5
8.0

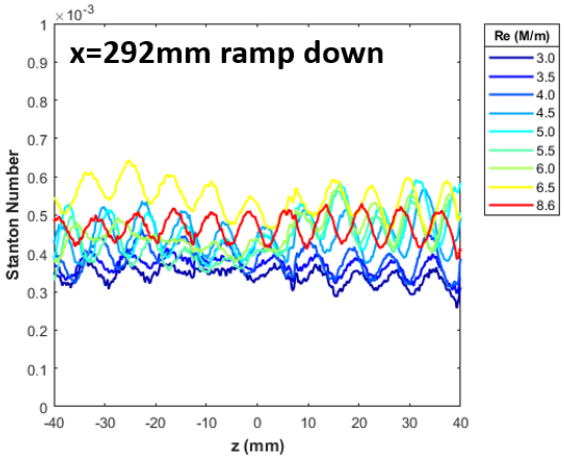
x=292mm ramp down
Stanton Number
z (mm)
Re (M/m)
3.0
3.5
4.0
4.5
5.0
5.5
6.0
6.5
8.6

Run 3403

Surface pressure measurements and IR thermography made over a Re sweep.

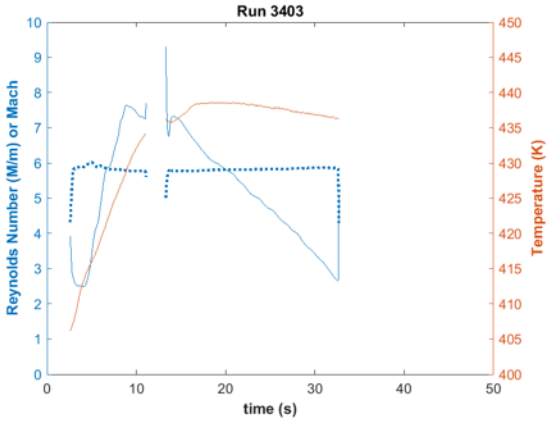

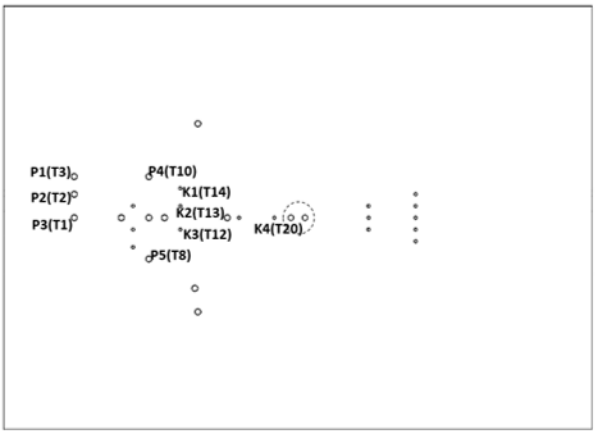

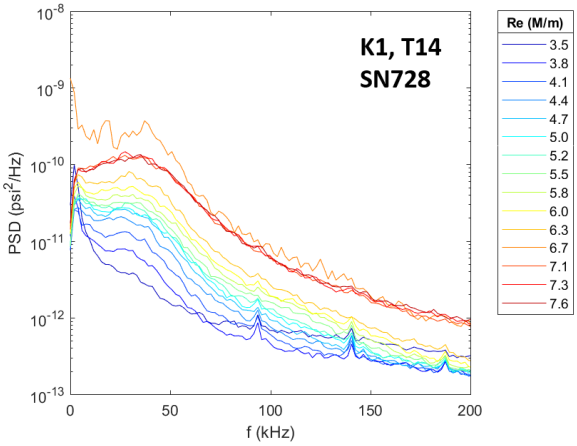

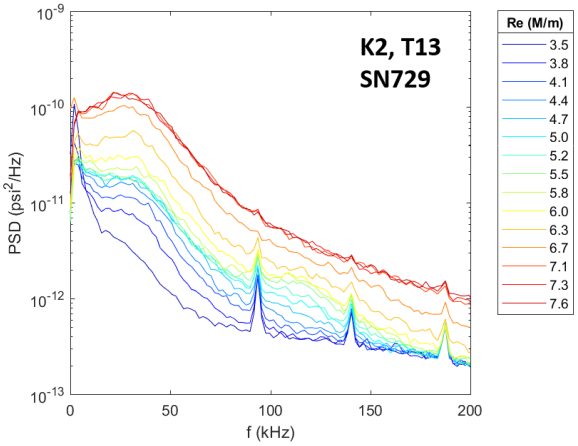

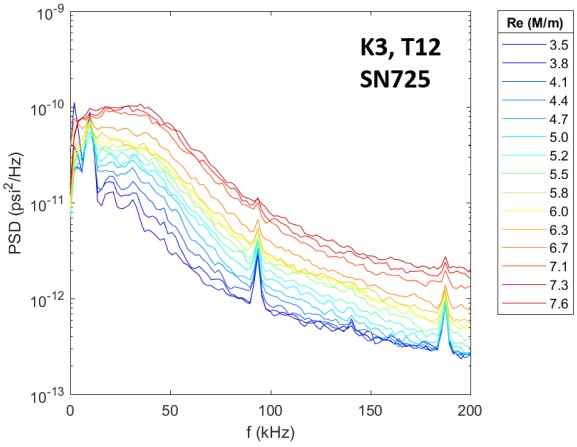

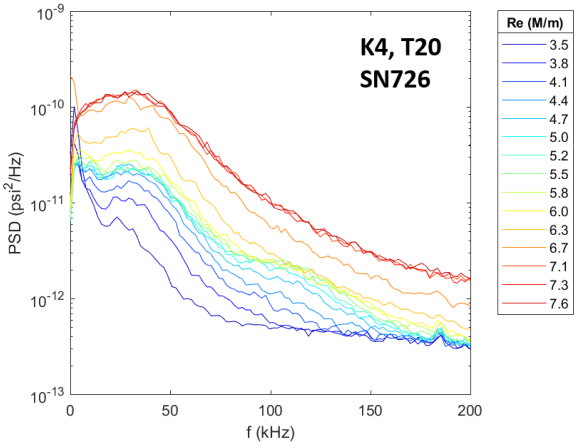

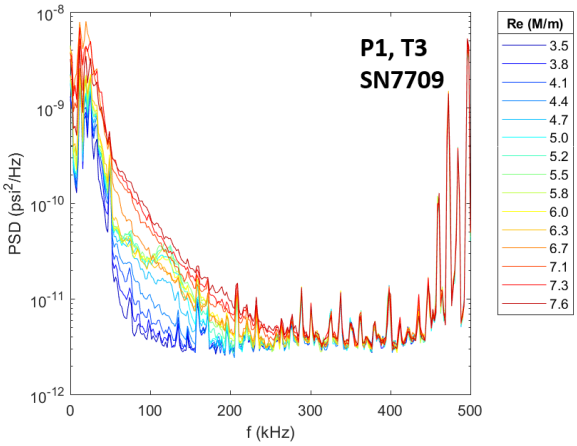
P1, T3
SN7709
PSD (psi²/Hz)
f (kHz)
Re (M/m)
3.5
3.8
4.1
4.4
4.7
5.0
5.2
5.5
5.8
6.0
6.3
6.7
7.1
7.3
7.6

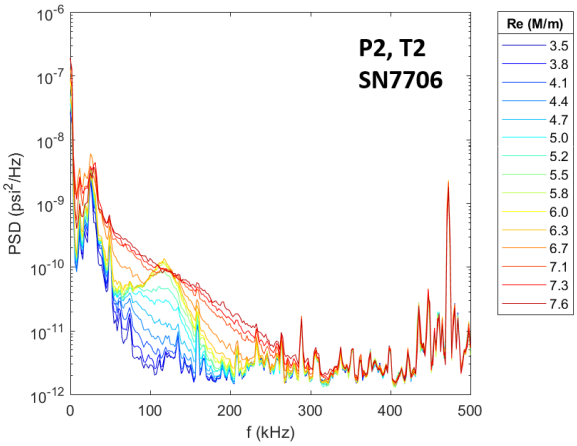
P2, T2
SN7706
PSD (psi²/Hz)
f (kHz)
Re (M/m)
3.5
3.8
4.1
4.4
4.7
5.0
5.2
5.5
5.8
6.0
6.3
6.7
7.1
7.3
7.6

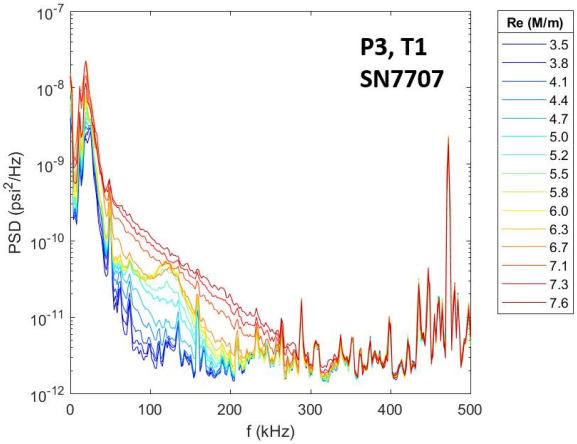
P3, T1
SN7707
PSD (psi²/Hz)
f (kHz)
Re (M/m)
3.5
3.8
4.1
4.4
4.7
5.0
5.2
5.5
5.8
6.0
6.3
6.7
7.1
7.3
7.6

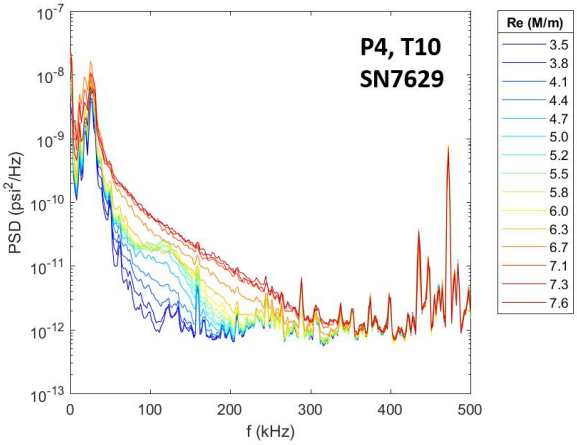
P4, T10
SN7629
PSD (psi²/Hz)
f (kHz)
Re (M/m)
3.5
3.8
4.1
4.4
4.7
5.0
5.2
5.5
5.8
6.0
6.3
6.7
7.1
7.3
7.6

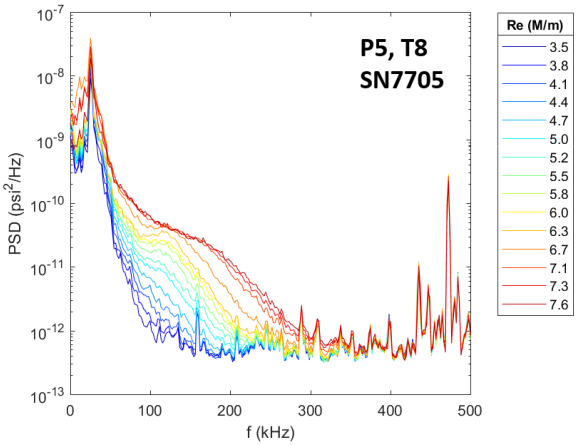
P5, T8
SN7705
PSD (psi²/Hz)
f (kHz)
Re (M/m)
3.5
3.8
4.1
4.4
4.7
5.0
5.2
5.5
5.8
6.0
6.3
6.7
7.1
7.3
7.6

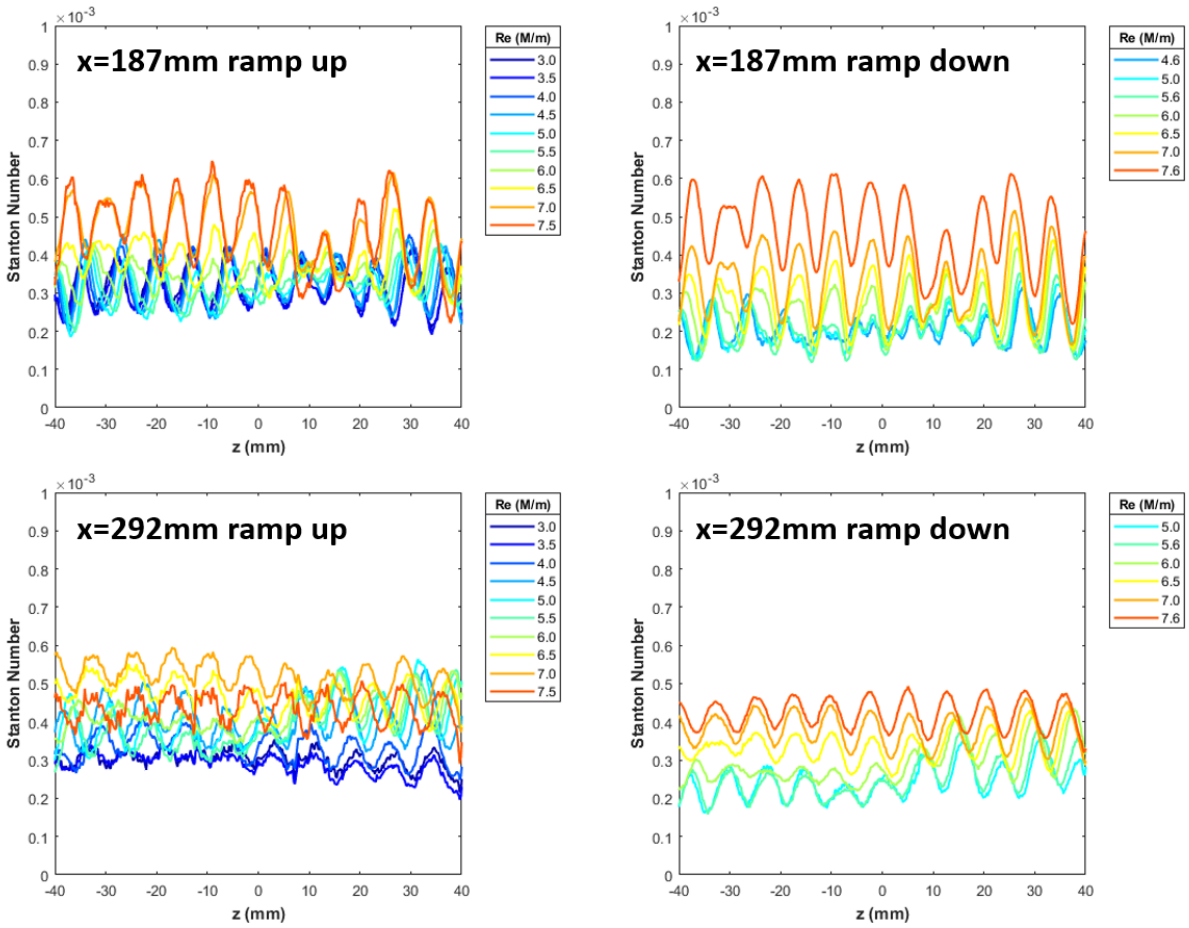

Run 3421

IR thermography on a Re sweep.

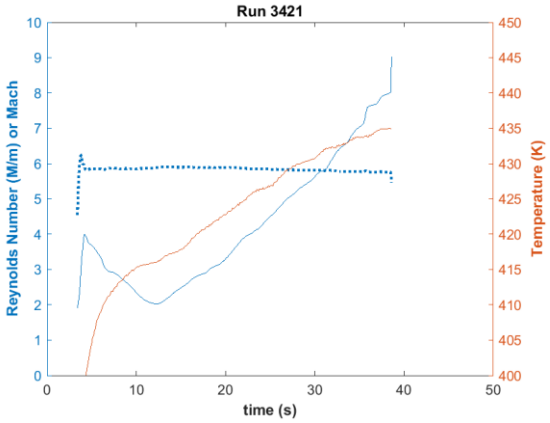

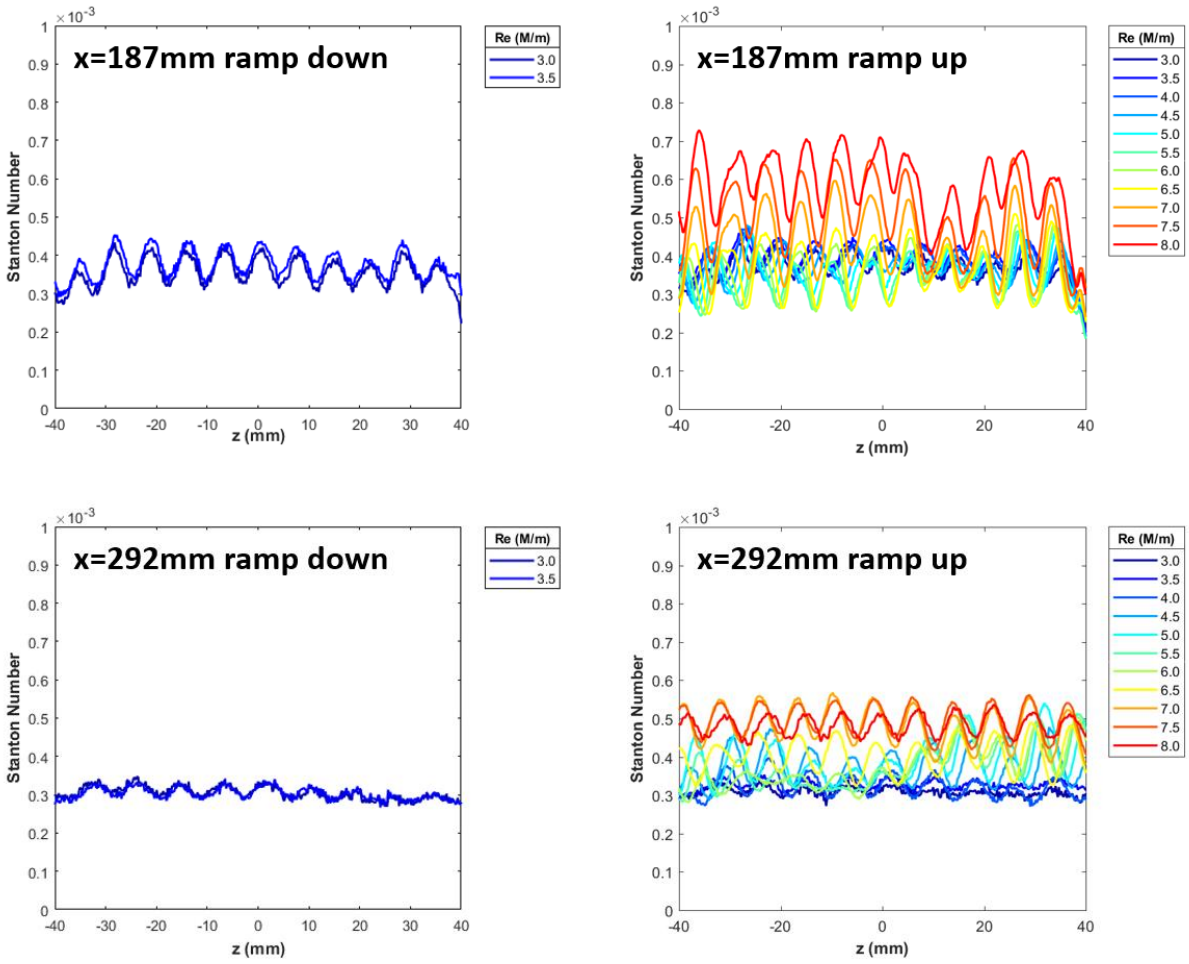

Trips, cylinder

Run 3422

IR thermography on a Re sweep.

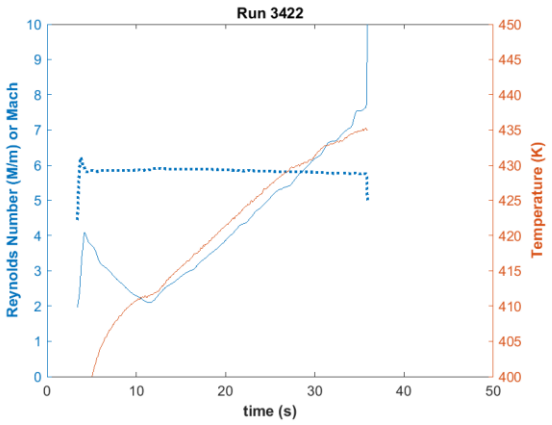

Region 2 profile heating

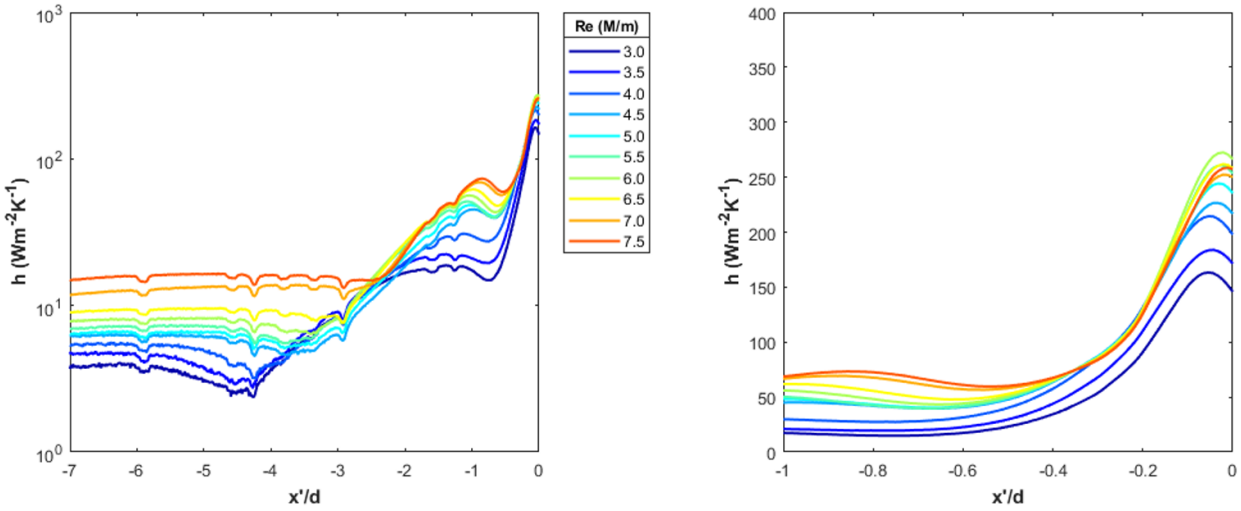

Run 3424

Surface pressure measurements, IR thermography, and schlieren made over a Re sweep.

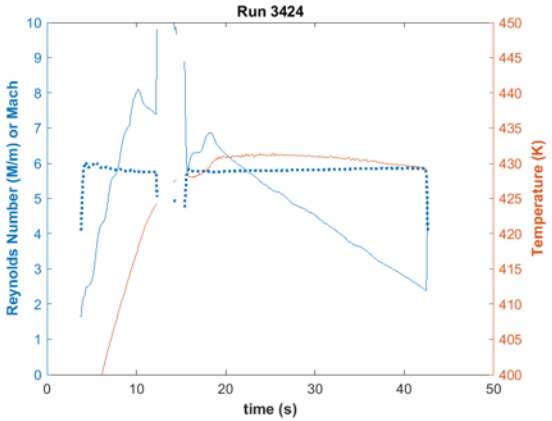

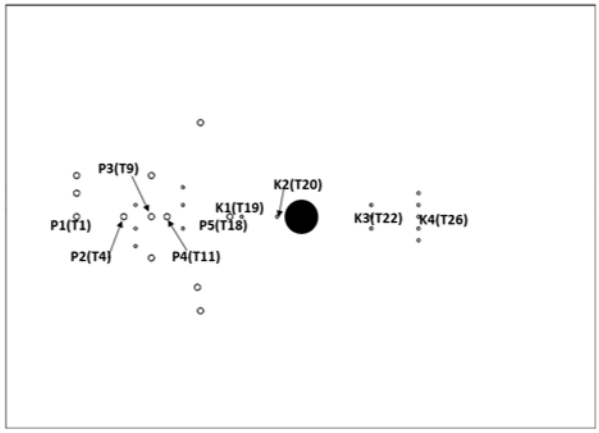

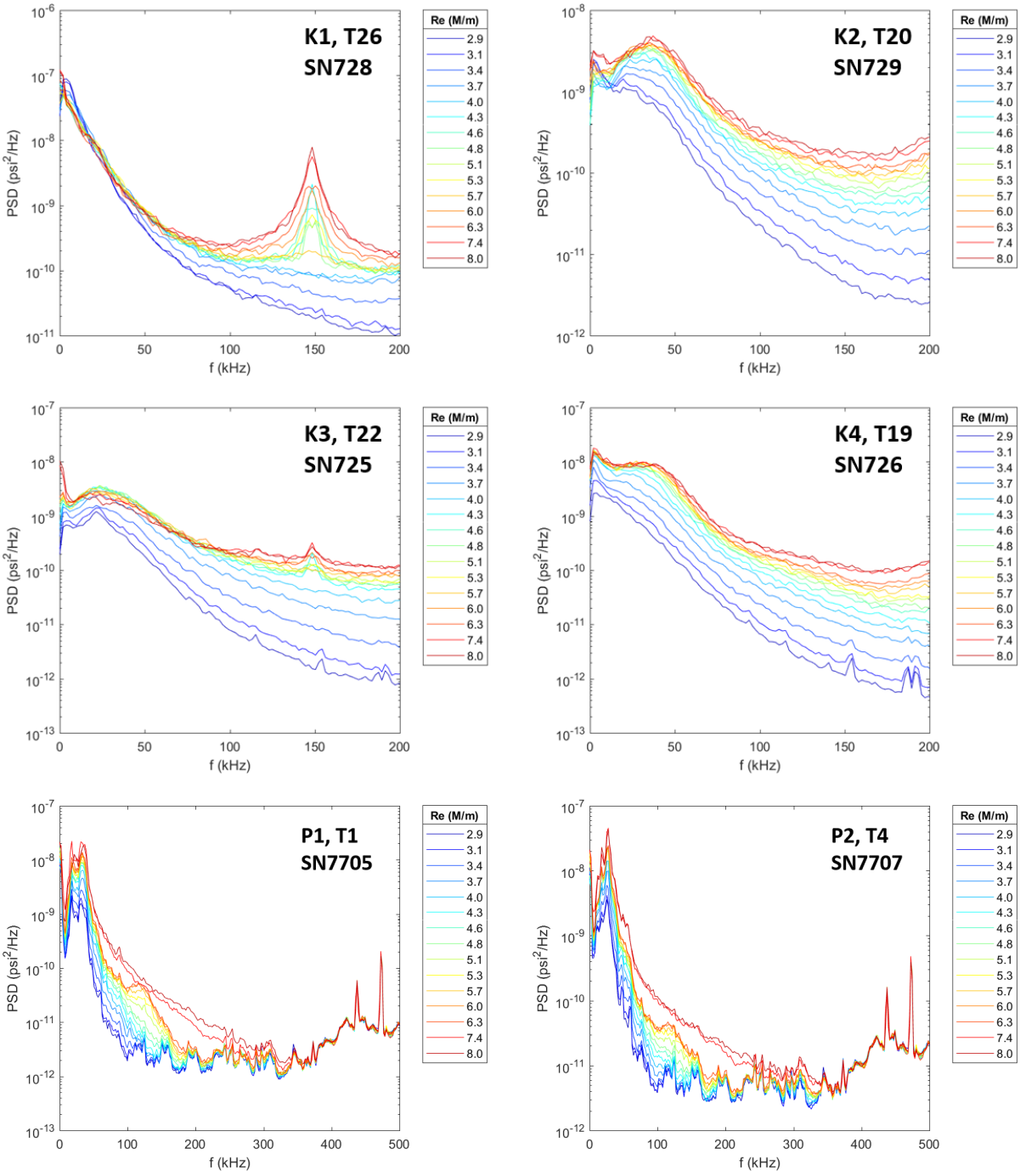
K1, T26
SN728
K2, T20
SN729
K3, T22
SN725
K4, T19
SN726
P1, T1
SN7705
P2, T4
SN7707
PSD (psi²/Hz)
f (kHz)
Re (M/m)
2.9
3.1
3.4
3.7
4.0
4.3
4.6
4.8
5.1
5.3
5.7
6.0
6.3
7.4
8.0

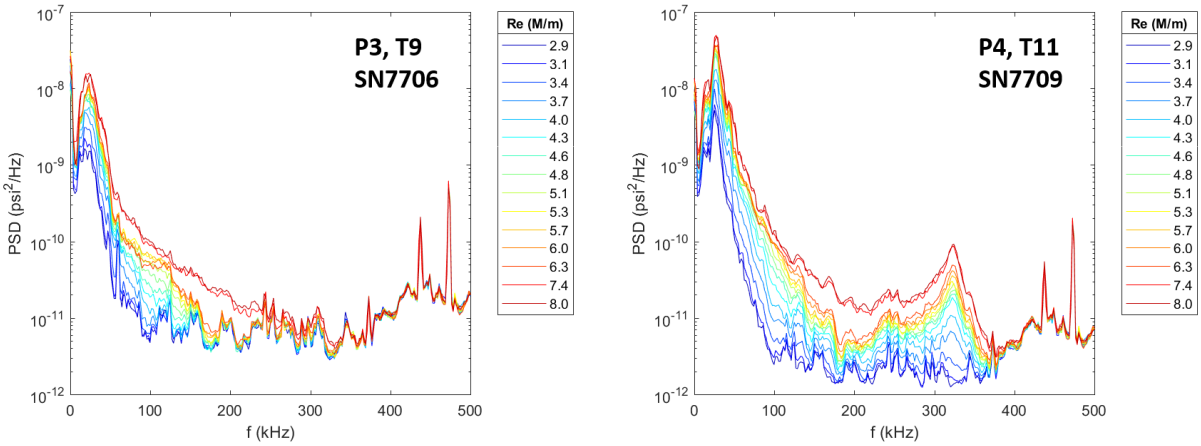

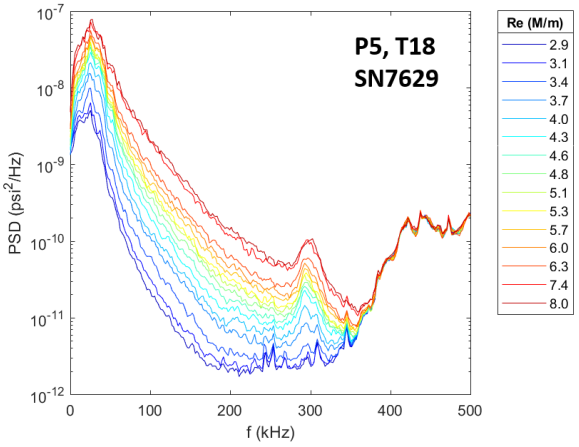

Region 2 profile heating

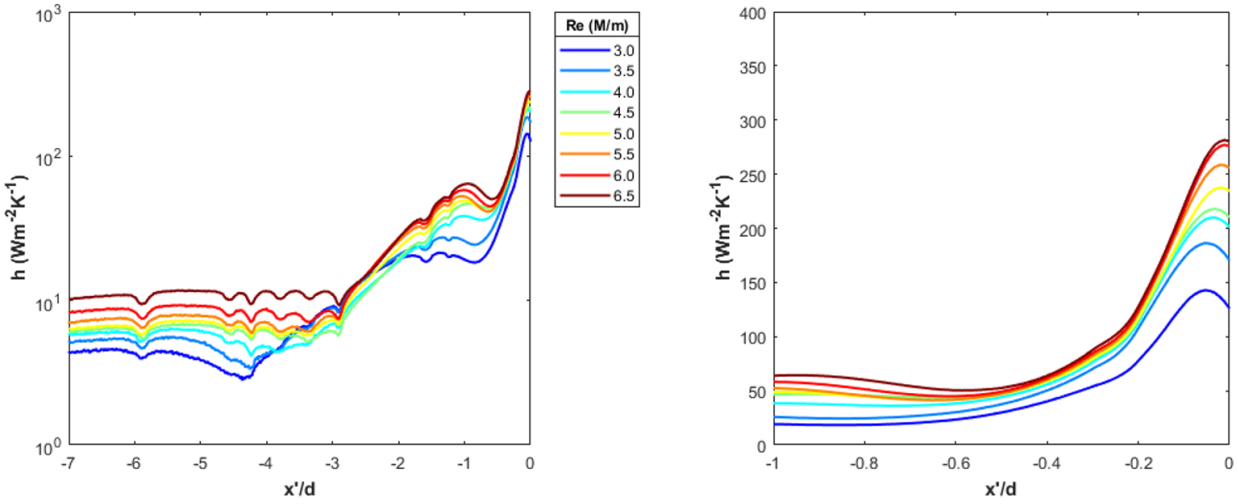

Run 3425

Surface pressure measurements, IR thermography, and high-speed schlieren made over Re steps.

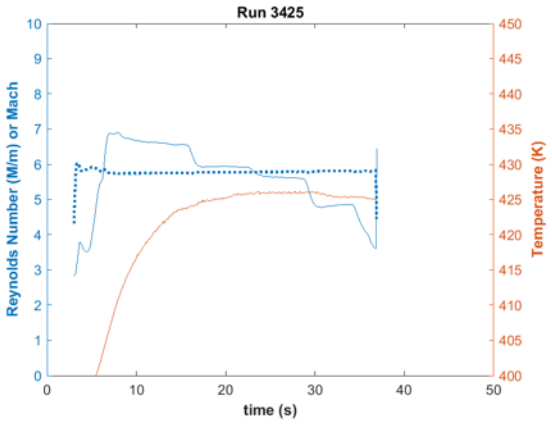

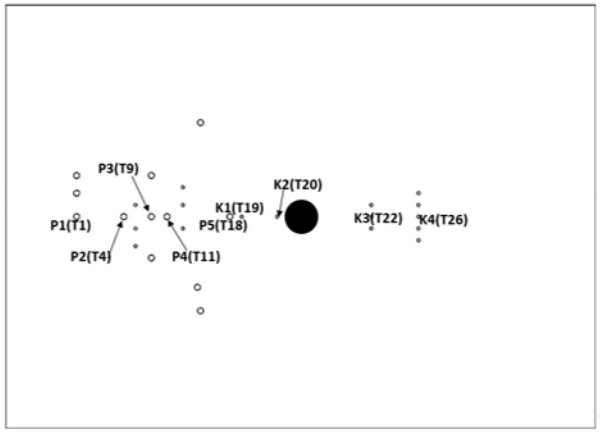

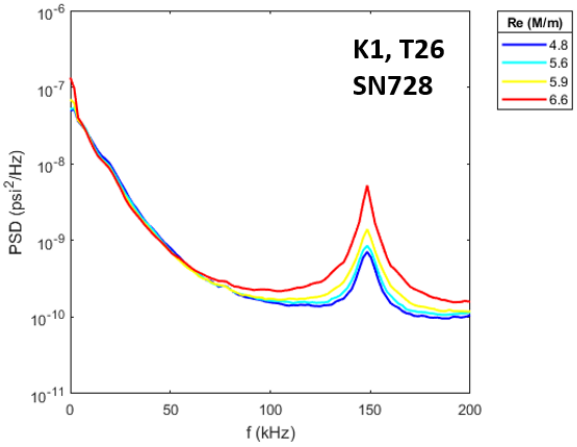

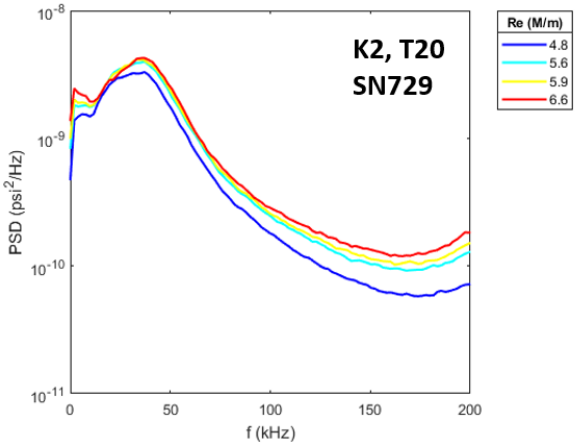

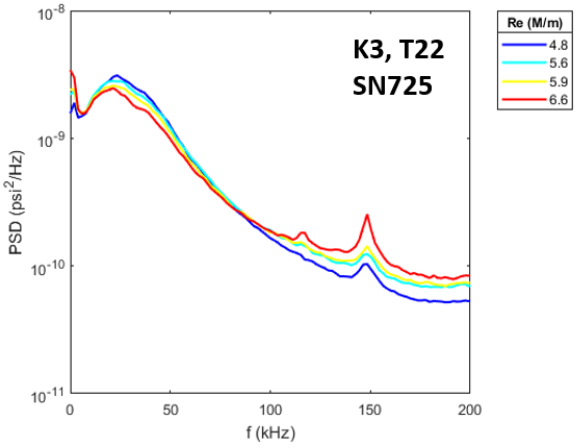

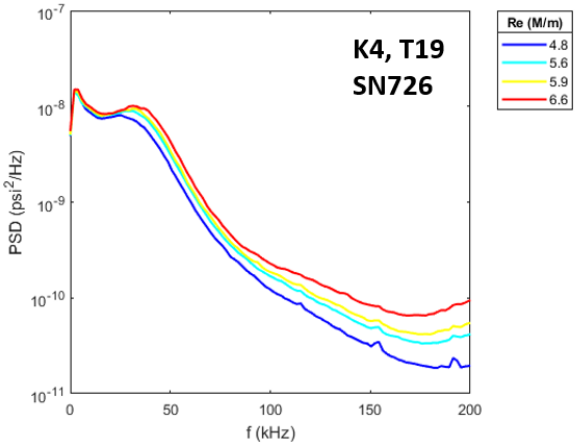

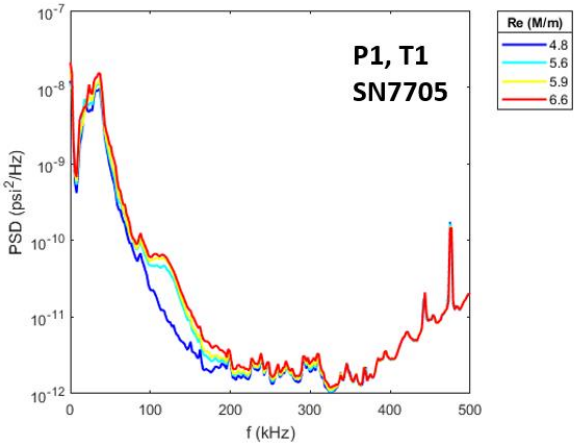
P1, T1
SN7705
Re (M/m)
4.8
5.6
5.9
6.6
PSD (psi²/Hz)
f (kHz)

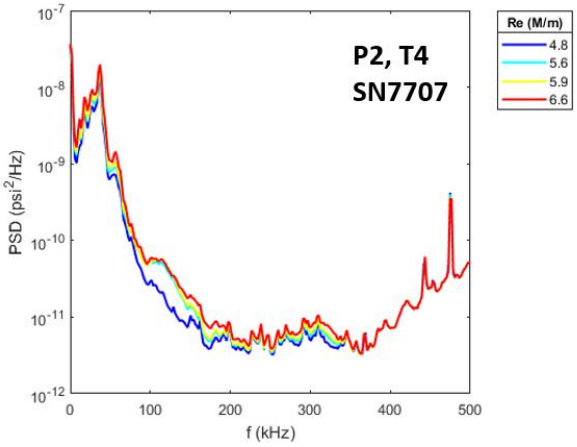
P2, T4
SN7707
Re (M/m)
4.8
5.6
5.9
6.6
PSD (psi²/Hz)
f (kHz)

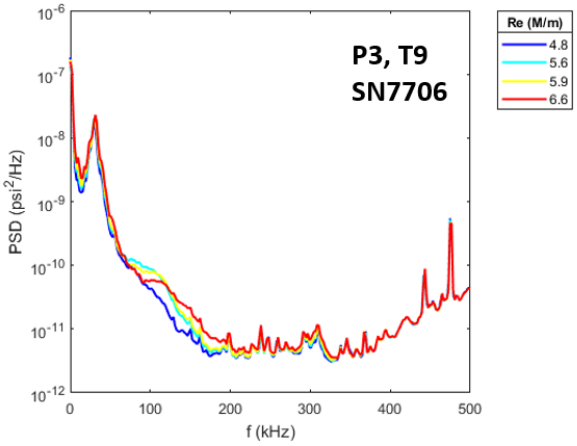
P3, T9
SN7706
Re (M/m)
4.8
5.6
5.9
6.6
PSD (psi²/Hz)
f (kHz)

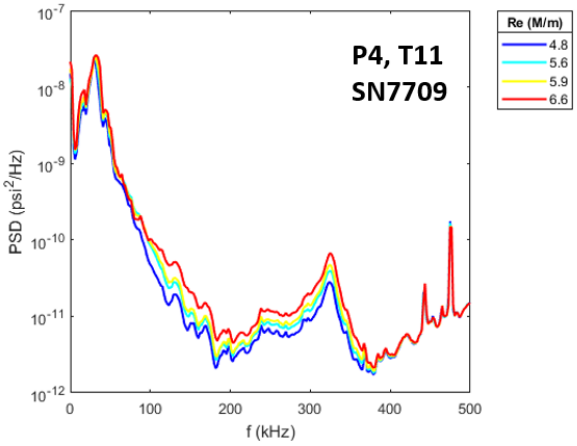
P4, T11
SN7709
Re (M/m)
4.8
5.6
5.9
6.6
PSD (psi²/Hz)
f (kHz)

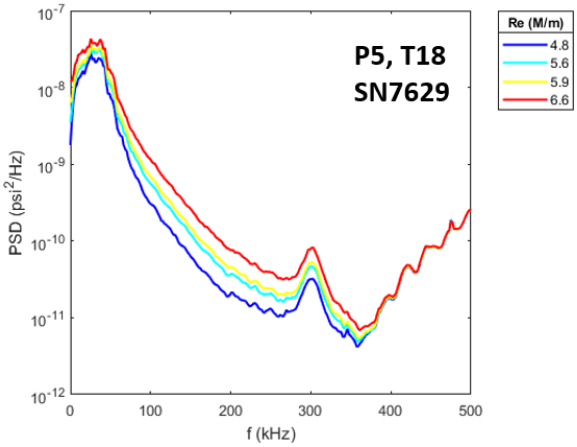
P5, T18
SN7629
Re (M/m)
4.8
5.6
5.9
6.6
PSD (psi²/Hz)
f (kHz)

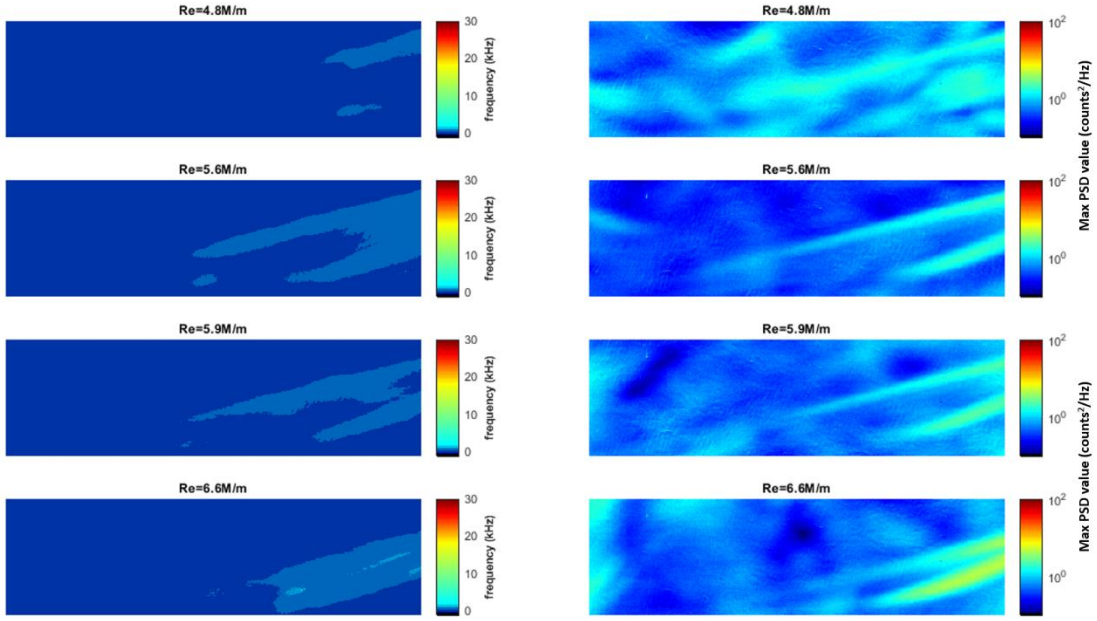
Re=4.8M/m
Re=5.6M/m
Re=5.9M/m
Re=6.6M/m
frequency (kHz)
Max PSD value (counts²/Hz)

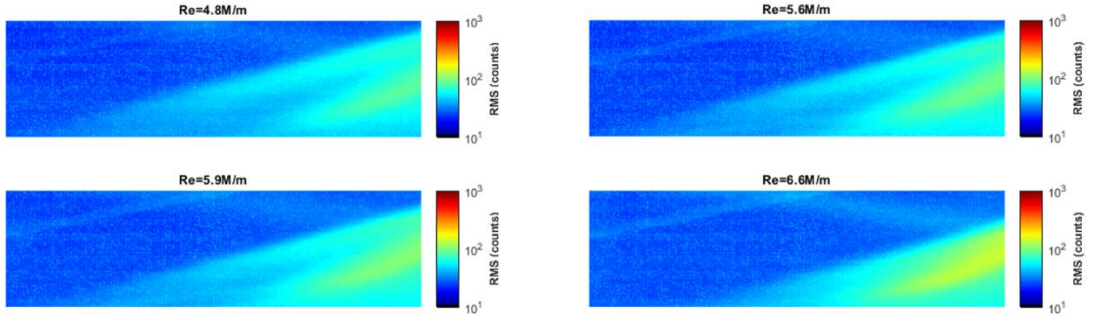
Re=4.8M/m
Re=5.6M/m
Re=5.9M/m
Re=6.6M/m
RMS (counts)

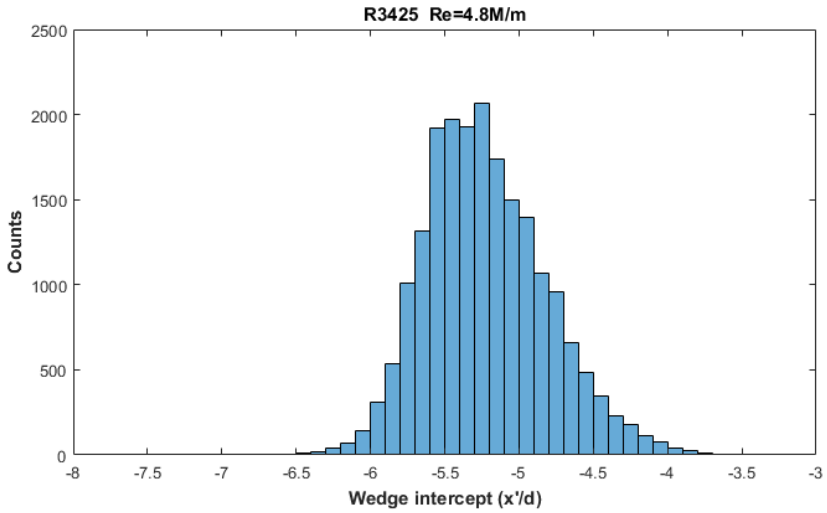
R3425 Re=4.8M/m
Counts
Wedge intercept (x'/d)

Run 3426

Surface pressure measurements, IR thermography, and high-speed schlieren made over Re steps.

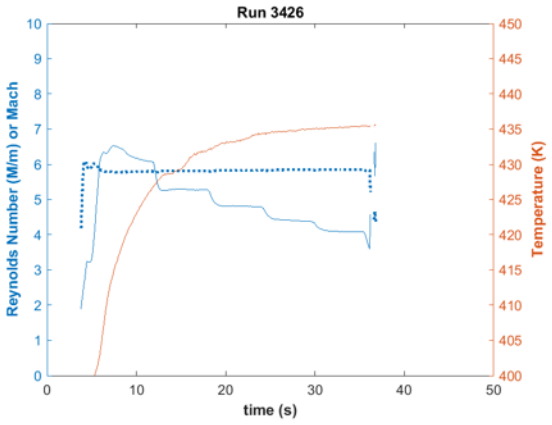

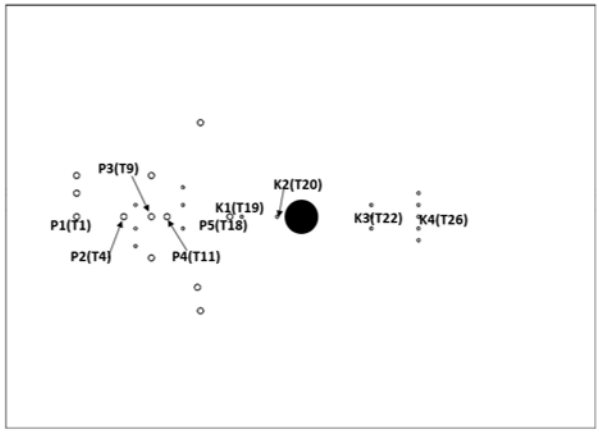

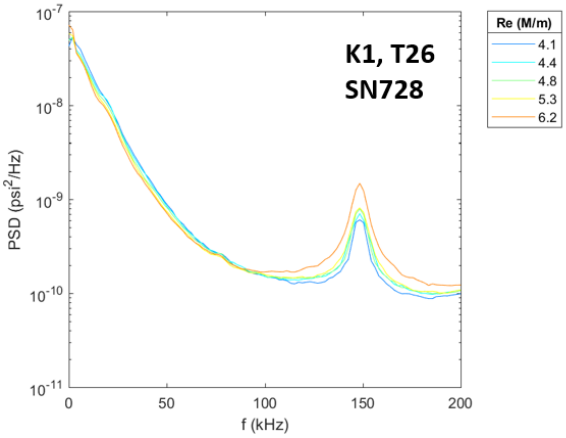

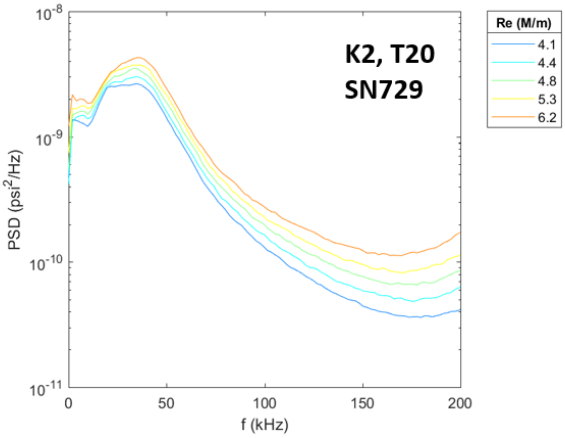

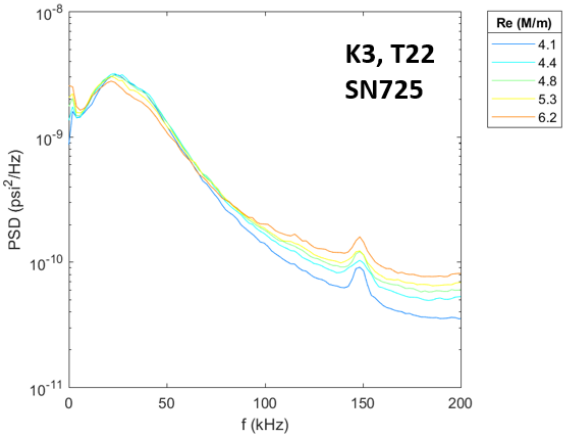

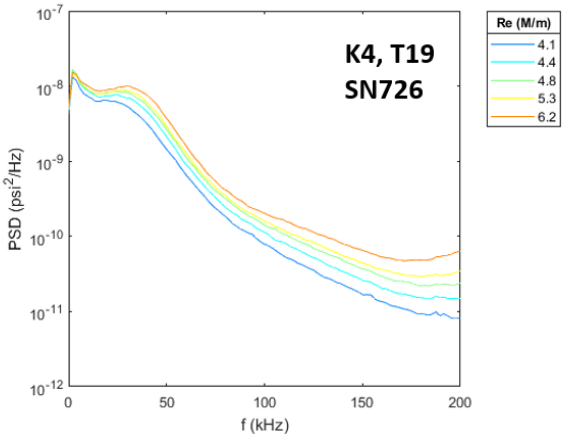

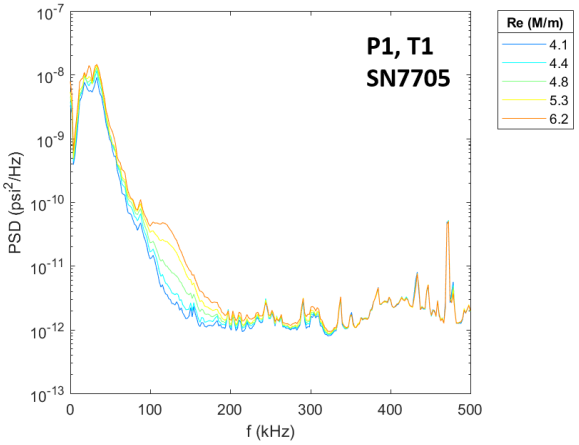
P1, T1
SN7705
Re (M/m)
4.1
4.4
4.8
5.3
6.2
PSD (psi²/Hz)
f (kHz)

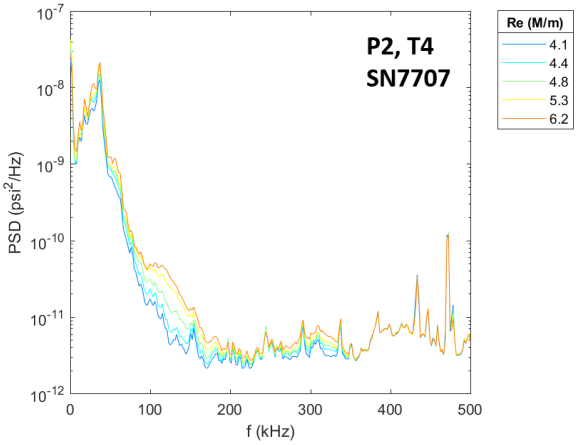
P2, T4
SN7707
Re (M/m)
4.1
4.4
4.8
5.3
6.2
PSD (psi²/Hz)
f (kHz)

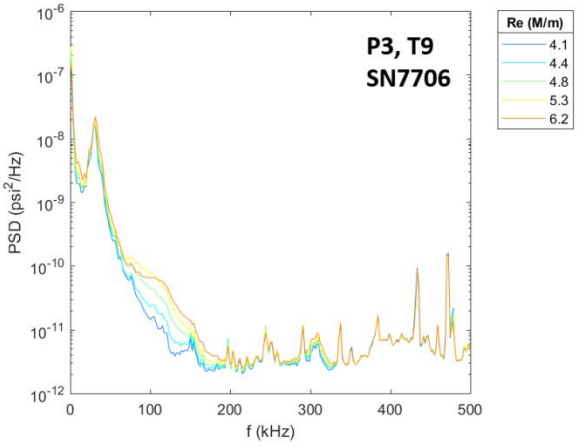
P3, T9
SN7706
Re (M/m)
4.1
4.4
4.8
5.3
6.2
PSD (psi²/Hz)
f (kHz)

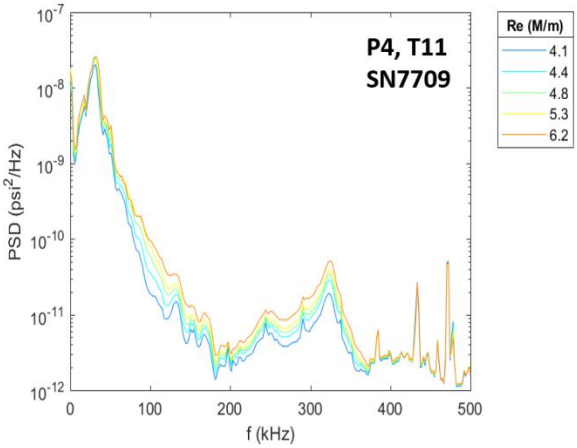
P4, T11
SN7709
Re (M/m)
4.1
4.4
4.8
5.3
6.2
PSD (psi²/Hz)
f (kHz)

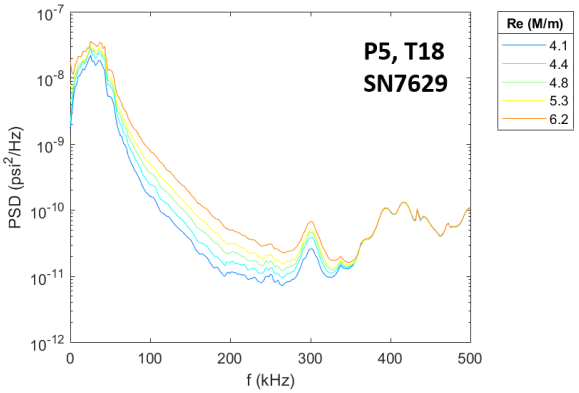
P5, T18
SN7629
Re (M/m)
4.1
4.4
4.8
5.3
6.2
PSD (psi²/Hz)
f (kHz)

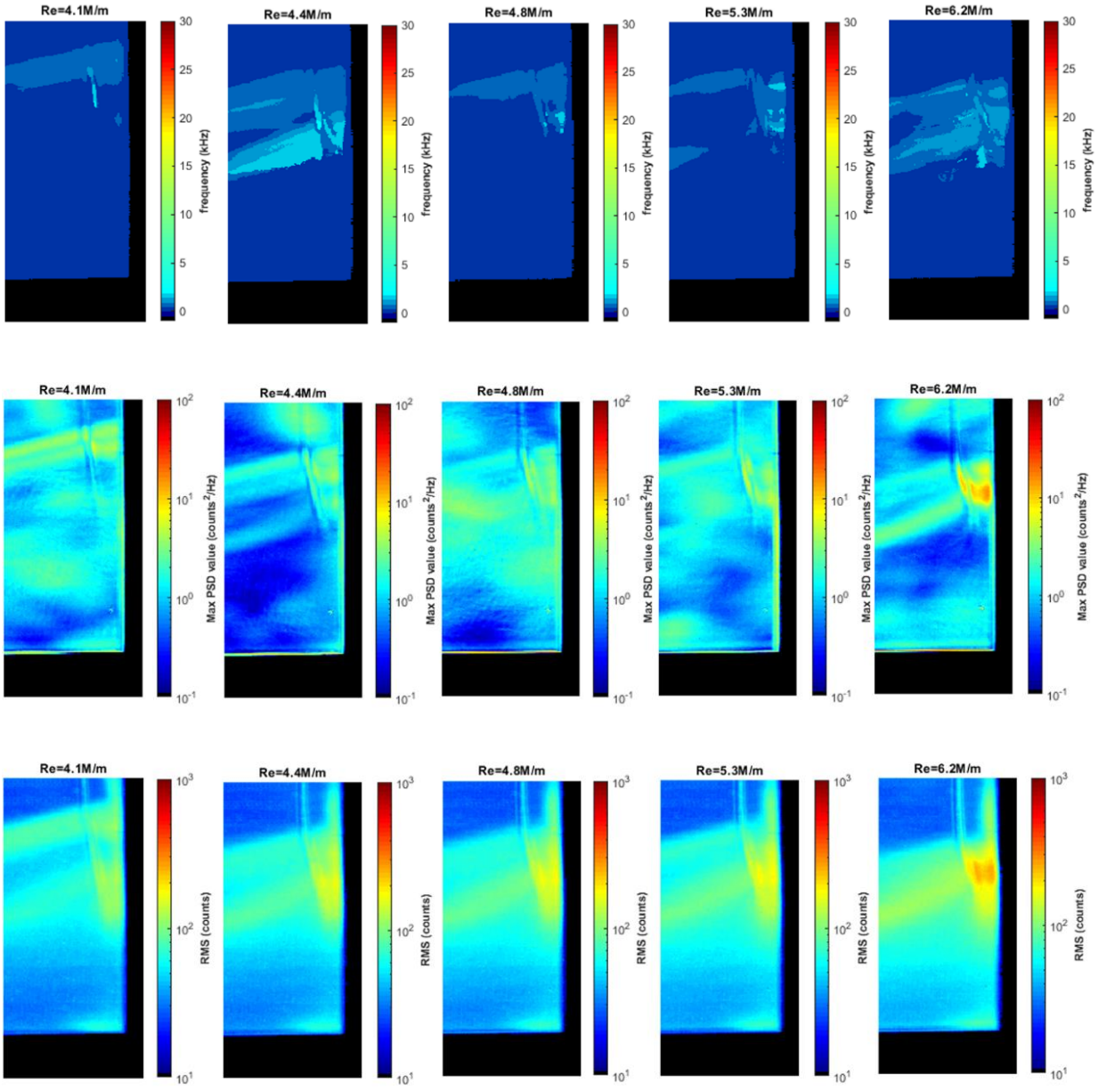
Re=4.1M/m
Re=4.4M/m
Re=4.8M/m
Re=5.3M/m
Re=6.2M/m
frequency (kHz)
Max PSD value (counts²/Hz)
RMS (counts)

Run 3427

Surface pressure measurements, IR thermography, and schlieren made over a Re sweep.

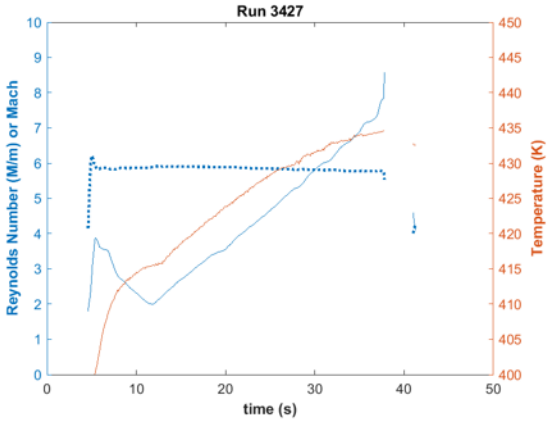

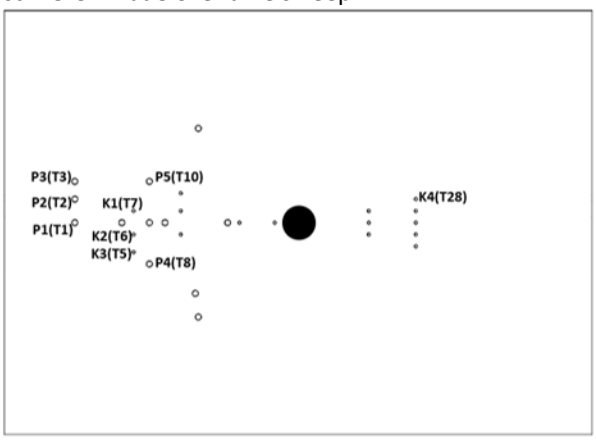

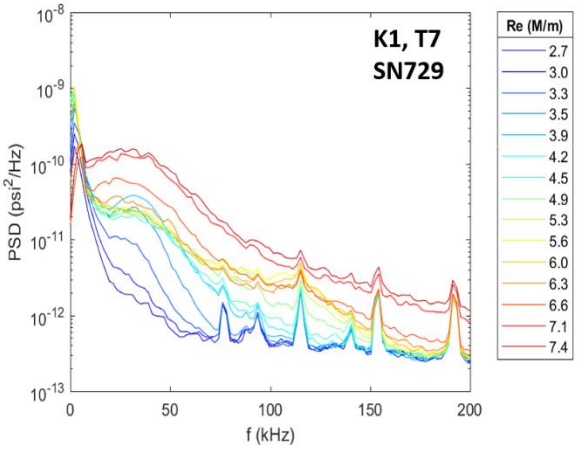

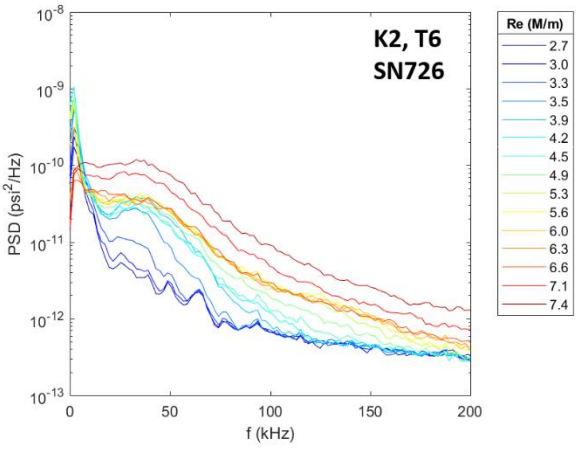

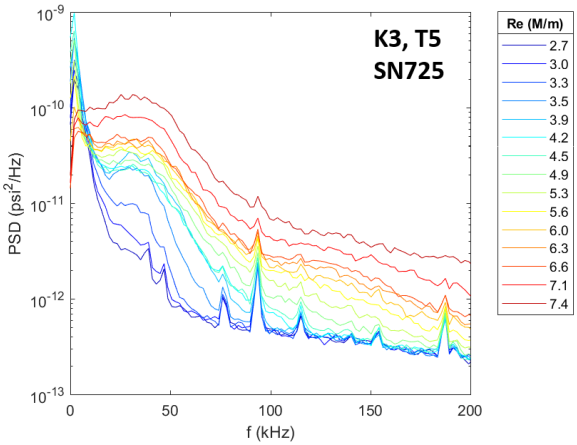

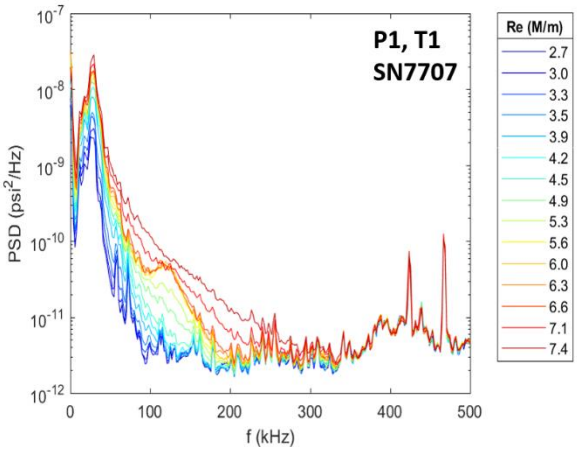
P1, T1
SN7707
Re (M/m)
2.7
3.0
3.3
3.5
3.9
4.2
4.5
4.9
5.3
5.6
6.0
6.3
6.6
7.1
7.4
PSD (psi²/Hz)
f (kHz)

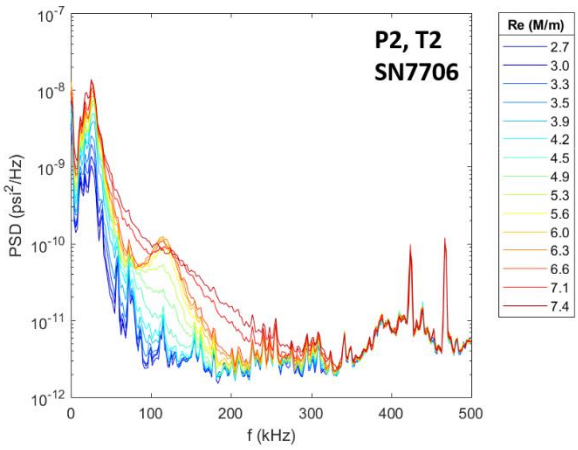
P2, T2
SN7706
Re (M/m)
2.7
3.0
3.3
3.5
3.9
4.2
4.5
4.9
5.3
5.6
6.0
6.3
6.6
7.1
7.4
PSD (psi²/Hz)
f (kHz)

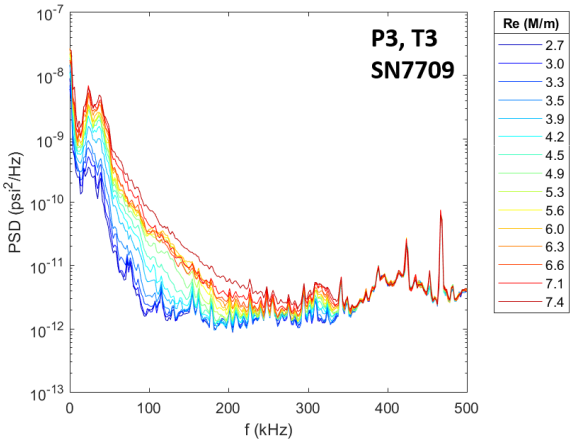
P3, T3
SN7709
Re (M/m)
2.7
3.0
3.3
3.5
3.9
4.2
4.5
4.9
5.3
5.6
6.0
6.3
6.6
7.1
7.4
PSD (psi²/Hz)
f (kHz)

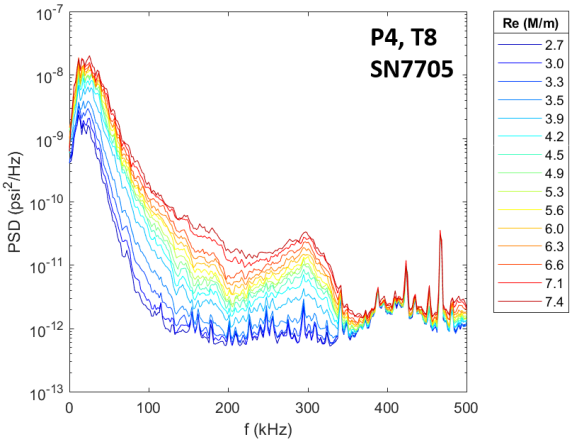
P4, T8
SN7705
Re (M/m)
2.7
3.0
3.3
3.5
3.9
4.2
4.5
4.9
5.3
5.6
6.0
6.3
6.6
7.1
7.4
PSD (psi²/Hz)
f (kHz)

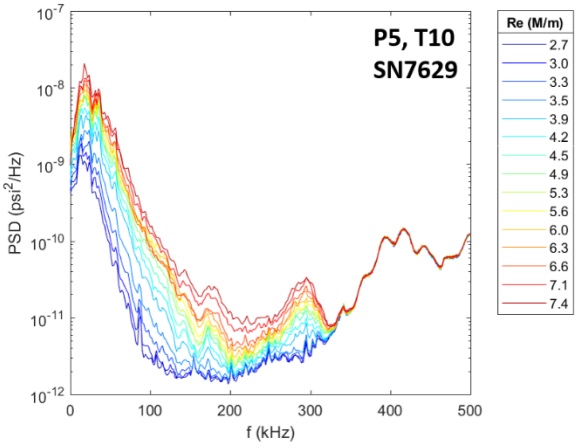
P5, T10
SN7629
Re (M/m)
2.7
3.0
3.3
3.5
3.9
4.2
4.5
4.9
5.3
5.6
6.0
6.3
6.6
7.1
7.4
PSD (psi²/Hz)
f (kHz)

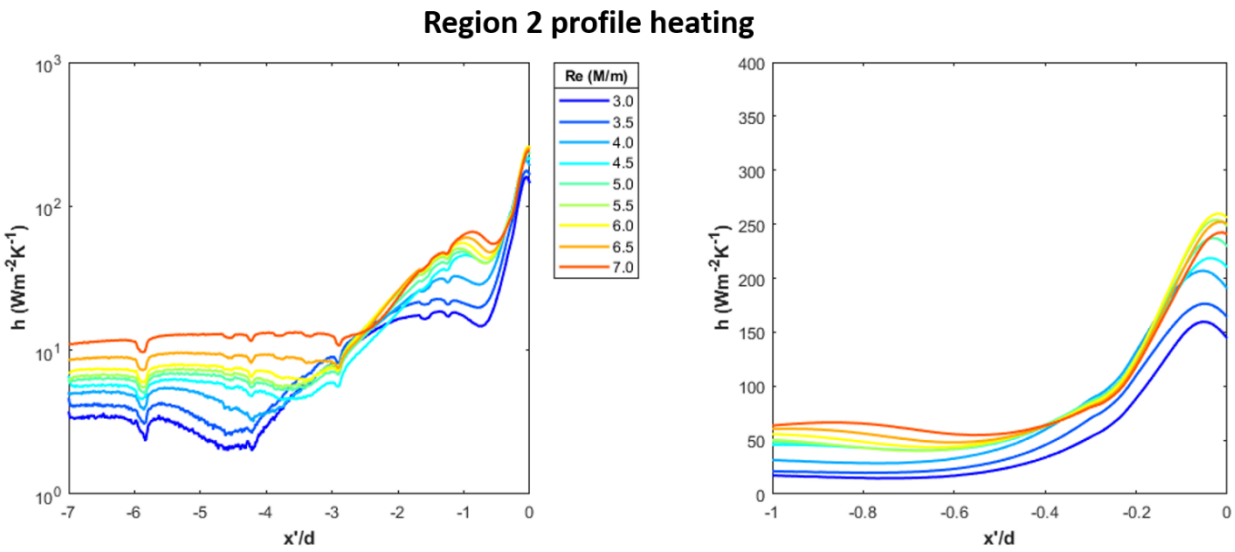

Run 3428

Surface pressure measurements, IR thermography, and high-speed schlieren made over Re steps.

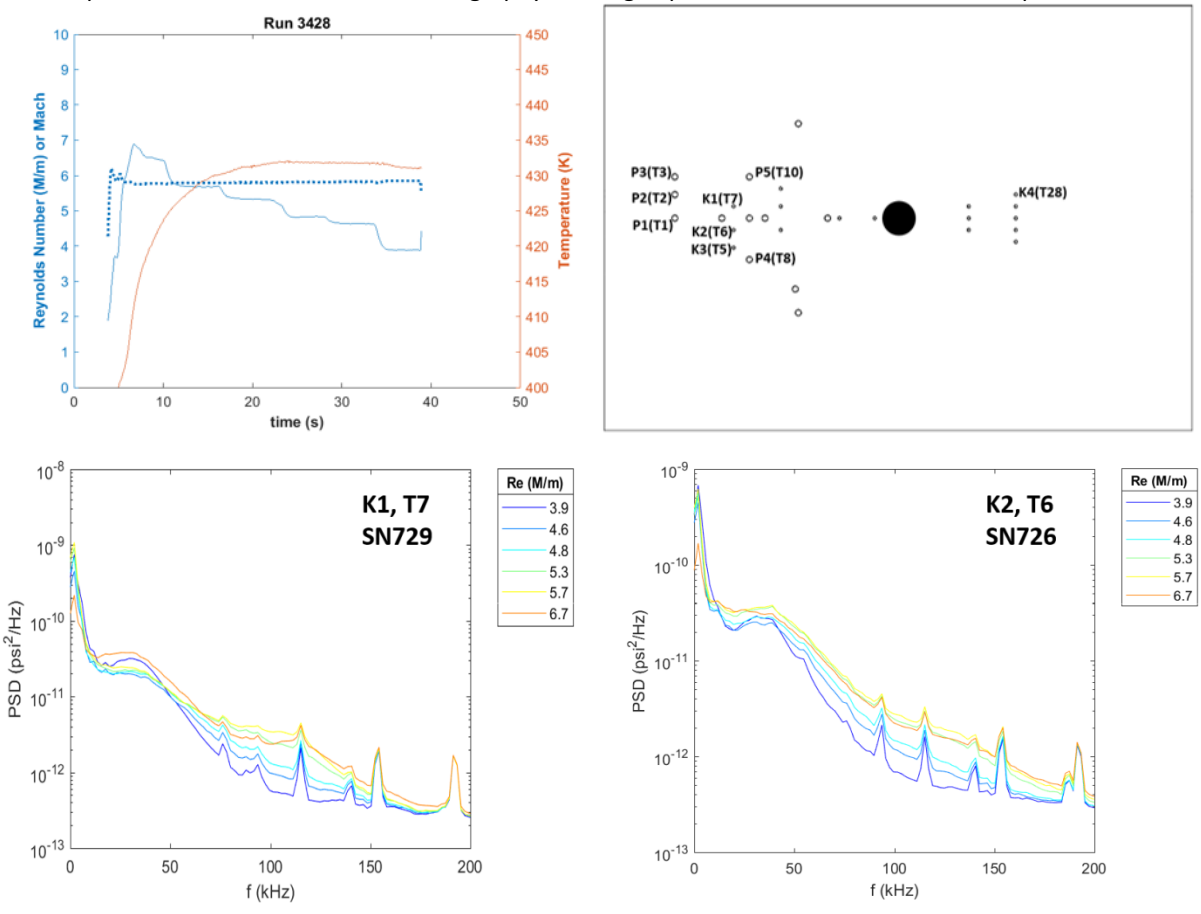

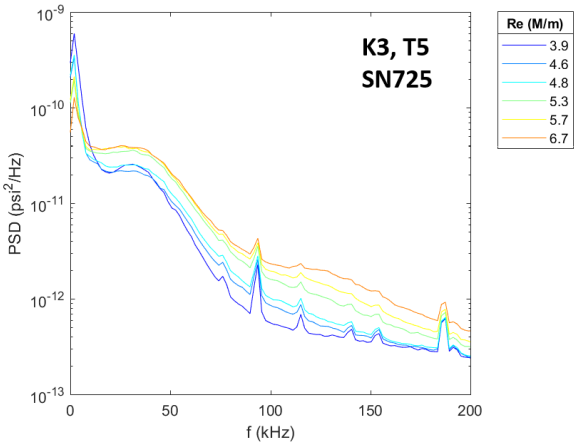
K3, T5
SN725
Re (M/m)
3.9
4.6
4.8
5.3
5.7
6.7
PSD (psi²/Hz)
f (kHz)

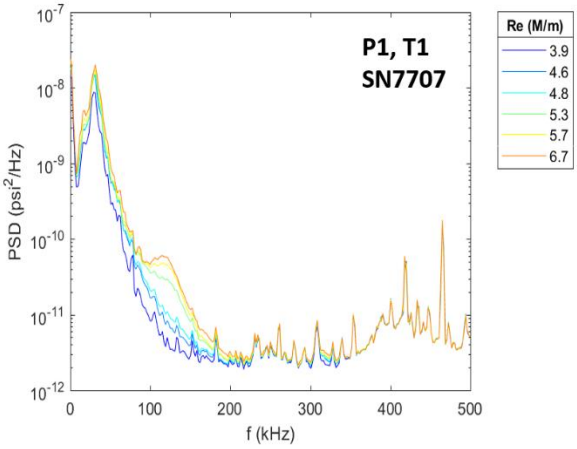
P1, T1
SN7707
Re (M/m)
3.9
4.6
4.8
5.3
5.7
6.7
PSD (psi²/Hz)
f (kHz)

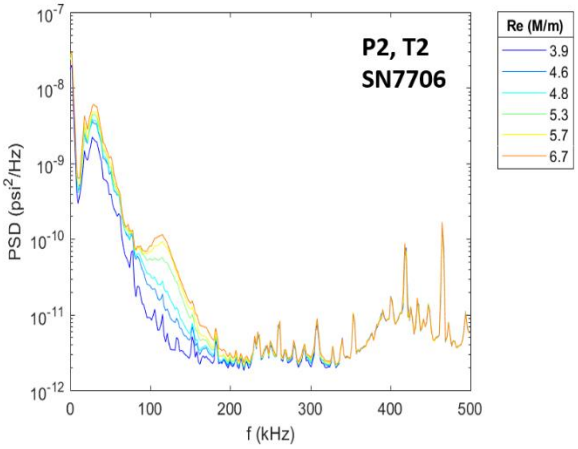
P2, T2
SN7706
Re (M/m)
3.9
4.6
4.8
5.3
5.7
6.7
PSD (psi²/Hz)
f (kHz)

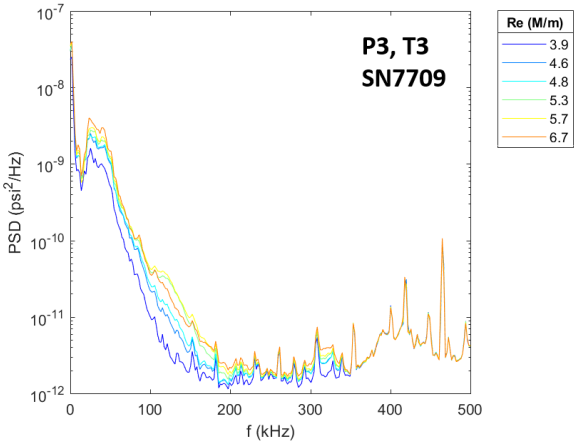
P3, T3
SN7709
Re (M/m)
3.9
4.6
4.8
5.3
5.7
6.7
PSD (psi²/Hz)
f (kHz)

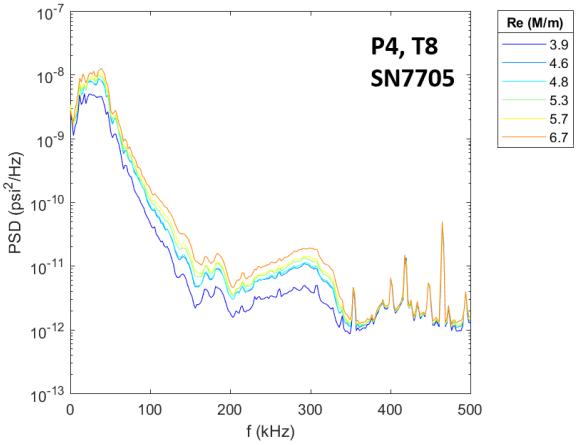
P4, T8
SN7705
Re (M/m)
3.9
4.6
4.8
5.3
5.7
6.7
PSD (psi²/Hz)
f (kHz)

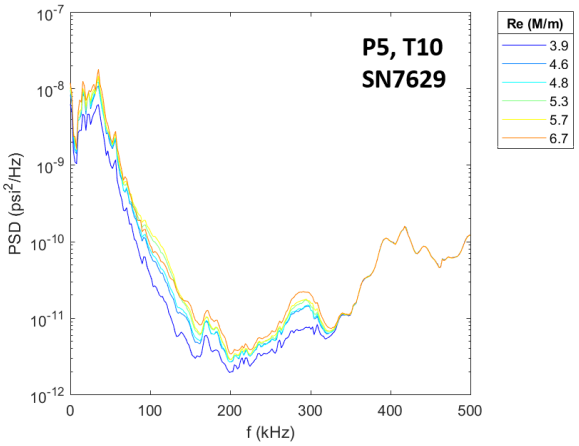
P5, T10
SN7629
Re (M/m)
3.9
4.6
4.8
5.3
5.7
6.7
PSD (psi²/Hz)
f (kHz)

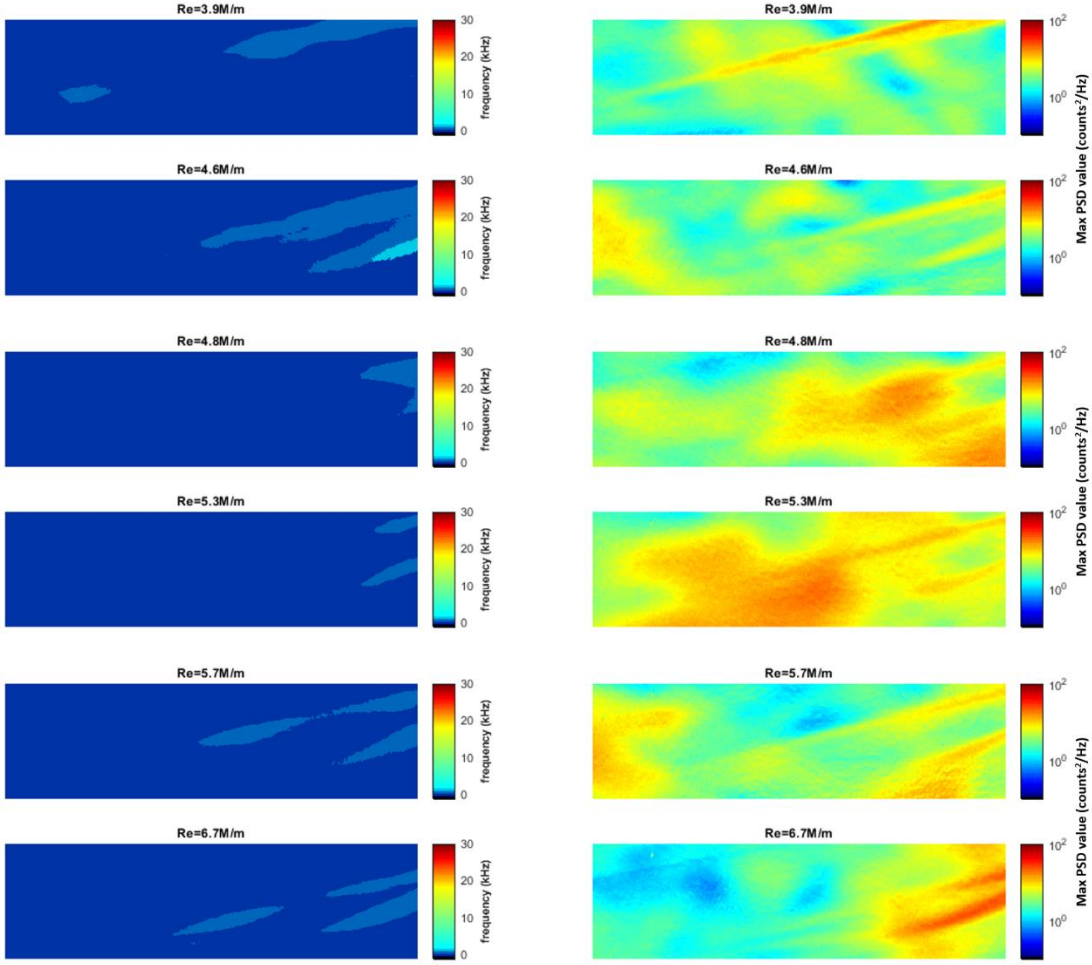
Re=3.9M/m
Re=4.6M/m
Re=4.8M/m
Re=5.3M/m
Re=5.7M/m
Re=6.7M/m
frequency (kHz)
Max PSD value (counts²/Hz)

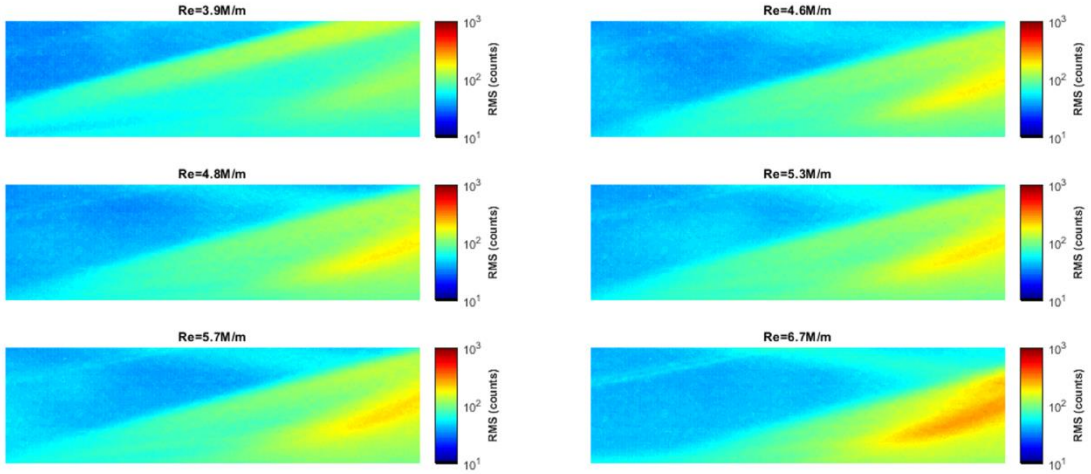
Re=3.9M/m
Re=4.6M/m
Re=4.8M/m
Re=5.3M/m
Re=5.7M/m
Re=6.7M/m
RMS (counts)
10^3
10^2
10^1

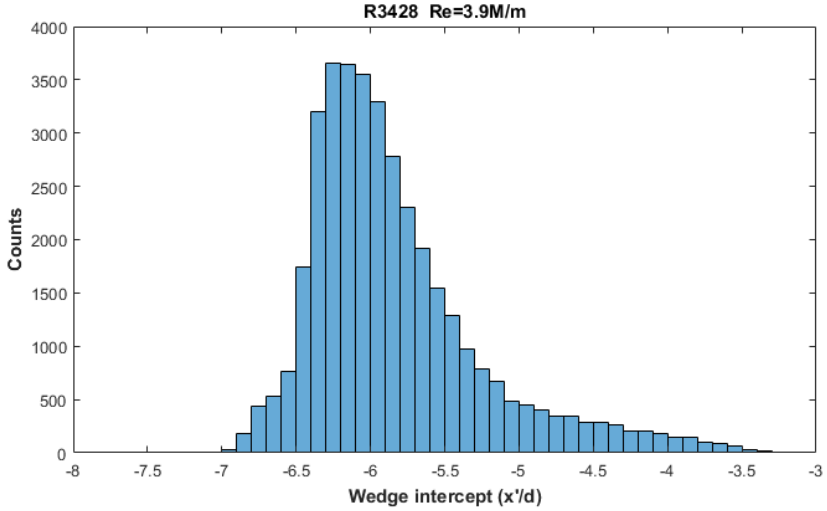
R3428 Re=3.9M/m
Counts
Wedge intercept (x'/d)
4000
3500
3000
2500
2000
1500
1000
500
0
-8
-7.5
-7
-6.5
-6
-5.5
-5
-4.5
-4
-3.5
-3

Run 3429

Surface pressure measurements, IR thermography, and high-speed schlieren made over Re steps.

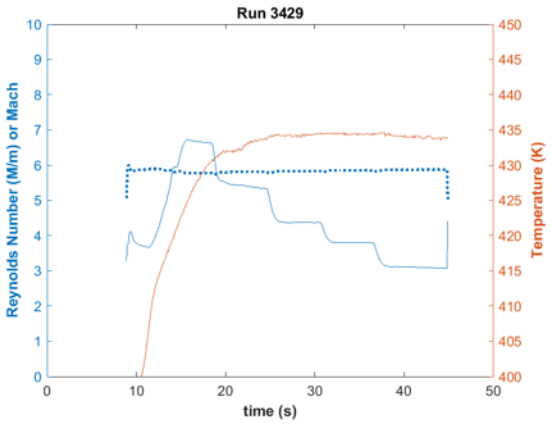

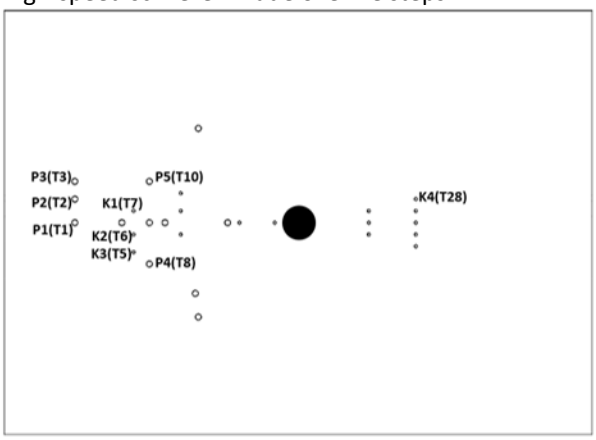

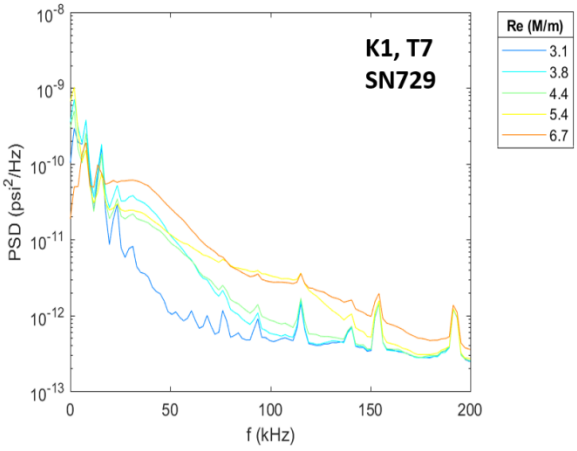

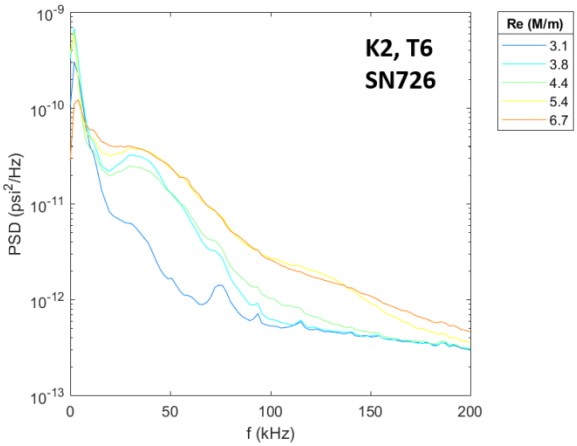

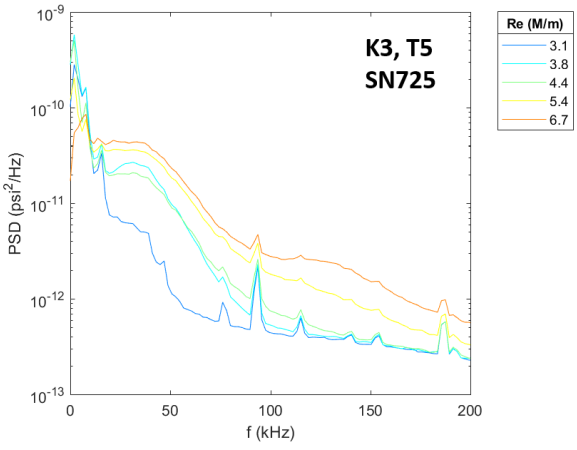

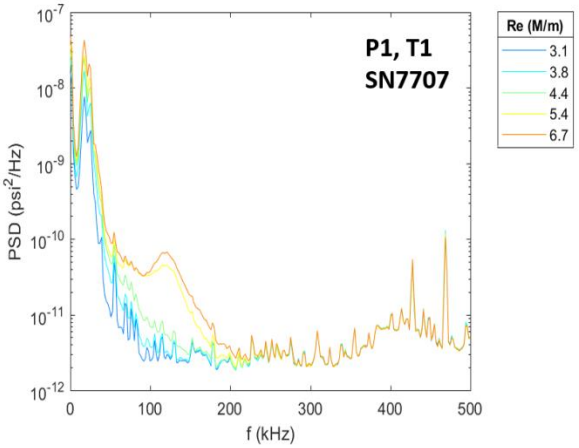
P1, T1
SN7707
Re (M/m)
3.1
3.8
4.4
5.4
6.7
PSD (psi²/Hz)
f (kHz)

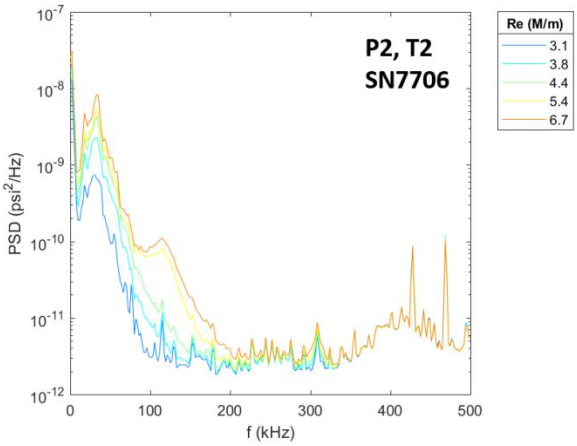
P2, T2
SN7706
Re (M/m)
3.1
3.8
4.4
5.4
6.7
PSD (psi²/Hz)
f (kHz)

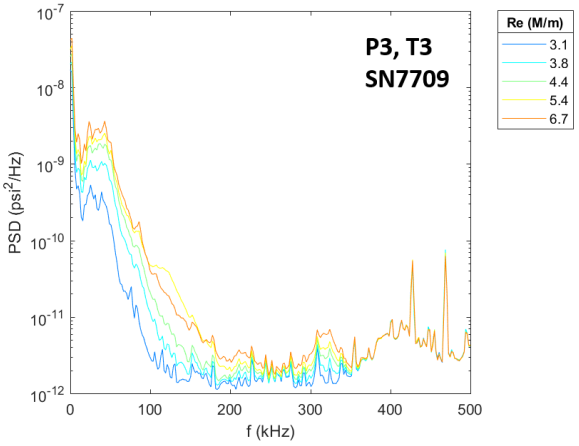
P3, T3
SN7709
Re (M/m)
3.1
3.8
4.4
5.4
6.7
PSD (psi²/Hz)
f (kHz)

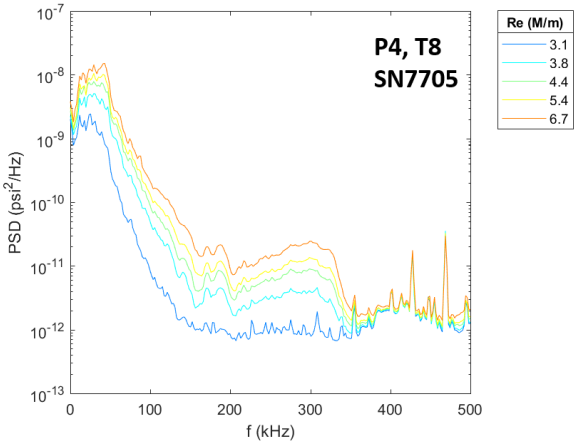
P4, T8
SN7705
Re (M/m)
3.1
3.8
4.4
5.4
6.7
PSD (psi²/Hz)
f (kHz)

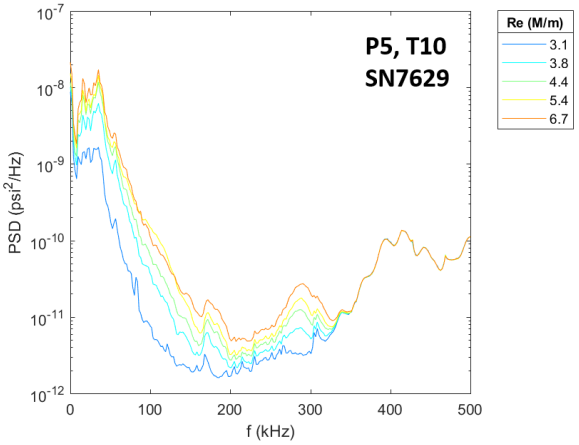
P5, T10
SN7629
Re (M/m)
3.1
3.8
4.4
5.4
6.7
PSD (psi²/Hz)
f (kHz)

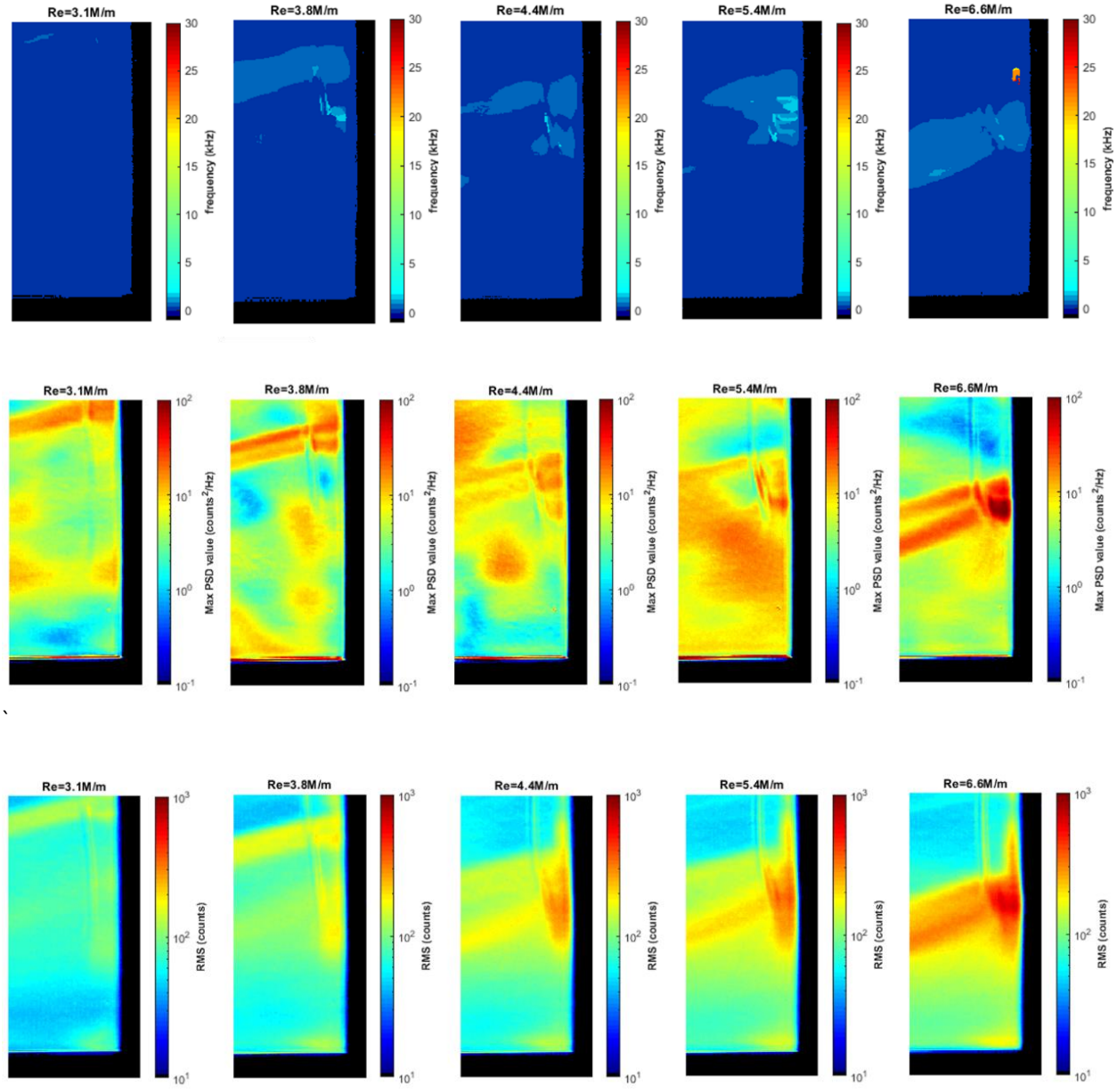
Re=3.1M/m
Re=3.8M/m
Re=4.4M/m
Re=5.4M/m
Re=6.6M/m
frequency (kHz)
Max PSD value (counts²/Hz)
RMS (counts)

Run 3436

Surface pressure measurements, IR thermography, and schlieren made over a Re sweep.

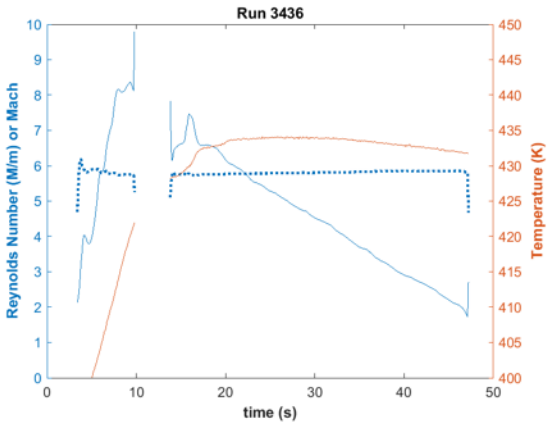

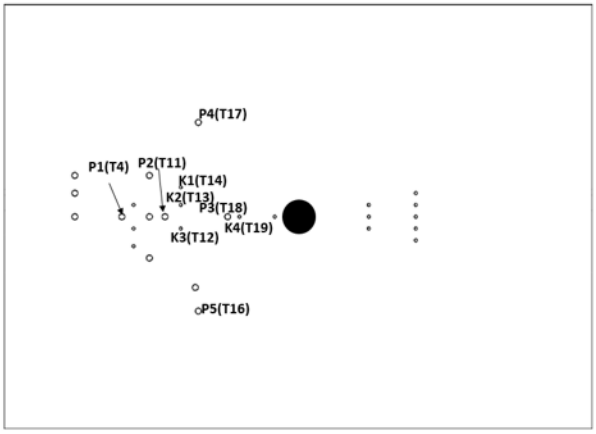

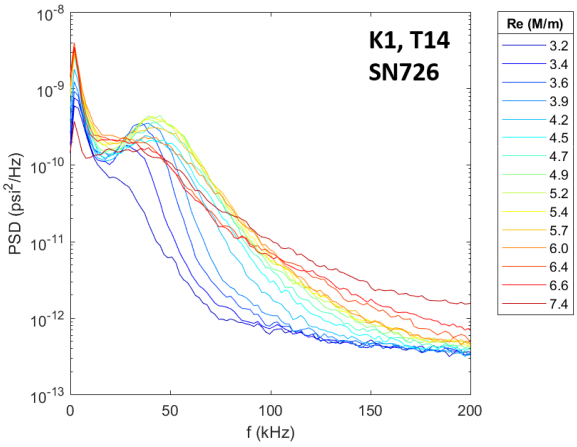

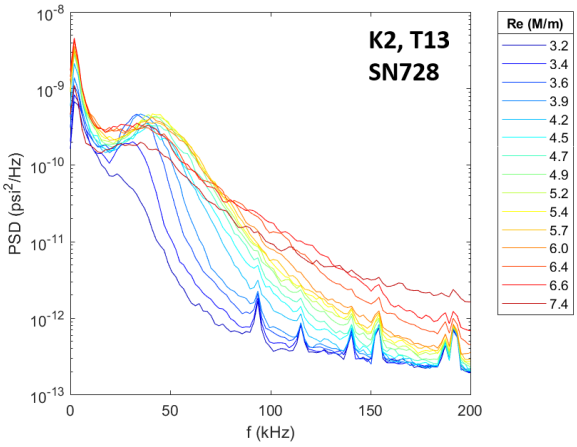

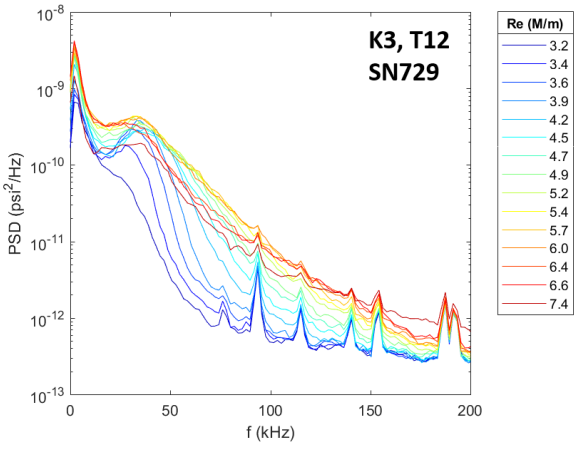

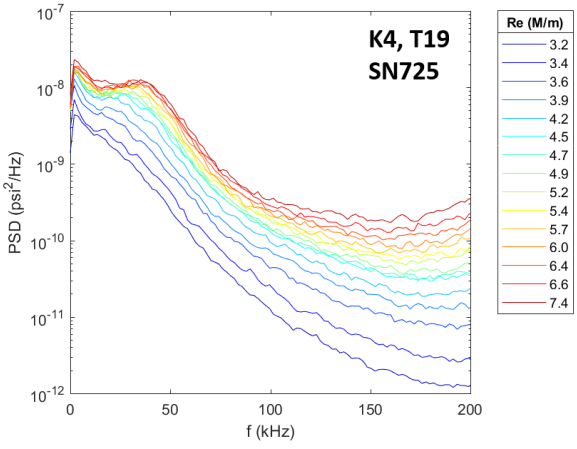

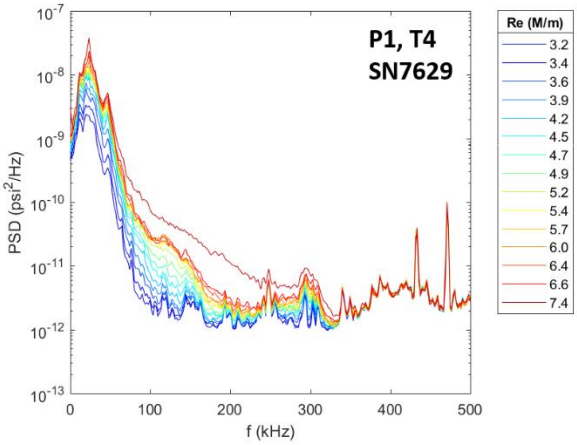
P1, T4
SN7629
PSD (psi²/Hz)
f (kHz)
Re (M/m)
3.2
3.4
3.6
3.9
4.2
4.5
4.7
4.9
5.2
5.4
5.7
6.0
6.4
6.6
7.4

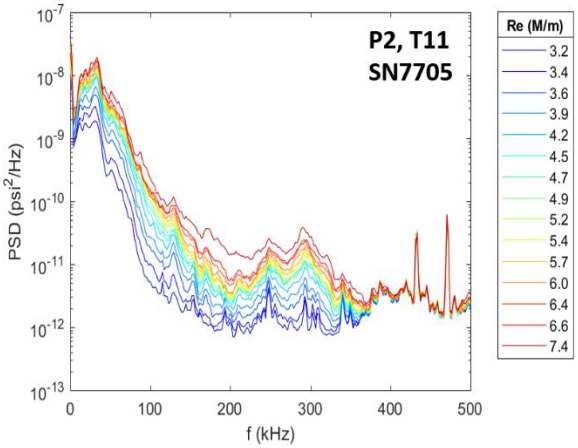
P2, T11
SN7705
PSD (psi²/Hz)
f (kHz)
Re (M/m)
3.2
3.4
3.6
3.9
4.2
4.5
4.7
4.9
5.2
5.4
5.7
6.0
6.4
6.6
7.4

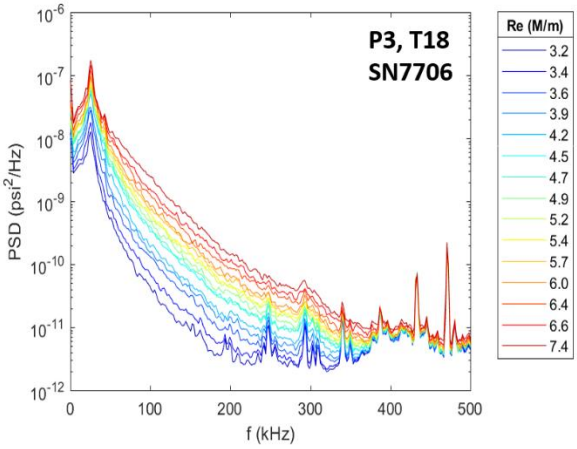
P3, T18
SN7706
PSD (psi²/Hz)
f (kHz)
Re (M/m)
3.2
3.4
3.6
3.9
4.2
4.5
4.7
4.9
5.2
5.4
5.7
6.0
6.4
6.6
7.4

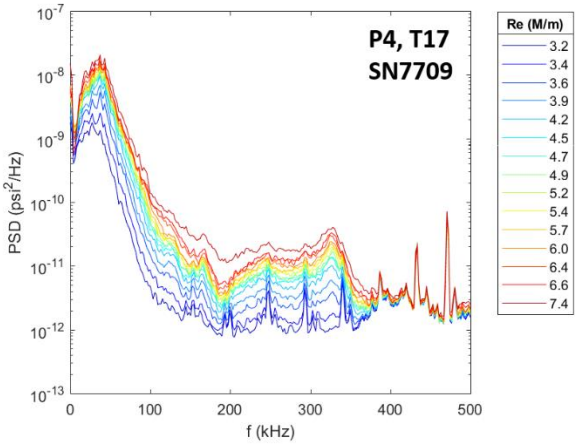
P4, T17
SN7709
PSD (psi²/Hz)
f (kHz)
Re (M/m)
3.2
3.4
3.6
3.9
4.2
4.5
4.7
4.9
5.2
5.4
5.7
6.0
6.4
6.6
7.4

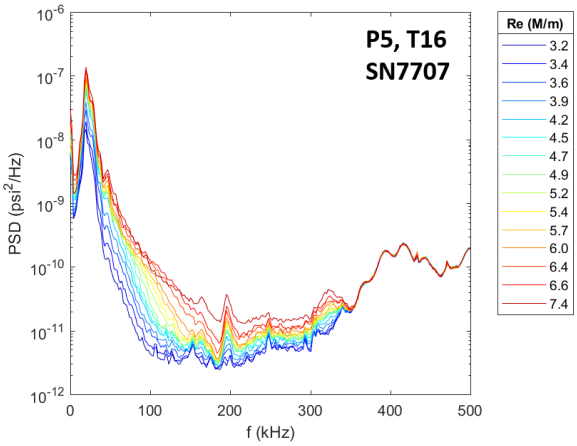
P5, T16
SN7707
PSD (psi²/Hz)
f (kHz)
Re (M/m)
3.2
3.4
3.6
3.9
4.2
4.5
4.7
4.9
5.2
5.4
5.7
6.0
6.4
6.6
7.4

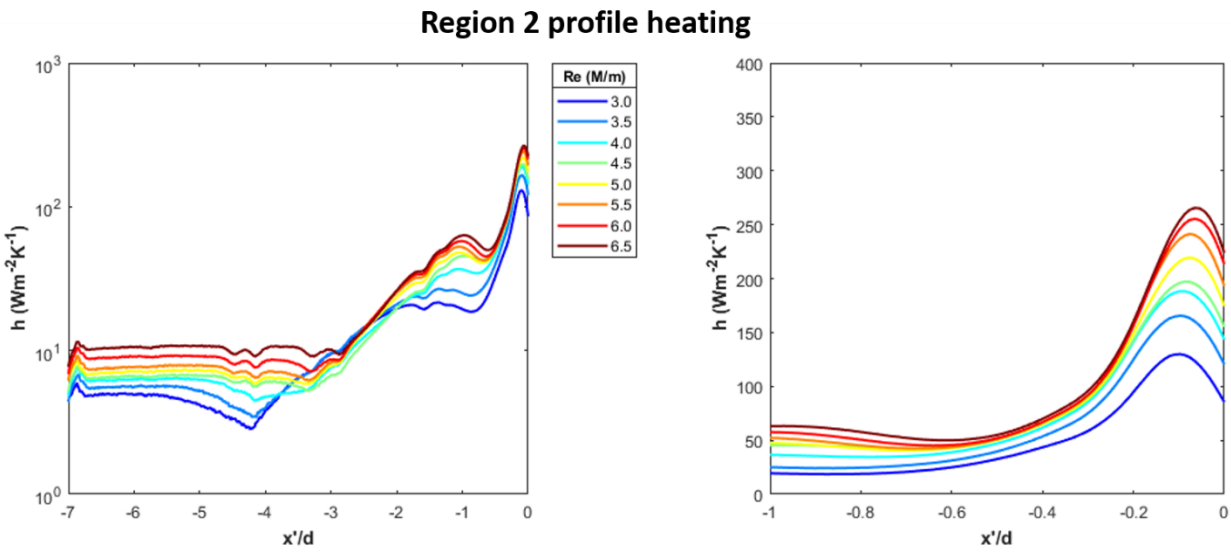

Run 3439

Surface pressure measurements, IR thermography, and high-speed schlieren made over Re steps.

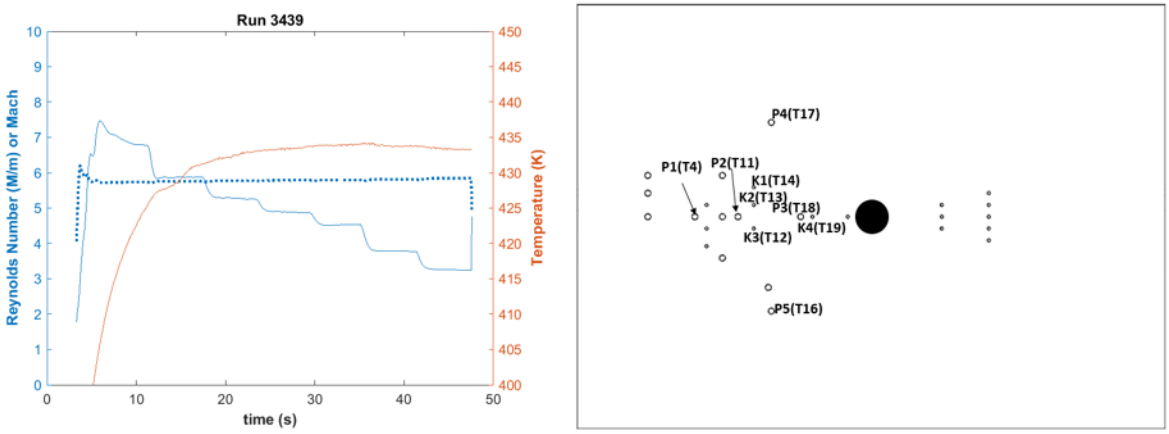

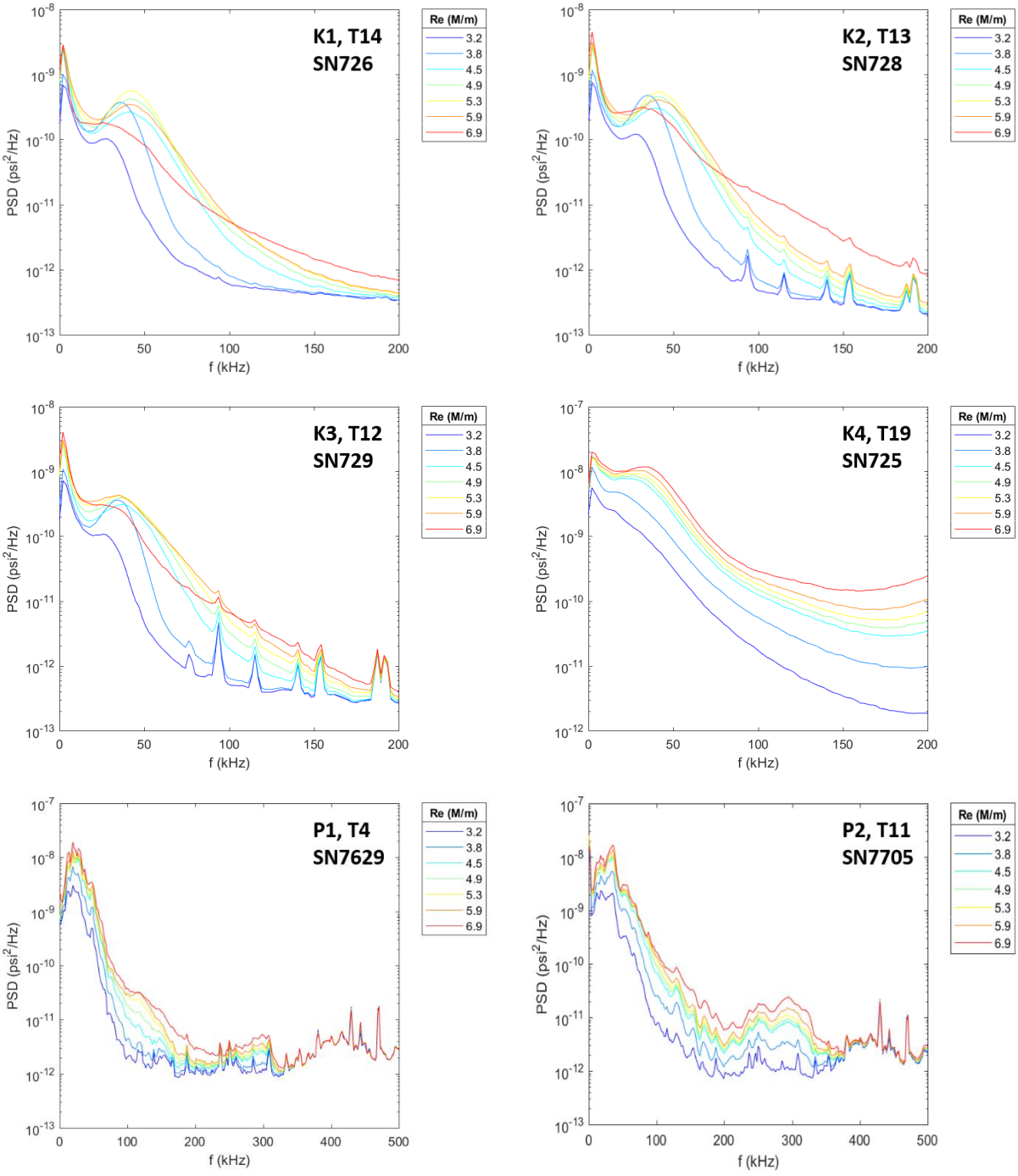
K1, T14
SN726
K2, T13
SN728
K3, T12
SN729
K4, T19
SN725
P1, T4
SN7629
P2, T11
SN7705
Re (M/m)
3.2
3.8
4.5
4.9
5.3
5.9
6.9
PSD (psi²/Hz)
f (kHz)

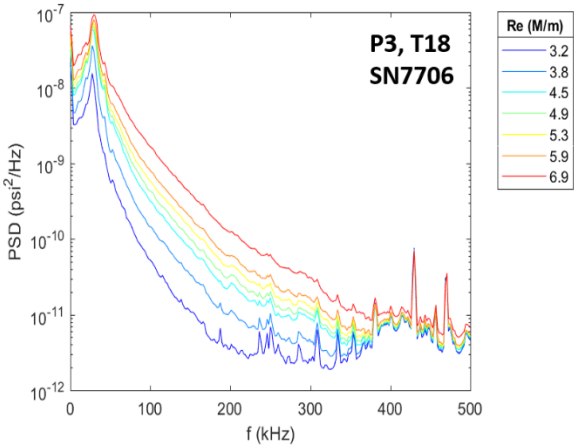
P3, T18
SN7706
Re (M/m)
3.2
3.8
4.5
4.9
5.3
5.9
6.9
PSD (psi²/Hz)
f (kHz)

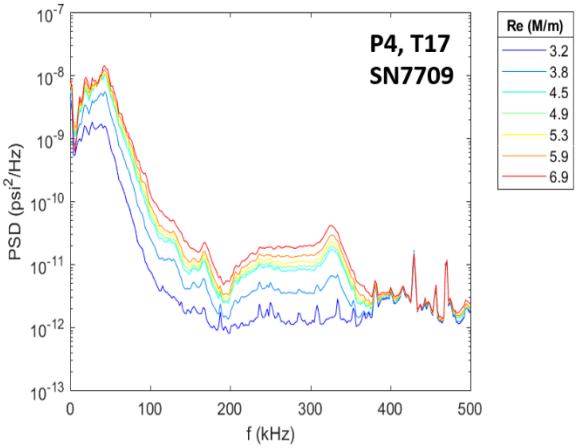
P4, T17
SN7709
Re (M/m)
3.2
3.8
4.5
4.9
5.3
5.9
6.9
PSD (psi²/Hz)
f (kHz)

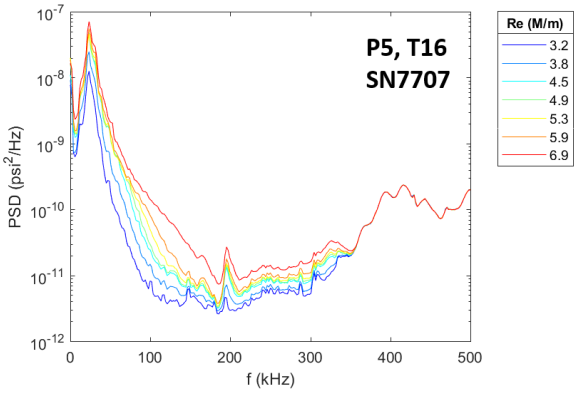
P5, T16
SN7707
Re (M/m)
3.2
3.8
4.5
4.9
5.3
5.9
6.9
PSD (psi²/Hz)
f (kHz)

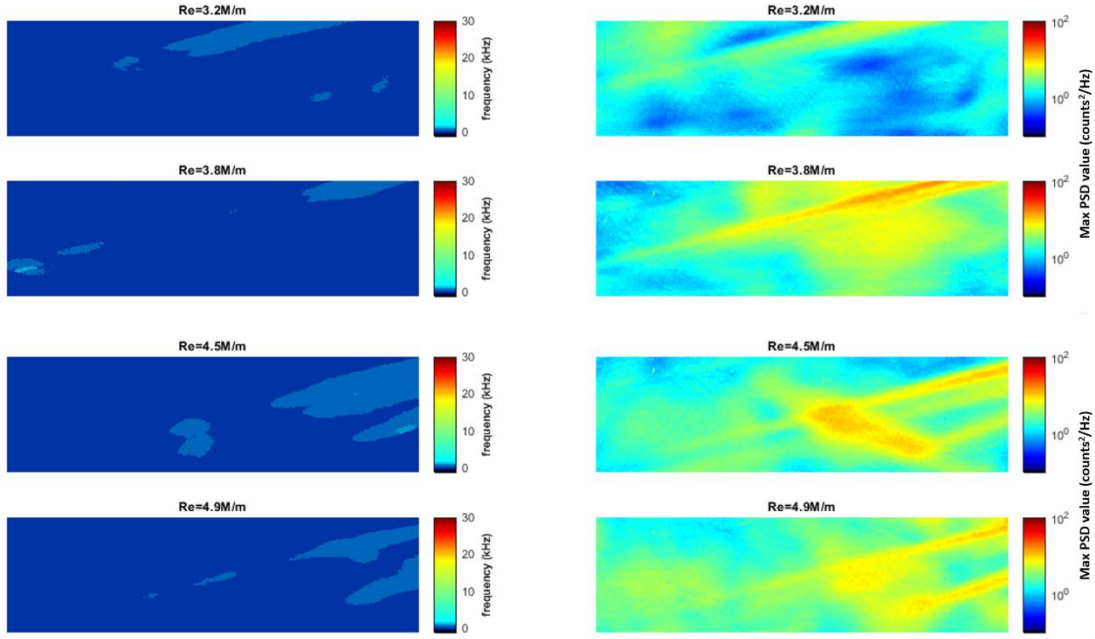
Re=3.2M/m
Re=3.8M/m
Re=4.5M/m
Re=4.9M/m
frequency (kHz)
Max PSD value (counts²/Hz)

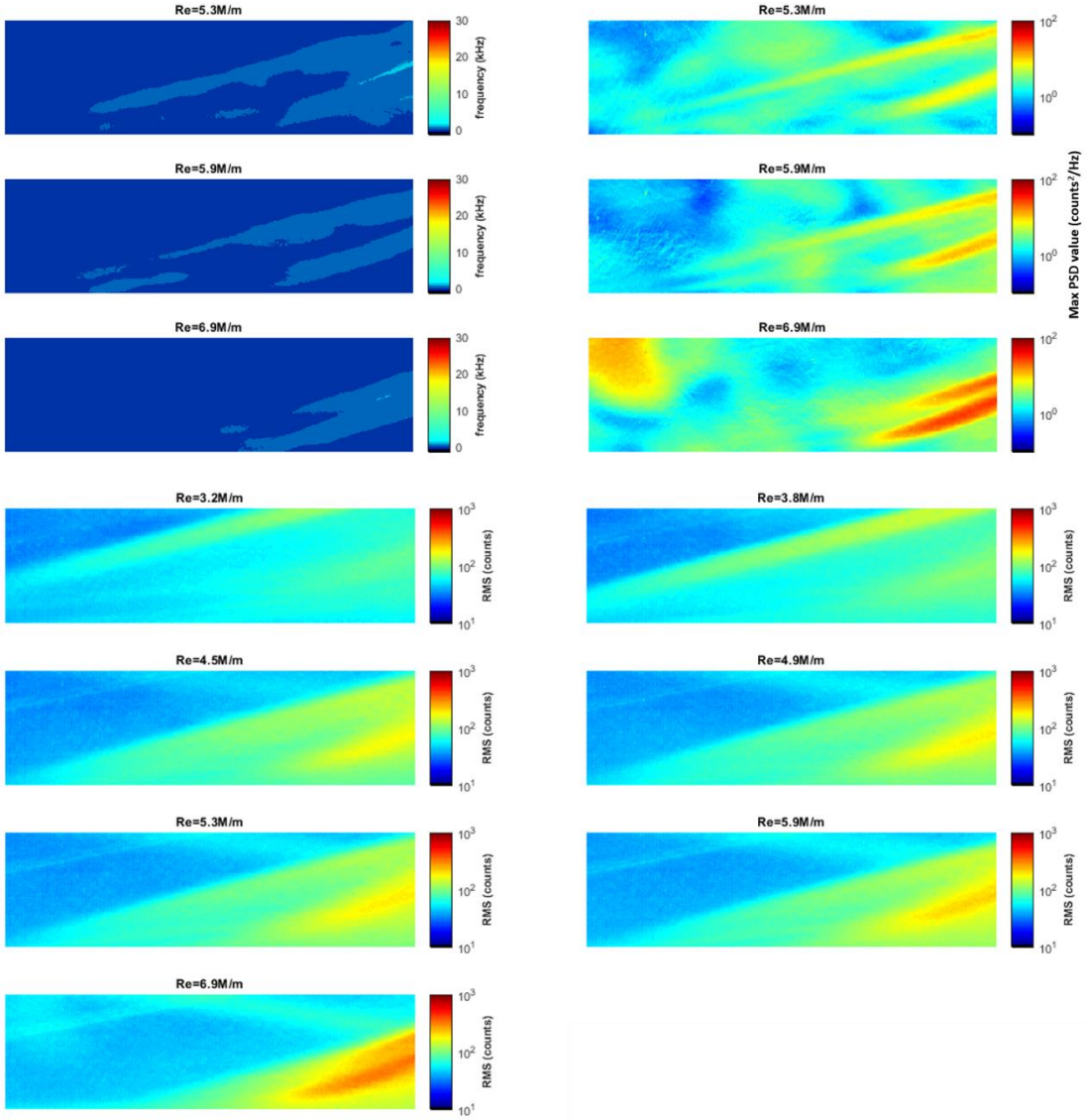
Re=5.3M/m
Re=5.9M/m
Re=6.9M/m
Re=3.2M/m
Re=4.5M/m
Re=5.3M/m
Re=6.9M/m
Re=5.3M/m
Re=5.9M/m
Re=6.9M/m
Re=3.8M/m
Re=4.9M/m
Re=5.9M/m
frequency (kHz)
RMS (counts)
Max PSD value (counts²/Hz)

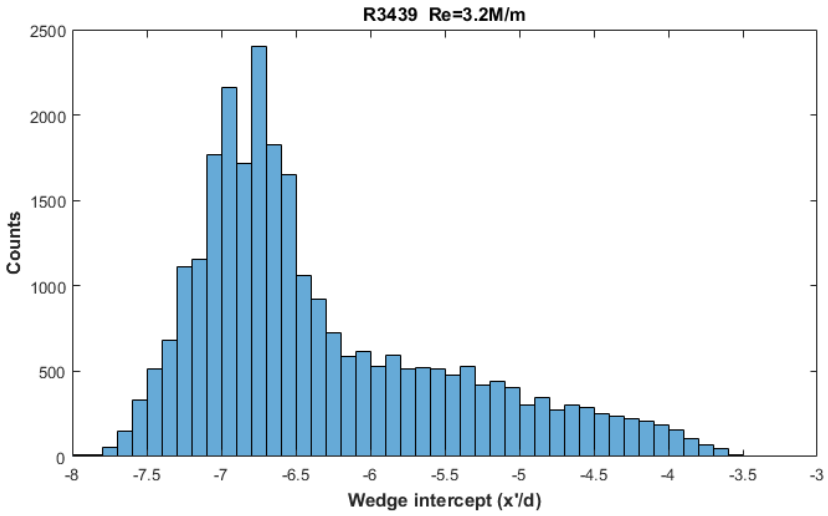
R3439 Re=3.2M/m
Counts
Wedge intercept (x'/d)

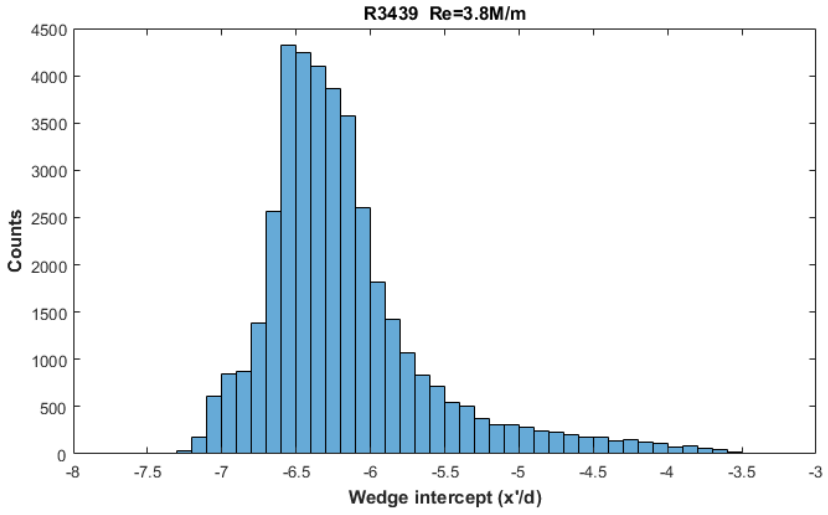
R3439 Re=3.8M/m
Counts
Wedge intercept (x'/d)

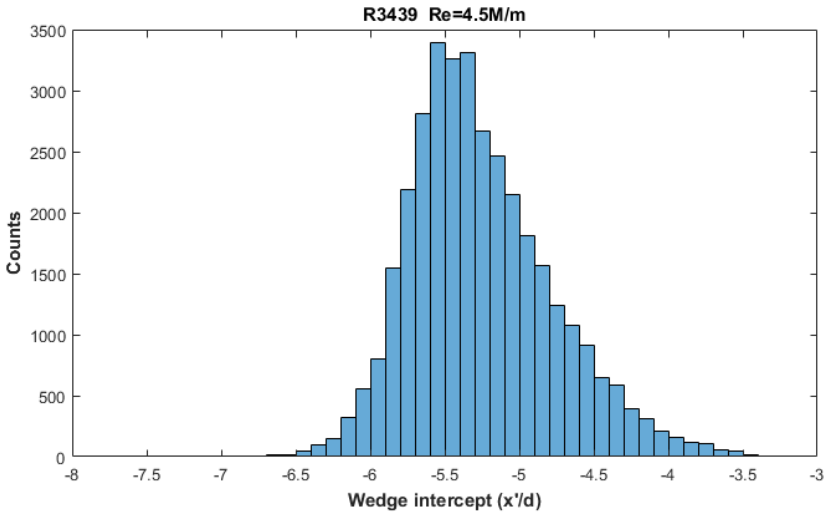
R3439 Re=4.5M/m
Counts
Wedge intercept (x'/d)

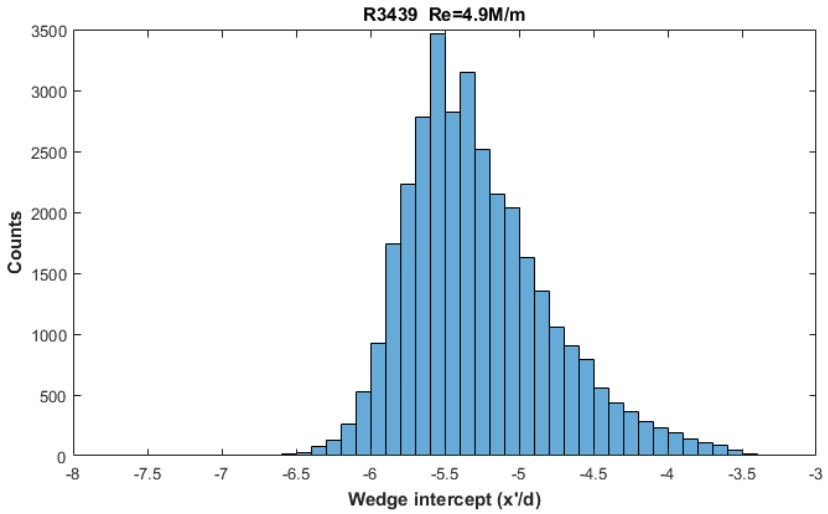
R3439 Re=4.9M/m
Counts
Wedge intercept (x'/d)
0
500
1000
1500
2000
2500
3000
3500
-8
-7.5
-7
-6.5
-6
-5.5
-5
-4.5
-4
-3.5
-3

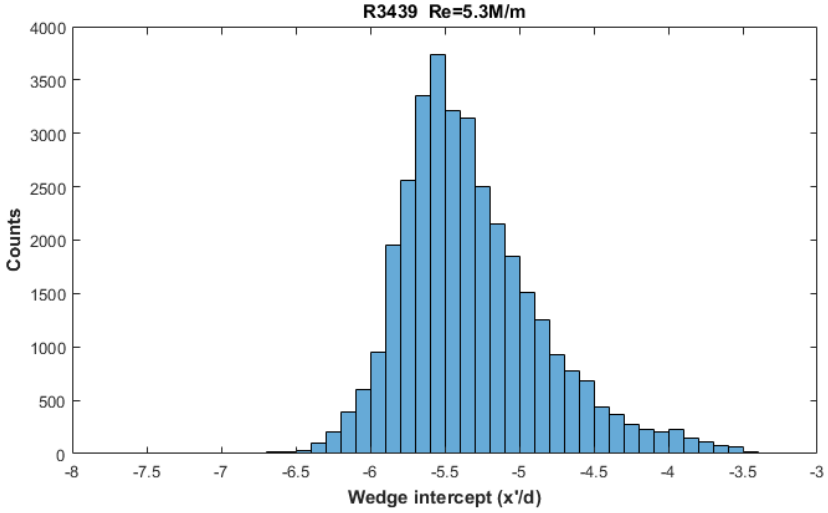
R3439 Re=5.3M/m
Counts
Wedge intercept (x'/d)
0
500
1000
1500
2000
2500
3000
3500
4000
-8
-7.5
-7
-6.5
-6
-5.5
-5
-4.5
-4
-3.5
-3

Run 3441

Surface pressure measurements, IR thermography, and high-speed schlieren made over Re steps.

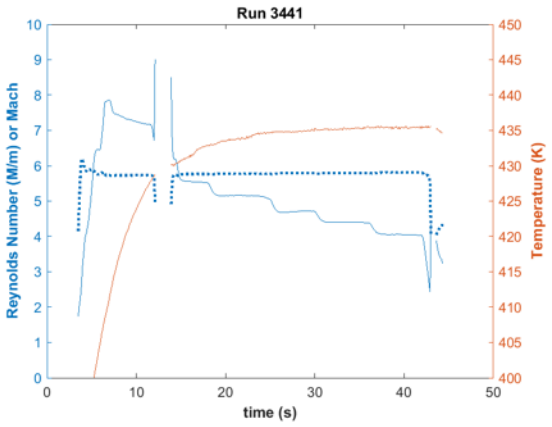

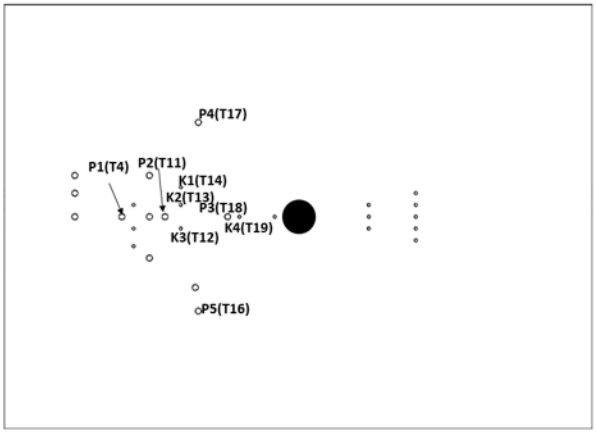

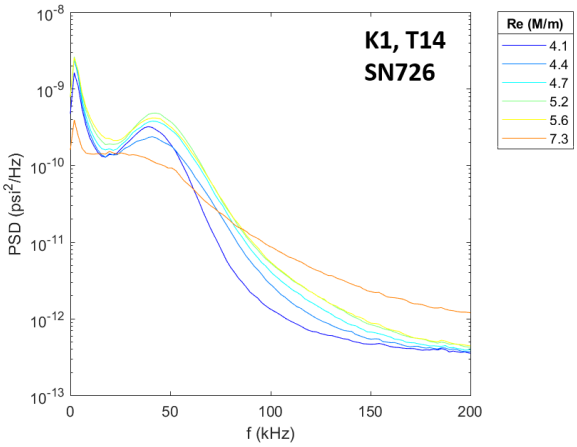

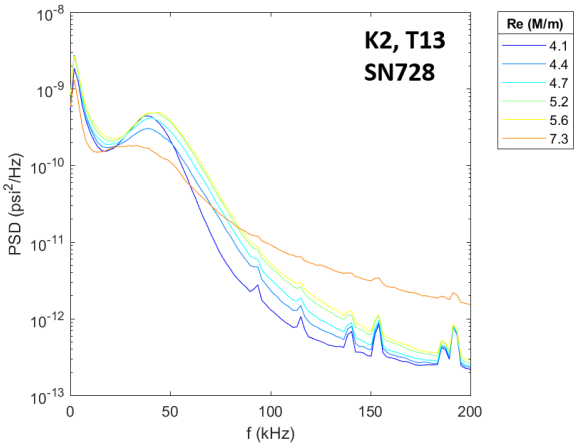

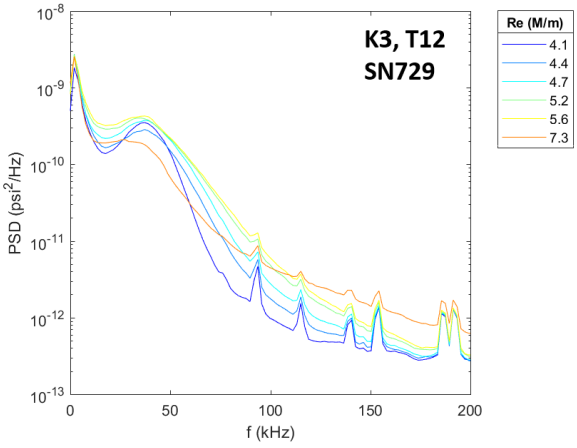

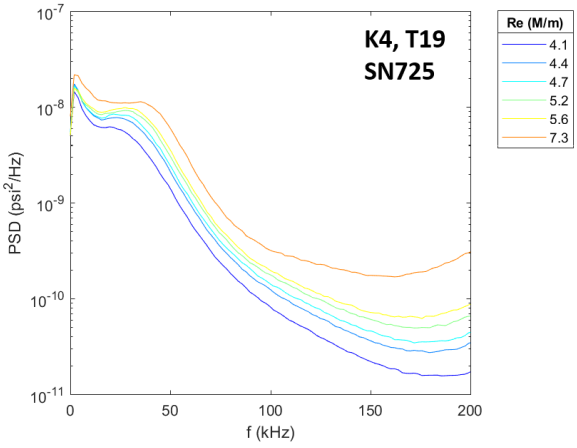

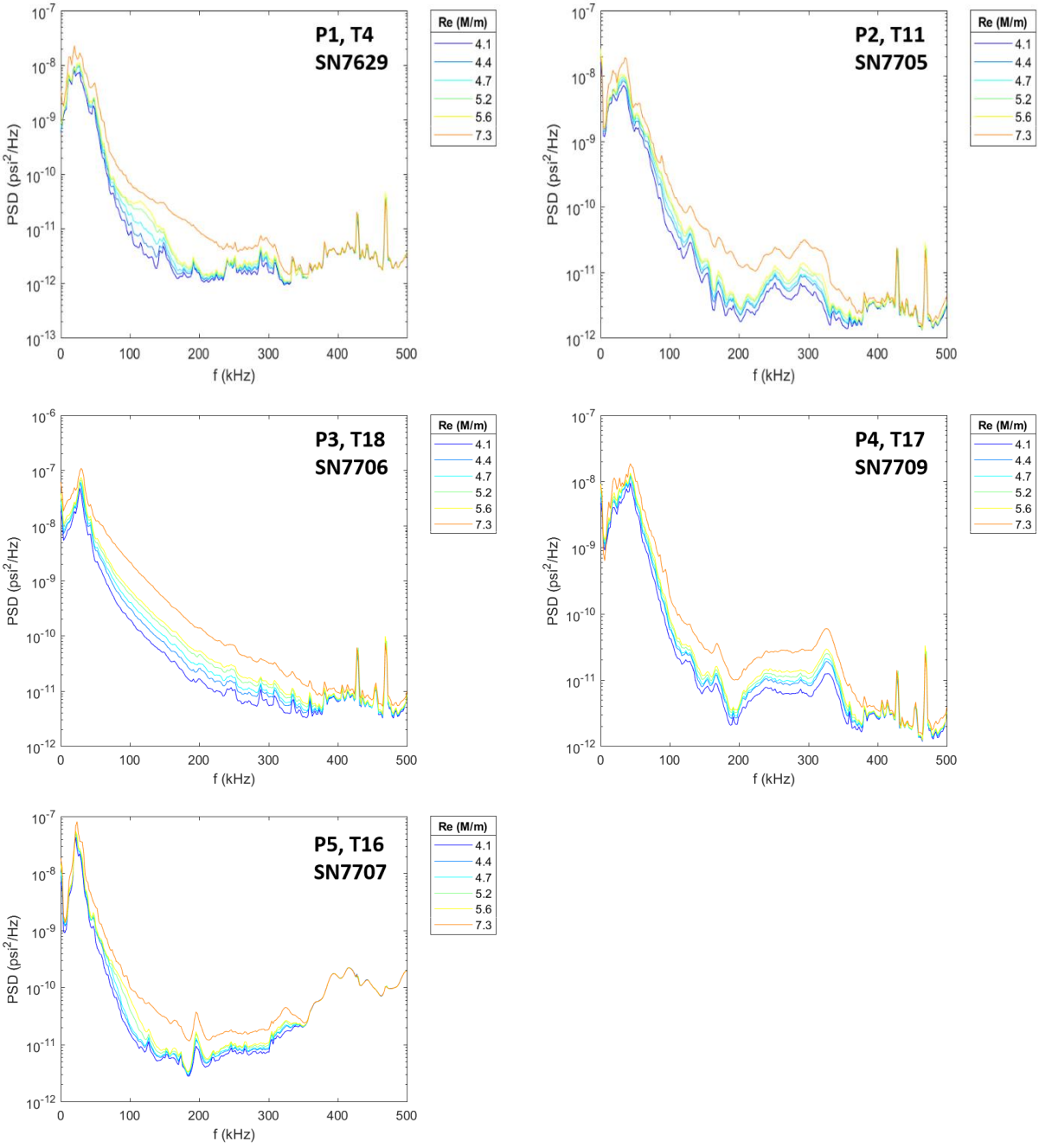
P1, T4
SN7629
P2, T11
SN7705
P3, T18
SN7706
P4, T17
SN7709
P5, T16
SN7707
Re (M/m)
4.1
4.4
4.7
5.2
5.6
7.3
PSD (psi²/Hz)
f (kHz)

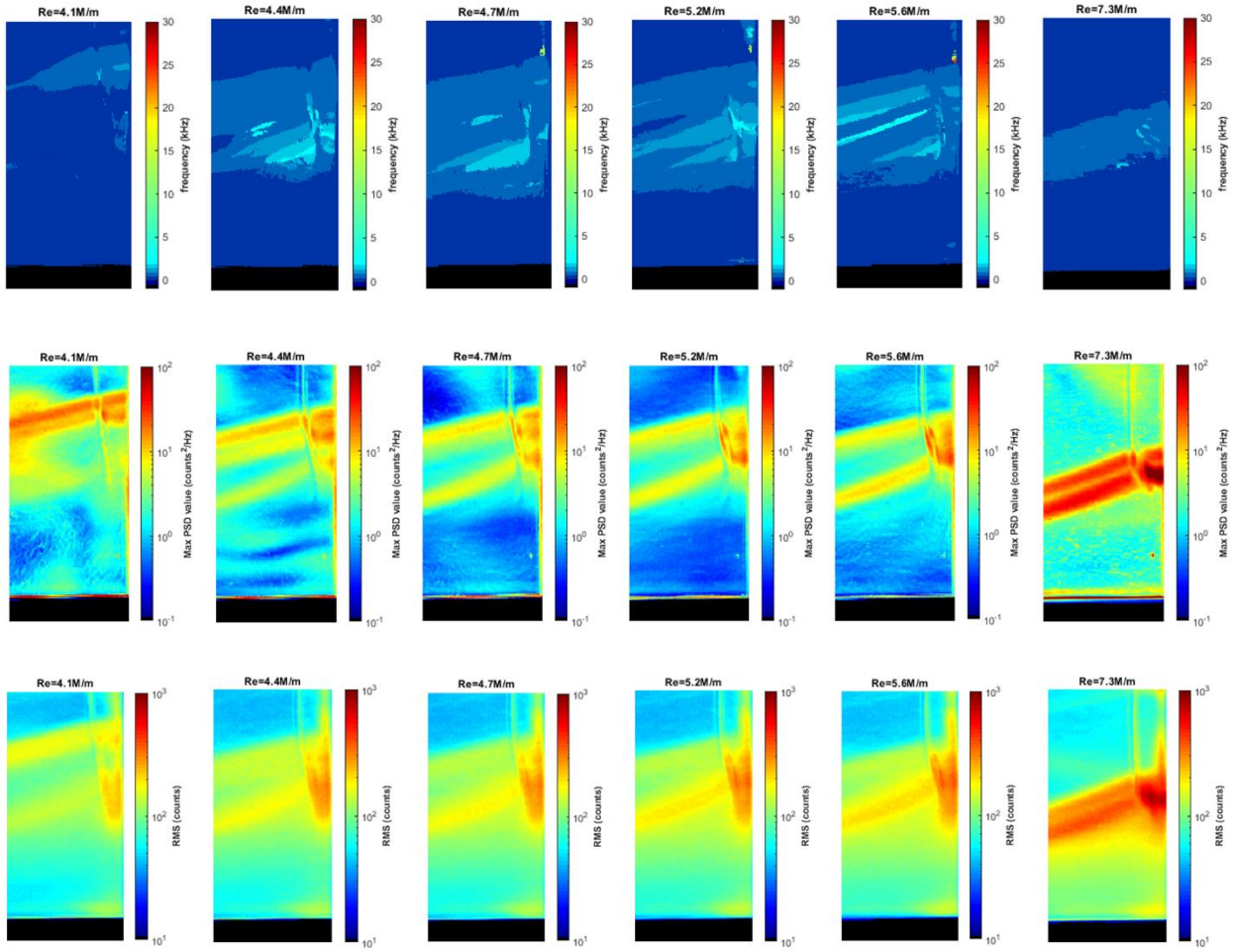

Run 3442

Surface pressure measurements, IR thermography, and schlieren made over a Re sweep.

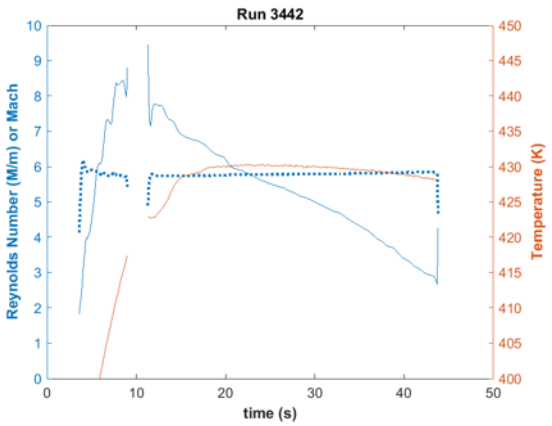

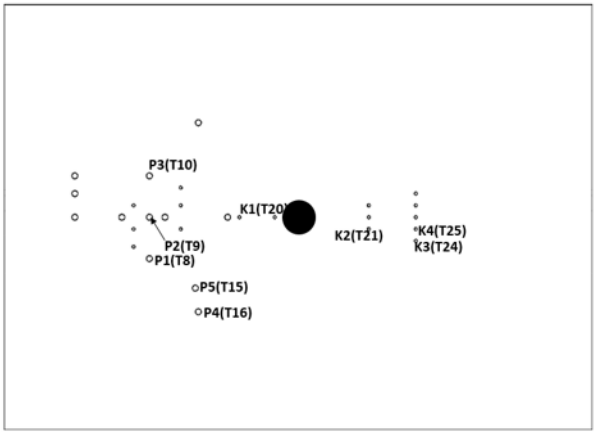

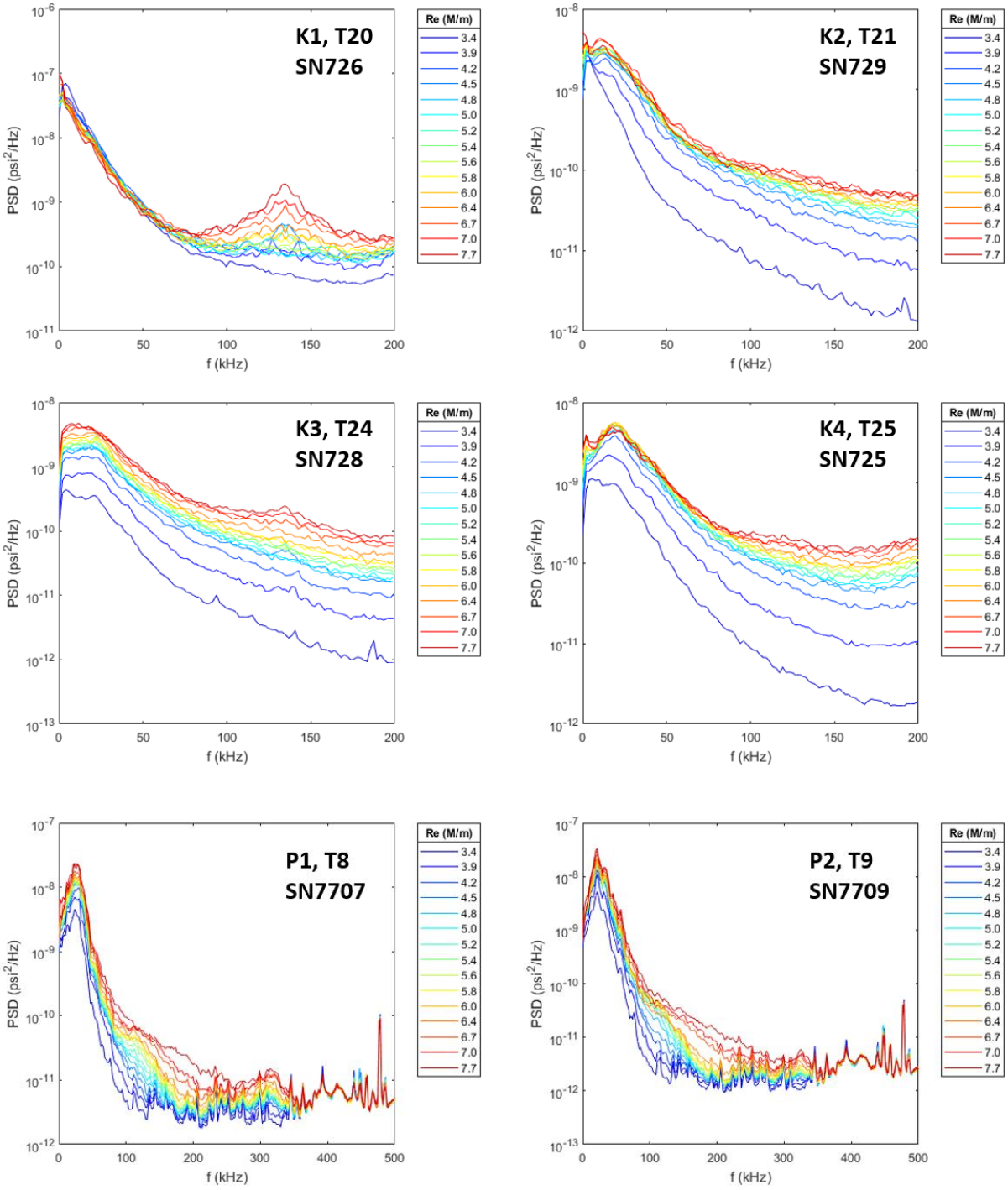
K1, T20
SN726
K2, T21
SN729
K3, T24
SN728
K4, T25
SN725
P1, T8
SN7707
P2, T9
SN7709
PSD (psi²/Hz)
f (kHz)
Re (M/m)
3.4
3.9
4.2
4.5
4.8
5.0
5.2
5.4
5.6
5.8
6.0
6.4
6.7
7.0
7.7

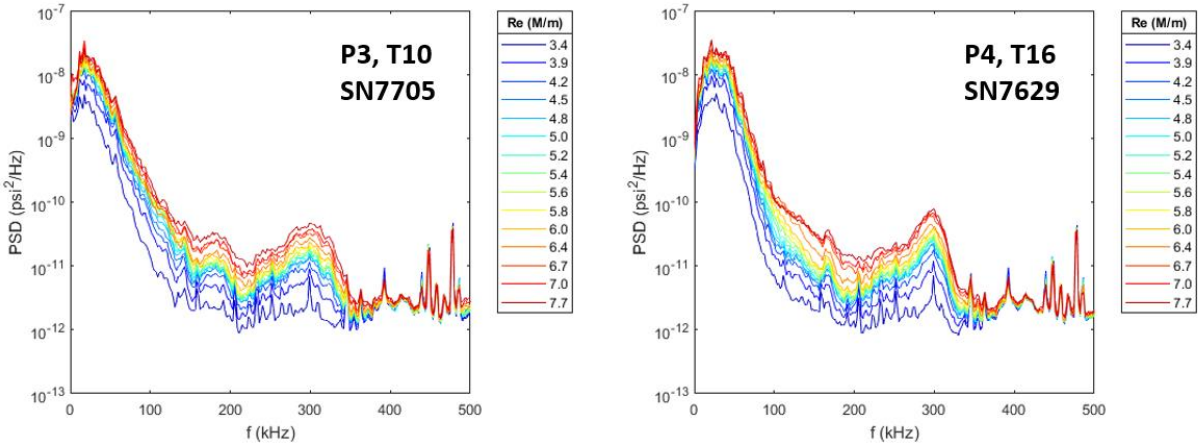

Region 2 profile heating

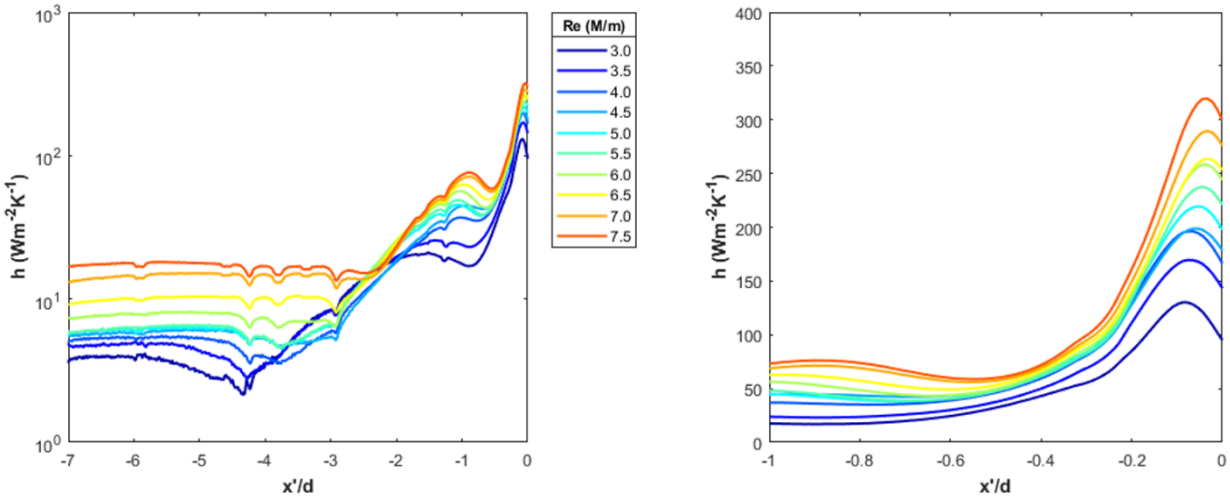

Run 3443

Surface pressure measurements, IR thermography, and high-speed schlieren made over Re steps.

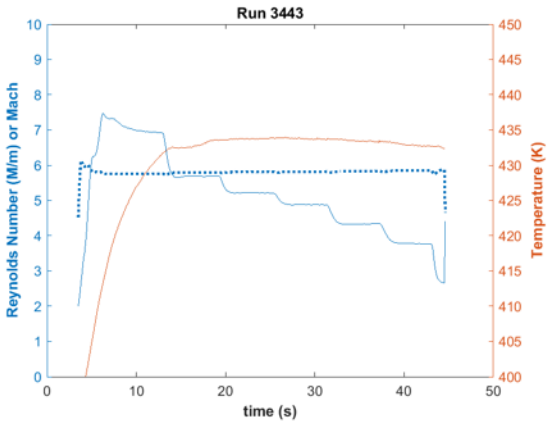

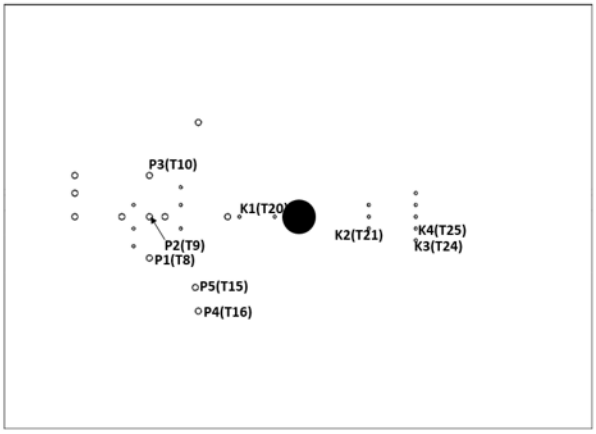

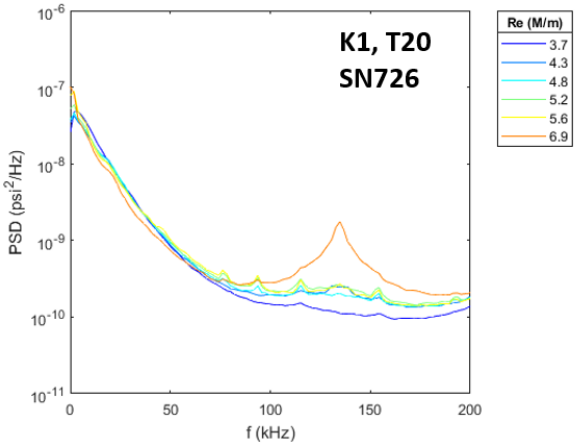

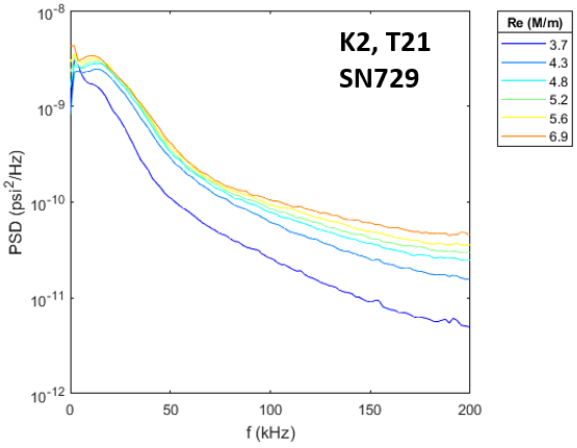

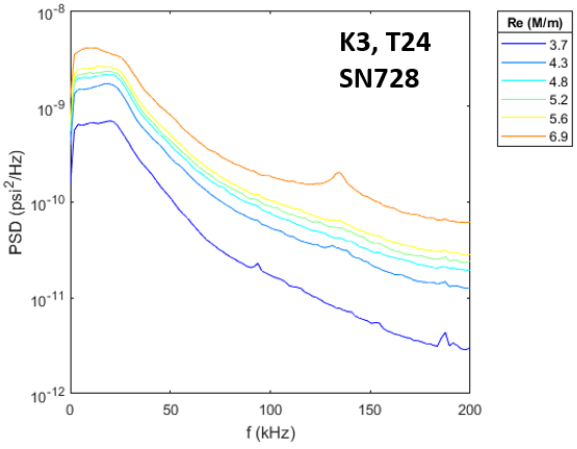

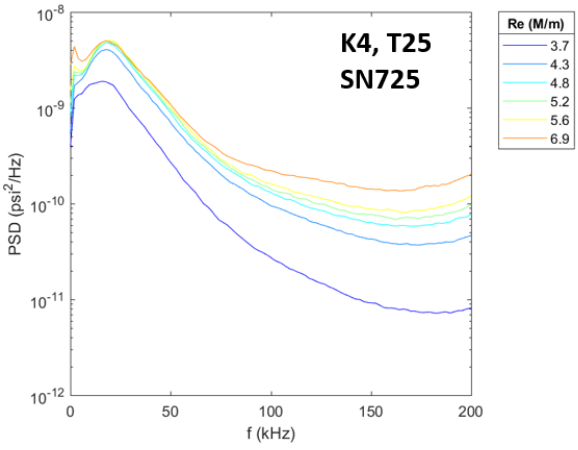

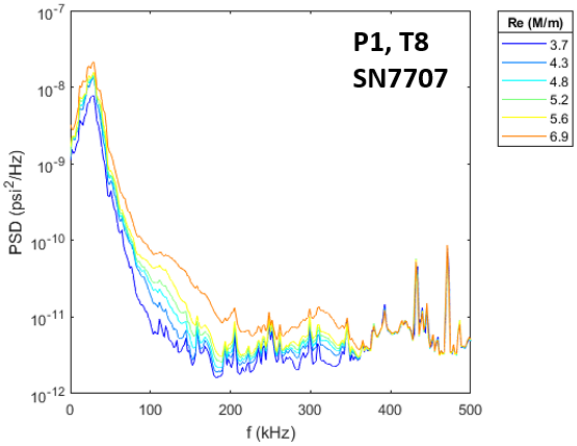
P1, T8
SN7707
Re (M/m)
3.7
4.3
4.8
5.2
5.6
6.9
PSD (psi²/Hz)
f (kHz)

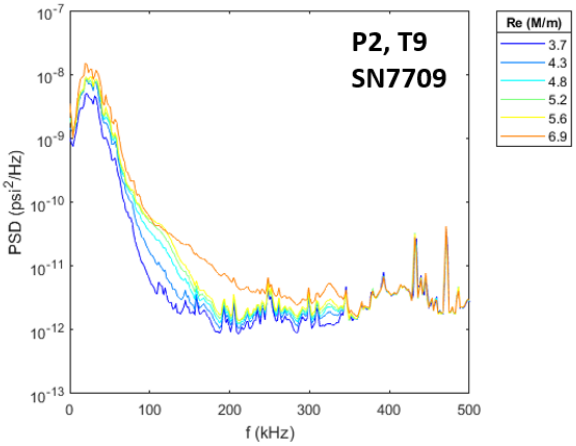
P2, T9
SN7709
Re (M/m)
3.7
4.3
4.8
5.2
5.6
6.9
PSD (psi²/Hz)
f (kHz)

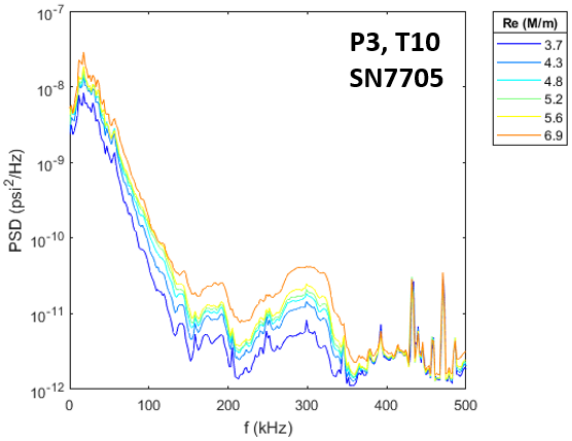
P3, T10
SN7705
Re (M/m)
3.7
4.3
4.8
5.2
5.6
6.9
PSD (psi²/Hz)
f (kHz)

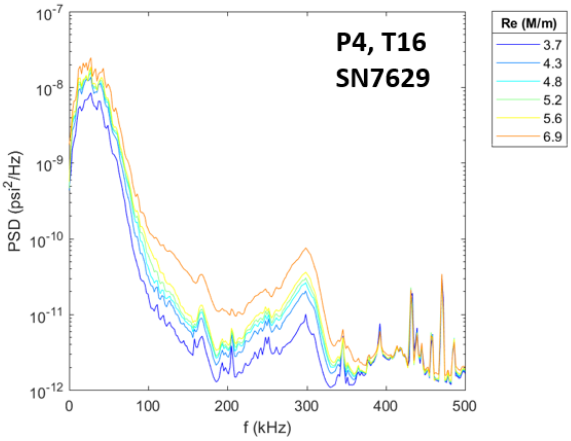
P4, T16
SN7629
Re (M/m)
3.7
4.3
4.8
5.2
5.6
6.9
PSD (psi²/Hz)
f (kHz)

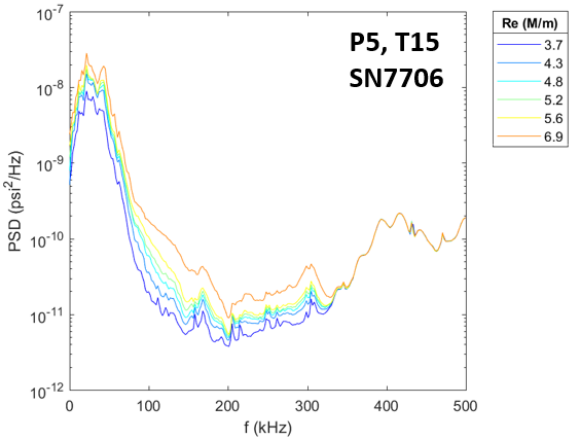
P5, T15
SN7706
Re (M/m)
3.7
4.3
4.8
5.2
5.6
6.9
PSD (psi²/Hz)
f (kHz)

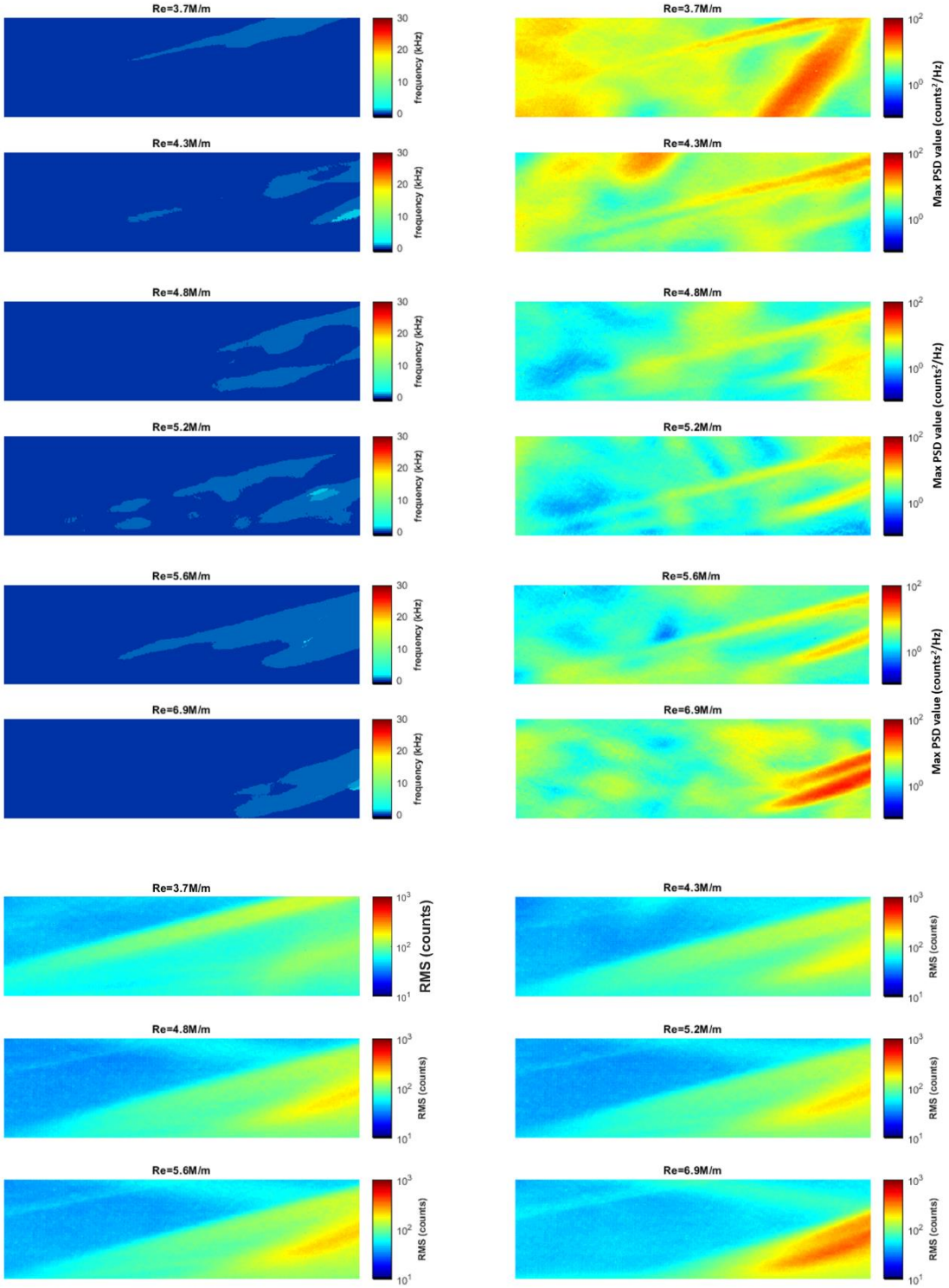
Re=3.7M/m
Re=4.3M/m
Re=4.8M/m
Re=5.2M/m
Re=5.6M/m
Re=6.9M/m
frequency (kHz)
Max PSD value (counts²/Hz)
RMS (counts)

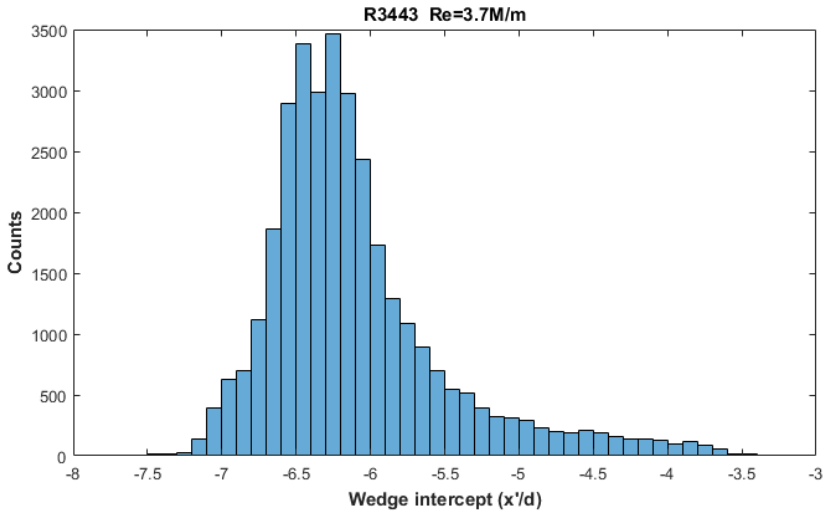
R3443 Re=3.7M/m
Counts
Wedge intercept (x'/d)

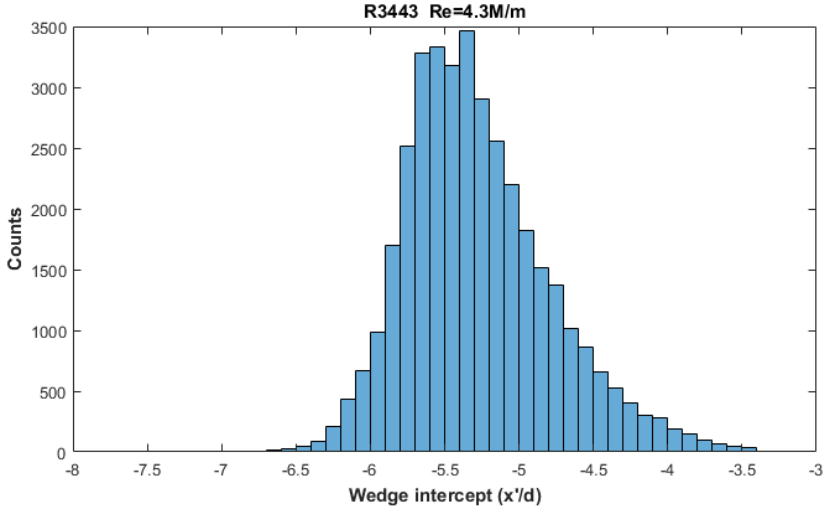
R3443 Re=4.3M/m
Counts
Wedge intercept (x'/d)

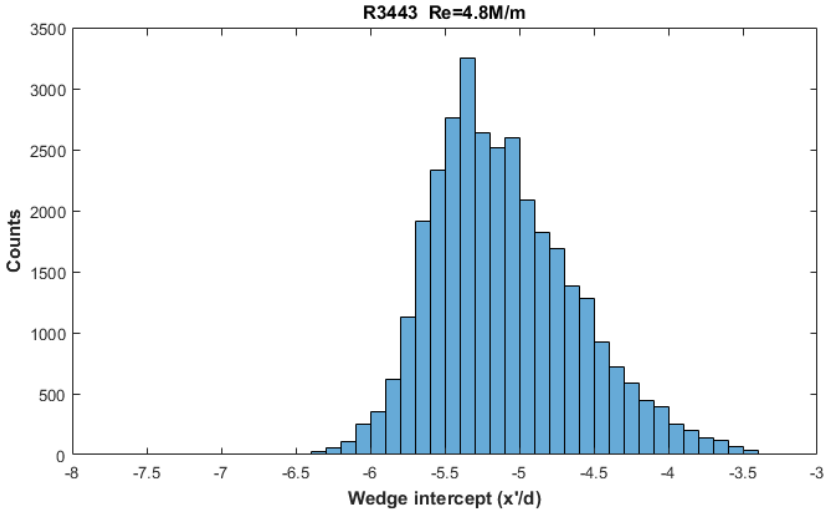
R3443 Re=4.8M/m
Counts
Wedge intercept (x'/d)

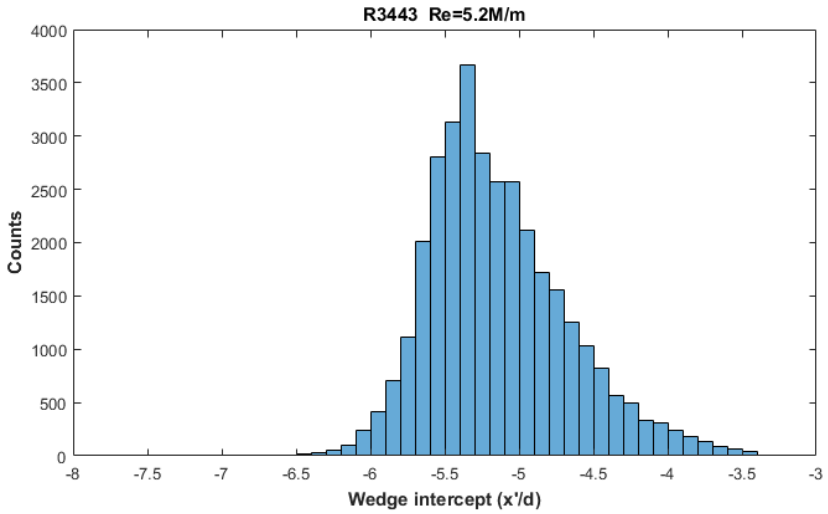

Run 3444

Surface pressure measurements, IR thermography, and high-speed schlieren made over Re steps.

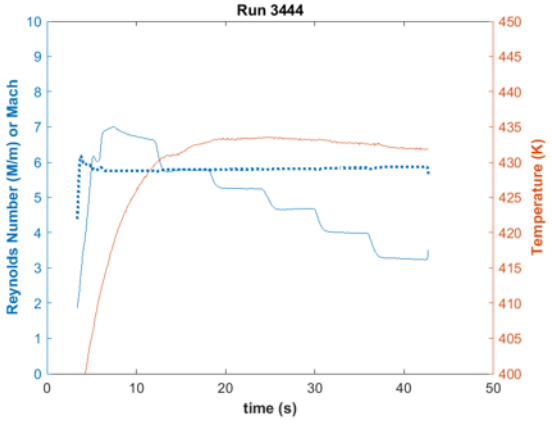

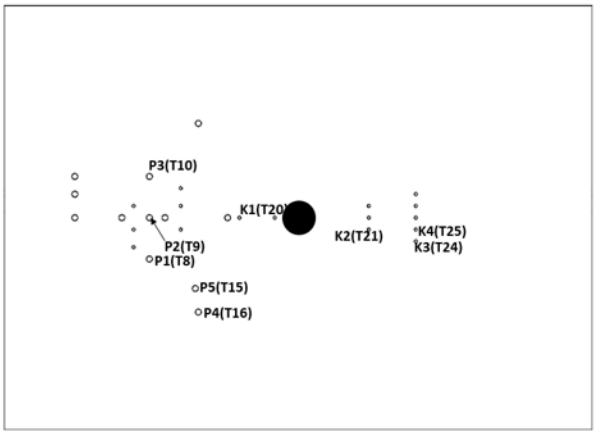

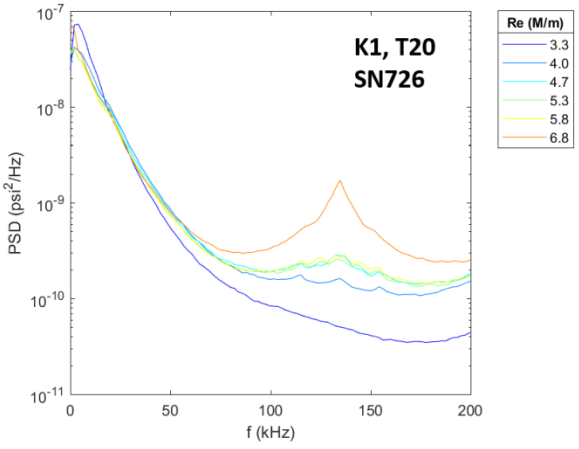

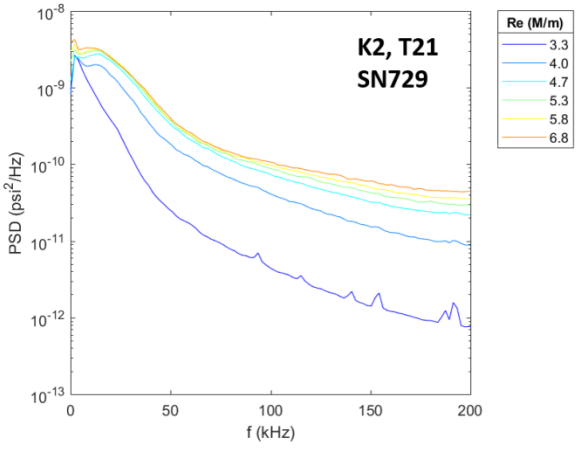

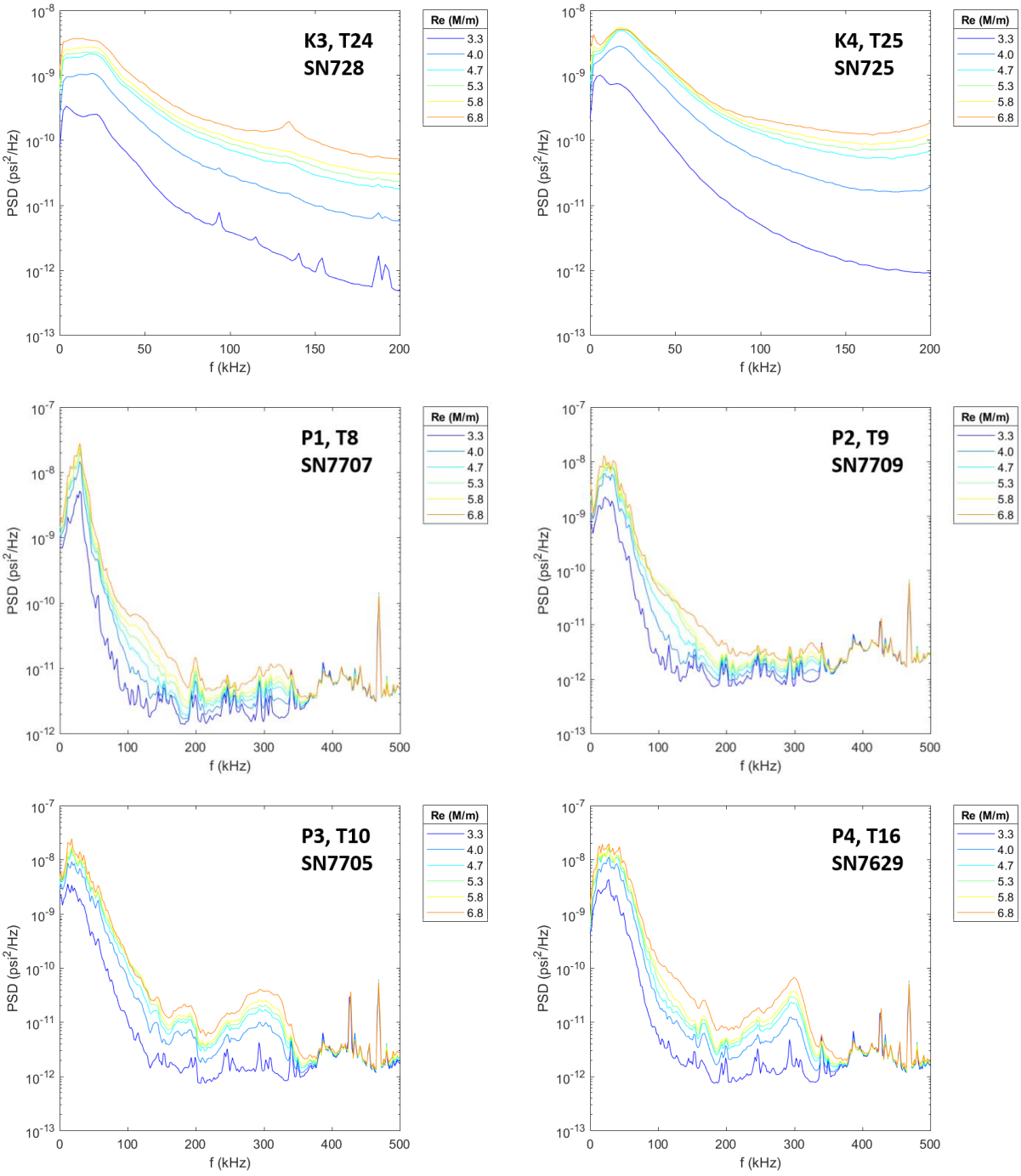
K3, T24
SN728
K4, T25
SN725
P1, T8
SN7707
P2, T9
SN7709
P3, T10
SN7705
P4, T16
SN7629
Re (M/m)
3.3
4.0
4.7
5.3
5.8
6.8
PSD (psi²/Hz)
f (kHz)

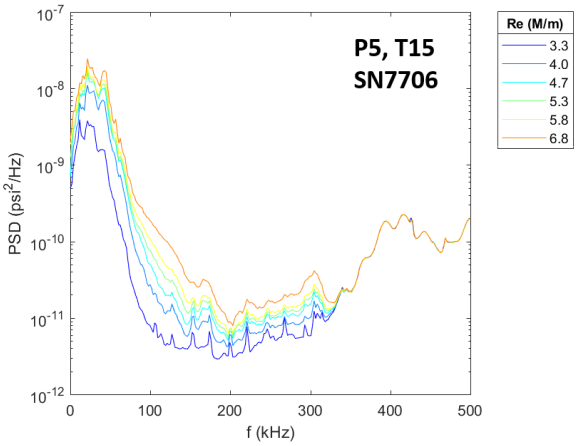
P5, T15
SN7706
Re (M/m)
3.3
4.0
4.7
5.3
5.8
6.8
PSD (psi²/Hz)
f (kHz)

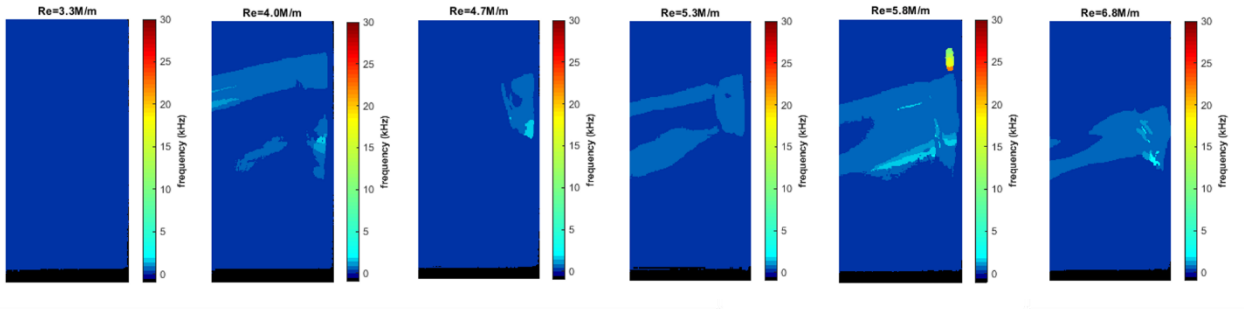
Re=3.3M/m
Re=4.0M/m
Re=4.7M/m
Re=5.3M/m
Re=5.8M/m
Re=6.8M/m
frequency (kHz)

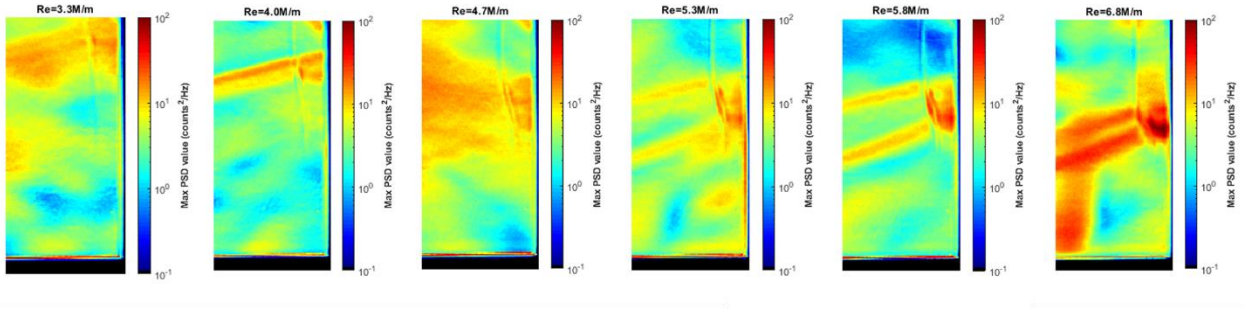
Re=3.3M/m
Re=4.0M/m
Re=4.7M/m
Re=5.3M/m
Re=5.8M/m
Re=6.8M/m
Max PSD value (counts²/Hz)

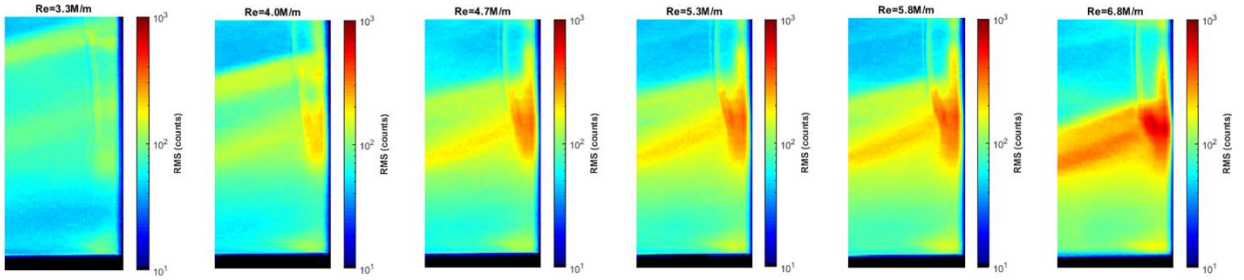
Re=3.3M/m
Re=4.0M/m
Re=4.7M/m
Re=5.3M/m
Re=5.8M/m
Re=6.8M/m
RMS (counts)

No trips, cylinder

Run 3458

Surface pressure measurements, IR thermography, and schlieren made over a Re sweep.

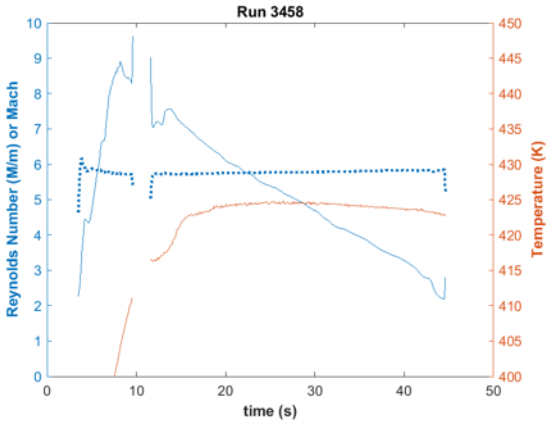

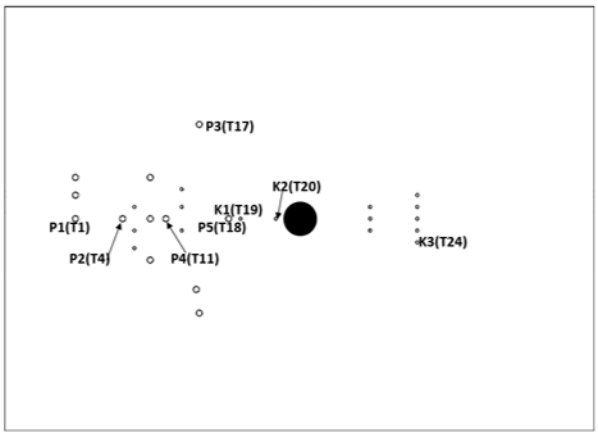

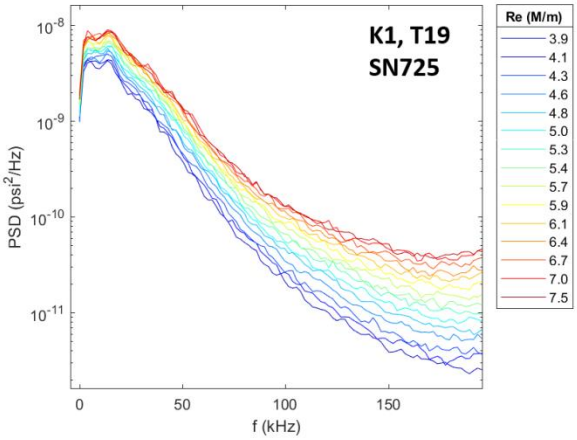

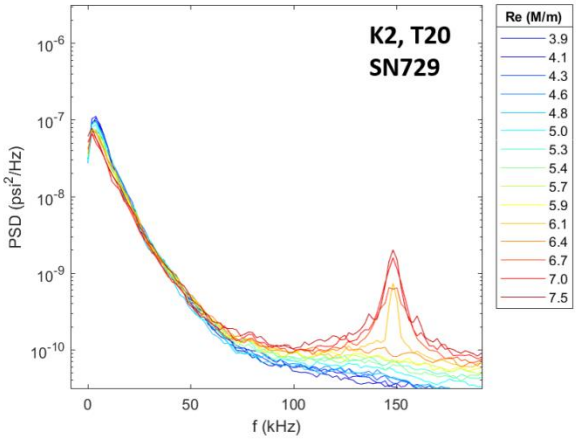

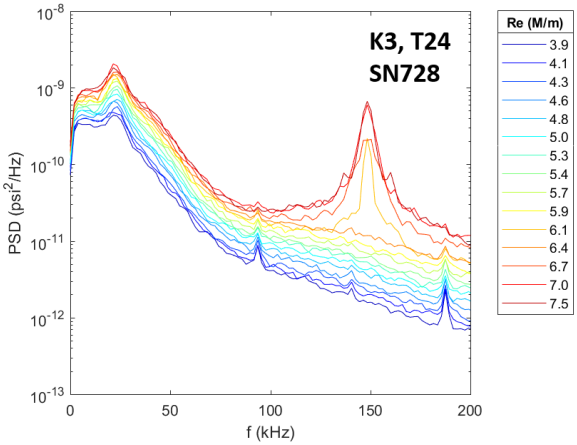

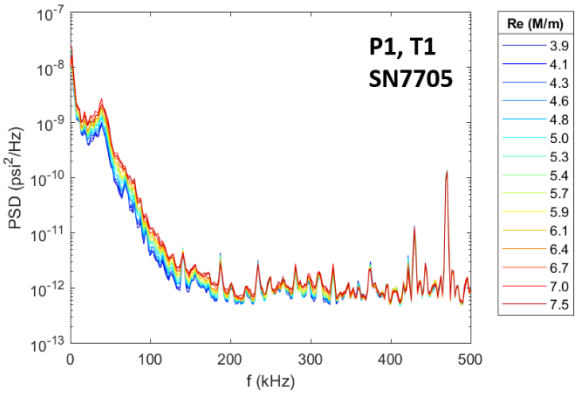
P1, T1
SN7705
PSD (psi²/Hz)
f (kHz)
Re (M/m)
3.9
4.1
4.3
4.6
4.8
5.0
5.3
5.4
5.7
5.9
6.1
6.4
6.7
7.0
7.5

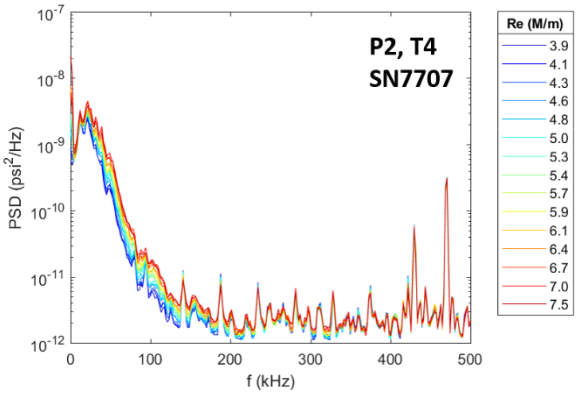
P2, T4
SN7707
PSD (psi²/Hz)
f (kHz)
Re (M/m)
3.9
4.1
4.3
4.6
4.8
5.0
5.3
5.4
5.7
5.9
6.1
6.4
6.7
7.0
7.5

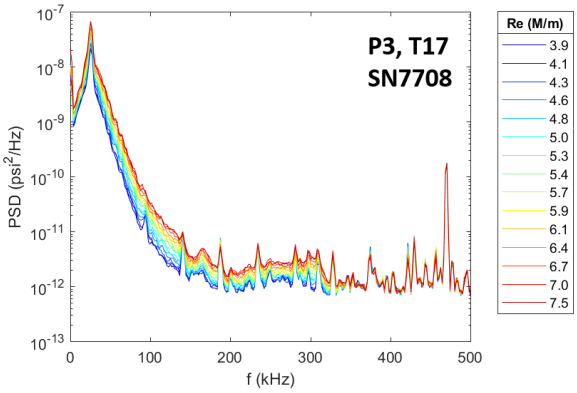
P3, T17
SN7708
PSD (psi²/Hz)
f (kHz)
Re (M/m)
3.9
4.1
4.3
4.6
4.8
5.0
5.3
5.4
5.7
5.9
6.1
6.4
6.7
7.0
7.5

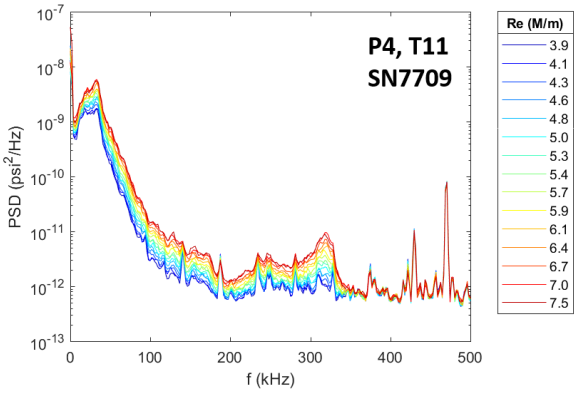
P4, T11
SN7709
PSD (psi²/Hz)
f (kHz)
Re (M/m)
3.9
4.1
4.3
4.6
4.8
5.0
5.3
5.4
5.7
5.9
6.1
6.4
6.7
7.0
7.5

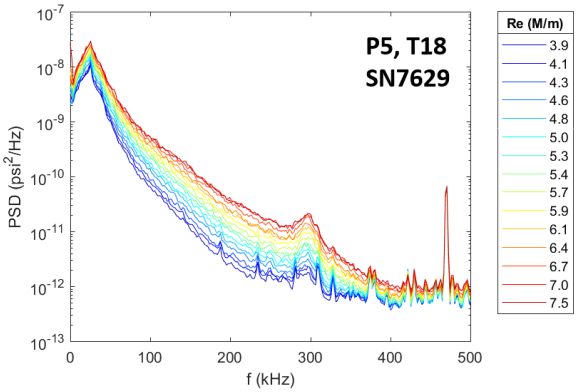
P5, T18
SN7629
PSD (psi²/Hz)
f (kHz)
Re (M/m)
3.9
4.1
4.3
4.6
4.8
5.0
5.3
5.4
5.7
5.9
6.1
6.4
6.7
7.0
7.5

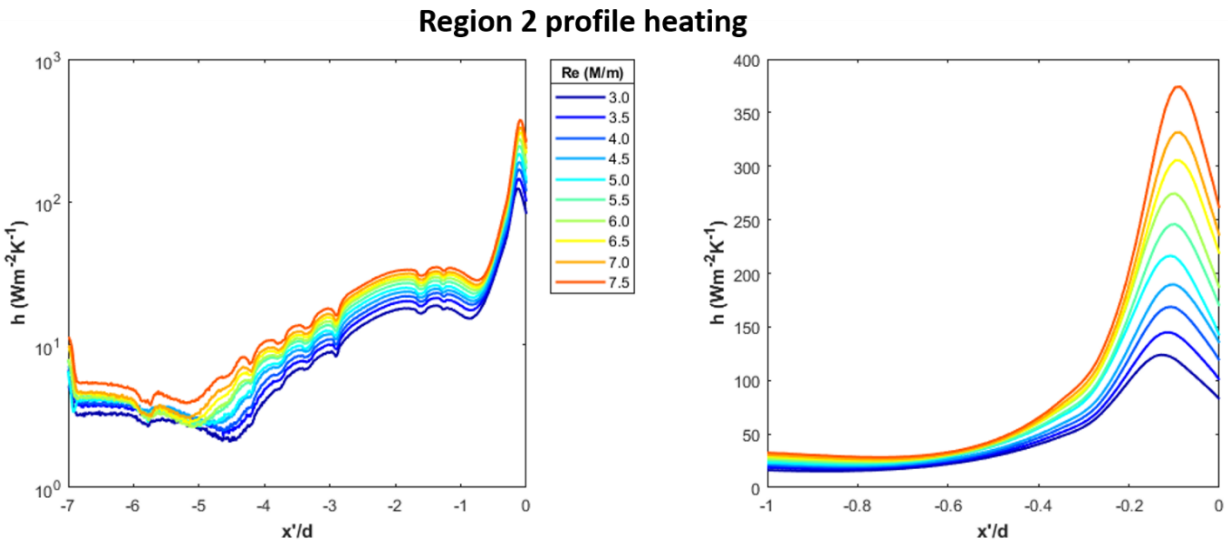

Run 3459

Surface pressure measurements, IR thermography, and high-speed schlieren made over Re steps.

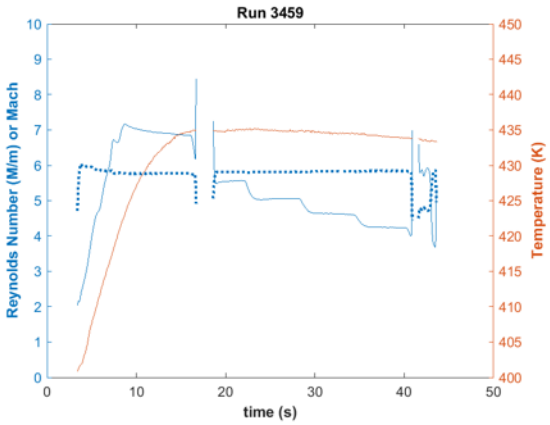

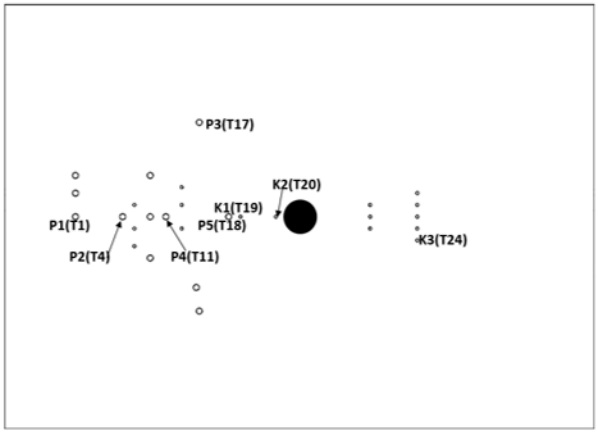

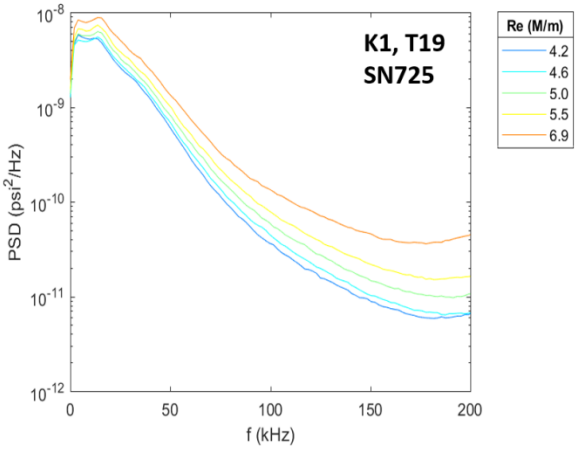

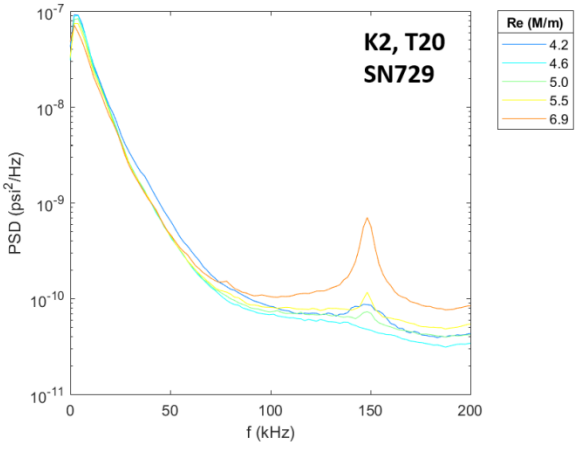

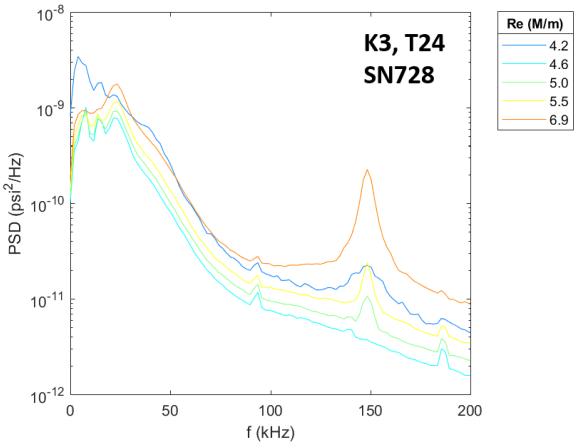
K3, T24
SN728
Re (M/m)
4.2
4.6
5.0
5.5
6.9
PSD (psi²/Hz)
f (kHz)

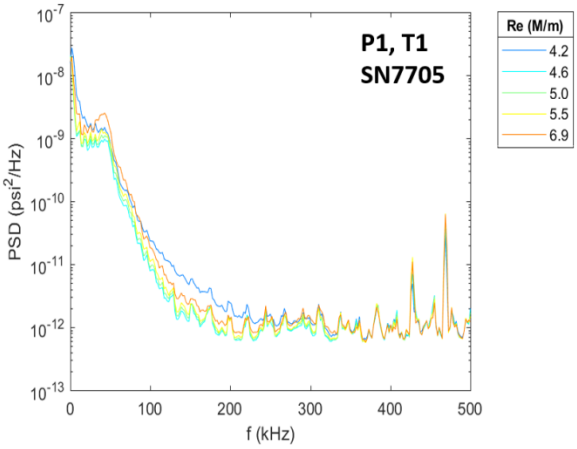
P1, T1
SN7705
Re (M/m)
4.2
4.6
5.0
5.5
6.9
PSD (psi²/Hz)
f (kHz)

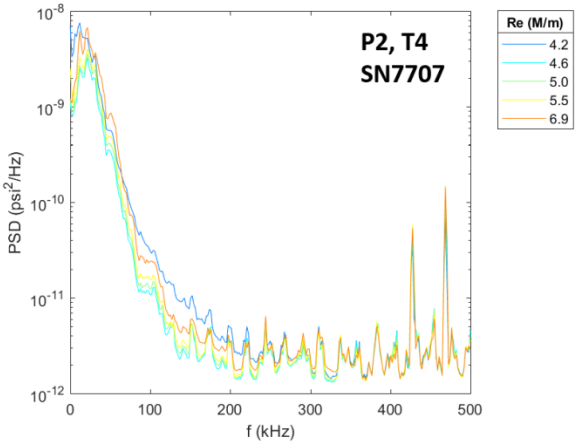
P2, T4
SN7707
Re (M/m)
4.2
4.6
5.0
5.5
6.9
PSD (psi²/Hz)
f (kHz)

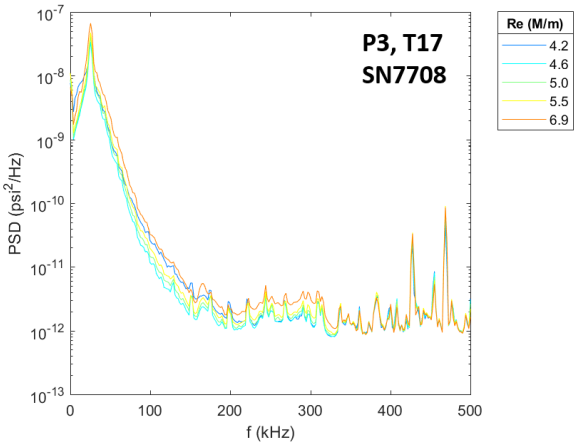
P3, T17
SN7708
Re (M/m)
4.2
4.6
5.0
5.5
6.9
PSD (psi²/Hz)
f (kHz)

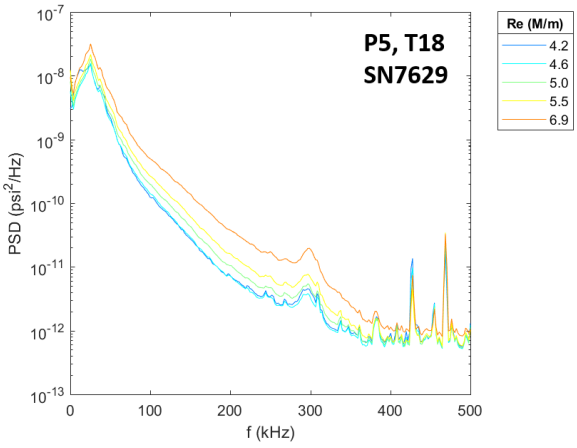
P5, T18
SN7629
Re (M/m)
4.2
4.6
5.0
5.5
6.9
PSD (psi²/Hz)
f (kHz)

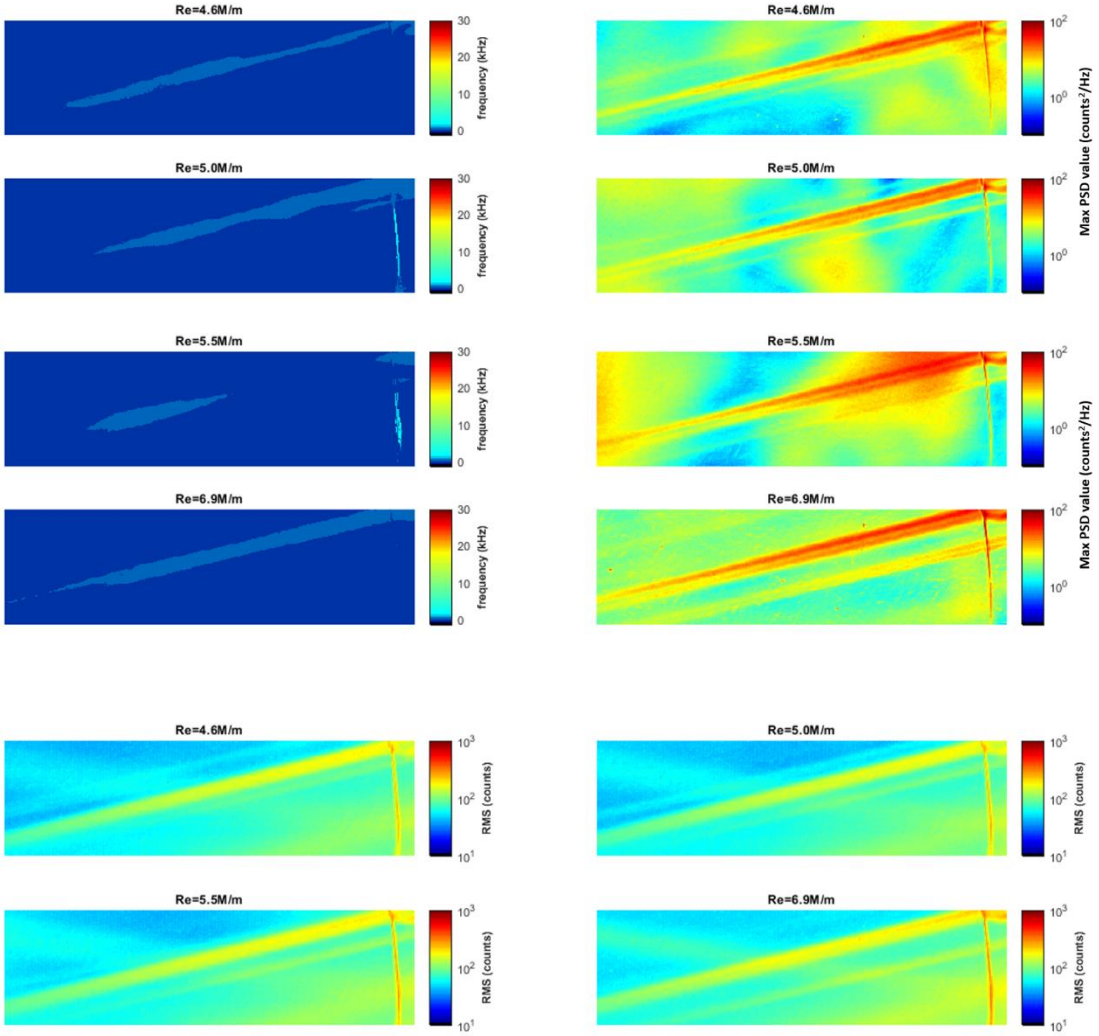
Re=4.6M/m
Re=5.0M/m
Re=5.5M/m
Re=6.9M/m
frequency (kHz)
Max PSD value (counts²/Hz)
RMS (counts)

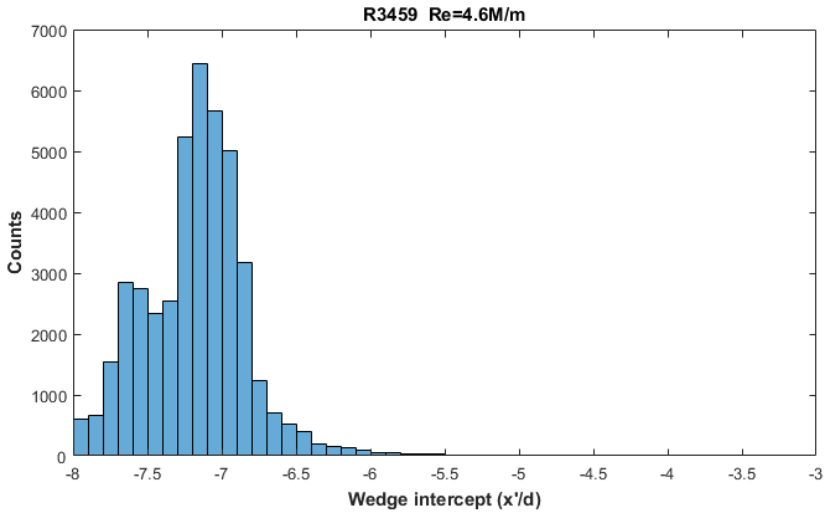
R3459 Re=4.6M/m
Counts
Wedge intercept (x'/d)
7000
6000
5000
4000
3000
2000
1000
0
-8
-7.5
-7
-6.5
-6
-5.5
-5
-4.5
-4
-3.5
-3

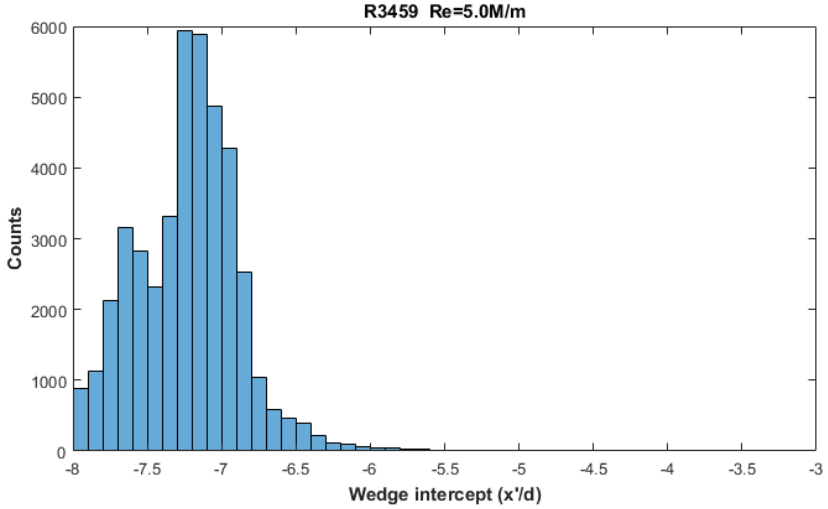
R3459 Re=5.0M/m
Counts
Wedge intercept (x'/d)
6000
5000
4000
3000
2000
1000
0
-8
-7.5
-7
-6.5
-6
-5.5
-5
-4.5
-4
-3.5
-3

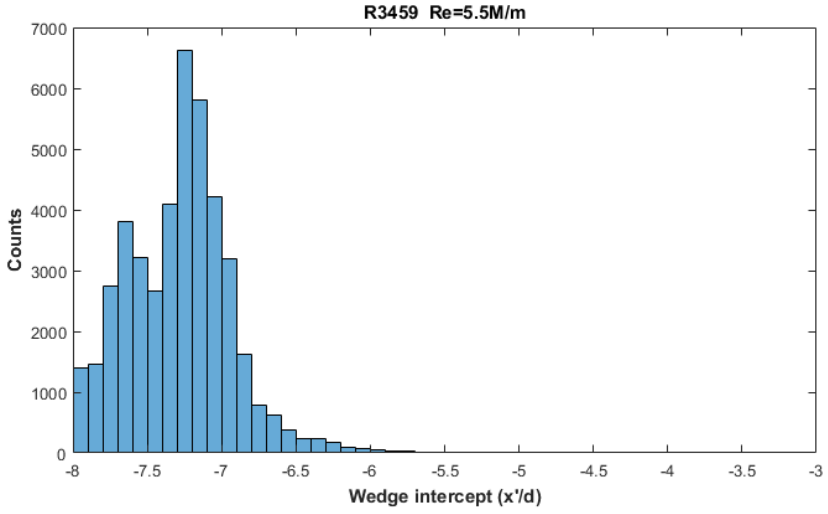
R3459 Re=5.5M/m
Counts
Wedge intercept (x'/d)
7000
6000
5000
4000
3000
2000
1000
0
-8
-7.5
-7
-6.5
-6
-5.5
-5
-4.5
-4
-3.5
-3

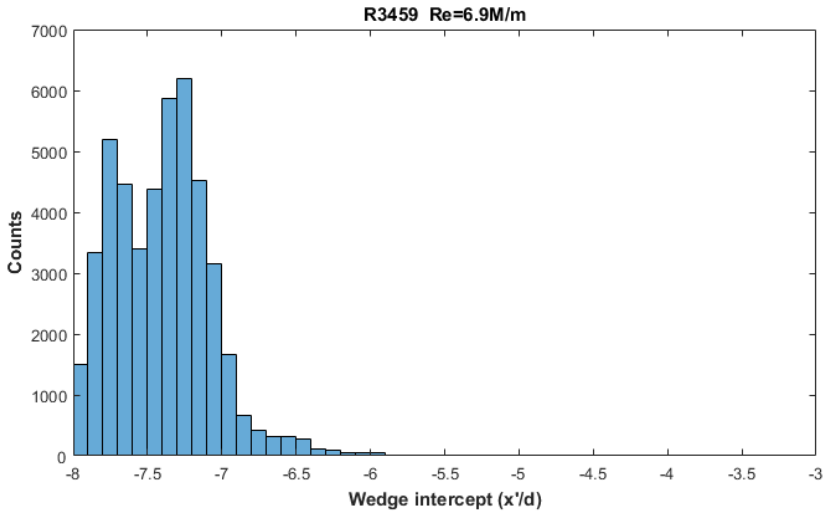

Run 3460

Surface pressure measurements, IR thermography, and high-speed schlieren made over Re steps.

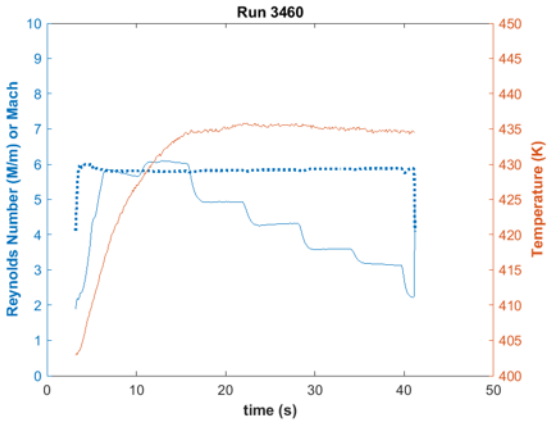

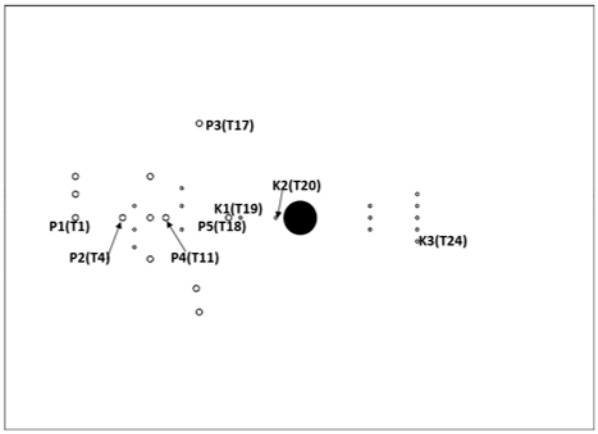

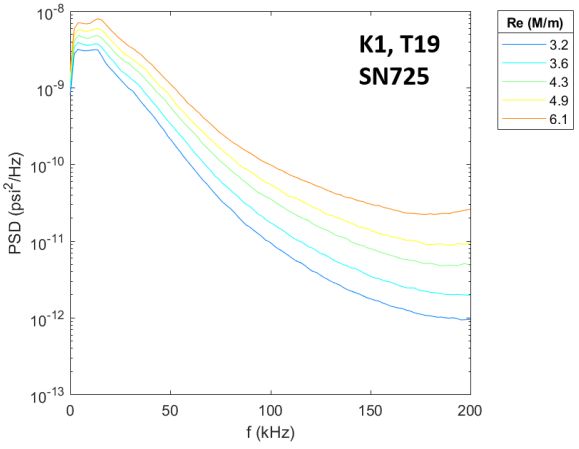

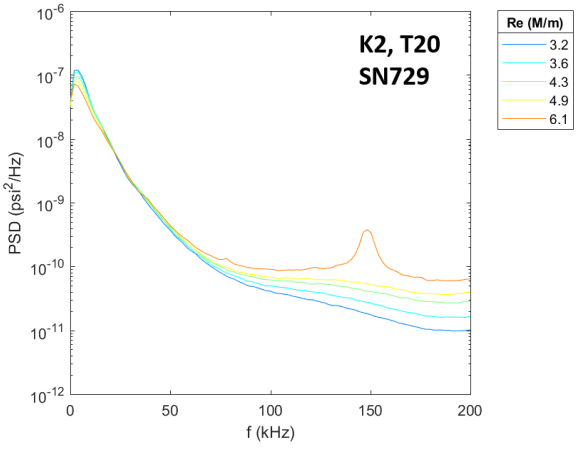

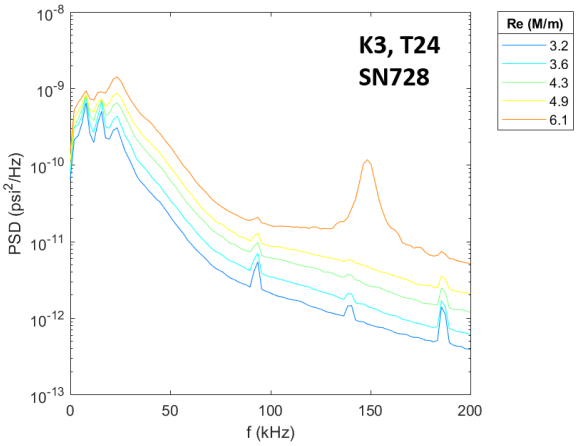
K3, T24
SN728
Re (M/m)
3.2
3.6
4.3
4.9
6.1
PSD (psi²/Hz)
f (kHz)

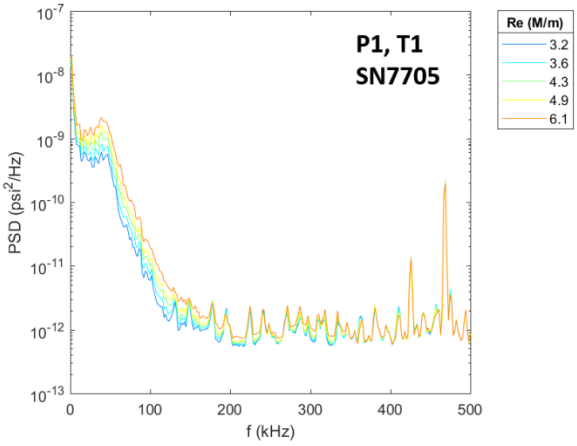
P1, T1
SN7705
Re (M/m)
3.2
3.6
4.3
4.9
6.1
PSD (psi²/Hz)
f (kHz)

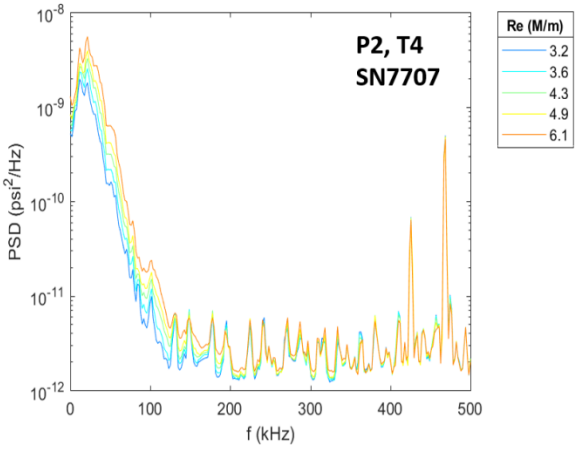
P2, T4
SN7707
Re (M/m)
3.2
3.6
4.3
4.9
6.1
PSD (psi²/Hz)
f (kHz)

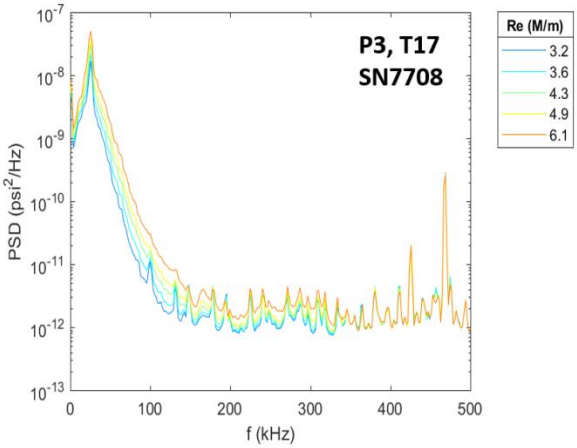
P3, T17
SN7708
Re (M/m)
3.2
3.6
4.3
4.9
6.1
PSD (psi²/Hz)
f (kHz)

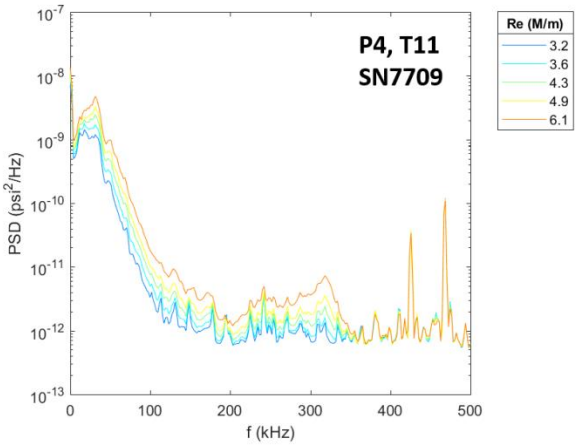
P4, T11
SN7709
Re (M/m)
3.2
3.6
4.3
4.9
6.1
PSD (psi²/Hz)
f (kHz)

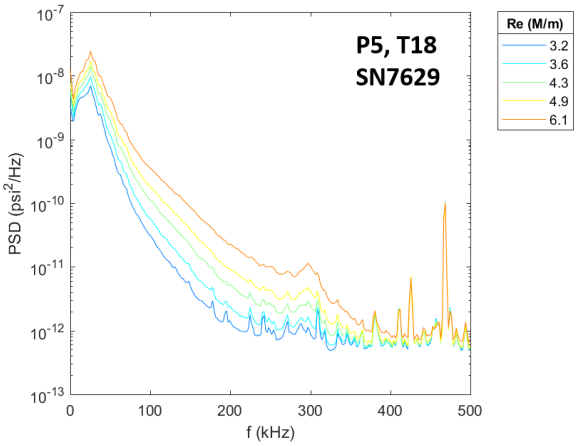
P5, T18
SN7629
Re (M/m)
3.2
3.6
4.3
4.9
6.1
PSD (psi²/Hz)
f (kHz)

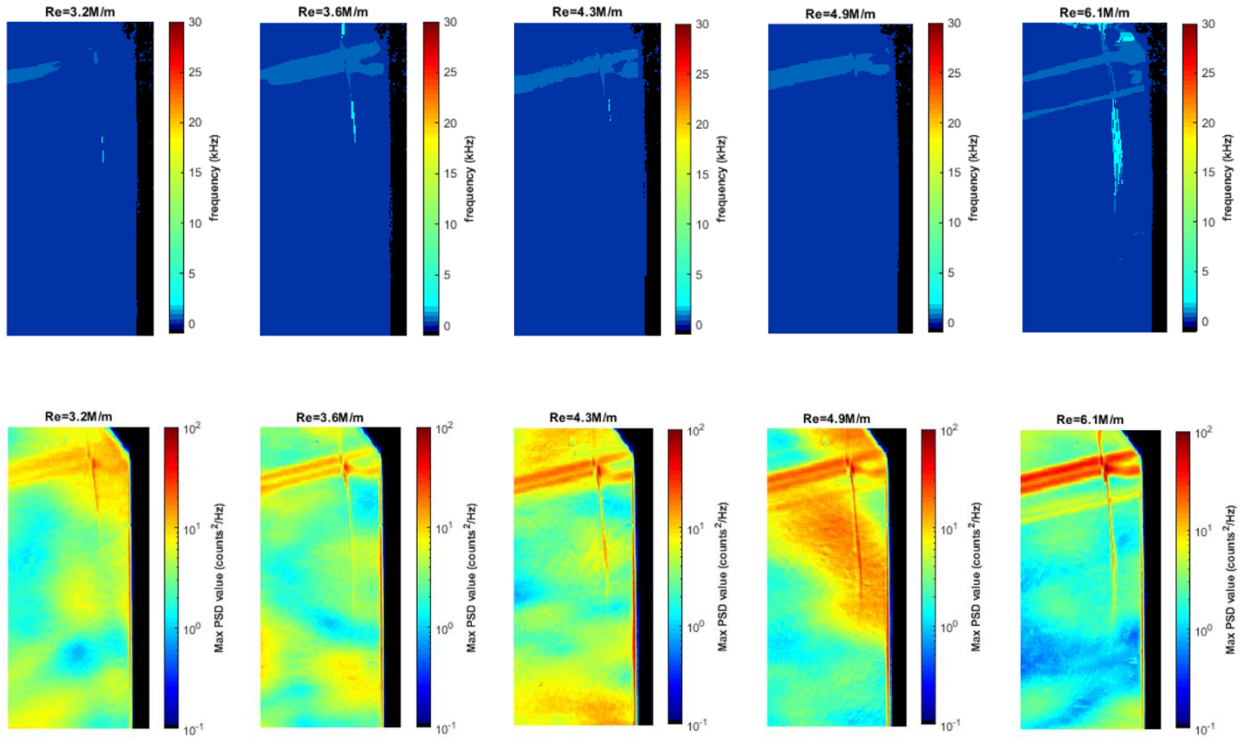
Re=3.2M/m
Re=3.6M/m
Re=4.3M/m
Re=4.9M/m
Re=6.1M/m
frequency (kHz)
Max PSD value (counts²/Hz)

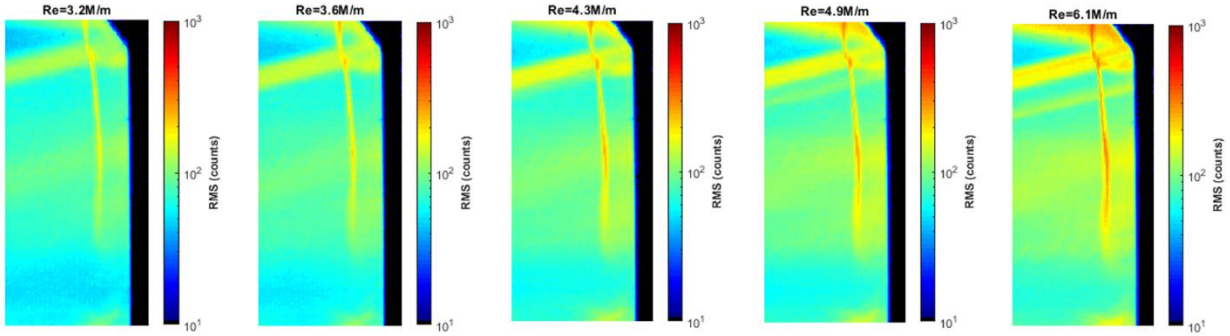

Run 3461

Surface pressure measurements, IR thermography, and schlieren made over a Re sweep.

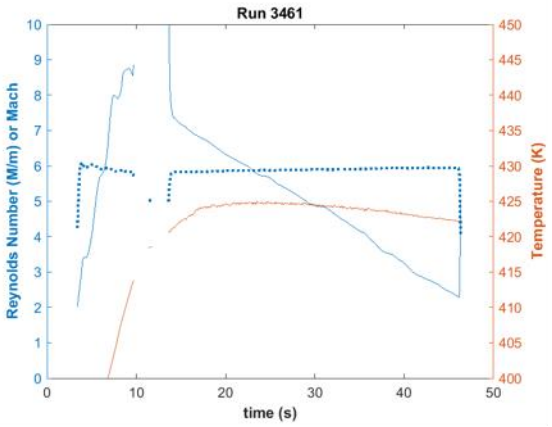

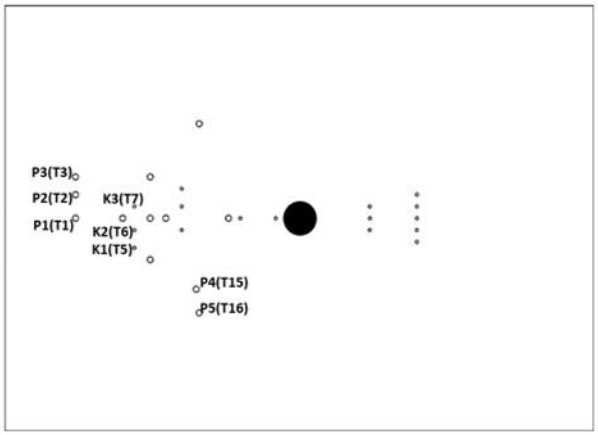

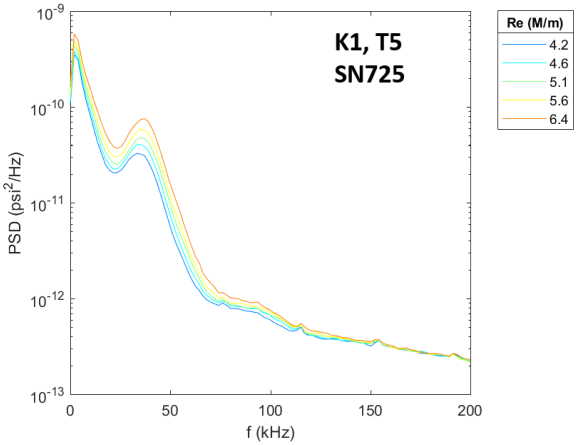

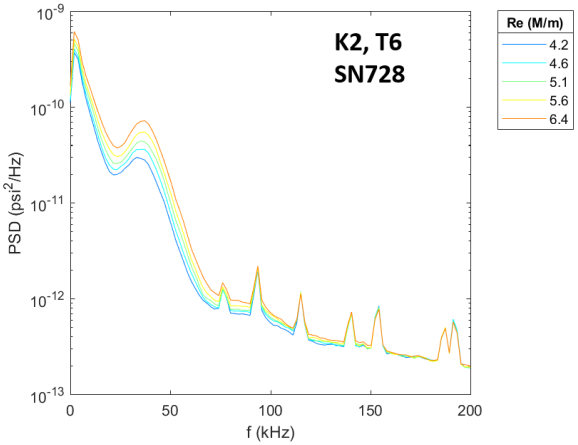

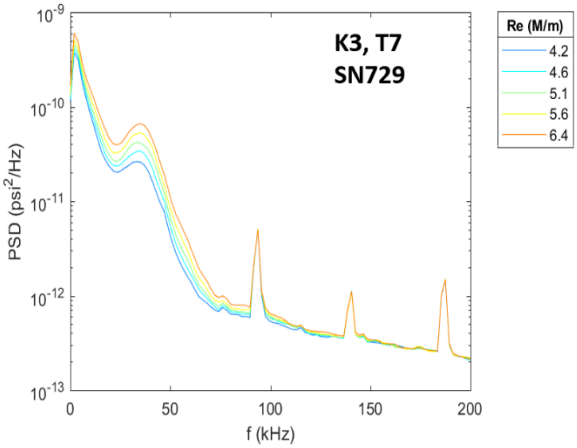
K3, T7
SN729
Re (M/m)
4.2
4.6
5.1
5.6
6.4
PSD (psi²/Hz)
f (kHz)

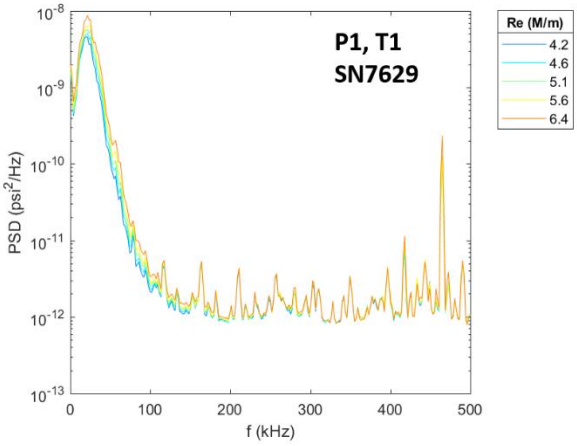
P1, T1
SN7629
Re (M/m)
4.2
4.6
5.1
5.6
6.4
PSD (psi²/Hz)
f (kHz)

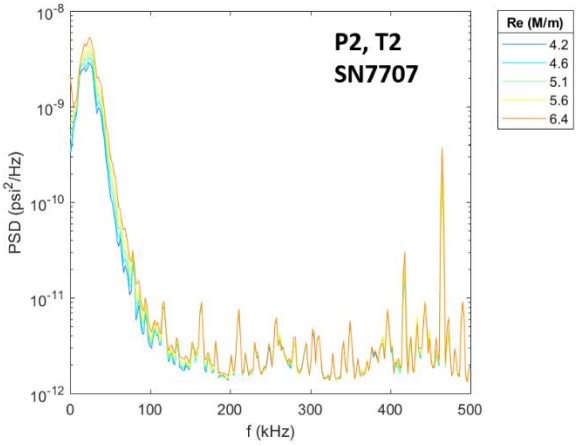
P2, T2
SN7707
Re (M/m)
4.2
4.6
5.1
5.6
6.4
PSD (psi²/Hz)
f (kHz)

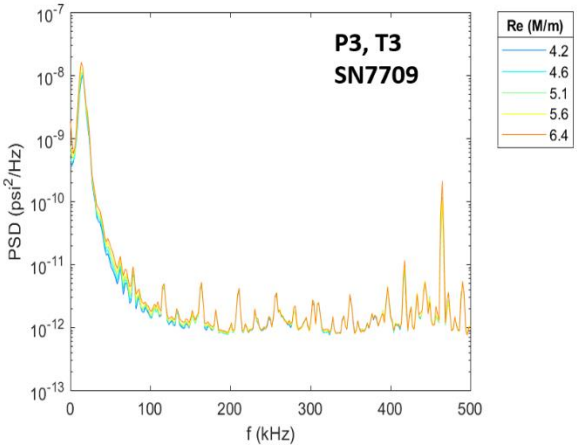
P3, T3
SN7709
Re (M/m)
4.2
4.6
5.1
5.6
6.4
PSD (psi²/Hz)
f (kHz)

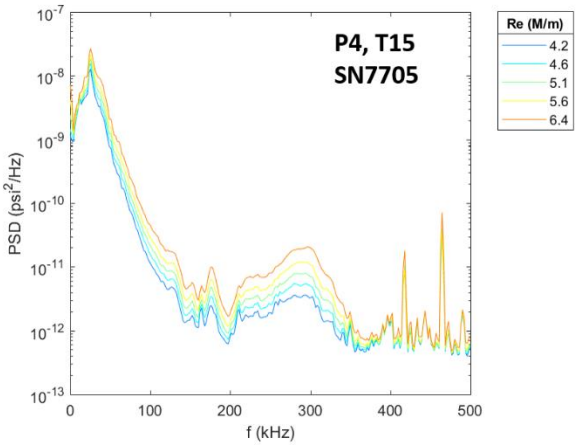
P4, T15
SN7705
Re (M/m)
4.2
4.6
5.1
5.6
6.4
PSD (psi²/Hz)
f (kHz)

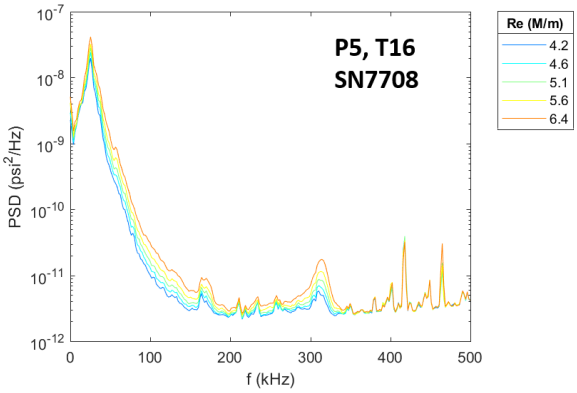

Run 3462

Surface pressure measurements, IR thermography, and high-speed schlieren made over Re steps.

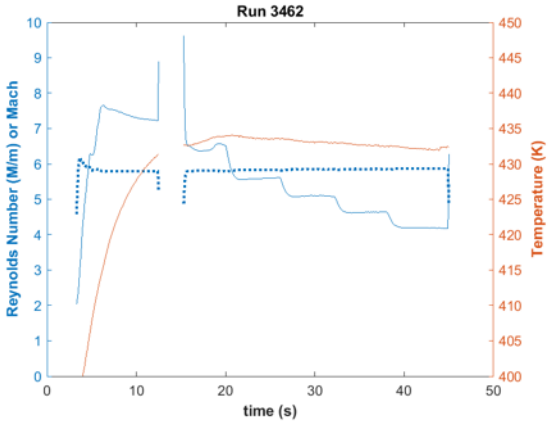

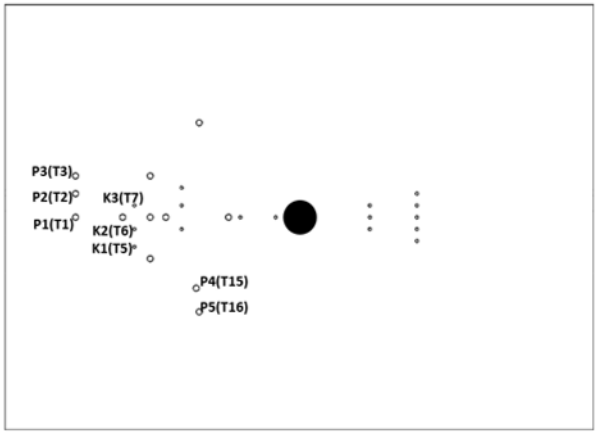

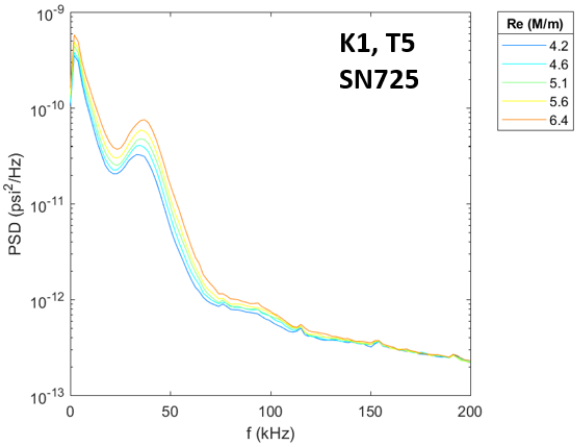

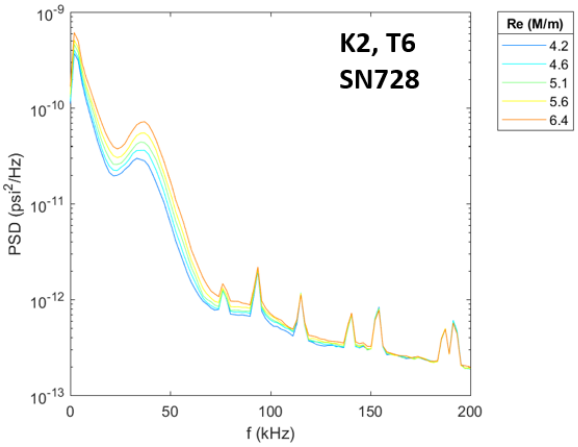

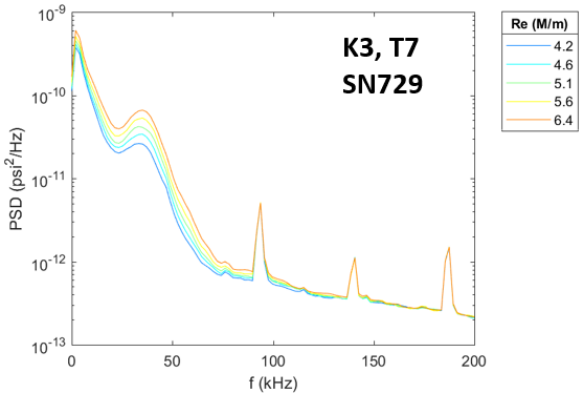
K3, T7
SN729
Re (M/m)
4.2
4.6
5.1
5.6
6.4
PSD (psi²/Hz)
f (kHz)

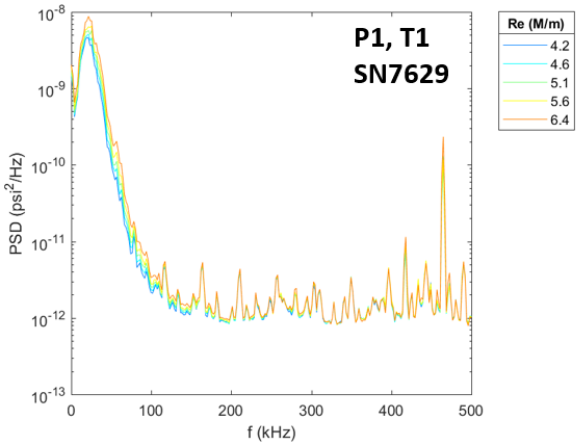
P1, T1
SN7629
Re (M/m)
4.2
4.6
5.1
5.6
6.4
PSD (psi²/Hz)
f (kHz)

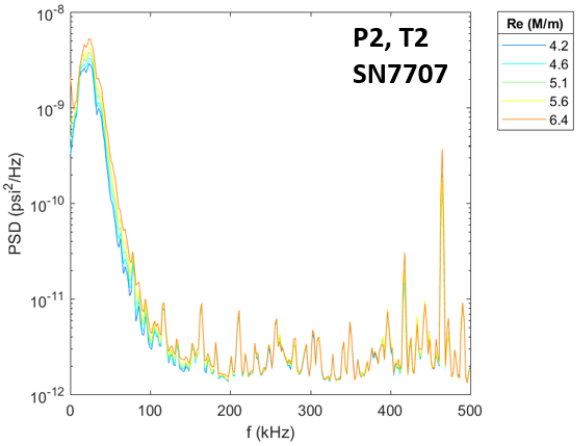
P2, T2
SN7707
Re (M/m)
4.2
4.6
5.1
5.6
6.4
PSD (psi²/Hz)
f (kHz)

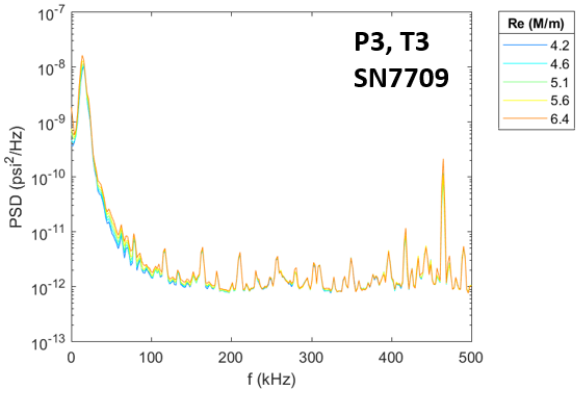
P3, T3
SN7709
Re (M/m)
4.2
4.6
5.1
5.6
6.4
PSD (psi²/Hz)
f (kHz)

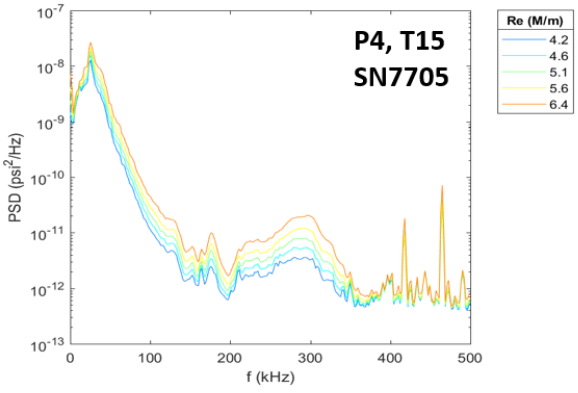
P4, T15
SN7705
Re (M/m)
4.2
4.6
5.1
5.6
6.4
PSD (psi²/Hz)
f (kHz)

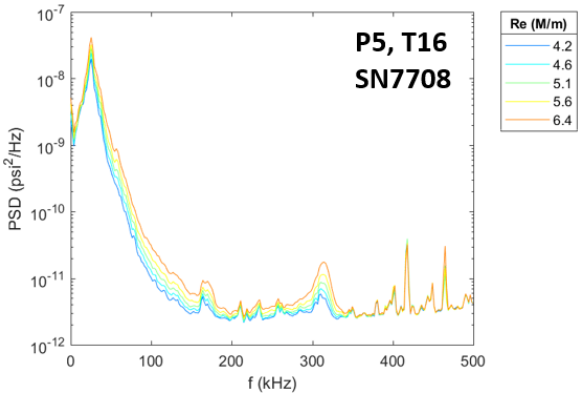
P5, T16
SN7708
Re (M/m)
4.2
4.6
5.1
5.6
6.4
PSD (psi²/Hz)
f (kHz)

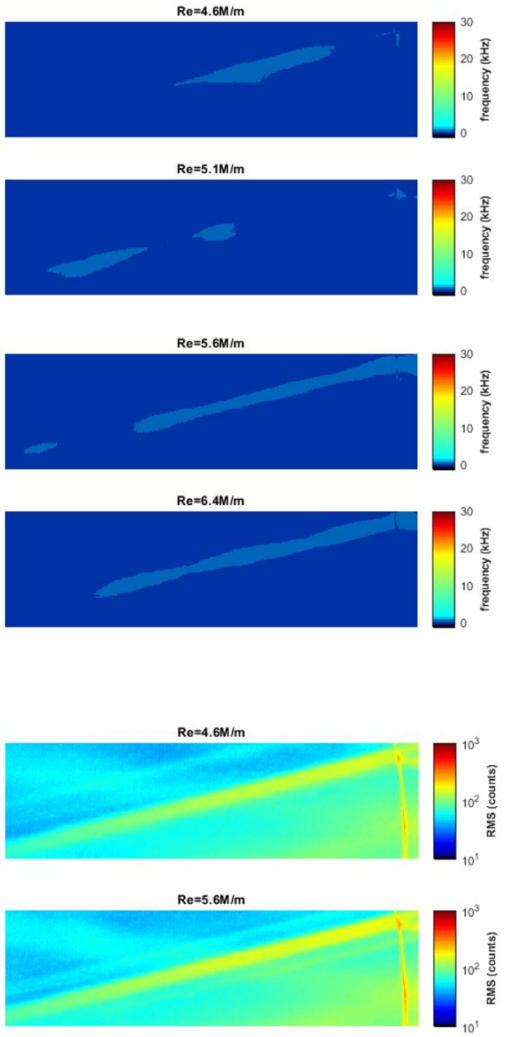
Re=4.6M/m
Re=5.1M/m
Re=5.6M/m
Re=6.4M/m
frequency (kHz)

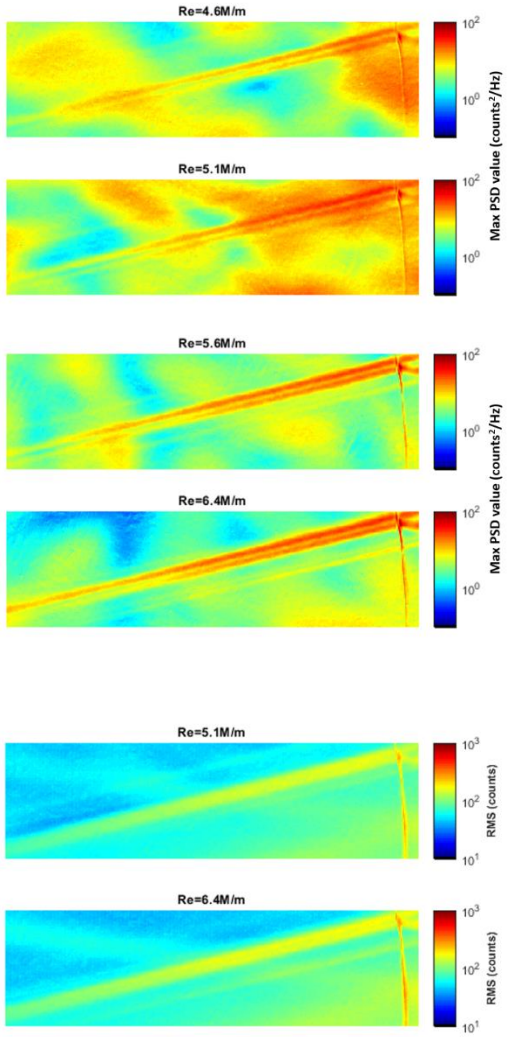
Re=4.6M/m
Re=5.1M/m
Re=5.6M/m
Re=6.4M/m
Max PSD value (counts²/Hz)

Re=4.6M/m
Re=5.6M/m
RMS (counts)

Re=5.1M/m
Re=6.4M/m
RMS (counts)

Run 3463

Surface pressure measurements, IR thermography, and high-speed schlieren made over Re steps.

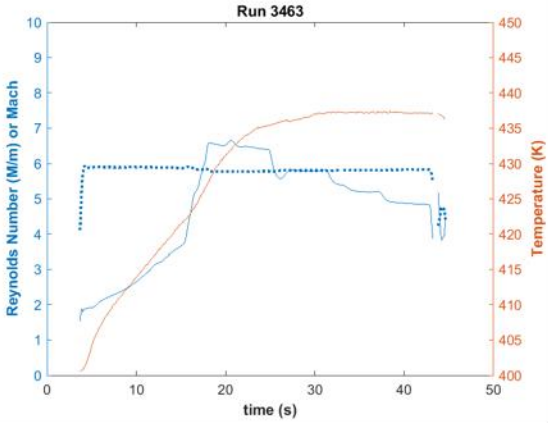

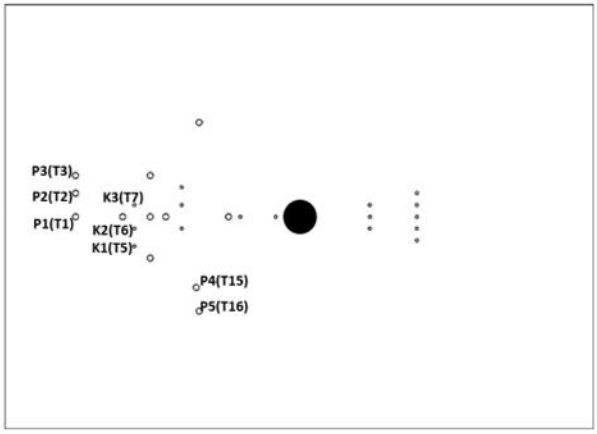

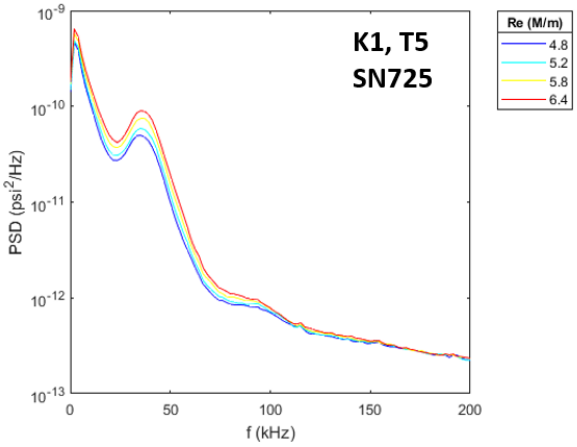

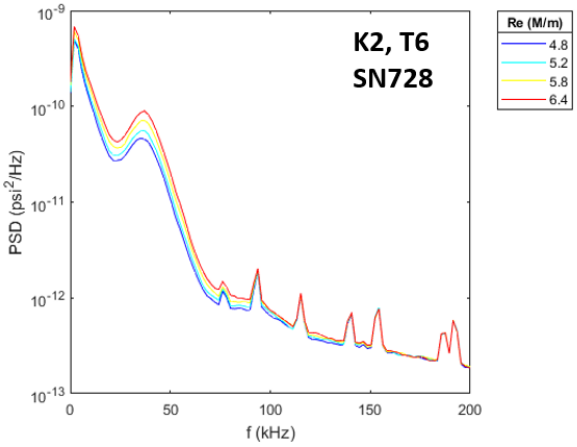

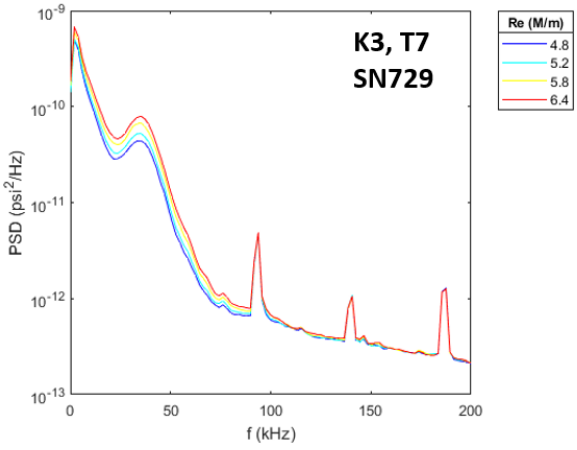

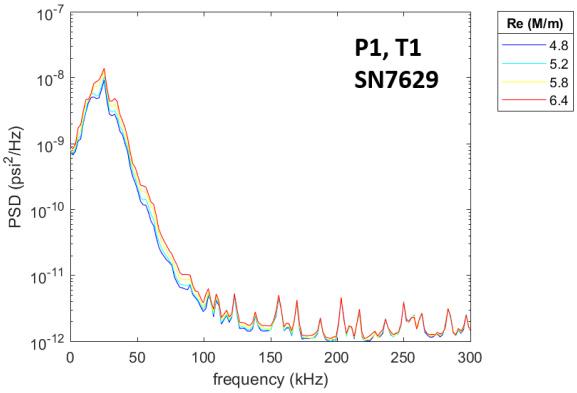
P1, T1
SN7629
Re (M/m)
4.8
5.2
5.8
6.4
PSD (psi²/Hz)
frequency (kHz)

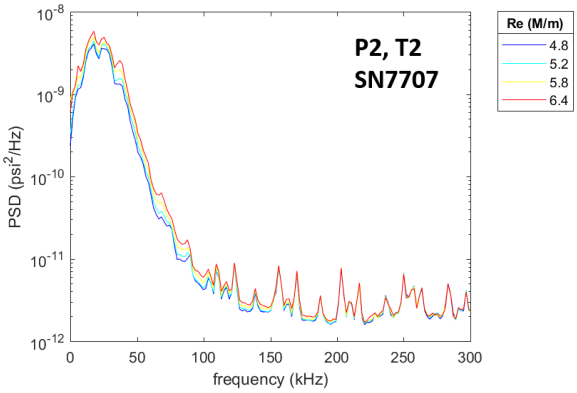
P2, T2
SN7707
Re (M/m)
4.8
5.2
5.8
6.4
PSD (psi²/Hz)
frequency (kHz)

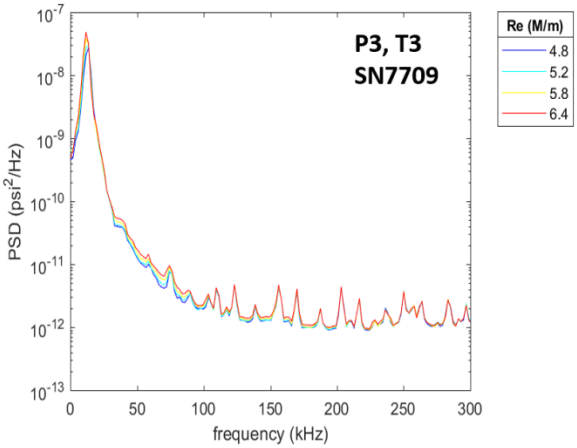
P3, T3
SN7709
Re (M/m)
4.8
5.2
5.8
6.4
PSD (psi²/Hz)
frequency (kHz)

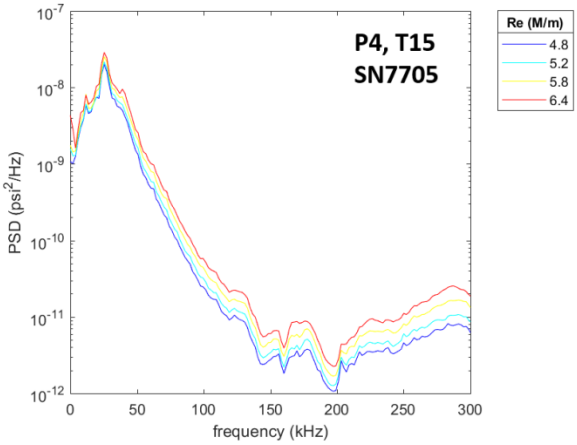
P4, T15
SN7705
Re (M/m)
4.8
5.2
5.8
6.4
PSD (psi²/Hz)
frequency (kHz)

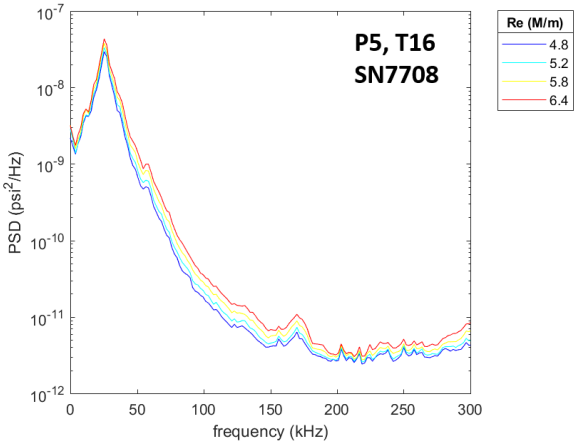
P5, T16
SN7708
Re (M/m)
4.8
5.2
5.8
6.4
PSD (psi²/Hz)
frequency (kHz)

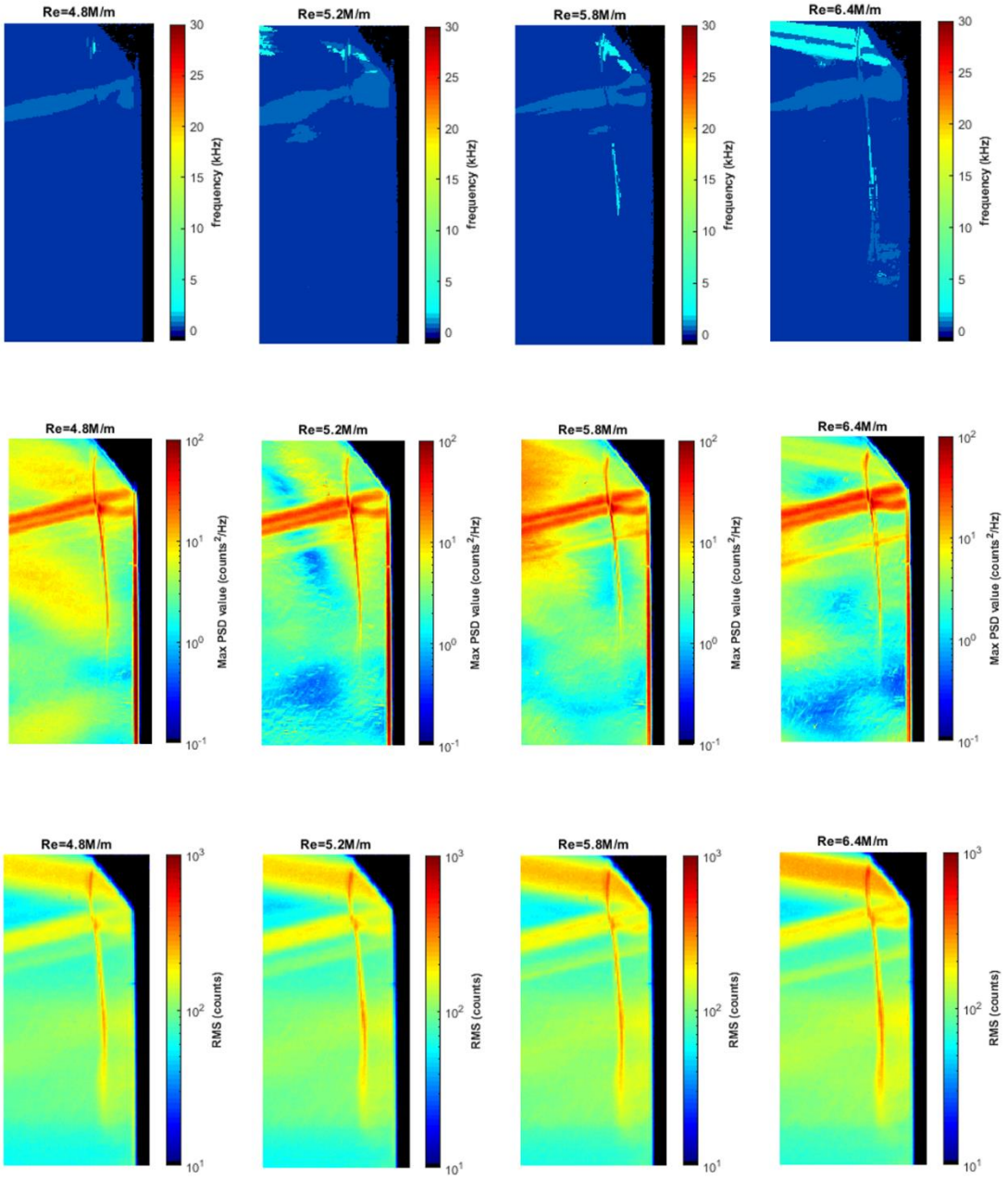

Run 3464. DAQ Error.

Run 3466

Surface pressure measurements, IR thermography, and schlieren made over a Re sweep.

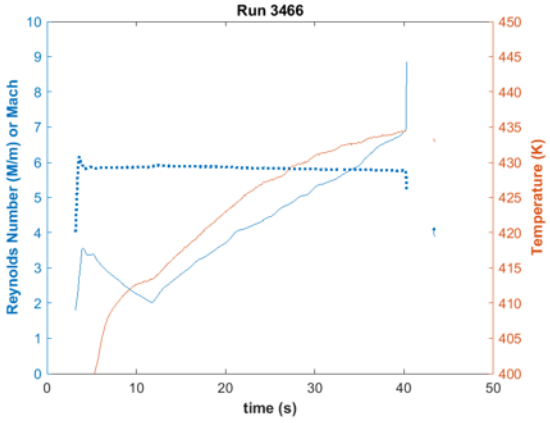

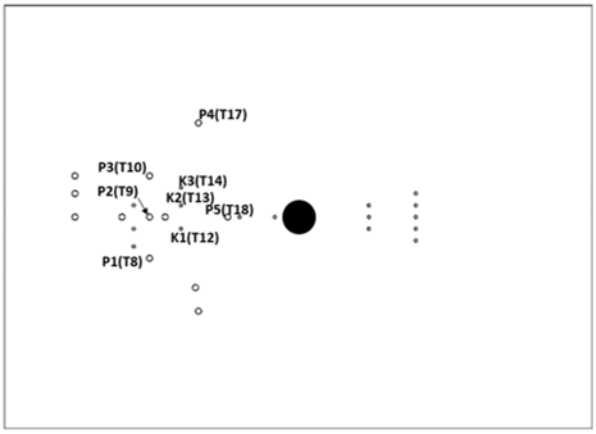

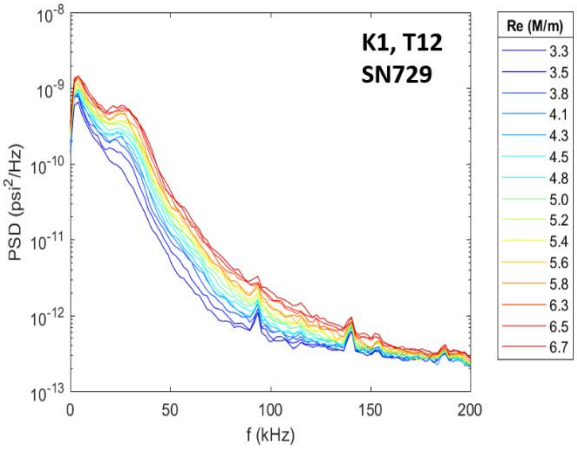

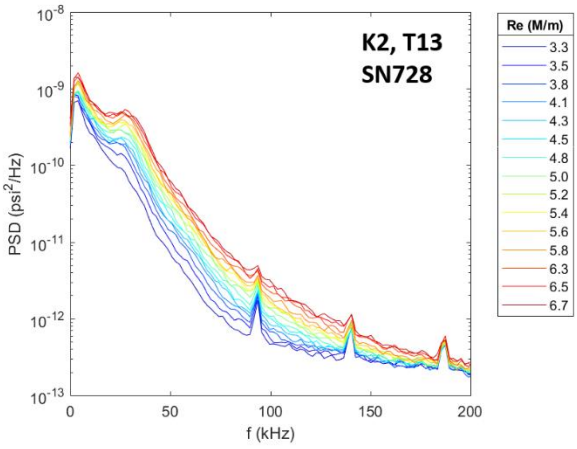

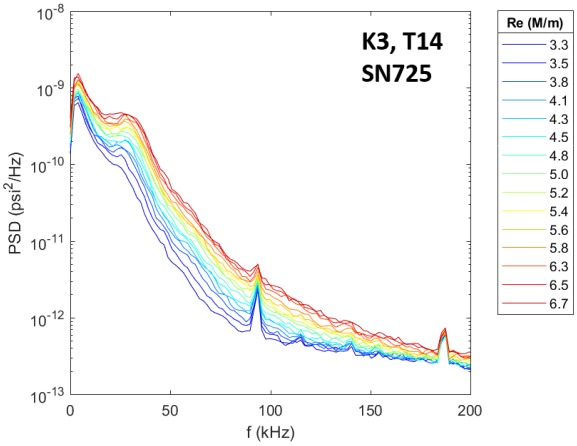

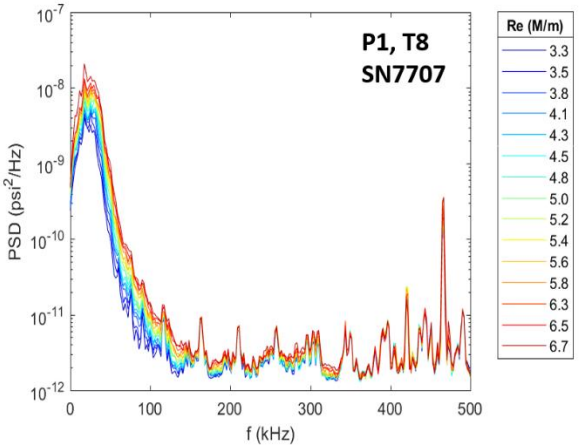
P1, T8
SN7707
PSD (psi²/Hz)
f (kHz)
Re (M/m)
3.3
3.5
3.8
4.1
4.3
4.5
4.8
5.0
5.2
5.4
5.6
5.8
6.3
6.5
6.7

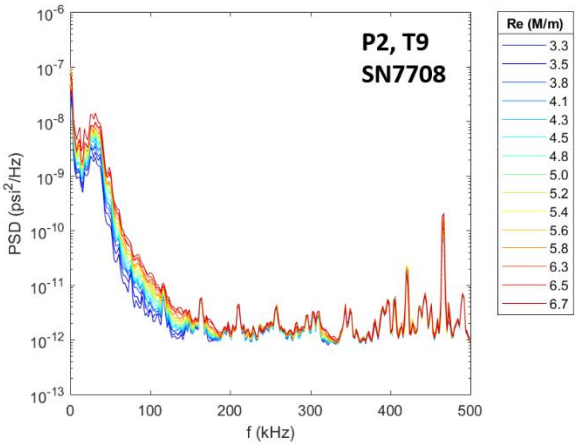
P2, T9
SN7708
PSD (psi²/Hz)
f (kHz)
Re (M/m)
3.3
3.5
3.8
4.1
4.3
4.5
4.8
5.0
5.2
5.4
5.6
5.8
6.3
6.5
6.7

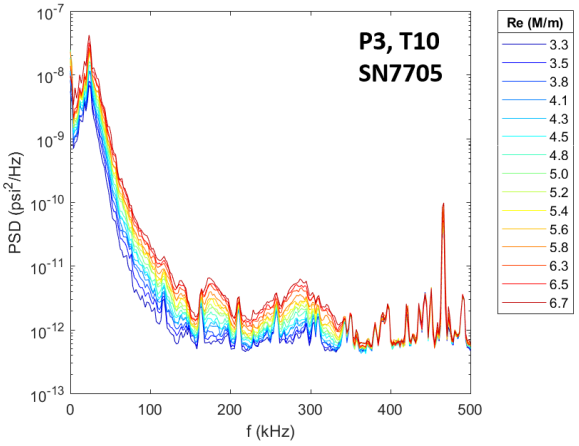
P3, T10
SN7705
PSD (psi²/Hz)
f (kHz)
Re (M/m)
3.3
3.5
3.8
4.1
4.3
4.5
4.8
5.0
5.2
5.4
5.6
5.8
6.3
6.5
6.7

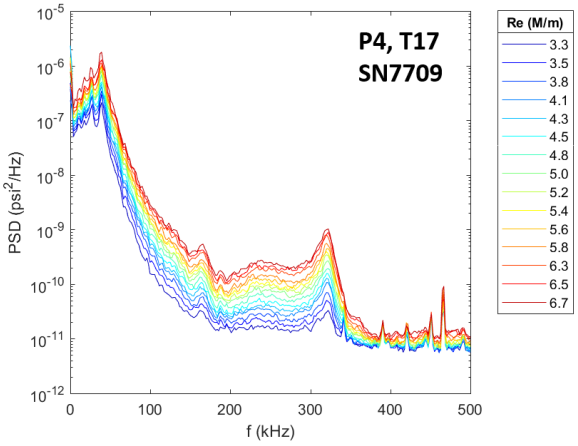
P4, T17
SN7709
PSD (psi²/Hz)
f (kHz)
Re (M/m)
3.3
3.5
3.8
4.1
4.3
4.5
4.8
5.0
5.2
5.4
5.6
5.8
6.3
6.5
6.7

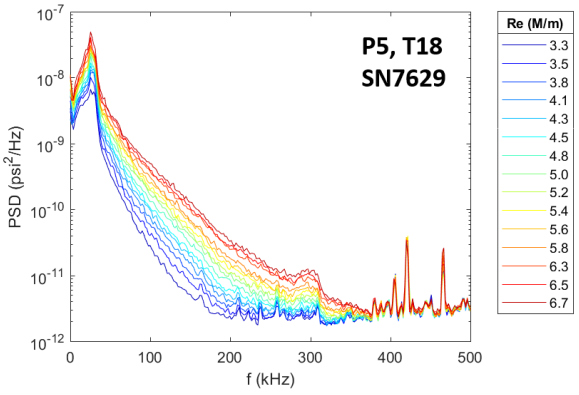
P5, T18
SN7629
PSD (psi²/Hz)
f (kHz)
Re (M/m)
3.3
3.5
3.8
4.1
4.3
4.5
4.8
5.0
5.2
5.4
5.6
5.8
6.3
6.5
6.7

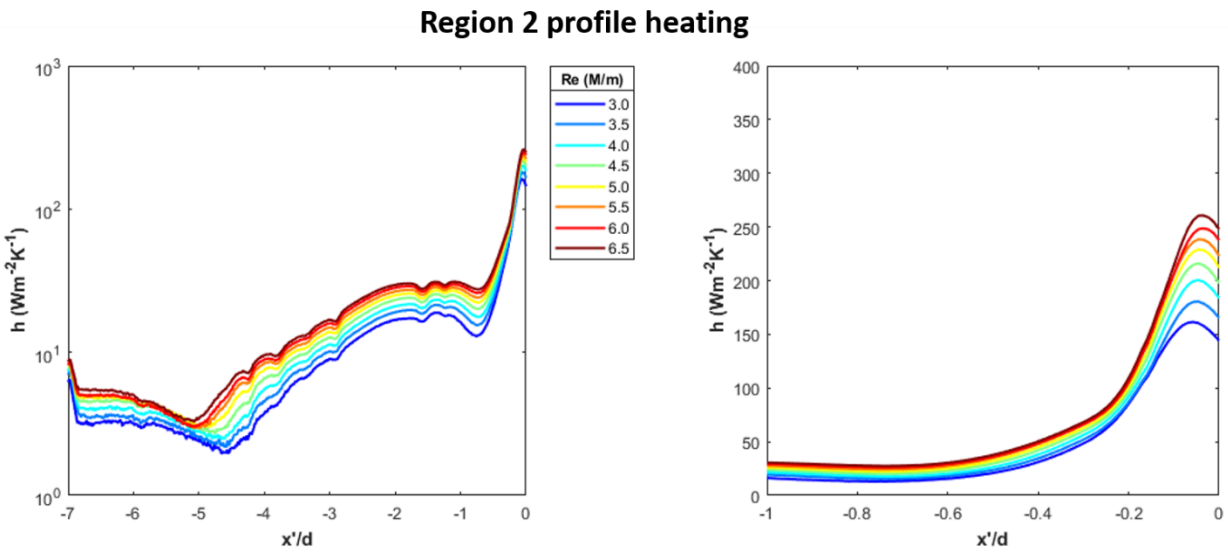

Run 3467

Surface pressure measurements, IR thermography, and high-speed schlieren made over Re steps.

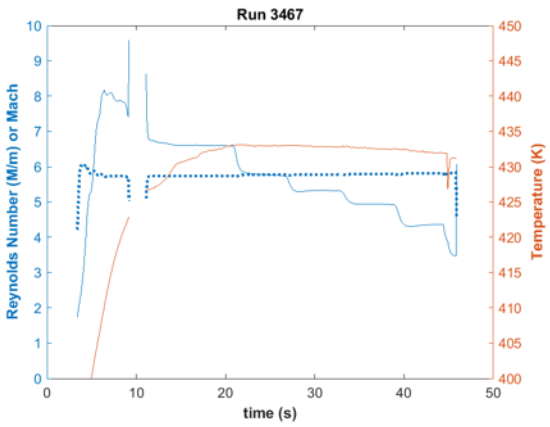

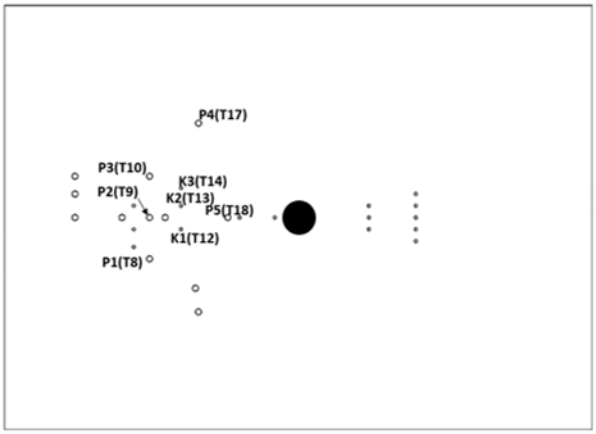

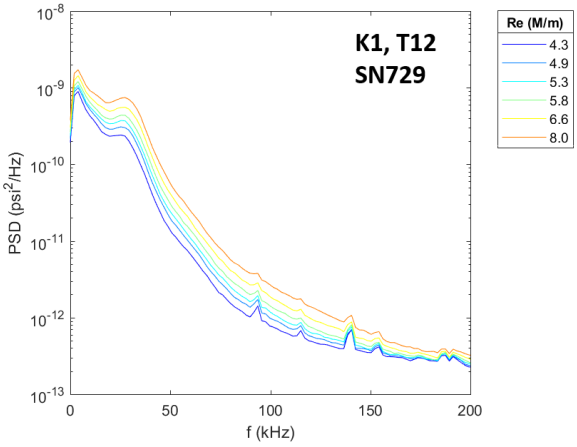

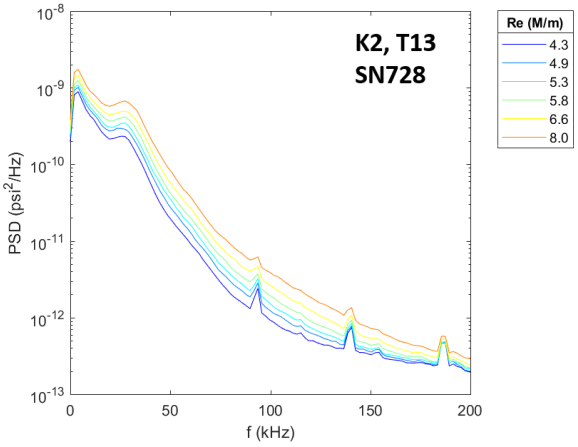

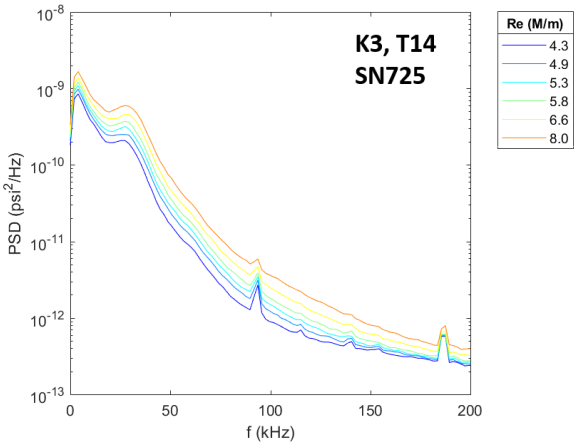
K3, T14
SN725
Re (M/m)
4.3
4.9
5.3
5.8
6.6
8.0
PSD (psi²/Hz)
f (kHz)

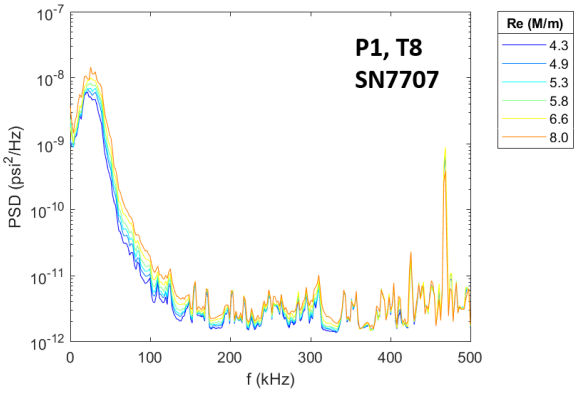
P1, T8
SN7707
Re (M/m)
4.3
4.9
5.3
5.8
6.6
8.0
PSD (psi²/Hz)
f (kHz)

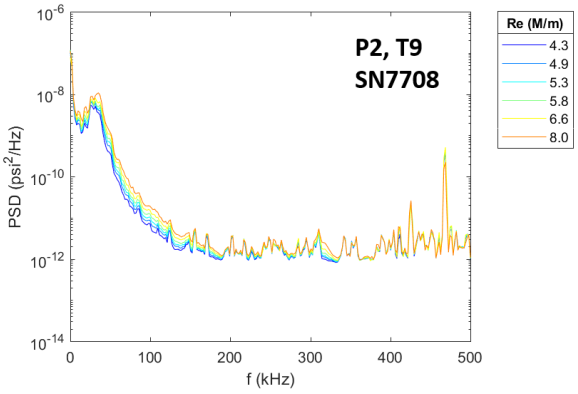
P2, T9
SN7708
Re (M/m)
4.3
4.9
5.3
5.8
6.6
8.0
PSD (psi²/Hz)
f (kHz)

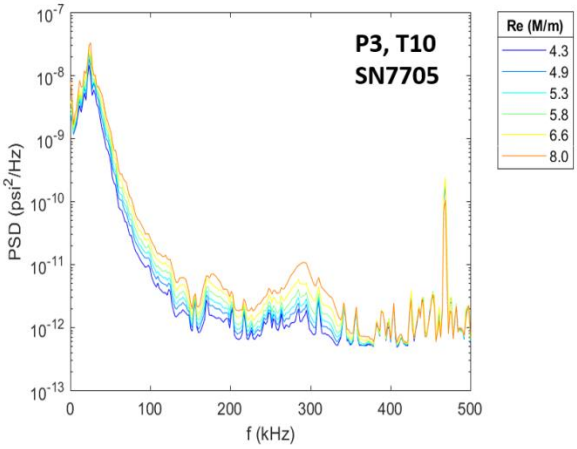
P3, T10
SN7705
Re (M/m)
4.3
4.9
5.3
5.8
6.6
8.0
PSD (psi²/Hz)
f (kHz)

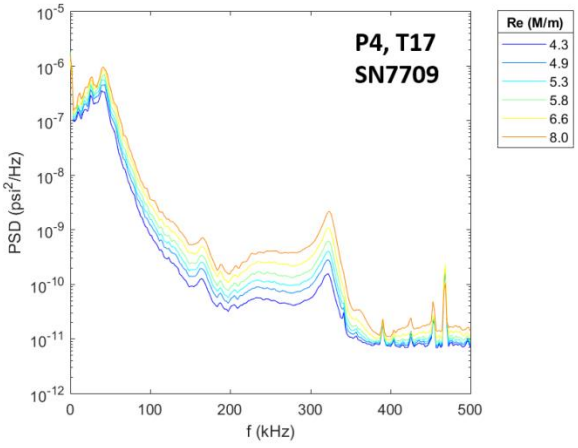
P4, T17
SN7709
Re (M/m)
4.3
4.9
5.3
5.8
6.6
8.0
PSD (psi²/Hz)
f (kHz)

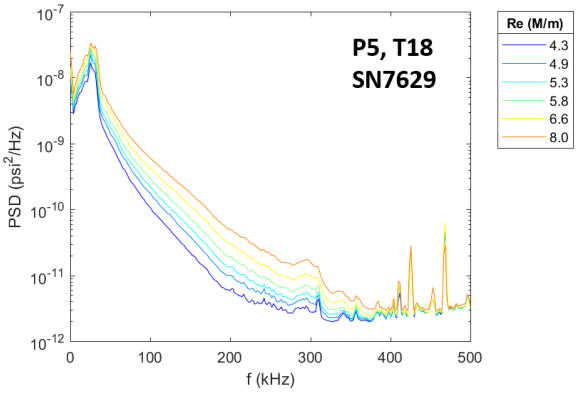
P5, T18
SN7629
Re (M/m)
4.3
4.9
5.3
5.8
6.6
8.0
PSD (psi²/Hz)
f (kHz)

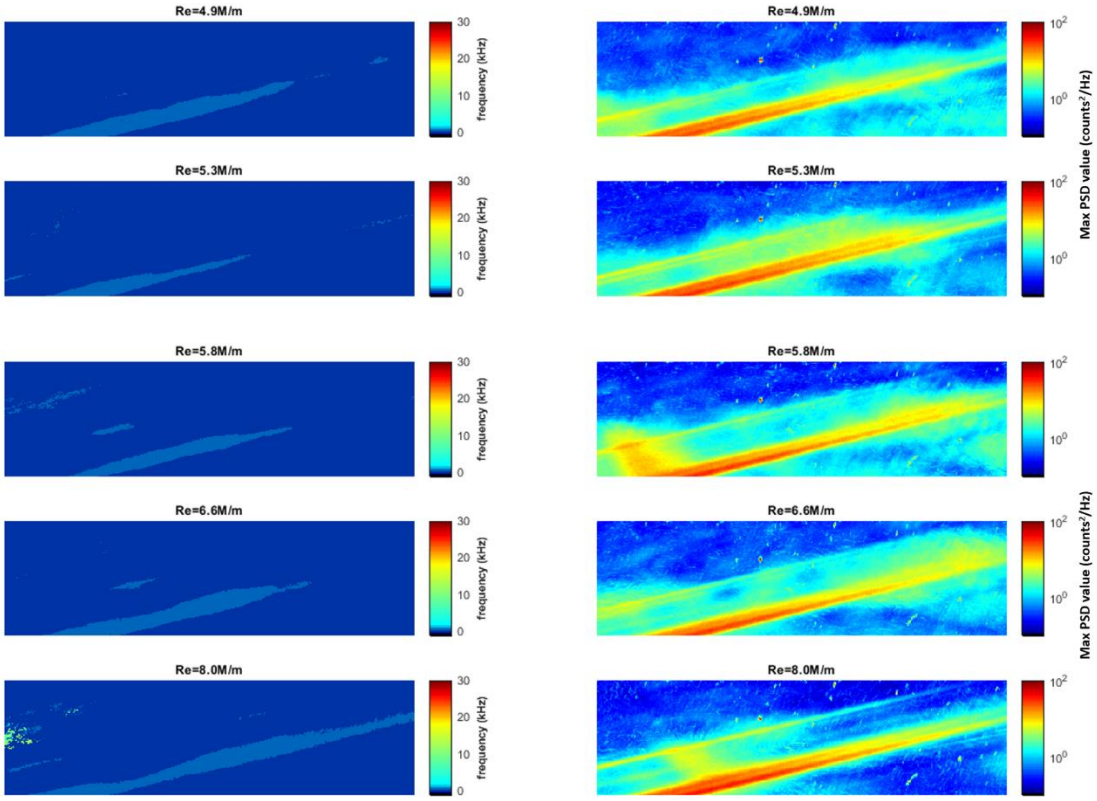
Re=4.9M/m
Re=5.3M/m
Re=5.8M/m
Re=6.6M/m
Re=8.0M/m
frequency (kHz)
Max PSD value (counts²/Hz)

Run 3468

Surface pressure measurements, IR thermography, and high-speed schlieren made over Re steps.

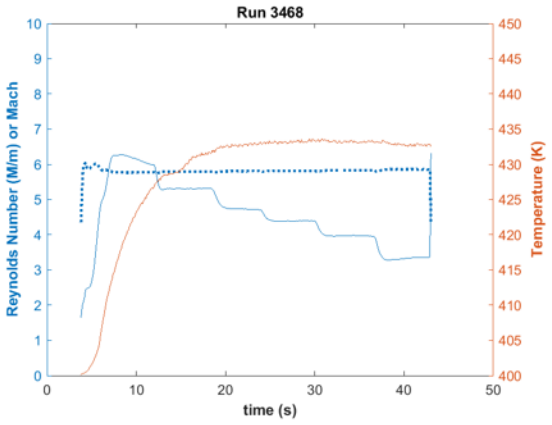

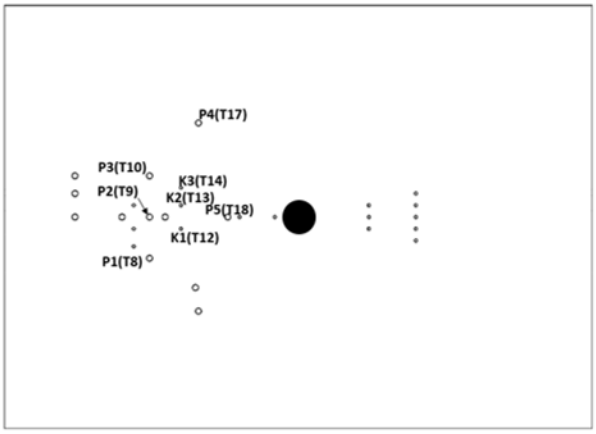

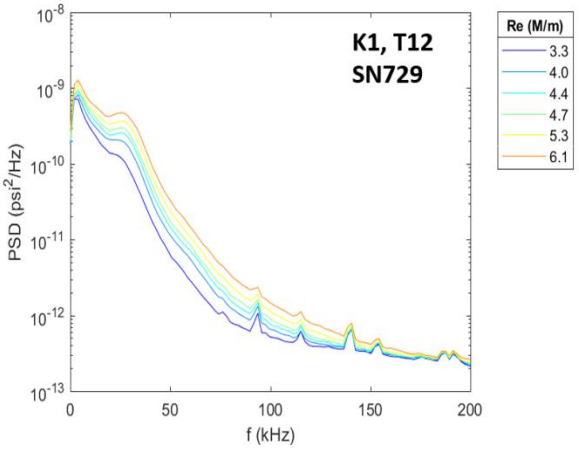

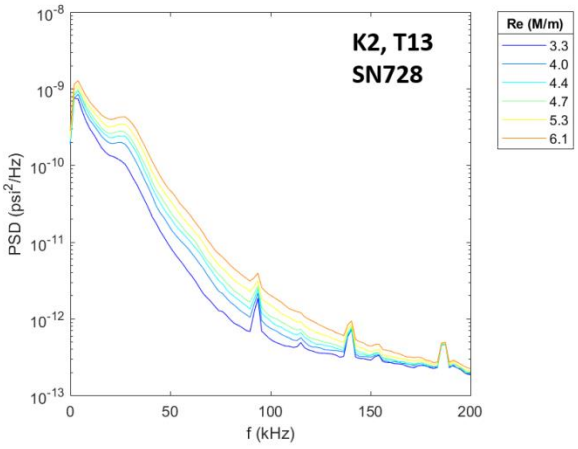

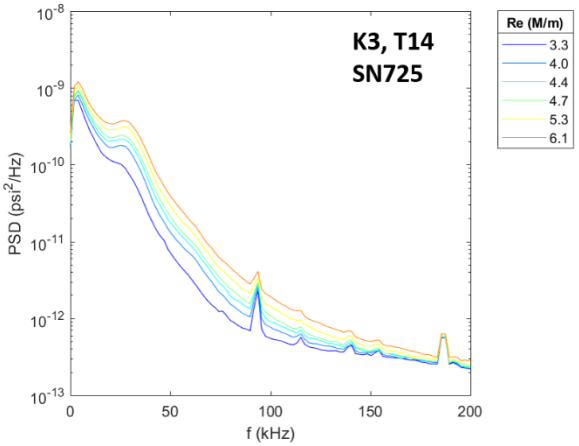

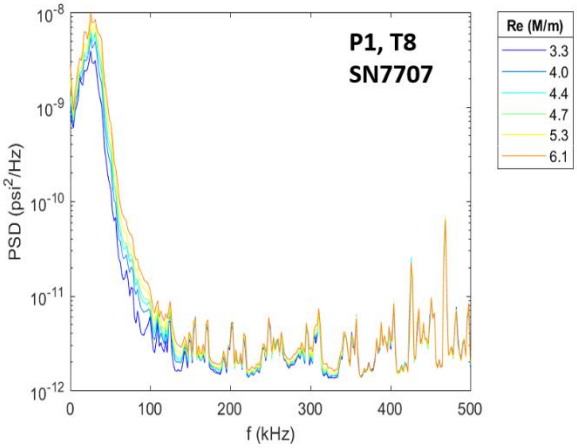
P1, T8
SN7707
Re (M/m)
3.3
4.0
4.4
4.7
5.3
6.1
PSD (psi²/Hz)
f (kHz)

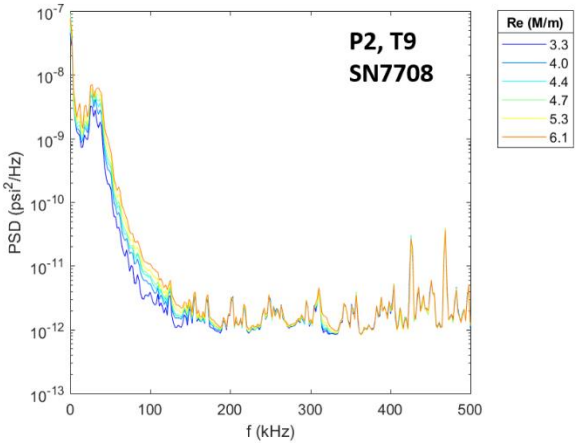
P2, T9
SN7708
Re (M/m)
3.3
4.0
4.4
4.7
5.3
6.1
PSD (psi²/Hz)
f (kHz)

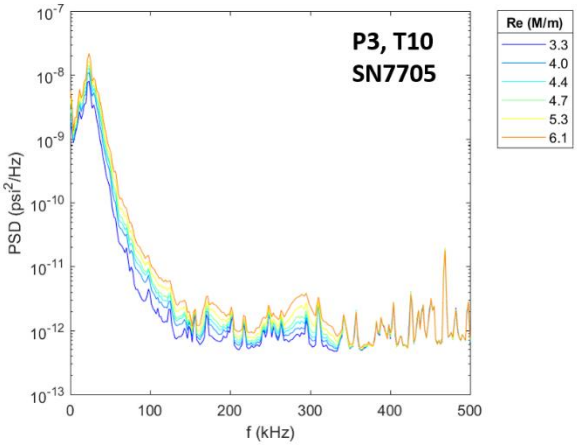
P3, T10
SN7705
Re (M/m)
3.3
4.0
4.4
4.7
5.3
6.1
PSD (psi²/Hz)
f (kHz)

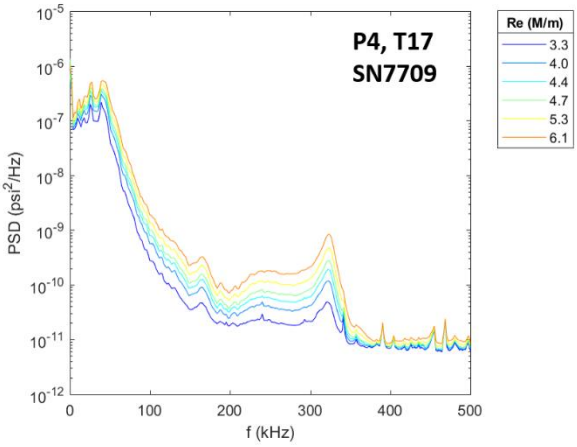
P4, T17
SN7709
Re (M/m)
3.3
4.0
4.4
4.7
5.3
6.1
PSD (psi²/Hz)
f (kHz)

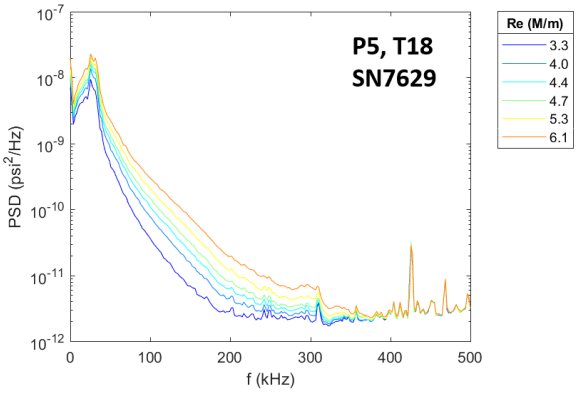
P5, T18
SN7629
Re (M/m)
3.3
4.0
4.4
4.7
5.3
6.1
PSD (psi²/Hz)
f (kHz)

No trips, no cylinder

Run 3469

Surface pressure measurements and IR thermography made over Re steps.

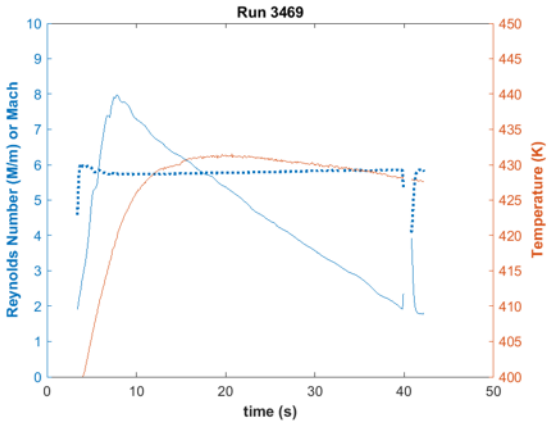

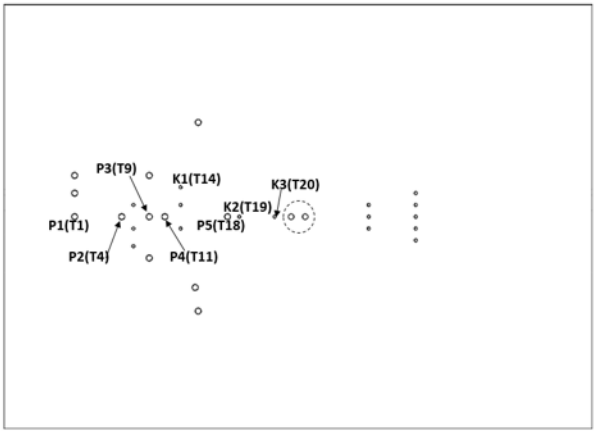

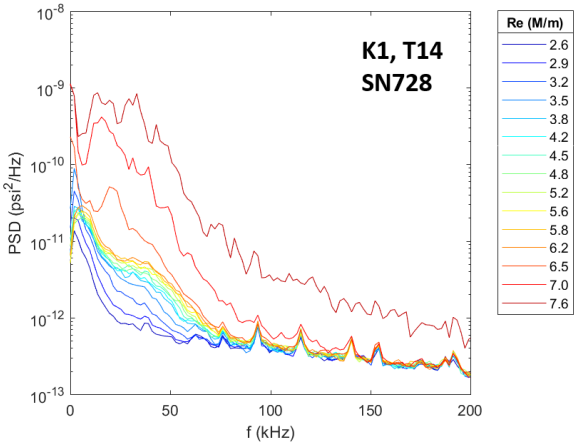

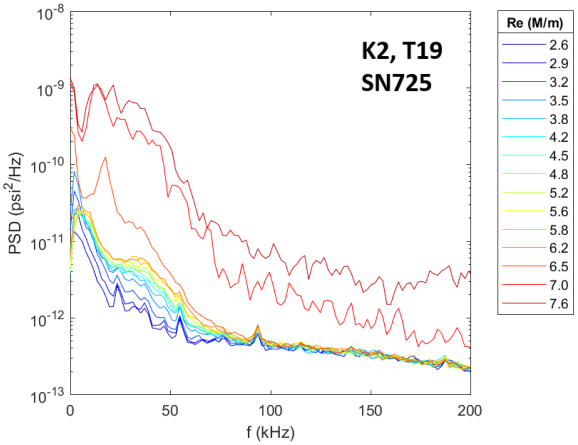

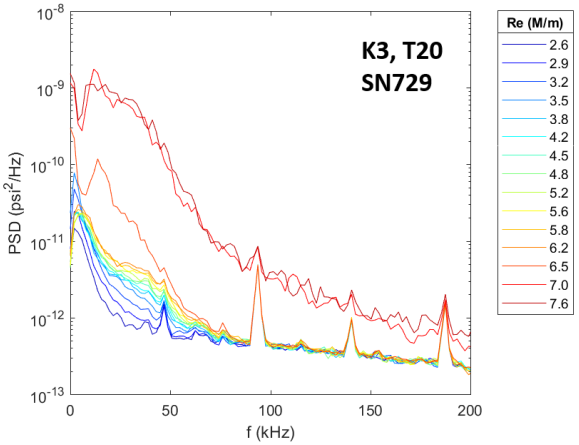

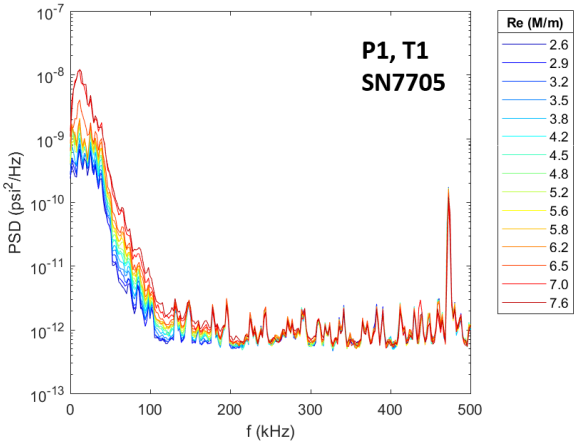
P1, T1
SN7705
PSD (psi²/Hz)
f (kHz)
Re (M/m)
2.6
2.9
3.2
3.5
3.8
4.2
4.5
4.8
5.2
5.6
5.8
6.2
6.5
7.0
7.6

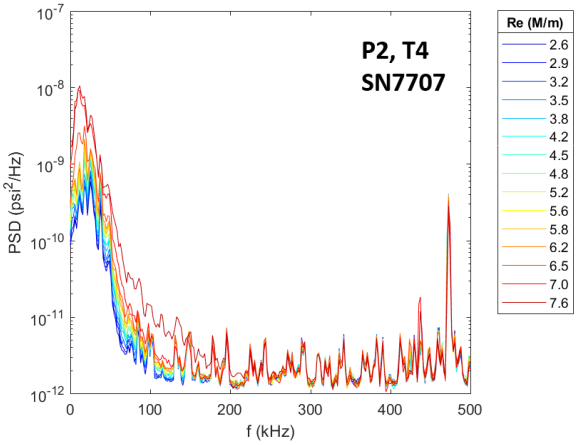
P2, T4
SN7707
PSD (psi²/Hz)
f (kHz)
Re (M/m)
2.6
2.9
3.2
3.5
3.8
4.2
4.5
4.8
5.2
5.6
5.8
6.2
6.5
7.0
7.6

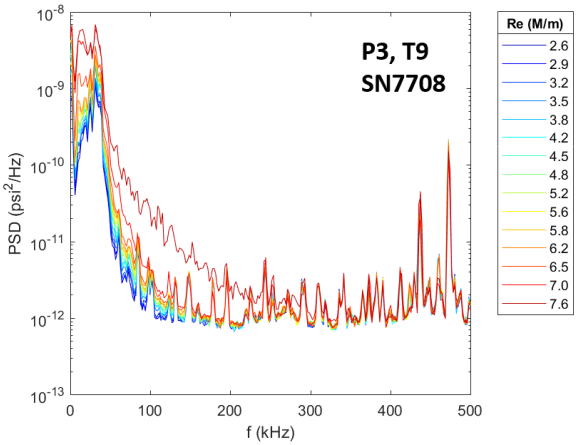
P3, T9
SN7708
PSD (psi²/Hz)
f (kHz)
Re (M/m)
2.6
2.9
3.2
3.5
3.8
4.2
4.5
4.8
5.2
5.6
5.8
6.2
6.5
7.0
7.6

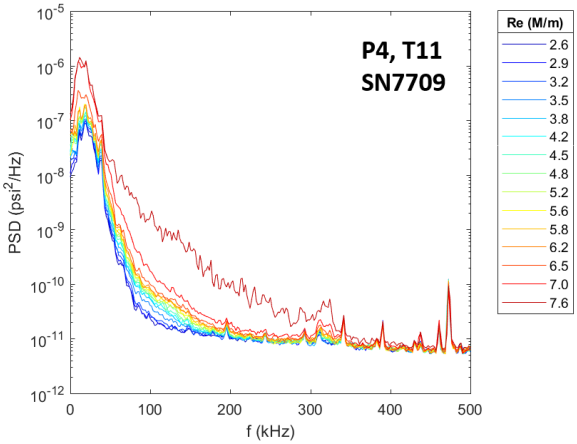
P4, T11
SN7709
PSD (psi²/Hz)
f (kHz)
Re (M/m)
2.6
2.9
3.2
3.5
3.8
4.2
4.5
4.8
5.2
5.6
5.8
6.2
6.5
7.0
7.6

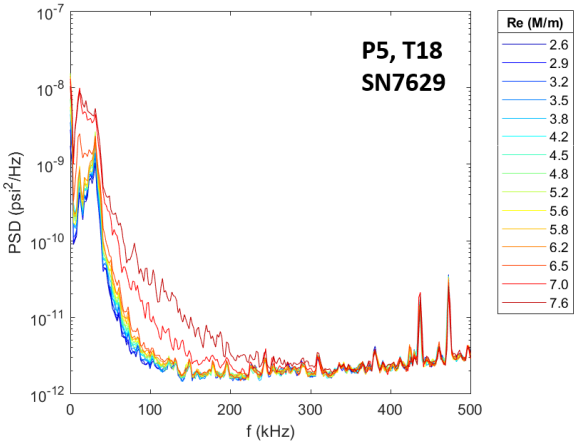
P5, T18
SN7629
PSD (psi²/Hz)
f (kHz)
Re (M/m)
2.6
2.9
3.2
3.5
3.8
4.2
4.5
4.8
5.2
5.6
5.8
6.2
6.5
7.0
7.6

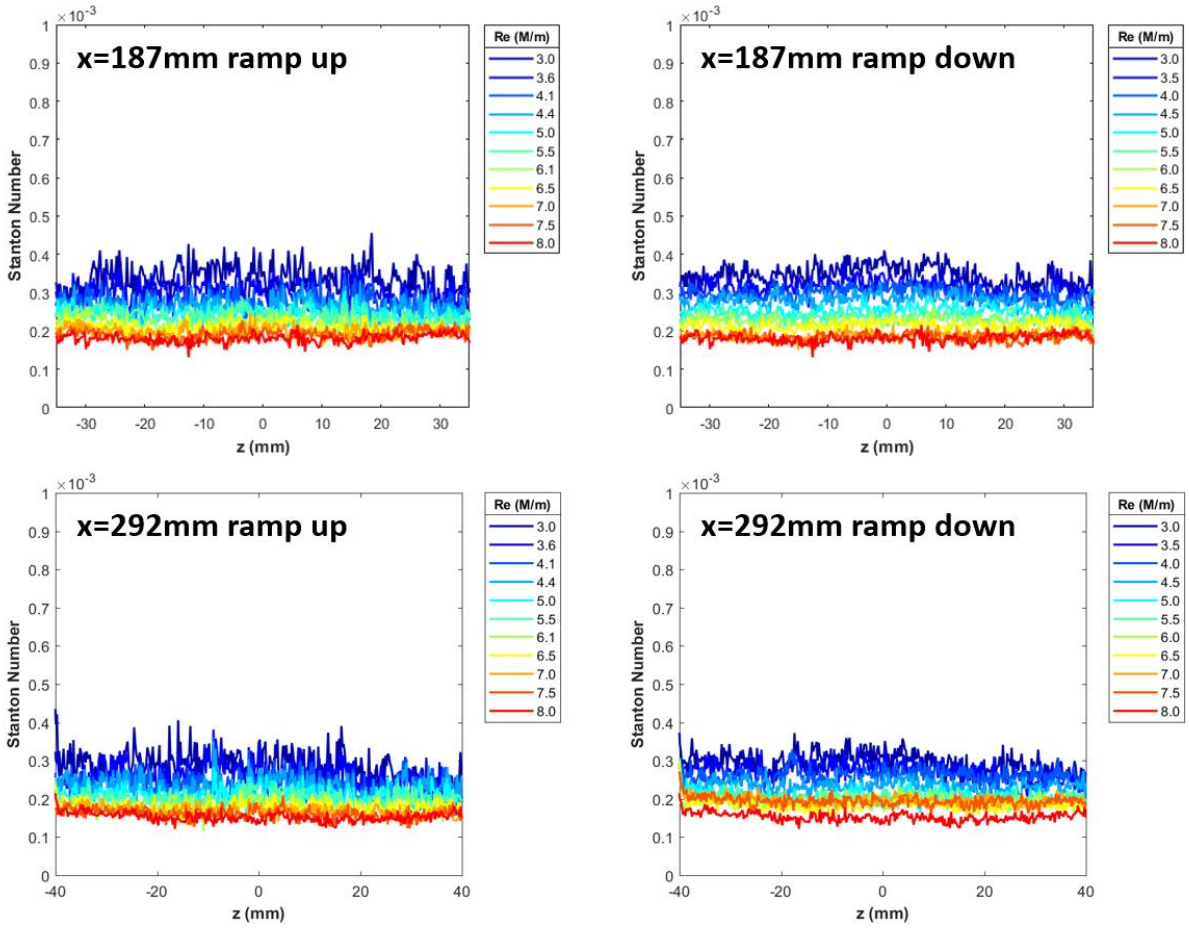

Run 3470. Attempted hot-wire traverse but jam and DAQ error.

Run 3471

Hot-wire traverse at x=187mm, z=0.4mm. Re near 4.9M/m.

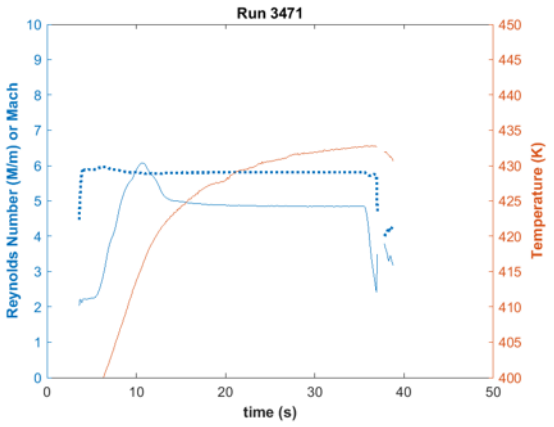

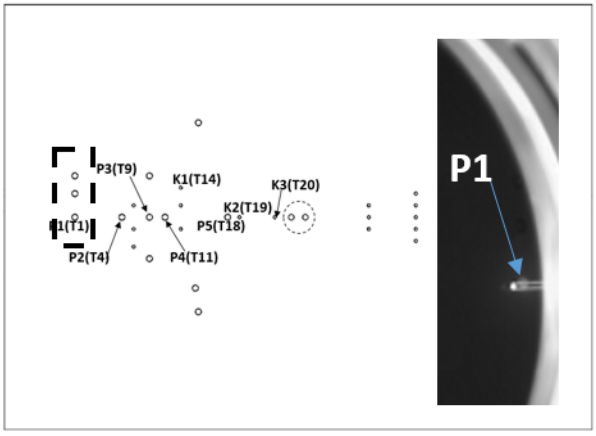

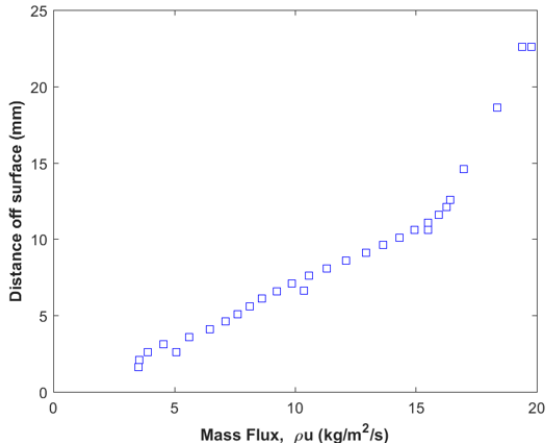
Distance off surface (mm)
Mass Flux, ρu (kg/m²/s)

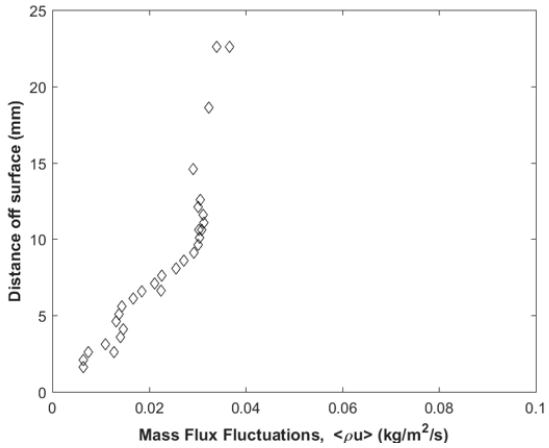
Distance off surface (mm)
Mass Flux Fluctuations, <ρu> (kg/m²/s)

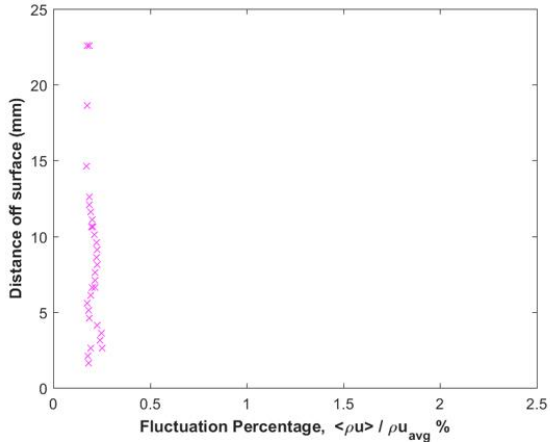
Distance off surface (mm)
Fluctuation Percentage, <ρu> / ρu_avg %

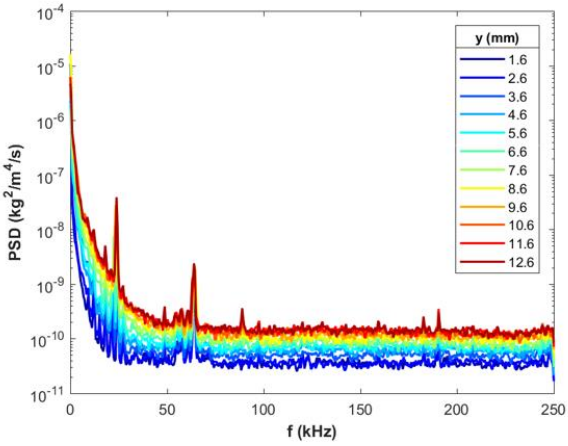
PSD (kg²/m⁴/s)
f (kHz)
y (mm)
1.6
2.6
3.6
4.6
5.6
6.6
7.6
8.6
9.6
10.6
11.6
12.6

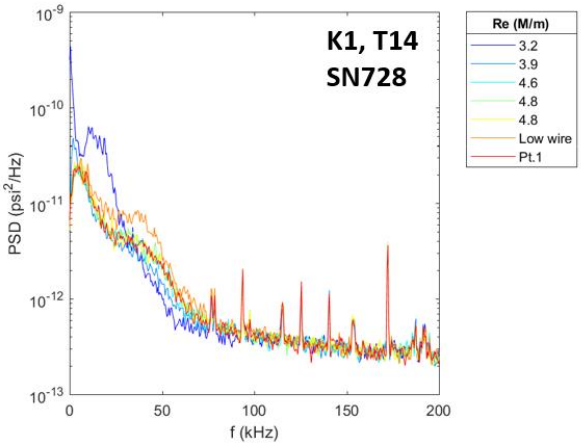
K1, T14
SN728
PSD (psi²/Hz)
f (kHz)
Re (M/m)
3.2
3.9
4.6
4.8
4.8
Low wire
Pt.1

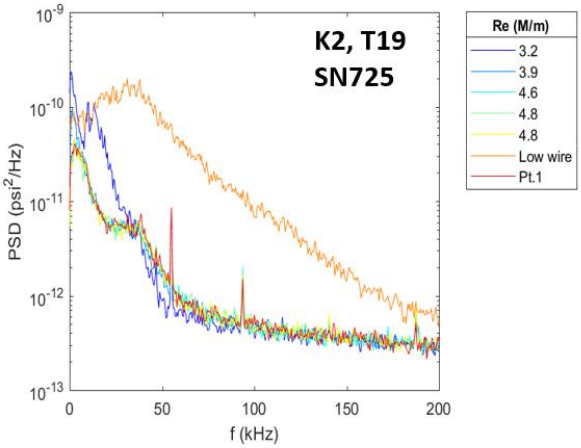
K2, T19
SN725
PSD (psi²/Hz)
f (kHz)
Re (M/m)
3.2
3.9
4.6
4.8
4.8
Low wire
Pt.1

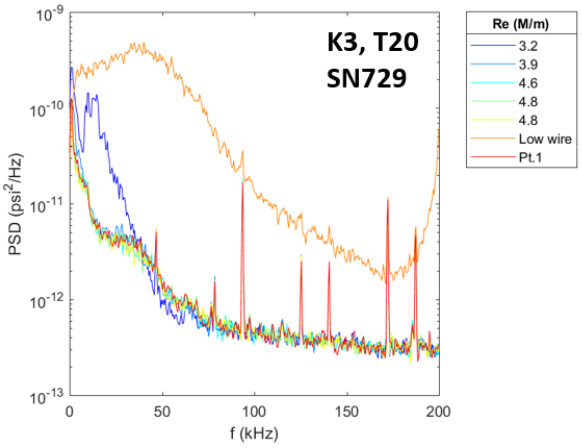
K3, T20
SN729
Re (M/m)
3.2
3.9
4.6
4.8
4.8
Low wire
Pt.1
PSD (psi²/Hz)
f (kHz)

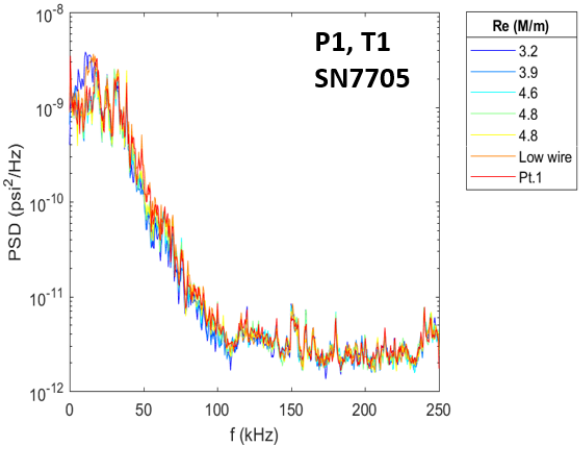
P1, T1
SN7705
Re (M/m)
3.2
3.9
4.6
4.8
4.8
Low wire
Pt.1
PSD (psi²/Hz)
f (kHz)

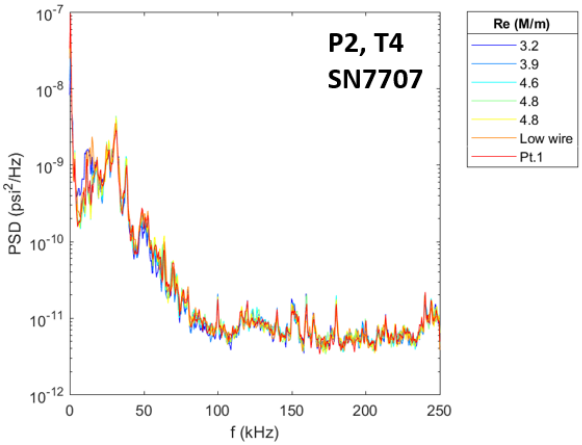
P2, T4
SN7707
Re (M/m)
3.2
3.9
4.6
4.8
4.8
Low wire
Pt.1
PSD (psi²/Hz)
f (kHz)

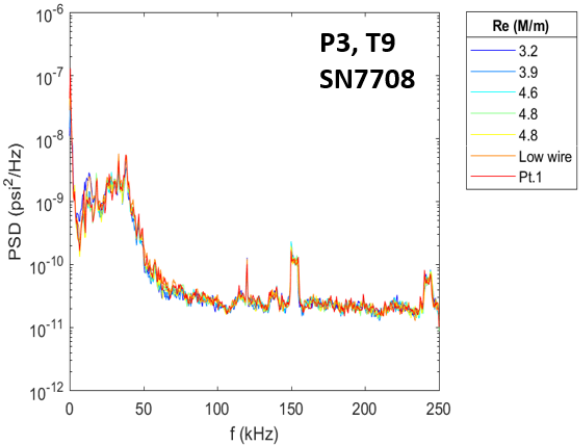
P3, T9
SN7708
Re (M/m)
3.2
3.9
4.6
4.8
4.8
Low wire
Pt.1
PSD (psi²/Hz)
f (kHz)

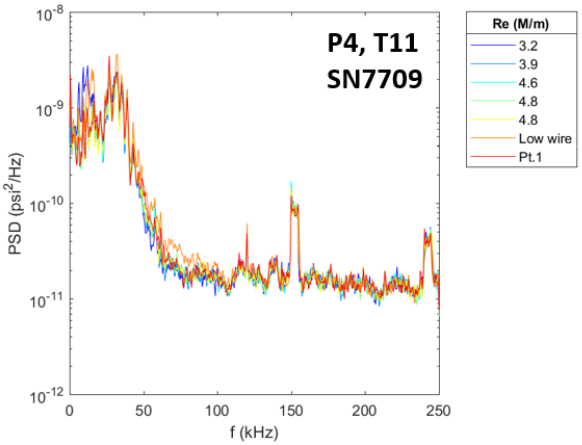
P4, T11
SN7709
Re (M/m)
3.2
3.9
4.6
4.8
4.8
Low wire
Pt.1
PSD (psi²/Hz)
f (kHz)

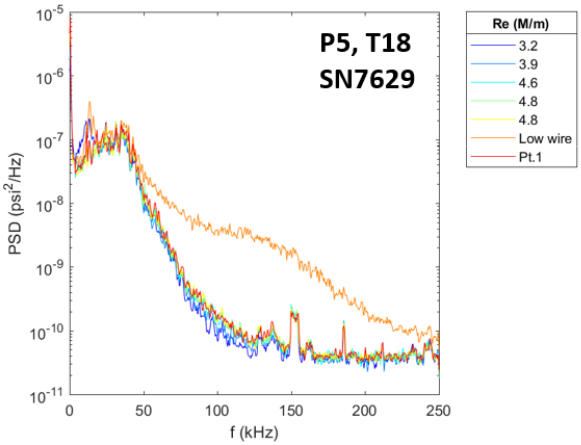
P5, T18
SN7629
Re (M/m)
3.2
3.9
4.6
4.8
4.8
Low wire
Pt.1
PSD (psi²/Hz)
f (kHz)

Run 3472

Hot-wire traverse at x=187mm, z=-1.6mm. Re near 4.8M/m.

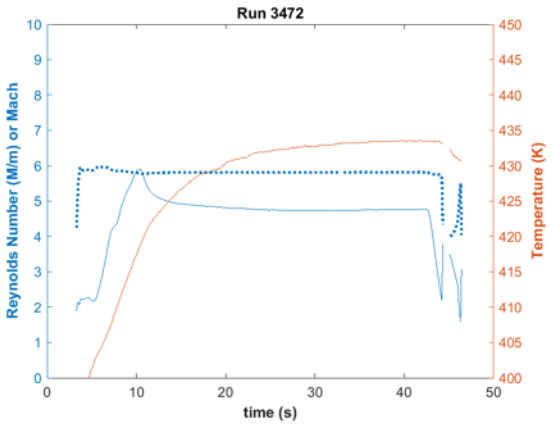

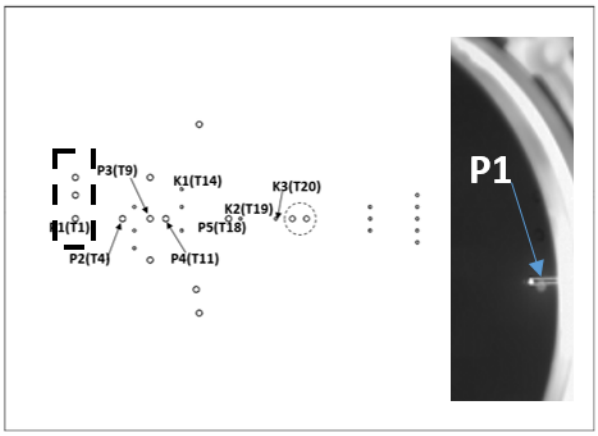

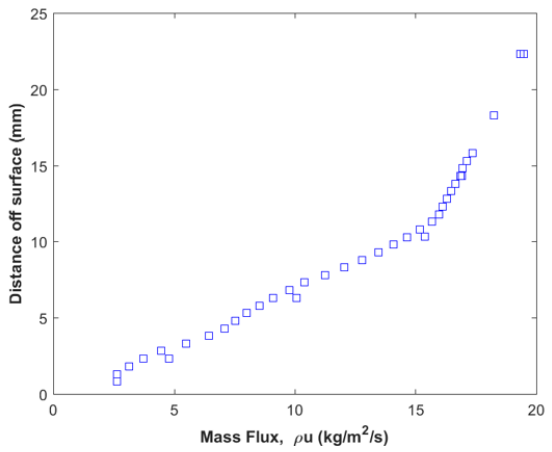

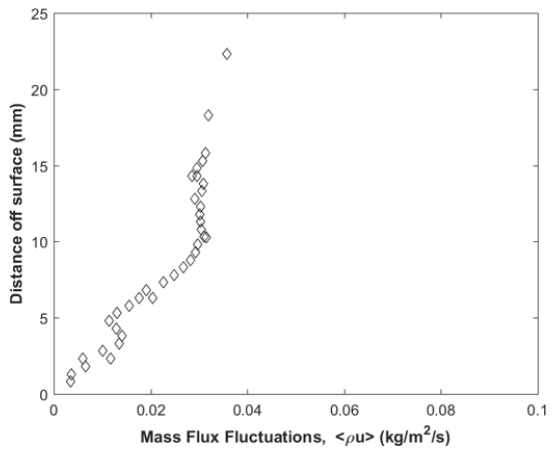

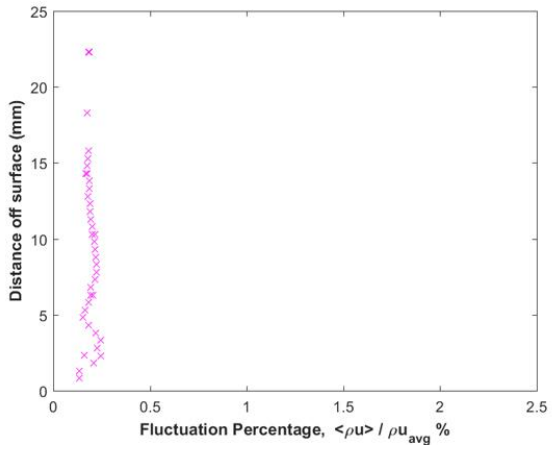

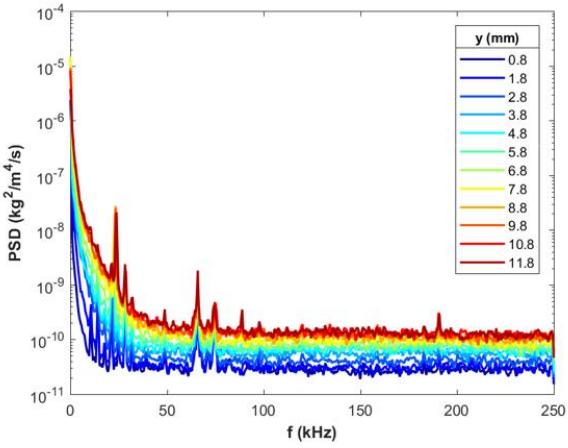

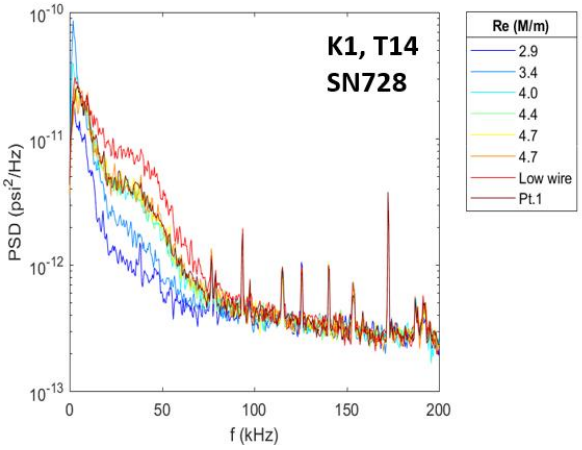
K1, T14
SN728
PSD (psi²/Hz)
f (kHz)
Re (M/m)
2.9
3.4
4.0
4.4
4.7
4.7
Low wire
Pt.1

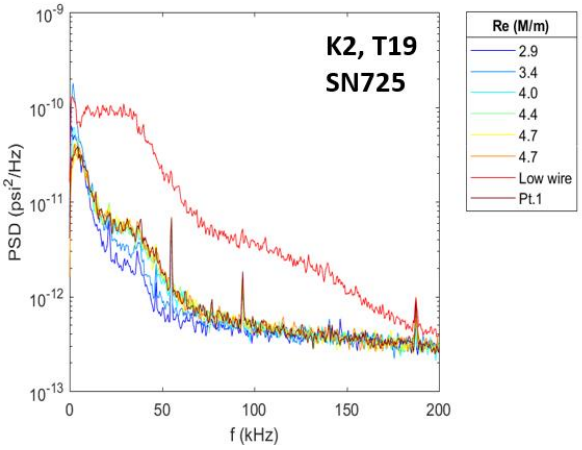
K2, T19
SN725
PSD (psi²/Hz)
f (kHz)
Re (M/m)
2.9
3.4
4.0
4.4
4.7
4.7
Low wire
Pt.1

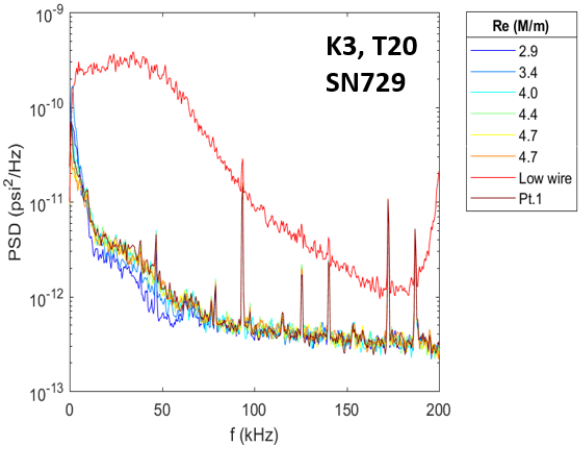
K3, T20
SN729
PSD (psi²/Hz)
f (kHz)
Re (M/m)
2.9
3.4
4.0
4.4
4.7
4.7
Low wire
Pt.1

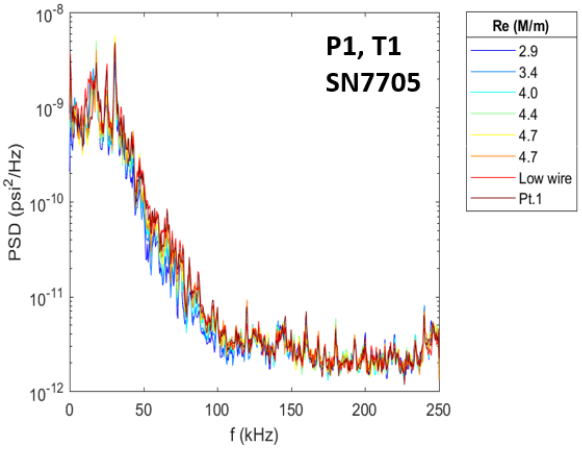
P1, T1
SN7705
PSD (psi²/Hz)
f (kHz)
Re (M/m)
2.9
3.4
4.0
4.4
4.7
4.7
Low wire
Pt.1

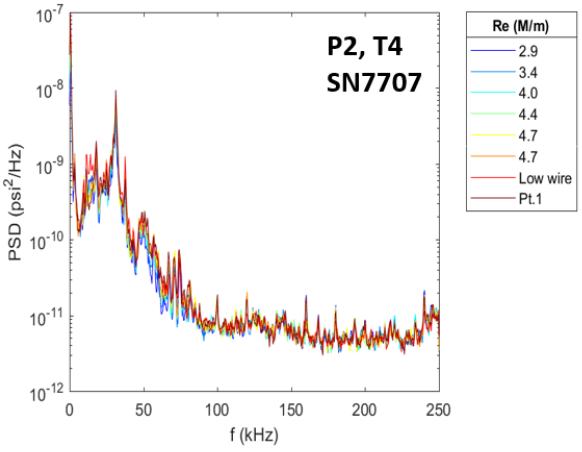
P2, T4
SN7707
PSD (psi²/Hz)
f (kHz)
Re (M/m)
2.9
3.4
4.0
4.4
4.7
4.7
Low wire
Pt.1

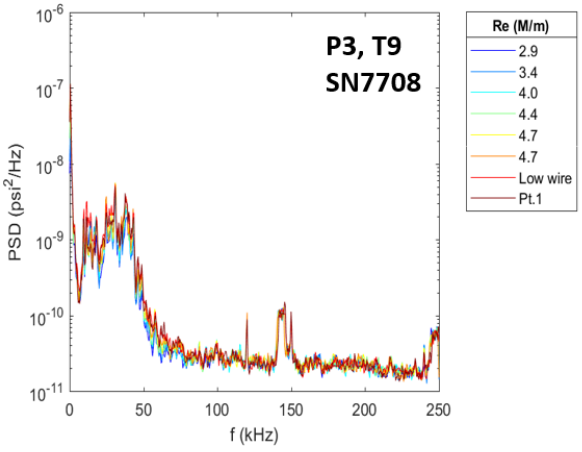
P3, T9
SN7708
PSD (psi²/Hz)
f (kHz)
Re (M/m)
2.9
3.4
4.0
4.4
4.7
4.7
Low wire
Pt.1

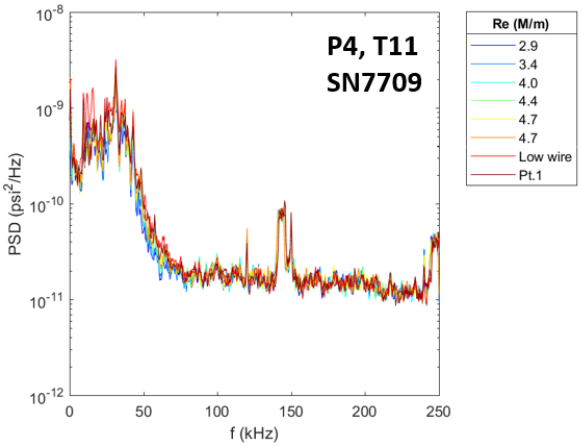

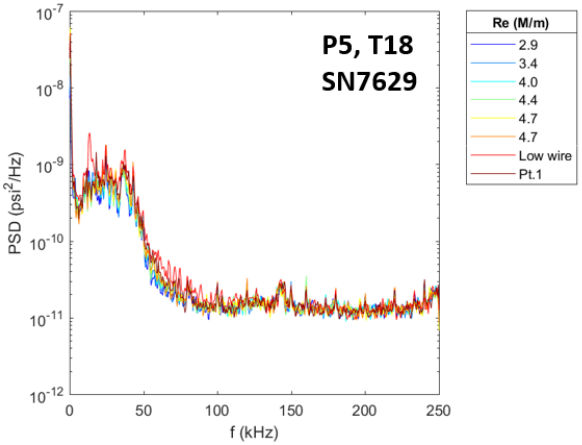

Run 3473

Hot-wire traverse at x=187mm, z=0.0mm. Re near 4.7M/m.

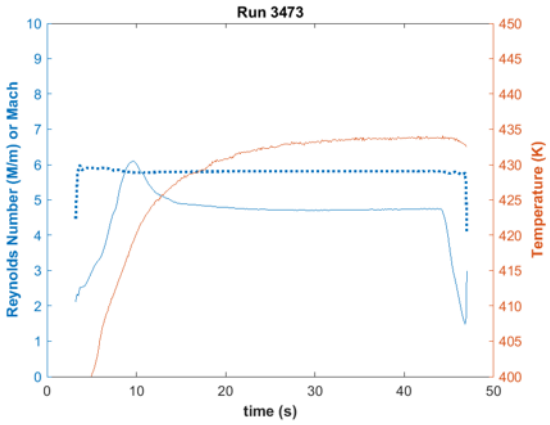

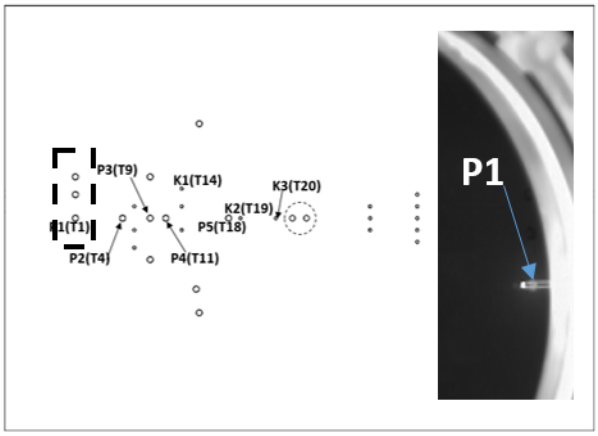

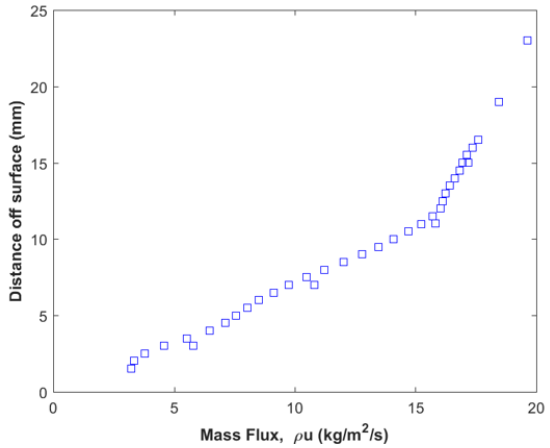

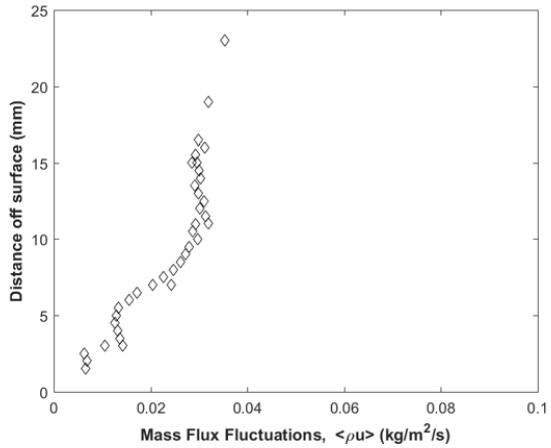

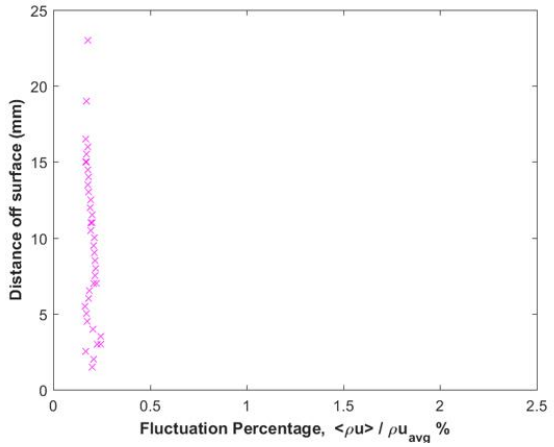
Distance off surface (mm)
Fluctuation Percentage, <ρu> / ρu_avg %

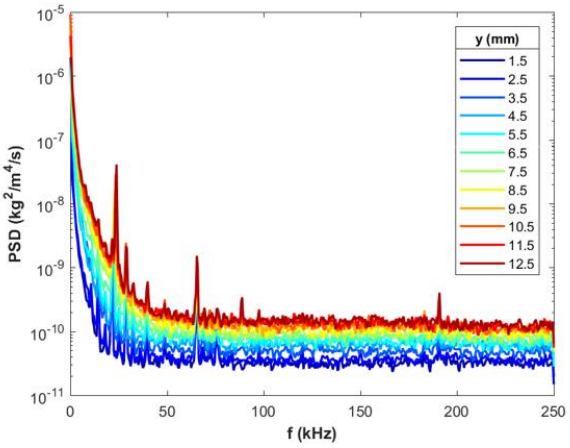
y (mm)
1.5
2.5
3.5
4.5
5.5
6.5
7.5
8.5
9.5
10.5
11.5
12.5
PSD (kg²/m⁴/s)
f (kHz)

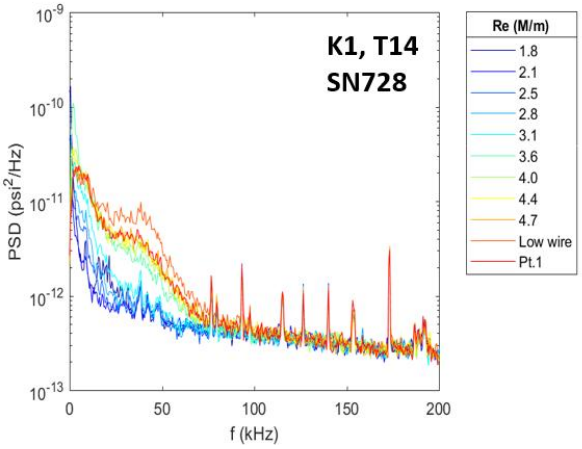
K1, T14
SN728
Re (M/m)
1.8
2.1
2.5
2.8
3.1
3.6
4.0
4.4
4.7
Low wire
Pt.1
PSD (psi²/Hz)
f (kHz)

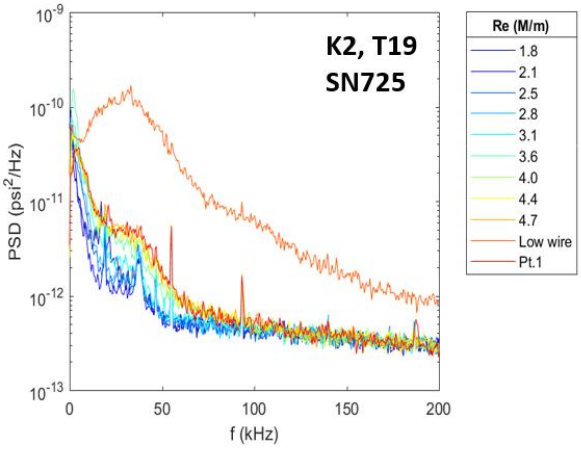
K2, T19
SN725
Re (M/m)
1.8
2.1
2.5
2.8
3.1
3.6
4.0
4.4
4.7
Low wire
Pt.1
PSD (psi²/Hz)
f (kHz)

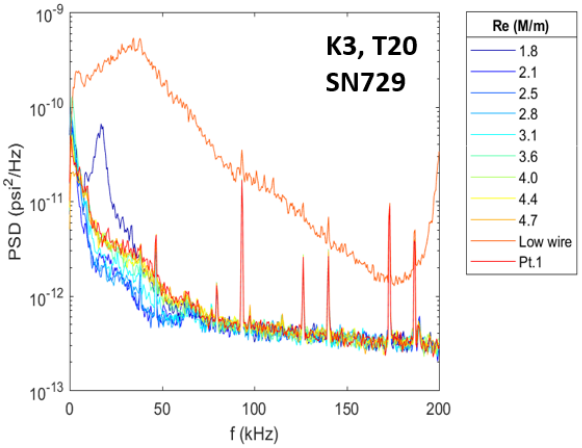
K3, T20
SN729
Re (M/m)
1.8
2.1
2.5
2.8
3.1
3.6
4.0
4.4
4.7
Low wire
Pt.1
PSD (psi²/Hz)
f (kHz)

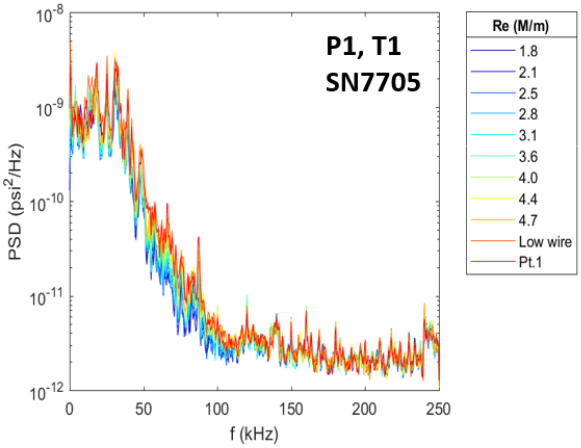
P1, T1
SN7705
Re (M/m)
1.8
2.1
2.5
2.8
3.1
3.6
4.0
4.4
4.7
Low wire
Pt.1
PSD (psi²/Hz)
f (kHz)

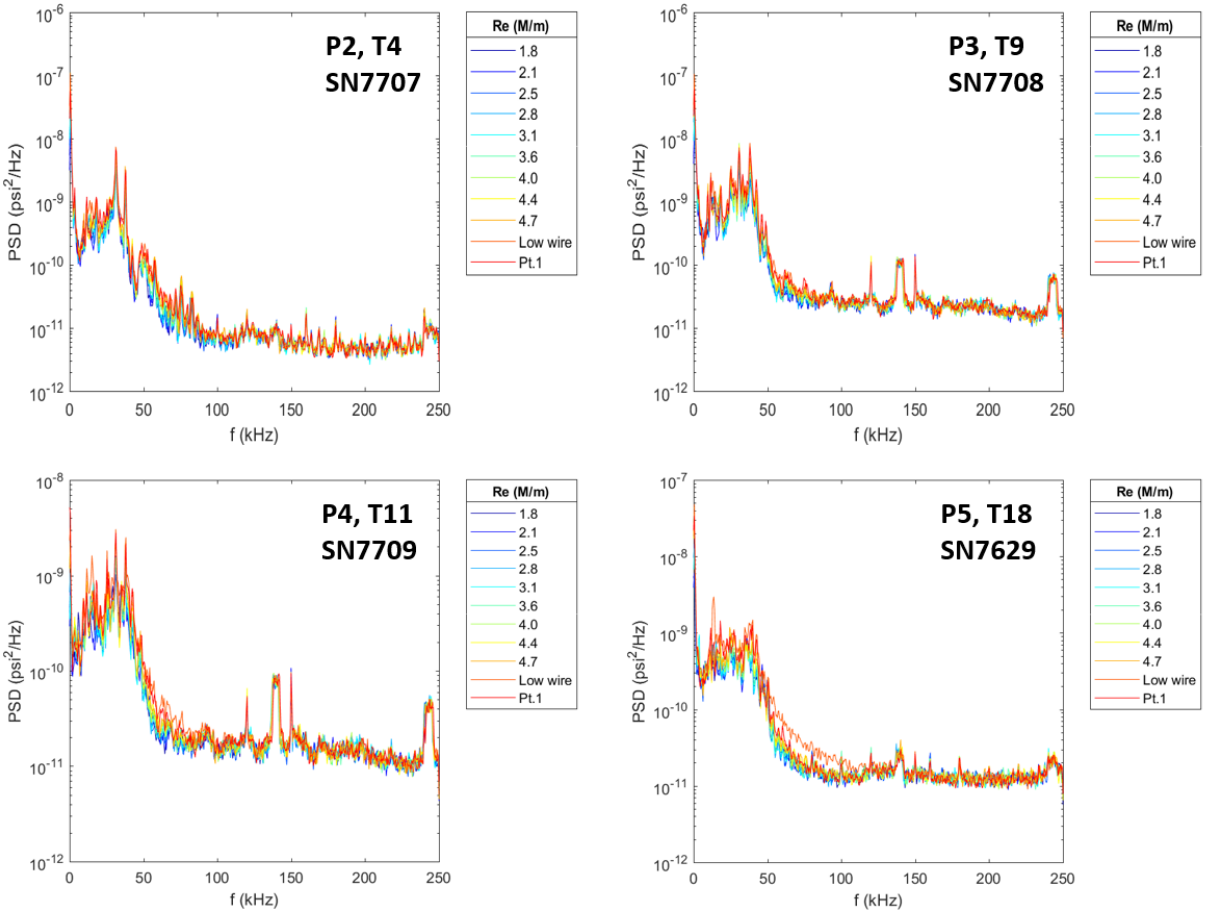

Run 3474

Hot-wire traverse at x=293mm, z=-1.2mm. Re near 4.7M/m.

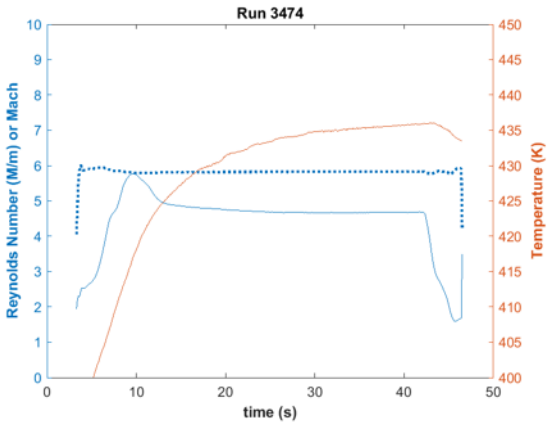

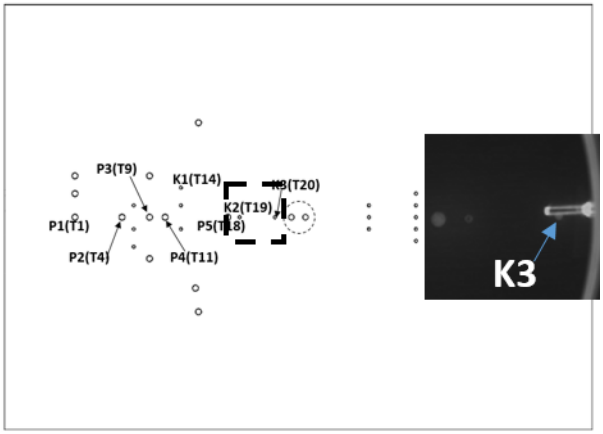

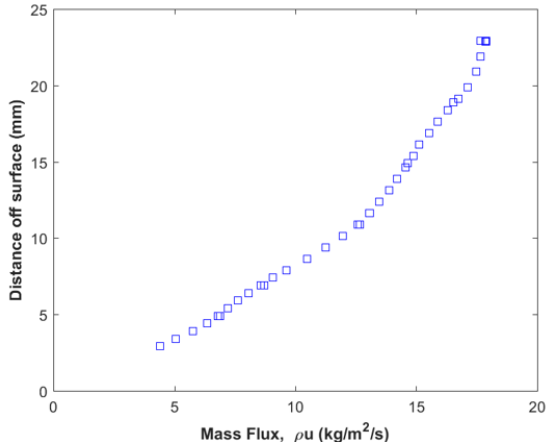
Distance off surface (mm)
Mass Flux, ρu (kg/m²/s)

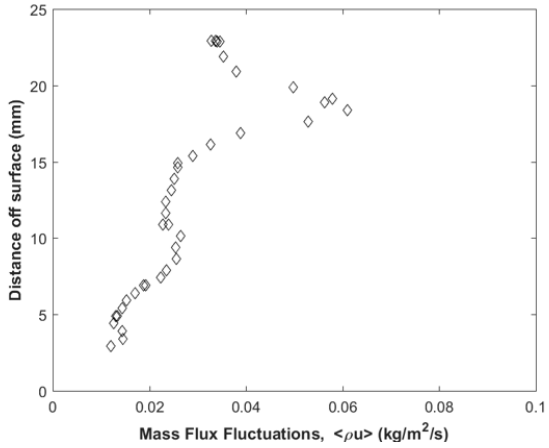
Distance off surface (mm)
Mass Flux Fluctuations, <ρu> (kg/m²/s)

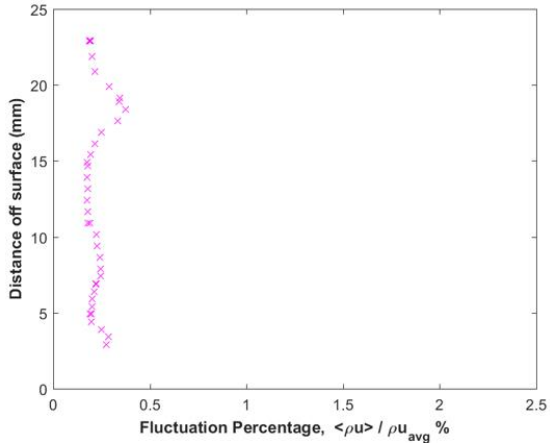
Distance off surface (mm)
Fluctuation Percentage, <ρu> / ρu_avg %

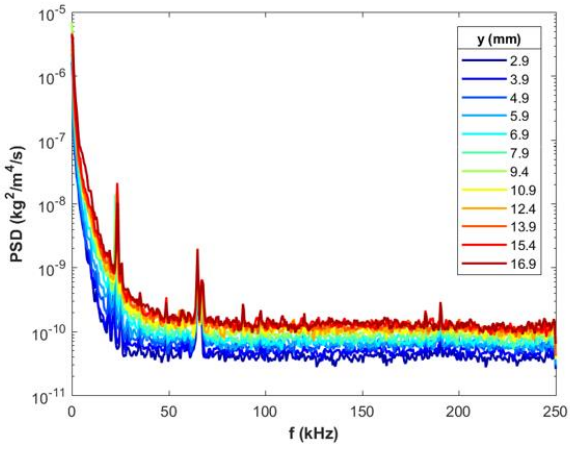
y (mm)
2.9
3.9
4.9
5.9
6.9
7.9
9.4
10.9
12.4
13.9
15.4
16.9
PSD (kg²/m⁴/s)
f (kHz)

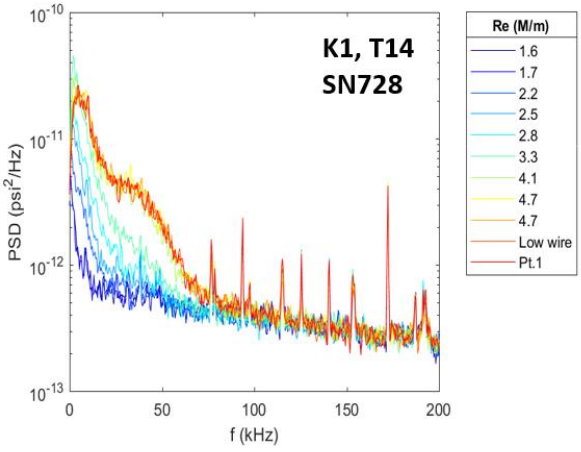
K1, T14
SN728
Re (M/m)
1.6
1.7
2.2
2.5
2.8
3.3
4.1
4.7
4.7
Low wire
Pt.1
PSD (psi²/Hz)
f (kHz)

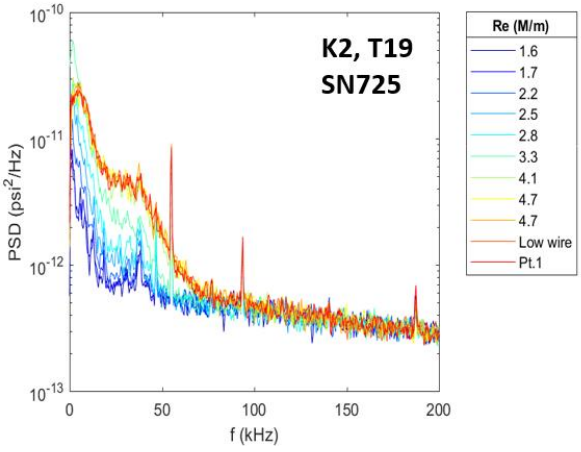
K2, T19
SN725
Re (M/m)
1.6
1.7
2.2
2.5
2.8
3.3
4.1
4.7
4.7
Low wire
Pt.1
PSD (psi²/Hz)
f (kHz)

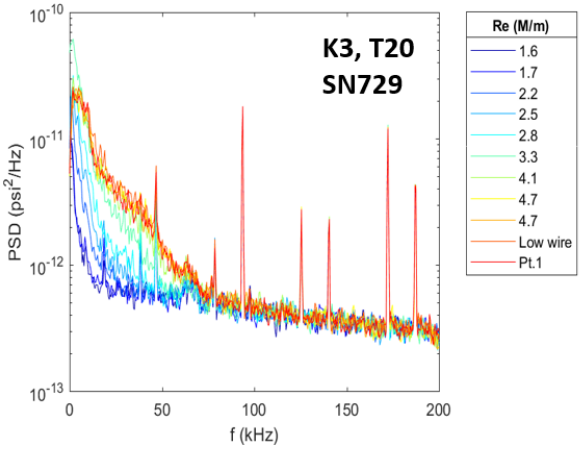
K3, T20
SN729
PSD (psi²/Hz)
f (kHz)
Re (M/m)
1.6
1.7
2.2
2.5
2.8
3.3
4.1
4.7
4.7
Low wire
Pt.1

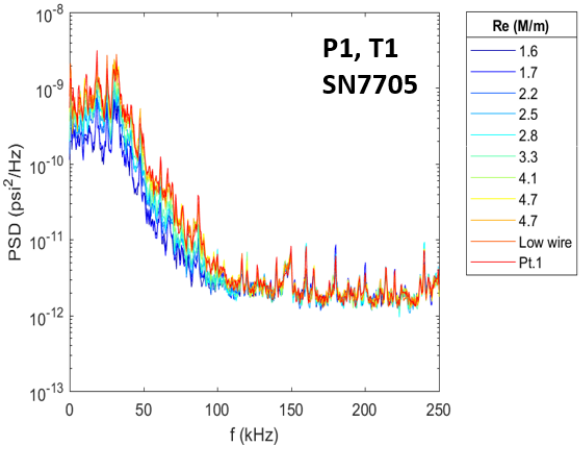
P1, T1
SN7705
PSD (psi²/Hz)
f (kHz)
Re (M/m)
1.6
1.7
2.2
2.5
2.8
3.3
4.1
4.7
4.7
Low wire
Pt.1

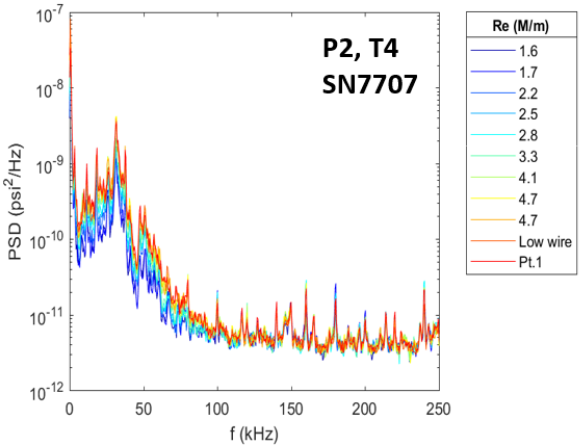
P2, T4
SN7707
PSD (psi²/Hz)
f (kHz)
Re (M/m)
1.6
1.7
2.2
2.5
2.8
3.3
4.1
4.7
4.7
Low wire
Pt.1

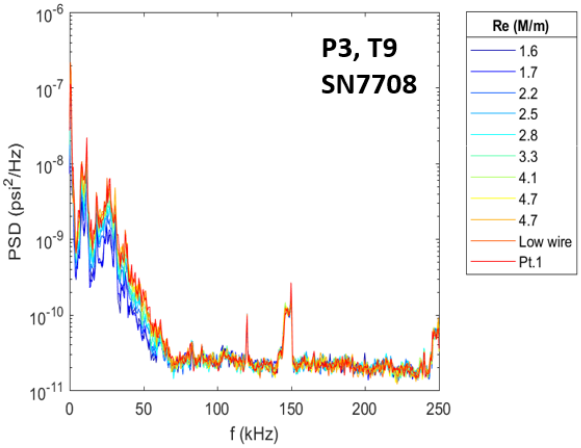
P3, T9
SN7708
PSD (psi²/Hz)
f (kHz)
Re (M/m)
1.6
1.7
2.2
2.5
2.8
3.3
4.1
4.7
4.7
Low wire
Pt.1

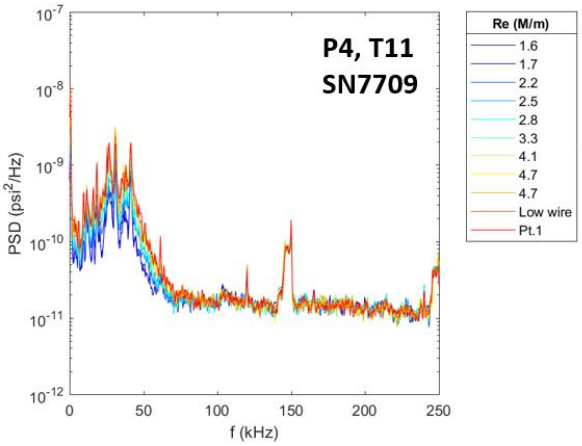
P4, T11
SN7709
PSD (psi²/Hz)
f (kHz)
Re (M/m)
1.6
1.7
2.2
2.5
2.8
3.3
4.1
4.7
4.7
Low wire
Pt.1

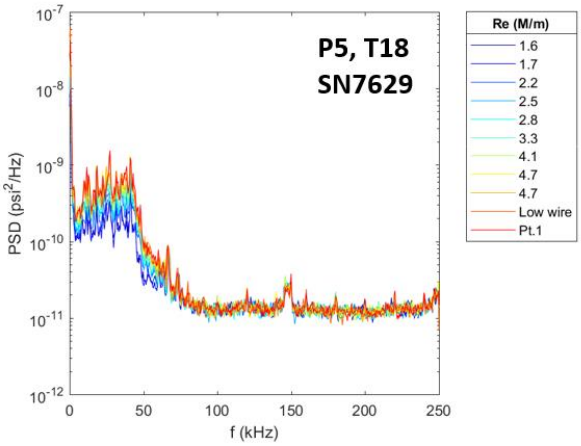
P5, T18
SN7629
PSD (psi²/Hz)
f (kHz)
Re (M/m)
1.6
1.7
2.2
2.5
2.8
3.3
4.1
4.7
4.7
Low wire
Pt.1

Run 3475

Hot-wire traverse at x=293mm, z=0.7mm. Re near 4.9M/m.

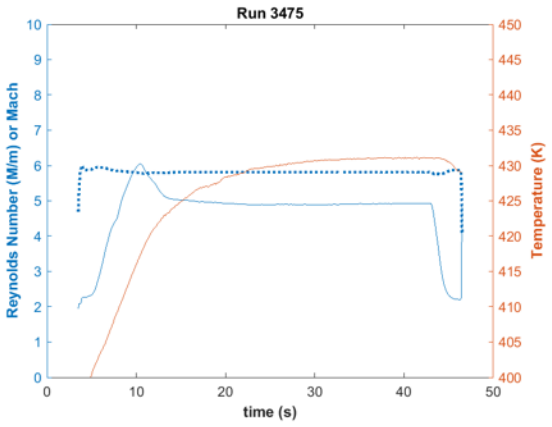

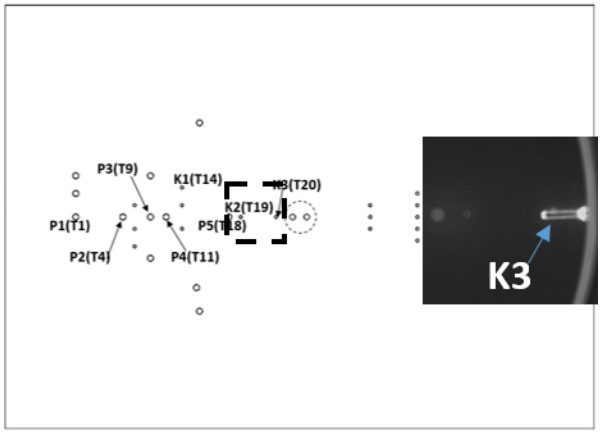

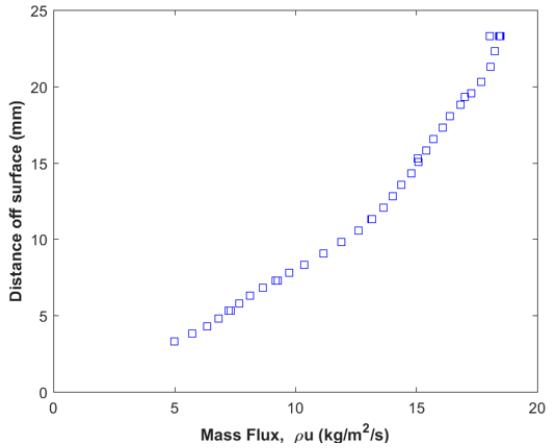

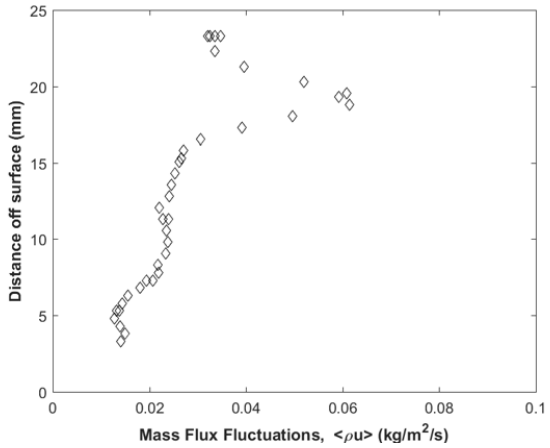

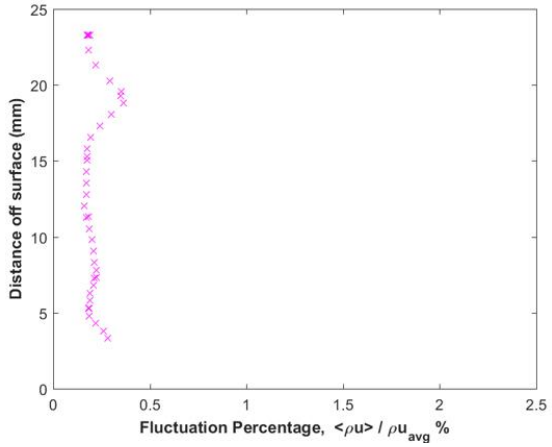

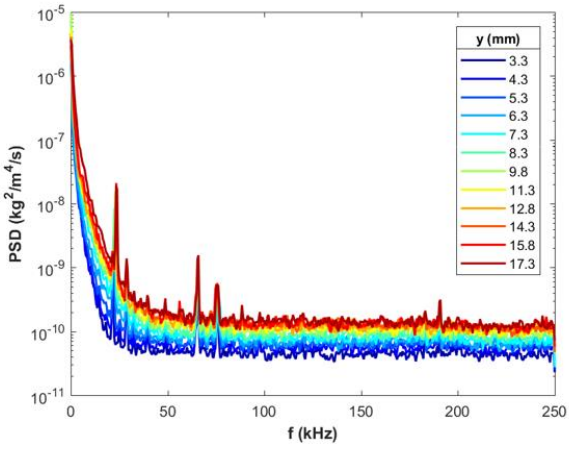

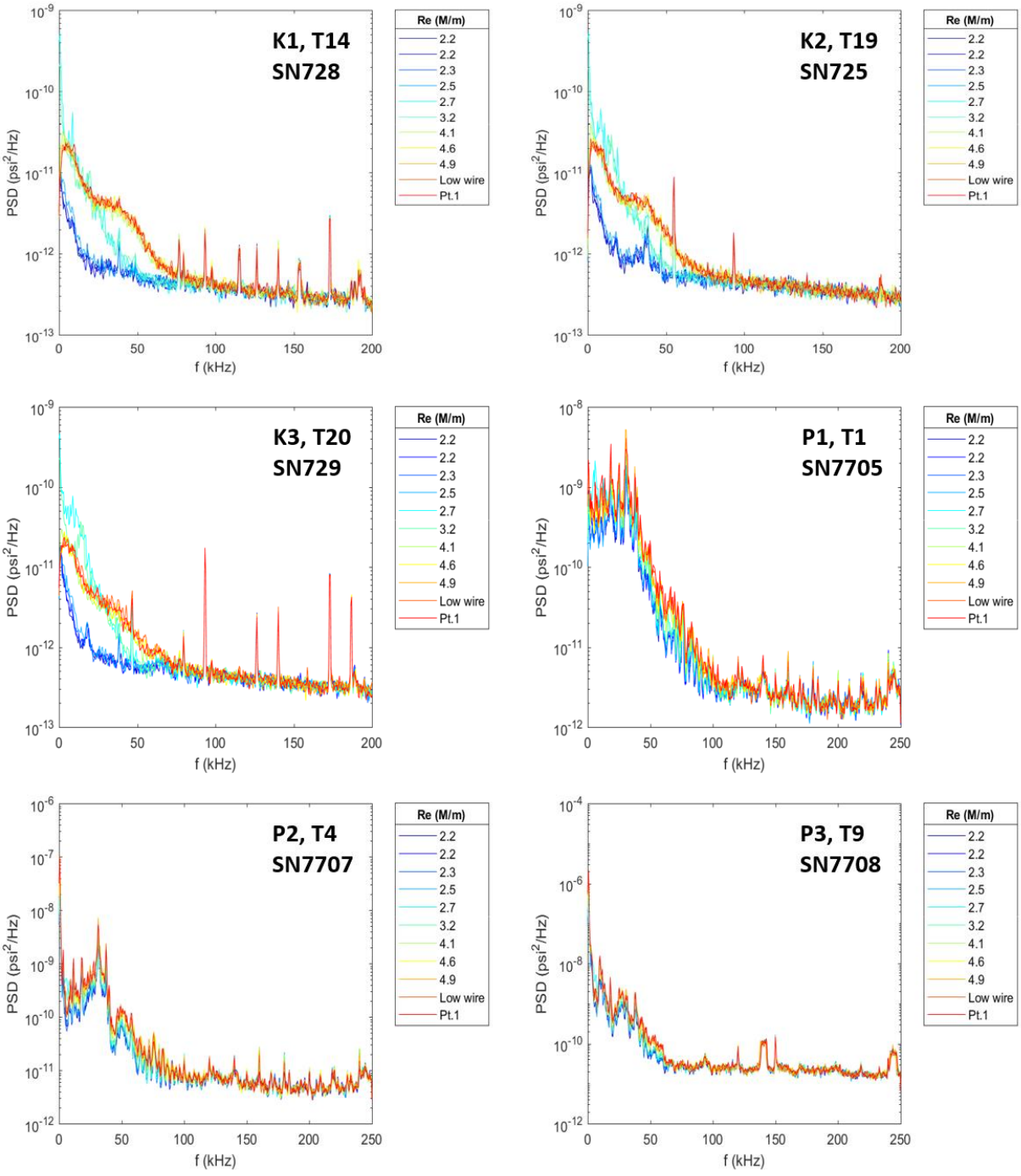
K1, T14
SN728
K2, T19
SN725
K3, T20
SN729
P1, T1
SN7705
P2, T4
SN7707
P3, T9
SN7708
PSD (psi²/Hz)
f (kHz)
Re (M/m)
2.2
2.2
2.3
2.5
2.7
3.2
4.1
4.6
4.9
Low wire
Pt.1

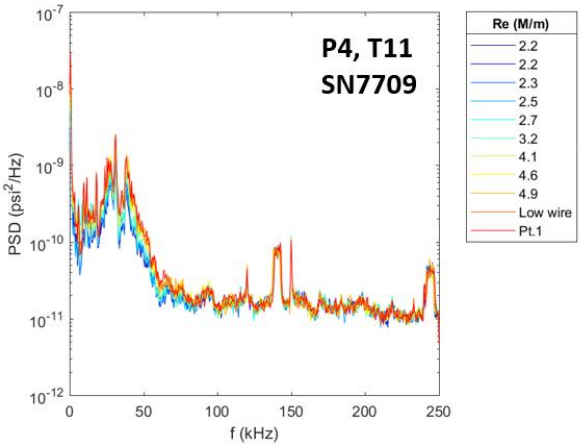

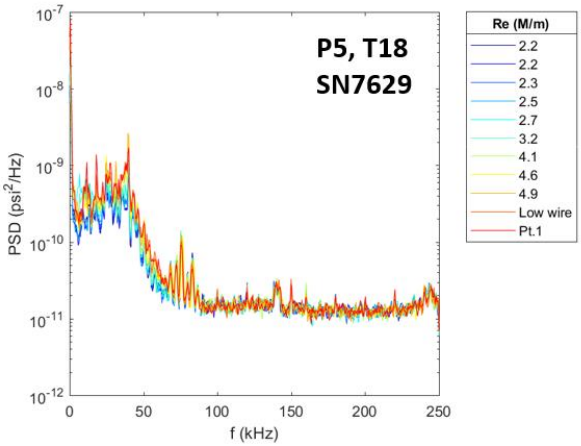

Cylinder wake

Run 3476

Hot-wire was positioned above K3(T24) and traversed from 20 to 40 mm above surface. Re near 4.9M/m.

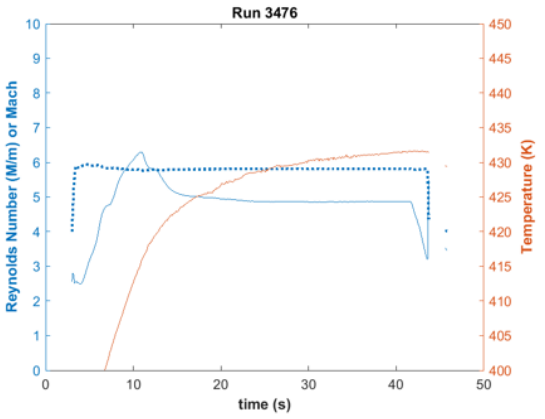

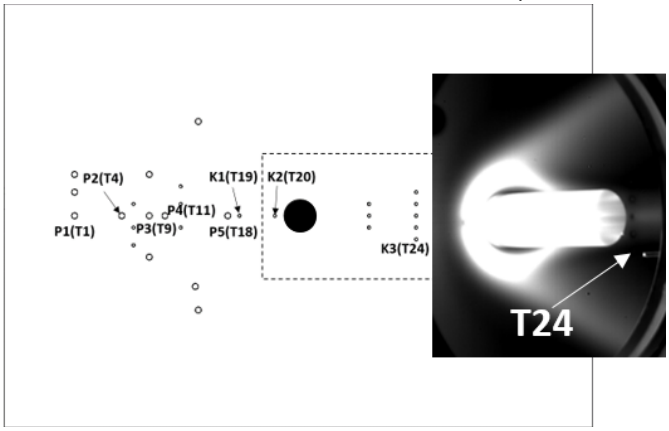

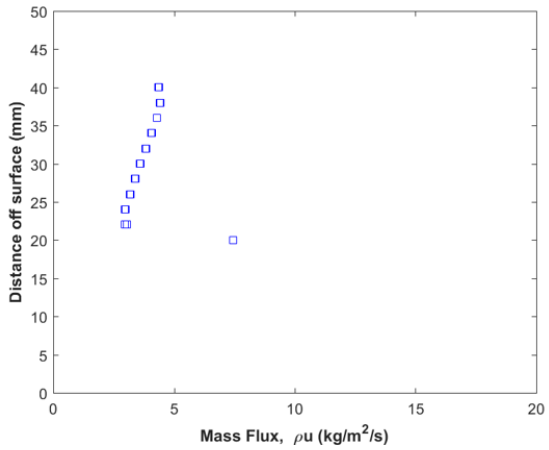

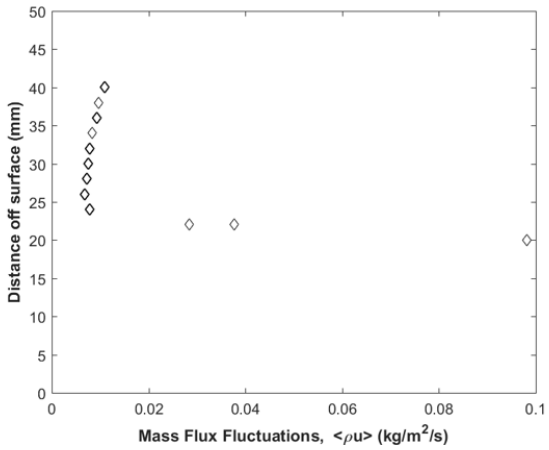

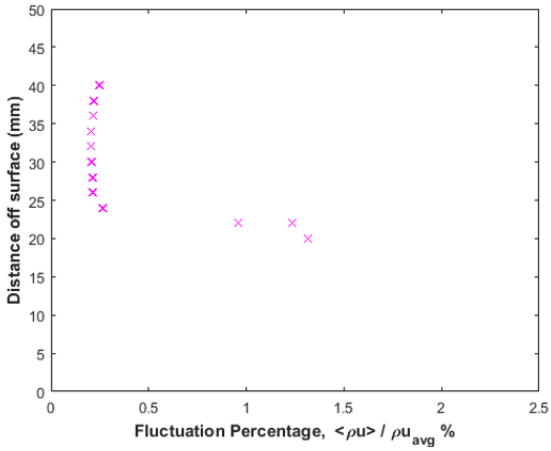
Distance off surface (mm)
Fluctuation Percentage, <ρu> / ρu_avg %

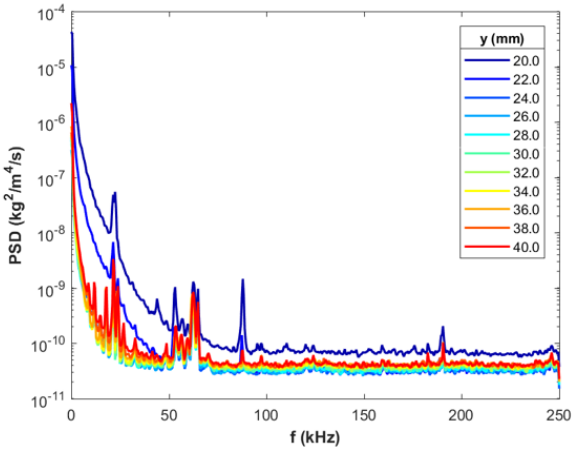
PSD (kg²/m⁴/s)
f (kHz)
y (mm)
20.0
22.0
24.0
26.0
28.0
30.0
32.0
34.0
36.0
38.0
40.0

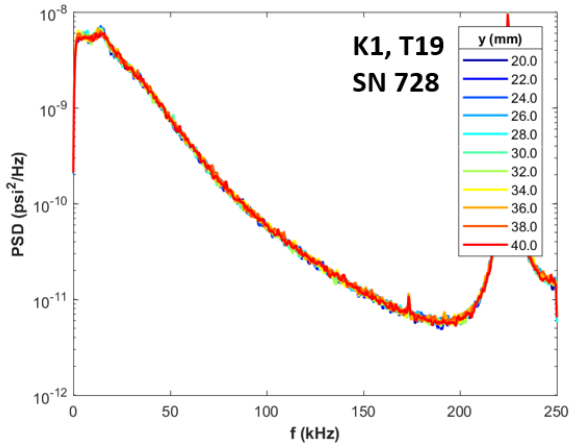
K1, T19
SN 728
PSD (psi²/Hz)
f (kHz)
y (mm)
20.0
22.0
24.0
26.0
28.0
30.0
32.0
34.0
36.0
38.0
40.0

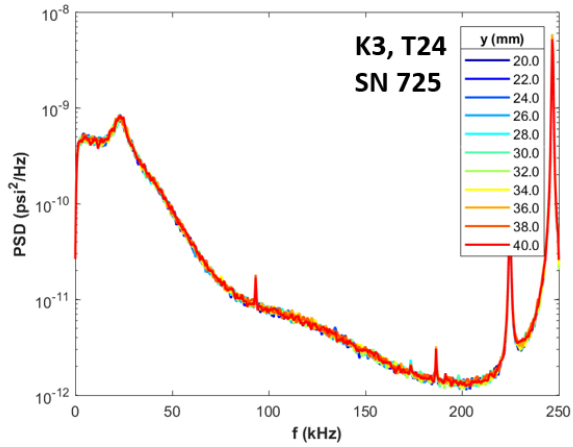
K3, T24
SN 725
PSD (psi²/Hz)
f (kHz)
y (mm)
20.0
22.0
24.0
26.0
28.0
30.0
32.0
34.0
36.0
38.0
40.0

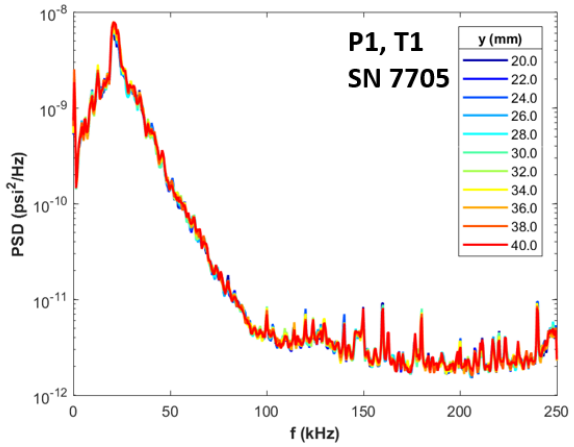
P1, T1
SN 7705
PSD (psi²/Hz)
f (kHz)
y (mm)
20.0
22.0
24.0
26.0
28.0
30.0
32.0
34.0
36.0
38.0
40.0

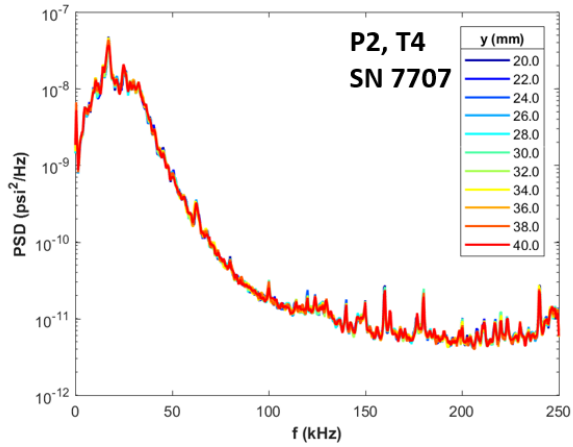
P2, T4
SN 7707
PSD (psi²/Hz)
f (kHz)
y (mm)
20.0
22.0
24.0
26.0
28.0
30.0
32.0
34.0
36.0
38.0
40.0

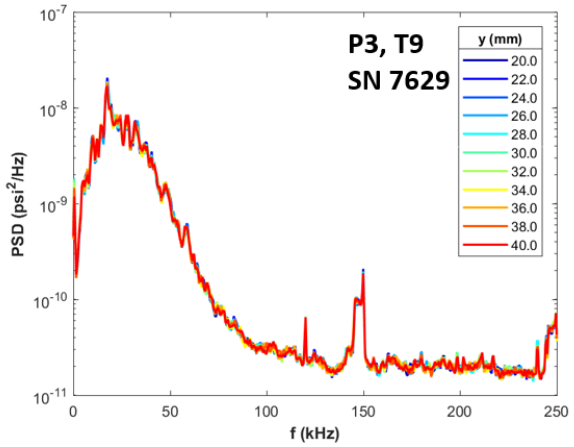

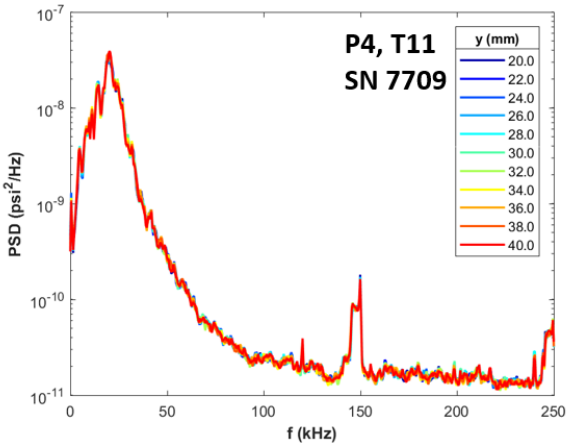

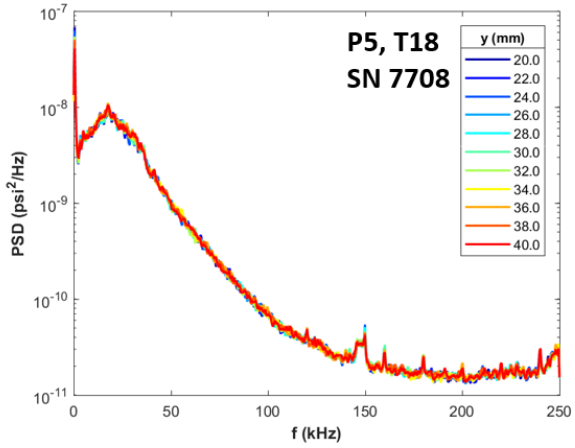

Run 3477

Hot-wire positioned at x/D = 1.7, z/D = 2.0, and traversed from 3.0 to 25.0 mm. Re near 4.7M/m.

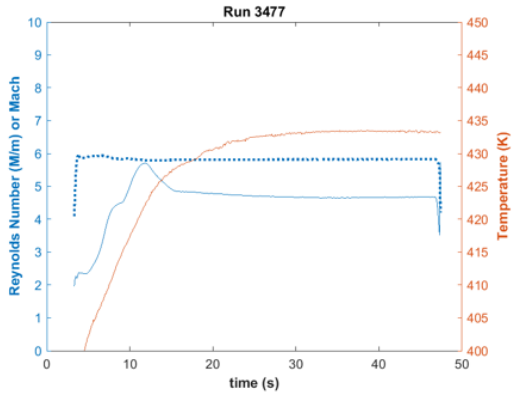

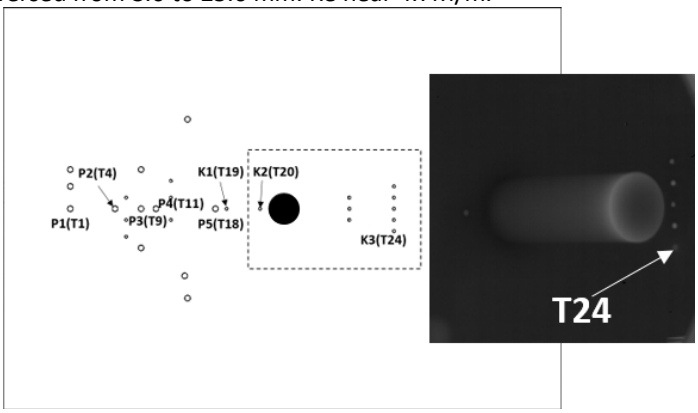

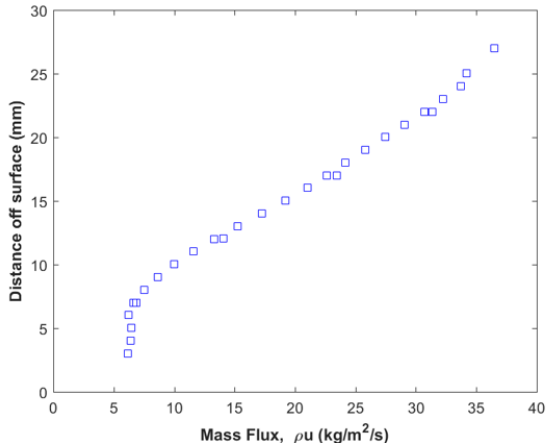
Distance off surface (mm)
Mass Flux, ρu (kg/m²/s)

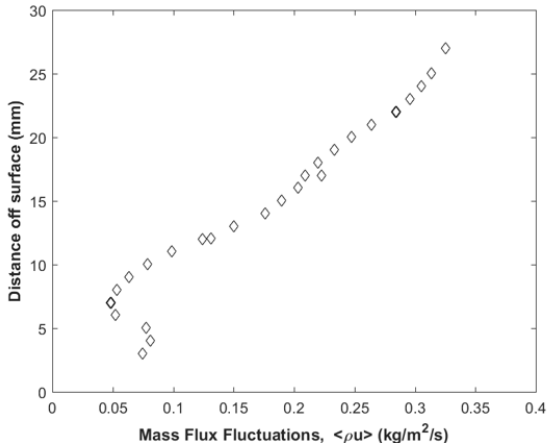
Distance off surface (mm)
Mass Flux Fluctuations, <ρu> (kg/m²/s)

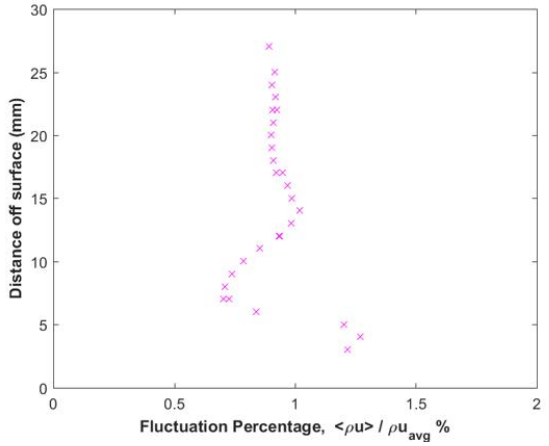
Distance off surface (mm)
Fluctuation Percentage, <ρu> / ρu_avg %

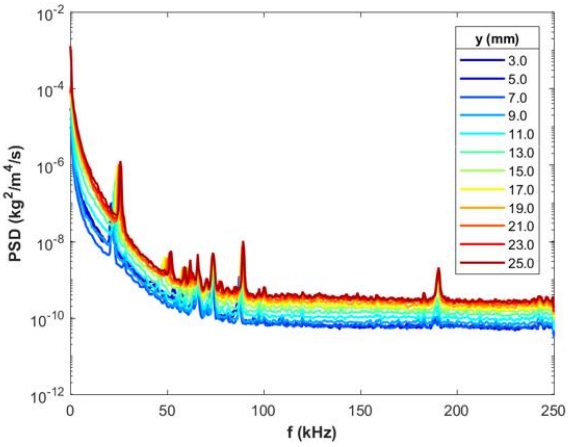
PSD (kg²/m⁴/s)
f (kHz)
y (mm)
3.0
5.0
7.0
9.0
11.0
13.0
15.0
17.0
19.0
21.0
23.0
25.0

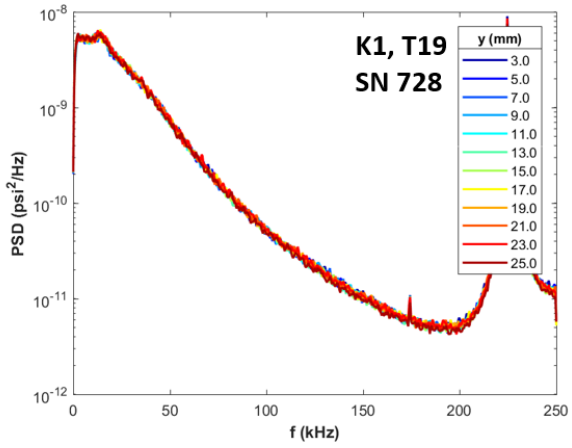
K1, T19
SN 728
PSD (psi²/Hz)
f (kHz)
y (mm)
3.0
5.0
7.0
9.0
11.0
13.0
15.0
17.0
19.0
21.0
23.0
25.0

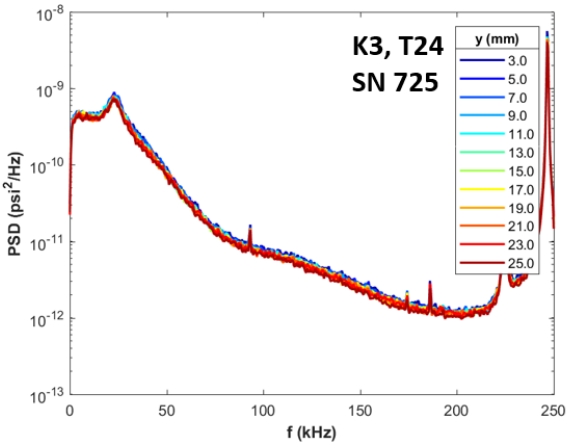
K3, T24
SN 725
PSD (psi²/Hz)
f (kHz)
y (mm)
3.0
5.0
7.0
9.0
11.0
13.0
15.0
17.0
19.0
21.0
23.0
25.0

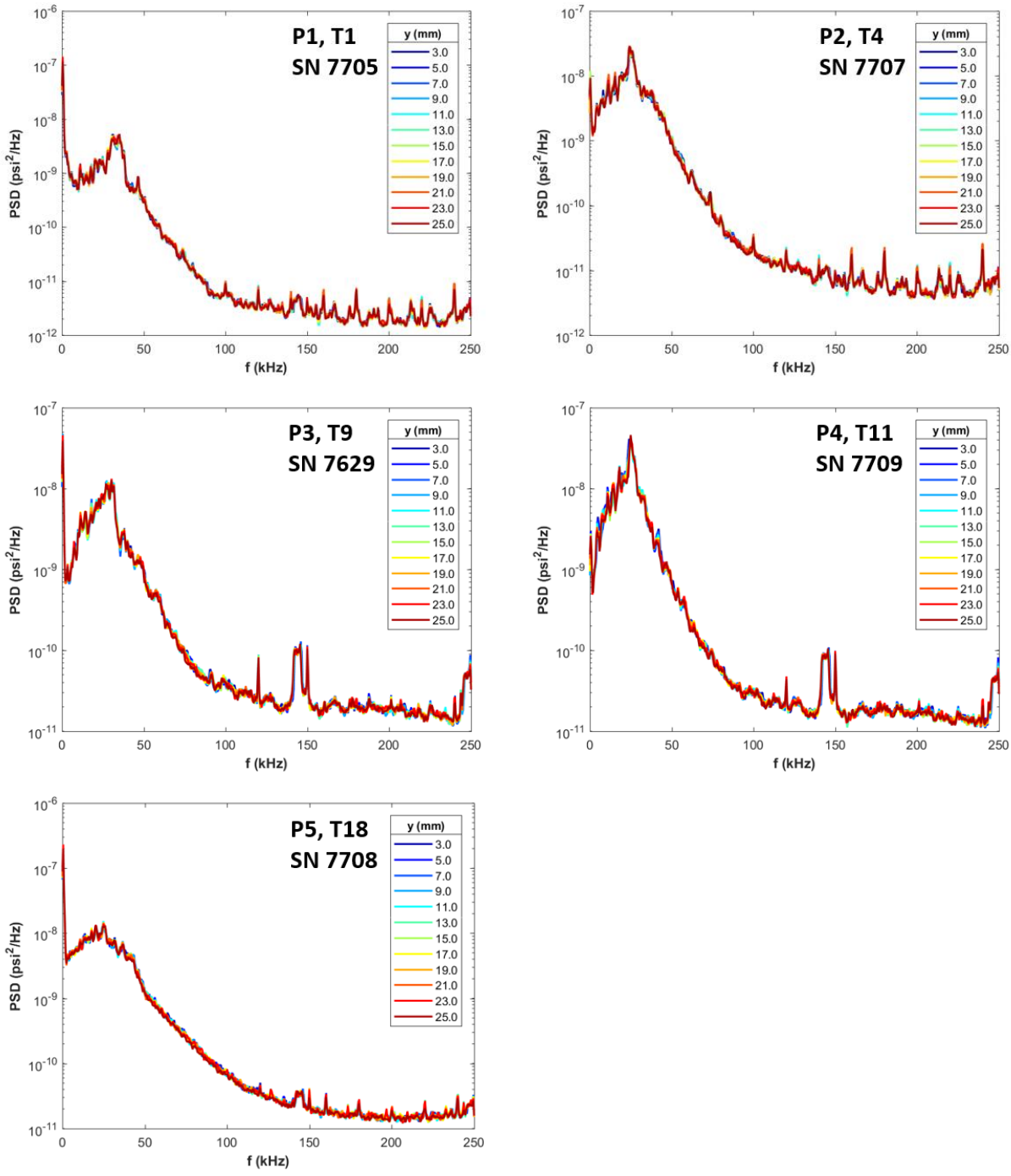

Run 3478. Traverse jam.

Run 3479

Hot-wire positioned at x/D = 1.7, z/D = 2.0, and traversed from 3.0 to 25.0 mm. Re near 4.9M/m. With trips.

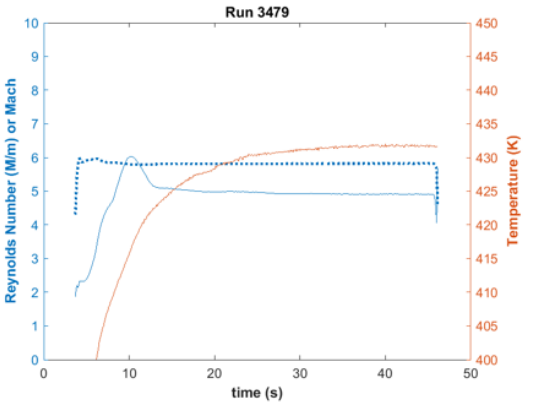

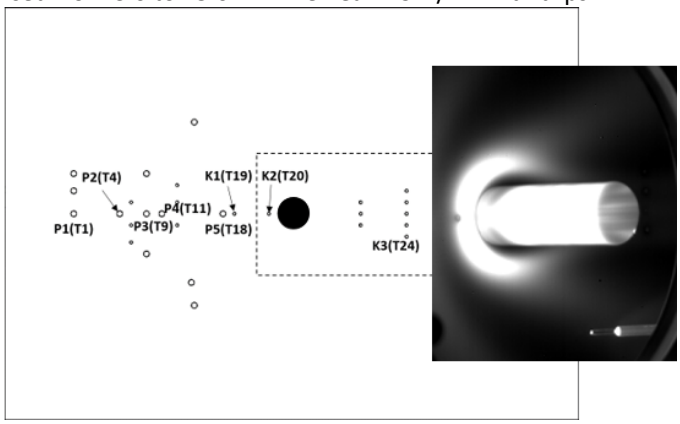

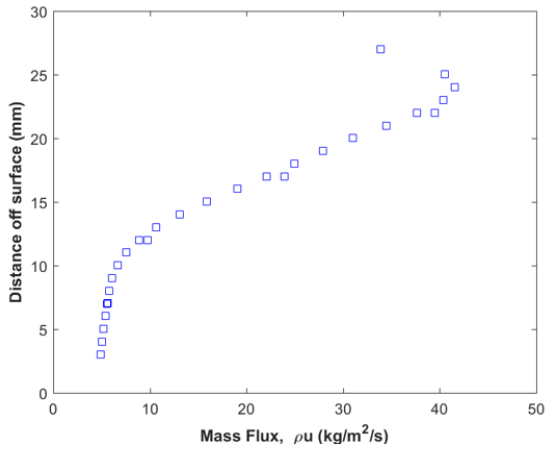

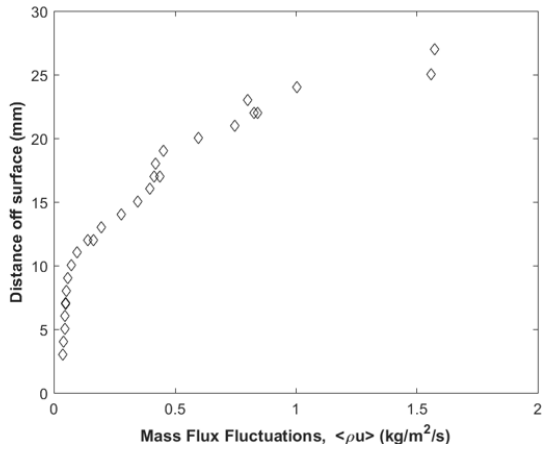

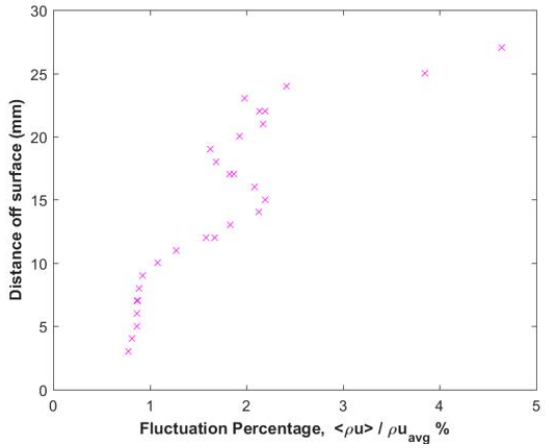

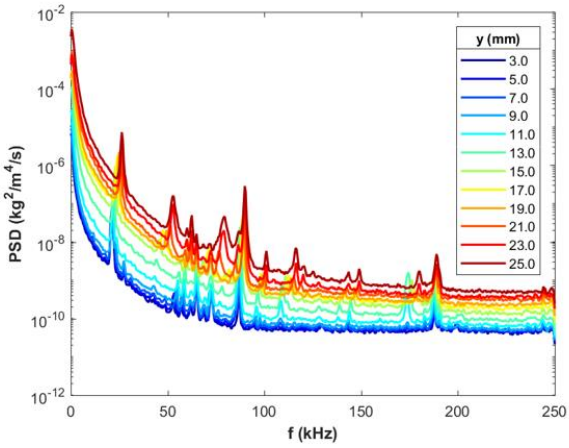

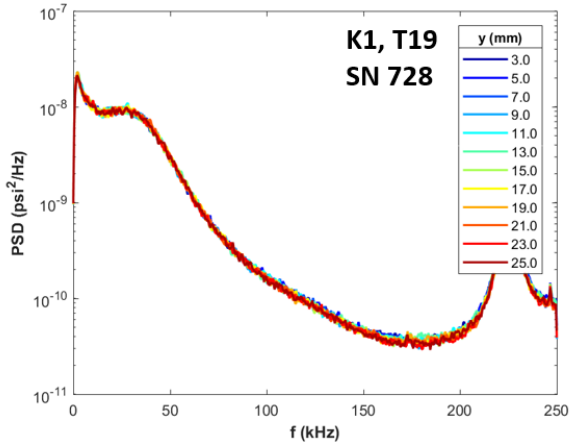
K1, T19
SN 728
y (mm)
3.0
5.0
7.0
9.0
11.0
13.0
15.0
17.0
19.0
21.0
23.0
25.0
PSD (psi²/Hz)
f (kHz)

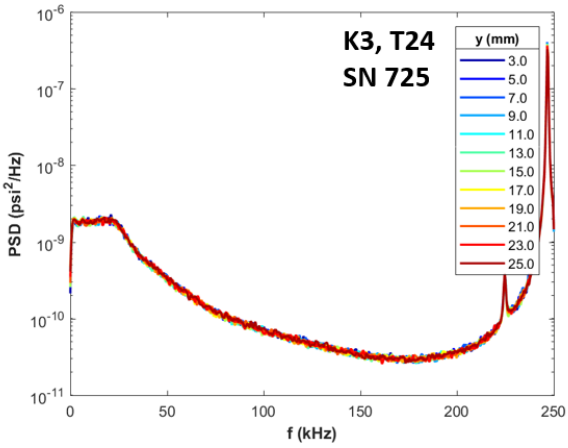
K3, T24
SN 725
y (mm)
3.0
5.0
7.0
9.0
11.0
13.0
15.0
17.0
19.0
21.0
23.0
25.0
PSD (psi²/Hz)
f (kHz)

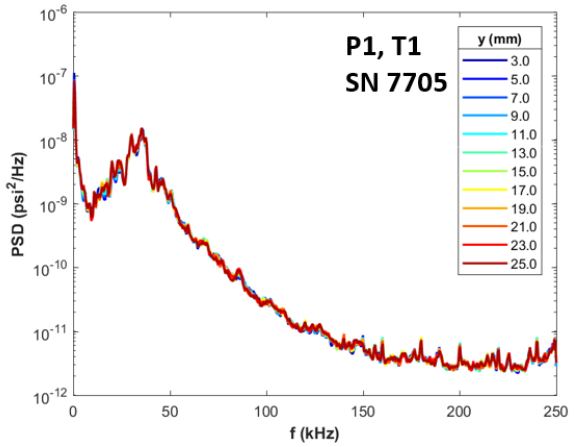
P1, T1
SN 7705
y (mm)
3.0
5.0
7.0
9.0
11.0
13.0
15.0
17.0
19.0
21.0
23.0
25.0
PSD (psi²/Hz)
f (kHz)

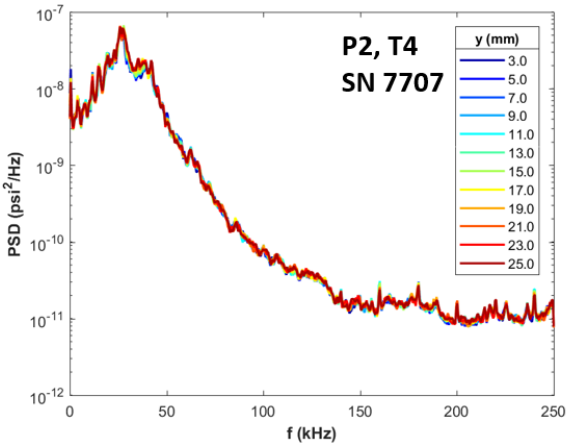
P2, T4
SN 7707
y (mm)
3.0
5.0
7.0
9.0
11.0
13.0
15.0
17.0
19.0
21.0
23.0
25.0
PSD (psi²/Hz)
f (kHz)

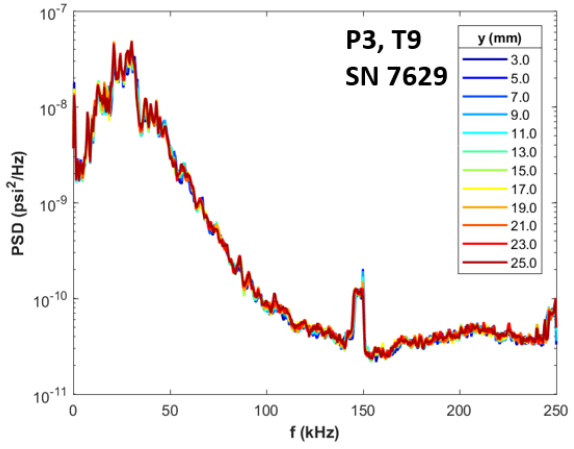
P3, T9
SN 7629
y (mm)
3.0
5.0
7.0
9.0
11.0
13.0
15.0
17.0
19.0
21.0
23.0
25.0
PSD (psi²/Hz)
f (kHz)

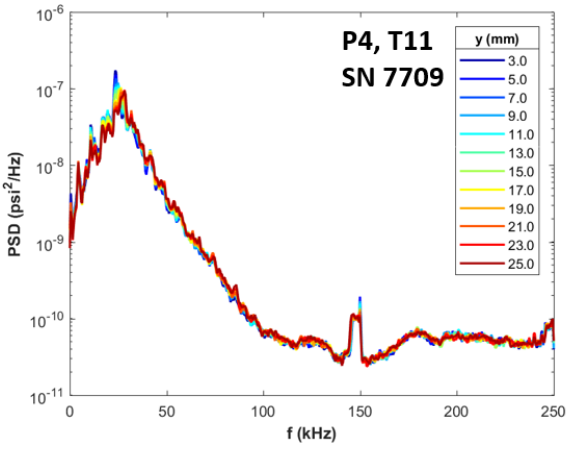
P4, T11
SN 7709
y (mm)
3.0
5.0
7.0
9.0
11.0
13.0
15.0
17.0
19.0
21.0
23.0
25.0
PSD (psi²/Hz)
f (kHz)

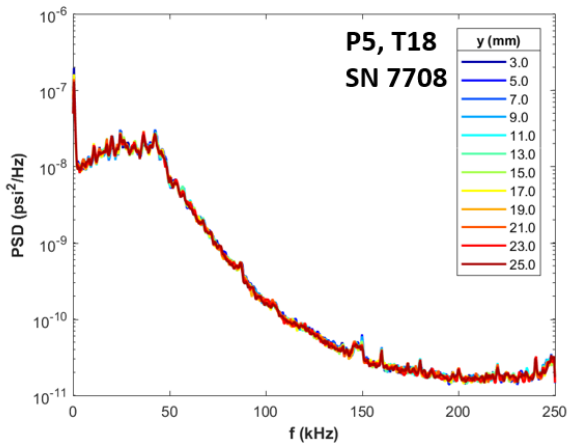

Run 3480

Wire fixed at same position as previous run at a height of 5mm. Reynolds number sweep from 5.8 to 1.9 M/m.

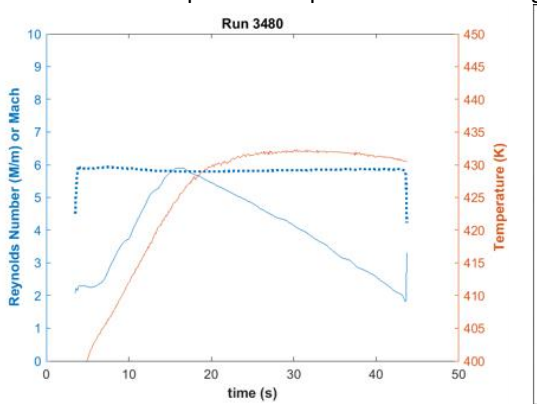

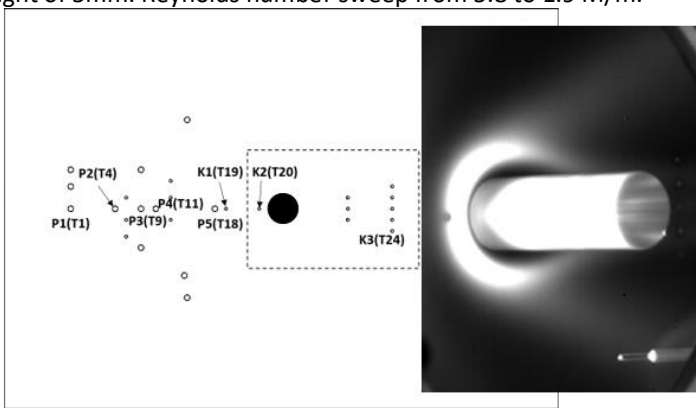

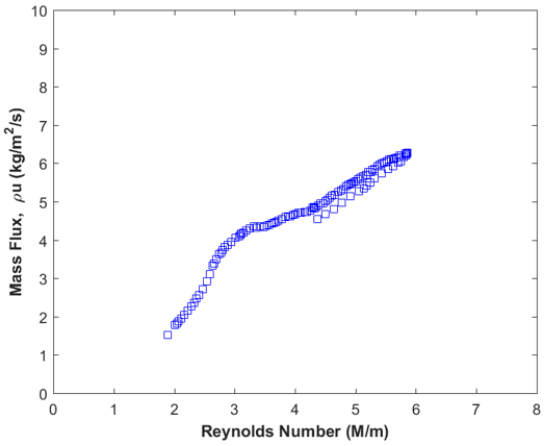

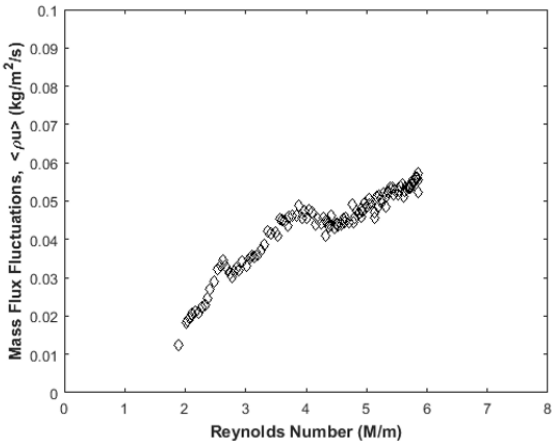

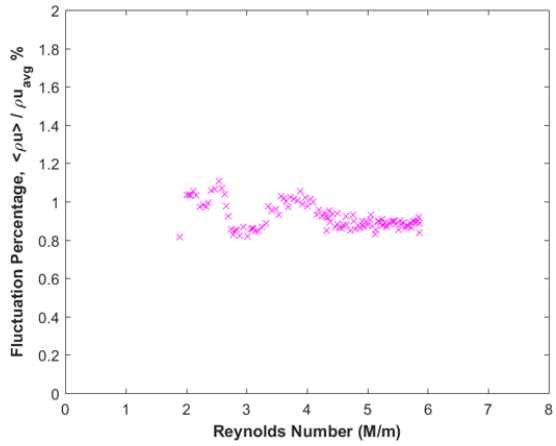
Fluctuation Percentage, <ρu> / ρu_avg %
Reynolds Number (M/m)

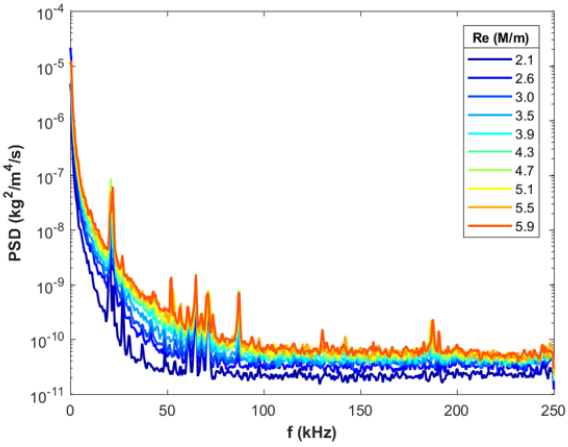
PSD (kg²/m⁴/s)
f (kHz)
Re (M/m)
2.1
2.6
3.0
3.5
3.9
4.3
4.7
5.1
5.5
5.9

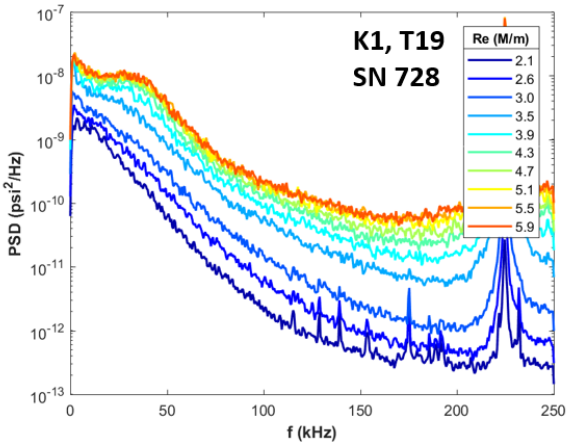
K1, T19
SN 728
PSD (psi²/Hz)
f (kHz)
Re (M/m)
2.1
2.6
3.0
3.5
3.9
4.3
4.7
5.1
5.5
5.9

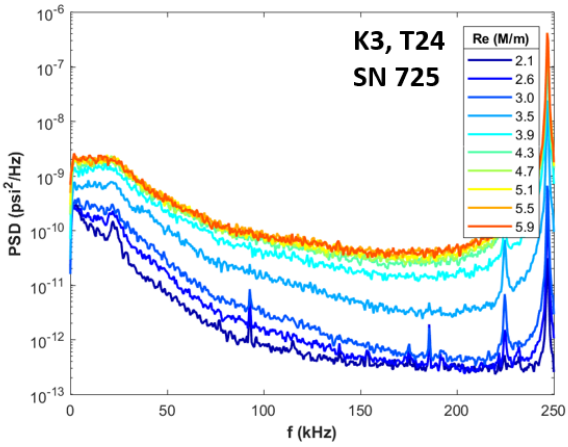
K3, T24
SN 725
PSD (psi²/Hz)
f (kHz)
Re (M/m)
2.1
2.6
3.0
3.5
3.9
4.3
4.7
5.1
5.5
5.9

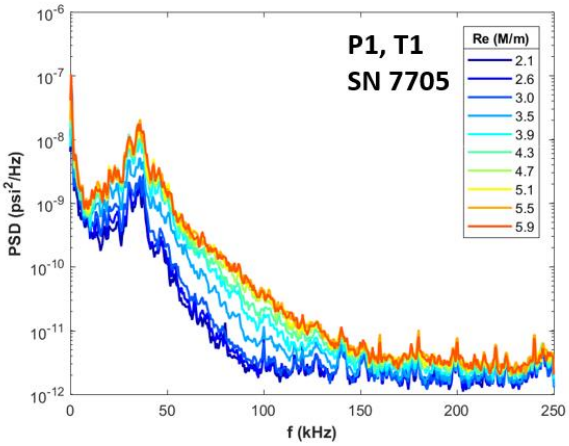
P1, T1
SN 7705
PSD (psi²/Hz)
f (kHz)
Re (M/m)
2.1
2.6
3.0
3.5
3.9
4.3
4.7
5.1
5.5
5.9

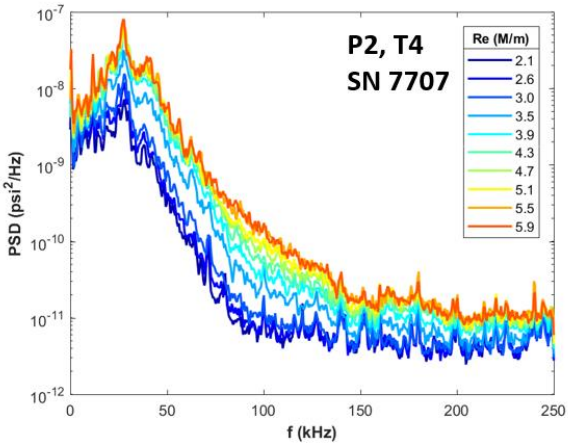
P2, T4
SN 7707
PSD (psi²/Hz)
f (kHz)
Re (M/m)
2.1
2.6
3.0
3.5
3.9
4.3
4.7
5.1
5.5
5.9

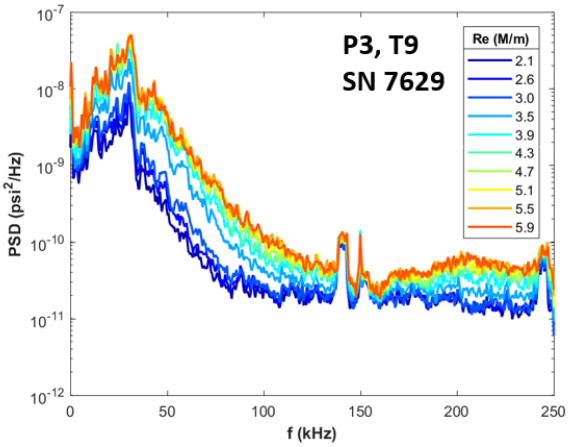

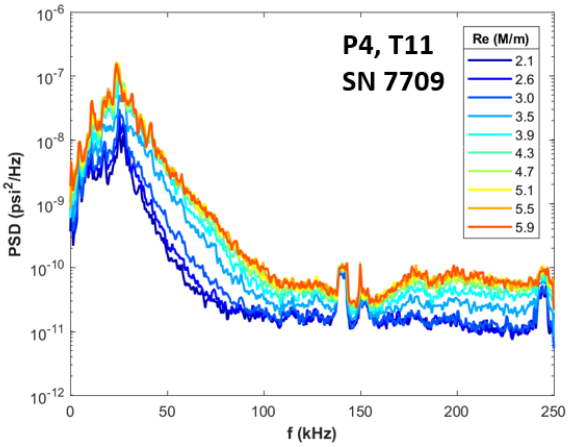

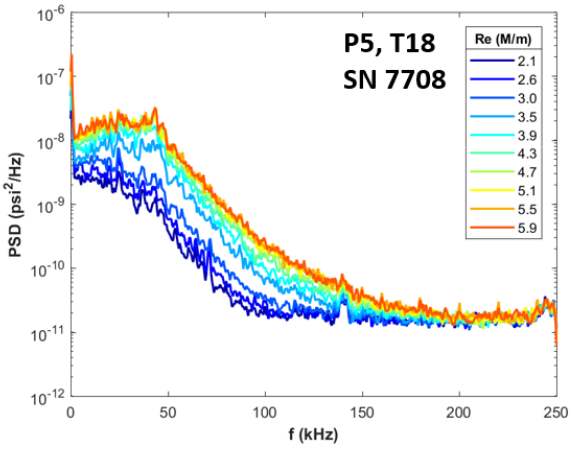

Run 3481

Hot-wire calibration run with wire positioned 1.7” upstream of what would be the model leading edge.

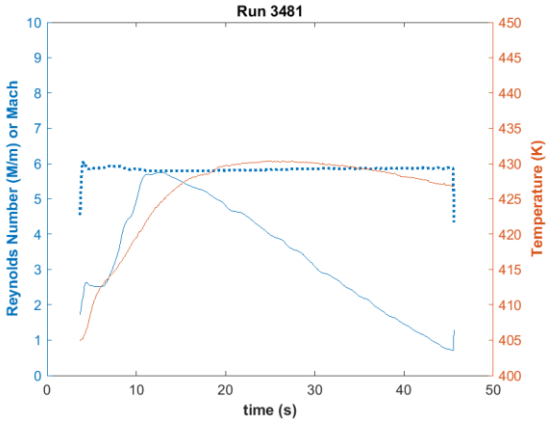

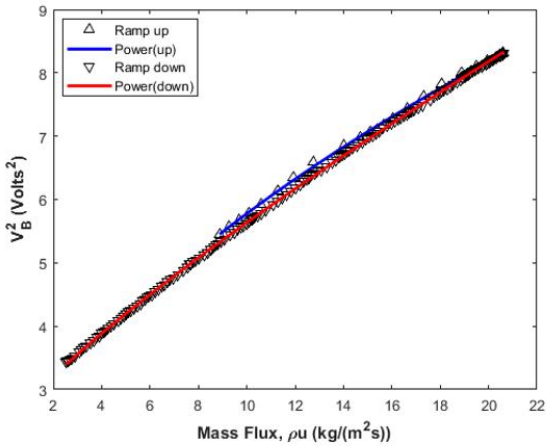
Ramp up
Power(up)
Ramp down
Power(down)
V_B^2 (Volts^2)
Mass Flux, ρu (kg/(m^{2}s))

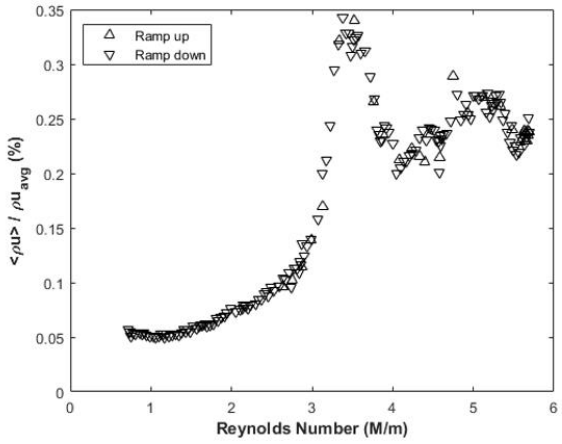
Ramp up
Ramp down
$<\rho u> / \rho u_{avg}$ (%)
Reynolds Number (M/m)

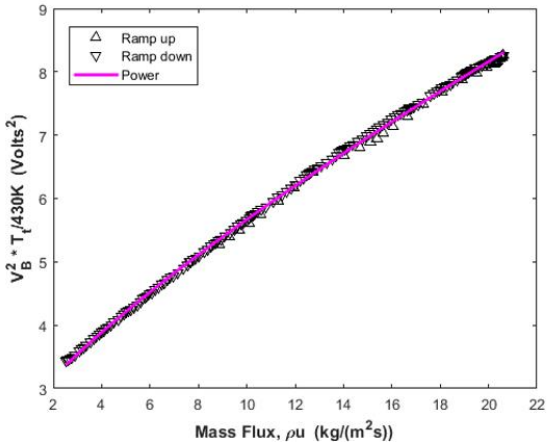
Ramp up
Ramp down
Power
$V_B^2 * T_t/430K$ (Volts^2)
Mass Flux, ρu (kg/(m^{2}s))

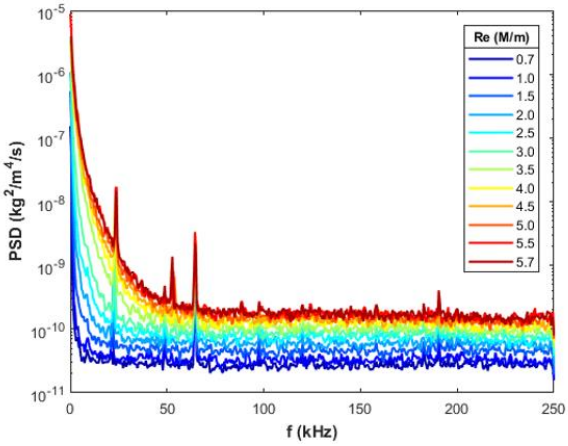
Re (M/m)
0.7
1.0
1.5
2.0
2.5
3.0
3.5
4.0
4.5
5.0
5.5
5.7
PSD (kg^2/m^4/s)
f (kHz)

Trips, angled cylinder

Run 3482

Surface pressure measurements, IR thermography, and schlieren made over a Re sweep. Cylinder was angled back 15°.

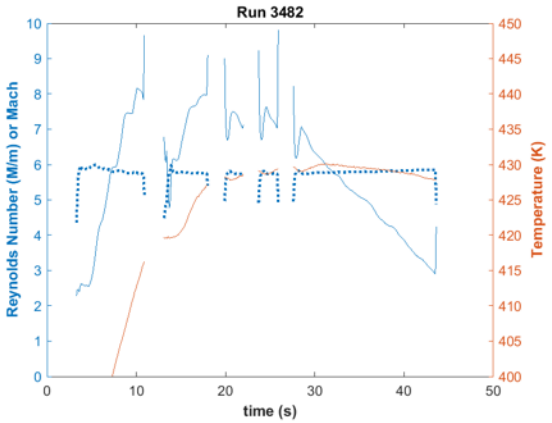

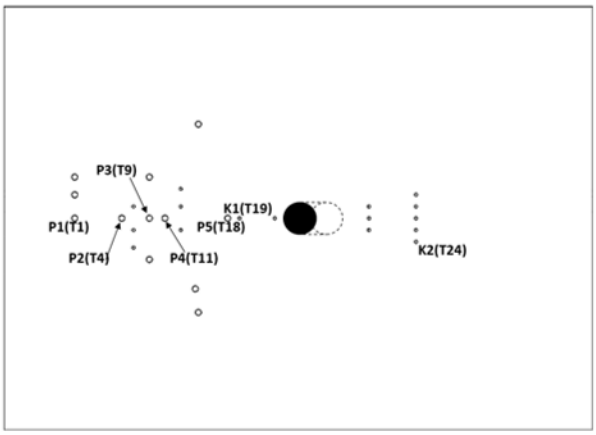

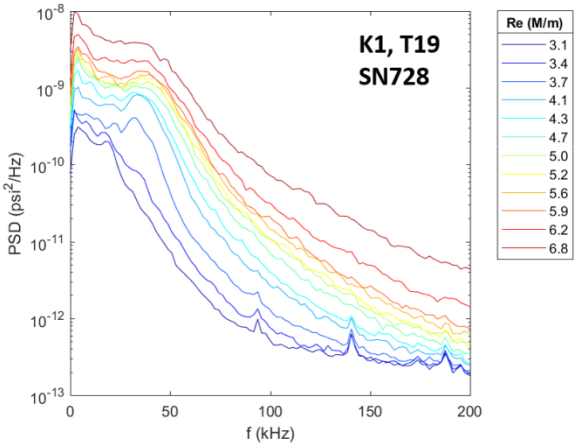

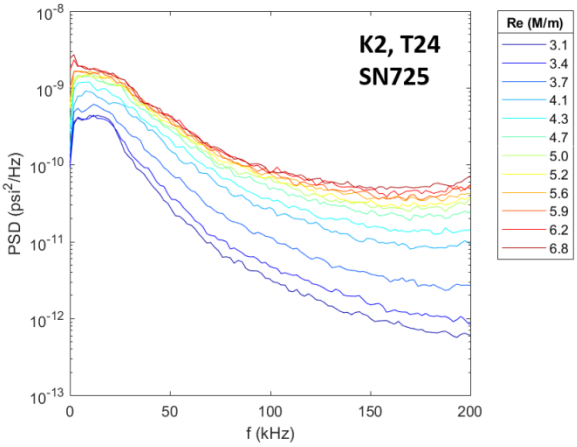

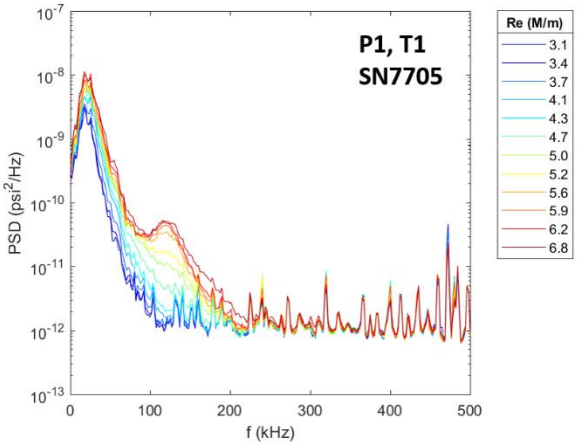

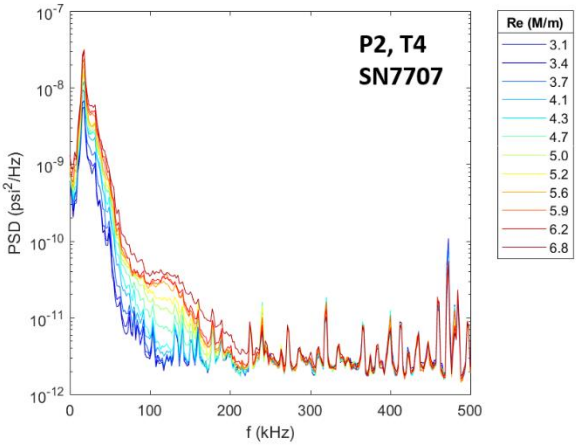

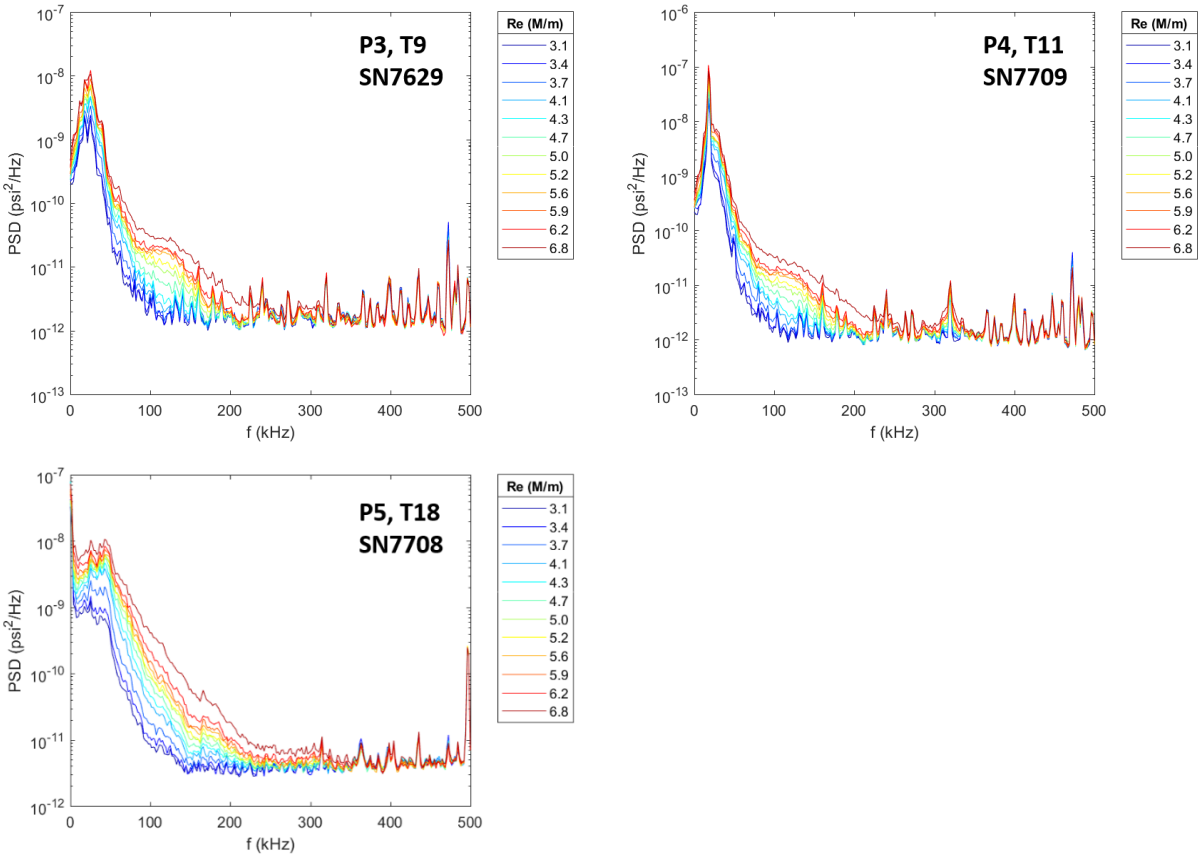

Run 3483

Surface pressure measurements, IR thermography, and schlieren made over a Re sweep. Cylinder was angled back 15°.

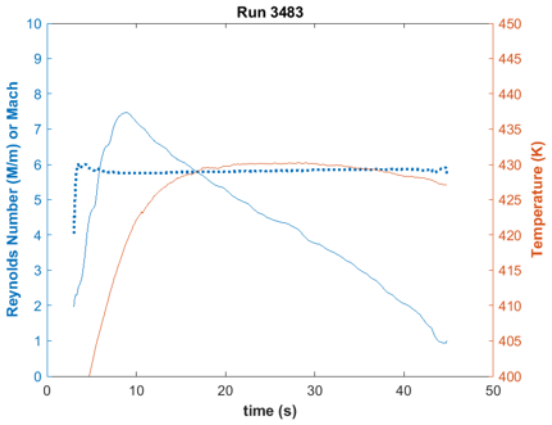

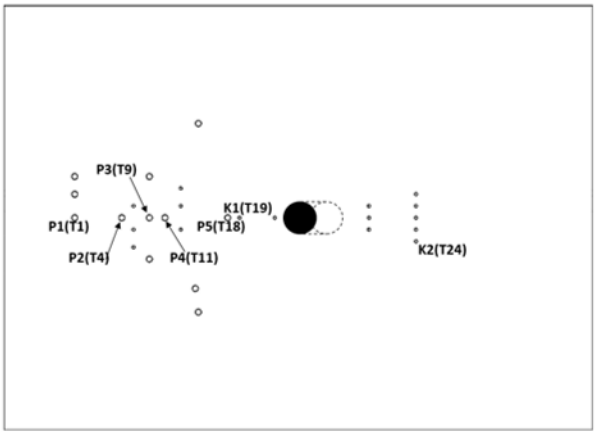

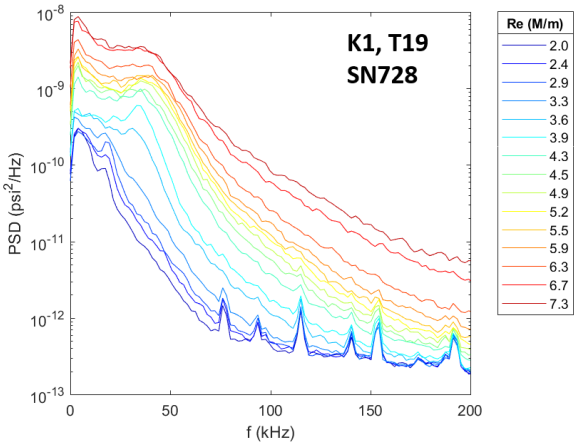
K1, T19
SN728
PSD (psi²/Hz)
f (kHz)
Re (M/m)
2.0
2.4
2.9
3.3
3.6
3.9
4.3
4.5
4.9
5.2
5.5
5.9
6.3
6.7
7.3

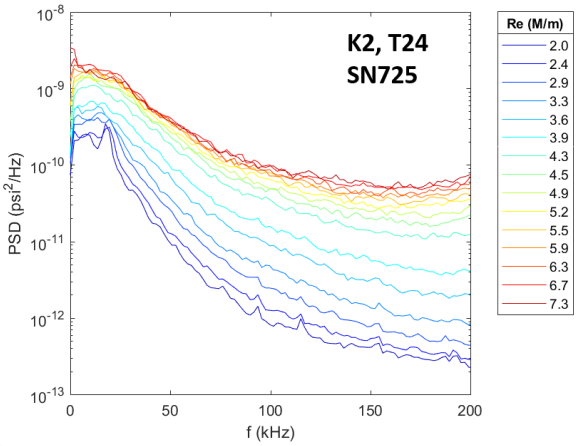
K2, T24
SN725
PSD (psi²/Hz)
f (kHz)
Re (M/m)
2.0
2.4
2.9
3.3
3.6
3.9
4.3
4.5
4.9
5.2
5.5
5.9
6.3
6.7
7.3

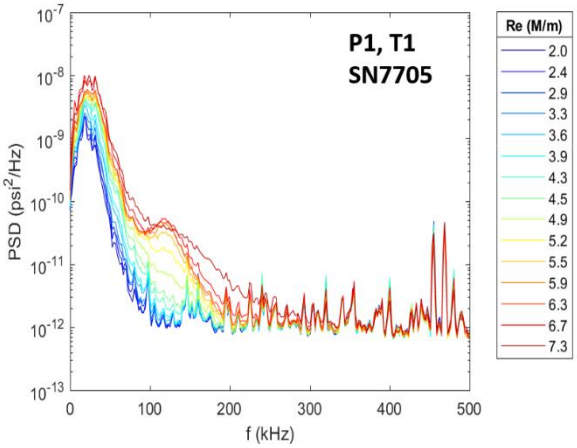
P1, T1
SN7705
PSD (psi²/Hz)
f (kHz)
Re (M/m)
2.0
2.4
2.9
3.3
3.6
3.9
4.3
4.5
4.9
5.2
5.5
5.9
6.3
6.7
7.3

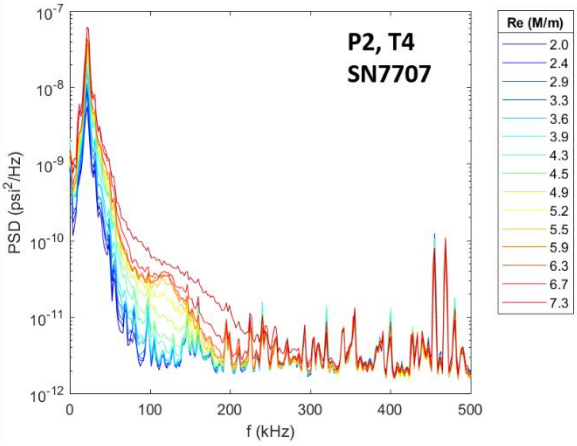
P2, T4
SN7707
PSD (psi²/Hz)
f (kHz)
Re (M/m)
2.0
2.4
2.9
3.3
3.6
3.9
4.3
4.5
4.9
5.2
5.5
5.9
6.3
6.7
7.3

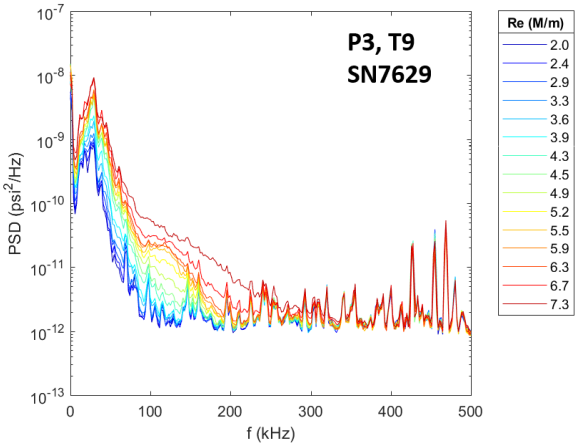
P3, T9
SN7629
PSD (psi²/Hz)
f (kHz)
Re (M/m)
2.0
2.4
2.9
3.3
3.6
3.9
4.3
4.5
4.9
5.2
5.5
5.9
6.3
6.7
7.3

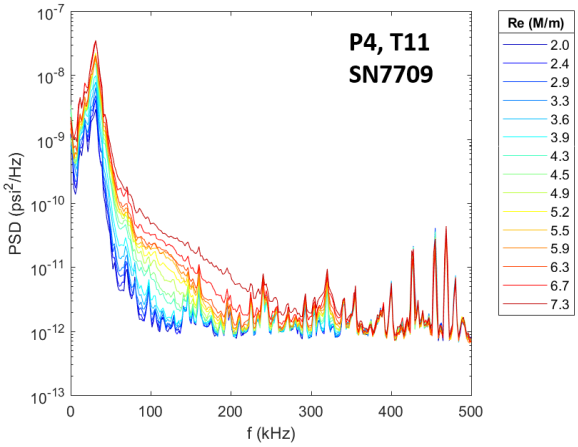
P4, T11
SN7709
PSD (psi²/Hz)
f (kHz)
Re (M/m)
2.0
2.4
2.9
3.3
3.6
3.9
4.3
4.5
4.9
5.2
5.5
5.9
6.3
6.7
7.3

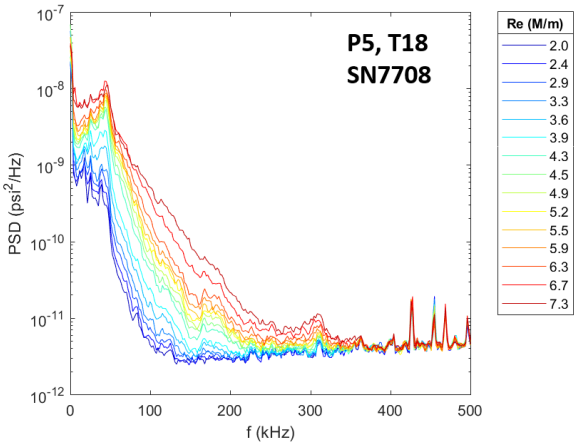

Run 3484

Surface pressure measurements, IR thermography, and high-speed schlieren made over Re steps. Cylinder was angled back 15°.

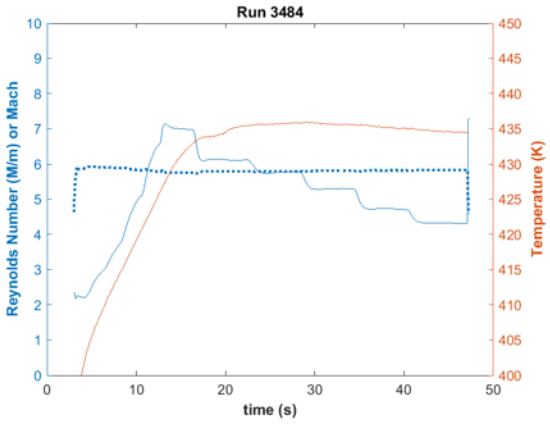

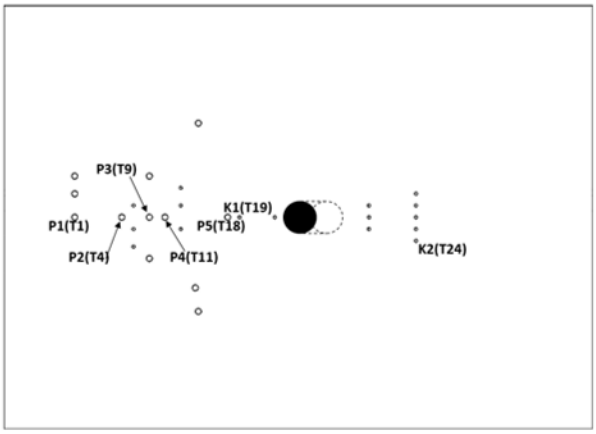

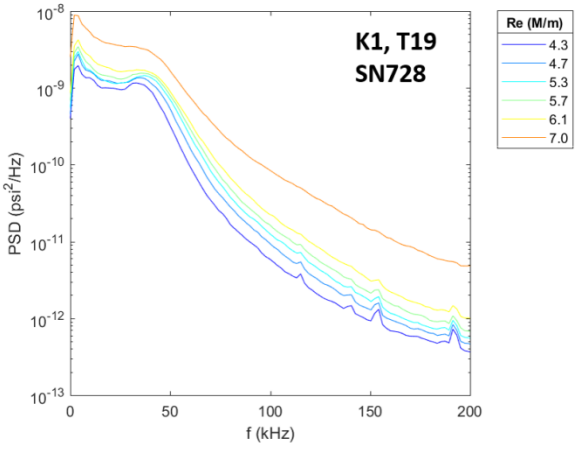

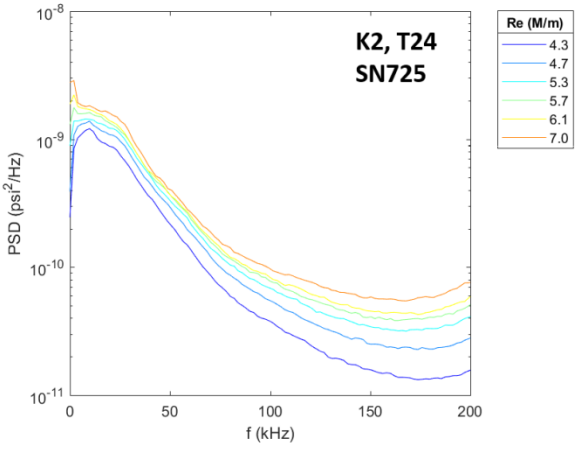

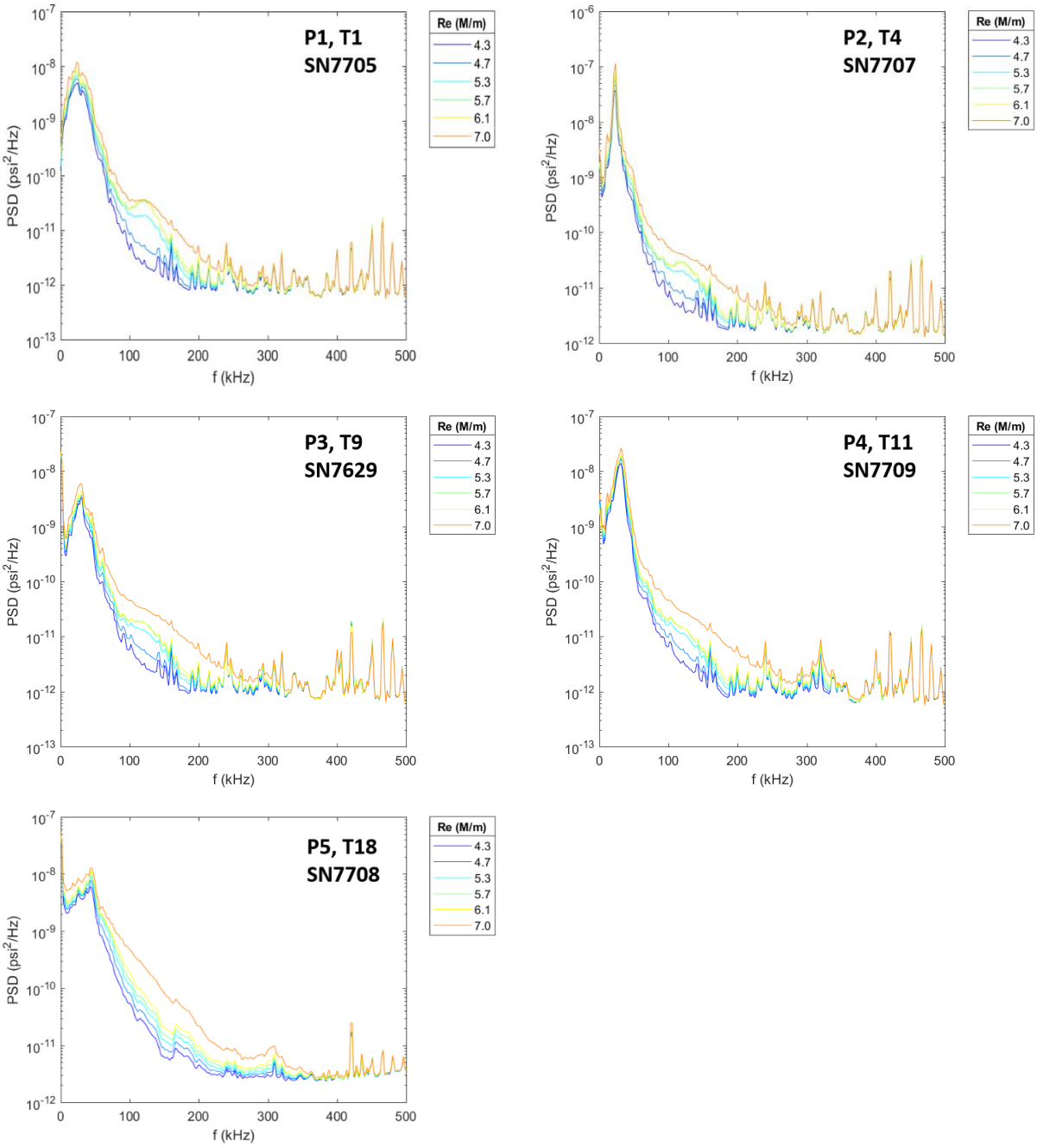
P1, T1
SN7705
P2, T4
SN7707
P3, T9
SN7629
P4, T11
SN7709
P5, T18
SN7708
Re (M/m)
4.3
4.7
5.3
5.7
6.1
7.0
PSD (psi²/Hz)
f (kHz)

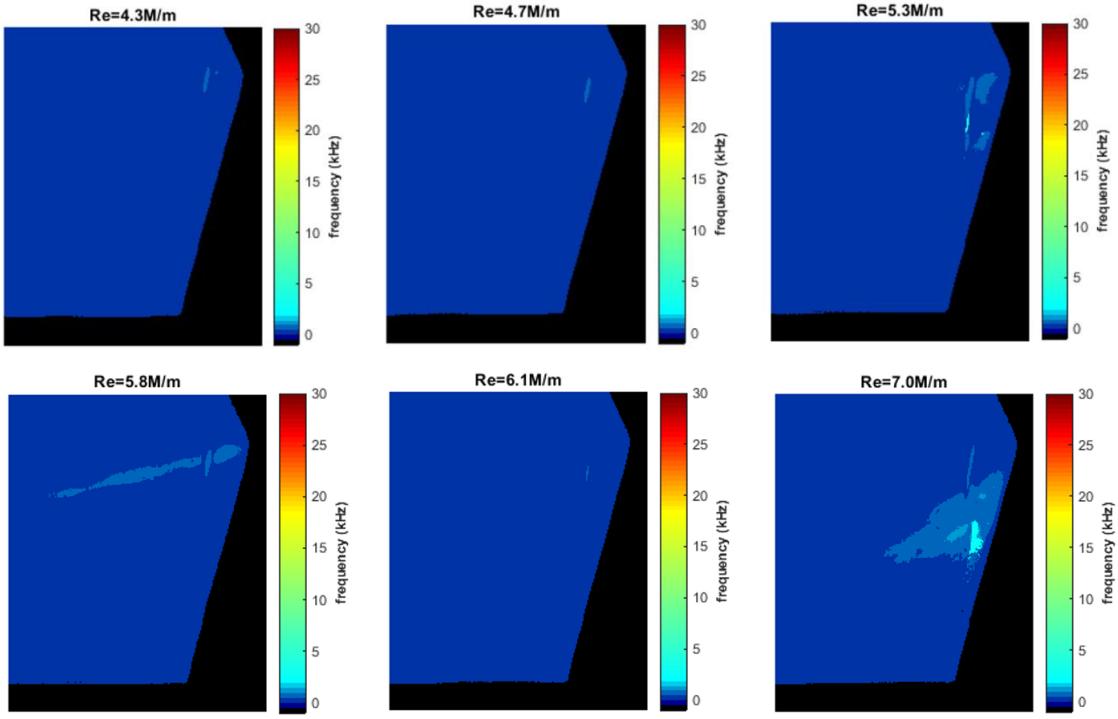
Re=4.3M/m
Re=4.7M/m
Re=5.3M/m
Re=5.8M/m
Re=6.1M/m
Re=7.0M/m
frequency (kHz)
0
5
10
15
20
25
30

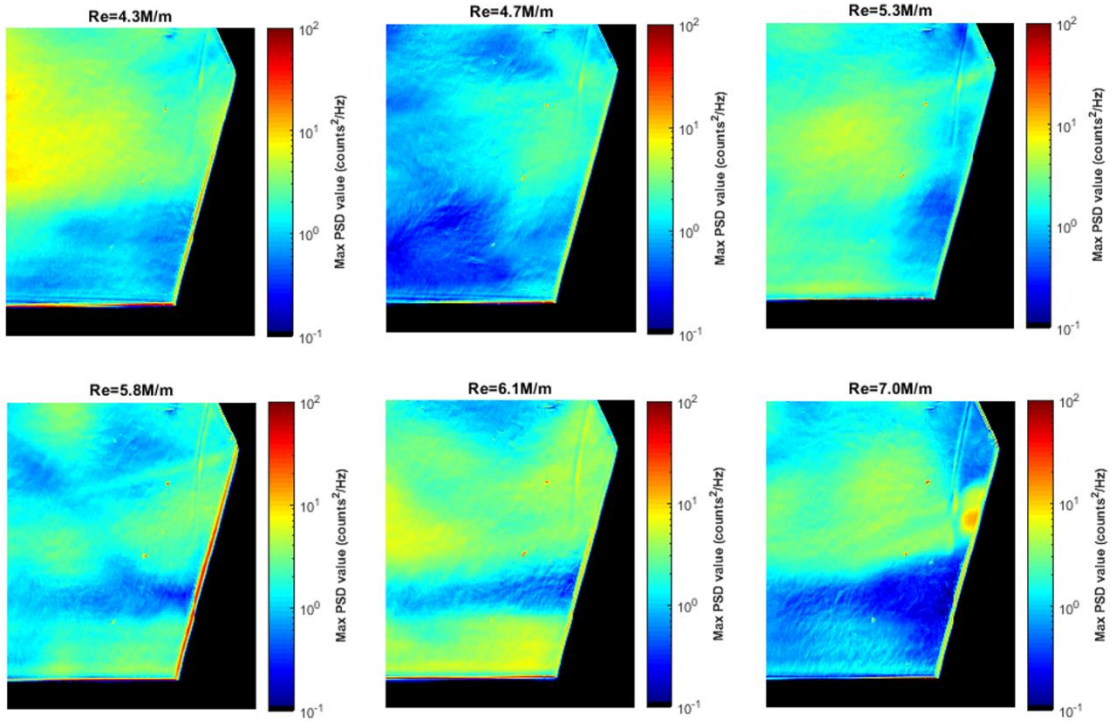
Re=4.3M/m
Re=4.7M/m
Re=5.3M/m
Re=5.8M/m
Re=6.1M/m
Re=7.0M/m
Max PSD value (counts²/Hz)
10⁻¹
10⁰
10¹
10²

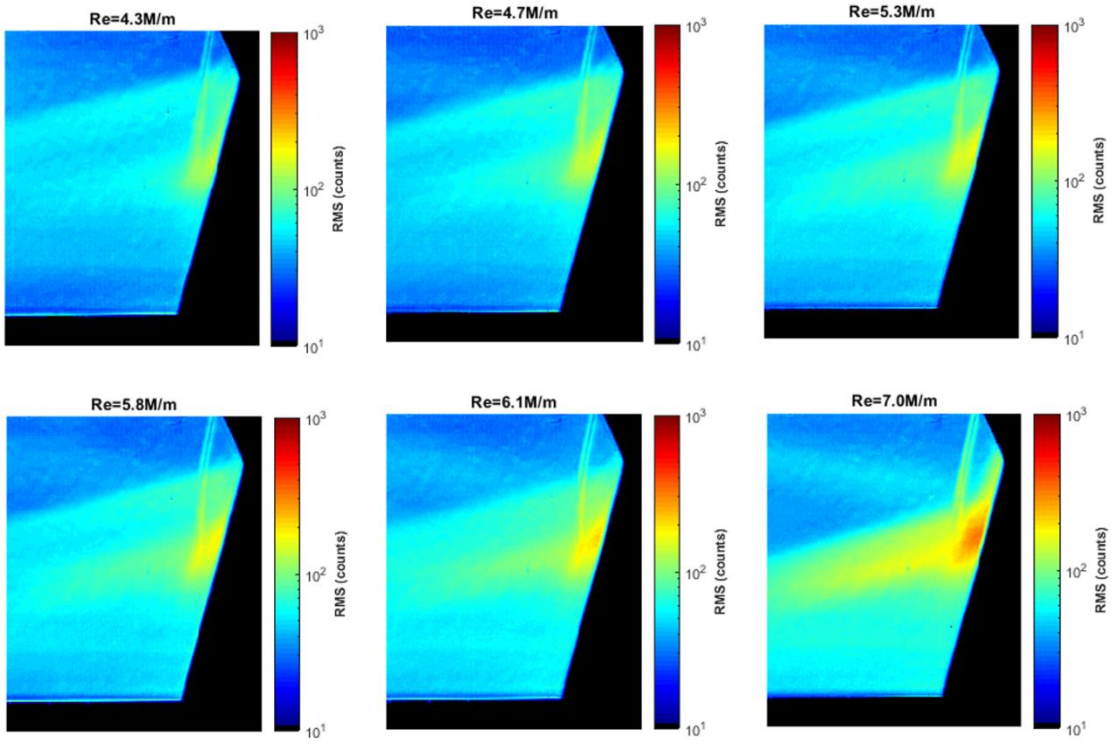

Run 3485

Surface pressure measurements, IR thermography, and schlieren made over a Re sweep. Cylinder was angled back 30°.

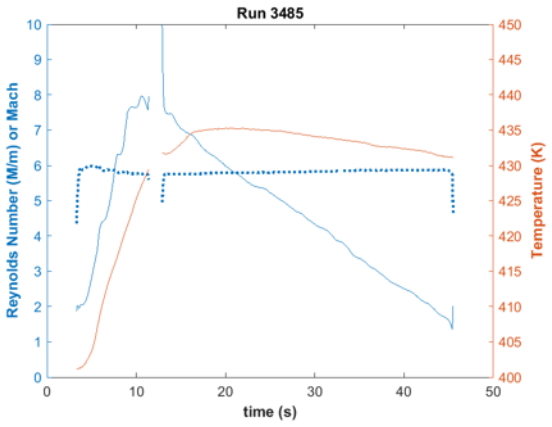

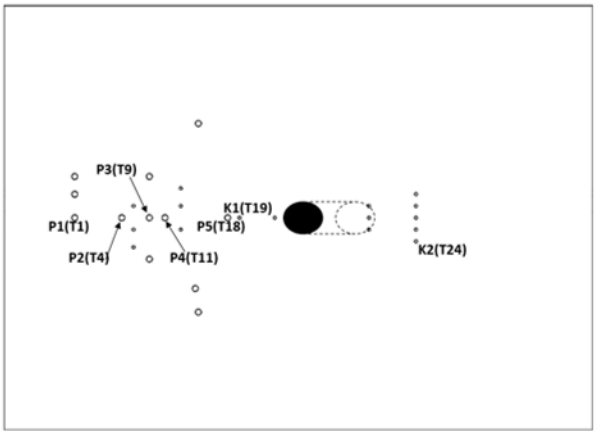

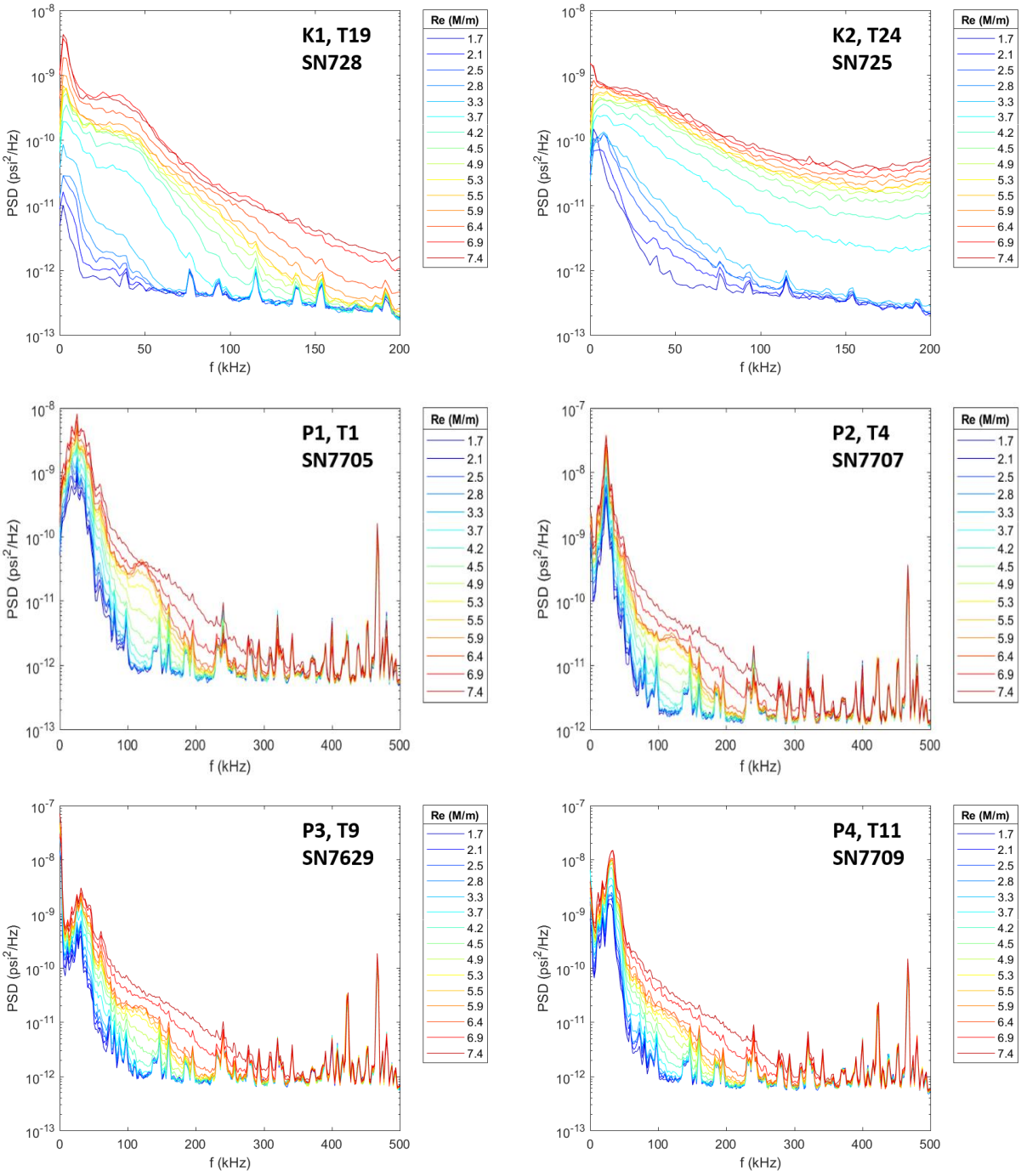
K1, T19
SN728
K2, T24
SN725
P1, T1
SN7705
P2, T4
SN7707
P3, T9
SN7629
P4, T11
SN7709
PSD (psi²/Hz)
f (kHz)
Re (M/m)
1.7
2.1
2.5
2.8
3.3
3.7
4.2
4.5
4.9
5.3
5.5
5.9
6.4
6.9
7.4

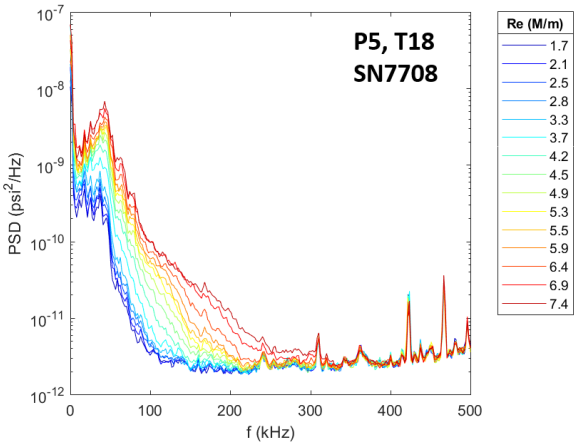

Run 3486

Surface pressure measurements, IR thermography, and high-speed schlieren made over Re steps. Cylinder was angled back 30°.

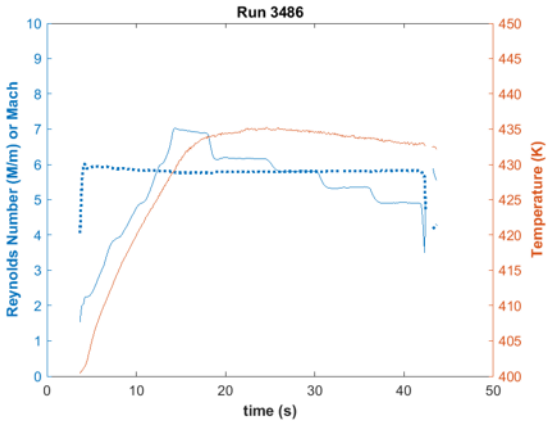

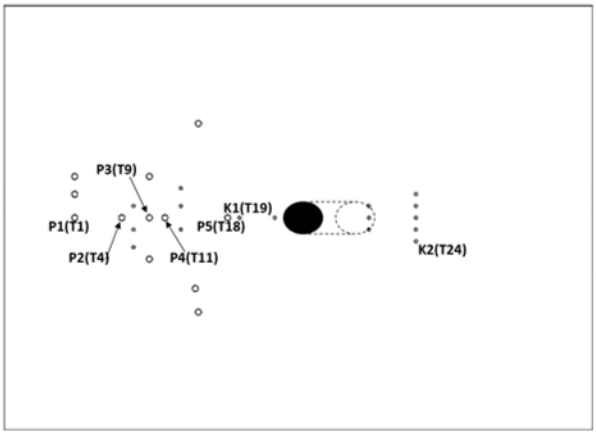

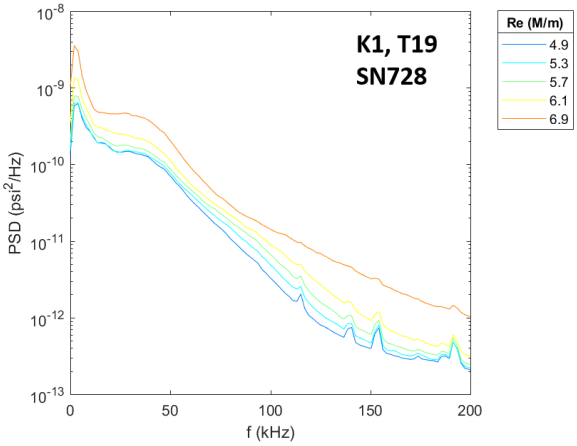

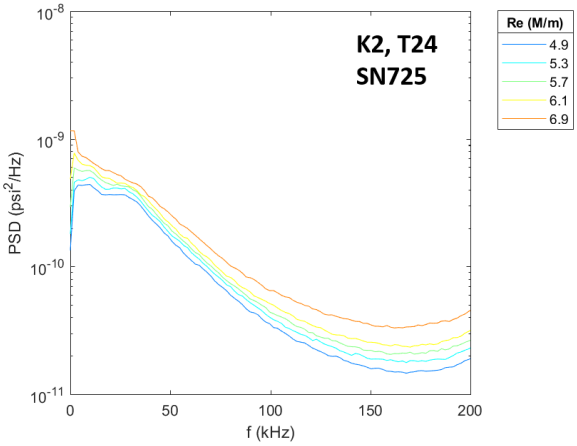

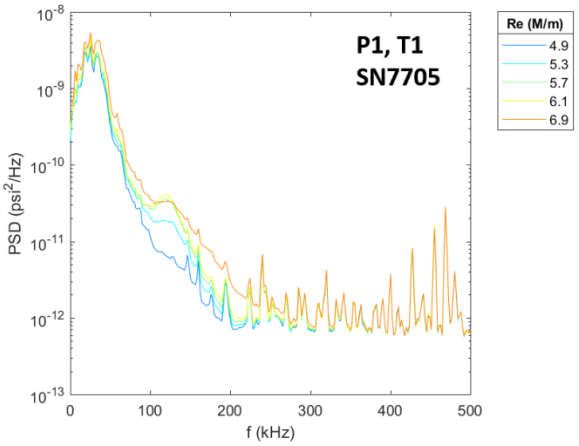
P1, T1
SN7705
Re (M/m)
4.9
5.3
5.7
6.1
6.9
PSD (psi²/Hz)
f (kHz)

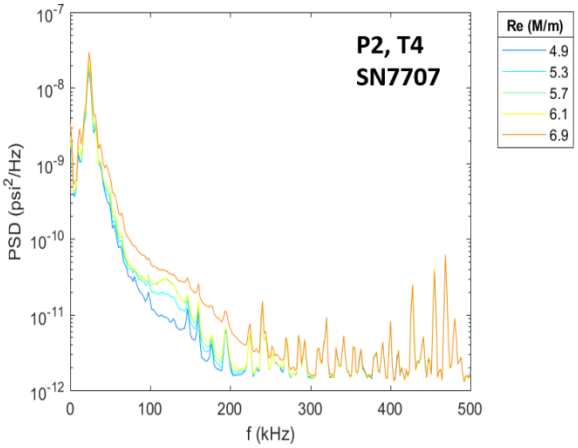
P2, T4
SN7707
Re (M/m)
4.9
5.3
5.7
6.1
6.9
PSD (psi²/Hz)
f (kHz)

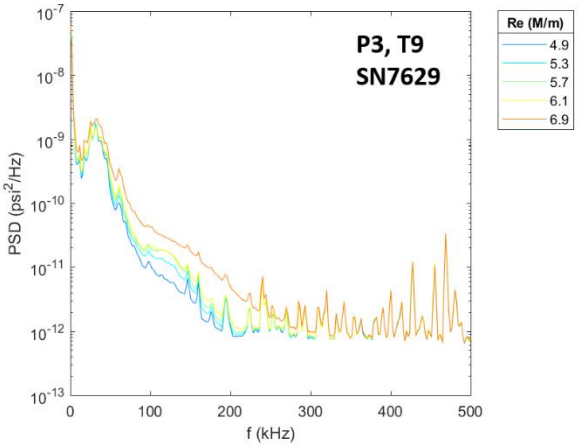
P3, T9
SN7629
Re (M/m)
4.9
5.3
5.7
6.1
6.9
PSD (psi²/Hz)
f (kHz)

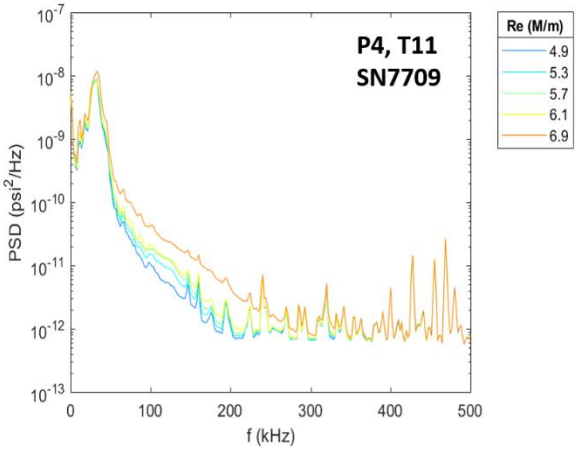
P4, T11
SN7709
Re (M/m)
4.9
5.3
5.7
6.1
6.9
PSD (psi²/Hz)
f (kHz)

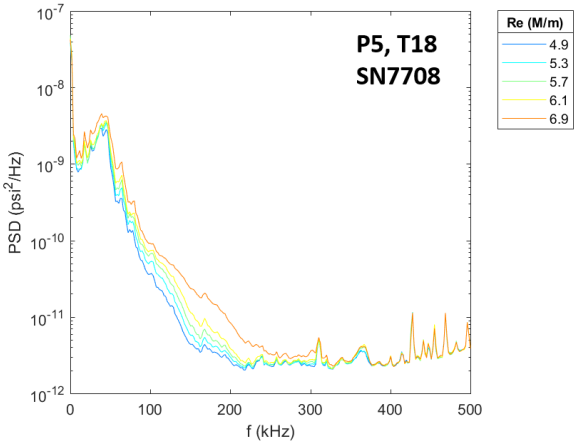
P5, T18
SN7708
Re (M/m)
4.9
5.3
5.7
6.1
6.9
PSD (psi²/Hz)
f (kHz)

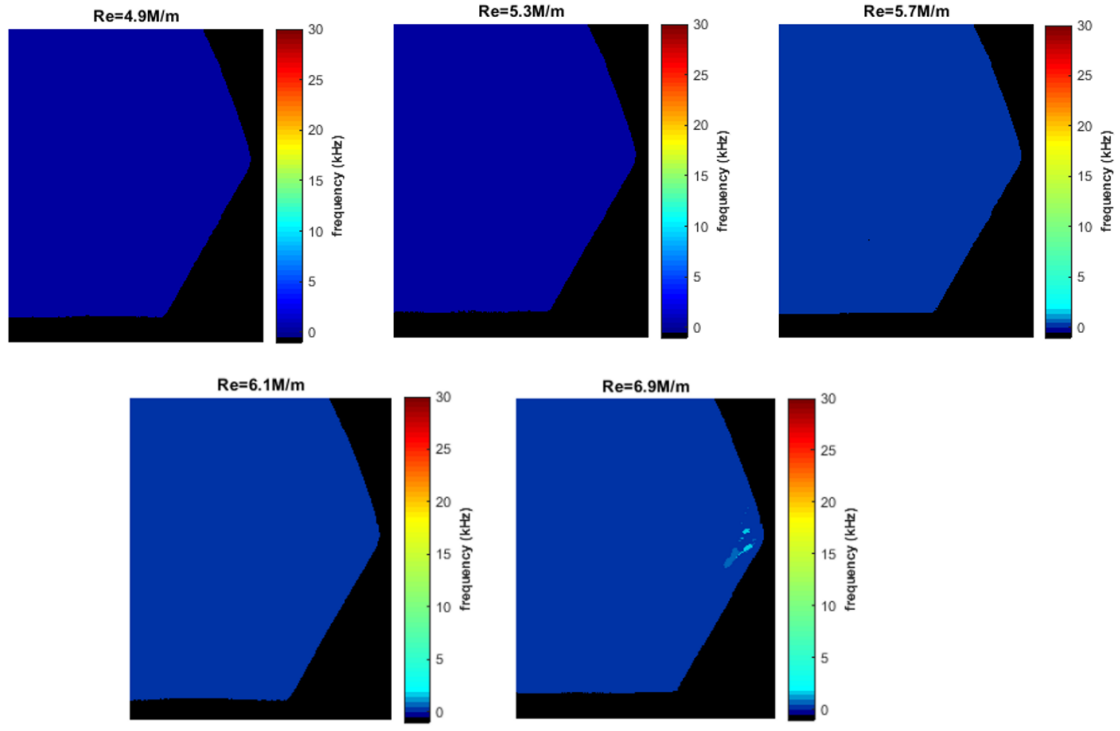
Re=4.9M/m
Re=5.3M/m
Re=5.7M/m
Re=6.1M/m
Re=6.9M/m
frequency (kHz)
0
5
10
15
20
25
30

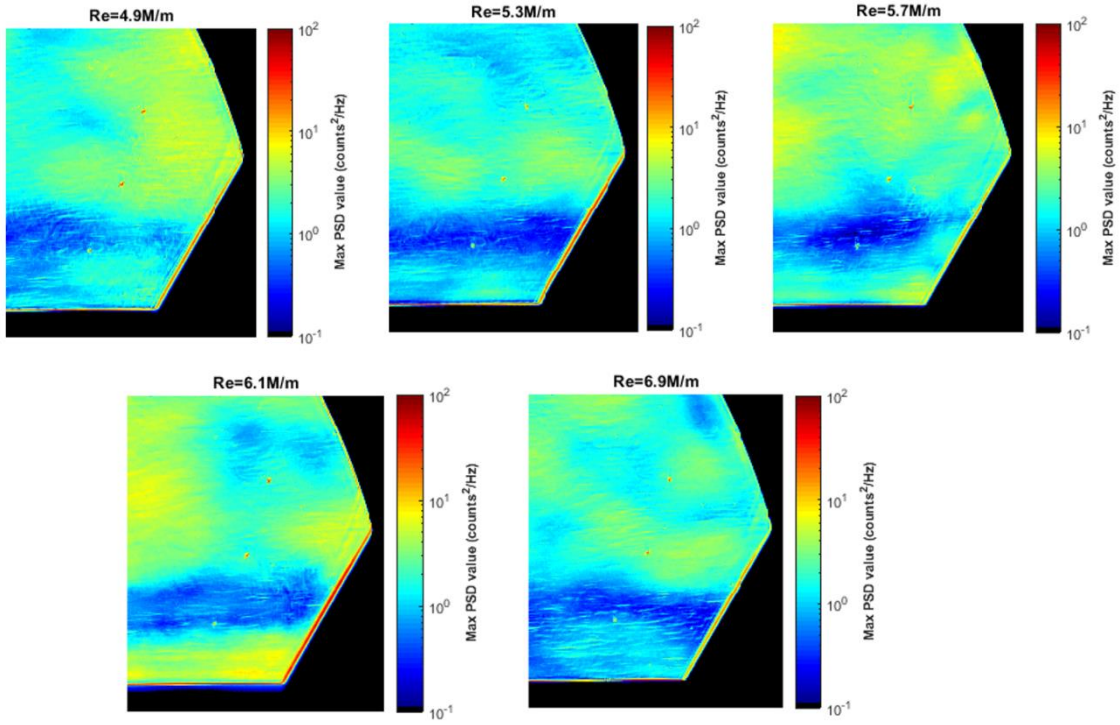
Re=4.9M/m
Re=5.3M/m
Re=5.7M/m
Re=6.1M/m
Re=6.9M/m
Max PSD value (counts²/Hz)
10⁻¹
10⁰
10¹
10²

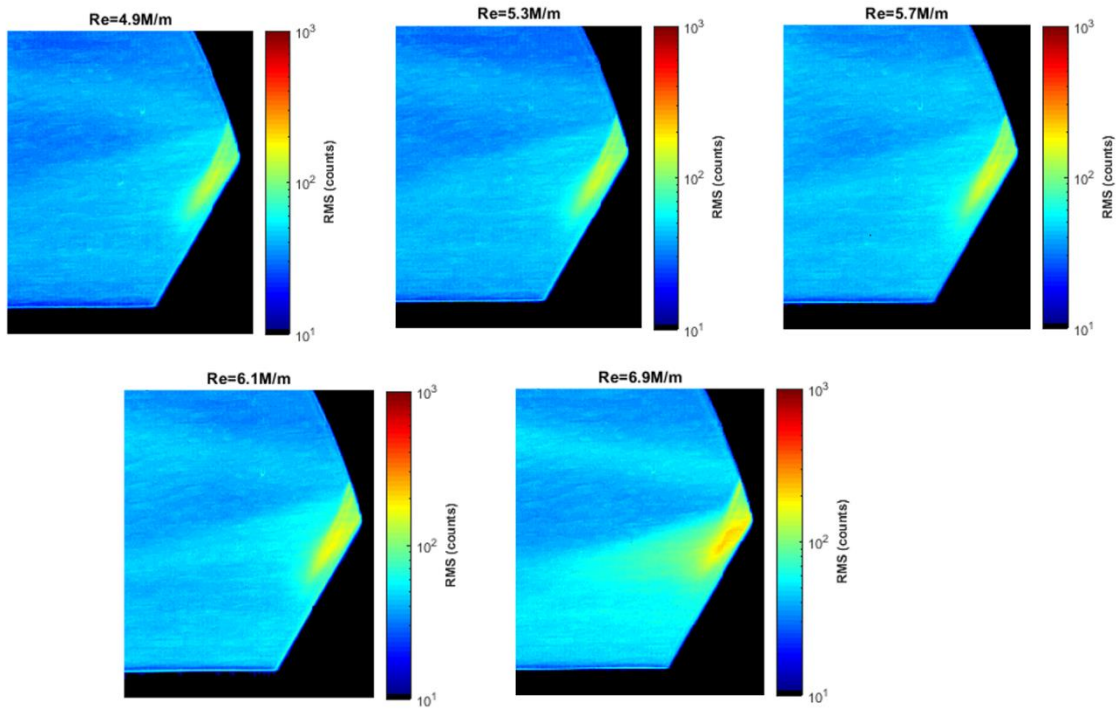

Run 3487

Surface pressure measurements, IR thermography, and schlieren made over a Re sweep. Cylinder was angled forward 15°.

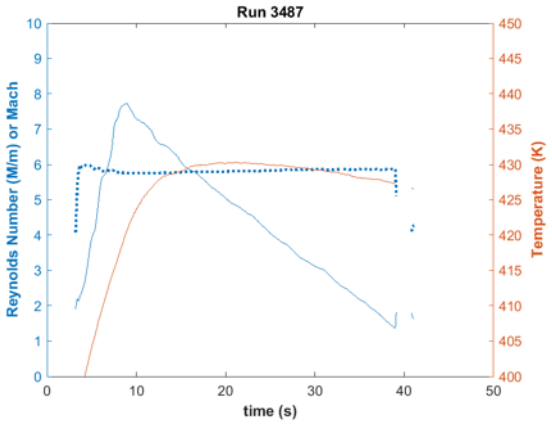

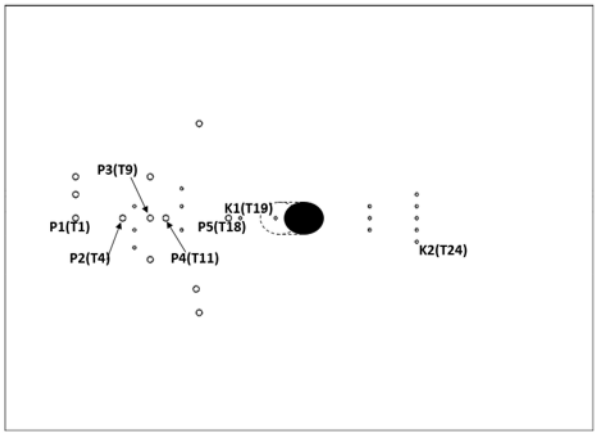

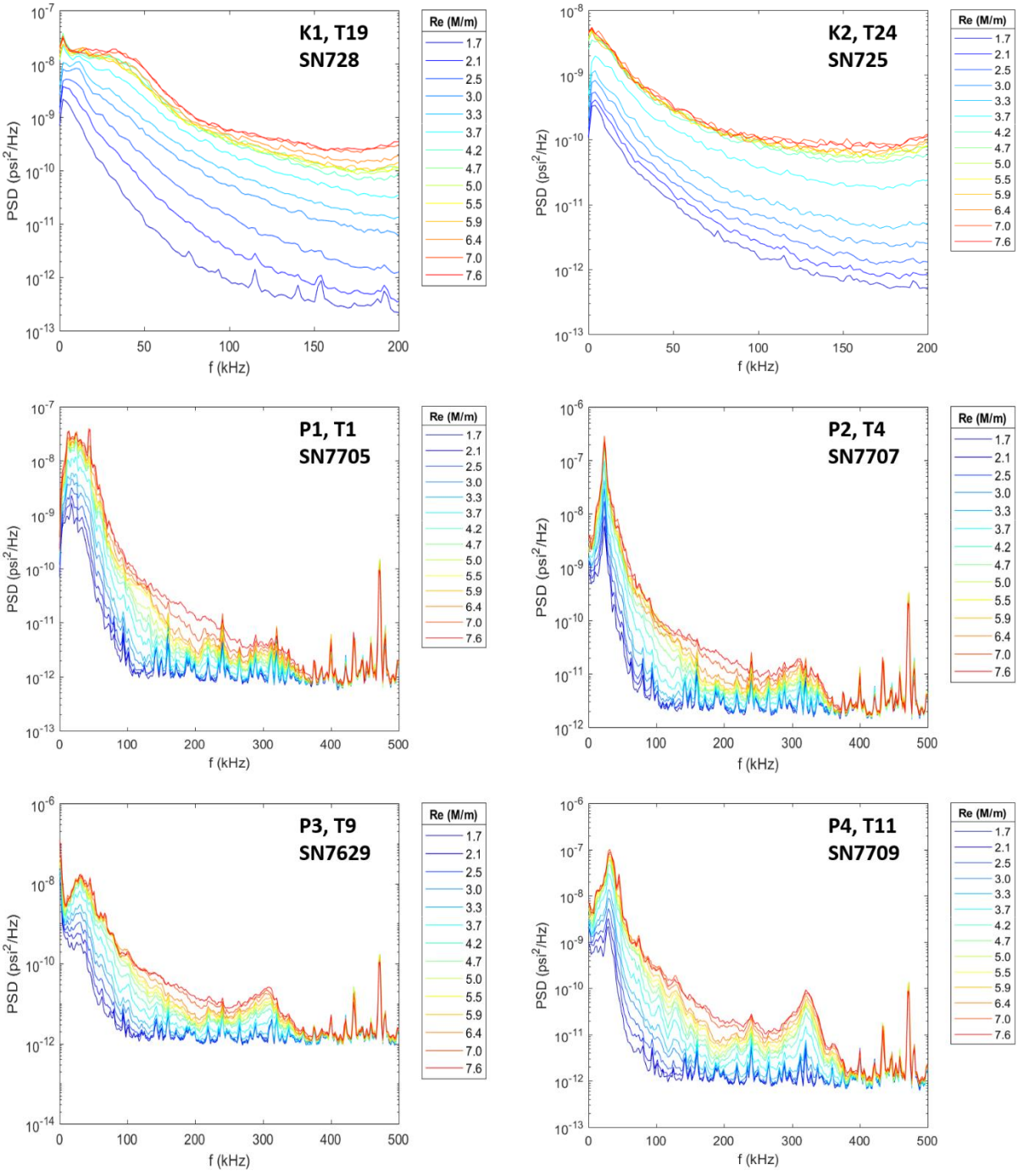
K1, T19
SN728
K2, T24
SN725
P1, T1
SN7705
P2, T4
SN7707
P3, T9
SN7629
P4, T11
SN7709
PSD (psi²/Hz)
f (kHz)
Re (M/m)
1.7
2.1
2.5
3.0
3.3
3.7
4.2
4.7
5.0
5.5
5.9
6.4
7.0
7.6

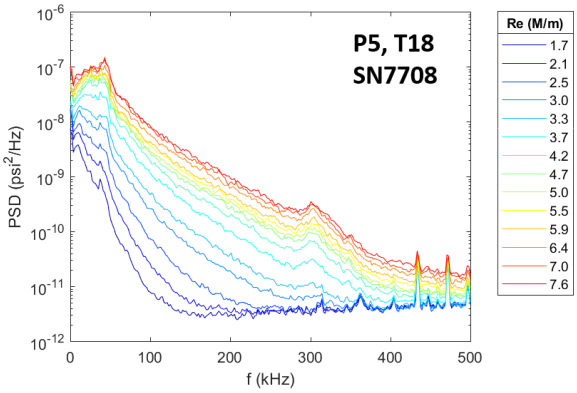

Run 3488

Surface pressure measurements, IR thermography, and high-speed schlieren made over Re steps. Cylinder was angled forward 15°.

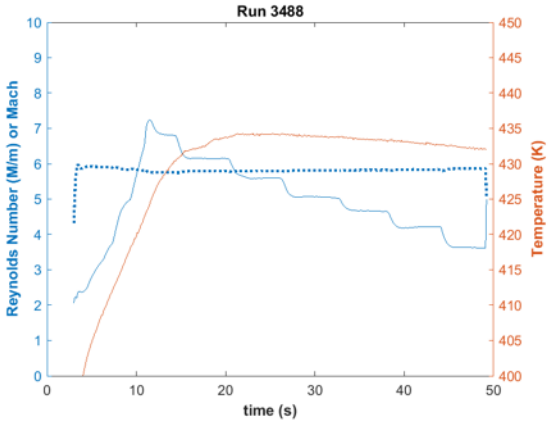

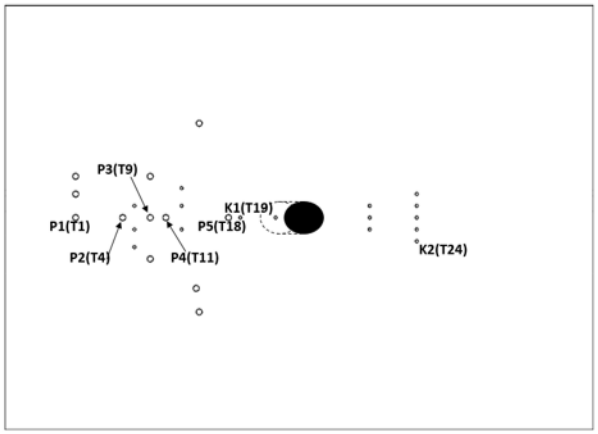

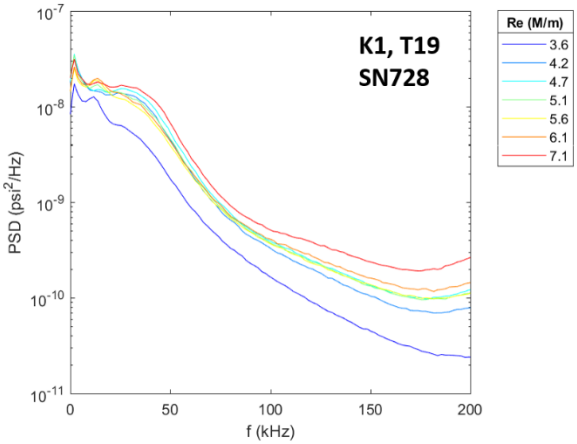

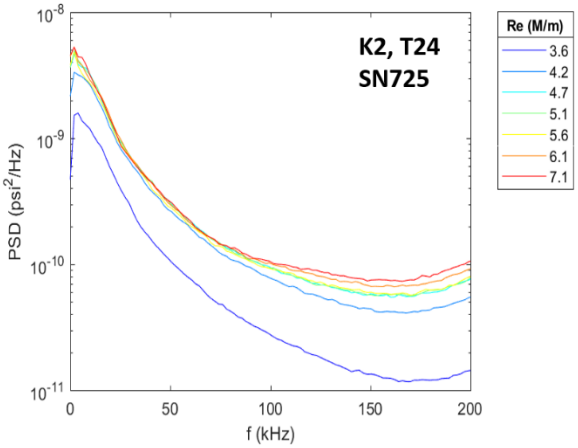

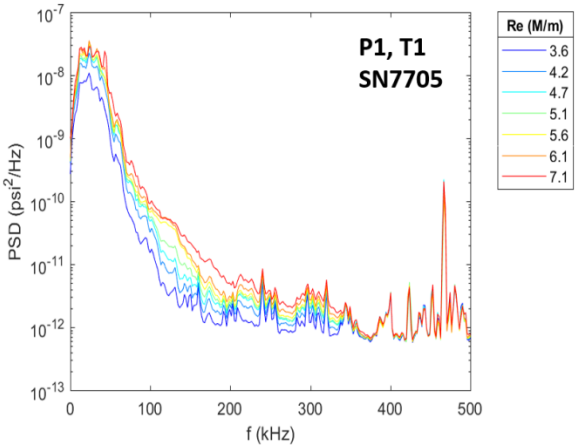
P1, T1
SN7705
Re (M/m)
3.6
4.2
4.7
5.1
5.6
6.1
7.1
PSD (psi²/Hz)
f (kHz)

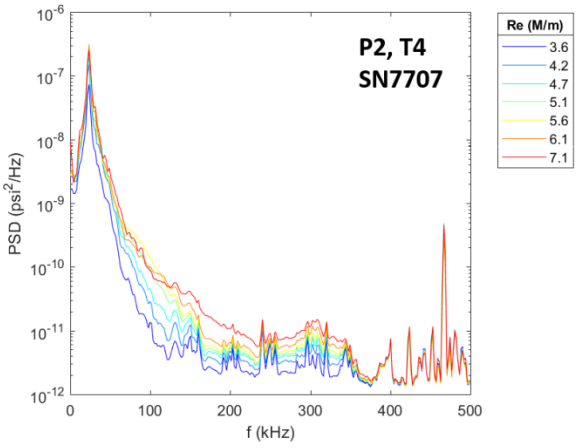
P2, T4
SN7707
Re (M/m)
3.6
4.2
4.7
5.1
5.6
6.1
7.1
PSD (psi²/Hz)
f (kHz)

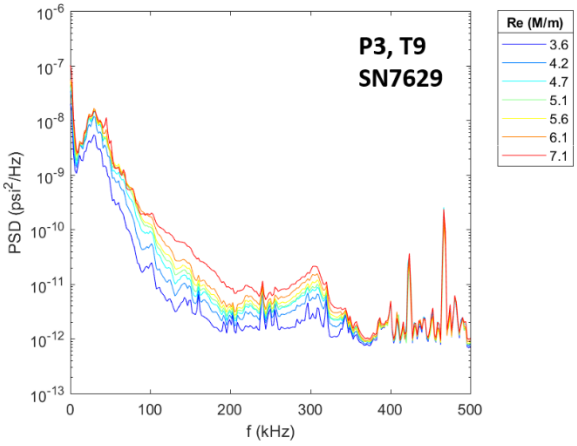
P3, T9
SN7629
Re (M/m)
3.6
4.2
4.7
5.1
5.6
6.1
7.1
PSD (psi²/Hz)
f (kHz)

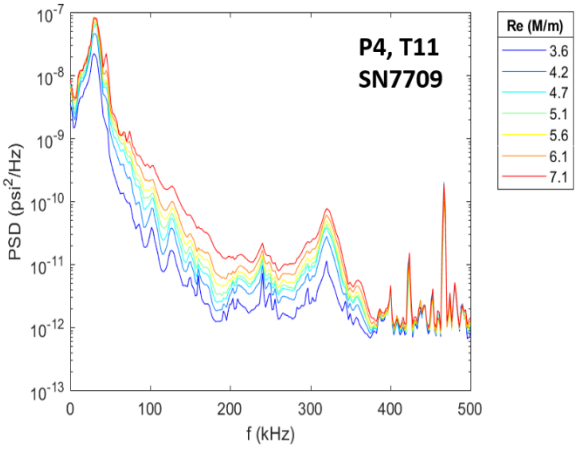
P4, T11
SN7709
Re (M/m)
3.6
4.2
4.7
5.1
5.6
6.1
7.1
PSD (psi²/Hz)
f (kHz)

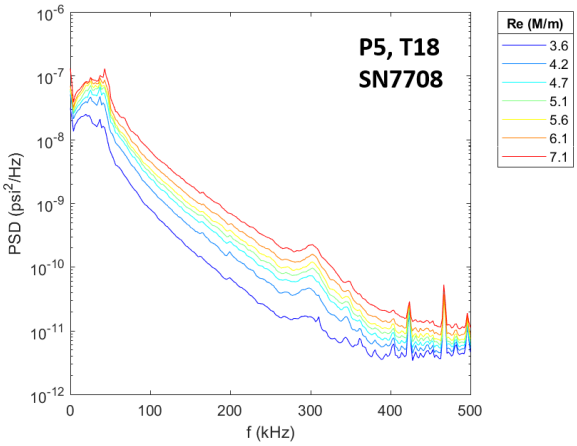
P5, T18
SN7708
Re (M/m)
3.6
4.2
4.7
5.1
5.6
6.1
7.1
PSD (psi²/Hz)
f (kHz)

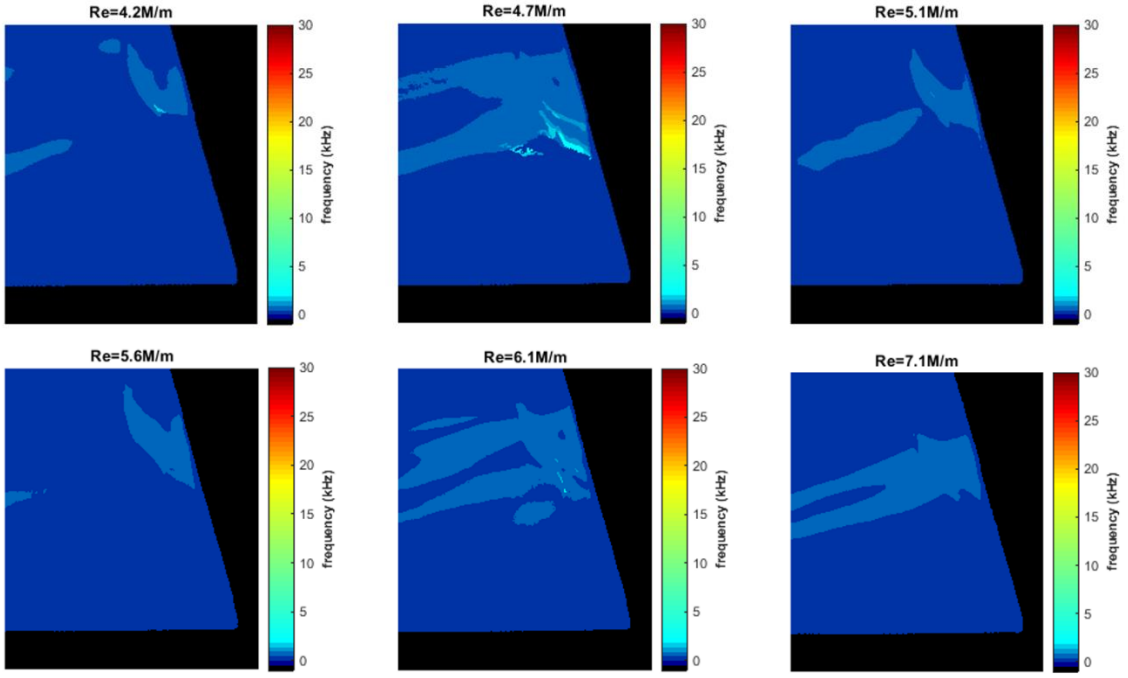
Re=4.2M/m
Re=4.7M/m
Re=5.1M/m
Re=5.6M/m
Re=6.1M/m
Re=7.1M/m
frequency (kHz)
0
5
10
15
20
25
30

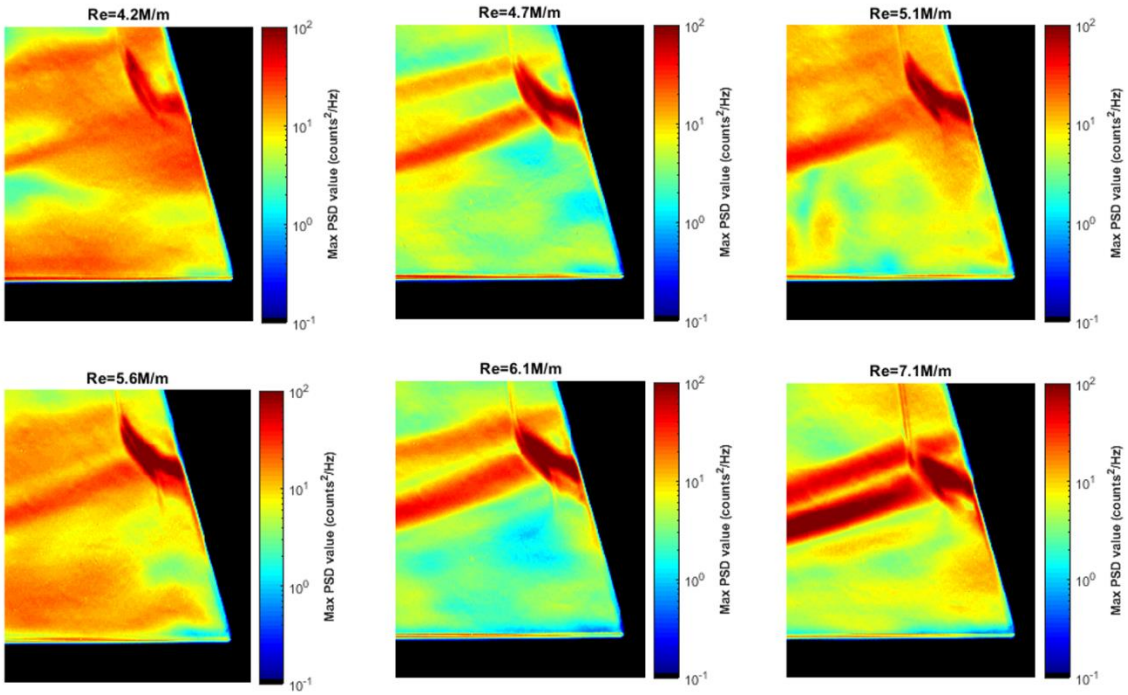
Re=4.2M/m
Re=4.7M/m
Re=5.1M/m
Re=5.6M/m
Re=6.1M/m
Re=7.1M/m
Max PSD value (counts²/Hz)
10⁻¹
10⁰
10¹
10²

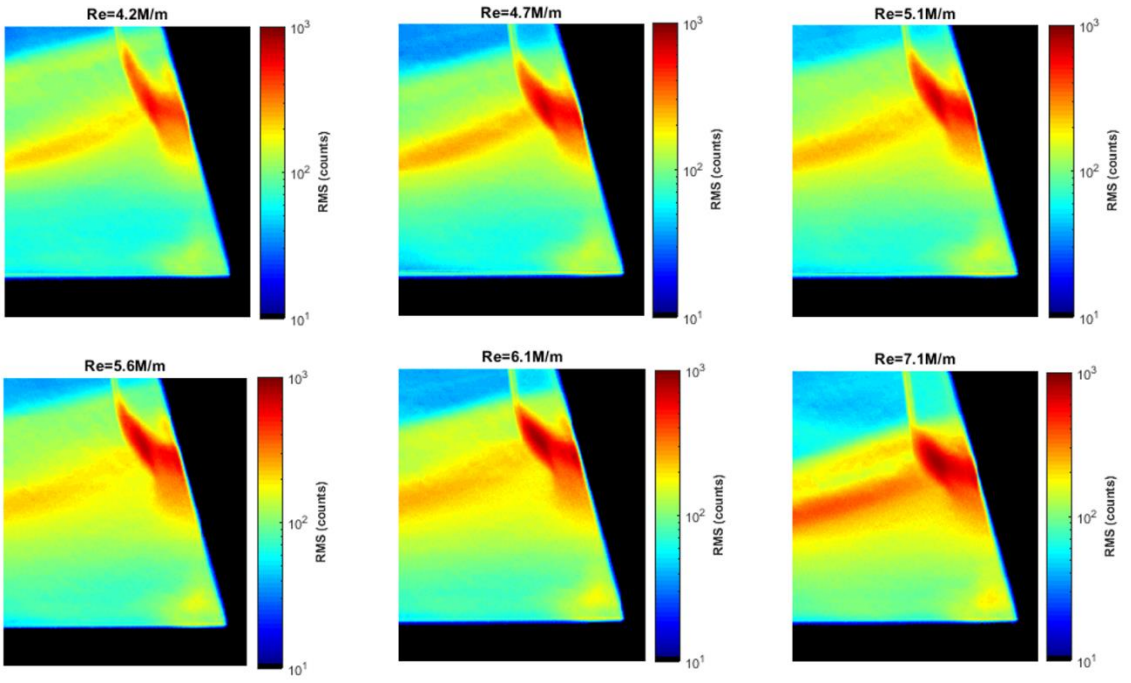

Run 3489

Surface pressure measurements, IR thermography, and high-speed schlieren made over Re steps. Cylinder was angled forward 15°.

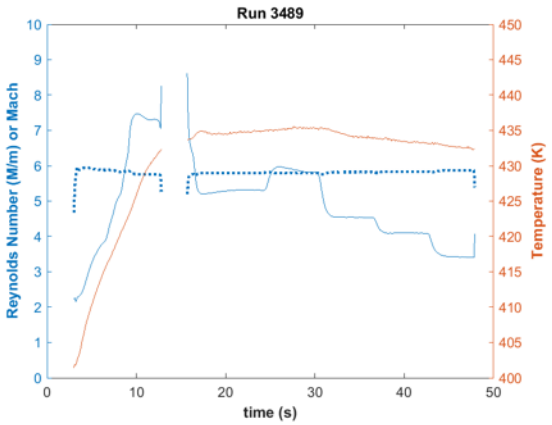

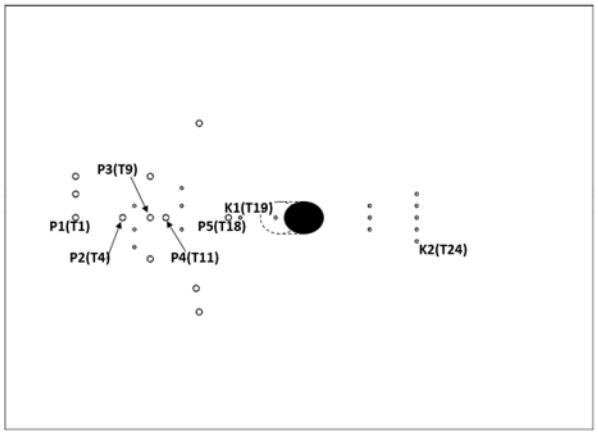

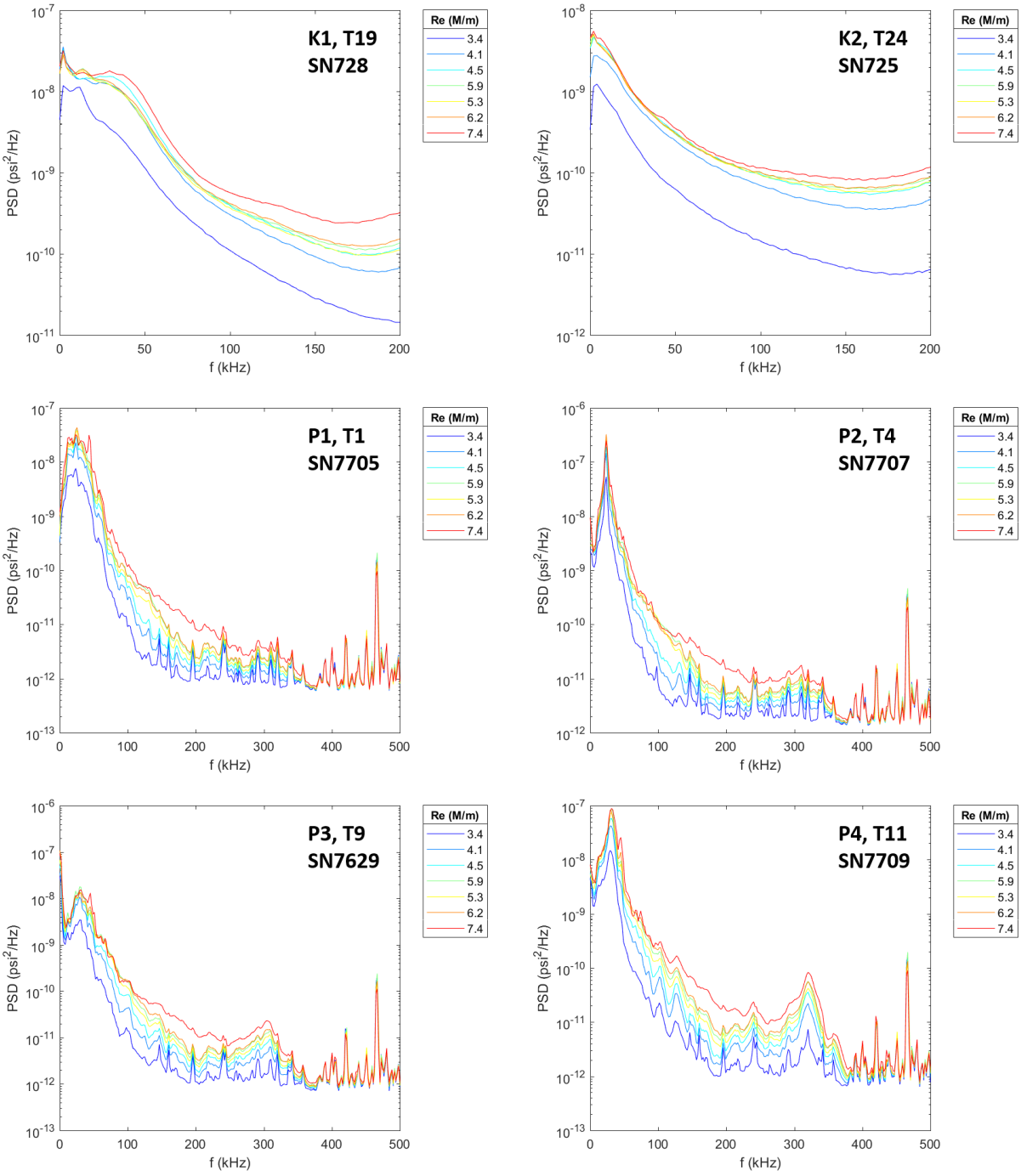
K1, T19
SN728
K2, T24
SN725
P1, T1
SN7705
P2, T4
SN7707
P3, T9
SN7629
P4, T11
SN7709
Re (M/m)
3.4
4.1
4.5
5.9
5.3
6.2
7.4
PSD (psi²/Hz)
f (kHz)

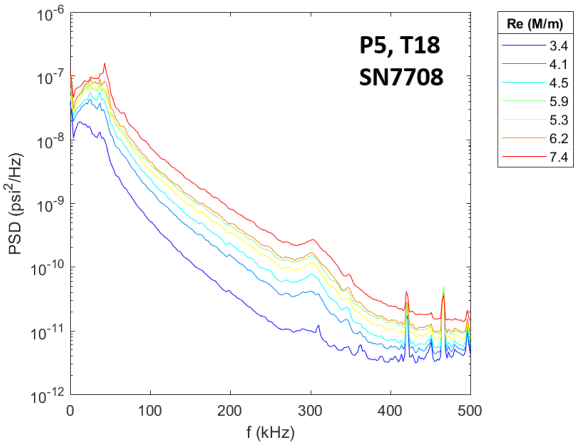
P5, T18
SN7708
Re (M/m)
3.4
4.1
4.5
5.9
5.3
6.2
7.4
PSD (psi²/Hz)
f (kHz)

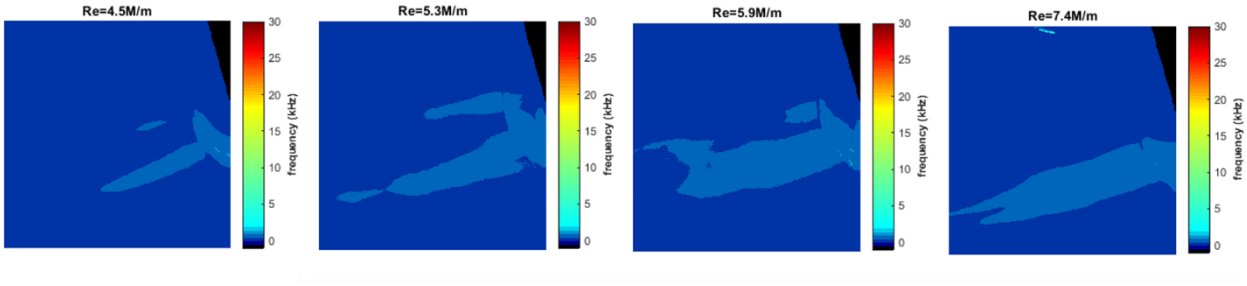
Re=4.5M/m
Re=5.3M/m
Re=5.9M/m
Re=7.4M/m
frequency (kHz)

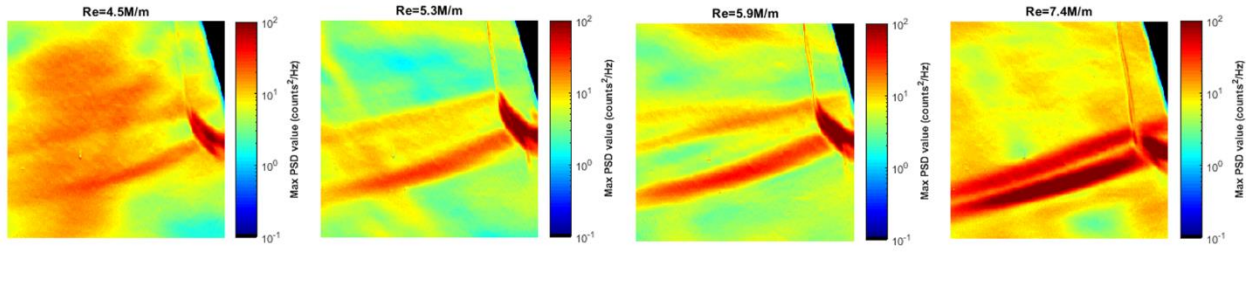
Re=4.5M/m
Re=5.3M/m
Re=5.9M/m
Re=7.4M/m
Max PSD value (counts²/Hz)

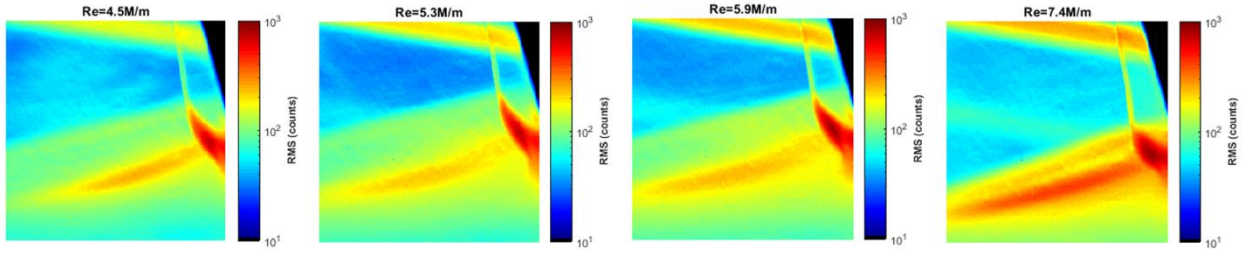
Re=4.5M/m
Re=5.3M/m
Re=5.9M/m
Re=7.4M/m
RMS (counts)

Focused schlieren

Run 3490

Focused schlieren on model with trips and 15° forward cylinder. Camera traverse was swept to sweep position of plane of focus. Re held near 4.9M/m.

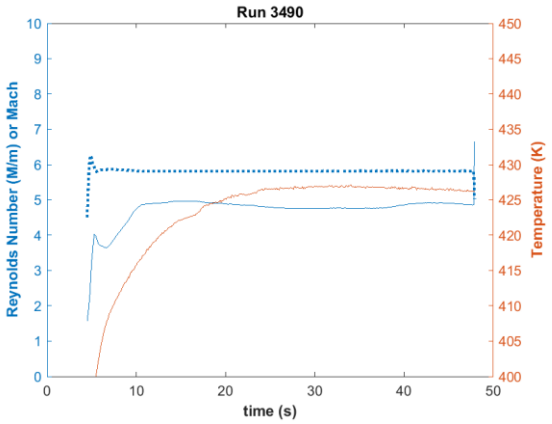

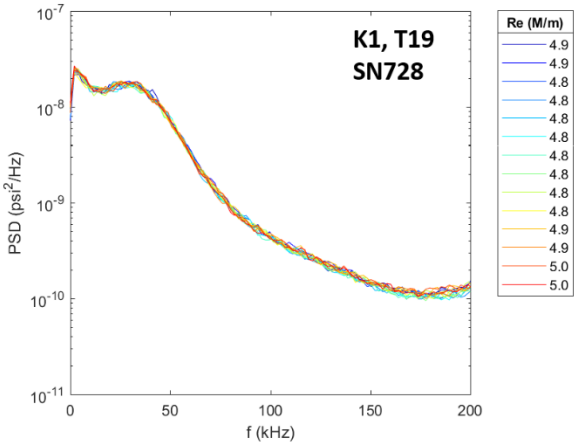

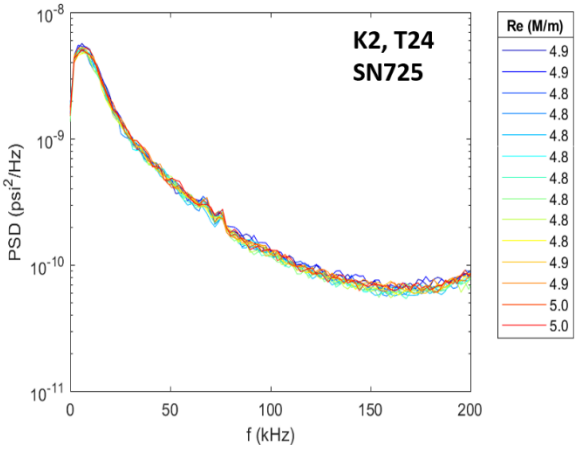

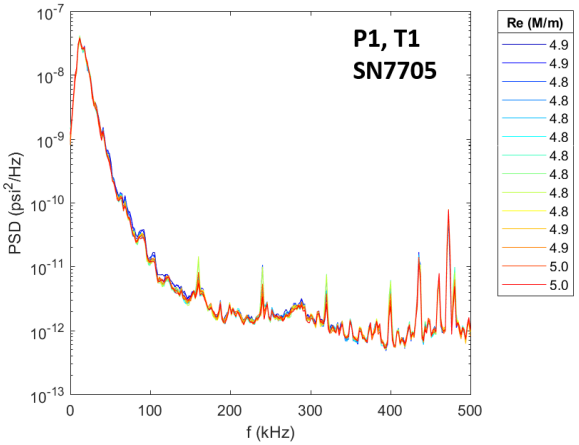

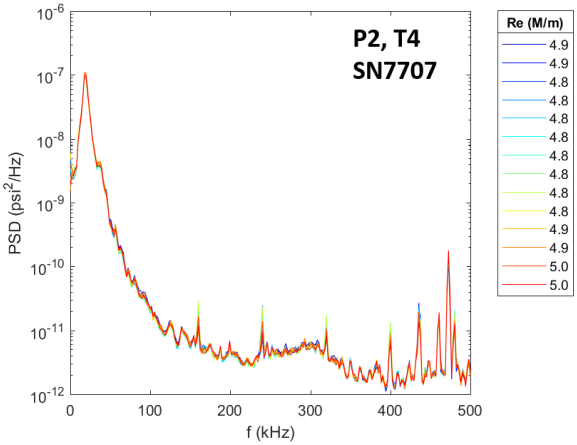

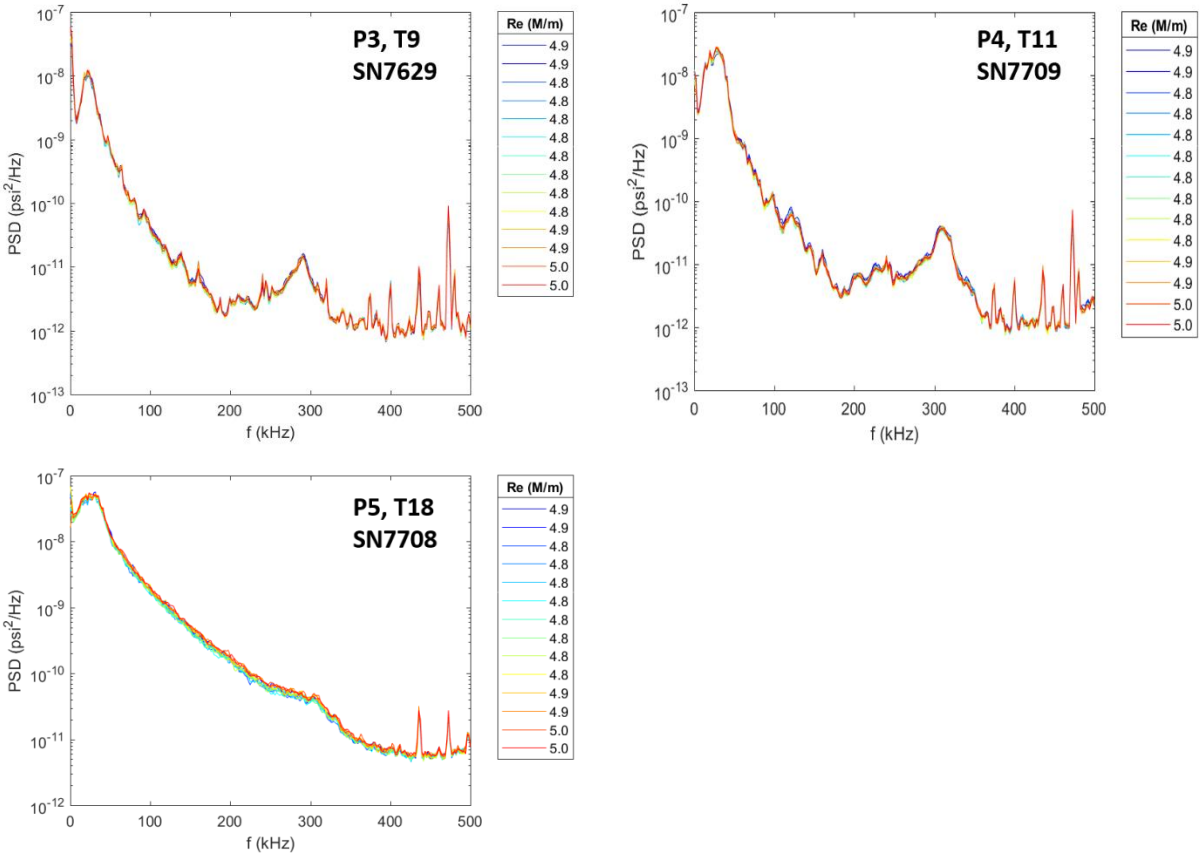

Run 3492

Focused schlieren on model with 15° forward cylinder. Camera traverse was stepped to step position of plane of focus. 150k fps and 30k images at each step. Re held near 4.9M/m.

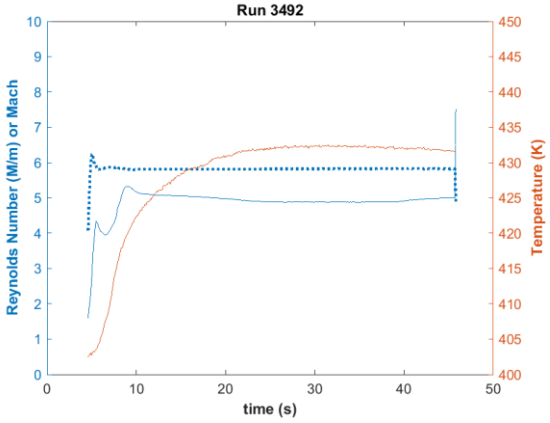

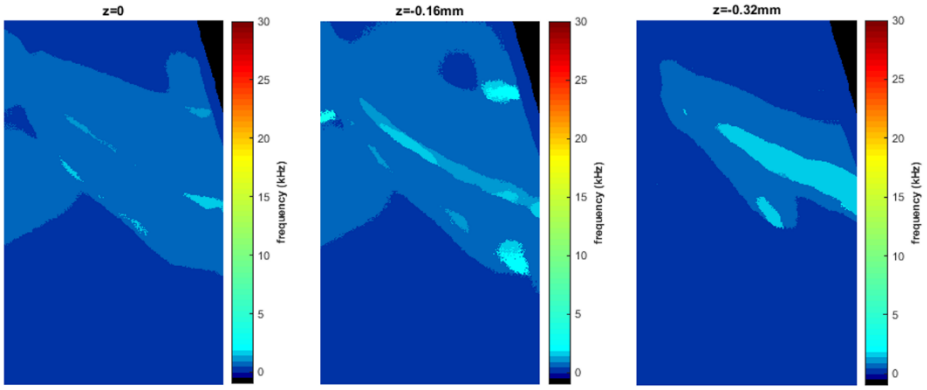
z=0
z=-0.16mm
z=-0.32mm
frequency (kHz)
0
5
10
15
20
25
30

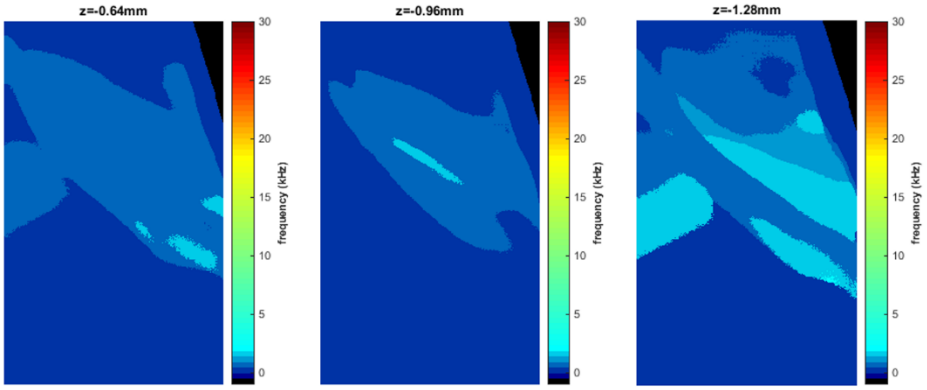
z=-0.64mm
z=-0.96mm
z=-1.28mm
frequency (kHz)
0
5
10
15
20
25
30

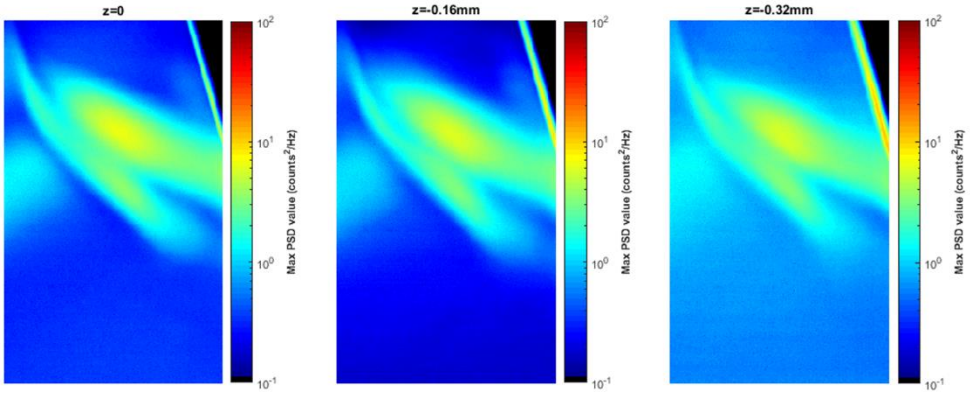
z=0
z=-0.16mm
z=-0.32mm
Max PSD value (counts²/Hz)
10⁻¹
10⁰
10¹
10²

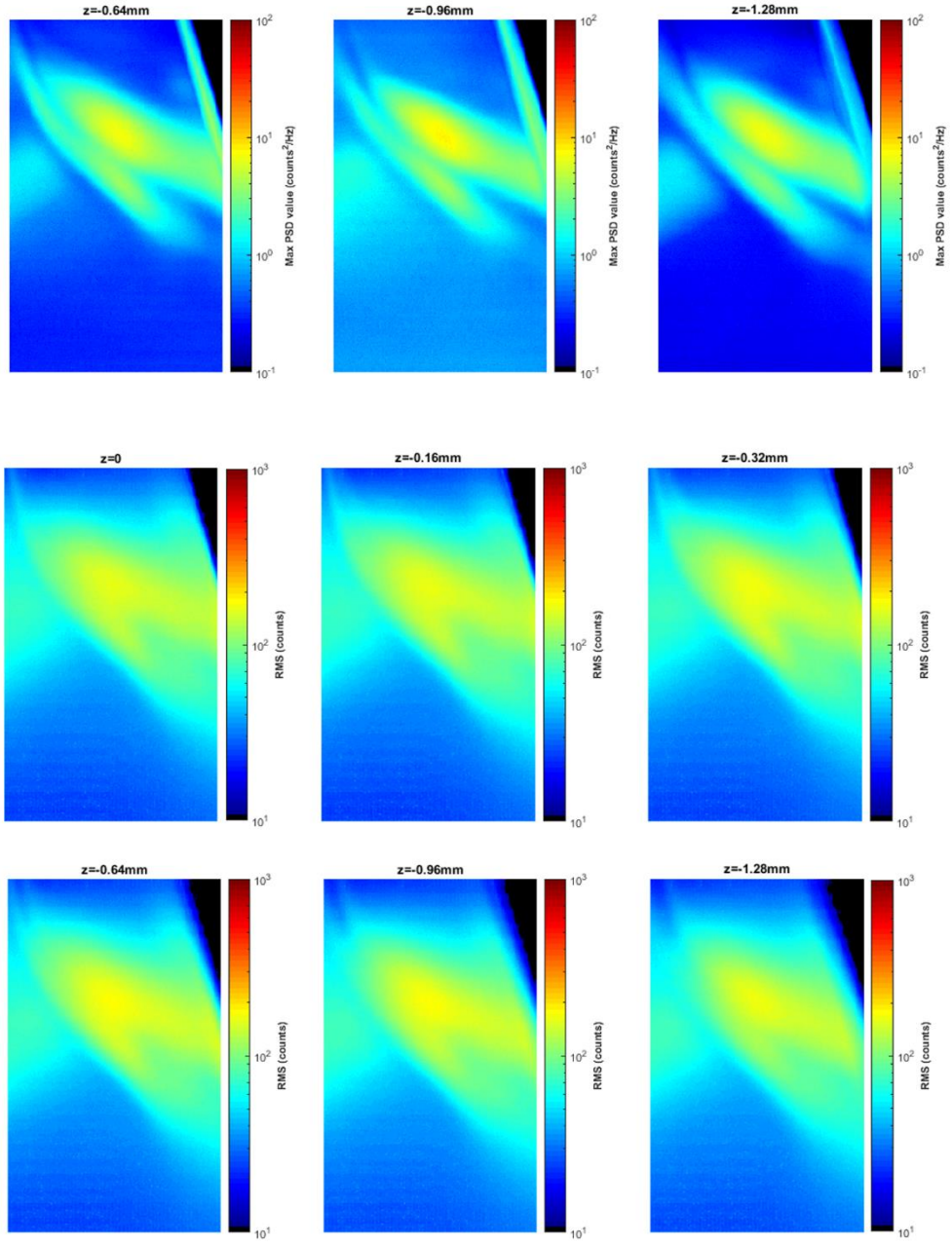
z=-0.64mm
z=-0.96mm
z=-1.28mm
Max PSD value (counts²/Hz)
z=0
z=-0.16mm
z=-0.32mm
RMS (counts)
z=-0.64mm
z=-0.96mm
z=-1.28mm
RMS (counts)

Run 3494

Focused schlieren on model with perpendicular cylinder. Camera traverse was stepped to step position of plane of focus. 150k fps and 30k images at each step. Re held near 4.9M/m.

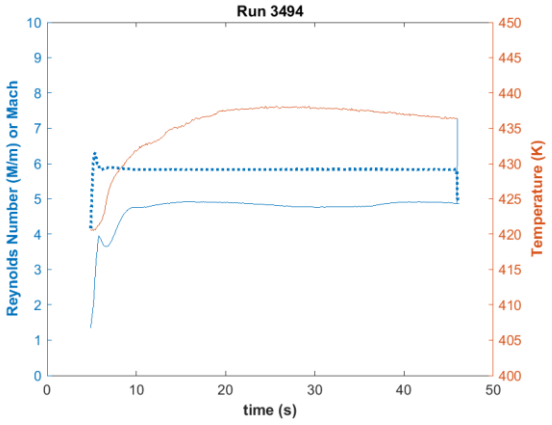

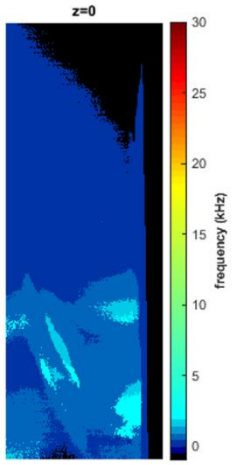

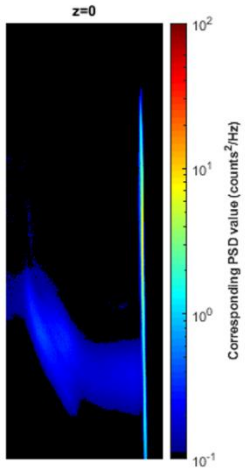

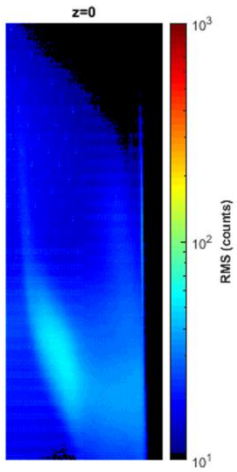

APPENDIX I

SOFTWARE SNAPSHOTS

A number of different software packages were used to configure the instrumentation and to monitor, collect, and process the data. The software and most commonly used files are listed in Table I-15. This section describes the utility of the software in terms of the data collected for the present campaign.

Table I-15. Software utilized in present campaign

Software	Filename	Purpose
Labview	NALDAQ 2013.vi	-Monitors tunnel/operating conditions in real-time -Writes conditions to file
Labview	OperatorPanel.vi	-Displays tunnel conditions on monitor above the regulators
Labview	HW_Traverse Controller_AL_DualDAQ_all channels.vi	-Moves traverse and samples all FastDAQ channels
Labview	ANLDoubleDAQsweep.vi ANLDoubleDAQhold.vi	-Samples FastDAQ channels and alerts user when sampling -Writes data to binary file
NI SignalExpress	HW Frequency Response_180304.seproj	-Displays wire response in real-time to aid in tuning
ResearchIR		-Samples infrared irradiance at user specified integration times -Exports data in various file formats
Photron FASTCAM Viewer		-Controls the Photron SA-Z camera -Exports data in different file formats
Ensemble Motion Composer		-Verifies motors are enabled -Moves traverse
MATLAB		-Data processing

The LabView Virtual Instruments (VIs) used during the present campaign were written by previous NAL students (most notably J.W. Hofferth), but some were modified to fit the data collection needs of this study. *NALDAQ 2013* and *OperatorPanel* were VIs used to monitor tunnel

conditions during preheat and during every run. *NALDAQ 2013* output two excel files for every run. The "raw data" file contained conditions for all transducers on the supply line, ejector line, and on ACE and the M6QT. These values were tabulated at 100 Hz for 60 seconds. The reduced data file tabulated the same conditions at 10 Hz and formed relevant plots.

The VI *HW_Traverse Controller_AL_DualDAQ_all channels* allowed for control of the traverse and sampling of all FastDAQ channels. Figure I-187 shows the front panel. An excel file was created before each hot-wire run, and read into the VI, giving the traverse coordinates that defined a survey. Data collection began once the tunnel conditions were reached by clicking the "MOVE AND RECORD" button on the front panel. Tunnel conditions (T_t, p_t, p, and M) and the FastDAQ samples were written to a binary (.sbi) file. The FastDAQ data included DC filtered, DC raw, AC filtered, and raw bridge voltage values. It also included surface pressure transducer voltage values for applicable runs.

Figure I-187. Front panel of the VI used to collect hot-wire data

Either *ANLDoubleDAQsweep* (shown in Figure I-188) or *ANLDoubleDAQhold* was used to sample the FastDAQ for the bulk of the campaign. They were essentially the same program but sampled at different rates to reflect either the Reynolds number sweeping or stepping nature of the run. The programs sampled every channel of the FastDAQ, which allowed for tunnel conditions, five PCBs, and 4 Kulites (both AC and DC signals). The large, red LED was illuminated when data were being sampling, which allowed the tunnel operator to time his pressure regulation outside of the time of sampling.

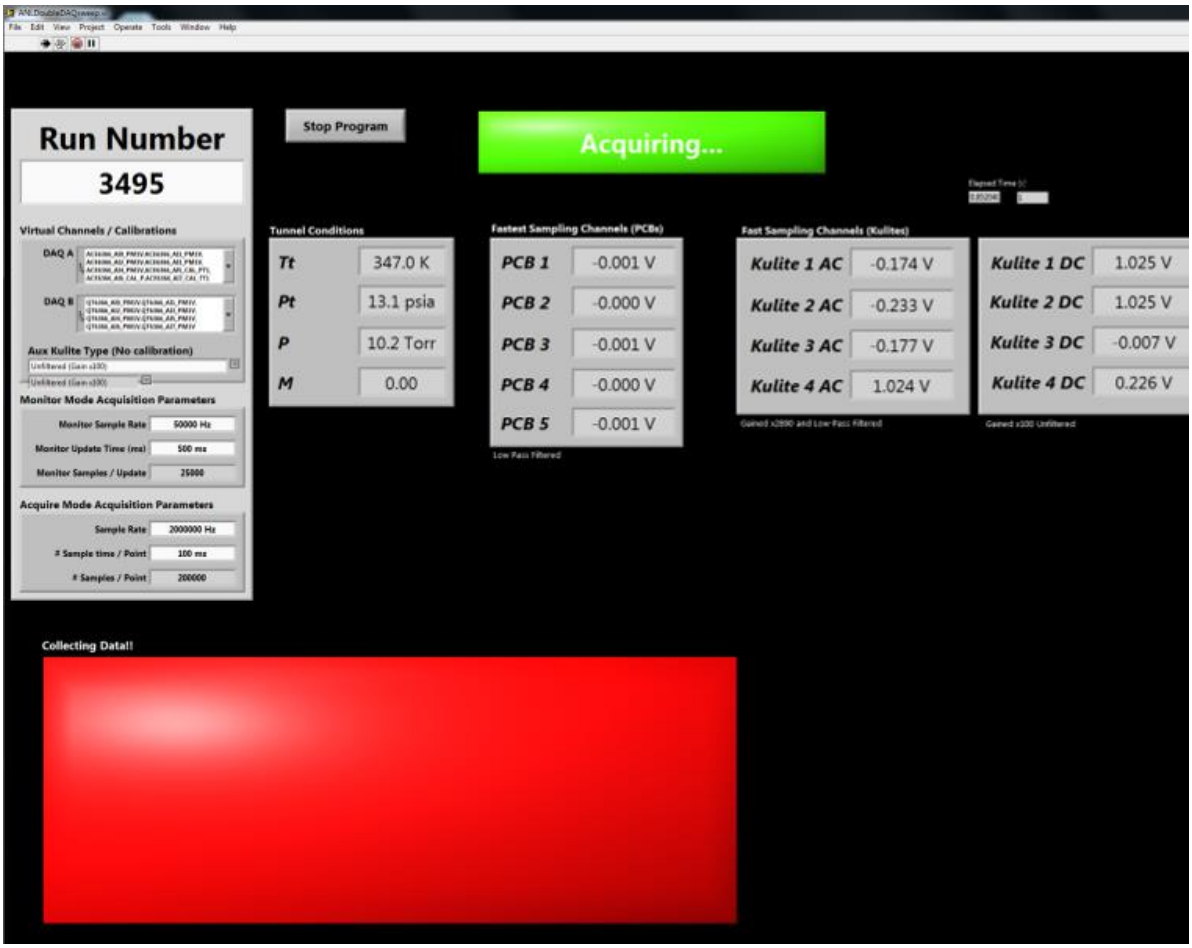

Figure I-188. Front panel of the VI used to collect surface pressure data

FLIR ResearchIR was used to perform calibrations (Camera -> User Calibration -> Perform) and to sample IR data during each run. A snapshot of the software playing back a video is given in Figure I-189. The “Record Settings” (Figure I-190) were verified for every run, ensuring the correct Prefix and run number were input. Snapshots were often taken with a ruler to know the field-of-view on the model. The presets and sampling rate were set in the “Camera Control” box on the main screen. The most commonly used options under the “Tools” tab were “File Operation” and “Make Self Viewing File”. “File Operation” allowed for background subtraction of a vacuum frame from frames for the entire run, which gave an effective sequence of ΔT maps. These maps often gave greater contrast for clarity in heating patterns. The file extension (.ats) was able to be read into MATLAB for data processing, so files were generally kept as they were sampled. However, File -> Export allowed for saving as other file types, and File -> Extract enabled reduction of frames and / or presets.

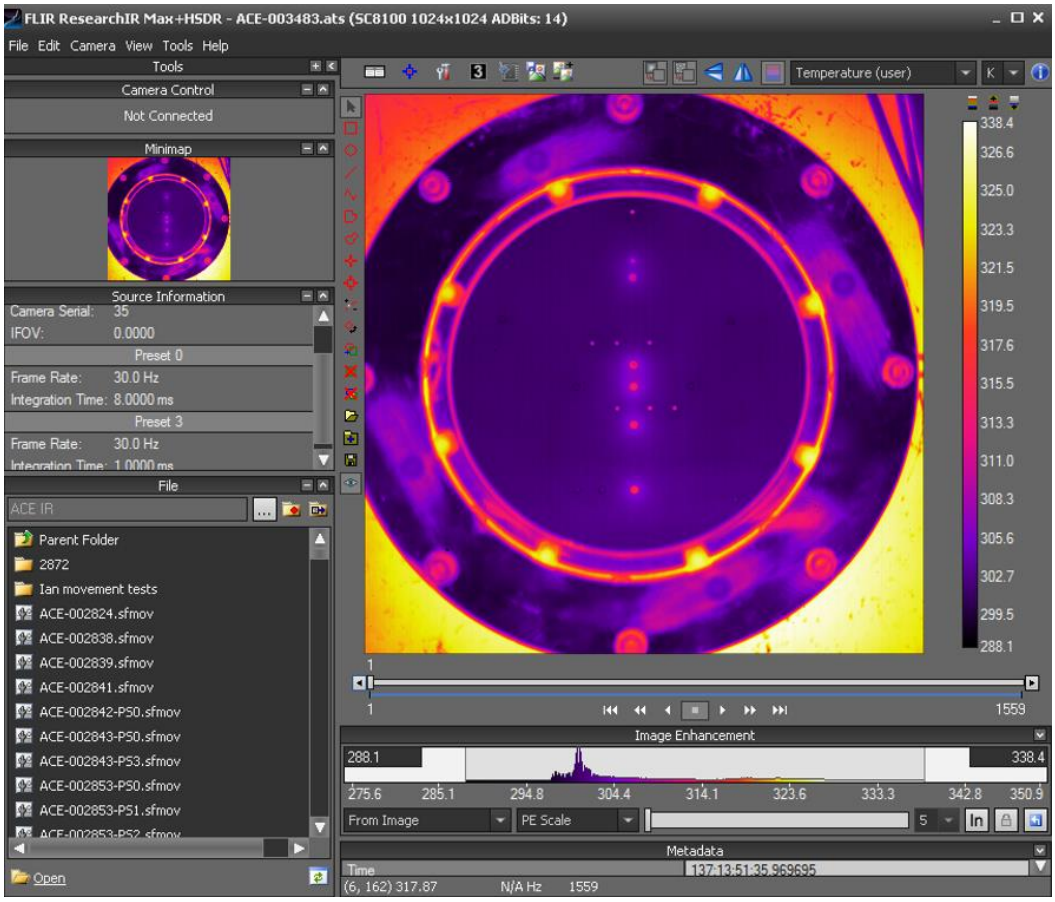

Figure I-189. FLIR ResearchIR primary interface

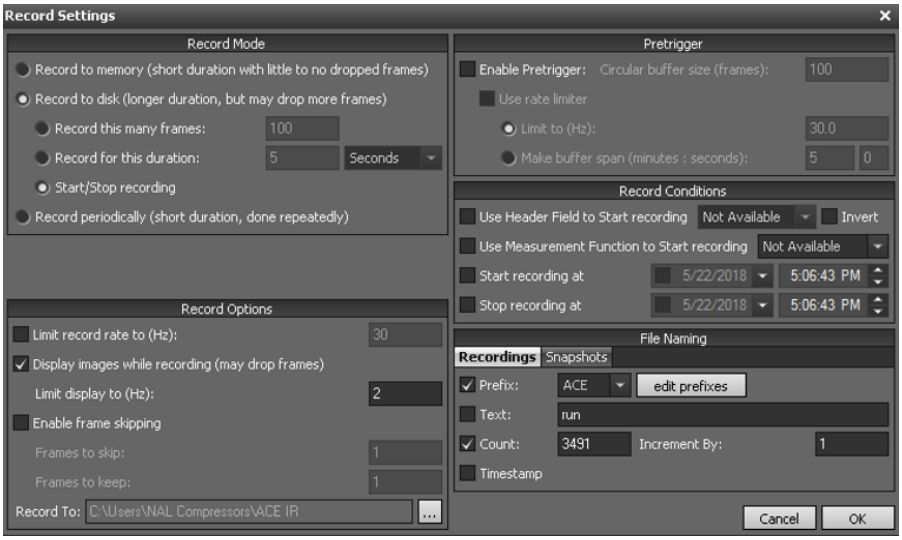

Figure I-190. FLIR ResearchIR record settings

Photron FASTCAM Viewer (PFV) controlled the FASTCAM SA-Z CMOS camera. Figure I-191 gives a screen shot of the software. A live view of the image took up the majority of the screen. Information for future recording settings was displayed in the upper left corner. The right panel, under the "LIVE" tab, allowed for the settings to be changed. The "Frame Rate" and "Resolution" were the most commonly changed parameters between the runs. The "Variable Setting (Resolution)" dialog box (Figure I-192, left) was utilized to set the parameters. Once these were set, "Shading", was enabled to clear up the image. The trigger mode was set to "Random", which allowed the camera to be triggered from a TTL pulse from the FastDAQ. The number of frames taken at each sampling period in "Random Mode" depended on the run type. Once a run was completed, the frames could be replayed at different rates under the "SAVE" tab. Clicking "Save" prompted a "Save Options Settings" dialog box (Figure I-192, right). This interface allowed the user to select a file path, format, and options to save data at different frame rates.

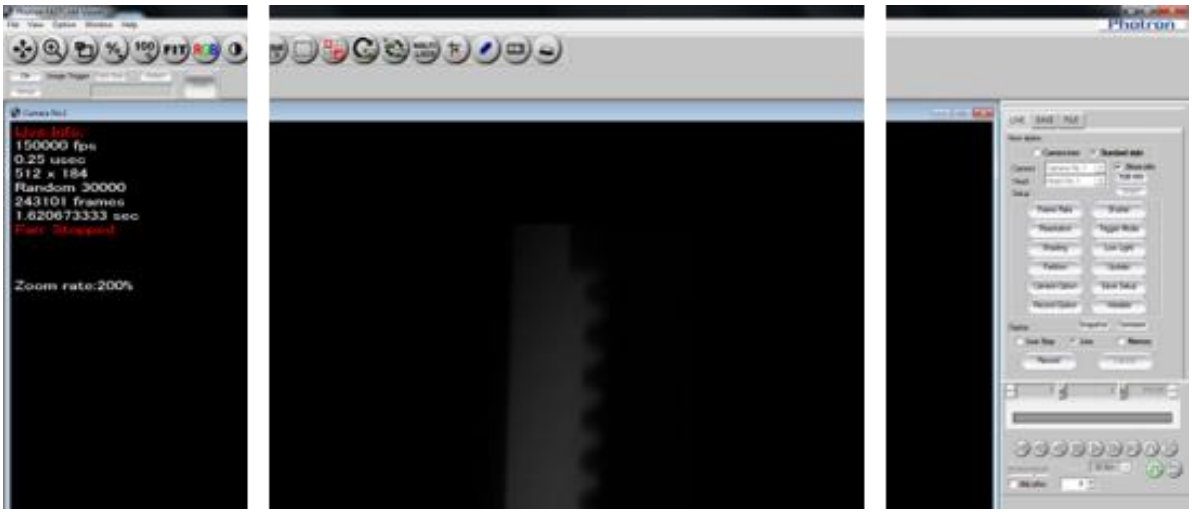

Figure I-191. PFV primary interface

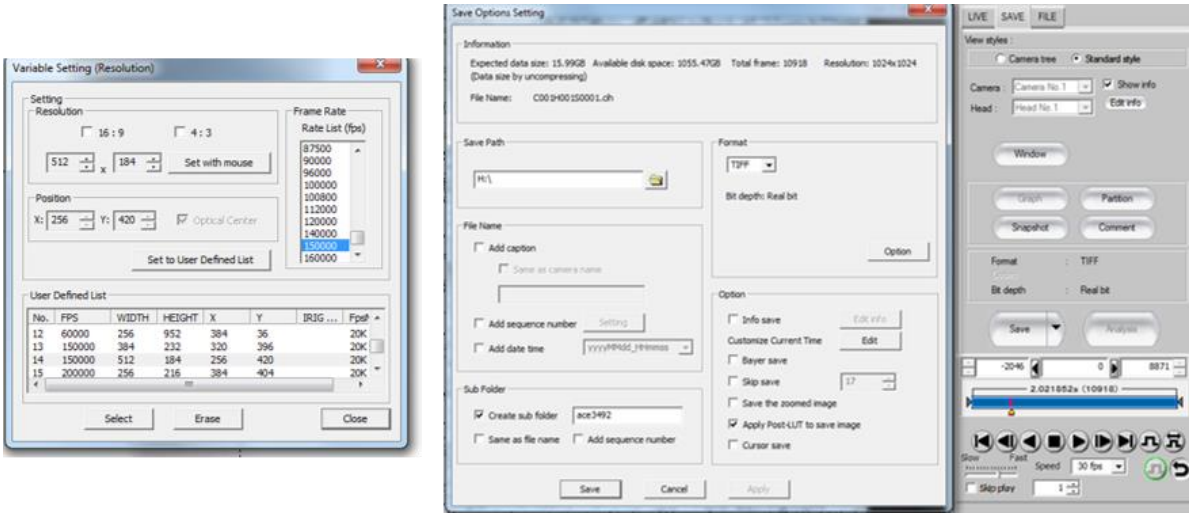

Figure I-192. PFV commonly utilized dialog boxes

MATLAB was used for data reduction. The most relevant segments of code for 1-D heat conduction, shock tracking, and schlieren dynamics are given below.

MATLAB Scripts

Heat flux

```
%QCALC.m – Calculates heat flux from a series of surface temperature maps
%They were saved as the 3 dimensional (space,space,time) variable "frame" in IR_3xxx.mat files

[filename,pathname]=uigetfile('.mat')        % have user select IR file location
Run-
Number=[3391,3393,3394,3395,3397,3398,3399,3400,3401,3402,3403,3421,3422,3424,3425,3427,3428,3436,3439,3442,3443,
3458,3459,3462,3466,3467,3469,3482,3483,3485,3487,3489,3490];      %all run numbers

for j=RunNumber
 clearvars -except j RunNumber pathname
 filename=['IR_',num2str(j),'.mat'];
 load(filename);


%Read in IR image files and metadata
frame_avg = 20;         %The number of frames averaged at the beginning of the run for the initial temperature

%Get initial surface temperature and average
for i=1:size(frame,3)
   Tint2(i)=mean(mean(frame(420:450,200:250,i)));     %average of a small patch of upstream pixels
end
```

```
Tinitial = mean(Tint2(1:frame_avg));    %initial temperature set to average small patch temperature of first 20 frames
initial_frame = sum(frame(:,:,1:frame_avg),3)/frame_avg;    %initial frame set to average of first 20 frames

for i=1:length(Time)
  frame(:,:,i)=frame(:,:,i)-initial_frame;    %calculate delta T for the full run
end

%Compute heat flux
Qout=zeros(size(frame,1),size(frame,2),size(Time,2)-frame_avg);   %initialize heat flux matrix

%PEEK properties
k=0.26; cp=1500; rho=1310;

bc1=Tinitial;
bc2=Tinitial;

frame= frame + bc1;   %bring frame back from delta T to T (reduces reflections)

%Parameters to write to file
TI(1,:)=frame(300,300,(frame_avg+1):end);
NTHI=size(TI,2); NODES=49; THICK=6.35/1000;
dt=Time(2)-Time(1);

%Solves function "Leidydiff.m" (given after this m-file)
h = waitbar(0,'I"m Working on it Geeze');
for i=1:size(frame,1)
  for j=1:size(frame,2)   %solves for one pixel at a time
    T1(:,1)=frame(i,j,(frame_avg+1):end);
    Qout(i,j,:)=Leidydiff(k,cp,rho,Time(1:end-frame_avg),dt,THICK,T1,bc1,bc2);
  end
  %i
  waitbar(i/size(frame,1))
end
close(h)

save(['IR_Q_',num2str(runnum)], 'Qout','k','cp','rho','Tinitial','NTHI','NODES','THICK','dt','frame8','-v7.3');
end
```

%Leidydiff.m - This function is essentially neeldiff.m (developed by Ian Neel) but adds one line for the adiabatic instead of isothermal boundary condition. The bottom node is set to the same temperature as the node above it. (T slope at bottom wall is zero) It uses both a central difference forward time scheme and a 5 point symmetric forward time scheme to compute the temperature profile.

```
function [q,T] = Leidydiff(k,cp,rho,Time,dt,len,T,bc1,bc2)    %values passed from QCALC.m

%inputs
surfacetemps=T;   %surface temperature value from "frame" in QCALC.m

a=(k/(rho*cp));      %thermal diffusivity
s=0.5;               %convergence parameter
dx=sqrt(a*dt/s);     %node spacing into material based on sampling rate

Maxtime = Time(end)-Time(1);      %final time step

Jmax = round(len/dx+1);          %number of nodes along “pixel rod”
```

```
Maxex = Jmax-1;                 %number of terms in exact solution

%Prepare coefficients
jmap = Jmax-1;
AJM = jmap;

%Create array of X locations for plotting
x=zeros(1,Maxex+1);
for i=2:Maxex+1
   x(i)=x(i-1)+dx;
end

T = NaN(round(Maxtime/dt)+1,AJM+1);      %initialize matrix for temperature storage
T= NaN(size(surfacetemps,1),AJM+1);

%Initial conditions
for i = 2:(size(T,2)-1)
   T(1,i)= bc2;          %sets initial temperature in "pixel rod" to value from QCALC.m
end
% boundary conditions
for i= 1:size(T,1)
   T(i,1)=surfacetemps(i);       %sets upper surface to frame values for all time
   T(i,end)=bc2;                 %this one will be overwritten below in the loop
end

%FTCS Finite Difference Loop  (internal temperature)
t=zeros(1,size(T,1));
for n=2:size(T,1) %loop time
   for j=2:size(T,2)-1  %loop j
      T(n,j)=s*T(n-1,j-1)+(1-2*s)*T(n-1,j) +s*T(n-1,j+1);   %sets temperature throughout the material
      T(n,(size(T,2))) = T(n,(size(T,2)-1));              %new line that sets bottom element to same Temp as element above it
   end
   t(n) = t(n-1)+dt;
end

%Heat Flux
q=zeros(1,size(Time,2));
for i=1:size(Time,2)
   q(i)=-k*((-(3/2)*T(i,1)+2*T(i,2)-0.5*T(i,3))/(dx));   %calculates heat flux from nodes at and near surface
end
end
```

Shock Tracking

```
%Line finding and propagation to model from schlieren images
appd1 = [782 640];   %cylinder base coordinates (px)
appd2 = [27 646];    %upstream point on model surface coordinates (px)
phi = atand((appd2(2)-appd1(2))/(appd2(1)-appd1(1)));    %model angle
origin = [67.7 26.6];    %upper left pix of reduced resolution box in mm units
res = 73.7;      %px/cm
```

```
FileList=dir('Re3p8/*.tif')
FileList={FileList.name}';

kk=1;
for i = 1:length(FileList)
   I = imread(['Re3p8/',FileList{i}]);
   pix(:,:,kk)=int16(I(:,:));     %stores all images
   kk=kk+1;
end

out = int16(mean(pix,3));
p2 = pix-out;          %mean subtracted images

ht = 128;        %height of image in pixels
wd = 456;        %width of image in pixels
threshold = 75;   %counts value difference
reach =7;
reachlow=2;      %2-7 pixels above/below defines window for comparison

%Defines the lines. The interrogated pixel value was compared to pixels offset between 2 and 7 above and below it. If the interrogated pixel value was below (mean-threshold) for pixels above and below it, it was taken as a potential line point.
p6 = zeros(ht,wd,length(FileList));
h = waitbar(0,'Runnin...isolate lines');
for k = 1:length(FileList)
   for i=1+reach:ht-reach
      for j=1:wd
         if(p2(i,j,k)<mean(p2(i-reach:i-reachlow,j,k))-threshold&&p2(i,j,k)<mean(p2(i+reachlow:i+reach,j,k))-threshold)
            p6(i,j,k) = 1;
         else
         p6(i,j,k) = 0;
         end
      end
   end
   waitbar(k/length(FileList),h)
end
close(h)

%Cleans up maps of potential line points. If surrounding points are not part of lines, interrogated point is not on a line either
p7=p6;
for k = 1:length(FileList)
for i=2:ht-1
   for j=2:wd-1
      if(p6(i,j)==1&&p6(i-1,j)==0&&p6(i+1,j)==0&&p6(i,j-1)==0&&p6(i,j+1)==0)
         p7(i,j) = 0;
      end
   end
end
end

%Runs a Hough transform to find lines in the maps of potential line points
h = waitbar(0,'Runnin...hough');
for k = 1:length(FileList)
   [N,T,R] = hough(p7(:,:,k));
   P = houghpeaks(N,10,'threshold',ceil(0.1*max(N(:))));
   lines = houghlines(p7(:,:,k),T,R,P,'FillGap',60,'MinLength',200);     %Minimum length of lines considered was 200 pixels, with a 60 pixel allowable gap size
   if length(lines)==0  %if lines are not found, values are set as zero for that image
```

```
      rh(k,1) = nan;  th(k,1) = nan;  sl(k,1) = nan;  ynau(k,1) = nan;  x1pt(k,1) = nan;  y1pt(k,1) = nan;  x2pt(k,1) = nan;  y2pt(k,1) =
nan;
   end
   for m =1:length(lines)
      if (lines(m).theta < 80 && lines(m).theta > 72)  %only considers lines in the anticipated direction (between bounds)
         rh(k,m) = lines(m).rho;
         th(k,m) = lines(m).theta;
         sl(k,m) = (lines(m).point2(2)-lines(m).point1(2))/(lines(m).point2(1)-lines(m).point1(1));
         ynau(k,m) = lines(m).point1(2)-sl(k,m)*lines(m).point1(1);
         x1pt(k,m) = lines(m).point1(1);                    %2 points defining every line detected are pulled out
         y1pt(k,m) = lines(m).point1(2);                    %these are in units of pixels in image coordinates
         x2pt(k,m) = lines(m).point2(1);
         y2pt(k,m) = lines(m).point2(2);
      else
         rh(k,m) = nan;  th(k,m) = nan;  sl(k,m) = nan;  ynau(k,m) = nan;  x1pt(k,m) = nan;  y1pt(k,m) = nan;  x2pt(k,m) = nan;
y2pt(k,m) = nan;
      end
   end
   waitbar(k/length(FileList),h)
end

%Sets zeros to nan
rh(rh==0) = nan;  th(th==0) = nan;  sl(sl==0) = nan;  ynau(ynau==0) = nan;  x1pt(x1pt==0) = nan;  y1pt(y1pt==0) = nan;
x2pt(x2pt==0) = nan;  y2pt(y2pt==0) = nan;

%If multiple lines are found in an image, they are sorted so the most leftmost line (upstream shock) is first in the array
[rho,I] = sort(rh,2,'ascend')
for k = 1:length(rho)
   for j = 1:size(rho,2)
      theta(k,j) = th(k,I(k,j));  slope(k,j) = sl(k,I(k,j));  y0(k,j) = ynau(k,I(k,j));  px1(k,j) = x1pt(k,I(k,j));  py1(k,j) = y1pt(k,I(k,j));
      px2(k,j) = x2pt(k,I(k,j));  py2(k,j) = y2pt(k,I(k,j));
   end
end

%Coordinate transformation and shock-model intercept
for k = 1:length(rho)
   for j = 1:size(rho,2)
      tp1(k,j) = atand(px1(k,j)/py1(k,j))+phi;    %rotation of pt1 from image origin (pt2 in table) reference to wedge
      x1pix(k,j) = sqrt(px1(k,j)^2+py1(k,j)^2)*sind(tp1(k,j));  %xdistance in ref to model from image origin
      y1pix(k,j) = sqrt(px1(k,j)^2+py1(k,j)^2)*cosd(tp1(k,j));  %ydistance in ref to model from image origin
      tp2(k,j) = atand(px2(k,j)/py2(k,j))+phi;
      x2pix(k,j) = sqrt(px2(k,j)^2+py2(k,j)^2)*sind(tp2(k,j));
      y2pix(k,j) = sqrt(px2(k,j)^2+py2(k,j)^2)*cosd(tp2(k,j));
      xcor1(k,j) = origin(1)- x1pix(k,j)/res*10;          % xdistance from model origin(mm)
      ycor1(k,j) = origin(2)- y1pix(k,j)/res*10;          % ydistance from model origin(mm)
      xcor2(k,j) = origin(1)- x2pix(k,j)/res*10;
      ycor2(k,j) = origin(2)- y2pix(k,j)/res*10;
      lnslp(k,j) = (ycor2(k,j)-ycor1(k,j))/(xcor2(k,j)-xcor1(k,j));   %slope of lines
      xint(k,j) = (xcor1(k,j)-ycor1(k,j)/lnslp(k,j))/(0.75*25.4);   %extrapolating line to wedge intercept (in terms of cylinder d)
   end
end
close(h)

save('G:\Raw_Data\M4-Composite_Wedge\C2-Cylinder\schlieren\ace3439\Tr3p8');
```

```
%Generation of PSD maps for a series of time resolved schlieren images
FileList=dir('Re6p6/*.tif')
FileList={FileList.name}';

stPic = 1;
endPic = 50000;   %number of images at a condition

ht = 128;         %height of image in pixels
d_wd = 76;        %width was split up to keep "pix" variable size manageable through processing
fs = 150*1000;

%Section was repeated through all width segments (in this case, 6)
kk=1;
for i=stPic:endPic
   I = imread(['Re6p6/',FileList{i}]);   %reads in an image
   pix(:,:,kk) = I(1:ht,1:d_wd);   %stores all image segments (partial width)
   kk=kk+1;
end
pix=double(pix);   %converts to appropriate datatype for PSD

pctoverlap = 50;
numpts=300;       %chosen for frequency resolution of 500Hz
noverlap = floor(pctoverlap/100*numpts);

%Runs a PSD for every pixel in the image segment
h = waitbar(0,'Runnin wd1/6..')
for i = 1:ht
   for j = 1:d_wd
      [Rpsd,f] = pwelch(squeeze(pix(i,j,:))-mean(squeeze(pix(i,j,:))),numpts,noverlap,numpts,fs);
      allpsds(i,j,:) = Rpsd;
   end
   waitbar(i/ht,h)
end
close(h)
clear pix        %frees up space for next image segment

%...Above section repeated 5 more times for other width segments

save('N:\NAL\Users\Andrew\Documents\XSBLIs\Data\Model\cylinder\schlieren\ace3425\r6p6f500');
```

APPENDIX J

CFD BASIC STATE SOLUTION

The computational results in this appendix represent the laminar flow basic state 2-D solution for the base model (no trips and no cylinder) in a Mach 5.8 freestream with *Re*=5M/m. The CFD solution was generated to obtain a more complete picture of the effects of the slightly blunted leading edge. Its impact on mass flux was experimentally demonstrated using a hot-wire anemometer. Credit to Daniel Mullen for gridding the geometry and running the simulation.

Figure J-194 shows Mach number contours for flow above the model. The top image gives the distribution over the entire model, while the bottom image examines the leading 6 cm. The theoretical Mach number across the shock should be 5.63 using the oblique shock relation. The image that is zoomed on the leading edge clearly demonstrates streamwise and wall-normal variation in Mach number with maximum values lower than the theoretical oblique shock value. The leading-edge curvature results in a reduction of Mach number to a maximum of 5.2 at *x*=10cm and 5.4 at *x*=20cm.

Figure J-195 shows mass flux contours for flow over the full model (top) and the first 20 centimeters (bottom). The effect of the leading-edge curvature on mass flux is that the jump in mass flux across the shock decreases with streamwise position (as the relative shock angle becomes more oblique). The mass flux also grows with wall-normal distance, from the model to the leading-edge shock. This trend was demonstrated in the boundary layer and leading edge hot-wire surveys. A comparison between a “no trips” boundary layer survey from Run 3471 and a computational survey at the same streamwise position (*x*=187mm) is presented in Figure J-. There is

excellent agreement overall. The mass flux throughout the boundary layer is a near perfect match, and the points just outside of the boundary layer demonstrate a similar gradient with a slight offset.

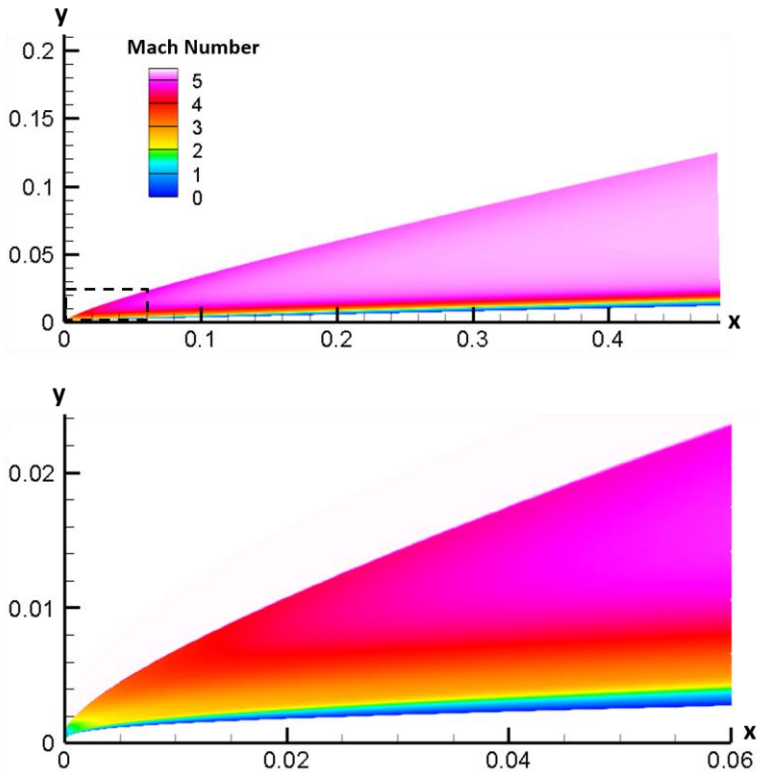

Figure J-193. Mach number distribution over entire model (top) and distribution near leading edge (bottom)

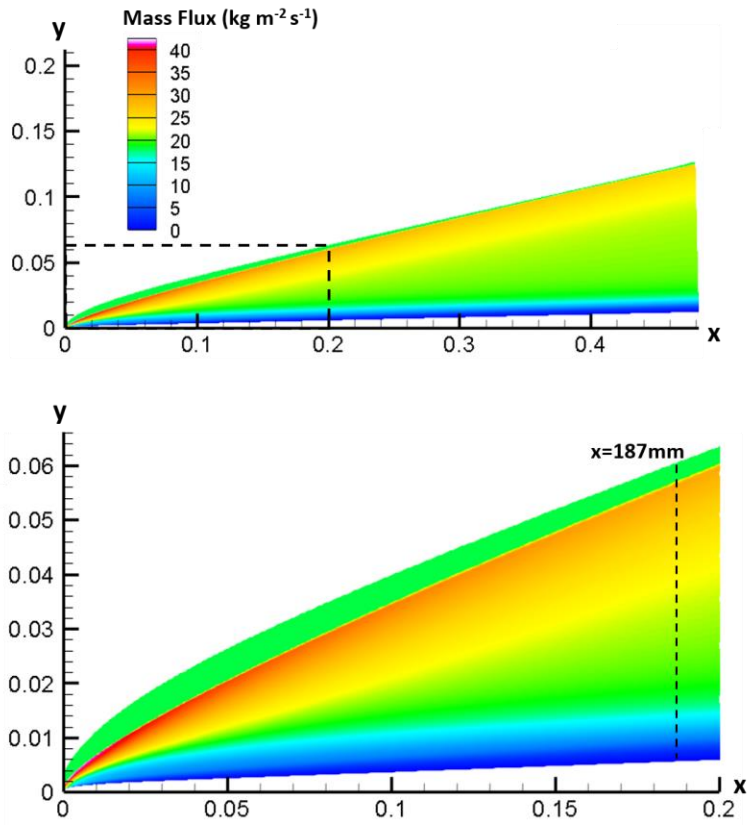

Figure J-194. Mass flux distribution over entire model (top) and distribution near leading edge (bottom)

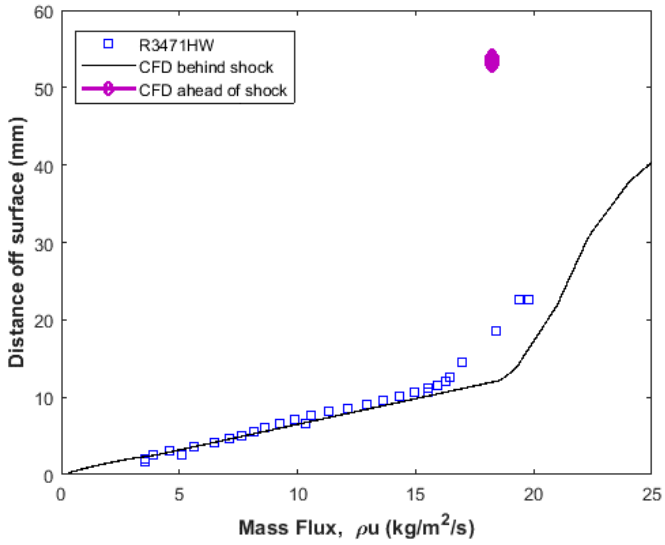

Figure J-195. Hot-wire and CFD mass flux surveys at *x*=187mm